NanoScience and Technology

R.A. Evarestov

Theoretical Modeling of Inorganic Nanostructures

Symmetry and ab-initio Calculations of Nanolayers, Nanotubes and Nanowires

Springer

NanoScience and Technology

Series editors

Phaedon Avouris, Yorktown Heights, USA
Bharat Bhushan, Columbus, USA
Dieter Bimberg, Berlin, Germany
Klaus von Klitzing, Stuttgart, Germany
Hiroyuki Sakaki, Tokyo, Japan
Roland Wiesendanger, Hamburg, Germany

The series NanoScience and Technology is focused on the fascinating nano-world, mesoscopic physics, analysis with atomic resolution, nano and quantum-effect devices, nanomechanics and atomic-scale processes. All the basic aspects and technology-oriented developments in this emerging discipline are covered by comprehensive and timely books. The series constitutes a survey of the relevant special topics, which are presented by leading experts in the field. These books will appeal to researchers, engineers, and advanced students.

More information about this series at http://www.springer.com/series/3705

R.A. Evarestov

Theoretical Modeling of Inorganic Nanostructures

Symmetry and ab-initio Calculations of Nanolayers, Nanotubes and Nanowires

Springer

R.A. Evarestov
Department of Chemistry
St. Petersburg State University
St. Petersburg
Russia

ISSN 1434-4904 ISSN 2197-7127 (electronic)
ISBN 978-3-662-44580-8 ISBN 978-3-662-44581-5 (eBook)
DOI 10.1007/978-3-662-44581-5

Library of Congress Control Number: 2014948754

Springer Heidelberg New York Dordrecht London

© Springer-Verlag Berlin Heidelberg 2015
This work is subject to copyright. All rights are reserved by the Publisher, whether the whole or part of the material is concerned, specifically the rights of translation, reprinting, reuse of illustrations, recitation, broadcasting, reproduction on microfilms or in any other physical way, and transmission or information storage and retrieval, electronic adaptation, computer software, or by similar or dissimilar methodology now known or hereafter developed. Exempted from this legal reservation are brief excerpts in connection with reviews or scholarly analysis or material supplied specifically for the purpose of being entered and executed on a computer system, for exclusive use by the purchaser of the work. Duplication of this publication or parts thereof is permitted only under the provisions of the Copyright Law of the Publisher's location, in its current version, and permission for use must always be obtained from Springer. Permissions for use may be obtained through RightsLink at the Copyright Clearance Center. Violations are liable to prosecution under the respective Copyright Law.
The use of general descriptive names, registered names, trademarks, service marks, etc. in this publication does not imply, even in the absence of a specific statement, that such names are exempt from the relevant protective laws and regulations and therefore free for general use.
While the advice and information in this book are believed to be true and accurate at the date of publication, neither the authors nor the editors nor the publisher can accept any legal responsibility for any errors or omissions that may be made. The publisher makes no warranty, express or implied, with respect to the material contained herein.

Printed on acid-free paper

Springer is part of Springer Science+Business Media (www.springer.com)

This book is dedicated to my teacher and friend

Professor Marija I. Petrashen

Preface

The present book is dedicated to the theoretical modeling of nanostructures being the second one published on this topic in Springer Series *Nanoscience and Technology*.

The first book of this kind *Nanostructures: Theory and Modeling* was published in 2004 [1]. The authors of the book Prof. C. Delerue and Prof. M. Lannoo wrote in the preface that it is an introduction to the theory of nanostructures providing basic concepts for the physics of nano-objects and reviewing the theoretical methods of the nanostructure modeling. The authors have tried to make the book accessible to inexperienced readers, and it only requires basic knowledge in quantum mechanics and solid state physics.

Since 2004, the science of nanostructures has had an explosive gross [2]. The carbon nanotubes have remained to be widely investigated, including not only electronics and sensor technology, but also nanocatalysis and nanobiotechnology. The varied developments in carbon nanotubes are covered in book [2], citing over 2,000 references.

However, the nanostructures of a variety of inorganic materials have since been synthesized, their properties and applications have been investigated. In the book [2], the numbers of references cited are 500 and 900, respectively, in the case of inorganic nanotubes and nanowires.

An essential information about the structure and properties of inorganic nano-objects has been obtained due to the theoretical modeling and ab initio calculations of the nanostructure electronic properties. The use of the symmetry of one-periodic models of nanotubes and nanowires allows their calculations to be extended to the systems, consisting of 300–400 atoms.

The description of the symmetry and first principles treatment of the inorganic nanotubes based on BN, TiO_2, and $SrTiO_3$ has been given by me recently in the chapter 13 of the book [3]. This book was published in 2012 as the second (enlarged) edition of my former book [4] in Springer Series in Solid State sciences, vol. 153. Since its online publication on January 18, 2013, there has been a total of 5,167 downloads for my book or its chapters on SpringerLink. This book was one of the top 25 % most downloaded eBooks in the relevant Springer eBook Collection in 2013.

I am sure that now it is time to cover the main results of the ab initio calculations made on the different inorganic nanostructures, describing in more detail their symmetry properties and overviewing the basic theoretical methods used, and the results obtained. This is the motivation of my book writing.

This book is divided in two parts.

Part I (Theory) of the book is intended for the experienced researchers who find in Chap. 2 the detailed description of the symmetry of the one-periodic (1D) nanotubes and nanowires. The basis of the modern ab initio methods of the nanostructure calculations is given in Chap. 3.

However, the book is also useful for the experimentalists who can omit the details of the ab initio methods description and read in Part II (Applications) the results of the theoretical modeling and ab initio calculations for the concrete inorganic nanostructures. To make such a work more convenient, I distributed the material in Part II over separate chapters in such a way that each chapter is dedicated to the concrete class of the inorganic nanostructures (boron compounds, tetravalent semiconductors, nitrides, oxides, sulfides).

Chaps. 4–6 in Part II include materials written by Prof. Yu. Zhukovskii (Institute of Solid State Physics, University of Latvia) and I am grateful to him for allowing me to use these materials in my book. He published a number of original papers on the ab initio treatment of inorganic nanostructures.

I am grateful to all my colleagues who took part in our joint nanostructure research (Prof. Yu. Zhukovskii, Dr. A. Panin, Dr. A. Bandura, Prof. D. Migas, Dr. S. Piskunov, D. Kuruch, M. Losev) or sent me fresh results of their research (Prof. M. Damnjanovic, Prof. P. Deak, Prof. R. Tenne, Dr. B. Aradi).

I would like to express my thanks to the members of the Quantum Chemistry Department of St. Petersburg State University, Dr. A. Panin and Dr. A. Bandura, for their help in preparing this book. I am especially indebted to Dr. C. Ascheron and Mrs. A. Duhm of Springer-Verlag for the cooperation in the preparation of this book.

St. Petersburg R.A. Evarestov

References

1. C.J. Delerue, M. Lannoo, *Nanostructures: Theory and Modeling* (Springer, Berlin, Heidelberg, 2004)
2. C.N.R. Rao, A. Govindaraj, *Nanotubes and Nanowires,* 2nd edn. RSC Nanoscience and Nanotechnology, vol. 18 (Royal Society of Chemistry, Cambridge, 2011)
3. R.A. Evarestov, *Quantum Chemistry of Solids. LCAO Treatment of Crystals and Nanostructures,* 2nd edn. Springer Series in Solid State Sciences, vol. 153 (Springer, Berlin, Heidelberg, New York, 2012)
4. R.A. Evarestov, *Quantum Chemistry of Solids. The LCAO First Principles Treatment of Crystals*. Springer Series in Solid State Sciences, vol. 153 (Springer, Berlin, 2007)

Contents

Part I Theory

1 Introduction 3
References 7

2 The Symmetry Groups in Three-Dimensional Space 9
2.1 Classification of the Symmetry Groups 10
2.2 Space (Triperiodic) Symmetry Groups of Bulk Crystals 12
2.2.1 Translation and Point Symmetry of Bulk Crystals 12
2.2.2 Symmorphic and Nonsymmorphic Space Groups. 19
2.2.3 Orbits of Triperiodic Groups. Wyckoff Positions 24
2.3 Bulk Crystal Structures 31
2.3.1 Structures with Cubic Lattices. 31
2.3.2 Structures with Tetragonal and Orthorhombic Lattices . . . 34
2.3.3 Structures with Hexagonal Lattices 39
2.4 Diperiodic (Layer) Symmetry Groups of Nanolayers 44
2.4.1 Two Factorizations of the Layer Groups. 44
2.4.2 Orbits of Layer Groups 50
2.4.3 Slab Models of Nanolayers. 51
2.5 Line and Rod Symmetry Groups of Stereo-Regular Polymers and Monoperiodic Nanostructures 58
2.5.1 Different Factorization of Line and Rod Groups 58
2.5.2 Rod Groups and their Settings as a Special Geometric Realizations of Line Groups 63
2.5.3 Orbits with Respect to Line and Rod Groups 66
2.5.4 Nanotube Rolling Up from 2D Systems 67
2.5.5 Hexagonal and Square Lattices 71
2.5.6 Rectangular Lattices 74
2.5.7 Symmetry of Double and Multiwall Nanotubes 75
2.5.8 The Nanowires Construction 77

2.6 Symmetry of Crystalline Orbitals in Periodic Systems: Space, Layer and Line Groups 81
2.6.1 Symmetry of Molecular and Crystalline Orbitals 81
2.6.2 Irreducible Representations of Space Groups. Symmetry of Crystalline Orbitals of Bulk Crystals. 83
2.6.3 Site Symmetry and Induced Representations of Space Groups 91
2.6.4 Irreducible Representations of Layer Groups. Symmetry of Crystalline Orbitals. 96
2.6.5 Irreducible Representations of Line Groups. 98
2.6.6 Site Symmetry for Line Groups of Families 4 and 8 102
2.7 CRYSTAL Program. Use of Symmetry in First-Principles LCAO Calculations of 3D, 2D, 1D Systems 106
References 110

3 First-Principles Simulations of Bulk Crystal and Nanolayer Properties 113
3.1 Basis Sets and Pseudopotentials in the Crystalline Electronic Structure Calculations. 114
3.1.1 Plane Wave and Localized Atomic Functions Basis Sets. 114
3.1.2 Gaussian Basis Sets for Solid State Calculations 125
3.1.3 Effective Core Potentials 133
3.2 LCAO Hartree-Fock Method for Periodic Systems. 144
3.2.1 Electron Correlation, One-Electron and One-Determinant Approximations 144
3.2.2 LCAO Hartree-Fock Method for Periodic Systems 147
3.3 Foundations of Density Functional Theory 153
3.3.1 Density Functional Theory 153
3.3.2 The Kohn–Sham Single-particle Equations 156
3.3.3 Climbing the Jacob's Ladder for Exchange-Correlation Functionals. 159
3.4 LCAO and Density Functional Tight Binding (DFTB) Methods for Periodic Systems 169
3.4.1 LCAO DFT Method for Periodic Systems 169
3.4.2 Exchange-Correlation Functionals for Periodic Systems 173
3.4.3 Density Functional Tight Binding (DFTB) Method 178
3.5 Plane Wave Hartree-Fock and DFT Methods for Periodic Systems 183
3.5.1 Projector Augmented-Wave Method 183
3.5.2 Plane Wave Hartree-Fock Method for Periodic Systems 184
3.5.3 Plane Wave Density Functional Method for Periodic Systems 187

3.6 Molecular Dynamics Approach 188
3.7 First-Principles Simulation of Bulk Crystal (3D) Properties 189
3.7.1 One-Electron Properties: Band Structure, Density of States 190
3.7.2 Equilibrium Structure, Bulk Modulus, Formation and Surface Energy 198
3.7.3 Phonon Frequencies and Relative Phase Stability Calculations 201
3.8 Nanostructure Formation, Surface and Strain Energy 207
References 208

Part II Applications

4 Boron and Metal Diborides 217
4.1 Boron Bulk and Nanolayers 218
4.2 Boron Nanotubes 223
4.2.1 Rolled-Up Single-Wall Nanotubes 223
4.2.2 Bundles of Rolled-Up Single-Wall Nanotubes 228
4.2.3 Rolled-Up Double-Wall Nanotubes 232
4.2.4 Polyhedral Nanotubes 235
4.3 Boron Nanowires 237
4.4 Metal Diboride Bulk and Nanolayers 239
4.5 Rolled-Up Metal Diboride Nanotubes 241
4.5.1 Single-Wall Nanotubes 241
4.5.2 MgB_2 and BeB_2 Nanotubes and Their Bundles 243
4.5.3 AlB_2 Nanotubes and Their Bundles 246
4.5.4 Single- and Double-Wall TiB_2 Nanotubes 248
References 250

5 Group IV Semiconductors 253
5.1 Silicon and Germanium Bulk and Nanolayers 254
5.2 Silicon and Germanium Nanotubes 257
5.2.1 Rolled-Up Si Nanotubes 257
5.2.2 Rolled-Up Ge Nanotubes 260
5.2.3 Faceted Si Nanotubes 261
5.2.4 Polyhedral Silicon Nanotubes 265
5.3 Silicon and Germanium Nanowires 268
5.3.1 Synthesis and Simulation of Si Nanowires 268
5.3.2 Cohesive and Electronic Properties of Si Nanowires 277
5.3.3 Thermal and Vibrational Properties of Si Nanowires 282
5.3.4 Elastic Properties of Si Nanowires 293
5.3.5 Prismatic and Circular-Type Ge Nanowires 297

5.4 Silicon Carbide and Germanium Silicide Bulk and Nanolayers 306
5.5 Silicon Carbide and Germanium Silicide Nanotubes 310
5.5.1 Rolled-Up and Polyhedral Single-Wall SiC Nanotubes . . . 310
5.5.2 Bundles of Rolled-Up Single-Wall SiC Nanotubes. 313
5.5.3 Rolled-Up Double-Wall SiC Nanotubes 315
5.5.4 Faceted SiC Nanotubes 317
5.5.5 Rolled-Up Single-Wall GeSi Nanotubes 319
5.6 Silicon Carbide and Germanium Silicide Nanowires 323
5.6.1 Polymorphism and Stability of SiC Nanowires 323
5.6.2 Electronic Properties of SiC Nanowires 328
5.6.3 Stability of GeSi and Hetero-Structured Ge/Si Nanowires 331
5.6.4 Electronic Properties of GeSi and Hetero-Structured Ge/Si Nanowires 336
References 342

6 Nitrides of Boron and Group III Metals 347
6.1 Boron Nitride Bulk and Nanolayers 349
6.2 Boron Nitride Nanotubes 351
6.2.1 Polyhedral and Rolled-Up Single-Wall Nanotubes 351
6.2.2 Vibrational Properties of Rolled-Up Single-Wall Nanotubes 354
6.2.3 A Growth Mechanism of Rolled-Up Single-Wall Nanotubes 360
6.2.4 Bundles of Rolled-Up Single-Wall Nanotubes. 362
6.2.5 Rolled-Up Double-Wall Nanotubes 366
6.3 Boron Nitride Nanoscrolls and Nanowires. 370
6.3.1 Nanoscrolls 370
6.3.2 Prismatic Nanowires 373
6.3.3 Monoatomic BN Linear Nanochains 378
6.4 Group III Metal Nitride Bulk and Nanolayers 382
6.5 Group III Metal Nitride Nanotubes 386
6.5.1 Rolled-Up Single-Wall AlN Nanotubes 386
6.5.2 Rolled-Up Single-Wall GaN Nanotubes 390
6.5.3 Rolled-Up Single-Wall (Al,Ga)N Nanotubes 392
6.5.4 Faceted AlN Nanotubes 396
6.6 Group III Metal Nitride Nanowires 400
6.6.1 Prismatic AlN Nanowires 400
6.6.2 Thermal and Vibrational Properties of AlN Nanowires 407
6.6.3 Elastic Properties of AlN Nanowires 410
6.6.4 Prismatic GaN Nanowires and Their Elasticity 415
References 422

7 Binary Oxides of Transition Metals 429
7.1 Zinc Oxide 430
7.1.1 Bulk Zinc Oxide and Nanolayers. 431
7.1.2 Symmetry of Zinc Oxide Nanostructures 436
7.1.3 ZnO Nanotubes. 439
7.1.4 ZnO Nanowires. 447
7.2 Titanium Oxide 450
7.2.1 Bulk and Nanolayers 450
7.2.2 Rolled-Up Single- and Double-Wall TiO_2 Nanotubes with Hexagonal Morphology. 458
7.2.3 Rolled up Singlewall TiO_2 Nanotubes with Rectangular Morphology 470
7.2.4 TiO_2 Nanowires 480
7.2.5 Orientation Effects in the Morphology and Electronic Properties of Rutile Nanowires, Anatase Nanowires and Facetted Nanotubes 507
7.3 ZrO_2 521
7.3.1 Bulk Zirconia 521
7.3.2 Structure and Stability of ZrO_2 Sheets 523
7.3.3 ZrO_2 Nanotubes 530
References 539

8 Ternary Oxides 545
8.1 $SrTiO_3$ 546
8.1.1 Bulk and Nanolayers 546
8.1.2 Symmetry of Rolled-Up $SrTiO_3$ Nanotubes 557
8.1.3 Calculations of Rolled-Up $SrTiO_3$ Nanotubes 560
8.1.4 $SrTiO_3$ Nanowires 566
8.2 $SrZrO_3$ 570
8.2.1 Bulk and Nanolayers 570
8.2.2 Rolled-Up $SrZrO_3$ Nanotubes 576
8.3 $BaTiO_3$ 578
8.3.1 Bulk and Nanolayers 579
8.3.2 Rolled-Up $BaTiO_3$ Nanotubes. 588
8.3.3 $BaTiO_3$ Nanowires 598
References 607

9 Sulfides 611
9.1 MoS_2 and WS_2 611
9.1.1 Bulk and Nanolayers 612
9.1.2 Nanotubes 619
9.1.3 Nanowires and Nanoribbons 626

9.2 TiS_2 and ZrS_2 631
9.2.1 Bulk and Nanolayers 631
9.2.2 Rolled-Up Single-Walled Nanotubes 638
9.2.3 Rolled-Up Double-Walled Nanotubes. 643
References 649

Appendix A: Space Groups 653

Appendix B: Layer Groups as Subroups of Space Groups. 657

Appendix C: Line Groups 661

Appendix D: Rod Groups as Subgroups of Space Groups 663

Index 667

Part I
Theory

Chapter 1
Introduction

Extensive experimental and theoretical investigations of nanostructures began in 1991 after the discovery of carbon nanotubes as tubular forms based on the graphite sheet (graphene) [1]. The results of carbon-based nanostructures studies (both experimental and theoretical ones) are summarized in several books [2–9]. The point defects influence on different properties of carbon nanotubes was studied in [10, 11]. In [11] the special attention was paid to the changes in the electronic properties of carbon nanotubes induced by the substitution of nitrogen, boron, or oxygen for C atoms.

However nanostructures are produced not only from carbon. In the last 20 years nanostructures of different inorganic compounds have been discovered and investigated. Researchers have synthesized not only inorganic nanotubes, but also inorganic nanoribbons, nanowires (nanorods) and nanowiskers [12, 13]. There have been reports on a variety of synthetic inorganic nanotubes [14], such as tungsten sulfide [15], silicon and boron nitrides [16, 17], vanadium, titanium and rare earth oxides [18–20]. Several reviews have appeared for the studies of inorganic nanotubes [21–27]. In [14] essential studies and topics are described concerning the synthesis, characterization and properties of individual nanotubular compounds or families.

Nanotubular materials are classified into three types [14]: single- and multi-walled rolled up nanotubes (that correspond to one or more sheets rolled into nanotube single or concentric cylindrical forms with no edge atoms) and a scrolled nanotube generated from a single straight sheet with both ends kept free.

Rolled up single- and multi-walled nanotubes are constructed from folded two-periodic (2D) layers, consisting of one or several sheets of atoms.

Multi-layered inorganic compounds (ZnO, for example) which have tubular forms are known, exhibit layers with the same hexagonal atom arrangement which have carbon nanotubes.

Examples of nonhexagonal layered structures, which may also form tubular structures are shown in Fig. 1.1 [25].

If the surface and interior of a finite-diameter 1D nanoobject is rigidly occupied by atoms, it is often called a nanowire or nanorod, and sometimes a “quantum” wire or “quantum” rod. The polyhedral nanotubes with a regular polyhedral shape are formed by nanowires with a hollow core.

© Springer-Verlag Berlin Heidelberg 2015

R.A. Evarestov, *Theoretical Modeling of Inorganic Nanostructures*,
NanoScience and Technology, DOI 10.1007/978-3-662-44581-5_1

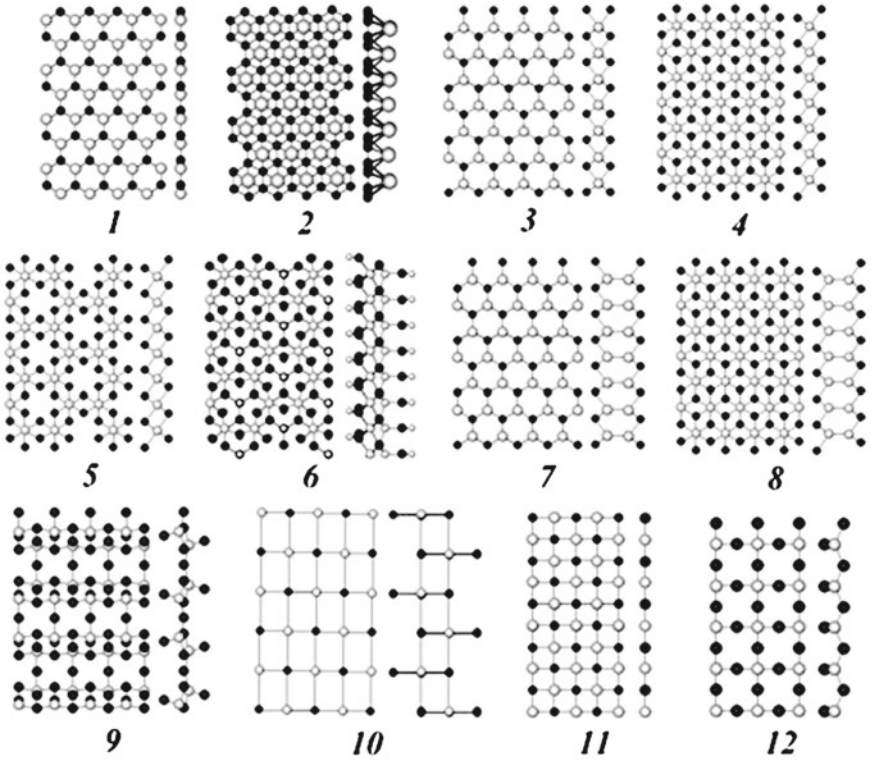

Fig. 1.1 Structures of the monolayers of some inorganic compounds: *1* BN, *2* AlB_2, MgB_2, *3* MoS_2, WS_2, $NbSe_2$, *4* TiS_2, ZrS_2, anatase TiO_2, $NiCl_2$, *5* $FeCl_3$, MoO_3, *6* imogolite $Al2O_3(OH)_3Si(OH)$, *7* GaS, GaSe, *8* metastable InS with a *hexagonal* lattice, *9 rectangular* V_2O_5, *10 centered rectangular* lepidocrocite TiO_2, *11 square* MgO and *12* SiO_2. The *empty circles* represent metal atoms, while *full circles* stand for nonmetal atoms, [25]

It has become common in the literature to use the designation "nanowire (nanorod)". The implication is that nanowire is the preferred terminology, and nanorod means nothing essentially different [28].

The qualifier "quantum" applied to dots, wires (or rods), is ambiguous, for it does not indicate whether the system is a free standing fragment of a crystal, or a region embedded in a host crystal, as in gate-patterned regions of a two-dimensional layer in a 3D crystal. In the opinion of Philip B. Allen [28], it is better not to use "quantum" except for the latter case, or unless the ambiguity is intentional.

Ordered nanowires fall into several structural classes, [28]: (1) helical nanowires, (2) molecular nanowires, and (3) nanocrystalline nanowires (NCNW).

Helical nanowires are filled nanotubes. Potassium halide-filled BN nanotube is an example of a helical nanowire, [29]. Its fillings are usually single crystals with lengths up to several micrometers.

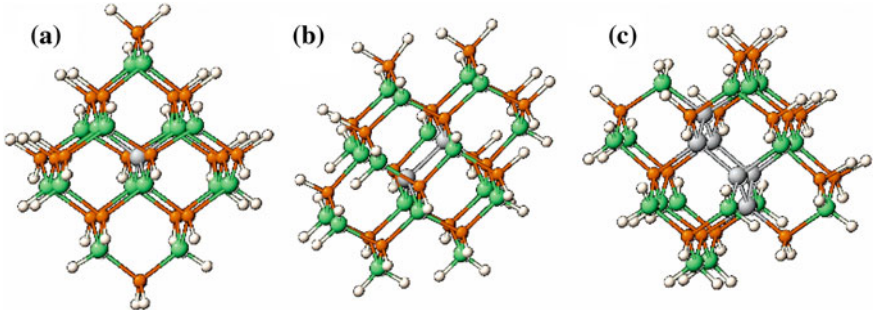

Fig. 1.2 Ball and stick model for the different nanocrystal symmetries. The atoms in *gray* represent the *center* of the nanocrystal. *Green* balls are for Se, *orange* for Cd, and *white* for pseudo-hydrogen atoms. **a–c** represent atom-centered (AC), bond-centered (BC), and hexagonal interstitia-centered (HC) nanocrystals, respectively (Reprinted figure with permission from Dalpian et al. [31], Copyright (2006) by the American Chemical Society)

Molecular nanowires can be fragments of quasi-1D crystals. For example, the non-helical inorganic polymer $(Mo_6S_6)_N$ (a fragment of the quasi-1D bulk crystal $M_2Mo_6X_6$, where M is an alkali and X = S,Se) is an example of a molecular nanowire, which has been studied experimentally and theoretically.

Finally, nanocrystalline nanowires (NCNW) are 1D fragments of bulk crystals where the bulk was a 3D (not a quasi-1D) material, [28]. The term "nanocrystal" is used for the fragments of bulk crystals that have only point group symmetry (0 D) typical of the molecules (the term "molecular cluster" is also used [30]). As an example, Fig. 1.2 shows nanocrystals constructed by cutting a spherical fragment of a CdSe bulk crystal with a zinc blende structure [31]. Point group symmetries are usually very important when one deals with molecules. Different symmetries usually lead to different properties in molecules, and this has been studied widely in the literature. Also it is very natural to expect symmetry to play an important role in the properties of nanocrystals [31].

Two parameters enter in the definition of a spherical nanocrystal: its radius and its center [31]. Nanocrystals with different centers and similar radii have different symmetries. For example, if a nanocrystal is centered in an atom (AC), as can be seen in Fig. 1.2a, it will have a T_d point group symmetry. The same will happen if the center is in a tetrahedral interstitial. These nanocrystals will be nonstoichiometric, that is, they will have a different number of cations and anions. Nanocrystals centered in a bond (BC) or in a hexagonal interstitial (HC), as can be seen in Figs. 1.2b, c, will be stoichiometric but will have lower symmetries (C_{3v}).

Simulations on monoperiodic nanostructures for different classes of inorganic substances are widely performed now, simultaneously with their synthesis and experimental study. A deep understanding of the composition and structure at the atomic level is key to understanding the relations between the unique properties of nanomaterials when compared with the bulk phase [32].

The theoretical difficulties one encounters in nanostructure study are as follows, [28]: (1) the precise atomic structure of inorganic nanomaterials is rarely known; (2) the computer techniques to exploit rotational as well as translational symmetry are not well developed.

Progress in nanoscience is becoming increasingly dependent on simulation and modeling, which is due to a combination of three factors [33]: the reduced size of nano-objects, the increasing power of computers and the development of new theoretical methods. The book by Delerue and Lannoo [33] is one of the first attempts to provide the theoretical background needed to simulate nanodevices, quantum dots and molecular devices.

The second edition of our previous book Quantum Chemistry of Solids [30] includes a chapter dealing with symmetry properties and the recent applications of the LCAO first-principles method to inorganic nanotubes, based on BN, TiO_2 and $SrTiO_3$ compounds. The chapter demonstrates the efficiency of first-principles calculations for predicting the structure and stability of single- and double-walled nanotubes.

In this book we discuss the symmetry and the results of the theoretical study of inorganic nanolayers, nanotubular materials and nanowires. Computational modeling is an essential part of this study so that our book effectively deals with **computational nanoscience**.

We present the basic results of the theoretical modeling of the structural and electronic properties of inorganic diperiodic (nanolayers) and monoperiodic (nanotubes and nanowires) nanostructures with different shapes and morphologies. Three models of monoperiodic nanostructures are considered: (i) nanocrystalline nanowires (obtained from 3D parent crystal structure sectioning it along the crystalline planes parallel to the chosen direction of the nanowire translation), (ii) rolled up nanotubes—single- and multi-walled (rolled from 2D nanolayers of parent crystal thin film) and (iii) polyhedral nanotubes. The symmetry of these models is described within the formalism of monoperiodic (line) symmetry groups for the conventional nanotubes. The nanowires and the polyhedral nanotube symmetry are described by 75 rod groups, forming a subset of an infinite number of line groups.

The three-dimensional triperiodic (3D) symmetry groups of the bulk crystals and the two-periodic (2D) layer symmetry groups of thin films are considered as the basis for the generation of monoperiodic (1D) symmetry groups of the nanostructures.

The formalism of the line symmetry groups is discussed and applied to the description of nanotubes and nanowires symmetry. The symmetry aspects of the nanotubes rolled up from the diperiodic layer are considered using the connection between the three dimensional diperiodic layer groups and monoperiodic line groups. The three-dimensional rod and layer subperiodic groups are considered in the context of three-dimensional space along with their concomitant relationships with the three-dimensional space groups. These relationships are the basis for the symbols and classification of the subperiodic groups, which are used in the symmetry description of nanowires and polyhedral nanotubes.

The first-principles methods applied to the LCAO and Plane Wave calculations of the electronic and vibrational properties of nanostructures are thoroughly described.

Understanding the theoretical aspects presented here provides greater scope for the synthesis of monoperiodic nanostructures with predictable morphology and a better interpretation of their properties.

Part II Applications gives numerous examples of the first-principles calculations of different inorganic nanostructures. We consider nanostructures based on: (1) α-*Boron* and metal diborides MeB_2 (Me = Al, Be, Mg, Ti); (2) tetravalent semiconductors—silicon, germanium, silicon carbide SiC, germanium silicide; (3) Boron and Group III metal nitrides; (4) binary oxides (ZnO, TiO_2, ZrO_2); (5) ternary oxides $Sr(Ba)TiO_3$, $SrZrO_3$; (6) disulfides MoS_2, WS_2, TiS_2, ZrS_2.

It is demonstrated that the properties of the inorganic nanostructures differ from those of the corresponding bulk crystal. This material helps the reader to understand potential of computer modelling for predicting the existence and describing the properties of inorganic nanostructures.

The majority of the first-principles 1D nanostructure DFT calculations were performed using Plane Waves (PW) basis requiring that periodic boundary conditions be used to model these nanostructures. Therefore an artificial vacuum space is inserted in the xy plane to separate adjacent nanowires, while the length of the 1D nanostructure is created by replication along the z-direction. In LCAO methods such an artificial periodicity is not necessary.

To determine the stability of nanoscale structures studied computationally, formation or binding energy was calculated. These energies are compared as a function of nanostructure dimension, usually diameter, as well as shape, and can give an indication of the relative stability of nanowires and nanotubes compared to the bulk or sheets. It is expected that when the dimensions of a material are reduced into the nano-region, unique and novel shapes and morphologies can form and, as a result, the bond distances and angles often differ from those in the bulk material [34]. It is therefore highly important to examine the structural changes of various nanostructures that affect their electronic and magnetic properties, including the density of states and band structure.

References

1. S. Ijima, Nature **354**, 56 (1991)
2. R. Saito, G. Dresselhaus, M.S. Dresselhaus, *Physical Properties of Carbon Nanotubes* (Imperial College Press, London, 1998)
3. F. Harris, *Carbon Nanotubes and Related Structures: New Materials for the Twenty-First Century* (Cambridge University Press, Cambridge, 1999)
4. M.S. Dresselhaus, G. Dresselhaus, Ph. Avouris (eds.), *Carbon Nanotubes: Synthesis, Structure, Properties, Applications and Electronics*. Topics in Applied Physics, vol. 80 (Springer, New York, 2001)
5. S. Reich, C. Thomsen, J. Maultzsh, *Carbon Nanotubes* (Wiley-VCH, Weinheim, 2004)
6. S.V. Rotkin, S. Subramoney (eds.), *Applied Physics of Carbon Nanotubes. Fundamentals of Theory, Optics, and Transport Devices* (Springer, New York, 2005)
7. A. Jorio, G. Dresselhaus, M.S. Dresselhaus (eds.), *Carbon Nanotubes*. Topics in Applied Physics, vol. 111 (Springer, New York, 2008)

8. P.N. Dyachkov, *Elektronnyje Svojstva i Primenenije Nanotrubok* (*Electronic Properties and Applications of Nanotubes*) (Binom, Moscow, 2010)
9. D. Jiang, Z. Chen, *Graphene Chemistry: Theoretical Perspectives* (Wiley, Hoboken, 2013)
10. S. Uryu, T. Ando, Phys. Rev. B **76**, 155434 (2007)
11. P.N. Dyachkov, Russ. J. Inorg. Chem. **56**, 1 (2011)
12. H.S. Nalwa (ed.), *Encyclopedia of Nanoscience and Nanotechnology*, vols. 1–10 (American Scientific Publishers, Valencia, 2004)
13. M. Rieth, W. Schommers (eds.), *Handbook of Theoretical and Computational Nanotechnology* (American Scientific Publishers, Stevenson Ranch, 2006)
14. T. Kijima (ed.), *Inorganic and Metallic Nanotubular Materials*. Topics in Applied Physics, vol. 117 (Springer, Berlin, 2010)
15. R. Tenne, L. Margulis, M. Genut, G. Hodes, Nature **360**, 444 (1992)
16. J.M. Hamilton, S.E. Dolan, R. Nesper, C.E. Manin, Y.O. Colijn, C.A. McDonald, S.G. Shore, Science **260**, 659 (1993)
17. N.G. Chopra, R.J. Luyken, K. Cherrey, V.H. Crespi, M.L. Cohen, S.G. Louie, A. Zettl, Science **269**, 966 (1995)
18. M.E. Spahr, P. Butterli, R. Nesper, M. Muller, F. Krumeich, H.U. Nissen, Angew. Chem. Int. Ed. **37**, 1263 (1998)
19. T. Kasuga, M. Niramatsu, A. Hoson, T. Sekino, K. Niihara, Adv. Mater. **11**, 1307 (1999)
20. M. Yada, J. Mihara, S. Moiri, M. Kuroki, T. Kijima, Adv. Mater. **14**, 309 (2002)
21. C.N.R. Rao, M. Nath, J. Chem. Soc. Dalton Trans. **1**, 1 (2003)
22. M. Remskar, Adv. Mater. **16**, 1497 (2004)
23. G.S. Zakharova, V.L. Volkov, V.V. Ivanovskaya, A.L. Ivanovskii, Russ. Chem. Rev. **74**, 587 (2005)
24. A.N. Enyashin, S. Gemming, G. Seifert, Springer Ser. Mater. Sci. **93**, 33 (2006)
25. R. Tenne, M. Remkar, A.N. Enyashin, G. Seifert, in *Carbon Nanotubes*, ed. by A. Jorio, G. Dresselhaus, M.S. Dresselhaus. Topics in Applied Physics, vol. 111 (Springer, Berlin, 2008), pp. 631–671
26. R. Tenne, G. Seifert, Annu. Rev. Mater. Res. **39**, 387 (2009)
27. R. Tenne, M. Redlich, Chem. Soc. Rev. **39**, 1423 (2010)
28. P.B. Allen, Nanoletters **7**, 6, 11, 1220 (2007)
29. W.Q. Han, C.W. Chang, A. Zettl, Nanoletters **4**, 1355 (2004)
30. R.A. Evarestov, *Quantum Chemistry of Solids. LCAO Treatment of Crystals and Nanostructures*, 2nd edn. Springer Series in Solid State Sciences, vol. 153 (Springer, New York, 2012)
31. G.M. Dalpian, M.L. Tiago, M. Lopez del Puerto, J.R. Chelikowsky, Nanoletters **6**, 501 (2006)
32. R. Levi, M. Bar-Sadan, R. Tenne, in *Springer Handbook for Nanomaterials, Chap. 16*, ed. by R. Vajtai (Springer, Berlin, 2013)
33. C.J. Delerue, M. Lannoo, *Nanostructures: Theory and Modeling* (Springer, Berlin, 2004)
34. M. Spencer, Prog. Mater. Sci. **57**, 437 (2012)

Chapter 2
The Symmetry Groups in Three-Dimensional Space

The theoretical modeling of inorganic nanostructures described in this book is based on the consideration of 3D-2D-1D three-dimensional objects (three-periodic bulk crystals, diperiodic nanolayers, monoperiodic nanotubes and nanorods).

First, the structure and properties of a bulk crystal with 3D periodicity are computed. The prototype bulk crystal structure is one of the main factors that influence the properties of nano-sized systems. This allows one to compare the results calculated with the existing experimental data and thereby check the validity of the calculation method used.

Second, the nanolayer structure and properties are calculated, as the structure and properties of the rolled up nanotubes depend on the slab, used in rolling up procedure.

Finally, the structure and properties of nanotubes and nanorods are calculated applying the same computational method as was applied for the bulk crystals and nanolayers.

The symmetry properties of the system are used in 3D-2D-1D calculations allowing one to make a classification of the electron and phonon states and drastically reduce the computational time.

In this chapter we discuss the following symmetry groups in the three-dimensional space: (1) space groups $G = G_3^3$—230 types of three dimensional groups with three-dimensional translations (triperiodic 3D), (2) layer groups $DG = G_2^3$—80 types of three dimensional groups with two-dimensional translations (diperiodic 2D) and (3) line groups $LG = G_1^3$—three dimensional groups with one-dimensional translations (monoperiodic 1D). 75 rod groups (RG) constitute a subset of the infinite number of line groups.

The description the bulk crystal requires the knowledge of the full symmetry group of the crystal (space group G) and its irreducible representations. The group G includes both translations, operations from the point groups of symmetry and combined operations. The application of symmetry transformations means splitting all space into systems of equivalent points known also as Wyckoff positions in crystals, irrespective of whether there are atoms in these points or not. The crystal-structure type is specified when one decides which sets of the Wyckoff positions for the corresponding space group are occupied by atoms. To distinguish between different

© Springer-Verlag Berlin Heidelberg 2015

R.A. Evarestov, *Theoretical Modeling of Inorganic Nanostructures*,
NanoScience and Technology, DOI 10.1007/978-3-662-44581-5_2

structures of the same type one needs the numerical values of lattice parameters and additional data if there exist occupied Wyckoff positions with free parameters in the coordinates.

We briefly discuss the 20 bulk crystal structures (cubic, tetragonal, orthorhombic and hexagonal) which form the basis of nanostructure modeling. Among them are structures with both symmorphic and nonsymmorphic space groups, structures with the same Bravais lattice and crystal class but different space groups, structures described by only lattice parameters or by both the lattice parameters and free parameters of the Wyckoff positions occupied by atoms.

The site symmetry approach extension to the layer and line groups is considered.

The symmetry of crystalline orbitals in bulk crystals and nanostructures is defined by the their symmetry group irreducible representations, which are also considered in this chapter.

2.1 Classification of the Symmetry Groups

Let G_m^n mean the symmetry group of the system in the n-dimensional space (n-dimensional group) with m-dimensional translation subgroup ($m \leq n$) [1].

In this chapter we discuss the symmetry groups in the three-dimensional space ($n = 3$): (1) space groups $G = G_3^3$—230 types of three dimensional groups with the three-dimensional translations (triperiodic 3D, $m = 3$), (2) layer groups $DG = G_2^3$—80 types of three dimensional groups with two-dimensional translations (diperiodic 2D, $m = 2$) and (3) line groups—$LG = G_1^3$ three dimensional groups with one-dimensional translations (monoperiodic 1D, $m = 1$). 75 rod groups (RG) constitute a subset of the infinite number of line groups.

17 plane groups $G = G_2^2$ and 7 frieze groups $G = G_1^2$ are the symmetry groups in the two-dimensional space ($n = 2$) being the subsets of the three-dimensional layer and rod groups, respectively.

2 groups in the one-dimensional space $LG = G_1^1$ are called by line groups in [2]. However, we use this term for all monoperiodic three dimensional groups with one-dimensional periodicity. These groups are called in [3] by commensurate line groups.

Independent study of polymers, or, in more rigorous terms, general 1-periodic three-dimensional objects, stimulated the analysis of 1-periodic symmetry groups which could include rotation axes of arbitrary order. Such groups received a collective name ‘line groups’. There are infinitely many line groups and their classification may be performed in a number of ways [3, 4]. Rod groups constitute a subset of the set of line groups but due to their origin enumeration, notations, and geometric realizations rod groups possess certain specificity as compared with the line groups. In this section we establish the explicit correspondence between rod groups and relevant geometric realizations of the corresponding line groups to lay a bridge between crystallography and symmetry description of stereoregular polymers. It seems to be of increasing importance due to the very fast developments in the field

of nanotubes, nanoribbons, and nanowires. These 1-periodic objects originate from crystalline solids but nanotube symmetry elements may include rotation axes of arbitrary order.

The three-dimensional triperiodic groups with the three lattice basic translation vectors $\mathbf{a}_1, \mathbf{a}_2, \mathbf{a}_3$ are called here space groups. The basic translation vectors define the primitive unit cell i.e. the minimal volume unit cell used to reproduce the whole lattice by the tree dimensional basic translations. The so called crystallographic (conventional) unit cell with the crystallographic translation vectors **a**, **b**, and **c** is defined as the minimal volume unit cell in the form of a parallelepiped constructed on vectors of translations and possessing the point symmetry of the lattice.

The layer groups and rod groups are known as subperiodic groups [5]. The three-dimensional rod and layer groups are considered in the context of a three-dimensional space along with their concomitant relationships with space groups. These relationships are the basis for the symbols and classification of the subperiodic groups which are used in [5]. Subperiodic groups are described, as are the space groups, see [2], by means of a crystallographic coordinate system, consisting of a crystallographic basis and a crystallographic origin. For subperiodic groups, not all vectors of the crystallographic basis are lattice vectors. For the three-dimensional layer groups and rod groups, the basis vectors are labeled **a**, **b**, and **c**. The basis vectors **a** and **b** are chosen as lattice vectors in the case of layer groups, and **c** is chosen as a lattice vector in the case of rod groups.

The three-dimensional crystallographic point groups $G = G_0^3$ form 32 crystal classes of space groups. Excluding 5 cubic point groups one obtains 27 classes of layer and rod groups. The 10 point symmetry groups $G = G_0^2$ in two-dimensional space and 2 point symmetry groups $G = G_0^1$ in one-dimensional space are subsets of the three-dimensional point groups $G = G_0^3$ [1].

The triperiodic (3D) space groups $G = G_3^3$ describe the symmetry of bulk crystals. The classification of the crystalline electron and phonon states requires the knowledge of the full symmetry group of a bulk crystal (triperiodic space group G) and its irreducible representations. The group G includes both the three-dimensional translations, operations from the 32 three-dimensional point symmetry groups $G = G_0^3$ and combined operations.

The diperiodic (layer) groups $DG = G_2^3$ are the symmetry groups of the thin films. These groups are used to describe the electronic structure of surface states of crystals in the slab model. In the *single-slab* model a crystal with a surface is approximated by a slab of finite thickness. The symmetry group of this model (diperiodic or layer group) allows the existence of the point symmetry operations that move the atoms out of the plane of the layer but bring them into positions occupied by other atoms of the slab. The diperiodic (layer) group DG includes both the two-dimensional translations, operations from the 27 three-dimensional point symmetry groups $G = G_0^3$ and combined operations.

The layer groups are subperiodic subgroups of the triperiodic groups.The knowledge of the space 3D groups allows one to generate the layer groups corresponding to the different surface orientations in the bulk crystal. The layer groups in turn are used as basic ones in the monoperiodic nanotubes modeling.

The commensurate line groups $LG = G_1^3$ (also called monoperiodic groups) are symmetry groups of three-dimensional objects translationally periodic along a line—stereoregular polymers, nanotubes and nanowires. The symmetry groups of nanoribbons and nanowires (75 rod groups RG) form a finite subset of an infinite number of line groups. Rod group includes both the one-dimensional translations, operations from the 27 three-dimensional point symmetry groups $G = G_0^3$ and combined operations.

2.2 Space (Triperiodic) Symmetry Groups of Bulk Crystals

2.2.1 Translation and Point Symmetry of Bulk Crystals

The classification of the molecular or the crystalline electron and phonon states requires the knowledge of the system symmetry group and its irreducible representations. In both molecules and bulk crystals the symmetry group is the set of transformations in three dimensional space that transforms any point of the space into an equivalent point. The systems of equivalent points are called orbits of points. In equivalent points the properties of a molecule or a crystal (electrostatic potential, electronic density, etc.) are all identical.

The symmetry of molecules in the three dimensional space is described by the three dimensional point groups $F = G_0^3$ without the periodicity. The group F consists of the orthogonal symmetry operations (rotations through symmetry axes, reflections in symmetry planes and their combinations) that transform the equilibrium configuration of the nuclei of a molecule into itself. They form a group F of molecular symmetry. There are no restrictions on the rotation axes order so that the number of point groups is formally infinite.

The space group is the triperiodic group $G = G_3^3$ in the three-dimensional space and includes both the three-dimensional translations, operations from the point groups of symmetry (the crystal classes) and combined operations. The condition of the compatibility of the point and translation symmetry operations restricts the rotation axes by order 1, 2, 3, 4, 6 and therefore the total number of the crystallographic point groups is 32.

As well as molecules, crystals possess point symmetry, i.e. equivalent points of space are connected by the point-symmetry transformations. But in a crystal the number of the point-symmetry elements (the rotation axis or reflection planes) is formally infinite. Therefore, it is impossible to find such a point of space where all the point-symmetry elements intersect. It is connected by the fact that, unlike molecules, in crystals among operations of symmetry there are translations of a group of rather small number of atoms to space. The presence of translation symmetry means the periodicity of the perfect crystals structure: translations of the primitive unit cell reproduce the whole crystal.

In real crystals of macroscopic sizes translation symmetry, strictly speaking, is absent because of the presence of borders. If, however, we consider the so-called bulk properties of a crystal (for example, distribution of electronic density in the volume of the crystal, determining the nature of a chemical bond) the influence of borders can not be taken into account (number of atoms near to the border is small, in comparison with the total number of atoms in a crystal) and we consider a crystal as a boundless system [6].

In the theory of electronic structure two symmetric models of a boundless crystal are used: or it is supposed that the crystal fills all the space (model of an infinite crystal), or the fragment of a crystal of finite size (for example, in the form of a parallelepiped) with the identified opposite sides is considered. In the second case we say, that the crystal is modeled by a cyclic cluster which translations as a whole are equivalent to zero translation (Born–von Karman Periodic Boundary Conditions–PBC). Between these two models of a boundless crystal there exists a connection: the infinite crystal can be considered as a limit of the sequence of cyclic clusters with increasing volume. In a molecule, the number of electrons is fixed as the number of atoms is fixed. In the cyclic model of a crystal the number of atoms (and thus the number of electrons) depends on the cyclic-cluster size and becomes infinite in the model of an infinite crystal. It makes changes, in comparison with molecules, to a one-electron density matrix of a crystal that now depends on the sizes of the cyclic cluster chosen. As a consequence, in calculations of the electronic structure of crystals it is necessary to investigate convergence of results with an increase of the cyclic cluster that models the crystal. For this purpose, the features of the symmetry of the crystal, connected with the presence of translations also are used.

Translation symmetry of a perfect crystal can be defined with the aid of three noncoplanar vectors: $\mathbf{a}_1, \mathbf{a}_2, \mathbf{a}_3$ basic translation vectors. Translation $t_{\boldsymbol{a}}$ through the lattice vector

$$\mathbf{a} = n_1\mathbf{a}_1 + n_2\mathbf{a}_2 + n_3\mathbf{a}_3 \tag{2.1}$$

where n_1, n_2, n_3 are integers, relates the equivalent points $\boldsymbol{r}$ and $\boldsymbol{r}'$ of the crystal:

$$\boldsymbol{r}' = \boldsymbol{r} + \boldsymbol{a} \tag{2.2}$$

Translations $t_{\boldsymbol{a}}$ are elements of the translation group T. If we draw all the vectors $\boldsymbol{a}$ from a given point (the origin), then their endpoints will form the Bravais lattice, or "empty" lattice, corresponding to the given crystal. The endpoints of the vectors in this construction are the lattice points (lattice nodes). Three of the basic translation vectors define the elementary parallelepiped called the primitive unit cell (PUC). The PUC contains lattice points only at the eight corners of the parallelepiped. Each corner belongs to eight PUC, so that by fixing the PUC by one lattice point at the corner we refer the remaining of the corners to the nearest seven PUC's. We note that the basic translation vectors cannot be chosen uniquely. However, whatever the choice of these vectors, the volume of the PUC is always the same. The PUC defines the smallest volume whose translations form the whole Bravais lattice (direct lattice). Usually, the basic vectors are chosen to be the shortest of all those possible.

Atoms of a crystal are not necessarily located in the direct lattice points. In the simplest case when all the crystal is obtained by translations of one atom (such crystals are termed monoatomic, many metals belong to this type) all atoms can be placed in direct lattice points.

As a set of points, the direct lattice possesses not only translation but also point symmetry, i.e. lattice points are interchanged when rotations around one of the axes of symmetry, reflections in planes of symmetry and their combinations are applied. All the point-symmetry operations of the Bravais lattice are defined when the origin of the coordinate system is chosen in one of the lattice points. The corresponding PUC can be defined as the reference unit cell (it is obtained by a zeroth translation ($n_1 = n_2 = n_3 = 0$ in (2.5)). Among point-symmetry operations of a direct lattice it is obligatory to include inversion I in the origin of coordinates since, together with translation on a vector $\boldsymbol{a}$ the group of translations T also includes translation on a vector $-\boldsymbol{a}$. The identity element of group T is t_0—a zeroth translation. Elements R of point group F^0 transform each lattice vector into a lattice vector: $R\boldsymbol{a} = \boldsymbol{a}'$. The point group F^0 of symmetry of the direct lattice determines the crystal system (or syngony). There are seven systems (syngonies) of direct lattices. It turns out that not all point groups can be lattice symmetry groups F^0. The requirement that both $\boldsymbol{a}$ and $R\boldsymbol{a}$ can simultaneously be lattice vectors restricts the number of possible point groups. Let us now establish these limitations [7].

To establish the rotations of the group F^0, let us take the basic lattice vectors $\boldsymbol{a}_1, \boldsymbol{a}_2, \boldsymbol{a}_3$ as the basis unit vectors in the space of the lattice vectors $\boldsymbol{a}$, and write down the matrix $D(R)$ of the transformation R in the new basis, in which all the lattice vectors have integer components. If the matrix of the orthogonal transformation R in this basis is denoted by $D'(R)$, then $D'(R) = U^{-1}D(R)U$, where U is a matrix of the transformation from the initial orthonormal basis to the basis $\boldsymbol{a}_1, \boldsymbol{a}_2, \boldsymbol{a}_3$. If R is a rotation (or mirror rotation) through an angle φ the traces of the matrices $D(R)$ and $D'(R)$ are equal:

$$\mathrm{Sp}D'(R) = \mathrm{Sp}D(R) = \pm 1 + 2\cos(\varphi) \tag{2.3}$$

Since, however, R should transform the lattice vector $\boldsymbol{a}$ into the lattice vector $\boldsymbol{a}' = R\boldsymbol{a}$ it follows that all the elements of $D'(R)$ and hence its trace, must be integers. It follows that $\cos(\varphi) = \cos(2\pi\frac{m}{n}) = \pm 1, \pm 2, 0$. Consequently, the group F^0 can contain only two-, three-, four- and sixfold axes. Finally, it can be shown that if the group F^0 contains the subgroup $C_n,\ n > 2$, it will also contain the subgroup C_{nv}. The above three limitations ensure that the point group of the lattice can only be one of the seven point groups: $S_2, C_{2h}, D_{2h}, D_{3h}, D_{4h}, D_{6h}, O_h$. This is why there are only seven syngonies: namely, triclinic, monoclinic, orthorhombic, rhombohedral, tetragonal, hexagonal and cubic. It is seen that, unlike molecules, in point groups of symmetry of crystals there is no axis of symmetry of the fifth order (rotations around such axes are incompatible with the presence of translations).

Two Bravais lattices with the same group of point symmetry F^0 fall into one type if they can be transferred to each other by the continuous deformation that is not decreasing the point symmetry of a lattice. In three-dimensional space there are

Table 2.1 Distribution of crystal classes F and Bravais lattices on singonies F^0

Syngony F^0 crystal classes F	Direct lattice types	Basic translation vectors	Bravais lattice param.
Triclinic S_2: $C_1, S_2(C_i)$	P	Any noncoplanar	$a, b, c,$ α, β, γ
Monoclinic C_{2h}: C_s, C_2, C_{2h}	P A, B, C	$(0, -b, 0), (a \sin\gamma, -a\cos\gamma, 0), (0, 0, c)$ $(0, -b, 0), (1/2)(a \sin\gamma, -a\cos\gamma, -c),$ $(1/2)(a \sin\gamma, -a\cos\gamma, c)$	a, b, c, γ
Orthorhombic D_{2h}: C_{2v}, D_2, D_{2h}	P A, B, C F I	$(0, -b, 0), (a, 0, 0), (0, 0, c)$ $(1/2)(a, -b, 0), (1/2)(a, b, 0), (0, 0, c)$ $(1/2)(a, 0, c), (1/2)(0, -b, c), (1/2)(a, -b, 0)$ $(1/2)(a, b, c), (1/2)(-a, -b, c), (1/2)(a, -b, -c)$	a, b, c
Tetragonal D_{4h}: $S_4, D_{2d}, C_4, C_{4v},$ C_{4h}, D_4, D_{4h}	P I	$(a, 0, 0), (0, a, 0), (0, 0, c)$ $(1/2)(-a, a, c), (1/2)(a, -a, c), (1/2)(a, a, -c)$	a, c
Hexagonal D_{6h}: $C_3, S_6, C_{3v}, C_{3h}, D_3,$ $D_{3d}, D_{3h}, C_6, C_{6h},$ C_{6v}, D_6, D_{6h}	H	$(a/2, -a/2, 0), (0, a, 0), (0, 0, c)$	a, c
Rhombohedral D_{3d}: $C_3, S_6, C_{3v}, D_3, D_{3d}$	R	$(a, 0, c), (-a/2, a/2, c), (-a/2, -a/2, c)$	a, c
Cubic O_h: T, T_d, T_h, O, O_h	P F I	$(a, 0, 0), (0, a, 0), (0, 0, a)$ $(1/2)(0, a, a), (1/2)(a, 0, a), (1/2)(a, a, 0)$ $(1/2)(-a, a, a), (1/2)(a, -a, a)(1/2)(a, a, -a)$	a

14 types of direct lattices whose distribution on syngonies is shown in Table 2.1. In addition to the translational subgroup T, the space group contains other transformations whose form depends on the symmetry of the Bravais lattice and the symmetry of the components of the crystal, i.e. on the symmetry of the PUC as the periodically repeating set of particles forming the crystal. This last fact frequently ensures that not all the transformations in the point group F^0 are included in the symmetry group of the crystal. Not all transformations that map the sites on each other need result in a corresponding mapping of the crystal components. It is therefore possible that the point group of a crystal F (crystal class) will only be a subgroup of a point group of an empty lattice. So the real crystal structure point-symmetry group F may coincide with the lattice point symmetry group F^0 or be its subgroup. The distribution of crystal classes F and Bravais lattices on syngonies is given in Table 2.1.

The lattice types are labeled by P (simple or primitive), F (face-centered), I (body-centered) and $A(B, C)$ (base-centered). Cartesian coordinates of basic translation vectors written in units of Bravais lattice parameters are given in the third column of Table 2.1. It is seen that the lattice parameters (column 4 in Table 2.1) are

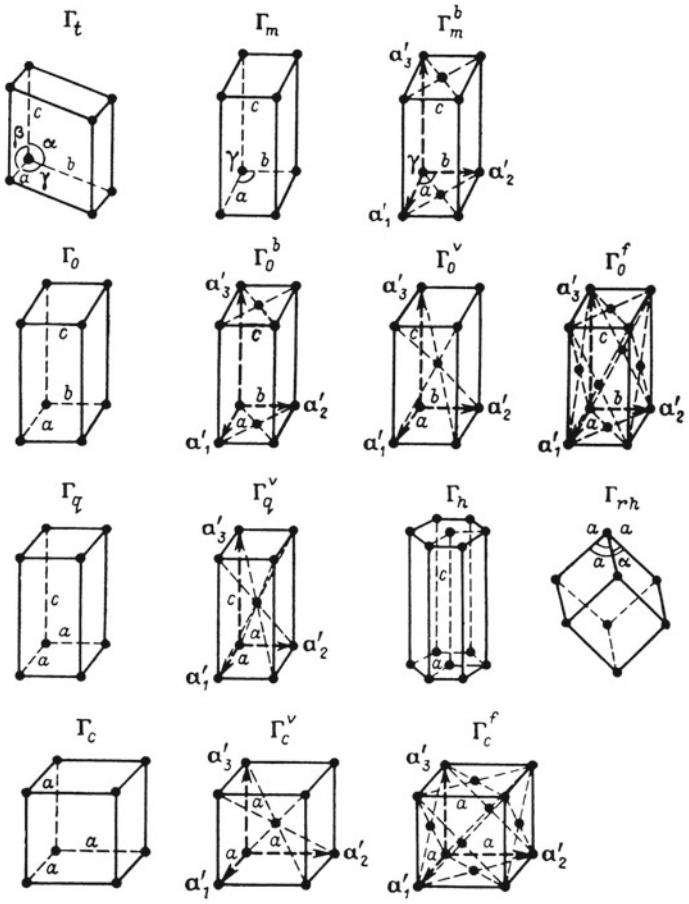

Fig. 2.1 Three-dimensional Bravais lattices

defined only by syngony, i.e. are the same for all types of Bravais lattices with the point symmetry F^0 and all the crystal classes F of a given syngony.

The point symmetry group of a *triclinic* lattice Γ_t (Fig. 2.1) consists of only inversion in the coordinates origin.

Therefore this lattice is defined by 6 parameters—lengths a, b, c of basic translation vectors and angles α, β, γ between their pairs $\boldsymbol{a}_2 - \boldsymbol{a}_3$, $\boldsymbol{a}_1 - \boldsymbol{a}_3$ and $\boldsymbol{a}_1 - \boldsymbol{a}_2$, respectively.

In simple Γ_m and base-centered Γ_m^b *monoclinic* lattices one of the vectors (with length c, for example) is orthogonal to the plane defined by two vectors with length a and b (γ is the angle between these vectors not equal to 90 or 120°). In lattice Γ_m^b the centered face can be formed by a pair of nonorthogonal lattice vectors. For example, in a C centered monoclinic lattice the lattice point appears on the face formed by $\boldsymbol{a}_1$ and $\boldsymbol{a}_2$ basic translation vectors. In the base-centered lattice one can consider so-called

conventional unit cell—the parallelepiped, reflecting the monoclinic symmetry of the lattice. For a simple monoclinic lattice Γ_m the conventional and primitive unit cells coincide, for a base-centered monoclinic lattice Γ_m^b the conventional unit cell contains 2 primitive unit cells (see Fig. 2.1).

All the three translation vectors of a simple *orthorhombic* lattice Γ_o are orthogonal to each other, so that the conventional cell coincides with the primitive cell and is defined by three parameters—lengths of the basic translation vectors. For base-centered Γ_o^b, face-centered Γ_o^f and body-centered Γ_o^v lattices the conventional unit cell contains two, four and two primitive cells, respectively (see Fig. 2.1).

The *tetragonal* lattices Γ_q (simple) and Γ_q^v (body-centered) are defined by two parameters, as two of the three orthogonal translation vectors of a conventional unit cell have the same length a.

The *hexagonal* lattice is defined by two parameters: a—length of two equal basic translation vectors (with the angle 120° between them) and c—length of the third basic translation vector orthogonal two the plane of first two vectors.

In a *rhombohedral(triclinic)* lattice all three translation vectors have the same length a, all three angles α between them are equal (but differ from 90°), so this lattice is defined by two parameters. There are two possibilities to define the rhombohedral lattice parameters. In the first case the parameters a and γ are given directly. In the second case the lengths a and c of the hexagonal unit-cell translation vectors are given: this cell consists of three primitive rhombohedral cells (so-called hexagonal setting for rhombohedral Bravais lattice).

Three *cubic* lattices (simple Γ_c, face-centered Γ_c^f and body-centered Γ_c^v) are defined by one lattice parameter a—the length of conventional cubic cell edge (see Table 2.1 and Fig. 2.1).

The unit cell of a crystal is defined as that volume of space that its translations allow all the space without intervals and superpositions to be covered. The PUC is the minimal volume $V_{\boldsymbol{a}} = \boldsymbol{a}_1[\boldsymbol{a}_2 \times \boldsymbol{a}_3]$ unit cell connected with one Bravais lattice point. Conventional unit cells are defined by two, four and two lattice points, for the base-, face- and body-centered lattices, respectively.

The 32 point groups, enumerated in Table 2.2, are known as crystallographic point groups and are given in Schönflies (Sch) notation. The Sch notation is used for molecules. In describing crystal symmetry the international notation (or Hermann–Mauguin notation) is also of use. In the latter, the point-group notation is determined from the principal symmetry elements: an n fold axis is denoted by the symbol n, a reflection mirror plane by symbol m. The symbols n/m and nm are used for the combinations of an n fold axis with the reflection plane perpendicular to the axis or containing the axis, respectively. Instead of mirror rotation axes, the international system uses inversion axes $\overline{n}$ when a rotation through an angle $2\pi/n$ is followed by the inversion operation. The full international notation of a point group consists of the symbols of group generators. Abbreviated international notations are also used. The Sch and international full and abbreviated notations of crystallographic point groups are given in Table 2.2.

Table 2.2 Crystallographic point groups: schoenflies and international notations

International			International		
Schoenflies	Full	Abbreviated	Schoenflies	Full	Abbreviated
C_n	n	n	D_2	32	32
$C_s(C_{1h})$	m	m	D_4	422	422
$C_i(S_2)$	I	T	D_6	622	622
S_4	$\overline{4}$	$\overline{4}$	D_{2h}	$2/m\ 2/m\ 2/m$	mmm
S_6	$\overline{3}$	$\overline{3}$	D_{3h}	$6m2$	$6m2$
C_{2h}	$2/m$	$2/m$	D_{4h}	$4/m\ 2/m\ 2/m$	$4/mmm$
C_{3h}	$\overline{6}$	$\overline{6}$	D_{6h}	$6/m\ 2/m\ 2/m$	$6/mmm$
C_{4h}	$4/m$	$4/m$	D_{2d}	$42m$	$42m$
C_{6h}	$6/m$	$6/m$	D_{3d}	$32/m$	$3m$
C_{2v}	$2mm$	$2mm$	T	23	23
C_{3v}	$3m$	$3m$	T_h	$2/m3$	$m3$
C_{4v}	$4mm$	$4mm$	T_d	$43m$	$43m$
C_{6v}	$6mm$	$6mm$	O	432	432
D_2	222	222	O_h	$4/m\ 3\ 2/m$	$m3m$

Let us make a linear transformation of PUC translation vectors:

$$\boldsymbol{A}_j = \sum_{i=1}^{3} l_{ji}\boldsymbol{a}_i, \quad |\det \boldsymbol{l}| = L \tag{2.4}$$

where the integer coefficients l_{ji} form the matrix l. Vectors $\boldsymbol{A}_j$ and their integer linear combinations

$$\boldsymbol{A_n} = \sum_{j=1}^{3} n_j \boldsymbol{A}_j \tag{2.5}$$

define for $L > 1$ new, "rare" Bravais lattice for which it is possible to consider various unit cells also. The primitive cell of a new lattice with volume $V_{\boldsymbol{A}} = L \times V_{\boldsymbol{a}}$ will be the so-called large unit cell (supercell), in relation to an initial primitive unit cell. At $L = 1$ transformation (2.4) means transferring to other vectors of the basic translations, to another under the form, but not on the volume primitive cell (see Fig. 2.2).

The so called crystallographic(conventional) unit cell with the translation vectors **a**, **b**, and **c** is defined as the minimal volume unit cell in the form of a parallelepiped constructed on vectors of translations and possessing the point symmetry of the lattice. The conventional unit cell coincides with the primitive unit cell for the simple lattices. The conventional unit cell for the centered lattices consists of integer number of the primitive unit cells forming the supercell of the Bravais lattice.

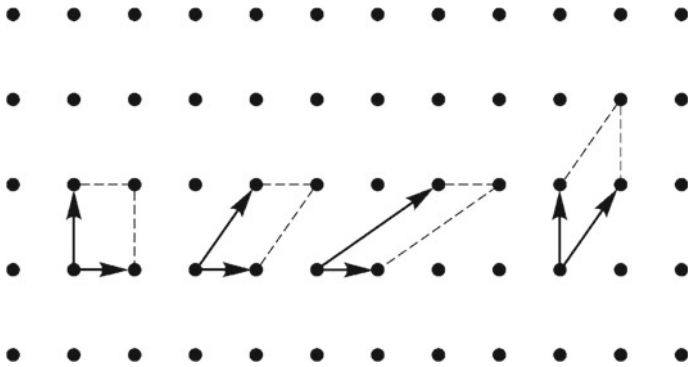

Fig. 2.2 Different primitive unit cell choices

Indeed, for simple lattices P of all syngonies, except for hexagonal (H), the defining primitive unit cell vectors of the basic translations $\boldsymbol{a}_1, \boldsymbol{a}_2, \boldsymbol{a}_3$ can be chosen in such a manner that the primitive cell constructed on them is crystallographic. For the centered lattices the crystallographic unit cells consist of 2, 4 and 2 primitive cells for base-, face- and body-centered lattices, respectively (Fig. 2.1). In the description of symmetry of a trigonal crystal both rhombohedral and hexagonal cells are used. The latter is defined by transformation (2.4) with a matrix

$$l = \begin{pmatrix} 2 & 1 & 0 \\ -1 & 1 & 0 \\ 1 & 1 & 1 \end{pmatrix} \tag{2.6}$$

and $L = 3$. As $L = 3$ for this matrix the hexagonal unit cell contains 3 rhombohedral unit cells.

2.2.2 Symmorphic and Nonsymmorphic Space Groups

As considered in the previous section Bravais lattices define the group T of lattice translations. The general symmetry transformation of a Bravais lattice ("empty" lattice) can be written in the form $t_{\boldsymbol{a}} R$. Operations R transform any translation vector $\boldsymbol{a}$ to another translation vector $R\boldsymbol{a}$ and form point group F^0 (holohedric point group). The combined operation $t_{\boldsymbol{a}} R$ transforms the point of space with radius-vector $\boldsymbol{r}$ to an equivalent point $\boldsymbol{r}' = R\boldsymbol{r} + \boldsymbol{a}$. The identity element of the Bravais lattice symmetry group is $t_{\boldsymbol{0}} E$. The multiplication law for operations $t_{\boldsymbol{a}} R$ is:

$$t_{\boldsymbol{a}_1} R_1 t_{\boldsymbol{a}_2} R_2 \boldsymbol{r} = R_1 R_2 \boldsymbol{r} + \boldsymbol{a}_1 + R_1 \boldsymbol{a}_2 = t_{\boldsymbol{a}_1 + R_1 \boldsymbol{a}_2} R_1 R_2 \boldsymbol{r} \tag{2.7}$$

so that

$$(t_{\boldsymbol{a}}R)^{-1}\boldsymbol{r} = R^{-1}\boldsymbol{r} - R^{-1}\boldsymbol{a} = t_{-R^{-1}\boldsymbol{a}}R^{-1}\boldsymbol{r} \tag{2.8}$$

The operations $t_{\boldsymbol{a}}$ and R do not commute. Indeed

$$t_{\boldsymbol{a}}R\boldsymbol{r} = R\boldsymbol{r} + \boldsymbol{a}; \quad \boldsymbol{a}\boldsymbol{r} = R(\boldsymbol{r} + \boldsymbol{a}) = R\boldsymbol{r} + t_{R\boldsymbol{a}} = t_{R\boldsymbol{a}}R\boldsymbol{r} \tag{2.9}$$

so that

$$t_{\boldsymbol{a}}R = Rt_{R^{-1}\boldsymbol{a}} \tag{2.10}$$

Operations $t_{\boldsymbol{a}}R$ form the space group G^0 of an "empty" Bravais lattice. As lattice translations (also called proper translations) $t_{\boldsymbol{a}}$ and point-symmetry operations R do not commute the space groups $G^0 = T \wedge F^0$ are a semidirect product of the translation and point groups of lattice symmetry. The point symmetry operations R form subgroup F^0 of space group G^0 (such space groups are termed symmorphic space groups). The group T of pure translations forms an invariant subgroup of G^0. As $\boldsymbol{t}_{\boldsymbol{a}}^{-1} = \boldsymbol{t}_{-\boldsymbol{a}}$ we have $(\boldsymbol{t}_{\boldsymbol{a}}R)^{-1}\boldsymbol{t}_{\boldsymbol{a}'}\boldsymbol{t}_{\boldsymbol{a}}R = (\boldsymbol{t}_{\boldsymbol{a}}R)^{-1}\boldsymbol{t}_{\boldsymbol{a}+\boldsymbol{a}'}R = \boldsymbol{t}_{R\boldsymbol{a}'}$.

The group of translations T is a subgroup of the full group symmetry G (space group) that also contains operations of point group F and their combinations with translations.

Any symmetry operation g of a crystal with space group G can be written in the form of $g_i = t_{\boldsymbol{v}_i+\boldsymbol{a}}R_i$ where $\boldsymbol{v}_i$ is the so-called improper (fractional) translation, depending on element R_i of a point group of a crystal and satisfying the requirements described below. The operation g_i transforms the point of space with radius-vector $\boldsymbol{r}$ to an equivalent point $\boldsymbol{r}' = g_i\boldsymbol{r} = R_i\boldsymbol{r} + \boldsymbol{v}_i$. The operations $t_{\boldsymbol{a}}$ are elements of the group of translations T – translations on the corresponding vector of the Bravais lattice.

In crystals, unlike molecules, together with rotations through axes of symmetry and reflections in planes there exist rotations through screw axes (rotation followed by translation along a rotation axis on a part of a vector of translation) and reflections in planes with partial translation in a plane (such planes are termed glide planes). Translation along a screw axis of symmetry cannot be arbitrary and depends on the order of this axis. Let the order of an axis be equal to n (n rotations through axis are equivalent to an identity operation). Thus, n translations along an axis should give a vector of translation of a lattice, i.e. an element of group T that forms a subgroup of a space group of a crystal. Otherwise, rotation through a screw axis will not be an operation of symmetry. For example, rotation through an axis of the fourth order can be accompanied by translation along this axis on a quarter or half of the vector of translation. A similar requirement is imposed on the operation of sliding reflection: two sequential reflections in a glide plane should be equivalent to translation on a vector of a lattice. By definition, any symmetry operation g of a space group transforms any atom of a crystal to equivalent atom. The equivalent atoms are always the atoms of the same chemical identity but the latter can be nonequivalent.

Therefore, fractional (improper) translations can appear only in those crystals that contain several equivalent atoms in the primitive unit cell. The presence of identical atoms in a primitive cell—a condition necessary, but insufficient for the occurrence of fractional translations in the space-group elements. As an example, we consider in Sect. 2.3 the perovskite $CaTiO_3$ structure with three equivalent oxygen atoms in a primitive unit cell and symmorphic space group O_h^1.

The set of fractional translations $\boldsymbol{v}$ in the space-group elements $g = t_{\boldsymbol{v}} R$ depends on the choice of origin (with respect to which the space-group elements are written) and on the labeling of axes (choice of setting) [2].

By definition, the symmorphic space groups contain, together with each element $t_{\boldsymbol{a}} R$, the elements R and $t_{\boldsymbol{a}}$ of the point group F and translation group T, respectively. This means that for a symmorphic space group the origin of the coordinate system may be chosen in such a way that the local (site) symmetry group of origin coincides with the point group of the crystal F. This means that all fractional translations $\boldsymbol{v}$ are zero. Such a choice of origin is accepted for symmorphic space groups in the International tables [2]. For nonsymmorphic space groups some fractional translations will be nonzero for any choice of origin.

The full information on space groups is given in the International Tables for Crystallography [2] and presented on a site [8]. The knowledge of general principles of the space-group designations is necessary to use the crystal-structure databases correctly.

There are three systems of designations of space groups. First, all groups are numbered from 1 upto 230 in order of increasing point symmetry of the corresponding Bravais lattice (syngonies from triclinic to cubic). For fixed syngony the ordering is made over Bravais lattice types and for the fixed Bravais lattice type—over crystal classes (point group F) beginning from the symmorphic space group. In this list, the space groups of "empty" lattices appear as the first ones for fixed type of the lattice. Secondly, the more informative Schönflis symbol is used for space groups. This contains the Schönflis symbol of point group F of a crystal class and the upper numerical index distinguishing space groups within the limits of one crystal class.

Thirdly, the most detailed information on a space group is contained in so-called international (Hermann–Mauguin) designations. In these is there both a symbol of the Bravais lattice type, and a symbol of a crystal class with the indication of the elements of symmetry (axes and planes).

For a designation of types of Bravais lattices the following symbols are used: P simple (or primitive); A, B, C—one face (base-) centered; F—face-centered; I—body-centered. For hexagonal and trigonal (rhombohedral) lattices symbols H and R are accepted.

The centering type symbol is followed by a set of characters indicating the symmetry elements. These sets are organized in the following way.

The two dimensional (plane) lattice symmetry directions are chosen along the conventional unit cell translation vectors **a** and **b**. The one or two entries refer to one or two kinds of the plane lattice symmetry directions.

The one, two or three entries after the centring letter refer to the one, two or three kinds of symmetry directions of the three-dimensional lattice belonging to the

space group. The three-dimensional lattice symmetry directions are chosen along the conventional unit cell translation vectors **a**, **b**, and **c** and occur either as singular directions (as in the monoclinic and orthorhombic crystal systems) or as sets of symmetrically equivalent symmetry directions (as in the higher-symmetrical crystal systems).

The (sets of) lattice symmetry directions and their sequence for the different lattices are summarized in Table 2.3 given in [2] for two-dimensional (plane) and three-dimensional lattices.Only one representative of each set is required. According to their position in this sequence, the symmetry directions are referred to as primary, secondary and tertiary directions.This sequence of lattice symmetry directions is transferred to the sequence of positions in the corresponding Hermann-Mauguin space-group symbols. Each position contains one or two characters designating symmetry elements (axes and planes) of the space group that occur for the corresponding lattice symmetry direction. Symmetry planes are represented by their normals; if a symmetry axis and a normal to a symmetry plane are parallel, the two characters (symmetry symbols) are separated by a slash. The plane lattices have only two lattice symmetry directions as the primary symmetry direction is the rotation point in plane. The plane lattices are discussed in the next section, where the layer groups are considered.

The list of 230 three-periodic space groups is given in Appendix A.

The seven holohedric point groups F^0 and all their subgroups form 32 crystallographic point groups (32 crystalline classes). By combining these 32 point groups with the translation groups of 14 Bravais lattices, 73 symmorphic space groups are obtained, including 14 space groups of the symmetry of empty Bravais lattices (see Table A.1). The remaining 157 space groups include point-symmetry operations with improper (partial) translations, i.e. rotations through screw axes and reflections in glide planes.

There exist only two triclinic space groups (1, 2) with symbols $P1$ (no point-symmetry operations) and $P\overline{1}$ (the inversion operation appears, this is the symmetry group of triclinic Bravais lattice). For monoclinic space groups (3–15) one symbol is needed that gives the nature of the twofold axis (rotation axis 2 or screw axis 2_1) or reflection plane (mirror plane m or glide plane c). Two settings are used for monoclinic space groups: y-axis unique, or, used in Table A.1, z-axis unique. Primitive and base-centered (z-axis unique) monoclinic Bravais lattices symmetry groups are $P2/m$ (10) and $C2/m$ (11), respectively.

The symbols of orthorhombic space groups (16–74) contain the three sets. For symmorphic groups as a symbol of a crystal class the international designation of point groups corresponding to it serves. In Table A.1 conformity of Schönflies's symbols (applied for molecules) and international symbols for point groups of symmetry of crystals is given. For example, $N225$, O_h^5 and $Fm\overline{3}m$—three symbols of the same space group of symmetry of a crystal with NaCl structure.

For nonsymmorphic groups in a symbol of the point group it is underlined also, which axes are screw and which planes are planes of the sliding reflections.

Table 2.3 Lattice symmetry directions for two and three dimensions

	Symmetry direction (position in Hermann-Mauguin symbol)		
	Primary	Secondary	Tertiary
Two dimensions			
Oblique	Rotation point in plane		
Rectangular		[10]	[01]
Square		$\left\{\begin{matrix}[10]\\[01]\end{matrix}\right\}$	$\left\{\begin{matrix}[1\bar{1}]\\[11]\end{matrix}\right\}$
Hexagonal		$\left\{\begin{matrix}[10]\\[01]\\[\bar{1}\bar{1}]\end{matrix}\right\}$	$\left\{\begin{matrix}[1\bar{1}]\\[12]\\[\bar{2}\bar{1}]\end{matrix}\right\}$
Three dimensions			
Triclinic	None		
Monoclinic	[010] ('unique axis b') [001] ('unique axis c')		
Orthorhombic	[100]	[010]	[001]
Tetragonal	[001]	$\left\{\begin{matrix}[100]\\[010]\end{matrix}\right\}$	$\left\{\begin{matrix}[1\bar{1}0]\\[110]\end{matrix}\right\}$
Hexagonal	[001]	$\left\{\begin{matrix}[100]\\[010]\\[\bar{1}\bar{1}0]\end{matrix}\right\}$	$\left\{\begin{matrix}[1\bar{1}0]\\[120]\\[\bar{2}\bar{1}0]\end{matrix}\right\}$
Rombohedral (hexagonal axes)	[001]	$\left\{\begin{matrix}[100]\\[010]\\[\bar{1}\bar{1}0]\end{matrix}\right\}$	
Rombohedral (rhombohedral axes)	[111]	$\left\{\begin{matrix}[1\bar{1}0]\\[01\bar{1}]\\[\bar{1}01]\end{matrix}\right\}$	
Cubic	$\left\{\begin{matrix}[100]\\[010]\\[001]\end{matrix}\right\}$	$\left\{\begin{matrix}[111]\\[1\bar{1}\bar{1}]\\[\bar{1}1\bar{1}]\\[\bar{1}\bar{1}1]\end{matrix}\right\}$	$\left\{\begin{matrix}[1\bar{1}0][110]\\[01\bar{1}][011]\\[\bar{1}01][101]\end{matrix}\right\}$

Directions that belong to the same set of equivalent symmetry directions are collected between braces. The first entry in each set is taken as the representative of that set

For example, for the group of symmetry of rutile structure it is possible to use designations $N136$, D_{4h}^{14} or $P4_2/mnm$, where the symbol 4_2 means that an axis of the fourth order is a screw axis, with translation on half a period along this axis on rotation by angle $\pi/2$, and a symbol n means that two of the four vertical planes are planes of sliding reflection. A more detailed explanation of the principles of international designations can be found in [2].

2.2.3 Orbits of Triperiodic Groups. Wyckoff Positions

To characterize a space group G an analytical description may be employed, which states for a space group the coordinates of all points that are equivalent to a chosen point $\boldsymbol{q}$ with coordinates (xyz). An analytical description of all 230 space groups is given in the International Tables for Crystallography [2] and is based on the fact that for a given space group G all points of a three-dimensional space are subdivided into sets of symmetrically equivalent points called crystallographic orbits (G-orbits).

All the points of a given crystallographic orbit may be obtained from one (arbitrary) G-orbit point $\boldsymbol{q}$ (generating point) by applying to the latter all the operations of space group G. Due to the infinite number of translations (in the model of an infinite crystal) there is an infinite number of points in each space group crystallographic orbit. Any one of the crystallographic orbit points may represent the whole crystallographic orbit, i.e. may be a generating point $\boldsymbol{q}$ of the crystallographic orbit.

All the space group G symmetry operations $t_{\boldsymbol{v}_i+\boldsymbol{a}}R_i = (R_i|\boldsymbol{v}_i + \boldsymbol{a}), i = 1, 2, \ldots, n_{\boldsymbol{q}}$ that satisfy the condition $t_{\boldsymbol{v}+\boldsymbol{a}}R\boldsymbol{q} = \boldsymbol{q}$ (i.e. map a point $\boldsymbol{q}$ onto itself) form a finite site-symmetry group $\mathrm{G}_{\boldsymbol{q}}$ of $\boldsymbol{q}$ with respect to G. This finite size group is called by stabilizer of the G-orbit. The site-symmetry group $\mathrm{G}_{\boldsymbol{q}}$ is isomorphic to one of the 32 crystallographic point groups. If the origin of the space group is at the position $\boldsymbol{q}$, the elements of the site-symmetry group $\mathrm{G}_{\boldsymbol{q}}$ will be of the form $t_{\boldsymbol{0}}R$.

The site-symmetry groups G_j of different points $\boldsymbol{q}_j$ of the same G-orbit are conjugate groups of $\mathrm{G}_1 = \mathrm{G}_{\boldsymbol{q}}$, i.e. the site-symmetry groups G_1 and G_j of points $\boldsymbol{q}_1 = \boldsymbol{q}$ and $\boldsymbol{q}_j$ of the same orbit are related by $g_j\mathrm{G}_1g_j^{-1} = G_j (g_j \in G, g_j \notin G_j, g_j\boldsymbol{q}_1 = \boldsymbol{q}_j)$. For a point $\boldsymbol{q}$ at a general position the site-symmetry group $\mathrm{G}_{\boldsymbol{q}}$ consists of only the identity operation $t_{\boldsymbol{0}}E = (E|\boldsymbol{0})$; the site-symmetry group of a point at a special position includes at least one other symmetry operation in addition to the identity operation.

An infinite number of crystallographic orbits for a given space group G can be subdivided into sets of so-called Wyckoff positions of G. All the crystallographic orbits that have the same set of stabilizers (not only isomorphic but the same!) belong to the same Wyckoff position and can be called by equivalent G-orbits. If the coordinates of the generating point of a crystallographic orbit do not contain free parameters, the corresponding Wyckoff position consists of only one crystallographic orbit; in other cases an infinite number of crystallographic orbits belongs to the same Wyckoff position with variable parameters.

The different Wyckoff positions are the sets of the non-equivalent G-orbits and are labeled by small Roman letters. The maximum number of different Wyckoff positions of a space group is 27 (in the orthorhombic space group D_{2h}^1—$Pmmm$). The various possible sets of Wyckoff positions for all the space groups are given in the International Tables for Crystallography [2] and reproduced on an Internet site [8]. The oriented site-symmetry symbols are employed to show how the symmetry elements at a site are related to the symmetry elements of the crystal lattice. The site-symmetry symbols display the same sequence of lattice symmetry directions as the space-group symbol (see Table 2.3). Sets of equivalent symmetry directions that do

not contribute any element to the site symmetry group are represented by a dot. In this way, the orientation of the symmetry elements at the site is emphasized as illustrated by the several examples in [2]. We consider here one of these examples—the cubic space group $G = Pn\bar{3}n$ (the space group number 222). G-orbit b consists of six points and has 42.2 as its oriented site-symmetry symbol. This cubic site-symmetry symbol displays a tetragonal site symmetry. The position of the dot indicates that there is no symmetry along the four secondary cubic directions. The fourfold axis is connected with one of the three primary cubic symmetry directions and two equivalent twofold axes occur along the remaining two primary directions. Moreover, the group contains two mutually perpendicular (equivalent) twofold axes along those two of the six tertiary cubic directions [110] that are normal to the fourfold axis. Each pair of equivalent twofold axes is given by just one symbol 2. (Note that at the six sites of position 6b the fourfold axes are twice oriented along the simple cubic lattice vector **a**, twice along **b** and twice along **c**.)

As a second example, Table 2.4 lists the oriented site-symmetry symbols for the space group $D_{4h}^{14}(P4_2/m2_1/n2/m)$, the symmetry group of a rutile structure (see Sect. 2.3.3).

For this group there are 11 different Wyckoff positions (11 types of non-equivalent orbits) denoted by letters from a to k. The number of crystallographic orbit points in the primitive unit cell (multiplicity) equals $n_F/n_{\boldsymbol{q}}$ where $n_F = 16$ is the order of the point group D_{4h} and $n_{\boldsymbol{q}}$ is the order of the site symmetry group $G_{\boldsymbol{q}}$. The number of points in a Wyckoff position and their coordinates are given in the International Tables with respect to the conventional unit cell of the lattice (for the space group D_{4h}^{14} with a simple Bravais lattice, the conventional unit cell coincides with the primitive unit cell). Use of the Wyckoff general position $k(xyz)$ points allows one to determine the appropriate Seitz space-group symbols for the coset representatives in the decomposition

$$G = \sum_{i=1}^{n_F} (R_i|\boldsymbol{v}_i)T = \sum_{i=1}^{n_F} t_{\boldsymbol{v}_i} R_i T \tag{2.11}$$

of space group G with respect to the translation group T. In Table 2.4 these symbols are written under the coordinates of the points obtained from the point $\boldsymbol{r}(x, y, z)$ by performing the space-group operation $t_{\boldsymbol{v}}R$. The orientation of the symmetry elements with respect to the tetragonal lattice translation vectors $\boldsymbol{a}_1(a, 0, 0)$, $\boldsymbol{a}_2(0, a, 0)$ and $\boldsymbol{a}_3(0, 0, c)$ is shown in Fig. 2.3. In the point group D_{4h} there are four rotations around twofold axes ($U_x, U_y, U_{xy}, U_{\bar{x}y}$) and four rotations (including the identity operation) around the main fourfold z-axis ($E, C_{4z}, C_{4z}^2 = C_{2z}, C_{4z}^3 = C_{4z}^{-1}$).

The remaining 8 symmetry operations are all products of inversion I with rotations: I, reflections $\sigma_x, \sigma_y, \sigma_{xy}, \sigma_{\bar{x}y}, \sigma_z$ in the planes perpendicular to the corresponding twofold axes and z-axis; mirror rotations S_{4z}^{-1}, S_{4z}. It is seen from Table 2.4 that the elements of the point group $D_{2h}(E, C_{2z}, U_{xy}, U_{\bar{x}y}, I, \sigma_z, \sigma_{xy}, \sigma_{\bar{x}y})$ appear in the cosets decomposition (2.11) without fractional translations. These elements form the site symmetry group of the coordinate system origin placed at the point

Table 2.4 Wyckoff positions of space group 136 ($P4_2/mnm$)

Multipl.	Wyck. letter	Site symm.	Coordinates
16	k	1	$(x, y, z)(-x, -y, z)(-y + 1/2, x + 1/2, z + 1/2)$ $(y + 1/2, -x + 1/2, z + 1/2)(-x + 1/2, y + 1/2, -z + 1/2)$ $(x + 1/2, -y + 1/2, -z + 1/2)(y, x, -z)(-y, -x, -z)$ $(-x, -y, -z)(x, y, -z)(y + 1/2, -x + 1/2, -z + 1/2)$ $(-y + 1/2, x + 1/2, -z + 1/2)(x + 1/2, -y + 1/2, z + 1/2)$ $(-x + 1/2, y + 1/2, z + 1/2)(-y, -x, z)(y, x, z)$
8	j	..m	$(x, x, z)(-x, -x, z)(-x + 1/2, x + 1/2, z + 1/2)$ $(x + 1/2, -x + 1/2, z + 1/2)(-x + 1/2, x + 1/2, -z + 1/2)$ $(x + 1/2, -x + 1/2, -z + 1/2)(x, x, -z)(-x, -x, -z)$
8	i	m..	$(x, y, 0)(-x, -y, 0)(-y + 1/2, x + 1/2, 1/2)$ $(y + 1/2, -x + 1/2, 1/2)(-x + 1/2, y + 1/2, 1/2)$ $(x + 1/2, -y + 1/2, 1/2)(y, x, 0)(-y, -x, 0)$
8	h	2..	$(0, 1/2, z)(0, 1/2, z + 1/2)(1/2, 0, -z + 1/2)$ $(1/2, 0, -z)(0, 1/2, -z)(0, 1/2, -z + 1/2)$ $(1/2, 0, z + 1/2)(1/2, 0, z)$
4	g	m.2 m	$(x, -x, 0)(-x, x, 0)(x + 1/2, x + 1/2, 1/2)$ $(-x + 1/2, -x + 1/2, 1/2)$
4	f	2.m m	$(x, x, 0)(-x, -x, 0)(-x + 1/2, x + 1/2, 1/2)$ $(x + 1/2, -x + 1/2, 1/2)$
4	e	2.m m	$(0, 0, z)(1/2, 1/2, z + 1/2)(1/2, 1/2, -z + 1/2)$ $(0, 0, -z)$
4	d	$\bar{4}$..	$(0, 1/2, 1/4)(0, 1/2, 3/4)(1/2, 0, 1/4)$ $(1/2, 0, 3/4)$
4	c	2/m..	$(0, 1/2, 0)(0, 1/2, 1/2)(1/2, 0, 1/2)(1/2, 0, 0)$
2	b	m.m m	$(0, 0, 1/2)(1/2, 1/2, 0)$
2	a	m.m m	$(0, 0, 0)(1/2, 1/2, 1/2)$

Equivalent sets of Wyckoff positions
(ab)(c)(d)(e)(fg)(h)(i)(j)(k)

of Wyckoff position $a(0, 0, 0)$. The second point of this position (1/2, 1/2, 1/2) is obtained from the first one by application of any symmetry operation from these eight (C_{4z}, C_{4z}^{-1}, S_{4z}, S_{4z}^{-1}, U_x, U_y, σ_x, σ_y) that come into the coset representatives in (2.15) with fractional translation $\boldsymbol{v} = (1/2, 1/2, 1/2)$. We therefore write the space group D_{4h}^{14} (for the case when the Wyckoff position a is taken as the origin) as

$$D_{4h}^{14} = \sum_{R \in D_{2h}} \left[(R|0)\mathrm{T} + (U_x|\frac{1}{2}\frac{1}{2}\frac{1}{2})(R|0)\mathrm{T} \right] \tag{2.12}$$

Considering the full international symbol $P4_2/m2_1/n2/m$ of the space group D_{4h}^{14}, we see that the coset representatives in the decomposition of (2.12) with respect

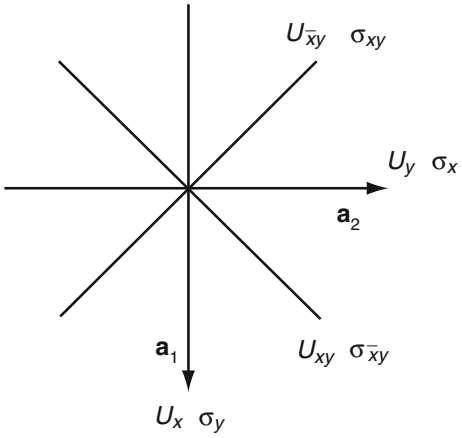

Fig. 2.3 Orientation of the symmetry elements with respect to the tetragonal lattice translations

to the translation group T correspond to this symbol. Indeed, in our example of a tetragonal lattice the three positions in this symbol correspond to the symmetry directions [001]; [100], [010]; and [1$\bar{1}$0], [110], respectively. Rotation through the angle $\pi/2$ about the z-axis is followed by translation along this axis by one-half of the translation vector $\boldsymbol{a}_3$ as is seen from the symbol for the element $(C_{4z}|l/2, 1/2, 1/2)$. The notations 2_1 and 2 for twofold x- and xy-rotation axes agree with the fourfold symbols for $(U_x|\frac{1}{2}\frac{1}{2}\frac{1}{2})$ and $(U_{xy}|000)$. Finally, the notations m, n, m for the reflection planes perpendicular to the corresponding symmetry directions in the international symbol for the space group agree with the Seitz symbols $\sigma_z|000)$, $(\sigma_x|\frac{1}{2}\frac{1}{2}\frac{1}{2})$, and $(\sigma_x y|000)$, respectively. The space group D_{4h}^{14} may also be described by its six generators: three primitive translations $t_{\boldsymbol{a}_i} = (E|\boldsymbol{a}_i)(i = 1, 2, 3)$ of the simple tetragonal lattice and three generating elements $(C_{4z}|1/2, 1/2, 1/2)$, $(U_x|1/2, 1/2, 1/2)$, $(I|0, 0, 0)$.

The coordinates of Wyckoff positions a, b, c, d do not contain free parameters (Table 2.4); those of e, f, g, h positions contain one free parameter; the coordinates of the positions i and j contain two free parameters. This means that an infinite number of Wyckoff sets e–f exists in the crystal but the sets a, b, c, d consist of only one crystallographic orbit. Pairs of Wyckoff positions a–b, f–g, and i–j have isomorphic site symmetry groups (D_{2h}, C_{2v} and C_s, respectively).

As is seen from the Table pairs of Wyckoff positions a–b and f–g have the same point-group symmetry and the same orientation of the symmetry elements with respect to the lattice. The orbits in each pair of these Wyckoff positions form physically equivalent orbits [9]. The physically equivalent orbits have the different sets of the stabilizers and therefore refer to the non-equivalent orbits. It becomes evident if one moves the coordinate system origin from a-point to b-point: the new set of a- and f- orbit stabilizers differs from the former one by the pure translations. At the same time the different origin choice can not change the physical properties of the crystal structure defined by a space group G. For example, the rutile TiO_2 structure with the space group $D_{4h}^{14}(P4_2/m2_1/n2/m)$ and two formula units in the

primitive cell (Z = 2) can be given in two equivalent descriptions: Ti($2a$)O($4f$) or Ti($2b$)O($4g$). The physically equivalent sets of Wyckoff positions for all the space groups can be found on the Internet site [8]. This information will be used in the next section for the description of different crystal lattice structures. This means that if equivalent points are occupied by atoms in the crystal lattice there are possible equivalent descriptions of this structure. For $NbOCl_3$ structure ($Z = 4$) with the same space group two equivalent descriptions can be given: Nb($4f$)O($4g$)Cl($4g$)Cl($8i$) and Nb($4g$)O($4f$)Cl($4f$)Cl($8i$). In this case, the Cl($8i$) position is the same but Cl($4f$) and Cl($4g$) positions interchange.

The difference between oriented site-symmetry groups of different Wyckoff positions is due to different orientations of the elements of the site-symmetry group $G_{\boldsymbol{q}}$ with respect to the lattice. The difference arises when similar symmetry elements (reflections in planes and rotations about twofold axes of symmetry) occur in more than one class of elements of the point group F. Only eleven site groups [$C_2(2)$, $C_s(m)$, $C_{2h}(2/m)$, $C_{2v}(2mm)$, $C_{3v}(3mm)$, $D_2(222)$, $D_3(322)$, $D_{2d}(42m)$, $D_{3d}(32m)$, $D_{2h}(mmm)$, and $D_{3A}(62m)$] can have different orientations with respect to the Bravais lattice. Oriented site-symmetry symbols show how the symmetry elements at a site are related to the symmetry elements of a space group. The site-symmetry symbols display the same sequence of symmetry directions as the space-group international symbol. Sets of equivalent symmetry directions that do not contribute any element to the site-symmetry group $G_{\boldsymbol{q}}$ are represented by a dot. In our example of the space group D_{4h}^{14} the site-symmetry groups G_a, G_b do not contain reflection in the planes σ_x, σ_y (the dot is at the second position) and the site group $G_e = 2.mm$ does not contain reflection in the plane σ_z (a dot is at the first position, Table A.1).

The *Bravais lattice* is an infinite set of points generated by three nonparallel basic translation vectors, such that each point is identical in itself and its surroundings, see Sect. 2.2.1. With each Bravais lattice point may be associated a number of atoms (so-called basis). If atomic coordinates relative to the lattice point are given, together with the lengths and directions of the lattice vectors chosen to define the axes of reference, the complete structure (crystal lattice) is defined. The Internet page [10] currently contains links to about 300 structures in more than 90 of the 230 space groups. A graphical representation as well as useful information about these crystal lattices can be obtained. Other sources of information can be found at various sites linked with [11].

The application of symmetry transformations means splitting all space into systems of equivalent points. The sets of these points for molecules are given in [12]. The sets of equivalent points for crystals are known as Wyckoff positions, irrespective of whether there are atoms in these points or not. The total number of possible splittings of the three-dimensional space of a crystal on systems of equivalent points is finite and for the three-dimensional periodicity case equals 230 (number of space groups of crystals) [2].

The crystal-structure type is specified when one states which sets of Wyckoff positions for the corresponding space group are occupied by atoms. To distinguish different structures of the same type one needs the numerical values of lattice

parameters and additional data if Wyckoff positions with free parameters in the coordinates are occupied. The various ways of filling of equivalent points by atoms generate a huge (hundreds of thousands) number of real crystalline structures.

When describing the crystal-structure type one also gives the value of Z (the number of formula units in the conventional unit cell). This information is, in principle, not necessary as Z is defined by the chemical formula of the compound and the multiplicity of Wyckoff positions in the unit cell occupied by atoms. It is also necessary to take into account that the primitive unit cell of any crystal contains half the number of atoms in a body-centered cell, one-quarter the number in a face-centered, and half the number in an A, B, or C base-centered cell. Trigonal cells contain one-third the number of atoms in the corresponding hexagonal cell. The Wyckoff-site description of a crystal-structure type is also origin dependent (see Sect. 2.2.3). It was shown that equivalent alternatives often arise if two or more sets of sites are physically equivalent (see Sect. 2.2.3). The crystal lattice structure types can be indexed in different ways [10]. In *Strukturbericht* designation symbols A and B are used for monoatomic and diatomic (with equal numbers of atoms of each type) crystal types, symbols C and D—for AB_2 and A_nB_m compounds, respectively. Symbols $E, F, G, \ldots, K$ specify more complex compounds, symbols L, O, and S specify alloys, organic compounds and silicates. *The Pearson symbol* indicates the crystal symmetry and the number of atoms in the conventional unit cell. For example, rocksalt NaCl structure has a face-centered (F) cubic (c) structure with 8 atoms in the cubic (nonprimitive!) unit cell, so it is designated $cF8$. The letters m, o, t, h, c are used in Pearson symbols for monoclinic, orthorhombic, tetragonal, hexagonal, trigonal and cubic Bravais lattice-types, respectively. Pearson symbols do not necessarily specify a unique structure: diamond, NaCl and zincblende $cF8$ structures differ by symbols $A, B1$ and $B3$ (numbers in symbols $B1$ and $B3$ were assigned in roughly the historical order of the study of crystal lattices). *The prototype index* is an index of the various crystal structures by prototype compound (diamond, rocksalt, zincblende structures). Some compounds can be associated with more than one prototype: ZnS compound can be found in zincblende and wurtzite structure. Finally, the *space group index* of a structure can be used. Space groups are listed in the order they appear in the International Tables [2]. As space groups refer to one of seven syngonies the structures are ordered as triclinic (space groups 1 and 2), monoclinic (3–15), orthorhombic (16–74), tetragonal (75–142), trigonal (143–167), hexagonal (168–194) and cubic (195–230). For example, cubic structures correspond to the three Pearson symbols cPn, cFn and cIn.

In the next subsections we give short descriptions of those crystal structures which are basis for the nanotubes and nanowires modeling discussed in Part II Applications. We use space-group and prototype indexes in subsection titles. In the corresponding tables we give for each structure all the mentioned indexes. These tables show that the same compound can be found in different structures (C—diamond, graphite, ZnS—sphalerite, wurtzite, $CaTiO_3$—cubic perovskite, distorted (orthorhombic) perovskite, TiO_2—rutile, anatase). Different structures can have the same Bravais lattice (diamond, NaCl, fluorite, sphalerite) or even the same space group (rocksalt NaCl—fluorite CaF_2). For any structure type we give the prototype, space group (number and

international symbol), number of formula units in the primitive and conventional unit cells, the occupation of Wyckoff positions by atoms and the equivalent Wyckoff-site description.

This possibility of different equivalent descriptions of the crystal-structure types has to be taken into account when the symmetry of electron and phonon states in crystals is analyzed. Furthermore, when preparing the input data for modern computer codes one usually takes crystal-structure data from the database or original papers. These data often contain information about the structure in the form accepted in ICSD (Inorganic Crystal Structure Database), see site [13].

As an example, we take the data for rutile structure given in this database (in brackets some clarifications are given).

COL ICSD Collection Code 82656

DATE Recorded June 26, 1998; updated Nov 30, 1999

NAME Titanium dioxide

MINERAL Rutile—synthetic at 1573 K

REFERENCE Journal of Solid State Chemistry 127 (1996) 240–247

CELL (lattice parameters for simple tetragonal lattice, unit cell volume and number of formula units in conventional cell): $a = 4.594(0)$ $b = 4.594(0)$ $c = 2.959(0)$ $\alpha = 90.0$ $\beta = 90.0$ $\gamma = 90.0$ $V = 62.4$ $Z = 2$

SGR (space group) $P\,4_2/m\,n\,m$ (136)—tetragonal

CLAS (point symmetry group F of crystal) $4/mmm$ (Hermann–Mauguin)—D_{4h} (Schoenflies)

PRS (Pearson symbol) tP6

PARM (Wyckoff positions occupied by atoms and their parameters)

Atom	*No*	*OxStat*	*Wyck*	---*X*---	---*Y*---	---*Z*---
Ti	1	4.000	2*a*	0.	0.	0.
O	1	−2.000	4*f*	0.3047(2)	0.3047(2)	0.

As $Z = 2$ (two formula units in primitive unit cell, the conventional unit cell coincides with the primitive one as the Bravais lattice is simple tetragonal) one needs 2 sets of coordinates for Ti atom (2a) and four sets for O atom (4f). As is seen for each Wyckoff position occupied by an atom there are given coordinates of only one representative. The others can be found on the site [8] for space group 136:

$$2a : (0,0,0)(\tfrac{1}{2},\tfrac{1}{2},\tfrac{1}{2});\ 4f : (x,x,0)(-x,-x,0)(-x+\tfrac{1}{2},x+\tfrac{1}{2},\tfrac{1}{2})(x+\tfrac{1}{2},-x+\tfrac{1}{2},\tfrac{1}{2})$$

In this case, $x = 0.3047$ as follows from the structure data. To the best of our knowledge only computer code CRYSTAL [14] allows one to include the space-group information in input data so that any occupied Wyckoff position can be presented by one representative. In the other computer codes the coordinates of all atoms in the PUC are introduced and the point symmetry of the structure is found by the code itself and used in calculations. From this example it is seen that the necessary information for structures requires the use not only of the database but also IT.

Obviously, atoms of different chemical elements are always nonequivalent in a crystal, i.e. cannot be connected by operations of symmetry. But atoms of one chemical element in a crystal can not to be connected by operations of symmetry. These atoms are not equivalent in a crystal structure even when they occupy the same Wyckoff position with different free parameters (examples of such the structures can be found in the next sections).

In the next section we consider those crystal structures which form the basis of the nanostructures modeling. As will be seen, the different crystal structures can be considered as one or another means of the distribution of the atoms between the Wyckoff positions of the corresponding space group. The crystal structure can also be described by Pearson symbol indicating the crystal lattice type and the number of atoms in the conventional (crystallographic) unit cell. The Bravais lattice type is given at the beginning of Pearson symbol: cP,cI,cF- for cubic lattices, tP,tI- for tetragonal lattices, oP,oS,oF- for orthorhombic lattices, hP and hR for hexagonal and rhombohedral lattices. The number of atoms in the crystallographic unit cell follows the Bravais lattice type.

2.3 Bulk Crystal Structures

2.3.1 Structures with Cubic Lattices

In Table 2.5 we give general information about all the cubic structures under consideration: prototype name, Pearson designation, space group symbol, Wyckoff positions occupations, and possible equivalent description of the structure. All these structures

Table 2.5 Cubic structures

Prototype	Pearsons symbol	Cubic lattice parameter a (Å)	Space group	Wyckoff positions	Equivalent description
Diamond (C)	cF8	3.567	Fd3m(227)	C(8a)	C(8b)
Fluorite (CaF_2)	cF12	5.463	$Fm\bar{3}m$(225)	Ca(4a) F(8c)	Ca(4b) F(8c)
Zincblende (ZnS)	cF8	5.409	$F\bar{4}3m$(216)	Zn(4a) S(4c)	Zn(4b) S(4d)
Perovskite (cubic) ($ATiO_3$)	cP5	3.795	$Pm\bar{3}m$(221)	A(1a) Ti(1b) O(3c)	Ti(1a) A(1b) O(3d)

Equivalent sets of Wyckoff positions for space groups [8]
216 (abcd)(e)(fg)(h)(i)
221 (ab)(cd)(ef)(g)(h)(ij)(kl)(m)(n)
225 (ab)(c)(d)(e)(f)(g)(hi)(j)(k)(l)
227 (ab)(cd)(e)(f)(g)(h)(i)

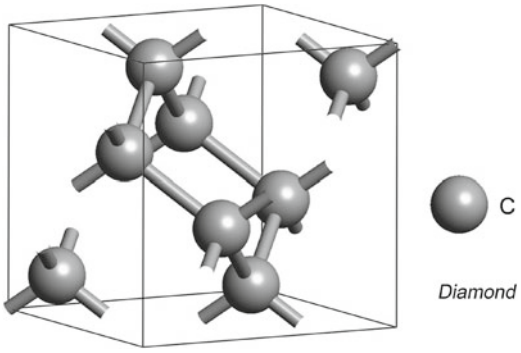

Fig. 2.4 Diamond structure

contain one formula unit in the primitive unit cell ($Z = 1$). For the structures cF with a face-centered cubic lattice the number of atoms is given for the cubic unit cell consisting of four primitive unit cells (this is traditional for crystal-structure databases). In computer calculations only the atoms inside the primitive unit cell have to be included: two atoms for diamond and zincblende, three and five atoms for fluorite and cubic perovskite structures, respectively.

The third column of Table 2.5 contains the numerical values of the cubic lattice parameter a, taken from [13].

Diamond structure (Fig. 2.4) is described by nonsymmorphic space group N227 with the face-centered cubic lattice: the macroscopic cubic symmetry of this crystal appears as the direct product of the first carbon atom site symmetry group T_d and inversion I at the center of C–C bond moving the first carbon to the equivalent second carbon atom in the primitive unit cell.

The coordinates of the carbon atoms can be given in fractions of primitive lattice vectors (these vectors are nonorthogonal for a face-centered cubic lattice) or in Cartesian coordinates. The primitive vectors themselves are usually given in Cartesian coordinates that for cubic lattices are directed along the translation vectors of the conventional (cubic) unit cell (see Fig. 2.1). To describe the diamond structure it is enough to give the numerical value of one parameter—the length of the cubic unit-cell translation vector (cubic lattice parameter a). One can find [10] the following numerical data for diamond structure (for an experimental value of 3.57 Å of the lattice parameter) in the form:

Primitive vectors $\boldsymbol{a}_1 = (0.000, 1.785, 1.785)$ $\boldsymbol{a}_2 = (1.785, 0.000, 1.785)$ $\boldsymbol{a}_3 = (1.785, 1.785, 0.000)$ Volume $= 11.37482325$. These numerical data correspond to the origin choice 2 for the space group N227 in [2] and the diamond structure description C(8a) with the shifted origin.

The space group N225 is the symmetry group of the *fluorite* CaF_2 structure (Ca(4a)F(8c)) (Fig. 2.5).

Some fluorite type compounds form the basis for the nanostructures: TiO_2, ZrO_2.

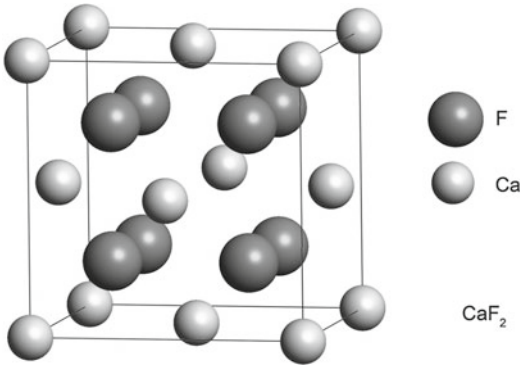

Fig. 2.5 Fluorite structure

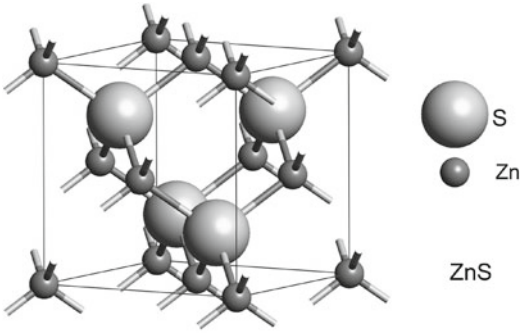

Fig. 2.6 Zincblende structure

The Ca atom in the fluorite structure can be placed also in Wyckoff position b (0.5, 0.5, 0.5). The symmorphic space group N225 is given in [2] for one origin choice (in Wyckoff position a with the site symmetry group O_h).

The point symmetry of the *sphalerite(zincblende)* ZnS (Fig. 2.6) structure is tetrahedral, but the lattice is cubic face-centered.

This structure can be obtained from the diamond structure by exchanging two carbon atoms with Zn and S atoms, so that the operation of interchange of two atoms in the primitive unit cell disappears. The zincblende structure is known for different compounds, which form nanotubes and nanowires (SiC, TiC, GeSi, BN, AlN, GaN). For an equivalent description of the structure the Zn and S atoms can be interchanged.

The *cubic perovskite* $CaTiO_3$ structure (Fig. 2.7) is more complicated and found as the high-temperature modification of different crystals ($SrTiO_3$, $BaTiO_3$, $PbTiO_3$, $SrZrO_3$, $PbZrO_3$). The structure is defined by one simple cubic lattice parameter a. In the cubic perovskite structure the Ti–O distance is equal to one half of the translation vector length. In the equivalent structure description (when Ca and Ti atoms are interchanged) the three oxygen atoms positions need to be taken as (0.5, 0.5, 0), (0.5, 0, 0.5) and (0, 0.5, 0.5).

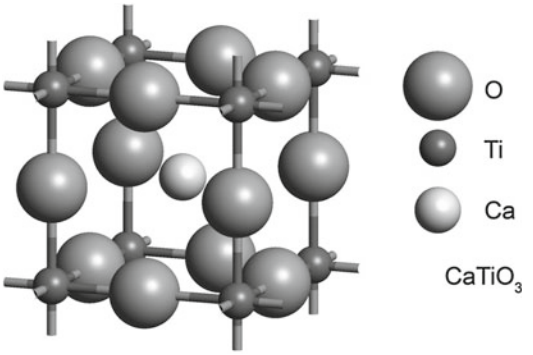

Fig. 2.7 Perovskite structure

The considered different cubic structures are defined by one numerical parameter—the cubic lattice constant. This is due to the fact that in these structures atoms occupy Wyckoff positions that have no free parameters. The definition of the more complicated structures requires the knowledge of both the lattice constants and the numerical values of the free parameters for the free-parameter-dependent Wyckoff positions occupied by atoms.

2.3.2 Structures with Tetragonal and Orthorhombic Lattices

In Table 2.6 we give general information about the tetragonal and orthorhombic crystals, being the basis of the nanostructures formation: two modifications (rutile and anatase) of titanium dioxide, zirconia, ferroelectric phases of the titanates, vanadium pentoxide and lepidocrocite. Tetragonal (a,c) and orthorhombic (a,b,c) lattice parameters are given in Åin the third column of Table 2.6.

Both TiO_2 modifications contain 6 atoms (two formula units) in the primitive cell.

The *rutile structure* (Fig. 2.8) belongs to the $P4_2/mnm$ nonsymmorphic space group.

The unit cell of the primitive tetragonal lattice is defined by the lattice vectors $\boldsymbol{a}_1 = \boldsymbol{a}_2$ (in the xy-plane) and $\boldsymbol{c}$ (along z-axis). The rotations through a fourth-order axis are followed by the improper translations along the z-axis of one half of the $\boldsymbol{c}$-vector length to ensure transformation of any of the oxygen atoms to another one, see Table 2.4. As is seen from Table 2.6 two Ti atoms of the primitive cell occupy Wyckoff position a(000;1/2, 1/2, 1/2), four oxygen atoms occupy Wyckoff position f with one free parameter v: $(\pm(v, v, 0); \pm(v + 1/2, 1/2 - v, 1/2))$. The Wyckoff positions coordinates are given in units of a, a, c. Thus, the rutile structure is defined by three parameters: a, c and v. The numerical data for rutile structure are given in [10].

The *anatase* structure (Fig. 2.9) belongs to the I4/amd nonsymmorphic space group.

Table 2.6 Tetragonal and orthorhombic structures

Prototype	Pearsons symbol	Lattice parameters (a,c) or (a,b,c) in Å	Space group	Wyckoff positions	Equivalent description
Rutile ($Ti(Sn)O_2$, MgF_2)	tP6	4.587.2.959	$P4_2/mnm(136)$	Ti(Mg)(2a)	Ti(Mg)(2b)
				O(F)(4f)	O(F)(4g)
Anatase (TiO_2)	tI12	3.764,9.502	$I4_1/amd(141)$	Ti(2a)	Ti(2b)
				O(4e)	O(4e)
Zirconia (ZrO_2)	tP6	3.598,5.165	$P4_2/nmc(137)$	Zr(2a)	Zr(2b)
				O(4d)	O(4d)
Strontium titanate ($SrTiO_3$)	tI14	5.513,7.807	I4/mcm(140)	Sr(4b)	Sr(4b)
				Ti(4c)	Ti(4c)
				O_1(4a)	O_1(4a)
				$O_2(8h)$	$O_2(8h)$
Barium(Lead) titanate ($Ba(Pb)TiO_3$)	tp5	4.318,4.106	P4mm(99)	Ba(Pb)(1a)	Ba(Pb)(1b)
				Ti(1b)	Ti(1a)
				O_1(1b)	O_1(1a)
				O_2(2c)	O_2(2c)
Barium titanate ($BaTiO_3$)	oS10	4.009,5.621,5.639	Amm2(38)	Ba(2a)	Ba(2b)
				Ti(2b)	Ti(2a)
				$O_1(2a)$	O_1(2b)
				O_2(4e)	O_2(4d)
Vanadium pentoxide (V_2O_5)	oP14	11.544,3.571,4.383	Pmmn(59)	V(4f)	V(4f)
				$O_1(4f)$	$O_1(4f)$
				O_2(4f)	O_2(4f)
				O_3(2b)	O_3(2a)
Lepidocrocite (FeO(OH))	oS16	3.072,12.516,3.873	Cmcm(63)	Fe(4c)	Fe(4c)
				O1(4c)	O1(4c)
				O_2(4c)	O_2(4c)
				H(8f)	H(8f)

Equivalent sets of Wyckoff positions for space groups [8]
136 (ab)(c)(d)(e)(fg)(h)(i)(j)(k)
137 (ab)(c)(d)(e)(f)(g)(h)
140 (a)(b)(c)(d)(e)(f)(g)(h)(i)(j)(k)(l)(m)
141 (ab)(cd)(e)(f)(g)(h)(i)
99 (ab)(c)(d)(f)(e)(g)(h)(ij)(k)(l)(m)(n)(o)
63 (ab)(c)(d)(e)(f)(g)(h)
59 (ab)(cd)(e)(f)(g)
38 (ab)(c)(de)(f)

The tetragonal unit cell of a body-centered tetragonal lattice is defined by the lattice vectors $\boldsymbol{a}_1 = \boldsymbol{a}_2$ (in the xy-plane) and $\boldsymbol{c}$ (along the z-axis) and contains 2 primitive unit cells. To describe the primitive unit cell the translation vectors $\boldsymbol{a}_1(a, 0, 0), \boldsymbol{a}_2(0, a, 0), \boldsymbol{a}_3(1/2a, 1/2a, 1/2c)$ are used. As is seen from Table 2.6. two Ti atoms of the primitive cell occupy Wyckoff position 2a(0, 0, 0; 0, 1/2, 1/4),

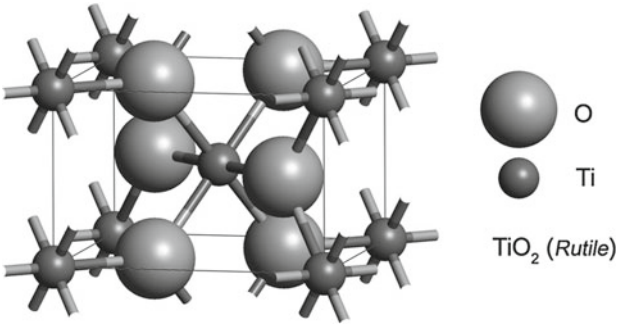

Fig. 2.8 Rutile structure

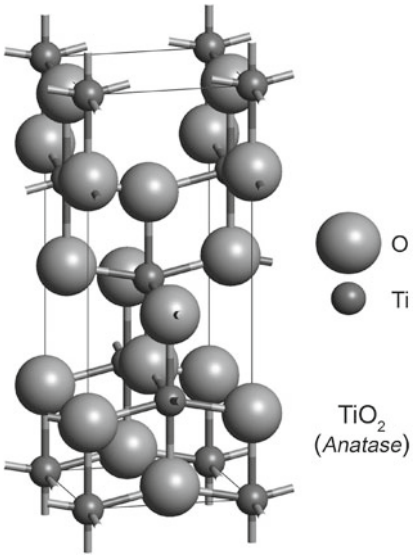

Fig. 2.9 Anatase structure

four oxygen atoms occupy Wyckoff position 4e $(0, 0, v; 1/2, 0, -v+1/2; 0, 1/2, v+1/4; 1/2, 1/2, -v+1/2)$. The anatase structure is defined by three parameters: a, c, v. The numerical data for anatase structure are given in [10]. These data correspond to the coordinate system origin shifted by $(1/8, -1/8, -1/4)$ (in the units of primitive translations), in comparison with the origin choice made in [2].

Zirconia is an oxide which exhibits a large variety of polymorphs. The properties of bulk ZrO_2 are well studied experimentally [15]. It was established that ZrO_2 has three zero-pressure modifications. At high temperatures (t $\geq$2,350 C), zirconia adopts a cubic fluorite structure, see Table 2.5 while at low temperatures (t$\leq$1,150 C), a monoclinic baddeleyite ($P2_1/c$) structure is preferred thus representing a ground state of zirconia. A tetragonal zirconia phase (see Fig. 2.10) belongs to the nonsymmorphic space group $P4_2/nmc$ and exists at intermediate temperatures; it can be

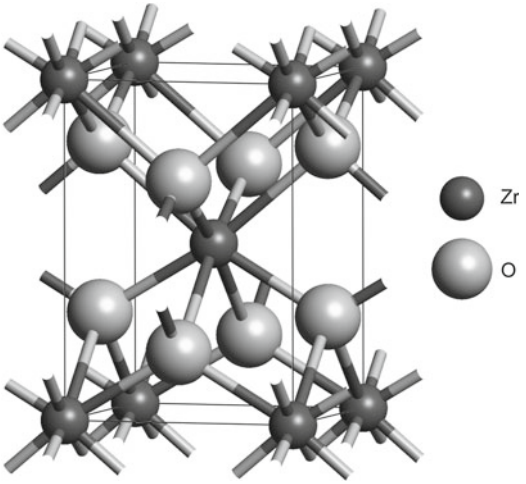

Fig. 2.10 Tetragonal zirconia structure

viewed as a simple perturbation of the cubic fluorite phase, see Fig. 2.5 in which the oxygen atoms are displaced alternately along the 4_2 axis by 0.2 Å. The relative stability of ZrO_2 zero pressure phases can be influenced by the crystallite size. It is well known that small zirconia particles suspended in a host matrix do not transform from tetragonal to monoclinic, even well below the bulk transition temperature unless subjected to an external stress field or heating above 700 K [16]. Moreover, Wang et al. [17] have found that tetragonal zirconia can be obtained in particles with sizes below 40 nm at room temperature. Structure studies [18] of ZrO_2 deposition on the amorphous silica have shown that the thin ZrO_2 film growth starting from the formation of amorphous phase proceeds with preferential growth of crystallites of tetragonal and cubic structures in the direction [001]. The structure analysis of the fabricated zirconia nanotubes (ZNT) also gives evidence that the small particle size may stabilize the virtually unstable phases. This means that ZNT can possess cubic, tetragonal or orthorhombic morphology.

The unit cell of the tetragonal zirconia primitive tetragonal lattice is defined by the lattice vectors $\boldsymbol{a}_1 = \boldsymbol{a}_2$ (in the xy-plane) and $\boldsymbol{c}$ (along z-axis). The rotations through a fourth-order axis are followed by the improper translations along the z-axis of one half of the $\boldsymbol{c}$-vector length to ensure transformation of any of the oxygen atoms to another one. As is seen from Table 2.6 two Zr atoms of the primitive cell occupy Wyckoff position $a(3/4, 3/4, 3/4; 1/4, 3/4, 1/4)$, four oxygen atoms occupy Wyckoff position d with one free parameter v: $(1/4, 1/4, v;\ 1/4, 1/4, v + 1/2;\ 3/4, 3/4, -v;\ 3/4, 3/4, -v + 1/2)$. The Wyckoff positions coordinates are given in units of a, a, c, the origin choice 2 is chosen, see [8]. Thus, the tetragonal zirconia structure is defined by three parameters: a, c and v. The numerical data for tetragonal zirconia structure are given in [13].

The structure of the $SrTiO_3$ low temperature antiferrodistortive (AFD) phase (Fig. 2.11b) belongs to the nonsymmorphic space group I4/mcm with the

body-centered tetragonal lattice and contains two formula units in the primirive unit cell (four formula units in the conventional cell of the body centered tetragonal lattice). The lattice parameters are: a = 5.511 Å, c = 7.796 Å.

The Sr and Ti atoms atom occupy Wyckoff positions 4b(0, 0.5, 0.25) and 4c (000), respectively. The nonequivalent oxygen atoms O_1 and O_2 occupy Wyckoff positions 4a(0, 0, 0.25) and 8h(0.2451, 0.2451.0), respectively. The structure is defined by two tetragonal lattice parameters (lengths of $\boldsymbol{a}_1 = \boldsymbol{a}_2$ primitive translations and of $\boldsymbol{c}$—translation vector of the tetragonal unit cell containing two primitive cells) and v-parameter defining the positions of O_2 atoms. The numerical data for this structure are given [10]. The primitive translation vector $\boldsymbol{a}_3$(1/2,1/2,1/2) is given in units of a, a, c.

$BaTiO_3$ (BTO) crystallizes either in the perovskite crystal structure or in its hexagonal modification. The crystal structure of the perovskite polymorph changes from cubic ($Pm\bar{3}m$) to tetragonal (P4 mm) at 403 K, then to orthorhombic (Amm2) at 278 K, and to rhombohedral (R3 m) at 183 K [19]. The cubic phase is paraelectric and the other phases are ferroelectric. In all four phases, there is one BTO formula unit in the unit cell so that phase transitions to ferroelectric phases are due to the soft mode

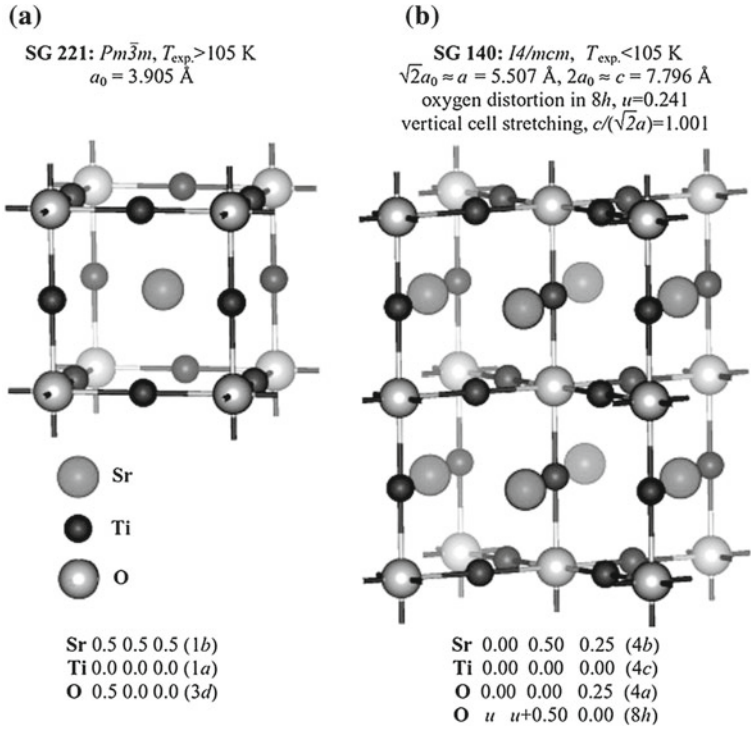

Fig. 2.11 Cubic (**a**) and tetragonal AFD (**b**) $SrTiO_3$ structures. Online (*Green balls*) Sr atoms, (*gray balls*) Ti, and (*red balls*) O atoms

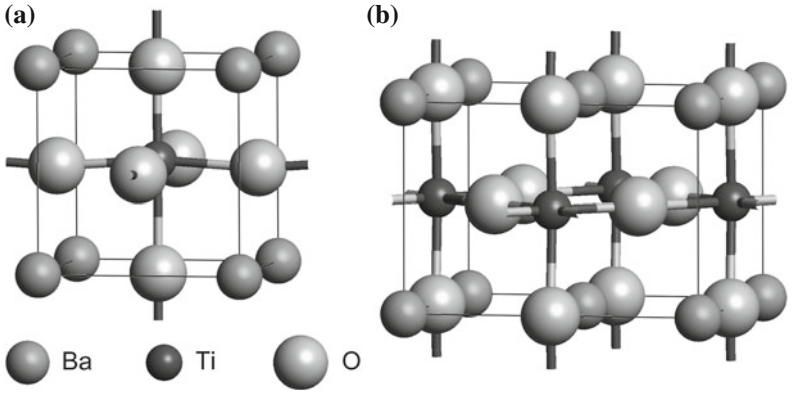

Fig. 2.12 Tetragonal (**a**) and Orthorhombic (**b**) Barium titanate structures

at Γ point of cubic BTO Brillouin zone (BZ). Lead titanate $PbTiO_3$ (PTO) is one of the simplest ferroelectrics with the perovskite structure and undergoes successive phase transitions from tetragonal to monoclinic to rhombohedral under pressure at low temperetures.

The structure of $BaTiO_3$ and $PbTiO_3$ zero-pressure ferroelectric tetragonal phases (Fig. 2.12a) belongs to the symmorphic space group P4mm with the simple tetragonal lattice and contains one formula unit in the primitive unit cell. The structure is defined by two tetragonal lattice parameters (lengths of $\boldsymbol{a}_1 = \boldsymbol{a}_2$ primitive translations and $\boldsymbol{c}$) and three v-parameters defining the positions of the Ti, O_1 and O_2 atoms. The lattice parameters are: a = 3.9988 Å, c = 4.0222 Å and a = 3.9009 Å, c = 4.1526 Å, for BTO and PTO, respectively [13]. The unit cell volumes are 64.32 (BTO) and 63.19 (PTO). The Ba (Pb) and Ti atoms atom occupy Wyckoff positions 1a(0, 0, 0) and 1b(0, 0, u_{Ti}), respectively. The nonequivalent oxygen atoms O_1 and O_2 occupy Wyckoff positions 1b(0, 0, u_1) and 2c(1/2, 0, u_2), (0, 1/2, u_2) respectively. The numerical data for these parameters taken from [13] are the following: $v_{Ti} = 0.5021(0.5340)$ for BTO(PTO); $v_1 = -0.0153(0.1120)$ for BTO(PTO); $v_2 = 0.5130(0.6220)$ for BTO(PTO).

Table 2.6 also gives the information about the orthorhombic structures of $BaTiO_3$, vanadium pentoxide V_2O_5 and lepidocrocite. The vanadium pentoxide contains two formula units V_2O_5 in the primitive cell (Z = 2) and forms nanotubes, which are not considered in this book. The lepidocrocite is used for TiO_2-based nanotube modeling after the change of iron atoms by titanium atoms and removing hydrogen atoms (see Chap. 7).

2.3.3 Structures with Hexagonal Lattices

In this section we consider hexagonal structures (graphite, BN honeycomb, MoS_2, titanium disulfide and diboride, ZnS (wurtzite), see Figs. 2.13, 2.14, 2.15, 2.16, 2.17 and 2.18, respectively).

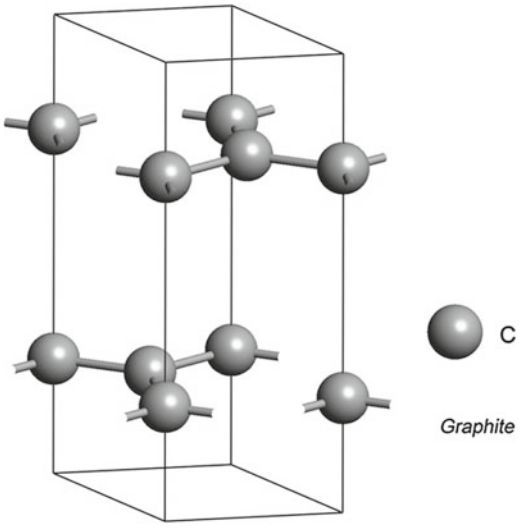

Fig. 2.13 Graphite structure

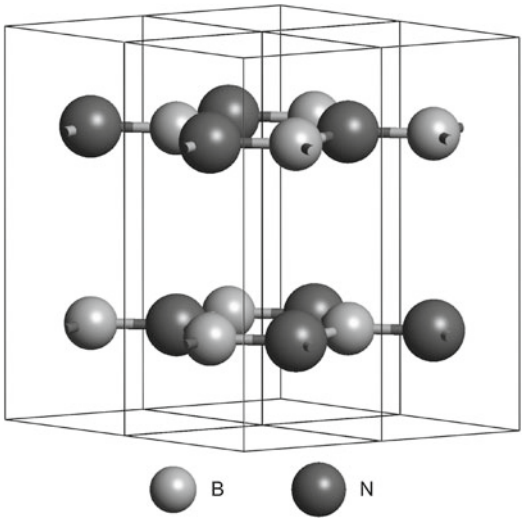

Fig. 2.14 Hexagonal BN structure

Table 2.7 shows that the graphite, hexagonal boron nitride BN and molibdenum disulfide MoS_2 structures, see Figs. 2.13, 2.14 and 2.15, belong to the nonsymmorphic space group $P6_3/mmc$. The symmorphic space groups $P\bar{3}m1(164)$ and $P6/mmm(191)$ describe the symmetry of TiS_2 and TiB_2 crystals, respectively. Wurtzite and α-quartz SiO_2 structures symmetry is given by nonsymmorphic groups $P6_3\,mc(186)$ and $P3_121(152)$, respectively. The rhombohedral structure of α boron

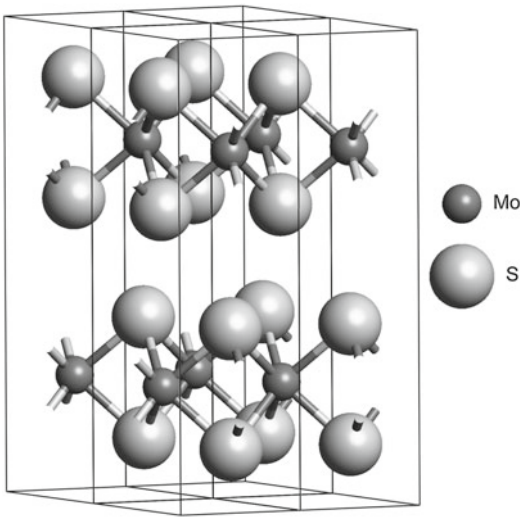

Fig. 2.15 Molybdenite MoS_2 structure

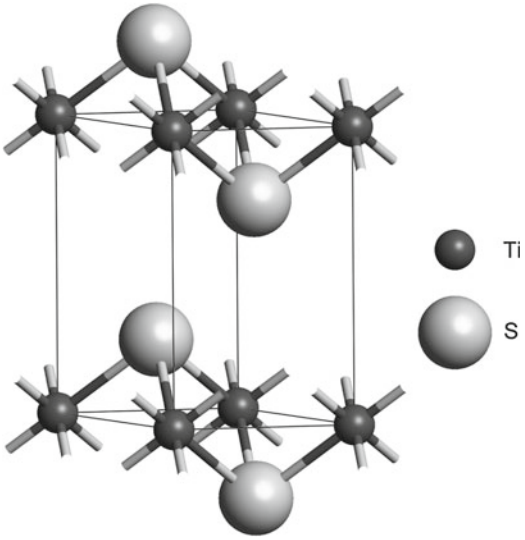

Fig. 2.16 Titanium disulfide TiS_2 structure

(symmorphic space group $R\bar{3}m(166)$) is given in the hexagonal setting (3 primitive unit cells in the hexagonal cell).

The unit cell of the hexagonal lattice is defined by the lattice vectors $\boldsymbol{a}_1 = \boldsymbol{a}_2$ (in the xy-plane) and $\boldsymbol{c}$ (along z-axis). The rotations through a six-order axis are followed by the improper translations along the z-axis of one half of the $\boldsymbol{c}$-vector

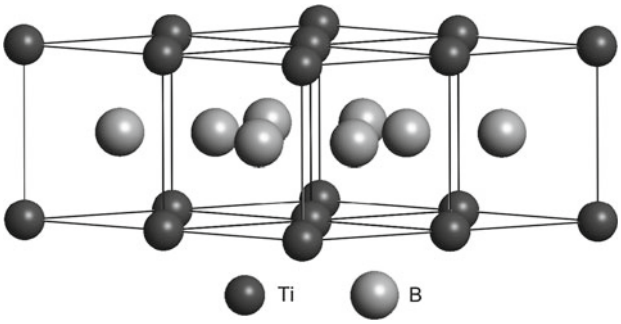

Fig. 2.17 TiB_2 structure

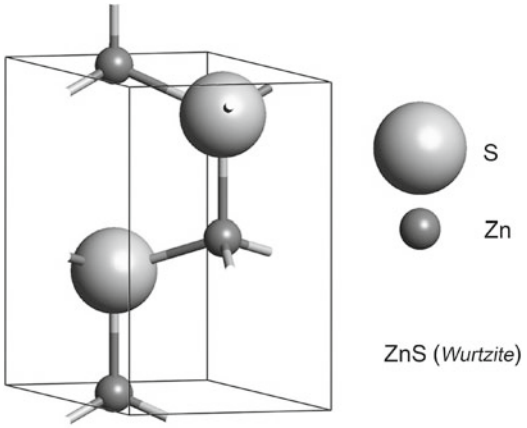

Fig. 2.18 Wurtzite structure

length. Belonging to the same space group, the three structures in consideration differ by the atom distribution over Wyckoff positions in the primitive unit cell of the hexagonal lattice. As it is seen from Table 2.7, the following Wyckoff positions of the space group $P6_3/mmc$ are used to describe the structures in consideration: 2b (0 0 1/4, 0 0 3/4), 2c (1/3 2/3 1/4, 2/3 1/3 3/4), 2d (2/3 1/3 1/4, 1/3 2/3 3/4) and 4f (1/3 2/3 z, 2/3 1/3 z+1/2, 2/3 1/3 −z, 1/3 2/3 −z+1/2). All the coordinates of Wyckoff positions are given in units of the three hexagonal lattice parameters.

In graphite structure four carbon atoms atoms occupy two nonequivalent Wyckoff positions 2b and 2c. The hexagonal lattice parameters are a = 2.4642 Å, c = 6.7114 Å, the unit cell volume is 35.29 [13]. The graphite structure consists of atomic layers separated by a distance larger than the interatomic distance in one layer. Therefore, the one-layer approximation (graphene layer) is used in nanotubes modeling: only two carbon atoms in the primitive cell of the plane hexagonal lattice are included in the graphene structure. In BN_{hex} structure two boron atoms and two nitrogen atoms occupy nonequivalent Wyckoff positions 2c and 2d. The hexagonal lattice

Table 2.7 Hexagonal structures

Prototype	Pearsons symbol	Lattice constants (a,c) in Å	Space group	Wyckoff positions	Equivalent description
Graphite C	hP4	2.464, 6.711	$P6_3/mmc(194)$	C(2b)	–
				C(2c)	
BN honeycomb	hP4	2.489, 6.561	$P6_3/mmc(194)$	B(2c)	B(2d)
				N(2d)	N(2c)
Molybdenite 2H (MoS_2)	hP6	3.169, 12.324	$P6_3/mmc(194)$	Mo(2c)	Mo(2d)
				S(4f)	S(4f)
Titanium Disulfide (TiS_2)	hP3	3.312, 5.449	$P\bar{3}m1(164)$	Ti(1a)	Ti(1b)
				S(2d)	S(2d)
Titanium Diboride (TiB_2)	hP3	3.024, 3.124	$P6/mmm(191)$	Ti(1a)	Ti (1b)
				B(2d)	B(2c)
Wurtzite (ZnS)	hP4	3.777, 6.188	$P6_3mc(186)$	Zn(2b)	–
				S(2b)	
Alpha quartz (SiO_2)	hP9	4.913, 5.405	$P3_121(152)$	Si(3a)	Si(3b)
				O(6c)	O(6c)
Alpha Boron (B)	hR12	4.906, 12.566	$R\bar{3}m(166)$	B_1(18h)	–
				B_2(18h)	

Equivalent sets of Wyckoff positions for space groups [8]
194 (a)(b)(cd)(e)(f)(g)(h)(i)(j)(k)(l)
164 (ab)(c)(d)(ef)(gh)(i)(j)
191 (ab)(cd)(e)(fg)(h)(i)(jk)(lm)(n)o(pq)
186 (a)(b)(c)(d)
152 (ab)(c)
166 (ab)(c)(de)(fg)(h)(i)

parameters are a = 2.4860 Å, c = 6.5160 Å, the unit cell volume is 34.88 [13]. As the graphite BN_{hex} consists of atomic layers separated by a distance larger than the interatomic distance in one layer. Therefore, the one-layer approximation is used in BN nanotubes modeling: only two atoms (boron and nitrogen) in the primitive cell of the plane hexagonal lattice are included in the structure. In molibdenum disulfide MoS_2 structure two molibdenum atoms and four sulfur atoms occupy Wyckoff positions 2c and 4f, respectively. The hexagonal lattice parameters are a = 3.1690 Å, c = 12.324 Å, the unit cell volume is 107.18 [13]. The sulfur atom position is defined by parameter z = 0.621. The layered structure of MoS_2 is used in nanotubes modeling.

The structure of titanium disulfide (TiS_2) belongs to the symmorphic space group $P3m1$ and contains one furmula unit in the primitive unit cell of the hexagonal lattice, see Fig. 2.16. Metal and sulfur atoms occupy parameter-free Wyckoff positions 1a (0 0 0) and 2d (1/3 2/3 1/2, 2/3 1/3 1/2), respectively. The structure of aluminium and titanium diborides (AlB_2,TiB_2) belongs to the symmorphic space group $P6/mmm$ and contains one furmula unit in the primitive unit cell of the hexagonal lattice, see Fig. 2.17. Metal and boron atoms occupy parameter-free Wyckoff

positions 1a (0 0 0) and 2d (1/3 2/3 1/2, 2/3 1/3 1/2), respectively. The structure is defined by the lengths a and c of the hexagonal lattice translation vectors $\boldsymbol{a}_1 = \boldsymbol{a}_2$ (in the xy-plane) and $\boldsymbol{c}$ (along z-axis) for AlB_2 (TiB_2): a = 3.016(3.024) Å, c = 3.268(3.154) Å, V = 25.74(24.98) [13].

The wurtzite structure of ZnS, see Fig. 2.18, is the hexagonal analog of the zincblende (sphalerite) structure of ZnS (see Sect. 2.3.1) and belongs to the nonsymmorphic space group $P6_3mc$ with a hexagonal lattice. The boron, aluminium and gallium nitrides (BN, AlN and GaN) and ZnO bulk crystals have the wurtzite structure. The primitive unit cell contains two formula units, two metal and two nitrogen (oxygen) atoms occupy the same Wyckoff position 2b(1/3, 2/3, z; 2/3, 1/3, z+1/2) with the different values of internal parameter z for metal atom and for sulfur atom. Thus, the wurtzite structure is defined by 4 parameters—two lattice and two internal ones. The numerical values of the structure data from [13] are the following for BN (AlN,GaN): a = 2.538 Å(3.115 Å, 3.221 Å); c = 4.197 Å(4.988 Å, 5.237 Å); V = 23.41(41.91, 47.05). The internal parameter $z_1 = 0$ for all the three structures, the internal parameter z_2 =0.373(0.305,0.378). The wurtzite structure can also be described in hexagonal axes.

The figures showing the α-Boron and α-quartz structures are given in Chap. 4 when the based on these structures nanotubes are considered.

2.4 Diperiodic (Layer) Symmetry Groups of Nanolayers

2.4.1 Two Factorizations of the Layer Groups

The diperiodic groups are the symmetry groups of the three-dimensional systems with translational periodicity in two directions. The diperiodic groups belong to the so-called subperiodic groups. The latter include 7 frieze groups (two-dimensional groups with one-dimensional translations), 75 rod groups (three-dimensional groups with one-dimensional translations), and 80 layer groups (three-dimensional groups with two-dimensional translations). The information presented about the subperiodic groups in [5] is in the same format and consists of the same content as that provided in [2] for space groups G. There are 80 diperiodic groups; 17 of them are plane, i.e. describe the symmetry of the two-dimensional systems with translational periodicity in two directions.

Diperiodic groups are subgroups of the three dimensional triperiodic space groups G. In the *single-slab* model a crystal with a surface is approximated by a slab of finite thickness. The symmetry group of this model allows the existence of symmetry operations that move the atoms out of the plane of the layer but bring them into positions occupied by other atoms of the slab. These are diperiodic groups (DG) in three dimensions. They are also called the layer groups. These groups also describe the symmetry of thin films. In layered crystals the interaction between the nearest layers is usually weaker than that between nearest atoms in the same layer plane.

Therefore, the slab model is a convenient approximation for such crystals. Layer groups describe the symmetry of this model.

Under standard crystallographic approach any diperiodic group (DG) may be presented in the form

$$\mathrm{DG} = \mathrm{T}(\mathbf{a})\mathrm{F} \tag{2.13}$$

where F is a finite system of representatives of DG decomposition in cosets of two-dimensional translation group T(**a**). Choice of representatives in not unique and any specific set F is, in general, not a subgroup of DG. However, since DG is the extension of G by T(a), F can be interpreted as a group with multiplication modulo pure two-dimensional translations. Factorization (2.13) of diperiodic group DG will be referred to as standard and is used in [5].

Any element of the layer group may be written as $(R_i|\boldsymbol{v}_i + \boldsymbol{a}_n)$, where $\boldsymbol{a}_n$ and $\boldsymbol{v}_i$ are lattice and improper translations, $i = 1, 2$.

Let $\boldsymbol{a}_3$ be a vector that does not lie in the layer plane. A set of elements $(E|n_3\boldsymbol{a}_3)$ forms a group T_3 of one-dimensional translations. Consider the elements

$$(R_i|\boldsymbol{v}_i + \boldsymbol{a}_n)(E|n_3\boldsymbol{a}_3), \quad (R_i|\boldsymbol{v}_i + a_n) \in \mathrm{DG}, i = 1, 2, \ (E|n_3\boldsymbol{a}_3) \in T_3 \tag{2.14}$$

The set (2.14) of symmetry operations contains a group of three-dimensional translations $(E|\boldsymbol{a}_n + n_3\boldsymbol{a}_3) \in \mathrm{T}$. The set (2.14) is some space group provided the translational symmetry (the group T) is compatible with the point symmetry $\mathrm{F_{DG}}$ of the layer group DG. This condition is fulfilled if the vector $\boldsymbol{a}_3$ is chosen perpendicular to the layer plane. Indeed, the translations $(E|\boldsymbol{a}_n) \in T^{(2)} \subset \mathrm{T}$ are compatible with $\mathrm{F_{FD}}$ as they are the elements of DG. The compatibility of the translations $(E|n_3\boldsymbol{a}_3) \in T_3$ with point group $\mathrm{F_{FD}}$ follows from the fact that the rotations (proper and improper) from DG transform the layer into itself and, therefore, the vector perpendicular to the layer is transformed into a vector also perpendicular to the layer. Thus, the set of elements (2.14) forms one of the three-periodic space groups G. Moreover, the translational group T_3 is invariant in G: with the translation $(E|\boldsymbol{a}_3)$ it contains also the translation $(E|R_i\boldsymbol{a}_3)$ for any R_i from (2.14). Therefore, the group G may be expressed as a semidirect product

$$\mathrm{G} = T_3 \wedge \mathrm{DG} \tag{2.15}$$

and be decomposed into cosets with respect to T_3

$$\mathrm{G} = \sum_i (R_i|\boldsymbol{v}_i + \boldsymbol{a}_n)T_3, \quad (R_i|\boldsymbol{v}_i + \boldsymbol{a}_n) \in \mathrm{DG}, \ i = 1, 2 \tag{2.16}$$

Thus, subperiodic layer group DG is isomorphic to factor group G/T_3. A relationship between factor groups of space groups and subperiodic groups is studied in [20, 21].

In [5] a relationship is considered between space (triperiodic) and subperiodic groups: given a crystal of a specific space-group symmetry and a plane transecting

the crystal, one can enquire as to what is the layer subgroup of the space group that leaves this plane invariant. The physical motivation for answering this question is clear as this problem arises, for example, in the surface modeling by a single slab. The information about subperiodic groups is followed in [5] by the scanning tables in which the layer symmetries of sectional planes are tabulated for all crystallographic orientations and for all positions (locations) of these planes. These tables also contain explicitly the orbits of these planes (an orbit is defined as a set of planes connected by the symmetry operations) and implicitly, via the so-called "scanning groups", information about the rod symmetries of straight lines that penetrate through the crystal.

Both the short and the full DG Hermann-Mauguin symbols consist of a letter indicating the centring type of the conventional cell (primitive P or centered rectangular C) and a set of characters indicating symmetry elements of the subperiodic group. The one or three entries after the centring letter refer to the one or three kinds of symmetry directions of the conventional crystallographic basis. Symmetry directions occur either as singular directions or as sets of symmetrically equivalent symmetry directions. Only one representative of each set is given. The sets of symmetry directions and their sequence in the Hermann-Mauguin symbol are summarized in Table 2.8.

Each position in the Hermann-Mauguin symbol contains one or two characters designating symmetry elements, axes and planes that occur for the corresponding crystallographic symmetry direction. Symmetry planes are represented by their normals; if a symmetry axis and a normal to a symmetry plane are parallel, the two characters are separated by a slash. Crystallographic symmetry directions that carry no symmetry elements are denoted by the symbol 1, e.g. P3m1 (DG69). If no misinterpretation is possible, entries 1 at the end of the symbol are omitted, as in p4 (DG49) instead of P411. Subperiodic groups that have in addition to translations

Table 2.8 Sets of symmetry directions and their positions in the Hermann-Mauguin symbol

	Symmetry direction (position in Hermann-Mauguin symbol)		
	Primary	Secondary	Tertiary
(*a*) *Layer groups and rod groups*			
Triclinic	None		
Monoclinic Orthorhombic	[100]	[010]	[001]
Tetragonal	[001]	[100]	$[1\bar{1}0]$
		[010]	[110]
Trigonal Hexagonal	[001]	[100]	$[1\bar{1}0]$
		[010]	[120]
		$[\bar{1}\bar{1}0]$	$[\bar{2}\bar{1}0]$
(*b*) *Frieze groups*			
Oblique	Rotation point in plane		
Rectangular		[10]	[01]

In the standard setting, periodic directions and their positions are [100] and [010] for the layer groups, [001] for the rod groups, and [10] for the frieze groups

no symmetry directions or only centres of symmetry have only one entry after the centring letter. These are the layer-group types P1 (DG1) and $p\bar{1}$ (DG2).

Table B.1 given in Appendix B, shows the correspondence DG $\leftrightarrow$ G$/T_3$ between three-dimensional diperiodic (DG) and three-periodic (G) space groups. This correspondence was at first given by Wood [22] in the setting that differs for rectangular diperiodic groups from that given in Table B.1 (the setting in this Table corresponds to the standard setting of [5]).

The second approach to the diperiodic groups description was suggested in [23] and is based on the non-standard factorization

$$\mathrm{DG} = \mathrm{ZP} \tag{2.17}$$

where Z is a cyclic generalized translation group, and P is a finite point group.

The non-standard DG factorization was used in [23] for the construction of the DG irreducible representations as the non-standard factorization allows the simple construction of irreducible representations, involving neither projective representations, nor the representations of the space supergroups.

Table B.2 is given in Appendix B and presents the non-standard factorization of the diperiodic space groups.The generalized translational group, Z describes the periodical arrangement of the elementary motifs along two independent directions (these two directions are assumed to be in the xy-plane). Therefore, Z can be formed of the generalized one-dimensional (1D) translational groups leaving the xy-plane invariant. There are only four generalized 1D translational groups satisfying this condition: (1) pure translational group T along an axis in the plane, (2) screw axis group 2_1 with the C_2 axis in the plane, (3) glide plane group T_h of the horizontal, xy, glide plane, (4) glide plane group T_v of the vertical glide plane (containing z-axis). All these groups are infinite cyclic groups. The first of them is generated by pure translation; as for the remaining three groups, pure translations are the index-2 subgroup generated by the square of the generator of the glide plane or the screw axis. The generalized 2D translational groups are direct or weak direct products of the listed four 1D generalized translations: (1) The pure 2D translational group T is the direct product of the two 1D translational groups T along independent directions, with, in general, different translational periods and an arbitrary angle between the translational directions. (2) The horizontal 2D glide plane group $T_h = TT_h$; translational periods of T and T_h may be different, and their directions form an arbitrary angle. (3) The 2D screw axis group $2_1 = T2_1$ (horizontal screw axis). (4) The vertical 2D glide plane group $T_v = TT_v$ (vertical glide plane). (5) The product 2_1T_h of the groups 2_1 and T_h generated by $(U_x|1/2, 0)$ and $(\sigma_h|0, 1/2)$ In the last three cases the screw axis (glide plane) can be chosen in the direction orthogonal to the translations of the group T or T_h, while the translational periods of the groups T and T_h are not related to those of 2_1 (respectively T_v).

These five 2D generalized translational groups form the lattices classified according to the four holohedries: the oblique (holohedry C_{2h}; arbitrary angle between the translational directions, with different periods), the rectangular (D_{2h}; orthogonal translational directions with different periods), the square one (D_{4h}; orthogonal

translational directions and equal periods) and the hexagonal one (D_{6h}; the angle $2\pi/3$ between the translational directions with the equal periods) [5]. If together with the primitive rectangular translations **a** and **b**, the lattice contains the vector $(\mathbf{a}+\mathbf{b})/2$ it is called the centred rectangular, to differ from the primitive ones (these generalized translational groups are emphasized by primes in the Table B.1). Depending on the type of the lattice, various orthogonal symmetries can be involved. They combine into the point factors, being the axial point groups, leaving the z-axis invariant. Since the crystallographic conditions on the order of the principal axis of rotation must be imposed (analogously to the space groups, but in the contrast to the line groups, see next section), the possible point factors are: C_n, C_{nv}, C_{nh}, D_n, D_{nh} (for $n = 1, 2, 3, 4, 6$), D_{nd} and S_{2n} (for $n = 1, 2, 3$). These are also the possible isogonal point groups, which are obtained by adding the orthogonal part of the generalized translational generators to the point factor (thus the point factor P is either the isogonal point group, or its index-2 subgroup).

Diperiodic group DG contains a subgroup of two-dimensional translations $T^{(2)}$ with elements $(E|\boldsymbol{a}_n)$, where

$$\boldsymbol{a}_n = n_1\boldsymbol{a}_1 + n_2\boldsymbol{a}_2 \tag{2.18}$$

is an arbitrary translation vector of the plane lattice, and $\boldsymbol{a}_1$, $\boldsymbol{a}_2$ are unit cell (primitive) translation vectors. The ends of all vectors $\boldsymbol{a}_n$ beginning at some origin O form a two-dimensional Bravais lattice. The point-symmetry group F_{DG} of this lattice must satisfy the following requirements: symmetry axes of order n (with $n > 2$) must be perpendicular to the plane of vectors $\boldsymbol{a}_1$, $\boldsymbol{a}_2$ (layer plane), reflection planes must be either perpendicular or parallel to this plane. These requirements restrict the number of possible two-dimensional lattices. The two-dimensional lattice of a layer group is also a two-dimensional lattice of a plane group (two-dimensional groups with two-dimensional translations). There exist five plane lattices, distributed over four crystal systems: oblique, rectangular (2 lattices—primitive and centered), square and hexagonal.

The point symmetry of the oblique, rectangular, square and hexagonal systems is given by C_2, C_{2v}, C_{4v} and C_{6v} point groups, respectively. Note that in a plane lattice the inversion at the origin of the coordinate system is equivalent to the rotation through the second-order axis normal to the plane. Screw axes in layer groups may be only the second-order axes lying in the layer plane. Improper translations in operations of reflection in glide planes (parallel or perpendicular to the layer plane) must be oriented along the layer plane.

One can find the information about subperiodic groups in [5] and on the Bilbao Crystallographic server [8]. These groups are specified by their number as given in [5] or by the international symbols. The international symbol of layer group DG contains, first, the information about the plane Bravais lattice type: P (primitive) or C (centered). Then the information about symmetry elements is given. The screw axes (of second order) have the subscript 1. The reflection planes are denoted as follows: m (mirror planes), n, a, b (glide planes, depending on the direction of the improper translations). The subperiodic groups are described by means of a crystallographic

coordinate system consisting of a crystallographic origin, denoted by O, and a crystallographic basis. The conventional basis vectors for the three-dimensional layer groups are labeled $\boldsymbol{a}$, $\boldsymbol{b}$, and $\boldsymbol{c}$. Unlike triperiodic space groups, not all basis vectors of the crystallographic basis are lattice vectors (for primitive lattices vectors $\boldsymbol{a}$ and $\boldsymbol{b}$ coincide with the primitive translations $\boldsymbol{a}_1$, $\boldsymbol{a}_2$).

Like space groups, the crystallographic coordinate system is used to define the symmetry operations and the Wyckoff positions. The symmetry operations are defined with respect to the directions of both lattice $\boldsymbol{a}$, $\boldsymbol{b}$ and nonlattice $\boldsymbol{c}$ basis vectors. A Wyckoff position, denoted by a coordinate triplet (x, y, z) for the three-dimensional layer groups, is defined in the crystallographic coordinate system by $O + \boldsymbol{r}$, where $\boldsymbol{r} = x\boldsymbol{a} + y\boldsymbol{b} + z\boldsymbol{c}$.

Like space groups, the term setting will refer to the assignment of the labels $\boldsymbol{a}$, $\boldsymbol{b}$, and $\boldsymbol{c}$ (and the corresponding directions [100], [010] and [001], respectively) to the basis vectors of the crystallographic basis. In the standard setting, those basis vectors that are also lattice vectors are labeled for layer groups with their two-dimensional lattice by $\boldsymbol{a}$ and $\boldsymbol{b}$. Note that the setting of the layer groups for rectangular lattices may be chosen different for the same group (symbols $P211$ or $P121$ refer to the same group in two different settings) but at the same time $P112$ and $P211$ denote different layer groups. In the first group the axis of second order (oriented along the z-axis) is perpendicular to the layer plane, in the second it lies in the layer plane xy and is directed along the x-direction. In the first case, the second-order axis is oriented along the plane translation lattice vector, in the second case along the nonlattice vector. Respectively, the Wyckoff positions for both groups are different, see [8].

For some layer groups of oblique and rectangular crystal systems (DG 1, 2, 8–18) the vector $\boldsymbol{a}_3$ may be inclined to the layer plane.

In the cases when a space group G may be represented as a semidirect product (2.15) in two different manners it generates two nonisomorphic layer groups. For example, the layer groups $P112$ and $P211$ are related to one space group $P2(C_2^1)$ with two different settings (the second-order axis is oriented along the z- and x-directions, respectively). The space group $P2/b$ (C_{2h}^4) generates two layer groups $P112/a$ and $P2/b11$. In the first group the rotation axis is perpendicular to the layer and the layer plane itself is a glide plane with an improper translation on a half-period along the x-direction. In the second group the rotation axis is directed along the x-axis; the glide reflection plane is perpendicular to the layer (and to the rotation axis) and reflection in this plane is followed by improper translation on the half-period along the y direction. The latter corresponds to the space group, with a nonconventional setting.

A particular case of layer groups is that of the so-called plane groups mentioned above. Formally, they are the symmetry groups of diperiodic systems in two dimensions. They correspond to the layer groups that do not contain the rotation axes lying in the layer plane and the reflection planes coinciding with the layer plane. Semi-infinite crystals with plane diperiodic surfaces have plane groups as the groups of symmetry.

2.4.2 Orbits of Layer Groups

The Wyckoff positions (the sets of non-equivalent orbits of the diperiodic groups -DG-orbits) for the 80-layer groups can be found in [5, 8]. The Wigner–Seitz (WS) cell for an arbitrary group DG is a right prism with a directrix lying in the layer plane. The projection of the Wigner–Seitz (WS) cell on the layer plane is a polygon constructed from the basis vectors $\boldsymbol{a}_1$ and $\boldsymbol{a}_2$ [6]. The WS cell of the corresponding triperiodic group G is derived by construction of additional planes perpendicular to the vectors $\boldsymbol{a}_3$ (and perhaps to their integer combinations with the vectors $\boldsymbol{a}_1$ and $\boldsymbol{a}_2$) and passing though their midpoints. Thus, the WS of the group G is a part of that for the corresponding group DG.

The site-symmetry groups of Wyckoff positions for the majority of positions belonging to both WS cells (of G and of DG) are identical since they are determined by the same set of symmetry operations. The only exception may be for the points on the sides of the group G cell that are absent in that of the group DG. The existence of translational symmetry in the third dimension in the group G may give rise to additional symmetry operations in site-symmetry groups for these points in the group G with respect to DG. The part of the WS cell of the layer group DG that has no common points with the cell of the corresponding group G contains the points of general position and the points with site symmetry defined by vertical planes and rotation axes. These types of site symmetry are already represented in the common part of the cells for G and DG. Therefore, the set of points with different types of site symmetry in the group G is larger than that in the group DG. Thus, the points of different types of site symmetry (Wyckoff positions) in DG may be specified by the same roman letters as in the corresponding groups G [8]. In layer groups the inversion center and the points of intersection of vertical and horizontal symmetry elements may be situated only in the layer plane. This means that the symmetry points of the Wigner–Seitz cell for a layer group DG may appear only in its intersection with the layer plane. An example illustrating the Wyckoff positions connection in space group C_{2h}^5 and layer DG 18, is given in [6].

Oriented site symmetry symbols for layer groups are used to show how the symmetry elements at a site are related to the conventional crystallographic basis. The site-symmetry symbols display the same sequence of symmetry directions as the subperiodic group symbol. Sets of equivalent symmetry directions that do not contribute any element to the site-symmetry group are represented by a dot. Sets of symmetry directions having more than one equivalent direction may require more than one character if the site-symmetry group belongs to a lower crystal system. For example, for the 2c position of tetragonal layer group P4mm (DG55), the site-symmetry group is the orthorhombic group 2 mm.. The two characters mm represent the secondary set of tetragonal symmetry directions, whereas the dot represents the tertiary tetragonal symmetry direction.

2.4.3 Slab Models of Nanolayers

The thin films and surface modeling is connected with the basic concepts, introduced by Tasker [24] in a discussion of the stability of surfaces of ionic or partly ionic crystals. According to classical electrostatic criteria, the stability of a compound surface depends on the characteristics of the charge distribution in the structural unit that repeats itself in the direction perpendicular to the surface. The surface can be studied by considering the crystal as a stack of atomic planes. Each plane consists of sublattices of nonequivalent atoms, a sum over each sublattice on each plane gives the total electrostatic potential. For perpendicular distances z greater than a few interionic spacings, the contribution from a planar sublattice reduces to the particularly simple form

$$V(z) = \frac{2\pi}{S} qz \tag{2.19}$$

where S is the area of the unit cell in the plane and q is the planar sublattice charge. This expression is identical to the potential due to an infinite charged plane of charge density $\rho = \frac{q}{S}$; the field $E = \frac{2\pi}{S} q$ due to the charged plane is constant. Since $V(z)$ and E do not diminish with increasing distance z the electrostatic sum must be over the whole crystal as stacks of planes unless cancellation of these terms occurs. Although the potential $V(z)$ becomes infinite at infinite distances from the plane, it should be noted that when the crystal is constructed as a neutral block the infinities cancel and the potential becomes constant at large distances. In fact, it becomes zero in all cases except where there is a dipole moment perpendicular to the surface. Similarly the field E cancels to zero outside a neutral crystal block, irrespective of the stacking sequence.

The repeat unit of a stack of planes is introduced when analyzing the distribution of the bulk structure atoms over the atomic planes in the direction z normal to the surface. This distribution depends on the crystal bulk structure and Miller index, defining the surface. The three different possible stacking sequences define three types of surfaces.

As a simplest case of the *type-1 surface* we can mention the (001) surface of MgO crystal with the sodium chloride structure. The neutral bulk unit cell consists of two atoms (Mg and O) and both of them occupy the same atomic plane. Each atomic plane has overall zero charge since it consists of both anions and cations in stoichiometric ratio. The potential $V(z)$ cancels on each plane since the contributions of the sublattices are equal and opposite. Additional planes in the surface of the crystal make no contribution to the energy of ions in the bulk of crystal, and the lattice sums required for the Madelung energy at any ion site need include only a few planes either side of that site.

The diperiodic symmetry groups of the rutile and the anatase and the corresponding 3D space groups are given in Table 2.9.

Table 2.9 Symmetry of slabs

Crystal	Index	Space Group		International Symbol		Layer Group	
		Even	Odd	Even	Odd	Even	Odd
Rutile	001	113	65	$P-42_1m$	Cmmm	58	47
	100	31	10	$Pm2_1n$	$P2/m11$	32	14
	101	14	14	$Pm2_1/b11$	$P2_1/b11$	17	17
	110	51	47	$Pmmb$	$Pmmm$	41	37
Anatase	001	51	115	$Pmmb$	$P-4m2$	41	59
	100	53	51	$Pman$	$Pmam$	42	40
	101	12	–	$C2/m11$	–	18	–
	110	13	21	$P112/b$	C222	7	22

Figure 2.19 shows stacking of densely-packed atomic planes under the (110), (100), (101) and (101) surfaces of rutile.

In the case of (110) and (101) slabs, the thinnest repeating layers consisting of three atomic planes each (with Ti atoms positioned in the middle of layer), i.e., $-O-Ti_2O_2-O-$ (Fig. 2.19a) and $-O_2-Ti_2-O_2-$ (Fig. 2.19c) are repeated along the directions of stacking which are inclined from the normal axes of slabs. Both types of layer units possess the zero dipole moment along the stacking direction although each of three planes inside the layer unit is charged (Fig. 2.19a, c). In two other densely-packed rutile slabs, the stacking directions are perpendicular to the slab surfaces while dipole moments of layer units equal to zero again. Inside the (100) slab (Fig. 2.19b), the repeating layer units consist of six $-O-Ti-O-O-Ti-O-$ atomic planes while inside the (001) slab (Fig. 2.19d), each of two TiO_2 atomic planes per repeating layer unit $-TiO_2-TiO_2-$ is electrically neutral. The layer symmetry groups of the rutile strucure thinnest slabs are the following: (110)-Pmmm; (100)-$Pm2_1n$; (101)-$P2_1/b11$; (001)-$P-42_1m$.

For the type-2 surface each plane contributes a term in the potential $V(z)$, but a sum over the planes in repeat units cancels the potential to zero. Addition of extra neutral repeat units at the type-2 surface of the crystal cannot therefore affect the energy of ions in the bulk, and again the Madelung sums for the potential at any ion site are rapidly convergent. The (110) surface of the TiO_2 rutile structure (Fig. 2.19a) is an example of a type-2 surface. Indeed, the bulk crystal unit Ti_2O_4 atoms are distributed over three planes with the surface unit cells consisting of one oxygen atom (two planes) or Ti_2O_2 units (one plane). The atomic planes in this repeating unit are charged (in the ionic model $q = -2$ for oxygen planes and $q = +4$ for Ti_2O_2 planes). However, the stacking of planes with the repeat unit as O–Ti_2O_2–O allows one to obtain zero as its dipole moment along the z-direction. Two other terminations (O–O–Ti_2O_2 and Ti_2O_2–O–O) give the repeat unit that bears a nonzero dipole moment. This example demonstrates that the surface orientation only is not always sufficient to refer the surface to the one of three types, especially when various terminations may be produced. The atomic TiO_2 planes in the repeat unit of the (001) surface of rutile (Fig. 2.19d) are neutral and the dipole moment of any stack of an integer number of such planes is again zero (type-2 surface). The repeat units for

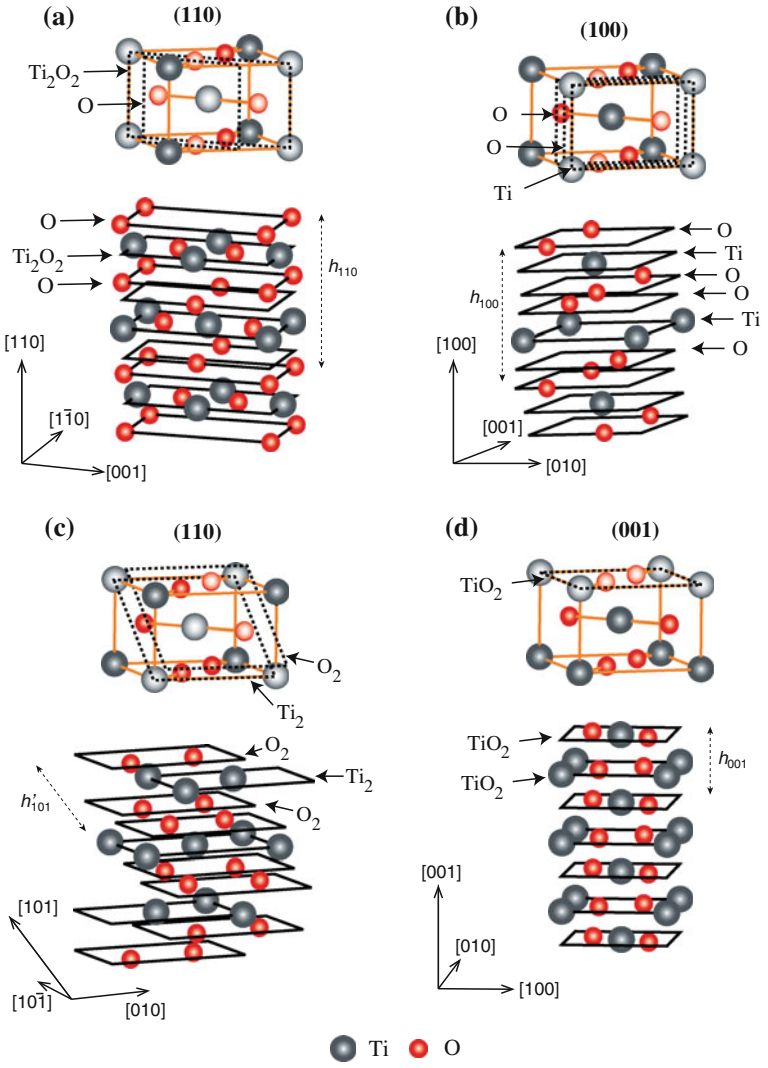

Fig. 2.19 Stacking of atomic planes for densely-packed rutile TiO_2 surfaces cut from bulk unit cells by planes imaged using *dashed lines*. One-two parallel section planes (110) (**a**), (100) (**b**) and (101) (**c**), crossing unit cells and containing oxygen atoms only are shown additionally. For (001) slab (**d**), no additional section plane is necessary. Directions of layer stacking for (110) (a) and (101) (c) slabs are inclined from the axes normal to slab surfaces, however, they are perpendicular to axes [1$\bar{1}$0] and [10$\bar{1}$], respectively. In the cases of (100) (b) and (001) (d) slabs directions of stacking coincide with the normal to slab surfaces

(100) and (101) type-2 surfaces have also zero dipole moment (O- and O_2-terminated repeat units of 6 and 3 atomic planes, respectively, can be chosen).

For the majority of cases of the oxide surfaces the stacking sequence of charged planes has a dipole moment perpendicular to the surface. In particular, the stacks of

alternately charged planes form the repeat unit for (101) surface of TiO_2 (Fig. 2.19c).

Figure 2.20 shows stacking of densely-packed atomic planes under the (001), (101), (110) and (100) surfaces of anatase.

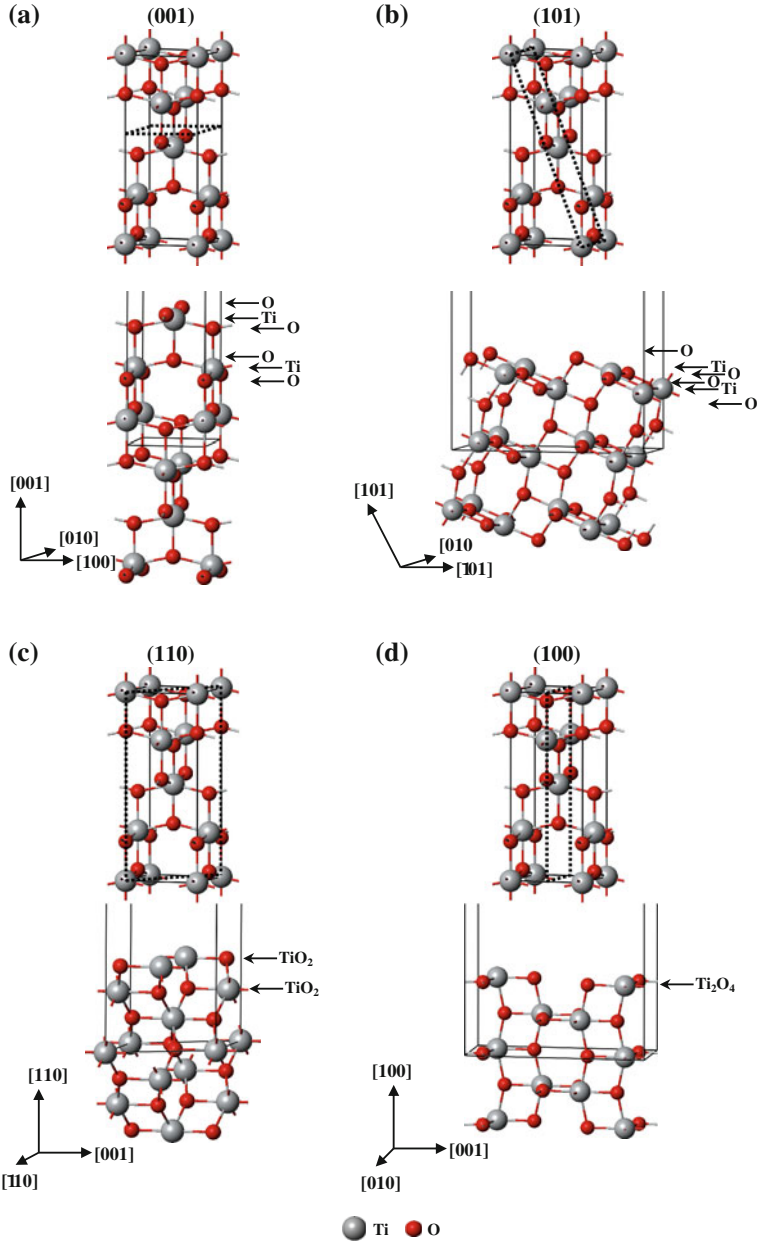

Fig. 2.20 Stacking of atomic planes for anatase TiO_2 surfaces

In the case of (110) and (101) slabs, the thinnest layers are repeated along the directions of stacking which are inclined from the normal axes of slabs. In two other densely-packed slabs, the stacking directions are perpendicular to the slab surfaces. The thinnest (110) layer consists of two $-TiO_2-TiO_2$ atomic planes, see Fig. 2.20c. The thinnest (001) and (101) layers consist of six $-O-Ti-O-O-Ti-O-$ atomic planes each, see Fig. 2.20a, b. At last, the thinnest (110) anatase slab consists of one plane $-Ti_2O_4-$, see Fig. 2.20d. In (100) and (001) densely-packed slabs, the stacking directions are perpendicular to the slab surfaces. All the four anatase layer units possess the zero dipole moment along the stacking direction. Each of six planes inside the (001) and (101) layer units is charged while $-Ti_2O_4-$ and $-TiO_2-TiO_2-$ planes in (100) and (110) layer units are electrically neutral. The thinnest layer symmetry groups of the anatase structure are the following: (110)-P112/b; (100)-Pmam; (101)-C2/m11; (001)-Pmmb.

Figure 2.21 shows the stacking of atomic planes for cubic perovskite ABO_3 surfaces.

All the surfaces in cubic perovskite structure are type-3 surfaces being stacks of alternately charged planes. It is less obvious in the case of the (001) surface in $A^{II}B^{IV}O_3$ as the repeat unit consists of neutral atomic planes (see below). It is also seen that the charge of the atomic plane depends both on the oxidation states of A and B atoms (the sum of oxidation states is in all cases 6) and Miller indexes of the surface.

For the stacking sequence of alternately charged planes (producing a dipole moment perpendicular to the surface) the two-plane repeat unit produces a potential at large distances whose magnitude is given by

$$V = 2\pi|q|\frac{a}{S} \tag{2.20}$$

where a is the interplanar spacing. Addition of an extra neutral repeat unit of two planes on the surface of the crystal will affect the energy of ions an infinite distance below the surface. Consequently, the Madelung sum cannot be truncated and must

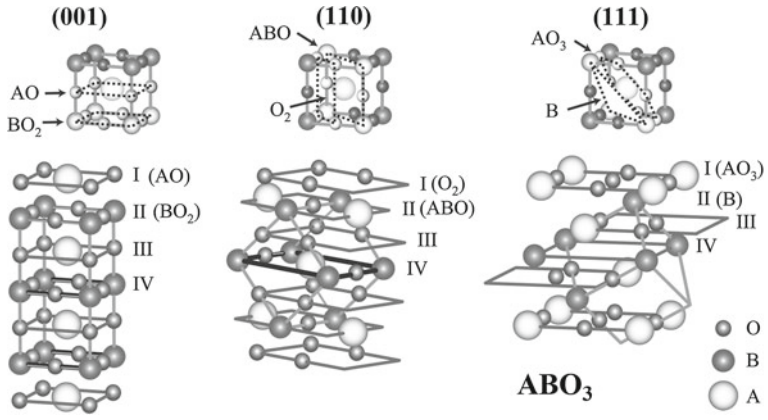

Fig. 2.21 Stacking of atomic planes for cubic perovskite ABO_3 surfaces

include contributions from every plane out to the surface. The potential at any ion site never reaches a constant bulk value, the energy of a neutral pair of ions never reaches the usual cohesion energy and the surface energy is infinite [24]. The stacking of planes for rutile (100), (101) and (111) type-3 surfaces is more complicated as it can not be named as the stacking sequence of alternatively charged planes.

The classification of the surfaces by Tasker is based on the formal ionicities (oxidation states) of metal atoms. As we already noted, the oxidation state and calculated atomic charges are close only in purely ionic compounds (MgO, for example). In fact, the transition-metal atoms charges differ essentially from the oxidation states due to the covalence part of the chemical bonding with oxygen atom.

Type-1 or -2 surfaces have a zero dipole moment in their repeat unit and are thus potentially stable. By contrast, polar type-3 surfaces have a diverging electrostatic surface energy due to the presence of a nonzero dipole moment not only on the outer layers, but on all the repeat units throughout the material [25]. An electrostatic instability of type-3 surfaces results from the presence of that macroscopic dipole. Type-3 surfaces can be stabilized when the macroscopic field is removed by surface reconstruction, absorption of charged specks and so on. The modification of the surface electronic structure due to the reconstruction introduces compensating charges in the outer planes, stabilizing the surface structure. The absorption of charged specks is also a very effective mechanism to achieve the stabilization of polar orientations. Indeed, polar orientations are generally much more reactive than cleavage planes [25].

The classification of surfaces considered above was introduced for ionic or semi-ionic metal oxides. In covalent solids, the creation of a surface requires cutting covalent bonds, which means that dangling bonds would be present at the surface. The saturation of dangling bonds by chemisorption is important, for example, in silicates. When a surface is cut out from the bulk, unstable Si–O radicals at the surface react readily with water to give a fully hydroxylated surface with hydrophilic character.

Tasker's classification of surfaces allows some qualitative conclusions to be made about the surface stability. The quantitative calculations of the surface formation energy in slab models are considered in the next sections.

The crystals with wurtzite structure are layered compounds. Figure 2.22 shows the stacking of the atomic planes in the ZnO wurtzite structure for different slabs. The bulk unit cell consists of two ZnO formula units.

The thinnest (001) layer consists of four $Zn - O - Zn - O$ atomic planes, see Fig. 2.22a. The (001) surface of wurtzite structure is the most stable and used in the nanostructures modeling. In the thinnest (110) all four atoms of the bulk unit cell occupy the same plane forming type-1 surface structure (2.22b). The layers (100) and (101) consist of two and four atomic planes respectively (see Fig. 2.22c, d). In the former each of two atomic planes is neutral (2D unit cell contains ZnO formula unit); in the latter each of four atomic planes O–O–Zn–Zn is monoatomic. The (110) and (100) surfaces refer to the type 1, while (001) and (101)- to the types 3 and 2, respectively. The relative stability of the different wurtzite surface structures depends also on the interlayer distance. In particular the most stable (001) slab in the wurtzite

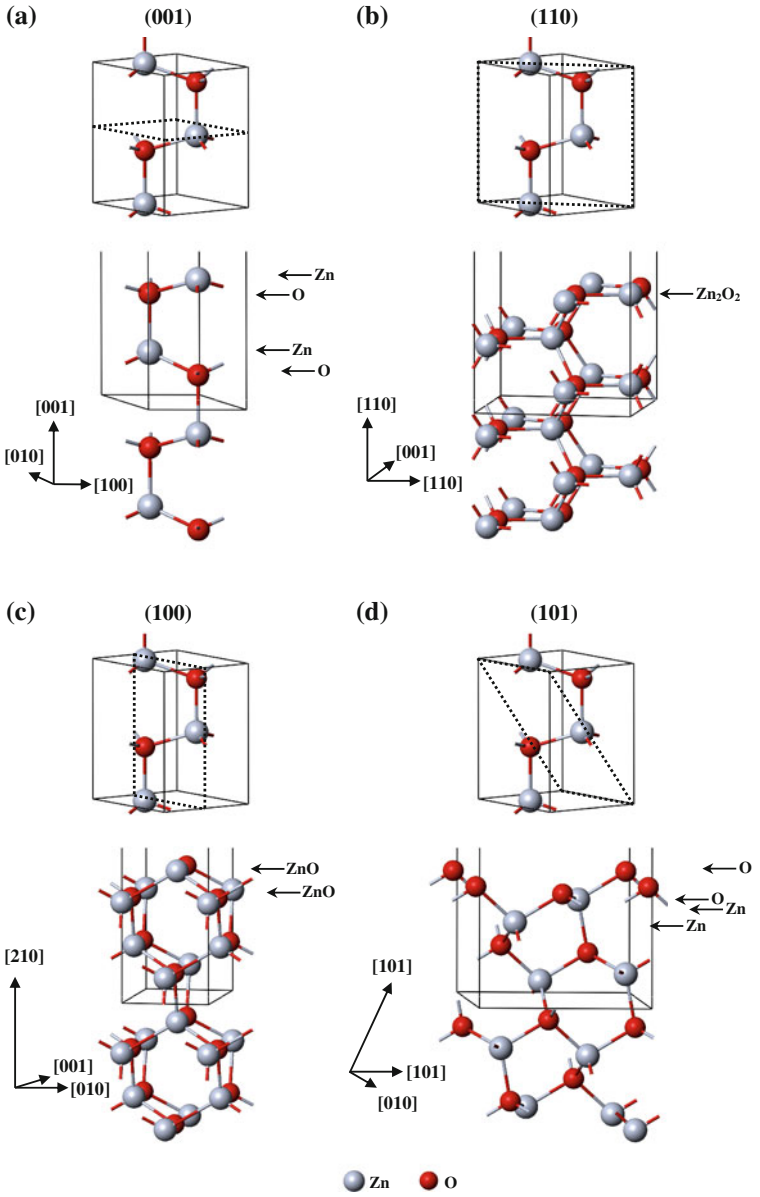

Fig. 2.22 Stacking of atomic planes for wurtzite ZnO surfaces

structure consists of two-plane neutral fragments separated by the relatively large interlayer distance.

Figure 2.23 shows atomic planes for TiS_2 structure (space group $P\tilde{3}m1$, hexagonal 3D lattice. The bulk unit cell consists of two formula units. The minimal size (001) slab consists of three atomic planes: the middle is formed of Ti atoms, while two

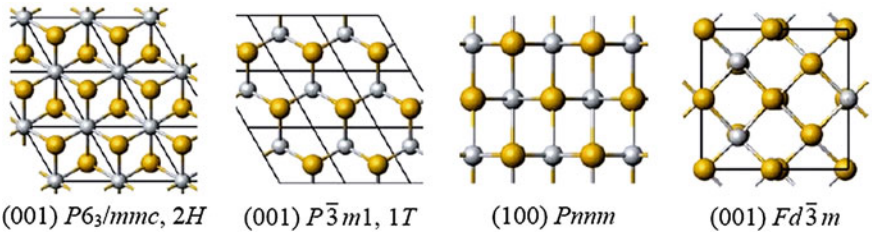

Fig. 2.23 Atomic planes in TiS_2 structures

other sheets are from sulfur atoms, see Fig. 2.23. Just this slab is used in the nanotube rolling for TiS_2 structure, see Sect. 3.5.

2.5 Line and Rod Symmetry Groups of Stereo-Regular Polymers and Monoperiodic Nanostructures

2.5.1 Different Factorization of Line and Rod Groups

Line groups L are divided into two classes: incommensurate and commensurate [3]. Incommensurate line groups contain rotohelical transformations $(C_\varphi|f)$ with rotation angles φ that are not commensurate with π.

By definition, commensurate line groups (also called monoperiodic groups) are discrete symmetry groups of three-dimensional objects translationally periodic along a line: stereo-regular polymers, nanotubes, nanowires, nanoribbons and quasi-one-dimensional subsystems in the bulk (threeperiodic) crystals. In the objects mentioned the basic constituents (monomers) are repeated regularly.

The number of line groups is infinite as the translation axis can be the rotation or screw axis of any integer order q. The relevance of line groups for polymers was discussed by Vainstein [1]. The derivation of commensurate line groups as the symmetry groups of stereo-regular polymer molecules was presented in [4].

Normally the z-axis is chosen as a line group principal axis and with such a convention the elements of pure translation subgroup T(a) are of the form $(E|0, 0, na)$, n-integer. Here a is a translation period defined as a smallest positive real number such that $(E|0, 0, a)$ belongs to the group under consideration. For elements of T(a) the symbol $(E|a)$ instead of $(E|0, 0, a)$ will be used. The symbol T will stand for the discrete group of pure translations along z-axis when $a = 1$.

Under the standard for crystallography approach any commensurate line group may be presented in the form

$$\mathrm{L} = \mathrm{T}(\vec{a})\mathrm{F} \tag{2.21}$$

where F is a finite system of coset representatives of line group decomposition in cosets of $\mathrm{T}(a)$-invariant subgroup of L. The choice of representatives in not unique

and any specific set F is, in general, not a subgroup of L. However, since L is the extension of F by T(a), F can be interpreted as a group with multiplication modulo pure translations (factor group L/T(a)). The group F is isomorphic to the axial point group P_I known as isogonal point group. Factorization (2.21) of line group L will be referred to as standard [26].

The derivation of the commensurate line groups is given in [4]. The line groups are described in the standard factorization (2.21) as an extension of a one-dimensional translation group by an isogonal point group. The isogonal point group is either cyclic or a semi-direct product of cyclic groups.

The method of derivation of the line groups consists of first extending by the cyclic isogonal point groups and then obtaining the rest of the line groups by unification within the Euclidean group. To this purpose, a simple test is given to decide whether two line groups multiply into a third one. The method displays the subgroup structure of the line groups, relevant to the construction of their irreducible representations. All the commensurate line groups are derived and tabulated in [4].

An alternative method considered in [3] exploits elementary group-theoretical means (with quite a bit of Number Theory) but embraces both commensurate and incommensurate line groups. This method is based on the factorization

$$\mathrm{L} = \mathrm{ZP} \tag{2.22}$$

where Z is a cyclic generalized translation group, and P is a finite point group. The requirement that L contains a subgroup of pure translations immediately implies that Z must be of one of the following two forms:

$$\mathrm{Z} = \mathrm{T}_q^r(f) = \langle (C_q^r|f) \rangle \quad \text{or} \quad \mathrm{Z} = \mathrm{T}'(a) = \langle (\sigma_v|\frac{a}{2}) \rangle \tag{2.23}$$

where f is a *fractional* translation, $\mathrm{r} = 0, 1, 2, \ldots, q-1$.

If the factorization (2.22) is used, then the structure of line groups may be studied in several steps.

As the first step it is reasonable to analyze the discrete point groups operating on cylindrical surfaces. Such an analysis (used also in [4]) is not complicated and gives 7 families of the point groups which leave cylinder invariant (the so-called axial point groups P_I):

$$\mathrm{C}_q, \quad \mathrm{S}_{2q}, \quad \mathrm{C}_{qh}, \quad \mathrm{D}_q, \quad \mathrm{C}_{qv}, \quad \mathrm{D}_{qd}, \quad \mathrm{D}_{qh} \tag{2.24}$$

Then step by step it is necessary to consider the products ZP to find out when each concrete product is a group, and to ascertain that it has not occurred at previous steps, probably in a different guise.

The orthogonal transformations of axial point groups P_I leave the z-axis invariant (rotations C_q around the z-axis, reflections σ_v in vertical planes) or reverse the direction of the z-axis (rotations U around the second order axis perpendicular to the z-axis, reflections σ_h in horizontal planes). The former transformations are called

the positive ones, the latter—the negative ones. As the product of negative elements is positive, the set of positive elements is either the whole group (positive group P_I^+) or a halving subgroup, when the group is called negative: $P_I^- = P_I^+ + p^- P_I^+$. It was shown that the isogonal point groups of equivalent line groups are necessarily conjugated by proper rotations which leave the z-axis invariant.

The construction of the physically distinct line groups in both factorizations is based on the fact that all isogonal point groups are either cyclic (C_q, S_{2q}) or the product of cyclic groups: $C_{qv} = C_q \wedge C_{1v}$; $C_{qh} = C_q \times C_{1h}$; $D_q = C_q \wedge D_1$; $D_{qd} = (C_q \wedge C_{1v}) \wedge D_1$; $D_{qh} = (C_q \wedge C_{1v}) \wedge C_{1h}$.

In Table C.1 (given in Appendix C) from [3] the result of such an analysis is presented: all line groups are divided into 13 families, each family includes infinitely many line groups. Among these families there are 5 symmorphic (families 2, 3, 6, 9, 11) for which factorization (2.22) coincides with the standard one. The families 1 and 5 contain both incommensurate and commensurate (symmorphic and nonsymmorphic) line groups.

Table C.1 lists the line groups of 13 families for any order q of the rotation or screw axis written in the form L = ZP, [3]. The line group decomposition:

$$L^{(F)} = \sum_{i=1}^{N_F} l_i^{(F)} L^{(1)} \tag{2.25}$$

contains the subgroup $L^{(1)}$—a set of all roto-helical transformations and in the case of the first family groups $L^{(1)}$ is the line group itself. For families $F = 2, 3, \ldots, 8$ it is a halving subgroup ($N_F = 2$), for the remaining families $F = 9, \ldots, 13$ the first family subgroup $L^{(1)}$ is a subgroup of index four ($N_F = 4$). The coset representatives $l_i^{(F)}$ are given in Table C.1 [3].

In the theory of line groups the 1st family, being one of the simplest, plays nevertheless the most important role. The reason is in the structure of axial groups P in (2.22): any such group contains C_n as its subgroup and, consequently, admits decomposition in cosets of C_n.

The main result concerning the line groups of the 1st family may be formulated as follows [3]:

For a fixed translation period *a commensurate* line groups of the 1st family are parametrized by triplets $(\tilde{q}, n, r) \in \mathbb{N}^+ \times \mathbb{N}^+ \times K$

$$L = T_{\tilde{q}n}^r (\frac{a}{\tilde{q}}) C_n = T(a)F \tag{2.26}$$

where $K = \{r : 0 \leq r \leq \tilde{q}$ & $\mathrm{GCD}(\tilde{q}, r) = 1\}$, GCD is the abbreviation for the greatest common divisor, and $\mathbb{N}^+$ is the set of positive natural numbers. Here

$$F = \bigcup_{t=0}^{\tilde{q}-1} \left(C_q^{rt} | \frac{a}{\tilde{q}} t \right) C_n, \quad q = \tilde{q}n \tag{2.27}$$

Note that, by definition, $\mathrm{GCD}(l, 0) = 1 \Leftrightarrow l = 1$ and, consequently, $r = 0$ corresponds to the case $\mathrm{T}_n^0(a) = \mathrm{T}(a)$. It is pertinent to emphasize as well that a (for fixed $(\tilde{q}, n, k)$) is a translation period of the maximal free 1-periodic subgroup $\mathrm{T}(a)$ of the line group (2.26). The analogous subgroup of the generalized group Z of translations has, in general, greater period ([3]).

Table C.1 shows that some line groups can be given with different factorizations. Rotations around the z-axis and translations along it commute, which implies that all the helical operations $(C_Q|f)$ (Q- is the rotation axis order, f is a partial translation) commute with pure rotations C_n around the z-axis i.e. rotations from the point group P_n. Therefore any group P_n is compatible with any group $T_Q(f)$ for any Q. Their products $T_Q(f)C_n$ comprise first family line groups $\mathrm{L}^{(1)}$ which are subgroups of all the other line groups. Similarly, all $T_Q(f)$ are compatible with groups D_n since $U(C_Q|f)^t = (C_Q|f)^{-t}U$. The products $\mathrm{T_Q(f)} \wedge \mathrm{D}_n$ comprise the fifth family groups $\mathrm{L}^{(5)}$. Other compatibility relations are as follows [3]. Mirror planes of intrinsic symmetry can be retained only if Q is rational, i.e. $Q = r/q$, where r and q are integers. It means that only commensurate helical groups allow a mirror plane. These helical groups are $T(f = a)$ and T_{2q}^1 $(f = a/2)$, where q is the order of the principal axis of a point group. On the other hand, the glide plane group T' is compatible with all axial point groups. The only requirement when a point group contains mirror planes or U-axes is that the glide plane should either coincide with them or bisect them, and different groups are obtained in these two cases. As a glide plane is commensurate, so are all the resulting groups. All the products of the point factor P and the generalized translation group Z define 11 remaining line group families, given in Table C.1. Thus one gets 13 infinite families of line groups. Each family includes all groups (with various parameters Q, f, n) with a fixed type of Z and P. Incommensurate line groups are either from the first or from the fifth family, while in all the other families the generalized translation group is either the glide plane reflections group T′, the pure translation group T, or the zigzag group T_{2n}^1. The products L = ZP are weak direct, Z is a cyclic group, the intersection of Z and P can only be the identity element. If one or both subgroups are invariant, this product becomes semi-direct (with the first factor invariant) or direct, respectively. It is well-known that some subgroups of the group of Euclidean transformations admit different geometric realizations. For example, group $\mathrm{C}_{qv}(\alpha) = \mathrm{C}_q \cup \sigma_\alpha \mathrm{C}_q$, where σ_α is a reflection in the vertical plane passing through z-axis and a line in the xy-plane with the direction vector $(\cos\alpha, \sin\alpha, 0)$ is a geometric realization of C_{qv} group defined by the setting angle α. Usually the setting angle is taken equal to zero which corresponds to choosing xz as a benchmark reflection plane. In particular, in the theory of line groups the setting angle is usually chosen equal to zero [3]. On the other hand, groups C_q stipulate a unique geometric realization as soon as the axis and direction of rotations are chosen.

Not being subgroups of space groups (unlike rod groups), line groups are a much wider class of symmetries. While rod groups describe only translationally periodical objects, line groups include symmetries of incommensurate structures. In the limit $q = \infty$ each family gives a continuous group P_∞. These limiting groups correspond to the symmetry of linear molecules and also behave as the isogonal

groups of incommensurate systems. Axial point groups P_I are descrete subgroups of the cylindrical point group P_∞.

When used to describe the symmetry of polymer molecules line groups can also be factorized as a weak direct product of the intrinsic point symmetry P of monomer and the group of generalized translations Z, arranging these monomers along the direction of periodicity, see [3] and references therein. The product of two subgroups is a group if and only if these subgroups commute, i.e. PZ = ZP(it does not mean that $Z_j P_i$ is equal to $P_i Z_j$). The symmetry operations of polymers are defined as geometrical transformations leaving the compound unchanged. These operations occur in two different ways: as periodicity of the regular arrangement of monomers (comprise group Z) and as the intrinsic symmetry P of a single monomer. However, the intrinsic symmetry of the monomer P_n is the symmetry of the whole polymer only if it leaves simultaneously all the monomers unchanged, i.e. if it is compatible with the periodical arrangement [3]. This fact was used in [27] for a line group classification: after an independent classification of all the possible arrangements and their symmetries, as well as of the symmetries of monomers, these two were combined in all possible compatible ways to get all the possible line groups. Such an approach allows one to consider the symmetry of both commensurate (one-periodic) and incommensurate (non-periodic) systems. Moreover, in such a way one can directly obtain important information on the specific structure of line groups and can use it to explore many significant physical consequences.

Under the standard approach any commensurate line group may be presented in the form

$$\mathrm{L} = \mathrm{T}(a)\mathrm{F} = \sum_{\mathrm{i}=1}^{\mathrm{n_p}} (\mathrm{R_i}|\mathrm{v_i})\mathrm{T(a)} \tag{2.28}$$

The choice of coset representatives $(R_i|v_i)$ in the standard factorization in not unique and any specific set F is, in general, not a subgroup of L. In (2.28) R_i and n_p are the operation and order of the isogonal point group P_I, respectively. Improper translations v_i appear only in nonsymmorphic line groups. Such a factorization of the line group is the same as that of rod groups. However in the former the rotation axis order q is any positive integer number, in the latter q = 1, 2, 3, 4, 6.

The first family commensurate line groups are represented in the standard factorization as $\mathrm{L} = q_p$ and as $\mathrm{L} = \mathrm{T}_q^r \times \mathrm{C}_n$ in factorization (2.22). In the standard factorization $L = (C_q^1|\frac{p}{q})$ where C_q^1 is the rotation by the angle $\frac{2\pi}{q}$ around the translation axis. Evidently $L = (C_q^r|\frac{rp}{q})$ so that $rp = n + lq$ (l is integer, $n = \mathrm{GCD}(q, r)$). These relations allow the two factorizations of the same line group to be written.

As an example we consider the line group $\mathrm{L} = q_{28}^{22}$ with q = 28, n = 2, p = 22. Therefore $22r = 2 + 28l$ and for l = 7 we obtain r = 9 so that in the factorization (2.22) this group is written as $T_{28}^9 C_2$. It will be seen later that such a line group is the symmetry group of the nanotube with the chirality (4,2) rolled up from the hexagonal lattice.

2.5.2 Rod Groups and their Settings as a Special Geometric Realizations of Line Groups

75 rod groups (RG) are known in crystallography as subperiodic subgroups of space groups (SG) [5] and form the finite subset of an infinite number of line groups as the order q of rotation or screw axis can only be 1, 2, 3, 4, 6. By analogy with a space (three-periodic) and layer (two-periodic) groups rod groups are factorized RG = TF as an extension of the one-dimensional translations group T (invariant subgroup of RG) by the factor group F = RG/T. A subperiodic rod group RG can contain the following elements [28]: translations $\boldsymbol{a}$ in one direction which by convention is designated as z-axis; a two-, three-, four- or sixfold rotation or screw axis pointed in this direction; the rotation U around twofold axes perpendicular to it; reflection planes containing translation vector (vertical planes σ_v) and reflection planes perpendicular to it (horizontal planes σ_h). Every RG is in correspondence with some three-periodic space group SG: it is a subgroup of SG and has the same point symmetry group F. To obtain RG, it is sufficient to keep translations only in one direction in a related SG. The related RG and SG groups have the same international notations.

Table D.1 (see Appendix D) gives the correspondence between rod and space groups—their international notation, the number of the corresponding SG and its Schönflis symbol. This Table can be compared with Table B.1 from Appendix B, where correspondence between three-dimensional two-periodic (DG) layer groups and three-dimensional three-periodic space groups (SG) is given. Screw axes in layer groups only can be the second-order axes, lying in the layer plane. Screw axes in rod groups are oriented along the translation direction and therefore can be axes of orders 2, 3, 4, 6. One can find information about rod groups on the Bilbao Crystallographic Server [8]. These groups are specified by their number or by international symbols. The first symbol P (primitive) is the same for all rod groups as the translations are made along the principal symmetry axis, formally forming primitive one-periodic lattice. Then the information about symmetry elements is given. The screw axis of the order q has subscript p (p = 0, 1, 2, …, $q-1$). The corresponding symmetry operations are rotations through $2\pi p/q$ about the z-axis. The reflection planes are denoted by m (mirror planes) and c (vertical glide planes containing the translation axis). The factor groups F of rod groups (called in crystallography by crystal classes) are isomorphic to axial point groups C_q, D_q, S_{2q}, C_{qv}, C_{qh}, D_{qd}, D_{qh}. For q = 1, 2, 3, 4, 6 there are 31 different axial point groups, defining the crystal class of the related space and rod groups. The point groups D_1, D_{1d}, D_{1h} are isomorphic to the point groups C_2,C_{2h}, C_{2v}, respectively; the point groups C_{1h}, C_{1v} are isomorphic to the point group C_s. This isomorphism is used in crystallographic description of rod groups distributed over 27 crystal classes. The corresponding space groups are given in their Schönflis notation in the second column in Table D.1. As can be seen from Table D.1, some rod groups are related to two different space groups as two possible RG settings can be chosen. For example, RG 46 (with the third order rotation axis along z) is related to the space groups D_3^2 and D_3^1 when the second order axis U is

directed along the x- and y-coordinate axes, respectively. However, two different rod groups 15 (Pmm2) and 18 (Pm2m) are subgroups of the same SG 25. Whereas, in RG 15 the second order rotation axis is directed along the translation direction z, in RG 18 the second order rotation axis is orthogonal to z. As in the latter case this axis can be directed along both the x and y Cartesian axes, RG 18 has two settings −P2mm and Pm2m, respectively. 75 rod groups can be distributed over 13 families, as is shown in Table D.2 (see Appendix D).

Family 1 consists of rod groups belonging to classes C_q and containing rotations q or q_p, p = 0, 1, ..., $q-1$ (in international notations) around q-order ($q = 2, 3, 4, 6$) rotation or screw axis. Family 5 consists of rod groups belonging to classes D_q and containing rotations q or q_p around the q-order rotation or screw axis and rotations U. The symmorphic rod groups of classes S_{2q}, C_{qh}, C_{qv}, D_{qd} and D_{qh} are related to families 2, 3, 6, 9 and 11, respectively. The remaining 6 families are formed by nonsymmorphic rod groups and include rotations around screw axes $(2q)_q$ with $q = 1, 2, 3$ (families 4, 8, 13) or reflections in vertical glide planes (families 7, 10, 12). As can be seen from Table D.2, rod groups 15 and 18 refer to families 6 (crystal class C_{2v}) and 11 (crystal class D_{1h}), respectively.

Table D.3 (see Appendix D) is taken from [3] and presents rod groups in the form accepted for a line group classification.

For the symmorphic RG a crystallographic factorization RG = TF coincides with that used for line groups (RG = TP_I). For nonsymmorphic RG difference appears: compare Tables D.2 and D.3.

The first family rod groups ($T_q^r C_n$) are represented in the standard factorization as q_p, q = 1, 2, 3, 4, 6; p = 0, 1, ..., $q-1$. In the standard factorization $L = (C_q^1|\frac{p}{q})$ where C_q^1 is the rotation by the angle $\frac{2\pi}{q}$ around the translation axis. Evidently $L = (C_q^r|\frac{rp}{q})$ so that $rp = n + lq$ (l is integer, $n = \mathrm{GCD}(q, r)$). These relations allow the two factorizations of the same rod group to be written. As an example we consider the rod group 57 ($L6_4$) of the first family: q = 6, n = 2, p = 4. Therefore $4r = 2 + 6l$, $r = 2$ (for l = 1) and the rod group 57 in the factorization (2.22) is written as $T_6^2 C_2$, see Table D.3.

Let us consider now rod groups belonging to family 4. In the crystallographic factorization these groups belong to classes C_{qh}, q = 1, 2, 3, see Table D.3. However, the factor group F contains rotations around the screw axis of the order $(2q)_q$ i.e. rotations around the translation axis are in fact rotohelical operations, including the rotation and improper translation by a half of the translation vector. The rod groups of family 4 can be factorized in such a way that the rotohelical operations are included in the cyclic group of the generalized translations Z (pure translations form the subgroup T of the group Z) and pure rotations are included in the point group P_n, see Table D.3. In this case rod groups of family 4 are written in the form ZP, where $Z = T_q^1$ and $P_n = C_{nh}$. Next we consider the example of the rod groups of family 12, belonging to crystallographic class D_{qh} and containing reflections in the vertical glide planes, see Table D.3. Now Z = T′ and contains all the pure translations and reflections in glide planes while $P_n = C_{nh}$, see Table D.3.

Rod groups being a special case of the line groups, arise as 1-periodic subgroups of space groups and it comes as no surprise that space groups may contain different geometric realizations of the same line group. Rod groups settings as a special geometric realizations of line groups are considered in [26]. For each of the 8 families of non-symmorphic line groups the explicit correspondence between rod groups and relevant geometric realizations of the corresponding line groups is established. The settings of rod groups and line groups are taken into account.

In crystallography different realizations of the same rod group are called *settings*. In the theory of line groups crystallographic settings manifest themselves as geometric realizations with specially chosen setting angles. Besides infinitely many geometric realizations of line groups containing reflections in vertical planes or Umklapp transformations there exist realizations which differ in the choice of a horizontal reflection plane. For example, instead of the point group $\mathrm{C}_{nh} = \mathrm{C}_n \cup \sigma_h \mathrm{C}_n$ it is possible to take the group $\mathrm{C}'_{nh} = \mathrm{C}_n \cup (\sigma_h|\frac{a}{2})\mathrm{C}_n$ which corresponds to selection as the reflection plane the affine plane parallel to the xy-plane but passing through the point $(0, 0, \frac{a}{4})$.

As we already mentioned, the rod groups are distinguished among general line groups by the orders q of principal axes of the isogonal groups which can take the values $q = 1, 2, 3, 4, 6$. For $q = 3, 6$ in tables of rod groups [5] the hexagonal coordinate system is used. The hexagonal coordinate system is obtained by the rotation of the y axis counter-clockwise by $\frac{\pi}{6}$ angle in the xy-plane. Basis vectors of the hexagonal coordinate system are connected with the Cartesian ones by the relations:

$$h_1 = e_1, \quad h_2 = -\frac{1}{2}e_1 + \frac{\sqrt{3}}{2}e_2, \quad h_3 = e_3 \tag{2.29}$$

To compare line and rod group realizations one should be able to proceed from the usual mathematical notation of affine transformations to that accepted in crystallography [5]. Symmetry elements (reflexion planes, axes, etc.) are defined in crystallography *parametrically*. For example, in Cartesian coordinates a triplet $x, 0, z$ defines a plane as a locus $\{xe_1 + ze_3 : x, z \in \mathbb{R}\}$. It is clear that the normal vector of this plane is $e_2 = (0, 1, 0)$. A triplet $x + s, -x, z$ defines the affine plane $\{(x + s)e_1 - xe_2 + ze_3 : x, z \in \mathbb{R}\}$ passing through the point $(s, 0, 0)$ and with the normal vector $e_1 + e_2 = (1, 1, 0)$. A triplet $x, -x, 0$ defines a line $\{xe_1 - xe_2 : x \in \mathbb{R}\}$ in the xy-plane. A triplet $x, -x, \frac{a}{4}$ is a line in the affine plane passing through the point $(0, 0, \frac{a}{4})$ in parallel with the xy-plane. The analogous convention is used in the case when the hexagonal coordinate system is used. For example, lines in the xy-plane having with the x-axis angles $-\frac{\pi}{3}, -\frac{\pi}{6}, 0, \frac{\pi}{6}, \frac{\pi}{3}, \frac{\pi}{2}, \frac{2\pi}{3}$ and passing through the origin have the following parametric presentation in hexagonal coordinate system: $0, y, 0$; $x, -x, 0$; $x, 0, 0$; $2x, x, 0$; $x, x, 0$; $x, 2x, 0$; $0, y, 0$.

Basic symmetry operations of rod groups in crystallography have the following designation: rotation $(C_{\pm n}|0)$ around the z-axis is designated as $n^{\pm}\ 0, 0, z$, screw rotation $(C_{\pm n}|f)$—as $n^{\pm}(f)\ 0, 0, z$, reflection $(\sigma_0|0)$ with respect to the xz-plane—as $m\,x, 0, z$, reflection $(\sigma_{\frac{\pi}{4}}|0)$—as $m\,x, x, z$, reflection $(\sigma_h|0)$—as $m\,x, y, 0$. Glide plane reflections of the type $(\sigma_0|\frac{a}{2})$ are encoded as $c\ x, 0, z$, transformations $(\sigma_h|\frac{a}{2})$—as

$m\ x, y, \frac{a}{4}$. Umklapp transformations are interpreted as rotations: for example, transformation $(U_{\frac{\pi}{2}}|0)$ is designated as $2\,0, y, 0$, and transformation $(U_{\frac{\pi}{2}}|\frac{a}{2})$—as $2\,0, y, \frac{a}{4}$. The notation for transformations of the type $(\sigma_h C_{\pm n}|f)$ is slightly more cumbersome and not unique: operation $(\sigma_h C_{\pm n}|0)$ is designated as $\bar{n}^{\pm}\,0, 0, z; 0, 0, 0$, and operation $(\sigma_h C_{\pm n}|\frac{a}{2})$—either as $\bar{n}^{\pm}(\frac{a}{2})\,0, 0, z; 0, 0, 0$ or as $\bar{n}^{\pm}\,0, 0, z; 0, 0, \frac{a}{4}$. In the last example ambiguity is connected with existence of two equivalent presentation of the transformation under consideration: $(\sigma_h C_{\pm n}|\frac{a}{2}) = (\sigma_h|\frac{a}{2})(C_{\pm n}|0) = (C_{\pm n}|\frac{a}{2})(\sigma_h|0)$. Inversion at the origin is encoded as $\bar{1}\,0, 0, 0$.

Line groups of the first family do not depend on the setting angle because their geometric realization is uniquely defined by the choice of the rotation axis and a convention about the direction of rotation (normally counter-clockwise). Therefore, each rod group of the first family should appear in the unique setting.

For each of the seven families of nonsymmorphic line groups the explicit correspondence between rod groups and relevant geometric realizations of the corresponding line groups is established in [29]. The settings of rod groups and line groups are taken into account. The results are presented in a table of 75 rod groups listed (in international and factorized notation) by families of the line groups according to the order of the principal axis q (q = 1, 2, 3, 4, 6) of the corresponding isogonal point group.

2.5.3 Orbits with Respect to Line and Rod Groups

Orbits are useful both in theory of molecules, polymers, and solids. Indeed, for arbitrary group G its orbit G.**x** contains points that should be occupied by atoms of the same element if at least one point, say **x**, is occupied by an atom of this type. In theory of molecules implicit subdivision of space into the union of orbits is performed as the first step in construction of symmetry adapted basis functions. Actual construction is performed either by application of certain projection operators or by diagonalization of specially selected matrices. It is normally assumed that irreducible matrix representations are tabulated and ready for use. Therefore the conception of stabilizer is not very fruitful here. The situation is different in line group theory. Stabilizers are used for site symmetry analysis and for construction of Frobenius induced representations. Line groups operate on the cylindrical (Cyl) surfaces of fixed radius and the corresponding orbits also lie on these surfaces. Type, or symmetry of orbit is defined by the set of stabilizers of its points: orbits of the same type have *identical* sets of stabilizers. Such orbits are called equivalent. Since non-degenerate cylindrical surfaces with fixed $\rho \neq 0$ are of dimension 2, sets of equivalent orbits as topological spaces can be of dimensions 2, 1, and 0 (isolated orbits). For $\rho = 0$ sets of equivalent orbits may be of dimension 1 and 0. It is convenient to introduce the notation $\mathbf{x}_\rho(\alpha+\beta, z) = (\rho\cos(\alpha+\beta), \rho\sin(\alpha+\beta), z)$ for general point belonging to Cyl_ρ where α will play the role of the *setting angle* and β angle will be used for orbit parametrization (along with the z- coordinate).

L-orbits and their types can not depend upon line group factorization. But it is possible to construct in a certain sense minimal sets of representatives of line group orbits which (i) uniquely define the orbit type, and (ii) can be used for *easy* generation of the whole L-orbit. These sets may depend on the line group factorization. It is clear that F-orbits can play a role of such sets of representatives in the case when the standard factorization is used. If the factorization $\mathrm{L} = \mathrm{ZP}$ is exploited then, as can be shown [3], either P or P^+-orbits satisfy the aforementioned requirements (i) and (ii) in *almost all* situations. Here P^+ is a subgroup of group P formed by orthogonal transformations leaving unchanged z- coordinate of any point. Ambiguity may arise in the case when the type of $\mathrm{P}(\mathrm{P}^+)$-orbit depends on the parity of n but the corresponding L-orbits turn out to be equivalent for all values of n. For example, if $\mathrm{P} = \mathrm{C}_{nv}(\alpha)$ then $\mathrm{C}_{nv}(\alpha)$ - orbits $\mathrm{C}_{nv}(\alpha)\mathbf{x}_\rho(\alpha, z)$ and $\mathrm{C}_{nv}(\alpha)\mathbf{x}_\rho(\alpha + \frac{\pi}{n}, z)$ are equivalent for odd and non-equivalent for even values of n. But the corresponding $\mathbf{T}^1_{2n}(a)\mathrm{C}_{nv}(\alpha)$-orbits (line groups of family 8) are equivalent without dependence on the parity of n. The analogous situation takes place for the line groups of family 13. And the second nuance is connected with the fact that even for symmorphic groups there may exist P^+-orbits whose actual type (symmetry) is determined by subgroups including transformations with *non-zero translational parts*. In more rigorous terms, if $\mathbf{x}$ is a point of P^+-orbit then it is possible that the stabilizer $\mathrm{P}^+_{\mathbf{x}}$ turns out to be only a proper subgroup of the full stabilizer $\mathrm{L}_{\mathbf{x}}$.

It is easy to see that $\mathrm{P}(\mathrm{P}^+)$-orbits are always the subsets of the corresponding F-orbits. The major difference between them is the following. L-orbit is obtained from the corresponding F-orbit by application to its points all possible pure translations along the z-axis. If the factorization (2.22) is used then either the screw axis group or the glide plane group must be applied to the points of the $\mathrm{P}(\mathrm{P}^+)$-orbit to get the whole L-orbit. Unfortunately in general there is no one-to-one correspondence between symmetry labels of orbits with respect to Line and Rod groups.

2.5.4 Nanotube Rolling Up from 2D Systems

The simplest description of nanotube symmetry and structure is based on so-called layer folding. Let $\mathbf{a}$ and $\mathbf{b}$ be the primitive translation vectors $\mathbf{a}_1$ and $\mathbf{a}_2$ of the two-periodic (2D) lattice of the layer and γ-the angle between them. Layer folding means the construction of the cylindrical surfaces of nanotubes by rolling up 2D crystalline layers. To specify the symmetry of nanotubes as monoperiodic (1D) systems, it is necessary to define the finite 1D translation vector $\mathbf{L} = l_1\mathbf{a} + l_2\mathbf{b}$ along the nanotube axis and normal to the chiral vector $\mathbf{R} = n_1\mathbf{a} + n_2\mathbf{b}$ (l_1, l_2, n_1 and n_2 are integers). The nanotube of the chirality (n_1, n_2) is obtained by folding the layer in a way that the chiral vector $\mathbf{R}$ becomes circumference of the tube. The orthogonal vectors $\mathbf{R}$ and $\mathbf{L}$ are connected with the 2D lattice translation vectors $\mathbf{a}$ and $\mathbf{b}$ by the transformation

$$\begin{pmatrix} \mathbf{R} \\ \mathbf{L} \end{pmatrix} = \mathbf{Q} \begin{pmatrix} \mathbf{a} \\ \mathbf{b} \end{pmatrix} \tag{2.30}$$

The determinant $q = \begin{vmatrix} n_1 & n_2 \\ l_1 & l_2 \end{vmatrix}$ of the matrix $\mathbf{Q} = \begin{pmatrix} n_1 & n_2 \\ l_1 & l_2 \end{pmatrix}$ is equal to the number of 2D lattice points in the plane lattice supercell formed by the chirality $\mathbf{R}$ and translation $\mathbf{L}$ vectors. The orthogonality relation $\mathbf{RL} = 0$ can be written in the form:

$$\frac{l_1}{l_2} = -\frac{n_2 b^2 + n_1 ab\cos\gamma}{n_1 a^2 + n_2 ab\cos\gamma} \tag{2.31}$$

where $a = |\mathbf{a}|$ and $b = |\mathbf{b}|$. If n is the greatest common devisor of n_1 and n_2 ($\tilde{n}_1 = n_1/n, \tilde{n}_2 = n_2/n$), one can introduce the reduced chirality vector $\tilde{\mathbf{R}}$ along the direction of the vector $\mathbf{R}$:

$$\tilde{\mathbf{R}} = \frac{1}{n}\mathbf{R}; \quad \begin{pmatrix} \tilde{\mathbf{R}} \\ \mathbf{L} \end{pmatrix} = \tilde{\mathbf{Q}} \begin{pmatrix} \mathbf{a} \\ \mathbf{b} \end{pmatrix}; \quad \tilde{\mathbf{Q}} = \begin{pmatrix} \tilde{n}_1 & \tilde{n}_2 \\ l_1 & l_2 \end{pmatrix}; \quad \tilde{q} = \det(\tilde{\mathbf{Q}}) \tag{2.32}$$

The comparison of (2.31), (2.32) shows that $q = n\tilde{\mathrm{q}}$ where $\tilde{q}$ is the number of the lattice points in the supercell formed by the reduced chirality $\tilde{\mathbf{R}}$ and translation $\mathbf{L}$ vectors.

Commensurate nanotubes, being monoperiodic systems, have a line group symmetry $\mathbf{L} = \mathbf{ZP}$ [30, 31], where $\mathbf{P}$ is the point factor and $\mathbf{Z}$ is the generalized translation group. The point factor $\mathbf{P}$ is a subgroup of the axial point group $\mathbf{P_I}$ belonging to one of the axial symmetry point groups. The group $\mathbf{Z}$ is infinite and cyclic, describing either the glide plane reflections $T' = (\sigma_v|\frac{1}{2})$ or the screw axis rotations by $\frac{2\pi}{n\tilde{q}}$ (for $\tilde{q} > 1$) generated by helical operations $T_q^r = (C_q^r|\frac{1}{\tilde{q}})$ where $r = 0, 1, \ldots, n-1$. For $n > 1$, pure rotations appear and form a subgroup of the point symmetry group $\mathbf{P_I}$. The smallest helical vector $\mathbf{H}$ is defined as $\mathbf{H} = h_1\mathbf{a} + h_2\mathbf{b} = \frac{r}{n\tilde{q}}\mathbf{R} + \frac{1}{\tilde{q}}\mathbf{L}$ and satisfies the following conditions: $\tilde{n}_1 h_2 - \tilde{n}_2 h_1 = 1$; $h_1 l_2 - h_2 l_1 = r$. The projections of the helical vector $\mathbf{H}$ on the chiral vector $\mathbf{R}$ and translation vector $\mathbf{L}$ (Fig. 2.24) define the rotational and translational parts of the helical rotation T_q^r, respectively. It is evident that the translational part of the helical vector $\mathbf{H}$ is the same for the ray of the nanotubes $(n_1, n_2) = n(\tilde{n}_1, \tilde{n}_2)$, differing by n.

The symmetry of a nanotube is defined by: (i) the nanotube chirality (n_1, n_2), (ii) translation vector components (l_1, l_2) found from the orthogonality relation (2.31), (iii) the point symmetry of the rolled 2D lattice (see below).

The orthogonality relation has different forms for different 2D lattices:

-rectangular primitive ($\cos\gamma = 0; a \neq b$);

$$\frac{l_1}{l_2} = -\frac{n_2 a^2}{n_1 b^2}, \quad \text{or} \quad l_1 n_1 b^2 = -l_2 n_2 a^2; \tag{2.33a}$$

- rectangular centered ($\cos\gamma \neq 0, \frac{1}{2}; a = b$);

$$\frac{l_1}{l_2} = -\frac{n_2 + n_1\cos\gamma}{n_1 + n_2\cos\gamma}; \tag{2.33b}$$

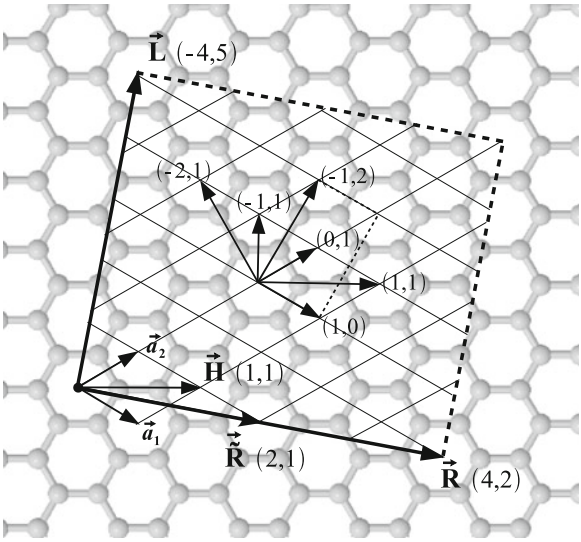

Fig. 2.24 Chirality vectors of the nanotubes from graphene layer

- square ($\cos\gamma = 0; a = b$);

$$\frac{l_1}{l_2} = -\frac{n_2}{n_1} \quad \text{or} \quad l_1 n_1 + l_2 n_2 = 0; \tag{2.33c}$$

- hexagonal ($\cos\gamma = \frac{1}{2}; a = b$);

$$\frac{l_1}{l_2} = -\frac{2n_2 + n_1}{2n_1 + n_2}. \tag{2.33d}$$

It is readily seen from (2.33) that the translational symmetry of the nanotube can exist for any arbitrary chirality (n_1,n_2) if the nanotube is obtained by folding the layer with square or hexagonal 2D lattices. However, there are restrictions on the possible chiralities for rectangular lattices: (n,0), (0,n) for rectangular primitive and ($-n$,n), (n,n) for rectangular centered ones.

The translations of the layer become rotohelical operations T_q^r on the nanotube, giving the first family subgroup $\mathbf{L}^{(1)} = \mathbf{ZP}(\mathbf{P} = \mathbf{C}_q)$ of the nanotube line group $\mathbf{L}$. The latter has the same parameters for the ray of the nanotubes $(n_1, n_2) = n(\tilde{n}_1, \tilde{n}_2)$, differing by n.

Apart from the translational invariance, the layer groups have rotational symmetry generated by the rotations around the z-axis perpendicular to the layer. For rectangular, square and hexagonal lattices the order of these rotation axes is 2, 4 and 6, respectively. In addition, non-oblique 2D lattices have both vertical mirror and glide planes. In the layer groups some of the 2D lattice symmetry operations are absent.

The symmetry operations matrices $G^{(3)} = (F^{(3)}|\mathbf{t}^{(2)})$, corresponding to the layer group, consist of orthogonal $F^{(3)}$ and translational $\mathbf{t}^{(2)}$ parts. Let the Cartesian axes x, y and z be directed along the chiral vector $\mathbf{R}$, the nanotube translation vector $\mathbf{L}$ and the layer principal axis perpendicular to the layer, respectively.

During the folding procedure after the transformation described by (2.30) of the 2D lattice the orthogonal symmetry operations survive if they do not change the z-coordinate (the layer is rolled up to the tube) and do not mix or interchange the x and y coordinates (chirality and translation vectors are assumed to be fixed). It means that after folding the layer, only those layer group symmetry operations survive which had the diagonal 2×2 submatrices

$$F^{Q} = \begin{pmatrix} \pm 1 & 0 \\ 0 & \pm 1 \end{pmatrix}$$

$$E = \begin{pmatrix} 1 & 0 \\ 0 & 1 \end{pmatrix}, \quad U = \begin{pmatrix} -1 & 0 \\ 0 & -1 \end{pmatrix}, \quad \sigma_v = \begin{pmatrix} -1 & 0 \\ 0 & 1 \end{pmatrix}, \quad \sigma_h = \begin{pmatrix} 1 & 0 \\ 0 & -1 \end{pmatrix} \tag{2.34}$$

The transformations (2.34) include the rotation U by π around the second order axis, normal to the tube, and reflections in planes, orthogonal to the 2D lattice plane and parallel to the tube axis, directed along the translation vector $\mathbf{L}(\sigma_v)$ or orthogonal to it (σ_h). In particular among the normal-to-layer rotation axes only the two-fold U-axes survive, being compatible with the monoperiodic symmetry. Therefore whenever the order of the principal axis of the layer is 2, 4 or 6, the symmetry of the nanotube is at least the fifth family line group $\mathbf{L}^{(5)} = \mathbf{ZP}(\mathbf{P} = \mathbf{D}_q)$.

The transformed translations $\mathbf{t}^{Q}$ can be written in the components of the vectors $\mathbf{R}$ and $\mathbf{L}$ as:

$$\mathbf{t}^{Q} = (0\ 0), \quad \left(\tfrac{1}{2n}\ 0\right), \quad \left(0\ \tfrac{1}{2}\right), \quad \left(\tfrac{1}{2n}\ \tfrac{1}{2}\right) \tag{2.35}$$

where $n = 1$ for the reduced chirality vector $\tilde{\mathbf{R}}$, while 1/2 in the second position produces the non-symmorphic line groups containing the helical rotation $T^{1}_{2n} = (C^{1}_{2n}|\frac{1}{2})$ or the reflection in glide plane $T' = (\sigma_v|\frac{1}{2})$. The nanotube symmetry groups are formed by the point symmetry operations (2.34) and translations (2.35) survive the folding and combined in such a way that they form the line group $\mathbf{L} = \mathbf{ZP}$.

The procedure described can be applied for finding the nanotube symmetry if the symmetry of the layer group used for folding is known [31]. A helical axis and pure rotations are always present in the line group of a nanotube, while mirror and glide planes appear only for special chiral vectors of rectangular, square and hexagonal lattices. Table 2.10 presents the rolling up correspondence of the line and diperiodic (layer) groups. For each family F of the line groups the roto-helical subgroup $\mathrm{L}^{(1)}$ and the isogonal group P^{I}_{q} (for irrational Q in families 1 and 5, q is infinite)are given in columns 2 and 3. The corresponding diperiodoc groups enumerated according to [5] follow: for an arbitrary chiral vector the rolling gives either the first or the fifth family line group (when the order of the orthogonal to the lattice plane axis is

Table 2.10 Rolling up correspondence of the line and diperiodic (layer) groups

F	$L^{(1)}$	P_q^I	Diperiodic groups
1	$T_Q C_n$	C_q	1,2,4,5,8,9,10,11,12,13,14,15,16,17,18,27,28,29,30, 31,32,33,34,35,36,65,66,67,68,69,70,71,72,74,78,79
5	$T_Q C_n$	D_q	3,6,7,19,20,21,22,23,24,25,26,37,38,39,40,41,42,43,44,45,46,47,48, 49,50,51,52,53,54,55,56,57,58,59,60,61,62,63,64,73,75,76,77,80
2	TC_q	S_{2q}	**a**:17,33,34; **b**:12,16,29,30
3	TC_q	C_{qh}	**a**:11,14,15,27,31,32; **b**:28
4	$T^1_{2q}C_q$	C_{2qh}	**e**:13,18,35; **d**:36; **h**:69,72,78; **g**:70,71,79
6	TC_q	C_{qv}	**a**:28; **b**:11,14,15,27,31,32
7	TC_q	C_{qv}	**a**:12,16,29,30; **b**: 17,33,34
8	$T^1_{2q}C_q$	C_{2qv}	**e**:36; **d**:13,18,35; **h**:70,71,79; **g**:69,72,78
9	TC_q	D_{qd}	**a**:42,45; **b**:24,38,40
10	TC_q	D_{qd}	**c**:25,39,43,44,56,60,62,63
11	TC_q	D_{qh}	**c**:23,37,41,46,55,59,61,64
12	TC_q	D_{qh}	**a**:24,38,40; **b**:42,45
13	$T^1_{2q}C_q$	D_{2qh}	**f**:26,47,48,55,56,57,58,61,62,63,64; **i**:77,80

2, 4, 6). The underlined diperiodic groups (following after the corresponding special chiral vectors) give other line group families below. The corresponding special chiral vectors are the following: $a = (n, 0)$, $b = (0, n)$, $c \in \{(n, 0), (0, n)\}$, $d = (n, n)$, $e = (-n, n)$, $f \in \{(n, n), (-n, n)\}$, $g \in \{(n, 0), (0, n), (-n, n)\}$, $h \in \{(n, n), (-n, 2n), (-2n, n)\}$, $i \in \{(n, 0), (0, n), (-n, n), (n, n), (-n, 2n), (-2n, n)\}$.

2.5.5 Hexagonal and Square Lattices

Different types of nanotubes can be rolled up from layers with a hexagonal plane lattice. We call them nanotubes with hexagonal morphology. Figure 2.25 shows the supercells of a graphene layer defining armchair (3,3), zigzag (3,0) and chiral (6,3) nanotubes.

The first reports on synthesis of carbon nanotubes [32] were followed by extensive symmetry investigation [3, 33] of the nanotubes with hexagonal morphology. Equation (2.33d) ensures the orthogonality of the chiral and translation vectors. From (2.32) we find the matrix $\tilde{\mathbf{Q}}$, its determinant $\tilde{q}$, the components h_1, h_2 of the smallest helical vector $\mathbf{H}$ and $r = h_1 l_2 - h_2 l_1$ for the special chiral vectors $\mathbf{R}$.

$$\mathbf{R}(n, n) : l_1/l_2 = -1; \quad \tilde{\mathbf{Q}} = \begin{pmatrix} 1 & 1 \\ -1 & 1 \end{pmatrix}; \ \tilde{q} = 2; \quad \mathbf{H}(0, 1), \ r = 1 \tag{2.36a}$$

$$\mathbf{R}(-n, n) : l_1/l_2 = 1; \quad \tilde{\mathbf{Q}} = \begin{pmatrix} -1 & 1 \\ -1 & -1 \end{pmatrix}; \ \tilde{q} = 2; \quad \mathbf{H}(-1, 0), \ r = 1 \tag{2.36b}$$

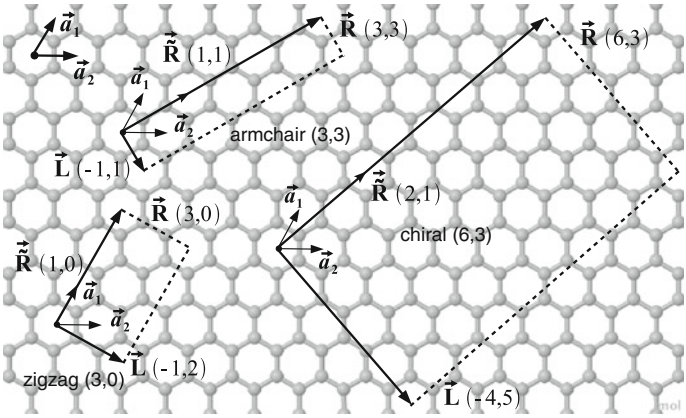

Fig. 2.25 Supercells of graphene layer defining armchair (3,3), zigzag (3,0) and chiral (6,3) nanotubes

$$\mathbf{R}(n,0): l_1/l_2 = -1/2; \quad \tilde{\mathbf{Q}} = \begin{pmatrix} 1 & 0 \\ -1 & 2 \end{pmatrix}; \ \tilde{q} = 2; \quad \mathbf{H}(0,1), \ r = 1 \tag{2.36c}$$

$$\mathbf{R}(-n,2n): l_1 = 1, \ l_2 = 0; \quad \tilde{\mathbf{Q}} = \begin{pmatrix} -1 & 2 \\ -1 & 0 \end{pmatrix}; \ \tilde{q} = 2; \quad \mathbf{H}(-1,1), \ r = 1 \tag{2.36d}$$

$$\mathbf{R}(-2n,n): l_1 = 0, \ l_2 = -1; \quad \tilde{\mathbf{Q}} = \begin{pmatrix} -2 & 1 \\ 0 & -1 \end{pmatrix}; \tilde{q} = 2; \quad \mathbf{H}(-1,1), \ r = 1 \tag{2.36e}$$

As $\tilde{q} = 2$ for all the special chiral vectors, the rototranslational part of the corresponding line group is $T^1_{2n} = (C^1_{2n}|\frac{1}{2})$ while $q = n\tilde{q}$ and $\mathbf{L} = \mathbf{T}^1_{2n}\mathbf{P}_n$. For the general chiral vector $\mathbf{R}(n_1, n_2)(n_1 \neq 0, n_2 \neq 0; n_2 \neq \pm n_1, -2n_1, -\frac{1}{2}n_1)$ we have

$$\tilde{\mathbf{Q}} = \begin{pmatrix} \tilde{n}_1 & \tilde{n}_2 \\ -(2\tilde{n}_2 + \tilde{n}_1) & (2\tilde{n}_1 + \tilde{n}_2) \end{pmatrix}, \ \tilde{q} = 2(\tilde{n}_1^2 + \tilde{n}_1\tilde{n}_2 + \tilde{n}_2^2); \ \tilde{n}_1 h_2 - \tilde{n}_2 h_1 = 1;$$
$$(2\tilde{n}_1 + \tilde{n}_2)h_1 + (2\tilde{n}_2 + \tilde{n}_1)h_2 = r$$

In this case the rotohelical operations are $T^r_q = (C^r_q|\frac{\tilde{t}}{\tilde{q}})$, $q = n\tilde{q}$ is the order of the screw axis, $r = 0, 1, 2 \ldots, q - 1$.

Keeping in mind these results let us analyze Table 2.10. The hexagonal lattice defines layer groups 65–80 (see Table in Chap. 11). In groups 65–68 and 74 the order 3 axes are orthogonal to the lattice plane and mirror planes are absent. Therefore these groups belong to Family one and the tubes rolled up from the corresponding layers have the same symmetry for any chiral vector $\mathbf{R}(n_1, n_2)$. The tubes rolled up from layers with diperiodic groups 69, 72, 78, 70, 71, 79 belong to families 4, 8 depending on the setting of the special chiral vector relative to the mirror planes.

In all these groups the mirror planes appear that are orthogonal to the x- or y-axis appear. Finally, the tubes rolled up from the layers with diperiodic groups 77, 80 belong to Family 13: in these layer groups there are mirror planes orthogonal both to the x- and y-axes.

Perovskite $SrTiO_3$, $BaTiO_3$ nanotubes are synthesized by a low temperature hydrothermal reaction [34]. These nanotubes have a square morphology, i.e. can be rolled up from layers with a square plane lattice ($\cos\gamma = 0; a = b$) [35]. From (2.33c) it follows that $l_1 n_1 + l_2 n_2 = 0$. Applying (2.32) we have

$$\mathbf{R}(n,0) : l_1 = 0,\ l_2 = 1;\quad \tilde{\mathbf{Q}} = \begin{pmatrix} 1 & 0 \\ 0 & 1 \end{pmatrix};\ \tilde{q} = 1;\quad \mathbf{H}(0,1),\ r = 0 \tag{2.37a}$$

$$\mathbf{R}(0,n) : l_1 = -1,\ l_2 = 0;\quad \tilde{\mathbf{Q}} = \begin{pmatrix} 0 & 1 \\ -1 & 0 \end{pmatrix};\ \tilde{q} = 1;\quad \mathbf{H}(-1,0),\ r = 0 \tag{2.37b}$$

As in (2.37a), (2.37b) $r = 0$, no screw axis appears either for $\mathbf{R}(n,0)$ or $\mathbf{R}(0,n)$ special chiral vectors.

$$\mathbf{R}(n,n) : l_1 = -1,\ l_2 = 1;\quad \tilde{\mathbf{Q}} = \begin{pmatrix} 1 & 1 \\ -1 & 1 \end{pmatrix};\ \tilde{q} = 2;\quad \mathbf{H}(0,1),\ r = 1 \tag{2.37c}$$

$$\mathbf{R}(-n,n) : l_1 = -1,\ l_2 = -1;\quad \tilde{\mathbf{Q}} = \begin{pmatrix} -1 & 1 \\ -1 & -1 \end{pmatrix};\ \tilde{q} = 2;\quad \mathbf{H}(-1,0),\ r = 1 \tag{2.37d}$$

As in (2.37c), (2.37d) $\tilde{q} = 2$, the rototranslational part of the corresponding line groups is $T^1_{2n} = (C^1_{2n}|\frac{1}{2})$ while $q = n\tilde{q} = 2n$ and $\mathbf{L} = \mathbf{T}^1_{2n}\mathbf{P}_n$.

For the general chiral vector $\mathbf{R}(n_1, n_2)$, $(n_1 \neq 0, n_2 \neq 0; n_2 \neq \pm n_1)$ we have

$$\tilde{\mathbf{Q}} = \begin{pmatrix} \tilde{n}_1 & \tilde{n}_2 \\ -\tilde{n}_2 & \tilde{n}_1 \end{pmatrix},\ \tilde{q} = \tilde{n}_1^2 + \tilde{n}_2^2;\ \tilde{n}_1 h_2 - \tilde{n}_2 h_1 = 1;\ \tilde{n}_1 h_1 + \tilde{n}_2 h_2 = r;$$
$$h_1 = \frac{1}{\tilde{q}}(r\tilde{n}_1 - \tilde{n}_2);\ h_2 = \frac{1}{\tilde{q}}(r\tilde{n}_2 + \tilde{n}_1) \tag{2.37e}$$

In this case the rotohelical operations are $T^r_q = (C^r_q|\frac{1}{\tilde{q}})$, $q = n\tilde{q}$ is the order of the screw axis, $r = 0, 1, 2, \ldots, q-1$.

Now let us analyze Table 2.10 for layer groups 49–64 with a square lattice. In all these groups the order four axis is orthogonal to the lattice plane. Therefore the tubes with the general chiral vector $\mathbf{R}(n_1, n_2)$ belong to the fifth family. In groups 49–54 there are no mirror planes orthogonal to the lattice plane. Therefore the line group of the corresponding nanotubes belong to the fifth family. As no screw axis appears for the tubes with the special chiral vectors $\mathbf{R}(n,0)$ and $\mathbf{R}(0,n)$, see (2.37a), (2.37b), the corresponding line groups 56, 60, 62, 63 and 55, 59, 61, 64 are symmorphic and belong to families ten and eleven, respectively. These two sets of groups differ in the type of the mirror plane: in the former the orthogonal to the x-axis plane is a glide plane, in the latter this plane is a mirror plane. In layer groups 57, 58 there are no

mirror or glide planes orthogonal to the x-axis. The special chiral vectors $\mathbf{R}(n, n)$ and $\mathbf{R}(-n, n)$, see (2.37c), (2.37d) generate tubes with line groups belonging to Family 13 with a rotochelical tube axis of the order $q = 2n$.

2.5.6 Rectangular Lattices

The layers with rectangular lattices are used for inorganic TiO_2 nanotube modeling [36–38].

For the primitive rectangular lattice ($\cos\gamma = 0; a \neq b$) we have $l_1 n_1 b^2 = -l_2 n_2 a^2$, see (2.33a). For commensurate nanotubes a/b has to be a rational number as it defines l_1/l_2 (l_1, l_2 are integers). It means that the nanotubes are commensurate only for the special chiral vectors.

$$\mathbf{R}(n,0) : l_1 = 1,\ l_2 = 0;\quad \tilde{\mathbf{Q}} = \begin{pmatrix} 1 & 0 \\ 0 & 1 \end{pmatrix};\ \tilde{q} = 1;\quad \mathbf{H}(0,1),\ r = 0 \tag{2.38a}$$

$$\mathbf{R}(0,n) : l_1 = 0,\ l_2 = 1;\quad \tilde{\mathbf{Q}} = \begin{pmatrix} 0 & 1 \\ -1 & 0 \end{pmatrix};\ \tilde{q} = 1;\quad \mathbf{H}(-1,0),\ r = 0 \tag{2.38b}$$

It is seen that for a primitive rectangular lattice the screw axis is absent ($r = 0$).

For the rectangular centered lattice ($cos\gamma \neq 0, 0.5; a = b$), see (2.33b), we have:

$$\frac{l_1}{l_2} = -\frac{n_2 + n_1 \cos\gamma}{n_1 + n_2 \cos\gamma};$$

The corresponding nannotubes are commensurate for the following special chiral vectors:

$$\mathbf{R}(n,n) : l_1 = -1,\ l_2 = 0;\quad \tilde{\mathbf{Q}} = \begin{pmatrix} 1 & 1 \\ -1 & 1 \end{pmatrix};\ \tilde{q} = 2;\quad \mathbf{H}(0,1),\ r = 1 \tag{2.39a}$$

$$\mathbf{R}(-n,n) : l_1 = -1,\ l_2 = -1;\quad \tilde{\mathbf{Q}} = \begin{pmatrix} -1 & 1 \\ -1 & -1 \end{pmatrix};\ \tilde{q} = 2;\quad \mathbf{H}(-1,0),\ r = 1 \tag{2.39b}$$

In this case the rotohelical operations are $T_q^r = (C_q^r | \frac{1}{\tilde{q}})$, $q = 2n$ is the order of the screw axis, $r = 0, 1, 2, \ldots, q-1$.

Now let us analyze Table 2.10 for layer groups 8–48 with rectangular primitive and centered lattices. In groups 8–10 there are no U axis or mirror planes and these groups generate nanotubes belonging to the first family. The two-fold axis orthogonal to the layer plane appears in layer groups 19–22, so that the corresponding nanotube symmetry belongs to the fifth family. The line groups generated by the rolling vectors $\mathbf{R}(n, 0)$ and $\mathbf{R}(0, n)$ are both symmorphic (families 2,3,6,9) or contain a glide plane (families 7,9,12). The line groups generated by the rolling vectors $\mathbf{R}(n, n)$ and $\mathbf{R}(-n, n)$ are nonsymmorphic (families 4,8,13).

For arbitrary single-walled nanotubes, the algorithm of rolled up nanotubes construction, described here theoretically within the formalism of line groups, is also implemented for composition of inputs in CRYSTAL code [14, 39] and is now actively used in LCAO calculations of the different inorganic nanotubes. Nanotubes of any size and order of symmetry can be built automatically by rolling up a 2D slab [40]. That is done by specifying a pair of integers to define a roll-up vector in terms of the slab unit vector components. The rolling vector is perpendicular to the nanotube axis and its modulus is the nanotube circumference.

2.5.7 Symmetry of Double and Multiwall Nanotubes

The symmetry groups of doublewall and multiwall nanotubes are considered in [3, 30, 41]. The symmetry of SW NTs is described by line group $\mathbf{L} = \mathbf{ZP}$, which is a product of axial point group $\mathbf{P}$ and the infinite cyclic group $\mathbf{Z}$ of generalized translations (see Subsection 2.5.1). The latter consists of rotations by $2\pi r/q$ around the q-order screw axis, translations $(n/q)a$ (a denotes the translational period) or reflections in the glide plane $(\sigma_v|a/2)$. Here $n = G(n_1, n_2)$ is the greatest common divisor and (n_1, n_2) define the chiral vector of SW NT.

The line symmetry group of a double-wall nanotube can be found as the intersection $\mathbf{L_2} = \mathbf{Z_2P_2} = (\mathbf{L} \cap \mathbf{L}')$ of the symmetry groups $\mathbf{L}$ and $\mathbf{L}'$ of its single-wall constituents [41]. The intersection $\mathbf{P_2} = (\mathbf{P} \cap \mathbf{P}')$ of the point groups is chosen independently of the generalized translational factor $\mathbf{Z_2}$ [30].

Let (n_1, n_2) and (n_1', n_2') define the chiral vectors of the single-wall constituents of a double-wall nanotube. Its axial point group $\mathbf{P}_2 = \mathbf{C}_N$ is the principal axis subgroup of the DW NT line group $\mathbf{L}_2$ with $N = G(n, n') = G(n_1, n_2, n_1', n_2')$. Only nanotubes composed exclusively of either (n, n) (armchair) or $(n, 0)$ (zigzag) SW constituents can have additional mirror or glide planes, as well as a rotoreflectional axis. The translational factor $\mathbf{Z}_2$ is completely absent for incommensurate DW NT, i.e. when the ratio a/a' is not rational [30]. As an example, we can mention DW NT formed from the hexagonal SW NTs with different types of chirality, both armchair and zigzag, i.e., $(n_1, n_1)@(n_2, 0)$, where the ratio $a/a' = \sqrt{3}$ (a, a' are lengths of the translation vectors of SW constituents).

The coaxial hexagonal DW NTs with $(n_1, n_1)@(n_2, n_2)$ and $(n_1, 0)@(n_2, 0)$ chiralities are commensurate: their translation period is the same as for the constituents: $\mathbf{L} = -\mathbf{a} + \mathbf{b}$ ((n,n)-chirality), $\mathbf{L} = -\mathbf{a} + \mathbf{2b}$ ((n,0)-chirality), as described by (2.33d). For the square lattice period of such DW NTs is the same as for the constituents: $\mathbf{L} = \mathbf{a} - \mathbf{b}$ ((n,n)-chirality), $\mathbf{L} = \mathbf{b}$ ((n,0) chirality), as described by (2.33c). For the commensurate DWNT the translational factor $\mathbf{Z}_2$ contains rotations around the screw axis, common to both SW components. Two possibilities for periodic DW NTs have been considered in [30]: (i) both n_1/N and n_2/N are odd—$\mathbf{L}_2$ contains the screw axis $(2N)_N$; (ii) either one or both n_1/N and n_2/N are even—$\mathbf{L}_2$ contains the rotation axis of order the N. As an example of the first possibility one has hexagonal DW NT $(6, 6)@(10, 10)$: $N = 2$, $n_1/N = 3$, $n_2/N = 5$, the screw axis 4_2.

For DW NT (12, 0)@(18, 0), we have $N = 6$, $n_1/N = 2$, $n_2/N = 3$, the rotation axis of order 6.

In the particular case of commensurate armchair $(n_1, n_1)@M(n_1, n_1)$ and zigzag $(n_1, 0)@M(n_1, 0)$ DW nanotubes with hexagonal morphology (i.e., $n_2 = Mn_1$), the symmetry group can be found from the results obtained in [30] for the full symmetry of multiwall nanotubes. For armchair and zigzag DW NTs with odd M, the line symmetry groups are the same as for their SW constituents—$(2n)_n/m$ (Family 4, point symmetry $\mathbf{C}_{2nh}$) and $(2n)_n mc$ (Family 8, point symmetry $\mathbf{C}_{2nv}$), respectively. For an even M, the rotations about the screw axis of the order $2n$ are replaced by rotations around the pure rotation axis of the order n so that DW NT line symmetry groups become n/m (family 3, point symmetry $\mathbf{C}_{nh}$) and nm (family 6, point symmetry $\mathbf{C}_{nv}$), for armchair and zigzag chiralities, respectively.

For each SW NT, the coordinate system can be chosen with its origin fixed in the initial nanosheet (slab) which the folding procedure has to be applied to. The normal to the slab plane passing through the origin can be defined as x axis in the SW NT coordinate system. Because of the coaxiality, the two parameters completely determine the relative positions of SW constituents in DW NT: the angle φ and length Δz by which the outer tube is rotated around z and translated along z, respectively (in regard to the initial configuration with the coinciding x and x′ axes of both shells) [30, 41]. Thus, the initial position of both SW constituents in DW NTs is characterized by $\varphi = 0$ and $\Delta z = 0$. In this case the maximum possible number of symmetry elements for both SW NTs coincide, and the symmetry of the initial DW NT structure is described by one of the line groups considered above. After atomic relaxation the values of φ and Δz can differ from zero. Presumably, the roto-translational part of DW NT symmetry group (independent of the relative SW NT positions) is not changed after the relaxation. However, other common symmetry elements of SW NTs (second-order U axes normal to the translation vector, reflection and glide planes) can be lost. Thus, the total symmetry of DW NT is reduced. The symmetry of DWNT with hexagonal and square morphology is considered in more detail in next subsections dealing with for BN, TiO_2 and $SrTiO_3$ nanotubes.

For multiwall nanotubes the following symmetry can be found [30]. If at least one of the single-wall constituents is chiral, there are two possibilities in the commensurate case: $\mathbf{T}_q^r\mathbf{C}_N$, corresponding to the general mutual position; and $\mathbf{T}_q^r\mathbf{D}_N$ in the special mutual positions with the common U axis. Similarly, the tube built of incommensurate components has a symmetry described by the point groups $\mathbf{C}_N$ or $\mathbf{D}_N$. If the nanotube is built of either single-wall $(n, 0)$,$(n', 0)$…tubes or single wall (n, n), (n', n'),…tubes, the order of the principal rotational axis is $N = G(n, n' \ldots)$. If the tube contains single-wall tubes of both types, no translational periodicity appears and its symmetry is described by a point group. On the other hand, for a tube composed of components of the same type, the translational period is equal to that of the components. Two different situations can occur: if all the integers n/N, n'/N,…are odd ("odd" case), the translations are refined by the screw axis $\mathbf{T}_{2N}^1$; otherwise, if at least one of these integers is even ("even" case), no screw axis emerges. Note that owing to the various arrangements of the components, any of the line and axial point groups can be the resulting symmetry for the commensurate and incommensurate

Table 2.11 Symmetry of the multiwall $(n, 0)$ (zigzag) and (n, n) (armchair) tubes

Relative position	Line group				Isogonal group		Point group
	Odd		Even		Odd	Even	
General	$\mathbf{T}^1_{2n}\mathbf{C}_N$	(1)	$\mathbf{TC}_N$	(1)	$\mathbf{C}_{2N}$	$\mathbf{C}_N$	$\mathbf{C}_N$
σ_h	$\mathbf{T}^1_{2n}\mathbf{C}_{Nh}$	(4)	$\mathbf{TC}_{Nh}$	(3)	$\mathbf{C}_{2Nh}$	$\mathbf{C}_{Nh}$	$\mathbf{C}_{Nh}$
σ_v	$\mathbf{T}^1_{2n}\mathbf{C}_{Nv}$	(8)	$\mathbf{TC}_{Nv}$	(6)	$\mathbf{C}_{2Nv}$	$\mathbf{C}_{Nv}$	$\mathbf{C}_{Nv}$
σ'_v	$\mathbf{T}^1_{2n}\mathbf{C}_{Nv}$	(8)	$\mathbf{T}_c\mathbf{C}_{Nv}$	(7)	$\mathbf{C}_{2Nv}$	$\mathbf{C}_{Nv}$	$\mathbf{C}_N$
(U, U')	$\mathbf{T}^1_{2n}\mathbf{D}_N$	(5)	$\mathbf{TD}_N$	(5)	$\mathbf{D}_{2N}$	$\mathbf{D}_N$	$\mathbf{D}_N$
σ_h, σ_v	$\mathbf{T}^1_{2n}\mathbf{D}_{Nh}$	(13)	$\mathbf{TD}_{Nh}$	(11)	$\mathbf{D}_{2Nh}$	$\mathbf{D}_{Nh}$	$\mathbf{D}_{Nh}$
σ_h, σ'_v	$\mathbf{T}^1_{2n}\mathbf{D}_{Nh}$	(13)	$\mathbf{T}_c\mathbf{C}_{Nh}$	(12)	$\mathbf{D}_{2Nh}$	$\mathbf{D}_{Nh}$	$\mathbf{C}_{Nh}$
(σ_h, σ'_h)	$\mathbf{T}^1_{2n}\mathbf{C}_{Nh}$	(4)	$\mathbf{TS}_{2N}$	(2)	$\mathbf{C}_{2Nh}$	$\mathbf{S}_{2N}$	$\mathbf{S}_{2N}$
$(\sigma_h, \sigma'_h), \sigma_v$	$\mathbf{T}^1_{2n}\mathbf{D}_{Nh}$	(13)	$\mathbf{TD}_{Nd}$	(9)	$\mathbf{D}_{2Nh}$	$\mathbf{D}_{Nd}$	$\mathbf{D}_{Nd}$
$(\sigma_h, \sigma'_h), \sigma'_v$	$\mathbf{T}^1_{2n}\mathbf{D}_{Nh}$	(13)	$\mathbf{T}_c\mathbf{S}_{2N}$	(10)	$\mathbf{D}_{2Nh}$	$\mathbf{D}_{Nd}$	$\mathbf{S}_{2N}$

components, respectively. The analysis of the special arrangements of constituents with common horizontal axes, mirror or glide planes, that increase the symmetry of the total system is summarized in Table 2.11. For periodic tubes, the line groups (and families) and the isogonal groups are in the "odd" columns if all the ratios n/N, $n'/N, \ldots$ are odd, and in the "even" columns otherwise. The point groups of the tubes with both zigzag ($(n, 0)$—chiralities) and armchair ((n, n)—chiralities) components are in the last column. In the first column the relative positions of the component tubes are characterized by coinciding symmetry elements (beside the common principal axis in the general position). Here (U, U') denotes the horizontal axis, which is the U axis in some of the constituents, and the U' axis in the remaining ones (thus, additional mirror or glide planes are excluded). Also, (σ_h, σ'_h) is a plane which is σ_h in some of the constituents (with n necessarily even) and σ'_h in the remaining tubes; in the incommensurate case, the same groups are obtained when they have commom σ'_h planes.

A single-wall MeS_2 nanotube is three layer sandwich and a building block for a multi-wall tubes. The symmetry analysis of these nanotubes is given in [42]. Depending on chirality, the symmetry group of NT belongs to one of three different families: chiral (n_1, n_2)-$T^r_q(f)C_n$; achiral(n, n)-$T^1_{2n}(f)C_{nh}$; achiral $(n, 0)$-$T^1_{2n}(f)C_{nv}$. Regardless of chirality, single-wall MeS_2 nanotube is a three-orbit system:each S-Me-S sheet is generated by the action of the transformations from the group $T^r_q(f)C_n$ on a single atom arbitrary chosen to represent the orbit. For achiral tubes this is the halving subgroup of the symmetry group, while for the chiral ones it is a complete group.

2.5.8 The Nanowires Construction

The symmetry of a nanowire is described by one of 75 rod groups (RG) considered above. As we have seen the order of the main rotation or screw axis in line groups can be any integer number while in RGs this order can only be the same as in a

bulk crystal, i.e., 1, 2, 3, 4, and 6. This circumstance causes specific conditions of NW geometry construction depending on morphology and symmetry of crystalline lattice. The NW symmetry is defined both by the structure of the prototype bulk crystal and by the direction of the one-dimensional translation periodicity.

The geometric constructions of possible atomic arrangments for inorganic nanowires are suggested in [43]: the nanowires are considered as fragments of bulk crystals (nanocrystalline nanowires). The basic idea of this approach is (1) choose a maximally linear, charge-neutral, and (if possible) dipole-free atomic cluster containing a single formula unit, and (2) using if possible the symmetry axis of this linear cluster as the nanowire growth axis, distributed by translations and screw rotations the atomic clusters to give a stoichiometric nanowire with some symmetry around the growth axis and minimal surface polarity. This approach is demonstrated in [43] for: (1) wurtzite structure (which occurs in [001] nanowires based on GaN and ZnO); (2) fluorite structure CaF_2 based nanowires, growing in [111] orientation; (3) rutile based nanowires growing in [001] and [110] directions and anatase based nanowires oriented along [001] direction. In both cases the charge neutral and dipole free linear TiO_2 units are chosen to construct the nanowire; (4) based on perovskite $BaTiO_3$ structure nanowires oriented along [111] direxion.

Since nanowires can be described as infinite prisms of different diameters, their stability depends on stability of lateral facets, according to Wulff's construction formalism [44]. Lateral facets of nanowire can be constructed basing on the two-periodic slab model used in the surface calculations. There are two approaches to such a construction: (1) choosing the slab in such away that its surface is normal to the chosen NW periodicity direction with subsequent removal of the slab translations and restoring the translation for NW; (2) choosing the nanowire periodicity along the one of the slab 2D translation vectors with subsequent removal of the second translation vector. The first approach is considered in Chap. 7 for the rutile TiO_2 based nanowires construction. Let us consider in more detail the second approach.

Let the nanowire periodicity direction **L** is defined by the set of integer numbers [l_1,l_2,l_3] in units of the bulk lattice translations $\mathbf{a}_1$, $\mathbf{a}_2$, and $\mathbf{a}_3$. One constructs the slab with the nanowire periodicity along the one of the slab 2D translation vectors with subsequent removal of the second translation vector. The rod symmetry group of such a nanowire is subgroup of the slab layer group. The slab surface becomes a facet of the rod obtained, being parallel to the nanowire periodicity direction **L**. All the possible slab surfaces (possible nanowire facets), parallel to **L**, are defined by the integer solutions of the equation

$$l_1k_1 + l_2k_2 + l_3k_3 = 0 \tag{2.40}$$

where the integer numbers k_1, k_2, k_3 are Miller indexes of the slab surface and equal to 0, ± 1 for the low index surfaces. In this case the reciprocal lattice vectors have only two independent integer components m and n for each of seven possible nanowires directions [l_1, l_2, l_3] : [001]→(m,n,0), [010]→(n,0,m), [100]→(0,m,n), [110]→(m,−m,0), [101]→(−m,n,m), [011]→(n,m,−m), [111]→(m,n,−m−n).

Table 2.12 Low index facets of nanowires cut from triclinic, monoclinic and orthorhombic lattices

Nanorod direction	Facets, **k**		Orthogonality, (±)		
	A	B	Triclinic	Monoclinic	Orthorhombic
[001]	(100)	(010)	−	+	+
	(110)	$(\bar{1}10)$	−	−	−
[010]	(001)	(100)	−	−	+
	(101)	$(10\bar{1})$	−	−	−
[100]	(010)	(001)	−	+	+
	(011)	$(0\bar{1}1)$	−	−	−
[110]	(001)	$(\bar{1}10)$	−	−	+
	$(\bar{1}11)$	$(1\bar{1}1)$	−	−	−
[101]	(010)	$(10\bar{1})$	−	+	+
	$(11\bar{1})$	$(\bar{1}11)$	−	−	−
[011]	(100)	$(0\bar{1}1)$	−	−	+
	$(1\bar{1}1)$	$(11\bar{1})$	−	−	−
[111]	$(\bar{1}10)$	$(11\bar{2})$	−	−	−
	$(10\bar{1})$	$(1\bar{2}1)$	−	−	−
	$(0\bar{1}1)$	$(\bar{2}11)$	−	−	−

The existence of (2.40) solutions depends on the nanowire periodicity direction and Miller indexes of the surfaces in consideration. The sign + in Tables 2.12 and 2.13 means that for a given nanowire direction and the crystal system chosen the orthogonality (2.40) is satisfied for A and B low index surfaces (facets). For monoclinic lattice $\beta \neq 90$. These tables allow to construct the nanowire models for the crystals with the different Bravais lattices.

Let us consider the NWs facets for the rutile TiO_2 structure with the primitive tetragonal lattice [45]. For the [001]-oriented NWs one can expect the {110} facets

Table 2.13 Low index facets of nanowires cut from tetragonal, hexagonal and cubic lattices

Nanorod direction	Facets, **k**		Orthogonality, (±)		
	A	B	Tetragonal	Hexagonal	Cubic
[001]	(100)	(010)	+	−	+
	(110)	$(\bar{1}10)$	+	+	+
[100]	(010)	(001)	+	+	
	(011)	$(0\bar{1}1)$	−	−	
[110]	(001)	$(\bar{1}10)$	+	+	+
	$(\bar{1}11)$	$(1\bar{1}1)$	−	−	−
[101]	(010)	$(10\bar{1})$	+	−	
	$(11\bar{1})$	$(\bar{1}11)$	−	−	
[111]	$(\bar{1}10)$	$(11\bar{2})$	+	+	+
	$(10\bar{1})$	$(1\bar{2}1)$	−	−	+
	$(0\bar{1}1)$	$(\bar{2}11)$	−	−	+

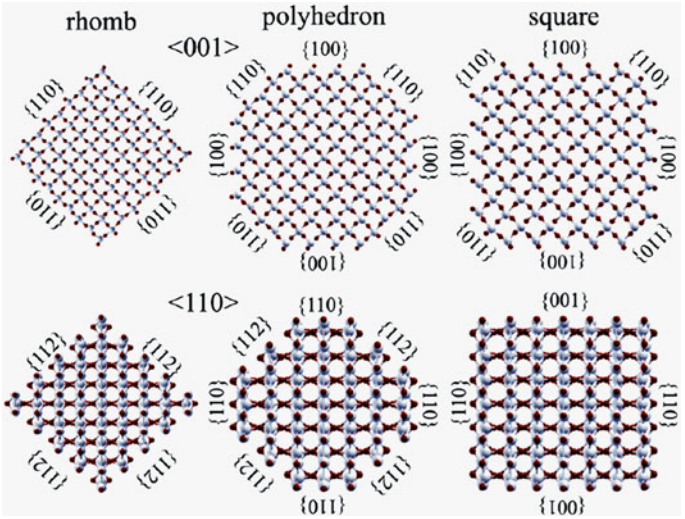

Fig. 2.26 Cross sections of the [001]-oriented TiO_2 NWs with diameters of about 3.9 nm (the *top* panel) and of the [110]-oriented TiO_2 NWs with diameters of 2.9 nm (the *bottom* panel) displaying three possible morphology (the rhomb, the polyhedron, and the square). The large, *light-blue* (*gray*) *balls* stand for Ti atoms, the small, *red* (*dark*) *balls* represent O atoms. All facets are indicated (Reprinted figure with permission from Migas et al. [45], Copyright (2010) by the American Chemical Society)

to characterize their surface (the rhomb case in Fig. 2.26) and this morphology has been observed experimentally [46]. One can also consider NWs in which the {110} and {100} facets are close in size (the polyhedron case in Fig. 2.26) and where the {100} facets dominate with small in size {110} facets playing the role of edges (the square case in Fig. 2.26). The unit cell parameter along the NWs axis ($a_{||}$) is equal to c_{bvlk}.

In the case of NWs with axis along the [110] directions, the facets the {110} and {001} are predicted to appear (the square case in Fig. 2.26). Some other possible morphology can be the polyhedron (the {110}, {001}, and {112} facets are close in size) and the rhomb (only the {112} facets are present), which are also shown in Fig. 2.26. Unfortunately, there is no information about the (112) surface and it is quite possible that such a surface is unstable as far as it has not been observed experimentally.

As a next example let us consider the construction of the nanowire with the periodicity direction $\mathbf{L} = [101]$ for the primitive tetragonal lattice. It is seen that the Miller indexes of the surfaces (010) and $(10\bar{1})$ satisfy (2.40). As the next step we construct the slab parallel to the surface $(10\bar{1})$ and after this remove the periodicity along the direction [010]. For the body centered tetragonal lattice the preliminary supercell transformation has to be made to obtain the teragonal direct lattice unit cell.

All the models in consideration are characterized by the TiO_2 stoichiometry.

The computer code CRYSTAL-14 [39] contains the option which allows the nanowire construction basing on the described above approach. To build nanowire starting from the corresponding 3D bulk structure one needs give in the code input the information about the crystal plane, termination and thickness of the two crystal planes defining the nanowire. The corresponding NW direction is then easily defined from the two tables given above [40]. At this stage, a nanowire can exhibit sharp and unphysical edges that can be smoothed out by further cutting the rod along additional crystal planes parallel to the periodic direction. The origin of the nanowire cell is shifted automatically to maximize symmetry of the rod group.

The NANOCUT code used recently for construction of TiO_2 nanowires with anatase and rutile structures [47] requires to introduce the cut-off radii along the cutting directions orthogonal to direction of NW periodicity. The choice of the cutting distance used as a parameter in that code could be simplified if the preliminary slab consideration is made.

2.6 Symmetry of Crystalline Orbitals in Periodic Systems: Space, Layer and Line Groups

2.6.1 Symmetry of Molecular and Crystalline Orbitals

The aim of the first-principles approaches in quantum chemistry is to calculate the properties of molecules and crystals without the use of empirical parameters. In principle, all the particles—electrons and nuclei—should be involved in such calculations. In fact, the solution of this complicated task is simplified in the Born–Oppenheimer approximation (also called the adiabatic approximation). In the first stage the electronic subsystem is studied for different nuclear configurations to calculate the potential-energy surface and to find the optimized atomic positions corresponding to the minimal total energy per primitive cell. The nuclear motion can be studied *a posteriori*, by considering the electronic energy surface as an external potential.

Quantum chemistry of solids concerns mainly those physical and chemical properties of solids that depend on the electronic structure. The problem of nuclear motion is solved in approaches using molecular-dynamics method. The calculations of the electronic subsystem in the adiabatic approximation are always connected with the choice of the electronic Hamiltonian. Formally, the symmetry of the electronic Hamiltonian may differ from the symmetry of the nuclear configuration. However, in the case of crystalline solids the approximate electronic Hamiltonians are usually chosen in such a way that the translational and point symmetry of a crystal is maintained. In this chapter we consider in more detail two of the mostly popular approximate methods of many-electron systems description—Hartree-Fock method and the density-functional theory. In both approaches the approximate many-electron function is introduced in such a way that the electron subsystem calculations are made for one-electron wavefunctions. The latter are known as molecular orbitals in molecules and crystalline orbitals in crystals.

The symmetry of the electronic Hamiltonian $\hat{\mathrm{H}}$ ensures that orbitals (one-electron functions for many-electron systems) can be classified according to the irreducible representations of point groups for molecules and space groups for crystals.

In the symmetry-adapted basis the diagonalizing of the Hamiltonian matrix H is reduced to the diagonalizing of its diagonal blocks. Every eigenvalue of the matrix $H^{(\alpha)}$ is repeated n_α times in the total list of the eigenvalues of the operator $\hat{\mathrm{H}}$. The eigenfunctions of the Hamiltonian $\hat{\mathrm{H}}$ corresponding to the same eigenvalue are the basis functions of an irrep of the symmetry group G of $\hat{\mathrm{H}}$ (in the absence of accidental degeneracy that is not due to the symmetry) and the degeneracies of eigenvalues are equal to dimensions of the irreps of G (also in the absence of accidental degeneracy). Thus, the eigenstates $\varphi(\boldsymbol{r})$ and their eigenvalues may be labeled by the irreps of the symmetry group G of the Hamiltonian $\hat{\mathrm{H}}$.

The symmetry properties of molecular orbitals and the degeneracy of the corresponding eigenvalues are defined by the irreducible representations of the point groups. The tables of these irreps characters are published in many books and their notations are well known and as a rule unambiguous. The energy-level degeneracy is usually 1 (a, b irreps), 2 (e irreps) and 3 (t or f irreps). As an exclusion, the icosahedral point symmetry group of the fullerene molecule C_{60} has 4- and 5-dimensional representations (g and h irreps, respectively).

For crystalline solids the translation symmetry of the Hamiltonian is taken into account in any electronic-structure calculations as it allows calculations to be made for the basis connected only with the primitive unit cell. In the translation-symmetry-adapted basis the matrix H has a quasidiagonal structure with identical blocks related to an irrep $\boldsymbol{k}$ of the translation symmetry group T. As the latter is Abelian its irreps are one-dimensional. The translation symmetry adapted functions are known as Bloch functions and numbered by wavevector $\boldsymbol{k}$. Use of the point symmetry of a crystal allows the number of Bloch functions calculated to be decreased and further block-diagonalization of Hamiltonian of a crystal to be made.

The numbering of the translation symmetry adapted functions (Bloch functions) remains when the trnslations become two-dimensional (layer groups) or one-dimensional (line groups).

The space symmetry of crystalline orbitals is defined by irreducible representations of space, layer or line groups. The structure of these irreps is more complicated than in the case of point groups. The dimensions of the space, layer and line group irreps and the corresponding degeneracy of energy levels are also different from those for point groups.

The time-reversal symmetry of the crystalline Hamiltonian introduces an additional energy-level degeneracy. Let the Hamiltonian operator $\hat{\mathrm{H}}$ be real. The transition in the time-dependent Schrodinger equation to a complex-conjugate equation with simultaneous time-inversion substitution

$$\mathrm{i}\frac{\partial\varphi(\boldsymbol{r},t)}{\partial t} = \hat{\mathrm{H}}\varphi(\boldsymbol{r},t),\ \mathrm{i}\frac{\partial\varphi^*(\boldsymbol{r},-t)}{\partial t} = \hat{\mathrm{H}}\varphi^*(\boldsymbol{r},-t) \tag{2.41}$$

shows that the functions $\varphi(\boldsymbol{r}, t)$ and $\varphi^*(\boldsymbol{r}, -t)$ are solutions of the same time-dependent Schrodinger equation. This combined operation (complex conjugation + time inversion) is called the time-reversal transformation. Applying this operation to the time-independent Schrödinger equation for the time-independent part of stationary-state wavefunctions

$$\hat{\mathrm{H}}\varphi(\boldsymbol{r}) = E\varphi(\boldsymbol{r}),\ \hat{\mathrm{H}}\varphi^*(\boldsymbol{r}) = E\varphi^*(\boldsymbol{r}) \tag{2.42}$$

we see that $\varphi(\boldsymbol{r})$ and $\varphi^*(\boldsymbol{r})$ are the eigenfunctions of the same real operator $\hat{\mathrm{H}}$ belonging to the same eigenvalue E. So with respect to the time-independent part of stationary states $\varphi(\boldsymbol{r})$ the time-reversal operator reduces to a simple complex conjugation

$$\hat{\mathrm{K}}\varphi(\boldsymbol{r}) = \varphi^*(\boldsymbol{r}) \tag{2.43}$$

Let φ_i $(i = 1, 2, \ldots, n)$ be eigenfunctions of a real Hamiltonian $\hat{\mathrm{H}}$ belonging to an eigenvalue E and also be the basis of a unitary irrep $D(g)$ of its symmetry group $G(g \in G)$. The functions $\hat{\mathrm{K}}\varphi_i = \varphi_i^*$ are also eigenfunctions of $\hat{\mathrm{H}}$ belonging to the same eigenvalue E, but transforming according to the irrep $D^*(g)$. The irreps $D(g)$ and $D^*(g)$ may be either equivalent or inequivalent. The functions φ_i and φ_i^* may be linearly dependent or linearly independent. There are three cases: (1) the functions φ_i and φ_i^* are linearly dependent and are bases of equivalent irreps ; (2) the functions φ_i and φ_i^* are linearly independent and transform according to inequivalent irreps; (3) the functions φ_i and φ_i^* are linearly independent and are bases of equivalent irreps. In cases 2 and 3 the eigenvalue E belongs to $2n$ states φ_i and φ_i^*. They form a basis of the rep of the group G that is the sum of two irreps $D(g)$ and $D^*(g)$ of the same dimension n. Thus, the degeneracy of the eigenvalue E doubles with respect to that caused by the symmetry group in the space. In case 1, there is no additional degeneracy. In tables of irreps of space, layer and line groups the complex conjugate irreps are usually united in one so-called physically irreducible rep. When analyzing the degeneracy of one-electron energy levels in crystals it is necessary to take into account the time-reversal symmetry. In particular, even in the case when the point-symmetry group F of a crystal does not include inversion the complex conjugated crystalline orbitals with wavevectors $\boldsymbol{k}$ and $-\boldsymbol{k}$ correspond to the same energy eigenvalue.

2.6.2 Irreducible Representations of Space Groups. Symmetry of Crystalline Orbitals of Bulk Crystals

The group T of pure translations $t_{\boldsymbol{a}}$ of an infinite lattice is a group of infinite order. By introducing cyclic boundary conditions one assumes that the infinite crystal consists of equivalent blocks in the form of parallelepipeds having sides $\boldsymbol{A}_1 = N_1\boldsymbol{a}_1, \boldsymbol{A}_2 = N_2\boldsymbol{a}_2, \boldsymbol{A}_3 = N_3\boldsymbol{a}_3$. It is assumed that the points of different

blocks connected by translations are physically equivalent, i.e. $t_{\boldsymbol{A}_j}^{N_j} = t_{\boldsymbol{0}}$. The large positive number $N = N_1N_2N_3$ defines the size of each block, also called the main region of a crystal (this block contains N primitive unit cells in the cyclic model of a crystal). Only the finite-order group $\mathrm{T}^{(N)}$ (modulo translations $\boldsymbol{A}_l, \boldsymbol{A}_2, \boldsymbol{A}_3$) of N translations $\boldsymbol{a}_n = \sum_{i=1}^{3} n_i \boldsymbol{a}_i$ inside the main region is considered when generating the irreps of the translation group. Because this group is Abelian all its irreps are one-dimensional. Moreover, the group $\mathrm{T}^{(N)}$ is a direct product of groups $\mathrm{T}^{(N_1)}$, $\mathrm{T}^{(N_2)}$ and $\mathrm{T}^{(N_3)}$, as all the translations $t_{\boldsymbol{a}_n}$ commute. Each group $\mathrm{T}^{(N_i)}$ of N_i translations $t_{n_i\boldsymbol{a}_i}$ has N_i one-dimensional irreps $D^j(t_{n_i\boldsymbol{a}_i})$, $j = 1, 2, \ldots, N_i$, satisfying the condition $\left[D^j(t_{\boldsymbol{a}_n})\right]^{N_j} = D^j(t_{N_j\boldsymbol{a}_n}) = D^j(t_{\boldsymbol{0}}) = 1$. Taking $D^j(t_{\boldsymbol{a}_i}) = \exp(-2\pi \mathrm{i} p_j/N_j)$ (where p_j is an integer) one satisfies this condition. The integer $p_j = 0, 1, \ldots, N_j - 1 (i = 1, 2, 3)$ denotes different irreps of the translation group $\mathrm{T}^{(N_i)}$. The irrep $D^{(p_1p_2p_3)}(t_{\boldsymbol{a}_n})$ of the translation group $\mathrm{T}^{(N)}$ can be written as

$$D^{(p_1p_2p_3)}(t_{\boldsymbol{a}_n}) = \exp\left[-2\pi \mathrm{i}(p_1n_1/N_1 + p_2n_2/N_2 + p_3n_3/N_3)\right] \tag{2.44}$$

There are $N = N_1N_2N_3$ sets of integers p_1, p_2, p_3 ($p_i = 0, 1, \ldots, N_i - 1$) that are used to label N different irreps of the translation group $\mathrm{T}^{(N)}$.

Introducing the primitive translation vectors $\boldsymbol{B}_1, \boldsymbol{B}_2, \boldsymbol{B}_3$ of the reciprocal lattice by

$$(\boldsymbol{a}_i \cdot \boldsymbol{B}_j) = 2\pi\delta_{ij}, \quad (i, j = 1, 2, 3) \tag{2.45}$$

one may define allowed $\boldsymbol{k}$ vectors (wavevectors) by $\boldsymbol{k} = \kappa_1\boldsymbol{B}_1 + \kappa_2\boldsymbol{B}_2 + \kappa_3\boldsymbol{B}_3$, where $\kappa_i = p_i/N_i (i = 1, 2, 3)$. Thus

$$(\boldsymbol{k} \cdot \boldsymbol{a}_n) = 2\pi(n_1p_1/N_1 + n_2p_2/N_2 + n_3p_3/N_3) \tag{2.46}$$

so that

$$D^{(\boldsymbol{k})}(t_{a_n}) = \exp(-\mathrm{i}\boldsymbol{k} \cdot \boldsymbol{a}_n) \tag{2.47}$$

The N irreps of $\mathrm{T}^{(N)}$ are now labeled by the N allowed $\boldsymbol{k}$ vectors. The point symmetry of reciprocal lattice coincides with that of the direct one. However, the type of reciprocal lattice may differ from that of the direct lattice.

Adding the reciprocal lattice vector

$$\boldsymbol{B}_{\boldsymbol{m}} = \sum_i m_i \boldsymbol{B}_i \tag{2.48}$$

to the allowed $\boldsymbol{k}$ vector we have

$$\begin{aligned} \exp(-\mathrm{i}(\boldsymbol{k} + \boldsymbol{B}_{\boldsymbol{m}}) \cdot \boldsymbol{a}_{\boldsymbol{n}})) &= \exp(-\mathrm{i}\boldsymbol{k} \cdot \boldsymbol{a}_{\boldsymbol{n}}) \exp(-\mathrm{i}\boldsymbol{B}_{\boldsymbol{m}} \cdot \boldsymbol{a}_{\boldsymbol{n}}) \\ &= \exp(-\mathrm{i}\boldsymbol{k} \cdot \boldsymbol{a}_{\boldsymbol{n}}) \end{aligned} \tag{2.49}$$

A pair of vectors $\boldsymbol{k}$ and $\boldsymbol{k}' = \boldsymbol{k} + \boldsymbol{B}_m$ is said to be equivalent since the irrep of $\mathrm{T}^{(N)}$ described by $\boldsymbol{k}$ can be equally well described by $\boldsymbol{k}'$. Therefore, the label $\boldsymbol{k}$ is determined up to within a reciprocal lattice vector and can be changed by vectors $\boldsymbol{B}_m$ of the reciprocal lattice.

The basis functions for the irreps of the translation group $\mathrm{T}^{(N)}$ are known as Bloch functions $\varphi(\boldsymbol{k}, \boldsymbol{r})$ and may be written in the form

$$\varphi(\boldsymbol{k}, \boldsymbol{r}) = \exp(\mathrm{i}\boldsymbol{k} \cdot \boldsymbol{r}) U(\boldsymbol{k}, \boldsymbol{r}) \tag{2.50}$$

where $U(\boldsymbol{k}, \boldsymbol{r}) = U(\boldsymbol{k}, \boldsymbol{r} + \boldsymbol{a}_n)$. Indeed

$$\begin{aligned} t_n \varphi(\boldsymbol{k}, \boldsymbol{r}) &= \exp(-\mathrm{i}\boldsymbol{k} \cdot \boldsymbol{a}_n) \exp(\mathrm{i}\boldsymbol{k} \cdot \boldsymbol{r}) U(\boldsymbol{k}, \boldsymbol{r} - \boldsymbol{a}_n) \\ &= \exp(-\mathrm{i}\boldsymbol{k} \cdot \boldsymbol{a}_n) \varphi(\boldsymbol{k}, \boldsymbol{r}). \end{aligned} \tag{2.51}$$

The Bloch functions are also called the $\boldsymbol{k}$ basis.

Applying a space group operator $g \equiv t_v R (g \in G)$ to the Bloch function $\varphi(\boldsymbol{k}, \boldsymbol{r})$ we obtain a Bloch function $\tilde{\varphi}(\boldsymbol{k}, \boldsymbol{r})$. Indeed

$$\begin{aligned} t_{a_n} t_v R \varphi(\boldsymbol{k}, \boldsymbol{r}) &= t_v R t_{R^{-1} a_n} \varphi(\boldsymbol{k}, \boldsymbol{r}) \\ &= \exp(-\mathrm{i}\boldsymbol{k} \cdot R^{-1} \boldsymbol{a}_n) t_v R \varphi(\boldsymbol{k}, \boldsymbol{r}) \\ &= \exp(-\mathrm{i} R\boldsymbol{k} \cdot \boldsymbol{a}_n) t_v R \varphi(\boldsymbol{k}, \boldsymbol{r}) \end{aligned} \tag{2.52}$$

i.e.

$$t_v R \varphi(\boldsymbol{k}, \boldsymbol{r}) = \tilde{\varphi}(R\boldsymbol{k}, \boldsymbol{r}) \tag{2.53}$$

As follows from (2.49) from the point of view of determining all the irreducible representations of a space group it is only necessary to consider the wavevectors in one unit cell of reciprocal space ($\boldsymbol{k}$ space) and the unit cell that is chosen is referred to as the first Brillouin zone (BZ). For most space groups it is not a primitive unit cell in $\boldsymbol{k}$ space. Instead, the unit cell of $\boldsymbol{k}$ space is the Wigner–Seitz unit cell. The latter is defined as consisting of all those points of $\boldsymbol{k}$ space that lie closer to $\boldsymbol{k} = \boldsymbol{0}$ than to any other reciprocal lattice point. Its boundaries are therefore the planes that are the perpendicular bisectors of the lines joining the point $\boldsymbol{k} = \boldsymbol{0}$ to the nearest and sometimes to the next-nearest reciprocal lattice nodes (the planes bisecting the line from $\boldsymbol{k} = \boldsymbol{0}$ to $\boldsymbol{k} = \boldsymbol{B}_m$ have the equation $\boldsymbol{k}\boldsymbol{B}_m = |\boldsymbol{B}_m|^2/2$). For some direct lattices (simple cubic, for example, see Fig. 2.27) only nearest-neighbor reciprocal lattice points are involved in the construction of the Brillouin zone but for others next-nearest neighbors are involved as well, see Fig. 2.28.

The advantage of this choice is that the Wigner–Seitz unit cell manifests the point-group symmetry F^0 of the appropriate crystal system. The disadvantage is that for certain Bravais lattices the appearance of BZ may be different for different values of lattice parameters. For all Bravais lattices except those of extremely low symmetry the advantage of this definition outweighs the disadvantage [48]. For monoclinic and triclinic space groups the problem of drawing of Brillouin zones for all possible

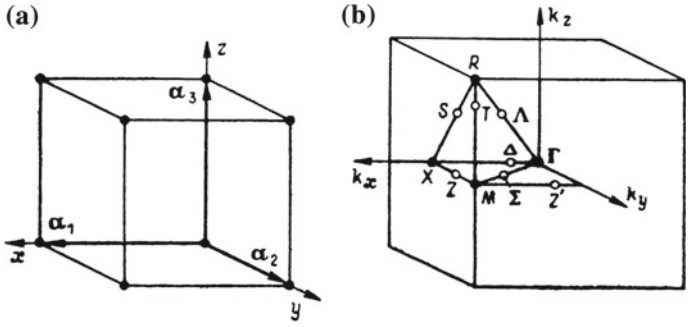

Fig. 2.27 Primitive unit cell (**a**) and Brillouin zone (**b**) for simple cubic lattice

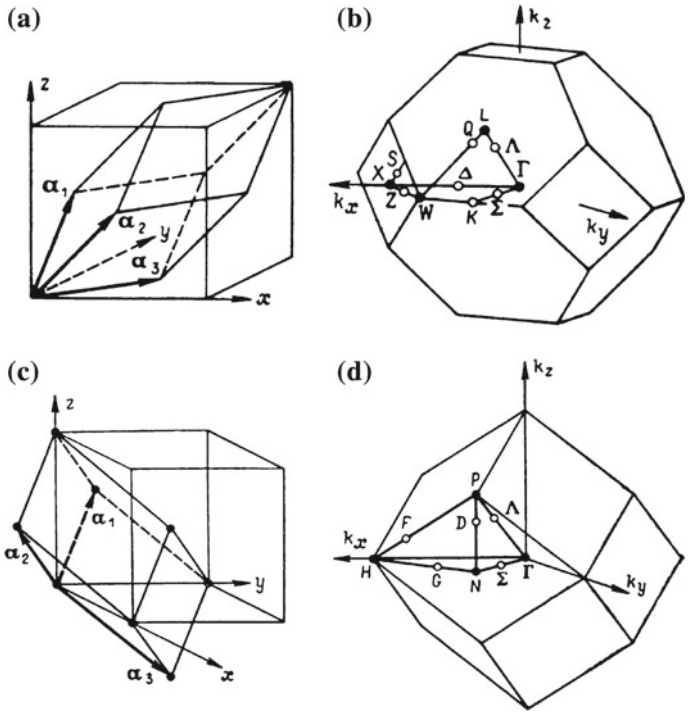

Fig. 2.28 Primitive unit cells (**a, c**) and Brillouin zones (**b, d**) for face-centered and body- centered cubic lattices

relative values of lattice parameters is so complicated that the primitive unit cell of the reciprocal lattice is used for the Brillouin zone. In [49] one can find Brillouin zones representations for all the Bravais lattices and for each set of possible restrictions on the lattice parameters. For cubic, hexagonal, simple tetragonal and simple orthorhombic lattices the shape of the Brillouin zone is unique, while for trigonal, body-centered tetragonal, body-, base- and face-centered orthorhombic lattices there

are two or more possible shapes depending on the relative lengths of the primitive translations and the angles between them.

By construction, the BZ contains N allowed $\boldsymbol{k}$ vectors when N primitive unit cells are included in the main region of a crystal. As the number N is assumed to be arbitrarily large, in the limiting case of $N = \infty$ the allowed $\boldsymbol{k}$ vectors take all values inside the BZ. In the electronic- structure calculations of crystals finite (and relatively small) numbers of $\boldsymbol{k}$ points are considered. However, the interpolation procedure used after calculation allows the one-electron energies to be shown as continuous functions of wavevectors (see, for example, Figs. 2.29 and 2.30 for band structures of $SrZrO_3$ and silicon, respectively).

Two vectors $\boldsymbol{k}$ and $\boldsymbol{k}'$ are said to be equivalent if $\boldsymbol{k}' = \boldsymbol{k} + \boldsymbol{B}_m$. By definition, no two interior points of a Brillouin zone can be equivalent; but every point on the surface of the Brillouin zone has at least one equivalent also on the surface of the Brillouin zone. For each BZ there is a basic domain Ω such that $\sum_R R\Omega$ is equal to the whole BZ, where R are the elements of the holosymmetric point group F^0 (F^0 is the point- symmetry group of the Bravais lattice and defines the appropriate crystal system). For each space group there is a representation domain Φ of the appropriate BZ (it is also called the irreducible part of the Brillouin zone), such that $\sum_R R\Phi$ is equal to the whole BZ, where the sum over R runs through the elements of the point-symmetry group $F \subseteq F^0$ (F is also called the isogonal point group and is obtained

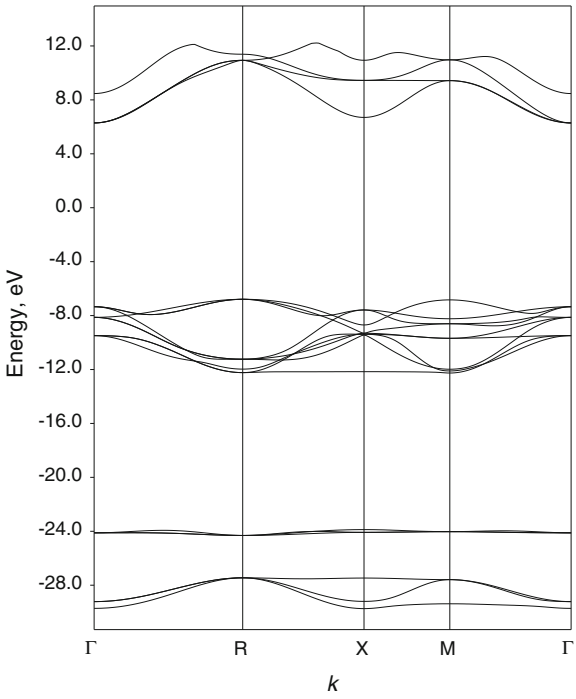

Fig. 2.29 Hartree-Fock energy bands for $SrZrO_3$ crystal

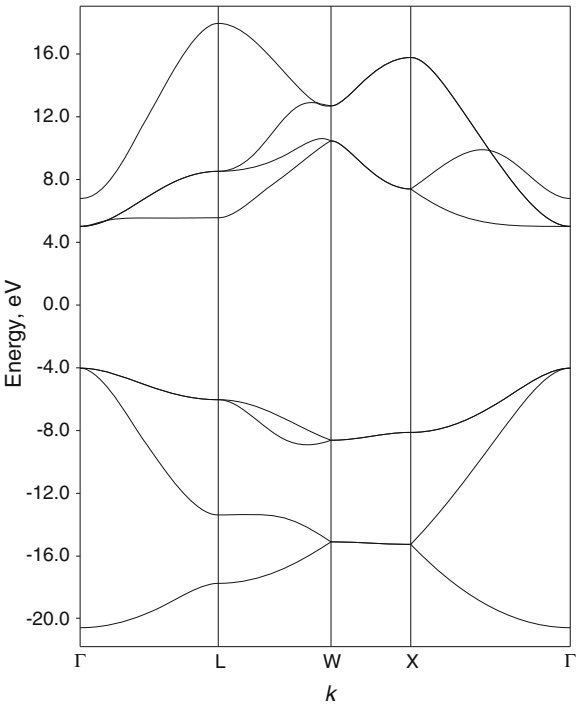

Fig. 2.30 Hartree-Fock energy bands for silicon crystal

by taking all the distinct elements R that are found in the elements $t_v R$ of space group G). For each holosymmetric space group (for which the set of all the distinct rotational parts of the space-group symmetry operations forms the holosymmetric point group F^0 of the appropriate crystal system) Φ can be taken to be identical with Ω. But for the remaining space groups the volume of Φ is some small-integer multiple of the volume of Ω. This multiple is equal to n_{F^0}/n_F, i.e. is defined by orders n_{F^0} and n_F of the holosymmetric point group n_{F^0} and crystal structure point group F. The majority of crystal structures considered in Sect. 2.3 have holosymmetric point groups. The exclusions refer to the structures of sphalerite and wurtzite with point groups T_d and C_{6v} being subgroups of cubic and hexagonal lattices point groups O_h and D_{6h}. In two cases under consideration (BZ for face-centered and hexagonal lattices, Figs. 2.28 and 2.31) the basic domain volumes are equal to 1/48 and 1/24 of the Brillouin-zone volume, the representation domains are two times larger.

Those elements of the point-symmetry group F^0 of the reciprocal lattice that transform a point $\boldsymbol{k}$ into itself or into some equivalent $\boldsymbol{k}$ point form the wavevector point-symmetry group $F_{\boldsymbol{k}} \subset F^0$. For example, for the direct face-centered cubic lattice ($F^0 = O_h$) BZ points Γ(0,0,0), X (1/2,1/2,0), L(1/2,1/2,1/2),W(1/4,1/2,3/4) (see Fig. 2.28) have point symmetry groups O_h, D_{4h}, D_{3d}, D_{2d}, respectively. The point group $F_{\boldsymbol{k}}$ of the $\boldsymbol{k}$ vectors F, Z, M, A (Fig. 2.32) for a simple tetragonal lattice

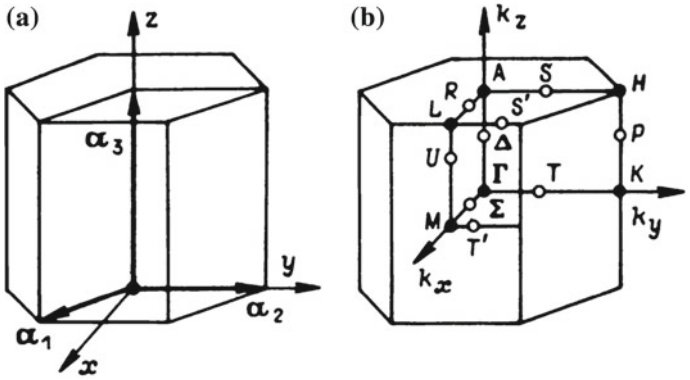

Fig. 2.31 Primitive unit cell (**a**) and Brillouin zone (**b**) for hexagonal lattice

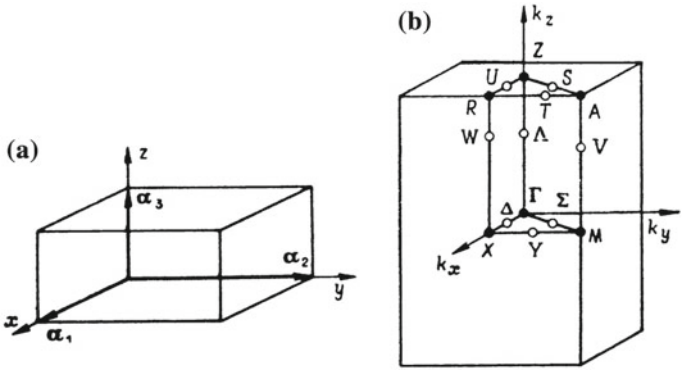

Fig. 2.32 Primitive unit cell (**a**) and Brillouin zone (**b**) for simple tetragonal lattice

coincides with the D_{4h} point group of the tetragonal lattice itself; the point group D_{2h} of the $\boldsymbol{k}$ vectors X and R is a subgroup of D_{4h}.

All the mentioned points of the BZ are called points of symmetry. By definition, $\boldsymbol{k}$ is a point of symmetry if there exists a neighborhood of $\boldsymbol{k}$ in which no point $\boldsymbol{k}'$ has the same symmetry group $\mathrm{F}_{\boldsymbol{k}}$ and $\mathrm{F}_{\boldsymbol{k}'} \subset \mathrm{F}_{\boldsymbol{k}}$. The Γ ($\boldsymbol{k} = \boldsymbol{0}$) point of the Brillouin zone is usually a symmetry point; exceptions here are the space groups of the crystallographic classes C_s, C_{nv}, C_n. All the other symmetry points are situated on the surface of the Brillouin zone and are usually denoted in a more or less unique way by capital Roman letters as in Fig. 2.32 for a simple tetragonal lattice.

If, in any sufficiently small neighborhood of $\boldsymbol{k}$, there is a line (plane) of points passing through $\boldsymbol{k}$ and having the same point group $\mathrm{F}_{\boldsymbol{k}}$ then $\boldsymbol{k}$ is said to be on a line (plane) of symmetry. The lines of symmetry are denoted both by Roman (on the surface of the Brillouin zone) and Greek (inside the Brillouin zone) capital letters. A symmetry line may be denoted by two symmetry points at the ends of this line: $\Lambda - \Gamma L(C_{3v})$, $\Sigma - \Gamma M(C_{2v})$, $\Delta - \Gamma X(C_{2v})$ (Fig. 2.28a); the corresponding

$F_{\boldsymbol{k}}$ groups are in parentheses. It is evident that the point groups C_{2v} of different wavevectors, being isomorphic to each other, do not coincide for all symmetry lines. For example, the second-order symmetry axis C_2 is along the X-coordinate axis for the ΓX line and along the XY symmetry axis for the ΓM line.

Tables of $\boldsymbol{k}$ vector types for BZ symmetry points and symmetry lines can taken from the site [8]. In fact, for all the space groups referring to the same crystal class and the same lattice type the $\boldsymbol{k}$ vector types are the same. This follows from the fact that in reciprocal space only the point-symmetry operations R transform the $\boldsymbol{k}$ vectors.

The representation theory of space groups uses a theorem that the translation group T is an invariant subgroup of G. Therefore, the little-group method [6] may be used for the generation of irreps of space group G from irreps of translation subgroup T. The one-dimensional irreps of translation group T transform under point-symmetry operations R of space group G according to relation (2.53) i.e. the Bloch function with wave vector $\boldsymbol{k}$ transforms to a Bloch function with wavevector $R\boldsymbol{k}$.

Let us suppose that $\mathrm{D}(g)$ is an irrep of G acting in a space L of dimension n. The operators $\mathrm{D}(g)$ for $g = t_{\boldsymbol{a}} \in \mathrm{T}$ form a rep of T that is in general reducible. Let it contain irreps of T characterized by the vectors $\boldsymbol{k} = \boldsymbol{k}_1, \boldsymbol{k}_2, \ldots, \boldsymbol{k}_n$. Therefore a basis can be found in space L that consists of Bloch functions $\varphi(\boldsymbol{k}_1, \boldsymbol{r}), \ldots, \varphi(\boldsymbol{k}_n, \boldsymbol{r})$. With respect to this basis, the elements of T are represented in the irrep $\mathrm{D}(g)$ by diagonal matrices with elements $\exp(-\mathrm{i}\boldsymbol{k}_p\boldsymbol{a})$, $p = 1, 2, \ldots, n$. The fact that $\mathrm{D}(g)$ is a rep of G implies that if we start with $\varphi(\boldsymbol{k}, \boldsymbol{r})$ and generate the Bloch functions $t_{\boldsymbol{v}} R\varphi(\boldsymbol{k}, \boldsymbol{r}) = \tilde{\varphi}(R\boldsymbol{k}, \boldsymbol{r})$, where $t_{\boldsymbol{v}} R \in \mathrm{G}$ then we obtain some linear combination of n Bloch functions of the initial basis. This means that $R\boldsymbol{k}$ is one of the vectors $\boldsymbol{k}, \boldsymbol{k}_2, \ldots, \boldsymbol{k}_n$.

In n-dimensional space L there are no nonzero subspaces invariant with respect to $\mathrm{D}(g)$ for all $g \in \mathrm{G}$.

Therefore, as we run over all elements of G operating on $\varphi(\boldsymbol{k}, \boldsymbol{r})$ by $\mathrm{D}(g)$, we generate the entire space L, i.e. each of the vectors $\boldsymbol{k}_1, \ldots, \boldsymbol{k}_n$ appears as the transform of $\boldsymbol{k}$ under some element of the point group F (point group of the space group G). It may be that the vectors $\boldsymbol{k}_1, \ldots, \boldsymbol{k}_n$ are not all different. A set of n_s distinct (non-equivalent) $\boldsymbol{k}$ vectors chosen from the set $\boldsymbol{k}_1, \ldots, \boldsymbol{k}_n$ is called the star of wavevector $\boldsymbol{k}$ and is denoted as ${}^*\boldsymbol{k}$. A star can be generated from one of its members by operating on it by elements of point group F. The Γ point of BZ forms one-ray star for any space group as it is a coordinate system origin for all the point- symmetry group F transformations in reciprocal space. The stars ${}^*X$, ${}^*L$ and ${}^*W$ (see Fig. 2.28 of the Brillouin zone for the fcc direct lattice) consist of 3, 4 and 6 rays, respectively.

The point group of the wavevector $\boldsymbol{k}$ (little cogroup of $\boldsymbol{k}$) $F_{\boldsymbol{k}} \subseteq F$, by definition, consists of all the rotations or reflections $R\boldsymbol{k}(i = 1, 2, ..., n_k)$ that rotate $\boldsymbol{k}$ into itself or an equivalent vector $R\boldsymbol{k} = \boldsymbol{k} + \boldsymbol{B}_m$.

By definition, the basic and representation domains in Brillouin zone include one representative of all wave vector stars defined by point groups F^0 and $\mathrm{F} \subset \mathrm{F}^0$, respectivelly.

The space-group irreps generation is described, for example, in [7, 26, 49]. It is shown that the dimension of a space-group representation (degeneracy of energy

levels in a crystal) for a given $\mathbf{k}$ is equal to the product of the number of rays in the star $\mathbf{k}^*$ and the dimension of the point group $F_{\mathbf{k}}$ irreducible representation (ordinary for symmorphic space groups or projective for nonsymmorphic space groups at the points on the surface of Brillouin zone). As to each of the degenerated states corresponds the same one-electron energy it is enough to identify energy levels only for one ray of the wavevector star as it is made in the figures showing the electronic band structure. To identify the one-electron energies at the symmetry lines the group-subgroup compatibility relations are used.

When the space group is realized in a crystalline structure the atomic states included in the LCAO basis define the symmetry of crystalline orbitals appearing in the electronic-structure calculations. The symmetry connection of atomic and crystalline orbitals is given by induced representations of space groups.

2.6.3 Site Symmetry and Induced Representations of Space Groups

In the previous section we examined the use of space-group irreducible representations for the classification of the delocalized (Bloch-type) crystalline states. In this traditional approach the crystal is considered as a whole system and the symmetry properties of the environment of constituent atoms are ignored. This results in a loss of information about the connection between the atomic and crystalline states. This information is widely used in the quantum chemistry of solids as it allows the crystalline properties to be explained from the knowledge of the chemical nature of the constituent atoms and their interactions. In the plane-waves methods of electronic-structure calculations the Bloch-type delocalized states are not directly connected with the states of the separate atoms. However, in the LCAO methods the Bloch-type delocalized functions are represented as the linear combination of the functions of separate atoms. Therefore, the symmetry connection between the delocalized Bloch and localized atomic states appears to be important. If we use not only the space symmetry of a crystal as a whole but also the site symmetry of different groups of constituent atoms we can considerably extend the possibilities of the group-theory applications. To study this in more detail the reader is referred to our previous book [6] where we examined the theory and the applications of the site-symmetry approach to the electron, phonon, magnetic properties of crystals and in the theory of phase transitions. In this section, we examine only those theoretical aspects of the site-symmetry approach that concern the electron states and allow analysis of the symmetry connection between the delocalized Bloch-type and localized Wannier-type electron states in crystals. This symmetry connection is described using representations of space groups induced by the irreps β of the site-symmetry subgroup $\mathrm{G}_{\mathbf{q}}$ of point $\mathbf{q}$ in the direct lattice space ($\beta \uparrow \mathrm{G}$). This type of induced rep of space groups was considered in [6].

All elements of the space group G can be written in the form $t_{\mathbf{v}_R+\mathbf{a}_n} R$, where $\mathbf{v}_R$ is a fractional lattice translation associated with the F point-group element R and $\mathbf{a}_n$ is a direct lattice translation vector.

The elements of the site-symmetry group $G_{\mathbf{q}} \subseteq G$ of the point $\mathbf{q}$ in the direct lattice space are those elements of G for which $g_{\boldsymbol{q}}\boldsymbol{q} = t_{\boldsymbol{v}_R+\boldsymbol{a}_n} R_{\boldsymbol{q}}\mathbf{q} = \boldsymbol{q}$. The space-group elements $g_{\mathbf{q}}$ are supposed to be given in the coordinate system whose origin is at one of the Wyckoff positions. The site-symmetry group elements for the other Wyckoff positions are mapped by the space-group elements with the point-symmetry operators R. Thus the site-symmetry group $G_{\mathbf{q}} \subseteq G$ is isomorphic with the point group $F_{\mathbf{q}}$ formed by $R_{\mathbf{q}}$. When the coordinate system origin is moved to the other Wyckoff position $\mathbf{q}_1$ the site-symmetry group elements of this new origin are elements of the point group $F_{\mathbf{q}_1}$ but the site-symmetry group elements $g_{\mathbf{q}}$ of the former origin $\mathbf{q}$ contain translations. As an example we consider the space group O_h^7 for the two origin choices given in the International Tables for Crystallography [2]. The site-symmetry group of Wyckoff position a(000) is mapped to the pure point-symmetry operations of the group for the first origin choice and to the set of operations with the translational part for the second origin choice.

Let the representatives $g_{jn} (j = 1, 2, \ldots, n_q = n_G/n_F)$ in the decomposition

$$G = \sum_{j,\mathbf{n}} g_{jn} G_{\mathbf{q}}, \quad g_{j\mathbf{n}} = t_{\mathbf{v}_j+\mathbf{a}_n} R_j \tag{2.54}$$

be chosen so that the points

$$\mathbf{q}_j = t_{\mathbf{v}_j} R_j \mathbf{q} \tag{2.55}$$

occupy the positions within the smallest unit cell (primitive or Wigner–Seitz). The operations $g_{j\mathbf{n}}$ generate from the point $\mathbf{q}$ sublattices $\mathbf{q}_j + \mathbf{a}_n (j = 1, 2, \ldots, n_q)$.

Let the local functions $W_{i1}^{(\beta)}(\mathbf{r}) \equiv W_i(\mathbf{r} - \mathbf{q}), (i = 1, 2, \ldots, n_\beta)$ be centered at point $\mathbf{q}$ of the direct lattice and span the space of the irrep β of the site-symmetry group $G_{\mathbf{q}} \subset G$ with matrices $d^{(\beta)}(g_{\mathbf{q}})$ and characters $\chi^{(\beta)}(g_{\mathbf{q}})(g_{\mathbf{q}} \in G_{\mathbf{q}})$. The nature of these functions depends on the physical problem under consideration. In the electron-band theory of crystals $W_i^{(\beta)}(\mathbf{r} - \mathbf{q}_A)$ are atomic functions of atom A. In phonon spectroscopy applications $W_i^{(\beta)}(\mathbf{r} - \mathbf{q}_A)$ mean the components of atomic displacements of an atom A, in magnetically ordered crystals these functions are the magnetic moments of atoms [6].

To specify the induced rep $\beta \uparrow G$ in the basis of local functions $W_{ij}^{(\beta)}(\mathbf{r} - \mathbf{a}_n)$ one has to indicate the symmetry center $\mathbf{q}$ of local functions by its Wyckoff position and the irrep β of the site-symmetry point group $G_{\mathbf{q}}$. Thus, in the $\boldsymbol{q}$ basis the induced rep $\beta \uparrow G$ is specified by the index $(\mathbf{q}, \beta)$.

As an example, we consider oxygen atom $2s$ functions in the perovskite $CaTiO_3$ structure. The oxygen atoms occupy Wyckoff position c of the space group O_h^1 with the site-symmetry D_{4h}. The $2s$-functions of an oxygen atom transform over a_{1g} irrep of the point group D_{4h}. Thus, the induced representation in $\mathbf{q}$ basis (c, a_{1g}) is three-dimensional at each $\mathbf{k}$ point $(d^{(\beta)} = a_{1g}, n_\beta = 1, n_{\mathbf{q}} = 3)$.

The labels of the induced rep $(\boldsymbol{q}, \beta)$ can be given in the $\boldsymbol{k}$ basis corresponding to those in the $\boldsymbol{q}$ basis, i.e. the results of the reduction of the induced rep over irreps of the group $G_{\boldsymbol{k}}$. All the information obtained can be specified by listing the symmetry

(the labels of irreps) of the Bloch states with wavevectors $\boldsymbol{k}$ corresponding only to a relatively small number of $\boldsymbol{k}$ points in the Brillouin zone forming a set K. The set K contains the inequivalent symmetry points of the Brillouin zone and one representative point from each inequivalent symmetry element (symmetry line or symmetry plane) if the latter does not contain the points of higher symmetry [26].

The symmetry properties of basis functions with other vectors $\boldsymbol{k}$ can be determined with the use of the compatibility relations.

Reducing the induced rep requires the characters of the irreps of the little group $G_{\boldsymbol{k}}$ (tabulated in [48] and on site [8]) and gives the induced rep index in the $\boldsymbol{k}$-basis. At the site [8] this procedure is programmed so that user can find the induced rep index in the $\boldsymbol{k}$-basis for any Wyckoff positions of 230 space groups.

Let us consider the induced representation (c, a_{1g}) of the space group O_h^1 formed by $2s$ functions of oxygen atoms in the perovskite structure. Using the site-symmetry option at the site [8] one obtains the induced band representation (c, a_{1g}) in the $\boldsymbol{k}$ basis in the form $\Gamma(1^+3^+)\mathrm{R}(5^+)\mathrm{M}(4^+5^-)\mathrm{X}(1^+3^-4^-)$. The labels of the small irreps of the little groups are taken from [48].

The theory of induced representations of space groups gives the answer to the question of whether it is possible to generate in the space of states of a given energy band the basis of localized functions? The answer to this question allows the symmetry connection between delocalized Bloch-type and localized Wannier-type crystalline orbitals to be obtained.

The following qualitative discussion should explain some features of band reps corresponding to real energy bands in crystals. Let a crystal be formed from isolated constituent atoms by decreasing the interatomic distances from very large ones to those corresponding to real crystalline structure. The crystal field may split the degenerate one-electron atomic levels due to symmetry requirements, leading to quite narrow energy bands, because of the interatomic interactions. The interatomic distances are sufficiently large that the crystalline orbitals corresponding to these bands are localized quite well at the atomic sites and are close to atomic functions. The Bloch states of these narrow energy bands span the spaces of some band reps that certainly have $\boldsymbol{q}$ basis, i.e. are induced representations. These reps are induced by those irreps of site-symmetry groups of atoms that describe the transformation properties of atomic states generating the energy bands. The further decrease of the interatomic distances may considerably transform the energy bands (join them together into more complicated ones and later split them up again into other simple ones) but a new electronic state of arbitrary symmetry cannot arise nor can any state disappear. At the same time, the wavefunctions of all possible symmetry types may change and corresponding one-electron energies may shift along the energy scale. Thus, an energy band corresponding to a band rep without a $\boldsymbol{q}$ basis (i.e. that is not an induced rep) may arise. However, this band, in joining with one or several neighboring ones, forms an energy band corresponding to a composite induced rep with $\boldsymbol{q}$ basis. In the joint space of these band states one can generate the basis of localized functions. Thus, the calculated one-electron energy band spectra of crystals may always be divided into bands connected with some simple or composite induced reps. When the interatomic distances are decreased to those in a real crystal

the atomic functions undergo more or less extensive modifications and become the Wannier functions of a crystal. When the latter arise directly from atomic functions one can use for them the same notation (s, p, d and so on). Let the atoms be at Wyckoff positions with the site symmetry group $G_{\boldsymbol{q}}$. Localized functions transforming according to irreps of the group $G_{\boldsymbol{q}}$ correspond to the bands arising from atomic levels split by a crystalline field. If, when the interatomic distances are decreased, the energy bands cross one another then the states of the resultant composite band also span the space of a composite induced rep. However, it may happen that this new band splits into several subbands related to localized functions that have centers of localization somewhat displaced from the atomic positions for further decreases in the interatomic distances. This case is typical for the electronic structure of crystals with covalent chemical bonding.

The space symmetry of crystalline orbitals generated by atomic orbitals of the LCAO basis can be found from induced representations of space groups. The knowledge of space symmetry of crystalline orbitals allows the pictures of electronic bands given as a result of electronic-structure calculations to be understood. It is also useful in localized crystalline orbitals generation. As an example, we show the energy bands for MgO (Fig. 2.33), silicon (Si) (Fig. 2.30) and $SrZrO_3$ crystals (Fig. 2.29). The LCAO calculations of these crystals were made using the Hartree-Fock LCAO method (see Chap. 3). MgO crystal has rocksalt structure

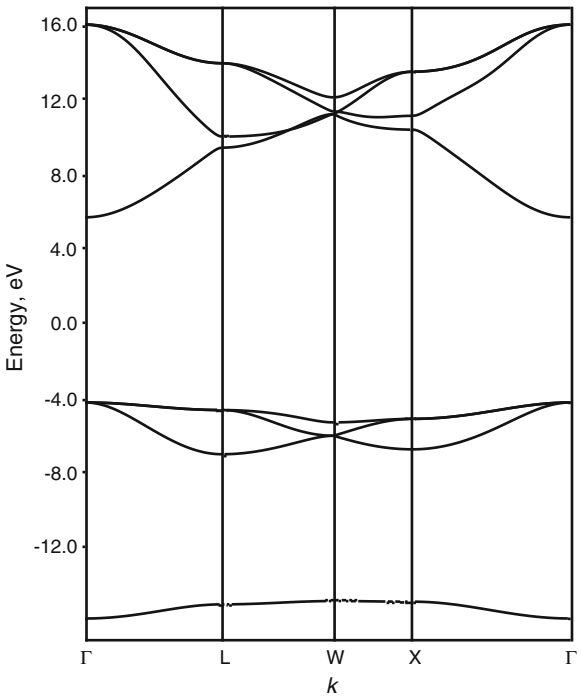

Fig. 2.33 Hartree-Fock energy bands for MgO crystal

with symmorphic space group O_h^5, Si crystal has diamond structure with nonsymmorphic space group O_h^7 and $SrZrO_3$ crystal has perovskite structure with symmorphic space group O_h^1, see Sect. 2.3. The translation symmetry of the first two crystals is described by the same face-centered cubic lattice, of the third one—by the simple cubic lattice. The point group $F = O_h$ of all the three crystals is holosymmetric (coincides with point group F^0 of the cubic lattice). For the first two crystals the wavevector belongs to the same Brillouin zone (Fig. 2.28), the representation domain coincides with the basic domain, the symmetry points of BZ are the same: $\Gamma(0, 0, 0)$, $X(1/2, 1/2, 0)$, $L(1/2, 1/2, 1/2)$ and $W(1/4, 1/2, 3/4)$ with the wavevector point groups O_h, D_{4h}, D_{3d} and D_{2d}, respectively. For the third crystal, the wavevector belongs to the simple cubic lattice Brillouin zone (Fig. 2.27), the representation domain also coincides with basic domain, the symmetry points of BZ are: $\Gamma(0, 0, 0)$, $R(1/2, 1/2, 1/2)$, $X(1/2, 0, 0)$ and $M(1/2, 1/2, 0)$ with the wavevector point groups O_h, O_h, D_{4h} and D_{4h}, respectively. For the symmorphic space groups O_h^5 and O_h^1 the small representations of little groups of symmetry points of BZ coincide with the ordinary (vector) irreducible representations of the corresponding wavevector point groups. For nonsymmorphic space group O_h^7 and the Γ and L the corresponding small representations are p-equivalent to ordinary representations of point groups O_h and D_{3d}. For the X and W points the small representations are not p-equivalent to ordinary irreducible representations of point groups D_{4h} and D_{2d}, respectively.

Let us connect the pictures of the calculated band structures with the symmetry of crystalline orbitals. As for MgO and silicon crystals the dimensions of the corresponding small representations are different at the X and W points, the splitting of the valence band to one-sheet and three-sheet subbands takes place for MgO, but for Si crystal the valence band is not split. In the symmetry directions of the Brillouin zone the compatibility relations are used to explain the energy-level splittings.

For the symmetry directions in the Brillouin zone $\Delta(\Gamma X)$, $\Lambda(\Gamma L)$, Σ (see Fig. 2.28) the small representations of both space groups are p-equivalent to ordinary irreducible representations of point groups C_{4v}, C_{3v} and C_{2v}. The notations of these representations are taken from [48]. For symmetry directions on the surface of the Brillouin zone $Z(XW)$, S small representations of space group O_h^5 are p-equivalent to ordinary irreducible representations of point group C_{2v}, for the symmetry direction Q – to ordinary irreducible representations of group C_s. For the nonsymmorphic space group O_h^7 small representations in the symmetry direction Z are not p-equivalent to ordinary irreducible representations of point group C_{2v}.

In Tables 2.14 and 2.15 we give the notations of induced representations in $\boldsymbol{k}$-basis for symmetry points of the Brillouin zone. We include only the band representations for upper valence bands of all the crystals under consideration.

These bands are induced by the oxygen atom $2s$, $2p$ states in MgO, by the silicon atom $3s$, $3p$ states in silicon, by the strontium atom $4p$ states and oxygen atom $2s$, $2p$ states in $SrZrO_3$. For all three crystals the short symbol of the band representation in $\mathbf{k}$-basis contains only the indices of the small IR s for the most symmetrical points of the BZ, because the indices for all other IR s contained in the BR are determined with the help of compatibility relations. These are the states responsible

Table 2.14 Band representations of space groups O_h^5 and O_h^7 for upper valence bands of MgO and Si crystals

	Γ	X	L	W	
MgO $-$ O_h^5					
$b(1/2, 1/2, 1/2)$	a_{1g}	1^+	1^+	2^-	4
	t_{1v}	5^-	2^-5^-	1^+3^+	1 5
Si $-$ O_h^7					
$a(0\,0\,0)$	a_1	1^+2^-	1	1^+2^-	1
	t_2	4^-5^+	1 3 4	$1^+2^-3^+3^-$	1 2 2

Table 2.15 Band representations for upper valence bands in $SrZrO_3$ crystal induced from Sr $4p-$, O $2s-$ and O $2p-$ atom-like states

Atom states	**q**-basis	Γ	R	M	X
Sr $4p-$	(b, t_{1v})	4^-	5^+	2^-5^-	1^+5^+
O $2s-$	(d, a_{1g})	1^+3^+	4^-	1^+5^-	$1^+2^+3^-$
O $2p_z-$	(d, a_{2v})	4^-	1^+3^+	$1^+2^+3^-$	1^+5^-
O $2p_{x,y}-$	(d, e_v)	4^-5^-	4^+5^+	$3^+4^+5^\pm$	$3^-4^-5^\pm$

for four-sheet valence bands in the first two crystals (Figs. 2.33 and 2.30) and for the 6- and 9-sheet valence bands in $SrZrO_3$ crystal (Fig. 2.29)

Due to the considered symmetry difference of crystalline orbitals in MgO and Si crystals the nature of chemical bonding in these crystals is also different. Indeed, in ionic MgO crystal the splitting of the valence band allows the crystalline orbitals localized on an oxygen atom to be generated and transformed over a_{1g} and t_{1v} irreducible representations of the oxygen site-symmetry group O_h. In covalent Si crystal all four sheets of the valence band have to be included in localization so that the localized orbitals found are centered at the middle of the Si $-$ Si bond.

In $SrZrO_3$ crystal oxygen $2s$ functions transform according to $\beta = a_{1g}$ IR of the oxygen site-symmetry group $G_{\mathbf{q}} = D_{4h}$ and generate a 3-sheeted BR. The symmetry of states in this band is fully determined by the $2s$ function of one of three oxygens in the primitive cell and may be labeled by the symbol (d, a_{1g}) as oxygen atoms occupy Wyckoff position d in space group O_h^1. In Table 2.15 this band, with the symbol of the BR (d, a_{1g}), is given in $\boldsymbol{k}$-basis (Γ, R, M, X are the symmetry points of the BZ).

Analysis of the space symmetry of crystalline orbitals is used to consider the possible centers of localization of chemical bonding in crystals.

2.6.4 *Irreducible Representations of Layer Groups. Symmetry of Crystalline Orbitals*

It can be shown that all the irreps of DG are contained in the irreps of the related space group G. The simple connection between the irreps of G and DG may be established using (2.15), i.e. isomorphism DG $\leftrightarrow$ G$/T_3$: every irrep of DG is related to a definite

irrep of G (of the same dimension). In these irreps of G all the elements of the coset $(R_i|\boldsymbol{v}_i + \boldsymbol{a}_n)T_3$ are mapped by the same matrix. In particular, all the translations in T_3 (coset $(E|\boldsymbol{0})T_3$) are mapped by unit matrices. We refer the reader to Chap. 6 in [6] for details. The same approach can be used to connect irreps of space group G with those of subperiodic rod group RG $\leftrightarrow$ G/$T^{(2)}$ ($T^{(2)}$ is the two-dimensional group of translations in a plane that does not contain the one-dimensional translations of a rod group), [28]. The two-dimensional plane groups and the corresponding layer groups are isomorphic (see Table B.2) and therefore have the same sets of irreps. The theory of induced reps described above for triperiodic space groups G may be easily applied to diperiodic groups DG. The tables of simple induced reps of DG may be directly constructed by using this theory [6]. The induced reps of layer groups are useful when analyzing electron-density localization on a crystal surface. Such analysis is important in the study of chemisorption of atoms and molecules.

In order to understand the principal features of the origin of surface states it is important to know how the energy bands of a crystal look in terms of the diperiodic specification. The comparison of bulk and surface states according to the symmetry is based on the relation between the irreps of the corresponding tri- and diperiodic groups G and DG. The bulk states are specified by the wavevector $\boldsymbol{k}^{(3)}$ in the three-dimensional BZ (BZ-3) for the group G. The surface states are classified by $\boldsymbol{k}^{(2)}$ in the two-dimensional BZ (BZ-2) of the layer (plane) group DG. The choice of the translation vectors $\boldsymbol{a}_1$ and $\boldsymbol{a}_2$ in the surface plane defines its orientation relative to the primitive translation vectors $\boldsymbol{a}_i^{(3)} (i = 1, 2, 3)$ of the corresponding space group G. The surface is identified by three integers (hkl)—Miller indices, specifying the atomic planes in the crystal by means of the components of a vector perpendicular to that plane. Planes perpendicular to crystallographic axes X, Y, Z are indicated $(h00)$, $(0k0)$ and $(00l)$, respectively. In particular, the planes closest to the origin are identified with indices (100), (010) and (001). Planes parallel to one of the three axes X, Y, Z are indicated $(0kl)$, $(h0l)$ and $(hk0)$, respectively. When the surface reconstruction effects (change of the surface plane translational symmetry with respect to that of the perfect crystal) may be neglected, the symmetry group DG of a crystal with a surface is a subgroup of the bulk crystal group G. However, the BZ-2 depends on the indices of the surface plane.

Consider, for example, crystals with face-centered cubic Bravais lattices. For the (001), (110) and (111) sections the plane lattices are square, rectangular and hexagonal, respectively. The basic translation vectors of the direct and reciprocal lattices for these three cases are given in Table 2.16 ($\boldsymbol{a}_1$ and $\boldsymbol{a}_2$ are given in units $a/2$, $\boldsymbol{B}_i$ in units $2\pi/a$, where a is the cubic lattice parameter). Note that for a cubic lattice the planes (100), (010) and (001) are equivalent. The equivalence takes place also for (110), (101), and (011) planes. We see that the vectors $\boldsymbol{B}_i (i = 1, 2)$ are now not the translation vectors of the three-dimensional reciprocal lattice. Therefore, the boundaries of BZ-2 do not coincide with those of BZ-3.

Figure 2.34 shows the Brillouin zones corresponding to the surface (001), (110) and (111) inscribed in the three-dimensional Brillouin zone for a face-centered cubic lattice.

Note that some nonequivalent points of BZ-3 become equivalent in BZ-2 (for example, the points X for the surface (001) and the points L for the (110) surface).

Table 2.16 Vectors of basis translations for three sections of a face-centered cubic Bravais lattice

Surface translation vectors	(001)	(110)	(111)
$\mathbf{a}_1$	110	−110	1 − 10
$\mathbf{a}_2$	1–10	002	10 − 1
$\mathbf{B}_1$	110	−110	2/3, −4/3, 2/3
$\mathbf{B}_2$	1–10	001	2/3, 2/3, −4/3

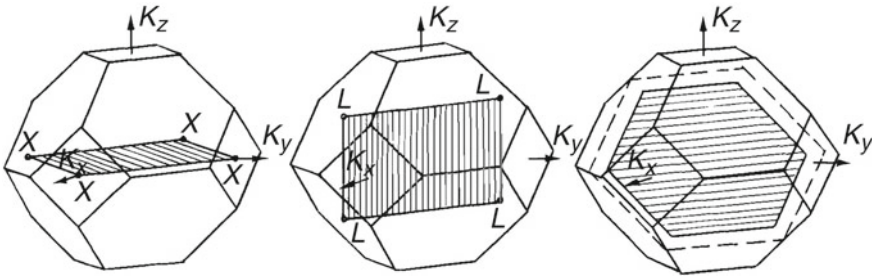

Fig. 2.34 Brillouin zones for a face-centered cubic lattice and surfaces **a** (001), **b** (110), **c** (111)

Some points of BZ-2 have higher symmetry than in BZ-3 (for example, the vertices of BZ-2 for the (111) surface). These properties of BZ-2 arise because the unit-cell vectors in the two-dimensional reciprocal space $\boldsymbol{B}_i$ are not the lattice vectors of the three-dimensional reciprocal lattice.

To obtain the crystal energy band structure in terms of a diperiodic specification it is necessary to represent the dispersion law $E = E_n(\boldsymbol{k}^{(3)})$ in the form

$$E_n^s(\boldsymbol{k}_\parallel^s) = E_n(\boldsymbol{k}_\parallel^s + \boldsymbol{k}_\perp - \boldsymbol{B}_n) \tag{2.56}$$

where $\boldsymbol{k}_\parallel^s$ is a projection of the three-dimensional wavevector $\boldsymbol{k}^{(3)}$ onto the surface and $\boldsymbol{k}_\perp$ is its component perpendicular to the surface. The vector $\boldsymbol{B}_n$ is assumed to be chosen so that the wavevector $\boldsymbol{k}_\parallel^s = \boldsymbol{k}_\parallel + \boldsymbol{B}_n$ takes values in the limits of BZ-2. In the projection of the energy bands of the three-dimensional crystal on the two-dimensional Brillouin zone forbidden energy lacunas can appear. When the surface is taken into account, a band of surface states appears inside the energy lacuna. These surface states are analogous to the local energy levels of point defects that appear in the forbidden energy gap of a perfect crystal. The energy levels of surface states may arise in the continuous energy spectrum of a bulk three-dimensional perfect crystal. These are the so-called resonance surface states. They are analogous to the point defect states in the spectrum of bulk-crystal states.

2.6.5 Irreducible Representations of Line Groups

The consideration the triperiodic translation group and its irreducible representations can easily be extended to the monoperiodic groups.

The one dimensional direct **a** and reciprocal **B** lattice translations are now one-dimensional vectors, satisfying the orthogonality relation $(\mathbf{aB}) = 2\pi$. Let the one-dimensional translations $t_{\mathbf{a}}$ be directed along z Cartesian axis.

In the standard factorization $L = TF$ the translations form the invariant subgroup of L and the factor group $P_I = L/T$ (isogonal point group) is isomorphic to one of the axial point groups C_q, $S_{2q} \leftrightarrow C_{2q}$, D_q,C_{qv},C_{qh},D_{qd},D_{qh}. In Line groups the rotation axis order q is any integer number (for Rod groups q = 1, 2, 3, 4, 6). The point groups P_I (isogonal point groups) of monoperiodic nanostructures can be considered as an analog of the crystal class introduced for the space and layer groups. The line groups from families 2, 3, 6, 9, 11 are symmorphic as these groups do not contain helical rotations or the reflections in the glide planes. The Line groups of families 1 and 5 can be both symmorphic and nonsymmorphic. For the symmorphic Line groups P_I are axial point groups; for nonsymmorphic Line groups P_I is isomorphic to the factor group L/T.

As in the case of the space groups the little-group method may be used for the generation of irreps of line group L from one-dimensional irreps of the translation subgroup T.

As in the case of 3D translations the Bloch function with wave vector $\boldsymbol{k}$ transforms to a Bloch function with wavevector $R\boldsymbol{k}$. Here R is the operation of the isogonal point group.

The point group of the wavevector $\boldsymbol{k}$ (little cogroup of $\boldsymbol{k}$) $F_{\boldsymbol{k}} \subseteq F$, by definition, consists of all the rotations or reflections $R\boldsymbol{k}(i = 1, 2, \ldots, n_k)$ that rotate $\boldsymbol{k}$ into itself or an equivalent vector $R\boldsymbol{k} = \boldsymbol{k} + \boldsymbol{B}$. The number of rays in the wave vector star is equal to n_F/n_k where n_F is the number of the elements in the group F.

The one-dimensional Brillouin zone is the segment connecting the reciprocal lattice points π/a and $-\pi/a$. The symmetry points of BZ are $\Gamma(0)$ and Z(1/2) (in units $2\pi/a$) with the one ray in the wave vector star. The number of rays in the star of other (general) **k**-points depends on the axial point group. The general **k**-points form one-ray stars for the isogonal point groups C_n, C_{nv} which do not contain the operations transforming **k** to $-\mathbf{k}$. For all the rest axial point groups the general **k**-points form two-rays stars, including both **k** and $-\mathbf{k}$ -points.

By definition, the little group $\mathrm{L}_{\boldsymbol{k}}$ of wavevector $\boldsymbol{k}$ consists of all elements $l_j^{\boldsymbol{k}} = t_{\boldsymbol{v}_j^{(k)}+\boldsymbol{a}} R_j^{(\boldsymbol{k})}$, $j = 1, 2, \ldots, n_k$, where $R_j^{(\boldsymbol{k})} \in \mathrm{F}_{\boldsymbol{k}}$. The group $\mathrm{L}_{\boldsymbol{k}} \subseteq \mathrm{L}$ is a group of order $N \cdot n_{\boldsymbol{k}}^j$ where N is the number of one-dimensional translations in the main region of a monoperiodic crystal.

The dimension of a Line group full representation (degeneracy of energy levels in a monoperiodic structure) for a given **k** is equal to the product of the number of rays in the star $\mathbf{k}^*$ and the dimension of the axial point group $F_{\mathbf{k}}$ irreducible representation (ordinary or projective).

The ordinary irreps of axial point groups are well known, the characters of their irreps can be found on the site [50]. These representations are one and two-dimensional. The projective irreps of these groups are not tabulated, their knowledge is necessary only for $Z(1/2)$ point of the one-dimensional BZ for the line group families 4, 5, 10, 12, 13.

The irreducible representations of the commensurate line groups are found and tabulated in [51–53] using the standard factorization. In order to obtain a complete set of non-equivalent representations of any line group of L^+ type it is sufficient to know all the reps of the corresponding isogonal point group C_q or C_{qv}, q = 1,2,... The representations of line group of L^- type are induced from those of its invariant subgroup L^+. The factorization (2.22) is used in [3] for the construction of irreps both for the commensurate and noncommensurate line group irreps. The construction of the line groups irreps starts with the first family group. In this case the line group is the direct product L = Z × P, both factors Z and P = C_n are the cyclic groups with the one-dimensional irreps $\exp(ilx)$, lx is a multiple of 2π, l is the order of the cyclic group.

The helical group Z irreps are classified with the help of the helical quasimomentum $\tilde{k}$ changing in the helical Brillouin zone - the segment connecting the reciprocal lattice points π/f and $-\pi/f$ where f is the partial translation. For the commensurate line groups the partial translation $f = \frac{ra}{q}$, r = 1,2,...q−1, so that the helical Brillouin zone is $\frac{q}{r}$ times larger than that of the quasimomentum k introduced in the standard line group factorization. Analogously, for the rotational subgroup C_n there are n different one-dimensional irreducible representations, given by the integer $\tilde{m}$. Thus the irreps of the first family line groups have the form

$$_{\tilde{k}}A_{\tilde{m}} = \exp(\mathbf{i}\tilde{k}f)\exp(\frac{\mathbf{i}\tilde{m}2\pi}{n}) \tag{2.57}$$

In the both classifications the irreducible representations are grouped into the so called bands, the property which will be inherited by all the other families. Namely, for fixed $\tilde{m}$, representations differ only by $\tilde{k}$. When $\tilde{k}$ varies within the helical Brillouin zone one obtains a series of representations to be referred to as a helical or $\tilde{m}$-band. Analogously, for commensurate groups, fixing m one gets series of the representations with k from the Brillouin zone, which is called linear or m-band [3]. The representations of the first family line groups have been used in [3] to construct the irreps of other groups. It is seen from Table D.2 that the first family group $L^{(1)}$ is the halving subgroup of the line groups of the families 2,...8. Therefore the induction procedure from a halving subgroup was used in [3] to construct the representations of the families 2,...,8. In the third step the representations of the families 9,...13 have been found using the reps of the positive families 6,7,8 and the induction procedure from a halving subgroup.

As an example we briefly describe how to construct irreducible representations of line groups belonging to the families 4 and 8. But to begin with, we remind the definition of a conjugate representation. If H is a normal subgroup of a group G and ρ is some matrix representation of H then for any $s \in$ G the representation $\rho^s(h) = \rho(s^{-1}hs)$ is called s - conjugate of ρ.

Family 4. L = $T^1_{2n}(\frac{a}{2})C_{nh}$ = H ∪ sH where H = $T^1_{2n}(\frac{a}{2})C_n$ is a zigzag group with generators $(C_{2n}|\frac{a}{2})$, $(C_n|0) \in$ H, and $s = (\sigma_h|0)$. Irreps of the normal subgroup H are 1-dimensional:

$$ {}_kA_m(C_{2n}|\frac{a}{2}) = e^{\mathbf{i}k\frac{a}{2}}e^{\mathbf{i}m\frac{\pi}{n}}, \quad {}_kA_m(C_n|0) = e^{\mathbf{i}m\frac{2\pi}{n}} \tag{2.58} $$

where $k \in \left(-\frac{\pi}{a}, \frac{\pi}{a}\right]$ and $m \in (-n, n]$. It is easy to ascertain that s-conjugate irreps of H are

$$ {}_kA^s_m(C_{2n}|\frac{a}{2}) = {}_{-k}A_m(C_{2n}|\frac{a}{2}) = e^{-\mathbf{i}k\frac{a}{2}}e^{\mathbf{i}m\frac{\pi}{n}}, \quad {}_kA^s_m(C_n|0) = e^{\mathbf{i}m\frac{2\pi}{n}} \tag{2.59} $$

In the case under discussion irrep of H is identical to its s-conjugate if and only if

$$ e^{\mathbf{i}k\frac{a}{2}} = e^{-\mathbf{i}k\frac{a}{2}} \Leftrightarrow k\frac{a}{2} = -k\frac{a}{2} + 2\pi l \tag{2.60} $$

and relevant solution of this equation is $k = 0$. Thus, 1-dimensional irreps of L are

$$ {}_kA^{\pm}_m(C_{2n}|\frac{a}{2}) = e^{\mathbf{i}k\frac{a}{2}}e^{\mathbf{i}m\frac{\pi}{n}}, \quad {}_kA^{\pm}_m(C_n|0) = e^{\mathbf{i}m\frac{2\pi}{n}}, \quad {}_kA^{\pm}_m(\sigma_h|0) = \pm 1 \tag{2.61} $$

For $k \neq 0$ irreps ${}_kA_m$ and ${}_kA^s_m$ of H are non-equivalent and the induced representations ${}_kE_m = Ind^{\mathrm{L}}_{\mathrm{H}}({}_kA_m)$ are irreducible:

$$ \begin{aligned} {}_kE_m(C_{2n}|\frac{a}{2}) &= \begin{pmatrix} e^{\mathbf{i}(k\frac{a}{2}+m\frac{\pi}{n})} & 0 \\ 0 & e^{\mathbf{i}(-k\frac{a}{2}+m\frac{\pi}{n})} \end{pmatrix} \\ {}_kE_m(C_n|0) &= \begin{pmatrix} e^{\mathbf{i}m\frac{2\pi}{n}} & 0 \\ 0 & e^{\mathbf{i}m\frac{2\pi}{n}} \end{pmatrix} \\ {}_kE_m(\sigma_h|0) &= \begin{pmatrix} 0 & 1 \\ 1 & 0 \end{pmatrix} \end{aligned} \tag{2.62} $$

It is easy to see that for $k \in (-\frac{\pi}{a}, \frac{\pi}{a})$ the induced irreps with k and $-k$ are equivalent and therefore the range of k reduces to $(0, \frac{\pi}{a})$ with $m \in (-n, n]$ for each k. The case $k = \frac{\pi}{a}$ requires special attention because for this value of k the interval of m values reduces to $(0, n]$.

Family 8. $\mathrm{L} = \mathrm{T}^1_{2n}(\frac{a}{2})\mathrm{C}_{nv} = \mathrm{H} \cup s\mathrm{H}$ where $\mathrm{H} = \mathrm{T}^1_{2n}(\frac{a}{2})\mathrm{C}_n$ is a zigzag group with generators $(C_{2n}|\frac{a}{2})$, $(C_n|0) \in \mathrm{H}$, and $s = (\sigma_v|0)$. Irreps of normal subgroup H are 1-dimensional and are given by (2.58). In this case s-conjugate irreps are

$$ \begin{aligned} {}_kA^s_m(C_{2n}|\frac{a}{2}) &= {}_kA_{-m}(C_{2n}|\frac{a}{2}) = e^{\mathbf{i}k\frac{a}{2}}e^{-\mathbf{i}m\frac{\pi}{n}} \\ {}_kA^s_m(C_n|0) &= {}_kA^s_{-m}(C_n|0) = e^{-\mathbf{i}m\frac{2\pi}{n}} \end{aligned} \tag{2.63} $$

and irrep of H is identical to its s-conjugate if and only if

$$ m\frac{\pi}{n} = -m\frac{\pi}{n} + 2\pi l \tag{2.64} $$

It is easy to see that the relevant solutions of this equation are $m = 0, n$ and 1-dimensional irreps of the line group under discussion are

$$
\begin{aligned}
&{}_kA_m(C_{2n}|\frac{a}{2}) = e^{\mathbf{i}k\frac{a}{2}}e^{\mathbf{i}m\frac{\pi}{n}}, \quad {}_kA^s_m(C_n|0) = 1, \quad {}_kA^s_m(\sigma_v|0) = 1 \\
&{}_kB_m(C_{2n}|\frac{a}{2}) = e^{\mathbf{i}k\frac{a}{2}}e^{\mathbf{i}m\frac{\pi}{n}}, \quad {}_kB^s_m(C_n|0) = 1, \quad {}_kB^s_m(\sigma_v|0) = -1
\end{aligned} \tag{2.65}
$$

where $k \in (-\frac{\pi}{a}, \frac{\pi}{a}]$ and $m = 0, n$. It seems pertinent to note that due to tradition 1-dimensional irreps which accept values $+1$ or -1 at the element $(\sigma_v|0)$ are denoted by capital letters A and B, respectively. For the remainder values of k and m we should induce to get

$$
\begin{aligned}
{}_kE_m(C_{2n}|\frac{a}{2}) &= \begin{pmatrix} e^{\mathbf{i}(k\frac{a}{2}+m\frac{\pi}{n})} & 0 \\ 0 & e^{\mathbf{i}(k\frac{a}{2}-m\frac{\pi}{n})} \end{pmatrix} \\
{}_kE_m(C_n|0) &= \begin{pmatrix} e^{\mathbf{i}m\frac{2\pi}{n}} & 0 \\ 0 & e^{-\mathbf{i}m\frac{2\pi}{n}} \end{pmatrix} \\
{}_kE_m(\sigma_v|0) &= \begin{pmatrix} 0 & 1 \\ 1 & 0 \end{pmatrix}
\end{aligned} \tag{2.66}
$$

where $k \in (-\frac{\pi}{a}, \frac{\pi}{a}]$ and $m \in (0, n)$. Note that here the range of m reduces to $(0, n)$ since 2-dimensional irreps with labels m and $-m$ are equivalent.

2.6.6 Site Symmetry for Line Groups of Families 4 and 8

The site symmetry approach used for the space and layer groups can be extended to the line groups using the induction procedure from the irreps of the orbit representative stabilizer being the subgroup of the line group. The other possibility is to use the restriction of Line group irreps to orbit stabilizers. As an example we apply the restriction procedure for the construction of the induced irreps of families 8 and 13 of Line groups. As soon as the induced representations from the irreps of orbit stabilizers are obtained, it is easy to construct the so-called dynamical representations of line groups which are defined as representations induced from the vector representations of orbit stabilizers (probably with subsequent multiplication by a certain permutation matrix). The use of the site-symmetry approach in lattice dynamics allows one to make a quick group theoretical analysis of the phonon symmetry not only at the Brillouine zone center but in the entire Brillouine zone. The knowledge of the symmetry of phonons at K=0 is necessary for interpretation of second order infrared and Raman spectra. Furthermore, this information can be used in the symmetry assignment of vibrational mode branches calculated by numerical methods

General character of a point group F we denote by the symbol $\chi(\mathrm{F})$. If an irrep of F is labeled by the symbol m, its character will be denoted as $\chi_m(F)$.

For example, $\chi_m(\mathrm{C}_n)$ will stand for the irrep $C_n^l \mapsto e^{\mathbf{i}m\frac{2\pi}{n}l}$ of C_n group where integer $m \in (-\frac{n}{2}, \frac{n}{2}]$.

The symbol $\chi_m(\mathrm{S}_{2n})$ will stand for the irrep $\sigma_h C_{2n}^l \mapsto e^{\mathbf{i}m\frac{\pi}{n}l}$ of the group S_{2n} with integer $m \in (-n, n]$.

For characters of the groups $\mathrm{C}_{1v} = \mathrm{C}_s, \mathrm{C}_{1h}, \mathrm{C}_i$ we will use the symbol $\chi_0^{\pm}(\mathrm{F}) = \{1, \pm 1\}$. These groups are just different geometric realizations of the same abstract group of order 2, but their representations are traditionally labeled as

$$\begin{aligned} &\chi_0^+(\mathrm{C}_s) = a_1, \quad \chi_0^-(\mathrm{C}_s) = a_2, \quad \chi_0^+(\mathrm{C}_{1h}) = a', \\ &\chi_0^-(\mathrm{C}_{1h}) = a'', \quad \chi_0^+(\mathrm{C}_i) = a_g, \quad \chi_0^-(\mathrm{C}_i) = a_v \end{aligned} \tag{2.67}$$

For C_{nv} group with $n > 1$ 1-dimensional irreps are usually denoted

$$\begin{aligned} &\chi_0^+(\mathrm{C}_{nv}) = a_1, \quad \chi_0^-(\mathrm{C}_{nv}) = a_2 \\ &\chi_{\frac{n}{2}}^+(\mathrm{C}_{nv}) = b_1, \quad \chi_{\frac{n}{2}}^-(\mathrm{C}_{nv}) = b_2 \text{ (for even } n) \end{aligned} \tag{2.68}$$

The irrep $\chi_0(\mathrm{C}_1)$ of the trivial group C_1 is denoted by the symbol a.

The restriction of line group irreps to representations of orbit stabilizers is well-defined and easy procedure. Expressions for the induced from irreps of orbit stabilizers representations of line groups will include integration over linear Brillouine zone or summation over finite set of k values if the periodic boundary conditions are imposed on the translations along the z axis. Let us consider in more detail the Line groups of Family 8.

Line groups of the 8th family are $\mathrm{L} = \mathrm{T}_{2n}^1(a)\mathrm{C}_{nv} = \mathrm{T}(a)\left(\mathrm{C}_{nv} \bigcup (C_{\frac{\pi}{n}} | \frac{a}{2})\mathrm{C}_{nv}\right)$. The isogonal group is C_{2nv} and transversal $\mathrm{F} = \mathrm{C}_{nv} \bigcup (C_{\frac{\pi}{n}} | \frac{a}{2})\mathrm{C}_{nv}$ contains $4n$ elements being a group modulo pure translations.

For $n > 1$ line groups from this family generate orbits of 3 types. The number of types reduces to 2 for $n = 1$.

For orbits of the type a_1 (Rod group label c) their representatives may be taken as $\mathbf{x}_\rho(\alpha + \beta, z)$ with $\beta \in (0, \frac{\pi}{n})$ and arbitrary z value. The stabilizer of orbit points is trivial and the restriction rules are

$$_kA_m \downarrow \mathrm{C}_1 = \chi_0(\mathrm{C}_1), \quad _kB_m \downarrow \mathrm{C}_1 = \chi_0(\mathrm{C}_1) \tag{2.69}$$

for $k \in (-\frac{\pi}{a}, \frac{\pi}{a}]$, $m = 0, n$, and

$$_kE_m \downarrow \mathrm{C}_1 = 2\chi_0(\mathrm{C}_1) \tag{2.70}$$

for $k \in (-\frac{\pi}{a}, \frac{\pi}{a}]$, $m \in (0, n)$.

The induction rules give regular representation as could be expected:

$$\chi_0(\mathrm{C}_1)\uparrow \mathrm{L} = \bigoplus_{k\in(-\frac{\pi}{a},\frac{\pi}{a}]}\left[\left(2\bigoplus_{m\in(0,n)} {}_kE_m\right)\oplus {}_kA_0\oplus {}_kB_0\oplus {}_kA_n\oplus {}_kB_n\right] \tag{2.71}$$

The corresponding dynamical representation is just a threefold regular one.

Orbits with representatives $\mathbf{x}_\rho(\alpha, z)$ are of the type b_1 (Rod group label b) and these representatives have stabilizer $\mathrm{C}_{1v}(\alpha) = \{(0, e), (0, \sigma_\alpha)\}$. The restriction of the line group irreps to C_{1v} group gives

$${}_kA_m\downarrow \mathrm{C}_{1v} = \chi_0^+(\mathrm{C}_{1v}),\quad {}_kB_m\downarrow \mathrm{C}_{1v} = \chi_0^-(\mathrm{C}_{1v}) \tag{2.72}$$

where $k \in (-\frac{\pi}{a}, \frac{\pi}{a}]$, $m = 0, n$, and

$${}_kE_m\downarrow \mathrm{C}_{1v} = \chi_0^+(\mathrm{C}_{1v})\oplus\chi_0^-(\mathrm{C}_{1v}) \tag{2.73}$$

where $k \in (-\frac{\pi}{a}, \frac{\pi}{a}]$, $m \in (0, n)$.

The corresponding induction rules are

$$\begin{aligned}\chi_0^+(\mathrm{C}_{1v})\uparrow \mathrm{L} &= \bigoplus_{k\in(-\frac{\pi}{a},\frac{\pi}{a}]}\left[\left(\bigoplus_{m\in(0,n)} {}_kE_m\right)\oplus {}_kA_0\oplus {}_kA_n\right]\\ \chi_0^-(\mathrm{C}_{1v})\uparrow \mathrm{L} &= \bigoplus_{k\in(-\frac{\pi}{a},\frac{\pi}{a}]}\left[\left(\bigoplus_{m\in(0,n)} {}_kE_m\right)\oplus {}_kB_0\oplus {}_kB_n\right]\end{aligned} \tag{2.74}$$

Vector representation is $2\chi_0^+(C_{1v})\oplus\chi_0^-(C_{1v})$ and

$$\begin{aligned}\rho^{dyn}(\mathrm{L}) &= (2\chi_0^+(\mathrm{C}_{1v})\oplus\chi_0^-(\mathrm{C}_{1v}))\uparrow \mathrm{L}\\ &= \bigoplus_{k\in(-\frac{\pi}{a},\frac{\pi}{a}]}\left[2({}_kA_0\oplus_k A_n)\oplus_k B_0\oplus_k B_n\oplus\bigoplus_{m\in(0,n)} 3{}_kE_m\right]\end{aligned} \tag{2.75}$$

Points $(0, 0, z)$ represent two-point F-orbits $\{(0, 0, z), (0, 0, z + \frac{a}{2})\}$ with group C_{nv} as a stabilizer of their points. We have

$${}_kA_m\downarrow \mathrm{C}_{nv} = \chi_0^+(\mathrm{C}_{nv}),\quad {}_kB_m\downarrow \mathrm{C}_{nv} = \chi_0^-(\mathrm{C}_{nv}) \tag{2.76}$$

where $k \in (-\frac{\pi}{a}, \frac{\pi}{a}]$ and $m = 0, n$. For 2-dimensional irreps we have

$$kE_m\downarrow \mathrm{C}_{nv} = e_m(\mathrm{C}_{nv}), m \in (0, \frac{n}{2})$$

$$ {}_kE_m \downarrow \mathrm{C}_{nv} = e_{m-[\frac{n}{2}]}(\mathrm{C}_{nv}), m \in (\frac{n}{2}, n) \tag{2.77} $$

The induction rules are

$$ \begin{aligned} \chi_0^+(\mathrm{C}_{nv}) \uparrow \mathrm{L} &= \bigoplus_{k\in(-\frac{\pi}{a},\frac{\pi}{a}]} {}_kA_0 \oplus {}_kA_n \\ \chi_0^-(\mathrm{C}_{nv}) \uparrow \mathrm{L} &= \bigoplus_{k\in(-\frac{\pi}{a},\frac{\pi}{a}]} {}_kB_0 \oplus {}_kB_n \\ e_m(\mathrm{C}_{nv}) \uparrow \mathrm{L} &= \bigoplus_{k\in(-\frac{\pi}{a},\frac{\pi}{a}]} \left[{}_kE_m \oplus {}_kE_{m+[\frac{n}{2}]} \right] \end{aligned} \tag{2.78} $$

where $m \in (0, \frac{n}{2})$. For even values of n and $m = \frac{n}{2}$

$$ {}_kE_{\frac{n}{2}} \downarrow \mathrm{C}_{nv} = \chi_{\frac{n}{2}}^+(\mathrm{C}_{nv}) \oplus \chi_{\frac{n}{2}}^-(\mathrm{C}_{nv}) \tag{2.79} $$

and the induction rules are

$$ \chi_{\frac{n}{2}}^+(\mathrm{C}_{nv}) \uparrow \mathrm{L} = \bigoplus_{k\in(-\frac{\pi}{a},\frac{\pi}{a}]} {}_kE_{\frac{n}{2}}, \quad \chi_{\frac{n}{2}}^-(\mathrm{C}_{nv}) \uparrow \mathrm{L} = \bigoplus_{k\in(-\frac{\pi}{a},\frac{\pi}{a}]} {}_kE_{\frac{n}{2}} \tag{2.80} $$

Three cases should be analyzed when dynamical representations are constructed.

For $n = 1$ the vector representation is $2\chi_0^+(C_{1v}) \oplus \chi_0^-(C_{1v})$ and

$$ \rho^{dyn}(\mathrm{L}) = (2\chi_0^+(\mathrm{C}_{1v}) \oplus \chi_0^-(\mathrm{C}_{1v})) \uparrow \mathrm{L} = \bigoplus_{k\in(-\frac{\pi}{a},\frac{\pi}{a}]} [2({}_kA_0 \oplus_k A_1) \oplus_k B_0 \oplus_k B_1] \tag{2.81} $$

For $n = 2$ the vector representation is $\chi_0^+(C_{1v}) \oplus \chi_1^+(C_{2v}) \oplus \chi_1^-(C_{2v})$ and

$$ \rho^{dyn}(\mathrm{L}) = (\chi_0^+(\mathrm{C}_{1v}) \oplus \chi_1^+(\mathrm{C}_{2v}) \oplus \chi_1^-(\mathrm{C}_{2v})) \uparrow \mathrm{L} = \bigoplus_{k\in(-\frac{\pi}{a},\frac{\pi}{a}]} ({}_kA_0 \oplus_k A_2 \oplus 2_kE_1) \tag{2.82} $$

For $n > 2$ we have the vector representation $\chi_0^+(C_{nv}) \oplus e_1(C_{nv})$ and

$$ \rho^{dyn}(\mathrm{L}) = (\chi_0^+(\mathrm{C}_{nv}) \oplus e_1(\mathrm{C}_{nv})) \uparrow \mathrm{L} = \bigoplus_{k\in(-\frac{\pi}{a},\frac{\pi}{a}]} ({}_kA_0 \oplus_k A_n \oplus_k E_1 \oplus_k E_{n-1}) \tag{2.83} $$

The case $n = 2$ is embraced by the last formula and its separate treatment is actually not required.

As an example we consider TiO_2-based nanotubes (NTs) of different morphology systematically synthesized and carefully studied as promising technological materials, see Chap. 7.

As we have seen above in most theoretical simulations on titanium nanotubes, the model $3D \longrightarrow 2D \longrightarrow 1D$ of structural transformations described was applied, i.e., the bulk ($3D$) phase first formed a lamellar product ($3D \longrightarrow 2D$) and then was bent and rolled to a nanotubular form ($2D \longrightarrow 1D$). The lamellar product is mainly formed by the anatase (101) surface, identified as prevailing in TiO_2. A further geometry optimization of the 3-sheet O–Ti–O layer for $2D \longrightarrow 1D$ transition results in the formation of titania nanotubes possessing hexagonal fluorite-like (111) morphology [26].

The three-layer nanosheets cut from the fluorite phase of the bulk TiO_2 (the space group 225 $Fm\bar{3}m$) have the symmetry of the layer group 72 $P\bar{3}m1$. Using the rolling up correspondence of the line and layer groups [31], one obtains line groups for special chiralities of TiO_2 nanotubes: (n,n)–Family 4, (n,0)–Family 8 with the isogonal point groups C_{2nh} and C_{2nv}, respectively. For n = 1,2,3 these line groups coincide with the crystallographic rod groups.

The symmetry of electron and phonon states for rod groups can be found using the site-symmetry approach [8] for the space groups as the Wyckoff positions of rod groups form subsets of those for space groups.

The site-symmetry approach described above can be applied to find the symmetry of phonon and electron d-states for (n,n) and (n,0) nanotubes rolled up from 3-sheet O–Ti–O layer (n = 1, 2, 3). The rod symmetry groups are $2n_n/m$ and $2n_nmc$ and belong to families 4 and 8, respectively. In this case the tube unit cell contains 6n atoms occupying three nonequivalent 2n-atom orbits (1 titanium orbit and 2 oxygen orbits), corresponding to Wyckoff positions d (stabilizer C_{1h}) and b (stabilizer C_{1v}) for families 4 and 8, respectively.

The corresponding general analytic expressions for the induced representations of all Line groups can be found in Tables published in [3] and are used in the computer code, generating the induced representations for any Wyckoff positions, belonging to Families 4 and 8 of Line groups. This code has been applied to the case of Rod groups and Wyckoff positions, described above for TiO_2 nanotubes. The results obtained by two different ways, coincide.

2.7 CRYSTAL Program. Use of Symmetry in First-Principles LCAO Calculations of 3D, 2D, 1D Systems

CRYSTAL is a general-purpose program for the study of crystalline solids, and the first which has been distributed publicly [39]. The first version was released in 1988 and then seven next versions have followed: CRYSTAL92, CRYSTAL95, CRYSTAL98, CRYSTAL03, CRYSTAL06, CRYSTAL09, CRYSTAL14.

The recent version of the CRYSTAL program -CRYSTAL14- [39] computes the electronic structure of periodic systems within Hartree-Fock, Density Functional or various hybrid approximations. The Bloch functions of the periodic systems are expanded as linear combinations of atom centred Gaussian functions

(LCAO). Powerful screening techniques are used to exploit real space locality. Restricted (Closed Shell) and Unrestricted (Spin-polarized) calculations can be performed with all-electron and valence-only basis sets with effective core pseudopotentials.

The program can automatically handle space symmetry of 230 space groups, 80 layer groups, 75 rod groups (99, if the different rod group settings are taken into account), 45 point groups. Point symmetries compatible with translation symmetry are provided for molecules. Helical symmetry of the polymers is available. Input tools allow the generation of a slab (2D system), or a cluster (0D system), from a 3D crystalline structure, or the creation of a supercell with a defect, nanotubes (1D system) from a single-layer slab model (2D system), nanorods (1D systems) from the bulk crystal (3D system).

The code may be used to perform consistent studies of the physical and chemical properties of molecules, polymers, nanotubes, nanorods, surfaces and crystalline solids: structural features, vibrational properties, electronic structure, magnetic properties, dielectric properties (linear and non-linear electric susceptibilities up to forth-order), elastic, piezoelectric and photoelastic properties [39].

The lack of the crystallographic restrictions for line groups makes translations just a small part of the full symmetry, in contrast to space and layer groups. While in the unit cell of a three-dimensional crystal there are typically several to hundred atoms, the unit cell of a typical nanotube includes hundreds or thousands of atoms. The majority of the existing ab initio numerical codes do not implement line group symmetry.

One of the first attempts of such an implementation was made in [54] to calculate the graphene nanotubes by the method of linear augmented cylindrical waves. Using the symmetry-adapted version of this method carbon nanotubes containing up to 118804 atoms per translational unit cell (the chiral vector $\mathbf{R}(100, 99)$, helical axis order 59402) were calculated. Even for the largest system with a huge unit cell, the band structure can be easily calculated and the results can be presented in the standard form of four curves for the valence band plus one curve for the low-energy states of the conduction band.

The rototranslational (helical) symmetry was implemented in CRYSTAL09 code, [14, 55] and used in the first-principles LCAO calculations of carbon nanotubes. To the best of our knowledge, this is the first complete, tested and documented implementation of helical point symmetry in a general purpose computer code. It has been shown that the use of the helical symmetry of nanotubes, usually quite high, permits one to drastically reduce the computational time and tackle large unit cell nanotubes with an extended basis set. The code permits one to pass from a 3D object (bulk crystal) to a 2D slab and then to a 1D nanotube in a fully automatic way.

In the direct space the helical symmetry is exploited for the calculation of mono- and bi-electronic integrals, so that only a small fraction (the irreducible wedge) of the Fock (Kohn-Sham) matrix F is explicitly computed. The saving factor in the computing time can be as large as N, where N is the number of point symmetry operators that characterize the system.

The symmetry in the reciprocal space is also exploited, as the matrices corresponding to each irreducible representation (IR) are individually diagonalized for the considered **k** points. By transforming the Bloch basis into a symmetry adapted basis the Fock matrix F(**k**) becomes block-diagonal, with each block corresponding to an irreducible representation (IR) of the point group. When the system is periodic only along one direction (z in our convention) and the rotation part of the symmetry operators acts on the Cartesian coordinates (x and y) orthogonal to the translation direction, the point group of each **k** point is the same, and contains the full set of point operators. The Fock matrix then factorizes in exactly the same way at each **k** point. As the cyclic group Z is Abelian, the number of IRs (and of blocks to be diagonalized) is equal to the number of rototranslation operators. In this case the saving factor is much larger than N, due to the third-to-fourth order scaling of the diagonalization process. As a matter of fact, the dimension of all the diagonalized matrices is $M = mN_{AO}$, where N_{AO} is the number of atomic orbitals describing each atom and m is the number of atoms in the layer unit cell.

Following [55] we consider the use of helical symmetry in the first-principles calculations of carbon nanotubes. The structure of a carbon nanotube is modelled by rolling up a single sheet of graphite (i.e. graphene) into a cylinder along the given translation vector $\mathbf{R}(n_1, n_2)$ in a plane hexagonal lattice with two carbon atoms in the primitive cell. The symmetry of graphene is given by layer group $80(P6/mmm)$. It is seen from Table 2.10 that this layer group generates nanotubes with the symmetry of the line group $\mathbf{L}^{(5)}$ (the fifth family) when the general chiral vector $\mathbf{R}(n_1, n_2)$ is used for rolling up the tube (chiral carbon nanotubes). Zigzag and armchair achiral nanotubes are obtained by rolling up the special chiral vectors $\mathbf{R}(n, 0)$ and $\mathbf{R}(n, n)$, respectively. The symmetry of these tubes is given by the line group $\mathbf{L}^{(13)}$, see Table 2.10. The isogonal point groups of the carbon chiral and achiral nanotubes are $\mathbf{D}_n$ and $\mathbf{D}_{2nh}$, with the helical symmetry axis orders equal to n and $2n$, respectively. The resulting nanotubes contain $2q$ and $4q$ atoms, respectively, i.e. dozens or hundreds of atoms in the unit cell, depending on the chiral vector choice. As an example, consider the (24,0) nanotube; with the basis set used for calculations in [55] (a 6-1111G^* contraction) the size of the Fock matrix in the AO basis is 2112 (22 AOs times 96 atoms); in the symmetry adapted basis there are 48 blocks, each containing 44 lines. Then 48 44×44 - matrices are diagonalized at each **k** point.

It is clear that the reduction in computational time due to this factorization is dramatic, in particular, in the case of highly symmetric systems with large unit cells, for which the diagonalization requires a large fraction of the overall computing time. Table 2.17 demonstrates the effect of using of the helical point symmetry in the simulation of carbon nanotubes of increasing size. The results are taken from [55]. The geometry of a set of carbon zigzag $(n, 0)$ nanotubes was optimized. Structure optimizations were performed by using analytical energy gradients with respect to atomic coordinates and unit-cell parameters. Convergence was checked on both gradient components and nuclear displacements. The hybrid B3LYP functional was adopted, together with a quite complete basis set containing $1s$, $4sp$, and $1d$ shells, that is 22 AOs per carbon atom (6-1111G^* contraction). The level of accuracy in evaluating the Coulomb and Hartree-Fock exchange series is controlled by

Table 2.17 Effect of the exploitation of point symmetry in the simulation of carbon nanotubes of increasing size [55]

	R	N_A	N_{AO}	N_R	$N_{\hat{S}}$	t_{SCF}	t_G	ΔE	δE
(8,0)	3.137	32	704	15.8	16	72.1	459.6	42.78	1.48
(9,0)	3.529	36	792	17.8	18	65.9	409.2	34.47	0.728
(10,0)	3.921	40	880	19.8	20	63.0	384.3	27.20	0.475
(11,0)	4.313	44	968	21.8	22	60.7	365.0	22.57	0.387
(12,0)	4.705	48	1,056	23.8	24	60.6	355.2	19.50	0.126
(13,0)	5.097	52	1,144	25.8	26	61.4	353.9	16.24	0.117
(14,0)	5.489	56	1,232	27.8	28	62.8	350.1	14.08	0.134
(15,0)	5.881	60	1,320	29.7	30	63.4	352.6	12.65	0.0518
(16,0)	6.273	64	1,408	31.7	32	65.2	346.9	10.88	0.0685
(17,0)	6.665	68	1,496	33.7	34	66.5	344.3	9.70	0.0750
(18,0)	7.058	72	1,584	35.7	36	67.9	341.0	8.93	0.0195
(19,0)	7.450	76	1,672	37.7	38	70.2	344.1	7.86	0.0320
(20,0)	7.842	80	1,760	39.6	40	72.5	344.6	7.14	0.0386
(21,0)	8.234	84	1,848	41.6	42	75.4	344.9	6.68	0.0151
(22,0)	8.626	88	1,936	43.6	44	78.4	347.1	5.97	0.0162
(23,0)	9.018	92	2,024	45.6	46	81.7	348.6	5.49	0.0243
(24,0)	9.410	96	2,112	47.6	48	85.6	351.5	5.20	8.63E-3

five parameters, [14] for which the 8 8 8 8 16 values were used. The threshold on the SCF energy was set to 10^{-8}Ha. The reciprocal space was sampled according to a regular sublattice with shrinking factor 10 (6 **k** vectors). The DFT exchange-correlation contribution was evaluated by numerical integration over the unit cell volume. In these calculations, a (75,974) grid was used which corresponds to a pruned grid with 75 radial and 974 angular points; the accuracy in the integration can be estimated by the error in the integrated electronic charge density in the unit cell ($\Delta_e = 810^{-4}|e|$ for a total of 576 electrons in the (24,0) nanotube).

Table 2.17 documents the effect of point symmetry use for a set of $(n, 0)$ nanotubes (all of them share the same rolling direction). In the first two columns, the (n_1, n_2) indices of the nanotubes and their radius, R (Å), are reported. N_A and N_{AO} are the number of atoms and atomic orbitals in $(6-1111G(d))$ basis set per unit cell, N_R is the ratio between the number of elements of the complete and irreducible Fock matrix, $N_{\hat{S}}$ is the number of symmetry operators. The cost of the calculation is documented in the t_{SCF} and t_G columns of Table 2.17; t_{SCF} and t_G are given in seconds and mean the time of a single SCF cycle and of the gradient calculation, respectively (single processor-Intel Xeon, 1.86 GHz, RAM 8 Gb). ΔE and δE (kJmol^{-1} per couple of C atoms) are the energy difference with respect to graphene and the relaxation energy after rigid rolling, respectively.

In going from (8,0) to (24,0), the number of atoms (N_A), basis functions (N_{AO}), and symmetry operators ($N_{\hat{S}}$) increase exactly by threefold (from 32 to 96, from 704 to 2112, and from 16 to 48, respectively). The complete Fock matrix for the largest

case is then about three times larger than for the (8,0) case, whereas the symmetry adapted matrix size is roughly constant. The (8,0) nanotube F matrix has about 11,500 elements that diminish to 10,000 for the (24,0) case. The number of elements N_R is extremely close to the number of symmetry operators $N_{\hat{S}}$. The time required for the calculation of bi-electronic integrals, the most expensive part of the SCF calculation, decreases for a while and then remains nearly constant. The same behavior is shown by the gradient, whose cost from (12,0) to (24,0) varies by less than 1 %. The overall cost of the SCF cycle increases (slowly) for three reasons. First, the diagonalization step scales linearly with N (i.e., with the number of symmetry operators and with the number of atoms). Second, the t_{SCF} and t_G AO $\rightarrow$ Bloch $\rightarrow$ symmetry adapted basis transformations, and the back transformations to the AO basis for building the density matrix, are matrix multiplications. In principle, AO $\rightarrow$ Bloch and Bloch $\rightarrow$ symmetry adapted basis transformations should scale as N_{AO}^2 and N_{AO}^3, respectively, with a low prefactor. In practice, the sparsity of all the involved matrices is exploited, so that the scaling of this stage is closer to N_{AO}^2 than to N_{AO}^3. Third, the overhead for the symmetry analysis increases with the number of symmetry operators. Overall, the total cost increases by less than 50 % for the SCF and remains constant for the gradient, whereas in a perfect linear scaling code, not exploiting the symmetry, the cost would increase by a factor of three. The last two columns provide the energy difference between the relaxed nanotube and graphene, $\Delta \mathrm{E} = \mathrm{E}_{\mathrm{relaxed}} - \mathrm{E}_{\mathrm{graphene}}$, and the relaxation energy after rigid rolling, δE (energy difference between unrelaxed and relaxed nanotubes). Roughly speaking, both ΔE and δE decrease regularly as n increases, as expected and in line with the previous findings. Actually, a finer analysis shows that δE data belongs to three different curves, describing the $(3n, 0)$, $(3n + 1, 0)$, and $(3n + 2, 0)$ cases; however, the differences are quite small and tend to disappear with the increase of the nanotube diameter. The stability of a nanotube family with respect to graphene calculated at the B3LYP level documents the feasibility of this kind of calculations, and the accuracy of the implementation [55].

The rototranslational symmetry subgroup of the line group was implemented in CRYSTAL09 code. The full line group symmetry was implemented in CRYSTAL14 code and gives the higher efficiency in the calculations of the nanotubes with the isogonal point groups C_{nv}, C_{nh}, D_{nd}, D_{nh}.

References

1. B.K. Vainstein, *Modern Crystallography: Fundamentals of Crystals, Symmetry and Methods of Structural Crystallography*, vol. 1 (Springer, Berlin, 1994) Kristallographia **4**, 842 (1959)
2. T. Hahn (ed.), *International Tables for Crystallography*. Space-group Symmetry, vol. A (Reidel, Dordrecht, 1983)
3. M. Damnjanović, I. Milošević, *Line Groups in Physics*. Lecture Notes in Physics, vol. 801 (Springer, Berlin, 2010)
4. M. Vujičić, I.B. Božović, F. Herbut, J. Phys. A: Math. Gen. **10**, 1271 (1977)

5. V. Kopsky, D.B. Litvin (eds.), *International Tables for Crystallography*. Subperiodic Groups, vol. E (Kluwer Academic Publishers, Dodrecht, 2002)
6. R.A. Evarestov, V.P. Smirnov, *Site Symmetry in Crystals: Theory and Applications*, 2nd edn. Springer Series in Solid State Sciences, vol. 108 (Springer, Berlin, 1997)
7. M.I. Petrashen, E.D. Trifonov, *Applications of Group Theory in Quantum Mechanics* (M.I.T. Press, Massachusetts, 1969)
8. *Bilbao Crystallographic Server. The Crystallographic Site at the Condensed Matter* (Physics Department of the University of the Basque Country), http://www.cryst.ehv.es/
9. L.L. Boyle, Acta Cryst. A **29**, 353 (1973)
10. http://cst-www.nrl.navy.mil/lattice/
11. http://cst-www.nrl.navy.mil/lattice/others.html
12. H.A. Jahn, E. Teller, Proc. R. Soc. Lond. A **161**, 220 (1937)
13. Inorganic Crystal Structure Database (ICSD), http://www.fiz-informationsdienste.de/en/DB/icsd/
14. R. Dovesi, V.R. Saunders, C. Roetti, R. Orlando, C.M. Zicovich-Wilson, F. Pascale, B. Civalleri, K. Doll, N.M. Harrison, I.J. Bush, P. D'Arco, M. Llunell, *CRYSTAL09 User's Manual* (University of Torino, Torino, 2010)
15. O.A. Graeve, Zirconia, in *Ceramic and Glass Materials: Structure, Properties and Processing*, ed. by J.F. Shackelford, R.H. Doremus (Springer Science, New York, 2008), p. 169
16. D. Vollath, F.D. Fischer, M. Hagelstein, D.V. Szabó, J. Nanopart. Res. **8**, 1016 (2006)
17. C.M. Wang, S. Azad, S. Thevuthasan, V. Shutthanandan, D.E. McCready, C.H.F. Peden, J. Mater. Res. **19**, 1315 (2004)
18. A. Aarik, A. Aidla, H. Mundar, T. Uustrate, V. Sammelselg, Thin Solid Films **408**, 97 (2002)
19. P. Goudochnikov, A.J. Bell, J. Phys.: Condens. Matter **19**, 176201 (2007)
20. V. Kopsky, Acta Cryst. A **45**, 805, 816 (1989)
21. V. Kopsky, Acta Cryst. A **56**, 370 (2000)
22. E.A. Wood, 80 Diperiodic Groups in Three Dimensions, Bell System Monograph No 4680 (1964)
23. I. Milosević, B. Nikolić, M. Damnjanović, M. Krčmar, J. Phys. A: Math. Gen. **31**, 3625 (1998)
24. P.W. Tasker, J. Phys. C: Solid State Phys. **12**, 4977 (1979)
25. F. Finocchi, F. Bottin, C. Noguera, in *Computational Materials Science*, ed. by C.R.A. Catlow, E.A. Kotomin (IOS Press, Amsterdam, 2003), p. 196
26. R.A. Evarestov, *Quantum Chemistry of Solids. LCAO Treatment of Crystals and Nanostructures*, 2nd edn. Springer Series in Solid State Sciences, vol. 153 (Springer, Berlin, 2012)
27. M. Damnjanović, M. Vujicić, Phys. Rev. B **25**, 6987 (1982)
28. V.P. Smirnov, P. Tronc, Phys. Solid State **48**, 1373 (2006)
29. R.A. Evarestov, A.I. Panin, Acta Cryst. A **68**, 582 (2012)
30. M. Damnjanović, I. Milosević, M. Vuković, R. Sredanivić, Phys. Rev. B **60**, 2728 (1999)
31. M. Damnjanović, B. Nikolić, M. Milosĕvić, Phys. Rev. B **75**, 033403 (2007)
32. S. Ijima, Nature **354**, 56 (1991)
33. E.B. Barros, A. Jorio, G.G. Samsonidze, R.B. Capaz, A.G.S. Filho, J.M. Filho, G. Dresselhaus, Phys. Rep. **431**, 261 (2006)
34. Y. Mao, S. Banerjee, S.S. Wong, Chem. Commun. **3**, 408 (2003)
35. R. Evarestov, IOP Conf. Ser.: Mater. Sci. Eng. **23**, 012012 (2011)
36. A.V. Bandura, R.A. Evarestov, Surf. Sci. **603**, L117 (2009)
37. R.A. Evarestov, A.V. Bandura, M.V. Losev, Russ. J. Gen. Chem. **80**, 1152 (2010)
38. R.A. Evarestov, Yu.F. Zhukovskii, A.V. Bandura, S. Piskunov, Cent. Eur. J. Phys. **9**, 492 (2011)
39. R. Dovesi, V.R. Saunders, C. Roetti, R. Orlando, C.M. Zicovich-Wilson, F. Pascale, B. Civalleri, K. Doll, N.M. Harrison, I.J. Bush, P. D'Arco, M. Llunell, M. Causa, Y. Noel, *CRYSTAL14 User's Manual* (University of Torino, Torino, 2014)
40. R. Dovesi, R. Orlando, A. Erba, C.M. Zicovich-Wilson, B. Civalleri, S. Casassa, L. Maschio, M. Ferrabone, M. Pierre, P. D'Arco, Y. Noel, M. Causa, M. Rerat, B. Kirtman, Int. J. Quant. Chem. **114**, 1287 (2014)
41. M. Damnjanović, I. Milosĕvić, T.V.E. Dobradzić, B. Nikolić, J. Phys. A **36**, 10349 (2003)

42. M. Damnjanović, T. Vuković, I. Milosĕvić, Acta Phys. Pol. A **120**, 224 (2011)
43. P.B. Allen, Nanoletters **7**, 6, 11, 1220 (2007)
44. C. Herring, Phys. Rev. **82**, 87 (1951)
45. D.B. Migas, V.L. Shaposhnikov, V.E. Borisenko, F.A. D'Avitaya, J. Phys. Chem. C **114**, 21013 (2010)
46. C.A. Chen, Y.M. Chen, A. Korotcov, Y.S. Huang, D.S. Tsai, K.K. Tiong, Nanotechnology **19**, 075611 (2007)
47. B. Aradi, P. Deak, H.A. Huy, A. Rosenauer, T. Frauenheim, J. Phys. Chem. C **115**, 18494 (2011)
48. A.P. Cracknell, B.L. Davies, S.C. Miller, W.F. Love, *Kronecker Product Tables, 1 General Introduction and Tables of Irreducible Representations of Space Groups* (IFI/Plenum, New York, 1979)
49. C.J. Bradley, A.P. Cracknell, *The Mathematical Theory of Symmetry in Solids* (Clarendon, Oxford, 1972)
50. http://gernot-katzers-spice-pages.com/character_tables/index.html
51. I.B. Božović, M. Vujičić, F. Herbut, J. Phys. A: Math. Gen. **11**, 2133 (1978)
52. I.B. Božović, M. Vujičić, J. Phys. A: Math. Gen. **14**, 777 (1981)
53. I. Božović, N. Božović, J. Phys. A: Math. Gen. **14**, 1825 (1981)
54. P.N. D'yachkov, D.V. Makaev, Phys. Rev. B **76**, 195411 (2007)
55. I. Noel, P. D'Arco, R. Demichelis, C.M. Zicovich-Wilson, R. Dovesi, J. Comput. Chem. **32**, 855 (2010)

Chapter 3
First-Principles Simulations of Bulk Crystal and Nanolayer Properties

In this chapter we consider the methods of first-principle calculations of the bulk crystal and nanostructure properties, which depend on the electronic structure.

The choice of the basis set is of particular importance when treating periodic systems where a large variety of chemical bonding can be found. The following two approaches to the basis-set choice define two types of methods of the electronic-structure calculations of periodic systems: plane-wave (PW) methods and localized atomic-like orbitals (LCAO) methods. Each method has its advantages and disadvantages.

In the case of monoperiodic (1D) systems (for example, nanotubes and nanowires) PW calculations one needs an introduction of two vacuum regions, both of which must be wide enough so that the 1D systems will not interact through the bulk crystal. LCAO calculations are free from this shortcoming. Therefore in the quantum chemistry of the systems with 2D and 1D periodicity the LCAO methods are more preferable. These methods are more flexible as they allow both Hartree-Fock and Kohn–Sham equations to be solved, are applicable in the correlated wavefunction approaches (for example, MP2 theory) and in the Kohn–Sham theory based on hybrid exchange-correlation functionals. Both all-electron and valence-electron—only calculations can be made in LCAO basis, while the PW methods always require using the effective core potential (ECP) for core electrons. Different choices of the ECP for solids are discussed.

The extension of one-electron approximation (Restricted, Unrestricted and Restricted Open shell one-determinant Hartree-Fock methods) to periodic systems is considered. The direct lattice summations in the Fock matrix elements and the **k** dependence of the one-electron density matrix, energy levels and crystalline orbitals are the main difficulties of the HF LCAO method for periodic systems, compared with molecules.

In the self-consistent calculations of the electronic structure of bulk crystals and nanostructures, both in the basis of plane waves and in the basis of localized atomic-type functions, one needs at every stage of the self-consistent procedure to evaluate the approximate electron-density matrix by integration over the Brillouin zone (BZ).

© Springer-Verlag Berlin Heidelberg 2015

R.A. Evarestov, *Theoretical Modeling of Inorganic Nanostructures*,
NanoScience and Technology, DOI 10.1007/978-3-662-44581-5_3

The progress in the electron-correlation study of solids is connected mainly with the density-functional theory (DFT), determining directly the various physical properties of a system without any knowledge of the many-electron wavefunction. Unfortunately, for the density-functional-based methods there is no procedure for a systematic improvement of the calculated results when a higher accuracy is desired. Modeling the exchange and correlation interactions becomes difficult within DFT as the exact functionals for the exchange and correlation are not known except for the homogeneous (uniform) electron gas. The problem of molecular exchange-correlation functional transferability to crystals is discussed. The climbing of the so called Jacob's Ladder for Exchange-Correlation Functionals defines approximations that permit the calculation of real periodic systems: LDA, GGA and hybrid Hartree-Fock/Kohn–Sham (orbital dependent) exchange correlation and screened exchange correlation functionals.

The Density Functional Tight Binding (DFTB) method is popular for 1D nanostructure calculations. This method uses Slater type atomic orbitals, applied to the two-center integrals introduction as free parameters. When these parameters are fitted to reproduce the results of the DFT calculations the electron correlation is also taken into account. Hamiltonian matrix elements can be modified by a self-consistent redistribution of Mulliken charges.

The application of the DFT and hybrid exchange-correlation functionals to simulations of nanostructures (nanolayers, nanotubes, nanowires) is discussed in Part II of this book. As we mentioned in Chap. 2, the study of nanostructures usually starts with calculations of the structure and properties of the corresponding bulk crystals. The bulk crystals play a role of benchmark systems to check the applicability of the selected computation method to reproducing the experimental data for different bulk crystal properties: the equilibrium atomic structure, one-electron properties (band structure and density of states), formation and atomization (cohesive) energy, bulk modulus and elastic constants, phonon frequencies and thermodynamical properties.

The results of the LCAO DFT(PBE0) calculations of the structure and electronic properties, bulk modulus and the relative energies of different phases are presented for several bulk crystals serving as a base for nanostructure modeling: binary oxides (rutile phase of TiO_2), ternary oxides ($SrTiO_3$, $SrZrO_3$, $BaTiO_3$) and sulfides (TiS_2, ZrS_2). Good agreement is demonstrated of the calculation results with the experimental data.

3.1 Basis Sets and Pseudopotentials in the Crystalline Electronic Structure Calculations

3.1.1 Plane Wave and Localized Atomic Functions Basis Sets

Although the same fundamental theory underlies the Hartree-Fock or the density-functional approach in both solid-state physics and molecular quantum chemistry

(for example, the same exchange-correlation functionals can be used in both disciplines), the detailed implementation is usually quite different [1]. First, this difference concerns the basis-set choice.

Since the electronic charge density of an isolated molecule is necessarily localized in a finite region of space, the traditional quantum-chemical method is LCGTO (MOs are expanded in a basis of localized Gaussian-type orbitals, centered on the atomic nuclei).

The choice of the basis set is of particular importance when treating periodic systems where a large variety of chemical bonding can be found. The following three approaches to the basis-set choice define three types of methods of the electronic-structure calculations in crystals [2]: plane-wave (PW) methods, atomic-sphere (AS) methods, LCAO methods. Each method has its advantages and disadvantages. The information about the existing computer codes using AS, PW and LCAO basis sets for the periodic structure calculations can be found on the site [3].

The tradition in solid-state physics is to use plane waves (PW) as a basis set for expanding the one-particle Kohn–Sham wavefunctions (crystalline orbitals) [4]. These can be used in their pure form in the first-principles Effective Core Potential (pseudopotential) method [5] or modified near the atomic cores (augmented plane waves [6]).

The basic idea of AS methods is to divide the electronic-structure problem, providing efficient representation of atomic-like features that are rapidly varying near each nucleus and smoothly varying functions between atoms [2]. The smooth functions are augmented near each nucleus by solving the Schrödinger equation in the sphere at each energy and matching to the outer wave function. The resulting APW (augmented plane waves) or KKR (Kohn–Korringa–Rostoker) methods are powerful but require solution of nonlinear equations. The linear modifications of AS methods (LAPW, LMTO) use the familiar form of a secular equation involving a Hamiltonian and overlap matrix. The linear modification of the all-electron (termed also full potential—FP) PW method (FPLAPW) provide the most precise solutions of the Kohn–Sham equations. However FPLAPW calculations are practically difficult as the core-states description requires a huge number of plane waves.

The simpler PW methods using the effective core potential (ECP) for core electrons (pseudopotential) are the most popular in the Kohn–Sham periodic-systems calculations. Plane waves are an orthonormal complete set; any function belonging to the class of continuous normalizable functions can be expanded with arbitrary precision in such a basis set. Using the Bloch theorem the single-electron wavefunction $\varphi_i(\mathbf{r})$ can be written as a product of a wave-like part and a cell-periodic part $\varphi_{i\boldsymbol{k}} = \exp(\mathrm{i}\boldsymbol{k}\boldsymbol{r})u_i(\boldsymbol{r})$ (see Chap. 2). Due to its periodicity in a direct lattice $u_i(\boldsymbol{r})$ can be expanded as a set of plane waves $u_i(\boldsymbol{r}) = \sum_{\boldsymbol{B}} C_{i\boldsymbol{B}} \exp(\mathrm{i}\boldsymbol{B}\boldsymbol{r})$, where $\boldsymbol{B}$ is the reciprocal lattice vector. Thus, in the PW basis the single-electron wavefunction can be written as a linear combination of plane waves

$$\varphi_{i\boldsymbol{k}}(\boldsymbol{r}) = \sum_{\boldsymbol{B}} C_{i\boldsymbol{B}} \exp(\mathrm{i}(\boldsymbol{k}+\boldsymbol{B})\boldsymbol{r}) \tag{3.1}$$

The number of basis functions used is controlled by the largest wavevector in the expansion (3.1). This is equivalent to imposing a cutoff on the kinetic energy as the kinetic energy of an electron with wavevector $(\boldsymbol{k} + \boldsymbol{B})$ is given by $\frac{|\boldsymbol{k}+\boldsymbol{B}|^2}{2}$. Thus, the size of the PW basis set is defined by the so-called cutoff energy, i.e. the kinetic energy for the largest reciprocal lattice vector included in the PW basis. The PW basis set is universal, in the sense that it does not depend on the positions of the atoms in the unit cell, nor on their nature [7]. One does not have to construct a new basis set for every atom in the periodic table nor modify them in different materials, as is the case with localized atomic-like functions and the basis can be made better (and more expensive) or worse (and cheaper) by varying a single parameter—the number of plane waves defined by the cutoff energy value. This characteristic is particularly valuable in the quantum molecular-dynamics calculations, where nuclear positions are constantly changing. It is relatively easy to compute forces on atoms. Finally, plane-wave calculations do not suffer from the basis-set superposition error (BSSE). In practice, one must use a finite set of plane waves, and this in fact means that well-localized core electrons cannot be described in this manner. One must either augment the basis set with additional functions (as in linear combination of augmented plane waves scheme), or use pseudopotentials to describe the core states. Both AS and PW methods, developed in solid-state physics are used to solve Kohn–Sham equations. We refer the reader to recently published books for the detailed description of these methods [2, 8–10]. The plane waves are a reasonable first approximation to conduction-band eigenfunctions and permit many formal simplifications and computational economies.

Nevertheless, PW methods have the disadvantage that very localized or inhomogeneous systems may require excessive numbers of waves for their representation. PW basis can be formally applied only to the systems with 3D periodicity i.e. bulk crystals. The main problem of PW basis use arises when the three-dimensional objects have 2D periodicity (nanolayers) or 1D periodicity (nanotubes, nanowires).

This problem can be especially serious in surface calculations, where the requirement of periodicity in three dimensions leads to a model with slabs repeating periodically along the surface normal. A surface may have periodicity in the plane of the surface, but it cannot have periodicity perpendicular to the surface. Therefore the artificial supercell for a surface calculation is introduced. The supercell contains a crystal slab and a vacuum region [5]. The supercell is repeated over all space, so the total energy of an array of crystal slabs is calculated. To ensure that the results of the calculation accurately represent an isolated surface, the vacuum regions must be wide enough so that faces of adjacent crystal slabs do not interact across the vacuum region, and the crystal slab must be thick enough so that the two surfaces of each crystal slab do not interact through the bulk crystal [5]. If the space between the slabs is wide enough to make interactions between them negligible, the “lattice constant” normal to the surface has to be quite large and the corresponding reciprocal lattice vector quite short, resulting in a large number of plane waves within a given kinetic-energy cutoff and hence a relatively expensive calculation. The distance between the

slabs needs to be even larger if adsorbate molecules are to be added to the surface, since these molecules also should not interact across the space between the slabs.

In the case of monoperiodic (1D) systems (for example, nanotubes and nanowires) one needs to use two vacuum regions in PW calculations and both must be wide enough so that the 1D systems do not interact through the bulk crystal.

Finally, even molecules (0D periodicity) can be studied in this fashion (three vacuum regions have to be introduced when PW basis set is used). Again, the supercell needs to be large enough so that the interactions between the molecules are negligible. The calculation of the charged molecular systems (molecular ions) requires the charge compensation by the surrounding medium.

To make the Hartree-Fock calculations in PW basis practically applicable one needs the introduction of the short- and long-range parts of the Hartree-Fock exchange (see Hartree-Fock method in PW basis subsection).

Localized-basis approaches to periodic systems do not suffer from these disadvantages. Very localized states, including core states if desired, can be represented by a suitable choice of atom-centered basis functions. The electronic charge density goes naturally to zero in regions of space where there are no atoms, and the lack of basis functions in such regions is not a problem unless a detailed description of energetic excitations, scattering states, or tunneling is required [1]. LCAO methods can be formulated equally easily for systems periodic in one, two or three dimensions. For surface modeling there is no need for periodicity normal to the surface; a single slab of sufficient finite thickness can be used. This facilitates the accurate treatment of molecule–surface interactions, especially when the molecules are relatively far from the surface. Also, if the basis functions are carefully constructed and optimized for the crystalline environment (see next subsection) it is possible to represent the valence-electron eigenstates with a relatively small number of basis functions: just enough to accommodate all the electrons, plus a few more functions to give the Kohn–Sham orbitals sufficient variational freedom. Thus, only a few tens of basis functions per atom are typically needed, versus hundreds per atom in typical plane-wave approaches.

The auxiliary basis sets needed to represent the charge density and, if desired, the exchange-correlation potential are also fairly modest in size. Once the basis set has been constructed and the required overlap and Hamiltonian matrices formed, the small (compared to plane wave) size of the basis can greatly reduce the computational cost of solving the Kohn–Sham equations.

Also, especially in systems with large unit cells, one can exploit sparsity in these matrices, since basis functions on distant centers will have negligible overlap and interaction (except for certain long-range Coulomb multipole interactions that can be summed according to Ewald's convention or screened). Advanced techniques can be applied to calculate multicenter integrals in LCGTO methods for solids. For example, in the implementation of periodic boundary conditions in the MO LCAO program [11, 12] all terms contributing to the KS Hamiltonian are evaluated in real space, including the infinite Coulomb summations, which are calculated with the aid of the fast multipole method. In LCGTO methods with PBC the $O(N)$ linear-scaling DFT calculations for large and complex systems are possible [11, 13]. For example,

carbon nanostructures up to C540 were calculated [14] using DFT LCAO with the numerical atomic basis.

In the quantum chemistry of the systems with 2D and 1D periodicity the LCAO methods are more preferable [7]. These methods are more flexible as they allow both Hartree-Fock and Kohn–Sham equations to be solved, are applicable in the correlated wavefunction approaches (for example, MP2 theory) and in Kohn–Sham theory based on hybrid exchange-correlation functionals. In comparison with plane waves, the use of all-electron LCAO calculations allows one to describe accurately electronic distributions both in the valence and the core region with a limited number of basis functions. The local nature of the basis allows a treatment both of finite systems and of systems with periodic boundary conditions in one, two or three dimensions. This has an advantage over plane-wave calculations of molecules, polymers or surfaces that work by imposing artificial periodicity: the calculation must be done on, e.g. a three-dimensional array of molecules with a sufficiently large distance between them (the molecule is placed at the center of a periodic supercell). LCAO total energies can be made very precise (i.e. reliable to many places of decimals) since all integrals can be done analytically (in practice, this is only true for Hartree-Fock calculations; density-functional theory LCAO calculations require a numerical integration of the exchange-correlation potential that reduces the attainable precision). Having an "atomic-like" basis facilitates population analyses, the computation of properties such as projected densities of states, and "pre-SCF alteration of orbital occupation" making the convergence of SCF calculations faster. As was already noted the LCAO basis allows easy comparison of the results obtained for molecules and solids at the same precision level of calculations.

As it is demonstrated in the next subsection, the molecular basis set atomic-like orbitals can be considered as a starting point to generate atomic basis sets to be used in crystalline compounds. Therefore, we begin with the molecular basis-sets description.

In molecular quantum chemistry two types of atomic-like basis sets are used: Slater-type orbitals (STO) and Gaussian-type orbitals (GTO). In fact, it is not really correct to call them "orbitals". They are better described as basis-set functions, since they are Slater-type or Gaussian-type functions used to approximate the shapes of the orbitals defined as one-electron wavefunctions. Using the acronyms accepted in solid-state theory it would be possible even call LCAO methods for crystals to "all-electron or full potential linear combination of Slater (Gaussian)-type functions—FP LS(G)TF method" [7], compare with the acronym FP LAPW (full potential linear combination of augmented plane waves).

The mathematical form of the normalized primitive Slater-type function (STF) in atom-centered polar coordinates is

$$\chi_{nlm}^{STF}(\boldsymbol{r}) = N_{nl}(\zeta) r^{n-1} \exp(-\zeta r) Y_{lm}(\theta, \varphi) = R_{nl}(r) Y_{lm}(\theta, \varphi) \tag{3.2}$$

where ζ is an orbital exponent, n is the principal quantum number, $Y_{lm}(\theta, \varphi)$ are the spherical harmonics, depending on the angular momentum quantum numbers l

and m. The Slater orbitals can be written in the form (3.2) with the orbital exponent $\zeta = \frac{Z-s}{n^*}$ and $n = n^*$.

The STF with the radial part in the form (3.2) and integer n can be used as the basis functions in Hartree-Fock–Roothaan calculations of atomic wavefunctions. The radial dependence of the atomic orbitals is an expansion in the radial Slater-type basis functions φ_{lmp} whose indices are l, running over $s, p, d, f, \ldots$ symmetries, and p counting serially over basis-set members for a given symmetry:

$$\varphi_{lmi} = \sum_p C_{lmp} R_{lp}(r) Y_{lm}(\theta, \varphi) \tag{3.3}$$

The radial expansion is independent of m; all electrons with a given l, i have the same radial dependence. The orbital angular dependence $Y_{lm}(\theta, \varphi)$ is a normalized spherical harmonic.

The Slater-type orbitals were the first to be used in the molecular quantum chemistry semiempirical calculations. Nowadays STO are used in DFTB method (see Sect. 3.4). Unfortunately, such functions are not suitable for fast calculations of multicenter integrals in ab-initio calculations. Gaussian-type functions (GTFs) were introduced to remedy the difficulties. GTFs are used in basis sets in practically all modern codes for LCAO calculations of molecules. We know two exclusions from this rule—KS LCAO codes SIESTA and ADF, see [3]. The SIESTA code uses a numerical AO basis set, the ADF code uses Slater-type basis set orbitals.

A primitive Gaussian-type function can be written in a local Cartesian coordinate system in the form

$$\chi^{GTF} = x^l y^m z^n \exp(-\alpha r^2) \tag{3.4}$$

where α is the orbital exponent, and the l, m, n are not quantum numbers but simply integral exponents of Cartesian coordinates. Gaussian primitives (3.4) can be factorized into their Cartesian components, i.e. $\chi^{GTF} = \chi_x^{GTF} \chi_y^{GTF} \chi_z^{GTF}$, where each Cartesian component has the form (introducing an origin such that the Gaussian is located at position A),

$$\chi_x^{GTF} = (x - x_A) \exp\left(-\alpha (x - x_A)^2\right) \tag{3.5}$$

This simplifies considerably the calculation of integrals. If we write the exponential part of an STF, $exp(-\alpha r)$ in Cartesian components we get $\exp(-\alpha\sqrt{x^2 + y^2 + x^2})$ that is not so separable. Note that the absence of the STO pre-exponential factor r^{n-1} restricts single Gaussian primitives to approximating only $1s$, $2p$, $3d$ etc. orbitals and not, e.g. $2s$, $3p$, $4d$, etc. However, combinations of Gaussians are able to approximate correct nodal properties of atomic orbitals if the primitives are included with different signs. The sum of exponents of Cartesian coordinates $L = l + m + n$ is used analogously to the angular-momentum quantum number for atoms to mark Gaussian primitives as s-type ($L = 0$), p-type ($L = 1$), d-type ($L = 2$), f-type ($L = 3$) etc. From six $3d$ GTFs ($x^2, xy, xz, yz, y^2, z^2$) there are only five linearly independent

and orthogonal atomic d-orbitals being linear combinations of Cartesian Gaussians $(3z^2 - r^2, xz, yz, x^2 - y^2, xy)$, the sixth combination $x^2 + y^2 + x^2 = r^2$ is Gaussian primitive of s-type.

It is clear that the behavior of a Gaussian is qualitatively wrong both at the nuclei and in the long-distance limit for a Hamiltonian with point-charge nuclei and Coulomb interaction. From this point of view Slater type orbitals would be preferable.

In so-called Pople basis sets, the basis functions are made to look more like Slater-type functions by representing each STF χ^{STF} as a linear combination of Gaussian primitives:

$$\chi^{STF} = \sum_{i=1}^{N} C_i \chi_i^{GTF} \tag{3.6}$$

where C_i is a fixed coefficient and N is the number of Gaussian primitives used to represent the Slater-type basis function. The sums (3.6) are known as the contracted Gaussian basis set. Linear combinations of Gaussian primitives allow the representation of the electron density close to the nucleus to be improved. Recall that STF has a cusp at the nucleus, while GTF does not. By taking linear combinations of Gaussian primitives, the cusplike behavior is better reproduced.

The Gaussian basis set can also be used without any connection with the Slater-type orbitals: HF equations solutions for atoms are reached by Roothaan's expansion method with Gaussian-type functions as was done with STFs. The details of both procedures—Gaussian expansion of Slater-type orbitals and atomic SCF calculations with Gaussian-type basis—are well known in molecular quantum chemistry. It was found that GTF expansions require inclusion of more primitives than STF expansions for the same accuracy in the total and one-electron SCF energies for atoms.

In molecular quantum chemistry Gaussian-type basis functions are expanded as a linear combination (contraction) of individually normalized Gaussian primitives $g_j(\boldsymbol{r})$ characterized by the same center and angular quantum numbers but with different exponents

$$\chi_i(\boldsymbol{r}) = \sum_{j=1}^{N} d_j g_j(\boldsymbol{r}), \quad g_j(\boldsymbol{r}) = g(\boldsymbol{r}; \alpha, l, m) = N_{lm}(\alpha) r^l Y_{lm}(\theta, \phi) \exp(-\alpha_j r^2) \tag{3.7}$$

where N is the length of the contraction, the α_j are the contraction exponents, the d_j are contraction coefficients. Gaussian primitives can be written in terms of real spherical harmonics including a normalization constant.

If accurate solutions for an atom are desired, they can be obtained to any desired accuracy in practice by expanding the "core" basis functions in a sufficiently large number of Gaussians to ensure their correct behavior. Furthermore, properties related to the behavior of the wavefunction near nuclei can often be predicted correctly, even without an accurately "cusped" wavefunction. In most molecular applications the asymptotic behavior of the density far from the nuclei is considered much

more important than the nuclear cusp [7]. The molecular wavefunction for a bound state must fall off exponentially with distance, whenever the Hamiltonian contains Coulomb electrostatic interaction between particles. However, even though an STFs basis would, in principle, be capable of providing such a correct exponential decay, this occurs in practice only when the smallest exponent in the basis set is $\zeta_{min} = \sqrt{2I_{min}}$, where I_{min} is the first ionization potential. Such a restriction on the range of exponent values, while acceptable for atomic SCF calculations, is far too restrictive for molecular and solid-state work. Some of these formal limitations have thus turned out to be of relatively little importance in practice.

By proper choice of the N, α_j, and d_j in the contraction (3.7) the "contracted Gaussians" may be made to assume any functional form consistent with the primitive functions used. One may therefore choose the exponents of the primitives and the contraction coefficients so as to lead to basis functions with desired properties, such as reasonable cusp-like behavior at the nucleus (e.g. approximate Slater functions or HF atomic orbitals). Integrals involving such basis functions reduce to sums of integrals involving the Gaussian primitives. Even though many primitive integrals may need to be calculated for each basis function integral, the basis function integrals will be rapidly calculated provided the method of calculating primitive integrals is fast, and the number of orbital coefficients in the wavefunction will have been considerably reduced. The exponents and contraction coefficients are normally chosen on the basis of relatively cheap atomic SCF calculations so as to give basis functions suitable for describing exact Hartree-Fock atomic orbitals. An approximate atomic basis function, whose shape is suitable for physical and chemical reasons, is thus expanded in a set of primitive Gaussians, whose mathematical properties are attractive from a computational point of view. Note that the physical motivation for this procedure is that, while many primitive Gaussian functions may be required to provide an acceptable representation of an atomic orbital, the relative weights of many of these primitives are almost unchanged when the atoms are formed into molecules or crystals. The relative weights of the primitives can therefore be fixed from a previous calculation and only the overall scale factor for this contracted Gaussian function need be determined in the extended calculation. It is clear that contraction will in general significantly reduce the number of basis functions.

For molecular basis sets of Gaussian-type functions (GTF) general acronyms and notations are used that are well known in molecular quantum chemistry.

A Minimal-basis sets are constructed by using one Slater-type orbital basis function of each type occupied in the separated atoms that comprise a molecule. If at least one p-type, d-type or f-type orbital is occupied in the atom, then the complete set (3 p-type, 5 d-type, 7 f-type) of functions must be included in the basis set. The simplest of these basis sets is that designated *STO*-3*G*, an acronym for *Slater-type-orbitals* simulated by 3 primitive Gaussians added together. The coefficients of the Gaussian functions are adjusted to give as good a fit as possible to the Slater orbitals.

Only one best fit to a given type of Slater orbital is possible for a given number of Gaussian functions. Hence, all STO-3G basis sets for any row of the periodic table are the same, except for the exponents of the Gaussian functions. The exponents are expressed as scale factors, the squares of which are used as multipliers of the

adjusted exponents in the original best-fit Gaussian functions. In this way, the ratios of exponents remain the same while the effective exponent of each orbital can be varied, [7]. The STO-3G basis set, and other minimal basis sets, usually do reasonably well at reproducing geometries of only simple organic molecules. The minimal basis sets do not allow alteration of the basis orbitals in response to a changing molecular environment and therefore make comparison between charged and uncharged species unreliable. Anisotropic environments are another problem for minimal basis sets [7].

Because the core electrons of an atom are less affected by the chemical environment than the valence electrons, the core electrons can be treated with a minimal basis set while the valence electrons are treated with a larger basis set. This is known as a *split-valence basis set*. In these bases, the AOs are split into two parts: an inner, compact orbital and an outer, more diffuse one. The coefficients of these two kinds of orbitals can be varied independently during construction of the MOs. Thus, the size of the AO can be varied between the limits set by the inner and outer functions. Basis sets that similarly split the core orbitals are called double zeta, DZ (implying two different exponents) or triple zeta, TZ (implying three different exponents). For example, the 3-21G notation of split valence basis set means that the core orbitals are represented by three Gaussians, whereas the inner and outer valence orbitals consist of two and one Gaussians, respectively. If we were to name bases consistently, of course, this one would be labeled STO-3-21G, but the STO is customarily omitted from all split-valence descriptors. Two other split-valence bases are the 6-31G and the 6-311G. Both have six Gaussian cores. The 6-311G is a triply split basis, with an inner orbital represented by three Gaussians, and middle and outer orbitals represented as single Gaussians. The triple split improves the description of the outer valence region.

Further improvement of the basis set is achieved including *polarization functions* in the basis set. For example, this is done by adding d-orbitals to the basis of all atoms having no d-electrons. For typical organic compounds these are not used in bond formation, as are the d-orbitals of transition metals. They are used to allow a shift of the center of an orbital away from the position of the nucleus. For example, a p-orbital on carbon can be polarized away from the nucleus by mixing into it a d-orbital of lower symmetry. One obvious place where this can improve results is in the modeling of small rings; compounds of second-row elements also are more accurately described by the inclusion of polarization. The presence of polarization functions is indicated in the Pople notation by appending an asterisk to the set designator. Thus, 3-21G* implies the previously described split valence basis with polarization added. Typically, six d-functions (x^2, y^2, z^2, xy, xz, and yz), equivalent to five d-orbitals and one s, are used (for computational convenience). Most programs can also use five real d-orbitals. An alternative description of this kind of basis is DZP: double zeta, polarization. A second asterisk, as in the 6-31G** basis set, implies the addition of a set of p-orbitals to each hydrogen to provide for their polarization. Again, an alternative notation exists: DZ2P(double zeta 2 polarization). An asterisk in parentheses signals that polarization functions are added only to second-row elements. Another alternative to the asterisk for specifying polarization functions is (d), placed after the G.

To provide more accurate descriptions of anions, or neutral molecules with unshared pairs, basis sets may be augmented with so-called *diffuse functions*. These are intended to improve the basis set at large distances from the nuclei, thus better describing the barely bound electrons of anions. Processes that involve changes in the number of unshared pairs, such as protonation, are better modeled if diffuse functions are included.

The augmentation takes the form of a single set of very diffuse (exponents from 0.1 to 0.01) *s* and *p* orbitals. The presence of diffuse functions is symbolized by the addition of a plus sign, +, to the basis set designator: 6-31+G. (Since these are *s*- and *p*-orbitals, the symbol goes before the G.)

Again, a second + implies diffuse functions added to hydrogens; however, little improvement in results is noted for this addition unless the system under investigation includes hydride ions.

All of the codes for molecular ab-initio calculations offer at least one set of diffuse functions. Still more extensive basis sets exist, and are described by more complicated notation.

Let us summarize the notations used for molecular GTO basis sets. Basis sets denoted by the general nomenclature N-M1G or N-M11G, where N and M are integers, are called Pople basis sets. The first, N-MlG, is a split-valence double-zeta basis set while the second, N-M11G is a split-valence triple-zeta basis set. The integers N and M in the basis set name give the number of Gaussian primitives used. For example, in the split-valence double-zeta basis set 6-31G for a carbon atom, the first number (N = 6) represents the number of Gaussian primitives used to construct the core orbital basis function (the 1*s* function). The second two numbers (M = 3 and 1) represent the valence orbitals, 2*s*, 2*s*′, 2*p*(3) and 2*p*′(3). The first number after the dash in the basis set name (3 in this case) indicates the number of Gaussian primitives used to construct the 2*s* and 2*p*(3) basis functions. The second number after the dash (1 in this case) gives the number of Gaussian primitives used to construct the 2*s*′ and 2*p*′(3) basis functions. There are two common methods for designating that polarization functions are included in a basis set. The first method is to use * or ** after the Pople basis set name; for example, 6-31G* or 6-31G**. The single * means that one set of *d*-type polarization functions is added to each nonhydrogen atom in the molecule. The double ** means that one set of *d*-type polarization functions is added to nonhydrogens and one set of *p*-type polarization functions is added to hydrogens. The second method for including polarization functions in the basis-set designation is more general. It is indicated by the notation (ll,l2) following the Pople basis-set name; for example, 6-31G(*d*) or 6-31G(*d*, *p*). The first label indicates the polarization functions added to nonhydrogen atoms in the molecule. The notations 6-31G(*d*) and 631G(*d*, *p*) mean that one set of *d*-type polarization functions is added to all nonhydrogens. The notation 6-31 l(2*df*) means that two sets of *d*-type and one set of *f*-type polarization functions are added to nonhydrogens. The second label in the notation (ll,l2) indicates the polarization functions added to hydrogen atoms. The basis set 6-31G(*d*) has no polarization functions added to hydrogen, while the basis 6-31G(*d*, *p*) has one set of *p*-type polarization functions added to hydrogen atoms. The basis set 6-31 1G(2*df*, 2*pd*) has two sets of *p*-type and one set of *d*-type

polarization functions added to hydrogen atoms. The use of diffuse functions in a Pople basis set is indicated by the notation + or ++. The + notation, as in 6-3l+G(*d*), means that one set of *sp*-type diffuse basis functions is added to nonhydrogen atoms (4 diffuse basis functions per atom). The ++ notation, as in 6-31++G(*d*), means that one set of *sp*-type diffuse functions is added to each nonhydrogen atom and one *s*-type diffuse function is added to hydrogen atoms.

In Table 3.1 we give a list of basis sets of orbitals that are commonly used in modern MO calculations. The H and C atomic orbitals that are included are listed. The first set contains "Gaussian-like orbitals". Outside of the STO-3G basis set, most Gaussian basis sets are "split-valence", which means that they use different numbers of Gaussian functions to describe core and valence atomic orbitals. Thus, a 6-31G basis set uses 6 Gaussians for the core orbitals, and two sets of Gassians for the valence orbitals, one with 3 Gaussians and another with one. Adding more Gaussians allows more flexibility in the basis set so as to give a better approximation of the true orbitals. Therefore, although some of the basis sets incorporate the same AOs, the larger ones provide a much better description of them. For each basis set, polarization (*), and diffuse functions (+) can also be added, which add flexibility into the basis set.

Alternate basis sets that are commonly used are the Dunning correlation-consistent polarized valence X zeta basis sets, denoted cc-pVXZ, see Table 3.2. Dunning pointed

Table 3.1 The basis sets and orbitals they include

Basis	AOs on C	AOs on H
STO-3G	1*s*, 2*s*, $2p_x$, $2p_y 2p_z$	1*s*
3-21G*	1*s*, 2*s*, 2*p*, 3*s*, 3*p*	1*s*, 2*s*
3-21+G*	1*s*, 2*s*, 2*p*, 3*s*, 3*p*, 4*s*, 4*p*	1*s*, 2*s*
6-31G	1*s*, 2*s*, 2*p*, 3*s*, 3*p*	1*s*, 2*s*
6-31G*	1*s*, 2*s*, 2*p*, 3*s*, 3*p*, 3*d*	1*s*, 2*s*
6-31G**	1*s*, 2*s*, 2*p*, 3*s*, 3*p*, 3*d*	1*s*, 2*s*, 2*p*
6-31+G*	1*s*, 2*s*, 2*p*, 3*s*, 3*p*, 3*d*, 4*s*, 4*p*	1*s*, 2*s*
6-311G*	1*s*, 2*s*, 2*p*, 3*s*, 3*p*, 3*d*, 4*s*, 4*p*	1*s*, 2*s*, 3*s*
6-11++G(2*df*, 2*pd*)	1*s*, 2*s*, 2*p*, 3*s*, 3*p*, 3*d*, 4*s*, 4*p*, 4*d*, 4*f*	1*s*, 2*s*, 2*p*, 3*s*, 3*p*, 3*d*, 4*s*

Table 3.2 Correlation-consistent polarized valence X zeta (XZ) basis sets

Basis	AOs on C	AOs on H
cc-pVDZ	1*s*, 2*s*, 2*p*, 3*s*, 3*p*, 3*d*	1*s*, 2*s*, 2*p*
cc-pVTZ	1*s*, 2*s*, 2*p*, 3*s*, 3*p*, 3*d*, 4*s*, 4*p*, 4*d*, 4*f*	1*s*, 2*s*, 2*p*, 3*s*, 3*p*, 3*d*
cc-pVQZ	1*s*, 2*s*, 2*p*, 3*s*, 3*p*, 3*d*, 4*s*, 4*p*, 4*d*, 4*f*, 5*s*, 5*p*, 5*d*, 5*f*, 5*g*	1*s*, 2*s*, 2*p*, 3*s*, 3*p*, 3*d*, 4*s*, 4*p*, 4*d*, 4*f*
cc-pV6Z	Total of 7*s*, 6*p*, 5*d*, 4*f*, 3*g*, 2*h*, *i*	

out that basis sets optimized at the Hartree-Fock level might not be ideal for correlated computations [15]. The "correlation consistent" basis sets are optimized using correlated wavefunctions and cc-pVXZ means a Dunning correlation-consistent, polarized valence, X-zeta basis; X = D,T,Q,5,6,7. In particular, the cc-pVDZ for C atom consists of $3s2p1d$, cc-pVTZ would be $4s3p2d1f$, cc-pVQZ would be $5s4p3d2f1g$. The advantage of these is that increasing basis-set size is systematic. In fact, if energies are calculated with the cc-pVDZ, cc-pVTZ and cc-pVQZ basis sets, then there is an analytical function that can be used to extrapolate to cc-pVmZ (the complete basis-set limit). Unfortunately, cc-pVQZ calculations are not commonly made. Moreover, cc-VXZ functions are more difficult to integrate than the Gaussian functions and these calculations take longer even for comparably sized basis sets. Dunning basis sets already contain polarization functions, but they can be augmented with diffuse functions.

The EMSL (the environmental molecular sciences laboratory) [16] library supplies a wide selection of atomic basis sets optimized for molecules. This library allows the extraction of Gaussian basis sets, and any related effective core potentials (the effective core potentials are considered in the next sections), from the Molecular Science Research Center's Basis Set Library. A user may request the basis set be formatted appropriately for a wide variety of popular molecular electronic-structure packages. In addition to the exponents and contraction coefficients that define the basis set, the user can obtain descriptive data that include the overall philosophy behind the basis literature citations, the angular momentum composition of the basis and many other pieces of information.

3.1.2 Gaussian Basis Sets for Solid State Calculations

Molecular AO basis sets can formally be used in periodic LCAO calculations but their adequacy must be carefully checked.

In the periodic systems the basis sets are chosen in such a way that they satisfy the Bloch theorem. Let a finite number m_A of contracted GTFs be attributed to the atom A with coordinate $\boldsymbol{r}_A$ in the reference unit cell. The same GTFs are then formally associated with all translationally equivalent atoms in the crystal occupying positions $\boldsymbol{r}_A + \boldsymbol{a}_n$ ($\boldsymbol{a}_n$ is the direct lattice translation vector). For the crystal main region of N primitive unit cells there are $N \sum_A m_A$ Gaussian-type Bloch functions (GTBF) constructed according to

$$\chi_{\boldsymbol{k}i}(\boldsymbol{r}) = \frac{1}{\sqrt{N}} \sum_{\boldsymbol{a}_n} \exp(\mathrm{i}\boldsymbol{k}\boldsymbol{a}_n)\chi_i(\boldsymbol{r} - \boldsymbol{r}_A - \boldsymbol{a}_n) \tag{3.8}$$

The total number M of GTBFs equals $M = \sum_A m_A$, where the summation is made over the atoms of the reference cell. Thus, in solids the basis-set functions are modulated over the infinite lattice: any attempt to use large uncontracted molecular or

atomic basis sets, with very diffuse functions can result in the wasting of computational resources [17]. Therefore exponents and contraction coefficients in the molecular and periodic systems are generally rather different, and with some exceptions, such as molecular crystals and certain covalent solids, molecular basis sets are not directly transferable to the study of crystalline solids.

As in the case of molecules, basis functions in solids are grouped into shells. In general, a shell contains all functions characterized by the same n and l quantum numbers (e.g. all the different d-functions in a $3d$ shell); this allows the partitioning of the total charge density into "shell charge distributions" and is useful in the selection of bielectronic integrals and in the evaluation of long-range interactions. A feature of the contraction schemes originally used in the basis sets of the Pople type (and often useful in calculations with the CRYSTAL code [17]) is the additional grouping into shells of basis functions with only the same principle quantum number; e.g. a $2sp$ shell, in which both $2s$ and $2p$ functions have the same set of exponents α_j but different contraction coefficients d_j. This procedure reduces the number of auxiliary functions to be calculated in the evaluation of electron integrals. Note that if the basis set is restricted to the s, p and d basis functions, only sp shells can be formed in this way. In certain circumstances it may actually represent an important constraint on the form of the basis functions. For relatively small calculations where the time and storage limitations are not an important factor, some consideration should be given to describing the s and p functions with separate sets of exponents. Most standard molecular codes use what is known as a segmented contraction scheme, in which the transformation from the larger primitive set to the smaller contracted set is restricted in such a way that each Gaussian primitive $g_j(\boldsymbol{r})$ contributes to exactly one contracted GTF. In contrast, the general contraction scheme makes no such assumptions, and allows each Gaussian primitive to contribute to several contracted GTFs. A considerable advantage of the general scheme is that the contracted GTFs reproduce exactly the desired combinations of primitive functions. For example, if an atomic SCF calculation is used to define the contraction coefficients in a general contraction, the resulting minimal basis will reproduce the SCF energy obtained in the primitive basis. This is not the case with segmented contractions. There are other advantages of the general contraction: for example, it is possible to contract inner-shell orbitals to single functions with no error in the atomic energy, making calculations on heavy elements much easier. Another advantage is a conceptual one: using a general contraction, it is possible to perform calculations in which the one-particle space is a set of atomic orbitals, a true LCAO scheme, rather than being a segmented grouping of a somewhat arbitrary expansion basis. The MOs or COs can then be analyzed very simply, just as with the original qualitative MO LCAO or CO LCAO approach, but in terms of "exact AOs" rather than relatively crude approximations to them.

The computational aspects of GTFs use in the calculations of solids are discussed in [7]. The important reason for the usefulness of a Gaussian basis set is embodied in the Gaussian product theorem (GPT), which in its simplest form states that the product of two primitive Gaussian functions with exponents α and β, located at the centers $\boldsymbol{A}$ and $\boldsymbol{B}$, is itself a primitive Gaussian with exponent $\gamma = \alpha + \beta$, multiplied

by a constant factor F, located at a point $\boldsymbol{C}$ along the line segment $\boldsymbol{A} - \boldsymbol{B}$, where $\boldsymbol{C} = \frac{\alpha \boldsymbol{A} + \beta \boldsymbol{B}}{\gamma}$ and $F = \exp\left(-\frac{\alpha\beta}{\gamma}(\boldsymbol{A} - \boldsymbol{B})^2\right)$.

The product of two polynomial GTF, of degree μ and ν and located at the points $\boldsymbol{A}$ and $\boldsymbol{B}$ is therefore another polynomial GTF located at $\boldsymbol{C}$ of degree $\mu + \nu$ in x_C, y_C and z_C, which can be expressed as a short expansion of one-center Gaussians:

$$\chi_{Ax}(x)\chi_{Bx}(x) = \sum_{i=0}^{\mu+\nu} C_i^{\mu+\nu} \varphi_{Ci}(x - x_C) \tag{3.9}$$

where $\varphi_{Ci}(x) = x^i \exp(-\alpha_p(x - x_c)^2)$ and $x_c = \frac{\alpha x_A + \beta x_B}{\alpha + \beta}$.

The product of two Gaussians that are functions of the coordinates of the same electron is referred to as an overlap distribution, and all the integrals that must be calculated involve at least one such overlap distribution. The most important consequence of the GPT is that all four-center two-electron integrals can be expressed in terms of two-center quantities. Even though the four-center bielectronic integrals can be written in terms of two-center quantities, the cost of evaluating them still scales nominally as N^4, where N is the number of functions in the expansion. This scaling must be reduced in order to treat large systems. One way of doing this that is used in the CRYSTAL code is the method of *prescreening*, where, rather than attempting to calculate the integrals more efficiently, one seeks, where possible, to avoid their evaluation altogether. The expression for an integral over primitive Gaussians can be formally written as

$$(ab|cd) = S_{ab} S_{cd} T_{abcd} \tag{3.10}$$

where S_{ab} is a radial overlap between the functions χ_a and χ_b, and T_{abcd} is a slowly varying angular factor. In many situations the product $S_{ab}S_{cd}$ thus constitutes a good estimate of the magnitude of the integral whose product is used as an estimate in screening out small integrals. In order to estimate these overlaps quickly, a single, normalized s-type Gaussian called an adjoined Gaussian is associated with each shell, whose exponent α is the smallest of the exponents in the shell contraction. This function thus reproduces approximately the absolute value of the corresponding AOs at intermediate and long range. The adjoined Gaussian is used in fast algorithms for estimating overlaps on the basis of which integrals are either evaluated exactly, approximately, or not at all. The level of approximation is user-definable through a set of tolerances given in the input. Such algorithms, and a consideration of the crystalline symmetry, mean that the integrals part of the CRYSTAL code scales at between N and N^2, depending on the size of the system. The most unpleasant scaling in this code is thus the SCF part that, since it involves the diagonalization of the Fock matrix, scales as approximately N^3.

The role of diffuse basis-set functions requires a special consideration in crystalline systems. Very diffuse functions can yield numerical instabilities and involve a risk of linear-dependent catastrophes [7]. Furthermore, due to the truncation criteria of the infinite sums, based on the overlap, when the exponents of the primitive

Gaussians decrease, the number of integrals to be calculated increases very rapidly. Too extended basis sets are not needed in periodic calculations because the complete basis-set limit is reached quicker than in molecular calculations. Furthermore, the risk of linear dependence problems increases. The choice of the AO basis set is a compromise between accuracy and costs. As accuracy must be the main goal of ab-initio calculations, good-quality basis sets should always be used in spite of their computational cost to avoid producing meaningless numbers.

The choice of the basis set (BS) is one of the critical points, due to the large variety of chemical bonding that can be found in a periodic system. For example, carbon can be involved in covalent bonds (polyacetylene, diamond) as well as in strongly ionic situations (Be_2C, where the Mulliken charge of carbon is close to -4). Some general principles of the basis-set choice for periodic systems are formulated [7, 17] and we briefly reproduce them here. The great deal of experience gained in the molecular computational chemistry can be used in the selection of basis sets for studies of crystalline solids. However, molecular quantum chemists do not, in general, optimize basis sets by varying the exponents or contraction coefficients to minimize the energy. Rather, there is a hierarchy of basis sets with perceived qualities, and for a difficult problem where accuracy is important, one would use a "good-quality" standard basis set from a library without modification. In crystalline systems, by contrast, basis-set optimization is usually necessary, essentially for two reasons. First, there is a much larger variety of binding than in molecules, and basis sets are thus less transferable. Secondly, hierarchical libraries of basis sets comparable to those available for molecules do not really exist for solids. For certain types of compounds, such as molecular crystals or many covalent materials, the molecular sets can sometimes be used largely unmodified, but this has to be done carefully. However, for strongly ionic crystals and metals the basis sets, particularly the valence states, need to be redefined completely. In essentially all cases, the core states may be described using the solutions of atomic calculations, as even in the presence of strong crystal fields the core states are barely perturbed and may be described by the linear variation parameters in the SCF calculation.

Redefining basis sets in this way is obviously time consuming and even more obviously rather boring, and so over the recent years various workers involved with the CRYSTAL code have contributed to the effort to develop libraries of basis sets to be made available on the Internet. The URL of the official site is: http://www.crystal.unito.it/basis-sets.php. We recommend the reader to use the information given on this site. The site shows a periodic table. Clicking on the symbol for the required element will reveal a text file containing various different basis sets that may have been used in different materials containing that element type. Accompanying each basis set is a list of authors, a list of materials where the set has been used, references to publications and hints on optimization where relevant. This table is obviously not complete (in particular, lanthanides and actinides are practically absent as the calculations with f-electrons are not included even in the CRYSTAL06 code). Additional information can be found on the site of the Cambridge basis set library: http://www.tcm.phy.cam.ac.uk/.

We follow [7] the discussion of optimization strategies for the basis sets given in the libraries mentioned and also the adaptation of molecular bases for various types of solids. First, a number of general principles are given that should be taken into account when choosing a basis set for a periodic system.

The *diffuse basis functions* are used in atoms and molecules to describe the tails of the wavefunction, which are poorly described by the long-range decay of the Gaussian function. In periodic systems the cost of HF/DFT calculations can more essentially increase when the diffuse basis functions are included (in the silicon and diamond crystals, for example, the number of bielectronic integrals can be increased by a factor of 10 simply by changing the exponent of the most diffuse single Gaussian from 0.168 to 0.078 (Si) and from 0.296 to 0.176 (C), [7]. Fortunately, in crystalline compounds in contrast to molecules, especially in nonmetallic systems, the large overlap between neighbors in all directions drastically reduces the contribution of low-exponent Gaussians to the wavefunction. This has the consequence that a small "split-valence" basis set such as 6-21G is closer to the Hartree-Fock limit in crystals than in molecules.

The *number of primitives* is an important feature of the basis set. A typical basis set for all electron calculations includes "core functions" with higher exponents and a relatively large number of primitives—these will have a large weight in the expansion of the core states. The "valence functions" with a large weight in the outer orbitals will have lower exponents and contractions of only a very few primitives. It is possible to get away with putting a lot of primitives in the core since core states have very little overlap with the neighboring atoms. The use of many primitives in the valence shells would add significantly to the cost of the calculation, but in many cases it is necessary.

There are several ways to improve a basis set [7]: (1) reoptimize the more diffuse exponents (and contraction coefficients if necessary); (2) decontract, i.e. convert the more diffuse contractions into single Gaussian primitives; (3) convert *sp* functions into separate s and p functions; (4) add polarization functions if not already present; (5) add more primitives (watch out for linear dependence problems); (6) use a better starting point for the basis set. Optimization in this sense means varying an appropriate subset of the basis-set parameters until the energy is minimized. In principle, this is a reasonably complex multidimensional minimization, but there are various standard shell scripts available. Two of them can be downloaded from the Internet sites: BILLY code http://www.tcm.phy.cam.ac.uk/mdt26/downloads/billy.tar.gz) and LoptCG code (http://www.crystal.unito.it/LoptCG/LoptCG.html).

The adequacy of the starting molecular basis sets depends on the type of crystalline compound.

To describe *covalent crystals* the small molecular split-valence basis sets can be used with confidence and essentially without modification. It is enough to reoptimize the exponent of the most diffuse shell, which produces a slightly improved basis, while reducing the cost of the calculation. That said, 6-21G* is not really all that good and a larger better basis set with more variation freedom is quite easy to make for these cases (see web libraries).

For *fully-ionic* crystals (like alkali halides, LiH or MgO) with an almost completely empty cation valence shell it often proves convenient to use a basis set containing only "core" functions plus an additional sp shell with a relatively high exponent. It is usually difficult, and often impossible, to optimize the exponents of functions that only have appreciable weight in almost empty orbitals. Anions present a different problem. Reference to isolated ion solutions is possible only for halides, because in such cases the ions are stable even at the Hartree-Fock level. For other anions, which are stabilized by the crystalline field, the basis set must be redesigned with reference to the crystalline environment. Consider, for example, the optimization of the oxygen basis set in Li_2O [7]. The difficulty is to allow the valence distribution to relax in the presence of two more electrons. We can begin from a standard STO-6G basis set, i.e. six contracted primitive Gaussians for the 1*s* shell, and six more to describe the 2*sp* shell. First, two more Gaussians were introduced into the 1*s* contraction, in order to improve the virial coefficient and total energy. The two outer Gaussians of the valence *sp* shell were then removed from the contraction and allowed to vary independently. The exponents of the two outer independent Gaussians and the coefficients of the four contracted ones were optimized in Li_2O. The best outer exponents of the ion were found to be 0.45 and 0.15, and are therefore considerably more diffuse than the neutral isolated atom, where the best exponents are 0.54 and 0.24. The rest of the oxygen valence shell is unchanged with respect to the atomic situation. The introduction of *d* functions in the oxygen basis set gives only a minor improvement in the energy, with a population of 0.02 electrons/atom/cell (*d* functions may be important in the calculation of certain properties, however). Thus, for anions, reoptimization of the most diffuse valence shells is mandatory when starting from a standard basis set.

The majority of crystals can be classified as *semi-ionic* (with chemical bonding being intermediate between covalent and purely ionic limits). For such crystals the adequacy of selected basis sets must be carefully tested as, is discussed in [7], for example, for semi-ionic compounds SiO_2 (quartz) and Al_2O_3 (corundum). The exponents of the outer shell for the two cations (Si and Al) used in molecular calculations prove to be too diffuse. For the Si atom in quartz, reoptimization in the bulk gives $\alpha = 0.15$ (instead of the molecular value 0.09). Corundum is more ionic than quartz, and in this case it is better to eliminate the most diffuse valence shell of Al, and to use two Gaussians of the inner valence shells as independent functions ($\alpha = 0.94$ and $\alpha = 0.3$, respectively).

For *metals* very diffuse Gaussians are required to reproduce the nearly uniform density so that has often been argued that plane waves are a more appropriate basis for these systems. It is generally impossible to optimize an atomic-like basis set in the Hartree-Fock calculations of metallic systems. However, Gaussian DFT studies indicate that GTFs are able to provide a reliable and efficient description of simple metallic systems (see, for example, metallic lithium calculations [18]). Thus, the effects of the basis set and Hamiltonian were separated.

UHF and hybrid DFT calculations (see Sects. 3.2 and 3.3) for strongly correlated *transition-element magnetic compounds* require reasonably good basis sets for the transition elements. These are not so widely available even to molecular quantum chemists since most of the effort in developing molecular GTF basis sets has been for

the first- and second-row atoms. One reason for this may be that molecules containing transition metal atoms tend to be very badly described at the Hartree-Fock level. Molecular bonds tend to have a fairly high degree of "covalency" and the existence of partially-occupied *d* states leads to a great many nearly degenerate levels, and thus to a large "static correlation" (i.e. the weight of the HF determinant in a CI expansion would be small, and a multideterminant treatment is more appropriate). Basis sets to describe the correlation using quantum chemistry correlated wavefunction techniques need to be much richer than those for systems well described at the HF level since they need to treat all of the unoccupied levels. It may seem surprising that single-determinant HF could be so successful in periodic crystalline magnetic insulators containing transition elements, but this is an important characteristic of these ionic materials. The highly symmetric environment and long-range Coulomb forces tend to separate the orbitals into well-defined subsets with a significant gap between the occupied and unoccupied states. Hence, the ground state of NiO (for example) is rather well described by a single determinant. In this sense, a strongly correlated magnetic insulator is in many ways a "simpler system" than many molecules. The success of UHF calculations in these materials (and also hybrid DFT schemes) is now well known.

Molecular GTF basis sets for transition elements have been reoptimized in the solid state and are available on the Torino and Cambridge Gaussian basis set library web sites referred to earlier.

There exist a number of different algorithms for the minimization of the many variables function, [19]. The comparative study of their efficiency for the basis set optimization in crystals was recently performed in [20]. As an example of LCAO basis set optimization in TiO_2 (anatase) calculations we mention here publication [21]. To optimize the BS, the minimization method without calculations on the total energy derivatives developed by Powell [22] and often called "the method of conjugate directions" was used. It believed to be one of the most efficient direct minimization methods. Interfaced with the CRYSTAL09 LCAO computational code [17] the program package OPTBAS [20] was applied for the BS optimization. BS exponential parameters less than 0.1 were excluded from the AOs and a bound-constrained optimization was performed for the remaining exponential parameters with a 0.1 lower bound. The diffuse exponents of valence s, p and d-orbitals were optimized for the stable anatase phase of bulk titania. Its atomic and electronic properties were reproduced in good agreement with the experiment (the experimental values are given in brackets): the lattice parameters a = 3.784 (3.782) and c = 9.508 (9.502), the dimensionless parameter for the relative position of the oxygen atom u = 0.2074 (0.2080), although the values of the bandgap are reproduced worse, being overestimated: 4.0 versus 3.2 eV. In any case, these results for the bulk titania (anatase) agree with the experimental data better than those given in [23] for both plane wave (PW) and LCAO calculations when one uses different exchange-correlation potentials.

In the final part of this section we shall discuss a rather serious problem, associated with Gaussian basis sets—the basis-set superposition error (BSSE). A common response to this problem is to ignore it, since it will go away in the limit of a complete basis but to achieve this limit one needs calculations that are seldom performed. The

problem of BSSE is a simple one: in a system comprising interacting fragments A and B, the fact that in practice the basis sets on A and B are incomplete means that the fragment energy of A will necessarily be improved by the basis functions on B, irrespective of whether there is any genuine binding interaction in the compound system or not. The improvement in the fragment energies will lower the energy of the combined system, giving a spurious increase in the binding energy. It is often stated that BSSE is an effect that one needs to worry about only in calculations on very weakly interacting systems. This is not really true [7]. BSSE is an ever-present phenomenon and accurate calculations should always include an investigation of BSSE. Examples of areas in which one should be particularly worried are the study of the binding energy of molecules adsorbed on surfaces (see, for example [24] for an interesting discussion) or the calculation of defect-formation energies.

The approach most commonly taken to estimate the effect of BSSE is the counterpoise correction of Boys [25]: the separated fragment energies are computed not in the individual fragment basis sets, but in the total basis set for the system including "ghost functions" for the fragment that is not present. These energies are then used to define the counterpoise-corrected (CPC) interaction energy, which by comparison with the perturbation theory, was shown to converge to the BSSE-free correct value [26].

Linear dependencies of Gaussian-type orbital basis sets employed in the framework of the HF SCF method for periodic structures, which occur when diffuse basis functions are included in the basis set in an uncontrolled manner, were investigated [27]. The basis sets constructed avoid numerical linear dependences, and were optimized for a number of periodic structures. The numerical AO basis sets for solids were generated in [28] by confining atoms within spheres and smoothing the orbitals so that the first and second derivatives go to zero at the boundary. This gives rise to small atomic-like basis sets that can be applied to solid-state problems and are efficient for treating large systems.

The concept of balanced Gaussian basis sets for periodic density functional theory calculations was analyzed in [29] for diamond and silicon bulk crystals using energy-optimized Gaussian basis sets and compared to the corresponding molecular cases. Benchmark calculations [29] show that explicitly optimized condensed phase basis sets have a slower basis set convergence than atomic optimized ones.

The first attempt to develop a consistent standard all-electron Gaussian basis set of a defined quality for H–Br elements for periodic calculations was made in [30]. The def-2 -TZVP (VTZ* in the former subsection) molecular basis sets [31, 32] were chosen as a starting point. These basis sets consist of highly contracted Gaussians for core shells and three less contracted or primitive Gaussians per valence shell. For every valence shell, there is at least one primitive or even contracted polarization function of higher angular momentum. Gaussian functions with orbital exponents smaller than 0.1 were removed. Pob-TZVP basis sets ("pob" means portable) inherit highly contracted core-shell Gaussians and three (contracted or primitive) basis functions per valence shell of the def2-TZVP molecular basis sets, but only one (instead of two) primitive polarization function of higher angular momentum is added as polarization for the complete shell. This scheme results in smaller numbers of contracted

and primitive Gaussians than in the original def2-TZVP basis. The orbital exponents and contraction coefficients of the valence shells were variationally optimized for selected solids using the hybrid DFT functional: the correlation functional is PW91, [33] whereas the exchange functional is a mixture of 80 % of PW91 exchange and 20 % of Hartree-Fock exchange, see Sect. 3.3 for hybrid exchange-correlation functionals description. This functional was shown to provide good agreement with the experiment for lattice parameters and cohesive energies [34–36].

The final basis sets obtained, denoted as pob-TZVP, are not fully variational for all reference systems. The final values of orbital exponents and contraction coefficients depend on the selected systems and on the DFT method that was used. However, as the changes necessary in the adjustments were relatively small, these basis sets are portable to other systems (pob-TZVP basis sets are given on the CRYSTAL code site http://www.crystal.unito.it). These basis sets were tested in [30] and the results obtained were compared with standard basis sets taken from the CRYSTAL code basis set database. The lattice constants and atomic positions were optimized using the hybrid exchange-correlation functional defined above. Figures 3.1, 3.2 and 3.3 give the relative error in the lattice constants for ionic compounds, semiconductors and transition metal oxides, respectively.

It is seen that the maximum and mean errors in the lattice constants obtained with pob-TZVP basis sets are less than those obtained with the standard basis sets. The pob-TZVP basis sets were also used in [30] for cubic metals. Although most of the optimization runs failed or gave bad results with the CRYSTAL standard basis sets, the pob-TZVP basis sets gave satisfactory results without further modifications, showing the portability of these basis sets. The results can be easily improved by adding diffuse valence functions with very small orbital exponents.

We considered the basis sets for all-electron calculations in which all the core electrons are involved explicitly. Both in molecular and solid-state quantum chemistry core states can be treated implicitly as creating an effective core potential (pseudopotential). The pseudopotential approximation becomes the most efficient for the crystalline compounds of heavy elements. Simultaneously, an important role is played by the relativistic effects on the electronic structure. In the next subsection we consider nonrelativistic and relativistic pseudopotentials used in the modern LCAO calculations of periodic systems. The choice of the corresponding valence basis sets is also discussed.

3.1.3 Effective Core Potentials

It is well known that most of the chemical properties of molecules and solids are determined by the valence electrons of the constituent atoms. The core states are weakly affected by changes in chemical bonding. The effect of core electrons is principally to shield the nuclear charges and to provide an effective potential for the valence electrons. The main reason for the limited role of the core electrons is the

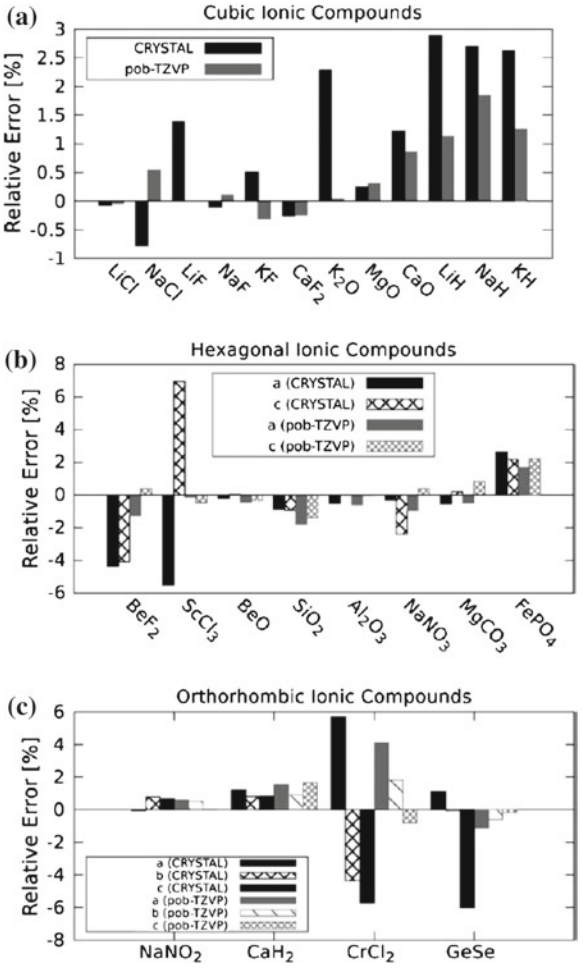

Fig. 3.1 Relative error in the lattice constants of ionic compounds with respect to experimental values: **a** cubic; **b** hexagonal; **c** orthorhombic [30]

spatial separation of the core and valence shells that originates from the comparatively strong binding of the core electrons to the nucleus.

The idea behind effective core potentials (ECPs), also called pseudopotentials (PP), is to treat the core electrons as creating effective averaged potentials rather than actual particles. Effective core potentials are based on the frozen-core approximation and serve to represent the potential generated by the core electrons, also incorporating relativistic effects. ECP application can introduce significant computational efficiencies as it allows the formulation of a theoretical method for dealing only with the valence electrons, while retaining the accuracy of all-electron methods.

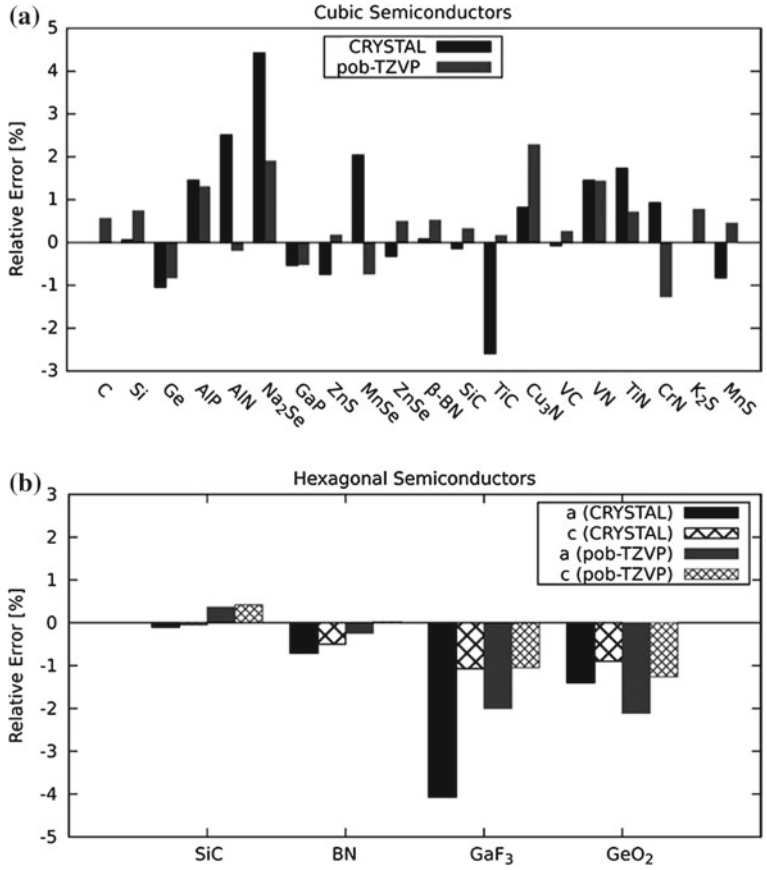

Fig. 3.2 Relative error in the lattice constants of semiconducting compounds with respect to experimental values: **a** cubic; **b** hexagonal [30]

As we already noted, pseudopotentials are essentially mandatory in plane-wave calculations of solids since the core orbitals have very sharp features in the region close to the nucleus and too many plane waves would be required to expand them if they were included. In atomic-like basis-set calculations pseudopotentials are formally not mandatory and have different characteristics from those designed for plane waves since localized basis functions actually have necessary sharp features in the core region. Nevertheless, ECP methods are also used in the LCAO calculations of molecules and solids since the difficulty of the standard LCAO methods rises rapidly with the number of electrons. If the CPU time in LCAO calculations were dominated by integrals calculation, PP introduction would not give very much since the number of integrals is controlled by more diffuse functions that overlap strongly with the neighboring atoms. These diffuse functions are introduced mainly to describe the change of atomic valence states. However, the use of ECP will decrease the

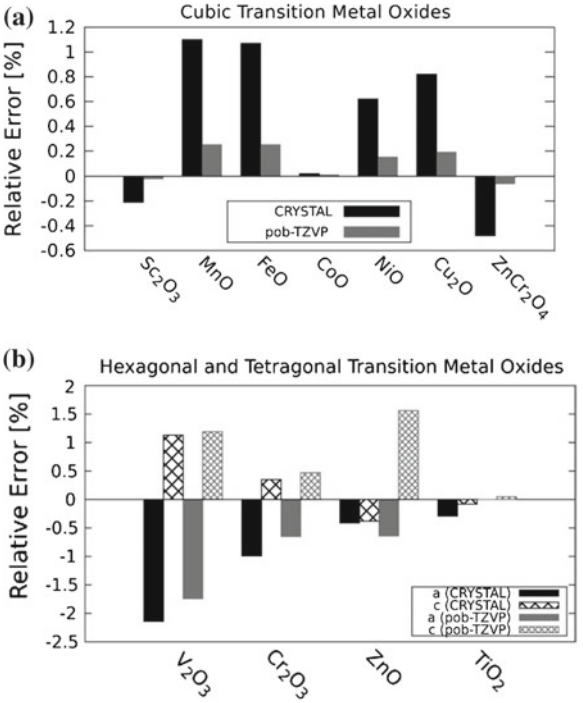

Fig. 3.3 Relative error in the lattice constants of transition metal oxides with respect to experimental values: **a** cubic; **b** hexagonal and tetragonal, [30]

number of coefficients in the one-electron wavefunctions and might give significant savings in the SCF part. It is also quite easy to incorporate relativistic effects into pseudopotentials, which is increasingly important for heavy atoms. All electron relativistic calculations are very expensive and in many cases are practically difficult.

The parameters and the underlying basis set of so-called energy-consistent ECPs can be adjusted in accordance with representative experimental data, not only for the ground state, but also for excited states, electron affinities, ionization potentials and so on. Being of semiempirical origin, they can perform remarkably well for a given system, but their transferability to other environments can be poorer than that of shape-consistent ECPs. So-called shape-consistent ECPs (known in computational condensed matter as the norm conserving ECPs) are rather easy to derive and contain no adjustable parameters, i.e. these are ab-initio ECPs. The construction of shape-consistent ECPs for molecules is based on the original proposal of Christiansen et al. [37], where shape consistency was introduced. Simultaneously, norm conserving ECPs were introduced in computational condensed-matter physics by Hamann et al. [38]. This example demonstrates practically independent development of ECPs for molecules and crystals as different terms are used for the same ECP property.

The work by Phillips and Kleinman (PK) [39] is an important step in ECP applications to solids. PK developed the pseudopotential formalism as a rigorous formulation of the earlier "empirical potential" approach. They showed that ECP that has plane-wave pseudo wavefunctions as its eigenstates could be derived from the all-electron potential and the core-state wavefunctions and energies. Thus a nonempirical approach to finding ECP was introduced.

The PK pseudopotential shortcomings are well known [40]: it depends explicitly on the one-electron eigenvalue and outside the core region the normalized pseudo orbital (PO) is proportional but not equal to the true orbital. Typically, generation of a pseudopotential proceeds as follows. First, a cutoff distance r_c for the core is chosen. In a PP approach all radial $R_{nl}(r)$ orbitals of the valence shell must be nodeless, as for each l all lower-lying states have to be projected out by the PP. In the case of oxygen, for instance, the $2s$-PO must be nodeless. It is, however, impossible to produce two (or more) nodeless orbitals in the same energy range with only a single spherical PP, as for fixed PP only the angular momentum term can generate differences.

Since PP replaces the potential of the nucleus and the core electrons, it is spherically symmetric and each angular momentum l can be treated separately, which leads to nonlocal l-dependent PP $V_l(r)$. Consequently, the total atomic PP usually consists of several components, one for each angular momentum present in the valence space. The PP dependence upon l means that, in general, PP is a nonlocal operator, that can be written in a semilocal (SL) form

$$\hat{V}^{PS} = \sum_{lm} |Y_{lm}(\theta, \varphi)\rangle V_l(r) \langle Y^*_{lm}(\theta, \varphi)| \tag{3.11}$$

where $Y_{lm}(\theta, \varphi)$ are spherical harmonics and $V_l(r)$ is the pseudopotential for the lth angular-momentum component. This is termed semilocal because it is nonlocal in the angular variables, but local in the radial variable: when operating on the function $f(r, \theta', \varphi')$, $\hat{V}^{PS}$ has the effect [2]

$$\left[\hat{V}^{PS} f\right]_{r,\theta,\varphi} = \sum_{lm} Y_{lm}(\theta, \varphi) V_l(r) \int d(\cos\theta') d\varphi' Y_{lm}(\theta', \varphi') f(r, \theta', \varphi') \tag{3.12}$$

All the PP information is in the radial functions $V_l(r)$. (We note that the HF exchange operator is fully nonlocal both in the angular and radial variables.) To generate PP an all-electron calculation (HF or DFT) of the free atom is performed. The DFT PP Hamiltonian includes the local (Hartree and exchange-correlation) and semilocal (PP) parts; the HF PP Hamiltonian includes local (Hartree), nonlocal (exchange) and semilocal (PP) parts. The set of PP parameters is chosen to accurately reproduce the eigenvalues and eigenfunctions of the valence states. Clearly, in the region of space where most of the electronic norm is concentrated, both orbitals must be very close, if not identical. On the other hand, the form of the valence orbitals in the core region, where the core electrons are moving, is less relevant. Otherwise, the core states themselves would play a more important role. In the core region one can thus

allow the pseudo-orbital (PO) to differ from the all-electron orbital (AO) without losing too much accuracy [41].

A giant step forward in pseudopotentials was taken by Hamann et al. [38], who introduced norm conserving pseudopotentials (NCPP). NCCP for the angular momentum l is chosen so that

(1) the resulting atomic valence PO agrees with the corresponding all-electron (AE) AO for all r larger than some l-dependent cutoff (core) radius

$$R_{nl}^{PS}(r) = R_{nl}^{AE}(r) \tag{3.13}$$

(2) the norm of the orbital is conserved,

$$\int_0^{r_{c,l}} |R_{nl}^{PS}(r)|^2 dr = \int_0^{r_{c,l}} |R_{nl}^{ae}(r)|^2 dr \tag{3.14}$$

(3) The logarithmic derivatives of the true and pseudowavefunctions and their first energy derivatives agree for $r > r_c$.

Condition 1 automatically implies that the real and pseudovalence eigenvalues agree for a chosen "prototype" configuration, as the eigenvalue determines the asymptotic decay of the orbitals.

Properties (2) and (3) are crucial for the pseudopotential to have optimum transferability among a variety of chemical environments [41].

The PP concept was motivated by the inertness of the atomic core states in binding so that the ionic core of the atom provides a fixed potential in which the valence electrons are moving, independently of the system (atom, molecule or solid) considered. However, in polyatomic systems the valence states undergo obvious modifications compared to the atomic valence orbitals, even if the polyatomic core potential is given by a simple linear superposition of atomic core potentials. Most notably, the eigenenergies change when atoms are packed together, which leads to bonding and antibonding states in molecules and to energy bands in solids. Thus, while PPs are designed to reproduce the valence AOs of some chosen atomic reference configuration (usually the ground state), it is not clear *a priori* that they will have the same property for all kinds of polyatomic systems and for other atomic configurations. Consequently, one has to make sure that the PP is *transferable* from its atomic reference state to the actually interesting environment. To check the transferability of PP one has to analyze the sensitivity of the agreement between atomic POs and AOs to the specific eigenenergy in the single-particle equation. One finds that the variation of the logarithmic derivative $R_{nl}^{PS}(r)/R_{nl}^{ae}(r)$ with the single-particle energy is determined by the norm contained in the sphere between the origin and r. This is true in particular in the neighborhood of one of the actual atomic eigenvalues ε_{nl}, i.e. for a bound atomic eigenstate. Thus, as soon as normconservation is ensured, the POs exactly reproduce the energy dependence of the logarithmic derivative of the AOs for $r > r_{c,l}$. Consequently, one expects the POs to react as the AOs when the

valence states experience some energy shift in a polyatomic environment—provided the underlying PPs are normconserving. This argument supporting the transferability of PPs emphasizes the importance of normconservation in a very explicit way. In practice, it is, nevertheless, always recommended to check the transferability explicitly examining some suitable atomic excitation process and the binding properties of simple molecular or crystalline systems [41].

The form of ECP used in the condensed-matter applications depends on the basis chosen—PW or LCAO. The numeric pseudopotentials in plane-wave calculations must be used with the density functional that was employed to generate them from the reference atomic state. This is a natural and logical choice whenever one of the plane-wave DFT codes is used. In PW calculations the valence functions are expanded in Fourier components, and the cost of the calculation scales as a power of the number of Fourier components needed in the calculation. One goal of PP is to create POs that are as smooth as possible and yet are accurate. In PW calculations maximizing smoothness is to minimize the range of Fourier space needed to describe the valence properties to a given accuracy [2]. Normconserving PPs achieve the goal of accuracy, usually at some sacrifice of smoothness. A different approach by Vanderbilt, known as "ultrasoft pseudopotentials" (US) [42] reaches the goal of accurate PW calculations by a transformation that re-expresses the problem in terms of the smooth function and the auxiliary function around each core that represent the rapidly varying part of the density. The generation code for Vanderbilt US pseudopotentials and their library can be found on site http://www.physics.rutgers.edu/dhv/uspp.

Ab-initio pseudopotentials for PW calculations of solids can be generated also by the fhiPP package [43], see also site http://www.fhi-berlin.mpg.de/th/fhimd/.

The numerical AO-based DFT code SIESTA [44] employs the same numeric pseudopotentials as plane-wave-based codes. An alternative approach is used in the Slater-orbital-based DFT code ADF [45], where so-called core functions are introduced. They represent the core-electron charge distribution, but are not variational degrees of freedom and serve as fixed core charges that generate the potential experienced by valence electrons [46].

In molecular quantum chemistry Gaussian-function-based computations, effective core potentials were originally derived from the reference calculation of a single atom within the nonrelativistic Hartree-Fock or relativistic Dirac–Fock approximations, or from some method including electron correlations (CI, for instance). A review of these methods, as well as the general theory of ECPs is provided in [47, 48].

Let us discuss the effective core potentials and the corresponding valence basis sets that are used for Gaussian-function-based LCAO periodic computations implemented in the computer codes CRYSTAL [17] and GAUSSIAN [49].

The ECP general form is a sum of the Coulomb term, the local term and the semilocal term

$$V_{PS}(r) = C + V_{loc} + V_{sl} = -\frac{Z_N}{r} + \sum_{k=1}^{M} r^{n_k} C_k \exp(-\alpha_k r^2) + \sum_{l=0}^{3} \left[\sum_{k=1}^{M_l} r^{n_{kl}-2} C_{kl} \exp(-\alpha_{kl} r^2) \right] \hat{P}_l \qquad (3.15)$$

where Z_N in the Coulomb term is the effective nuclear charge (total nuclear charge minus the number of electrons represented by ECP). The local term is a sum of products of polynomial and Gaussian radial functions. The semilocal term is a sum of products of polynomial radial functions, Gaussian radial functions and angular-momentum projection operators $\hat{P}_l$. Therefore, to specify the semilocal ECP one needs to include a collection of triplets (coefficient, power of r and exponent) for each term in each angular momentum of ECP.

Hay and Wadt (HW) ECP [50] are of the general form (3.15). The procedure employed for the generation of ECPs includes the following sequence of steps: (1) the "core" orbitals to be replaced and the remaining "valence" orbitals are defined. This step defines whether the small-core (the outermost core electrons are explicitly treated along with the valence electrons) or a large-core HW pseudopotential is generated; (2) the true numerical valence orbitals are obtained from self-consistent nonrelativistic Hartree-Fock (or relativistic Dirac–Fock) calculations for $l = 0, 1, \ldots, L$, where L, in general, is greater than the highest angular-momentum quantum number of any core orbital; (3) smooth, nodeless pseudo-orbitals (PO) are derived from the true Hartree-Fock (Dirac–Fock) orbitals so that PO behave as closely as possible to HF orbitals in the outer, valence region of the atom; (4) numerical effective core potentials V_l^{PS} are derived for each l by demanding that PO be a solution in the field of V_l with the same orbital energy ε as the Hartree-Fock (Dirac–Fock) orbital; (5) the numerical potentials are fit in the analytic form with Gaussian functions, the total potential is represented as (3.15); (6) the numerical POs are also fit with Gaussian functions to obtain basis sets for molecular or periodic calculations. In the case of large-core ECP the primitive Gaussian bases (3s2p5d), (3s3p4d) and (3s3p3d) are tabulated for the first, second, and third transition series atoms, respectively. The figures in brackets mean the number of primitive Gaussians in ns, np and $(n-1)d$ contracted AOs for $n = 4, 5, 6$. In the case of small-core ECP $(n-1)s$, $(n-1)p$ contracted AOs are added and given as the linear combinations of primitive Gaussians. Hay-Wadt ECPs and valence-electron basis sets are also generated for main-group elements: large core—for Na to Xe, and Cs to Bi, small core—for K, Ca, Rb, Sr, Cs, Ba.

The other known ECP and valence-electron basis sets were generated using the procedure described for Hay–Wadt ECP generation. The Durand–Barthelat large-core semilocal ECP [51] and the corresponding valence-electron basis sets are generated for 3d-transition elements and the main-group elements Li to Kr.

Compact one- and two-Gaussian expansions for the components of the effective potentials of atoms in the first two rows are presented by Stevens–Basch–Krauss [52]. Later, the list of ECP was extended to the third-, fourth- and fifth-row atoms [53] and includes relativistic ECP (RECP). The pseudo-orbital basis-set expansions

for the first two rows of atoms consist of four Gaussian primitives using a common set of exponents for the s and p functions. Analytic SBK RECP are generated in order to reproduce POs and eigenvalues as closely as possible. The semilocal SBK ECP are given by

$$r^2 V_l(r) = \sum_k A_{lk} r^{n_{l,k}} \exp(-B_{l,k} r^2) \tag{3.16}$$

The potentials and basis sets were used to calculate the equilibrium structures and spectroscopic properties of several molecules. The results compare extremely favorably with the corresponding all-electron calculations.

Stuttgart–Dresden (SD) ECP (formerly Stoll and Preuss ECP) are under constant development [54]. SD semilocal ECPs are written in the form

$$V_{sl} = \sum_{l=0}^{3} \left[\sum_{k=1}^{\mu_k} r^{n_{kl}-2} C_{kl} \exp(-\alpha_k r^2) \right] \hat{P}_l \tag{3.17}$$

Note the different convention for the factor $r^{n_{kl}-2}$ compared to (3.15). The database of SD ECP include relativistic ECP (RECP) generated by solving the relativistic Dirac–Fock equation for atoms. Improved SD pseudopotentials exist for many of the main-group elements, and the pseudopotentials are also available for 5d and other heavier elements. The most recent ECP parameters, optimized valence-electron basis sets, a list of references and guidelines for the choice of pseudopotentials can be found at site http://www.theochem.uni-stuttgart.de.

The use of atomic pseudopotentials (or effective core potentials–ECPs) considerably simplifies the quantum-mechanical description of polyatomic systems (molecules and crystals) as the much more localized and chemically inert core electrons are simulated by ECP introduction. The choice of the norm conserving and transferable ECPs ensures that the valence states are reproduced in the majority of cases as accurately as would be done in all-electron calculations.

Pseudopotentials are also used as embedding potentials when some special region of a covalently bonded solid or very large molecule is modeled by a modest-size cluster. This model is applied when one is interested in the electronic structure and properties of some small region of a large system such as a localized point defect in a solid, an adsorbed molecule on a solid surface or an active site in a very large biological molecule. In such a case one can model the region of interest by cutting a modest-sized but finite cluster out of a larger system and performing the calculation on it. For ionic solids the surrounding crystal can be modeled by the system of point charges. More difficult is the case when the environment is a covalently bonded system and the boundary between the cluster and the environment passes through chemical bonds (covalent or partly covalent). In this case, the distant and nearest parts of the environment should be treated separately [55]. In the distant part, only the electrostatic potential representing the ionic component of the environment should be retained. The nearest part, corresponding to the "broken or dangling bonds", needs special consideration. Each atom of the cluster boundary surface has unsaturated

"dangling bonds" that cause spurious effects unless saturated in some way, usually by adding hydrogen or pseudoatoms [56]. This is better than leaving the dangling bond but clearly the termination is still imperfect in the sense that the bond to the attached atom is different from the bond to whatever atom is situated there in the real system [57]. The use of the embedding potentials (EP) to saturate the dangling bonds of the cluster gives a cluster surface bond identical to that in the real large system.

Heavy-element systems are involved in many important chemical and physical phenomena. However, they still present difficulties to theoretical study, especially in the case of solids containing atoms of heavy elements (with the nuclear charge $Z \geq 50$). The description of the relativistic electronic-structure theory for molecular systems is given, for example, in [58] and in our earlier book [59]. For a long time the relativistic effects inherent in heavy atoms were not considered important for chemical properties because they appear primarily in the core atomic region. However, now the importance of these effects, which play an essential and vital role in the total nature of electronic structures for heavy-element molecular and periodic systems, is recognized [58].

While accurate relativistic calculations of simple heavy-atom molecules can be performed on modern computers, the relativistic calculations of periodic systems are mainly made using the relativistic effective core potential (RECP).

There are several reasons for using RECPs in calculations of complicated heavy-atom molecules, molecular clusters and periodic solids. Like nonrelativistic ECP approaches, RECP approaches allow one to exclude from calculations a large number of chemically inactive electrons and explicitly treat only valence and outermost core electrons. The oscillations of the valence spinors are usually smoothed in heavy-atom cores simultaneously with the exclusion of small components from explicit treatment (quasirelativistic approximation). As a result, the number of primitive basis functions can be essentially reduced; this is especially important for the calculation and transformation of two-electron integrals when studying many-atomic systems with very heavy elements including lanthanides and actinides. The RECP method is based on a well-developed earlier nonrelativistic technique of pseudopotential calculations; however, effective scalar-relativistic and spin-orbit interaction effects are taken into account by means of the RECP operator. In the RECP method, the interactions with the excluded inner core shells (spinors!) are described by spin-dependent potentials, whereas the explicitly treated valence and outer core shells can be described by spin-orbitals. This means that some "soft" way of accounting for the core-valence orthogonality constraints is applied in the latter case [60]. Meanwhile, the strict core-valence orthogonality can be retrieved after the RECP calculation by using the restoration procedures. The use of the spin-orbitals allows one to reduce dramatically the expenses at the stage of correlation calculation.

In LCAO calculations of heavy-atom molecules and periodic systems the relativistic "energy-consistent" pseudopotentials by the Stuttgart–Dresden–Cologne group are also actively used [54, 61]. To generate "energy-consistent" RECP, direct adjustment of two-component pseudopotentials is performed (scalar-relativistic + spin-orbit potentials) to atomic total energy valence spectra. The latter are derived from the

four-component multiconfiguration Dirac-Hartree-Fock all-electron atomic calculations. The "energy-consistent" RECPs are now tabulated for all the elements of the periodic table at the site http://www.theochem.uni-stuttgart.de. The adjustment of the pseudopotential parameters was done in fully numerical atomic calculations, valence basis sets were generated a posteriori via energy optimization. A complete set of potentials includes one-component (nonrelativistic and scalar-relativistic) effective-core potentials (ECP), spin-orbit (SO) and core-polarization potentials (CPP); only one-component ECPs are listed in full. The "energy-consistent"pseudopotentials are under continuous development and extension [61, 62] and the corresponding Gaussian basis sets are published [63–65].

In plane-wave calculations of solids and in molecular dynamics, separable pseudopotentials [66] are more popular now because they provide linear scaling of the computational effort with the basis-set size in contrast to the radially local RECPs. Contrary to the four-component wavefunction used in full relativistic calculations, the pseudowavefunction in the RECP case can be both two- and one-component. The RECP operator simulates, in particular, interactions of the explicitly treated electrons with those that are excluded from the RECP calculations.

The consideration of the relativistic effects in the compounds of heavy atoms is most easily carried out in scalar-relativistic (one-component) calculations with the use of the relativistic effective core potential (RECP). Following [67], we discuss a problem of practical importance, i.e. to what extent the application of the RECP of an uranium atom to scalar-relativistic calculations is useful in reproducing the dissociation energy and spectrum of one-electron energies found in the full-electron relativistic calculation by the DHF method. The validity of RECP method is studied in [67] using the UF_6 molecule. Uranium hexafluoride UF_6 became the subject of numerous experimental and theoretical studies owing to the fact that it is used in the enrichment of uranium with a molecular laser. The difficulties in the calculation of the electronic structure of this molecule are connected both with the necessity to take into account the relativistic effects and with the influence of electronic correlation effects in the case of the localized f-electrons of the uranium atom. The main results of the study [67] are the following.

According to the full-electron nonrelativistic calculation by the HF method, the dissociation energy of the UF_6 molecule is 13.7 eV, which reproduces only 43 % of the experimental value. If relativistic effects are taken into account this value increases to 23.5 eV (73 % of the experimental value), and the energies of MOs corresponding to the core states $1s$, $2s$, and $3s$ of the uranium atom are essentially reduced as compared to the HF calculation. At the same time, for MOs that are higher in energy (arising from the $6s$ and $6p$ states of the uranium atom) the reduction is noticeably less. For MOs containing the filled $3d$, $4d$, $5d$, and $4f$-orbitals of the uranium atom the one-electron energies increase as a consequence of the increasing screening of the nucleus by the inner electrons when the relativistic effects are taken into account. It is evident from the aforesaid that the consideration of the relativistic effects in the full-electron calculation of the UF_6 molecule is essential.

The results of scalar-relativistic calculations on the UO_2 crystal and the comparative study of UN, U_2N_3 and UN_2 crystals are discussed in [59] and demonstrate the efficiency of RECP use for the periodic systems.

In the next sections we discuss in short the Hartree-Fock (also called the wave function based) and Density Functional Theory (DFT) methods used nowadays in periodic structures modeling, in particular for nanotubes and nanowires.

3.2 LCAO Hartree-Fock Method for Periodic Systems

3.2.1 Electron Correlation, One-Electron and One-Determinant Approximations

Electrons in molecules and crystals repel each other according to Coulomb's law, with the repulsion energy depending on the interelectron distance as r_{12}^{-1}. This interaction creates a correlation hole around any electron, i.e. the probability to find any pair of electrons at the same point of spin-coordinate space is zero. From this point of view only the Hartree product Ψ_H of molecular or crystalline spin-orbitals $\psi_i(\boldsymbol{x})$:

$$\Psi_H(\boldsymbol{x}_1, \boldsymbol{x}_2, \ldots, \boldsymbol{x}_{N_e}) = \psi_1(\boldsymbol{x}_1)\psi_2(\boldsymbol{x}_2), \ldots, \psi_{N_e}(\boldsymbol{x}_{N_e}) \tag{3.18}$$

is a completely uncorrelated function. The Hartree product (3.18) describes the system of N_e electrons in an independent particle model. This independence means that the probability of simultaneously finding electron 1 at $\boldsymbol{x}_1$, electron 2 at $\boldsymbol{x}_2$, etc. ($\boldsymbol{x}$ means the set of coordinate $\boldsymbol{r}$ and spin σ variables) is given by

$$\begin{aligned} &|\Psi_H(\boldsymbol{x}_1, \boldsymbol{x}_2, \ldots, \boldsymbol{x}_{N_e})|^2 d\boldsymbol{x}_1 d\boldsymbol{x}_2, \ldots, d\boldsymbol{x}_{N_e} \\ &= |\psi_1(\boldsymbol{x}_1)|^2 d\boldsymbol{x}_1 |\psi_2(\boldsymbol{x}_2)|^2 d\boldsymbol{x}_2, \ldots, |\psi_{N_e}(\boldsymbol{x}_{N_e})|^2 d\boldsymbol{x}_{N_e} \end{aligned} \tag{3.19}$$

which is the probability of finding electron 1 at $\boldsymbol{x}_1$ times the probability of finding electron 2 at $\boldsymbol{x}_2$, etc., i.e. product of probabilities.

The well-known Extended Hückel semiempirical method for molecules and the Tight Binding (TB) approach to crystals are examples of the models with full absence of electron correlation in the wavefunction. The Hamiltonian in these methods does not include explicitly electron–electron interactions (such a Hamiltonian is known as the one-electron Hamiltonian) so that the total many-electron wavefunction is a simple product (3.18) of the one-electron functions and the total electron energy is a sum of one-electron energies. If the semiempirical parameters are used in these methods the electron correlation is taken into account at least partly. When the TB parameters are fitted to reproduce the results of DFT calculations (see DFTB method) the electron correlation is also taken into account but it is not known precisely how large is the correlation part included.

The difference between the one-electron Hamiltonian and the Hamiltonian of the one-electron approximation (HF method) is the following. The former does not include electron–electron interaction so that the calculation of its eigenvalues and eigenvectors does not require a self-consistent procedure. The Hamiltonian of the one-electron approximation includes explicitly the interelectron interactions, the one-electron approximation is made only in the many-electron wavefunction. The one-electron approximation Hamiltonian depends on the one-electron wavefunctions unknown at the beginning of the calculation (for example, the Coulomb and exchange parts of the Hamiltonian in the Hartree-Fock method, see next section) and the self-consistent calculation is required.

The Hartree-Fock (HF) self-consistent (SCF) method replaces the instantaneous electron–electron repulsion with the repulsion of each electron with an average electron charge cloud. The HF method assumes that the many-electron wavefunction can be written as one Slater determinant. The Hartree-Fock method is usually defined as "uncorrelated". However, the electron motions are no longer completely independent. Indeed, no two electrons with the same spin can be at the same place. This is called the Fermi hole. Thus, *same-spin electrons are correlated in Hartree-Fock, different-spin electrons are not*. Sometimes, it is said that HF methods take into account the so-called spin correlation.

The HF methods are also called by the independent electrons approximation [68] but this independence is restricted by the Pauli principle.

In modern molecular quantum chemistry the correlation energy is defined as the difference between the exact energy and the HF energy in a complete basis (Hartree-Fock limit). As one does not know the exact energy one uses the experimental total energy (the sum of the experimental cohesive energy and free-atom energies) or calculates the exact energy for a given one-electron basis set and defines the basis set correlation energy as the difference between the exact and HF energies calculated for the same one-electron basis set. In molecular systems, the correlation energy is about 1 eV per electron pair in a bond or lone pair.

One of the first attempts to include the electron-correlation in calculations was made by Fock et al. [69], who suggested the incomplete separation of variables for two-valent atoms.

The key distinction between the Hamiltonian operator and the Fock operator is the following, [70]: the former returns the electronic energy for the many-electron system, the latter is really not a single operator, but the set of all of the interdependent one-electron operators that are used to find the one-electron functions (molecular or crystalline orbitals) from which the HF wavefunction is constructed as a Slater determinant. The HF wavefunction corresponds to the lowest possible energy for a single-determinant many-electron wavefunction formed from the chosen basis set.

Including electron-correlation in MO theory means an attempt to modify the HF wavefunction to obtain a lower electronic energy when we operate on that modified wavefunction with the Hamiltonian. This is why the name post-Hartree-Fock methods is traditionally used for the methods including the electron-correlation.

In the unrestricted Hartree-Fock approximation (where the coordinate dependence of spin-up and spin-down MOs was allowed to differ) the one-determinant

many-electron wavefunction is, in the general case, not an eigenfunction of the total spin operator S^2. To repair that deficiency the technique of projection is used [71] so that the resulting wavefunction becomes a sum of several Slater determinants and therefore partly takes into account electron-correlation, i.e. goes beyond the one-determinant HF approximation. However, the coefficients in the sum of Slater determinants are defined only by the projection procedure, i.e. the total spin-symmetry requirements introduced for the many-electron wavefunction.

The sum of Slater determinants

$$\Psi = C_0\Psi_{HF} + C_1\Psi_1 + C_2\Psi_2 + \cdots \tag{3.20}$$

is used also in other post-HF approaches: configuration interaction (CI), multiple-configuration SCF (MCSCF) and coupled-cluster (CC) methods applied to include the electron-correlation in molecules.

Often, the HF approximation provides an accurate description of the system and the effects of the inclusion of correlations with CI or MCSCF methods are of secondary importance. In this case, the correlation effects may be considered as a smaller perturbation and as such treated using the perturbation theory. This is the approach of Möller–Plesset [72] or many-body perturbation theory for the inclusion of correlation effects. In the MP2 approximation only the second-order many-body perturbations are taken into account.

The above-mentioned quantum-chemical approaches to electron-correlations in molecules (also called wavefunction-based correlation methods) are described in detail in monographs [68, 70], review articles [73, 74] and are implemented in modern computer codes.

The main disadvantage of the wavefunction-based correlation methods is the high scaling of the computational cost with the number of atoms N in a molecule, at least when the canonical MOs are used. The scaling of the computational complexity is $O(N^5)$ for the simplest and cheapest method—second-order perturbation theory MP2. For the CC theory the computational cost scales are $O(N^6)$ and even $O(N^7)$ for the truncated beyond doubles and triples substitutions, respectively. Such a high "scaling wall" [75] restricts the application range of the wavefunction-based correlation methods to molecules of rather modest size. For this reason the density-functional-based correlation methods remain until now the main way to treat large molecular systems. The main disadvantages of the latter methods are the principal impossibility for systematic improvements, the underestimation of transition-state energies, and the inability to describe weak interactions (dispersive forces).

The essential progress in the correlation effects inclusion was achieved in the so-called local correlation methods [75, 76] taking into account the short-range nature of the correlation. In these methods, the localized MOs are generated from the occupied canonical MOs since different localization criteria. For the virtual space the atomic-orbital basis is projected out of the occupied MO space.

As compared to the molecules the wavefunction-based correlation methods for periodic systems are practically reliable only when the molecular cluster model is used. Unfortunately, the well-known problems of the cluster choice and the influence

of the dangling bonds on the numerical results restricts the application range of the molecular cluster model to the essentially ionic systems.

The more sophisticated incremental scheme [77–80] maintains the infinite nature of periodic systems but the correlation effects are calculated incrementally using standard quantum-chemical codes.

Only recently was the MP2 theory applied to the periodic systems based on the local correlation methods and use of Wannier functions [75, 81].

While for the molecules the local correlation methods are already implemented in computer codes the implementation of this approach to the periodic systems is the main goal of the new CRYSCOR project [82].

3.2.2 LCAO Hartree-Fock Method for Periodic Systems

In molecular quantum chemistry the molecular orbital (MO) is expanded in terms of GTO. Different atomic functions used in calculations of molecules and crystals were considered above. For the moment, we restrict ourselves by representation of MO $\varphi_i(\boldsymbol{r})$ as a linear combination of atomic orbitals $\chi_{\mu A}(\boldsymbol{r})$ (MO LCAO approximation):

$$\varphi_i(\boldsymbol{r}) = \sum_{\mu A} C_{i\mu}\chi_{\mu A}(\boldsymbol{r}) \tag{3.21}$$

where μ numbers all basis functions centered on atom A and summation is made over all the atoms in the molecular system. The MO LCAO approximation (also known as the Hartree-Fock–Roothaan approximation [83]) is practically the only way to make first-principles calculations for molecular systems. In the standard derivation of the Hartree-Fock equations relative to a closed-shell system, the constraint that each molecular orbital is populated by two electrons or vacant is introduced (Restricted Hartree-Fock theory—RHF).

In the MO LCAO approximation RHF method transforms to the matrix equations

$$\mathbf{FC} = \mathbf{SCE} \tag{3.22}$$

where **F** and **S** are the Fock and the overlap matrices, **C** and **E** are the matrices of eigenvectors and eigenvalues. The dimension M of square matrices **F**, **S**, **C** is equal to the number of items in the sum (3.21), i.e. the total number of AO used in the calculation.

The Fock matrix **F** is the sum of one-electron **H** and two-electron **G** parts. The former includes the kinetic (T) and nuclear attraction (Z) energy, the latter is connected with the electron–electron interactions.

By definition, in the molecular states with closed shells all MO are fully occupied by electrons or empty. The corresponding many-electron wavefunction can be written as a single Slater determinant, each MO is occupied by an equal number of electrons

with α and β spins. Such a function describes the ground state of a molecule with total spin $S = 0$ and with the symmetry of identity representation of the point-symmetry group.

In the case of open-shell molecular systems a single Slater determinant describes a state with the fixed spin-projection (equal to the difference of n_α and n_β electrons) but is not the correct spin eigenfunction. Indeed, let in the open-shell configuration the highest one-electron energy level be occupied by one electron with α spin. As there are no spin interactions in the Hartree-Fock Hamiltonian the same electron energy corresponds to the function with β-spin electrons on the highest occupied level. This means that in order to get the correct total spin eigenfunction transforming over the identity representation of the point group it is necessary to use a sum of Slater determinants. The molecules with an odd number of electrons, the radicals and the magnetic systems have the open shells in the ground state.

The restricted open-shell Hartree-Fock (ROHF) and the unrestricted Hartree-Fock Method (UHF) approximations permit, however, open-shell systems to be described, while maintaining the simplicity of the single-determinant approximation. This is made at the stage of self-consistent electronic-structure calculations. Afterwards, the obtained spin-orbitals can be used to get the correct total spin many-determinant wavefunction and to calculate the corresponding electron energy.

The ROHF [84] many-electron wavefunction is, in the general case, a sum of Slater determinants; each determinant contains a closed-shell subset, with doubly occupied orbitals and an open-shell subset, formed by orbitals occupied by a single electron.

In one particular case, the ROHF wavefunction reduces to a single determinant: this is the so-called half-closed- shell cases, where it is possible to define two sets of orbitals, the first n_d occupied by paired electrons and the second n_s, by electrons with parallel spins. The total number of electrons $n = n_d + n_s$. In all molecular programs ROHF means a single-determinant wavefunction with maximal spin projection that is automatically eigenfunctions of S^2 with the maximal spin projecton value $S = n_s/2$. So, for the ROHF method projection on a pure spin state is not required. The space symmetry of the Hamiltonian in the ROHF method remains the same as in the RHF method, i.e. coincides with the space symmetry of nuclei configuration. The double-occupancy constraint allows the ROHF approach to obtain solutions that are eigenfunctions of the total spin operator. The molecular orbitals diagram for the ROHF half-closed shell is given in Fig. 3.4, (left).

In the UHF method, keeping a single-determinant description, the constraint of double occupancy of molecular orbitals is absent as α electrons are allowed to occupy orbitals other than those occupied by the β electrons. The greater variational freedom allows the UHF method to produce wavefunctions that are energetically more stable, i.e. give lower electron energy. Another advantage of the UHF method is that it allows solutions with locally nonzero negative or positive spin density (i.e. ferromagnetic or antiferromagnetic systems). However, UHF solutions are formed by a mixture of spin states and are eigenfunctions only of the total spin-projection operator S_z.

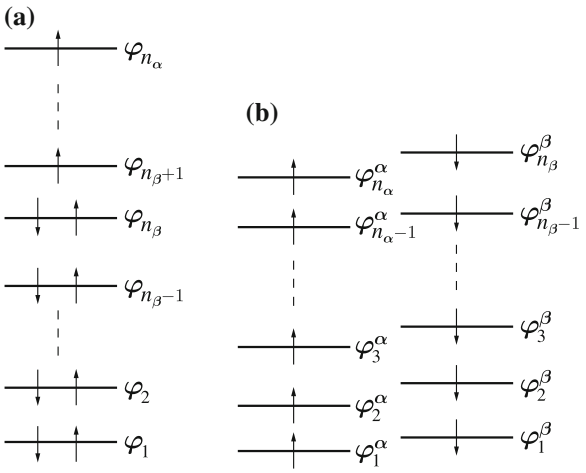

Fig. 3.4 The one-electron levels filling in **a** ROHF and **b** UHF methods

In the UHF approach, the single-determinant wavefunction is computed using n_α MOs $\varphi^\alpha(\boldsymbol{r})$ and n_β MOs $\varphi^\beta(\boldsymbol{r})$, corresponding to the electrons with α and β spin, respectively.

Let us we examine the main modifications in the Hartree-Fock–Roothaan equations (3.22), it being necessary to take into account the translation symmetry of periodic systems.

The first most important difference appears in the LCAO representation of the crystalline crbitals (CO) compared to the molecular orbitals (MO).For the periodic system the AO symmetrization over the translation subgroup of the space group is made giving the Bloch sums of AOs:

$$\chi_{\mu\boldsymbol{k}}(\boldsymbol{r}) = \frac{1}{\sqrt{N}} \sum_{\boldsymbol{R}_n} \exp(\mathrm{i}\boldsymbol{k}\boldsymbol{R}_n)\chi_\mu(\boldsymbol{r} - \boldsymbol{R}_n) \tag{3.23}$$

In (3.23), the index μ labels all AOs in the reference primitive unit cell ($\mu = 1, 2, \ldots, M$) and $\boldsymbol{R}_n$ is the translation vector of the direct lattice (for the reference primitive cell $\boldsymbol{R}_n = 0$). The summation in (3.23) is supposed to be made over the infinite direct lattice (in the model of the infinite crystal) or over the inner primitive translations $\boldsymbol{R}^0_n$ of the cyclic cluster (in the cyclic model of a crystal).

In the LCAO approximation crystalline orbital (CO) is the Bloch function as it is expanded over the Bloch sums of AOs:

$$\varphi_{i\boldsymbol{k}}(\boldsymbol{r}) = \sum_\mu C_{i\mu}(\boldsymbol{k})\chi_{\mu\boldsymbol{k}}(\boldsymbol{r}) \tag{3.24}$$

In the MO LCAO approximation the index i in the expansion (3.21) numbers the MOs (their total number M is equal to the number of atomic orbitals used in the expansion (3.21)). In the case of closed shells the N_e electrons of the molecule occupy $N_e/2$ MOs and $(M - N_e/2)$ MOs are empty.

The total number of COs of the cyclic cluster equals $M \times N$ (N is the number of the primitive unit cells in the cyclic cluster; M is the number of AO basis functions per primitive unit cell). For the cyclic cluster containing $N_e = N \times n$ electrons (n is the number of electrons per primitive unit cell) $N_e/2$ crystalline orbitals are occupied by electrons and $(M \times N - N_e/2)$ orbitals are empty. The numbering of crystalline orbitals is made by two indices i and $\boldsymbol{k}$: the one-electron states of a crystal form the energy bands numbered by index i and joining the N states with the same i. The closed-shell case (the nonconducting crystals) means that all the energy bands are filled or empty (there are no partly filled energy bands).

For $N \to \infty$ the total number of COs also becomes infinite, the one-electron energy levels form the continuous energy bands, but the total number of energy bands remains finite and is equal to M. For the closed-shell case $n/2$ electrons occupy the lowest-energy bands for each $\boldsymbol{k}$-vector. The forbidden gap in the nonconducting crystals is the crystalline analog of the HOMO (highest-occupied MO)–LUMO (lowest-unoccupied MO) one-electron energies difference.

On the basis of Bloch functions, the Fock and overlap matrices F and S become

$$F_{\mu\nu}(\boldsymbol{k}) = \sum_{\boldsymbol{R}_n} \exp(\mathrm{i}\boldsymbol{k}\boldsymbol{R}_n) F_{\mu\nu}(\boldsymbol{R}_n); \quad S_{\mu\nu}(\boldsymbol{k}) = \sum_{\boldsymbol{R}_n} \exp(\mathrm{i}\boldsymbol{k}\boldsymbol{R}_n) S_{\mu\nu}(\boldsymbol{R}_n) \tag{3.25}$$

where $F_{\mu\nu}(\boldsymbol{R}_n)$ is the matrix element of the Fock operator between the μth AO located in the reference (zero) cell and the νth AO located in the $\boldsymbol{R}_n$ cell. The matrix element $S_{\mu\nu}(\boldsymbol{R}_n)$ is the overlap integral of the same AOs. The row index can be limited to the reference cell for translational symmetry. Matrices represented on the Bloch basis (or in $\boldsymbol{k}$-space) take a block-diagonal form, as Bloch functions are bases for irreducible representations of the translation group T ($\mathrm{T}^{(N)}$ for the cyclic cluster of N primitive cells); each block has the dimensions of the AO basis in the primitive cell, M,

$$\mathrm{F}(\boldsymbol{k})\mathrm{C}(\boldsymbol{k}) = \mathrm{S}(\boldsymbol{k})\mathrm{C}(\boldsymbol{k})\mathrm{E}(\boldsymbol{k}) \tag{3.26}$$

In the HF LCAO method, (3.26) for the periodic systems replaces (3.22) written for the molecular systems. In principle, the above equation should be solved at each SCF procedure step for all the (infinite) $\boldsymbol{k}$-points of the Brillouin zone. Usually, a finite set $\{\boldsymbol{k}_j\}(j = 1, 2, \ldots, L)$ of $\boldsymbol{k}$-points is taken (this means the replacing the infinite crystal by the cyclic cluster of L primitive cells). The convergence of the results relative to the increase of the $\boldsymbol{k}$-points set is examined in real calculations, for the convergent results the interpolation techniques are used for eigenvalues and eigenvectors as these are both continuous functions of $\boldsymbol{k}$ [85]. The convergence of the SCF calculation results is connected with the density matrix properties.

The overlap matrix elements in the AO basis are the lattice sums of the overlap integrals between AOs, numbered now by indices of AO in the zero (reference) cell and of the cell defined by the translation vector $\boldsymbol{R}_n$.

The Fock matrix elements (as in the case of molecules) are the sums of one-electron (the kinetic energy T and the nuclear attraction energy Z) and two-electron (Coulomb J and exchange energies) parts. The difference of these matrices from the molecular analogs is the appearance of the sums over a direct lattice, containing one-electron (kinetic energy and nuclear attraction) and two-electron integrals.

The spinless one-electron density matrix (DM) elements are defined in the LCAO approximation as

$$P_{\lambda\sigma}(\boldsymbol{R}_{m'}) = 2\int d\boldsymbol{k} e^{i\boldsymbol{k}\boldsymbol{R}_{m'}} \sum_i C^*_{i\lambda}(\boldsymbol{k}) C_{i\sigma}(\boldsymbol{k}) \theta(\epsilon_F - \epsilon_i(\boldsymbol{k})) \tag{3.27}$$

where ϵ_F is the Fermi energy, the integration in (3.27) extends to the first Brillouin zone and corresponds to the model of the infinite crystal. In the cyclic-cluster model the integration is replaced by the summation over $\boldsymbol{k}$-points numbering the irreps of the group of the inner cyclic-cluster translations. The DM elements depend on the eigenvectors $C_i(\boldsymbol{k})$ of the $F(\boldsymbol{k})$ matrix. The integration or summation over $\boldsymbol{k}$ in DM elements makes it impossible to solve (3.26) for different $\boldsymbol{k}$ independently.

The electron energy of the crystal (per primitive unit cell) as calculated within the HF LCAO approximation can be expressed in terms of the one-electron density matrix (DM) and includes the lattice sums

$$E_e = \frac{1}{2}\sum_{\mu\nu}^{M}\sum_{\boldsymbol{R}_n} P_{\mu\nu}(\boldsymbol{R}_n)\left(F_{\mu\nu}(\boldsymbol{R}_n) + T_{\mu\nu}(\boldsymbol{R}_n) + Z_{\mu\nu}(\boldsymbol{R}_n)\right) \tag{3.28}$$

The direct lattice summations in the Fock matrix elements and the $\boldsymbol{k}$ dependence of the one-electron DM, energy levels and COs are the main difficulties of the HF LCAO method for periodic systems, compared with molecules. A special strategy must be specified for the treatment of the infinite Coloumb and exchange series as well as for the substitution of the integral that appears in DM with a weighted sum extended to a finite set of $\boldsymbol{k}$-points. The efficient solution of these problems has been implemented in the CRYSTAL code [86]. These problems are also valid for UHF and ROHF LCAO methods for periodic systems.

In self-consistent calculations of the electronic structure of crystals both in the basis of plane waves and in the basis of localized atomic-type functions, one needs in every stage of the self-consistent procedure to evaluate an approximate electron-density matrix by integration over the Brillouin zone (BZ):

$$\rho(\mathbf{r}, \mathbf{r}') = \int_{BZ} Q_{\mathbf{r},\mathbf{r}'}(\mathbf{k}) d\mathbf{k}, \qquad Q_{\mathbf{r},\mathbf{r}'}(\mathbf{k}) = \sum_v \psi^*_v(\mathbf{k}, \mathbf{r}')\psi_v(\mathbf{k}, \mathbf{r}) \tag{3.29}$$

where the sum is over occupied electronic states of the crystal. In practice, $\psi(\mathbf{k}, \mathbf{r})$ (and $\varphi(\mathbf{k}) \equiv Q_{\mathbf{r},\mathbf{r}'}(\mathbf{k})$) are calculated in some finite meshes of $\mathbf{k}$-points. Therefore, one needs for the evaluation of the integral (3.29) to construct the interpolation formula of the numerical integration based on an interpolation procedure by means of some set of interpolation functions.

The functions $\varphi(\mathbf{k}) \equiv Q_{\mathbf{r},\mathbf{r}'}(\mathbf{k})$) are periodic in the reciprocal space with periods determined by the basic translation vectors $\mathbf{b}_i$ of the reciprocal lattice and having the full point symmetry of the crystal (F is a point group of order n_F of the crystal).

$$\varphi(\mathbf{k} + \mathbf{b_m}) = \varphi(\mathbf{k}) = \varphi(f\mathbf{k}), \quad f \in F, \quad \mathbf{b_m} = \sum_{i=1}^{3} m_i \mathbf{b}_i \tag{3.30}$$

The plane waves $\exp(\mathrm{i}\mathbf{k} \cdot \mathbf{a_n})$ seem to be the most convenient as interpolation functions for the integrand in the BZ integration, where $\mathbf{a_n} = \sum_{i=1}^{3} n_i \mathbf{a}_i$ are direct lattice translation vectors and $\mathbf{a}_i$ are primitive translations. It is easy with plane waves to take into account the translational and point symmetry of the crystal.

In the problem of BZ integration, nodes for the interpolation ($\mathbf{k}$-points of the BZ) were called special points (SP).

Many procedures for special points generation have been proposed. The most popular special-points (SP) sets are meshes obtained by a very simple algorithm proposed by Monkhorst and Pack (MP) in [87]:

$$\mathbf{k}_{\mathbf{p}}^{(n)} = \sum_{i=1}^{3} u_{p_i}^{(n)} \mathbf{b}_i, \; n = 1, 2, \ldots, p_i = 1, 2, \ldots, n, \quad u_{p_i}^{(n)} = \frac{2p_i - n - 1}{2n} \tag{3.31}$$

These meshes are widespread in modern Hartree-Fock and density-functional theory calculations of crystals and are automatically generated in the corresponding computer codes. But MP meshes of SP have at least one shortcoming, which may be understood if one oversees the problem from the point of view of the more general large unit cell–small Brillouin zone (LUC–SBZ) method of SP generation [59].The MP method is a particular case of the LUC–SBZ method. In [88] the modification of the MP meshes was suggested that makes faster and more regular convergence of the results of the self-consistent calculations of the electronic structure of crystals.

The suggested in [88] modification of Monkhorst–Pack special-points meshes for Brillouin-zone integration is essentially useful for crystals with many atoms in a primitive unit cell or for point-defect calculations in a supercell model. In these cases each step of the self-consistent procedure in Hartree-Fock or DFT calculations is time consuming, so that the higher efficiency of $\mathbf{k}$-point meshes shortens the computing time. It is also important for the lattice parameters or atom-position optimization in crystals, when the self-consistent procedure is repeated for different atomic structures. LUC–SBZ method of the special point set generation can be applied both in LCAO and plane-wave calculations to approximate the density matrix of a crystal.

3.3 Foundations of Density Functional Theory

3.3.1 Density Functional Theory

The low computational cost, combined with useful accuracy, has made Density Functional Theory (DFT) a standard technique in most branches of chemistry and materials science [89]. The number of papers given by Web of Knowledge when DFT is searched as a topic will soon reach 10,000 per year [89]. The applications to materials will soon outstrip those in chemistry. It is demonstrated in the next chapters that the majority of the published nanostructure calculations are also based on the DFT approach.

Density-functional theory has its conceptual roots in the Thomas–Fermi model of a uniform electron gas [90, 91] and the Slater local exchange approximation [92]. A formalistic proof for the correctness of the Thomas–Fermi model was provided by Hohenberg–Kohn theorems, [93]. DFT has been very popular for calculations in solid-state physics since the 1970s. In many cases DFT with the local-density approximation (LDA) and plane waves as basis functions gives quite satisfactory results, for solid-state calculations, in comparison to experimental data at relatively low computational costs when compared to other ways of solving the quantum-mechanical many-body problem.

In DFT, the one-electron density $\rho(\boldsymbol{r})$

$$\rho(\boldsymbol{r}) = N \int d^3\boldsymbol{r}_2 \int d^3\boldsymbol{r}_3 \ldots \int d^3\boldsymbol{r}_N \Psi^*(\boldsymbol{r}, \boldsymbol{r}_2, \ldots, \boldsymbol{r}_N)\Psi(\boldsymbol{r}, \boldsymbol{r}_2, \ldots, \boldsymbol{r}_N) \quad (3.32)$$

becomes the key variable: DFT can be summarized by the sequence

$$\rho(\boldsymbol{r}) \rightarrow \Psi(\boldsymbol{r}_1, \boldsymbol{r}_2, \ldots, \boldsymbol{r}_N) \rightarrow V(\boldsymbol{r})$$

i.e. knowledge of $\rho(\boldsymbol{r})$ implies knowledge of the wavefunction and the potential, and hence of all other observables. This also represents the fact that ultimately the electron density and not a wavefunction is the observable. Although this sequence describes the conceptual structure of DFT, it does not really represent what is done in actual applications of it and does not make explicit the use of many-body wavefunctions.

Some chemists until now consider DFT as a containing " semiempirism"(not ab-initio) method but recognize that the small number of semiempirical parameters are used in DFT and these parameters are "universal to the whole chemistry" [94]. It took a long time for quantum chemists to recognize the possible contribution of DFT. A possible explanation of this is that the molecule is a very different object to the solid as the electron density in a molecule is very far from uniform [94]. DFT was not considered accurate enough for calculations in molecular quantum chemistry until the 1990s, when the approximations used in the theory were greatly refined to better model the exchange and correlation interactions. DFT is now a leading method for electronic-structure calculations in both fields.

Whereas the many-electron wavefunction is dependent on $3N$ variables, three spatial variables for each of the N electrons, the density is only a function of three variables and is a simpler quantity to deal with both conceptually and practically.

The literature on DFT and its applications is large. Some representative examples are the following: books [95–101], separate chapters of monographs [2, 70, 102, 103] and review articles [104–110]. The short essay [111] introduces newcomers to the basic ideas and uses of modern electronic DFT theory,

The DFT recent progress (in particular, for materials and nanoscience) and ongoing challenges are discussed in [89].

Two core elements of DFT are the Hohenberg–Kohn (HK) theorems [4, 93] and the Kohn–Sham equations [112]. The former is mainly conceptual, but via the second the most common implementations of DFT have been done.

The first HK theorem states that the external potential of the system, and hence the total energy, is a unique functional of the electron density. This theorem demonstrates the existence of a one-to-one mapping between the ground-state electron density and the ground-state wavefunction of a many-particle system. The first Hohenberg–Kohn theorem is only an existence theorem, stating that the mapping exists, but does not provide any such exact mapping. It is in these mappings that approximations are made.

Hohenberg and Kohn proved [93] that to a given ground-state density $\rho(\boldsymbol{r})$ it is in principle possible to calculate the corresponding ground-state wavefunction $\Psi_0(\boldsymbol{r}_1, \boldsymbol{r}_2, \ldots, \boldsymbol{r}_N)$. This means that for a given ground-state density for some system we cannot have two different external potentials V. This means that the electron density $\rho(\boldsymbol{r})$ defines all terms in the Hamiltonian and therefore we can, in principle, determine the complete N electron wavefunction for the ground-state by only knowing the electron density. The first HK theorem shows only that it is possible to calculate any ground-state property when the electron density is known but does not give the means to do it. Since the wavefunction is determined by the density, we can write it as $\Psi_0 = \Psi_0[\rho]$, which indicates that Ψ_0 is a function of its N spatial variables, but a *functional* of $\rho(\boldsymbol{r})$. More generally, a functional $F[n]$ can be defined as a rule for going from a function to a number, just as a function $y = f(x)$ is a rule (f) for going from a number (x) to a number (y). A simple example of a functional is the total number of electrons in a system N

$$N = \int d^3\boldsymbol{r}\rho(\boldsymbol{r}) = N[\rho(\boldsymbol{r})] \tag{3.33}$$

which is a rule for obtaining the number N, given the function $\rho(\boldsymbol{r})$. Note that the name given to the argument of ρ is completely irrelevant, since the functional depends on the *function* itself, not on its variable. Hence we do not need to distinguish $F[\rho(\boldsymbol{r})]$ from, e.g. $F[\rho(\boldsymbol{r}')]$. Another important case is that in which the functional depends on a parameter, such as in

$$V_H[\rho(\boldsymbol{r})] = \int d^3\boldsymbol{r}' \frac{\rho(\boldsymbol{r}')}{|\boldsymbol{r} - \boldsymbol{r}'|} \tag{3.34}$$

that is a rule that for any value of the parameter $\boldsymbol{r}$ associates a value $V_H[\rho(\boldsymbol{r})]$ with the function $\rho(\boldsymbol{r}')$. This term is the so-called one-electron Hartree potential of the Coulomb field created by all electrons of the system, with the electron in question included.

DFT explicitly recognizes that nonrelativistic Coulomb systems differ only by their external potential $V(\boldsymbol{r})$, and supplies a prescription for dealing with the universal operators T and U once and for all. This is done by promoting the electron density $\rho(\boldsymbol{r})$ from just one of many observables to the status of the key variable, on which the calculation of all other observables can be based. In other words, Ψ_0 is a unique functional of ρ, i.e. $\Psi_0[\rho]$ and consequently all other ground-state observables O are also functionals of ρ

$$\langle O\rangle[\rho] = \langle \Psi_0[\rho]|\hat{O}|\Psi_0[\rho]\rangle \tag{3.35}$$

From this it follows, in particular, that also the ground-state energy is a functional of ρ

$$E_0 = E[\rho] = \langle \Psi_0[\rho]|T + V + U|\Psi_0[\rho]\rangle \tag{3.36}$$

where the contribution of the external potential can be written explicitly in terms of the density

$$V[\rho] = \int V(\boldsymbol{r})\rho(\boldsymbol{r})d^3\boldsymbol{r} \tag{3.37}$$

The functionals $T[\rho]$ and $U[\rho]$ are called universal functionals, while $V[\rho]$ is obviously nonuniversal, as it depends on the system under study. Having specified a system, i.e. V is known, one then has to minimize the functional

$$E[\rho] = T[\rho] + U[\rho] + \int V(\boldsymbol{r})\rho(\boldsymbol{r})d^3\boldsymbol{r} \tag{3.38}$$

with respect to $\rho(\boldsymbol{r})$, assuming one has got reliable expressions for $T[\rho]$ and $U[\rho]$.

The second HK theorem states that the ground state energy can be obtained variationally: the density that minimizes the total energy is the exact groundstate density i.e. this theorem proves that the ground-state density minimizes the total electronic energy of the system. It states that once the functional that relates the electron density with the total electronic energy is known, one may calculate it approximately by inserting approximate densities ρ'. Furthermore, just as for the variational method for wavefunctions, one may improve any actual calculation by minimizing the energy functional $E[\rho']$. A successful minimization of the energy functional will yield the ground-state density ρ_0 and thus all other ground-state observables. A practical scheme for calculating ground-state properties from electron density was provided by the approach of Kohn and Sham [112] considered in the next section.

3.3.2 The Kohn–Sham Single-particle Equations

Within the framework of Kohn–Sham (KS) DFT, the intractable many-body problem of interacting electrons in a static external potential is reduced to a tractable problem of noninteracting electrons moving in an effective potential. The functional in (3.38) is written as a fictitious density functional of a noninteracting system

$$E_{eff}[\rho] = \langle \Psi_{eff}[\rho] | T_{eff} + V_{eff} | \Psi_{eff}[\rho] \rangle \tag{3.39}$$

where T_{eff} denotes the noninteracting electrons kinetic energy and V_{eff} is an external effective potential in which the electrons are moving. It is assumed that the fictitious (model) system has the same energy as the real system. Obviously, $\rho_{eff}(\boldsymbol{r}) = \rho(\boldsymbol{r})$ if V_{eff} is chosen to be

$$V_{eff} = V + U + (T - T_{eff}) \tag{3.40}$$

Thus, one can solve the so-called Kohn–Sham equations of this auxiliary noninteracting system with the effective Hamiltonian

$$H_{eff} = \sum_{i=1}^{N} \left[-\frac{1}{2}\Delta_i + V_{eff}(\boldsymbol{r}_i) \right] = \sum_{i=1}^{N} h_{eff}(\boldsymbol{r}_i) \tag{3.41}$$

that yields the orbitals $\varphi_i(\boldsymbol{r})$ that reproduce the density $\rho(\boldsymbol{r})$ of the original many-electron system $\rho(\boldsymbol{r}) = \rho_{eff}(\boldsymbol{r}) = \sum_{i=1}^{N} |\varphi(\boldsymbol{r})|^2$. The effective single-electron potential $V_{eff}(\boldsymbol{r})$ can be written as

$$V_{eff}(\boldsymbol{r}) = V + \int \frac{\rho_{eff}(\boldsymbol{r}')}{|\boldsymbol{r} - \boldsymbol{r}'|} d^3\boldsymbol{r}' + V_{XC}\left[\rho_{eff}(\boldsymbol{r})\right] \tag{3.42}$$

where the second term denotes the so-called Hartree term describing the electron–electron Coulomb repulsion, while the last term V_{XC} is called the exchange correlation potential and includes all the many-electron interactions. Since the Hartree term and V_{XC} depend on $\rho(\boldsymbol{r})$ that depends on the φ_i, which in turn depend on V_{eff}, the problem of solving the Kohn–Sham equation has to be done in a self-consistent (i.e. iterative) way. Usually, one starts with an initial guess for $\rho(\boldsymbol{r})$, then calculates the corresponding V_{eff} and solves the Kohn–Sham equations for the φ_i. From these one calculates a new density and starts again. This procedure is then repeated until convergence is reached.

There are only single-particle operators in (3.41). Therefore, the solution to the Schrödinger equation for a model system of noninteracting electrons can be written exactly as a single Slater determinant $\Psi = |\varphi_1, \varphi_2, \ldots, \varphi_N|$, where the single-particle orbitals φ_i are determined as solutions of the single-particle equation

$$h_{eff}\varphi_i = \varepsilon_i \varphi_i \tag{3.43}$$

Furthermore, $\rho(\boldsymbol{r}) = \sum_{i=1}^{N} |\varphi_i(\boldsymbol{r})|^2$, where the summation runs over the N orbitals with the lowest eigenvalues ε_i.

The main problem is that we do not know the exact form of the effective potential V_{eff}, i.e. the so-called exchange-correlation energy and potential. There exist approximations to these (LDA, GGA, hybrid exchange-correlation potentials) that are good approximations in very many cases. On the other hand, by introducing an approximation in the Schrödinger equation for the model noninteracting particles, we do not know whether improved calculations (e.g. using larger basis sets) also lead to improved results (compared with, e.g. experiment or other calculations). The success of the Kohn–Sham approach is based on the assumption that it is possible to construct the model system of noninteracting particles moving in an effective external potential. Thus, it is indirectly assumed that for any ground-state density there exists an effective potential (the corresponding density matrix is called V representative). There exist (specifically constructed) examples where this is not the case, but in most practical applications, this represents no problem [102].

HK theorems and KS equations can be extended to the spin-polarized systems where the electron- density components $\rho_\alpha(\boldsymbol{r})$, $\rho_\beta(\boldsymbol{r})$ for spin-up and spin-down orbitals differ i.e. the spin-density $\rho^s(\boldsymbol{r}) = \rho_\alpha(\boldsymbol{r}) - \rho_\beta(\boldsymbol{r})$ is nonzero.

The result is that the total energy and any other ground-state properties become a functional not only of $\rho(\boldsymbol{r})$ but also of spin-density $\rho^s(\boldsymbol{r})$, i.e. $E_{eff} = E[\rho(\boldsymbol{r}), \rho^s(\boldsymbol{r})]$. Spin-density-functional theory (SDFT) is a widely implemented and applied formalism of DFT.

Since 1990 there has been an enormous amount of comparison for molecules between DFT KS and HF (MO) theory. Such a comparison is easily extended to crystals when we consider CO instead of MO. The discussion of advantages and disadvantages of DFT compared to MO theory can be found for example, in [70] and is briefly reproduced here. The most fundamental difference between DFT and MO theory is the following: DFT optimizes an electron density, while MO theory optimizes a wavefunction. So, to determine a particular molecular property using DFT, we need to know how that property depends on the density, while to determine the same property using a wavefunction, we need to know the correct quantum-mechanical operator. As a simple example, consider the total energy of interelectronic repulsion. Even if we had the exact density for some system, we do not know the exact exchange-correlation energy functional, and thus we cannot compute the exact interelectronic repulsion. However, with the exact wavefunction it is a simple matter of evaluating the expectation value for the interelectronic repulsion operator to determine this energy. Thus, it is easy to become confused about whether there exists a KS "wavefunction". Formally, the KS orbitals are pure mathematical constructs useful only in construction of the density. In practice, however, the shapes of KS orbitals tend to be remarkably similar to canonical HF MOs and they can be quite useful in qualitative analysis of chemical properties. If we think of the procedure by which they are generated, there are indeed a number of reasons to prefer KS orbitals to HF orbitals. For instance, all KS orbitals, occupied and virtual, are subject to the same external potential. HF orbitals, on the other hand, experience varying potentials, and, in particular, HF virtual orbitals experience the potential that would be felt by

an extra electron being added to the molecule. As a result, HF virtual orbitals tend to be too high in energy and anomalously diffuse compared to KS virtual orbitals. This fact is especially important for crystalline solids and explains why HF bandgaps are overestimated compared to those in DFT and experiment. Unfortunately, for some choices of exchange-correlation potential DFT bandgaps are too small in comparison with the experimental data. In *exact* DFT, it can also be shown that the eigenvalue of the highest KS MO is the exact first ionization potential, i.e. there is a direct analogy to Koopmans' theorem for this orbital—in practice, however, *approximate* functionals are quite poor at predicting IPs in this fashion without applying some sort of correction scheme, e.g. an empirical linear scaling of the eigenvalues.

The Slater determinant formed from the KS orbitals is the exact wavefunction for the fictitious *noninteracting* system having the same density as the real system. This KS Slater determinant has certain interesting properties by comparison to its HF analogs. It is an empirical fact that DFT is generally much more robust in dealing with open-shell systems where UHF methods show high spin contamination, i.e. incorporates some higher spin states (doublets are contaminated by quartets and sextets, while triplets are contaminated by pentets and heptets). The degree of spin contamination can be estimated by inspection of $\langle S^2 \rangle$, which should be 0.0 for a singlet, 0.75 for a doublet, 2.00 for a triplet, etc. Note, incidentally, that the expectation values of S^2 are sensitive to the amount of HF exchange in the functional. A "pure" DFT functional nearly always shows very small spin contamination, and each added per cent of HF exchange tends to result in a corresponding percentage of the spin contamination exhibited by the HF wavefunction. This behavior can make the hybrid HF-DFT functionals useful for open-shell systems (see next subsection).

The formal scaling behavior of DFT is, in principle, no worse than N^3, where N is the number of basis functions used to represent the KS orbitals. This is better than HF by a factor of N, and very substantially better than other methods that include electron correlation.

The most common methods for solving KS equations proceed by expanding the Kohn–Sham orbitals in a basis set. DFT has a clear advantage over HF in its ability to use basis functions that are not necessarily contracted Gaussians. The motivation for using contract GTOs is that arbitrary four-center two-electron integrals can be solved analytically. In the electronic-structure programs where DFT was added as a new feature to the existing HF code the representation of the density in the classical electron-repulsion operator is carried out using the KS orbital basis functions. Thus, the net effect is to create a four-index integral and these codes inevitably continue to use contracted GTOs as basis functions. In particular, such a scheme is used in the CRYSTAL code [17]. However, if the density is represented using an auxiliary basis set, or even represented numerically, other options are available for the KS orbital basis set, including STFs. The SIESTA density-functional code [44] for crystalline solids uses the numerical AO basis instead of GTO. STO have the advantage that fewer of them are required (since they have correct cusp behavior at the nuclei), and certain advantages associated with symmetry that can be used even more readily, so they speed up calculations considerably. The Amsterdam density-functional code

and its BAND version for solids [45] makes use of STO basis functions covering atomic numbers 1–118.

Another interesting possibility is the use of plane waves as basis sets in periodic infinite systems (crystalline solids) represented using periodic boundary conditions. While it takes an enormous number of plane waves to properly represent the decidedly aperiodic densities that are possible within the unit cells of interesting chemical systems, the necessary integrals are particularly simple to solve, and thus this approach has found wide use in solid-state physics.

3.3.3 Climbing the Jacob's Ladder for Exchange-Correlation Functionals

The effective potential (3.40) includes the external potential and the effects of the Coulomb interactions between the electrons, e.g. the exchange and correlation interactions. In principle, it also includes the difference in kinetic energy between the fictitious noninteracting system and the real system. In practice, however, this difference is ignored in many modern functionals as empirical parameters appear that necessarily introduce some kinetic-energy correction if they are based on experiment [70].

Modeling the exchange and correlation interactions becomes difficult within KS DFT as the exact functionals for exchange and correlation are not known except for the homogeneous (uniform) electron gas. However, approximations exist that permit the calculation of real systems.

Perdew [113] described a Jacobs ladder in which the "rungs" (levels of sophistication) of density functional approximations ultimately lead to the "Heaven" of chemical accuracy [114], see Fig. 3.5.

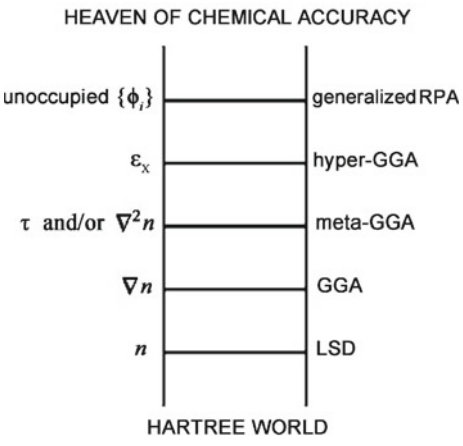

Fig. 3.5 Jacob's ladder of density functional approximations to the exchange-correlation energy, n is an electron density (Reprinted figure with permission from Perdew et al. [113], Copyright (2005) by the AIP Publishing LLC)

The first "rung" consists of density functionals that are classified as local spin density approximation (LSD) and local density approximation (LDA). The second "rung" consists of semilocal density functionals that depend explicitly on both the electron density and the density gradient and are referred to as generalized gradient approximations (GGAs). The GGA density functionals increase the level of accuracy previously achieved by the LDA.

More accurate functionals of higher "rungs" can be called "beyond-GGA functionals" or nonlocal functionals.

The third-"rung" consists of density functionals that in addition to the electron density and the density gradient depend explicitly on the kinetic energy-density, expressed in terms of the occupied KS orbitals. Density functionals in the third "rung" are called Meta-GGA (MGGA) and they strive for wider applicability and better accuracy than LDA or GGA functionals [114, 115].

Fourth-rung hybrid functionals mix a fraction of the Hartree-Fock exchange ϵ_x into the DFT exchange functional i.e. the wave-function-based HF method is combined with the density-based theory. Walter Kohn, the Nobel Prize Winner in chemistry writes in his Nobel lecture [4] that wave-function- based and density-based theories, will in complementary ways, continue not only to give us quantitatively more accurate results, but also contribute to a better physical/ chemical understanding of the electronic structure of matter.

MGGA and hybrid functionals can be called orbital-dependent functionals because they are not only represented in terms of the electron density, but also contain parts represented in single-particle Kohn–Sham orbitals $\varphi_i(\boldsymbol{r})$. In MGGA functionals the kinetic energy density $\tau(\boldsymbol{r}) = 1/2\sum_i |\nabla\varphi_i(\boldsymbol{r})|^2$ is included. In hybrid functionals the nonlocal HF exchange energy is also an orbital-dependent functional. Still another type of orbital functional is the self-interaction correction (SIC).

The fifth "rung" density-functionals, called double-hybrid, are considerably more complex. A double hybrid functional includes a certain amount of HF exchange and the perturbative second-order correlation part PT2 (hence double hybrid) [116]. In this case the unoccupied KS orbitals are included in the calculation.

The simplest approximation is the local-density approximation (LDA), based upon the exact exchange energy for a uniform electron gas, which can be obtained from the Thomas–Fermi (TF) model, and from fits to the correlation energy for a uniform electron gas.

In the TF model it is suggested that the number of electrons is so large that the system could be treated using quantum-statistical arguments. The approximation in the TF model concerns kinetic energy. For a homogeneous interaction-free electron gas the density is constant and the average kinetic energy per particle is $\varepsilon_t^{hom} = Cn^{5/3}$. The kinetic energy per unit volume in this model is $n\varepsilon_t^{hom}$. If the electron density varies sufficiently slowly in space $T^{LDA} = \int d^3\boldsymbol{r}\varepsilon_t^{hom}(\rho(\boldsymbol{r}))$ can serve as a workable approximation for the kinetic-energy functional.

If this is combined with the expression for the nuclei–electron attractive potential and the electron–electron Hartree repulsive potential we have the TF expression for the energy of a homogeneous gas of electrons in a given external potential:

$$E_{TF}[\rho(\boldsymbol{r})] = C_F \int \rho^{5/3}(\boldsymbol{r}) d^3\boldsymbol{r} - \sum_j \frac{Z_j}{|\boldsymbol{r} - \boldsymbol{R}_j|}\rho(\boldsymbol{r}) + \frac{1}{2}\int\int \frac{\rho(\boldsymbol{r})\rho(\boldsymbol{r}')}{|\boldsymbol{r} - \boldsymbol{r}'|} d^3\boldsymbol{r} d^3\boldsymbol{r}' \tag{3.44}$$

The importance of this equation lies not so much in how well it is able to really describe even the energy of an atom, as in that the energy is given completely in terms of the electron density $\rho(\boldsymbol{r})$.

This is an example of a density-functional for energy allowing us to map the density $\rho(\boldsymbol{r})$ onto the energy E without any additional information required. Furthermore, the TF model employs the variational principle assuming that the ground state of the system is connected to the electron density for which the energy (3.44) is minimized under the constraint of $N = \int d^3\boldsymbol{r}\rho(\boldsymbol{r})$.

The exchange-correlation energy E_{XC} is approximated by a sum of the exchange E_X and correlation E_C energies.

In LDA, for the exchange energy calculation the Dirac–Slater exchange energy is used

$$E_X[\rho] = C_X \int \rho^{4/3}(\boldsymbol{r}) d^3\boldsymbol{r} \tag{3.45}$$

or the more complicated suggested by Barth and Hedin [117].

For the correlation energy functional $E_C[\rho(\boldsymbol{r})]$ the situation is more complicated since even for a homogeneous electron gas it is not known exactly. Early approximate expressions for correlation in homogeneous systems were based on applying the perturbation theory. With the advent of highly precise calculations of correlation energy for the electron liquid by Ceperley and Alder (CA) [118] the approximations for the correlation energy in a homogeneous system are made by a parameterization of CA data for a free-electron gas. There are known parameterizations of Vosko–Wilk–Nisair [119], Perdew–Zunger [120] and Perdew–Wang [121]. The three latter parameterizations of the LDA are implemented in most standard DFT program packages (both for molecules and solids) and in many cases give almost identical results. On the other hand, the earlier parameterizations of the LDA, based on perturbation theory can deviate substantially and should be better avoided.

The functional dependence of E_{XC} on the electron density is expressed as an interaction between the electron density and "an energy density" ε_{XC} that is dependent on the electron density

$$E_{XC}[\rho(\boldsymbol{r})] = \int \rho(\boldsymbol{r})\varepsilon_{XC}[\rho(\boldsymbol{r})] d^3\boldsymbol{r} \tag{3.46}$$

The energy density ε_{XC} is treated as a sum of individual exchange and correlation contributions. Two different kinds of densities are involved [70]: the electron density is a per unit volume density, while the energy density is a per particle density. The LDA for E_{XC} formally consists in

$$E_{XC}^{LDA}[\rho(\boldsymbol{r})] = \int d^3\boldsymbol{r}\left[\varepsilon_X^{hom}[\rho(\boldsymbol{r})] + \varepsilon_C^{hom}[\rho(\boldsymbol{r})]\right] = \int d^3\boldsymbol{r}\varepsilon_{XC}^{hom}[\rho(\boldsymbol{r})] \tag{3.47}$$

The energy densities ε_X^{hom}, ε_C^{hom} refer to a homogeneous system, i.e. the exchange-correlation energy is simply an integral over all space with the exchange-correlation energy density at each point assumed to be the same as in a homogeneous electron gas with that density. Nevertheless, LDA has proved amazingly successful, even when applied to systems that are quite different from the electron liquid that forms the reference system for the LDA.

In the local spin-density approximation (LSDA) the exchange-correlation energy can be written in terms of either of the two spin densities $\rho^\alpha(\boldsymbol{r})$ and $\rho^\beta(\boldsymbol{r})$

$$\begin{aligned} E_{XC}^{LSDA}[\rho^\alpha(\boldsymbol{r}), \rho^\beta(\boldsymbol{r})] &= \int d^3\boldsymbol{r}\rho(\boldsymbol{r})\varepsilon_{XC}^{hom}[\rho^\alpha(\boldsymbol{r}), \rho^\beta(\boldsymbol{r})] \\ &= \int d^3\boldsymbol{r}\rho(\boldsymbol{r})\left[\varepsilon_X^{hom}\left[\rho^\alpha(\boldsymbol{r}), \rho^\beta(\boldsymbol{r})\right] + \varepsilon_C^{hom}\left[\rho^\alpha(\boldsymbol{r}), \rho^\beta(\boldsymbol{r})\right]\right] \end{aligned} \tag{3.48}$$

or the total density $\rho(\boldsymbol{r})$ and the fractional spin polarization $\zeta(\boldsymbol{r}) = (\rho^\alpha(\boldsymbol{r}) - \rho^\beta(\boldsymbol{r}))/\rho(\boldsymbol{r})$.

For many decades the LDA has been applied in, e.g. calculations of band structures and total energies in solid-state physics. The LDA provides surprisingly good results for metallic solids with delocalized electrons, i.e. those that most closely resemble the uniform electron gas (jellium). At the same time, there are well-known disadvantages of the LDA for solids. It revealed systematic shortcomings in the description of systems with localized electrons and as a result the underestimation of the bond distances and overestimation of the binding energies. LDA calculations as a rule give calculated bandgaps that are too small. In the quantum chemistry of molecules the LDA is much less popular because the local formulation of the energy expression does not account for the electronic redistribution in bonds. For well-localized electrons the nonexact cancellation of the self-energy part (self-interaction) of the Hartree term in the LDA exchange functional is important (in HF energy the self-energy part in the Hartree term is cancelled by the corresponding part of the exchange term). The LDA fails to provide results that are accurate enough to permit a quantitative discussion of the chemical bond in molecules (so-called "chemical accuracy" requires calculations with an error of not more than about 1 kcal/mol per particle). The LDA exploits knowledge of the density at the point $\rho(\boldsymbol{r})$. Real systems, such as molecules and solids, are inhomogeneous (the electrons are exposed to the spatially varying electric fields produced by the nuclei) and interacting (the electrons interact via the Coulomb interaction). The way density-functional theory, in the local-density approximation, deals with this inhomogeneous many-body problem is by decomposing it into two simpler (but still highly nontrivial) problems: the solution of the spatially uniform many-body problem (the homogeneous electron liquid) yields the uniform exchange-correlation energy, and the solution of a spatially inhomogeneous noninteracting problem (the inhomogeneous electron gas) yields the particle density. Both steps are connected by the local-density approximation, which shows how the exchange-correlation energy of the uniform interacting system enters the equations for the inhomogeneous noninteracting system.

We note that both the local density approximation and the local exchange approximation use only the diagonal part of the density matrix $\rho(\boldsymbol{r}, \boldsymbol{r}')$, i.e. $\rho(\boldsymbol{r}) = \rho(\boldsymbol{r}, \boldsymbol{r})$. However these approximations are different in their nature. In LDA the local density is used to include both the exchange and correlation of electrons, in the local exchange approximation to the HF exchange the electron correlation is not taken into account at all.

The particular way in which the inhomogeneous many-body problem is decomposed, and the various possible improvements over the LDA, are behind the success of DFT in practical calculations, in particular, those of materials. The most important improvement over LDA is the attempt to introduce a spatially varying density and include information on the rate of this variation in the functional. The corresponding functionals are known as semilocal functionals [107].

The first successful extensions for the LDA were developed in the early 1980s, when it was suggested that the density $\rho(\boldsymbol{r})$ be supplemented at a particular point $\boldsymbol{r}$ with information about the gradient of the electron density at this point in order to account for the nonhomogeneity of the true electron density [100]. LDA was interpreted as the first term of the Taylor expansion of the uniform density, the form of the functional was termed the gradient expansion approximation (GEA). The authors expected to obtain better approximations of the exchange-correlation functional by extending the series with the next lowest term. In practice, the inclusion of low-order gradient corrections almost never improves the LDA, and often actually makes it worse. The reason for this failure is that for GEA the exchange-correlation hole has lost many of the properties that made the LDA hole physically meaningful [100]. Higher-order corrections, on the other hand, are exceedingly difficult to calculate, and little is known about them.

It was a major breakthrough when it was realized, in the early 1980s, that instead of power-series-like systematic gradient expansions one could experiment with more general functions of $\rho(\boldsymbol{r})$ and $\nabla\rho(\boldsymbol{r})$, which do not need to proceed order by order. Such functionals, of the general form

$$E_{XC}^{GGA}[\rho_\alpha, \rho_\beta] = \int d^3\boldsymbol{r} f(\rho_\alpha, \rho_\beta, \nabla\rho_\alpha, \nabla\rho_\beta) \tag{3.49}$$

have become known as generalized-gradient approximations (GGAs), [122]. GGA functionals are the workhorses of the current density-functional theory. Different GGAs differ in the choice of the function $f(\rho, \nabla\rho)$. Note that this makes different GGAs much more different from each other than the different parameterizations of the LDA: essentially there is only one correct expression for $\varepsilon_{XC}^{hom}(\rho)$ and the various parameterizations of the LDA are merely different ways of writing it [107]. On the other hand, depending on the method of construction employed for obtaining $f(\rho, \nabla\rho)$, one can obtain very different GGAs. In particular, GGAs used in molecular quantum chemistry typically proceed by fitting parameters to test sets of selected molecules. On the other hand, the GGAs used in solid state theory tend to emphasize exact constraints on the density-functional for the exchange-correlation energy [113].

In this approach, the density-functional approximations are assigned to various rungs according to the number and kind of their local ingredients [113].

The semiempirical functionals are fitted to selected data from experiment or from the ab-initio calculations. The higher the rung of the functional the larger is the number of parameters (functionals with as many as 21 fit parameters are popular in chemistry). Is DFT ab-initio or semiempirical? As was suggested in [113], it can fall in between as a nonempirical theory when the functionals are constructed without empirical fitting.

The best nonempirical functional for a given rung is constructed to satisfy as many exact theoretical constraints as possible while providing satisfactory numerical predictions for real systems [113]. Once a rung has been selected, there remains little choice of which constraints to satisfy (but greater freedom in how to satisfy them), [113]. Accuracy is expected to increase up the ladder of rungs as additional local ingredients enable the satisfaction of additional constraints. A short summary of the exact constraints on $E_{XC}[\rho]$ can be found in [113]. In this paper some useful recommendations for DFT users are also given. Users should not randomly mix and match the functionals, but use exchange and correlation pieces designed to work together, with their designer-recommended local parts. They should not shop indiscriminately for the functional that "works best". Users should always specify which functional they used, with its proper name and literature reference, and why they chose it. Statements like "we used the density-functional theory" or "we used the generalized gradient approximation" are almost useless to a reader or listener who wants to reproduce the results.

Nowadays, the most popular (and most reliable) GGA functionals are PBE (denoting the functional proposed in 1996 by Perdew et al. [123] in physics, and BLYP (denoting the combination of Becke's 1988 exchange functional [124] with the 1988 correlation functional of Lee et al. [125]) in chemistry. A detailed consideration of the PBE functional can be found in [126].

PWGGA denotes the GGA functional suggested by Perdew and Wang [33, 122]. Many other GGA-type functionals are also available, and new ones continue to appear. The new meta-GGA (MGGA) functional TPSS (Tao–Perdew–Staroverov–Scuseria) [127] supersedes the older PKZB (Perdew–Kurth–Zupan–Blaha) functional [128]. The known functionals are modified as has been done recently for the PBE functional to improve its accuracy for the thermodynamic and electronic properties of molecules [115, 129].

Recently, several new GGA functionals have been proposed to improve the description of solids: Armiento-Mattsson (AMO5) [130], Wu-Cohen (WC06) [131] and the modified PBE GGA for solids (PBEsol) [132]. A short discussion of them can be found in [133]. Both WC06 and PBEsol are based on the PBE functional. In the former, the exchange part of the PBE functional is slightly modified to recover the fourth-order parameters of the gradient expansion in the limit of the slowly varying electron density. The PBEsol functional has the same analytical form as the PBE except that of the two parameters are changed in order to satisfy the constraints that are more appropriate for solids. The AM05 functional was developed in quite a different framework, the so-called subsystem functional scheme in which a

general functional is obtained by combining functionals obtained from different model systems. All these new functionals have been systematically investigated for comprehensive sets of solids with different bonding characters, and have shown significant improvements over the LDA and PBE, in particular for equilibrium lattice constants [134]. On the other hand, these new GGA functionals still suffer from the failure to treat the van der Waals dispersion interaction. The layered materials (being the base for the nanotube production, see Part II) are characterized by quasitwo-dimensional layered structure, and the inter-layer interaction is usually held to be of van der Waals character. The performance of LDA and GGA functionals for layered materials has been rarely investigated. In [135], $MoSe_2$ was included in a set of solids to test different GGA functionals. It was found that while the PBE overestimates the lattice constant c by 17 %, WC06 does it by only 2 %. A systematic investigation of LDA and GGA functionals for the layered materials ZrX_2 and HfX_2 (X = S,Se) is performed in [133], using the FPLAPW method.

The PBE functional [128] has two nonempirical derivations based on the exact properties of the XC hole [123] and energy [136].

The PBE GGA correctly reduces to LSD for uniform electron densities, its correlation component recovers the slowly varying ($t \to 0$) and rapidly varying ($t \to \infty$) limits of the numerical GGA. Under uniform scaling ($\rho(\boldsymbol{r}) \to \lambda^3 \rho(\lambda \boldsymbol{r})$), the PBE exchange energy scales like λ (as does the exact exchange functional) and the PBE correlation energy correctly scales to a constant as $\lambda \to \infty$. For small-amplitude density variations around a uniform density, LSD is a very good approximation. The PBE functional recovers this limit. The PBE functional satisfies the Lieb–Oxford bound [137]:

$$E_X^{PBE}[\rho_\alpha, \rho_\beta] \geq E_{XC}^{PBE}[\rho_\alpha, \rho_\beta] \geq 2.273 E_X^{LDA}[\rho] \tag{3.50}$$

A useful way to compare GGA functionals is to write

$$E_{XC}^{GGA}[\rho_\alpha, \rho_\beta] \approx \int d^3\boldsymbol{r} \rho \varepsilon_X(\rho) F_{XC}(r_s, \zeta, s) \tag{3.51}$$

where the enhancement factor $F_{XC}(r_s, \zeta, s)$ over the local exchange depends upon the local radius r_s ($r_s \lesssim 1$ for the core electrons and $r_s \gtrsim 1$ for the valence electrons), the spin polarization ζ and inhomogeneity s. The s-dependence of F_{XC} is the nonlocality of the GGA. We see that the nonempirical PBE functional best fulfils many of the physical and mathematical requirements of DFT. The application of the PBE functional in the calculations of bulk crystals and nanostructures is considered in Part II of this book.

At the same time, there are some failures of the PBE functional essential for extended systems. For example, the exact exchange-correlation hole in crystals can display a diffuse long-range tail that is not properly captured by the GGA (such a diffuse hole arises in the calculation of the surface energy of a metal). Neither the LSD nor the GGA correctly describes the long-range tail of the van der Waals interaction. Corrections of these failures might be made possible by using orbital-dependent or hybrid functionals.

The density-functional theory, even with rather crude approximations such as the LDA and the GGA, is often better than Hartree-Fock: the LDA is remarkably accurate, for instance, for geometries and frequencies, and the GGA has also made bond energies quite reliable. Therefore, "the aura of mystery" appeared around DFT (see discussion of this by Baerends and Gritsenko [138]). The simple truth is not that LDA/GGA is particularly good, but that Hartree-Fock is rather poor in the two-electron chemical-bond description. This becomes clear when one considers the statistical two-electron distribution, which is usually cast in terms of the exchange-correlation hole: a decrease in the probability of finding other electrons in the neighborhood of a reference electron, compared to the (unconditional) one-electron probability distribution [100].

The concept of electron density, which provides an answer to the question "how likely is it to find one electron of arbitrary spin within a particular volume element while all other electrons may be anywhere" can be extended to the probability of finding not one but a pair of two electrons with spins σ_1 and σ_2 simultaneously within two volume elements $d\boldsymbol{r}_1$ and $d\boldsymbol{r}_2$, while the remaining $N-2$ electrons have arbitrary positions and spins [100].

The exchange-correlation hole describes the change in the conditional probability caused by the correction for self-interaction, exchange and Coulomb correlation, compared to the completely uncorrelated situation. It can formally be split into the Fermi hole, $h_x^{\sigma_1=\sigma_2}(\boldsymbol{r}_1,\boldsymbol{r}_2)$ and the Coulomb hole $h_c^{\sigma_1,\sigma_2}(\boldsymbol{r}_1,\boldsymbol{r}_2)$

$$h_{xc}(\boldsymbol{x}_1,\boldsymbol{x}_2) = h_x^{\sigma_1=\sigma_2}(\boldsymbol{r}_1,\boldsymbol{r}_2) + h_c^{\sigma_1,\sigma_2}(\boldsymbol{r}_1,\boldsymbol{r}_2) \tag{3.52}$$

The exchange hole h_x applies only to electrons with the same spin, the correlation hole h_c has contributions for electrons of either spin and is the hole resulting from the $1/r_{12}$ electrostatic interaction. This separation is convenient but only the total xc hole has a real physical meaning. In the HF method the Fermi hole is accounted for through the use of a single Slater determinant, whereas the Coulomb hole is neglected. Like the total hole, the Fermi hole contains exactly the charge of one electron $\int h_x(\boldsymbol{r}_1,\boldsymbol{r}_2)d\boldsymbol{r}_2 = -1$ and takes care of the self-interaction correction (SIC). The exchange hole h_x is negative everywhere $h_x(\boldsymbol{r}_1,\boldsymbol{r}_2) < 0$ and its actual shape depends not only on the Fermi correlation factor but also on the density at $\boldsymbol{r}_2$. As a consequence, h_x is not spherically symmetric.

The Coulomb hole must be normalized to zero and this result is independent of the positions of electrons with $\sigma' \neq \sigma$: $\int h_c(\boldsymbol{r}_1,\boldsymbol{r}_2)d\boldsymbol{r}_2 = 0$.

The essential error of the Hartree-Fock method arises from the fact that in the HF model the exchange-correlation hole in a two-electron bond is not centered around the reference electron, but is too delocalized, having considerable amplitude on both atoms involved in the bond. The LDA and GGA models incorporate, simply by using an electron-centered hole, an important part of the effect of the interelectron Coulomb repulsion. To improve the LDA and GGA models orbital-dependent functionals are introduced. The introduction of orbital dependence, not only density and gradient dependence, into the functionals can be realized in different ways [107]. Hybrid HF-DFT functionals are the most popular beyond-GGA functionals. These

functionals mix a fraction of the HF exchange into the DFT exchange functional and use the DFT correlation part. But why is the exact HF exchange mixed with the approximate DFT exchange part? How can one find the weights of this mixing? May be it would be possible to use the exact HF exchange and rely on approximate functionals only for the part missing in the HF model, i.e. the electron correlation: $E_{xc} = E_x^{HF} + E_c^{KS}$ (EXX—orbital-dependent exact exchange functional). The HF exchange is calculated using the KS orbitals so that the EXX energy will be slightly higher than the HF energy. The orbital-dependent exact-exchange (EXX) group of methods has received much attention in the literature. Two advantages of the EXX functional are often mentioned: (a) the self-interaction correction is incorporated in this functional; (b) it is natural to break up the total problem of electron–electron interaction in the large (due to self-interaction correction) exchange part and the small correlation part. The hope is of course that it will be simpler to find an accurate density-functional for the small correlation energy.

Critical analysis of the EXX method in DFT can be found, for example, in [100, 138]. The true xc hole is substantially more localized around the reference electron. That is why rough localized model holes, like those of the GGA, which approximate this total hole, are so successful.

The LDA and GGA total holes are localized around the reference electron, which is a definite advantage, as EXX approximation cannot be regarded to be the next improvement over the GGA. There are other possibilities of such an improvement: (1) to develop orbital-dependent functionals, which represent exchange and correlation simultaneously; (2) use HF-DFT exchange mixing.

The first possibility was realized recently, for example, in [139] where the virtual orbital-dependent xc functional E_{xc}^{BB} (BB, Buijse–Baerends) is suggested:

$$E_{xc}^{BB}\left[\{\varphi_j\},\{\varphi_a\}\right] = -\frac{1}{2}\sum_{i}^{M}\sum_{j}^{M}\sqrt{w_i w_j}\int d\boldsymbol{r}_1 d\boldsymbol{r}_2 \frac{\varphi_i(\boldsymbol{r}_1)\varphi_i(\boldsymbol{r}_2)\varphi_j(\boldsymbol{r}_1)\varphi_j^*(\boldsymbol{r}_2)}{r_{12}} \quad (3.53)$$

and applied in the calculations of hydrogen chains H_n and small molecules. Here $w_i[\rho]$ is the xc orbital weight, which governs the involvement of the occupied/virtual orbital φ_i in the xc functional. It is important that the summation in (3.53) is made over $M = N_{occ} + N_v$ orbitals, where N_{occ} and N_v are the numbers of occupied and virtual KS orbitals. By giving weights to the virtual orbitals one can incorporate the effect of correlation. In [140] the functional form of w_i was approximated with the Fermi-type distribution

$$w_i = \frac{2}{1+\exp(f(\varepsilon_i - \varepsilon_F))} \quad (3.54)$$

where ε_i are the KS orbital energies and ε_F is the Fermi-level parameter. We do not consider the E_{xc}^{BB} functional in more detail as its possibilities for crystals are not well understood.

The second possibility of GGA improvement—the mixing of HF and DFT exchange—is used in the well-known B3LYP, B3PW and PBE0 hybrid functionals.

In Kohn–Sham density-functional theory, the exchange-correlation energy is rigorously given by

$$E_{xc} = \frac{1}{2}\int \rho(\boldsymbol{r}) \int \frac{h_{xc}(\boldsymbol{r},\boldsymbol{r}')}{|\boldsymbol{r}'-\boldsymbol{r}|} d^3\boldsymbol{r}' d^3\boldsymbol{r} \tag{3.55}$$

$$h_{xc}(\boldsymbol{r},\boldsymbol{r}') = \int_0^1 h_{xc}^{\lambda}(\boldsymbol{r},\boldsymbol{r}')d\lambda \tag{3.56}$$

known as the "adiabatic connection" or "coupling strength integration". In this most fundamental of DFT formulas, h_{xc} is an effective exchange-correlation hole, and λ is a coupling-strength parameter that switches on interelectronic $1/r_{12}$ repulsion, subject to a fixed electronic density (achieved, in principle, by suitably adjusting the external potential as a function of λ). The Kohn–Sham h_{xc} is therefore a coupling strength average of h_{xc}^{λ} as it evolves from $\lambda = 0$ through $\lambda = 1$ [141].

In an atom, the size of the hole is relatively insensitive to λ and remains of roughly atomic size. In a molecule, the changes in the character and size of the hole occur as λ varies from its noninteracting $\lambda = 0$ to its fully interacting $\lambda = 1$ limits. At $\lambda = 0$ (pure exchange with no correlation whatsoever) delocalization of the hole over two or more centers is characteristic. Accurate DFTs must recognize this $\lambda = 0$ nonlocality. As λ increases, the hole is localized by the long-range, nondynamical, left–right correlations that are absent in atoms but operative in molecules. At the fully interacting limit ($\lambda = 1$), the hole is localized to roughly atomic size. To incorporate the necessary nonlocality Becke [142] proposed so-called hybrid functionals

$$E_{xc}^{hyb} = E_{xc}^{KS} + a_{mix}\left(E_x^{HF} - E_x^{KS}\right) \tag{3.57}$$

The difference from the EXX functional is the following: the exact HF exchange E_x^{HF} is mixed with the DFT (LDA, GGA) exchange-correlation energy in hybrid functionals and with the DFT correlation energy in EXX functionals. The mixing parameter a_{mix} is used to patch an appropriate amount of HF exchange into the exchange-correlation energy. Even the simplest "half-half" hybrid functional ($a_{mix} = 0.5$) greatly improves the calculated properties, compared with the pure DFT results. Becke developed 3-parameter functional expressions known as B3PW and B3LYP hybrid functionals:

$$E_{xc}^{B3PW} = E_{xc}^{LSDA} + a\left(E_x^{HF} - E_x^{LSDA}\right) + b\Delta E_x^{Becke} + c\Delta E_x^{PW} \tag{3.58}$$

$$E_{xc}^{B3LYP} = E_{xc}^{LSDA} + a\left(E_x^{HF} - E_x^{LSDA}\right) + b\Delta E_x^{Becke} + c\Delta E_x^{LYP} \tag{3.59}$$

The B3PW functional (3.58) uses in E_{xc} the Becke [124] exchange and Perdew–Wang exchange-correlation [122], while in the B3LYP functional (3.59) the correlation part is that suggested by Lee–Yang–Parr [125]. The a, b, c parameters were optimized

to fit the experimental data and do not depend on the molecule under consideration. It is clear that the choice of hybrid functionals is motivated by reasonable physical arguments. The term $a\left(E_x^{HF} - E_x^{LSDA}\right)$ replaces some electron-gas exchange with the exact exchange to capture the proper small-λ limit in (3.55). The coefficient a reflects the rate of onset correlation as it increases from zero. The other terms allow optimum admixtures of exchange and correlation-type gradient corrections. These hybrid functionals are the simplest mixture of the exact exchange, the LSDA for exchange-correlation, and gradient corrections of exchange and correlation type, that exactly recovers the uniform electron-gas limit. The B3LYP functional is the most popular one in molecular quantum chemistry. Nevertheless, the correct amount of HF exchange included in any hybrid functional cannot be a constant over all species or even all geometries of a single species [143]. The rationale for mixing the exact exchange with the DFT approximation is discussed in [144]. The authors write the hybrid functional in the form

$$E_{xc} \cong E_{xc}^{KS} + \frac{1}{n}\left(E_x - E_x^{KS}\right) \tag{3.60}$$

where the optimum integer n can be found from the perturbation theory and $n = 4$ for the atomization energies of typical molecules. Such a formally parameter-free hybrid functional with a PBE exchange-correlation part is known as the PBE0 hybrid functional. A simplification of hybrid exchange-correlation functionals was suggested by Becke [141], based on the simulation of delocalized exact exchange by local density-functionals. A simple model was introduced that detects exchange hole delocalization in molecules through a local variable related to kinetic-energy density.

In the next section we consider the extension of DFT methods to the periodic systems, including the monoperiodic nanostructures.

3.4 LCAO and Density Functional Tight Binding (DFTB) Methods for Periodic Systems

3.4.1 LCAO DFT Method for Periodic Systems

We discuss here the KS LCAO method for crystals in comparison with the HF LCAO approach (Sect. 3.2). The electronic energy of the crystal (per primitive cell) as calculated within the HF approximation (E_{HF}) and DFT (E_{DFT}) can be expressed in terms of the one-electron density matrix (DM) of the crystal defined as $P(\boldsymbol{k})$ in terms of the Bloch sums of AOs, or as $\rho(\boldsymbol{R}, \boldsymbol{R}')$ in coordinate space. These expressions are:

$$E_{HF}[\rho] = E_0[\rho] + E_H[\rho] + E_X[\rho] \tag{3.61}$$

$$E_{DFT}[\rho] = E_0[\rho] + E_H[\rho] + E_{XC}[\rho] \tag{3.62}$$

where $E_0[\rho]$ is defined as the expectation value of the one-electron operator $\hat{h}(\boldsymbol{R})$

$$E_0[\rho] = \frac{1}{N} \int\limits_{V_N} d^3\boldsymbol{R}[\hat{h}(\boldsymbol{R})\rho(\boldsymbol{R}, \boldsymbol{R}')]_{\boldsymbol{R}'=\boldsymbol{R}} \tag{3.63}$$

$E_H[\rho]$ is the Coulomb (Hartree) energy,

$$E_H[\rho] = \frac{1}{N} \int\limits_{V_N} d^3\boldsymbol{R} \int\limits_{V_N} d^3\boldsymbol{R}' \frac{\rho(\boldsymbol{R}, \boldsymbol{R})\rho(\boldsymbol{R}', \boldsymbol{R}')}{|\boldsymbol{R} - \boldsymbol{R}'|} \tag{3.64}$$

$E_X[\rho]$ is the HF exchange energy,

$$E_X[\rho] = -\frac{1}{2N} \int\limits_{V_N} d^3\boldsymbol{R} \int\limits_{V_N} d^3\boldsymbol{R}' \frac{|\rho(\boldsymbol{R}, \boldsymbol{R}')|^2}{|\boldsymbol{R} - \boldsymbol{R}'|} \tag{3.65}$$

and $E_{XC}[\rho]$ in (3.62) is the exchange-correlation energy functional of density $\rho(\boldsymbol{R}, \boldsymbol{R}) = \rho(\boldsymbol{R})$ (different expressions for this functional depend on the DFT version and were discussed in the next subsection). The electron position vector $\boldsymbol{R}$ is supposed to be written as the sum $\boldsymbol{R} = \boldsymbol{r} + \boldsymbol{R}_n$, where $\boldsymbol{R}_n$ specifies the primitive cell and $\boldsymbol{r}$ is the position vector of an electron within this primitive cell. The difference between the HF exchange energy E_X and DFT exchange-correlation energy E_{XC} is the following: the former depends on the total DM $\rho(\boldsymbol{R}, \boldsymbol{R}')$, the latter only on DM diagonal elements $\rho(\boldsymbol{R})$, i.e. electron density.

In the HF approximation and DFT, the crystal orbitals are solutions to the equations

$$\hat{F}(\boldsymbol{k})\varphi_i(\boldsymbol{k}) = \varepsilon_i(\boldsymbol{k})\varphi_i(\boldsymbol{k}) \tag{3.66}$$

where the one-electron operator $\hat{F}(\boldsymbol{k})$ is either the HF operator, $\hat{F}^{HF}(\boldsymbol{k})$

$$\hat{F}^{HF}(\boldsymbol{k}) = \hat{H}(\boldsymbol{k}) + \hat{J}(\boldsymbol{k}) + \hat{X}(\boldsymbol{k}) \tag{3.67}$$

or the Kohn–Sham operator $\hat{F}^{KS}(\boldsymbol{k})$,

$$\hat{F}^{KS}(\boldsymbol{k}) = \hat{H}(\boldsymbol{k}) + \hat{J}(\boldsymbol{k}) + \hat{V}_{XC}(\boldsymbol{k}) \tag{3.68}$$

Here, $\hat{H}(\boldsymbol{k})$ is a one-electron operator that describes the motion of an electron in the crystal and is equal to the sum of the kinetic-energy operator and the Coulomb interaction operator between the electron and fixed atomic nuclei and $\hat{J}(\boldsymbol{k})$ and $\hat{X}(\boldsymbol{k})$ are the Coulomb and exchange operators, respectively, which describe the interaction of the given electron with the other electrons of the crystal.

In the LCAO basis, both the Hartree-Fock and Kohn–Sham equations are :

$$F(\boldsymbol{k})C(\boldsymbol{k}) = S(\boldsymbol{k})C(\boldsymbol{k})E(\boldsymbol{k}) \tag{3.69}$$

The HF and KS operators in the reciprocal space are represented by the Fock matrices $F^{HF}_{\mu\nu}(\boldsymbol{k})$ and Kohn–Sham matrices $F^{KS}_{\mu\nu}(\boldsymbol{k})$, which are related to the matrices in the coordinate space by the relations

$$F^{HF}_{\mu\nu}(\boldsymbol{k}) = \sum_{\boldsymbol{R}_n} \exp(i\boldsymbol{k}\boldsymbol{R}_n)\left[h_{\mu\nu}(\boldsymbol{R}_n) + j_{\mu\nu}(\boldsymbol{R}_n) + x_{\mu\nu}(\boldsymbol{R}_n)\right] \tag{3.70}$$

$$F^{KS}_{\mu\nu}(\boldsymbol{k}) = \sum_{\boldsymbol{R}_n} \exp(i\boldsymbol{k}\boldsymbol{R}_n)\left[h_{\mu\nu}(\boldsymbol{R}_n) + j_{\mu\nu}(\boldsymbol{R}_n) + v^{XC}_{\mu\nu}(\boldsymbol{R}_n)\right] \tag{3.71}$$

where $h_{\mu\nu}(\boldsymbol{R}_n), j_{\mu\nu}(\boldsymbol{R}_n)$ and $x_{\mu\nu}(\boldsymbol{R}_n)$ are the one-electron, Coulomb, and exchange parts of the Fock matrix in the coordinate space. In the DFT, instead of the nonlocal-exchange interaction matrix $x_{\mu\nu}(\boldsymbol{R}_n)$, the exchange-correlation matrix $v^{XC}_{\mu\nu}(\boldsymbol{R}_n)$ is used, with different exchange-correlation functional approximations being employed in various versions of the DFT. In particular, in the local-density approximation (LDA), it is assumed that

$$\begin{aligned} v^{XC}_{\mu\nu}(\boldsymbol{R}_n) &= \int d^3\boldsymbol{R}\varphi_\mu(\boldsymbol{R})v^{XC}(\boldsymbol{R})\varphi_\nu(\boldsymbol{R}-\boldsymbol{R}_n) \\ v^{XC}(\boldsymbol{R}) &= \frac{\partial}{\partial\rho}\varepsilon[\rho(\boldsymbol{R})] \end{aligned} \tag{3.72}$$

The CO-LCAO calculations based on both the HF method and DFT allow one not only to make a comparison between the results obtained within these two approximations but also to employ a combination of these approximations used in hybrid HF-DFT methods. The HF self-consistent electron density of the crystal can be used to calculate correlation corrections to the total HF energy a posteriori [145]. In some cases it is useful to use the HF self-consistent density matrix to make the convergence of the DFT LCAO self-consistent procedure faster.

The extension of the existing HF-LCAO computer codes to DFT-LCAO ones allows a very direct comparison between these methods using the same code, the same basis set, and the same computational conditions. The modification of the HF LCAO code with PBC to perform DFT calculations is straightforward in principle. It is required only to delete the HF exchange and instead to evaluate the matrix elements of exchange-correlation operator, that is, to solve KS rather than HF equations in each iteration of the SCF procedure [146]. The main difficulty of this modification arises in the calculations of matrix elements of the exchange-correlation operator. Different approaches to this problem were suggested.

The principal merit of the HF LCAO scheme is the possibility to calculate the matrix elements of the Fock matrix analytically. This merit may be retained in the DFT LCAO calculation if the exchange-correlation potential is expanded in

an auxiliary basis set of Gaussian-type functions, with even-tempered exponents. At each SCF iteration the auxiliary basis set is fitted to the actual analytic form of the exchange-correlation potential, which changes with the evolving charge density [147].

The numerical integration also can be used to calculate the matrix elements of the exchange-correlation potential. For the numerical integration, the atomic partition method proposed by Savin [148] and Becke [149] has been adopted and combined with Gauss–Legendre (radial) and Lebedev (angular) quadratures [150]. The Kohn–Sham LCAO periodic method based on numerical integration at each cycle of the self-consistent-field process is computationally more expensive than the periodic LCAO Hartree-Fock method that is almost fully analytical.

In conclusion of this section we give some comments concerning the meaning of the KS eigenvalues and orbitals [9]. Strictly speaking, the KS eigenvalues and eigenvectors do not have the physical meaning of one-electron energies and wavefunctions as in the HF theory. Also, the single-determinant many-electron wavefunction constructed out of the KS orbitals does not correspond to the exact wavefunction of the system of interacting electrons; it is merely a wavefunction of the corresponding fictitious noninteracting system. The HF eigenvalues for occupied and empty states are calculated with different potentials, but KS eigenvalues with the same. Therefore, one should be careful with the KS eigenvalues of the states lying above the "occupied" ones. For example, the energy gap between the uppermost valence and the lowermost conduction bands in a solid is strongly underestimated in the majority versions of DFT. Note that the gap is always overestimated in the HF theory. It can be shown that similarly to Koopman's theorem in the HF theory, the ionization energy in the KS theory is given by the KS energy in the highest-occupied state. But this result cannot be applied to other occupied KS states since in the KS theory all states must be occupied sequentially from the bottom to the top: one cannot remove an electron below the highest-occupied state leaving a hole there.

As an advantage of the DFT LCAO method one can mention the possibility of linear scaling in calculations of complex molecules and crystals.

The *Siesta* (Spanish Initiative for Electronic Simulations with Thousands of Atoms) method [13, 14] achieves linear scaling by the explicit use of localized Wannier-like functions and numerical pseudoatomic orbitals confined by a spherical infinite-potential wall.The SIESTA method provides a very general scheme to perform a range of calculations from very fast to very accurate, depending on the needs and stage of the simulation, of all kinds of molecule, material and surface. It allows DFT simulations of more than a thousand atoms in modest PC workstations, and over a hundred thousand atoms in parallel platforms [151]. The numerous applications of the Siesta DFT LCAO method can be found on the Siesta code site [44]. These applications include nanotubes, surface phenomena and amorphous solids. As the restriction of the Siesta method we mention the difficulty of the all-electron calculations and use of only LDA/GGA exchange-correlation functionals.

The second DFT LCAO linear-scaling method by Scuseria and Kudin (SK method) [11] uses Gaussian atomic orbitals and a fast multipole method, which achieves not only linear-scaling with system size, but also very high accuracy in

all infinite summations. This approach allows both all-electron and pseudopotential calculations and can be applied also with hybrid HF-DFT exchange-correlation functionals.

3.4.2 Exchange-Correlation Functionals for Periodic Systems

Are Molecular Exchange-correlation Functionals Transferable to Crystals? This question arises due to the well-known fact that the properties of crystals are quite often different from those of molecular systems. The difference is particularly evident for ionic and semi-ionic solids, in which the long-range electrostatic forces provide a strong localizing field for the electronic states that is not present in molecules. In this situation the shortcomings of standard LDA and GGA functionals, linked to the missing electronic self-interaction, are likely to be most severe [152]. This explains why the electronic-structure calculations in molecular quantum chemistry and solid-state physics were for a long time developing along two independent lines. While in the molecular quantum chemistry the wavefunction-based approaches (HF and post-HF) in the LCAO approximation were mainly used, in solid-state physics DFT-based methods with plane wave (PW) basis were popular. These two standard approaches were for a long time poorly transferable between the two fields [152]: early DFT functionals underperform post-HF techniques in reproducing the known properties of small molecules, while the extension of accurate post-HF methods to solid-state systems is difficult or has prohibitive computational expense.

The formulation of hybrid HF/DFT exchange-correlation functionals and their extension to periodic systems changed the situation; the combined HF-DFT approach has adequate accuracy for most needs in both quantum chemistry of molecules and solids, retaining a tractable computational cost and even allowing the system-size linear-scaling. One appealing feature of this approach is that it can readily exploit the progress and tools available to the quantum chemists for calculating the HF exchange.

Numerous solid-state studies have been performed with molecular hybrid functionals, providing valuable experience on their accuracy and applicability. In the review article [152] the results are summarized of publications in which hybrid exchange functionals have been applied under PBC to represent crystalline solids. The list of later publications, using LCAO basis set, can be found on the site http://www.crystal.unito.it.

The next step in the HF/DFT extension to solids was made by Scuseria and coworkers who coded the HF/DFT method with PBC in LCAO basis [153] and included a linear-scaling hybrid exchange-correlation HSE functional. Later HSE hybrid functional was implemented in VASP code [154], based on use of PW basis set.

The performance of hybrid density-functionals (HDF) in solid-state chemistry is examined in a review article [152] and the original publications [131, 155–164]. The HDF method has been used in considering the bulk crystal structure and electronic properties [23, 158, 165], phase transitions in solids [59, 166–168], the vibrational

properties and lattice dynamics [21, 169–171], surfaces [172, 173], point defects in crystals [174–179]. The references are given here only on few recent publications demonstrating that the HDF methods allow the calculation of different properties of solids in good agreement with the experiment.

However, the electronic structure calculations [160] of prototypical ferroelectric oxides $BaTiO_3$ and $PbTiO_3$ using the most popular exchange-correlation functionals show that it is difficult to obtain simultaneously good accuracy for structural and electronic properties. On the one hand, all the usual DFT functionals reproduce the structural properties with various degrees of success, the recently introduced GGA–Wu–Cohen [131] being by far the most accurate, but severely underestimate the band gaps. On the other hand, the B3LYP and PBE0 hybrid functionals correct the band-gap problem, but overestimate the volumes and atomic distortions giving a supertetragonality comparable to that rendered by the GGA-PBE for the tetragonal phases. It has been found the supertetragonality inherent to B3LYP and PBE0 calculations is mostly associated with the GGA exchange part and, to a lesser extent, to the exact–exchange contribution. To bypass this problem, a different hybrid B1–WC functional has been suggested by combining the GGA–WC functional with a small percentage of exact HF exchange $A = 0.16$ (instead of $A = 0.25$ in PBE0). With this B1–WC, very good structural, electronic, and ferroelectric properties have been obtained in LCAO calculations [160] as compared to experimental data for $BaTiO_3$ and $PbTiO_3$. Indeed, DFT(B1–WC) calculations give for $SrTiO_3$ and $BaTiO_3$ cubic phases the lattice constant a values 3.880 Å(3.905 Å) and 3.971 Å(4.00 Å), respectively. The calculated indirect band gaps are 3.57 eV (3.25) eV and 3.39 eV (3.20 eV), respectively. The experimental values are given in brackets.

In solid-state calculations, however, the use of hybrid functionals is not a common practice because of the high computational cost that exact exchange involves. A recent alternative to conventional hybrid functionals is a screened exchange hybrid functional developed by Heyd, Scuseria, and Ernzerhof (HSE) [156, 180, 181]. This functional uses a screened Coulomb potential for the exact exchange interaction, drastically reducing its computational cost, and providing results of similar quality to traditional hybrid functionals. It was demonstrated that the screened HF exchange (neglect of the computationally demanding long-range part of HF exchange) exhibits all physically relevant properties of the full HF exchange. The HSE functional for solids is much faster than regular hybrids and can be used in metals also.

The range of the exchange interaction in insulators decays exponentially as a function of the bandgap [182]. In metallic systems the decay is algebraic. To render the HF exchange tractable in extended systems, either the exchange interactions need to be truncated artificially or their spatial decay accelerated [181]. Various truncation schemes have been proposed to exploit the exponential decay in systems with sizable bandgaps. Truncation schemes are very useful for systems with localized charge distributions where the HF exchange decays rapidly over distance. However these approaches fail to significantly decrease the computational effort in systems with small or no gaps. In delocalized systems truncation leads to severe convergence problems in the self-consistent-field (SCF) procedure as well as uncertainties in the predicted energy of the system. The second option, accelerating the spatial

decay, circumvents both of these problems but still neglects interactions that might be physically important.

The HSE hybrid density-functional includes the spatial decay acceleration using a screened Coulomb potential and attempts to compensate for the neglected interactions. A screened Coulomb potential is based on a splitting of the Coulomb operator into short-range (SR) and long-range (LR) components. The choice of splitting function is arbitrary as long as SR and LR components add up to the original Coulomb operator. HSE use the error function to accomplish this split since it leads to computational advantages in evaluating the short-range HF exchange integrals: the error function can be integrated analytically when using Gaussian basis functions. The following partitioning is used for the full $1/r$ Coulomb potential:

$$\frac{1}{r} = \left(\frac{erfc(\omega r)}{r}\right)_{SR} + \left(\frac{erf(\omega r)}{r}\right)_{LR} \tag{3.73}$$

where the complementary error function $erfc(\omega r) = 1 - erf(\omega r)$ and ω is an adjustable parameter. For $\omega = 0$, the long-range term becomes zero and the short-range term is equivalent to the full Coulomb operator. The opposite is the case for $\omega \to \infty$. In the HSE approach the screened Coulomb potential is applied only to the exchange interaction. All other Coulomb interactions of the Hamiltonian, such as the Coulomb repulsion of the electrons, do not use a screened potential. The exchange energy in the PBE0 functional $E_{xc}^{PBE0} = a_{mix}E_x^{HF} + (1 - a_{mix})E_x^{PBE} + E_c^{PBE}$ is split into short- and long-range components

$$\begin{aligned} E_x^{PBE0} = {} & a_{mix}E_x^{HF,SR}(\omega) + a_{mix}E_x^{HF,LR}(\omega) + (1 - a_{mix})E_x^{PBE,SR}(\omega) \\ & + E_x^{PBE,LR}(\omega) - a_{mix}E_x^{PBE,LR}(\omega) \end{aligned} \tag{3.74}$$

where ω is an adjustable parameter governing the extent of short-range interactions. For the exchange-mixing parameter value $a_{mix} = 0.25$ and $\omega = 0$ (3.74) is equal to the exchange part of the PBE0 parameter-free functional. Numerical tests based on realistic ω values ($\omega \approx 0.15$) indicate that the HF and PBE long-range exchange contributions of this functional are rather small (just a few per cent), and that these terms tend to cancel each other [180].

Thus, if we neglect them and work under the assumption that this approximation may be compensated by other terms in the functional, one obtains a screened Coulomb potential hybrid density-functional of the form:

$$E_{xc}^{\omega PBE} = a_{mix}E_x^{HF,SR}(\omega) + (1 - a_{mix})E_x^{PBE,SR}(\omega) + E_x^{PBE,LR}(\omega) + E_c^{PBE} \tag{3.75}$$

where ω is an adjustable parameter governing the extent of short-range interactions. The hybrid functional (3.75) is equivalent to PBE0 for $\omega = 0$ and asymptotically reaches PBE for $\omega \to \infty$.

The short-range component of the HF exchange can be obtained by using the SR Coulomb potential when calculating the electron-repulsion integrals for the HF

exchange energy:

$$(\mu\nu|\lambda\sigma)^{SR} = \int\int d\boldsymbol{r}_1 d\boldsymbol{r}_2 \varphi_\mu(\boldsymbol{r}_1)\varphi_\nu(\boldsymbol{r}_1)\frac{erfc(\omega r_{12})}{r_{12}}\varphi_\lambda(\boldsymbol{r}_2)\varphi_\sigma(\boldsymbol{r}_2) \tag{3.76}$$

over contracted Gaussian-type functions. For these calculations the algorithm of Gill and Pople [183] was modified [180] so that the evaluation of integrals (3.76) is only slightly more time consuming than the regular electron-repulsion integrals.

To calculate the screened Coulomb exchange PBE functional the exchange model hole J_x^{PBE} of the PBE functional constructed in a simple analytical form by Ernzerhof and Perdew [184] is used. The model hole reproduces the exchange energy density of the PBE approximation for exchange and accurately describes the change in the exchange hole upon the formation of single bonds. In the HSE functional this PBE exchange hole is screened by employing the short-range Coulomb potential from (3.73).

The PBE long-range exchange contribution is then defined as the difference of the exchange-hole-based PBE and the SR PBE exchange energy densities.

In the so-called revised HSE03 hybrid functional [181] the improvement was introduced in the calculation in the integration procedure of the PBE exchange hole. This modification made the calculations numerically more stable and ensures that the HSE03 hybrid functional for $\omega = 0$ is closer to the PBE0 hybrid. The HSE03 (denoted also as $E^{\omega PBE}$) functional was incorporated into the development version of the GAUSSIAN code [185]. It was demonstrated for molecular systems that the HSE03 hybrid functional delivers results (bond lengths, atomization energies, ionization potentials, electron affinities, enthalpies of formation, vibrational frequencies), that are comparable in accuracy to the nonempirical PBE0 hybrid functional [181].

The HSE03 hybrid functional was extended to periodic systems [181]. The calculations were made for 21 metallic, semiconducting and insulating solids. The examined properties included lattice constants, bulk moduli and bandgaps. The results obtained with HSE03 exhibit significantly smaller errors than pure DFT calculations.

The influence of the exchange screening parameter ω on the performance of screened hybrid functionals has been reexamined in [156]. It has been shown that variation of the screening parameter influences solid band gaps the most. Other properties such as molecular thermochemistry or lattice constants of solids change little with ω. A new version of HSE (HSE06) with the screening parameter $\omega = 0.11$ has been recommended for further use. Compared to the original implementation, the new parameterization yields better thermochemical results and preserves the good accuracy for band gaps and lattice constants in solids.

The two-parameter space (ω, a) of the HSE functional has been systematically examined in [186, 187] to assess the performance of hybrid screened exchange functionals and to determine a balance between improving accuracy and reducing the screening length, which can further reduce computational costs. The suggested in [187] HSE12 functional is a range-minimized functional that matches the overall accuracy of the existing HSE06 parameterization but reduces the Fock exchange

length scale by half. Analysis of the error trends over parameter space produces useful guidance for future improvement of density functionals.

The preliminary screening of the integrals is necessary to take advantage of the rapid decay of short-range exchange integrals for periodic systems [181]. Two different screening techniques are used. In the first technique (Schwarz screening) substituting the SR integrals in place of the $1/r$ integrals yields an upper bound of the form

$$|(\mu\nu|\lambda\sigma)_{SR}| \leq \sqrt{(\mu\nu|\mu\nu)_{SR}}\sqrt{(\lambda\sigma|\lambda\sigma)_{SR}} \tag{3.77}$$

The $(\mu\nu|\lambda\sigma)$ integrals are then evaluated for each batch of integrals and only batches with nonnegligible contributions are used in calculating the HF exchange. The SR screening integrals are evaluated by the same procedure as the SR exchange integrals.

The second—distance-based multipole screening technique—uses multipole moments introducing the following screening criterion

$$T_n = \sum_{M\in\mu\nu}\sum_{M\in\lambda\sigma} C_{\mu\nu}^{max}\frac{1}{r^{l+M_{\mu\nu}^{low}+M_{\lambda\sigma}^{low}}}C_{\lambda\sigma}^{max} \tag{3.78}$$

where T_n is an estimate for the contribution of a shell quartet and M is a multipole in the multipole expansion of a given shell pair. M_{ij}^{low} are the lowest-order multipoles that can contribute to the integral and C_{ij}^{max} are the maximum coefficients in each order of multipoles. Replacing the $1/r$ potential with the $erfc(\omega r)/r$ short-range potential yields

$$T_n^{SR} = \sum_{M\in\mu\nu}\sum_{M\in\lambda\sigma} C_{\mu\nu}^{max}\frac{erf\left(\omega r^{l+M_{\mu\nu}^{low}+M_{\lambda\sigma}^{low}}\right)}{r^{l+M_{\mu\nu}^{low}+M_{\lambda\sigma}^{low}}} \tag{3.79}$$

This provides a distance-based upper bound for the SR exchange contribution of a given shell quartet.

The implementation of periodic boundary conditions relies on evaluating all terms of the Hamiltonian in real space [11]. The HF exchange is evaluated using replicated density matrices. All interactions within a certain radius from a central reference cell are calculated and the rest are neglected. This so-called near-field exchange (NFX) method [188] allows calculation of the HF exchange in time, scaling linearly with system size. It works reasonably well for insulating solids since the corresponding density matrix elements decay rapidly. In systems with smaller bandgaps, however, the spatial extent of nonnegligible contributions to the exchange energy is large. This large extent results in a large number of significant interactions. To render the computation tractable, the truncation radius must be decreased. Thus, significant interactions are neglected that leads to errors in the total energy of the system and introduces instabilities into the self-consistent field procedure.

Screened Coulomb hybrid functionals do not need to rely on the decay of the density matrix to allow calculations in extended systems [181]. The SR HF exchange interactions decay rapidly and without noticeable dependence on the bandgap of the system. The screening techniques do not rely on any truncation radius and provide

much better control over the accuracy of a given calculation. In addition, the thresholds can be set very tightly, without resulting in extremely long calculations.

A series of benchmark calculations [181] on three-dimensional silicon (6–21G basis was used) demonstrates the effectiveness of the screening techniques. The time per SCF cycle was studied given as a function of the distance up to which exchange interactions were included in the calculation. As this radius grows, the number of replicated cells grows as $O(N^3)$. The PBE0 curve tracks this growth since regular HF exchange has a large spatial extent. The relatively small bandgap of silicon (1.9 eV in this calculation) is insufficient for density matrix elements to decay noticeably. HSE, on the other hand, only shows a modest increase in CPU time as the system becomes larger. Beyond 10 Å, the CPU time only increases due to the time spent on screening. The HSE calculation of the total energy converges very rapidly and only cells up to 10 Å from the reference cell contribute to the exchange energy. PBE0, by comparison, converges significantly slower. Thus, HSE not only reduces the CPU time drastically, but also decreases the memory requirements of a given calculation since fewer replicated density matrices need to be stored in memory. In practice, HSE calculations can be performed with the same amount of memory as pure DFT calculations, whereas traditional hybrid methods have larger memory demands. Given the fast decay of the SR HF exchange interactions and the high screening efficiency, the HSE hybrid functional was successfully applied to a variety of three-dimensional solids. It was demonstrated that the screened Coulomb hybrid density-functional HSE not only reduces the amounts of memory and CPU time needed, when compared to its parent functional PBE0, but it is also at least as accurate as the latter for the structural, optical and magnetic properties of solids.

In nanostructure calculations the monoperiodic unit cell can contain several hundreds of atoms so that not only hybrid but even pure DFT exchange-correlation functionals are not practically applicable. The DFTB method allows one to simplify the calculation scheme maintaining the DFT accuracy of the results.

3.4.3 Density Functional Tight Binding (DFTB) Method

General information about the DFTB method and its implementation in computer codes is given on sites [189, 190]. The Density Functional based Tight binding (DFTB) method is based on a second-order expansion of the Kohn–Sham total energy in Density-Functional Theory (DFT) with respect to charge density fluctuations. The zeroth order approach is equivalent to a common standard non-self-consistent (TB) scheme, while at second order a transparent, parameter-free, and readily calculable expression for generalized Hamiltonian matrix elements can be derived. These are modified by a self-consistent redistribution of Mulliken charges (SCC).

Besides the usual “band structure” and short-range repulsive terms the final approximate Kohn–Sham energy additionally includes a Coulomb interaction between the charge fluctuations. At large distances this accounts for long-range electrostatic forces between two point charges and approximately includes self-interaction contri-

butions of a given atom if the charges are located at one and the same atom. Due to the SCC extension, DFTB can be successfully applied to problems where deficiencies within the non-SCC standard TB approach become obvious.

In the last few years, the DFTB method has been significantly extended to allow the calculation of optical and excited state properties. The GW formalism as well as the time dependent DFTB was implemented. Furthermore, the DFTB was used to calculate the Hamiltonian for transport codes, using Green function techniques.

We list here some selected references allowing the study of the DFTB method foundations and practical applications [191–201].

Based on DFT, the DFTB formalism introduces several approximations. The electronic charge density is written as a superposition of atomic densities. Likewise, the effective potential can be written as a superposition of atomic contributions so that the exchange-correlation energy is also decomposed into atomic contributions.

For large interatomic distances, the integral describing the electron-nucleus interaction is approximated through a point-charge approximation. In turn, the atomic population converges to the nuclear charge in the limit of large distances, and the energy terms from nuclear–nuclear repulsion and electron nuclear energy compensate for each other for large distances. In addition, in the large distance range, the two-center terms containing the potential vanish. In total, the many-center terms vanish at large interatomic distances.

For small interatomic distances, these arguments are not valid anymore. Therefore, the compensating terms are calculated using the atomic densities and potentials and then summarized together with the nuclear repulsion energy terms into a sum of pairwise repulsive energy terms. For short interatomic distances, the nuclear repulsion dominates. In this limit, the pairwise energy terms are repulsive, and they asymptotically approach zero in the long range. The second-order terms are represented in a multipole expansion considering only the monopolar terms.

KS-like equations can be set up, in which the effective potential consists of the sum of the atomic potentials and the corresponding contributions related to the second-order terms. The corresponding KS orbitals are written within the LCAO approach. They are represented in a minimal basis of optimized orthogonal atomic orbitals. These pseudoatomic basis functions are obtained by self-consistently solving the KS equations for a spherical symmetric spin-unpolarized neutral atom.

The approximations above formulated contain two-center terms only and lead to the same structure of the secular equations as in the other nonorthogonal TB schemes. It is important to emphasize that all matrix elements are calculated within the DFT.

The notations and formalism of the DFTB method are described in detail in [192]. The approximations in the formulated DFTB method, which contains two–center terms only in Hamiltonian matrix elements, lead to the same structure of the secular equations as in the non-orthogonal TB schemes or the extended Huckel method, but the important advantage is that all the matrix elements are calculated within the DFT.

Within the DFT, the total energy can be written as follows:

$$E_{\text{tot}}[\rho(\boldsymbol{r})] = T[\rho(\boldsymbol{r})] + E_{\text{ext}} + \overbrace{\frac{1}{2}\int\int \frac{\rho(\boldsymbol{r})\rho(\boldsymbol{r}')}{|\boldsymbol{r}-\boldsymbol{r}'|}d\boldsymbol{r}d\boldsymbol{r}'}^{E_{\text{H}}} + E_{\text{nn}} + E_{\text{xc}}[\rho(\boldsymbol{r})] \quad (3.80)$$

Here, T is the kinetic energy of the electrons, and E_{ext}, E_{H}, and E_{nn} are the electron-nuclei, the meanfield (Hartree), and the nuclear interaction energies, respectively. $E_{\text{xc}}[\rho(\boldsymbol{r})]$ denotes the functional of the exchange-correlation (xc) energy.

The electron-density distribution

$$\rho(\boldsymbol{r}) = \sum_{i}^{\text{occ}} \psi_i^*(\boldsymbol{r})\psi_i(\boldsymbol{r}) \quad (3.81)$$

can be obtained through the solution of the KS equations

$$\begin{aligned}
&\left[-\frac{1}{2}\nabla^2 + V_{\text{eff}}(\boldsymbol{r})\right]\psi_i(\boldsymbol{r}) = \varepsilon_i\psi_i(\boldsymbol{r}),\\
&V_{\text{eff}} = V_{\text{ext}} + V_{\text{H}} + V_{\text{xc}},\\
&V_{\text{H}} = \int \frac{\rho(\boldsymbol{r}')}{|\boldsymbol{r}-\boldsymbol{r}'|}d\boldsymbol{r},\ V_{\text{ext}} = -\sum_j \frac{Z_j}{r_j}\boldsymbol{r},\\
&V_{\text{xc}} = \frac{\delta E_{\text{xc}}}{\delta\rho}.
\end{aligned} \quad (3.82)$$

Using (3.82) the total energy can also be written as follows:

$$\begin{aligned}
E_{\text{tot}} = &\sum_{i}^{\text{occ}} \langle\psi_i|\overbrace{-\frac{1}{2}\nabla^2 + V_{\text{eff}}}^{\hat{h}^0}|\psi_i\rangle - \frac{1}{2}\left[\int V_{\text{eff}}\rho d\boldsymbol{r} - \int V_{\text{ext}}\rho d\boldsymbol{r}\right] + E_{xc}[\rho]\\
&- \frac{1}{2}\int V_{\text{xc}}\rho d\boldsymbol{r} + E_{\text{nn}}
\end{aligned} \quad (3.83)$$

Because E_{tot} is variational with respect to the density variations, the total energy may be calculated from an approximate electronic charge density obtained by knowing roughly the reference density distribution ρ_0. The reference density should be close to the exact density $\tilde{\rho}$, but one can further improve it [192].

As the whole Hamiltonian and overlap matrices contain one- and two-center contributions only, they can be calculated and tabulated in advance as functions of the distance between the atomic pairs. Thus, it is not necessary to recalculate any integral during the actual calculation. The pairwise tabulated integrals have to be transformed to a specific coordinate system by transformations of the angle-dependent part of the basis functions–atomic orbitals.

Because the atomic charges Δq_j in the second-order contributions depend on the orbitals ψ_i via the KS ansatz for the charge density in (3.81), the eigenvalue problem has to be solved self-consistently. However, in contrast to a full DFT calculation, the self-consistency has not to be achieved for the charge density, but for the charges Δq_j of the atoms in the system only. Such a restricted self-consistency is called a self-consistent charge (SCC) treatment.

The charge of an atom in a molecule or a solid is not uniquely defined. In line with the minimal valence basis ansatz for the KS orbitals, the most obvious way to define the charges is via the projection of the atomic orbitals onto each atom. The partitioning of the overlapping contributions can simply be done within the Mulliken approach. The resulting charges then correspond to the widely used Mulliken charges.

After the solution of the approximate KS equations, the total energy or the binding energy can be calculated. The repulsive energy contributions can be calculated also; but in practice, these pairwise contributions are fitted to full DFT calculations. In principle, any high-level calculation method could be used in full DFT calculations. The pairwise repulsive energy can be fitted to, for example, the following type polynomials:

$$V_{\text{rep}}(R) = \begin{cases} \sum_{n=2} d_n (R_c - R)^n, & \text{for } R < R_c, \\ 0, & \text{otherwise.} \end{cases} \tag{3.84}$$

Thereby, the repulsive potential has to be fitted for each pair of elements, not for each pair of atoms. It can be tabulated as the Hamiltonian and overlap matrix elements. It is also important to note that the repulsive terms are rather short-ranged, i.e., R_c is in the order of $\approx$1.5 times of the typical interatomic bonding distance. This characteristic makes V_{rep} rather well transferable from one system to another.

Analytical expressions for the forces on the atoms can be derived as well [192].

It should be noted that the computation of derivatives of the Hamiltonian and the overlap matrices can be performed, because the integrals are stored in tables. An efficient calculation of the forces is essential for the realization of molecular-dynamics (MD) simulations within the DFTB approach.

Corresponding formulations of the second derivative of the energy with respect to the nuclear coordinates exist as well. These are needed, e.g. for the calculation of vibrational spectra. However, a numerical differentiation of the forces turned out to be more practical.

In the materials science one needs to study the macroscopic properties of aggregates of atoms or molecules (an infinite molecular crystal, a molecular liquid, a polymer, or large biomolecule). Within these systems, one needs not only to take care of the covalent or ionic forces that bond the units, but also of the weak forces that contribute to the long range. The most important one is the London dispersion that belongs to the class of van der Waals interactions.

Within the DFT, the correct description of the London dispersion interactions is complicated. Therefore, the standard DFT does not include these forces. The

same holds for the DFTB in the standard and the SCC approach as only short-range atomic potentials are used and the Hamiltonian matrix elements are negligible at large interatomic distances, where van der Waals forces have a significant effect. However, the van der Waals interactions may be included into the DFTB approach a posteriori, which means that one calculates the van der Waals contributions independently after a DFTB or SCCDFTB cycle and add the result E_{disp} to the total energy. The typical van der Waals decay is with R^6 so that a Lennard–Jones potential can be used. The full periodic–table force–field for molecular mechanics and molecular–dynamics simulations is given in [202]. However, the R^{12} term in the Lennard-Jones potential is repulsive for short-range distances, in which the energy is calculated within the quantum-mechanical DFT or DFTB approach. Therefore, the potential has to be modified, so that no repulsive terms occur (the details of this correction are considered in [192]).

The force-field consideration of van der Waals interactions suggests the inclusion of further nonquantum–mechanically calculated interactions (QM/MM-quantum mechanics-molecular mechanics) methodology [203]. In such a treatment, the total energy is written as $E_{tot} = E_{QM} + E_{MM} + E_{QM/MM}$, where E_{QM} is the energy of the quantum mechanically described part of the system, and E_{MM} is the energy of the classically described part. For the QM part, the DFTB approach can be used; for the classical molecular-mechanics part, one can choose an empirical force field. $E_{QM/MM}$ describes the energy contribution resulting from the linkage of the QM to the MM region.

The QM/MM is a very practical approach for large systems, in which only parts of the processes are of interest, or in which a special process occurs in only a small region of a large system. With an approximate QM method such as the DFTB, one can even describe large parts of a biomolecule quantum mechanically, see references in [192].

The advantages of QM/MM calculations are that they are much faster than a full quantum-mechanical description, which in most cases is not even possible. However, there are also several drawbacks of the QM/MM approach. Molecular mechanics is not able to properly describe bond breaking and bond formation. Therefore, one has to make sure that the MM part in the system is restricted to the area where the bonds will not be broken during the simulation.

The DFTB approach is used to calculate not only ground-state properties. It has been extended to the excited states using the Time Dependent DFTB (TD–DFTB) scheme [192, 204].

A critical point in using the DFTB in any implementation is still the fitting procedure for the repulsive energy. To obtain meaningful results, it is vital that this procedure is done with greatest care for receiving meaningful results. Because the repulsive energy depends on the fitting procedure, its tables are not generally transferable from one class of systems to another. This is the reason why these parameters are not available publicly for all the elements of the periodic table. Attempts have been made to automatize this procedure [205].

The discussion of the DFTB method concludes the description of LCAO basis set use for the periodic systems calculations. In the next section we consider Plane Wave approaches to periodic systems.

3.5 Plane Wave Hartree-Fock and DFT Methods for Periodic Systems

3.5.1 Projector Augmented-Wave Method

The Hartree-Fock and DFT Plane Wave methods for periodic systems are realized using the projector-augmented wave method (PAW) technique. It is a generalization of the pseudopotential and linear augmented-plane-wave methods, and allows density functional theory calculations to be performed with greater computational efficiency [206]. The formal relationship between the ultrasoft (US) and the PAW method is derived in [207].

The valence wavefunctions tend to have rapid oscillations near the ion cores due to the requirement that they be orthogonal to core states. The PAW approach addresses this issue by transforming these rapidly oscillating wavefunctions into smooth wavefunctions which are more computationally convenient. The PAW method is typically combined with the frozen core approximation, in which the core states are assumed to be unaffected by the ion's environment. However the PAW method is an exact all- electron (AE) method for a complete set of partial waves [207]. Therefore, the method should yield results that are indistinguishable from any other frozen core AE method. In the US-PP method additional approximations are made.

The formalism of the PAW approach is described in [207, 208].

The AE (all-electron) wave functions Ψ_{nk}, with the n index corresponding to the summation over the bands and k indexing the **k**-points, are obtained starting from the PS (pseudo) $\widetilde{\Psi}_{nk}$ by using a linear transformation:

$$|\Psi_{nk}\rangle = \widetilde{\Psi}_{nk} + \sum_i (|\Phi_i\rangle - |\widetilde{\Phi}_i\rangle)\langle\widetilde{p}_i|\widetilde{\Psi}_{nk}\rangle \tag{3.85}$$

The index i stands for the atomic position $\boldsymbol{R}$, the angular momentum (l, m) and an additional index n to label different partial waves for the same site and angular momentum. The AE Φ_i and PS $\widetilde{\Phi}_i$ partial waves are equal outside the PAW sphere. Therefore, as in the norm conserving and ultra-soft scheme, $\Psi_n = \widetilde{\Psi}_n$ outside the core radius r_c^l. The projector functions $\widetilde{p}_i$ are dual to the PS partial waves:

$$\langle\widetilde{p}_i|\widetilde{\Phi}_j\rangle = \delta_{ij} \tag{3.86}$$

In the PAW method, two grids are used: a radial one inside the PAW sphere and a regular mesh in the whole simulation cell. As a consequence, on the one hand, the

partial waves and projector functions are separated between the angular and radial parts:

$$\Phi_i(\boldsymbol{r}) = \frac{\Phi_{n_i l_i}(r)}{r} S_{l_i m_i}(\hat{r}); \quad \widetilde{\Phi}_i(\boldsymbol{r}) = \frac{\widetilde{\Phi}_{n_i l_i}(r)}{r} S_{l_i m_i}(\hat{r}) \tag{3.87}$$

$$\widetilde{p}_i(\boldsymbol{r}) = \frac{\widetilde{p}_{n_i l_i}(r)}{r} S_{l_i m_i}(\hat{r}) \tag{3.88}$$

with $S_{lm}(\hat{r})$ the real spherical harmonics, see the Appendix A in [208]. On the other hand, the pseudized wave functions are expanded on a plane wave basis set:

$$\widetilde{\Psi}_{nk}(\boldsymbol{r}) = \sqrt{\frac{1}{\Omega}} \sum_{\boldsymbol{B}} c_{nk}(\boldsymbol{B})\, e^{i(\boldsymbol{k}+\boldsymbol{B})\cdot\boldsymbol{r}} \tag{3.89}$$

with Ω the volume of the unit cell.

By using (3.85) and the completeness relation of the projector-partial wave set,

$$\sum_i |\widetilde{\Phi}_i\rangle\langle\widetilde{p}_i| = 1 \tag{3.90}$$

the AE valence charge density becomes:

$$\rho_v(\boldsymbol{r}) = \sum_{nk} f_{nk} |\Psi_{nk}|^2 = \widetilde{\rho}(\boldsymbol{r}) + \rho^1(\boldsymbol{r}) - \widetilde{\rho}^1(\boldsymbol{r}) \tag{3.91}$$

with f_{nk} the occupation factors.

The pseudized charge density $\widetilde{\rho}$ is analogous to the one obtained in the norm-conserving pseudopotential case, whereas ρ^1 and $\widetilde{\rho}^1$ are the AE and pseudized partial densities, which are only defined within the PAW spheres.

A discussion of the PAW method application to the forces and stress tensor calculations can be found in [208].

The PAW method has been implemented in several codes using Plane Waves as the basis set [208]. The PAW technique is also used for the Hartree-Fock Plane Wave method realization for periodic systems, considered in the next subsection.

3.5.2 Plane Wave Hartree-Fock Method for Periodic Systems

For periodic systems the long-range nature of the Fock exchange interaction and the resultant large computational requirements present a major drawback [209]. This is especially true for metallic systems, which require a dense Brillouin zone sampling. Therefore the Hartree-Fock method in the basis of plane waves is usually realized using the screened density functional approach [209].

The nonlocal Fock exchange energy E_x in real space can be written as

$$E_x = -\frac{1}{2}\sum_{\mathbf{k}n,\mathbf{q}m} 2w_{\mathbf{k}}f_{\mathbf{k}n} \times 2w_{\mathbf{q}}f_{\mathbf{q}m} \times \int\int d^3\mathbf{r}d^3\mathbf{r}' \frac{\phi^*_{\mathbf{k}n}(\mathbf{r})\phi_{\mathbf{q}m}(\mathbf{r})\phi^*_{\mathbf{q}m}(\mathbf{r}')\phi_{\mathbf{k}n}(\mathbf{r}')}{|\mathbf{r}-\mathbf{r}'|} \tag{3.92}$$

Here $\phi_{\mathbf{k}n}$ is a set of one-electron Bloch states of the system and the corresponding set of (possibly fractional) occupational numbers $f_{\mathbf{k}n}$. The sums over $\mathbf{k}$ and $\mathbf{q}$ need to be performed over all the $\mathbf{k}$ points chosen to sample the Brillouin zone (BZ), whereas the sums over m and n are performed over all the bands at these $\mathbf{k}$ points. The $w_{\mathbf{k}}$ are $\mathbf{k}$ -point weights and the factors 2 account for the fact that we are considering a closed-shell system with doubly occupied one-electron states.

The corresponding nonlocal Fock exchange potential is given by

$$\begin{aligned} V_x(\mathbf{r},\mathbf{r}') &= -\sum_{\mathbf{q}m} 2w_{\mathbf{q}}f_{\mathbf{q}m}\frac{\phi^*_{\mathbf{q}m}(\mathbf{r}')\phi_{\mathbf{q}m}(\mathbf{r})}{|\mathbf{r}-\mathbf{r}'|} \\ &= -\sum_{\mathbf{q}m} 2w_{\mathbf{q}}f_{\mathbf{q}m}e^{-i\mathbf{q}\cdot\mathbf{r}'}\frac{u^*_{\mathbf{q}m}(\mathbf{r}')u_{\mathbf{q}m}(\mathbf{r})}{|\mathbf{r}-\mathbf{r}'|}e^{i\mathbf{q}\cdot\mathbf{r}} \end{aligned} \tag{3.93}$$

where $u_{\mathbf{q}m}$ is the cell periodic part of the Bloch state, $\phi_{\mathbf{q}m}$ at $\mathbf{k}$ point $\mathbf{q}$ with the band index m. Using the decomposition of the Bloch states $\phi_{\mathbf{q}m}$, in plane waves ($\mathbf{B}$-reciprocal lattice vector)

$$\phi_{\mathbf{q}m}(\mathbf{r}) = \frac{1}{\sqrt{\Omega}}\sum_{\mathbf{B}} C_{\mathbf{q}m}(\mathbf{B})e^{i(\mathbf{q}+\mathbf{B})\cdot\mathbf{r}} \tag{3.94}$$

Equation (3.93) can be rewritten as

$$V_x(\mathbf{r},\mathbf{r}') = \sum_{\mathbf{k}}\sum_{\mathbf{B}\mathbf{B}'} e^{i(\mathbf{k}+\mathbf{B})\cdot\mathbf{r}}V_{\mathbf{k}}(\mathbf{B},\mathbf{B}')e^{-i(\mathbf{k}+\mathbf{B}')\cdot\mathbf{r}'} \tag{3.95}$$

where

$$\begin{aligned} V_x(\mathbf{B},\mathbf{B}') &= \langle\mathbf{k}+\mathbf{B}|\hat{V}_x|\mathbf{k}+\mathbf{B}'\rangle \\ &= -\frac{4\pi e^2}{\Omega}\sum_{m\mathbf{q}} 2w_{\mathbf{q}}f_{\mathbf{q}m} \times \sum_{\mathbf{G}''}\frac{C^*_{\mathbf{q}m}\left(\mathbf{B}'-\mathbf{B}''\right)C_{\mathbf{q}m}\left(\mathbf{B}-\mathbf{B}''\right)}{|\mathbf{k}-\mathbf{q}+\mathbf{B}''|^2} \end{aligned} \tag{3.96}$$

is the representation of the Fock exchange potential in reciprocal space [210].

To avoid the calculation of expensive integrals over the slowly decaying long-ranged part of the Fock exchange, Heyd et al. [180] proposed replacing it with the corresponding density functional counterpart. The resulting expression for the exchange-correlation energy in the hybrid DFT-HF HSE03 approach is given by

$$E_{xc}^{\mathrm{HSE03}} = \frac{1}{4}E_x^{\mathrm{sr},\mu} + \frac{3}{4}E_x^{\mathrm{PBE,sr},\mu} + E_x^{\mathrm{PBE,lr},\mu} + E_c^{\mathrm{PBE}} \tag{3.97}$$

As can be seen from (3.97), only the exchange component of the electron-electron interaction is separated into a short- (sr) and a long-range (lr) part. The complete electronic correlation is represented by the standard correlation part of the PBE density functional.

A simple decomposition of the Coulomb kernel can be obtained using the construction

$$\frac{1}{r} = S_\mu(r) + L_\mu(r) = \frac{\mathrm{erfc}(\mu r)}{r} + \frac{\mathrm{erf}(\mu r)}{r} \tag{3.98}$$

where μ is the parameter that defines the range separation related to a characteristic distance $2/\mu$ at which the short-range interactions become negligible. In the context of the HSE03 functional, it was empirically established that the optimum range-separation parameter, μ is approximately 0.3 $\mathrm{Å}^{-1}$. Using the decomposed Coulomb kernel (3.98) and (3.92) one obtains straightforwardly

$$E_x^{\mathrm{sr},\mu} = -\frac{e^2}{2}\sum_{\mathbf{k}n,\mathbf{q}m} 2w_{\mathbf{k}}f_{\mathbf{k}n}2w_{\mathbf{q}}f_{\mathbf{q}m} \times \int\int d^3\mathbf{r}d^3\mathbf{r}' \frac{\mathrm{erfc}(\mu\,|\mathbf{r}-\mathbf{r}'|)}{|\mathbf{r}-\mathbf{r}'|} \times \phi^*_{\mathbf{k}n}(\mathbf{r})\phi_{\mathbf{q}m}(\mathbf{r})\phi^*_{\mathbf{q}m}(\mathbf{r}')\phi_{\mathbf{k}n}(\mathbf{r}') \tag{3.99}$$

The representation of the corresponding short-range Fock exchange potential in reciprocal space is given by

$$V_{\mathbf{k}}^{\mathrm{sr},\mu}(\mathbf{B},\mathbf{B}') = \langle \mathbf{k}+\mathbf{B}|\hat{V}_x^{\mathrm{sr},\mu}|\mathbf{k}+\mathbf{B}'\rangle = -\frac{4\pi e^2}{\Omega}\sum_{m\mathbf{q}} 2w_{\mathbf{q}}f_{\mathbf{q}m} \times \sum_{\mathbf{B}''} \frac{C^*_{\mathbf{q}m}\left(\mathbf{B}'-\mathbf{B}''\right)C_{\mathbf{q}m}\left(\mathbf{B}-\mathbf{B}''\right)}{|\mathbf{k}-\mathbf{q}+\mathbf{B}''|^2} \times \left(1-e^{-|\mathbf{k}-\mathbf{q}+\mathbf{B}''|^2/4\mu^2}\right) \tag{3.100}$$

The only difference from the reciprocal space representation of the complete (undecomposed) Fock exchange potential, given by (3.96), is the second factor in the summand in (3.100), representing the complementary error function in reciprocal space. Note that (3.100) shows the range-separated exchange interaction to belong to the class of screened exchange interactions.

The short-range PBE exchange energy and potential, as well as their long-range counterparts, are arrived at using the same decomposition (3.98), in accordance with Heyd et al. [180]. It is easily seen from (3.98) that the long-range term becomes zero

for $\mu = 0$ and the short-range contribution then equals the full Coulomb operator, whereas for $\mu \to \infty$ it is the other way around.

A detailed comparison of the performance of the HSE03 and PBE0 functionals for a set of archetypical solid state systems is presented in [209] by calculating lattice parameters, bulk moduli, heats of formation, and band gaps. The results indicate that the hybrid functionals indeed often improve the description of these properties, but in several cases the results are not yet close to the standard gradient corrected functionals. This concerns in particular metallic systems for which the bandwidth and exchange splitting are seriously overestimated.

3.5.3 Plane Wave Density Functional Method for Periodic Systems

The Kohn–Sham equations take on a very simple form when one uses plane waves [5]

$$\left\{ \sum_{\boldsymbol{B}'} \left(\frac{1}{2} |\boldsymbol{k} + \boldsymbol{B}|^2 \delta_{\boldsymbol{B}\boldsymbol{B}'} + V_{eN}(\boldsymbol{B} - \boldsymbol{B}') + V_{ee}(\boldsymbol{B} - \boldsymbol{B}') \right. \right.$$
$$\left. \left. + V_{XC}(\boldsymbol{B} - \boldsymbol{B}') \right) \right\} C_{i,\boldsymbol{k}+\boldsymbol{B}'} = C_{i,\boldsymbol{k}+\boldsymbol{B}} \varepsilon_{i\boldsymbol{k}} \tag{3.101}$$

where $V_{eN}(\boldsymbol{B} - \boldsymbol{B}')$, $V_{ee}(\boldsymbol{B} - \boldsymbol{B}')$, and $V_{XC}(\boldsymbol{B} - \boldsymbol{B}')$ are the Fourier transforms of the electronic–nuclei, electron–electron Coulomb, and exchange-correlation potentials. In this form, the kinetic energy is diagonal.

The solution of (3.101) proceeds by diagonalization of a Hamiltonian matrix whose matrix elements $H_{\boldsymbol{k}+\boldsymbol{B},\boldsymbol{k}+\boldsymbol{B}'}$ are given by the terms in the brackets above. The size of the matrix is determined by the choice of cutoff energy, and will be intractably large for systems that contain both valence and core electrons. This is a severe problem. A plane-wave basis set is usually very poorly suited to expanding electronic wave functions because a very large number of plane waves are needed to expand the tightly bound core orbitals and to follow the rapid oscillations of the wave functions of the valence electrons in the core region. An extremely large plane-wave basis set should be required to perform an all-electron calculation, and a vast amount of computational time would be required to calculate the electronic wave functions [5]. The pseudopotential approximation allows the electronic wave functions to be expanded using a much smaller number of plane-wave basis states. A list of PW DFT codes for periodic systems is given at [211].

3.6 Molecular Dynamics Approach

Complex quantum-mechanical systems that molecules and crystals are, as they consist of a great number of atomic nuclei and electrons, can in many cases be modeled by the nonrelativistic Hamiltonian having the form

$$\hat{\mathrm{H}} = -\frac{1}{2}\sum_{i=1}^{2N_e} \Delta_{\boldsymbol{r}_i} - \frac{1}{2}\sum_{j=1}^{N_a} \frac{1}{M_j}\Delta_{\boldsymbol{R}_j} + V(\boldsymbol{r}, \boldsymbol{R}) \tag{3.102}$$

where $\boldsymbol{r}_i$ are the coordinates of electrons ($i = 1, 2, \ldots, 2N_e$), $\boldsymbol{R}_j$ are the coordinates of nuclei ($j = 1, 2, \ldots, N_\mathrm{a}$) and $V(\boldsymbol{r}, \boldsymbol{R})$ is the energy of the Coulomb interaction of the electrons and nuclei:

$$V(\boldsymbol{r}, \boldsymbol{R}) = \sum_{j<j'} \frac{Z_j Z_{j'}}{|\boldsymbol{R}_j - \boldsymbol{R}_{j'}|} + \sum_{i<i'} \frac{1}{|\boldsymbol{r}_i - \boldsymbol{r}_{i'}|} - \sum_{ij} \frac{Z_j}{|\boldsymbol{r}_i - \boldsymbol{R}_j|} \tag{3.103}$$

The Hamiltonian (3.101) is approximate as it does not take into account the spin-orbit interaction and other relativistic effects. The calculation of eigenfunctions and eigenvalues of the operator (3.102), i.e. the solution of the time-independent Schrodinger equation

$$\hat{\mathrm{H}}\Phi = E\Phi \tag{3.104}$$

is possible only after applying some approximations. The first of them is the adiabatic approximation. It permits the motion of electrons and nuclei to be considered separately and is based on the large difference in electron and nuclear masses ($m_e \ll M_j$).

In the adiabatic approximation, first the problem of electronic motion is solved for the fixed positions of nuclei

$$\left[-\frac{1}{2}\sum_{i=1} \Delta_{\boldsymbol{r}_i} + V(\boldsymbol{r}, \boldsymbol{R})\right] \psi(\boldsymbol{r}, \boldsymbol{R}) = W(\boldsymbol{R})\psi(\boldsymbol{r}, \boldsymbol{R}) \tag{3.105}$$

The wavefunctions $\psi(\boldsymbol{r}, \boldsymbol{R})$ and the eigenvalues $W(\boldsymbol{R})$ in (3.105) depend on the nuclear coordinates $\boldsymbol{R}$ as parameters. Then, the found eigenvalues $W(\boldsymbol{R})$ are used as the operators of potential energy in the equation determining the nuclear motion:

$$\left[-\frac{1}{2}\sum_{j=1} \frac{1}{M_j}\Delta_{\boldsymbol{R}_j} + W(\boldsymbol{R})\right] \chi(\boldsymbol{R}) = \varepsilon\chi(\boldsymbol{R}) \tag{3.106}$$

This way of solving (3.104) is equivalent to the representation of the wavefunction Φ in the form of the product

$$\Phi(\boldsymbol{r}, \boldsymbol{R}) = \psi(\boldsymbol{r}, \boldsymbol{R})\chi(\boldsymbol{R}) \tag{3.107}$$

Further corrections of this reasonable approximation may be obtained from adiabatic perturbation theory by using, as the small parameter, the value $(\frac{1}{M})^{1/4}$, where M is the average mass of the nuclei. Equation (3.105) is often considered as an independent problem without any relation to the more general problem (3.104). This is motivated by the following reasoning. If the temperature is not very high, the nuclei vibrate about some equilibrium positions $\boldsymbol{R}^{(0)}$. Thus, in calculating the electronic structure, only configuration with the nuclei fixed at their equilibrium positions $\boldsymbol{R}^{(0)}$ is considered. The latter are typically known from experimental data (e.g. from X-ray or neutron-scattering crystallographic data). This means of electronic-structure calculation without using any other experimental data (except the equilibrium positions of the nuclei) is often considered as made from first-principles. Often, the first-principle calculations are made with geometry optimization when the positions of nuclei are found from the total-energy minimization. Formally, the results of such calculations correspond to zeroth temperature.

The temperature dependence of the structure can be found using the Molecular Dynamics (MD) approach [5]. The simplest MD approach uses classical mechanics to find solutions of the (3.106). The familiar Newton equations of motion are solved

$$\sum_{j=1} \frac{1}{M_j} \Delta_t \boldsymbol{R}_j(t) = -\sum_{j=1} \nabla_j V(\boldsymbol{R}_j(t)) \tag{3.108}$$

The potential $V(\boldsymbol{R}_j(t))$ can be found basing on the force field approach or from the solution of the ground state time-independent Schrodinger equation for the fixed nuclei configuration $\boldsymbol{R}$. In the first case this approach is known as the classic mechanics-molecular mechanics method, in the second case - the quantum mechanics-molecular mechanics method.

3.7 First-Principles Simulation of Bulk Crystal (3D) Properties

The applications of the DFT and hybrid exchange-correlation functionals for simulations of nanostructures (nanolayers, nanotubes, nanowires) are discussed in Part II of this book. However, the study of nanostructures usually starts with calculations of the structure and properties of the corresponding bulk crystals. The bulk crystals play a role of benchmark systems to check the applicability of the computational method selected to reproduce the experimental data for different bulk crystal properties: the equilibrium atomic structure, one-electron properties (band structure and density of states), formation and atomization (cohesive) energy, bulk modulus and elastic constants, phonon frequencies and thermodynamical properties.

3.7.1 One-Electron Properties: Band Structure, Density of States

The local properties of chemical bonding in crystals are defined by the electron-density distribution in real space described by a one-electron density matrix (DM). The latter is calculated self-consistently for the finite set of L discrete $\boldsymbol{k}$-points in BZ and corresponds to the cyclic cluster of L-primitive unit cells modeling the infinite crystal:

$$\rho_{\mu\nu}(\boldsymbol{R}_n) = \frac{1}{L}\sum_{i=1}^{M}\sum_{j=1}^{L}\exp(-\mathrm{i}\boldsymbol{k}\boldsymbol{R}_n)C_{i\mu}(\boldsymbol{k}_j)C^*_{i\nu}(\boldsymbol{k}_j)n_i(\boldsymbol{k}_j) \tag{3.109}$$

The total number M of the bands in (3.109) equals the number of AOs (both in LCAO and PW calculations) associated with the primitive unit cell. The one-electron energy levels form energy bands consisting of L levels in each band. Therefore, each energy band can allocate $2 \times L$ electrons; if in a unit cell there are n electrons, and the bands do not cross, the lowest $n/2$ bands are occupied and are separated from the empty bands. In this case the occupation numbers in (3.109) are $n_i = 2, 0$ for the occupied and empty bands, respectively (insulators and semiconductors). However, if n is odd, or if the valence and conduction bands cross, more than $n/2$ bands are partially occupied (metal).

The eigenvalue spectrum of an infinite periodic system does not consist of discrete energy levels as the wavevector $\boldsymbol{k}$ changes continuously along the chosen direction of the BZ. The DM of an infinite crystal is written in the form where the summation over the discrete $\boldsymbol{k}$-vectors of the BZ is replaced by the integration over the BZ. In particular in the LCAO approximation DM (calculated for the cyclic-cluster in the coordinate space) is replaced by

$$\begin{aligned}\rho_{\mu\nu}(\boldsymbol{R}_n) &= \sum_{i=1}^{M}\rho^{(i)}_{\mu\nu}(\boldsymbol{R}_n)\\ &= \frac{1}{V_{BZ}}\sum_{i=1}^{M}\int_{BZ}\exp(-\mathrm{i}\boldsymbol{k}\boldsymbol{R}_n)C_{i\mu}(\boldsymbol{k})C^*_{i\nu}(\boldsymbol{k})\,(\varepsilon_F - \varepsilon_i(\boldsymbol{k}))\,d\boldsymbol{k}\end{aligned} \tag{3.110}$$

where $\rho^{(i)}_{\mu\nu}(\boldsymbol{R}_n)$ is the contribution of the ith energy band.

For the infinite crystal at each cycle of the SCF process, an energy ε_F (the Fermi energy) must be determined, such that the number of one-electron levels with energy below ε_F is equal to the number of electrons (or, in other words, the number of filled bands below ε_F is equal to half the number of electrons in the unit cell). The Fermi surface is the surface in reciprocal space that satisfies the condition $\varepsilon_i(\boldsymbol{k}) = \varepsilon_F$. By limiting the integration over the BZ to states with energy below ε_F, a Heaviside step

function $\theta(\varepsilon_F - \varepsilon)$ excludes the empty states from the summation over the energy bands. In fact, the band structure of the infinite crystal is obtained after the cyclic-cluster self-consistent calculation by the interpolation of the one-electron energy levels considered as continuous functions $\varepsilon(\boldsymbol{k})$ of the wavevector. The band structure of solids is an important feature, defining their optical, electrostatic and thermal properties. Both the electron charge distribution and the band structure are defined by the self-consistent DM of a crystal.

For example, two binary oxides—cubic MgO in sodium chloride structure and teragonal TiO_2 in rutile structure—differ significantly in the character of metal-oxygen chemical bonding, which is due to the electron-density distribution being much different in them. Mg–O bonding is practically ionic, Ti–O bonding is an essentially covalent one.

We discuss now the differences in the band structures of these crystals.

The electronic structures of both compounds have been well studied experimentally. The experimental data show that the MgO crystal is a wide-bandgap insulator ($E_g = 7.8$ eV); titanium dioxide TiO_2 in the rutile structure is a semiconductor with an experimental bandgap of approximately 3 eV. These differences are reproduced in the band structure of these two binary oxides, calculated in [212] by HF and LDA LCAO methods and shown in Figs. 3.6 and 3.7, respectively. The details of the AO basis-set choice and BZ summation can be found in [212].

In MgO (in accordance with the results of other calculations), the two highest valence bands are the oxygen *s*- and *p*-like bands, respectively, whereas the conduction bands are more complicated. The upper valence bands in TiO_2 are also oxygen *s*- and *p*-like bands; however, they consist of 4 and 12 sheets, respectively, because the primitive cell of titanium oxide contains four oxygen atoms.

The lowest conduction band in TiO_2 consists of 10 branches formed by $3d$-states of two titanium atoms and is noticeably separated in energy from the upper conduction bands. The symmetry of the one-electron states can be found using the band representation theory of space groups and data on the crystalline structures.

Evidently the symmetry of band states does not depend on the basis choice for the calculation (LCAO or PW); the change of basis set can only make changes in the relative positions of one-electron energy levels.

An important parameter in the band theory of solids is the Fermi-level energy (see Figs. 3.6 and 3.7), the top of the available electron energy levels at low temperatures. The position of the Fermi level in relation to the conduction band is a crucial factor in determining electrical and thermal properties of solids. The Fermi energy is the analog of the highest-occupied MO energy (HOMO) in molecules. The LUMO (the lowest unoccupied MO) energy in molecules corresponds to the conduction-band bottom in solids. The HOMO-LUMO energy interval in a solid is called the forbidden energy gap or simply bandgap.

Depending on the translation symmetry of the corresponding Bloch states the gap may be direct or indirect. In HF and LDA calculations of both crystals under consideration the bandgap is direct, i.e. the one-electron energies at the top of the valence band and the bottom of the conduction band belong to the same Γ-point of the BZ (this result agrees both with the experiment and other band-structure calculations).

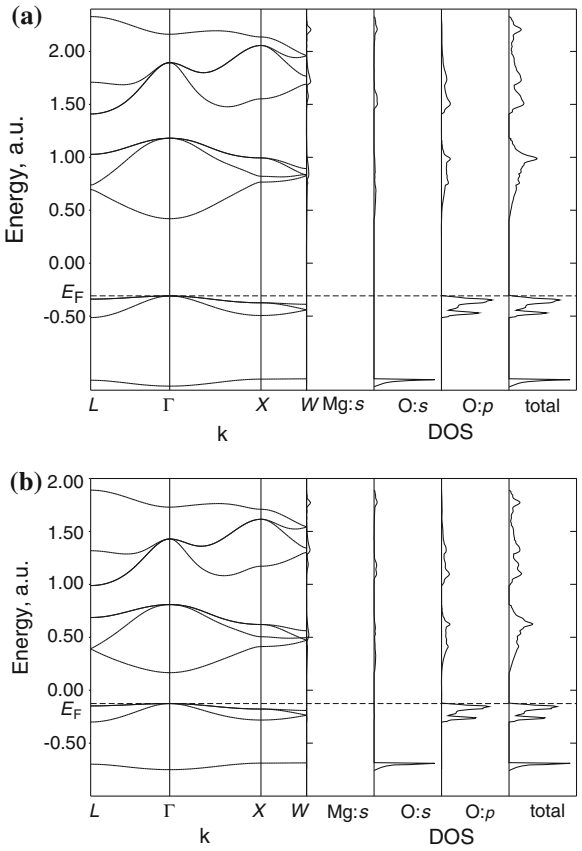

Fig. 3.6 Band structure and DOS of MgO crystal [212]: **a** HF LCAO method; **b** DFT(LDA) LCAO method

It is seen that the HF bandgap in both crystals is essentially overestimated and decreases in LDA calculations mainly due to the lowering of the conduction-band bottom energy. The influence of the correlation effects on the valence-band states is smaller.

Figures 3.6 and 3.7 show that the oxygen $2p$ bandwidth in ionic crystal MgO is smaller than that in TiO_2. The bandwidth is a measure of dispersion in the $\boldsymbol{k}$-space and depends on the magnitude and the range of interactions within the crystal: for the more covalent rutile crystal the oxygen-oxygen interactions are stronger. The core bands of both crystals (not shown on the figures) are separated by a large energy gap from the valence bands and are completely flat due to the high localization of core states near the atomic nuclei.

The Fermi energy of a crystal with n electrons in the primitive unit cell is defined from the condition

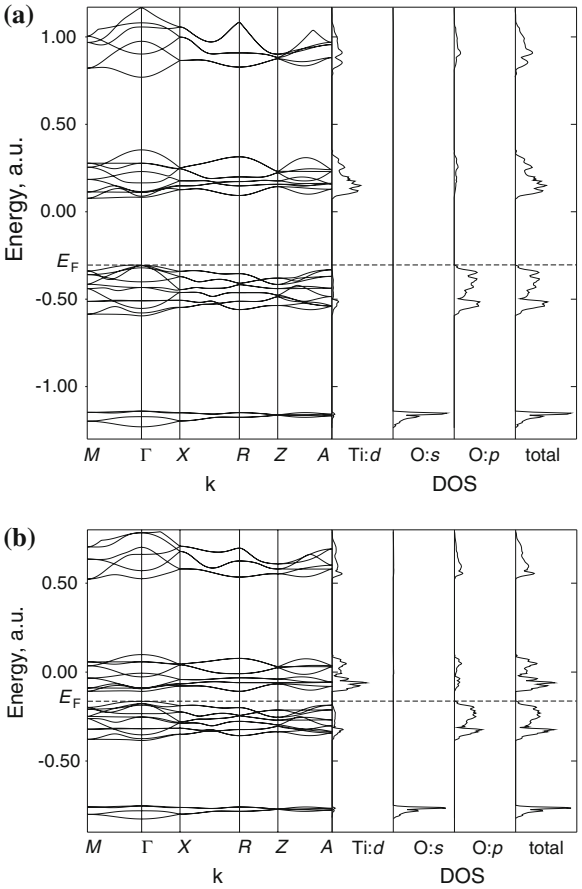

Fig. 3.7 Band structure and DOS of rutile TiO_2 crystal [212]: **a** HF LCAO method; **b** DFT(LDA) LCAO method

$$n = 2\sum_{i=1}^{M}\int_{-\infty}^{\varepsilon_F}\frac{1}{V_B}\int_{BZ}\theta(\varepsilon-\varepsilon_i(\boldsymbol{k}))d\boldsymbol{k} = \int_{-\infty}^{\varepsilon_F} n(\varepsilon)d\varepsilon = \sum_i\int_{-\infty}^{\varepsilon_F} n_i(\varepsilon)d\varepsilon \qquad (3.111)$$

where $n(\varepsilon)$ is the total density of states (DOS) per unit energy. DOS is an important quantity calculated for crystals. The total DOS can be expressed as the sum of contributions $n_i(\varepsilon)$ from individual energy bands, see (3.111). The total DOS definition is independent of the basis set choice (PW or LCAO); the product $n_i(\varepsilon)d\varepsilon$ defines the number of states with energy in the interval $d\varepsilon$. Each energy band spans a limited energy interval between the minimal and maximal one-electron energies ε_{min}, ε_{max} so that $\int_{\varepsilon_{min}}^{\varepsilon_{max}} n(\varepsilon)d\varepsilon$ gives DOS in the corresponding energy interval.

The connection between the electronic structure of a crystal and the one-electron states of the constituent atoms is given by the projected density of states (PDOS), associated with the separate AOs, their shells or individual atoms.

Let us rewrite the total DOS as

$$n(\varepsilon) = \sum_{i=1}^{M} n_i(\varepsilon) = \frac{1}{V_B} \sum_{i=1}^{M} \int_{BZ} f^i(\boldsymbol{k}) \delta(\varepsilon - \varepsilon_i(\boldsymbol{k})) d\boldsymbol{k} \tag{3.112}$$

The weighting function $f^{(i)}(\boldsymbol{k})$ in (3.112) chosen as

$$f^{(i)}(\boldsymbol{k}) = C_{i\mu}(\boldsymbol{k}) C^*_{i\nu}(\boldsymbol{k}) \exp(-\mathrm{i}\boldsymbol{k}\boldsymbol{R}_n) \tag{3.113}$$

defines PDOS associated with AO μ in the reference cell and AO ν in the cell with the translation vector $\boldsymbol{R}_n$. After summation over band index i and integration up to ε_F PDOS (3.113) gives the density matrix elements (3.110).

According to Mulliken population analysis, the DOS projected onto a given set of AOs $\{\lambda\}$ (belonging to the given shell or to the whole atom), is defined by the weight function

$$f^{(i)}_{\{\lambda\}}(\boldsymbol{k}) = \sum_{\mu \in \{\lambda\}} \sum_{\nu} C_{i\mu}(\boldsymbol{k}) C^*_{i\nu}(\boldsymbol{k}) S_{\mu\nu}(\boldsymbol{k}) \tag{3.114}$$

where $S_{\mu\nu}(\boldsymbol{k})$ is Fourier component of the overlap integral.

Let the set $\{\lambda\}$ consist of one AO from the reference cell. The summation of (3.114) over the direct lattice translations $\boldsymbol{R}_n$ and integration over BZ gives the orbital DOS

$$n_\mu(\varepsilon) = \frac{1}{V_{BZ}} \sum_i \sum_\nu \sum_{\boldsymbol{R}_n} \int_{BZ} C_{i\mu}(\boldsymbol{k}) C^*_{i\nu}(\boldsymbol{k}) \exp(\mathrm{i}\boldsymbol{k}\boldsymbol{R}_n) S_{\mu\nu}(\boldsymbol{k}) \delta(\varepsilon - \varepsilon_i(\boldsymbol{k})) d\boldsymbol{k} \tag{3.115}$$

The DOS of an atom A $n_A(\varepsilon)$ and the total DOS $n_{tot}(\varepsilon)$ are caluculated from the orbital DOS:

$$n_A(\varepsilon) = \sum_{\mu \in A} n_\mu(\varepsilon); \; n_{tot}(\varepsilon) = \sum_A n_A(\varepsilon) \tag{3.116}$$

The total DOS and PDOS give rich information on the chemical structure of a system, connecting the calculated band structure with the atomic states. We demonstrate this by considering total and projected DOS for binary oxides MgO, TiO_2 and ternary oxides $SrTiO_3$ and $SrZrO_3$ with cubic perovskite structure (see Figs. 3.6, 3.7 and 3.8).

The analysis of total and partial DOS demonstrates that in all the three oxides under consideration the upper valence band is predominantly formed by the O 2*p* states. It can also be seen that Mg 3*s*, Ti 3*d* and Zr 4*d* states make the dominant contribution to the bottom of the conduction band.

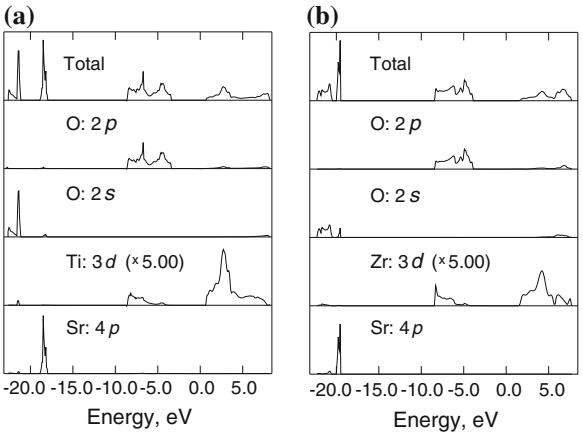

Fig. 3.8 Full and partial DOS in **a** $SrTiO_3$ and **b** $SrZrO_3$ crystals

As is seen from Fig. 3.9, the inclusion of correlation effects moves the valence and conduction bands to the higher and lower energies, respectively, which decreases the bandgap. In more ionic stronzium zirconate the energy bands are narrower than in less-ionic strontium titanate.

The ground-state electron-charge density in a crystal can be expressed as

$$\rho(\boldsymbol{r}) = \sum_{\mu\nu} \sum_{\boldsymbol{R}_n} \sum_{\boldsymbol{R}_m} \rho_{\mu\nu}(\boldsymbol{R}_n - \boldsymbol{R}_m)\chi_\mu(\boldsymbol{r} - \boldsymbol{R}_n)\chi_\nu(\boldsymbol{r} - \boldsymbol{R}_m) \tag{3.117}$$

and reproduces the essential features of the electron-density distribution near atomic nuclei and along interatomic bonds. For each $\boldsymbol{r}$ the sums over $\boldsymbol{R}_n$ and $\boldsymbol{R}_m$ are restricted to those direct lattice vectors such that the value of $\chi_\mu(\boldsymbol{r} - \boldsymbol{R}_n)$ and $\chi_\nu(\boldsymbol{r} - \boldsymbol{R}_m)$ are nonnegligible.

The total electron-density maps provide a pictorial representation of the total electronic distribution and are obtained by calculation of the charge density in a grid of points belonging to some planes. More useful information is obtained by considering difference maps, given as a difference between the crystal electron-density and a "reference" electron density. The latter is a superposition of atomic or ionic charge distributions.

Figure 3.10 shows the total and difference maps for Cu_2O crystal, obtained in HF LCAO calculations [213].

Two important quantities that require an integration involving $\rho(\boldsymbol{r})$ are the electrostatic potential and the electric field [214]. In particular, maps of the electrostatic potential created by electrons and nuclei at a crystal surface may be useful for gathering information about reaction paths and active sites of electrophilic or nucleophilic chemical processes at the surface. As concerns the electric field, it may be of interest to calculate the electric-field gradient at the location of nuclei with a nonzero nuclear

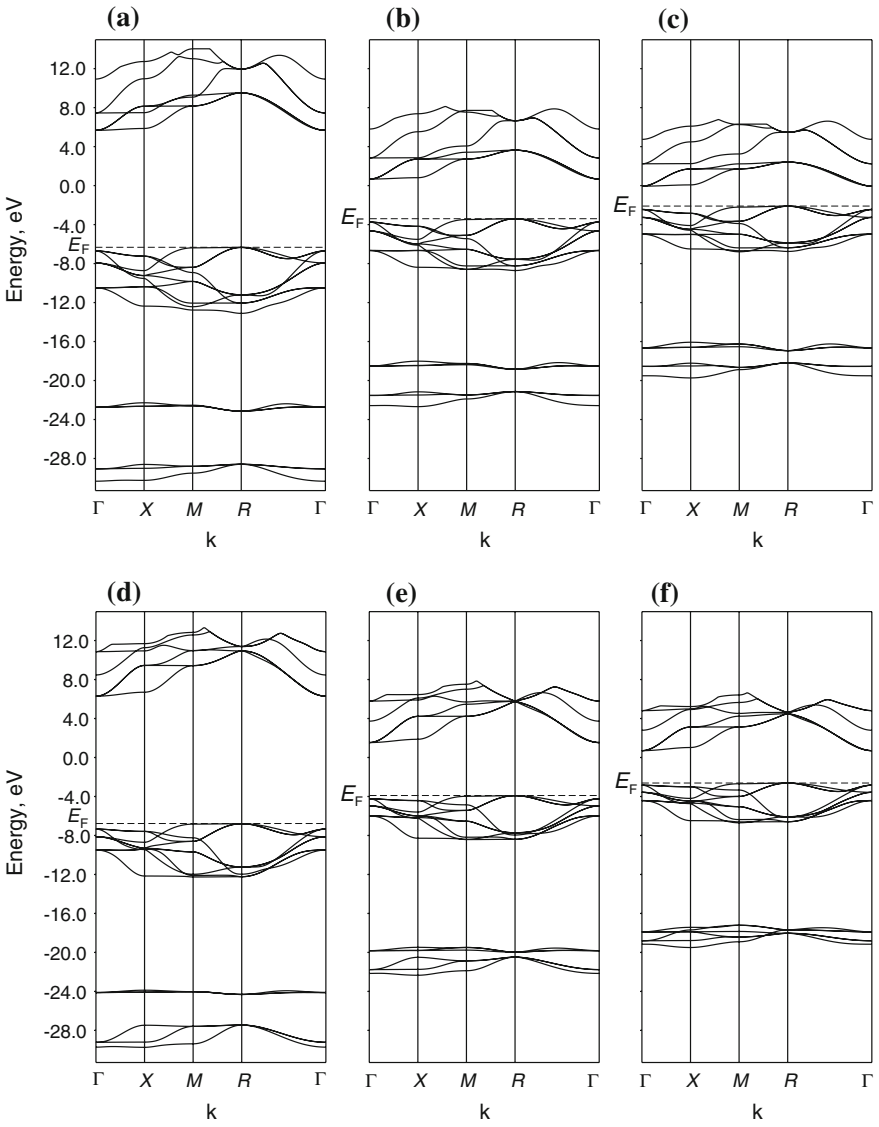

Fig. 3.9 Band structure of cubic crystals: **a**, **b**, **c** $SrTiO_3$, **d**, **e**, **f** $SrZrO_3$. **a**, **d** HF LCAO method; **b**, **e** hybrid HF-DFT(PBE0) LCAO method; **c**, **f** DFT(PBE) LCAO method

quadrupole moment, since comparison with experimental data is possible in such cases.

Three functions may be computed that have the same information content but different use in the discussion of theoretical and experimental results [86]: the electron

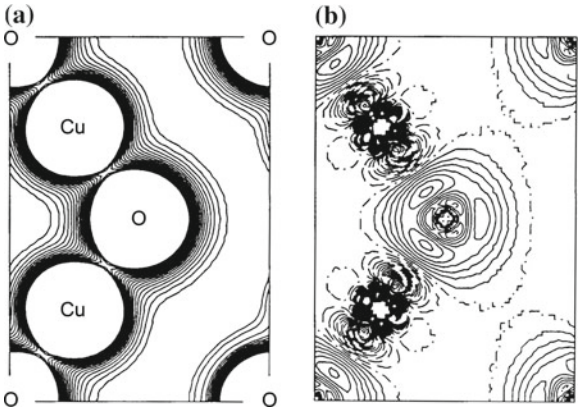

Fig. 3.10 Electron-density maps obtained for Cu_2O on a (110) plane [213]. **a** Total electron density. **b** Density difference maps, bulk minus neutral atom superposition. Values corresponding to neighboring isodensity lines differ by 0.01 e/Bohr^3. The full and broken curves in (**b**) indicate density increase and decrease, respectively

momentum density itself (EMD) $\rho(\boldsymbol{p})$; the Compton profile (CP) function $J(\boldsymbol{p})$; the autocorrelation function, or reciprocal space form factor, $B(\boldsymbol{r})$.

Let $\chi_\mu(\boldsymbol{p})$ be defined as the Fourier transform of AO $\chi_\mu(\boldsymbol{r})$ belonging to atom A

$$\chi_\mu(\boldsymbol{p}) = \int \exp(\mathrm{i}\boldsymbol{p}\boldsymbol{r})\chi_\mu(\boldsymbol{r})d\boldsymbol{r} \tag{3.118}$$

and $\boldsymbol{s}_\mu$ is the fractional coordinate of atom A in the reference cell.

EMD is defined as the diagonal element of the six-dimensional Fourier transform of the one-electron density matrix from coordinate to momentum space:

$$\rho(\boldsymbol{p}) = \sum_{\mu\nu}\sum_{\boldsymbol{R}_n} \rho_{\mu\nu}(\boldsymbol{R}_n)\exp\left(-\mathrm{i}\boldsymbol{p}(\boldsymbol{R}_n + \boldsymbol{s}_\mu - \boldsymbol{s}_\nu)\right)\chi_\mu(\boldsymbol{p})\chi_\nu(\boldsymbol{p}) \tag{3.119}$$

The Compton profile function is obtained by 2D integration of the EMD over a plane through and perpendicular to the direction

$$J(\boldsymbol{p}) = \int \rho(\boldsymbol{p} + \boldsymbol{p}'_\perp)d\boldsymbol{p}'_\perp \tag{3.120}$$

after indicating with $\boldsymbol{p}'_\perp$ the general vector perpendicular to $\boldsymbol{p}$.

It is customary to make reference to CPs as functions of a single variable p, with reference to a particular direction $\langle hkl\rangle$ identified by a vector $\boldsymbol{e} = (h\boldsymbol{a}_1 + k\boldsymbol{a}_2 + l\boldsymbol{a}_3)/|h\boldsymbol{a}_1 + k\boldsymbol{a}_2 + l\boldsymbol{a}_3|$. We have

$$J_{\langle hkl\rangle}(p) = J(p\boldsymbol{e}) \tag{3.121}$$

The function $J_{\langle hkl\rangle}(p)$ is referred to as directional CPs. The weighted average of the directional CPs over all directions is the average CP. In the so-called impulse

approximation, $J_{\langle hkl\rangle}(p)$ may be related to the experimental CPs, after correction for the effect of limited resolution [86].

Once the directional CPs are available, the numerical evaluation of the corresponding autocorrelation function, or reciprocal-space form factor, $B(\boldsymbol{r})$ is given by the 1D Fourier transform:

$$B_{\langle hkl\rangle}(\boldsymbol{r}) = \frac{1}{\pi}\int_{-\infty}^{\infty} J_{\langle hkl\rangle}(p)\exp(\mathrm{i}\boldsymbol{p}\boldsymbol{r})d\boldsymbol{p} \tag{3.122}$$

The structural and electronic properties of Cu_2O have been studied in [213] using the HF LCAO method and *a posteriori* density-functional corrections. The electronic structure and bonding in Cu_2O were analyzed and compared with X-ray photoelectron spectroscopy spectra, showing a good agreement for the valence-band states. The Fourier transform of the ground-state charge density of a crystalline system provides the X-ray structure factors of the crystal, which can be determined experimentally by X-ray diffraction. To check the quality of the calculated electron density in Cu_2O crystal, structure factors have been calculated in [213], showing a good agreement with the available experimental data.

3.7.2 Equilibrium Structure, Bulk Modulus, Formation and Surface Energy

The comparison of the parameters of the bulk rutile calculated using DFT-LCAO and DFT-PW methods with those obtained previously was made in [215].

Large-scale DFT-GGA-PBE LCAO calculations of the bulk rutile TiO_2 with total geometry optimization was performed using the CRYSTAL-09 [17]. An all-valence basis set (BS) in the form of 6s–311sp–1d Gaussian–type functions (GTFs) was used for the O atom [216]; for the Ti atom, the small-core effective-core pseudopotential (SCECP), was employed for the internal shells, and the BS includes valence (3s, 3p, 3d, 4s electrons) and virtual shells, i.e., GTF configuration is *SCECP*–5*s*–6*sp*–5*d* [217]. The optimization of BSs both for the O and Ti atoms was performed, the self-consistent procedure was performed on the 6×6×6 MonkhorstPack [87] **k**-mesh. To estimate effective atomic charges within the LCAO method, the Mulliken population analysis was used.

For large-scale DFT-PW calculations on rutile with the total geometry optimization, the scalar relativistic pseudopotentials combined with the Projector Augmented Wave (PAW) method, as implemented in the VASP computer code [154], were employed. The same PBE-GGA nonlocal exchange-correlation functional was used both in DFT-LCAO and DFT-PW calculations. To estimate effective charge distribution on atoms within plane wave methods, the Bader approach has been used.

Results calculated in [215] and a previous study using both DFT-LCAO and DFT-PW approaches are compared between themselves, see Table 3.3. Comparison of

Table 3.3 Structural and electronic properties of optimized rutile-based TiO_2 bulk [215]

Calculation method	Lattice parameters			Parameters of bonds and atoms				Band gap
and reference source	a, Å	c, Å	u	$r_{Ti-O(I)}$, Å	$r_{Ti-O(II)}$, Å	q_O, e	q_{Ti}, e	$\Delta\varepsilon_g$, eV
DFT-LCAO-PBE	4.647	2.980	0.306	1.964	2.006	−1.097	+2.194	1.74
DFT-PAW-PBE	4.619	2.964	0.305	1.956	1.990	−1.159	+2.318	1.79
DFT-USPP-PW91	4.630	2.981	0.305	1.965	1.995	−1.151	+2.302	1.89
Results of other	4.540	2.930	0.303	1.910	1.970	−1.00	+2.00	1.80
Calculations [23]	4.65	3.00	0.307	1.95	2.04	−1.36	+2.72	2.1
Experimental data	4.593	2.958	0.305	1.949	1.980	–	–	3.03 [218]

the structure parameters for titania bulk calculated using different methods clearly shows qualitative correlation between themselves and their correspondence to the experimental values, although a certain dispersion of results (obtained using different methods) can be observed. It is also true for the Ti–O bond lengths inside the first (I) and second (II) coordination shells consisting of the four and two O atoms, respectively, around each Ti atom. Calculated values of the effective charges q_O and q_{Ti} look also quite reasonable, which are found to be qualitatively comparable with the corresponding data obtained earlier.

As for the large difference between the experimental and calculated values of band gaps $\Delta\varepsilon_g$, it is well-known that standard DFT calculations essentially underestimate $\Delta\varepsilon_g$ for semiconductors and insulators. Nevertheless, DFT-PW-GGA methods were found to be quite applicable for qualitative description of a number of properties for the bulk rutile.

Table 3.4 shows the results TiS_2(ZrS_2) bulk crystal LCAO(PBE0) calculations [219].

Table 3.4 shows that the difference between the theoretical and experimental structure parameters does not exceed 1 % for the two sulfides under consideration. Also, a good estimate of the formation energy of TiS_2 and ZrS_2 is provided. This fact can be considered as the verification of the sufficient accuracy of PBE0 approximation in the special case of these layered crystals. This success of hybrid DFT method in the reproducing of weak van der Waals-type interlayer forces may be explained by the large contribution of the induced electrostatic interactions due to the large polarizability of sulfur atom. In agreement with the experimental observations, the 1To polymorphs were found to be the most stable modifications among all the considered phases. This can be clearly seen from Table 3.4 where the formation energy (per formula unit) of other presupposed phases is given with respect to that of 1To phase. The most encouraging thing is that the calculated energy of the observed 1To polytype proved to be lower than the energy of 2Ho (with $P6_3mc$ symmetry) and 3R-o (with R3m symmetry) polytypes, which have the same octahedral morphology of the three-plane atomic layers but were not actually observed.

Table 3.4 Calculated lattice parameters, formation energy E_{form}[a], and band gaps E_g of different TiS_2 and ZrS_2 phases [219] (experimental values are given in parenthesis)

Polymorph	Space group	a, Å	b, Å	c, Å	E_{form}, eV	E_g, eV
TiS_2						
Hexagonal, 1T-o (trigonal)	164($P\bar{3}m1$)	3.411 (3.408 [220])	3.411	5.656 (5.699 [220])	13.9[b] (14.9[c])	1.4 (0.3 [221])
Hexagonal, 2H-o	186($P6_3mc$)	3.412	3.412	11.541	0.013	1.5
Cubic	227($Fd\bar{3}m$)	9.723	9.723	9.723 (9.739 [222])	0.046	0.8
Rhombohedral, 3R-o	166($R\bar{3}m$)	3.420	3.420	19.151	0.066	1.5
Hexagonal, 2H-t	194($P6_3/mmc$)	3.322	3.322	12.045	0.597	1.6
Tetragonal	137($P4_2/nmc$)	4.178	4.178	6.070	1.244	1.1
ZrS_2						
Hexagonal, 1T-o (trigonal)	164($P\bar{3}m1$)	3.674 (3.650 [223])	3.674	5.891 (5.840 [223])	16.5[b] (17.7[c])	2.7 (1.7 [224])
Hexagonal, 2H-o	186($P6_3mc$)	3.676	3.676	11.912	0.001	2.8
Cubic	227($Fd\bar{3}m$)	10.396	10.396	10.396	0.020	2.1
Rhombohedral, 3R-o	166($R\bar{3}m$)	3.678	3.678	19.813	0.031	2.9
Tetragonal	137($P4_2/nmc$)	4.396	4.396	6.341	0.654	2.2
Hexagonal, 2H-t	194($P6_3/mmc$)	3.563	3.563	12.391	0.664	1.4

[a] Formation energy with respect to the 1T phase
[b] Calculated atomization energy
[c] Atomization energy estimated from the experimental data [225]

Ab initio PW simulations of surface properties use both isolated slab and repeated slab models, compared in HF studies of surface properties of $BaTiO_3$ in [226]. Ab initio schemes implemented with plane-wave based computational methods are quite convenient and effective for 3D periodic bulk crystals, but cannot treat directly isolated slabs. With plane-wave-based methods, slabs must be treated with periodically repeated supercells, which contain a vacuum space separating the slabs. Two major differences then result between isolated-slab and periodic-slab calculations [226]. The first one is the presence of spurious interactions among the periodically repeated slabs. Secondly, isolated-slab calculations can assume the proper boundary condition of a vanishing electric field in the vacuum regions, while periodic-slab calculations must assume the boundary condition of a vanishing average field over the supercell. This is a major problem when dealing with slabs with asymmetric terminations, even in the absence of a macroscopic polarization. Since the work functions of the two nonequivalent surfaces are generally different in that case, there is a potential difference across the slab. However, periodic boundary conditions force a periodic potential, which amounts to imposing a fictitious external field. This problem is unavoidable with periodic-slab calculations, where self consistency is achieved in such a fictitious field. Presumably, both of these problems for periodically repeated slabs diminish with increasing thickness of the vacuum regions separating the slabs. On the other

hand, even moderate vacuum separations greatly increase the computational burden, particularly when plane-wave-like basis sets are used.

The results of the very first ab initio study of surface properties of $BaTiO_3$ using isolated slabs were reported in [226]. The ability to deal with isolated slabs is due to the localized basis implementation that has been adopted in [226]. A localized-basis set not only allows one to perform calculations for genuinely finite and isolated systems, but also permits the introduction of arbitrarily large vacuum separations in periodic systems without any essential increase in the computational burden. That allows one to test periodic-slab calculations with various thicknesses of vacuum space in between. The results obtained in [226] indicate that periodic-slab calculations are substantially affected by the two problems mentioned above, even at quite large vacuum separations. On the other hand, the results for truly isolated slabs are quite consistent with fast convergence to genuine surface properties.

Several surface properties of $BaTiO_3$ have been calculated in [226]: namely, the surface charge, surface energy, and surface dynamical charges, within an ab initio HF scheme scheme. These properties have been studied as functions of the thickness and termination of the slabs. Both genuinely isolated slabs and periodically repeated slabs, with different terminations have been used. The ability to deal with genuinely isolated slabs is a virtue of the localized-basis implementation adopted in [226]. In particular, the slab surface charge provides a value for the spontaneous polarization in excellent agreement with the calculation of the latter as a Berry phase, and with experiment as well. On the other hand, it has been found that when periodically repeated slabs are used, the interactions among slabs and the fictitious field imposed by the periodic boundary conditions can significantly affect the accuracy of the calculations, even at quite large vacuum separations.

3.7.3 Phonon Frequencies and Relative Phase Stability Calculations

The second-order derivatives of the energy with respect to the nuclear coordinates are involved in lattice dynamics, in particular, in the calculation of vibrational (phonon) spectra. We shall begin from the molecular case [227]. The decoupling of the nuclear from the electronic motion is made in the adiabatic approximation. Let u_i represents a displacement of the ith cartesian coordinate from its equilibrium value ($i = 1, 2, \ldots, 3N$), where N is the number of nuclei in a molecule, and $q_i = \sqrt{M_i}u_i$ are the generalized coordinate (M_i is the mass of the atom associated with the ith coordinate) and its derivative with respect to time $\dot{q}_i = p_i$. In the harmonic approximation the classical vibrational Hamiltonian of a polyatomic molecule becomes

$$H = T + V = \frac{1}{2}\left(\sum_i M_i \dot{u}_i^2 + \sum_{ij} H_{ij} U_j\right) + V_0 = \frac{1}{2}\left(\langle p|p\rangle + \langle q|W|q\rangle\right) + V_0 \tag{3.123}$$

Here V_0 is the electron energy for the equilibrium atomic coordinates, and H_{ij} are the Hessian matrix elements

$$H_{ij} = \frac{1}{2}\left[\frac{\partial^2 V}{\partial u_i \partial u_j}\right]_0 \tag{3.124}$$

evaluated at equilibrium. The relation $W_{ij} = \frac{H_{ij}}{\sqrt{M_i M_j}}$ defines the elements of the weighted Hessian.

The eigenvalues $\varkappa_j$ of the Hermitian matrix W are the generalized force constants. The Hamiltonian (3.123) then can be factorized into $3N$ one-dimensional harmonic Hamiltonians

$$H = \sum_\nu h_\nu = \sum_\nu \frac{1}{2}\left(P_\nu^2 + \omega_\nu^2 Q_\nu^2\right) \tag{3.125}$$

Thus each of the $3N-6$ vibrational modes can be interpreted as a collective oscillatory movement with frequency $\omega_\nu = \sqrt{\varkappa_\nu}/2\pi$ and the problem of calculating vibrational spectra reduces to the diagonalization of matrix W to find the set of eigenvalues $\varkappa_j$.

For periodic systems, the translation invariance of the potential energy and Hessian matrix should be used. The generalized coordinates obey the Bloch theorem and are written in the form

$$q_i(\boldsymbol{k}) = N \sum_{\boldsymbol{g}} \exp(-\mathrm{i}\boldsymbol{k}\boldsymbol{g}) q_i^{\boldsymbol{g}} \tag{3.126}$$

The vibrational problem is block-factorized into a set of problems (one for each $\boldsymbol{k}$ point in BZ) of dimension $3N - 6$ where N is the number of atoms in the primitive unit cell.

The $\boldsymbol{k}$-block of the $\boldsymbol{k}$-factorized W matrix takes the form

$$W_{ij}(\boldsymbol{k}) = \sum_{\boldsymbol{g}} \exp(\mathrm{i}\boldsymbol{k}\boldsymbol{g}) \frac{H_{ij}^{\mathbf{0}\boldsymbol{g}}}{\sqrt{M_i M_j}} \tag{3.127}$$

where $H_{ij}^{\mathbf{0}\boldsymbol{g}}$ is the second derivative of potential energy at equilibrium with respect to atom i in the reference cell $\mathbf{0}$ and atom j in cell $\boldsymbol{g}$. The number of equations (3.127) to be solved equals the number of $\boldsymbol{k}$-points in the BZ, i.e. is infinite for the infinite crystal. In practice, the calculations of phonon frequencies are made for a finite number of $\boldsymbol{k}$-points and the interpolation is used to obtain so-called phonon branches $\omega_1(\boldsymbol{k}), \ldots, \omega_i(\boldsymbol{k}), \ldots, \omega_{3N}(\boldsymbol{k})$ (like one-electron energies are obtained in SCF calculations for a finite set of $\boldsymbol{k}$-points and then interpolated to form the electron-

energy bands). The relationship between phonon frequencies ω and wavevector $\boldsymbol{k}$ determines the phonon dispersion.

Comparing the vibrational branches and electronic bands calculations we note that in the former case the equations for different $\boldsymbol{k}$ values are solved independently while in the latter case the self-consistent calculation is necessary due to the BZ summation in the HF or KS Hamiltonian.

Once the phonon dispersion in a crystal is known, thermodynamic functions can be calculated on the basis of statistical mechanics equations. As an example, the Helmholtz free energy, F, can be obtained as:

$$\langle F \rangle = \sum_{i\boldsymbol{k}} \left\{ \frac{1}{2}\hbar\omega_{i\boldsymbol{k}} + k_B T \ln \left[1 - \exp\left(-\frac{\hbar\omega_{i\boldsymbol{k}}}{k_B T} \right) \right] \right\} \tag{3.128}$$

where the sum is extended to all lattice vibrations, $\omega_{i\boldsymbol{k}}$, and k_B is the Boltzmann's constant. Another way of computing thermodynamic functions is based on the use of the phonon density of states. The evolution of the crystal structure as a function of temperature and pressure can also be simulated by minimizing $G = F + pV$. The procedure requires a sequence of geometry optimizations, and lattice-vibration calculations [228].

Lattice vibrations can be measured experimentally by means of classical vibration spectroscopic techniques (infrared and Raman) or neutron inelastic scattering. However, only the latter technique allows one to measure the full spectrum in a range of $\boldsymbol{k}$ vectors, whereas with infrared and Raman spectroscopy, only lattice vibrations at $\Gamma(\boldsymbol{k} = \boldsymbol{0})$ are usually detected (the second-order spectra, corresponding to nonzero wavevector $\boldsymbol{k} \neq \boldsymbol{0}$ are demanding). The calculations of the vibrational frequencies only at Γ point require the solution of only one equation

$$\det |W(0)| = 0, \quad W_{ij}(0) = \sum_{\boldsymbol{g}} \frac{H_{ij}^{\boldsymbol{0g}}}{\sqrt{M_i M_j}} \tag{3.129}$$

The knowledge of phonon symmetry is useful in the analysis of infrared and Raman spectra of solids as the symmetries of active phonons in these spectra are governed by selection rules following from the symmetry restrictions imposed on the transitions matrix elements [229]. Using the symmetry of the phonons found one can establish which vibrational modes are active in the first- and second-order infrared and Raman spectra.

To analyze the symmetry of phonon states the method of induced reps of space groups can be used [229]. The procedure of analysis of the phonon symmetry is the following. Arranging atoms in the primitive cell over the Wyckoff positions of the periodic system symmetry group (the space, layer or line group) and using the induced reps of this group one can determine the symmetry of the phonons. Only those of the induced reps that are induced by the irreps of the site-symmetry groups according to which the components of the vectors of the local atomic displacements

Table 3.5 Phonon symmetry in rutile TiO_2 crystal with space group D_{4h}^{14}

$\boldsymbol{q}$-basis		$\boldsymbol{k}$-basis					
$G_{\mathbf{q}}$	Rep. of $G_{\boldsymbol{q}}$	Γ	M	Z	A	X	R
Ti(2a)	$b_{1u}(z)$	$2^-, 3^-$	$2^-, 3^-$	1	1	1	1^-
(000)	$b_{2u}(x-y)$	5^-	5^-	3	3	2	1^-
D_{2h}	$b_{3u}(x+y)$	5^-	5^-	4	4	2	1^-
O(4f)	$a_1(x+y)$	$1^+, 4^+, 5^-$	$1^+, 4^+, 5^-$	1, 4	1, 4	2, 2	$1^+, 1^-$
$(xx0)$	$b_2(x-y)$	$2^+, 3^+, 5^-$	$2^+, 3^+, 5^-$	2, 3	2, 3	2, 2	1^+1^-
C_{2v}	$b_1(z)$	$2^-, 3^-, 5^+$	$2^-, 3^-, 5^+$	1, 3	1, 3	1, 1	1^+1^-

transform are used. The total dimension n of the induced rep (called the mechanical representation) equals $3N$ (N is the number of atoms in the primitive cell).

As an example, Table 3.5 shows the phonon symmetry in rutile TiO_2 crystal.

There is a one-to-one correspondence between irreps of crystal point group D_{4h} and irreps of the space group at Γ point: $A_{1g,u} - 1^{\pm}$, $A_{2g,u} - 3^{\pm}$, $B_{1g,u} - 2^{\pm}$, $B_{2g,u} - 4^{\pm}$, $E_{g,u} - 5^{\pm}$. The atomic displacements of six atoms in the primitive cell generate the 18-dimensional reducible representation, which contains three acoustic modes and 15 optical modes ($A_{1g}+A_{2g}+A_{2u}+B_{1g}+2B_{1u}+B_{2g}+E_g+3E_u$). Three acoustic modes have zero frequency at the Γ point and are associated with the translation of the entire crystal along any direction in space. These branches are called *acoustic* modes as the corresponding vibrations behave as acoustic waves. The translation of the entire crystal along the z-axis corresponds to irrep 3^- (A_{2u}) at Γ point, translation in the plane xy – 5^- (E_u).

Both acoustic modes are polar and split into transverse A_{2u} (TO) and longitudinal E_u (LO) with different frequencies due to macroscopic electric field. All other branches show finite nonzero frequencies at Γ and are known as optical modes, because they correspond to unit-cell dipole moment oscillations that can interact with an electromagnetic radiation.

In the model of a finite crystal the rotation of the entire crystal around the z- and xy-axis corresponds to the irreps 3^+ and 5^+, respectively, including the displacements of only oxygen atoms, see Table 3.5. As seen from Table 3.5, the phonons of even symmetry ($1^+, 2^+, 3^+, 4^+, 5^+$) are connected only with the oxygen-atom displacements. Due to the different atomic masses of oxygen and titanium atoms, the corresponding lines can appear in different parts of the vibrational spectra, making its interpretation easier.

The calculation of phonon frequencies of the crystalline structure is one of the fundamental subjects when considering the phase stability, phase transitions, and thermodynamics of crystalline materials. The approaches of ab-initio calculations fall into two classes: the *linear response* method [230] and the *direct* method, see [231] and references therein.

In the first method, the dynamical matrix is expressed in terms of the inverse dielectric matrix describing the response of the valence electron-density to a periodic

lattice perturbation. For a number of systems, in particular, the nanostructures, the linear-response approach is difficult, since the dielectric matrix must be calculated in terms of the electronic eigenfunctions and eigenvalues of the perfect crystal.

There are two variants of the direct method.

In the frozen-phonon approach the phonon energy is calculated as a function of the displacement amplitude in terms of the difference in the energies of the distorted and ideal lattices. Another approach of the direct method uses the forces $\left(\frac{\partial E}{\partial u_i}\right)_{eq}$ calculated in the total-energy calculations, derives from them the values of the force-constant matrices and hence the dynamical matrix and phonon-dispersion curves.

The direct method calculations are restricted to phonons whose wavelength is compatible with the periodic boundary conditions (PBC) applied to the supercell used in the calculations [232]. Let the supercell is defined by the linear transformation (2.4) with matrix $\mathbf{l}$. The determinant L of this matrix defines the number of the primitive unit cells in the supercell.

The eigenvectors of the dynamical matrix $D(\mathbf{k}; \mu, \nu)$ are Bloch functions with the wave vectors $\mathbf{K}^{(s)} = \sum_i s_i \mathbf{B}_i (\|s_i\| \leq \|1/2\|)$ belonging to BZ of the initial reciprocal lattice, defined by the basic translation vectors $\mathbf{B}_i, i = 1, 2, 3$. Let $\mathbf{b}_i$ be basic translation vectors of the reciprocal lattice corresponding to the direct lattice Γ_2 of supercells and defining the reduced BZ. By definition of a reciprocal lattice $(\mathbf{a}_i \mathbf{B}_j) = (\mathbf{A}_j \mathbf{b}_i) = 2\pi\delta_{ij}$. The transformation (2.4) of the direct lattice is accompanied by the transformation of reciprocal lattices $\mathbf{b} = \mathbf{l}^{-1}\mathbf{B}$. For the symmetrical transformation $\mathbf{l}$ the transformation $\mathbf{l}^{-1}$ is also symmetrical [229], and L points of the initial BZ $\mathbf{K}^{\mathbf{k}_0} (i = 1, 2, \ldots, L)$ become equivalent to point $\mathbf{k}_0$ of the reduced BZ:

$$\mathbf{K}_i^{\mathbf{k}_0} = \mathbf{k}_0 + \sum_{ij} q_{ij} \mathbf{b}_j, i = 1, 2, \ldots L \tag{3.130}$$

where q_{ij} are integers.

Introducing PBC for a supercell means that only $\Gamma(\mathbf{k} = 0)$ point in the reduced BZ is considered so that $\mathbf{k}_0 = 0$ in (3.130). The corresponding $\mathbf{K}_i^{(s)}$ points of initial BZ have to be the translation vectors of the new reciprocal lattice i.e. $\mathbf{K}^{(s)} = \sum_{j'} m_{j'} \mathbf{b}_{j'}$ so that

$$\sum_{j'} m_{j'} \mathbf{b}_{j'} \sum_j n_j \mathbf{A}_j = \sum_{j'j} m_{j'} n_j (\mathbf{b}_{j'} \mathbf{A}_j) = 2\pi \sum_j m_j n_j \tag{3.131}$$

However,

$$\begin{aligned} (\mathbf{K}^{(s)} \mathbf{A}_n) &= \sum_{i'} s_{i'} \mathbf{B}_{i'} \sum_j n_j \sum_i l_{ji} \mathbf{a}_i \\ &= \sum_{i'} \sum_j \sum_i s_{i'} l_{ji} n_j (\mathbf{B}_{i'} \mathbf{a}_i) = 2\pi \sum_j \sum_i s_i l_{ji} n_j \end{aligned} \tag{3.132}$$

where m_j, n_j are zero or integers. Thus, the relation

$$\sum_i l_{ji} s_i = m_j, \; i, j = 1, 2, 3 \tag{3.133}$$

is fulfilled for the wave vectors $\mathbf{K}^{(s)} = \sum_j m_j \mathbf{b}_j$. These wave vectors are called commensurate with the supercell, defined by matrix $\mathbf{l}$.

The majority of calculations were performed based on DFT PW method, for example to study phonons in the rutile structure [233]. The calculation of the vibrational frequencies of crystals was implemented in the LCAO CRYSTAL code (see http://www.crystal.unito.it) and applied to different oxides bulk crystals [59].

In the LCAO approximation frequencies at Γ are evaluated in the direct method in the same way as for molecules [227]: a set SCF calculations of the unit cell are performed at the equilibrium geometry and incrementing each of the nuclear coordinates in turn by u (use of symmetry can reduce the number of the required calculations). Second-order energy derivatives are evaluated numerically. Obtaining frequencies at wavevector symmetry points different from Γ would imply the construction of appropriate supercells due to the one-to one correspondence between the supercell choice and the set of $\boldsymbol{k}$-points equivalent to the Γ point in the reduced BZ. A finite range of interaction in the lattice sum (3.129) is assumed, usually inside the supercell chosen. In the case of ionic compounds, long-range Coulomb effects due to coherent displacement of the crystal nuclei are neglected, as a consequence of imposing the periodic boundary conditions [227]. Therefore, $W_{ij}(0)$ needs to be corrected for obtaining the longitudinal optical (LO) modes [234]. For this reason, in some cases only transverse optical (TO) parts of the phonon spectrum are calculated as is done in the combined DFT PW-DFT LCAO lattice dynamics study of TiO_2 rutile [235]. The phonon frequencies computed in [235] for the rutile optimized crystal structure are reported in Table 3.6 and compared with experimental data.

The LDA frequencies are in excellent agreement with the experimental frequencies, especially if compared with the frequencies measured at low temperature ($T \sim 4$ K), when these data are available. The deviation between the LDA and experimental frequencies is $\sim$13 cm^{-1} at most, and is often much smaller than that. For instance, the deviation drops to no more than $\sim$2 cm^{-1} for the two stiffest modes, B_{2g} and A_{1g}, and it remains small also for several of the softer modes. Both PBE and PW91 results are much less satisfactory. With the exception of the B_{1g} mode, the GGA functionals systematically underestimate the LDA and measured frequencies. It is found in [235] that this discrepancy between LDA and GGA results is mostly due to the difference in the equilibrium lattice parameters at zero pressure predicted by the functionals. The LDA frequency is the highest because LDA predicts the smallest equilibrium volume, and the PBE equilibrium volume is large enough to lead to an imaginary frequency.

All the results discussed were obtained within the plane-wave pseudopotential implementation of DFT. For all functionals, calculations were repeated with the all-electron LCAO scheme for the equilibrium geometries, bulk moduli and energy

Table 3.6 Calculated and measured frequencies (in cm^{-1}) relative to the Γ-point of bulk TiO_2 rutile [235]*

Mode	PBE	PW91	LDA	Neutrons	IR and Raman
Raman					
B_{2g}	774.3	780.9	824.7	825	827
A_{1g}	565.9	572.0	611.6	610	612 (611)
E_g (2)	429.2	434.2	463.2	445	447 (455)
B_{1g}	154.2	151.7	137.0	142	143 (143)
Silent					
A_{2g}	423.6	425.4	421.7	Not found	–
B_{2u}	357.5	363.4	393.0	406	–
B_{1u}	79.2	99.2	104.0	113	–
Infrared					
E_u (TO)	468.6	472.0	488.4	494	500
E_u (TO)	353.5	357.1	383.9	Not found	388
E_u (TO)	124.0	127.4	191.4	189	183
A_{2u} (TO)	186.3	47.1	154.4	173 (142)	167 (144)

* The double degeneracy of the E_g mode is indicated by the label (2). The references to the experimental neutron-scattering and the infrared (IR) and Raman data are given in [235]. When available, the low-temperature ($T \sim 4$ K) experimental frequencies are reported in brackets

profiles along the ferroelectric TO A_{2u} mode. Apart from slight quantitative differences, in all cases the all-electron LCAO calculations agree well with the plane-wave, pseudopotential results, confirming their independence of the particular numerical scheme used to implement DFT. We note that the hybrid HF-DFT LCAO calculations could in principle give better agreement with experimental data for phonon frequencies of rutile as was shown in the B3LYP LCAO calculations of the vibrational spectrum of calcite $CaCO_3$ [236]. In this case the mean absolute error is less than 12 cm^{-1} (frequencies range from 100 to 1600 cm^{-1}).

The phonon frequencies calculations allow one to estimate the relative stability of the different bulk crystal phases. Table 3.7 shows the results of LCAO DFT(PBE0) calculations [237] of the phonon frequencies in $BaTiO_3$ bulk crystal. It is seen that, in agreement with the experimental data, only the rhombohedral $BaTiO_3$ phase is stable at low temperatures (the smallest phonon frequencies are imaginary for all the three other phases).

3.8 Nanostructure Formation, Surface and Strain Energy

In the part II Applications we consider the results of the calculations of the inorganic nanostructures (nanolayers-slabs, nanotubes-NT, nanowires-NW) based on boron compounds, tetravalent semiconductors, boron and Group III metal nitrides, oxides (binary and ternary) and sulfides.

Table 3.7 Calculated formation energies and the smallest phonon frequencies of the rhombohedral, orthorhombic, tetragonal and cubic phases of $BaTiO_3$ [237]

Phase	E_{form}[a], meV	The smallest phonon frequency (cm^{-1})
Rhombohedral (SG 160)	0	180
Orthorhombic (SG 38)	10	66i
Tetragonal (SG 99)	20	139i
Cubic (SG 221)	60	257i

[a] Formation energy relative to rhombohedral phase

For nanolayers, nanotubes and nanowires in consideration the calculated formation energy E_{form}, surface energy E_{surf} and strain energy E_{str} are given as defined by the following equations.

The formation energy E_{form} of the stoichiometric slabs was calculated via the equation:

$$E_{form} = E_{slab}/n_{slab} - E_{bulk}/n_{bulk} \tag{3.134}$$

where E_{slab}, n_{slab} and E_{bulk}, n_{bulk} are the total energy and the number of formula units per primitive cell in the slab and bulk crystal, correspondingly.

Stoichiometric nanotube (nanowire) formation energy E_{form} can be calculated using the total energy $E_{NT}(E_{NW})$ and the number of formula units n_{NT} (n_{NW}) per primitive cell for the nanotube (nanowire) instead of the slab values.

The stoichiometric slab surface energy was estimated as

$$E_{surf} = (E_{slab} - n_{slab}E_{bulk}/n_{bulk})/(2S_{slab}) \tag{3.135}$$

where S_{slab} is the surface area of the final slab structure. The term layer is used for the designation of the smallest possible group of close (but separated from others) atomic planes in the slab, which obey the bulk crystal stoichiometry.

The nanotube strain (rolling) energy was calculated by the equation:

$$E_{str} = E_{NT}/n_{NT} - E_{slab}/n_{slab} \tag{3.136}$$

This quantity may be interpreted as the energy of NT formation from the corresponding slab having the optimized structure.

References

1. J.E. Jaffe, A.C. Hess, J. Chem. Phys. **105**, 10983 (1996)
2. R. Martin, *Electronic Structure. Basic Theory and Practical Methods* (Cambridge University Press, Cambridge, 2004)
3. http://www.psi-k.org/codes.shtml
4. W. Kohn, Rev. Mod. Phys. **71**, 1253 (1999)

5. M.C. Payne, M.P. Teller, D.C. Allan, J.A. Arias, J.D. Joannopoulos, Rev. Mod. Phys. **64**, 1045 (1992)
6. http://www.wien2k.at
7. M. Towler, An introductory guide to Gaussian basis sets in solid state electronic structure calculations, http://www.theochem.unito.it/crystal_tuto/mssc2013_cd/tutorials/index.html
8. E. Kahiras, *Atomic and Electronic Structure of Solids* (Cambridge University Press, Cambridge, 2003)
9. L. Kantorovich, *Quantum Theory of the Solid State* (Kluwer Academic Publishers, Dordrecht, 2004)
10. R. Catlow, A. Sokol, A. Walsh, *Computational Approaches to Energy Materials* (Wiley, Chichester, 2013)
11. K.N. Kudin, G.E. Scuseria, Phys. Rev. B **61**, 16440 (2000)
12. V.N. Staroverov, G.E. Scuseria, J. Tao, J.P. Perdew, Phys. Rev. B **69**, 075102 (2004)
13. E. Artacho, D. Sanchez-Portal, P. Ordejon, A. Garcia, J.M. Soler, Phys. Status Solidi (B) **215**, 809 (1999)
14. P. Ordejon, E. Artacho, J.M. Soler, Phys. Rev. B **53**, R10441 (1996)
15. T.H. Dunning, J. Chem. Phys. **90**, 1007 (1989)
16. http://bse.pnl.gov/bse/portal
17. R. Dovesi, V.R. Saunders, C. Roetti, R. Orlando, C.M. Zicovich-Wilson, F. Pascale, B. Civalleri, K. Doll, N.M. Harrison, I.J. Bush, P. D'Arco, M. Llunell, *CRYSTAL09 User's Manual* (University of Torino, Torino, 2010)
18. K. Doll, N.M. Harrison, V.R. Saunders, J. Phys.: Condens. Matter **11**, 5007 (1999)
19. B.D. Bunday, *Basic Optimization Methods* (Edward Arnold Ltd., London, 1984)
20. R.A. Evarestov, A.I. Panin, A.V. Bandura, M.V. Losev, J. Phys.: Conf. Ser. **117**, 012015 (2008)
21. R.A. Evarestov, Yu.F. Zhukovskii, A.V. Bandura, S. Piskunov, Cent. Eur. J. Phys. **9**, 492 (2011)
22. W.H. Press, S.A. Teukolski, V.T. Vetterling, B.P. Flannery, *Numerical Recipes in FORTRAN 77: The Art of Scientific Computing*, vol. 1, 3rd edn. (Cambridge University Press, Cambridge, 2007)
23. F. Labat, P. Baranek, C. Domain, C. Minot, C. Adamo, J. Chem. Phys. **126**, 154703 (2007)
24. J. Sauer, P. Ugliengo, E. Garrone, V.R. Saunders, Chem. Rev. **94**, 2095 (1994)
25. S.F. Boys, F. Bernardi, Mol. Phys. **19**, 553 (1970)
26. M. Gutowski, J.G.G.M. van der Rijdt, J.H. van Lenthe, F.B. van Duijneveldt, J. Chem. Phys. **98**, 4728 (1993)
27. A. Gruneich, B.A. Hess, Theor. Chem. Acc. **100**, 253 (1998)
28. S.D. Kenny, A.P. Horsfield, H. Fujitami, Phys. Rev. B **62**, 4899 (2000)
29. F. Jensen, Theor. Chem. Acc. **132**, 1380 (2013)
30. M.F. Peintinger, D.V. Oliveira, T. Bredow, J. Comput. Chem. **34**, 451 (2013)
31. F. Weigend, R. Ahlrichs, Phys. Chem. Chem. Phys. **7**, 3297 (2005)
32. F. Weigend, F. Furche, R. Ahlrichs, J. Chem. Phys. **119**, 12753 (2003)
33. J.P. Perdew, A. Zunger, Phys. Rev. B **45**, 13244 (1992)
34. T. Bredow, A. Gerson, Phys. Rev. B **61**, 5194 (2000)
35. T. Bredow, Phys. Rev. B **75**, 144102 (2007)
36. V.V. Maslyuk, M.M. Islam, T. Bredow, Phys. Rev. B **72**, 125101 (2005)
37. A.P. Christiansen, Y.S. Lee, K.S. Pitzer, J. Chem. Phys. **71**, 4445 (1970)
38. D.R. Hamann, M. Schlüter, C. Chiang, Phys. Rev. Lett. **43**, 1494 (1979)
39. J.C. Phillips, L. Kleinman, Phys. Rev. **116**, 287 (1959)
40. L. Kleinman, D.M. Bylander, Phys. Rev. Lett. **48**, 1425 (1982)
41. http://www.physik.uni-frankfurt.de/~engel/ncpp.html
42. D. Vanderbilt, Phys. Rev. B **41**, 7892 (1990)
43. M. Fuchs, M. Scheffer, Comput. Phys. Commun. **119**, 67 (1999)
44. http://www.uam.es/departamentos/ciencias/fismateriac/siesta/
45. http://www.scm.com/Doc/Doc2006.01
46. A. Alkauskas, A. Baratoff, C. Bruder, J. Phys. Chem. A **108**, 6863 (2004)

47. M. Krauss, W.J. Stevens, Annu. Rev. Phys. Chem. **35**, 357 (1984)
48. M. Dolg, in *Modern Methods and Algorithms of Quantum Chemistry*, ed. by J. Grotendost, NIC Series, **1**, 479 (2000), **3**, 507 (2000), online http://www.fz-juelich.de/nic-series/NIC-Series-e.html
49. Gaussian 09, M.J. Frisch, G.W. Trucks, H.B. Schlegel, G.E. Scuseria, M.A. Robb, J.R. Cheeseman, J.A. Montgomery Jr., T. Vreven, K.N. Kudin, J.C. Burant, J.M. Millam, S.S. Iyengar, J. Tomasi, V. Barone, B. Mennucci, M. Cossi, G. Scalmani, N. Rega, G.A. Petersson, H. Nakatsuji, M. Hada, M. Ehara, K. Toyota, R. Fukuda, J. Hasegawa, M. Ishida, T. Nakajima, Y. Honda, O. Kitao, H. Nakai, M. Klene, X. Li, J.E. Knox, H.P. Hratchian, J.B. Cross, V. Bakken, C. Adamo, J. Jaramillo, R. Gomperts, R.E. Stratmann, O. Yazyev, A.J. Austin, R. Cammi, C. Pomelli, J.W. Ochterski, P.Y. Ayala, K. Morokuma, G.A. Voth, P. Salvador, J.J. Dannenberg, V.G. Zakrzewski, S. Dapprich, A.D. Daniels, M.C. Strain, O. Farkas, D.K. Malick, A.D. Rabuck, K. Raghavachari, J.B. Foresman, J.V. Ortiz, Q. Cui, A.G. Baboul, S. Clifford, J. Cioslowski, B.B. Stefanov, G. Liu, A. Liashenko, P. Piskorz, I. Komaromi, R.L. Martin, D.J. Fox, T. Keith, M.A. Al-Laham, C.Y. Peng, A. Nanayakkara, M. Challacombe, P.M.W. Gill, B. Johnson, W. Chen, M.W. Wong, C. Gonzalez, J.A. Pople (Gaussian Inc., Wallingford CT, 2009), http://www.gaussian.com/citation.htm
50. P.J. Hay, W.R. Wadt, J. Chem. Phys. **52**, 270, 284, 299 (1985)
51. P. Durand, J.C. Barthelat, Theor. Chim. Acta **38**, 283 (1975)
52. W.J. Stevens, H. Basch, M. Krauss, J. Chem. Phys. **81**, 6026 (1984)
53. W.J. Stevens, M. Krauss, H. Basch, P.J. Jasic, Can. J. Phys. **70**, 612 (1992)
54. H. Stoll, B. Metz, M. Dolg, J. Comput. Chem. **23**, 767 (2002)
55. I.V. Abarenkov, I.I. Tupitsyn, J. Chem. Phys. **115**, 1650 (2004)
56. T.A. Kaplan, S.D. Mahanti (eds.), *Electronic Properties of Solids Using Cluster Methods* (Plenum Press, New York, 1994)
57. I.V. Abarenkov, I.M. Antonova, Int. J. Quant. Chem. **100**, 649 (2004)
58. T. Nakajima, T. Yanai, K. Hirao, J. Comput. Chem. **23**, 847 (2002)
59. R.A. Evarestov, *Quantum Chemistry of Solids. LCAO Treatment of Crystals and Nanostructures*, 2nd edn. Springer Series in Solid State Sciences, vol. 153 (Springer, New York, 2012)
60. A.V. Titov, N.S. Mosyagin, Int. J. Quant. Chem. **71**, 359 (1999)
61. D. Figgen, G. Rauhut, M. Dolg, H. Stoll, Chem. Phys. **311**, 227 (2005)
62. M. Dolg, Theor. Chem. Acc. **114**, 297 (2005)
63. K.A. Peterson, C. Puzzarini, Theor. Chem. Acc. **114**, 283 (2005)
64. X. Cao, M. Dolg, J. Mol. Struct. (Theochem) **673**, 203 (2004)
65. X. Cao, M. Dolg, H. Stoll, J. Chem. Phys. **118**, 487 (2003)
66. G. Treurich, N.A. Hill, Phys. Rev. B **64**, 073106 (2001)
67. R.A. Evarestov, A.I. Panin, A.V. Bandura, Russ. J. Gen. Chem. **78**, 1823 (2008)
68. P. Flude, *Electron Correlations in Molecules and Solids*, 3rd edn. Springer Series in Solid State Sciences, vol. 100 (Springer, Berlin Heidelberg New York, 1995)
69. V. Fock, M. Vesselow, M. Petrashen, Zh. Exsp. Theor. Fiz. **10**, 723 (1940)
70. C.J. Cramer, *Essentials of Computational Chemistry*, 2nd edn. (Wiley, New York, 2004)
71. M.J. Wong, L. Radom, J. Phys. Chem. **99**, 8582 (1995)
72. C. Moller, M.S. Plesett, Phys. Rev. **46**, 618 (1934)
73. P.-O. Löwdin, Int. J. Quant. Chem. **55**, 77 (1995)
74. P. Knowles, M. Schütz, H.-J. Werner, in *Proceedings of Modern Methods and Algorithms of Quantum Chemistry*, 2nd edn. ed. by J. Grotendorst. NIC Series, vol. 3 (John von Neumann Institute for Computing, Julich, 2000), p. 97
75. C. Pisani, M. Busso, G. Capecchi, S. Casassa, R. Dovesi, L. Maschio, C. Zicovich-Wilson, M. Schutz, J. Chem. Phys. **122**, 094113 (2005)
76. P. Fulde, Adv. Phys. **51**, 909 (2002)
77. H. Stoll, Chem. Phys. Lett. **191**, 548 (1992)
78. A. Shukla, M. Dolg, P. Fulde, H. Stoll, Phys. Rev. B **60**, 5211 (1999)
79. B. Paulus, Chem. Phys. Lett. **371**, 7 (2003)
80. P. Fulde, H. Stoll, Found. Phys. **30**, 2049 (2000)

81. K.N. Kudin, G.E. Scuseria, J. Chem. Phys. **113**, 7779 (2000)
82. http://www.theochem.unito.it/lcc2004/cryscor.pdf
83. C.C.J. Roothaan, Rev. Mod. Phys. **23**, 69 (1951)
84. C.C.J. Roothaan, Rev. Mod. Phys. **32**, 179 (1960)
85. N.W. Ashcroft, N.D. Mermin, *Solid State Physics* (Cole, London, 1976)
86. V.R. Saunders, R. Dovesi, C. Roetti, R. Orlando, C.M. Zicovich-Wilson, N.M. Harrison, *CRYSTAL-2003 Users Manual* (University of Torino, Torino, 2003)
87. H.J. Monkhorst, J.D. Pack, Phys. Rev. B **13**, 5188 (1976)
88. R.A. Evarestov, V.P. Smirnov, Phys. Rev. B **70**, 233101 (2004)
89. K. Burke, J. Chem. Phys. **136**, 150901 (2012)
90. L.H. Thomas, Proc. Camb. Philos. Soc. **23**, 542 (1927)
91. E. Fermi, Z. Phys. **48**, 73 (1928)
92. J.C. Slater, Phys. Rev. **91**, 528 (1953)
93. P. Hohenberg, W. Kohn, Phys. Rev. **136**, B864 (1964)
94. N.C. Handy, Mol. Phys. **102**, 2399 (2004)
95. R.M. Dreizler, E.K.U. Gross, *Density Functional Theory* (Springer, Berlin, 1990)
96. N.H. March, *Electron Density Theory of Atoms and Molecules* (Academic Press, London, 1992)
97. H. Eschrig, *The Fundamentals of Density Functional Theory* (Teubner, Leipzig, 1996)
98. J.F. Dobson, G. Vignale, M.P. Das (eds.), *Density Functional Theory: Recent Progress and New Directions* (Plenum, New York, 1998)
99. V.E. Van Doren, K. Van Alsenoy, P. Geerlings (eds.), *Density Functional Theory and Its Applications to Materials* (American Institute of Physics, Melville, 2001)
100. W. Koch, M.C. Holthausen, *A Chemist's Guide to Density Functional Theory*, 2nd edn. (Wiley, New York, 2002)
101. D.S. Sholl, J.A. Steckel, *Density Functional Theory. A Practical Introduction* (Wiley, Hoboken, 2009)
102. M. Springborg, *Methods of Electronic Structure Calculations* (Wiley, Chichester, 2000)
103. J.R. Reimers, *Computational Methods for Large Systems: Electronic Structure Approaches for Biotechnology and Nanotechnology* (Wiley, Hoboken, 2011)
104. R.O. Jones, O. Gunnarsson, Rev. Mod. Phys. **61**, 689 (1989)
105. R. Neumann, Mol. Phys. **87**, 1 (1996)
106. J.P. Perdew, S. Kurth, Lect. Notes Phys. **620**, 1 (2003)
107. K. Capelle, *A Birds-eye View of Density Functional Theory*, http://arXiv.org/archive/cond-mat/0211443v4
108. K. Burke, *The ABC of DFT*, http://chem.ps.uci.edu/~kieron/dft/book
109. L. Goerigk, S. Grimme, Phys. Chem. Chem. Phys. **13**, 6670 (2011)
110. G.D. Sherrill, J. Chem. Phys. **132**, 110902 (2010)
111. K. Burke, L.O. Wagner, Int. J. Quant. Chem. **113**, 96 (2013)
112. W. Kohn, L.J. Sham, Phys. Rev. **140**, A1133 (1965)
113. J.P. Perdew, A. Ruzsinszky, J. Tao, V.N. Staroverov, G.E. Scuseria, G.I. Csonka, J. Chem. Phys. **123**, 062201 (2005)
114. F. Zahariev, S.S. Leang, M.S. Gordon, S. Grimme, J. Chem. Phys. **138**, 244108 (2013)
115. J. Tao, J.P. Perdew, V.N. Staroverov, G.E. Scuseria, Phys. Rev. B **69**, 075102 (2004)
116. S. Grimme, F. Neese, J. Chem. Phys. **127**, 150901 (2007)
117. U. von Barth, L. Hedin, J. Phys. C: Condens. Matter **5**, 1629 (1972)
118. D.M. Ceperley, B.J. Alder, Phys. Rev. Lett. **45**, 566 (1980)
119. S.J. Vosko, L. Wilk, M. Nussair, Can. J. Phys. **1980**, 1200 (1980)
120. J.P. Perdew, A. Zunger, Phys. Rev. B **23**, 5048 (1981)
121. J.P. Perdew, Y. Wang, Phys. Rev. B **40**, 3389 (1989)
122. J.P. Perdew, A. Zunger, Phys. Rev. B **33**, 8800 (1986)
123. J.P. Perdew, K. Burke, Y. Wang, Phys. Rev. B **54**, 16533 (1996)
124. A.D. Becke, Phys. Rev. A **38**, 3098 (1988)
125. C. Lee, W. Wang, R.G. Parr, Phys. Rev. B **37**, 785 (1988)

126. P. Ziesche, S. Kurth, J.P. Perdew, Comput. Mater. Sci. **11**, 122 (1998)
127. J. Tao, J.P. Perdew, V.N. Staroverov, G.E. Scuseria, Phys. Rev. Lett. **91**, 146401 (2003)
128. J.P. Perdew, S. Kurth, A. Zupan, P. Blaha, Phys. Rev. Lett. **82**, 2544 (1999)
129. X. Xin, W.A. Goddard III, J. Chem. Phys. **121**, 4068 (2004)
130. R. Armiento, A.E. Mattsson, Phys. Rev. B **72**, 085108 (2005)
131. Z. Wu, R.E. Cohen, Phys. Rev. B **73**, 235116 (2006)
132. J.P. Perdew, A. Ruzsinszky, G.I. Csonka, O.A. Vydrov, G.E. Scuseria, L.A. Constantin, X. Zhou, K. Burke, Phys. Rev. Lett. **100**, 136406 (2008)
133. H. Jiang, J. Chem. Phys. **134**, 204705 (2011)
134. P. Haas, F. Tran, P. Blaha, Phys. Rev. B **79**, 085104 (2009)
135. F. Tran, R. Laskowski, P. Blaha, K. Schwarz, Phys. Rev. B **75**, 115131 (2007)
136. J.P. Perdew, K. Burke, M. Ernzerhof, Phys. Rev. Lett. **77**, 3865 (1996)
137. E.H. Lieb, S. Oxford, Int. J. Quant. Chem. **19**, 427 (1981)
138. E.J. Baerends, O.V. Gritsenko, J. Chem. Phys. **123**, 062202 (2005)
139. M.A. Buijse, E.J. Baerends, Mol. Phys. **100**, 401 (2002)
140. M. Gruning, O.V. Gritsenko, E.J. Baerends, J. Chem. Phys. **118**, 7183 (2003)
141. A.D. Becke, J. Chem. Phys. **112**, 4020 (2000)
142. A.D. Becke, J. Chem. Phys. **98**, 1372, 5468 (1993)
143. O.V. Gritsenko, P.R.T. Schipper, E.J. Baerends, Int. J. Quant. Chem. Symp. **30**, 1375 (1996)
144. J.P. Perdew, M. Ernzerhof, K. Burke, J. Chem. Phys. **105**, 9982 (1996)
145. A. Lichanot, M. Merawa, M. Causa, Chem. Phys. Lett. **246**, 263 (1995)
146. M. Towler, A. Zupan, M. Causa, Comput. Phys. Commun. **98**, 181 (1996)
147. A. Zupan, M. Causa, Int. J. Quant. Chem. **56**, 337 (1995)
148. A. Savin, Int. J. Quant. Chem. **S22**, 457 (1988)
149. A.D. Becke, J. Chem. Phys. **96**, 2155 (1992)
150. M. Causa, Lect. Notes Chem. **48**, 91 (1996)
151. J.M. Soler, E. Artacho, J.D. Gale, A. Garcia, J. Junquera, P. Ordejón, D. Sánchez-Portal, J. Phys.: Condens. Matter **14**, 2745 (2002)
152. F. Cora, M. Alfredsson, G. Mallia, D. Midlemiss, W.C. Mackrodt, R. Dovesi, R. Orlando, Struct. Bond. **113**, 171 (2004)
153. http://www.gaussian.com
154. G. Kresse, J. Furthmuller, *VASP the Guide* (Universität Wien, Wien, 2007)
155. F. Cora, Mol. Phys. **103**, 2483 (2005)
156. A.V. Krukau, O.A. Vydrov, A.F. Izmaylov, G.E. Scuseria, J. Chem. Phys. **125**, 224106 (2006)
157. A.E. Mattsson, R. Armiento, J. Paier, G. Kresse, J.M. Wills, T.R. Mattsson, J. Chem. Phys. **128**, 084714 (2008)
158. R. Wahl, D. Vogtenhuber, G. Kresse, Phys. Rev. B **78**, 104116 (2008)
159. B. Civalleri, D.S. Middlemiss, R. Orlando, C.C. Wilson, P. Ugliengo, Chem. Phys. Lett. **451**, 287 (2008)
160. D.I. Bilc, R. Orlando, R. Shaltar, G.M. Rignanese, J. Iniguez, Ph. Ghosez, Phys. Rev. B **77**, 165107 (2008)
161. S.J. Clark, J. Robertson, Phys. Rev. B **82**, 085208 (2010)
162. R.M. Irelan, T.M. Henderson, G.E. Scuseria, J. Chem. Phys. **135**, 094105 (2011)
163. T.M. Henderson, J. Paier, G.E. Scuseria, Phys. Status Solidi (B) **248**, 767 (2011)
164. B.G. Janesko, T.M. Henderson, G.E. Scuseria, Phys. Chem. Chem. Phys. **11**, 443 (2009)
165. S. Park, B. Lee, S.H. Jeon, S. Han, Curr. Appl. Phys. **11**, 5337 (2011)
166. R. Demichelis, B. Civalleri, P. D'Arco, R. Dovesi, Int. J. Quant. Chem. **110**, 2260 (2010)
167. F. El-Mellouhi, E.N. Brothers, M.J. Lucero, I.W. Bulik, G.E. Scuseria, Phys. Rev. B **87**, 035107 (2013)
168. A. Kuzmin, A. Kalinko, R.A. Evarestov, Acta Materialia **61**, 371 (2013)
169. R. Demichelis, B. Civalleri, M. Ferrabone, R. Dovesi, Int. J. Quant. Chem. **110**, 406 (2010)
170. L. Machio, M. Ferrabone, A. Meyer, J. Garza, R. Dovesi, Chem. Phys. Lett. **501**, 612 (2011)
171. A.V. Bandura, R.A. Evarestov, J. Comput. Chem. **33**, 1554 (2012)
172. A.V. Bandura, R.A. Evarestov, D.D. Kuruch, Surf. Sci. **604**, 1591 (2010)

173. A.V. Bandura, R.A. Evarestov, Comput. Mater. Sci. **65**, 395 (2012)
174. P. Deak, B. Aradi, T. Frauenheim, E. Janzen, A. Gali, Phys. Rev. B **81**, 153203 (2010)
175. A. Janotti, J.B. Varley, P. Rinke, N. Umezawa, G. Kresse, G.G. Van de Walle, Phys. Rev. B **81**, 085212 (2010)
176. H.A. Huy, B. Aradi, T. Frauenheim, P. Deak, Phys. Rev. B **83**, 155201 (2011)
177. R. Ramorasad, H. Zhu, P. Rinke, M. Scheffler, Phys. Rev. Lett. **108**, 066404 (2012)
178. P. Deak, B. Aradi, T. Frauenheim, Phys. Rev. B **86**, 195206 (2012)
179. E. Blokhin, E. Kotomin, A. Kuzmin, J. Purans, R. Evarestov, J. Maier, Appl. Phys. Lett. **102**, 112913 (2013)
180. J. Heyd, G.E. Scuseria, M. Ernzerhof, J. Chem. Phys. **118**, 8207 (2003)
181. J. Heyd, G.E. Scuseria, J. Chem. Phys. **120**, 7274 (2004)
182. W. Kohn, Int. J. Quant. Chem. **56**, 229 (1995)
183. M.W. Gill, J.A. Pople, Int. J. Quant. Chem. **40**, 753 (1991)
184. M. Ernzerhof, J.P. Perdew, J. Chem. Phys. **109**, 3313 (1998)
185. GAUSSIAN Development Version, Revision B.07, M.J. Frisch, G.W. Trucks, H.B. Schlegel, G.E. Scuseria, M.A. Robb, J.R. Cheeseman, J.A. Montgomery Jr., T. Vreven, K.N. Kudin, J.C. Burant, J.M. Millam, S.S. Iyengar, J. Tomasi, V. Barone, B. Mennucci, M. Cossi, G. Scalmani, N. Rega, G.A. Petersson, H. Nakatsuji, M. Hada, M. Ehara, K. Toyota, R. Fukuda, J. Hasegawa, M. Ishida, T. Nakajima, Y. Honda, O. Kitao, H. Nakai, M. Klene, X. Li, J.E. Knox, H.P. Hratchian, J.B. Cross, V. Bakken, C. Adamo, J. Jaramillo, R. Gomperts, R.E. Stratmann, O. Yazyev, A.J. Austin, R. Cammi, C. Pomelli, J.W. Ochterski, P.Y. Ayala, K. Morokuma, G.A. Voth, P. Salvador, J.J. Dannenberg, V.G. Zakrzewski, S. Dapprich, A.D. Daniels, M.C. Strain, O. Farkas, D.K. Malick, A.D. Rabuck, K. Raghavachari, J.B. Foresman, J.V. Ortiz, Q. Cui, A.G. Baboul, S. Clifford, J. Cioslowski, B.B. Stefanov, G. Liu, A. Liashenko, P. Piskorz, I. Komaromi, R.L. Martin, D.J. Fox, T. Keith, M.A. Al-Laham, C.Y. Peng, A. Nanayakkara, M. Challacombe, P.M.W. Gill, B. Johnson, W. Chen, M.W. Wong, C. Gonzalez, J.A. Pople (Gaussian Inc., Pittsburg, 2003)
186. O.A. Vydrov, J. Heyd, A.V. Krukau, G.E. Scuseria, J. Chem. Phys. **125**, 074106 (2006)
187. J.E. Moussa, P.A. Schultz, J.R. Chelikowsky, J. Chem. Phys. **136**, 204117 (2012)
188. J.C. Burant, G.E. Scuseria, M.J. Frisch, J. Chem. Phys. **105**, 8969 (1996)
189. http://www.dftb.org
190. http://www.dftb-plus.info
191. G. Seifert, J. Phys. Chem. A **111**, 5609 (2007)
192. G. Seifert, WIRESs Comput. Mol. Sci. **2**, 456 (2012)
193. Z. Bodrog, B. Aradi, Phys. Status Solidi (B) **249**, 259 (2012)
194. Z. Bodrog, B. Aradi, T. Frauenheim, J. Chem. Theor. Comput. **7**, 2654 (2011)
195. G. Dolgonos, B. Aradi, N.H. Moreira, T. Frauenheim, J. Chem. Theor. Comput. **6**, 266 (2010)
196. B. Aradi, B. Hourahine, T. Frauenheim, J. Phys. Chem. A **111**, 5678 (2007)
197. P. Koskinen, V. Makinen, Comput. Mater. Sci. **47**, 237 (2009)
198. A.F. Oliveira, G. Seifert, T. Heine, H.A. Duarte, J. Braz. Chem. Soc. **20**, 1193 (2009)
199. G.M. de Seabra, R.C. Walker, M. Elstner, D.A. Case, A.E. Roitberg, J. Phys. Chem. A **111**, 5655 (2007)
200. T. Frauenheim, G. Seifert, M. Elstner, T. Niehaus, C. Kohler, M. Amkreutz, M. Sternberg, Z. Hajnal, A. di Carlo, S. Suhai, J. Phys.: Condens. Matter **14**, 3015 (2002)
201. T. Frauenheim, G. Seifert, M. Elstner, Z. Hajnal, G. Jungnickel, D. Porezag, S. Suhai, R. Scholz, Phys. Status Solidi (B) **217**, 41 (2000)
202. A.K. Rappe, C.J. Casewit, K.S. Colwell, W.A. Goddard III, W.M. Skiff, J. Am. Chem. Soc. **114**, 10024 (1992)
203. Q. Cui, M. Elstner, E. Kaxiras, T. Frauenheim, M. Karplus, J. Phys. Chem. B **105**, 569 (2001)
204. T.A. Niehaus, S. Suhai, F. Della, Sala, P. Lugli, M. Elstner, G. Seifert, T. Frauenheim. Phys. Rev. B **63**, 085108 (2001)
205. J.M. Knaup, B. Hourahine, T. Frauenheim, R.C. Walker, J. Phys. Chem. A **111**, 5637 (2007)
206. P.E. Blochl, Phys. Rev. **50**, 17953 (1994)
207. G. Kresse, D. Joubert, Phys. Rev. **59**, 1758 (1999)

208. M. Torrent, F. Jollet, F. Bottin, G. Zerah, X. Gonze, Comput. Mater. Sci. **42**, 337 (2008)
209. J. Paier, M. Marsman, K. Hammer, G. Kresse, I.C. Gerber, J.G. Angyan, J. Chem. Phys. **124**, 154709 (2006)
210. F. Gygi, A. Baldereschi, Phys. Rev. B **34**, 4405 (1986)
211. http://dft.sandia.gov
212. R.A. Evarestov, D.E. Usvyat, V.P. Smirnov, Phys. Solid State **45**, 2072 (2003)
213. E. Ruiz, S. Alvarez, P. Alemany, R. Evarestov, Phys. Rev. B **56**, 7189 (1997)
214. C. Pisani, R. Dovesi, C. Roetti, *Hartree-Fock ab-initio Treatment of Crystalline Systems*. Lecture Notes in Chemistry, vol. 48 (Springer, Berlin, 1988)
215. R.A. Evarestov, D.B. Migas, Yu.F. Zhukovskii, J. Phys. Chem. C **116**, 13395 (2012)
216. A. Schäfer, C. Huber, R. Ahlrichs, J. Chem. Phys. **100**, 5829 (1994)
217. M.M. Hurley, L.F. Pacios, P.A. Christiansen, R.B. Ross, W.C. Ermler, J. Chem. Phys. **84**, 6840 (1986)
218. H. Tang, F. Levi, H. Berger, P.E. Schmid, Phys. Rev. B **52**, 7771 (1995)
219. R.A. Evarestov, A.V. Bandura, Phys. Scr. **89**, 044001 (2014)
220. J.R. Dahn, W.R. McKinnon, R.R. Haering, W.J.L. Buyers, B.M. Powell, Can. J. Phys. **58**, 207 (1980)
221. C.Y. Chen, W. Fabian, F.C. Brown, K.C. Woo, B. Davies, B. DeLong, A.H. Thompson, Phys. Rev. B **21**, 615 (1980)
222. P. Lightfoot, F. Krok, J.L. Nowinski, P.G. Bruce, J. Mater. Chem. **2**, 139 (1992)
223. G. Haegg, N. Schoenberg, Arkiv fur kemi **7**, 371 (1954)
224. M. Moustafa, T. Zandt, C. Janowitz, R. Manzke, Phys. Rev. B **80**, 035206 (2009)
225. V.P. Glushko, V.A. Medvedev, L.V. Gurvich (eds.), *Thermal Constants of Substances* (Wiley, New York, 1999)
226. L. Fu, E. Yaschenko, L. Resca, R. Resta, Phys. Rev. B **60**, 2697 (1999)
227. F. Pascale, C.M. Zicovich-Wilson, F. Lopez, B. Civalleri, R. Orlando, R. Dovesi, J. Comput. Chem. **25**, 888 (2004)
228. R. Dovesi, B. Civalleri, R. Orlando, C. Roetti, V.R. Saunders, Rev. Comput. Chem. **21**, 1 (2005)
229. R.A. Evarestov, V.P. Smirnov, *Site Symmetry in Crystals: Theory and Applications*, 2nd edn. Springer Series in Solid State Sciences, vol. 108 (Springer, Berlin, 1997)
230. S. Baroni, S. de Gironcoli, A. Dal Corso, P. Giannozzi, Rev. Mod. Phys. **73**, 515 (2001)
231. K. Parlinski, Z.Q. Li, Y. Kawazoe, Phys. Rev. Lett. **78**, 4063 (1997)
232. R.A. Evarestov, M.V. Losev, J. Comput. Chem. **30**, 2645 (2009)
233. P. Sikora, J. Phys. Chem. Solids **66**, 1069 (2005)
234. P. Umari, A. Pasquarello, A. Dal Corso, Phys. Rev. B **63**, 094305 (2001)
235. B. Montanari, N.M. Harrison, Chem. Phys. Lett. **364**, 528 (2002)
236. M. Principe, F. Pascale, C.M. Zicovich-Wilson, V.R. Saunders, R. Orlando, R. Dovesi, Phys. Chem. Miner. **31**, 559 (2004)
237. R.A. Evarestov, A.V. Bandura, J. Comput. Chem. **33**, 1123 (2012)

Part II
Applications

Chapter 4
Boron and Metal Diborides

In this chapter, *written by Yu.F. Zhukovskii* (*quantzh@latnet.lv*), boron- and metal diborides-based nanostructures are considered.

Preliminary information about boron bulk and nanolayer structure allows one to analyze the results of the rolled-up single-walled (SW) boron nanotube theoretical calculations, made by DFT (LDA and GGA), as well as molecular dynamics methods. Single-wall nanotubes of different morphology are compared in order to make conclusions about their relative stability. The morphology, binding energy and electronic structure of double-walled boron nanotubes and polyhedral nanotubes supplements the discussion. The morphological evolution of boron nanotubes in close-packed bundles in the crystalline phase is discussed basing on the first-principles calculations, performed for a specific case of single-walled boron nanotubes with a small diameter and triangular-type chirality. The difference in the inter-nanotube interaction between the bundles of boron NTs with armchair- and zigzag-chiralities was found to be mainly due to the differences in their bonding features in the respective pristine single-walled boron nanotubes.

The results of LCAO DFT calculations of the relative stability of boron nanowires possessing different morphologies are discussed. According to the analysis of the electronic structure of 1D boron nanostructures, most of them, unlike the boron bulk, are found to be metallic, although a few BNT and BNW configurations can be classified as narrow band gap semiconductors.

Basing on the analysis of the MeB_2 structure and the chemical bonding in these compounds, the calculations of rolled up MgB_2, BeB_2, AlB_2 and TiB_2 single-walled nanotubes and their bundles are considered, performed using DFT (LDA and GGA), tight binding as well as molecular dynamics methods. MgB_2 NTs remain superconducting, analogously to the bulk, while the conductivity in the nanotubes of other metal borides is reduced in the sequence BeB_2, AlB_2 and TiB_2. The single-wall nanotubes of the latter diboride exhibit semiconducting properties.

© Springer-Verlag Berlin Heidelberg 2015

R.A. Evarestov, *Theoretical Modeling of Inorganic Nanostructures*,
NanoScience and Technology, DOI 10.1007/978-3-662-44581-5_4

4.1 Boron Bulk and Nanolayers

Boron (B) is known as the easiest metalloid element which forms a large number of compounds [1]. Bulk boron has exceptional properties of low volatility and a high melting point, its durability is larger as compared to steel while hardness is higher than that of corundum [2]. As a hard material with a small energy band gap, boron plays an important role in semiconductor and spacecraft applications, farmacology and medicine [3].

A variety of crystal structures of bare boron are related to its electron deficiency (as compared to carbon crystalline polymorphs), from which chemical versatility stems [4, 5].

Among boron bulk structures, the most energetically stable were found to be rhombohedral α- and β-B described by space group $R\bar{3}m$ [6]. Both steady quasi-molecular bulk structures are built from B_{12} icosahedra (Fig. 4.1) grouped inside rhombohedral crystal (other possible bulk boron phases are formed in the presence of impurities). The shape of β-B unit cell can be considered as $2 \times 2 \times 2$ supercell of empty α-B UC, however, the interior of β-boron UC is not empty and contains six internal distorted icosahedra (shown as dark) and a single B atom in the center of UC

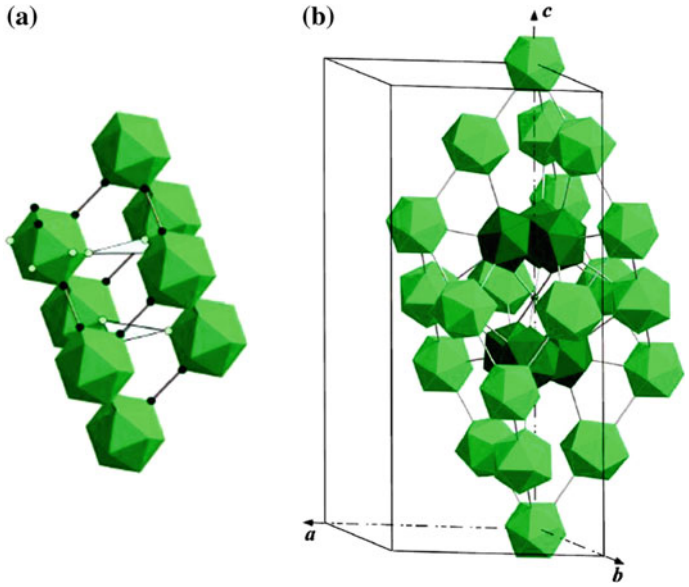

Fig. 4.1 Idealized rhombohedral unit cells of α- (**a**) and β- (**b**) boron bulk phases contain 12 and 105 atoms, respectively [6]. In α-B bulk, B_{12} icosahedra are arranged at each vertex of UC rhombohedron (i.e., one icosahedron *per* UC). In β-B bulk, each UC consists of four B_{12} icosahedra imaged light, two dark B_{28} units formed by three condensed icosahedra in each (with shared 8 atoms) and one single B atom in the UC center (point-like *circle*) [7]. As to a real bulk structure of β-B, it can correspond to 106.66 boron atoms *per* UC [8]

(Fig. 4.1b). In the alternative model of β-B UC [9], its rhombohedral configuration is similar to that of α-B (without B_{12}-centered bonds as shown in Fig. 4.1b), however, each vertex of the rhombohedron serves as the center of B_{84} polyhedron, the central icosahedron of which is surrounded by 12 B_6 pentagonal pyramids, moreover, each of such a unit cell contains B atom in its center and two semi-icosahedrons B_{10} around it. There are two independent atomic positions in the idealized α-B structure: six equivalent "polar" atoms (black points in Fig. 4.1a) form the upper and lower triangles of B_{12} icosahedron, while six "equatorial" atoms (white points) between them are arranged in a puckered hexagon. "Polar" icosahedron atoms of α-B form two-centered bonds with atoms of neighboring icosahedra while equatorial atoms form complex three-centered bonds with atoms.

Although 3D boron solids are usually considered as either band insulators or wide-gap semiconductors, they can become narrow-gap superconductors or metals under high pressure [10]. Meanwhile, boron nanostructures, e.g., 2D nanolayers (BNLs), 1D nanotubes (BNTs) and nanowires (BNWs), as well as 0D fullerene-type clusters, most of which were shown to be metallic, gained wide practical interest [3, 11]. Although no 2D planar boron structure exists in its quasi-molecular crystals since they do not possess laminar structures, the existence of quasi-planar B nanoflakes was established experimentally [12].

As discussed in Chap. 3, 2D $\rightarrow$ 1D structural transformation is usually applied for NT construction from nanolayers bent and rolled up to a nanotubular form. Thus, simulation of boron nanolayers (BNLs) is the first step for a further study of BNTs. Generally, in-plane bonds formed from overlapping sp^2 hybrids are stronger than off-plane-bonds derived from p_z orbitals, so a structure that optimally fills in-plane bonding states should be most preferable. Following this principle, Fig. 4.2 shows the projected densities of states (PDOS) for five B sheets mentioned above with separate in-plane (the superposition of s, p_x and p_y) and out-of-plane p_z projections [13].

Five main types of 2D BNLs were considered initially for the further construction of 1D nanotubes (Fig. 4.2): flat hexagonal graphitic-type (a) and triangular BNLs (b) were found to be metastable as described below [14]; stable BNLs composed of buckled triangular motifs t-BNLs (c), according to Aufbau principle [15]; stable planar BNLs composed of hexagonal motifs containing symmetrically distributed hollow hexagons either separated from each other by triangular regions (α-BNLs, d) or forming parallel stripes from hexagonal and triangular areas (β-BNLs, e) [13]. The most stable BNLs structures occur when hexagonal holes are distributed as evenly as possible, i.e., α-BNLs, followed by β-BNLs and t-BNLs (less stable than α-sheet by 0.05 and 0.12 eV/atom, respectively) which can be explained by the nature of electronic bonding in them as explained below.

Generally, in-plane bonds formed from overlapping sp^2 hybrids are stronger than off-plane-bonds derived from p_z orbitals, so a structure that optimally fills in-plane bonding states should be most preferable. Following to this principle, Fig. 4.2 shows the projected densities of states (PDOS) for five types of B nanolayers mentioned above with separate in-plane (the superposition of s, p_x, and p_y as well as out-of-plane (p_z) projections.

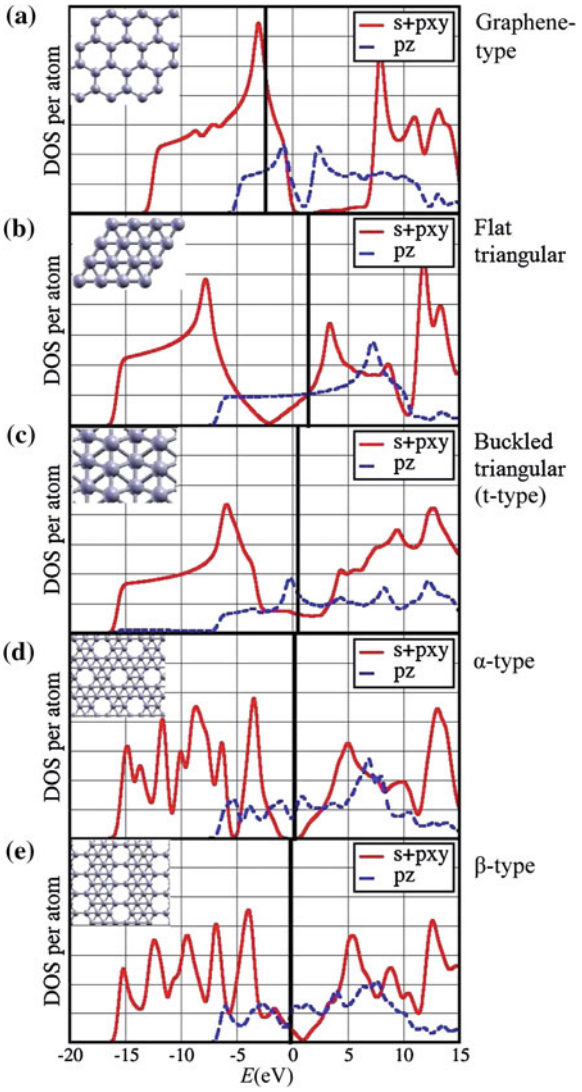

Fig. 4.2 Five morphologies of boron nanolayers and PDOS corresponding to them [13]. Projections are onto in-plane (sum of s, p_x, and p_y, *solid line*) and out-of-plane orbitals (p_z, *dashed line*). *Thick vertical solid lines* show the Fermi energies ϵ_F

(a) In the hexagonal graphene-type NL (Fig. 4.2a), all sp^2 hybrids are oriented along the nearest-neighbor vectors, so that overlapping hybrids produce the canonical two-center bonds [13]. In the case of graphene, the four valence electrons *per* atom completely fill the sp^2 and the p_z bonding states, leading to a highly stable structure. Since a boron atom possesses only three valence electrons, some of the strong in-plane

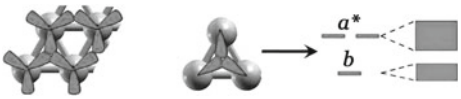

Fig. 4.3 Three-center bonding scheme in *flat triangular* nanolayers [13]. *Left* orientation of sp^2 hybrids. *Center* and *right* overlapping hybrids within a *triangle* (D_{3h} symmetry) yield bonding (**b**) and two anti-bonding (**a***) orbitals. Due to inter-triangle interactions, they broaden into bands

sp^2 bonding states are found to be unoccupied, explaining the relative instability of such a sheet as shown in Fig. 4.2a.

(b) In the flat triangular NL (Fig. 4.2b) each atom possesses six nearest neighbors, but only three valence electrons. Since the absence of two-center bonding scheme, typical for graphene, demands a proper description of this 2D structure, a three-center bonding scheme was suggested for this case [13] where three hybrids overlapping within an equilateral triangle are formed by three neighboring atoms (Fig. 4.3). According to the group theory, one low-energy symmetric bonding orbital **b** and two degenerated high-energy anti-bonding orbitals **a*** form the "closed" three-center bonding by three neighboring atoms [16]. These sp^2 orbitals then expand into bands due to inter-triangle couplings. Separately, the p_z orbitals also broaden into a single band. Figure 4.2b shows that the in-plane PDOS becomes zero at the energy separating in-plane bonding and anti-bonding states i.e., Fermi level ϵ_F should be at the zero point of the in-plane PDOS in Fig. 4.2b. However, ϵ_F lies noticeably above the ideal position and makes some electrons to occupy in-plane **a*** states. As a result, such a sheet has a surplus of electrons in anti-bonding states, which makes this structure metastable.

(c) In the flat triangular NL, however, buckles are under small perturbations along z axis [14]. The buckling mixes in-plane and out-of-plane states (some out-of-plane states move below ϵ_F as indicated in the corresponding PDOS shown in Fig. 4.2c) and can be considered as a symmetry reducing distortion that enhances binding inside BNLs and makes them stable.

(d) The flat hexagonal and triangular nanolayers are unstable separately, however, if the system is able to turn into a mixture of both phases in the right proportion, it will certainly benefit [13]. Such a structure is similar to carbon-boron stripe-type flat heterojunction simulated earlier [17]. Specifically, the hexagon-triangle mixture in BNLs with the highest stability should place ϵ_F precisely at the zero-point of in-plane PDOS (Fig. 4.2d), filling all available in-plane bonding states but none of the anti-bonding ones. From the doping perspective, the three-center flat triangular regions should act as donors while the two-center hexagonal regions should act as acceptors. The remaining electrons should fill low-energy p_z-derived states, leading to a metallic system. In fact, the stable α-BNL (Fig. 4.2d) satisfies this condition precisely.

(e) β-BNL, where hexagonal holes separated by single B–B bonds form parallel stripes (Fig. 4.2e), is a less stable nanolayer than α-BNL. Unlike the latter, β-BNL has a slight shift of ϵ_F from the ideal position.

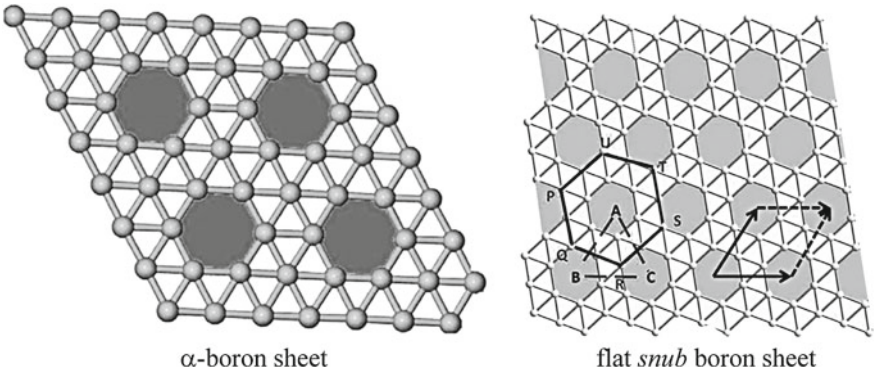

Fig. 4.4 Models of α- and *s*-BNLs (Reprinted figure with permission from Zope and Baruah [18], Copyright (2010) by the Elsevier B.V. All rights reserved)

In the recent study [18], the structure of α-BNL was modified to a snub boron sheet, *s*-BNL (Fig. 4.4). Unlike the former, in which the triangular regions form extended stripes, in the *s*-BNL these stripes are a zigzag-type. Moreover, α-BNL possesses two types of boron atoms: those at the centered hexagonal rings with a six-fold coordination versus B atoms which are part of the hollow hexagonal ring with a five-fold coordination. On the other hand, in the *s*-BNL (and in the related nanostructures), all boron atoms have five nearest neighbors. The hexagonal hole density (η) for a snub sheet is 1/7 (equal to that of β-BNL), which is larger than 1/9 for the α-sheet. On the other hand, the calculations [18] show that the *s*-BNL is energetically less stable than the α-sheet (by ~0.02 eV/atom). In any case, both α- and *s*-BNLs were found to be energetically more stable than β- and *t*-BNLs considered above (by ~0.05–0.07 and ~0.10–0.12 eV/atom, respectively [13]). Obviously, it would be possible to reduce the density of hexagonal holes by filling some of them with B atoms and gaining some binding energy at the cost of the loss of a uniform five-fold coordination. However, such 2D structures are certainly less symmetric.

Both boron nanolayers shown in Fig. 4.4 possess symmetrically distributed hexagonal holes, the centers of which (A, B, C etc.) correspond to the point group C_{6h} (that, e.g., describes hexagon PQRSTU), being isolated from each other by flat triangular regions. Vectors like ***AB*** and ***AC*** form the unit cells of both hexagonal nanolayers [18]. For the description of flat triangular boron sheets (Fig. 4.2b), the hexagonal symmetry (C_{6h}) is also applied [15], similar to puckered BNLs (C_{6v}, apex above hexagon [19]). For buckled *t*-BNLs (Fig. 4.2c), the centered-rectangular symmetry (C_{2v}) was found to be the most appropriate as shown in Fig. 4.5 [20]. As to β-BNL phase (Fig. 4.2e), its flat structure with quasi-linear distribution of hexagons [13] can be attributed to the low-symmetry monoclinic type.

Most of theoretical calculations on boron nanolayers and nanotubes of different morphologies were performed using both *ab initio* plane-wave DFT methods within LDA and GGA approaches [9, 13–15, 17–22] as well as DFT-LCAO method [23] and full-potential linear-muffin-tin-orbital molecular dynamics method (FP LMTO MD) [24].

4.2 Boron Nanotubes

4.2.1 Rolled-Up Single-Wall Nanotubes

Experimentally, hollow boron nanostructures were fabricated repeatedly, e.g., as elongated clusters [25] and single-wall (SW) quasi-1D tubules within diameter 0.3 nm [26]. In the first systematic theoretical study of small boron nanotubules [27], various hollow fullerene-type tubular systems were compared to their quasi-planar counterparts, including a boron nanolayer hypothetically rolled up to form a nanotube, which proceeds over a pronounced barrier. The majority of boron nanotubes with different morphologies were predicted to be metallic, possessing noticeable densities of states at Fermi levels [15].

Obviously, understanding the structure and properties of boron nanolayers is crucial for the prediction of those for BNTs. The majority of theoretical simulations performed so far focused on boron nanotubes constructed from *t*-BNLs [14, 15, 17, 20, 22]. The geometrical construction of *t*-NTs from *t*-BNLs is similar to that for carbon nanotubes obtained from a graphene sheet [28]: the basic tubular structure is characterized by a chirality vector $\boldsymbol{R}$ that defines a rectangular area on the BNL (Fig. 4.5) rolled up to a cylinder, i.e., this vector becomes the circumference of the BNT and its radius equals to $R = |\boldsymbol{R}|/2\pi$ [20]. Figure 4.5 illustrates that besides constructing a BNT by repeating a *tubular* unit cell (UC), one can also build a nanotube by repeating a *helical* unit cell along a spiral winding around the surface of a nanotube. The direction of this spiral is given by the helical vector $\boldsymbol{H}$ which, when uncoiled into a plane, defines the direction of a translational symmetry [20]. The helical unit cell is specified by vectors $\boldsymbol{H}$ and $\boldsymbol{K} \perp \boldsymbol{H}$. When introducing vector $\boldsymbol{T} \| \boldsymbol{H}$, a chirality vector of tubular UC can be defined as $\boldsymbol{R} = \boldsymbol{K} + \boldsymbol{T}$. In order to simplify

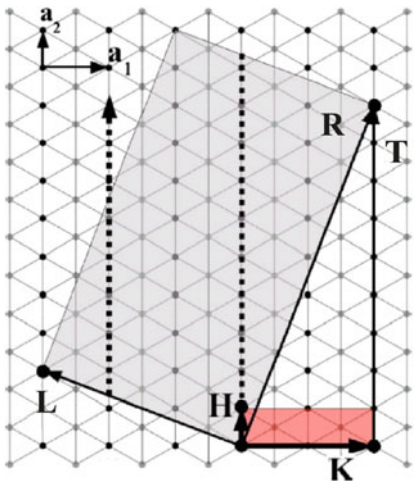

Fig. 4.5 Two different ways for construction of buckled boron nanotubes [20]. The *tubular* unit cell marked as *light gray* is repeated along the nanotube's axis, which lies parallel to vector $\boldsymbol{L}$. The *helical* unit cell marked as *dark gray* is translated along spirals (represented by the *dotted lines*) on the surface of the nanotube

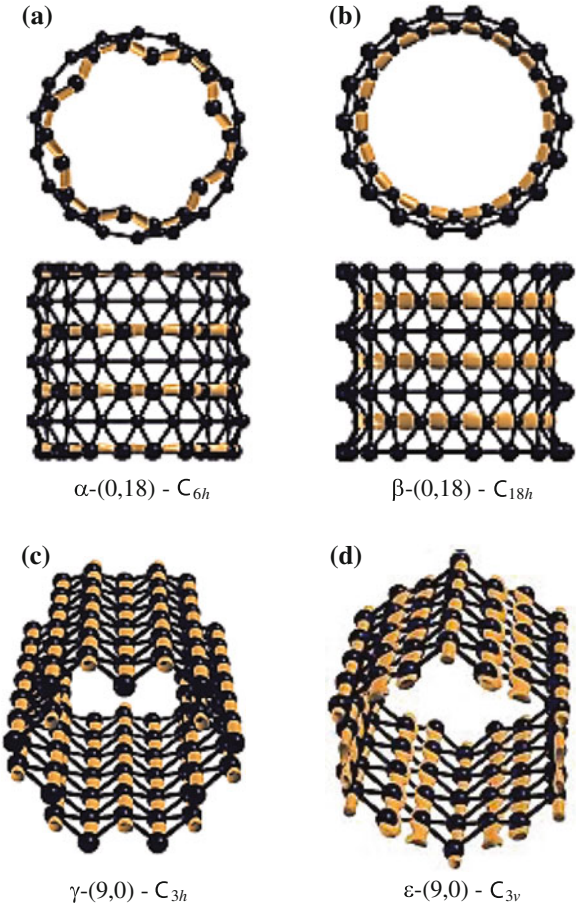

Fig. 4.6 Armchair- (**a**), (**b**) and zigzag- (**c**), (**d**) types of *t*-BNTs with circumference and straight directions of σ-bonds (indicated as *thick light lines*), respectively, which possess convex (**a**, **d**) and concave (**b**, **c**) morphologies [20]

simulation, the helical vectors were set as $\boldsymbol{H} = \boldsymbol{a}_2 = (0,1)$, $\boldsymbol{K} = (k,0)$ and $\boldsymbol{T} = (0,t)$ (Fig. 4.5).

Both the concave and convex configurations of the buckled *t*-BNTs possessing armchair- and zigzag-type chiralities, respectively, as imaged in Fig. 4.6 (translation along either $\boldsymbol{a}_1$ or $\boldsymbol{a}_2$ vectors shown in Fig. 4.5), are generated by using the construction formalism described above. Unlike *t*-BNLs, they are described by a different rotational symmetry since the nanotube buckling differs from that in sheets.

Rather low strain energies in zigzag *t*-BNTs, where translation vector and direction of σ-bonds coincide with direction of buckling rows, lead to a whole bunch of possible structural isomers since a nanotube without any significant amount of strain energy will not be able to maintain a circular cross section as in the case of armchair-type nanotubes (Fig. 4.6). This can result in a certain instability of the former. The existence and mutual orientation of σ-bonds is crucial for understanding the basic

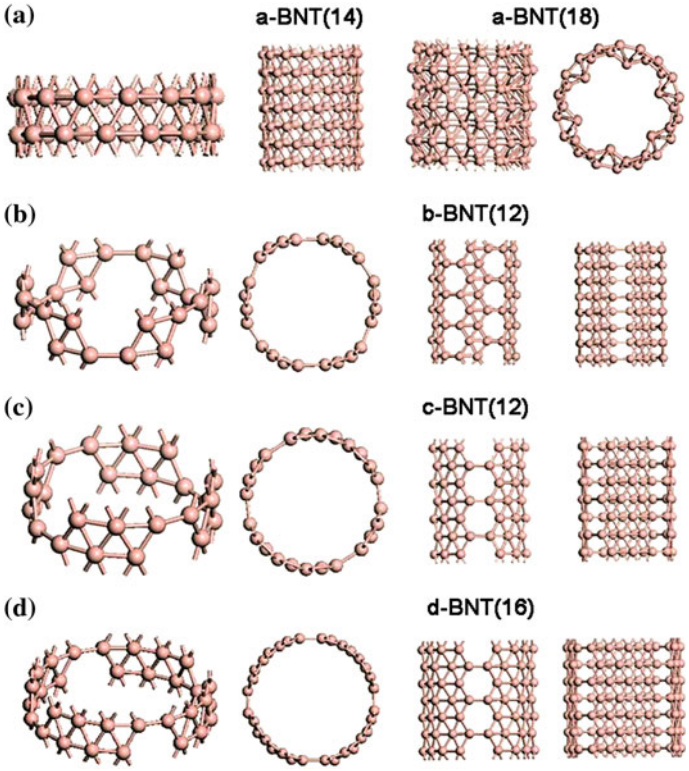

Fig. 4.7 *Front* and *top* view of the basic units and corresponding nanotubes. The data *in brackets* indicate the numbers of the boron atoms on each *ring* of the nanotubes [19]

mechanical and energetic properties of *t*-BNTs because the strain energy of the nanotube is mainly generated by bending these bonds. Multi-center bonds seem to have no real effect on the strain energy [14, 20].

The hexagonal boron nanotube in the form of double-ring basic units (where the number of B atoms in each ring is *n*) is shown in Fig. 4.7a [19]. By increasing the ring diameter, *a*-type nanotube was found to be buckled (similar to those *t*-BNTs considered above). The B–B bond length was shortened in each ring, but was prolonged between two rings. Figure 4.7a shows the *a*-type BNTs, both flat and buckled, where the number of boron atoms are 14 and 18 on each ring, respectively. For the buckled *a*-BNTs, B atoms on one ring form not a circular configuration but a zigzagged structure. The BNT geometries presented in Fig. 4.7b–d shows basic units with one boron atom being removed per interval of four, six, and eight atoms on each ring, respectively, which results in appearance of tubular structures with morphology similar to that of obtained by rolling up the β-BNL (Fig. 4.2e) parallel to the row of hexagonal holes. The binding energy *per* atom for BNTs containing hexagonal holes (*b–d*) was found to be $\sim$0.2 eV larger than in the buckled *a*-BNT,

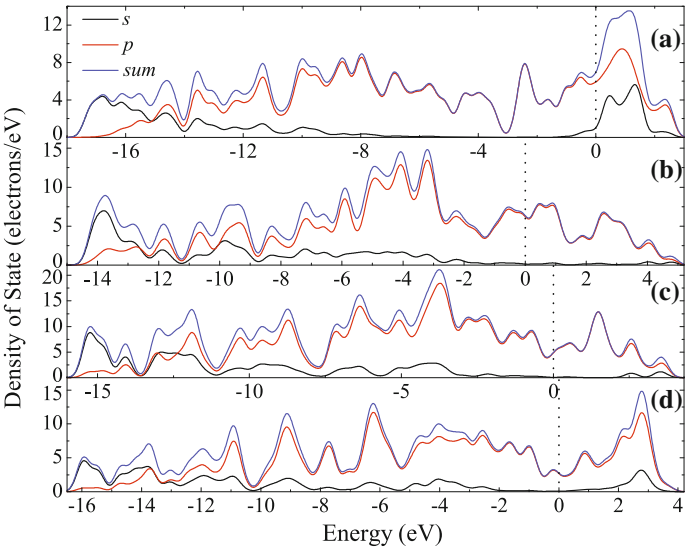

Fig. 4.8 Total and orbital-decomposed density of states for BNTs of *a*-, *b*-, *c*- and *d*-configurations (Reprinted figure with permission from Tian et al. [19], Copyright (2010) by the AIP Publishing LLC)

due to the strengthening of B–B bond between the rings by discarded atoms (e.g., the electronic population of such an inter-ring B–B bond grows from 1.01 *e* of *a*-type to 1.25 *e* in *b*-type) [19]. The BNT stability enhances as the ring diameter increases. This result confirms the larger stability of β-BNL (Fig. 4.2e) in comparison with *t*-BNL (Fig. 4.2c) as described above.

Figure 4.8 shows the density of states for B nanotubes corresponding to *a, b, c*, and *d* configurations (Fig. 4.7). The number of B atoms for these rings are 15, 16, 24, and 16, respectively. Clearly, the metallic behavior of all the BNT configurations is illustrated by the existence of electron states at Fermi level. To get more understanding of states on Fermi level, the projected orbital density of states onto *s* and *p* orbitals is displayed in Fig. 4.8, which shows that the states at Fermi level are dominated by *p* orbital electrons. However, for *a*-type nanotubes, electrons from *s* orbital also contribute to the states at Fermi level. Moreover, the occurrence of a pseudo-gap near Fermi level indicates the enhanced stability of *c*- and *d*-type nanotubes containing hexagonal holes.

Energetically stable configurations of boron nanotubes were found to be α-BNTs [21] (Fig. 4.9) and *s*-BNTs [18] which are obtained by rolling up the corresponding BNLs perpendicular or parallel to the direction of the diagonal formed by unit cell vectors (Fig. 4.4) for armchair- and zigzag-type chiralities, respectively. Moreover, α-BNTs were also constructed using an alternative polyhedral model [24] as described in a more detail in Sect. 4.2.4. To cover a reasonable range of diameters for both morphologies, four (*n,n*) and three (*n*,0) nanotubes were considered [21].

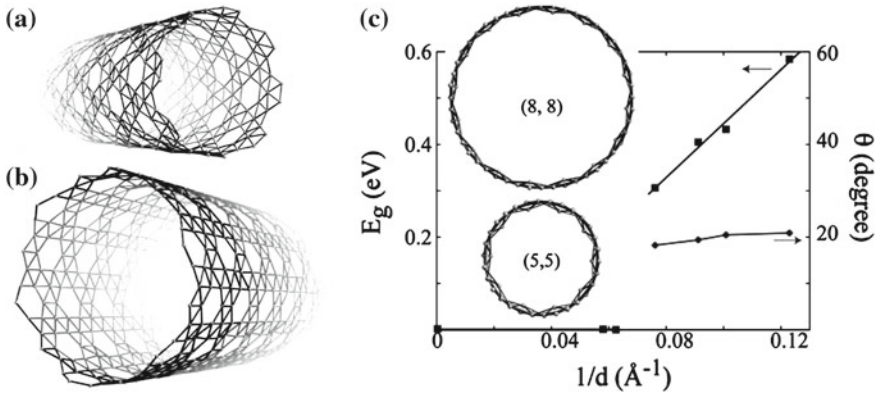

Fig. 4.9 Relaxed structures of **a** armchair (8,8), and **b** zigzag (18,0) α-BNTs. Part **c** shows plots of the band gap E_g (*left axis*) and dihedral angle θ formed by the central B atom and the plane of filled hexagon (*right axis*) versus curvature, $1/d$, for the studied armchair nanotubes. Axial view of (5,5) and (8,8) α-BNTs illustrates the degree of atomic buckling, inset in (**c**) (Reprinted figure with permission from Singh et al. [21], Copyright (2008) by the American Chemical Society)

NT relaxation was found to be diameter dependent and occurred mostly around the filled hexagons (positioned between the hollow ones as shown in Fig. 4.4), where the central B atom is located, relative to a hexagon tiling of the corresponding hexagonal CNT structures. Generally, these central B atoms buckle inward by departing off the plane of the hexagons (Fig. 4.9c, inset). Not all the central atoms buckle (it rather happens in every second filled hexagon). With the increasing diameter, the central B atoms systematically move back into the plane of hexagons (Fig. 4.2c). Irrespective of these transformations, the stability of α-BNTs was confirmed by the direct nanotube energy minimization in PW DFT PBE calculations [21]. This mode of geometrical relaxation appeared to have an important effect on the electronic structure of the nanotubes.

As a basic vibrational property of α-nanotubes, the Raman detectable radial breathing frequency (RBF) was calculated (120–240 cm^{-1}, decreasing with the growth of BNT diameter) which differ from the experimental data 70 cm^{-1} [26]. Such a discrepancy could indicate the difference between the real BNT structure and that of α-BNT. Additional distinction between this nanotube model and other BNTs is the appearance of small band gaps in nanotubes with diameters smaller than 1.5–2.0 nm, due to the orbital relaxation buckling in atomic positions leading to their rehybridization [21]. The combination of structural, electronic and vibrational properties makes α-BNT a promising material for various chemical, electronic and optical applications.

4.2.2 Bundles of Rolled-Up Single-Wall Nanotubes

Several experimentally detectable properties of CNTs, which where synthesized as pristine nanotubes, could appear only in the condensed state [29], where they tend to form close-packed bundles [30]. It is, therefore, of great interest to understand how boron nanotubes can be assembled into stable 3D form *via* inter-tubular interactions in the condensed phase, taking into account that the chemical bonding in BNT is quite different from that in CNT since the strain energy and inter-tubular interactions in the former are both diameter and chirality dependent, in contrast to carbon nanotubes [20, 31]. To investigate morphological evolution of boron nanotubes in the close-packed bundles in the crystalline phase, a specific case of SW BNTs with a small diameter and triangular-type chirality (Fig. 4.5) was studied [23]. Specifically, for simulation of bonding, stability, thermodynamic, and electronic properties of SW BNT bundles the DFT-LCAO method was found to be the most reliable.

First principles simulations of NT bundles and multi-wall NTs have been performed so far for nanotubes of equal diameters and the same chirality, otherwise computational expenditures exceed the limit of contemporary *ab initio* codes due to incompatibility of unit cell lengths for nanotubes of different chiralities [32]. For a highly symmetric configuration of the close-packed bundle structure, boron nanotubes with the chirality of either (0,*m*) armchair-type (Fig. 4.6a, b) or (*n*,0) zigzag-type (Fig. 4.6c, d) should be chosen. Two distinct morphologies of SW BNT bundles were considered for *ab initio* calculations on their 3D condensed structures, which presented (0,6) or (6,0) chiralities [23]. The crystalline bundles of SW BNTs were represented by arrays of identical nanotubes arranged in a hexagonal lattice, initial configuration of which (defined as sparse) is characterized by a large enough value of the nearest inter-nanotube distance (Fig. 4.10). These NTs are of infinite length and are not capped. A rhombic unit cell of BNT bundle can be characterized by two parameters: (i) a defined as a sum of the diameter of nanotube (d_{NT}) and its inter-tubular distance ($r_{\mathrm{NT-NT}}$), as well as (ii) c which represents the periodicity of a SW BNT along its tubular axis (l_{NT}).

Figure 4.11 shows the calculated potential energy surface (i.e., total energy versus UC volume) of the SW BNT bundles where the lattice parameters as well as the internal coordinates of the tubular configurations were optimized on the energy surface at each value of UC volume [23]. The sparse configuration is defined on the energy surface as the configuration where a bundle consists of weakly interacting SW BNTs which is true for $r_{\mathrm{NT-NT}} > 0.3$ nm. However, the equilibrium configuration is associated with the lowest total energy of the given type of bundles. The calculated equilibrium volumes are 200 and 165 Å^3 for *zz*- and *ac*-type bundles, respectively. There appears to be a crossover of the stability of bundles as the inter-tubular interaction becomes stronger between SW BNTs of a smaller diameter. As the overall trend, *zz*-type bundles are more stable in the sparse configuration, due to their high stability in static energy as pristine NTs, whereas *ac*-type bundles become more stable in the equilibrium configuration by settling down in rather compact, interlinked bundles (Fig. 4.10). This fact was reflected in a relatively large change of the cohesion energy

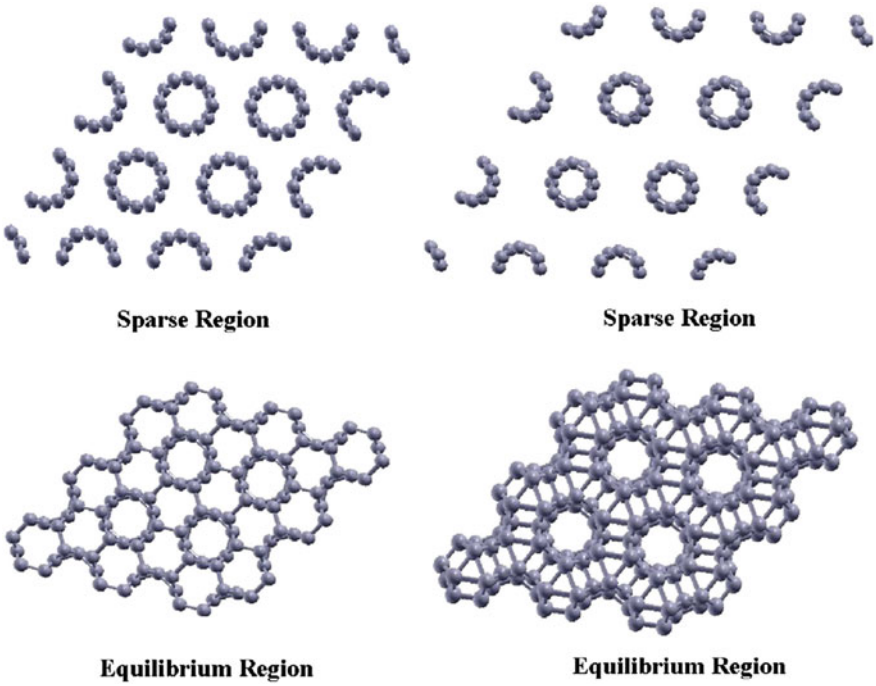

Fig. 4.10 *Top* views of supercells of SW BNT crystalline bundles corresponding to the sparse and equilibrium configurations, where individual nanotubes possess either zigzag-type (6,0) or armchair-type (0,6) chiralities (*left* and *right panels*, respectively) [23]

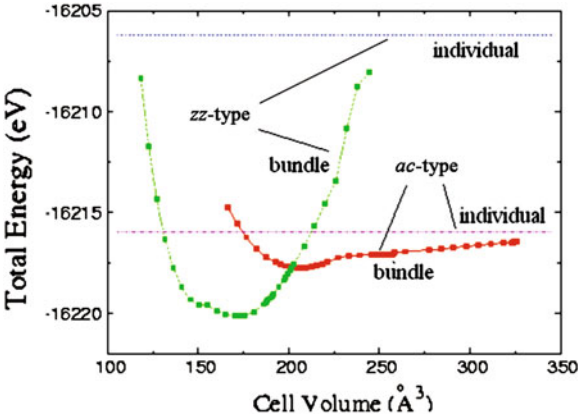

Fig. 4.11 The optimized energy curves represented by total energy versus UC volume in different morphologies, namely the sparse and equilibrium configurations of both *ac*- and *zz*-types of SW BNT bundles (Fig. 4.10). In the sparse region, UC volume exceeds 240 Å^3 associated with $r_{\mathrm{NT-NT}} > 0.3$ nm. *Straight lines* represent the total energy of isolated BNTs of *ac*- and *zz*-chiralities [23]

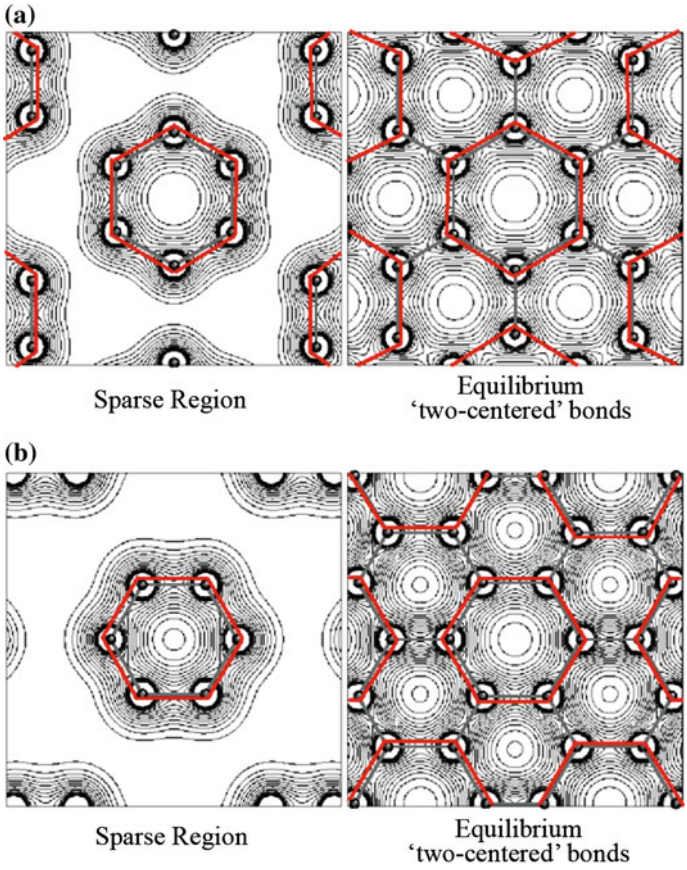

Fig. 4.12 *Top* views of the electronic charge density plots on the 2D plane for *zz*-type (**a**) and *ac*-type (**b**) SW BNT bundles in both the sparse and equilibrium configurations (as shown in the *left* and *right* columns, respectively). The *hexagonal box* in each plot represents the outline of the *top* view of SW BNT within the bundle [23]

ΔE_{coh} for *ac*-type bundles (~0.59 eV/atom [23]) from the sparse configuration to the equilibrium configuration, gaining almost 10 % of cohesive energy relative to α-B bulk (Fig. 4.1a). For the small d_{NT} values, the *ac*-type SW BNT is not energetically preferable relative to the *zz*-type NT, though a stronger inter-tubular interaction within the bundles is crucial for stabilizing *ac*-type bundles over *zz*-type bundles.

In the sparse configuration of the crystalline BNT bundles, there was almost no total charge density distribution in the inter-tubular region (Fig. 4.12). The total charge density is nearly equivalent to the superposition of charge densities of individual pristine nanotubes. For bundles in the equilibrium configuration, the Mulliken population analysis was used to estimate the strength of intra-tubular and inter-tubular bonds in terms of the degree of overlap population in units of the electron charge (e) among the nearest B neighbors [23]. For the *zz*-type of bundles, the dominance

of σ bonds was found, which interconnected the "triangle-square-triangle" along the tubular axis, over the π bonds associated with B atoms along the triangular network in the intra-tubular region. The two-centered bonds in BNT bundles, therefore, appeared to be as rigid as those in isolated nanotubes. For the *ac*-chirality of bundles, the inter-tubular interaction was described by both two- and three-centered bonds, both having significant strengths. The strength of the latter was found to be nearly the same in both inter- and intra-tubular regions. The presence of "buckling" induced two-centered σ bonds in the intra-tubular and inter-tubular regions of BNT bundles was confirmed too, though they were not present in the isolated *ac*-SW BNTs.

The difference in the inter-nanotube interaction between bundles of BNTs with *ac*- and *zz*-chiralities was found to be mainly due to the differences in their bonding features in the respective pristine SW BNTs [23]. In bundles of *zz*-SW BNTs, the bonding was dominated by two-centered σ bonds with the population of $\sim$0.66 e, whereas the bonding features in bundles consisting of *ac*-SW BNT are dominated by three-centered σ bonds with nearly a homogeneous electron distribution and bond population of $\sim$0.41 e. In the case of small diameters of BNTs brought together to form a bundle, the rigid two-centered σ bonds along the tubule axial direction in the *zz*-type SW BNTs (Fig. 4.6c, d) could not be easily deformed, leading to a weaker B–B bond population ($\sim$0.33 e). At the same time, for the *ac*-type bundles of SW BNTs, relatively weak two-centered σ bonds lying along the circumferential direction (Fig. 4.6a, b) were found to be easily distorted [23], to yield stronger inter-tubular two- and three-centered bonds (with bond populations $\sim$0.52 and $\sim$0.36 e, respectively). The distortion of circumferential σ bonds was expected to enhance the chemical reactivity caused by unsaturated dangling bonds on nanotube surface of *ac*-type of SW BNTs.

The crystalline SW BNT bundles mainly demonstrated metallic features, similar to the pristine boron nanotubes, regardless of composition and chirality [23], in contrast to the corresponding case of carbon nanotubes where chirality determines the exposure of electronic properties either metallic or semiconducting. However, it was found that the elemental boron nanowires (to be considered in Sect. 4.3) can exhibit semiconducting features [33]. Obviously, the number of available one-electron states near the Fermi energy determine the electron transport properties of the BNT bundle [34]. For the sparse configuration of a bundle, the corresponding DOSs could be well correlated with those for pristine boron nanotubes. As the inter-tubular interaction became dominant in the *zz*-type of BNT bundles (Fig. 4.10), the multiple bands associated with intra-tubular and inter-tubular bonds crossed at the Fermi level (Fig. 4.13a). A higher value of the conductance associated with the *ac*-type of SW BNT bundles were attributed to the valence electrons of boron which were shared uniformly, thus creating delocalized three-centered bonds enhancing the probability of the electron conduction along the nanotube axial direction [23]. In contrast to the *zz*-type bundles, the strong inter-tubular two- and three-centered bonds found in the *ac*-type bundles were mostly located in the occupied valence bands below the Fermi level, thus, making no contribution to the intrinsic conductance. The metallic crystalline bundles of a small diameter single-wall boron nanotubes were also predicted to be thermodynamically stable [23] and possessing a number of novel

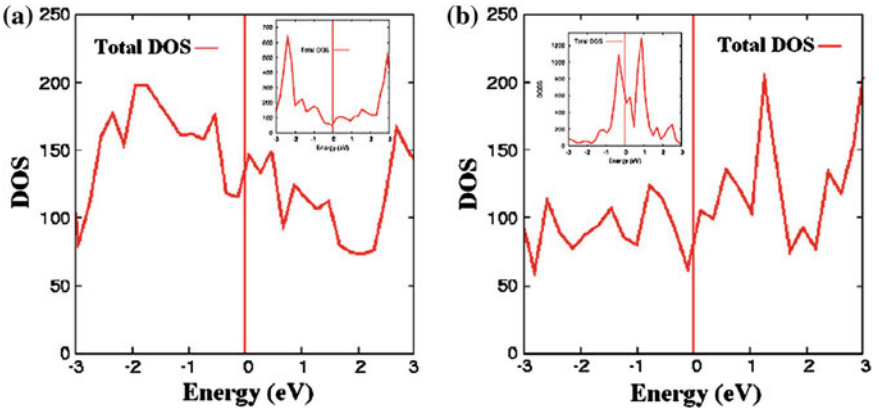

Fig. 4.13 The total density of states for *zz* (**a**) and *ac* (**b**) chiralities of BNT bundles. In both DOS plots, the range of ± 3 eV around Fermi level is shown, where $\epsilon_F = 0$. The insets in both plots show the DOS of sparse crystalline bundles for both configurations, which mimic the DOS of pristine SW BNT in both cases [23]

properties. On the whole, the dominance of inter-tubular interactions involving two- and three-centered bonding features in SW BNT bundles relative to the Van der Waals interactions yielded structural, mechanical, and electronic properties different from those of isolated BNTs. Within the small radii regime, it was predicted that if isolated or sparse bundles of a small diameter SW BNTs were grown, the *zz*-type of bundles was found to be energetically preferred. On the other hand, the close-packed *ac*-type of BNT bundles was found to be preferred in the equilibrium configuration [23].

4.2.3 Rolled-Up Double-Wall Nanotubes

SW BNTs possessing the same buckled triangular morphology (Fig. 4.6), as used for simulations on boron nanotube bundles described in the previous subsection, were applied also for the construction of commensurate double-wall (DW) BNTs of different chiralities and sizes as well as for calculations of their properties [9]. Three pairs of DW BNTs of either *ac*- or *zz*-chirality (i.e., (0,m_1) @ (0,m_2), where $m_2 > m_1$, and (n_1,0) @ (n_2,0), respectively) were modeled (Fig. 4.14a, b). The initial arrangement of internal and external single-wall shells corresponded to the preservation of the highest possible symmetry for DW BNTs, which depended on SW NT chiralities. During the optimization of the DW nanotube geometry, the outer atoms of the inner walls were matched to the inner atoms of the outer walls, which resulted in the appearance of both chemical inter-wall bonding, dependent on the inter-tubular distance $r_{\mathrm{NT-NT}}$. When internal (6,0) *zz*-BNT was worn by the (10,0) or (12,0) nanotubes, it shrank radially, and as a result, stretched longitudinally because of the electrostatic

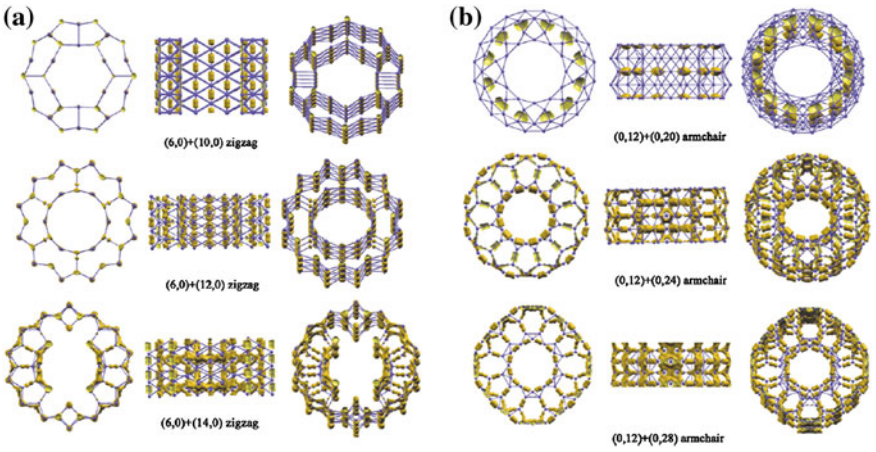

Fig. 4.14 Across, aside and axonometric views of commensurate DW BNTs, with *zz*-chirality (**a**) and *ac*-chirality (**b**), for fixed d_{NT} of the *internal shells* and changed diameters of the *outer shells*. Isosurfaces of their total valence electron density were taken at 0.80 $e \cdot \text{Å}^{-3}$ (except for 0.75 $e \cdot \text{Å}^{-3}$ in the case of (6,0) @ (10,0) *zz*-configuration) [9]

potential induced by the outer nanotube [9]. The average initial value of d_{NT} for (6,0) NT reduced from 6.42 Å in isolated SW NT down to 6.06 and 6.22 Å, respectively, while the average value of $r_{\text{NT}-\text{NT}}$ increased from 1.62 Å up to 1.69 and 1.70 Å for the same external shells. When the outer shell was replaced by (14,0) nanotube, the optimization trend changed in such a way that the internal shell was disrupted, while the bonds between the shells along the radial direction were essentially stretched (Fig. 4.14a). On the contrary, when the internal (0,12) *ac*-BNT was covered by the outer (0,20), (0,24), or (0,28) shell, the inter-tubular distances $r_{\text{NT}-\text{NT}}$ were almost unchanged (slight increase) [9], as a consequence, d_{NT} of internal shell grew from 5.28 Å to 5.80, 6.86 and 7.12 Å, respectively, without any disruption of (0,12) NT (Fig. 4.14b).

Binding energies *per* atom in DW BNT ($E_{bind} = E_{at} - E_{\text{NT}-\text{UC}}/n$), where E_{at} is a total energy of B atom, $E_{\text{NT}-\text{UC}}$ total energy of nanotube unit cell while n is the number of atoms *per* UC) were found to be somewhat larger than those in SW BNTs which indicated the existence of the inter-shell binding in double-wall nanotubes of different sizes. The most energetically stable configuration of DW BNT was found to be the armchair-type (0,12) @ (0,24) ($E_{bind} = 6.27$ eV/atom, which was larger than that in any other DW BNT configuration) [9].

Figure 4.15 depicts the total and angular momentum projected density of states for the corresponding DW BNTs imaged in Fig. 4.14. The calculated DOS of both *zz*- and *ac*-type DW BNTs show no gap with a finite DOS at the Fermi energy level ϵ_F, which confirms their metallic properties [9]. In each of these structures there were many valence and/or conduction bands crossing the Fermi energy. Thus, DW BNTs were predicted to be metallic as in most configurations of the SW BNTs. Moreover, analogically to DW CNTs [32] metallicity of double-wall boron nanotubes is

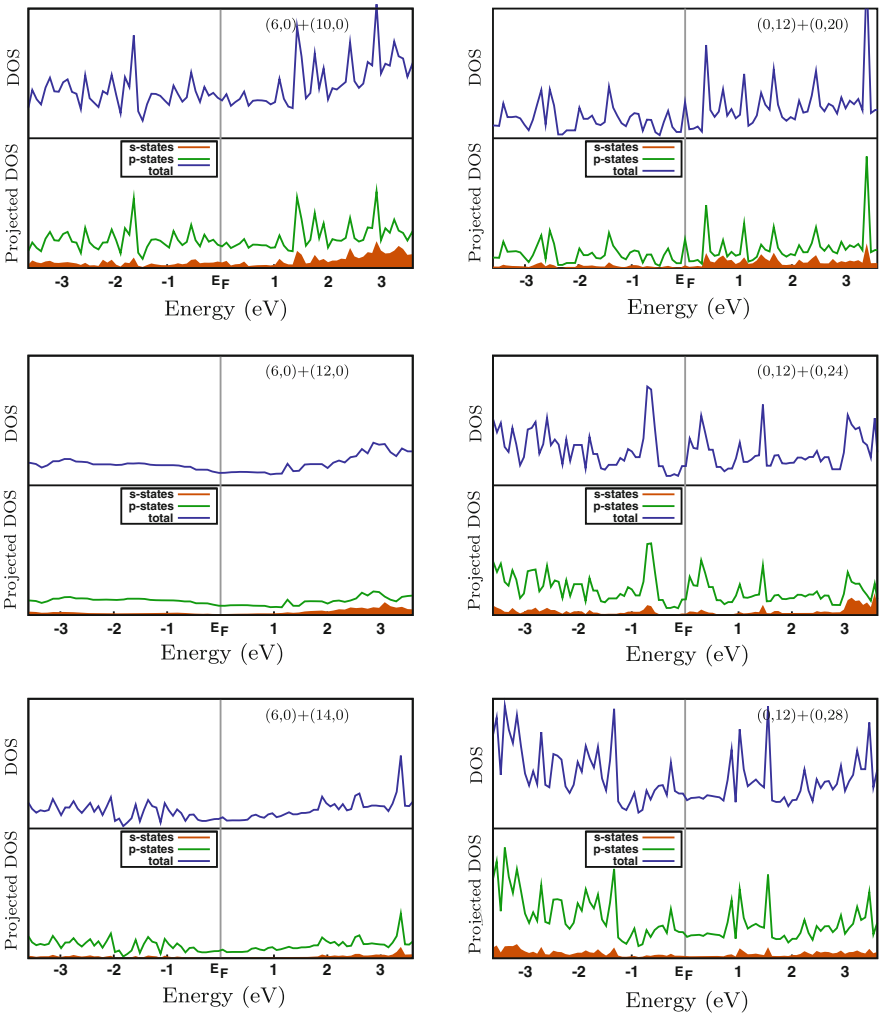

Fig. 4.15 The total and angular momentum decomposed densities of states for various configurations of DW BNTs (Fig. 4.14). Both total and projected DOSs (i.e., *s*- and *p*-states, where the former are shown as *shaded* background) are given in arbitrary units (Reprinted figure with permission from Sebetci et al. [9], Copyright (2008) by the Elsevier Ltd. All rights reserved)

likely higher than that in any of their single-wall constituents. The smoothness of DOSs in some energy intervals can be considered as a result of the dispersion of the bands which stems from puckering of nanotube walls, symmetry of the atomic arrangements, and the axial and circumferential bonding characteristics [9]. Double-wall BNTs exhibit, dominantly, *p*-channel conductivity along the nanotube axis, which is consistent with the DOS diagrams in the vicinity of the Fermi levels presented in Fig. 4.15. On the other hand, the *s*-bonding accounts for the stability of the tubular structure rather than conductivity. Moreover, the higher values of E_{bind}

were observed for DW BNT configurations which have stronger circumferential, longitudinal, and/or radial *s* bonds (Fig. 4.14a, b). Still, the availability of the bonding and non-bonding *p* states which extended along the nanotubular axis was the main reason for the conducting behavior of DW BNTs. For example, in (6,0) @ (10,0) and (0,12) @ (0,20) boron nanotubes, the *s*-states contribute to the conduction bands more than to the valence bands within 3 eV neighborhood of ϵ_F (top plots in Fig. 4.15), which makes these structures energetically less stable as compared to other DW BNTs [9].

Some of the initially fully occupied valence bands become partially occupied after the geometry optimization of DW BNT. The corresponding shift of the Fermi level with respect to the valence and conduction peaks of the DOS can be observed in Fig. 4.15. That becomes clear when one considers the positioning of ϵ_F with respect to the two successive peaks at $\sim$1 eV and with respect to the first peak among the valence bands (at about -0.3 eV in the case of (0,12)@(0,28) DW NT). These characteristic peaks can be identified in the DOS of (0,12)@(0,24) DW NT so that the two successive conduction peaks are just above ϵ_F while the valence peak is positioned close to -1 eV [9]. Consequently, when d_{DWNT} decreases with the double-wall nanotube configuration changes from (0,12) @ (0,28) to (0,12) @ (0,24), Fermi level appears to be shifted up as if it moved in the plateau between the valence and conduction peaks (Fig. 4.15).

4.2.4 Polyhedral Nanotubes

An alternative to traditional rolled-up model of nanotubes was proposed as a new polyhedral model, applied firstly for construction of SW CNTs [35] and then for a few SW NTs generated from widespread inorganic materials (B, BN, Si) [24]. Within that model, the NT morphology was determined by the character of bonding, being triangular in boron, rhombohedral in silicon as well as hexagonal in boron nitride and carbon nanotubes. The general polyhedral model for the construction of single-wall nanotubes was based on two fundamental postulates: (i) the corresponding bonds lying on the same helix are equal in length, which are assumed generally to be distinct, depending on their directions relatively to a nanotube axis; (ii) all atomic nuclei are equidistant from the NT axis. Thus, the nanotube diameter depends on the bond lengths and the chiral vector numbers (*n, m*), so that when the bond lengths are not equal, the NT diameter may vary from the predictions of the traditional rolled-up models. Since such features cannot be ignored, the traditional rolled-up models were extended in order to include distinct bond lengths, e.g., for BNTs [24].

SW BNTs are assumed to be formed by sp^2 hybridization and π-bonds (Fig. 4.16). The lattice structures for boron nanotubes that have been proposed, as considered in Sect. 4.2.1, in order to include (i) flat equilateral triangles, (ii) puckered equilateral triangles and (iii) a novel lattice pattern that is a triangular lattice structure with 1/9 hexagonal holes, a structure which is believed to be energetically more stable than a pure triangular lattice (α-BNLs and α-BNTs). However, the analysis of the raw data reveals a far more complex structure and the model of Yang [36] involves three distinct radii: three-quarters of the atoms have a hexagonal based radius, 1/8th

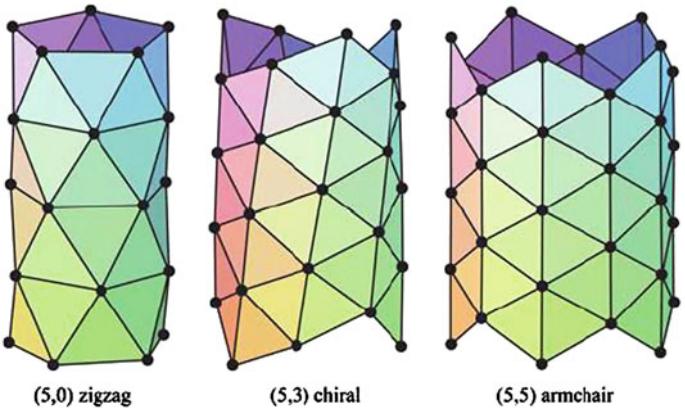

Fig. 4.16 General polyhedral model for boron nanotubes for zigzag, chiral and armchair morphologies, respectively (Reprinted figure with permission from Lee et al. [24], Copyright (2010) by the Royal Society of Chemistry)

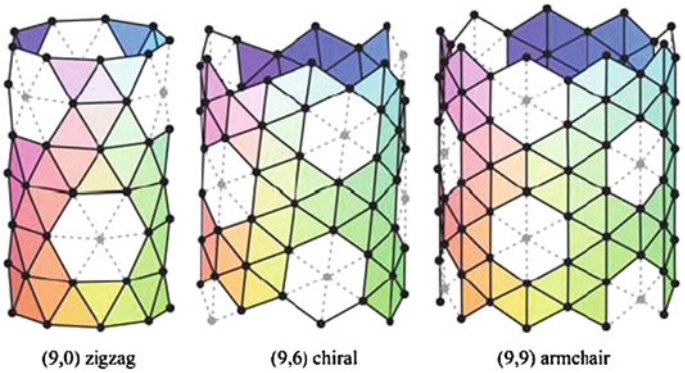

Fig. 4.17 Polyhedral models for BNTs of zigzag, chiral and armchair chiralities, with a concentration of 1/9 *hexagonal holes per* nanotube unit cell (Reprinted figure with permission from Lee et al. [24], Copyright (2010) by the Royal Society of Chemistry)

have a puckered outer radius and 1/8th have a puckered inner radius. Since the polymorphism of boron nanotubes is an important consideration with a number of possible structures which may be more stable than a homogeneous triangular lattice, such a lattice is considered for BNTs which comprises only the equilateral triangles with vertices which are all equidistant from a common nanotube axis. As a result, the nanotube lattice assumed here comprises a flat triangular pattern as shown in Fig. 4.16. In generalizing polyhedral model [37] a rolled-up model for boron nanotube was proposed with distinct bond lengths a_1, a_2 and a_3. Due to such an assumption, three different adjacent bond angles also exist, which are defined as the angles between two of the bonds where the atoms that are being bonded comprise a single triangle in the nanotube lattice. Figure 4.17 describes a general polyhedral

model for hole-containing α-BNTs. The missing atoms are represented by gray dots while the image bonds between the missing B atoms are shown by gray dashed lines.

4.3 Boron Nanowires

In the past few years, various chemical and physical methods have been successfully used to synthesize 1D boron nanomaterials, mainly nanowires (NWs), as well as nanobelts, nanocones, and nanotubes [11]. Three categories of methods were used for the synthesis: (i) chemical vapor deposition (CVD) with gas or solid precursors, (ii) magnetron sputtering (MS), and (iii) laser ablation (LA). A number of BNW properties and applications were experimentally studied using different methods, e.g.: (i) the electrical conductivity of single crystalline BNWs with a rhombohedral, structure of β-B phase (Fig. 4.1b) and (ii) BNW sources for emitting electrons at low electric field. Although the synthesis of BNWs becomes almost a routine procedure, unlike BNT synthesis [25, 26], theoretical simulations on boron nanowires still remain rather exotic [2], while the modeling of numerous boron nanotubes of different morphology continues during the last 16 years as analyzed in Sect. 4.2. A possible reason for such an imbalance could be the complexity of BNW structure which does not allow one to construct simple high-symmetric models for further large-scale *ab initio* calculations as in the case of BNTs. First principles spin-polarized calculations of boron nanowires possessing either α- or β-morphology (Fig. 4.18) have been performed recently [2] using DFT-LCAO method as implemented in SIESTA computation code [38]. The first stage of these simulations has included calculations on

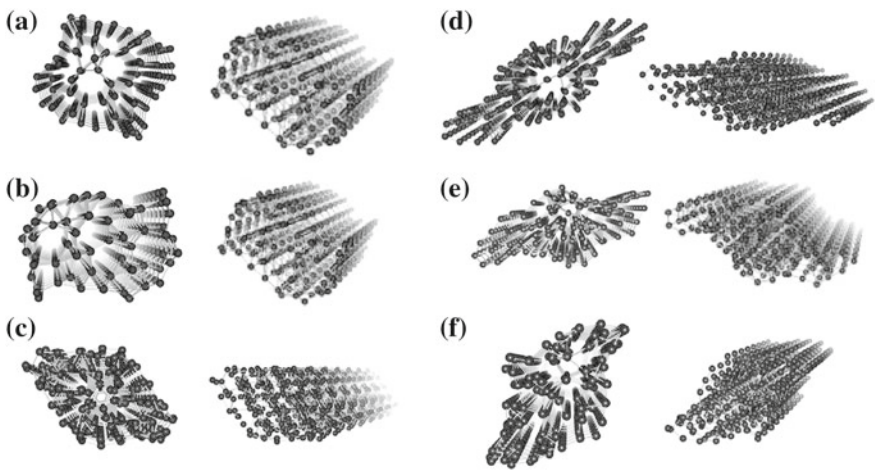

Fig. 4.18 Optimized configurations of six types of BNWs (circles show B atoms while sticks are the bonds between them): **a** α-a [100], **b** α-b [010], **c** α-c [001], **d** β-a [100], **e** β-b [010], and **f** β-c [001]. The *left* and *right* images are across and aside views of BNWs, respectively [2]

α- and β-B bulk (Fig. 4.1), in order to check the availability of *ab initio* calculations for the proper reproduction of cohesion energies and magnetic moments known from the experiments [2]. Six possible BNWs with different orientations and structures have been simulated (Fig. 4.18), three of them were obtained from the UCs of α-B growing along three base vectors, respectively, and the other three were analogically generated from β-B UC. The corresponding BNWs are denoted according to the directions of their axes. Structure of all these boron nanowires were optimized, including their spin moments too. The obtained results reveal that the optimized configurations of the six considered BNWs still keep the same perfect B–B bond structure as those in bulk boron. To evaluate the stability of these boron nanowires, their cohesive energies *per* atom (E_{coh}) were determined and they were found 0.6–0.8 eV smaller than cohesive energies of α- and β-B bulk [2]. Due to the relatively higher values of E_{coh} (6.8–6.9 eV/atom for α-BNW and 6.7–6.8 eV/atom for β-BNW), some of the considered nanowires may be metastable, i.e., experimental researchers need to seek the way of synthesizing these materials. Meanwhile, spin-polarized calculations allowed one to estimate also magnetic moments M. It was found that α-c [001] and β-c [001] oriented BNWs were magnetically active (values of their moments were estimated to be 1.98 and 2.62 μ_B, respectively), while other nanowires and bulk were found neutral [2]. Spin-polarized calculations also demonstrated that α-c [001] and β-c [001] oriented NWs possessed antiferromagnetic (AFM) order, the difference between the total energies for AFM and FM states was found to be 0.03 and 0.10 eV, respectively [2].

Figure 4.19 shows the band structures of the six types of considered boron nanowires (Fig. 4.18), in which the Fermi levels are denoted by a horizontal dashed line. For boron nanowires, having no magnetic moments, the band structures were recalculated without spin polarization [2], as shown in Fig. 4.19a, b, d and e. For both magnetic nanowires, the band structures were calculated using the spin-polarized DFT method. Obviously, most BNWs under consideration are metallic, with the electronic energy bands across ϵ_F. However, the band structure of the boron nanowire with α-c [001] orientation and phase structure essentially differs from that of the other metallic boron nanowires, i.e., the α-c [001] oriented BNW is a narrow band gap semiconductor with a direct energy gap of 0.19 eV at X point. Due to the well-known shortcoming of DFT method in the description of the excited states, this band gap value was certainly underestimated [2]. Nevertheless, it clearly indicates that the electronic properties of α-c [001] BNW differ from those of bulk boron and other considered nanowires.

In addition, the considered electronic properties of the boron nanowires formed as a result of infinite extension of the unit cell of the α-B bulk are also NW direction dependent. Obviously, these orientational dependence of the electronic and magnetic properties of boron nanowires would be reflected on the photoelectronic properties of these materials and bring them to have a number of promising applications that are novel for bulk boron [2]. Hence, the considered BNWs possess the dependence of ferromagnetic and semiconducting properties on nanowire orientation, which are distinctly different from those of the boron bulk that is not magnetic. The physical origins of ferromagnetic and semiconducting properties of BNWs were pursued and

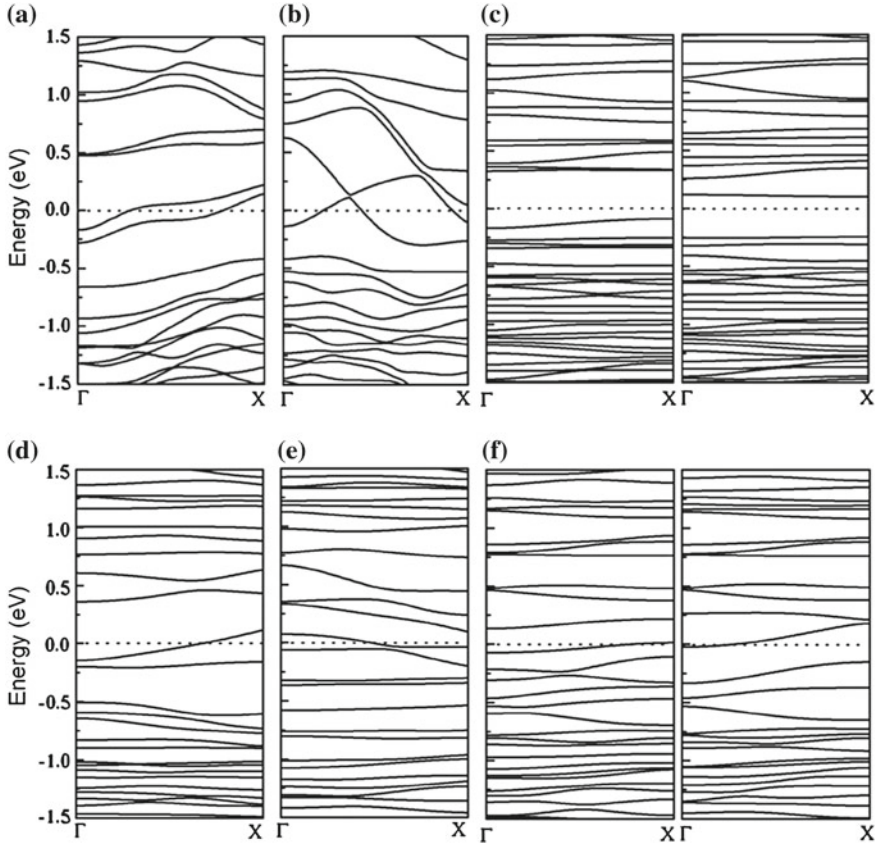

Fig. 4.19 The band structures of boron nanowires near the Fermi level: **a** α-a [100], **b** α-b [010], **c** α-c [001], **d** β-a [100], **e** β-b [010], and **f** β-c [001]. For **c** and **f**, the *left* and *right* plots represent the bands of spin-up and spin-down electrons. The *dashed lines* represent the Fermi level ϵ_F [2]

attributed to the unique surface structures. Therefore, these theoretical findings seem to open a way toward the applications of boron nanowires in electronics, optoelectronics, and spintronics [2].

4.4 Metal Diboride Bulk and Nanolayers

The discovery of high-temperature superconductivity (HTSC) for MgB_2 at $T_c = 39$ K [40] resulted in the enhanced interest to this class of materials with the structure close to the lattice instability boundary [41]. The next superconductor with a similar morphology was discovered soon at a markedly lower temperature (5 K), that was found to be ZrB_2 [42]. Superconductivity was observed not only in 3D diboride

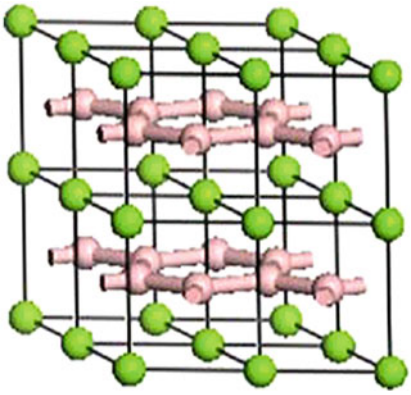

Fig. 4.20 Fragment of MeB_2 lattice where metal atoms are joined by *thin solid lines* [39]

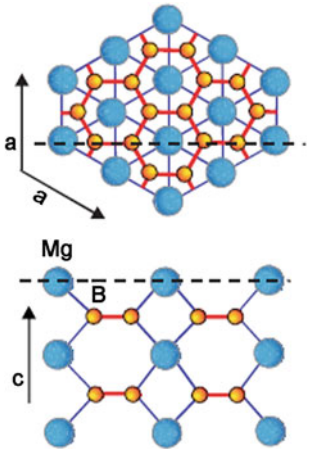

Fig. 4.21 Fragment of 5-layer $MgB_2(0001)$ slab [43]

single crystals and ceramics [43] but also in 2D thin films [44] as well as in 1D nanowires [45]. Except for the two experimental studies on the synthesis of non-crystalline nanotubes consisting of metal alloy diborides [46] and iron boride NT bundles [47], the information on reproducibly synthesized MeB_2 nanotubes is still not available, although a few methods were suggested for such a synthesis [48, 49], and a number of theoretical simulations predict their numerous properties, both electronic and structural [39, 41, 50–53].

Unlike boron, metal diboride structure is attributed to the layered crystals composed of periodically repeated bilayers consisting of boron and metal monolayers (Fig. 4.20) described by the hexagonal space group *P*6/*mmm* [39]. Atoms in a boron monolayer are arranged in a hexagonal graphite-type network while metal atoms form a triangular lattice that is located halfway between the honeycomb layers, positioned so that the atoms are projected onto the centers of the boron hexagons (Figs. 4.20 and 4.21). The primitive unit cell of MeB_2 contains three atoms (one formula unit). The family of layered diborides consists of a wide variety of metal atoms [50] attributed to at least 22 elements ranging from 2.58 (MnB_2) to 3.61 Å (GdB_2) by

an effective metallic diameter. Both atoms of light *sp*-metals and metals possessing *d*- and *f*-electrons can be accommodated in such a lattice. The ability of the MeB_2 single crystal to incorporate metals which differ so much in size and electronic structure creates the possibility of forming alloys between the members of that structural family. As discussed in the Sect. 4.1, some sp^2 bondsing states of trivalent boron atoms in graphene-like B monolayer (Fig. 4.2a) are unoccupied, which results in its relative instability. Just metal atoms were found essential in maintaining the charge neutrality and the honeycomb geometry of boron network. This can be illustrated by the simplified approach in which metal atoms donate the electron density (∼2e) to the nearest boron atoms [41], i.e., the network of Me^{2+} ions stabilize the negatively charged B^- layers the anions of which are strongly covalently bonded inside hexagonal lattice [39]. In any case, the strong covalent B–B bonding in boron layers prevail in MeB_2 bulk (Fig. 4.20), the polar interlayer Me–B bonds are weaker by one order of magnitude, while the interactions between Me cations are just lacking [52].

In 2D (0001) slab cut from MeB_2 crystal (Fig. 4.21), the ratio of strengths between B–B and Me–B bonds remains the same as in bulk, however, a noticeable covalent Me–Me bonding appears inside the metallic layer, the strength of which is comparable with that of Me–B bonding [52].

4.5 Rolled-Up Metal Diboride Nanotubes

4.5.1 Single-Wall Nanotubes

Analogously to graphene, the hexagonal B monolayer of arbitrary MeB_2 bilayer can be wrapped in boron cylinder inside the metal diboride nanotube, while the formation of co-axial metal cylinder follows this wrapping. If $\boldsymbol{a}_1$ and $\boldsymbol{a}_2$ are primitive vectors of the honeycomb boron layer, the wrapping vector for NT construction $\boldsymbol{R} = n\boldsymbol{a}_1 + m\boldsymbol{a}_2$ [48] defines the structure of a single-wall nanotube with arbitrary (*n, m*) chirality (as considered in Chap. 3). Interatomic distances inside the boron shell were initially assumed to be equal to the in-plane B–B distances, whereas the distance between the nearest coaxial boron and metal shells—to the inter-layer Me–B distances in the optimized bilayer (Fig. 4.21).

The two possible models of MeB_2 NTs have been considered so far: a metal cylinder located outside (a) and inside (b) B cylinder (Fig. 4.22). Termination of bilayer MeB_2 NTs depends mainly on the nature of Me atoms: for light metal atoms, B-termination was found to be more preferable [48, 50], while Me-termination prevails in nanotubes containing transition metal atoms, including Ti [49, 53]. The MeB_2 nanotubes with both *ac*- and *zz*-chiralities (Fig. 4.23) were simulated earlier [41, 48, 49, 52]. Their rotohelical morphologies can be described by point groups D_{nh} and C_{nv}, respectively. It was shown that *ac*-NTs were energetically more preferable compared to zigzag-type nanotubes [41, 48], although the latter were more stable at elevated temperatures [49]. In the B-terminated MeB_2 nanotubes (Fig. 4.22b), the

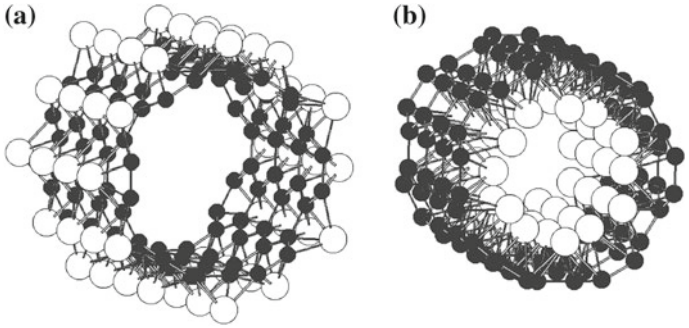

Fig. 4.22 Models of MeB_2 (6,6) *ac*-NT configurations: metallic cylinder is outside (**a**) and inside (**b**) a boron nanotube (Me and B atoms are shown as large *white* and small *black circles*, respectively) [48]

Me–Me bonds become stronger compared to bulk and sheets since metal atoms are in the "compressed" state with respect to their arrangement in the bulk crystal. Thus, the sequence of bond population in MeB_2 NT can be expressed *via* the following sequence: $p_{B-B} > p_{Me-Me} > p_{Me-B}$, i.e., interactions between metal and boron shells are the weakest [52]. On the other hand, in Me-terminated metal diboride nanotubes (Fig. 4.22a), $p_{Me-Me} < p_{Me-B}$ since metal atoms are "stretched" compared to MeB_2 bulk. For both NT terminations, B–B and Me–Me bonds become anisotropic. In particular, the difference in orientation of non-equivalent bonds (parallel, perpendicular, or at an angle to the translation vector of the nanotube) depends on the NT geometry and diameter. In this Subsection, we consider three types of the most widespread metal diboride nanotubes: MgB_2 (and isoelectronic BeB_2, for comparison), AlB_2 as well as TiB_2 with different number of valence electrons in metal atoms (two, three and four, respectively) and, thus, peculiarities of bonding in each case. Using (11,11) *ac*-nanotubes, as an example, it was found in [48] that changes in the electronic structure for a sequence of nanotubes ($MgB_2 \rightarrow AlB_2 \rightarrow TiB_2$) are determined by two main factors: (i) the growth of the electron number (from 176 to 220 *e*/UC for MgB_2 and TiB_2, respectively) is responsible for the growth of the valence band occupation; (ii) the nature of the metal atom determines the composition of the valence band and the interatomic Me–B and Me–Me interactions. When the dimensionality of MeB_2 varies (3D $\rightarrow$ 1D) while its formal stoichiometry remains the same, the morphology of metal diboride nanotubes plays the decisive role in the electronic spectrum near the Fermi level (and, consequently, in electro-physical properties). For example, the calculations performed earlier demonstrate that for B-terminated SW TiB_2 (6,6) nanotube, ϵ_F is localized near the DOS minimum. Besides, the Me-terminated SW NT of titanium diboride (Fig. 4.22a) was found to be a semiconductor [53], whereas MgB_2 and AlB_2 nanotubes possess high conductivity irrespective of NT termination [48, 50]. Analogously to BNSs and BNTs, the majority of *ab initio* calculations on MeB_2 sheets and nanotubes of different morphologies were performed using the plane-wave DFT methods within both LDA and

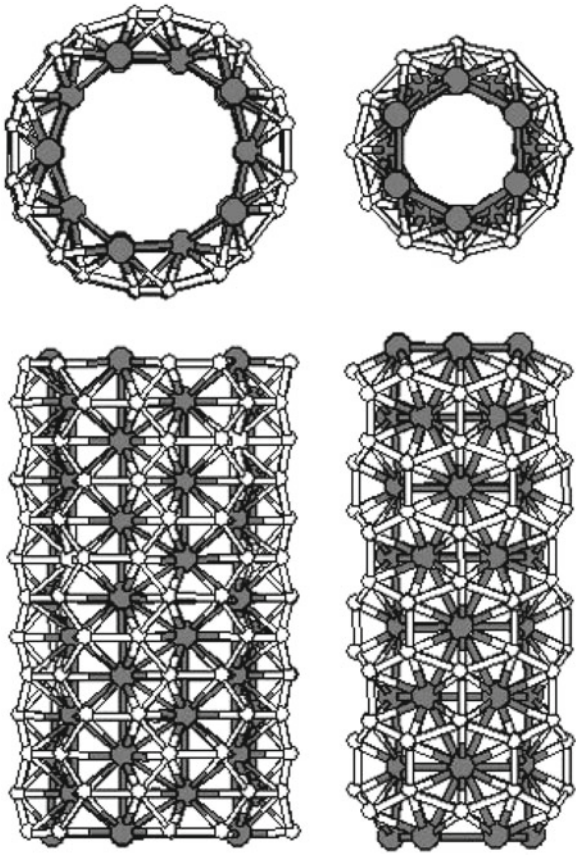

Fig. 4.23 Models of B-terminated MeB_2 nanotubes (Fig. 4.22b) which possess armchair (5,5) and zigzag (6,0) chiralities (*left* and *right panels*, respectively). Me and B atoms are shown as *large gray* and *small white circles*, respectively [41]

GGA approaches [39, 44, 49–51], parallel with the methods of LCAO-DFT [53], semi-empirical tight binding [48, 52] and molecular dynamics [41, 49].

4.5.2 MgB_2 and BeB_2 Nanotubes and Their Bundles

Both Mg and Be atoms may donate two valence electrons to the neighboring boron honeycomb layers inside the MeB_2 lattice, i.e., the B network becomes isoelectronic to graphite crystal [51]. These naturally layered structures motivated the investigation of single-wall MgB_2 and BeB_2 sheets as possible archetypes for nanotubular structures. MgB_2 NTs are expected to be high-temperature superconductors, even

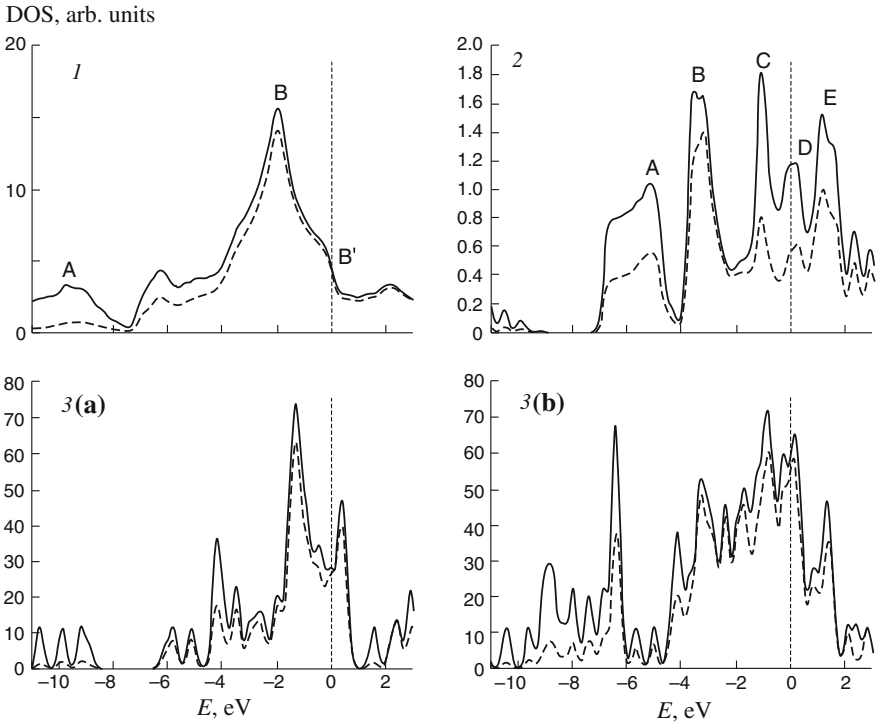

Fig. 4.24 Densities of states (the total DOS, *solid line*, and PDOS on the B(2*p*) states, *dashed line*) for 3D → 1D structures of MgB_2: (*1*) bulk, (*2*) sheet, (*3*) *ac*-(11, 11) (*a*) and *zz*-(20, 0) (*b*) nanotubes. The DOSs for NTs are given for a more stable configurations (Fig. 4.22b). The ϵ_F levels are shown by *vertical lines* [52]

more so because the well-known metallic carbon nanotubes, with markedly lower density of states at the Fermi level, were found to be displaying HTSC properties [48]. In SW MgB_2 nanotubes, the charge distribution was found to be different from that in bulk [39]: (i) the negative charge of boron shell is ∼0.73–0.84 *e per* B atom, depending on NT diameter and chirality; (ii) in the case of B-terminated nanotubes (Fig. 4.22a), a metal shell donates to boron ∼1.2 *e per* Mg atom while in the case of alternative NT termination, the charge transfer may approach 2 *e per* metal atom. As to the difference between the sizes of Be and Mg atoms, it results in a different geometry of the corresponding sheets and nanotubes [51]. Whereas the Mg atom in the single-wall 2D or 1D structures rests high above the boron plane (Fig. 4.21), the smaller Be atom drops from 1.4 Å above the boron layer in the bulk to only 0.5 Å above the plane in SW BeB_2 sheet. The B–B bonds elongate accordingly, from 1.66 to 1.72 Å, to accommodate the nearly coplanar Be atom. Under the appropriate conditions, SW BeB_2 NT may coalesce in a monolayer tubular form.

The DOSs for 3D → 1D forms of magnesium diboride, as present in Fig. 4.24, were firstly calculated using the tight-binding EHT method for the periodic structures [52]. The valence band of MgB_2 bulk (Fig. 4.24-(1)) consists of the filled B(2*s*, 2*p*)

states (A) and B($2p$) states (B), while ϵ_F is located in the region of bonding B($2p$) states (shoulder B'). The B($2p$) states can be decomposed to (i) B($2p_{x,y}$) ones, whose orbitals are coplanar with the boron network, forming the four σ-states responsible for the strong intra-layer covalent B–B bonds, and (ii) B($2p_z$) states, whose orbitals are perpendicular to the boron sheets, forming the two π-states responsible for the weak inter-layer bonds. One of the most important features of the MgB_2 band structure is the occurrence of hole B($2p_{x,y}$) states responsible for the superconductivity [52]. These states mainly contribute to the DOS near ϵ_F and determine metallic properties of MgB_2. Distinctly different DOSs were calculated for the isolated (0001) bilayer of MgB_2 (Fig. 4.24-(2)). The spectrum shows clearly pronounced "surface" DOS resonances (A-E), one of which (peak D) coincides with the Fermi level. This specific feature of the outer-layer states distribution of MgB_2 is believed to favor the increase in T_c in thin films compared to that in bulk [43]. Another important difference between 3D and 2D MgB_2 structures is a noticeable contribution of Mg states to the occupied part of the spectrum [52]. The comparison of the total one-electron energy spectra for *ac*- and *zz*-chiralities of magnesium diboride nanotubes (Figs. 4.24-(3a) and 4.24-(3b), respectively) with opposite terminations of nanotube shells (Fig. 4.22) shows that NT structures with magnesium cylinders inside boron shells are more stable [52]. Their spectra are of the metal type, and ϵ_F is located in the vicinity of B($2p$) states (Fig. 4.24). Contributions of Mg($3s$, $3p$) states to the valence band are found to be noticeably smaller. Such parameters of nanotube geometry as diameter and orientation of B–B bonds along the chirality vector distort both DOS and PDOS profiles. According to Fig. 4.24-3, for the *ac*-(11,11) NT (some B–B bonds are normal to the chirality direction), the Fermi level coincides with the local DOS minimum. On the contrary, for the *zz*-(20,0) nanotube (some bonds are aligned along the chirality direction), ϵ_F is localized near the local DOS maximum, with a high density of B($2p$) states; these MgB_2 NTs seem to be more promising for the search of materials with enhanced electro-physical (e.g., HTSC) parameters.

Analogous DOS-analysis was also performed for Be-terminated *ac*- and *zz*-type SW BeB_2 NTs using plane-wave DFT-LDA calculations [51]. Such nanotubes of both chiralities, (5,5) and (8,0), respectively, were found to be metallic over the whole energy spectrum while the corresponding Fermi levels coincided with the local DOS minima. The densities of states for these BeB_2 nanotubes at ϵ_F level were found markedly lower than for MgB_2 NTs and significantly higher than those for metallic CNTs. It means that beryllium diboride can possess low-temperature superconductive properties for all types of periodic structures (3D $\rightarrow$ 1D) as well as for large electron-phonon coupling matrix elements and can demonstrate distinct reactivity plus adsorption behavior of the outer shell atoms of BeB_2 NLs and NTs [51]. The models of MgB_2 and BeB_2 NTs have been described above for single nanotubes. However, although BNTs and CNTs as well as other types of earlier synthesized nanotubes can exist on their own, this is not always true for nanotubes of metal diborides, especially for B-terminated MeB_2 NTs [50]. The local atomic structure of 2D and 1D MeB_2 systems suggests that additional metal atoms are necessary to stabilize boron layers in MeB_2 bilayers and nanotubes derived from

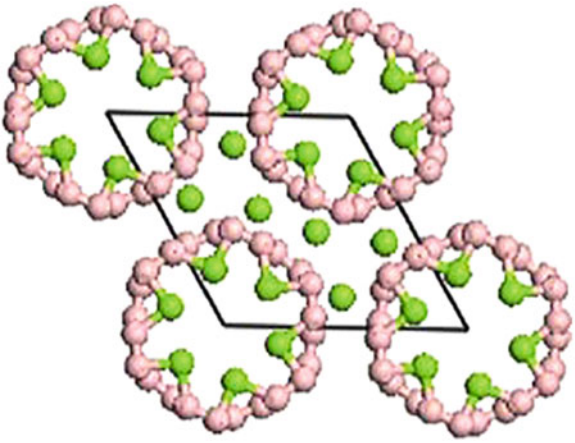

Fig. 4.25 The unit cell of hexagonal bundle of B-terminated MeB_2 nanotubes (Fig. 4.22b) strengthened by inter-tube Me atoms [39]

them. In bulk, each Me atom is bound with 12 neighboring B atoms (Fig. 4.20) since Me–Me bonds are too weak. However, a number of metal atoms located inside the boron shells of nanotubes is not enough to stabilize B-terminated SW MeB_2 NTs and they are more likely aggregated in bundles of boron shells with metal atoms both inside and between the nanotubes (Fig. 4.25), serving in part to bind the nanotubes together [39].

4.5.3 AlB_2 Nanotubes and Their Bundles

Pioneering DFT calculations on the structural and electronic properties of MeB_2 nanotubes were performed just for aluminum diboride [50] although the AlB_2 system was earlier considered to elucidate the quasi-planar configurations found for pure boron [15]. Since both B and Al are elements of group III, the whole family of metal diborides is attributed to AlB_2 lattice type [1]. It is interesting to note that if B is substituted for Al in Fig. 4.21, the structure becomes a puckered layer of six-fold coordinated boron considered in Sect. 4.1. It would be the construction procedure described elsewhere [15] and labeled by a pair of integers that describe cuts along the unit vectors of a triangular lattice. According to the plane-wave DFT-LDA calculations [50], unlike single boron nanotubes rolled up from B sheets, AlB_2 NTs prefer to be aggregated in bundles of metal nanotubes as shown in Fig. 4.25. Such a representation is shown in Fig. 4.26 and serves to emphasize the bonding between both boron and aluminum diboride nanotubes of the same *ac*-chirality (6,6) sitting on the hexagonal superlattice and possessing hexagonal morphology. Noticeable BNT-BNT bonding along the direction of this superlattice is evident from Fig. 4.26a. Obviously, there is a slight faceting due to undulations from the basic hexagonal lattice of the

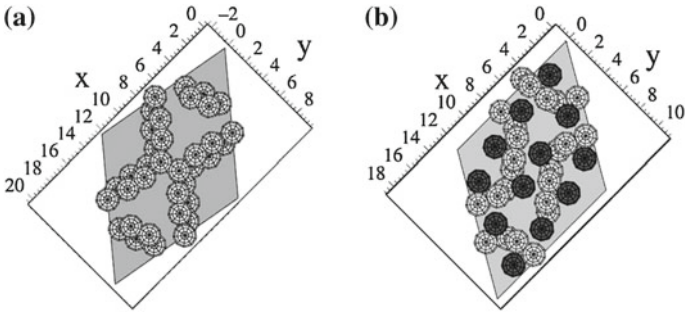

Fig. 4.26 Cross sections of SW Boron (6,6) NT (**a**) and AlB_2 NT (**b**) bundles incorporated in hexagonal superlattice. Units of surrounding *boxes* are given in Å. B and Al atoms are shown as *filled light* and *dark circles* [50]

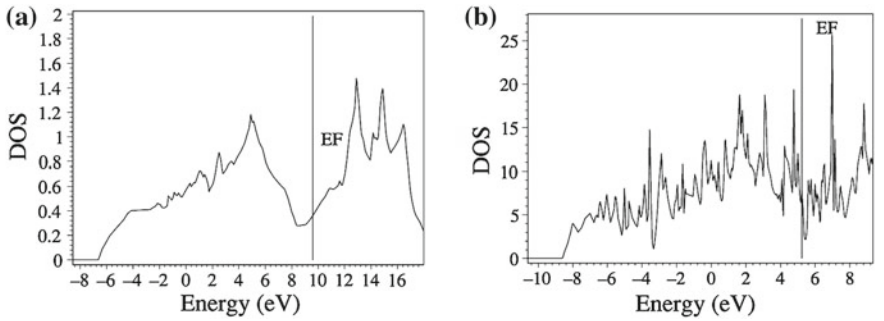

Fig. 4.27 DOSs in states/eV/cell versus energy in eV for crystalline AlB_2 bulk and AlB_2 SW (6,6) nanotube. Both systems are metallic [50]

quasi-planar reference structure. It was reasonable to take the relaxed (6,6) BNT as a good reference structure when looking for AlB_2 nanotube. The latter (Fig. 4.26b) was generated from BNT by substituting Al for boron at the six positions located along the directions of hexagonal bundle superlattice, both on the outside layer of the puckered nanotube, and on the inside NT layer. In the optimized bundle structure [50], AlB_2 NTs were rotated from the orientations they adopt in the superlattice of pure BNTs in such a way that Al atoms sticking out from the adjacent nanotubes do not face each other, but rather sit between boron layers. Such an arrangement locks the tubes together in a gear-like fashion and creates a local environment similar to that in crystalline AlB_2. The inclusion of aluminum atoms inside BNTs was found to be important for stabilizing the structure of hexagonal bundle superlattice.

The electronic densities of states calculated for crystalline AlB_2 bulk and AlB_2 NTs are plotted in Fig. 4.27 [50] showing that they both are metallic. This result was already predicted before and based on qualitative arguments related to both tight-binding models [54] and *ab initio* calculations [15]. Those predictions were found to be valid even after a complete structural relaxation. The overall shapes of the DOSs

for both crystalline and nanotubular AlB_2 look similar [50] due to similarities in the local atomic environments. The DOS for AlB_2 nanotube, however, has a much more fine structure, which can be understood in terms of the back-folding of the bands of crystalline AlB_2 into the reduced Brillouin zone of the tubular lattice. Obviously, the total densities of states for both AlB_2 bulk and (6,6) NT (Fig. 4.27) as well as MgB_2 bulk and (11,11) NT (Fig. 4.24) have certain qualitative similarities, due to identical arrangement of boron shells inside metal diborides. They also have differences caused by various electronic structures of Al and Mg atoms. The most essential difference of both materials is the fact that at the vicinity of Fermi level the density of states of AlB_2 is significantly lower than that of MgB_2 in periodic structures of different dimensionalities, i.e., the former cannot manifest a high-temperature superconductivity.

4.5.4 Single- and Double-Wall TiB_2 Nanotubes

Diborides of light *sp*-metals, as considered above, provide the formation of negatively charged B^- honeycomb layers by donating almost all the electronic density from the valence shells of Me atoms (BeB_2 and MgB_2) or its substantial part (AlB_2). On the contrary, diborides of transition metals, including TiB_2, possess an enhanced reactivity, especially in nanotubular form due to the presence of *d*-electrons not involved in chemical bonding [49, 53]. Some peculiarities of transition metal diborides distinguish the corresponding nanotubes from MeB_2 NTs described above [48]. For example, Ti shells are usually arranged outside the boron shells in SW TiB_2 NTs of both chiralities. Otherwise, Ti-B network would break in case if titanium atoms are inserted inside the boron nanotubes of small diameters [49]. For larger diameters of TiB_2 NTs, Ti-terminated nanotubes were found to be more stable than B-terminated nanotubes by at least 0.1 eV per atom. SW TiB_2 NTs can exist as well-separated from other nanotubes (free-standing), which make them active for either passivation by gas, e.g., hydrogen [49], or consequent growth as multi-wall nanotubes [53].

Figure 4.28 illustrates an initial stage of possible MW TiB_2 NT growth [53]. According to Fig. 4.28a, the B (Ti) shell is assumed to be the internal (external) cylinder of a bilayer SW TiB_2 *zz*-(6,0) NT. The radius of the internal boron shell was constrained to be so that the nearest neighbor B–B distances remain the same as that in the optimized TiB_2 bulk. The radius of the external titanium shell was determined through the optimization of the interlayer distance between B and Ti shells. The reduction in the number of B–Ti bonds, as compared to the bulk, led to the increase of B–Ti interactions and a smaller inter-shell distance. The inter-wall interaction inside a DW TiB_2 NT was explored through the study of a SW TiB_2 (6,0) NT incorporated in the external (12,0) boron nanotube (Fig. 4.28b) whose stability is provided by two *d*-electrons remaining in the valence shell of Ti atoms donated to (12,0) BNT. The B–B distance in the additional (12,0) tube is also taken as that of TiB_2 bulk (as for the (6,0) B shell). This determines the radius of the external boron wall.

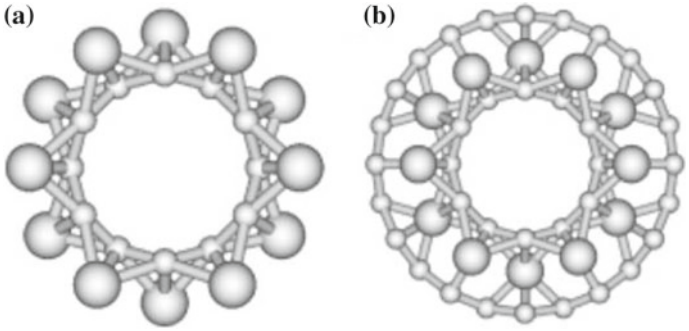

Fig. 4.28 Schematic representation of **a** SW TiB_2 (6,0) nanotube and **b** quasi-DW TiB_2 (6,0) @ B (12,0) NT. The *small* (*big*) *balls* represent B (Ti) atoms (Reprinted figure with permission from Guerini and Piquini [53], Copyright (2003) by the Elsevier Science Ltd. All rights reserved)

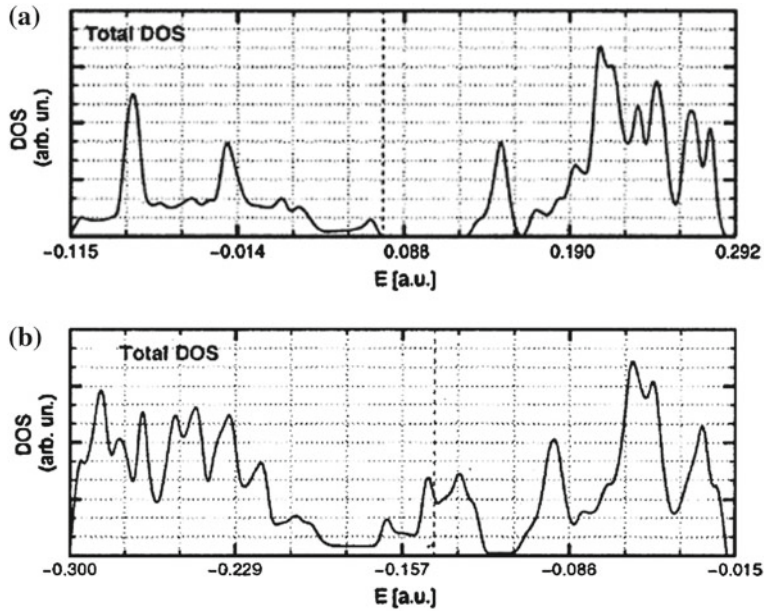

Fig. 4.29 The calculated total densities of states for both SW (6,0) TiB_2 NT (**a**) as well as quasi-DW TiB_2 (6,0) @ B (12,0) NT (**b**) [53]

The comparison between the total DOSs of both SW TiB_2 (6,0) and quasi-DW TiB_2 (6,0) @ B(12,0) (calculated using DFT-LCAO method [53]) is presented in Fig. 4.29. A well-separated single-wall TiB_2 *zz*-(6,0) NT displays presence of energy gap (1.32 eV), typical for a semiconductor (Fig. 4.29a). The additional external boron (12,0) nanotube wall imitating the formation of quasi-DW TiB_2 NT presents a markedly different density of states compared to a SW TiB_2 NT, showing a metallic

behavior, with the DOS at the Fermi level coming mainly from the external boron shell (Fig. 4.29b). This transition from semiconducting to metallic TiB_2 NTs could be explored in electronics [53] to build nanoscale junctions just by a variation of one cylindrical B shell. The enhanced reactivity of Ti-terminated TiB_2 NTs can also serve for hydrogen storage on titanium diboride nanotubes as predicted using the results of the plane-wave DFT-GGA calculations on H_2 molecule adsorption outside SW (5,5) and (8,0) TiB_2 NTs [49]. It was shown that in the case of one hydrogen molecule *per* external Ti atom the adsorption energy (E_{ads}) equals 0.47 (0.30) eV or 0.35 (0.34) eV for parallel (perpendicular) orientation of H_2 bound with nanotube of *ac*- or *zz*-chirality, respectively. For bimolecular hydrogen adsorption, the perpendicular orientation of H_2 was found to be more preferable, with $E_{ads} = 0.24\,(0.20)$ eV *per* H_2 for the same nanotubes of *ac*-(*zz*-) chiralities. Since hydrogen adsorption and further concentration was experimentally observed upon the TiB_2 (0001) surface [55] and then was confirmed in the corresponding DFT-GGA calculations [49], the results of analogous simulations obtained for nanotubes can be considered as realistic. Thus, TiB_2 nanotubes may be appealing candidates for the room-temperature hydrogen storage with the predicted capacity of 5.5 wt% and the desirable binding energies of 0.2–0.6 eV/H_2 [49].

Crystalline nanowires of metal diborides (mainly MgB_2 possessing HTSC properties mentioned in Sect. 4.4), diameters of which changed from 10 nm up to several hundreds nm, were repeatedly synthesized during last years using different methods: high-temperature vaporization of BNWs by magnesium obtained by sputtering of MgO substrate [56], direct pyrolysis of metal diboride nanoparticles [45], low-pressure chemical vapor deposition [57], etc. However, no reference on theoretical simulations of these nanowires have been found in literature so far, maybe this is a question of the nearest future.

References

1. E.L. Muetterties, *The Chemistry of Boron and Its Compounds* (Wiley, New York, 1967)
2. J.L. Li, T. He, G. Yang, Nanoscale Res. Lett. **7**, 678 (2012)
3. N.S. Hosmane (ed.), *Boron Science: New Technologies and Applications* (CRC Press, Boca Raton, 2011)
4. K. Smith, Nature **348**, 115 (1990)
5. E.D. Jemmis, M.M. Balakrishnarajan, P.D. Pancharatna, Chem. Rev. **102**, 93 (2002)
6. H. Werheit, V. Filipov, U. Kuhlmann, U. Schwarz, M. Armbrüster, A. Leithe-Jasper, T. Tanaka, I. Higashi, T. Lundström, V.N. Gurin, M.M. Korsukova, Sci. Technol. Adv. Mater. **11**, 023001 (2010)
7. H. Werheit, Solid State Sci. **13**, 1786 (2011)
8. E.D. Jemmis, D.L.V.K. Prasad, J. Solid State Chem. **179**, 2768 (2006)
9. A. Sebetci, E. Meteb, I. Boustani, J. Phys. Chem. Solids **69**, 2004 (2008)
10. Q.B. Yan, Q.R. Zheng, G. Su, Phys. Rev. B **77**, 224106 (2008)
11. J. Tian, Z. Xu, C. Shen, F. Liu, N. Xu, H.J. Gao, Nanoscale **2**, 1375 (2010)
12. H.J. Zhai, B. Kiran, J. Li, L.S. Wang, Nat. Mater. **2**, 827 (2003)
13. H. Tang, S. Ismail-Beigi, Phys. Rev. Lett. **99**, 115501 (2007)
14. M.H. Evans, J.D. Joannopoulos, S.T. Pantelides, Phys. Rev. B **72**, 045434 (2005)

15. I. Boustani, A. Quandt, E. Hernández, A. Rubio, J. Chem. Phys. **110**, 3176 (1999)
16. P.J. Durrant, B. Durrant, *Introduction to Advanced Inorganic Chemistry* (Wiley, New York, 1962)
17. A. Quandt, I. Boustani, Chem. Phys. Chem. **6**, 2001 (2005)
18. R.R. Zope, T. Baruah, Chem. Phys. Lett. **501**, 193 (2011)
19. F. Tian, Y. Wang, V.C. Lo, J. Sheng, Appl. Phys. Lett. **96**, 131901 (2010)
20. J. Kunstmann, A. Quandt, Phys. Rev. B **74**, 035413 (2006)
21. A.K. Singh, A. Sadrzadeh, B.I. Yakobson, Nano Lett. **8**, 1314 (2008)
22. W. Guo, Y. Hu, Y. Zhang, S. Du, H. Gao, Chin. Phys. B **18**, 2502 (2009)
23. K.C. Lau, R. Orlando, R. Pandey, J. Phys.: Condens. Matter **20**, 125202 (2008)
24. R.K.F. Lee, B.J. Cox, J.M. Hill, Nanoscale **2**, 859 (2010)
25. B. Kiran, S. Bulusu, H. Zhai, S. Yoo, X.C. Zeng, L. Wang, Proc. Natl. Acad. Sci. USA **102**, 961 (2005)
26. D. Ciuparu, R.F. Klie, Y. Zhu, L. Pfefferle, J. Phys. Chem. B **108**, 3967 (2004)
27. I. Boustani, A. Quandt, Europhys. Lett. **39**, 527 (1997)
28. R. Saito, G. Dresselhaus, M.S. Dresselhaus, *Phyical Properties of Carbon Nanotubes* (Imperial College Press, London, 1998)
29. J. Tersoff, R.S. Ruoff, Phys. Rev. Lett. **73**, 676 (1994)
30. J.P. Salvetat, G.A.D. Briggs, J.M. Bonard, R.R. Bacsa, A.J. Kulik, T. Stöckli, N.A. Burnham, L. Forró, Phys. Rev. Lett. **82**, 944 (1999)
31. K.C. Lau, R. Pati, R. Pandey, A.C. Pineda, Chem. Phys. Lett. **418**, 549 (2006)
32. Yu.F. Zhukovskii, S. Piskunov, S. Bellucci, Nanosci. Nanotechnol. Lett. **4**, 1074 (2012)
33. C.J. Otten, O.R. Lourie, M. Yu, J.M. Cowley, M.J. Dyer, R.S. Ruoff, W.E. Buhro, J. Am. Chem. Soc. **124**, 4564 (2002)
34. S. Datta, *Electronic Transport in Mesoscopic Systems* (Cambridge University Press, Cambridge, 2003)
35. B.J. Cox, J.M. Hill, Carbon **45**, 1453 (2007)
36. X. Yang, Y. Ding, J. Ni, Phys. Rev. B **77**, 041402 (2008)
37. R.K.F. Lee, B.J. Cox, J.M. Hill, J. Phys. Chem. C **113**, 19794 (2009)
38. J.M. Soler, E. Artacho, J.D. Gale, A. Garcia, J. Junquera, P. Ordejón, D. Sánchez-Portal, J. Phys.: Condens. Matter **14**, 2745 (2002)
39. D.L.V.K. Prasad, E.D. Jemmis, J. Mol. Struct. (Theochem) **771**, 111 (2006)
40. J. Nagamatsu, N. Nakagawa, T. Muranaka, Y. Zenitani, J. Akimitsu, Nature **410**, 63 (2001)
41. L.A. Chernozatonskii, JETP Lett. **74**, 335 (2001)
42. V.A. Gasparov, N.S. Sidorov, I.I. Zver'kova, M.P. Kulakov. JETP Lett. **73**, 532 (2001)
43. C. Buzea, T. Yamashita, Supercond. Sci. Technol. **14**, R115 (2001)
44. I.G. Kim, J.I. Lee, B.I. Min, A.J. Freeman, Phys. Rev. B **64**, 020508(R) (2001)
45. R. Ma, Y. Bando, T. Mori, D. Golberg, Chem. Mater. **15**, 3194 (2003)
46. Y. Zhu, F. Liu, W. Ding, Xu. Guo, Y. Chen, Angew. Chem. Int. Ed. **45**, 7211 (2006)
47. Y. Zhu, Xi. Guo, M. Mo, Xu. Guo, W. Ding, Y. Chen, Nanotechnology **19**, 405602 (2008)
48. V.V. Ivanovskaya, A.N. Enjashin, A.A. Sofronov, Yu.N. Makurin, N.I. Medvedeva, A.L. Ivanovskii, J. Mol. Struct. (Theochem) **625**, 9 (2003)
49. S. Meng, E. Kaxiras, Z. Zhang, Nano Lett. **7**, 663 (2007)
50. A. Quandt, A.Y. Liu, I. Boustani, Phys. Rev. B **64**, 125422 (2001)
51. P. Zhang, V.H. Crespi, Phys. Rev. Lett. **89**, 056403 (2002)
52. V.G. Bamburov, V.V. Ivanovskaya, A.N. Enyashin, I.R. Shein, N.I. Medvedeva, Yu.N. Makurin, A.L. Ivanovskii, Dokl. Phys. Chem. **388**, 43 (2003)
53. S. Guerini, P. Piquini, Microelectron. J. **34**, 495 (2003)
54. D. Pettifor, *Bonding and Structure of Molecules and Solids* (Oxford University Press, Oxford, 1995)
55. D.M. Zhang, Z.Y. Fu, J.K. Guo, Key Eng. Mater. **249**, 119 (2003)
56. Y. Wu, B. Messer, P. Yang, Adv. Mater. **13**, 1487 (2001)
57. T.T. Xu, A.W. Nicholls, R.S. Ruoff, Nano **1**, 55 (2006)

Chapter 5
Group IV Semiconductors

In this chapter, *written by Yu.F. Zhukovskii* (*quantzh@latnet.lv*), theoretical models of 1D nanostructures and their properties for both silicon and germanium as well as silicon carbide and germanium silicide semiconductors are considered and discussed.

Silicon and germanium are advanced semiconductors with a huge variety of technological applications. Not only rolled-up SW and DW as well as polyhedral nanotubes of silicon were simulated as in the case of boron, but also faceted nanotubes. These three types of Si nanotubes with different morphology were compared in order to make conclusions about their relative stability. The faceted nanotubes were found to be energetically the most stable under hydrogenation. The phonon band structure and the vibrational density of states were calculated for the polyhedral models of Si NTs. Theoretical calculations of Si and Ge nanotubes were performed using DFT (LDA and GGA), as well as DFTB and molecular dynamics methods.

Due to the enhanced technological interest, silicon nanowires are attributed to the most widespread chemical class of simulated nanowires, according to the total number of publications that have appeared so far. The optimized morphology, cohesive and elastic properties, electronic and vibrational structure of prismatic and circular-type Si NWs are calculated using the formalism of interatomic empirical potentials, the continuum and finite element models, the Monte-Carlo method, molecular dynamics, the DFT tight-binding (e.g., DFTB) methods and the first-principles methods of the density functional perturbation theory (DFTP). Hydrogenation of silicon nanowires essentially enhances their energetic stability. The faceting of nanowires oriented along the chosen crystallographic direction can be determined using the Wulff construction formalism. Analogous simulations were performed for the prismatic models of Ge nanowires.

Silicon monocarbide (SiC), one of the hardest materials suitable for electronic devices, and GeSi exhibit polymorphism characterized by different stacking of atomic layers, which was observed in their nanostructures too. The rolled-up models of SiC NTs are used for the construction of single- and double-walled nanotubes as well as bundles of SW NTs, while for alternative simulations, models of faceted SiC NTs are used. Theoretical calculations of equilibrium morphology, cohesive and electronic properties of SiC and GeSi nanotubes were performed using the PW DFT

© Springer-Verlag Berlin Heidelberg 2015

R.A. Evarestov, *Theoretical Modeling of Inorganic Nanostructures*,
NanoScience and Technology, DOI 10.1007/978-3-662-44581-5_5

methods within both the LDA and GGA approaches, the LCAO-DFT and LCAO-hybrid HF-DFT methods, tight binding and molecular dynamics methods.

Simulations of the cohesive and electronic properties of SiC nanowires of various morphologies were performed using the formalism of interatomic empirical potentials, tight-binding model, methods of molecular dynamics, DFT-LCAO and PW DFT methods within both the LDA and GGA approaches. Theoretical calculations on GeSi and hetero-structured Ge/Si nanowires of different morphologies were performed using the PW DFT and DFT-LCAO methods within both the LDA and GGA approaches, DFPT and tight-binding methods, as well as the formalism of interatomic empirical potentials. Ge_{core}-Si_{shell} NWs are believed to have the most stable structure among GeSi nanowires. They have negative values of formation enthalpy and for them the creation of a nanoalloy is preferable.

5.1 Silicon and Germanium Bulk and Nanolayers

Silicon is well known as an important and multi-useable semiconducting material, dominating in modern electronic technology [1]. The invention of the transistor and its monolithic integration in silicon substrate led to the implementation of Si-based devices in computer technology and telecommunication systems, thus, creating foundations for the semiconductor industry [2]. The continuously shrinking size of silicon devices (less than 65 nm) has raised interest to the properties of silicon at the nanoscale, both in the form of clusters and nanoparticles and in quasi-one-dimensional structures such as nanotubes and nanowires [3]. It was found that monoperiodic silicon nanostructures have potential for the development of Si-based devices such as sensors, logical gates, memories, and systems for optoolectronic and biological applications.

Germanium, whose morphology and properties are similar to those of silicon, was also widely applied in a number of technological branches, e.g., in electronics [4]. Obviously, both Ge and Si structures of different dimensionalities can be considered as complementary materials with slightly different parameters of the same types of crystalline lattice and similar chemical properties. Their description can be unified within this Subsection.

Si (Ge) crystal can be attributed to either more stable cubic diamond-type (*d*) structure (Fig. 5.1a) or less stable hexagonal wurtzite-type (*w*) structure (Fig. 5.1c) existing at high pressures [7]. Distribution of atoms in both phases differs by bond orientation in the 4th coordination spheres (Fig. 5.1b), i.e., directions of bonds 2, 3 and 4 in the former can be determined by rotation of those in the latter around the bond 1 by π [6]. Two phases of Si (Ge) bulk crystal are described by space groups $Fd\bar{3}m$ and $P6_3mc$ [8], respectively. The energetically most favorable surfaces for the two phases of crystalline lattice are determined by Miller indices (111) and (0001), respectively, along which both crystals are preferentially cleaved [2]. Figure 5.2 shows the structural stacking in diamond- and wurtzite-type Si (Ge) crystals where each atom has a tetrahedral coordination [8]. In *d*-Si (Ge), the stacking follows the series *ABCABC*

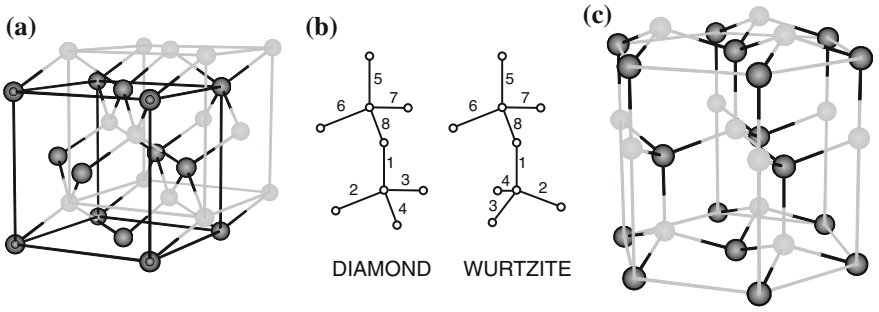

Fig. 5.1 Models of two possible silicon (germanium) single-crystal structures possessing lattices with cubic diamond-type (**a**) and hexagonal wurtzite-type (**c**) morphology showing the two pairs of interpenetrating *fcc* and *hcp* unit cells [5]. *Black* and *gray* balls show atoms attributed to the first or second unit cells for both types of Si (Ge) sublattices, respectively. Sketch (**b**) schematically represents the spatial distribution of Si-Si (Ge-Ge) bonds in diamond and wurtzite structures [6]

Fig. 5.2 Comparison of the structural stacking in diamond- (**a**) and wurtzite-type (**b**) structures of Si (Ge) bulk [8]

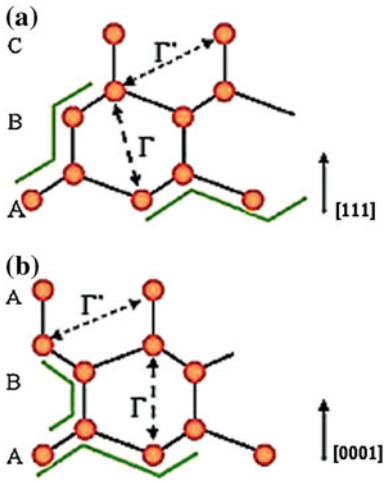

across the [111] direction (Fig. 5.2a), while the series in *w*-Si (Ge) is *ABAB* across the [0001] direction (Fig. 5.2b). Bilayers *A* are identical in both types of bulk structure whose projections on the corresponding (111) and (0001) planes form hexagonal quasi-sheets (Fig. 5.3a), which can be used for generation of SW Si (Ge) nanotubes [9]. However, the perfect Si (Ge) crystal possesses a non-layered lattice unlike carbon, where the most stable structure is a layered graphite lattice consisting of periodically distributed and relatively remote graphene monolayers [10]. On the other hand, reproducibly synthesized 1D Si structures were found to be either nanowires (NWs) with diamond-like morphology [11] or Si NTs with thick amorphous or faceted crystalline-structured walls [12]. The former were found to be energetically more

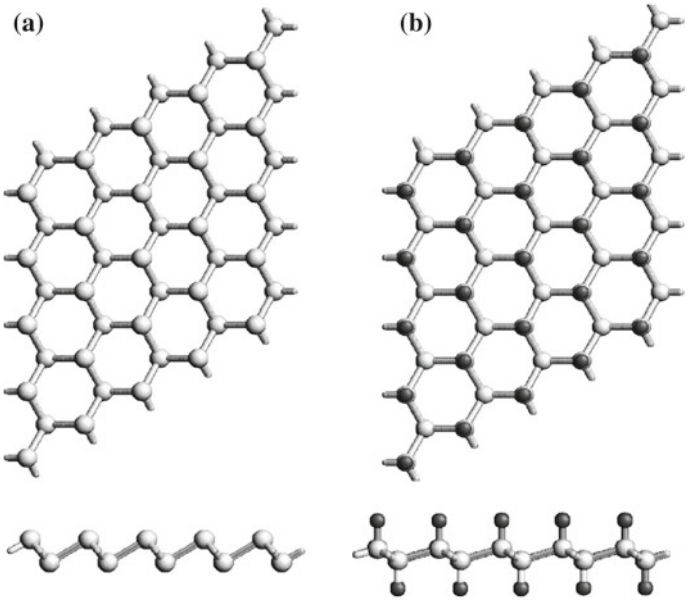

Fig. 5.3 The *top* views and *across* views of both silicide (**a**) and SiH_2 bilayers (**b**) [9]

favorable than the latter. As for carbon, the diamond NW-like nanostructures (DNWs) were found to be energetically less favorable than CNTs [13]. This difference can be easily explained since Si tendency for sp^3 hybridization originates from both the relatively small energy between *s* and *p* orbitals (5.66 eV), compared to carbon (10.60 eV), and the poor p-π overlap in Si=Si bond, being by the order of magnitude smaller than the corresponding value in C=C bond [9], which provides structural stability of 2D graphene monolayers and 1D single-wall carbon nanotubes. Therefore, the cohesive energy of hypothetical sp^2-bonded Si NTs achieves only 82 % of that for diamond-type silicon bulk (*cf.* with the 99 % energy ratio between CNTs and graphite bulk) [14].

The layered silicon-containing structures favorable for generation of nanotubes can exist among the inorganic crystalline modifications [9]. For example, alkaline-earth-metal disilicides (as $CaSi_2$), consist of hexagonal Si layers separated by the alkaline-earth-metal layers [15]. Analogously to B layers in MeB_2, as considered in Sect. 4.4, each Si atom in these silicides is threefold-coordinated by neighboring silicon atoms and possesses a negative charge (e.g., $-Si^{-}-Ca^{2+}-Si^{-}-$, similarly to B atoms in MeB_2, Fig. 4.21). Thus, Si layers become isoelectronic to the layered structure of black phosphorus (*b*-P), which was found to be a prototype for generation of stable PNTs [16]. Similarly as in *b*-P, the Si layers in metal silicides are not graphene-type planar but form buckled bilayers (as shown in Fig. 5.3a). On the other hand, the top view of this layered structure greatly resembles a graphene monolayer.

At this point, silicon may form stable nanotubes based on the basis of the silicide layer structure corresponding to phosphorus [16].

The DFTB calculations [9] qualitatively confirmed the values of structural data for Si bilayers (Si-Si bond length, 2.41 Å, Si-Si-Si bond angle, 104.8°, etc.) observed in $CaSi_2$ experimentally [15] and predicted for *b*-P theoretically [16]. Recent theoretical simulations of the silicide-type layer growth upon the Ag(111) substrate [17] confirms its stability due to a minimal mismatch between silicene and silver counterparts. Furthermore, the silicides may also be used for the synthesis of polymeric SiH_2 (whose Si-H bond length, 1.51 Å, is similar to that in disilane Si_2H_6 [18]). Obviously, SiH_2 may form a buckled tetralayer (as illustrated in Fig. 5.3b), a candidate for Si-based nanotube structures as a precursor. Analogically to models of silicon faceted NTs [12] and NWs [19], which are considered in more detail in Sects 5.2.3 and 5.3.1, respectively, hydrogen passivation is necessary also for termination of silicon dangling bonds in Si nanotubes [9]. Stabilization of silicon-based nanostructures is also achieved by oxidation, e.g., leading to the creation of SiO- and SiO_2-types of nanotubes [20–22]. One of the possible ways for SiO_2 NT generation was found to be the formation of silica monolayers based on 2D network consisting of SiO_4 tetrahedra grown on a Mo substrate (and rolled-up further on it [23]). Moreover, single-crystalline Si nanotubes synthesized in nanochannels of amorphous porous alumina using different methods are wrapped in amorphous SiO_2 walls [24]. In addition, a number of new routes to control and engineer the Si NTs surface chemistry were provided by functionalization of the inner and outer surfaces of nanotubes by the organic molecular layers containing different functional groups of hydrophobic/hydrophilic chemical nature. It was provided *via* covalent bonding, in order to give nanotubular structures with dual chemical properties [25].

The calculations on Si (Ge) nanolayers (e.g., honeycomb silicene monolayers) and nanotubes of different morphologies were performed using the PW DFT methods within both LDA and GGA approaches [10, 17, 26, 27], the LCAO-DFT methods [7, 12, 14, 21, 28], the semi-empirical DFTB method [9, 16, 29] and methods of molecular dynamics [7, 17, 30–32]. The discussion which follows is based on the results of these calculations.

5.2 Silicon and Germanium Nanotubes

5.2.1 Rolled-Up Si Nanotubes

Initial configurations of the nanotubes were constructed by folding a 2D graphene-like silicon nanolayer with a Si-Si bond distance obtained for the silicide nanolayer [9]. These nanostructures were constructed from initially flat nanolayers rather than the buckled structure shown in Fig. 5.3. However, the high symmetry of the hexagonal structures, which possessed both *ac*- and *zz*-NT (*n*,*n*) and (*n*,0) chiralities, was broken by small random displacements of atoms during the geometry optimization

procedure, in order to facilitate the convergence of the calculations. As a result, a different axial strain on the nanotube was imposed, with the aim of finding the atomic configuration and lattice parameter of the minimum energy, which exactly corresponds to the buckled structures of a Si(111) nanolayer.

Figure 5.4a, d illustrate the optimized structures found for silicide-type (*n*,*n*) and (*n*,0) nanotubes, respectively, which can be understood in terms of conventional graphitic CNTs by simply replacing the flat hexagons present in the latter with the cyclohexane-like rings, just in the same way as the layered structure of the silicides is related to that of graphene [9]. The analogical result was also obtained in the case of DFT-LCAO structural optimization on smooth Si NTs of *zz*-chirality [12]. They also were found to be structurally similar to those of the corresponding phosphorus nanotubes [16] although PNTs were non-charged. On the other hand, the neutral *ac*- and *zz*-SiH_2 nanotubes possessed the two morphologies where the arrangement of hydrogen atoms can be shown as either alternating inside/outside, i.e., SiH-*io* (Fig. 5.4b, e), or all bound outside the NT surface, i.e., SiH-*sf* (Fig. 5.4c, f). The total energy optimization for all the four configurations of SiH_2 NTs resulted in formation of the buckled nanotube structures, the same as in the case of silicide-type Si NTs [9]. Stability of Si^- and SiH_2 nanotubes can be described by strain energy as a function of the nanotube diameter (Fig. 5.5a). The strain energy (E_{strain}) is the energy difference *per* atom or formula unit between an NT and the reference nanolayer structures shown in Fig. 5.3. For a given diameter, the strain energy of Si NTs is only slightly larger than that of CNTs, but smaller than that of PNTs [9]. They all converge as $\sim 1/D^2$ towards the zero value of the reference nanolayer structure as the diameter D is increased.

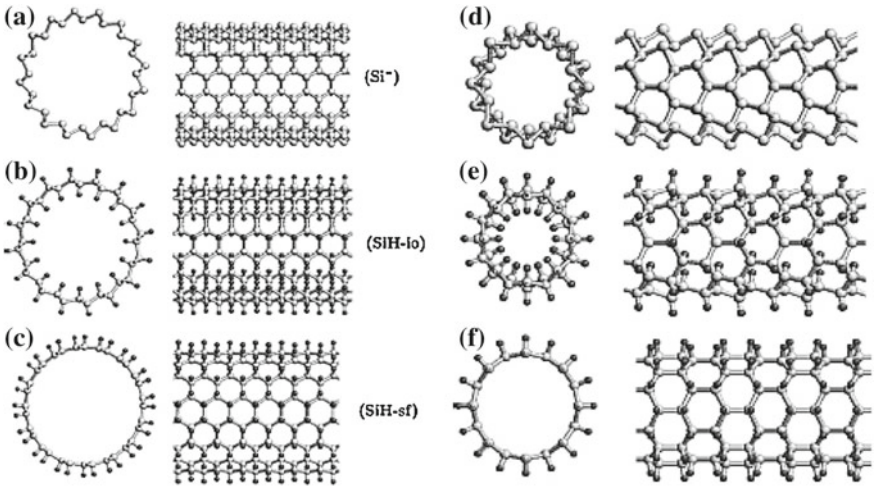

Fig. 5.4 Optimized structures of rolled-up (8,8) and (8,0) silicide-type (**a, d**), SiH-*io* (**b, e**), and SiH-*sf* (**c, f**) nanotubes, whose symmetry may be described by D_{nh} and C_{nv} point groups, respectively. The across- and aside-views are shown on the *left* and *right* sides of each panel [9]

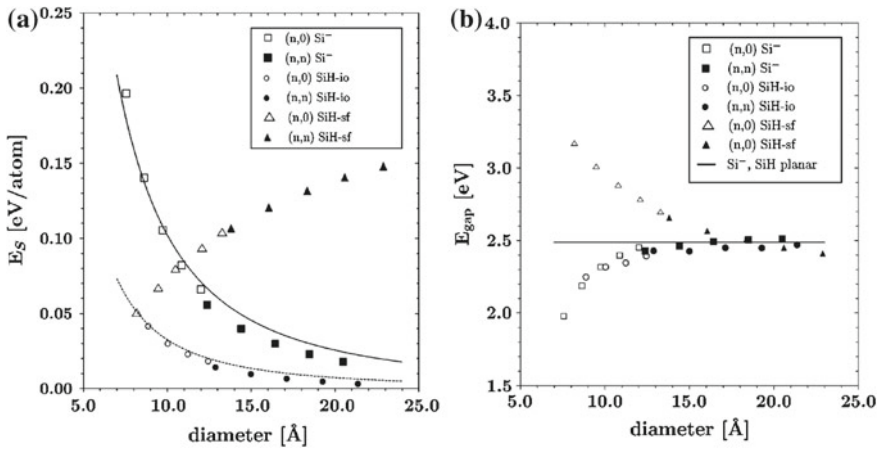

Fig. 5.5 Strain energies (**a**) and band gaps (**b**) of (*n*,*n*) and (*n*,0) silicide (Si^-), SiH-*io* and SiH-*sf* nanotubes as functions of the nanotube diameter [9]

The SiH-*io* NTs are energetically more favorable than Si^- NTs of the same chirality. Still, the behavior of SiH-*sf* nanotubes can be understood since due to the increase of the nanotube diameter and the simultaneous decrease of Si-Si-H curvature the bond angle is steadily forced towards 90^o, while the ideal tetrahedral angle of 109.5^o for fourfold-coordinated silicon in the SiH-*io* nanotubes can be achieved by increasing the diameter (Fig. 5.5a). A flat 2D SiH-*sf* nanolayer would not be stable at all, but it bends spontaneously and favors the creation of SiH-*sf* NTs with small diameters. The flat silicide and SiH_2 nanolayers as well as all the NTs considered were found to be semiconducting. Figure 5.5b shows the NT band gap $\Delta\epsilon$ as a function of the average diameter. For silicide and SiH-*io* NTs, the gap size rapidly grows towards the value of flat silicide and SiH_2 nanolayers with the increase in the nanotube diameter. For SiH-*sf* NTs, this behavior is opposite: the gap sizes shrink to the value of the flat nanolayer, in contrast to CNTs, but analogically to PNTs.

The double-wall silicon nanotube with a *zz*-chirality of both shells (Fig. 5.6) was firstly calculated using the DFT-LCAO method, with a total geometry optimization [12]. Each DW NT shell consists of two Si-Si bond types with equilibrium lengths of 2.31 and 2.33 Å, respectively, which were found to be shorter by 0.04 and 0.02 Å than in silicon bulk (2.35 Å). Each Si atom in these nanotubes is threefold coordinated, possessing a dangling bond. The optimized NT diameters were found to be 11.65 and 18.96 Å. Formation energies of constituent shells (E_{form}) were estimated to be 0.830 and 0.847 eV/atom for (9,0) (Fig. 5.6a) and (15,0) (Fig. 5.6b) nanotubes, respectively. Analogically to the other types of rolled-up double-wall nanotubes, a cylindrical DW Si NT is built by assembling the single-wall shells in a coaxial configuration (9,0)@(15,0) (Fig. 5.6c). The nearest Si-Si distance between both inner and outer NT shells equals to 3.19 Å, indicating that no covalent bond is formed between them [12]. The cylindrical DW Si NT has a lower $E_{form} \approx 0.74$ eV/atom

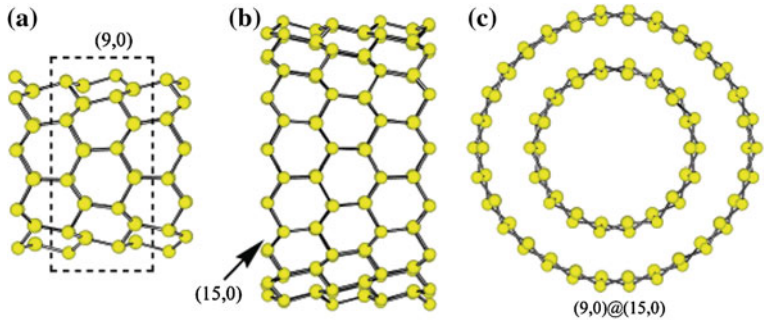

Fig. 5.6 Equilibrium configurations of rolled-up SW and DW Si nanotubes. *Side views* of **a** (9,0) and **b** (15,0) SW Si NTs; **c** *top view* of DW Si NT built by assembling both *zz*-SW Si NTs with a coaxial structure [12]

(compared with the corresponding values for the isolated nanotube constituents mentioned above), because of the attraction between them. However, this cylindrical DW Si NT is quite unstable at room temperature, undergoing considerable transformations towards amorphous silicon nanotubes by the formation of additional covalent bonds between the inner and outer shells, as revealed by both molecular dynamics simulations based on the empirical force-field method [30] as well as the first-principles DFT-LCAO calculations [12].

5.2.2 Rolled-Up Ge Nanotubes

By analogy with silicon, germanium nanolayers (NLs) can exist in 2D layered structures of Zintl-phase, like calcium digermanide [33] which includes periodically distributed hexagonal Ge NLs. Recently synthesized Ge-based polymers (polygermines) [34], possess a strong photoluminescence centered at ∼1.4 eV, and contain only hydrogen, similar to polysilanes, mentioned above [29]. Thus, the H-terminated Ge nanolayer with a morphology close to the one presented in Fig. 5.3b can serve as a prototype for generation of rolled-up Ge NTs (Fig. 5.7) with morphology similar to SiH-*io* configurations shown in Fig. 5.4b, e. As it is known, germanium nanotubes have not been synthesized yet, thus, the comparison of their properties with those calculated for Ge bulk and NLs [29] as well as for Si bulk, NLs and NTs [9] (using the same DFTB method) may help in analyzing and verifying the obtained results. The analogous comparison was performed for the finite cluster models of Si and Ge NTs (where open ends were passivated by H atoms) calculated using the hybrid first principle method [28]. Both series of NT simulations confirmed that Ge nanotubes possess substantially smaller band gaps and cohesive energies *vs*. larger bond lengths than in the corresponding Si NTs. At the same time, qualitative similarities

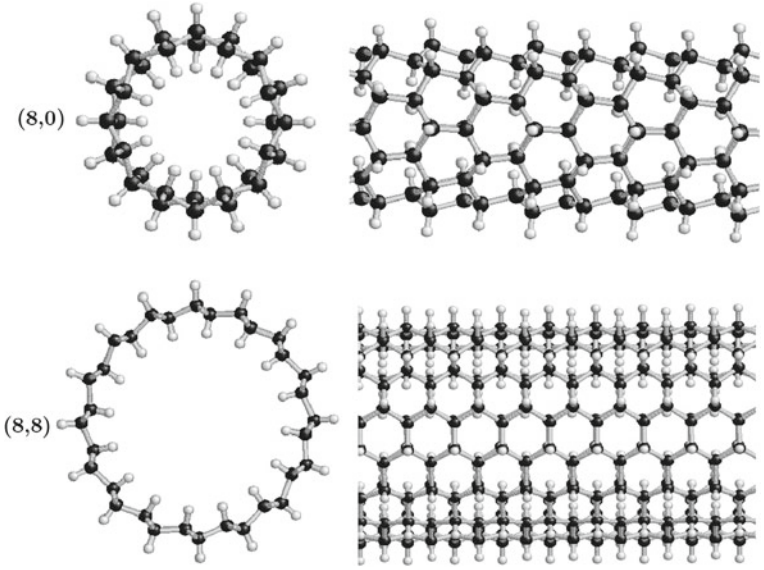

Fig. 5.7 Optimized structures of rolled-up (8,0) and (8,8) GeH_2 nanotubes as shown in *upper and lower panels*, respectively. On the *left and right sides* of each panel, the across- and aside-views are shown (Reprinted figure with permission from Seifert et al. [29], Copyright (2001) by the Elsevier Science Ltd. All rights reserved)

exist between functions $E_{strain}(d_{\mathrm{NT}})$ (Fig. 5.5a) and $\Delta\epsilon(d_{\mathrm{NT}})$ (Fig. 5.5b) for SiH-*io* nanotubes and analogous functions for GeH_2 NTs [29].

5.2.3 *Faceted Si Nanotubes*

An alternative model for the description of silicon nanotubes was chosen to be the faceted Si NT which may consist of several quasi-layers [12, 32]. This 1D nanostructure can be obtained by the removal of the core nanowire shell (symmetrically arranged around the NW axis) from the larger NW of the same faceting (Fig. 5.8). The two types of faceted DW Si NTs are usually considered [12]: with hexagonal (*h*-NT) and tetrahedral (*t*-NT) structures (as they were revealed like stable forms of thin Si NWs [35]). These faceted silicon nanotubes have fourfold coordinated cores and threefold coordinated NT surfaces (both exterior and interior), unlike the cylindrical SW Si NTs whose surfaces are purely threefold coordinated. Moreover, these faceted models can be easily implemented to describe multi-wall (MW) Si NTs with different diameters and wall thicknesses.

The annealing process allows one to obtain a faceted *h*-DW Si NT (Fig. 5.8) with the value of E_{form} (0.542 eV/atom) lower than any of its amorphous isomers [12]. Being different from the cylindrical SW Si NTs (Figs. 5.4 and 5.6), this faceted

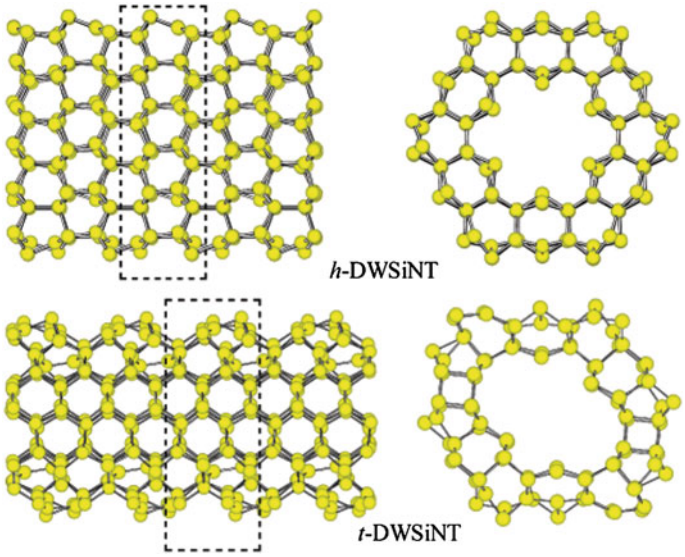

Fig. 5.8 Side (*left*) and *top* (*right*) views of DW Si NTs with hexagonal (*h*-) and tetrahedral (*t*-) facetting [12]

h-DW NT has a hexagonal cross-section with D_{3h} symmetry. The outer diameter of the *h*-DW Si NT was found to be ~19.8 Å, while the nearest Si-Si distance between the inner and the outer walls (2.41 Å) indicated the formation of Si-Si covalent bonds. The atomic arrangement in the *h*-DW silicon nanotube displays the characters of hexagonal lattices with the tube axis oriented along the [0001] direction enclosed by six highly reconstructed $\{10\bar{1}0\}$ lateral facets as shown in the upper panel of Fig. 5.8. The faceted *h*-DW Si NT was also found to be more stable than the cylindrical DW NT (Fig. 5.6). According to the rules of NT generation described above, the faceted Si NTs with larger diameters and wall thicknesses can be simply built as well, unlike the cases of rolled-up multi-wall (MW) nanotubes. Obviously, the faceted MW Si NTs with a hexagonal-like structure would become more stable when the wall thickness is large enough.

The DW Si NT in a tetrahedral form (*t* as shown in the lower panel of Fig. 5.8) was built by the following steps. The initial configuration of the *t*-DW NT with a hexagonal cross section was enclosed by four {111} and two {001} facets, while the nanotube axis was oriented along the [110] direction created by cutting from silicon single crystal (Fig. 5.1a). This hexagonal prism was then treated using the method of molecular dynamics at 500 K [12], to obtain the equilibrium configuration as shown in Fig. 5.8. A (2×1) dimerization along the axial direction occurred on the two reconstructed {001} facets, whereas the four {111} facets underwent considerable distortion. In other words, initially perfect {111} facets outside and inside the *t*-DW Si NT were quite unstable without hydrogen passivation. However, the tetrahedral feature of the atomic arrangement was maintained in that highly deformed faceted

nanotube. It was also found that the highly symmetric *h*-DW NT and the deformed *t*-DW NT had very close formation energies with a difference of < 0.2 meV/atom. Although the diamond structure *d*-Si is the most stable form for bulk silicon, the hexagonal form *h*-Si (Fig. 5.1c) is very close by energy to the diamond structure. Moreover, in the case of the smallest diameter in the faceted DW NW, the large contribution of the surface energy may even reverse the energetic order in favor of the hexagonal form [36]. To overcome structural instability of the faceted *h*- and *t*-DW Si nanotubes caused by the presence of dangling bonds outside and inside NTs, their termination by hydrogen atoms was simulated [12]. The stable configurations of H-passivated DW Si NTs obtained by their full relaxation are shown in Fig. 5.9. The atomic arrangement in the hydrogenated *h*-DW silicon nanotube clearly displays a hexagonal structure with D_{6h} symmetry, while the lateral surfaces are very similar to the perfect $(10\bar{1}0)$ surface of hexagonal lattices (Fig. 5.9a, b). The hydrogen passivation in the *t*-DW Si NT recovers the four perfect {111} and two dimerized {001} facets of bulk silicon in the diamond structure (Fig. 5.9c, d). The H-passivated *h*-DW

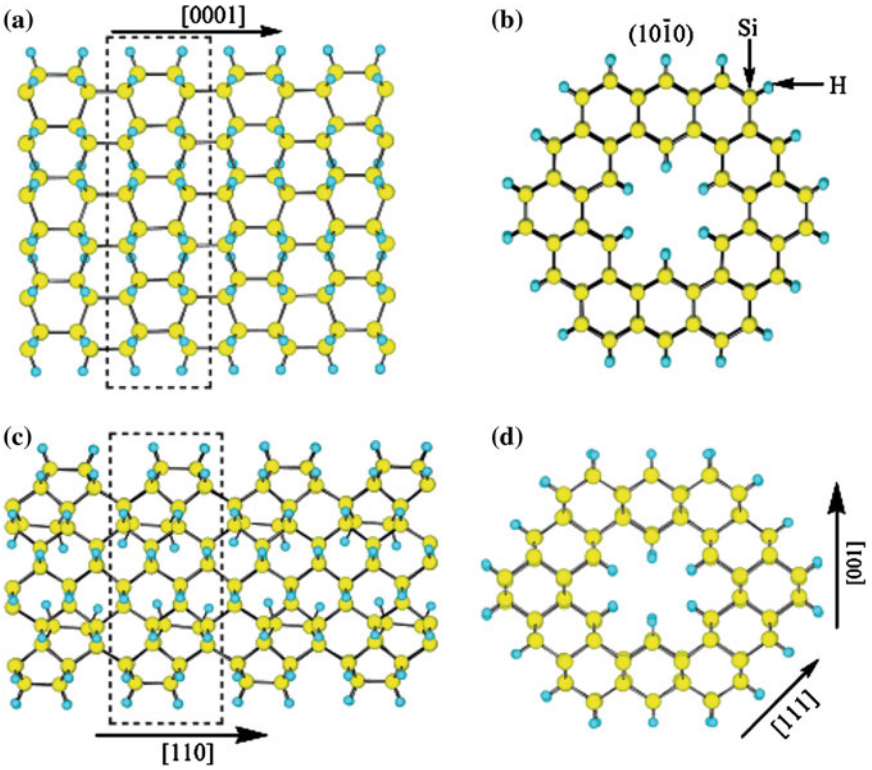

Fig. 5.9 Side view (*left*) and *top* view (*right*) of hydrogen-passivated *h*-DW Si NT (**a, b**) and *t*-DW Si NT (**c, d**) (Reprinted figure with permission from Zhao et al. [12], Copyright (2007) by the American Chemical Society)

NT is energetically comparable to the hydrogenated *t*-DW NT with a difference of <10 meV/atom.

Although *h*- and *t*-DW silicon nanotubes possess rather close formation energies, their electronic structures are quite different, as follows from the results of DFT-LCAO calculations [12]. The *h*-DW Si NT has an indirect band gap of 0.21 eV, which is much narrower than that of bulk silicon. The top of the highest occupied valence band (HOVB) and the bottom of the lowest unoccupied conduction band (LUCB) are at Γ (0,0,0) π/a and X (0,0,1) π/a points, respectively (Fig. 5.10a). However, the *t*-DW Si NT has a direct band gap of 0.11 eV at Γ point (Fig. 5.10b). This is quite different from those results obtained for pristine cylindrical SW NTs, which were found to be either quasi-metals or direct band gap semiconductors [27]. It was also found that the wave function of the HOVB displays the characters of sp^3 orbitals while that of the LUCB mainly arises from the p_z orbitals. It was related to the different arrangements of the threefold coordinated Si atoms on the lateral facets, a half of which extruded out and displayed the characters of sp^3 bonding type, whereas others demonstrated mainly sp^2 bonding type. It indicates that the flat bands near the Fermi level, which narrow the band gap, originate from the surface states. Upon H-passivation, the surface states near the Fermi level in the faceted DW Si NTs were substantially influenced by the presence of hydrogen atoms [12]. As a result, the band gaps increased up to 1.32 and 1.55 eV for the *h*- and *t*-DW silicon nanotubes, respectively. The H-passivated *h*-DW Si NT had an indirect band gap with the top of HOVB and the bottom of LUCB at Γ (0,0,0) π/a and (0,0,3/4) π/a points, respectively (Fig. 5.10c), whereas the hydrogenated *t*-DW Si NT had a direct band gap at Γ point only (Fig. 5.10d).

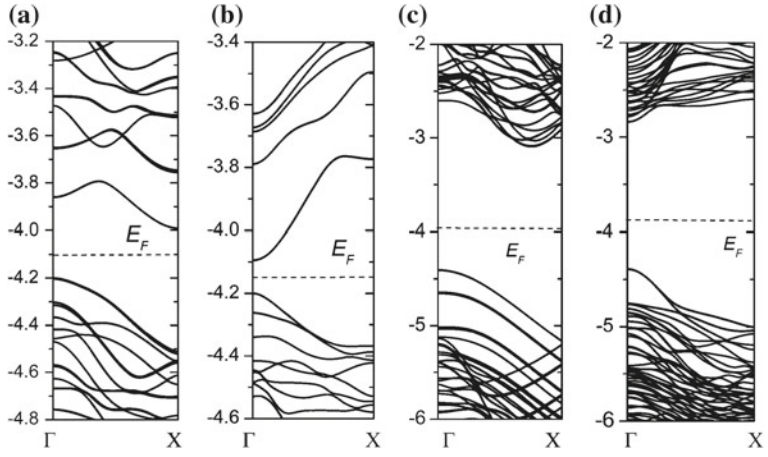

Fig. 5.10 Band structures of **a** *h*-DW Si NT and **b** *t*-DW Si NT as well as H-passivated **c** *h*-DW NT and **d** *t*-DW NT along Γ (0,0,0) π/a - X(0,0,1) π/a direction. The *dashed lines* indicate the Fermi levels (Reprinted figure with permission from Zhao et al. [12], Copyright (2007) by the American Chemical Society)

5.2.4 Polyhedral Silicon Nanotubes

Another alternative to the rolled-up model of nanotubes was shortly described in Sect. 4.2.4. Extension of the traditional rolled-up NT model was performed in this case to include distinct lengths of bonds depending on their orientation in relation to the NT axis. This formalism was applied e.g., for silicon nanotubes [37]. Since silicon prefers sp^3 bond formation [31], it was predicted that the four-coordinated atoms form a skewed rhomboid lattice as shown in Fig. 5.11. In principle, such a single-wall model is compatible with a morphology of (001) monolayer cut from *d*-Si bulk (Fig. 5.1a) while nanotube models described above were constructed from (111) sheets of diamond-like silicon (the same as from (0001) sheets of *h*-Si). Firstly, a similar approach was applied for finite cluster models of Si NTs (whose open ends were H-passivated [7]) simulated using both the hybrid first principle method and the classical molecular dynamics approach. Three structural types of prismatic nanotubules were considered in [31] (Fig. 5.12). Initial MD simulations were performed for molten silicon (beginning with T > 2,500 K down to melting point at 1,690 K) incorporated in chemically inert cylindrical nanopores of different diameters. It was found that in the case of nanopore with 10.65 Å diameter, the lower temperature phase (at 1877 K) gave a hexagonal NT (Fig. 5.12c). In the nanopores with diameters 9.82 and 8.98 Å, the observed structured solid-like phase was a pentagonal or square nanotubules, respectively (Fig. 5.12a, b). Ab initio calculations showed that the bonding features of the H-terminated $Si_{5n}H_{10}$ pentagonal nanotubules were very similar to those of the corresponding infinite SW silicon nanotubes [7], namely, the coordination number of any Si atom remained fourfold as in silicon bulk.

The DOS calculations performed for $Si_{5n}H_{10}$ pentagonal nanotubules using the first principles hybrid method indicated the consequent decrease of the band gap with

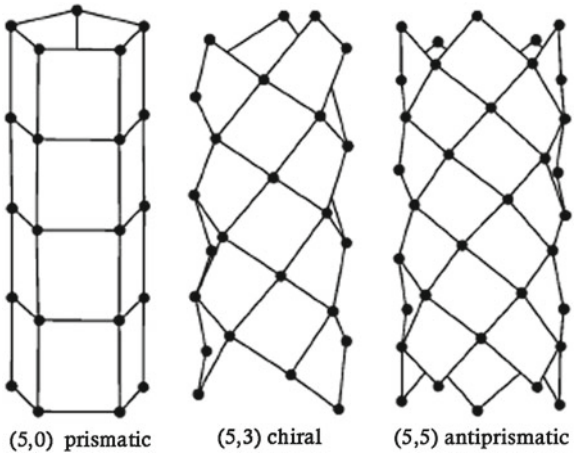

Fig. 5.11 General polyhedral model for silicon nanotubes for prismatic, chiral and antiprismatic chiralities (Reprinted figure with permission from Lee et al. [38], Copyright (2010) by the Royal Society of Chemistry)

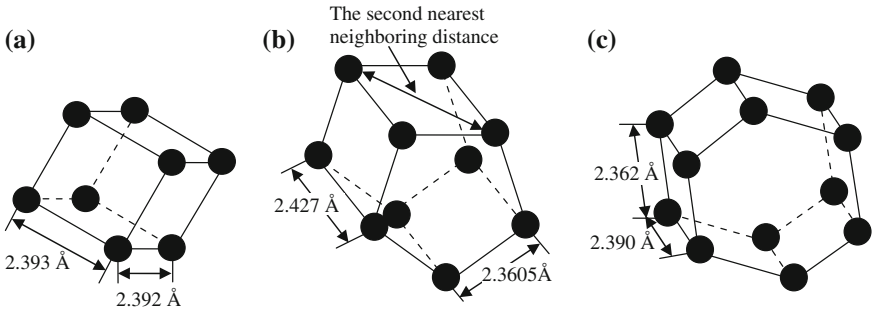

Fig. 5.12 Schematic images for the structure of **a** rectangular, **b** pentagonal, and **c** hexagonal SW Si nanotubules (Reprinted figure with permission from Wang et al. [31], Copyright (2007) by the Elsevier B.V. All rights reserved)

the increase of n from 2.26 eV ($n = 3$) down to 0.89 eV ($n = 8$). When substituting these cluster models by an infinite polyhedral NT with a prismatic chirality (Fig. 5.12a), the band gap was found to be zero since the conduction band was slightly overlapped by the valence band (the periodic calculations were performed using the PW DFT-GGA method) [7], i.e., the infinite single-wall silicon nanotube with a square-like morphology of (001) facets can be metallic. This conclusion was confirmed for all the three Si NT models presented in Fig. 5.12, in contrast with the results obtained for rolled-up and faceted models, both pristine and H-terminated, as analyzed above [9, 12, 29]. In the recent study [14], the vibrational properties of prismatic pentagonal and hexagonal SW Si NTs (Fig. 5.13b, c) were calculated using the DFT-LCAO method within the frozen phonons approach. The phonon dispersion curves obtained for 5- and 6-facetted silicon (001) nanotubes are shown in the right panels of Fig. 5.13, while the corresponding vibrational DOSs (VDOSs) are presented in the left panels. No negative frequencies were present in the phonon band structure, which is a clear indication of the stability for both NTs. The main features of VDOS for both nanotubes are in a qualitative agreement with the more complicated VDOS for Si NW reported elsewhere [39]. In particular, the two local maxima of the VDOS are found at 90 cm^{-1} (acoustic modes) and 344 cm^{-1} (optical modes) for a pentagonal NT, and at 83 cm^{-1} and 312 cm^{-1} for a hexagonal NT, respectively. The breathing modes (graphically imaged in Fig. 5.14) are located between 230 cm^{-1} and 315 cm^{-1} for 5-Si NT, while in the case of 6-Si NT they are shifted towards the lower frequencies (between 160 cm^{-1} and 250 cm^{-1}).

The effect of isotopic substitution upon the VDOS of the studied Si NTs was analyzed as well [14]. The layers of Si NTs were formed not only by the most abundant and stable ^{28}Si atoms, but also by varied number of slightly less stable ^{30}Si isotopes (~3 % of natural abundance [40]) distributed inside the whole chosen polygonal cross-sections of prismatic silicon nanotubes. Both Si NTs exhibit a depletion of

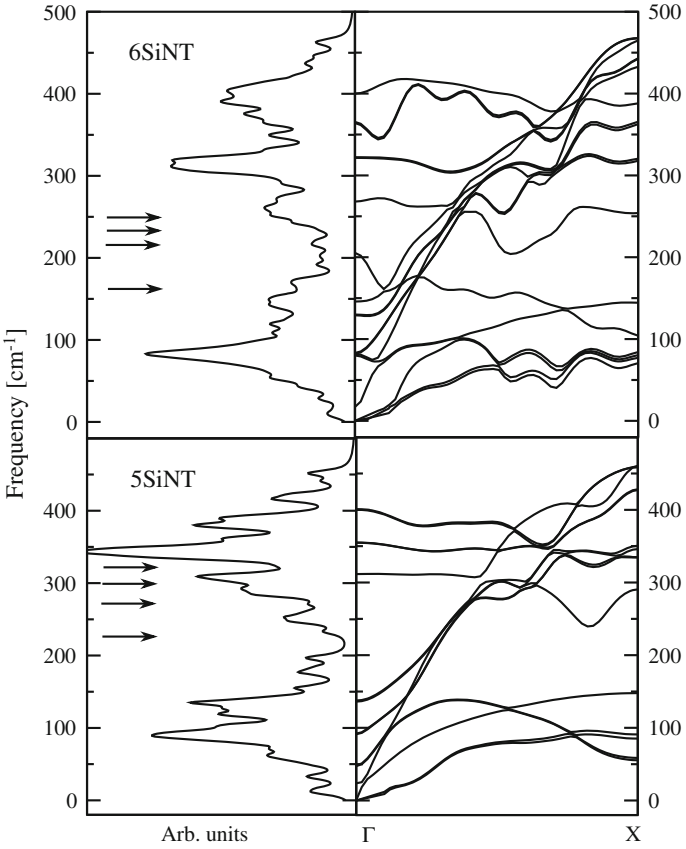

Fig. 5.13 Phonon's band structure and the vibrational density of states for the 5-Si and 6-Si NTs. Breathing modes are indicated by *arrows* (Fig. 5.14 gives the geometric representations of the breathing modes) (Reprinted figure with permission from Bogdan et al. [14], Copyright (2012) by the Elsevier B.V. All rights reserved)

the VDOS peaks in the region of 300–400 cm^{-1}. The visible changes in VDOSs ($\sim$20 % in the amplitude of the largest peak) were well observed beginning with the concentrations of 38 versus 47 % of polygons filled by ^{30}Si isotopes *per* supercell for pentagonal versus hexagonal NT morphologies, respectively [14].

Thus, the metallic character and the unique thermal properties of polyhedral silicon nanotubes make them the ideal candidates for various technological applications as suggested in [41, 42]. Obviously, the ultimate confirmation for the synthesis of stable ultrathin polyhedral SW Si NTs must undergo a series of reliable experiments.

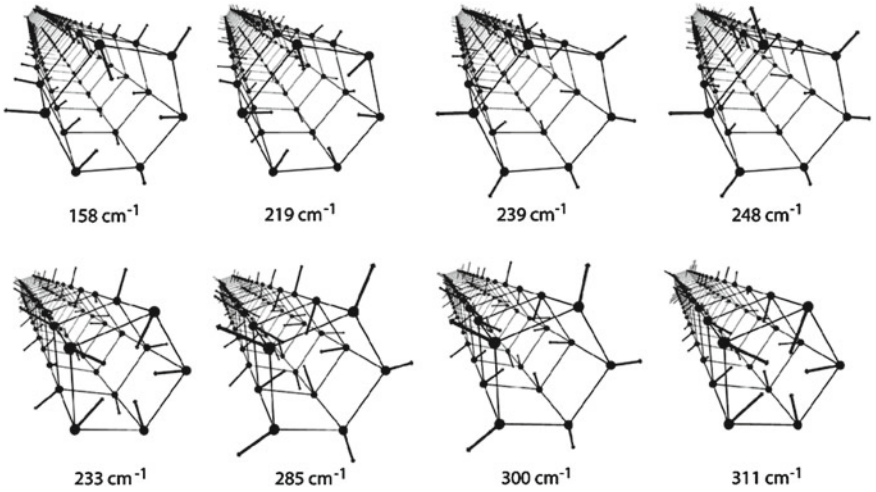

Fig. 5.14 Graphical representation for the breathing modes indicated by *arrows* in Fig. 5.13 for supercells of pentagonal (*bottom panel*) and hexagonal (*top panel*) Si NTs (Reprinted figure with permission from Bogdan et al. [14], Copyright (2012) by the Elsevier B.V. All rights reserved)

5.3 Silicon and Germanium Nanowires

5.3.1 Synthesis and Simulation of Si Nanowires

Silicon nanowires have attracted enhanced scientific interest due to their promising technological applications and experimental possibilities to synthesize structurally reproducible Si NWs when using the vapour-liquid-solid (VLS) method [43]. Moreover, silicon nanowires look like a very appealing choice, since they provide the ideal interface with the existing macro and micro Si devices while taking advantage from a tractable material technology [44]. For example, several advanced nanodevices were fabricated by the incorporation of Si NWs (e.g., those which include various dopants and point defects), such as (*i*) bipolar junction transistors (BJTs) [45], (*ii*) *p-n* diodes [46], (*iii*) logic gates [47], (*iv*) sensors for chemical and biological substances [48], (*v*) non-volatile memories [49], (*vi*) field-effect transistors (FETs) [50], (*vii*) photovoltaics [51], etc. Moreover, Si NWs found their relevance in nanotechnology as potential interconnects between different nanodevices [52]. In that respect, both conduction and contact properties of stable nanowire structures are very important. The VLS technique was elaborated one half century ago [53] for the reproducible growth of microscopic crystalline whiskers upon silicon substrate of a certain surface morphology covered by gold droplets. During the last decades this technique was transformed for synthesis of Si NWs upon analogous silicon substrate covered by Au nanoparticles [54], which are used as catalysts in order to decompose the vapor

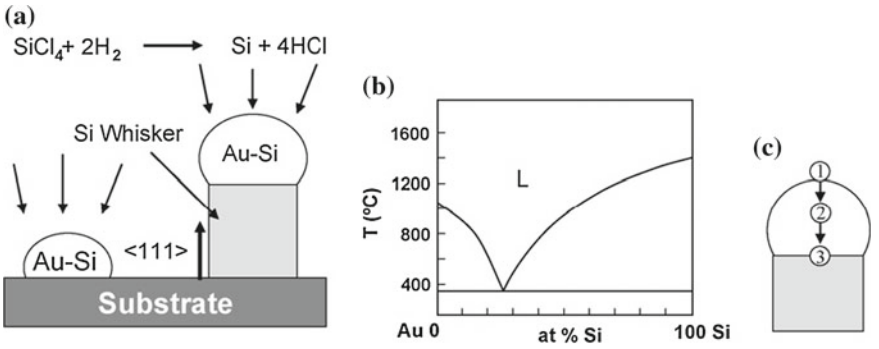

Fig. 5.15 Schematic illustration of the Si whisker growth from vapor phases via Au-Si catalytic droplets: **a** the Au-Si droplet formed upon the silicon substrate catalyzes the whisker (NW) growth; **b** the Au-Si phase diagram, **c** a possible diffusion path of a Si atom through a metal droplet [43]

mixture of $SiCl_4$ with H_2 and then to incorporate the releasing Si atoms, thus creating conditions for the growth of silicon nanowires (Fig. 5.15).

The VLS method can result in unidirectional growth of a wide spectrum of various nanomaterials, e.g., nanowires, becoming a quite popular technique for fabricating different 1D samples that include elemental metalloids, numerous semiconductors of II-VI and III-V groups, as well as various oxides and carbides [43]. A number of new techniques have been developed recently, to synthesize nanowires, such as laser-assisted chemical vapor deposition (CVD) [55], oxide-assisted CVD (without a metal catalyst) [43], thermal CVD [56], metal-catalyzed molecular beam epitaxy (MBE) [57, 58], chemical beam epitaxy (CBE) [59], etc. Though various kinds of nanowires fabricated *via* different techniques dramatically increase every year, understanding of the basic process of 1D nanostructure formation has not reached maturity yet. How to fabricate the desired nanowires with the tailored atomic structures and how to integrate functional nanostructures into devices still remain challenging issues for materials scientists [43].

The facets of Si NWs were often passivated with an oxidized layer or the dangling bonds were H-terminated (as mentioned in Sects. 5.1 and 5.2 for silicon nanolayers and nanotubes). This provided both stability of the nanowires and a big gain in their optical properties compared with the pristine Si NWs, due to a change in the band gap (*cf.* different plots in Fig. 5.10). Most of theoretical studies consider just hydrogen-terminated Si NWs since it is relatively easy to model them (*cf.* models for faceted Si NTs imaged in Figs. 5.8 and 5.9). As to an oxide layer on nanowires, it could be thicker than an atomic layer and could involve matching at the interface which is very complex [60]. The typical growth directions of nanowires with cubic structure of *d*-Si (Fig. 5.1a) were considered to be [111], [110], [112] (Fig. 5.16) as well as [001] (Fig. 5.19). The orientation of Si NWs was found to be thickness dependent. Nanowires with the diameter >13 nm were usually [111]-oriented, those having diameter between 7 and 13 nm grew preferably along the [112] direction, while Si NWs having diameters in the range of 3–7 nm were detected to be mainly [110]-oriented [61]. On the other hand, the thinnest synthesized Si NWs (with the diameters

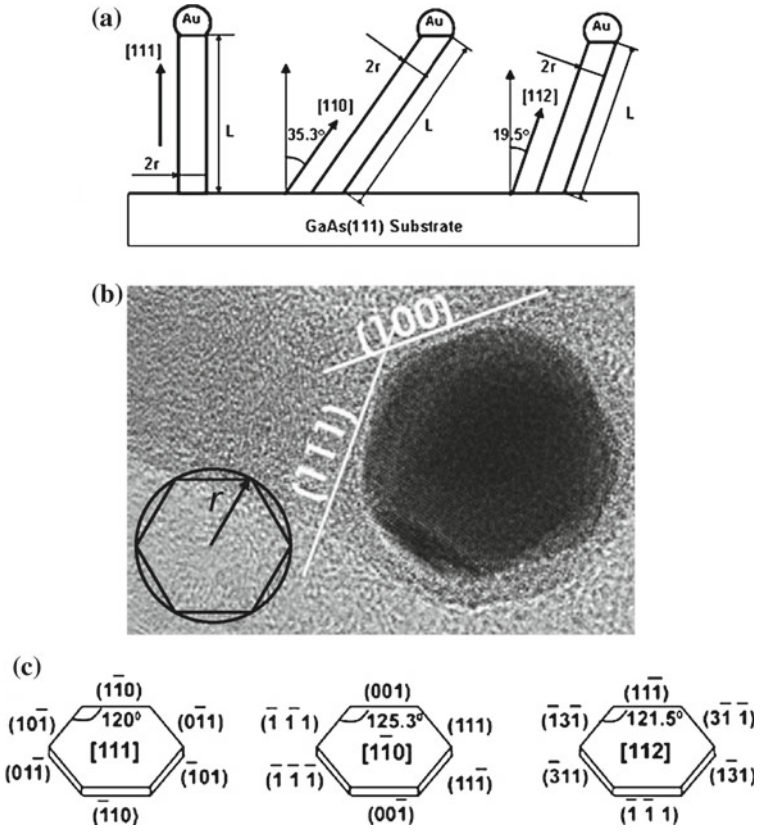

Fig. 5.16 **a** Models of the nanowire nuclei grown upon GaAs(111) substrate along [111], [110] and [112] directions. **b** *Top* view of a nanowire tip with Au catalyst; the shape of the catalyst/nanowire section is close to a hexagon. **c** The growing nanowires of different orientations possessing shapes of quasi-hexagonal prisms are characterized by different faceting as shown in their models (Reprinted figure with permission from Wang et al. [43], Copyright (2008) by the Elsevier B.V. All rights reserved)

of 1.3 nm) were again [112]-oriented [62] while 4 nm-thick [001]- and [110]-oriented silicon nanowires were reproducibly synthesized as well [63]. Obviously, all the four aforementioned types of Si NWs can be reliably used for the first principles simulations.

The interface structures of differently oriented nanowires show distinct morphologies. In relation to the [111]-oriented nanowires, the interfaces at Au catalysts are flat (111) planes perpendicular to NW axis (left panel of Fig. 5.16a). For the [110] and [112] NWs, the interfaces are generally along the (111) planes which are not perpendicular to NW axis (two other panels of Fig. 5.16a). The reason why the (111) planes are dominant at the interfaces is simply due to their lowest surface energy as compared to other planes while the next lowest surface energy were attributed to (001) and (110) planes) [43]. According to the results of theoretical analysis, for single

crystalline non-hydrogenated silicon surfaces, the surface energy order was shown to be $E_{surf}(111) < E_{surf}(100) < E_{surf}(110)$, which is different from the results obtained for H-passivated surfaces: $E_{surf}(111) < E_{surf}(110) < E_{surf}(100)$ [64]. This can be related to the effect of hydrogen termination since the surface energies of different hydrogenated Si surfaces were found to be dependent on the hydrogen chemical potential [65]. The energetic balance between different Si planes could suggest that [110]-oriented Si NWs are energetically the most favorable since they consist of {111} and {001} facets. However, the decline of these NWs towards the substrate plane allows one to predict that the [111] growth direction can be energetically the most favorable [43]. The choice of the most favorable shape of an arbitrary nanowire can be solved using the Wulff construction formalism or rule, which relates the equilibrium shape with the surface free energy of the facets involved [44]. Solving the energy minimization problem for $\Sigma s\gamma_s$, where s is the number of surface unit cells and γ_s the corresponding energy, leads to the proper choice of the optimum shape. Re-examination of the Wulff construction was performed within the determination of the equilibrium cross sections of Si NWs [66]. It was shown that the conventional formulation of the Wulff criterion lacks two important aspects: (*i*) in solids and smooth spherical particles, the energy of the edges between facets is neglected as compared to the surface contribution and (*ii*) the bulk is assumed already at its minimum and, thus, invariant. Hence, the following generalization for the Wulff energy (F) was proposed [44]:

$$F = E_e + \sum_s s\gamma_s + E_b, \tag{5.1}$$

where E_e is the energy of the matching adjacent facets (i.e., the energy of the edges) and E_b is the energy of the bulk, releasing the constraint on the innermost part of NW which can be changed.

The application of the modified Wulff construction formalism described by ((5.1)) [44] for [110]-oriented Si nanowire with the diameter up to 5 nm, taking into account NW construction around the bulk core (which seems to be a favored mechanism during the growth period), correctly predicted the formation of the hexagonal cross sections, which is in a good agreement with the experiments [61, 62], as shown in Fig. 5.17. However, when for the same [110]-oriented Si NW, the aforementioned condition on nanowire construction around the bulk core was removed, its ground-state structure was found to be a pentagonal cross section [66] constructed of the joined five prisms cut out of a Si(110) plane (Fig. 5.18). Such a structure was seldom observed experimentally too [67]. The most important result obtained when using this formalism was the emphasis of the roles of both the edges and the interplay between the edges and facets in determining the reconstruction of Si NWs.

The modified Wulff construction formalism was expanded to the Si NW grown along the [001] axis, the orientation of which favors a square cross section with the {100} facets (Fig. 5.19b), as an energetically cheaper choice compared to a square cross section with the {111} facets [69]. Since the abrupt match between the {100} facets results in an energetically higher cost, due to a large value of E_e in ((5.1)),

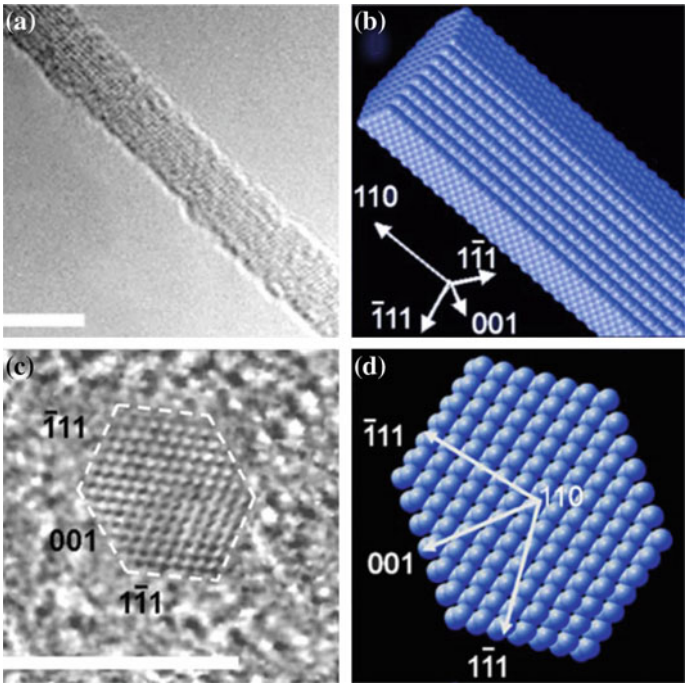

Fig. 5.17 Hexagonal cross section of [110]-oriented Si nanowire: **a** TEM images of 3.8 nm Si NWs grown along the [110] direction, **c** high-resolution TEM cross-sectional image, as well as equilibrium shapes for **b** the NW aside image and **d** the NW cross sections both predicted by Wulff construction. The scale bars are 5 nm (Reprinted figure with permission from Wu et al. [61], Copyright (2004) by the American Chemical Society)

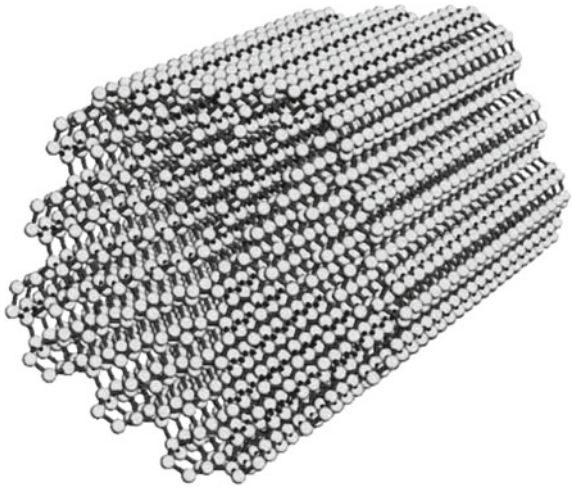

Fig. 5.18 Model of pentagonal [110]-oriented Si NW found for $d_{\mathrm{NW}} < 6$ nm [66]

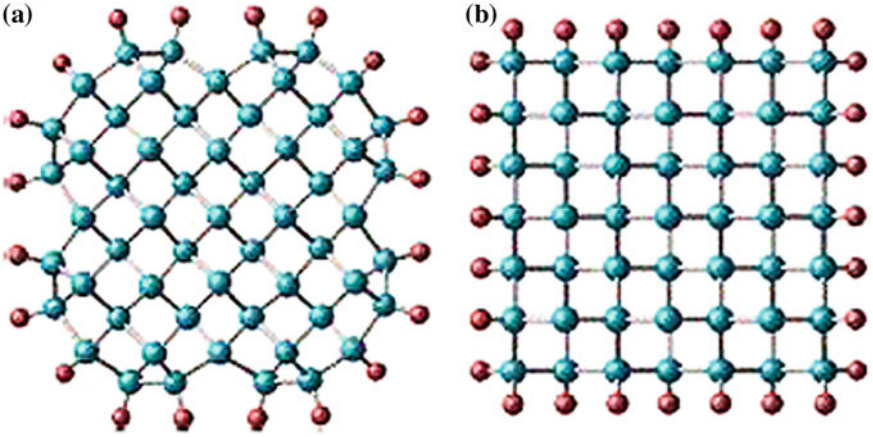

Fig. 5.19 Optimized structures of possible *square* cross sections of hydrogenated Si NWs (H atoms are shown small) grown along [001] direction in the cases of application of the modified Wulff construction formalism (**a**) and without it (**b**) [68]

the minimization of the energy may be achieved by forming smaller transition {110} facets at square corners and centers (Fig. 5.19a) that allow a smoother match between the dominant {100} facets and a partial release of the stress accumulated at the edge [44]. However, such a description of the NW shape smoothening is favored only beyond the 1.7 nm diameter, whereas thin and ultrathin Si NWs (some of them can possess even triangular prismatic forms [64]) prefer sharp edges, i.e., the removal of the edges does not pay back. To elucidate the role of different facets for NW stability, the cross sections bounded by different facet compositions should be examined at each growth orientation [70]. For the [001]-oriented Si NWs, for instance, all {100} and {110} facets, as well as three intermediate combinations between them were considered. The development of this approach allowed the formulation of the universal scaling law in terms of the NW perimeter, according to which the nanowire energy per atom always lies within two limiting energy lines, which are directly related to the character of the prevailing facets [44].

The shape smoothening of the [111]-oriented H-passivated nanowire possessing $d_{\mathrm{NW}} = 1.5\,\mathrm{nm}$ resulted in the formation of a circular-like Si NW [19], the cross-section of which is shown in Fig. 5.20. Moreover, cylindrical-type [001]-oriented nanowires were fabricated using the CVD method [71]. Basically, the stability of the Si NW circular cross-section was found to be superior as compared to the square cross-section. The radii of the circular NW cross-sections cut from Si bulk along the [001] axis without further hydrogenation (these models were used for simulations of the electronic conductance in nanowires [71]) were set at $0.8a_0$, $1.2a_0$, $1.5a_0$ and $2.5a_0$ respectively (where a_0 represents the lattice constant of the Si bulk equal to 5.43 Å), as shown in Fig. 5.21. It was noted that the radius $2.5a_0$ is quite closely approximated to the technological requirements and can be verified by the advanced fabrication. It can be explained that just for the case of $2.5a_0$, the [001]-oriented NW

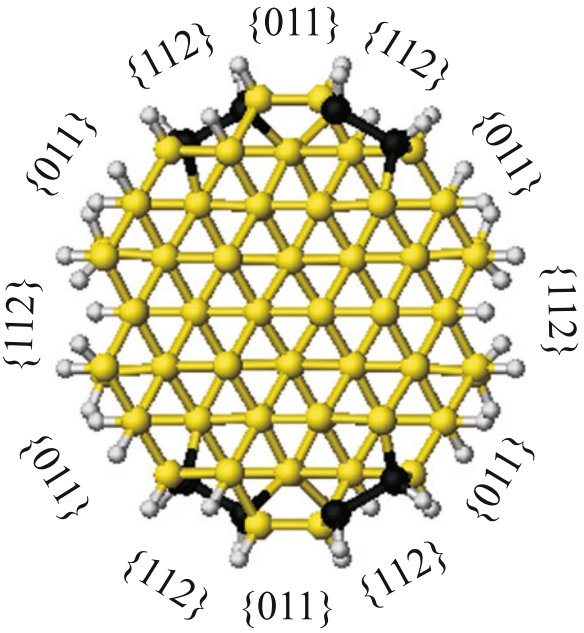

Fig. 5.20 Cross section of [111]-oriented Si NW. Outer H atoms are shown as *small balls* around Si nanowire. All lateral NW facets are indicated. Si dimers on the 112 facets are shown in *black* [19]

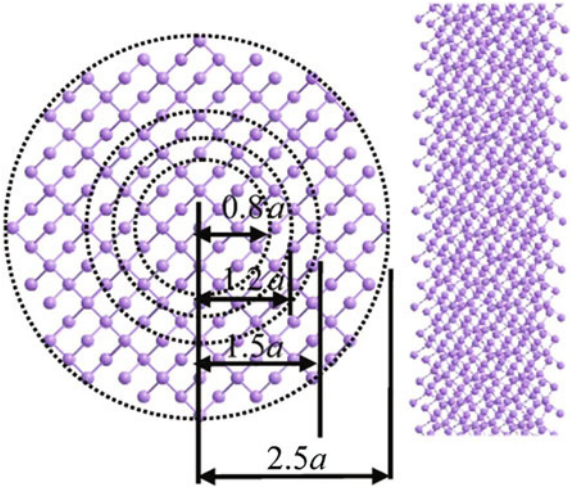

Fig. 5.21 Four configurations of [001]-oriented circular Si NW model [71]

structure remained almost unchanged after the structural optimization (even without H-passivation), so that it has the property fairly similar to that of the Si bulk.

However, circular-type smoothening of NW shape was not found to be true for nanowires of ultrathin diameters since in the absence of H-passivation they suffered essential distortion, the level of which increased with the decreasing diameter. For NW radii equal to $0.8a_0$, $1.2a_0$, $1.5a_0$ and $2.5a_0$, the corresponding average total energies per Si atom calculated using the PW-DFT method were found to be -4.76 eV, -4.82 eV, -4.95 eV and -5.13 eV, respectively [71]. Thus, as the diameter of the circular cross-section increased, the average NW energy reduced, i.e., the crystalline structure of silicon nanowire consequently achieved higher stability approaching to that in bulk.

The alternative structural models were suggested for MD simulations of Si NWs with diameters less than 6 nm [35], considering tetrahedral (based on *d*-Si structure shown in Fig. 5.1a), cage-like and polycrystalline nanowires (Fig. 5.22). All these NW types were fully relaxed without any symmetry constraints when using the formalism of the generalized tight-binding molecular dynamics (GTBMD) [72]. All of four NWs were taken of infinite length and modeled by large supercells incorporating a constant pressure ensemble, which served for a simultaneous relaxation of the lattice and basis degrees of freedom. The energetic preference of these NWs (the highest for (*a*) and the lowest for (*d*) structures shown in Fig. 5.22) is identical to that obtained in ab initio calculations [73]. The growth direction for the tetrahedral NWs was chosen along the [111] axis. The polycrystalline Si nanowire (*d*) was essentially tetrahedral in morphology, with stacking fault-type grain boundaries as defects. For (*b*) and (*c*) NW types (Fig. 5.22), their growth directions were chosen to be symmetrically crossing clathrate-type cages Si_{34} and Si_{46}, respectively (which are the most stable

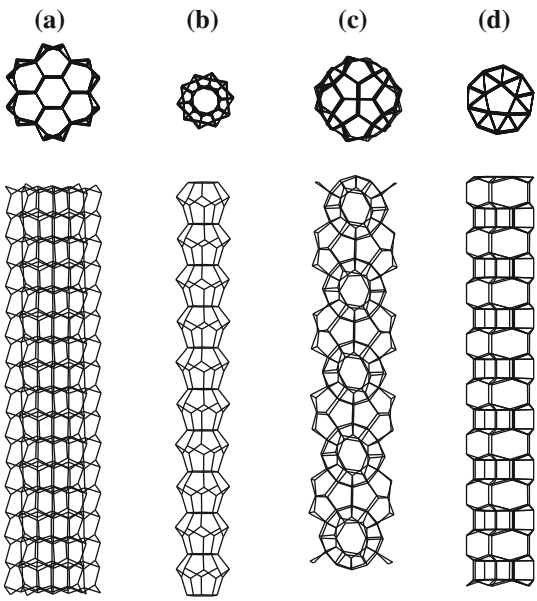

Fig. 5.22 Models of Si NWs presenting **a** tetrahedral, **b, c** cage-like and **d** polycrystalline structures [35]

clathrate forms in Si bulk), attached each other along the directions of NW axes, thus forming infinite chains [35].

Another type of Si 1D nanostructures, which may be attributed to the class of nanowires, was considered to be the string-type monoatomic chains [52]. The motivation of their theoretical simulations was supported by the reproducible synthesis of stable finite-size silicon nanochains [74]. Amongst several possible configurations of the atomic ordering in infinite 1D string-type chains, three forms were selected (Fig. 5.23) as the most simple for simulations. According to the results of the first principles calculations, the silicon monoatomic chain of the NZ configuration (possessing binding energy 4.1 eV/atom) was found to be energetically preferable over WZ and LC structures (with $E_{bind} = 3.9$ and 3.4 eV/atom, respectively) [52], which can be explained by the formation of additional triangular bonding in the former. The properties of finite-size Si monoatomic chains can be deduced from the calculated properties of infinite periodic chains, with the exception of termination effects. The characteristics of possible interconnect or device applications of these nanochains can be modified depending on their size, doping, type of electrodes they are connected to, the substrate they are placed on, or encapsulation. The most important application of finite Si chains is their incorporation between the two metallic electrodes, which provides the regime of ballistic conductance [52]. The possibilities of theoretical simulations on BN atomic chains, e.g., their arrangement between the two semi-infinite Al NWs, are considered in detail in Sect. 6.3.3.

Due to the enhanced technological interest, Si NWs are attributed to the most widespread chemical class of simulated nanowires, according to the total number of publications that have appeared so far [3, 44]. (Only partly these publications are considered in this Section.) Some of the key atomistic models used for simulations of different Si NW properties are shortly described above. Several methods were applied for their calculations: the formalism of interatomic empirical potentials [75–78], the continuum and finite element models [79, 80], the Monte-Carlo method [81], molecular dynamics [32, 35, 79, 82–86], the tight-binding (e.g., DFTB) methods [35, 64, 72, 78], the first principles methods of DFT-LCAO [12, 36, 69, 87, 88], the DFT-PW within both LDA and GGA approaches [19, 39, 52, 60, 66, 68–71,

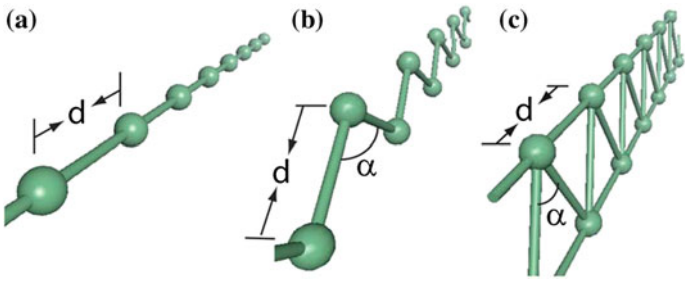

Fig. 5.23 Three models of infinite Si monoatomic strings: **a** linear chain (LC), **b** planar wide (WZ) and **c** planar narrow zigzag-type chain (NZ), where d is the bond length and α is the apex angle [52]

77, 89–97] as well as the Density Functional Perturbation Theory (DFPT) [39]. In most papers describing simulations of Si NWs, the main attention is focused on the equilibrium geometry and the electronic properties of nanowires, although a number of theoretical studies are devoted to analysis of their thermal and vibration properties [32, 39, 75–78, 81, 83, 86, 97], optical properties [90, 91], mechanical stability and elasticity [70, 79, 80, 82, 84, 85, 92–94, 96] as well as electric conductivity [35, 52, 71, 78].

5.3.2 Cohesive and Electronic Properties of Si Nanowires

The comparative theoretical analysis of Si NWs with the low Miller index directions of growth, i.e., [112]-, [110]-, [111]- and [100]-oriented nanowires enclosed by low-index {111}, {110} and {100} facets (Fig. 5.24), was performed based on DFTB calculations [64]. NW cross-sectional areas were varied between 0.3 and 12.6 nm^2, with different ranges for different nanowire orientations. Figure 5.24 shows 23 different NW cross-sections, although the total number of Si NW models considered in that study was 99 and many of them were not included in the Figure, due to a low symmetry of various NW configurations and their energetic disadvantages. As a result, the [112]-oriented nanowire was presented by only one rectangular configuration enclosed by two {111} and two {110} facets. Meanwhile, this rectangular cross section, a pentagonal cross section of the [100]-oriented NW as well as both triangular and hexagonal cross section of the [110]-oriented NW (as shown in Fig. 5.25) were experimentally visualized when using microscopic TEM and STM methods [62, 98]. All the considered Si NW structures were hydrogenated and placed in the supercell with a vacuum space at least 1 nm outside the nanowire at each lateral orientation [64], which was enough to eliminate the influence of the nanowires in adjacent cells (Fig. 5.25).

In the presence of external H atoms upon Si NWs, the symmetry of nanowires was found to be dependent on the NW orientation, diameter, shape of its cross section and relaxation [90]: for the case of $d_{NW} \approx 1$ nm, [100]-, [110]- and [111]-oriented NWs were described by C_{2h}, C_{2h} and C_{3v} point groups (for both the initial and relaxed morphologies), respectively, while for $d_{NW} \approx 3$ nm, the corresponding symmetry groups were C_i (C_s), C_{2h} (C_s) and C_{3v} (C_{3v}), respectively (groups for relaxed NW morphologies are shown in the brackets). The relaxed configurations of Si NWs exhibited slight deviations of Si-Si bond lengths from the Si crystal value: [100]-, [110]- and [111]-oriented nanowires were elongated by about 2, 2 and 1 per cents along their axial directions, respectively, while [112]-oriented NWs were contracted by about 1 % along the same direction. Differences in Si-Si bond lengths were caused by different deviations of Si-Si-Si bond angles from that of the perfect crystal (109.5°). NW surface lattice deformations were generally reduced with the increasing NW diameter converging to the perfect Si crystal due to the decrease of size effect and the increase of lattice rigidity. Two different {100} facet configurations of the [110]-oriented Si NW were considered when the dihydride plane defined by the

Si-H_2 bonds was either (*i*) parallel to nanowire or (*ii*) perpendicular to it (Fig. 5.25c, d). All the lateral spacings of Si rows in the latter configuration of [110]-oriented nanowires were contracted, which resulted in NW instability and could explain the appearance of the single domains observed in STM images of the {100} facets [62]. Fig. 5.26 shows three groups of curves corresponding to the cohesive energy *per* atom, (5.17), and the band gap versus the nanowire cross-sectional area for all four Si NW configurations considered above (Fig. 5.24) [64]. In Fig. 5.26a, the cohesive energies of [112]-oriented Si NWs are compared to those of [110]-oriented Si NWs, so that this comparison enables estimation of the surface energies for the different enclosing facets. In Fig. 5.26b, the cohesive energies of [112]-oriented Si NWs are compared to those of both [111]- and [100]-oriented Si NWs. The cohesive energy becomes lower (more negative) with the increasing nanowire cross-sectional area (or NW diameter).

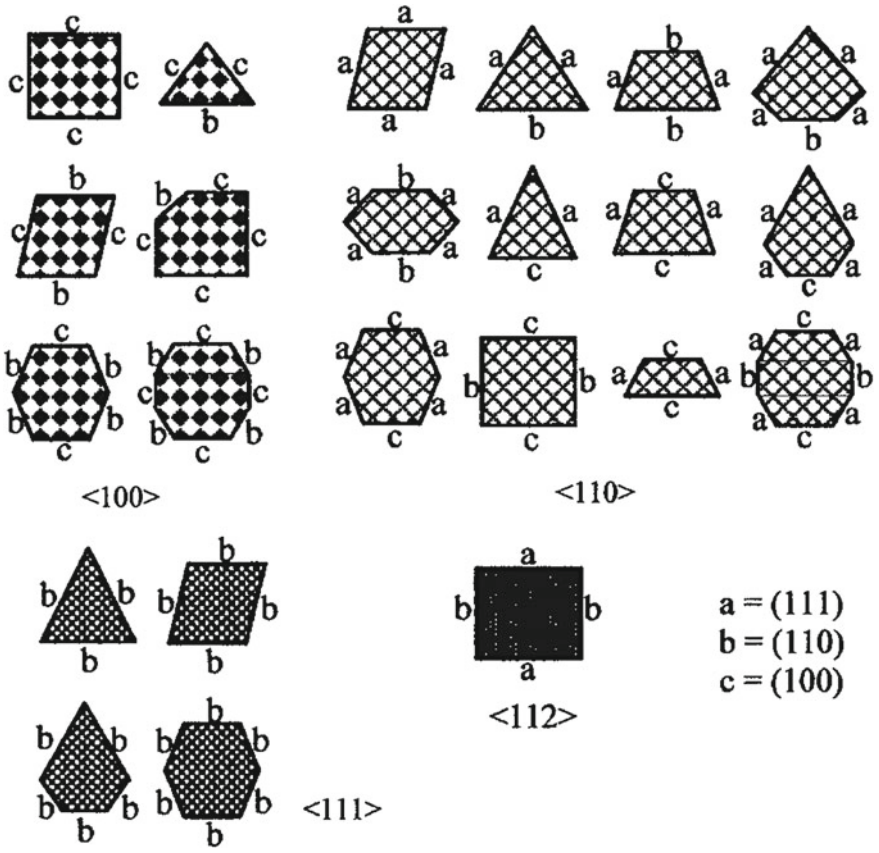

Fig. 5.24 Cross sections of energetically favorable [100]-, [110]-, [111]-, and [112]-oriented Si NWs (Reprinted figure with permission from Zhang et al. [64], Copyright (2005) by the AIP Publishing LLC)

Silicon nanowires with the same orientation, e.g., [110] (Fig. 5.26a), and different enclosing facets enable the evaluation of the effect of the enclosing H-terminated surfaces on the cohesive energy. Among [110]-oriented Si NWs with the different faceting those enclosed by only four {111} facets (rhomboidal cross section *aaaa*, higher right panel in Fig. 5.24) possessed the lowest cohesive energy, indicating that the (111) surface is the most favorable energetically. The [110]-oriented hexagonal-type Si NWs enclosed by four {111} and two {110} facets (*abaaba*, Fig. 5.24) possessed lower cohesive energies than the ones enclosed by four {111} and two {100} facets (*acaaca*, the same panel of Fig. 5.24). Similarly, the rectangular [110]-oriented nanowires containing two {110} and two {100} facets (*bcbc*, the same panel of Fig. 5.24) possessed lower cohesive energies than the rectangular [100]-oriented NWs containing four 100 facets (*cccc*, higher left panel, Fig. 5.24), which allowed one to deduce that the (110) surface possessed a lower energy than the (100) surface. Obviously, the surface energies of different NW facets are inversely proportional to

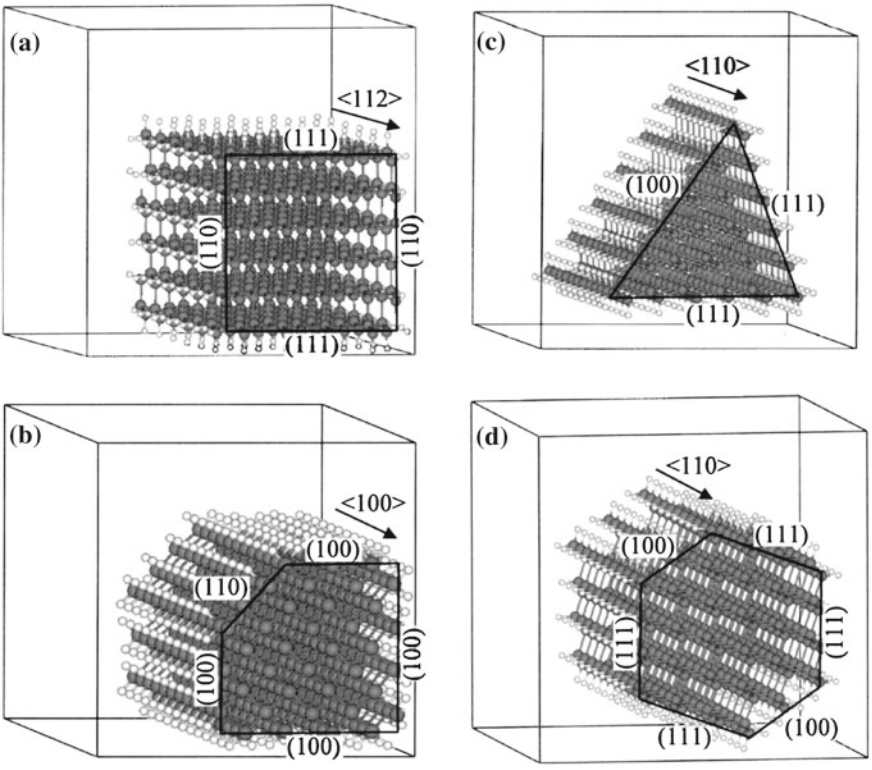

Fig. 5.25 Ball-and-stick models of selected H-passivated Si NWs in super cells **a** [112]-oriented NW enclosed between two {111} and two {110} facets, **b** [100]- oriented NW enclosed between four {100} and one {110} facets, **c** [110]-oriented NW enclosed between two {111} and one {100} facets, as well as **d** [110]-oriented NW enclosed between four {111} and two {100} facets, which were observed experimentally (Reprinted figure with permission from Zhang et al. [64], Copyright (2005) by the AIP Publishing LLC)

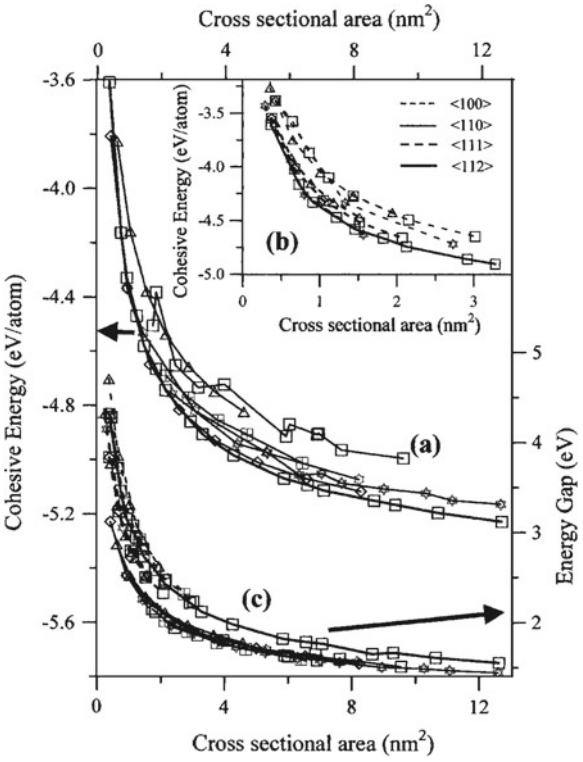

Fig. 5.26 The potential curves for H-passivated Si nanowires of different shapes and thicknesses are drawn separately for [110] and [112] NW orientations (**a**) as well as for [111], [100] and [112] ones enclosed in inset (**b**). For all the considered NW types, the band gap dependencies on nanowire thickness are drawn too (**c**). *Lines* in inset determine attribution of energy curves to different orientations of Si NWs while symbols □, △, ◇ and ∗ denote prismatic NWs with *rectangular*, *triangular*, *rhomboidal* and *hexagonal* cross sections (Reprinted figure with permission from Zhang et al. [64], Copyright (2005) by the AIP Publishing LLC)

the surface atomic densities of these facets [64]. However, it was rather surprising, that [112]-oriented Si NWs containing only two {111} facets and two {110} facets were energetically more favorable than the most stable [110]-oriented nanowire surrounded by four {111} facets only (Fig. 5.24). A plausible explanation of this result was found to be the smaller surface-to-volume ratio of [112]-oriented Si NW compared to aforementioned [110]-oriented nanowire (the first had a rectangular cross section, whereas the second was rhomboidal). For [111]-oriented Si NWs shown in Fig. 5.24 (all enclosed by {110} facets) the stability was the largest for the hexagonal nanowire, second for the rectangular NW, and the smallest was found to be for the triangular nanowire, in accordance with their surface-to-volume ratio. The same argument can also explained why the stability of the hexagonal [111]-oriented NW with six 110 facets approached that of the rectangular [112]-oriented NW with two {111} and two {110} facets.

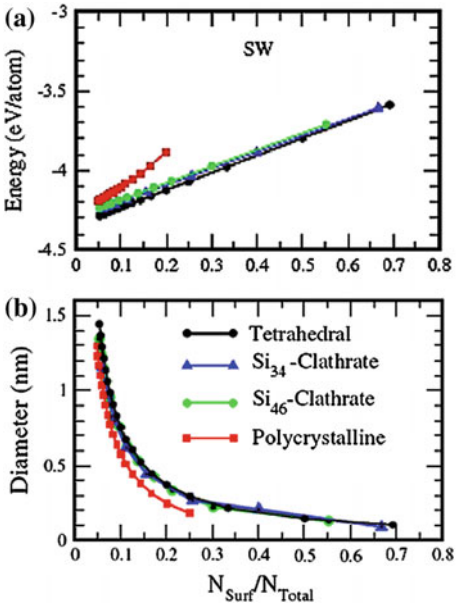

Fig. 5.27 Various dependences of Si NW cohesive energy (**a**) and diameter (**b**) on surface to volume ratio. The legends for four types of *curves* corresponding to nanowires imaged in Fig. 5.22 are indicated in the *lower panel* [35]

The aforementioned stability analysis was additionally illustrated by plotting the cohesive energies of four types of Si NWs imaged in Fig. 5.22 as functions of their surface to volume ratios (N_{surf}/N_{vol}, where numerator and denominator include the numbers of the corresponding atoms per NW UC) as presented in Fig. 5.27 [35]. The surface and volume Si atoms possess either threefold or fourfold coordination, respectively. Figure 5.27a shows the results obtained using MD simulations within the formalism of Stillinger-Weber (S-W) potential [99]. As shown in the lower panel of Fig. 5.27, for the same diameter, the N_{surf}/N_{vol} ratios of the polycrystalline nanowires in all the cases are smaller than the N_{surf}/N_{vol} ratios for single crystalline NWs. This is expected since the formation of stacking fault type defects in polycrystalline nanowires minimizes the surface to volume ratios for the given diameter. The total cohesive energies, including the contributions from the bulk, surface, and stacking fault defect type atoms, as the function of the N_{surf}/N_{vol} ratio were found to be valid criteria for comparing the stability of these nanowires, e.g., instability of the polycrystalline NWs for higher surface to volume ratio or smaller NW diameters up to 1.8 nm. For smaller diameters, these nanowires can collapse into mixed configurations with no clear distinction between surface and bulk type atoms. Among the single crystalline nanowires (Fig. 5.22) the monolithic tetrahedral-type nanowires were found to be slightly more favorable energetically than clathrate-type NWs [35].

Figure 5.26c shows the calculated band gaps of different NWs versus the nanowire cross-sectional area [64]. The dependence of $\Delta\epsilon_{gap}$ on the facet combinations was found to be much less important than that of cohesive energies. The values of band

gaps for Si NWs followed the order of $\Delta\epsilon_{gap}[100] > \Delta\epsilon_{gap}[112] > \Delta\epsilon_{gap}[111] > \Delta\epsilon_{gap}[110]$, with a strong dependence on NW diameters (Fig. 5.26c). On the whole, the parameters of Si NW band gaps obtained in the DFTB calculations [64] were found to be in a good qualitative accordance with the corresponding results of ab initio calculations [19, 87, 89] and experimental data [62]. For example, DFT PW calculations performed for H-passivated Si NWs possessing the same four low-index orientations as considered above [19, 89] showed a dependence of the band gap width on the factors such as (*i*) proper implementation of the Wulff construction formalism, (*ii*) the shape of nanowire (rhomboidal, polyhedral, square- or circular-types) as well as (*iii*) the formation of Si dimers on NW facets and their configuration (Fig. 5.20). In the absence of the proper passivation for Si NWs, their lateral surfaces were found to be strongly reconstructed [69], forming a case of series of buckled dimers with a pattern similar to Si(100) surfaces. Depending on the reconstruction, the surface states that cross the Fermi level can form, what leading to metallic or semi-metallic Si NWs. Under such circumstances, doping is no longer needed to have highly conducting nanowires. The possibility of tailoring Si NWs that are conducting without the need of doping is particularly relevant in very thin wires where typical doping concentrations require a precision in the fraction of impurities per atom that is extremely difficult to control. Although experiments available so far have not thoroughly explored the possibility of surface reconstruction or nanowire conductance without doping, these results show a promising venue of joint experimental and theoretical studies of pure silicon nanowires [69].

5.3.3 Thermal and Vibrational Properties of Si Nanowires

An accurate prediction of the thermal transport in nanocrystalline structures was found to be very important for both fundamental physics and engineering applications [81]. For example, a comprehensive analysis of Si NW thermal conductivity can lead to a deeper understanding of phonon scattering mechanisms, which is of basic theoretical significance. All the more so since the values of thermal conductance ζ(T) were earlier measured experimentally [100]. Initially, the continuous elasticity theory and the Boltzmann transport equation were used for theoretical simulation of ζ(T) for Si NW [101]. However, the discrete atomistic models considered later [75] were found to be more fitted for a more adequate description of thermal conductance. Two main models were considered depending on the regimes of phonon transport: (*i*) ballistic, when phonons are considered without elastic collisions along the mean free path L, (*ii*) a more general diffusive regime, where both ballistic and diffusive (inelastic) types of scattering are considered. If the phonons are transmitted ballistically, thermal conductance can be expressed as [75]:

$$\zeta_{bal}(\mathrm{T}) = \sum_{\alpha} \int_{0}^{\pi/a_z} [\hbar\omega\nu_z(\alpha, k_z)\frac{df_{\mathrm{B}}(\mathrm{T})}{d\mathrm{T}}]\frac{dk_z}{2\pi} = \frac{\hbar\omega}{2\pi}\int_{0}^{\infty}\theta_{bal}(\omega)\frac{df_{\mathrm{B}}(\mathrm{T})}{d\mathrm{T}}d\omega, \quad (5.2)$$

where α is a set of discrete quantum numbers labeling particular subbands in one-dimensional phonon dispersion relations, ω is a phonon frequency, k_z and ν_z are projections of the wave vector and the speed of the phonon on the NW direction, $f_{\mathrm{B}}(\mathrm{T}) = (e^{\hbar\omega/k_{\mathrm{B}}} - 1)^{-1}$ is the Bose-Einstein distribution function, $\hbar$ and k_{B} are Planck and Boltzmann constants while $\theta_{bal}(\omega)$ is the transmission function corresponding to the number of phonon subbands crossing frequency ω when considering the ballistic regime of phonon transport. In the case of diffusion regime of phonon transport, the corresponding expression for thermal conductance is written as [75]:

$$\zeta_{diff}(\mathrm{T}) = \sum_{\alpha} \int_{0}^{\pi/a_z} [\hbar\omega\nu_z(\alpha, k_z)\frac{\lambda(\alpha, k_z)}{L}\frac{df_{\mathrm{B}}(\mathrm{T})}{d\mathrm{T}}]\frac{dk_z}{2\pi} = \frac{\hbar\omega}{2\pi}\int_{0}^{\infty}\theta_{diff}(\omega)\frac{df_{\mathrm{B}}(\mathrm{T})}{d\mathrm{T}}d\omega, \quad (5.3)$$

where $\lambda(\alpha, \omega)$ is a characteristic relaxation length along the nanowire direction in the frequency interval $\omega_\alpha^l < \omega < \omega_\alpha^u$ only (indices l and u denote the lower and upper limits outside which $\lambda(\alpha, \omega) = 0$). If the phonon modes' lifetimes $\tau(\omega)$ are independent of the subband being dependent on the frequencies only, the relaxation lengths can be defined as $\lambda(\alpha, \omega) = \tau(\omega)\nu_z(\alpha, \omega)$. In the case of the known values of $\omega_\alpha(k_z)$ and $\tau(\omega)$, (5.3) allows computing the thermal conductance. Though, it was useful to recast (5.3) into a form equivalent to the right part of (5.2), so that to explicitly retain the "transmission function" of the $\theta(\omega)$ concept. Unlike ballistic regime of phonon transport, the number of phonon subbands crossing frequency ω in the latter case is defined as [75]:

$$N_b(\omega) = \sum_{\alpha} \delta'(\omega - \omega_\alpha^l)\delta'(\omega_\alpha^u - \omega), \quad (5.4)$$

where each of δ'-functions equals to zero if $\omega_\alpha^l > \omega$ or $\omega > \omega_\alpha^u$. In other cases $N_b(\omega) > 0$. Thus, if $\theta_{diff}(\omega) = N_b(\omega)\tau(\omega)\langle\nu_z(\omega)\rangle$, where the brackets denote the averaging of phonon's velocities estimated from the dispersion relations, the right parts of (5.2) and (5.3) look equivalent [75]. Thus, the thermal conductivity defined for both regimes of the NW thermal conductance as $\kappa(\mathrm{T}) = (L/s)\zeta(\mathrm{T})$, where s is the area of NW cross section while L the mean free path, can be expressed:

$$\kappa(\mathrm{T}) = \frac{L}{s}\frac{\hbar\omega}{2\pi}\int_{0}^{\infty}\theta(\omega)\frac{df_{\mathrm{B}}(\mathrm{T})}{d\mathrm{T}}d\omega = \frac{\hbar\omega}{2\pi}\int_{0}^{\infty}\Theta(\omega)\frac{df_{\mathrm{B}}(\mathrm{T})}{d\mathrm{T}}d\omega, \quad (5.5)$$

where the generalized transmission function $\theta(\omega)$ can be considered as either $\theta_{bal}(\omega)$ or $\theta_{diff}(\omega)$ depending on the conductance regime, while $\Theta(\omega) = \frac{L}{s}\theta(\omega)$.

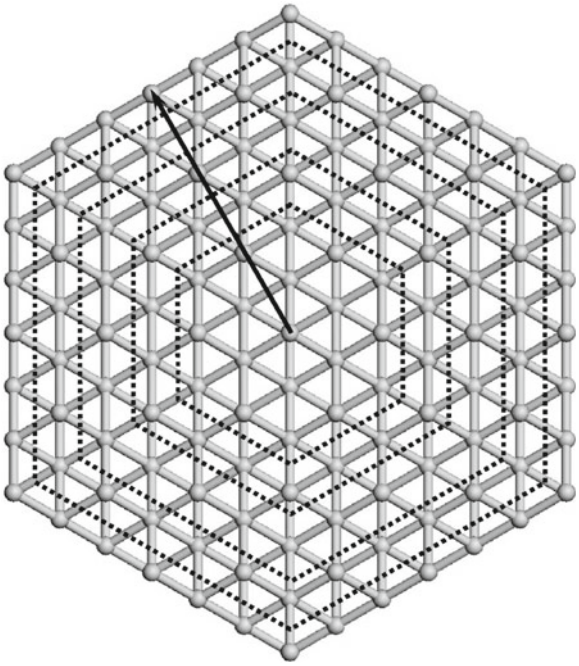

Fig. 5.28 Hexagonal cross sections of [111]-oriented Si NWs cleaved from bulk (*dotted*). The *arrow* indicates the counting atomic layers N_L from the NW axis to the {110} facet. For $N_L = 1$, $d_{\mathrm{NW}} = 6.2$ Å (Reprinted figure with permission from Zhang et al. [83], Copyright (2007) by the AIP Publishing LLC)

The dependence of thermal properties on the nanowire size was studied for hexagonal-type [111]-oriented Si NWs of different diameters [83]. Its initial structure was directly cleaved from the Si bulk, with six equivalent {110} facets exposed to vacuum as displayed in Fig. 5.28. The size of this type of Si NWs can be defined as the number N_L of hexagonal atomic layers around the central axis of the nanowires towards the {110} facets as indicated by the arrow. The periodic boundary condition was chosen along the axial direction perpendicular to the NW cross section with $l_{\mathrm{NW}} = 2c$, i.e., the nanowire supercell consisted of two NW UCs [83]. To obtain the lowest-energy structures of Si NWs, the simulated MD annealing procedure was used. The simulation of each Si NW configuration started with a high enough temperature (500 K), being slowly cooled down to 0 K. The interaction between Si atoms was described by the Stillinger-Weber potential mentioned above [99] and widely used to study structural properties of low dimensional Si nanostructures [35, 70].

Figure 5.29 shows the initial and relaxed structures of Si NWs after the S-W MD treatment [83]. The relaxed Si NW structure with $N_L = 4$ essentially differs from the non-relaxed NW structure. After relaxation, the shape of Si NW cross section changes from a hexagon to a quasi-circle (Fig. 5.29) and the structure does not keep the tetrahedral arrangement. The relaxed NW structure possesses C_3 point symmetry, similar to that obtained within the DFT-PW formalism [92]. For Si NWs

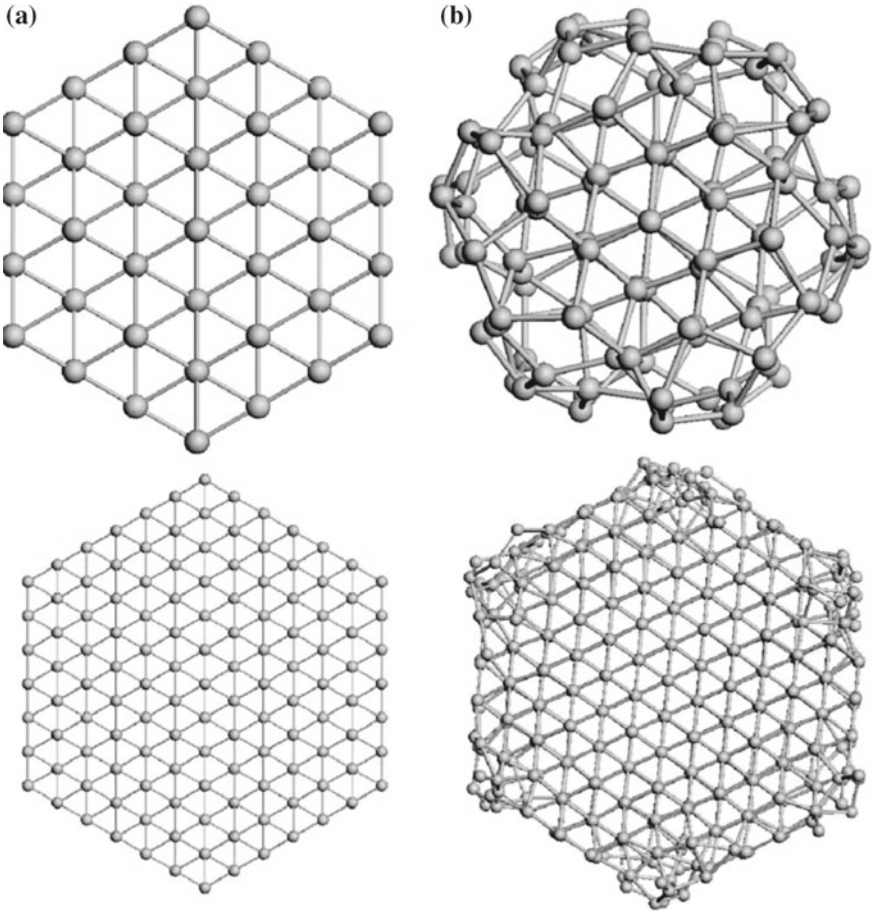

Fig. 5.29 The initial (**a**) and relaxed (**b**) structures when using S-W MD potentials for $N_L = 4$ and $N_L = 7$ Si NWs (*upper and lower panels*) [83]

with $N_L = 7$, the core structure is close to that of Si bulk while surface atoms do not reside on the ideal tetrahedral positions anymore. Thus, the results of MD simulations proved that the tetrahedral bulk silicon corresponded to the global minimum for S-W potential, which is quite suitable for simulation of Si NWs relaxations [83]. The influence of Si NW diameter on its thermal conductivity is illustrated in Fig. 5.30. A better fitting of the energy curve $\kappa_{\mathrm{NW}}(d_{\mathrm{NW}})$ was achieved when using the correcting expression $\kappa_{\mathrm{NW}} = \kappa_{bulk} + k/(d_{\mathrm{NW}})^{\alpha}$, where constants α and k were optimized taking into account the influence of the shift of phonon frequency of thin Si NWs due to the dimensional constraint [83]. For ultrathin Si NWs, the latter factor was essential according to the inset of Fig. 5.30. When the temperature of the nanowire was not high, only low frequency phonon modes were activated and contributed to the thermal conductivity. Thus, the analysis of influence of the phonon structure on NW properties is necessary.

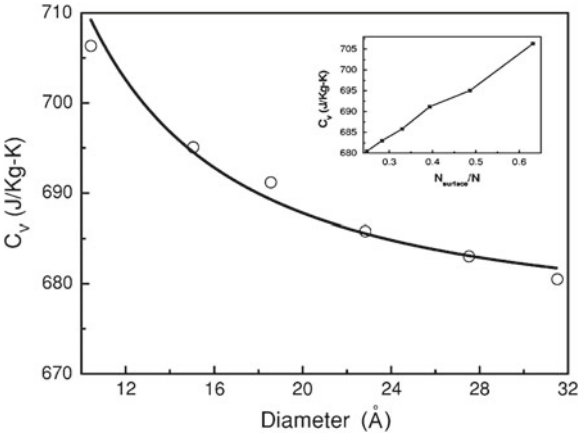

Fig. 5.30 Dependence of C_v (correlated with κ) on d_{NW} for [111]-oriented Si NW at room temperature. The inset connects with κ versus the ratio N_{surf}/N_{vol} (Sect. 5.3.2) (Reprinted figure with permission from Zhang et al. [83], Copyright (2007) by the AIP Publishing LLC)

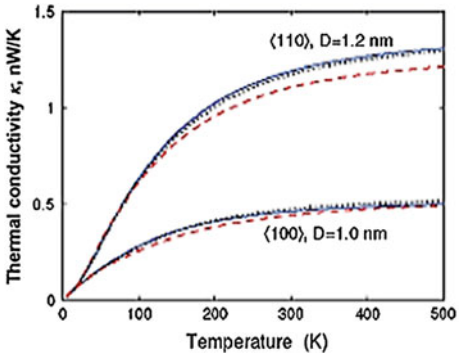

Fig. 5.31 The energy *curves* κ(T) for [110]- and [100]-oriented Si NWs with diameters 1.2 nm and 1.0 nm, respectively: (*solid lines*) TEP without H-passivation; (*dotted lines*) TEP with H-passivation; (*dashed lined*) DFT [77]

Figure 5.31 shows the dependencies of the thermal conductivity on the temperature for Si NWs with the alternative low-index NW orientations ([110] and [100]) calculated within the Tersoff empirical potential model (TEP) which is quantitatively similar to those obtained when performing the DFT-PW calculations [77]. Obviously, the [110]-oriented NWs possess a considerably higher thermal conductivity compared to [100]-ones, which directly correlates with the essentially larger cohesive energy of the former (Fig. 5.26). Leaving out the hydrogen atoms from H-passivated models of Si NWs in the TEP calculations was quite justified, similarly to nanowire models for MD simulations (Figs. 5.28, 5.29 and 5.30). The results presented in Fig. 5.31 were taken as a validation of relatively simple and fast empirical potential calculations on pure silicon nanowires. The study of much thicker nanowires would be very time-consuming when performing DFT calculations [77].

The top panel of Fig. 5.32 presents the atomic structure in the unit cells periodically repeated along the NW axes with [100], [110] and [111] orientations, initial

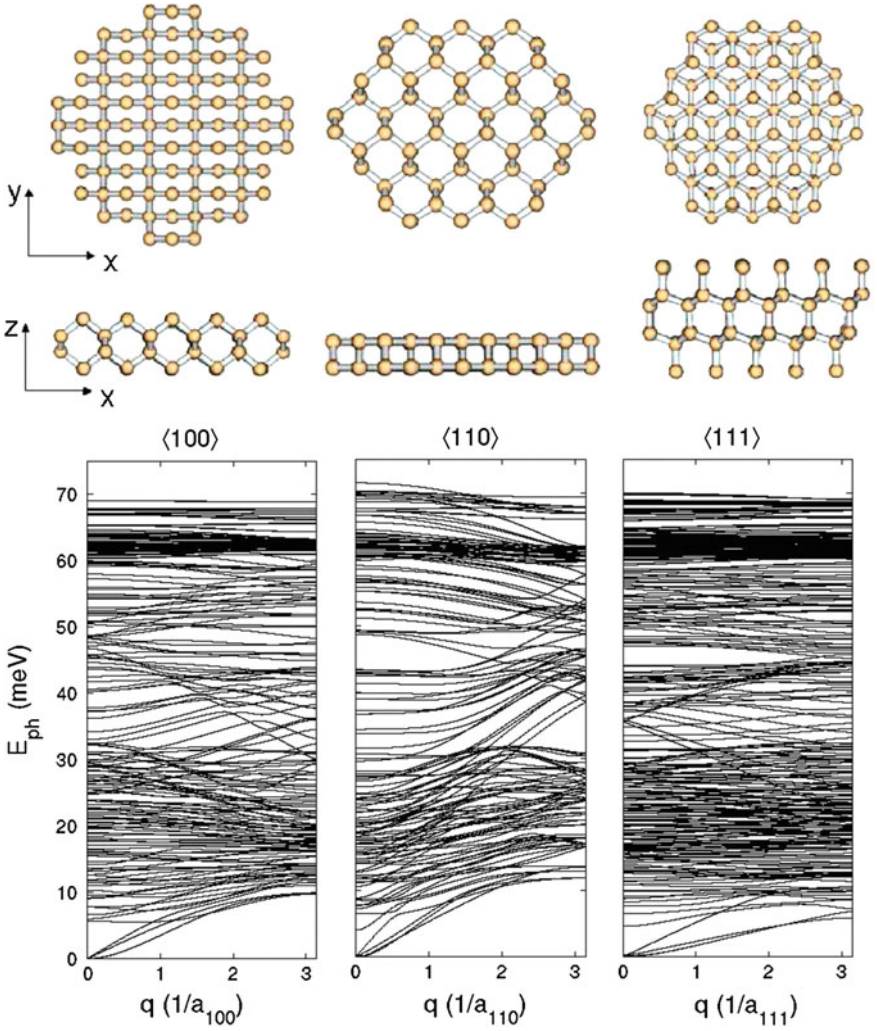

Fig. 5.32 Cross sections and aside views (*top and middle panels*, respectively) together with the full vibrational band structures (*bottom*) of Si NWs with orientations [100] (*left*), [110] (*middle*), and [111] (*right*). The phonon wave vectors, **q**, are all in the respective NW directions and are shown in units of the reciprocal UC lengths, with initial values $a_{100} = 5.4$, $a_{110} = 3.8$, and $a_{111} = 9.4$ Å. The areas of the corresponding NW cross-sections were defined as $s_{100} = 8.9$, $s_{110} = 11.2$ and $s_{111} = 9.0\,\text{nm}^2$ (Reprinted figure with permission from Markussen et al. [77], Copyright (2008) by the American Chemical Society)

diameters of which were defined from the lattice parameters of Si bulk [77]. Each NW type contained $3N_a$ subbands (N_a is the number of atoms *per* unit cell). Different NW orientations corresponded to different UC lengths, a_{hkl}, and, thus, different N_a numbers as well. At low phonon energies, there were only four acoustic modes: (*i*) the dilatational and (*ii*) the torsional modes, both with linear dispersions as well as

(*iii*) two flexural modes with quadratic dispersions [102]. Many relatively flat subbands starting right above the acoustic modes ($\hbar\omega \leq 4$ meV) denoted shear modes and originated from the bulk acoustic bands that were folded into the NW axis, whereas many closely lying bands around 63 meV corresponded to Si bulk longitudinal optical (LO) phonon energy. An important qualitative feature was that the bands of the [110]-oriented NW generally had a larger slope (velocity) than two other NW orientations containing many flat bands. Due to the larger slope, there were more bands at a given energy for [110]-oriented nanowires, leading to their larger thermal conductivity [77].

Since the thermal conductance of Si NWs and other nanostructures is mainly governed by phonons (e.g., their dispersion and interactions), the knowledge of the phonon spectrum and its interpretation is important for a better understanding of the corresponding conductivity mechanism [39]. One of the possible applications of such a notion is the low-field phonon mobility, which depends strongly on the scattering with acoustic phonons, the surface roughness and impurities. The phonon spectrum can also be identified with the structural instability of the system in the case of the of imaginary eigenfrequencies' occurrence, which, e.g., was found in ultrathin metallic nanowires [103]. A number of theoretical studies of Si NW vibrational properties employed empirical models with parameters obtained from the bulk, e.g., those mentioned above [32, 76, 77, 81, 83, 86, 101], although it was rather problematic to assess the accuracy of those model calculations in spite of identification of several unique phonon properties. This is why the analysis of comprehensive ab initio simulations of Si NW vibrational spectra was required too. Since the majority of synthesized Si NWs of a small diameter (<13 nm) were oriented along the [110] or [112] directions as mentioned in Sect. 5.3.1 [61] and theoretical studies confirmed these observations (Fig. 5.26), ab initio calculations of the phonon properties were performed mainly on [110]-oriented Si NWs, which are structurally more simple as compared to those with [112] orientation [39, 97]. Figure 5.33 shows a relaxed structure of the [110]-oriented Si NW, the diameter of which was chosen to be minimum (1.2 nm) among considered nanowires of the same type (with diameters 1.8 and 2.2 nm) [97]. To achieve its low-energy configuration, which is necessary to avoid unstable vibrational modes as pointed above, the dangling bonds above the facets and ribs of the nanowire were H-terminated (Fig. 5.33).

The calculated densities of vibrational modes (DOVMs) at Γ point of [110]-oriented Si nanowires for three different diameters are presented in Fig. 5.34b–d. For comparison, the corresponding DOVM of bulk Si is shown in Fig. 5.34a, whose two main features were found at around 4 and 15 THz, respectively. As the diameter of the nanowire increases, its DOVM profile becomes more and more close to the corresponding profile of Si bulk (*cf*. Fig. 5.34a, b). On the other hand, since the structure of Si NWs has a lower symmetry than that of bulk silicon (space group T_d), the degeneracy of many phonon modes is lifted, resulting in a wider distribution of modes in the DOVM of Si NWs [97]. In addition, quantum confinement can introduce modes that do not exist in the bulk, further broadening the DOVM features in Si NWs. Since the quantum confinement plays an extremely important role to govern the electrical and thermal properties of semiconducting nanostructures, those

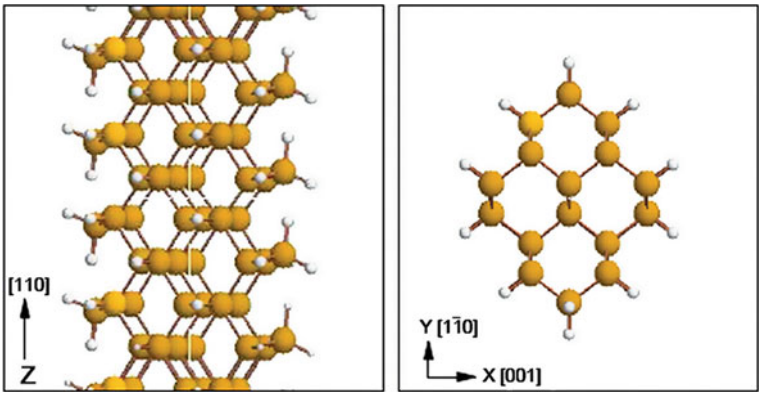

Fig. 5.33 Structure of thin [110]-oriented Si NW. The *left* and *right* images correspond to aside and across nanowire views, respectively. The NW facets were hydrogenated for structural stabilization (Reprinted figure with permission from Yang and Chou [97], Copyright (2011) by the American Chemical Society)

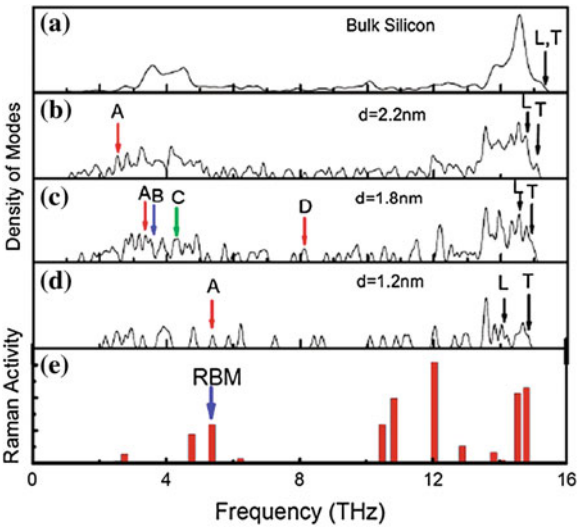

Fig. 5.34 Density of vibrational modes (DOVMs) for bulk silicon and three [110]-oriented Si NWs with different diameter sizes (**a–d**). L and T denote the LO and TO modes (longitudinal and transverse optical), respectively. A-D peaks correspond to the collective (confined) modes shown in Fig. 5.35. A 0.05 THz Gaussian broadening is applied for DOVMs. The Raman activity of the 1.2 nm Si NW with an arbitrary unit and the radial breathing mode (RBM) is marked (**e**) (Reprinted figure with permission from Yang and Chou [97], Copyright (2011) by the American Chemical Society)

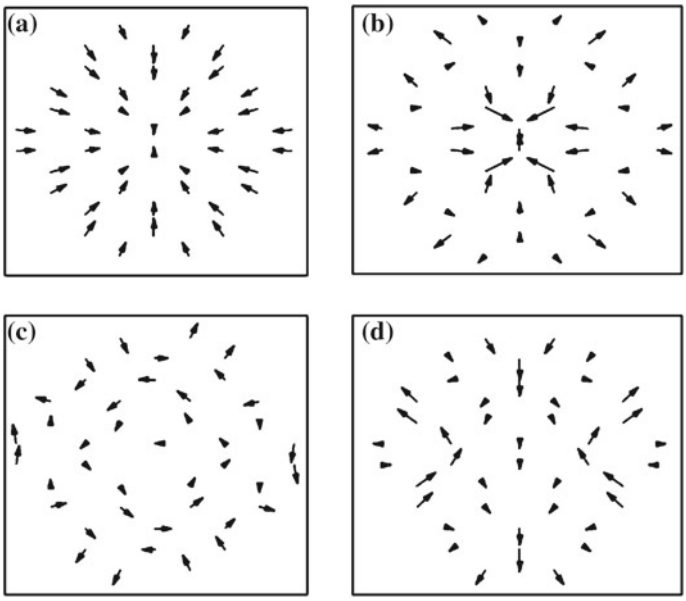

Fig. 5.35 Typical confined modes of a Si NW ($d_{NW} = 1.8$ nm) shown in plots (**a**)–(**d**) correspond to A–D peaks of vibrational spectrum imaged in Fig. 5.34c (Reprinted figure with permission from Yang and Chou [97], Copyright (2011) by the American Chemical Society)

vibrational modes resulting from the confinement and located within the low-frequency (acoustic) regime (8 THz in Fig. 5.34) attract an enhanced interest [104].

Figure 5.35 images representative confined modes of a nanowire (possessing special symmetries) different from the lattice vibrational modes in bulk silicon. One type of them is the RBM shown in Fig. 5.35a, b with atomic displacements along the radial direction only [97]. Because of the boundary conditions of a NW, there exists an amplitude modulation along the radial direction, generating a nodal structure as shown in Fig. 5.35b. Figure 5.35c illustrates a rotational mode whose atomic displacements have mainly the angular component. The vibrational mode in Fig. 5.35d possesses both radial and angular components, and each of these two components has its own spatial modulations. Because of the size dependence of the confined modes, they are usually regarded to have a practical importance in order to estimate diameter of nanowires through measurements of the Raman scattering (Fig. 5.34e) [97]. Because of the highly anisotropic nature of Si NWs, the construction of the Raman spectrum foresees both the space averaging and inclusion of the depolarization effect [105]. Figure 5.34e clearly shows that the RBM and other confined modes shown in Fig. 5.35 are Raman-active, depending on the NW diameter. In particular, the RBM is strongly active in the case of a narrow Si NW ($d_{NW} \approx 1.2$ nm), which could be used as an efficient quantity to estimate the thickness of narrow nanowires. However, it was found that the Raman activity of the confined modes decayed and gradually disappeared when the thickness of Si NWs increased, since only the prominent peak

associated with the high-frequency optical modes (right edges of the spectra imaged in Fig. 5.34a–d) appears in the first-order Raman spectrum of bulk silicon.

Therefore, the high frequency optical modes could be considered as a better candidate to provide a consistent measurement of the Si NW thickness over a large range of synthesized nanowires [97]. Obviously, these three high-frequency optical modes degenerate in the perfect bulk silicon crystal (Fig. 5.34a). The reduced symmetry in Si NWs split them into two groups: two transverse optical modes (TO1 and TO2) with their atomic displacements perpendicular to the axis, and one longitudinal optical mode (LO) with its atomic displacements along the axis. The details of the displacements of these optical modes are plotted in Fig. 5.36. The frequencies of these optical modes are marked in Fig. 5.34; the two TO modes are nearly degenerated and substantially separated from the LO mode. The separation increases as d_{NW} of Si NWs decreases. At the same time, the frequencies of all three optical modes decrease

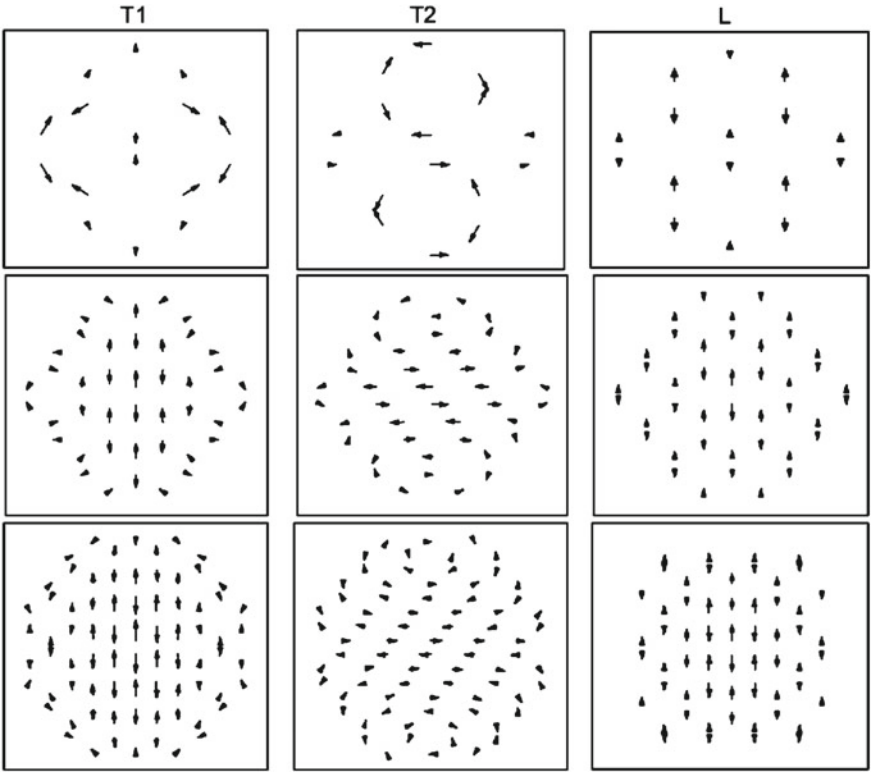

Fig. 5.36 Three high-frequency optical modes in Si NWs ($d_{NW} = 1.2$, 1.8 and 2.2 nm shown in the *top, middle and bottom panels*, respectively). Each column represents a specific type of optical modes: TO1, TO2 and LO (shown as L and T in Fig. 5.34). The atomic positions are rescaled, to compare their displacements (Reprinted figure with permission from Yang and Chou [97], Copyright (2011) by the American Chemical Society)

with the decreasing d_{NW} value [97]. The Raman activities of these high-frequency optical modes are presented in Fig. 5.34e. Because of the depolarization effect, only T-type modes are highly active. As compared with the RBM, the splitting of three high-frequency optical modes provides a better approach for estimating the thickness of bigger NWs [97]. The vibrational spectra of H-terminated Si NWs in Fig. 5.34b, c and d do not contain peaks associated with Si-H vibrations since their frequencies are much higher than the limit of the interval of frequencies considered there (>18 THz). The description of these vibrations was made in the other study where calculations on the Si NW phonon structure were performed using both LDA-PW and DFPT methods [39].

To better understand the evolution of the phonon spectrum as a function of the nanowire diameter, three different NW thicknesses were considered: 0.5, 1.2 and 1.6 nm, respectively (Fig. 5.37). According to the calculated phonon spectra of Si NWs presented in both Figs. 5.34 and 5.37, the growth of d_{NW} leads to a decrease of both optical and RBM frequencies since the fitting function for each type of vibrations was proportional to $(1/d_{NW})^{\alpha}$ where optimal values of α were found to be 1.2 for RBM and 1.2–1.5 for optical modes [97]. The calculated peaks $2100\,cm^{-1}$ were attributed to the stretching of Si-H bonds [39]. For all the considered nanowires, the number of "hydrogen modes" corresponded to the number of H atoms per NW unit cell. Similarly, the modes around 630 and 870 cm^{-1} were linked to the bending of Si-H bonds.

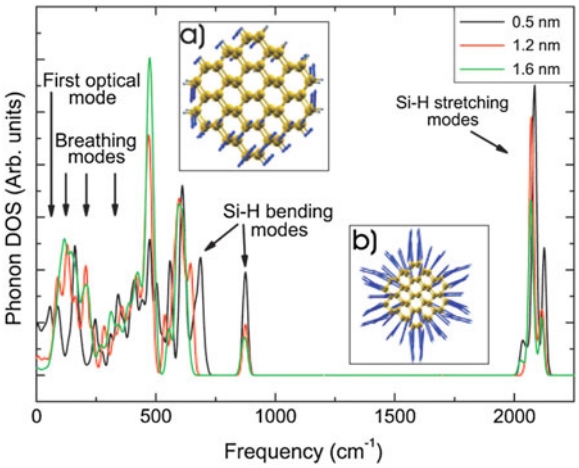

Fig. 5.37 Phonon density of states (DOS) for Si NWs with different diameter. The *arrows* indicate special eigenmodes. The resulting DOS is normalized with respect to the number of bands, so that a direct comparison is possible. Exact frequencies of the breathing mode are indicated by three *arrows* for the different NW diameters. The eigenmodes of the first optical mode (*a*) and the breathing mode (*b*) for the 1.6 nm nanowire are shown in the insets (Reprinted figure with permission from Peelaers et al. [39], Copyright (2009) by the American Chemical Society)

The phonon structure including acoustic and optical modes of hexagonal [111]-oriented Si NWs, which were experimentally found to be stable for nanowire diameters exceeding 13 nm [61], were studied using empirical potentials within the Stillinger-Weber formalism [76]. Development of this approach allowed the authors to describe clamped boundary conditions (when all the facet atoms displacements are set to be zero) for both types of phonon modes in real free-standing periodic nanowire models of different diameters with the atomistic structure.

5.3.4 Elastic Properties of Si Nanowires

As the sizes of synthesized silicon nanowires approach the smallest diameters (<10 nm), exploration of the changes in NW mechanical properties on the nanometer scale is vitally important [84]. According to (5.1), the surface energy and the energy of matching the adjacent facets play an important role in the energy balance of nanowires (due to the high surface to volume ratio) determining their specific elastic and mechanical properties. Moreover, the role of H-passivation of Si NW facets in achieving the stability of the nanowires is known (as described in Sect. 5.3.1), but little is known so far about the effect of the surface reconstruction which may impact the NW elasticity. It is also little known about the influence of strain effects on the electronic properties of Si nanowires [96] although the NW strain is a very important factor from the point of view of the growth and application aspect of nanodevices. Firstly, strain is rather unavoidable during the epitaxial growth if there is a lattice mismatch between the grown nanostructure and the substrate. Secondly, it was shown in many applications that electrons flow 70 % faster through strained Si than through a non-strained Si, and a strained chip design can be 35 % faster than a standard design [106]. Silicon nanowires are also expected to be essential building blocks for innovative applications in various nano-electrical-mechanical systems (NEMS) [84]. A predictive theory of nanomechanics remains an open problem both at the fundamental level and in terms of technological implementation since the continuum elastic theory (and more generally continuum mechanics) is only partly valid for nanoscale systems due to their composition of discrete atoms. Only during a gradual transition to nanosystems from those at micro- and macroscale levels, which do not contain structural irregularities and phase inhomogeneity, the continuum mechanics could show the possible limits of its applicability. Indeed, somewhat larger nanoscale structures may be described by continuum mechanics provided that the theory suitably extended to account for the occurrence of effects irrelevant in larger structures. However, a number of such attempts for Si NWs was found to be rather scarce [79, 80].

Among various mechanical properties, the Young's modulus E_Y is of particular interest as an important parameter in numerous functions of nanoscale devices containing, e.g., nanowires [102]. As mentioned above, properties of a Si NW surface layer (including also external H atoms which terminate the dangling bonds of outer Si atoms) differ from those of the NW core, it also holds true for elastic properties.

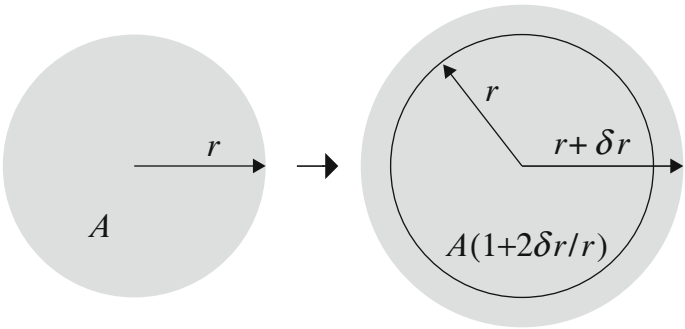

Fig. 5.38 The size effect defining the cross-sectional area consisting of core (*left circle*) as well as both core and surface layer (*right circle*). A is a cross-sectional area of core cylinder, r its radius while δr the thickness of surface layer (outer shell) [94]

To decompose the description of E_Y on the moduli of the core and surface shell, i.e., E_Y^{core} and E_Y^{shell}, respectively (Fig. 5.38), a cylindrical model of continuum mechanics was considered first [80]. The Young's modulus for a cylinder is defined as the ratio of the stress applied along its longitudinal axis to the resulting elongation strain ε_{zz}. Obviously, both the core and the outer shell undergo the same strain ε_{zz} and the surface is traction-free. Since the stress in arbitrary material is the product of its bulk (Young's modulus E_Y^{bulk} and ε_{zz}), the total force supported by the cylinder is the sum of the forces carried by each region. That force is the product of the axial stress and the cross-sectional area over which it acts. The total Young's modulus E_Y can be expressed via the following correlation [80]:

$$A_{tot}E_Y\varepsilon_{zz} = A_{core}E_Y^{core}\varepsilon_{zz} + A_{shell}E_Y^{shell}\varepsilon_{zz}, \tag{5.6}$$

where $A_{core} = \pi r^2$, $A_{tot} \approx A_{core}(1 + 2\delta r/r)$ and $A_{shell} \approx 2A_{core}\delta r/r$. This approach is valid for $\delta r << r$ only. Obviously, (5.6) can be transformed to the correlation between E_Y and E_Y^{core} [94]:

$$E_Y = E_Y^{core}(1 + \frac{2\delta r\delta E_Y}{r + 2\delta r}), \tag{5.7}$$

where $\delta E_Y = (E_Y^{shell} - E_Y^{core})/E_Y^{core}$ [80]. Thus, the total Young's modulus E_Y is changed by $\approx 2(\delta r/r)E_Y^{core}\delta E_Y$. This change modifies the value coefficient of the surface-area-to-volume ratio term in the Young's modulus, so when calculating this coefficient, its value is considered with respect to the location of the surface. The uncertainty vanishes as the system size is increased, i.e., the surface-to-volume ratio is decreased, so that this level of ambiguity is completely negligible for the modulus of macroscale structures [94].

Until now, several theoretical studies have been devoted to simulations on the elastic and mechanical properties of Si NWs of different low-index orientations including their influence on the electric, electronic and thermal properties [70, 79, 80, 82, 84,

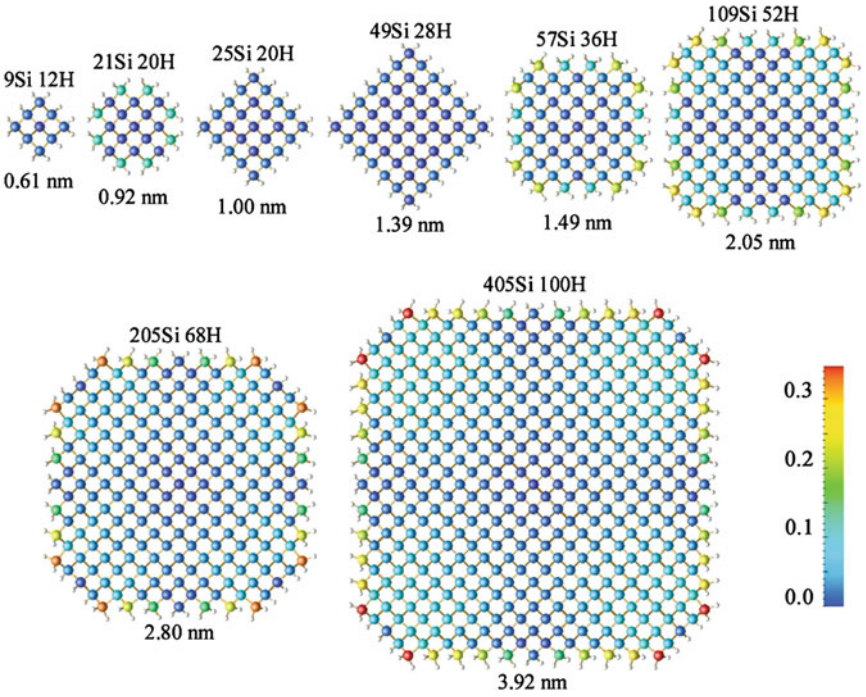

Fig. 5.39 Cross sections of fully relaxed hydrogen-terminated nanowires, with each Si atom colored as shown in the legend on the *right side* of figure corresponding to its transverse relaxation in Å. The numbers above the nanowires stand for the number of Si and H atoms *per* NW unit cell. The numbers below represent the nanowire width defined as the *square root* of the cross-sectional area [94]

85, 92–94, 96]. For example, large-scale DFT-PW calculations were performed for [001]-oriented Si NWs, cross-sectional shapes of which were chosen as truncated squares containing four pairs of alternating {100} and {110} facets (Fig. 5.39). However, nanowires of small diameters were chosen to be terminated by four energetically more stable {110} facets only, without canting {100} facets (as shown on the left side of Fig. 5.39) [94]. For the truncated NWs, the ratio of the facet areas is taken to be roughly compatible with the Wulff shape for a bare nanowire with $\{100\} - p(2 \times 2)$ and $\{110\} - (1 \times 1)$ surface reconstructions, i.e., the ratio of {100} to {110} area is 3.5:1 [94].

The reason for using the Wulff shape of bare nanowires was that the effect of surface condition on the material stiffness could be addressed by comparing H-passivated and bare NWs. In the Wulff shape of H-terminated nanowires, the {110} area would be larger than the {100} area due to the lower energy of the former facet, opposite to the Wulff shape of bare nanowires. It was found to be advantageous to use a bare NW shape not only because the surface energy of a bare slab could be exactly determined, whereas that of a slab with the H-passivated surface depends on the adsorbate chemical potential. Due to a common cross section, one could focus on the size or the role of the surface condition apart from any other effects due to the

shape [94]. For each of NW geometries shown in Fig. 5.39, the Si atoms were initially positioned at their bulk lattice sites and hydrogen atoms were added to terminate the dangling bonds at the surfaces, and then this configuration was relaxed. The surface structure, such as the ground-state canted dihydride {100} surface, was obtained naturally from the relaxation and did not require any initial seeding. The supercell size of each nanowire was one cubic UC length along the NW axis.

A number of physical phenomena can cause a residual stress along a nanowire. One example is the residual stress coming from the surface stress due to interactions in the passivation layer around a Si NW. This stress is equated to the axial stress when the longitudinal NW lattice spacing is fixed at the bulk value, $\sigma_{zz}(L_0)$, the argument of which corresponds to the length of the periodic supercell held fixed at Si bulk lattice spacing in the longitudinal direction [94]. The relaxed total energy was calculated for each NW shown in Fig. 5.39 in a series of longitudinal strains at increments of roughly 0.5 %. The corresponding total energy values were then fitted to a polynomial. The residual stress and other important properties were obtained from the strain derivatives of the polynomial: the first derivative gives the axial stress, σ_{zz}, the minimum of the polynomial, ε_{zz-eq}, gives the strain corresponding to the equilibrium length, and the value of the curvature at the minimum gives the Young's modulus of a nanowire, E_Y, i.e., [94]:

$$\sigma_{zz}(\varepsilon_{zz}) = \frac{1}{V_{SC}} \frac{\partial E_{tot}}{\partial \varepsilon_{zz}}, \tag{5.8}$$

$$\sigma_{zz}(\varepsilon_{zz-eq}) = 0, \tag{5.9}$$

$$E_Y = \frac{1}{V_{SC}} \frac{\partial^2 E_{tot}}{\partial \varepsilon_{zz}^2}|_{\varepsilon_{zz-eq}}, \tag{5.10}$$

where V_{SC} is the optimized volume of a NW supercell and E_{tot} is its calculated total energy. The equilibrium length of the NW supercell, L_{eq}, can be determined from the values of ε_{zz-eq} and L_0:

$$L_{eq} = L_0(1 + \varepsilon_{zz-eq}). \tag{5.11}$$

Equations (5.8–5.10) do not contain a surface shell and the internal core components of the NW Young's modulus E_Y as well as the axial stress zz as was considered in (5.6–5.7) within the approach of continuum mechanics (Fig. 5.38). As to the surface shell of H-terminated Si NWs, it consists of two sub-regions with two types of interactions: (*i*) the extrinsic surface H-H repulsions between the adjacent hydrogen adatoms, (*ii*) the intrinsic surface stress which is rather small since the dangling Si bonds are well terminated with H atoms while the Si-Si bond order is not significantly different from that in the bulk and the NW core. The extrinsic stress on the {100} facets quantitatively accounts for both the compressive residual stress $\sigma_{zz}(L_0)$ and the elongated equilibrium length L_{eq}. As a result, they were related to the leading order through the NW elasticity [94]:

$$\sigma_{zz}(\varepsilon_{zz}) = \sigma_{zz}(core) + \frac{1}{A}\sum_i \tau^{(i)}{}_{zz} w_i, \tag{5.12}$$

$$\sigma_{zz}(core) = \frac{8C_{12}\tau^{\{100\}}}{\pi d_{\mathrm{NW}}(C_{11}+C_{12})}, \tag{5.13}$$

$$E_Y^{core} = \frac{L_{eq}\sigma_{zz}(L_0)}{L_{eq}-L_0}, \tag{5.14}$$

where the axial stress in the core, $\sigma_{zz}(core)$, was averaged across the nanowire, A is the cross-sectional area (Fig. 5.38), while $\tau_{zz}^{(i)}$, $\tau^{\{100\}}$ and w_i are the longitudinal surface stress of the facets i in (5.12) and {100} in (5.13) as well as their widths, respectively. C_{11} and C_{12} are the elastic constants of Si bulk. Equation (5.14) is written in harmonic approximation since the strains are small. The surface shell contribution to the NW Young's modulus was determined mainly by H-H repulsions:

$$\Delta E_Y^{\mathrm{H-H}} = \frac{1}{A}\sum_i S_{11}^{\mathrm{H-H}} w_i^{\{100\}}, \tag{5.15}$$

where $S_{11}^{\mathrm{H-H}}$ is the extrinsic contribution to the surface elastic constant S_{11} from the H-H interaction, which could be approximately defined by the expression [94]:

$$S_{11}^{\mathrm{H-H}} \approx \frac{C_{11}}{\sqrt{2}A^{\mathrm{H-H}}(C_{11}+C_{12})}\frac{\partial^2 E_{tot}^{\mathrm{H-H}}}{\partial \varepsilon_{zz}^2}, \tag{5.16}$$

where $A^{\mathrm{H-H}}$ is the area covered by one silane group SiH_2 while $E_{tot}^{\mathrm{H-H}}$ is the contribution of the H-H bond to the total calculated energy of the nanowire.

Figure 5.40 shows that $E_Y(d_{\mathrm{NW}})$ curve is qualitatively well described by both the continuum model considered above and using ab initio calculations of atomistic models (Fig. 5.39). The Young's modulus becomes softer monotonically with the reduced size [94] dropping from the bulk value roughly in proportion to the ratio of surface area versus. volume. It does not exhibit a strong dependence on the ratio of the {100} to {110} area seen in the equilibrium length. The smallest Young's modulus was found for any of the nanowires studied (29.4 GPa), which corresponded to the thinnest 0.61 nm Si NW. Since the shapes were set different, direct comparison is rather challenging, however, the experimental stress-strain curve is complex. As to the cross-sectional elastic Si NW deformations, well visible in a lower part of Fig. 5.39 (for larger nanowire diameters), their description is done for AlN NWs (as considered in Sect. 6.6.3).

5.3.5 *Prismatic and Circular-Type Ge Nanowires*

Irrespective of structural proximity of Ge and Si single crystals (Fig. 5.1), each of them possesses some specific features. For example, germanium has a few

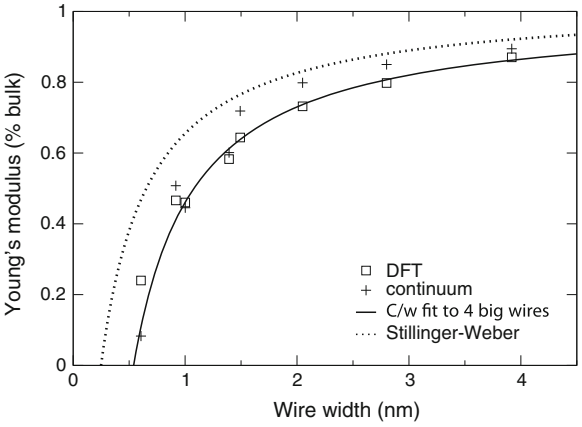

Fig. 5.40 Young's modulus for Si NWs as a function of NW width, w (Fig. 5.39), calculated using different methods enumerated in inset. The surface elastic constants were obtained from the {100}-canted slabs and the {110} slabs. The *solid curve* $E_Y = E_Y^{bulk} - C/w$, with $C = 66.1$ GPa/nm and $E_Y^{bulk} = 122.5$ GPa, was found to be the best fit for pure surface area to volume size dependence [94]

advantages over silicon for some electronic applications, such as higher intrinsic carrier concentration and mobility, larger excitonic Bohr radii and stronger quantum-confinement effects [107]. Although the whole range of Ge applications is still essentially smaller than that for Si, both synthesis and experimental studies of Ge nanostructures, first of all nanowires, attract significant interest [108–113]. To synthesize Ge NWs, the same methods of Si NWs growth were applied, as shortly described in Sect. 5.3.1, e.g., laser ablation, low-temperature CVD, vapor-liquid-solid synthesis, etc. Theoretical studies on Ge NWs, including simulations of their equilibrium geometry, electronic, elastic, optical and thermal properties depending on the initial structural parameters of a nanowire (diameter, orientation and shape) [88, 91, 95, 107, 114–120], have been found to be relatively scarce as compared to their silicon counterparts considered in the previous Subsections. A few studies included comparative analysis of the calculated properties for silicon and germanium nanowires of the similar geometry [88, 91, 95]. First principles methods were mainly applied for the corresponding calculations, either DFT-LCAO [88] or DFT-PW within both LDA and GGA approaches [91, 95, 107, 114–120]. Four energetically stable low-index nanowire orientations ([001], [110], [111] and [112]) have been considered so far in theoretical studies of Ge NWs, analogically to Si NWs (Fig. 5.24). Figure 5.41 represents the optimized structures of [001]-, [110]- and [111]-oriented H-terminated Ge nanowires possessing two different diameters each (∼2 and ∼3 nm, respectively) [118]. The optimized structures of NWs were kept highly symmetric, without significant surface reconstruction, due to the passivation of the dangling bonds by H atoms. According to Fig. 5.41, NW surface atoms relaxed more than those atoms closer to the center. The bond lengths between Ge atoms at the surface were relaxed by ∼1 %, whereas practically no relaxation

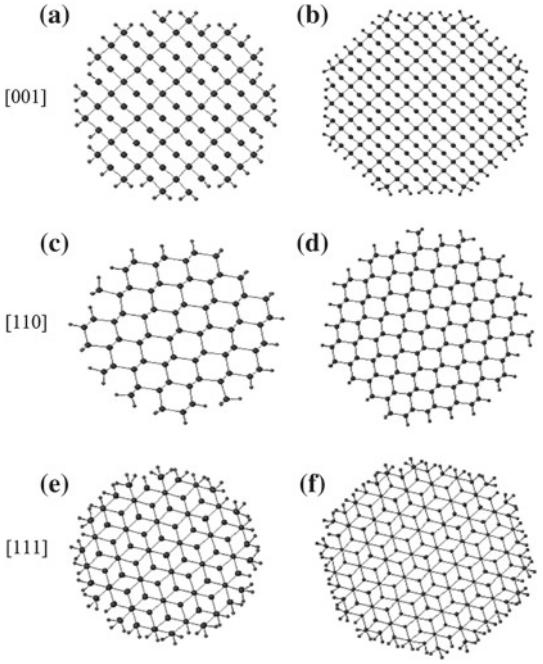

Fig. 5.41 Across images of the relaxed Ge NWs of different thicknesses and orientations: **a** $d_{[001]-\mathrm{NW(89Ge44H)}} \approx 2.03\,\mathrm{nm}$, **b** $d_{[001]-\mathrm{NW(185Ge60H)}} \approx 3.03\,\mathrm{nm}$, **c** $d_{[110]-\mathrm{NW(69Ge32H)}} \approx 2.12\,\mathrm{nm}$, **d** $d_{[110]-\mathrm{NW(133Ge40H)}} \approx 3.30\,\mathrm{nm}$, **e** $d_{[111]-\mathrm{NW(170Ge66H)}} \approx 2.11\,\mathrm{nm}$, **f** $d_{[111]-\mathrm{NW(326Ge90H)}} \approx 3.03\,\mathrm{nm}$ (brackets contain numbers of Ge and H atoms *per* NW unit cells). External small *circles* represent H atoms used to saturate NW dangling bonds. Local structural patterns depend on orientations of the nanowire axis: *square*-type shapes for [001], hexagonal for [110] and parallelograms for [111] orientations [118]

was observed for atoms in the interior region. Cross sections of [110]-oriented Ge NWs were found to be circular-type for all diameters while [001] and [111]-oriented nanowires possessed circular cross sections for $d_{\mathrm{NW}} < d_c$ only. The critical value of d_c, above which nanowire cross section acquired a faceted shape, lied in the range of $2.0\,\mathrm{nm} < d_c < 3.0\,\mathrm{nm}$ for [001] and [111] NW orientations. The value of d_c was determined by the competition to lower the total energy between the energies of the different exposed facets of H-terminated Ge, under the constraint of a fixed volume along the [001] direction (Fig. 5.41) to have a rectangular bonding geometry rather than the expected square surface arrangement of atoms in a single (001) surface layer [118] since the latter in a diamond-type lattice was not formed by the nearest neighboring atoms (Fig. 5.41a). The rectangular structure arose because the middle atoms (along the longer side of the rectangle) were the nearest neighbors of the top layer atoms (one layer below the top layer). For $d_{\mathrm{NW}} > 2.15\,\mathrm{nm}$ [001]-oriented nanowires, their cross sections were found to be octagonally-shaped with the {100} and {110} facets normal to the [001] axis (Fig. 5.41b). [111]-oriented

Ge NWs with $d_{NW} > 2.11$ nm were found to be hexagonally-shaped with {110} facets normal to the [111] axis (Fig. 5.41f). Due to the different atomic densities in different facets, in the case of a fixed diameter, [111]-oriented nanowires possess a larger number of atoms compared to [001]-oriented NWs, which, in turn, have a larger number of atoms compared to [110]-oriented NWs. The surface energies calculated for Ge NWs reflected the relative energy contributions of the exposed facets to the total NW energy [118]. Moreover, the energy per Ge atom in any NW decreased with the increasing diameter and approached the energy of the perfect Ge bulk *per* atom.

The electronic band structures of the relaxed germanium nanowires (Fig. 5.41) were calculated from $\Gamma(0,0,0)$ point to $X(0,0,2\pi/l_{NW})$ along one of the three considered NW axes where l_{NW} is the unit cell length. Figure 5.42 shows the NW band structures over half this range for all six NW types shown in Fig. 5.41 [118]. Obviously, the dispersion of the valence band (VB) for approximately the same values of d_{NW} is the greatest for [110]-oriented and the smallest for [111]-oriented nanowires. As expected from the quantum size effect, the absolute value of the VB maximum decreases in energy and the absolute value of the conduction band (CB) minimum increases in energy as the NW thickness (d_{NW}) decreases. Analogically to Si NWs, This also leads to the increase of the electronic band gap $\Delta\varepsilon_{gap}$ with the decreasing d_{NW}. The band gap could be either direct or indirect, depending on the

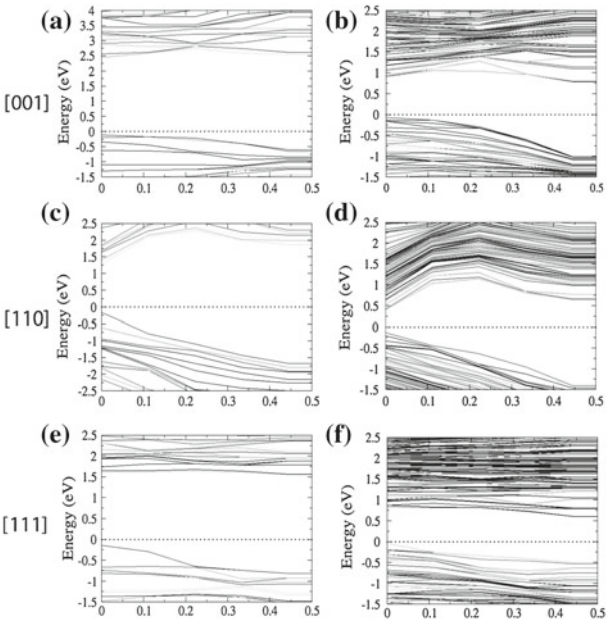

Fig. 5.42 The band structures of Ge NWs for [001] (**a, b**), [110] (**c, d**) and [111] (**e, f**) nanowire orientations. The Fermi level in each panel is set to zero being shown by the *dotted line*. Each band structure corresponds to the NW configuration of H-terminated Ge NWs described under the same label in Fig. 5.41 [118]

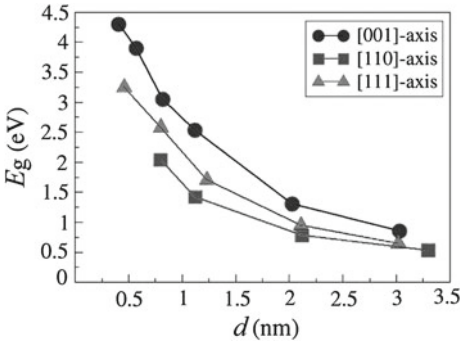

Fig. 5.43 Three *curves* of $\Delta\varepsilon_{gap}(d_{\mathrm{NW}})$ for three orientations of Ge NWs [118]

crystallographic orientation and the Ge NW diameter. It was found that all the gaps of [110]-oriented NWs were direct at Γ point (Fig. 5.42), the same as those of [001]-oriented NWs with $d_{\mathrm{NW}} < 1.3$ nm, which are quite suitable for applications in optics. In contrast, all the gaps of [111]-oriented NWs were found to be indirect, the same as those of [001]-oriented NWs with $d_{\mathrm{NW}} > 1.3$ nm [118]. Analogous qualitative conclusions were drawn for band gaps of the unrelaxed H-terminated Ge NWs [114].

Figure 5.43 shows the plot of $\Delta\varepsilon_{gap}(d_{\mathrm{NW}})$, which clearly depicts that the band gap depends on both the thickness of a Ge NW and its orientation. Among the band structures of Ge NWs the largest value of $\Delta\varepsilon_{gap}$ (4.3 eV), calculated using DFT-LCAO method, was found for an ultrathin [001]-oriented nanowire with thickness 0.41 nm (Fig. 5.43) consisting of 5 Ge and 12 H atoms per NW UC [118]. According to $\Delta\varepsilon_{gap}(d_{\mathrm{NW}})$ plots, the band gaps approach 0.4 eV with the value of d_{NW} increasing until the infinity, which corresponds to that of germanium bulk (the experimental values for Ge and Si bulk at 0 K were found to be 0.74 eV versus 1.17 eV, respectively [121], while at 300 K they decreased to 0.66 and 1.11 eV, respectively). The largest and smallest band gaps for the same value of d_{NW} correspond to [001]- and [110]-oriented NWs, respectively (Fig. 5.43).

Certain differences in the behavior of $\Delta\varepsilon_{gap}(d_{\mathrm{NW}})$ were found for nanowires of Ge as compared to those of Si. For example, unlike [111]-oriented Ge NWs possessing indirect band gaps (Fig. 5.42e, f), the same orientation of Si NWs was characterized by direct band gaps at Γ point for $d_{\mathrm{NW}} < 2.2$ nm [118]. The comparison of the band structures for [110]-oriented defective Ge and Si NWs calculated using the DFT-LCAO method [88] showed an essentially thicker band gap for the latter (Fig. 5.44). Both band structures were identical to those of the perfect nanowires, except for the appearance of a half-occupied band in the gap due to the absence of one H atom *per* UC. The dispersion of this band was found to be larger for Ge NWs (0.09 eV vs. 0.03 eV for Si NW [88]).

The parameters of the atomic and electronic structure for [112]-oriented H-terminated Ge NWs of different thicknesses with rectangular shapes of cross sections were obtained using the DFT-GGA plane wave calculations [107]. To classify those Ge NWs of different sizes, the notation A_nB_m was used (Fig. 5.45) where the labels

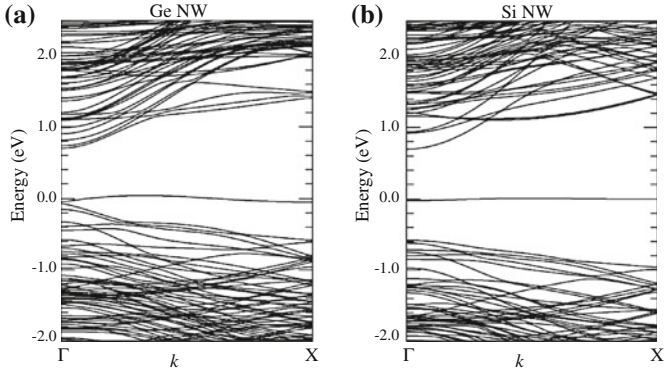

Fig. 5.44 Electronic band structures of Ge (**a**) and Si (**b**) [110]-oriented nanowires ($d_{NW} \approx 2.0$ nm) with one surface dangling bond defect (absence of one H atom above NW) per unit cell [88]

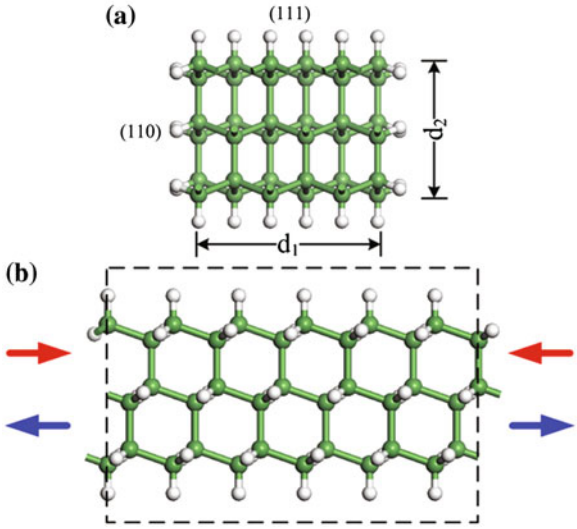

Fig. 5.45 Top (**a**) and lateral (**b**) views of [112]-oriented H-terminated Ge NW (A_3B_6) under possible uniaxial strains (shown by *arrows*) (Reprinted figure with permission from Zhang et al. [107], Copyright (2012) by the IOP Publishing)

A and B represented the {111} and {110} facets respectively, while the numbers n and m denoted the numbers of grids in the projected view. For example, an A_3B_6 configuration consisted of three (111) and six (110) planes, as shown in Fig. 5.45a. In each nanowire, the core contained solely Ge atoms in a quasi-single crystal along the [112] direction, while the surface dangling bonds were passivated by H atoms forming the external shell. Two parameters were defined to characterize the configuration of each NW: the cross-sectional area ($d_1 \times d_2$) along the [112] axis and the cross-sectional aspect ratio (d_1/d_2) of the {111} to the {110} facet, where d_1 and

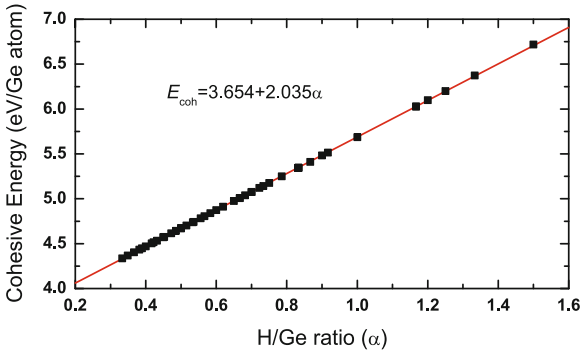

Fig. 5.46 Cohesive energy of H-terminated [112]-oriented Ge Ns as a function of $\alpha = n_H/n_{Ge}$ ratio (Reprinted figure with permission from Zhang et al. [107], Copyright (2012) by the IOP Publishing)

d_2 are shown in Fig. 5.45a. The uniaxial tensile and compressive strains were taken into consideration by changing the axial lattice constant of the nanowire, as shown in Fig. 5.45b. The relative axial lattice constants were varied in the range extending from −3 %(compression) to 3 %(expansion). A 3 %-strain could be experimentally realized because experiments measured a maximum yield strength corresponding to about 13 % strain in Ge NWs [122]. After changing the axial lattice constant, all the atoms were relaxed to their equilibrium positions using the conjugate gradient method [107]. To calculate the electronic properties of different Ge NWs oriented along the [112] axis, their optimized geometries were used.

To estimate the influence of external hydrogen atoms on the stability of H-terminated [112]-oriented Ge NWs, the cohesive energy of a NW *per* Ge atom was defined [107]:

$$E_{coh} = [n_{Ge}E_{Ge} + n_H E_H - E_{tot}]/n_{Ge} = 2E_{Ge-Ge} - \alpha(0.5E_{Ge-Ge} - E_{Ge-H}), \tag{5.17}$$

where E_{tot} is the total energy of a nanowire, E_{Ge} and E_H are the energies of isolated Ge and H atoms, respectively, n_{Ge} and n_H their numbers *per* UC, E_{Ge-Ge} and E_{Ge-H} are the energies of Ge-Ge and Ge-H bonds, respectively, while $\alpha = n_H/n_{Ge}$. Obviously, the cohesive energy clearly shows a linear relationship in relation to α (Fig. 5.46). Through a linear fitting of the calculated cohesive energy, its dependence on α was expressed as $E_{coh} = 3.654 + 2.035\alpha$ [107]. This linear function coincided with the earlier proposed model for the stability of H-terminated Si nanostructures, in which the ratio between the number of H and Si atoms was determined to be a universal predictor of the energetic stability [123]. Based on the calculations of E_{Ge-Ge} and E_{Ge-H}, the slope was found to be 2.096, which agreed well with the fitted value (2.035) [107]. According to Fig. 5.46, the cohesive energy *per* Ge atom linearly decreased with the n_H/n_{Ge} ratio. A simple algebraic deduction allowed predicting that when the number of Ge atoms was fixed, the number of H atoms should correspond those in a more stable structure for [112]-oriented Ge NW, i.e., A_2B_4 ($\alpha = 1$, $s_{NW} = 0.25\,nm^2$), A_3B_6 ($\alpha = 2/3$, $s_{NW} = 0.75\,nm^2$) (Fig. 5.45), A_4B_8 ($\alpha = 1/2$, $s_{NW} = 1.53\,nm^2$), etc. [107].

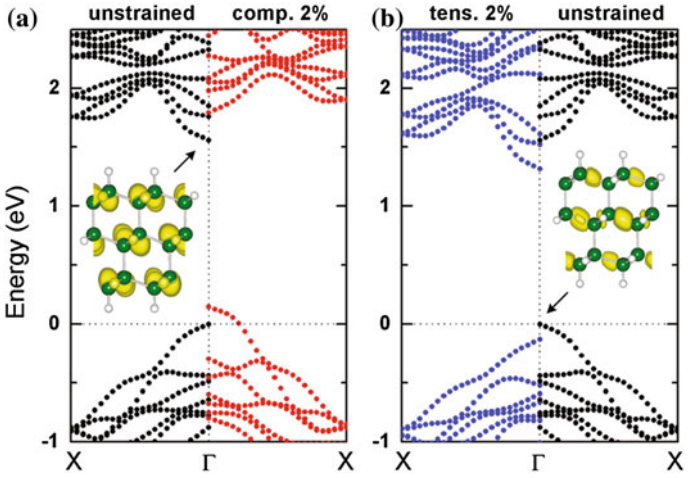

Fig. 5.47 Band structures of A_3B_6-type [112]-oriented H-terminated Ge NW: **a** unstrained and 2 % compressive strain (*red*) and **b** 2 % tensile strain (*blue*) and unstrained. The VB of unstrained nanowire was set to zero. Inset: isosurfaces of the electron density for the CB (*left*) and the VB (*right*), which correspond to 25 % of the maximum density. The *large* and *small spheres* show Ge and H atoms, respectively (Reprinted figure with permission from Zhang et al. [107], Copyright (2012) by the IOP Publishing)

To study the equilibrium properties of A_nB_{2n} shaped [112]-oriented Ge NWs under strain, the axial lattice constant l_{NW} (along the z direction) was first optimized, depending on the varied cross sectional area s_{NW}. Under the applied strain, the band gap of the nanowire decreased or increased as the strain was either tensile or compressive, respectively [107]. Figure 5.47 shows the band structures with strain and without it, under 2 % compressive (tensile) strain. Generally, strain significantly affects both the top of the valence band (VB) and the bottom of the conduction band, as well as the width of the band gap. The different strain dependences of the VB and CB can be explained by the decomposed charge densities, which redistribute the interatomic spaces of the Ge atoms and reflect the bonding character. Under the uniaxial tensile strain of the nanowire, the confining *xy* plane experiences a compressive radial strain, which means that the Ge-Ge bonds projected onto this plane are reduced, resulting in the enhanced Ge-Ge bond strength and stability, and the lowering of energy. Consequently, the energies of both the VB and CB decrease, as shown in Fig. 5.47b. In contrast, the uniaxial compressive strain leads to the expansion of the *xy* plane. The Ge-Ge bond lengths projected onto this plane increase, weakening the bond or increasing the energy. As a result, the energies of both the VB and CB increase (Fig. 5.47a). It explains the general trends for the variation of the energies of the VB and CB under the small external strain [107].

Analogically to the shape-induced transition of the band gap type found in [112]-oriented Si NWs [124], the dependence of the band gap indirect-to-direct transition on the shape of [112]-oriented Ge NW was studied too (Fig. 5.48) [107]. For all the [112]

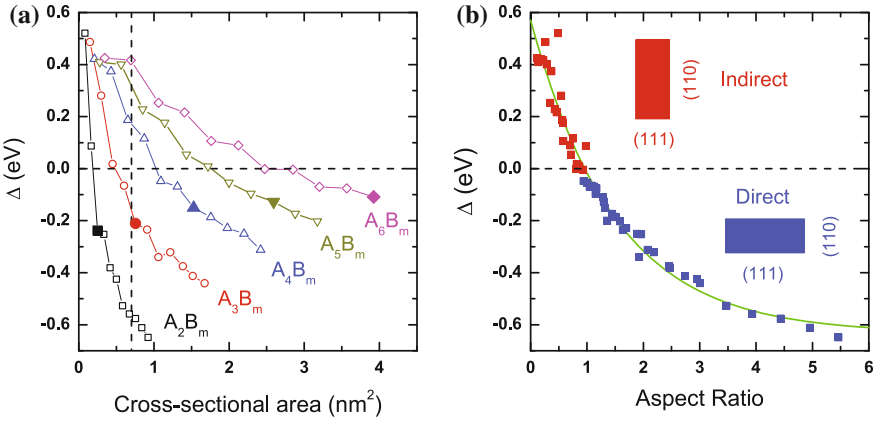

Fig. 5.48 **a** Energy difference (Δ) versus cross-sectional area of [112]-oriented Ge NWs. The filled points denote Δ for A_nB_{2n} type of Ge NWs. **b** Δ versus the cross-sectional aspect ratio of the {111} to the {110} side facets. The *shaded rectangles* represent the cross-sections of [112]-oriented Ge NWs. The *horizontal line* at zero is a reference level to indicate the demarcation between direct and indirect band dispersions or gaps. The *vertical line* denotes the cross-sectional area of 0.7 nm^2 (Reprinted figure with permission from Zhang et al. [107], Copyright (2012) by the IOP Publishing)

Ge NWs studied there, the top of the VB was always located at the Γ point, whereas the bottom of the CB was either located at the Γ point (Fig. 5.47) or somewhere between Γ and X points. For the description of the possible shape-induced band gap transition, the difference between the indirect and direct band dispersion Δ was introduced by defining it as the energy difference between the energy of the CB edges at the Γ and the energy of the CB minimum at the k point near or at the X point. As a result, a positive represents an indirect band gap, whereas a negative implies a direct band gap. For each curve in Fig. 5.48a, the {111} facet of Ge NWs was kept fixed while the {110} facet was treated as a variable. Obviously, each curve intersects the $\Delta = 0$ line, thus indicating that all of the five series of [112]-oriented Ge NWs experience an indirect-to-direct transition with the increasing NW thickness [107]. To reveal the relationship between the NW shape and the band gap type, the dependence of Δ on the cross-sectional aspect ratio is shown in Fig. 5.48b. The data points imaged there fall on a single curve, which was fitted to an exponential function, and decreases with the increase in the aspect ratio of the {111} to the {110} side facet (which is in contrast to the case for [112]-oriented Si NWs [124]). This indicates that the variation of Δ with the aspect ratio is independent of the Ge NW thickness. Thus, the electronic band structure of [112]-oriented Ge NWs can be simply tuned by increasing the {111} facets. Moreover, the energetically stable configurations of A_nB_{2n} considered above exhibit direct band gap characteristics, which can be useful for the application of Ge NWs in different optoelectronic devices [107].

5.4 Silicon Carbide and Germanium Silicide Bulk and Nanolayers

Silicon monocarbide (SiC) is one of the hardest materials suitable for electronic devices designed for operations in extreme environments [125]. Because of high thermal conductivity and stability, chemical resistivity, excellent mechanical properties, high refractive index and radiation resistance, SiC is widely applied in modern technology, e.g., for the use in high temperatures and radiation environments. The unique properties of SiC bulk, along with the properties arisen due to quantum size effects, are also reflected in SiC nanostructures (e.g., nanotubes). Indeed, the possibilities and promises abound for SiC nanostructures make them applicable for nanosensors and nanodevices which can be operated at high temperatures, frequencies and powers.

Not only Si and Ge but also SiC and GeC crystals possess considerable energy differences between sp^2 and sp^3 bonds which suppress stability of hexagonal phase typical for graphite bulk [126]. Thus, the crystals of Si (Ge) monocarbides can be attributed to the cubic diamond-type structure (Fig. 5.1a) or hexagonal wurtzite-type structure (Fig. 5.1c), as mentioned above, where a half of Si (Ge) atoms are substituted by C atoms in positions of the nearest neighbors. while the symmetry of the simplest hexagonal SiC (GeSi) structure can be described by the same space group as that of pure silicon or germanium ($P6_3mc$), being attributed to the wurtzite type of crystalline lattice. For the cubic SiC (GeSi) structure, the symmetry is different from that of d-Si (*cf.* $F\overline{4}3m$ and $Fd\overline{3}m$, respectively), due to the absence of inversion operations. The nomenclature name of this cubic structure is sphalerite (or zinc-blende). One of the aspects making SiC fascinating from a fundamental point of view is that it is not a simple single-crystal but a whole class of structures, due to polytypism [127]. In other words, 1D polymorphism, which provides a different stacking of the basic structural elements, e.g., (111) sphalerite and (0001) wurtzite faces, is not observed in silicon bulk were stacking is strictly determined (Fig. 5.2). More than 200 SiC polytypes have been reported so far [125] although only few of them are of practical importance (Fig. 5.49). There are mainly hexagonal α-polytypes (2H-SiC, which corresponds to a wurtzite phase shown in Fig. 5.2b, with *ABABAB* stacking, and more complicated 4H- and 6H-SiC possessing *ABCBAB* and *ABCACB* stackings, respectively) as well as cubic β-polytypes (first of all this is true for a sphalerite phase 3C-SiC with *ABCABC* stacking, according to Fig. 5.2a)

Obviously the procedure of rolled-up nanotube generation described in Sect. 5.2.1 can be applied for the construction of SiC nanotubes as well. For this purpose, the simplest SiC polytypes are usually chosen, i.e., 2H and 3C [129], which give identical hexagonal morphology for a single-layer (0001) and (111) nanolayers, respectively (Fig. 5.2). The main difference of silicon monocarbide from silicon is that the carbon atoms stabilize both SiC nanolayers and nanotubes, due to some charge transfer from Si to C (which was found to be different when using different calculation methods and models, cf. 0.3 e [130] and 0.6 e [131]). The electronic charge transfer from Ge to Si atom in germanium silicide is much smaller than that from Si to C atom in SiC (i.e., 0.09 e versus 0.40 e, respectively, according

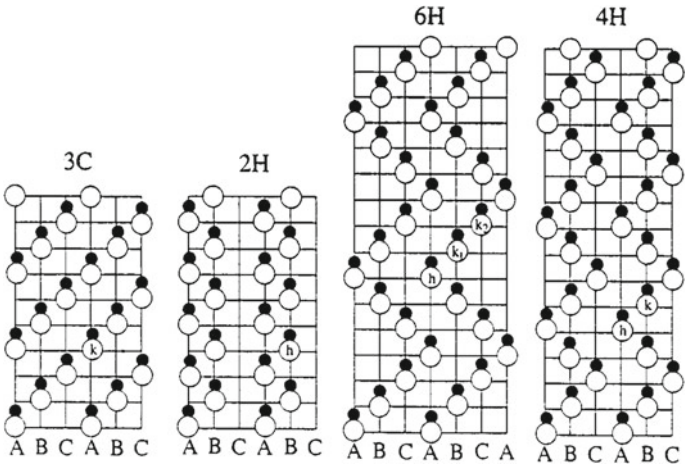

Fig. 5.49 Distribution of Si (*open circles*) and C (*filled circles*) atoms in the polytypes 3*C*, 2*H*, 6*H* and 4*H*. Letters inside *open circles* indicate types of non-equivalent sites ("k" denote *cubic* while "h" *hexagonal* sites) [128]

to LMTO estimate of ionicity in crystals of binary tetralides [132]). Thus, contrary to pure silicon less-dimensional structures, no special stabilizing H-passivation is necessary for SiC and partly for GeSi, although slightly charged and shifted Si (Ge) atoms are quite attractive for H adsorption making SiC (GeSi) nanostructures good candidates for hydrogen storage as compared to those of carbon. Moreover, SiC nanotubes are expected to have some advantages over CNTs because they possess highly reactive exterior surface facilitating sidewall decoration as well as stability at high temperatures. Different techniques, e.g., substitution reactions with Si atoms replacing C atoms attributed to MW CNTs, high-temperature reactions between silicon powders and multi-walled carbon nanotubes as well as between CH_4 with SiO, sputtering of polymer nanofibers upon silicon wafers, *etc.*, were employed for the synthesis of SiC NTs [133–138]. A series of theoretical simulations on SiC and GeSi nanolayers and nanotubes of different morphologies, e.g., SW and DW NTs, as well as SW NT bundles were performed for both infinite 1D models [129, 130, 139–146] and finite open-shell edge-passivated nanotubules [131, 139, 147–150]. Their calculations were performed using the PW DFT methods within both LDA and GGA approaches [130, 141–144, 146], the LCAO-DFT and LCAO-hybrid HF-DFT methods [129, 131, 139, 140, 147–150], the semi-empirical TB methods [139, 145] and methods of molecular dynamics [129, 139, 146].

Two types of infinite 2D SiC nanolayers (initially planar), optimized using the tight-binding method [139], are shown in Fig. 5.50. Both types correspond to Si to C ratio of 1:1. The hexagonal network consists of alternating Si and C atoms (Fig. 5.50a) where each silicon atom is surrounded by the nearest C neighbors and vice versa as considered above. This is type-1 of SiC graphene-like nanolayer. In the alternative atomic configuration of nanolayer (containing periodically distributed Si-Si dimers), the nearest neighbors of each Si atom are two C atoms and another Si atom as shown

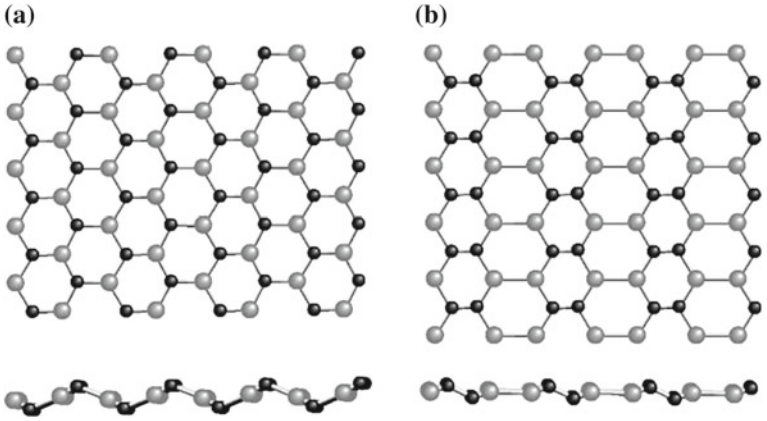

Fig. 5.50 Type-1 (**a**) and type-2 (**b**) SiC nanolayers with Si to C ratio of 1:1 obtained after structural relaxation of initial silicene-shaped monolayers. The surface reconstruction results in the appearance of nanolayer buckling. The *top* and *bottom* panels in (a) and (b) show *top* and side views of both nanolayers, respectively. In both configurations, Si atoms (colored as *grey*) are located in a single plane, while C atoms (*black*) are displaced above and below this *plane* [139]

in Fig. 5.50b. This is type-2 of SiC nanolayer. As it is seen in both bottom panels, the optimized structures exhibit rather wavelike or buckled features where all Si atoms are coplanar and C atoms are shifted up and down.

Ab initio TBMD calculations performed on various SiC nanolayers [139] show a noticeably higher energetic stability of type-1 structures as compared to those of type-2 (by 0.43 eV *per* Si C bond). On the other hand, a nanolayer of structural type-1 is essentially more rumpled as compared to that of type-2. In addition to these types of SiC nanolayers, type-3 of the surface structure has been considered [147, 148], which is equivalent in its non-relaxed form to type-2, since it contains one atom of the same kind (either C or Si) amongst the nearest neighbors. The difference between both structural types is determined by orientation of either C-C or Si-Si bonds relatively to the vector of potential wrapping that coincides with the vertical direction in Fig. 5.51. The cohesion energies *per* atom for type-2 and type-3 structures

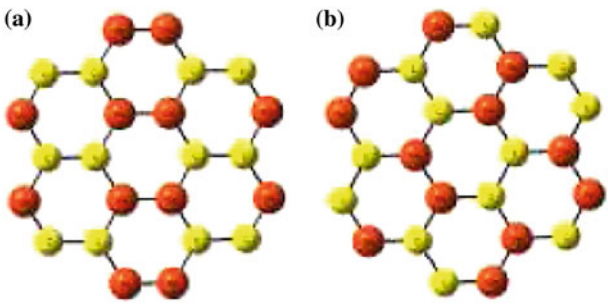

Fig. 5.51 *Top* views of non-relaxed SiC nanolayer fragments with atomic arrangements according to structural type-2 (**a**) and type-3 (**b**). Si and C atoms are colored as *grey* and *black*, respectively [148]

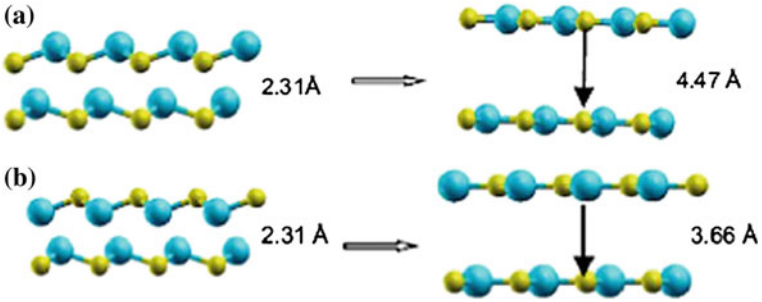

Fig. 5.52 Cross-section views of graphitic-like SiC bilayer with type-1 structure (Fig. 5.50a) before and after relaxation with two different stackings. **a** C-C (*top panel*) and **b** Si-C (*bottom panel*). C and Si atoms are shown as small *light* and large *dark balls*, respectively. Both types of orderings are indicated by the *vertical arrows* in the *right* column [130]

of SiC nanolayers have also been found to show close parameters (with the energy difference ∼0.01–0.02 eV) but noticeably smaller than those for type-1 (by ∼0.18–0.19 eV) [148]. This is the reason why more symmetric type-1 structures of binary compounds are mainly considered for simulation of SiC nanolayers and nanotubes (not speaking about ionic-covalent BN nanolayers and NTs which are described in Sects. 6.1 and 6.2, respectively). GeSi nanosystems with smaller polarity and energy difference between three structural types are discussed in Sect. 5.5.5. Obviously, the interaction between the adjacent nanolayers (Fig. 5.50) of multi-layer SiC sheet depends on their mutual orientation. The optimized interlayer spacing of flattened SiC graphitic-like multi-layer sheets has been found to depend on the ordering of atoms in different nanolayers of the honeycomb structure, for example, in the case of SiC double-layer [130] as shown in Fig. 5.52. Interlayer separations were found to be ∼3.7 Å for Si-C sequence of bilayer stacking versus ∼4.5 Å for Si-Si or C-C sequences of bilayer stacking. This is noticeably larger than the corresponding separation between the nearest honeycomb monolayers in graphite and multi-layer CNTs (∼3.4 Å [151]). Primarily buckled multi-layered structures were composed as in distorted graphite (left panels of Fig. 5.52) not as in either β-SiC bulk along the (111) direction or α-SiC bulk along the (0001) direction, respectively (Fig. 5.2), where the interlayer interaction is too strong to provide the formation of a flattened multi-layer structure. Calculations of hexagonal graphitic-like bilayers with type-1 morphology [130], on the contrary, indicate that the flattened multi-layer SiC structure can be obtained after optimization, with the interlayer spacing larger than initially (Fig. 5.52), which can be attributed to the interlayer Coulomb interaction caused by a slight charge redistribution between the nearest atoms positioned in the opposite nanolayers. An attractive Si-C interatomic ordering (Fig. 5.52b) favors to a more stable bilayer structure with a smaller separation between the flattened layers [130]. On the contrary, a repulsive C-C or Si-Si ordering (Fig. 5.52a) noticeably increases the interlayer spacing inside SiC bilayer and slightly reduces its stability (as follows from the energy curves shown in Fig. 5.58).

5.5 Silicon Carbide and Germanium Silicide Nanotubes

5.5.1 Rolled-Up and Polyhedral Single-Wall SiC Nanotubes

Single-wall silicon carbide nanotubes of different chiralities and diameters with the Si/C ratio of 1 can be constructed by rolling up type-1, type-2 and type-3 silicene monolayers (Figs. 5.50 and 5.51) using both infinite 1D models and finite 0D models of open-shell nanotubules with H-passivated edges. However, only rolled-up NTs of type-1 are surveyed for SiC, due to their noticeable energetic preferences over two other types of SiC nanotube morphologies [139, 147, 148, 150].

The sizes of SW SiC NTs described using the standard chiral vector notation (*n,m*), as applied for hexagonal rolled-up NTs, were chosen in [139] to be (6,6) and (12,0) for *ac*- and *zz*-chiralities, respectively (Fig. 5.53), possessing diameters 10.4 and 12.0 Å. The optimized structure of these NTs consists of two slightly separated concentric cylinders with positively charged Si atoms forming the inner shell and negatively charged C atoms forming the outer shell (this is a typical NT buckling which is determined by a difference between radii of the corresponding shells; the larger is the NT diameter, the smaller is the buckling [146]). The total energy optimization revealed the (6,6) SiC NT to be slightly more stable than the (12,0) SiC NT (by 0.05 eV *per* Si-C bond [139]). The Si-C bond lengths were found to be practically independent on the nanotube chirality and diameter (1.87 Å) [145] being close to arithmetic average of bond lengths in CNTs (1.42 Å [151]) and Si NTs (2.32 Å [12]).

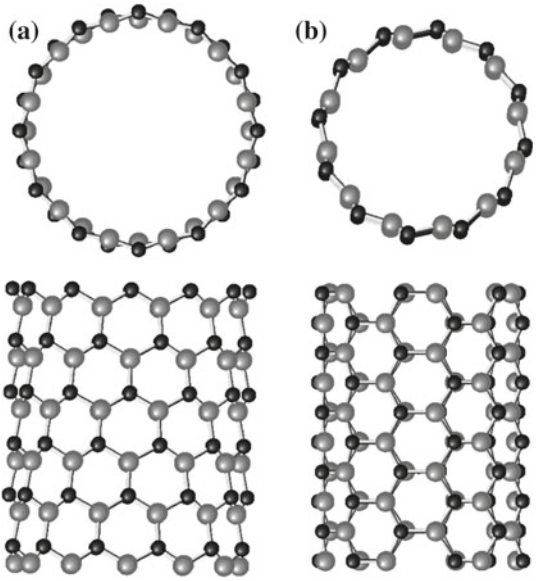

Fig. 5.53 Cross sections and side views of single-wall SiC nanotubes of *zz*- and *ac*-chiralities (**a** and **b**, respectively) obtained by rolling up the type-1 graphene-like sheet (Fig. 5.35a). C and Si atoms are shown as *black* and *grey balls* [139]

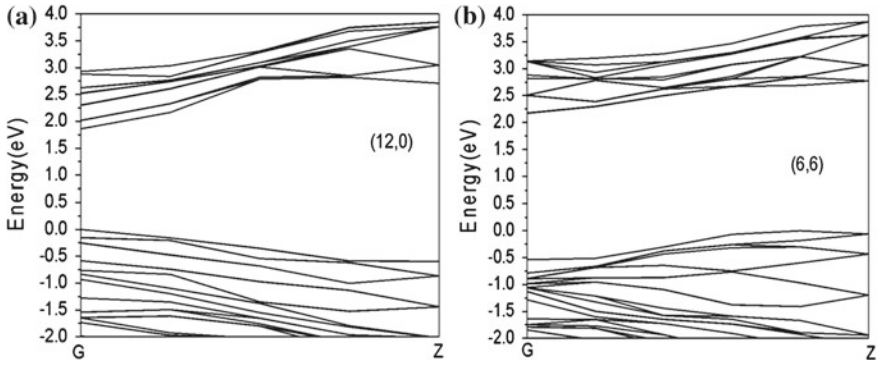

Fig. 5.54 The band structures and the density of states for *zz*-(12,0) (**a**) and *ac*-(6,6) (**b**) chiralities of silicon carbide nanotubes [141]

The band structures for (12,0) and (6,6) SiC NTs calculated using the plane wave DFT-GGA method [141] are plotted in Fig. 5.54, where the top of the valence band (VB) was taken as a reference and set to zero. For both *zz*- and *ac*-NTs, the degeneracy of energy levels at Z(0.5) point of one-dimensional BZ (equivalent to X point considered for NTs in Fig. 5.10) was found to be higher as compared to that at $\Gamma(0)$ point, while the band gaps ($\Delta\epsilon_{gap}$) were either direct or indirect (1.8 eV and 2.2 eV for *zz*- and *ac*-NTs, respectively). The area below the top VB can be divided into two diapasons: (*i*) the bottom of the valence-band region is mainly composed of C(2*s*) states, with a noticeable contribution from the hybrid Si(3*s*,3*p*) states; (*ii*) C(2*p*) states, which were found to be partially overlapped with Si(3*s*,3*p*) states, mainly contribute to the top of the VB region. The lowest conduction bands above the Fermi level mainly consist of Si(3*p*) states. The growth of the SiC NT diameter results in the growth of a band gap and vice versa. Tight binding (TB) calculations of band gaps in these nanotubes [145] showed different trends of their changes within the two sets of NT thicknesses: (*i*) with the decreasing chirality index of *zz*-nanotubes from (20,0) down to ultrathin (4,0) (the diameters of which are reduced from 10.0 to 2.0 Å, respectively) a substantial fall of $\Delta\epsilon_{gap}$ was observed (from 2.16 to 0.57 eV) (*ii*) when chirality indices of *ac*-NTs decreased from (10,10) down to (2,2) (the optimized diameters of which were changed from 8.5 to 1.7 Å, respectively), the band gap was reduced only from 2.12 to 1.83 eV. It means that ultrathin SiC nanotubes with *zz*-chirality can be transformed to conducting, especially in the presence of substitution impurities, while *ac*-NTs always remain semiconducting. A more detailed analysis of ultrathin SiC NT properties was made when performing the DFT-LCAO calculations on nanotubes under uniaxial compression from zigzag to armchair morphology [143] where the chirality index n was changed from 2 to 5 (Fig. 5.55). An unusual fourfold-coordinated nanotube (*H*-type), which corresponds to prismatic rhomboidal NT structures considered above for silicon (Sect. 5.2.4 and Fig. 5.11), possessed a distinct energy minimum along the transformation path $zz \rightarrow ac$. The valence bands of the *H*-type NTs were distinctly different from those of the *zz*- and *ac*-phase nanotubes, due to the stronger ionic character of Si-C bonds

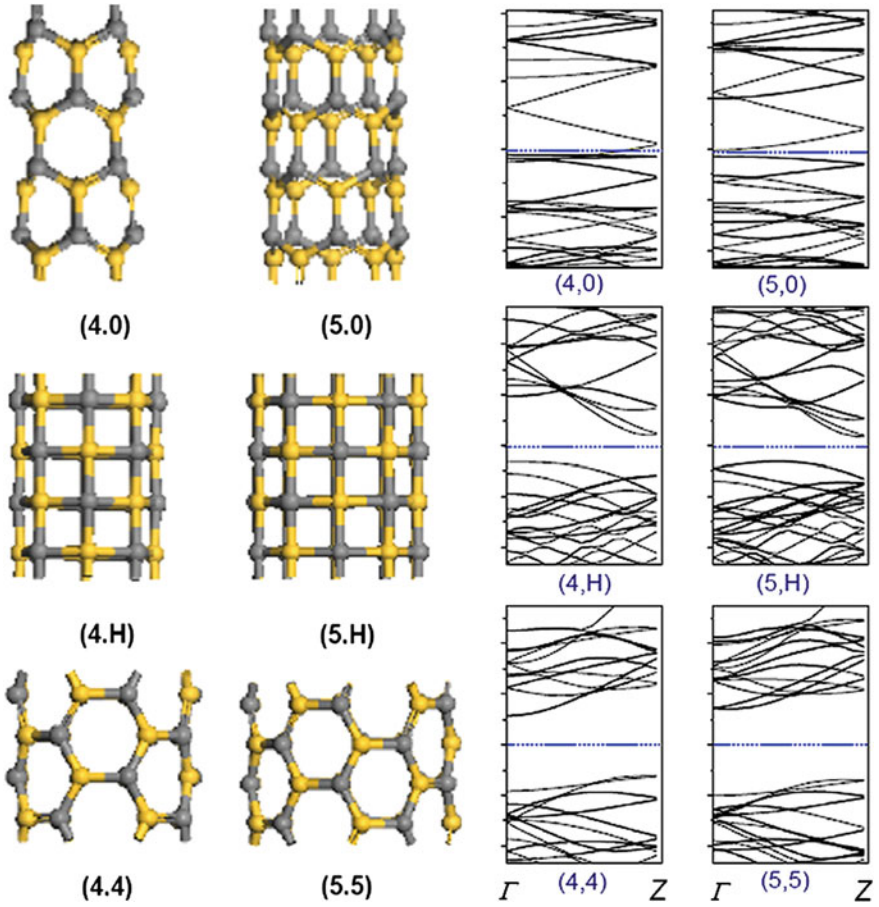

Fig. 5.55 The models (*left panel*) and the corresponding band structures (*right panel*) of ultrathin SiC nanotubes with *zz*-, prismatic rhomboidal (Fig. 5.11) and *ac*-chiralities (*top, middle* and *bottom* parts, respectively). C and Si atoms are shown as *dark* and *light balls*, respectively [143]

possessing four-fold coordination. While in silicon H-type bonding can exist as described above [37], no signs of its presence in CNTs were found [143], which can be understood from the pure covalent bonding in graphene monolayer. Within the considered interval of chirality indices, (2,0), (3,0), (4,0), (5,0), both *ac*- and H-type NTs were identified as semiconducting, with a gradually increasing indirect gap when n grows (widths of the latter are smaller). However, *zz*-type NTs were found to be metallic, with the appearance of ultra-narrow direct gap for $n = 5$ and NTs of a larger diameter (Fig. 5.55). On the other hand, the quasi-conductivity of ultrathin SiC *zz*-NTs, partly confirmed by recent DFT-GGA calculations [130], does not correspond to the results of TB simulations discussed above [145], which can be caused by abreak well-known deficiency of the standard DFT technique, significantly underestimating the band gaps [143].

5.5.2 *Bundles of Rolled-Up Single-Wall SiC Nanotubes*

Parallel with bundles of SW NTs for MgB_2 (Fig. 4.15), AlB_2 (Fig. 4.16) and other inorganic substances, the crystalline bundle structures of SiC SW NTs were simulated as well, using the DFT-LDA method within LAPW approach [142, 144] applied for hexagonal primitive unit cells, containing 12 Si and 12 C atoms for (6,6) NT bundle as well as 16 Si and 16 C atoms for (8,0) NT bundle (Fig. 5.56). Obviously, a nanotube inside a bundle interacts with its nearest neighbors. The values of the total energy per atom for (8,0) and (6,6) SiC NT bundles were found to be lower than for isolated SiC nanotubes, i.e., the former are more stable. The interaction energy of NTs in a bundle *per* atom can be defined as

$$E_{\mathrm{NT-NT}}^{bundle} = E_{\mathrm{NT}}^{bundle} - E_{\mathrm{NT}}^{isolated}, \tag{5.18}$$

where E_{NT}^{bundle} and $E_{\mathrm{NT}}^{isolated}$ are the total energies *per* atom of a selected nanotube in the bundle and isolated from other nanotubes, respectively [142]. The optimized equilibrium inter-shell distances and interaction energies were found to be 3.53 Å and 0.016 eV/atom for (6,6) NT bundle versus 3.48 Å and 0.021 eV/atom for (8,0) NT bundle. For comparison of equilibrium intershell distances and interaction energy of CNT and SiC NT bundles, analogous quantities were also calculated using the same method for (10,0) CNT bundle [142], the corresponding values were found to be 3.07 Å and 0.04 eV/atom. Thus, the intershell interaction in the bundle of *zz*-SiC NTs is weaker as compared to the *zz*-CNT bundle, while the intershell distance in SiC nanotube is large, although both isolated nanotubes have approximately the same diameter. This can be explained by a decreased aromaticity of SiC NT leading to a weak-stacking ability with the neighboring nanotubes in the bundle. The performed calculations also show that the bundling of small radius SiC NTs, e.g., with (8,0) and (6,6) chiralities, only slightly disturbs the geometry of the individual

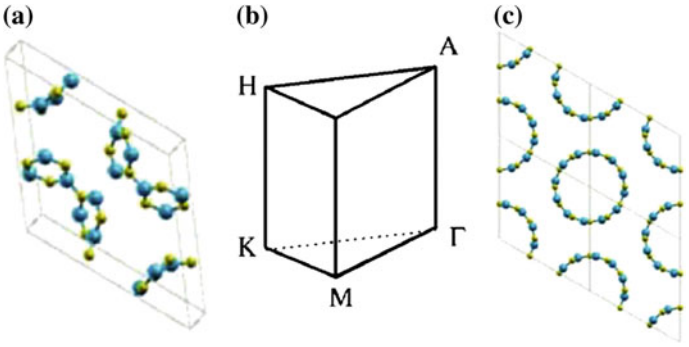

Fig. 5.56 The unit cell of (6,6) SiC NT bundle (**a**), the irreducible part of the *hexagonal* BZ for this bundle (**b**) as well as the cross-section of bundle (**c**). C and Si atoms are shown as small and large balls, respectively. [142]

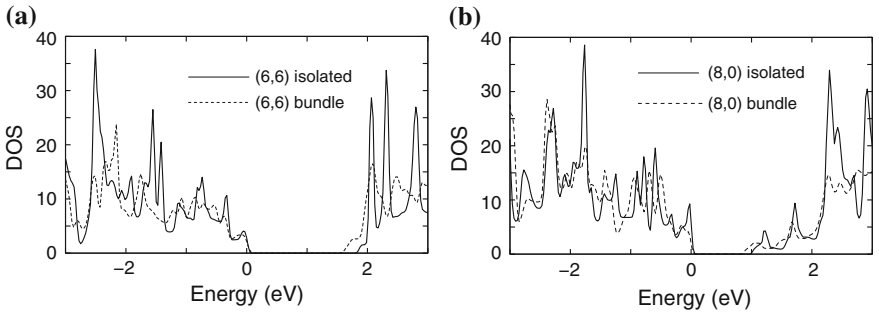

Fig. 5.57 The total densities of states for isolated SiC NTs and bundles with (6,6) (**a**) and (8,0) (**b**) chiralities of nanotubes, respectively [142]

nanotubes and causes almost neglecting radial buckling reduction in them, with an amplitude of ∼0.02 Å [142]. The formation of a crystalline bundle changes also the electronic properties of the constituent nanotubes. For example, intershell interactions in the CNT bundle break the rotational symmetry of nanotubes and give rise to the appearance of a pseudo-gap at the Fermi level [152]. The most remarkable change in SiC NT bundles was found to be the band splitting that occurred in both *ac*- and *zz*-nanotubes [142], i.e., the doubly degenerated states of the isolated (8,0) and (6,6) SiC NTs were splitted into non-degenerated states in the bundles, which resulted in the decrease of band gaps (Fig. 5.57). Moreover, the valence and conduction bands in both nanotubes were significantly expanded too. The interaction between nanotubes in a bundle does not only change the band structure along the NT axis but also causes the dispersion in the plane perpendicular to it. Such a dispersion is larger for (6,6) NT bundles than for (8,0) NT bundles indicating different interactions between the nanotubes in each bundle. As shown in Fig. 5.57a, b, the perpendicular dispersion leads to the total broadening of DOSs in bundled nanotubes.

In addition to the bundles of SiC nanotubes, detailed ab initio calculations using the same LAPW DFT-LDA method were recently performed for the geometric structure and electronic properties of Li-intercalated (6,6) SiC NT bundles [144]. Almost a complete charge transfer occurred between Li atoms of different arrangement and concentration as well as SiC NTs, indicating mainly ionic character of interactions in the Li-containing bundle. Both geometric and electronic structures of the bundles consisting of SiC NTs were significantly changed after Li intercalation as a result of the electronic charge transfer towards the constituent nanotubes. The most visible changes in the band structure were found to be a shift of the Fermi level towards the conduction band as well as metallic character of all the configurations of Li-intercalated SiC NT bundles. It was also found that the arrangement of Li atoms inside the nanotubes was energetically favorable as interstitial sites for intercalation. This may lead to high lithium storage ability for the bundles of SiC nanotubes which should activate direct experimental explorations of new nanostructured materials for technologically important Li-ion battery applications [153].

5.5.3 Rolled-Up Double-Wall SiC Nanotubes

Obviously, there is no clear one-to-one Si-C or C-C ordering when SiC graphitic-like multi-layers (Fig. 5.52) are rolled up to form multi-wall SiC nanotubes. Therefore, a competition between the interlayer C-C/Si-Si and Si-C interactions becomes more complex [130]. However, the inter-shell spacing of SiC MW NTs still depends on the combined effect of repulsive interactions between C (Si) and C (Si) atoms and attractive interactions between C and Si atoms, both in different shells. To clarify, how this combined effect influences the intershell spacing of SiC MW NTs, the relaxations and energetics of two sets of commensurate SiC DW nanotubes, namely, *zz*-NTs composed of (5,0)@(*m*,0) (with $m = 12$, 13, 14, 15, 17 and 20) as well as *ac*-NTs composed of (5,5)@(*m,m*) (with $m = 9$–15) (Fig. 5.58) were calculated using PW DFT-GGA method for periodic nanotube models [130]. A relative energy *per* atom of the relaxed SiC DW NT is expressed in (5.19).

$$\Delta E^{\mathrm{DWNT}} = E_{total}^{\mathrm{DWNT}} - E_{total}^{in\mathrm{SWNT}} - E_{total}^{out\mathrm{SWNT}}, \tag{5.19}$$

where $E_{total}^{\mathrm{DWNT}}$, $E_{total}^{in\mathrm{SWNT}}$ and $E_{total}^{out\mathrm{SWNT}}$ are the total energies *per* atom corresponding to the isolated SiC DW NT as well as its inner and outer SW shells, respectively

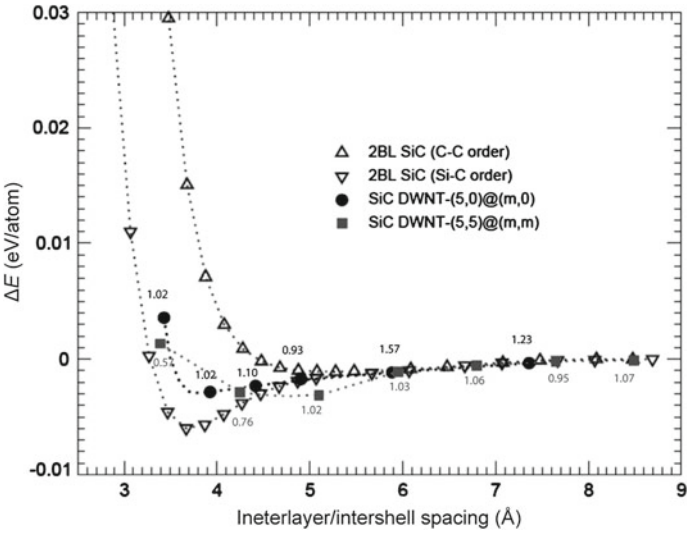

Fig. 5.58 The relative energies *per* atom corresponding to (*i*) the pair of graphitic-like bilayers (2BL) (Fig. 5.52) described by equation $\Delta E = E_{tot}(\mathrm{2BL})\text{-}2E_{tot}(\mathrm{1ML})$ and (*ii*) the pair of double-wall NTs described by (5.19), both shown as functions of the inter-layer and the inter-shell spacings ΔR, respectively (all the *curves* are marked by the corresponding labels). The values of α are written above and below the energy *curves* corresponding to *zz*- and *ac*- chiralities of DW NTs, respectively [130]

[130], shown as a function of the intershell spacing in Fig. 5.58 for double-wall commensurate *ac*-NTs (filled squares) and *zz*-NTs (filled circles). The two energy curves $\Delta E^{\mathrm{DWNT}}(\Delta R)$ (where ΔR is gradually changed inter-shell spacing) corresponding to the two sets of SiC DW NTs can be viewed as quasi-framed within the borders of the two curves corresponding to the two bilayer graphitic-like structures of C-C/Si-Si and Si-C orderings, respectively. The curve for the *zz*-DW NTs (5,0)@(*m*,0) exhibits the energy minimum at ~3.8 Å, while, for the *ac*-DW NTs (5,5)@(*m*,*m*), the curve exhibits a shallow energy minimum valley extending from 4.2 to 5.1 Å, with the minimum at ~4.8 Å [130]. These results confirm the experimental observations [133] which are similar to the cases of multi-layered SiC graphitic-like structures.

To shed some light on this correlation between DW NT geometry and energy, the value $\alpha = n_{\mathrm{Si-C}}/(n_{\mathrm{Si-Si}} + n_{\mathrm{C-C}})$ was introduced [130], which is a ratio of the number of the nearest Si-C pairs ($n_{\mathrm{Si-C}}$) to the total number of the nearest C-C and Si-Si pairs ($n_{\mathrm{C-C}}$ and $n_{\mathrm{Si-Si}}$, respectively) *per* unit cell of DW NTs. A ratio larger than 1 indicates that there are more Si-C pairs (attractive interactions) than the sum of C-C and Si-Si pairs (i.e., repulsive interactions), combined within the whole range of nanotube diameters, while a ratio less than 1 indicates the opposite. An atomic pair in this study is defined as two atoms located separately at the inner and outer shells of a SiC DW NT at a certain distance. They are counted within a range that corresponds to the optimized inter-shell separation (ΔR_0). The calculated ratio for each DW NT is indicated by the number close to the data representing a particular configuration of DW NT in Fig. 5.58. The examination of each ratio shows that almost all of those for *zz*-DW NTs exceed 1, with the only one exception ($\alpha = 0.93$ at ~4.9 Å) while those for *ac*-DW NTs in the vicinity of the equilibrium intershell separation (~4.8 Å) are substantially less than 1, whereas other *ac*-configurations exceed it. Obviously, the attractive interaction dominates for the *zz*-DW NTs in the vicinity of ΔR_0^{zz} (ratios larger than 1), while for the *ac*-DW NTs in the vicinity of ΔR_0^{ac} (with ratios less than 1), the repulsive interaction prevails, both consistent with the cases of the graphitic-like bilayers (Fig. 5.52). Analogically to the bundles of SiC SW NTs [142], the radial buckling in SiC DW NTs is reduced with the increasing diameter of both SW shells, whereas band gaps in DW NTs are noticeably smaller than those in their SW constituents [130].

Thus, the nature of the intershell neighbors is the key factor determining the corresponding ΔR_0. For SiC MW NTs of arbitrary chirality, its determination is not feasible computationally because the structure of their shells is incommensurate in general [130]. Therefore, it would be reasonable to suggest, based on the above consideration, that the two ranges of intershell spacing experimentally observed in SiC MW NTs (~3.8 and ~4.8 Å) are the results of the competition between interlayer attractive and repulsive Coulomb interactions.

5.5.4 *Faceted SiC Nanotubes*

In spite of the successful synthesis of cylinder-shaped SiC nanotubes [133, 135, 136, 138], they were found to demonstrate a rather metastable phase which will likely transform into SiC NWs under certain conditions [133]. The bundles of SiC NTs, prepared using sacrificial alumina membrane as a template, possessed crystalline structures, which are different from the layered multi-wall NTs [137]. Therefore, theoretical models of the crystalline-type SiC NTs (analogous to those of *h*-DW Si NT as shown in Fig. 5.8) are needed rather than those of cylindrical layered NTs [129]. 2*H*-polytype of SiC crystal (Fig. 5.49) was found to be the most unstable form, while 3*C*-polytype proved to be the most stable one at low temperatures. However, SiC NWs and crystalline NTs (Fig. 5.59) display essentially different energetic orders, due to the faceting effect. According to the theoretical analysis performed elsewhere [154], the hexagonal faceted NWs stabilize 2*H*-polytype when the nanowire diameter is smaller than 20 nm (in the range of possible first principles calculations) whereas the NWs in 3*C* form become energetically more favorable when their diameters are larger than 20 nm.

Obviously, single-crystalline *h*-SiC DW NTs, possessing the point symmetry D_{3h}, can be formed by the removal of the core nanowire symmetrically arranged around the [0001] axis from the larger NW of the same faceting (Fig. 5.59). The morphology of those NTs was characterized as hexagonal prisms with [0001]-oriented axis enclosed by six facets. The faceted SiC NTs were indexed by the number of $(10\bar{1}0)$ bilayers across the wall (*m*) and designated as *m*NTs. Their optimized radius was defined *via* an averaged distance from the central axis of the prism to the outmost atoms on its edge, while the wall thickness was represented by the distance between the inner and outer walls.

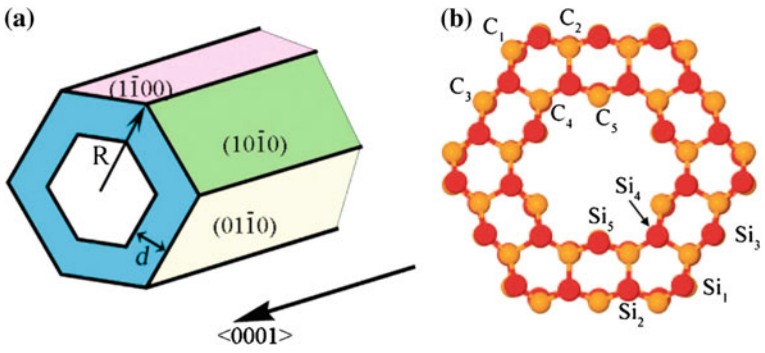

Fig. 5.59 Double-shell SiC nanotube with hexagonal faceted morphology: **a** sketch representation with definitions of the radius (*R*) and wall thickness (*d*); **b** *top* view of 2NT [129]. The projected densities of states for C and Si atoms (shown as *light* and *dark* balls, respectively) enumerated in *right panel* are present in Fig. 5.60

Ab initio and MD calculations on faceted SiC *m*NTs (Fig. 5.59) were performed using the DFT-LCAO method and formalism developed within the Tersoff bond-order interatomic potential (TP), respectively [129]. The NT surface atoms were found to relax inwards, with much more significant relaxation of Si atoms as compared to that of C atoms, i.e., analogously to the rolled-up SiC NTs, faceted nanotubes are predominantly C-terminated. The results of calculations [129] have proved that

(i) the faceted NTs are energetically more favorable as compared to the cylindrical layered SiC NTs (moreover, structurally similar to faceted 2NTs, rolled-up DW NTs undergo severe structural distortion even at a room temperature: Si-C bonds are formed bridging the inner and outer walls, and eventually, the cylindrical morphology transforms into a faceted configuration);
(ii) due to a larger surface area of rolled up NTs they are less stable than the faceted NWs with similar diameters,
(iii) values of formation energies of *m*NTs are close to those of NWs possessing a smaller radius (for example, this is true for both NWs with a radius of 7.59 Å and 3NTs with a radius of 10.67 Å and a wall thickness of 5.15 Å).

Figure 5.60 presents the projected electron density of states (PDOS) given by projecting the total DOS onto the atoms on internal and external 2NT facets. Obviously, the states near the Fermi level mainly arise from the states of the under-coordinated atoms on the facets. The top of the VB and the bottom of the CB originate mainly from the C(2*p*) and Si(3*p*) states of surface atoms, respectively. Such a feature is caused by the electron density transfer from Si to C atoms, due to their different electronegativities [140]. The PDOSs are also consistent with the spatial distribution

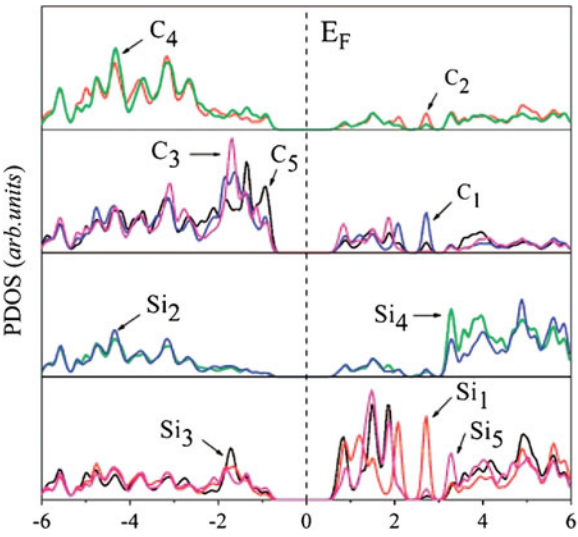

Fig. 5.60 PDOS of SiC 2NT obtained by projecting the total density of states onto the atoms specified in Fig. 5.59b. The energy at the Fermi level is set to zero [129]

of the wave functions around the atoms, which are responsible for the formation of the top of the VB and the bottom of the CB states. The isosurfaces for the corresponding wave functions are highly localized on the facets, Thus, the wave functions for SiC 2NT at the bottom of the CB reside at six corners of the hexagonal prisms, whereas at the top of the VB they are localized on the inner and outer facets (Fig. 5.59). The narrower band gaps of faceted NTs (as compared with SiC bulk) should make their electronic and optoelectronic properties, e.g., photoluminescence spectrum, different from those of SiC crystal [129].

5.5.5 *Rolled-Up Single-Wall GeSi Nanotubes*

Unlike well-described in literature SiC nanotubes, there is rather scarce information on synthesis and theoretical simulations of GeSi NTs, although these materials are quite perspective for various applications in semiconductor science and technology [149, 155–157]. Nanotubes (nanoscrolls) and free-standing flexible helical coils were fabricated for the first time from the strained Ge_xSi_{1-x}/Si heterolayers [155] as shown in Fig. 5.61. The procedure of fabrication was based on self-rolling of a highly strained

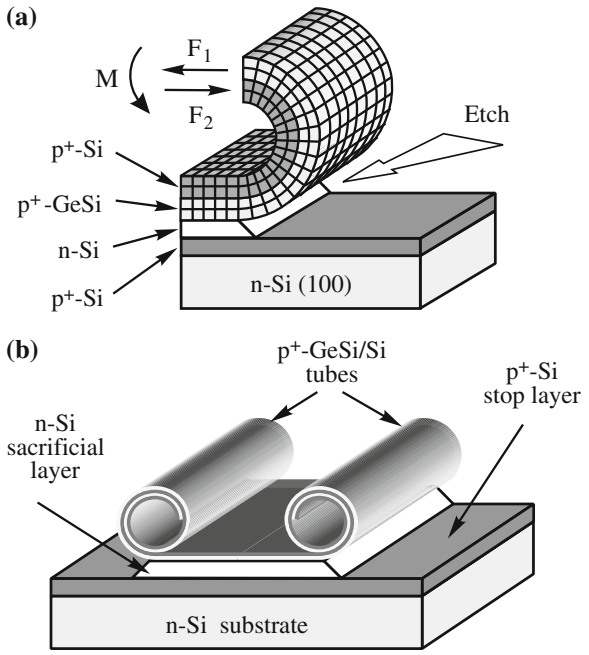

Fig. 5.61 Scheme of the nanoscroll formation: **a** strain-induced bending of GeSi/Si bilayer detached from the substrate by lateral undercut etching; **b** self-rolling of bilayer during etching of sacrificial layer. The oppositely directed forces F_1 and F_2 give rise to a moment of forces M, tending to bend the bilayer (Reprinted figure with permission from Golod et al. [155], Copyright (2001) by the IOP Publishing)

epitaxial ultrathin Ge_xSi_{1-x}/Si bilayer film detached from the silicon substrate. To ensure an easy detachment of the strained epitaxial bifilm from the substrate and its subsequent self-rolling into a nanotube-scroll, an additional sacrificial layer was specially introduced between the substrate and the bifilm (Fig. 5.61a). It is a layer that has to be subsequently removed by the selective etching. The diameters of the obtained nanoscrolls varied from 10 nm to 13 μm, depending on the thickness and lattice mismatch of the GeSi/Si bilayer. GeSi/Si NT and helical coils, up to 70 nm in diameter, exhibited quite good conducting properties and a high mechanical strength.

Recent MD simulations confirmed that a free standing Si nanofilm can bend into a nanotube with Ge as an inner layer, opposite to the normal bending configuration defined by a misfit strain [157]. Moreover, GeSi is a markedly less polar substance than SiC, as mentioned at the beginning of Sect. 5.4, since the charge transfer from Ge to Si atom is more than four times smaller than that from Si to C atom [132]. Thus, all three structural types of Ge and Si atomic arrangements in GeSi sheets (analogically to those shown in Figs. 5.50 and 5.51) are considered for the generation of rolled-up SW GeSi NTs, having a small difference between their cohesion energies. After the rolling up, the more negative Si atoms will occupy the outer shell, while Ge atoms can be arranged inside the buckled GeSi nanotube.

First ab initio study of SiGe NTs in both *ac*- and *zz*-configurations of those three types (Fig. 5.62) satisfying the initial honeycomb lattice structure has been carried out within the finite open-shell model of 0D nanotubules with H-passivated edges using the hybrid HF-DFT LCAO method [149] which can reproduce the band gaps of semiconductors better than traditional PW DFT methods. Obviously, NT of type 1 contains only one kind of bonds present throughout the nanotube, namely Ge-Si, whereas NTs of types 2 and 3 contain also Ge-Ge, and Si-Si bonds. The difference between GeSi SW NTs of types 2 and 3 consists in the arrangement of the adjacent Si (Ge) atoms: in the former type, any ring perpendicular to the NT axis contains only one kind of atoms, while in the latter, analogical rings contain alternating Ge and Si atoms.

Ab initio calculations were performed on the whole family of (n, n) and $(n,0)$ GeSi SW NTs, where n changed from 3 to 11, for all three structural types [149]. Figure 5.63 presents the plots of cohesive (binding) energy *per* atom versus. the number of atoms for all six sets of nanotubes. Among armchair GeSi NTs, the overall highest stability was found to be achieved for type-2 nanotubes, whereas the highest cohesive energy values of *zz*-NTs were obtained for type-1 structures. For *ac*-NTs, the binding energy *per* atom tends to increase monotonically achieving near saturation at (11,11) (Fig. 5.63a). Such a monotonous growth of the binding energy was also noticed in GeSi zigzag nanotubes (Fig. 5.63b). As long as NT diameter increases, both short- and long-range atomic interactions help stabilize nanotubes, possibly approaching the behavior of infinite tubes. Moreover, NTs of a larger diameter are more planar as compared to highly curved NTs of a smaller diameter, which reduces the $\sigma - \pi$ hybridization of the former, thus, increasing the stability of higher diameter nanotubes. On the other hand, both Si and Ge atoms favor sp^3 hybridization, whereas all GeSi NTs considered above were based on the graphite templates which made the atoms essentially three-fold coordinated or sp^2 hybridized. During NT optimization,

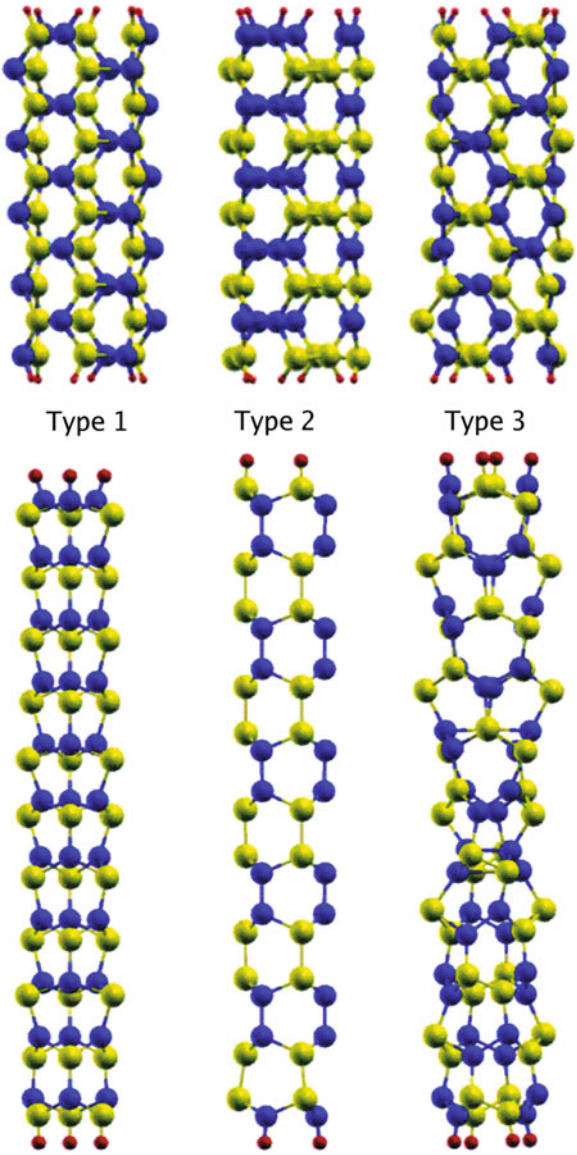

Fig. 5.62 Ultrathin GeSi NTs of three structural types with *ac*-(3,3) (*top*) and *zz*-(3,0) (*bottom*) chiralities. Ge and Si atoms are shown as *dark* and *light balls*, respectively, while small balls at tubular edges designate passivating H atoms [149]

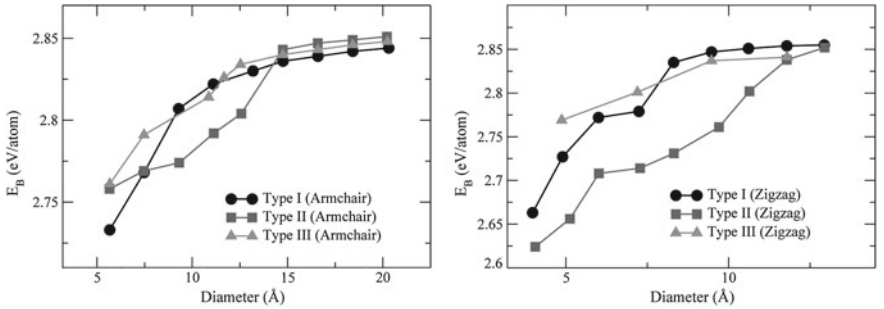

Fig. 5.63 Six sets of plots for binding (cohesion) energy versus diameter for GeSi SW NTs of different chiralities and structural types (Reprinted figure with permission from Rathi and Ray [149], Copyright (2008) by the Elsevier B.V. All rights reserved)

Si and Ge atoms try to retain their preferred sp^3 hybridization state which accounts not only for distortion in the tubular structure but also for the differences in bond lengths for different nanotubes. Small diameter nanotubes by virtue of their strong curvature are highly strained, therefore, the maximum bond expansion is noticed with minimization of the strain energy. Obviously, the layered type construction is favored by both Si-Si and Ge-Ge bonds and this, along with other factors, contribute to the relatively higher stability of GeSi SW *ac*-NTs of type-2 and *zz*-NTs of type-1. Analogically to SiC NTs, the values of nanotube buckling decrease with NT diameter growth. The Mulliken population analysis confirm a noticeable charge transfer from Ge to Si atoms since the latter are relatively more electronegative than Ge [149]. Armchair structures of type 1 exhibit a higher polarity than those of types 2 and 3 since only Ge-Si bonds are present in type 1 structures. Since the structures of types 2 and 3 contain Ge-Ge, Ge-Si and Si-Si bonds, the nature of their bonding is a mixture of ionic and covalent contributions. Mixed nature of bonding has been reported for zigzag GeSi nanostructures as well. For *zz*-chirality, GeSi NTs of types 1 and 3 also show a charge transfer between Si and Ge atoms. As the radii of Si atoms are smaller compared to Ge atoms, the stronger nuclear forces compel the charge accumulation over the former, although the main source of charge is the outer shell of Ge atoms. At the same time, structural type 2 shows a *unique* spread of the electronic charge along *zz*-NTs. For example, a nanotube with chirality indexes (11,0) was divided by two well-separated positively and negatively charged areas, irrespective of the electronegativities of the atoms. Such a feature can be exploited in developing p−n junction type devices where their different sections have different charge concentrations [149].

5.6 Silicon Carbide and Germanium Silicide Nanowires

5.6.1 Polymorphism and Stability of SiC Nanowires

The SiC nanowires possess superior structural stability and mechanical properties at high temperatures and, thus, can be utilized for possible applications in high-frequency and high-temperature both electronic and micromechanical devices as well as in thermal insulating materials for aerospace vehicles [158]. Moreover, these NWs are of particular interest due to the superior quantum confinement in quasi-one-dimensional (Q1D) nanostructures, which makes them excellent candidates for nanodevice construction [47]. SiC NWs were synthesized using a number of methods, e.g.: (*i*) interaction of multi-wall carbon nanotubes with Si oxide or halide species in a vapor-solid reaction, yielding SiC nanorods with effective diameters ranging from 2 to 30 nm [159]; (*ii*) a solid-solid reaction of SW CNTs with silicon carbide nanoclusters for fabrication of SiC heterostructures with crystalline interface [160]; (*iii*) chemical vapor deposition on porous Si substrates in the presence of Fe catalyst yielding SiC NWs with diameters 5–20 nm [161]; (*iv*) nanowires with effective diameter less than 10 nm synthesized using the arc-discharge method [162]. Different methods of synthesis, properties and applications of SiC NWs were reviewed elsewhere [163].

As shortly described in Sect. 5.4, SiC bulk polytypes consist of differently ordered stacking sequences of atomic double layers in a SiC single-crystal (Fig. 5.49), the stability of which depends on the synthesis conditions [154]. For example, the polytype-controlled epitaxial growth of 4*H*- and 6*H*-SiC was achieved by utilizing the step-flow growth on off-oriented SiC(0001) substrates, mainly by the chemical vapor deposition [164]. Obviously, a polymorphism can be also attributed to 1D SiC nanowires since their cores overcome the disadvantage of sp^2 hybridization typical for silicon carbide nanolayers (Sect. 5.4) as well as rolled-up and, in particular, faceted nanotubes (Sect. 5.5). The as-synthesized SiC NWs possessed mainly the single-crystalline core of 3*C* form (Fig. 5.49) oriented along the [111] direction [165], which was confirmed by large-scale DFT-LCAO calculations on this type of nanowires [166], although 6*H*-polytype SiC nanowires were also synthesized [167]. On the other hand, ab initio calculations on SiC NWs and faceted NTs performed earlier predicted the formation energy preference of 2*H*-polytype [0001]-oriented nanowires over 3*C* [111]-ones for $d_{\mathrm{NW}} < 20$ nm [129, 154]. The alternative first principles simulations gave the preference to 3*C*-oriented ultrathin NWs over 2*H* [0001]- and 3*C*-ones [145]. Simulations on SiC nanowires of various morphologies were performed using the formalism of interatomic empirical potentials [154], tight-binding model [145], methods of molecular dynamics [158, 168], DFT-LCAO methods [129, 166, 169], as well as PW DFT methods within both LDA and GGA approaches [154, 168, 170]. To perform these simulations, NW models were constructed as both finite [145, 158, 168, 169] and infinite [129, 145, 154, 166, 169, 170].

Four high-symmetric prismatic configurations of SiC NWs attributed to both 3*C* and 2*H* polytypes of a single-crystalline structure (Fig. 5.64) were calculated using DFT-LCAO method [166]. The NW hydrogenation was necessary in order to stabilize the facets, especially those with high density of dangling bonds. As a result, no visible surface reconstruction occurred in these H-terminated SiC nanowires, in contrast with non-hydrogenated NWs [129], which led to a difference in formation energies and their ratio for the same nanowire configurations. The average Si-H and C-H bond lengths upon the NW facets (Fig. 5.64) were found to be 1.499 and 1.106 Å, close to the corresponding values in CH_4 and SiH_4 molecules (1.483 and 1.091 Å), thus indicating chemical bonding of the outer H atoms onto the facets [166]. Because the densities of dangling bonds are different for various facets of these NWs, their stoichiometries differ too, from one nanowire to another. To evaluate the energetic stability of the SiC NWs with different stoichiometries, the formation energy (E_{form}) of each type of hydrogenated nanowires was defined using the following expression:

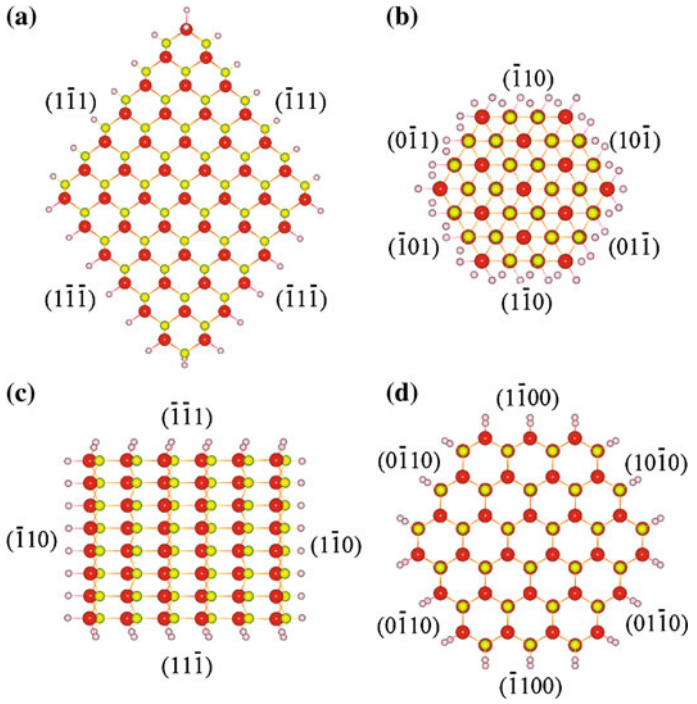

Fig. 5.64 Top images of the relaxed configurations of H-terminated SiC nanowires, each of which possesses three atomic coordination spheres around NW axes (NW3), enclosed by low-index facets written at the perimeter of each image. Orientations of nanowires corresponded to [110] (**a**), [111] (**b**), and [112] (**c**) possess structures of 3*C* polytypes, while [0001] (**d**) is a 2*H* polytype. C, Si, and H atoms are shown as *yellow*, *red*, and *small light lilac balls*, respectively (Reprinted figure with permission from Wang et al. [166], Copyright (2009) by the American Chemical Society)

$$E_{form} = E_{tot} + n_{\mathrm{Si-H}}\varepsilon_{\mathrm{Si-H}} + n_{\mathrm{C-H}}\varepsilon_{\mathrm{C-H}} - n_{\mathrm{SiC}}\mu_{\mathrm{SiC}} - n_{\mathrm{H}}\mu_{\mathrm{H}}, \tag{5.20}$$

where E_{tot} is the total energy of a H-terminated NW, n_{SiC} and μ_{SiC} are the number and chemical potential of SiC formula units, respectively, n_{H} and μ_{H} are the corresponding values of H atoms, while $n_{\mathrm{Si-H}}$ and $\varepsilon_{\mathrm{Si-H}}$ ($n_{\mathrm{C-H}}$ and $\varepsilon_{\mathrm{C-H}}$) are the number and zero-point vibrational energy of Si-H (C-H) bonds on the nanowire facets, respectively. Since the chemical potential of each species highly depends on the experimental conditions, such as temperature, pressure, and solution environment, these values estimated from ab initio calculations were correlated [166].

Figure 5.65 gives the formation energies of various types of SiC NWs (Fig. 5.64) for different values of d_{NW}, as a function of μ_{H}. Unlike clean SiC NWs which have positive formation energies [129], all the H-terminated nanowires possess negative values of E_{form}, suggesting that surface hydrogenation can effectively stabilize these NWs. The values of formation energies per SiC unit cell decrease linearly with the

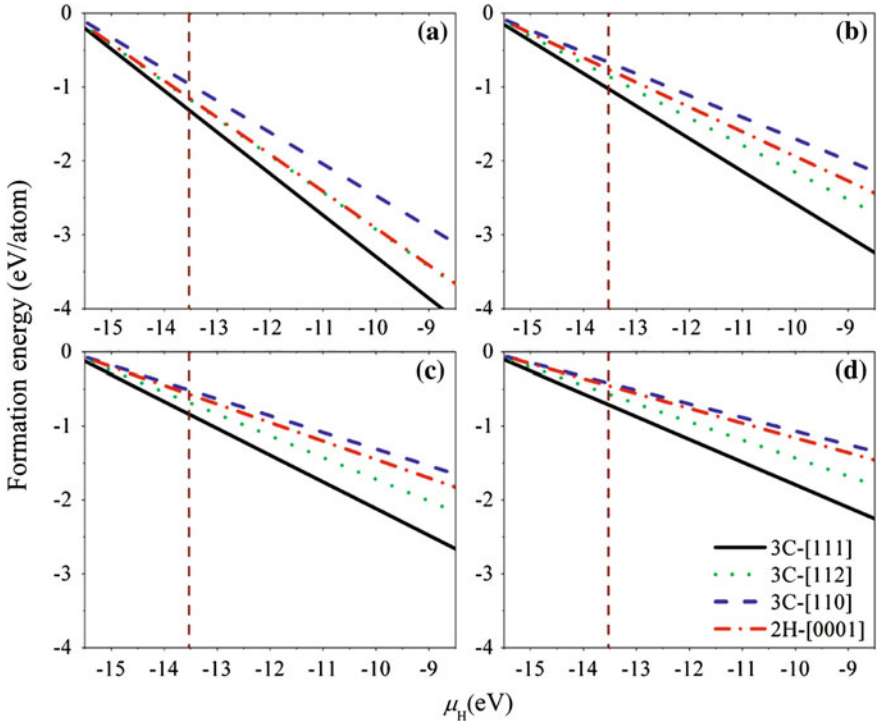

Fig. 5.65 Formation energies of differently oriented SiC nanowires of 3*C* and 2*H* polytypes (Fig. 5.49) as a function of μ_{H}. The chemical potential of atomic H in a vacuum was calculated to be -13.53 eV (as indicated by the *vertical dashed lines* at figures (**a**)–(**d**). NW1–NW4 configurations correspond to a number of atomic coordination spheres around nanowire axis (Fig. 5.64a–d correspond to NW3) (Reprinted figure with permission from Wang et al. [166], Copyright (2009) by the American Chemical Society)

increase of μ_H. Obviously, the energetic stability of these SiC NWs depends on their orientations (Fig. 5.65). The [111]-orientated nanowires of 3*C*-polytype with hexagonal cross sections were found to be energetically the most favorable, followed by [112]-oriented NWs of the same polytype and [0001]-oriented NWs of 2*H*-polytype [166]. The [110]-orientated SiC NWs of 3*C*-polytype look like energetically the most unfavorable. The differences in formation energies between the NWs with close diameters decrease with the increase of d_{NW} represented by the number of SiC formula units *per* supercell. This could be related to the H/SiC ratios of these NWs which decrease with the increasing d_{NW}. The superior stability of [111]-orientated nanowires over other kinds of SiC NWs was found to be in a good agreement with the corresponding experimental findings [171]. Additionally, Fig. 5.65 implies that the surface stability criteria could be changed as μ_H is lower than −16 eV. However, the lower is the chemical potential, the more difficult is the surface hydrogenation of SiC NWs. The nanowire hydrogenation reactions most likely occur between SiC NWs and atomic H whose chemical potential is about −13.5 eV.

Figure 5.66 shows a branched 3*C*-polytype Y-shaped SiC NW firstly designed by connection of the [110]-oriented SiC stem with the two [100]-oriented SiC branches possessing a typical crystallographic angle of 90° between them [168]. Execution of similar simulations is quite justified due to the experimental synthesis of branched SiC NWs [172]. A number of finite Y-shaped nanowire models with different diameters as well as lengths of both the stem and branches were designed [168] as initial configurations before their structural optimization. To relax the atomic structure and to calculate the elastic properties of these branched SiC NWs, the classical method of molecular dynamics with Tersoff potential [173] was used, which is known to describe adequately the nanostructured phases of SiC [166]. Simulation of the external pressure onto Y-shaped SiC nanowires was also performed [168].

Alternative models of SiC NWs were chosen similar to clathrate-type 1D Si NW chains (Fig. 5.22b, c) described in Sect. 5.3, where fullerene-type $(SiC)_{12}$ nanocage was considered as a structural element for the two types of nanowires (Fig. 5.67)

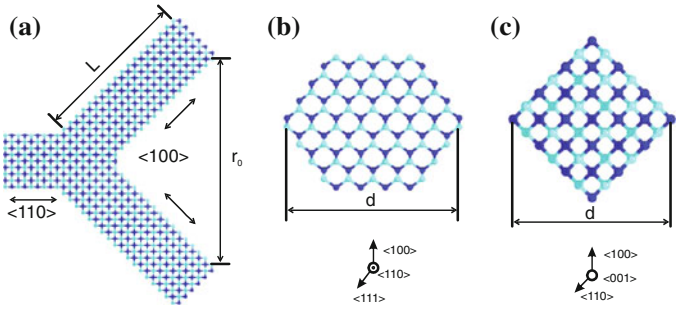

Fig. 5.66 The model of Y-branched SiC nanowire, where L is the branch length and r_0 is the initial distance between the branches (**a**); the perpendicular cross-sections in [110]-oriented stem (**b**) and [001]-oriented branches (**c**). Effective diameter (d) was estimated as the maximal distance between apexes on the opposite sides of nanowire cross-sections [168]

[169]. The first step of this model construction was both substantiation and structural optimization of nanocage unit. As in the case of SiC nanolayers (Fig. 5.50a) and nanotubes, the alternating allocation of Si and C atoms in $(SiC)_n$ nanocages was found to be most stable. Moreover, the polyhedrons of arbitrary fullerene-like $(XY)_n$ clusters having four-membered rings (4MRs) and six-membered rings (6MRs) on the cage facets show higher structural stability when consisting of six 4MRs and eight 6MRs, i.e., $(SiC)_{12}$, with maximum separation of 4MRs as shown in Fig. 5.67a [169]. This $(SiC)_{12}$ nanocage is described by the T_h symmetry group.

Large-scale DFT-LCAO calculations were performed for the construction of $(SiC)_{12}$-based nanostructures, both finite dimers (Fig. 5.67b, c) and infinite nanowires (Fig. 5.67d, e) [169]. The two $(SiC)_{12}$–$(SiC)_{12}$ dimers were just obtained from single nanocages by coalescing either two 4MRs of two $(SiC)_{12}$ (Fig. 5.67b) or two 6MRs of the same SiC clusters (Fig. 5.67c), followed by the global structure optimization. Both dimer structures keep axial symmetry, therefore, the $(SiC)_{12}$-based NWs can be formed by the translational symmetry (Fig. 5.67d, e).

To estimate the stability of either finite dimers or infinite nanowires, their binding energies E_{bind} were calculated and compared with that of $3C$-SiC bulk [169]. The cohesive energies of bulk and $(SiC)_{12}$ nanocage were found to be -8.28 and -6.99 eV/atom, respectively. The values of E_{bind} for dimer (I) and dimer (II)

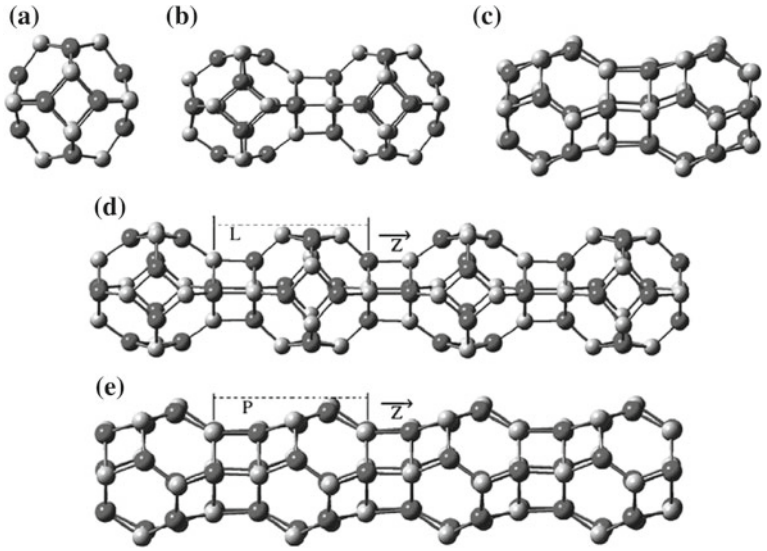

Fig. 5.67 The optimized configurations of the fullerene-like cage $(SiC)_{12}$ and $(SiC)_{12}$-based SiC nanostructures: **a** fullerene-like cage $(SiC)_{12}$, **b** $(SiC)_{12}$-$(SiC)_{12}$ dimer (I), **c** $(SiC)_{12}$-$(SiC)_{12}$ dimer (II), **d** $(SiC)_{12}$-based nanowire (I), and **e** $(SiC)_{12}$-based nanowire (II) obtained from coalescing of $(SiC)_{12}$-$(SiC)_{12}$ units in the dimer. The translational periodicity of the two kinds of SiC NWs along the z axis shown in (**d**) and (**e**) was optimized to be $L = 7.35$ Å and $P = 6.48$ Å, respectively. *Dark* and *light* balls correspond to Si and C atoms, respectively (Reprinted figure with permission from Li et al. [169], Copyright (2007) by the Elsevier B.V. All rights reserved)

(Fig. 5.67b, c, respectively) were estimated to be about 0.14 and 0.20 eV/atom, respectively, therefore, $(SiC)_{12}$-$(SiC)_{12}$ dimers are energetically more stable than a single 12-atom nanocage, while dimer (II) is more stable than dimer (I). The cohesive energies of the two $(SiC)_{12}$-based SiC NWs shown in Fig. 5.67d, e were found to be −7.27 and −7.38 eV/atom, respectively [169]. It means that in terms of the energy favorable order, among all the aforementioned structures, bulk 3*C*-SiC is the most stable one, followed by the $(SiC)_{12}$-based SiC nanowires (II) and (I), the $(SiC)_{12}$-$(SiC)_{12}$ dimers (II) and (I), while the most unstable is the $(SiC)_{12}$ nanocage (Fig. 5.67). Therefore, if the fullerene-like $(SiC)_{12}$ nanocage had an inherent special stability and could be synthesized experimentally, it would be easier to synthesize the $(SiC)_{12}$-based SiC NWs [169]. This gives experimentalists a guide to search for novel nanowires as a new kind of SiC nanomaterials, which are expected to find novel applications for nanotechnology.

5.6.2 Electronic Properties of SiC Nanowires

Electronic properties of SiC NWs (Fig. 5.64) depend mainly on the orientation of a nanowire and its diameter [166]. In contrast to the indirect band gap features of bulk 3*C*-SiC crystal, those of 3*C*-SiC NWs oriented along the [110] and [111] directions and as well as of the [0001]-oriented 2*H*-SiC NWs have direct band gaps at Γ points, while the [112]-oriented 3*C*-SiC NWs possess indirect band gaps (Fig. 5.68). Bulk 3*C*-SiC crystal has an indirect band gap with the valence band maximum (VBM) and the conduction band minimum (CBM) located at Γ and X points, respectively. When the [110]-oriented NW is constructed (Fig. 5.64a), the energy level of the CBM at $(1,0,0)2\pi/a$ and $(0,1,0)2\pi/a$ are upshifted due to the 1D confinement and the bands

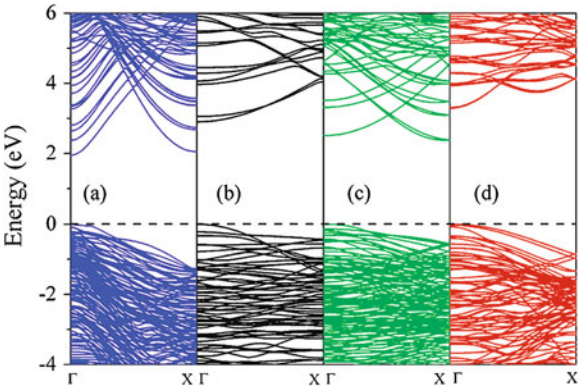

Fig. 5.68 Electronic band structures of SiC nanowires (with NW3 thickness as defined above and imaged in Fig. 5.64) oriented along **a** [110], **b** [111], **c** [112], and **d** [0001] crystallographic axes [166]

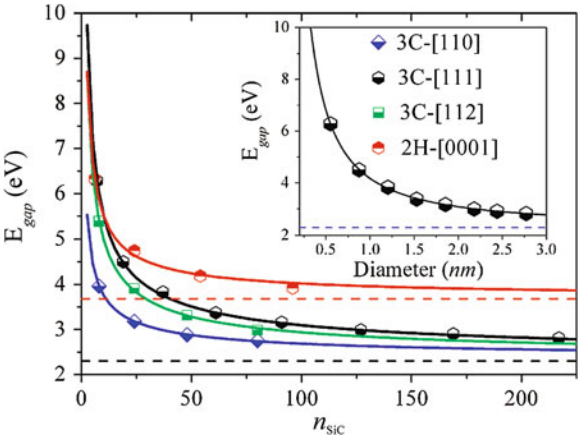

Fig. 5.69 Band gaps of SiC NWs with different orientations as functions of the number of atoms *per* SiC unit cells. The *solid lines* are constructed using (5.21). The inset shows band gaps of 3*C* [111]-oriented nanowires as a function of the NW diameter: $\Delta\varepsilon_{gap}(d) = 2.3 + 1.87d^{-1.27}$ (eV) (Reprinted figure with permission from Wang et al. [166], Copyright (2009) by the American Chemical Society)

at (0,0,1)$2\pi/a$ are projected onto the Γ point. This gives a rise to the direct band gap at the Γ point (Fig. 5.68a). The direct band gaps of [111]-oriented SiC nanowires (Fig. 5.68b) obtained in calculations [166] can arise from the quantum-confinement effects in these NWs. A similar conclusion can be drawn for the band structure of [0001]-oriented 2*H*-SiC NW (Fig. 5.68d). However, in the case of [112]-oriented SiC NWs (Fig. 5.64c), no CBM can be folded into the Γ point, and these nanowires possess indirect band gaps (Fig. 5.64c), similar to that of 3*C* SiC bulk [166].

Due to the quantum-confinement effects, the band gaps of SiC NWs decrease with the increase of the nanowire size. This was justified since the band gaps of SiC NWs ($\Delta\varepsilon_{gap}^{\mathrm{NW}}$) can be fitted via parameters α and β using the following expression [166]:

$$\Delta\varepsilon_{gap}^{\mathrm{NW}} = \Delta\varepsilon_{gap}^{bulk} + \beta(n_{\mathrm{SiC}})^{-\alpha}, \tag{5.21}$$

where $\Delta\varepsilon_{gap}^{bulk}$ is the band gap width of the corresponding SiC bulk of 3*C*- or 2*H*-polytypes and n_{SiC} is the number of SiC units *per* unit cell. Obviously, for a certain kind of SiC NWs, the $(n_{\mathrm{SiC}})^{0.5}$ is proportional to d_{NW}. The fitting parameters for these SiC NWs were suggested to be the following: $\alpha = 0.58$ and $\beta = 5.51$ for the [110]-oriented NWs, $\alpha = 0.60$ and $\beta = 12.7$ for the [111]-oriented NWs, $\alpha = 0.63$ and $\beta = 11.4$ for the [112]-oriented NWs, while $\alpha = 0.73$ and $\beta = 9.89$ for the [0001]-oriented 2*H*-NWs [166]. Figure 5.69 presents the dependencies $\Delta\varepsilon_{gap}(d_{\mathrm{NW}})$ for all four SiC NW configurations shown in Fig. 5.64, according to which the order of band gap widths is the following: $\Delta\varepsilon_{gap}[110] < \Delta\varepsilon_{gap}[112] < \Delta\varepsilon_{gap}[111] < \Delta\varepsilon_{gap}[0001]$. The band gap values of [111]-oriented 3*C*-SiC NWs (2.81–2.68 eV) were found to

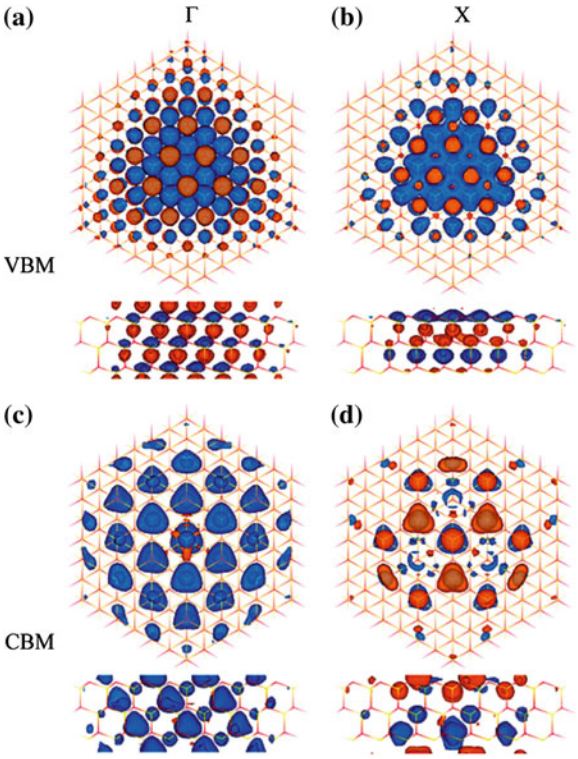

Fig. 5.70 Isosurfaces of the Kohn-Sham states, (**a**) and (**b**), of the valence band maximum as well as the conduction band minimum, (**c**) and (**d**), at Γ and X points distributed across and along (*upper* and *lower* plots) of the [111]-oriented 3*C*-SiC nanowire (Reprinted figure with permission from Wang et al. [166], Copyright (2009) by the American Chemical Society)

be consistent with the maximum of the emission band (440–560 nm) measured for SiC nanocrystallites [174].

The electron wave functions of the states, corresponding to the VBM and CBM of [111]-orientated SiC NWs were calculated at the Γ and X points of the Brillouin zone in order to reveal the origination of the bands near the Fermi level [166]. The isosurfaces of these wave functions are drawn in Fig. 5.70 being mainly distributed around the carbon and silicon atoms in the core region of the nanowire, respectively. This is also consistent with the orbital-resolved partial density of states, which shows that the electron states at VBM and CBM originate mainly from the C(2*p*) and Si(3*p*) states in the core region, respectively, while the surface states are removed from the band gap. This differs significantly from the bared SiC NWs where the electron bands near the Fermi level arise from the surface states [129].

The electronic energy band structures of the $(SiC)_{12}$ nanocage-based SiC nanowires (Fig. 5.67d, e) were also calculated [169]. Figure 5.71a, b present the energy bands near the Fermi surface for nanowires (I) and (II), respectively (Fig. 5.67),

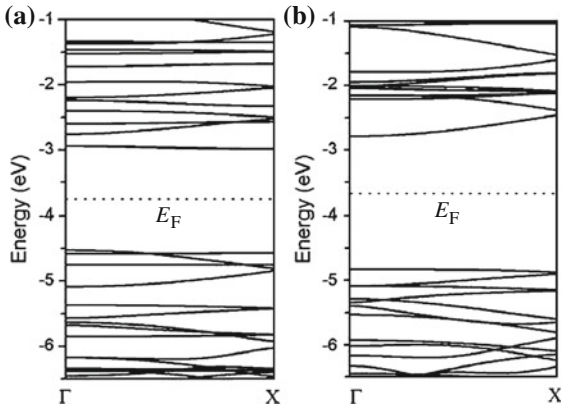

Fig. 5.71 The band structures of $(SiC)_{12}$ nanocage-based **a** SiC nanowire (I) and **b** SiC nanowire(II) (Fig. 5.67d, e, respectively) (Reprinted figure with permission from Li et al. [169], Copyright (2007) by the Elsevier B.V. All rights reserved)

where the Fermi levels of both SiC NWs are denoted by the dashed line in this figure. The two band structures clearly show the finite gaps, the widths of which were found to be 1.59 and 2.06 eV for the $(SiC)_{12}$-based SiC nanowires (I) and (II), respectively, which are slightly smaller than those of 3*C*- and 2*H*-SiC. It was clearly shown that although the formation of the tubular linkage structures does not cause the essential changes in the band-gap width $\Delta\varepsilon_{gap}$, it provides a way of adjusting the gap width by forming different nanostructures [169]. Obviously, the $(SiC)_{12}$ nanocage-based NW (I) can be considered as a semiconductor possessing an indirect gap (Fig. 5.71a), unlike the $(SiC)_{12}$-based nanowire(II) which was found to be a direct gap semiconductor (Fig. 5.71b).

The energy band structures of both $(SiC)_{12}$-based SiC nanowires were estimated to be qualitatively similar with those of the SiC nanotubes (Fig. 5.54) as they are always semiconductors with wide gaps [175].

5.6.3 Stability of GeSi and Hetero-Structured Ge/Si Nanowires

Unique electronic, transport and optical properties of Si NWs and Ge NWs partially mentioned in Sect. 5.3 can be extended and modulated when considering Ge_xSi_{1-x} nanowires (e.g., quasi-stoichiometric GeSi NWs with regular or disordered morphologies shown in Fig. 5.72a, b, d versus Fig. 5.72c, respectively) because they possess the same crystalline structure and display the total solubility [156]. Single crystalline [110]-oriented Ge_xSi_{1-x} nanowires were successfully synthesized using an Au catalyst-assisted chemical vapor method while their band gap modulation from 0.68 to 2.25 eV was observed for Ge concentrations within the interval $0 \leqslant x \leqslant 1$ and diameters from 9 to 100 nm [176]. In contrast with pure Si and Ge nanowires, the

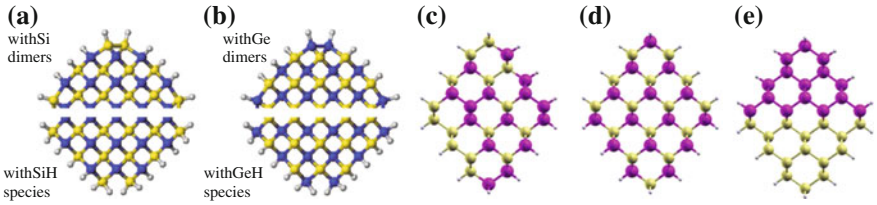

Fig. 5.72 The cross sections of hydrogenated either [001]-oriented GeSi NWs with and without dimers on the facets shown in (**a**) and (**b**) as half-sectioned images [156] or stoichiometric [110]-oriented nanowires with disordered (random) (**c**), regular (mixed) (**d**), and half-abrupt (**e**) morphologies [177]. Si and Ge atoms are shown as middle *light* and *dark* balls, respectively, while the surrounding H atoms are drawn as *small white balls*

possibility to modulate the band structure and optical spectra of Ge_xSi_{1-x} NW was determined by changing not only the NW diameter but also its chemical composition and morphology [177]. The interaction between Si and Ge atoms in a nanowire leads to the quantum confinement effect (QCE) different from that of pure NWs and the equilibrium band offset between the two different materials creating a spatial localization of electrons and holes [178], which can remarkably modify the transport and optical properties and be useful for photovoltaics.

For GeSi NWs, particular attention was focused on the coaxial core/shell nanowires [179], where a further possibility of tuning the band gap was envisaged by varying the composition of the hetero-structures and the geometry of interface between the two constituents (Fig. 5.73). The ultrahigh vacuum chemical vapor deposition method was used to grow Ge_xSi_{1-x} epitaxial core-shell nanowires with the Ge/Si shell content tuned to enable both a radial band and strain engineering [181]. These core/shell nanowires demonstrated important performance as high-mobility field effect transistors (NWFETs) [182] and low-temperature quantum devices [183], compatible with the actual Si technology.

Alternative types of hetero-structured Ge/Si NWs were considered as well: (*i*) $Ge_{0.5}Si_{0.5}$ nanowires consisting on Ge and Si semi-prisms (Fig. 5.72e) [177] and (*ii*) alternating pure Si and Ge nanorods (Fig. 5.74) contacting between them-

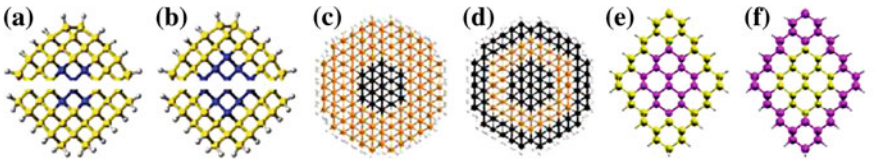

Fig. 5.73 The cross sections of hydrogenated coaxial core/shell [001]-oriented Ge/Si NWs with and without dimers on the facets possessing different Ge core diameters shown in (**a**) and (**b**) as half-sectioned images [156], [111]-oriented nanowires terminated by either Si (**c**) or Ge (**d**) shells (the latter contains two germanium shells) [178] as well as [110]-oriented NWs possessing Si (**e**) and Ge (**f**) terminations [180]. Si and Ge atoms are shown as *light* and *dark* balls, respectively while outer H atoms are drawn as *small white balls*

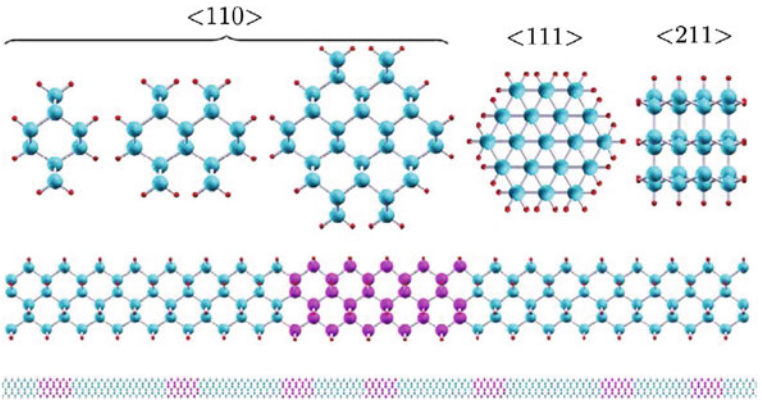

Fig. 5.74 The *top panel* shows cross-sections of H-terminated [110]-. [111]- and [211]-oriented hetero-structured Ge/Si NWs. Their diameters (*left*-to-*right*) after optimization were found to be: 0.78 nm, 1.02 nm, 1.44 nm, 1.14 nm and 1.06 nm, respectively. The *middle panel* images incorporate a pure Ge nanorod in the side hetero-structure of a Si NW (Ge and Si atoms are drawn in *magenta* and *blue*, respectively). The *bottom panel* describes a multiple hetero-structural nanowire (MHNW) with an arbitrary distribution of Ge hetero-structures [185]

selves along the NW axis [88, 184, 185]. The latter hetero-structures possess higher thermoelectricity as compared to pure Si or Ge NWs.

Theoretical calculations on GeSi and hetero-structured Ge/Si nanowires of different morphologies were performed using the PW DFT methods within both LDA and GGA approaches [156, 177–180, 185, 186], the LCAO-DFT method [88, 187, 188] and the DFPT method [184], the tight-binding method [189] as well as the formalism of interatomic empirical potentials [185, 190]. In majority of theoretical studies on GeSi NWs, their cohesive and electronic properties were simulated; additionally, transport and vibrational properties [184, 185, 189, 190], elasticity [186] as well as electro- and thermo-conductivity [184, 188] of these nanowires were simulated too.

Most comprehensive studies have been so far performed on [110]-oriented GeSi and Ge/Si NWs, both theoretically and experimentally [88, 176, 177, 179, 180, 185, 186, 188, 189]. Relative energetic stability of GeSi NW configurations shown in Figs. 5.72, 5.73 and 5.74 was determined via formation enthalpies [177]:

$$\Phi^*(\mathrm{Si}_n\mathrm{Ge}_m\mathrm{H}_l) = E_{tot}(\mathrm{Si}_n\mathrm{Ge}_m\mathrm{H}_l) - m\frac{E_{tot}(\mathrm{Ge}_N\mathrm{H}_l)}{N} - n\frac{E_{tot}(\mathrm{Si}_N\mathrm{H}_l)}{N}, \qquad (5.22)$$

where $N = m+n$ is the total number of Ge and Si atoms per NW cell, $E_{tot}(\mathrm{Si}_n\mathrm{Ge}_m\mathrm{H}_l)$, $E_{tot}(\mathrm{Ge}_N\mathrm{H}_l)$ and $E_{tot}(\mathrm{Si}_N\mathrm{H}_l)$ are calculated total energies of H-terminated GeSi, Ge and Si nanowires (to calculate the two latter energies, Si or Ge atoms were substituted by Ge or Si atoms, respectively). Figure 5.75 presents the relative enthalpy curves in dependence on d_{NW} [177] calculated for [110]-oriented GeSi NWs shown in Fig. 5.72c-e using (5.22), where $\Phi^* = 0$ for both $\mathrm{Ge}_N\mathrm{H}_l$ and $\mathrm{Si}_N\mathrm{H}_l$ configurations irrespective of d_{NW}. It was found that for $d_{\mathrm{NW}} > 0.9$ nm, the most stable SiGe

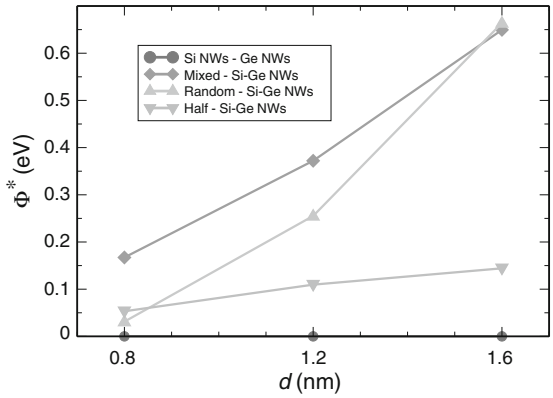

Fig. 5.75 Formation enthalpies for random (Fig. 5.72c), mixed (Fig. 5.72d), and half-abrupt (Fig. 5.72e) [110]-oriented GeSi NW configurations as a function of their diameter. The same quantity for the corresponding pure Si and Ge NWs is also shown (the two *curves* here coincide, both being zero for any diameter) [177]

NWs are those with a half-abrupt configuration (Fig. 5.72e). For $d_{\mathrm{NW}} > 1.6\,\mathrm{nm}$, the regular NW configuration (Fig. 5.72d) becomes more stable than a disordered one (Fig. 5.72c), which can be explained by a higher stability of the former in GeSi bulk. At the same time, these NW configurations are evidently less stable than those of Ge and Si NWs, either separated or joint.

Figure 5.76 presents the relative enthalpy curves for [110]-oriented Ge/Si core-shell NWs on concentrations of Ge and Si atoms for different values of d_{NW} according to (5.22) [180]. It is clear that for $\mathrm{Si}_{core}/\mathrm{Ge}_{shell}$ NWs, the formation enthalpy Φ^* is always positive, indicating their instability in relation to the pure NWs ($\Phi^* = 0$). This instability is more pronounced with the increase of the NW diameter. As opposed to this, $\mathrm{Ge}_{core}/\mathrm{Si}_{shell}$ nanowires possess negative values of Φ^*, thus indicating a higher stability compared to the pure Si and Ge NWs, GeSi NWs and $\mathrm{Si}_{core}/\mathrm{Ge}_{shell}$ NWs. It means that for this kind of geometry, Ge atoms tend to occupy the core of a nanowire, decreasing the formation enthalpy of the system. However, the size of the experimental SiGe NWs is one order of magnitude bigger than the size of theoretically simulated nanowires [180]; so the comparison between the results of the simulations and experimental data can be considered only as qualitative one. Still, the results presented in Figs. 5.75 and 5.76 allow extracting a trend of the formation enthalpy for abrupt, random and mixed configurations of GeSi NWs [177] as well as $\mathrm{Ge}_{core}/\mathrm{Si}_{shell}$ and $\mathrm{Si}_{core}/\mathrm{Ge}_{shell}$ NWs configurations [180]. In the case if all the aforementioned nanowires possess $d_{\mathrm{NW}} = 1.6\,\mathrm{nm}$ with the composition x_{Ge} nearly 0.5, the energy balance between different [110]-oriented H-terminated GeSi NW configurations is the following: $\Phi^*(\mathrm{Ge}_{core}/\mathrm{Si}_{shell}) < \Phi^*(pure\ \mathrm{Ge}\ or\ \mathrm{Si}) < \Phi^*(half - abrupt\ \mathrm{GeSi}) < \Phi^*(regular\ \mathrm{GeSi}) < \Phi^*(disordered\ \mathrm{GeSi}) < \Phi^*(\mathrm{Si}_{core}/\mathrm{Ge}_{shell})$.

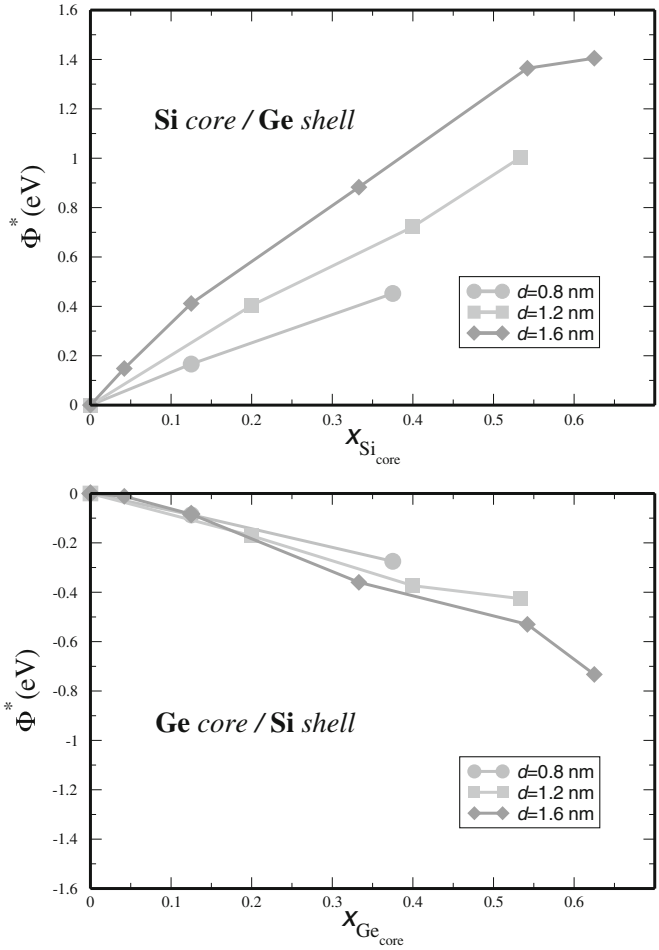

Fig. 5.76 Formation enthalpy for H-terminated [110]-oriented Si_{core}/Ge_{shell} and Ge_{core}/Si_{shell} nanowires as a function of NW composition and d_{NW}. $\Phi^* = 0$ for pure Si and Ge NWs for any d_{NW} (5.22) [180]

Thus, the most stable structure of GeSi nanowires can be considered Ge_{core}/Si_{shell} NWs, which have negative values of formation enthalpy and for which the creation of a nanoalloy with this geometry is favorable. All the other GeSi NW structures have positive values of Φ^*, so for these NWs the mixing of Ge and Si atoms is unfavorable compared to the pure Ge or Si nanowires. The least-favored configuration of the [110]-oriented H-terminated GeSi NW is Si_{core}/Ge_{shell} [180].

5.6.4 Electronic Properties of GeSi and Hetero-Structured Ge/Si Nanowires

Figure 5.77 illustrates the trend of the band gap width $\Delta\varepsilon_{gap}$ as the function of nanowires' diameter d_{NW} [177] for disordered, regular and half-abrupt [110]-oriented GeSi NWs (Fig. 5.72c, d, e, respectively) as well as for nanowires of Ge (Fig. 5.43) and Si (Fig. 5.33) with the same orientations, all calculated using the same DFT-LDA method. The most interesting result here is the finding that the half-abrupt NWs show a strongly reduced quantum confinement effect (RQCE) for $d_{\mathrm{NW}} > 0.9$ nm. This property is not found in regular and disordered NWs, which have gap close to those obtained for pure Si and Ge NWs, even if they have the same composition as the half NWs ($x_{\mathrm{Si}} = 0.5$ and $x_{\mathrm{Ge}} = 0.5$). This effect is related to the geometry of a nanowire, in particular, to the atomic configuration in a NW unit cell and to the presence of a clear interface between Si and Ge regions. Particularly, its physical origin is due to the well-pronounced interface between Si and Ge atoms, which is related to the consequent spatial carrier localization (SCL). Since the contribution to QCE for Si and Ge is very different, this creates a different alignment of the conduction and valence states and, as a consequence, a reduced width of $\Delta\varepsilon_{gap}$ compared to the pure NWs of the same diameter.

The analysis of the electronic structures of different GeSi NW configurations clearly shows that the contribution to the total DOS from a NW is principally due to Ge atoms for the valence and to Si atoms for the conduction states [177]. This is well observed in Fig. 5.78 where electrons are distributed in the Si-atom region of a nanowire while the hole is localized on the top of the central Ge atom near the Si/Ge interface, confirming straightforward tendency to an e−h separation in these

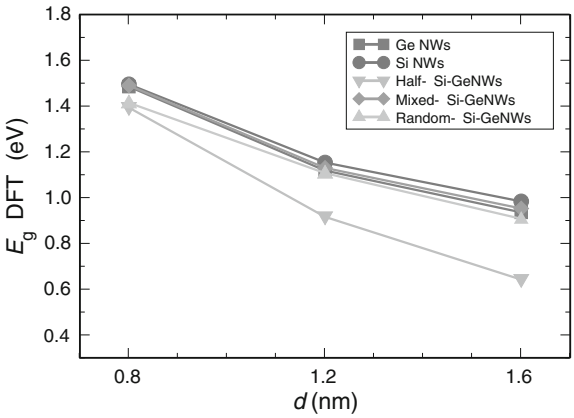

Fig. 5.77 The width of band gaps $\Delta\varepsilon_{gap}$ as the function of [110]-oriented GeSi NW diameter for disordered (random), mixed (regular), and half-abrupt NWs with a fixed composition. The corresponding gaps of pure Si and Ge NWs are also shown [177]

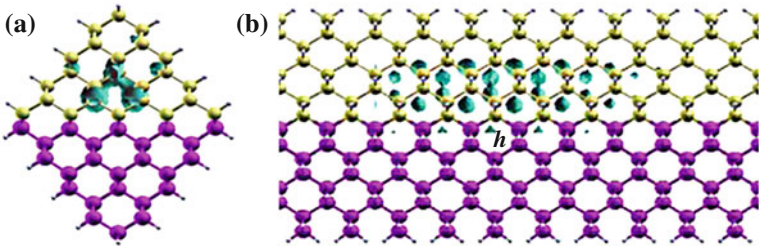

Fig. 5.78 Across (**a**) and side (**b**) views of the electron charge distribution in half-abrupt GeSi nanowire ($d_{NW} = 1.6$ nm); the hole (h) position is fixed on the top of the central Ge atom. *Light* and *dark spheres* represent Si and Ge atoms, respectively while the small spheres are H atoms used to saturate the dangling bonds. The isosurface of the $e - h$ distribution probability is shown in celestial [177]

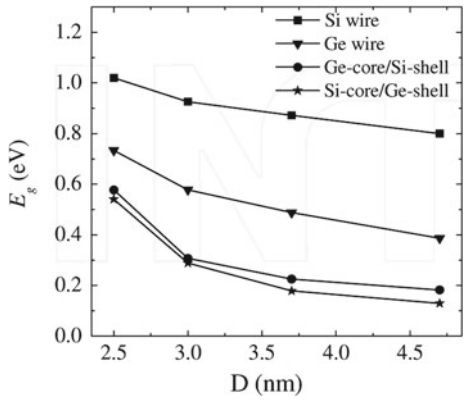

Fig. 5.79 Dependencies $\Delta\varepsilon_{gap}(d_{NW})$ for [110]-oriented Ge, Si as well as hetero-structured Ge- and Si-containing core-shell nanowires [186]

NW configurations. From the right panel of Fig. 5.78, an exciton localization along the wire axis of about 25 Å can be estimated.

Figure 5.79 confirms the conclusion drawn on the reduced band gap of the half-abrupt GeSi NW in comparison with the corresponding Ge and Si NWs (Fig. 5.77) for both Ge_{core}/Si_{shell} and Si_{core}/Ge_{shell} nanowires possessing $d_{NW} \geqslant 2.5$ nm. This difference was explained by the intrinsic strain of the core-shell wires due to a certain difference of their structural parameters [186]. For example, the Si-core in the 3.0 nm Si_{core}/Ge_{shell} NW experienced a 2.2 % tensile strain, while the Ge-shell was contracted with a 0.8 % compressive strain. Since the CBM/VBM states (i.e., the minimum of the conduction band and the maximum of the valance band) in the core-shell nanowire are primarily contributed by Si/Ge composition, the CBM energy variation with strain was examined for the pure Si NW of 1.5 nm diameter (represented the core) while the VBM energy variation with the strain was considered for the pure 3.0 nm Ge NW (i.e., the outer nanowire diameter).

At the same time, the origin of different behavior of the Ge_{core}/Si_{shell} and Si_{core}/Ge_{shell} NWs can be related to the variation in the distribution of the electronic

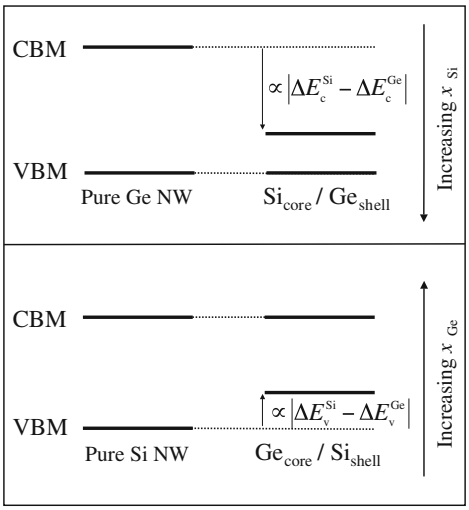

Fig. 5.80 Qualitative model of for RQCE in core-shell NWs. The mechanism of the reduction in the energy band gap with respect to the pure NWs is shown in the *bottom panel* for Ge_{core}/Si_{shell} NWs and in the *upper panel* side for Si_{core}/Ge_{shell} NWs [180]

states as the size of the core and the shell varies [180]. The valence band that presents a less significant discretisation of states is less affected by the increase of the Si core and roughly conserves the value of VBM of the pure Ge NW (Fig. 5.80). These two combined effects induce a reduction of $\Delta\varepsilon_{gap}$ with respect to the pure Ge NW. The conduction band of the Ge_{core}/Si_{shell} nanowire that presents a less significant discretisation of states is less affected by the increase of the Ge core and is localized in the Si shell, roughly conserving the value of CBM of the pure Si NW (Fig. 5.80). The origin of the weak RQCE with respect to the Ge_{core}/Si_{shell} NW is related to the fact that the differences of the CBM shift for pure Si and pure Ge NWs are bigger than those of VBM ($|\ \Delta E_{CB}^{Si} - \Delta E_{CB}^{Ge}\ | > |\ \Delta E_{VB}^{Si} - \Delta E_{VB}^{Ge}\ |$) [180]. In the first case of Ge_{core}/Si_{shell}—a more pronounced RQCE was obtained than that observed in Si_{core}/Ge_{shell} (as illustrated in Fig. 5.80).

Typical electronic band dispersions in the [110]-oriented core-shell Ge/Si and Si/Ge NWs (Fig. 5.73e, f) are shown in Fig. 5.81, which demonstrates a clear feature inside the dashed frame that the energy level spacing near the band gap is larger than that away from the gap [179]. The discrete set of states in the conduction band is more significant in the NW with a silicon core, while the discrete set of states in the valence bands is more noticeable in the NW with a germanium core. These discrete bands suggest additional confinement in the core or shell region for these core-shell nanowires. It means that there exist "band offsets" in these NWs that provide an additional geometrical confinement that can be tuned by varying the size and composition of the core-shell region. Similar results were also obtained for the [111]-oriented core-shell NWs (Fig. 5.73c) [179].

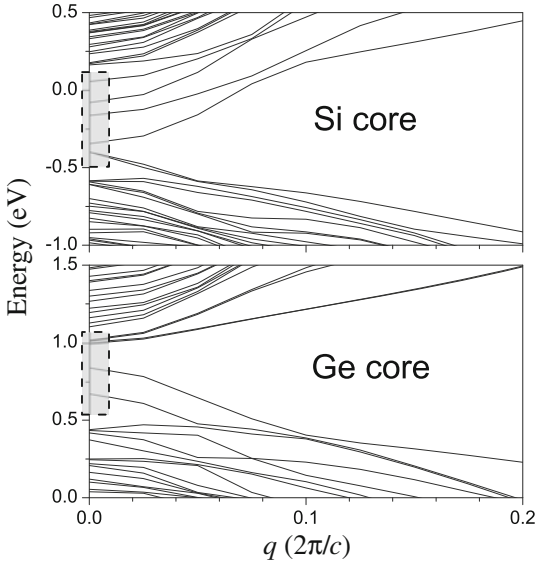

Fig. 5.81 Band dispersions of the [110]-oriented core-shell Ge/Si and Si/Ge NWs with 42 atoms in the core and 220 atoms in the shell. The *top* figure is for the NW with Si core whereas the *bottom* one is for the NW with Ge core. The *dashed frames* indicate the energy regions of interest [179]

Due to a specific morphology of the [001]-oriented GeSi (Fig. 5.72a, b) and core-shell Ge/Si (Fig. 5.73a, b) NWs, including dimerisation of the surface Ge and Si atoms, the results of their simulation are considered separately [156]. The band structures of regularly-structured GeSi NWs along with Si NWs and Ge NWs are shown in Fig. 5.82. All nanostructures are characterized by the direct transition in the point except the Ge NW with dimers. In the latter case, the minimum of the conduction band is located at 0.4 of the distance along the Γ-Z direction. The last valence band of these nanostructures displays two maxima separated by a few meV: one is at Γ and the other is at 0.2Γ-Z. The minimum of the first conduction band at Γ is evident for all nanowires imaged in Fig. 5.82 while for Ge NWs with and without dimers, a sizable decrease of the band at the Z point is also pronounced [156]. The dispersion of the bands near the gap region is similar to those reported previously for Si NWs [89, 90] and Ge NWs [114].

The Si_{core}/Ge_{shell} NWs (Fig. 5.83a) mostly possess the direct gap situated at Γ except the configuration without dimers (Fig. 5.73a) where the maximum of the VB is shifted from Γ to 0.1Γ-Z. The dispersion of the last valence band for these NWs with and without dimers is close to that of Si NWs, Ge NWs, and SiGe NWs displaying two maxima, while a progressive rising of the first conduction band at the Z point with the size of the Si core is clearly seen. The character of the states at Z was examined resulting in the fact that the main contributions came from the atomic sites close to the center and to the NW facets [156]. With the increase in the size of

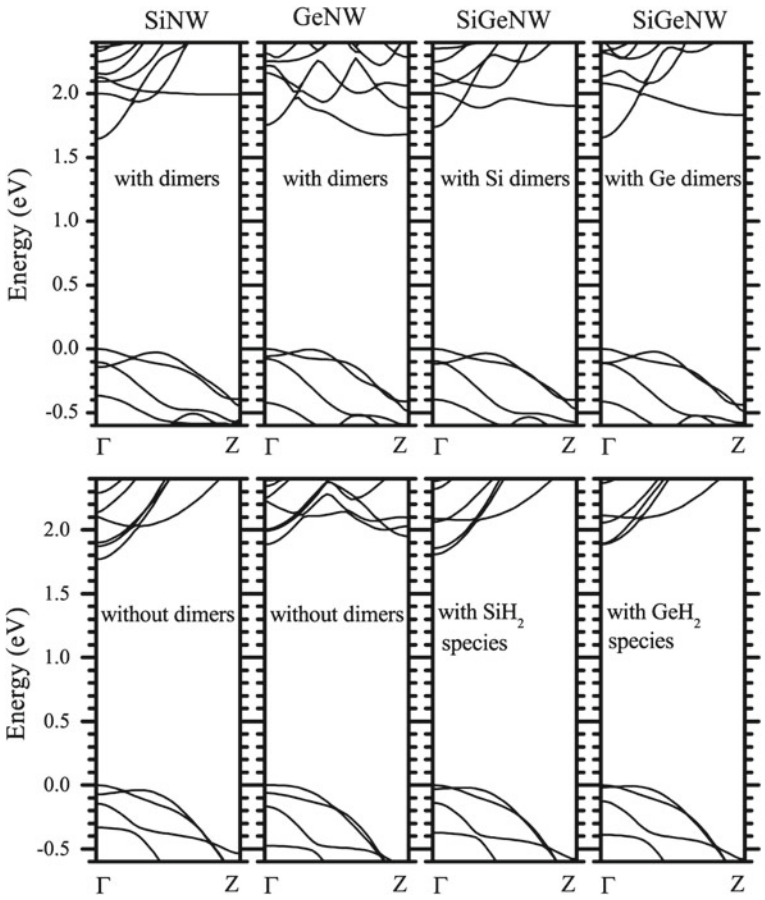

Fig. 5.82 Band structures of Si NWs, Ge NWs and GeSi NWs with and without Si (Ge) dimers [156]

the silicon core (Fig. 5.83a), Si atoms provide the main contributions to the states at Z, lifting, in their turn, the first conduction band up in the energy compared to the corresponding band structures for Si NWs and Ge NWs in Fig. 5.82.

In the case of Ge_{core}/Si_{shell} NWs (Fig. 5.83b), the valence band maximum at 0.4Γ-Z is more pronounced compared to that of Si NWs, GeNWs and GeSi NWs (Fig. 5.82), as well as Si_{core}/Ge_{shell} NWs (Fig. 5.83a). In addition, for the core of a larger diameter (right panels of Fig. 5.83b), the valence band maximum is located at 0.4Γ-Z, leading to the indirect character of the gap. Moreover, the first conduction band at Z shifts down with the increaseing of the Ge core for nanostructures with and without dimers.

It was also found that the increase of the NW period (l_{NW}) can stabilize the direct character of its gap in such nanostructures, while the decrease of l_{NW} mainly provides

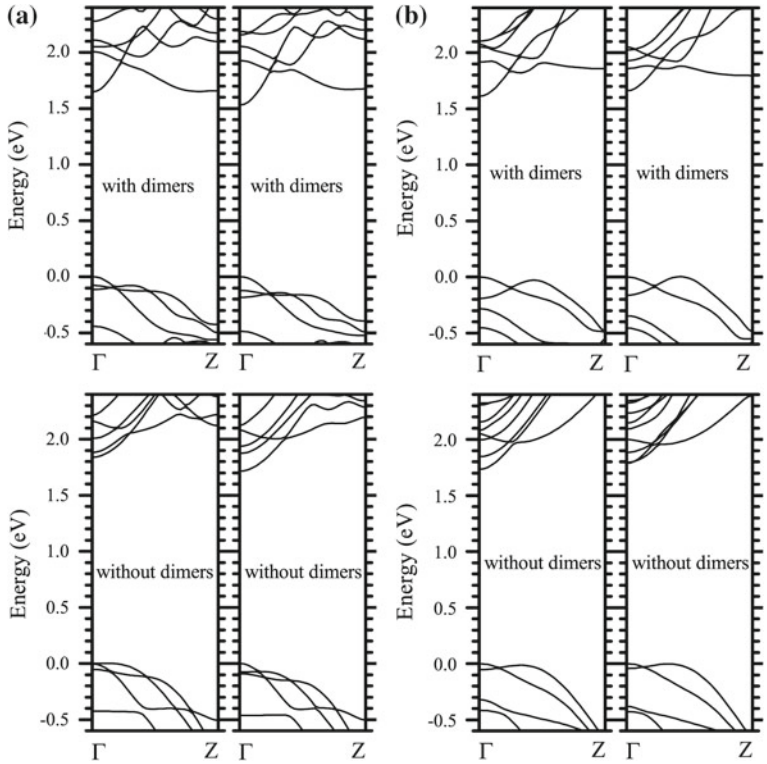

Fig. 5.83 Band structures of Si_{core}/Ge_{shell} NWs (**a**) and Ge_{core}/Si_{shell} NWs (**b**). *Left* (**a**) and *Right* (**b**) panels in band structures correspond to smaller and larger diameters of NW shell (corresponding to Fig. 5.73a, b, respectively) [156]

the indirect transition [156]. One possible way to increase l_{NW} in nanowires with dimers is to break some dimers and form SiH_2 species (Figs. 5.72a, b and 5.73a, b) because NWs with dimers possess a smaller l_{NW} as compared to that of NWs without dimers. The structural relaxation of GeSi NWs and Ge/Si core-shell NWs as well as Si NWs and Ge NWs of ~2 nm diameter included optimization of l_{NW} because the latter parameter can affect the dispersion of bands near the gap region. All NWs with dimers were found to possess higher oscillator strength of the first direct transition in the Γ point than NWs without dimers mainly because of the variation in the orbital angular character of the states [156]. Regular GeSi NWs of 2 nm diameter, with either Si or Ge dimers displaying the direct band gap and appreciable oscillator strength of the first direct transition can be considered as potential candidates for light emitting devices. Ge_{core}/Si_{shell} NWs are also promising candidates, although stabilization of the direct band gap is necessary in this case. Even though the direct character of the gap is predicted for Si_{core}/Ge_{shell} NWs, their low oscillator strength does not seem to be suitable for application in light emitting devices [156].

References

1. M. Hartmann, *Semiconductor Detectors for Nuclear Physics* (Springer, Berlin, 2009)
2. Ch. Schelling, *Growth and Characterization of Self-Organized and Organized Si and* $Si_{1-x}Ge_x$ *Nanostructures* (PhD Thesis, Johannes-Kepler-Universität, Linz, 2000)
3. V. Kumar (ed.), *Nanosilicon* (Elsevier, Oxford, 2007)
4. C. Claeys, E. Simoen, *Germanium-based Technologies. From Materials to Devices* (Elsevier, Oxford, 2007)
5. B. Pajot, B. Clerjaud, *Optical Absorption of Impurities and Defects in Semiconducting Crystals. II. Electronic Absorption of Deep Centres and Vibrational Spectra* (Springer, Berlin, 2013)
6. J. Sánchez-Dehesa, J.A. Vergés, C. Tejedor, Solid State Commun. **38**, 871 (1981)
7. J. Bai, X.C. Zeng, H. Tanaka, J.Y. Zeng, Proc. Natl. Acad. Sci. USA **101**, 2664 (2004)
8. A. Fontcuberta i Morral, J. Arbiol, J.D. Prades, A. Cirera, J.R. Morante, Adv. Mater. **19**, 1347 (2007)
9. G. Seifert, Th. Köhler, H.M. Urbassek, E. Hernández, Th. Frauenheim, Phys. Rev. B **63**, 193409 (2001)
10. S.B. Fagan, R.J. Baierle, R. Mota, A.J.R. da Silva, A. Fazzio, Phys. Rev. B **61**, 9994 (2000)
11. W.I. Park, G. Zheng, X. Jiang, B. Tian, C.M. Lieber, Nano Lett. **8**, 3004 (2008)
12. M. Zhao, R.Q. Zhang, Y. Xia, C. Song, S.-T. Lee, J. Phys. Chem. C **111**, 1234 (2007)
13. V.V. Pokropivny, A.L. Ivanovskii, Russ. Chem. Rev. **77**, 837 (2008)
14. D. Bogdan, R. Isai, A. Calborean, C. Morari, Physica E **44**, 1441 (2012)
15. K.H. Janzon, H. Schäfer, A. Weiss, Z. Anorg. Allg. Chem. **87**, 372 (1970)
16. G. Seifert, E. Hernández, Chem. Phys. Lett. **318**, 355 (2000)
17. J. Gao, J. Zhao, Sci. Rep. **2**, 00861 (2012)
18. E. Lukevitz, O. Pudova, R. Sturkovich, *Molecular Structure of Organosilicon Compounds* (Ellis Horswood Ltd., Chichester, 1989)
19. D.B. Migas, V.E. Borisenko, Nanotechnology **18**, 375703 (2007)
20. A.K. Singh, V. Kumar, Y. Kawazoe, Phys. Rev. B **72**, 155422 (2005)
21. M. Zhao, J.Z. Zhu, Y. Xia, M. Lu, J. Phys. Chem. C **111**, 2942 (2007)
22. M. Zhao, Z.H. Zhu, J.D. Gale, Y. Xia, G.Q. Lu, J. Phys. Chem. C **111**, 9652 (2007)
23. J.L. Lu, S. Kaya, J. Weissenrieder, T.K. Todorova, M. Sierka, J. Sauer, H.J. Gao, S. Shaikhutdinov, H.J. Freund, Surf. Sci. **600**, L164 (2006)
24. Y.H. Tang, L.Z. Pei, Y.M. Chen, C. Guo, Phys. Rev. Lett. **95**, 116102 (2005)
25. M. Ben-Ishai, F. Patolski, J. Am. Chem. Soc. **133**, 1545 (2011)
26. A.S. Barnard, S.P. Russo, J. Phys. Chem. B **107**, 7577 (2003)
27. X. Yang, J. Ni, Phys. Rev. B **72**, 195426 (2005)
28. A.K. Ray, P. Prodhan, J. Comput. Theor. Nanosci. **3**, 128 (2006)
29. G. Seifert, Th. Köhler, Z. Hajnal, Th. Frauenheim, Solid State Commun. **119**, 653 (2001)
30. J.W. Kang, J.J. Seo, H.J. Hwang, J. Nanosci. Nanotechnol. **2**, 687 (2002)
31. X. Wang, Z. Huang, T. Wang, Y.W. Tang, X.C. Zeng, Physica B **403**, 2021 (2008)
32. J. Chen, G. Zhang, B. Li, Nano Lett. **10**, 3978 (2010)
33. H.J. Wallbaum, Naturwissenschaften **32**, 76 (1944)
34. G. Vogg, M.S. Brandt, M. Stutzmann, Adv. Mater. **12**, 1278 (2000)
35. I. Ponomareva, M. Menon, D. Srivastava, A.N. Andriotis, Phys. Rev. Lett. **95**, 265502 (2005)
36. R. Kagimura, R.W. Nunes, H. Chacham, Phys. Rev. Lett. **95**, 115502 (2005)
37. R.K.F. Lee, B.J. Cox, J.M. Hill, J. Math. Chem. **47**, 569 (2010)
38. R.K.F. Lee, B.J. Cox, J.M. Hill, Nanoscale **2**, 859 (2010)
39. H. Peelaers, B. Partoens, F.M. Peeters, Nano Lett. **9**, 107 (2009)
40. J.K. Böhlke, J.R. De Laefer, P. De Bievre, H. Hidaka, H.S. Peiser, K.J.R. Rosman, P.D.P. Taylor, J. Phys. Chem. Ref. Data **34**, 57 (2005)
41. A.I. Hochbaum, R. Chen, R.D. Delgado, W. Liang, E.C. Garnett, M. Najarian, A. Majumdar, P. Yang, Nature **451**, 163 (2008)

42. A.I. Boukai, Y. Bunimovich, J. Tahir-Kheli, J.K. Yu, W.A. Goddard III, J.R. Heath, Nature **451**, 168 (2008)
43. N. Wang, Y. Cai, R.Q. Zhang, Mater. Sci. Eng. R **60**, 1 (2008)
44. R. Rurali, Rev. Mod. Phys. **82**, 427 (2010)
45. Y. Cui, C.M. Lieber, Science **291**, 851 (2001)
46. X. Duan, Y. Huang, Y. Cui, J. Wang, C.M. Lieber, Nature **409**, 66 (2001)
47. Y. Huang, X. Duan, Y. Cui, L.J. Lauhon, K.H. Kim, C.M. Lieber, Science **294**, 1313 (2001)
48. Y. Cui, Q. Wei, H. Park, C.M. Lieber, Science **293**, 1289 (2001)
49. X. Duan, Y. Huang, C.M. Lieber, Nano Lett. **2**, 487 (2002)
50. Y. Cui, Z. Zhong, D. Wang, W.U. Wang, C.M. Lieber, Nano Lett. **3**, 149 (2003)
51. T.J. Kempa, B. Tian, D.R. Kim, J. Hu, X. Zheng, C.M. Lieber, Nano Lett. **8**, 3456 (2008)
52. R.T. Senger, S. Tongay, E. Durgun, S. Ciraci, Phys. Rev. B **72**, 075419 (2005)
53. R.S. Wagner, W.C. Ellis, Appl. Phys. Lett. **4**, 89 (1964)
54. J. Westwater, D.P. Gosain, S. Tomiya, S. Usui, H. Ruda, J. Vac. Sci. Technol. B **15**, 554 (1997)
55. A.M. Morales, C.M. Lieber, Science **279**, 208 (1998)
56. Z.W. Pen, Z.R. Dai, Z.L. Wang, Science **291**, 1947 (2001)
57. L. Schubert, P. Werner, N.D. Zakharov, G. Gerth, F.M. Kolb, L. Long, U. Gösele, Appl. Phys. Lett. **84**, 4968 (2004)
58. Y. Cai, S.K. Chan, I.K. Sou, Y.F. Chan, D.S. Su, N. Wang, Adv. Mater. **18**, 109 (2006)
59. M.T. Björk, B.J. Ohlsson, T. Sass, A.I. Persson, C. Thelander, M.H. Magnusson, K. Deppert, L.R. Wallenberg, L. Samuelson, Appl. Phys. Lett. **80**, 1058 (2002)
60. A.K. Singh, V. Kumar, Y. Kawazoe, in *Nanosilicon*, ed. by V. Kumar (Elsevier: London, 2007), pp. 217–257
61. Y. Wu, Y. Cui, L. Huynh, C. Barrelet, D. Bell, C. Lieber, Nano Lett. **4**, 433 (2004)
62. D.D.D. Ma, C.S. Lee, F.C.K. Au, S.Y. Tong, S.T. Lee, Science **299**, 1874 (2003)
63. J.D. Holmes, K.P. Johnson, R.C. Doty, B.A. Korgel, Science **287**, 1471 (2000)
64. R.Q. Zhang, Y. Lifshitz, D.D.D. Ma, Y.L. Zhao, Th. Frauenheim, S.T. Lee, Y. Tong, J. Chem. Phys. **123**, 144703 (2005)
65. S. Hong, M.Y. Chou, Phys. Rev. B **57**, 6262 (1998)
66. Y. Zhao, B.I. Yakobson, Phys. Rev. Lett. **91**, 035501 (2003)
67. M. Takeguchi, M. Tanaka, H. Yasuda, K. Furuya, Surf. Sci. **493**, 414 (2001)
68. A. Singh, V. Kumar, R. Note, Y. Kawazoe, Nano Lett. **6**, 920 (2006)
69. R. Rurali, N. Lorente, Nanotechnology **16**, S250 (2005)
70. J.F. Justo, R.D. Menezes, L.V.C. Assali, Phys. Rev. B **75**, 045303 (2007)
71. N.C. Tsai, Y.R. Chiang, S.L. Hsu, Appl. Phys. A **98**, 135 (2010)
72. M. Menon, K.R. Subbaswamy, Phys. Rev. B **55**, 9231 (1997)
73. K. Moriguchi, S. Munetoh, A. Shintani, Phys. Rev. B **62**, 7138 (2000)
74. P. Soukiassian, Mater. Sci. Eng. B **96**, 115 (2002)
75. N. Mingo, Phys. Rev. B **68**, 113308 (2003)
76. T. Thonhauser, G.D. Mahan, Phys. Rev. B **69**, 075213 (2004)
77. T. Markussen, A.P. Jauho, M. Brandbyge, Nano Lett. **8**, 3771 (2008)
78. T. Markussen, A.P. Jauho, M. Brandbyge, Phys. Rev. B **79**, 035415 (2009)
79. H.S. Park, P.A. Klein, Comput. Methods Appl. Mech. Eng. **197**, 3249 (2008)
80. R.E. Rudd, B. Lee, Mater. Simul. **34**, 1 (2008)
81. Y. Chen, D. Li, J.R. Lukes, A. Majumdar, J. Heat Transf. **127**, 1129 (2005)
82. K. Kang, W. Cai, Philos. Mag. **87**, 2169 (2007)
83. Y. Zhang, J.X. Cao, Y. Xiao, X.H. Yan, J. Appl. Phys. **102**, 104303 (2007)
84. W.W. Zhang, Q.A. Huang, H. Yu, L.B. Lu, Adv. Mater. Res. **60–61**, 315 (2009)
85. K. Kang, W. Cai, Int. J. Plast. **26**, 1387 (2010)
86. D.L. Nika, A.I. Cocemasov, C.I. Isacova, A.A. Balandin, V.M. Fomin, O.G. Schmidt, Phys. Rev. B **85**, 205439 (2012)
87. H. Scheel, S. Reich, C. Thomsen, Phys. Status Solidi (B) **242**, 2474 (2005)
88. R. Kagimura, R.W. Nunes, H. Chacham, Phys. Rev. Lett. **98**, 026801 (2007)
89. D.B. Migas, J. Appl. Phys. **98**, 054310 (2005)

90. T. Vo, A.J. Williamson, G. Galli, Phys. Rev. B **74**, 045116 (2006)
91. M. Bruno, M. Palummo, S. Ossicini, R. Del Sole, Surf. Sci. **601**, 2707 (2007)
92. J.X. Cao, X.G. Gong, R.Q. Wu, Phys. Rev. B **75**, 233302 (2007)
93. B. Lee, R.E. Rudd, Phys. Rev. B **75**, 041305 (2007)
94. B. Lee, R.E. Rudd, Phys. Rev. B **75**, 195328 (2007)
95. H. Peelaers, B. Partoens, F.M. Peeters, Physica E **40**, 2169 (2008)
96. X.H. Peng, A. Alizadeh, S.K. Kumar, S.K. Nayak, Int. J. Appl. Mech. **1**, 483 (2009)
97. L. Yang, M.Y. Chou, Nano Lett. **11**, 2618 (2011)
98. C.P. Li, C.S. Lee, X.L. Ma, N. Wang, R.Q. Zhang, S.T. Lee, Adv. Mater. (Ger.) **15**, 607 (2003)
99. F. Stillinger, T. Weber, Phys. Rev. B **31**, 2384 (1985)
100. D. Li, Y. Wu, P. Kim, L. Shi, P. Yand, A. Majumdar, Appl. Phys. Lett. **83**, 2934 (2003)
101. J. Zou, A. Balandin, J. Appl. Phys. **89**, 2932 (2001)
102. A. Cleland, *Foundations of Nanomechanics* (Springer, New York, 2003)
103. M.J. Verstraete, X. Gonze, Phys. Rev. B **74**, 153408 (2006)
104. J. Krti, G. Kresse, H. Kuzmany, H. Phys. Rev. B **58**, 8869 (1998)
105. G.S. Duesberg, I. Loa, M. Burghard, K. Syassen, S. Roth, Phys. Rev. Lett. **85**, 5436 (2000)
106. L.M. Lee, E.A. Fitzgerald, J. Appl. Phys. **94**, 2590 (2003)
107. C. Zhang, A. De Sarkar, R.Q. Zhang, J. Phys.: Condens. Matter **24**, 015301 (2012).
108. Y.F. Zhang, Y.H. Tang, N. Wang, C.S. Lee, I. Bello, S.T. Lee, Phys. Rev. B **61**, 4518 (2000)
109. S. Mathur, H. Shen, V. Sivakov, U. Werner, Chem. Mater. **16**, 2449 (2004)
110. B.V. Kamenev, V. Sharma, L. Tsybeskov, T.I. Kamins, Phys. Status Solidi (A) **202**, 2753 (2005)
111. P. Nguyen, H.T. Ng, M. Meyyappan, Adv. Mater. **17**, 549 (2005)
112. X.H. Sun, C. Didychuk, T.K. Sham, N.B. Wong, Nanotechnology **17**, 2925 (2006)
113. B.S. Kim, T.W. Koo, J.H. Lee, D.S. Kim, Y.C. Jung, S.W. Hwang, B.L. Choi, E.K. Lee, J.M. Kim, D. Whang, Nano Lett. **9**, 864 (2009)
114. A.N. Kholod, V.L. Shaposhnikov, N. Sobolev, V.E. Borisenko, F.A.D. Avitaya, S. Ossicini, Phys. Rev. B **70**, 035317 (2004)
115. M. Bruno, M. Palummo, A. Marini, R. Del Sole, V. Olevano, A.N. Kholod, S. Ossicini, Phys. Rev. B **72**, 153310 (2005)
116. S.P. Beckman, J. Han, J.R. Chelikowsky, Phys. Rev. B **74**, 165314 (2006)
117. J.T. Arantes, A. Fazzio, Nanotechnology **18**, 295706 (2007)
118. D. Medaboina, V. Gade, S.K.R. Patil, S.V. Khare, Phys. Rev. B **76**, 205327 (2007)
119. H. Peelaers, B. Partoens, F.M. Peeters, Appl. Phys. Lett. **90**, 263103 (2007)
120. P. Logan, X. Peng, Phys. Rev. B **80**, 115322 (2009)
121. C. Kittel, *Introduction to Solid State Physics*, 6th edn. (Wiley, New York, 1986)
122. L.T. Ngo, D. Almécija, J.E. Sader, B. Daly, N. Petkov, J.D. Holmes, D. Erts, J.J. Boland, Nano Lett. **6**, 2964 (2006)
123. H. Xu, X.B. Yang, C.S. Guo, R.Q. Zhang, Appl. Phys. Lett. **95**, 253106 (2009)
124. A. Hmiel, Y. Xue, Phys. Rev. B **80**, 241410 (2009)
125. W.R.L. Lambrecht, S. Limpijumnong, S.N. Rashkeev, B. Segall, Phys. Status Solidi (B) **202**, 5 (1997)
126. M.T. Yin, M.L. Cohen, Phys. Rev. B **29**, 6996 (1984)
127. A.P. Verma, P. Krishna, *Polymorphism and Polytypism in Crystals* (Wiley, New York, 1966)
128. W. van Haeringen, P.A. Bobbert, W.H. Backes, Phys. Status Solidi (B) **202**, 63 (1997)
129. Z. Wang, M. Zhao, T. He, X. Zhang, Z. Xi, S. Yan, X. Liu, Y. Xia, J. Phys. Chem. C **113**, 856 (2009)
130. M. Yu, C.S. Jayanthi, S.Y. Wu, Phys. Rev. B **82**, 075407 (2010)
131. A. Mavrandonakis, G.E. Froudakis, M. Schnell, M. Mühlhäuser, Nano Lett. **3**, 1481 (2003)
132. U. Schmid, N.E. Christensen, M. Cardona, Phys. Rev. B **41**, 5919 (1990)
133. X.H. Sun, C.P. Li, W.K. Wong, N.B. Wong, C.S. Lee, S.T. Lee, B.K. Teo, J. Am. Chem. Soc. **124**, 14464 (2002)
134. E. Borowiak-Palen, M.H. Ruemmeli, T. Gemming, M. Knupfer, K. Biedermann, A. Leonhardt, T. Pihler, R.J. Kalenczuk, J. Appl. Phys. **97**, 056102 (2005)

135. A. Huczko, M. Bystrzejewski, H. Lange, A. Fabianowska, S. Cudzilo, A. Panas, M. Szala, J. Phys. Chem. B **109**, 16244 (2005)
136. T. Taguchi, N. Igawa, H. Yamamoto, S. Shamoto, S. Jitsukawa, Physica E **28**, 431 (2005)
137. H. Wang, X.D. Li, T.S. Kim, D.P. Kim, Appl. Phys. Lett. **86**, 173104 (2005)
138. J. Zhou, M. Zhou, Z. Chen, Z. Zhang, C. Chen, R. Li, X. Gao, E. Xie, Surf. Coat. Technol. **203**, 3219 (2009)
139. M. Menon, E. Richter, A. Mavrandonakis, G. Froudakis, A.N. Andriotis, Phys. Rev. B **69**, 115322 (2004)
140. M. Zhao, Y. Xia, F. Li, R.Q. Zhang, S.T. Lee, Phys. Rev. B **71**, 085312 (2005)
141. S.P. Huang, D.S. Wu, J.M. Hu, H. Zhang, Z. Xie, H. Hu, W.D. Cheng, Opt. Express **15**, 10947 (2007)
142. R. Moradian, S. Behzada, R. Chegel, Physica B **403**, 3623 (2008)
143. X. Wang, B. Wang, J. Zhao, G. Wang, Chem. Phys. Lett. **461**, 280 (2008)
144. R. Moradian, S. Behzada, R. Chegel, Phys. Lett. A **373**, 2260 (2009)
145. A.D. Patrick, X. Dong, T.C. Allison, E. Blaisten-Barojas, J. Chem. Phys. **130**, 244704 (2009)
146. T.A. Hilder, R. Yang, D. Gordon, A.P. Rendell, S.H. Chung, J. Phys. Chem. C **116**, 4465 (2012)
147. K.M. Alam, A.K. Ray, Nanotechnology **18**, 495706 (2007)
148. K.M. Alam, A.K. Ray, Phys. Rev. B **77**, 035436 (2008)
149. S.J. Rathi, A.K. Ray, Chem. Phys. Lett. **466**, 79 (2008)
150. K. Adhikari, A.K. Ray, Solid State Commun. **151**, 430 (2011)
151. R.A. Jishi, M.S. Dresselhaus, G. Dresselhaus, Phys. Rev. B **47**, 16671 (1993)
152. M. Ouyang, J.L. Huang, C.L. Cheung, C.M. Lieber, Science **292**, 702 (2001)
153. Yu.F. Zhukovskii, P. Balaya, E.A. Kotomin, J. Maier, Phys. Rev. Lett. **96**, 058302 (2006)
154. T. Ito, K. Sano, T. Akiyama, K. Nakamura, Thin Solid Films **508**, 243 (2006)
155. S.V. Golod, V.Ya. Prinz, V.I. Mashanov, A.K. Gutakovsky, Semicond. Sci. Technol. **16**, 181 (2001)
156. D.B. Migas, V.E. Borisenko, Phys. Rev. B **76**, 035440 (2007)
157. J. Zang, M. Huang, F. Liu, Phys. Rev. Lett. **98**, 146102 (2007)
158. M.A. Makeev, D. Srivastava, M. Menon, Phys. Rev. B **74**, 165303 (2006)
159. H. Dai, E.W. Wong, Y.Z. Lu, S. Fan, C.M. Lieber, Nature (London) **375**, 769 (1995)
160. Y. Zhang, T. Ichihashi, C. Landree, F. Nihey, S. Iijima, Science **285**, 1719 (1999)
161. X. Zhou, H. Lai, H. Peng, C.F.C.K. Au, L. Liao, N. Wang, I. Bello, C. Lee, S. Lee, Chem. Phys. Lett. **318**, 58 (2000)
162. T. Seeger, P. Redlich, M. Rühle, Adv. Mater. **12**, 279 (2000)
163. W. Zhou, Y. Zhang, X. Niu, G. Min, in *One-Dimensional Nanostructures*. Series, Lecture Notes in Nanoscale Science and Technology, vol. 3, ed. by Z.M. Wang (Springer, New York, 2008), pp. 17–59
164. H. Matsunami, T. Kimoto, Mater. Sci. Eng. R **20**, 125 (1997)
165. X. Duan, C.M. Lieber, Adv. Mater. **12**, 298 (2000)
166. Z. Wang, M. Zhao, T, He, H. Zhang, X. Zhang, Z. Xi, S. Yan, X. Liu, Y. Xia. J. Phys. Chem. C **113**, 12731 (2009)
167. J. Zhu, J. Jia, F.L. Kwong, D.H.L. Ng, Diam. Relat. Mater. **33**, 5 (2013)
168. P.B. Sorokin, D.G. Kvashnin, A.G. Kvashnin, P.V. Avramov, L.A. Chernozatonskii, J. Nanosci. Nanotechnol. **10**, 4992 (2010)
169. J. Li, Y. Xia, M. Zhao, X. Liu, C. Song, L. Li, F. Li, B. Huang, Chem. Phys. Lett. **442**, 384 (2007)
170. B. Yan, G. Zhou, W. Duan, J. Wu, B.L. Gu, Appl. Phys. Lett. **89**, 023104 (2006)
171. M. Bechelany, A. Brioude, D. Cornu, G. Ferro, P. Miele, Adv. Funct. Mater. **17**, 939 (2007)
172. A. Dąbrowska, M. Soszyński, A. Huczko, Phys. Status Solidi (B) **250**, 2713 (2013)
173. J. Tersoff, Phys. Rev. Lett. **61**, 2879 (1988)
174. X.L. Wu, J.Y. Fan, T. Qiu, X. Yang, G.G. Siu, P.K. Chu, Phys. Rev. Lett. **94**, 026102 (2005)
175. M.W. Zhao, Y.Y. Xia, F. Li, R.Q. Zhang, S.T. Lee, Phys. Rev. B **71**, 085312 (2005)
176. J.E. Yang, C.B. Jin, C.J. Kim, M.H. Jo, Nano Lett. **6**, 2679 (2006)

177. M. Amato, M. Palummo, S. Ossicini, Phys. Rev. B **79**, 201302(R) (2009)
178. A. Nduwimana, R. Musin, A. Smith, X. Wang, Nano Lett. **8**, 3341 (2008)
179. L. Yang, R.N. Musin, X.Q. Wang, M.Y. Chou, Phys. Rev. B **77**, 195325 (2008)
180. M. Amato, M. Palummo, S. Ossicini, Phys. Rev. B **80**, 235333 (2009)
181. K.M. Varahramyan, D. Ferrer, E. Tutuc, S.K. Banerjee, Appl. Phys. Lett. **95**, 033101 (2009)
182. J. Xiang, W. Lu, Y. Hu, Y. Wu, H. Yan, C.M. Lieber, Nature **441**, 489 (2006)
183. Y. Hu, H.O.H. Churchill, D.J. Reilly, J. Xiang, C.M. Lieber, Nat. Nanotechnol. **2**, 622 (2007)
184. J. Garg, N. Bonini, N. Marzari, Nano Lett. **11**, 5135 (2011)
185. M. Shelley, A.A. Mostofi, Europhys. Lett. **94**, 67001 (2011)
186. X. Peng, F. Tang, P. Logan, in *Nanowires - Fundamental Research*, ed. by A. Hashim (InTech Publication, Rieka, 2011), pp. 81–100
187. M. Amato, S. Ossicini, R. Rurali, Nano Lett. **11**, 594 (2011)
188. M. Amato, S. Ossicini, R. Rurali, Nano Lett. **12**, 2717 (2012)
189. S.R. Mehrotra, P. Long, M. Povolotskyi, G. Klimeck, Phys. Status Solidi (RRL) **7**, 903 (2013)
190. Z. Wang, N. Mingo, Appl. Phys. Lett. **97**, 101903 (2010)

Chapter 6
Nitrides of Boron and Group III Metals

In this chapter, *written by Yu.F. Zhukovskii* (*quantzh@latnet.lv*), theoretical models of 1D BN, AlN, GaN nanostructures as well as their properties are described and discussed.

Boron nitride semiconductors with stable *h*- and *c*-crystalline structures attract enhanced technological attention due to their unique properties. The formation of hexagonal BN NTs, both single- and multi-walled, can be considered as a result of the rolling-up of an *h*-BN(0001) honeycomb nanolayer (boronitrene), which is similar to the construction of carbon nanotubes from graphene. Like the latter, boronitrene is an almost flat hexagonal monolayer formed by a periodic network of sp^2 B-N bonds (where the influence of sp^3 bonding is neglected). Rolled-up SW and DW nanotubes as well as their bundles have been simulated in a large number of studies. According to the numerous publications, rolled-up BN NTs are the second most wide-spread type of nanotubes after CNTs. Other types of hollow 1D nanostructures of BN were simulated too, e.g., polyhedral nanotubes and nanoscrolls. To model BN NTs, both finite cage-like tubules (with either semi-fullerene caps or H-passivated edges) and periodic 1D nanotubes are used.

Equilibrium BN NT structures with different chiralities for single-, double- and triple-wall configurations, their cohesive, electronic and vibrational properties are studied by a number of methods: atomistic formalism of many-body empirical potentials, dynamical shell model, molecular dynamics and tight-binding methods, as well as the first principles methods of DFT-LCAO, PW DFT and DFT-LACW (Linearized-Augmented Cylindrical Waves). A growth mechanism for rolled-up single-wall BN nanotubes synthesized using the CVD (Chemical Vapor Deposition) method was simulated too.

The formation of BN nanoscrolls is dominated by two major energy contributions: an elastic energy increase caused by bending the BN layer (decreasing stability) and a free energy decrease generated by the van der Waals interaction energy of overlapping regions of the layer (increasing stability). As the structure is rolled up, the layer curvature increases before the layers overlap, and so do the torsion and inversion contributions to the strain energy. Thus, the rolled nanostructure becomes

© Springer-Verlag Berlin Heidelberg 2015

R.A. Evarestov, *Theoretical Modeling of Inorganic Nanostructures*,
NanoScience and Technology, DOI 10.1007/978-3-662-44581-5_6

less stable in relation to the undistorted (planar) configuration, which makes the transition from planar to rolled nanostructures energy-assisted.

Similar to diamond nanowires, theoretical studies on BN NWs were performed based mainly on their densely-packed *c*-BN structure. The structural, electronic and thermal properties of BN nanowires with optimized zinc-blende morphology were carefully simulated using the DFTB and molecular dynamics methods. The homogeneous BN NWs represented infinitely extended 1D prismatic crystallites cut from a *c*-BN crystal perpendicular to the (001), (111), and (110) section planes. BN NW stability strongly depends on the nanowire morphology. Apart from prismatic-type BN nanowires, theoretical simulations are performed also on BN nanofilaments of atomic diameters with the structure of the linear chain -B-N-B-N-, which can be doped by different atoms and functionalized. When joined to metallic electrodes (e.g., Al and Au) fragments of monoatomic BN filaments, which were found to be semiconducting, give rise to ballistic conductance along the linear $(BN)_m$ chains.

Two stable 3D morphologies of the technologically important group-III metal nitrides (AlN and GaN) are known: the hexagonal wurtzite (*w*) and the cubic (*c*) zinc-blende (sphalerite). 2D nanolayers of AlN and GaN were studied mainly for the densely-packed polar surfaces (0001) and (111) of the wurtzite and zinc-blende, respectively. A bilayer cut from the densely-packed *n*-type slabs with either *w*-(0001) or *c*-(111) termination forms buckled sp^3-bonded honeycomb 2D nanostructures, whose atop images are hexagonal like as those of the quasi-flat sp^2-bonded boronitrene.

Finite cage-like and infinite tubule models were used for the theoretical simulations on the SW AlN, GaN and $Al_xGa_{1-x}N$ nanotubes. Variation of Al concentration in $Al_xGa_{1-x}N$ nanotubes results in both linear and non-linear band gap change between the extreme values from the perfect GaN and AlN NTs. The latter are preferred in the growth of a faceted hexagonal-shaped nanotube wall continuing along the radial direction, analogously to faceted Si and SiC NTs. A wide spectrum of methods was applied in these calculations: atomistic formalism of the many-body empirical potentials, the method of molecular dynamics, DFTB and the ab initio PW DFT and LCAO DFT methods.

For the simulations of AlN and GaN nanowires, two traditional ab initio methods have been applied: the LCAO DFT and PW DFT. The latter method was used for the nanowires incorporated in the repeating tetragonal supercells of a dimension such that the interaction between NWs and their nearest images was negligible. The corresponding 1D NW models were exclusively chosen as those possessing a single-crystalline *w*-NW morphology (space group $P6_3mc$) with the growth direction along the [0001] axis, although the structure of their lateral facets could not be directly identified in the experiments. The cohesive, electronic, elastic and vibrational properties of AlN and GaN nanowires have been simulated so far. Both continuous and finite element models were used for the detailed description of mechanical (e.g., elastic) NW properties and their comparison with those found with the atomistic models.

6.1 Boron Nitride Bulk and Nanolayers

Boron nitride (BN) is a synthetic III–V compound with extraordinary mechanical, thermal, electrical, optical and chemical properties which are widely applied for various technological purposes [1]. First BN crystalline samples were synthesized at room temperature and atmospheric pressure as structures containing hexagonal sp^2-bonded monolayers isomorphic with graphene [2].

Stacked as planes, these honeycomb monolayers form a layered hexagonal boron nitride (*h*-BN), structurally similar to graphite, differed by the space arrangement of atoms in lattice [3], however, both described by the space group $P6_3/mmc$ [4]. In *h*-BN lattice, hexagonal rings of the basal planes are located directly above each other, with a sequence of atoms along vertical axis B-N-B-N-achieved via rotation between alternate layers by 180° (Fig. 6.1a). In graphitic structure (*g*-BN), only half of atoms of one plane lie above or below atoms of the adjacent layers while another half of atoms lie above or below the centers of the adjacent hexagons (as shown in Fig. 6.1b for *h*-BN with graphite structure). The former crystalline morphology was found to be energetically the most stable as compared to the latter or other structural polytypes of *h*-BN [4], due to larger electrostatic interaction between layers. Another essential difference between *h*-BN and *g*-BN is that the latter provides semi-metallic conductance mainly via noticeably delocalized π-electrons (with orbitals parallel to the honeycomb monolayers, while the ionicity of *h*-BN makes it a semiconductor with a wide band gap, experimentally estimated to be 5.97 eV [5].

The cubic allotrope of a non-layered BN with a sphalerite-type (zinc-blende) structure described by the space group $F\bar{4}3m$ and known as borazon (Fig. 6.2) is a synthetic material with the second highest hardness and thermal conductivity only

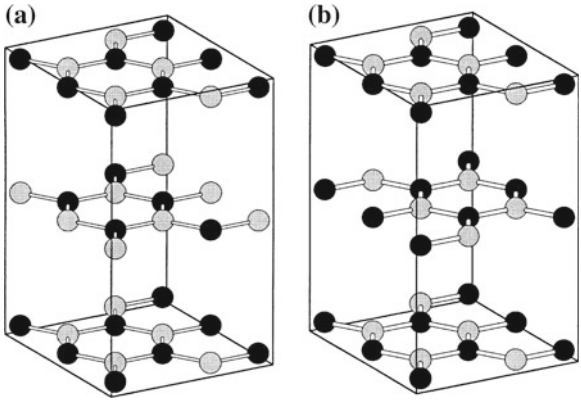

Fig. 6.1 Models of layered hexagonal binary BN allotropes with stable structures of *h*-BN (**a**) and graphitic *g*-BN (**b**). B and N atoms are shown as *gray* and *black balls*, respectively [4]

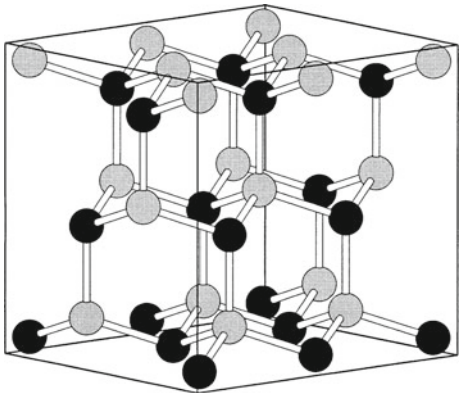

Fig. 6.2 Sphalerite-type boron nitride lattice (*c*-BN). B and N atoms are shown as *gray* and *black balls* (Reprinted figure with permission from Mosuang and Lowther [4], Copyright (2002) by the Elsevier Science Ltd. All rights reserved)

preceded by diamond [1]. In analogy to *c*-SiC considered in Sect. 5.4, *c*-BN is a sp^3-bonded crystal acting as an electrical insulator and an excellent thermally stable conductor of heat with a high resistance to oxidation. The cubic boron nitride can be obtained under a high pressure and a high temperature treatment of *h*-BN [4]. Besides energetically stable *h*- and *c*-crystalline structures, several metastable phases of boron nitride were also synthesized [1, 6]: (i) *w*- and *rs*-BN (wurtzite and rock-salt structures, respectively, with sp^3 hybridization), (ii) *r*- and *t*-BN (sp^2 rhombohedral and turbostratic structures, respectively) as well as (iii) amorphous *a*-BN. Unlike SiC and the majority of pnictides, which crystallize mainly in sp^3 *c*- and *w*-phases, whereas their sp^2 hexagonal phase was found to be rather metastable, *h*-BN can be easy synthesized just as a stable compound and then be transformed to *c*-BN [1]. This structural difference between similar types of binary compounds is obviously caused by a specific nature of the chemical bonding in BN, which can be characterized by considerable values of both ionicity (with charge transfer 1.01 *e* from B to N atom) and covalency (B-N bond population was estimated to be 0.58 *e*) [3]. The maximum of the electron density is localized closer to the midpoint along the semi-covalent bond, which can be explained by the proximity of ionic radii of B and N atoms as a result of the electronic charge transfer [7].

The formation of hexagonal BN NTs, both single- and multi-walled, can be considered as a result of the rolling up of an *h*-BN(0001) honeycomb nanolayer (boronitrene) [8], analogically to the construction of CNTs from graphene. Similar to graphene, boronitrene is almost a flat hexagonal monolayer (Fig. 6.3) formed by a periodic network of sp^2 B-N bonds (where the influence of sp^3 bonding is neglected), without noticeable buckling observed in a SiC monolayer (Sect. 5.4) and caused by a competition between sp^2 and sp^3 bonding. Figure 6.3 shows the fragment of quasi-flat boronitrene.

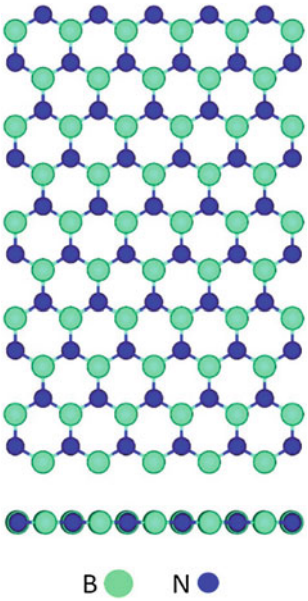

Fig. 6.3 Fragment of BN(0001) layer: *top* and *across* views. B and N atoms are shown as *middle light* and *small dark balls* [3]

6.2 Boron Nitride Nanotubes

6.2.1 Polyhedral and Rolled-Up Single-Wall Nanotubes

Comprehensive experimental studies of BN nanotubes (e.g., their synthesis) were carried out beginning with the middle of 90s [9] when MW NTs with the inner diameters on the order of 1–3 nm and with the lengths up to 200 nm were produced in a carbon-free plasma discharge between a BN-packed tungsten rod and a cooled Cu electrode. Nowadays, BN NTs are synthesized mainly via catalytic vapor–liquid–solid (VLS) mechanism at a temperature higher than 1000 °C, using different experimental methods (arc discharge, laser ablation and chemical vapor deposition) [10–14]. The most efficient method for the production of BN NTs includes the heating of MgO (particularly doped by SnO) and a boron powder mixture followed by the formation of B_2O_2 gas and its further reaction with NH_3 [10, 14]. Under certain experimental conditions not only SW and MW BN NTs were synthesized but also ropes containing numerous SW or MW nanotubes of similar morphology (bundles) [14].

Since the mechanism of BN NT growth is still not well defined [15], its theoretical simulations continue to attract enormous attention. A large number of atomistic calculations on BN nanotubes (regular, deformed and defective) have been performed so far for both SW and MW NT models of armchair, zigzag and chiral morphology possessing a wide range of uniform diameters (0.5–5 nm) as well as for their bundles. According to the total number of publications, the rolled-up BN NTs is the second widespread type of nanotubes after CNTs. Other types of hollow 1D nanostructures of BN were simulated too, e.g., nanoscrolls [16] and nanoarches [17]. To model BN

NTs, both finite cage-like tubules (with either semi-fullerene caps or H-passivated edges) [16, 18–20] and periodic 1D nanotubes [3, 8, 17, 21–42] were used. A number of methods were applied for their calculations: atomistic formalism of many-body empirical potentials [27], dynamical shell model [24], molecular dynamics [16, 18, 20], semi-empirical tight-binding (TB) methods [19, 23] and MNDO [15], first principles methods of DFT-LCAO [3, 17, 19, 20, 32, 35, 38–40, 42] as well as DFT-PW [8, 21, 22, 25, 26, 28–30, 33, 34, 37, 38, 41] and DFT-LACW (Linearized-Augmented Cylindrical Waves) [36]). In a few theoretical studies parallel with the prediction of the nanotube morphology and the electronic structure, the elastic and vibration properties were analyzed [20, 23–26, 29, 39] as well as thermodynamic conditions for the growth of nanotubes from nuclei [15, 18] and dislocation formation as a result of the strain relief [20].

In spite of the flat structure of boronitrene (Fig. 6.3), the polyhedral model for single-wall boron nitride nanotubes presents a two-shell structure [41]. Within this formalism, the boron atoms have a flatter structure of bonds, which are located closer to the nanotube axis as compared to the nitrogen atoms, which are fixed at pyramidal vertices above a triangular-type boron 1D polyhedron marked by gray lines (Fig. 6.4). The appearance of buckling in BN nanotubes of small diameters can be understood by re-hybridization and the weakening of π-bonds caused by the nanotube curvature [27]. As a result, B atoms tend to keep the sp^2 bonding with inter-bond angles of 120° while N atoms adhere an admixture of sp^3 hybridization, which leads to a smaller bond angle. These effects are contributive to the change of bond lengths and diameters in BN NTs. Except for buckling effects, boron nitride nanotubes with polyhedral quasi-hexagonal morphology (marked by black lines) constructed for different chiralities (Fig. 6.4) look qualitatively similar to the corresponding polyhedral models of CNTs. Optimization of the bond lengths and inter-bond angles in such models of both BN NTs and CNTs was performed using the DFT-GGA method [41].

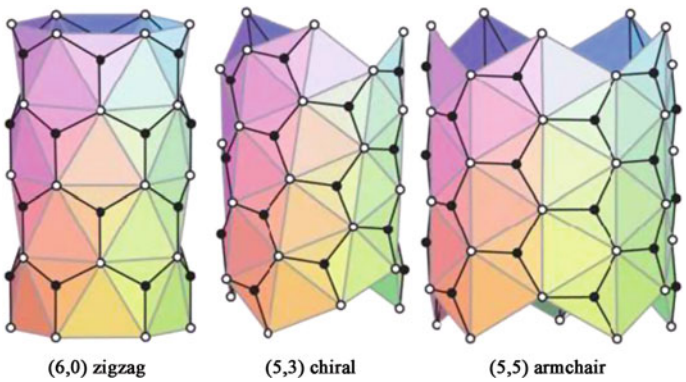

Fig. 6.4 General polyhedral models of BN nanotubes for three types of chirality. B and N atoms are shown as *white* (*hollow*) and *black balls* (Reprinted figure with permission from Lee et al. [41], Copyright (2010) by the Royal Society of Chemistry)

A number of SW BN NT simulations performed within the traditional rolled-up model, mainly for *ac*- and *zz*-chiralities, considered dependencies of different nanotube properties on gradually growing diameter D_{NT} varied from 0.5 up to 5.0 nm [3, 25–27, 35, 39]. Similar to *ac*- and *zz*-SiC nanotubes described in Sect. 5.5.1, both (6,6) and (12,0) SW BN NTs possessing the diameters of 8.4 and 9.6 Å, respectively, are shown in Fig. 6.5a, b [3]. The effect of buckling in these BN nanotubes reduces with the growth of their diameters (Fig. 6.6) achieving practically negligible values for SW BN NTs of larger diameters shown in Fig. 6.5c, d (24.9 and 28.7 Å corresponding to (18,18) and (36, 0) chirality indices, respectively).

Since hypothetical SW BN NTs with the infinite diameter should coincide with a boronitrene layer, a consequent growth of nanotube diameters leads to a substantial decrease of strain energies per formula unit, as defined in (6.1) and shown in Fig. 6.7a, similarly to that considered for Si NTs (Sect. 5.2.1). At the same time, the values of bond lengths ($d_{\mathrm{B-N}}$), effective atomic charges (q_{B} and q_{N}) as well as the band gap ($\Delta\epsilon_{gap}$) (Fig. 6.7b) approach to the same values as were calculated for the BN(0001) nanolayer (1.44 Å, 0.99 e and 7.09 eV, respectively) [3].

$$E_{strain} = \frac{1}{m}(E_{\mathrm{NT}} - kE_{slab}), \tag{6.1}$$

(a) optimized single-wall (6,6)*ac*-BN NT (aside and across images), D_{NT} = 0.84 nm;

(b) optimized single-wall (12,0)*zz*-BN NT (aside and across images), D_{NT} = 0.96 nm;

(c) optimized single-wall (18,18)*ac*-BN NT (aside and across images), D_{NT} = 2.49 nm;

(d) optimized single-wall (36,0)*zz*-BN NT (aside and across images), D_{NT} = 2.87 nm.

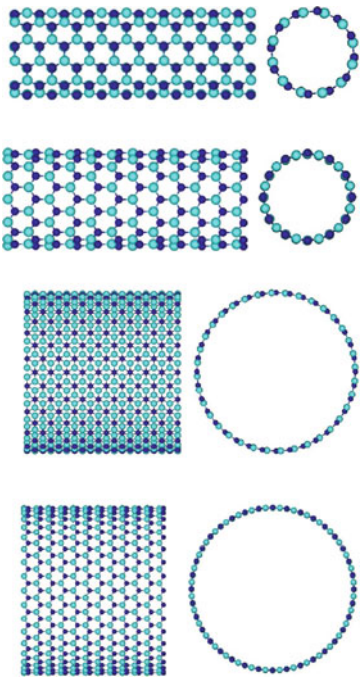

Fig. 6.5 Lateral and cross-section images of rolled-up SW BN NTs of different diameters possessing different chiralities. B and N atoms are shown as *light* and *dark balls*, respectively [3]

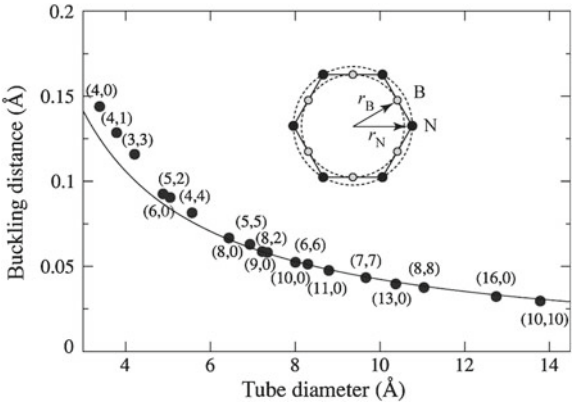

Fig. 6.6 Buckling distance in BN single-wall nanotube ($\delta r_{\mathrm{BNNT}} = r_{\mathrm{N}} - r_{\mathrm{B}}$) as a function of NT diameter [25]

where k is a number of slab unit cells with the same number of BN formula units (m) as in nanotube unit cells, while E_{NT} and E_{slab} are the total energies *per* corresponding unit cells. The energy curves $E_{strain}(D_{\mathrm{NT}})$ for BN nanotubes of both chiralities qualitatively coincide for $D_{\mathrm{NT}} > 1.0$ nm (Fig. 6.7a), i.e., just NT diameter determines the strain energy. As to $\Delta\epsilon_{gap}(D_{\mathrm{NT}})$ curves (Fig. 6.7b), they approach to each other and to the gap of BN nanolayer for $D_{\mathrm{NT}} > 1.5$ nm. On the other hand, because of some distortion of B-N bonds, their orientation in relation to the NT axis as well as due to the nanotube buckling, the dependences of arbitrary $d_{\mathrm{B-N}}$ and $q_{\mathrm{B}}(q_{\mathrm{N}})$ on D_{NT} and NT chirality are quite complicated [35]. Moreover, Fig. 6.7 shows that the properties of ultrathin BN NTs, e.g., those corresponding to indices (4,4) and (6,0) for *ac*- and *zz*-chiralities, respectively, substantially differ from the properties of thicker SW NTs, which can be explained by a slightly different bonding nature in the former ones, as described above.

6.2.2 *Vibrational Properties of Rolled-Up Single-Wall Nanotubes*

Reproducible synthesis of single-wall BN NTs and experimental studies of a number of their structural, electronic and vibrational properties [43, 44] provide possibilities for reliable verification of the corresponding theoretical predictions. One of the most convenient and effective experimental tools for identification of SW NTs was found to be Raman and infrared (IR) spectroscopy [44]. A number of phonon calculations for CNTs were performed using the force constant approach [45, 46] where these interatomic constants were fitted to experimental data up to the fourth nearest-neighbor interaction. Such an approach provides a fast estimate and, in combination with the zone-folding method (i.e., finding of the nanotube phonon frequencies from those of a corresponding nanolayer to be rolled into it) [46], results

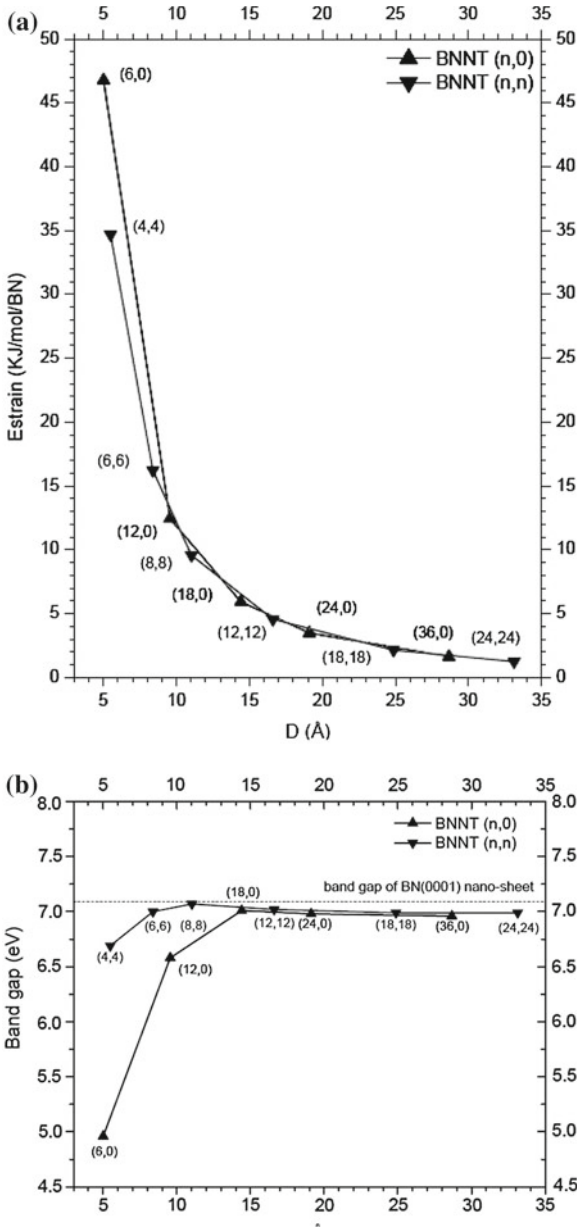

Fig. 6.7 Strain energies (**a**) and band gaps (**b**) of *ac*- and *zz*-BN nanotubes (Fig. 6.5) as functions of NT diameters [3]

in a good qualitative understanding of the vibrational properties of the nanotubes. Going beyond the force constant approach, the phonon dispersion in CNTs was calculated using tight-binding, DFT-LCAO and DFT-PW techniques, but the latter was

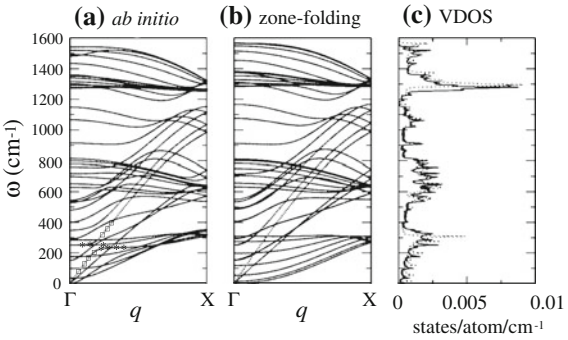

Fig. 6.8 Phonon dispersions and VDOSs for *ac*-BN NT calculated using ab initio and zone-folding methods. The *solid and dotted lines* in VDOS panel (**c**) correspond to the two plots of vibrational band structure (**a** and **b**), respectively. The *boxes* and *asterisks* in the left panel are described in text [25]

estimated as a more precise due to a better agreement with the experimental data [47]. The phonons in SW BN NTs have been calculated so far using the TB technique [23], the dynamical shell model [24], as well as ab initio methods of DFT-PW [25, 26, 29] and DFT-LCAO [39].

The phonon dispersion relations as well as the corresponding vibrational densities of states (VDOSs) obtained for a (6,6) BN nanotube using the first principles and zone-folding methods [25] are compared in Fig. 6.8. (A similar comparison was recently made for polyhedral Si NTs as considered in Sect. 5.2.4 [48].) Both approaches differ mainly in the low-frequency part of the spectrum, due to the coupling of in-plane and out-of-plane modes of nanolayer upon rolling into a nanotube. This results in a stiffening of the low-frequency nanotube modes. Another pronounced difference is the avoided crossings in the ab initio dispersion relation. According to the non-crossing rule of von Neumann and Wigner [49], the energy levels of modes, which have the same symmetry, do not cross when an adiabatic parameter (the phonon wave vector in this case) is changed. A prime example is the longitudinal (L) optical mode marked by boxes, which starts from zero frequency at Γ point of the Brillouin zone with the same slope as the L mode of nanolayer and displays evidently avoided crossing with the radial breathing mode (RBM at 251 cm^{-1}) marked by asterisks. Both modes possess A_1 symmetry at point Γ (Fig. 6.8). Figures 6.9 and 6.10 demonstrate the mapping of the three optical modes of nanolayer at Γ point onto the corresponding A modes of zz-NT [25]. The out-of-plane optical

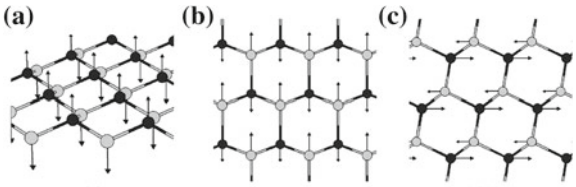

Fig. 6.9 Sketch of the optical phonon modes at Γ point in hexagonal BN nanolayer: **a** out-of-plane (ZO) mode, **b** transverse optical (TO) mode, and **c** longitudinal optical (LO) mode. (B and N atoms are shown as *light gray* and *black balls*.) For the assignment of "transverse" and "longitudinal", the phonon wave vector points in a horizontal direction with $q \to 0$ [25]

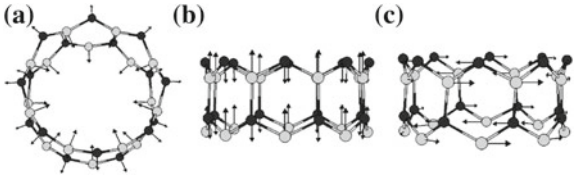

Fig. 6.10 Sketch of high-frequency *A* modes in *zz*-BN NT: **a** radial buckling (R) mode, **b** bond-stretching or longitudinal (L) mode, and **c** bond-bending or tangential (T) mode [25]

(ZO) modes of nanolayer transform to radial "buckling" (R) nanotube modes where all B atoms move inwards (outwards) simultaneously and all N atoms move outwards (inwards), giving rise to an oscillation of the NT buckling amplitude. The transverse optical (TO) mode of BN nanolayer maps onto the L NT mode, and, accordingly, the longitudinal optical (LO) mode of nanolayer maps onto a transverse or tangential (T) NT mode. In the *A* modes, all atoms along the circumference move in phase. In the modes of E_i symmetry, there are $2i$ nodes along the circumference (i nodal planes containing the symmetry axis of the tube). The *B* modes of NTs (n, n) and (n,0) contain $2n$ nodes along the circumference which means that a rotation by certain angle (with the proper translation along the tube axis) maps the mode onto its negative. In other words, for the *B* modes, the neighboring "columns" of atoms oscillate with a phase difference of π [25].

The points in the BZ of BN nanolayer give rise to the Raman- and IR-active *A*, E_1 and E_2 modes of NT. With a larger NT diameter (when increasing n of (n,n) and (n,0) nanotubes), the BZ points giving rise to the E_1 and E_2 modes converge towards BZ point of the BN(0001) nanolayer. Therefore, for a rough estimate of the frequencies of active modes for NTs of larger diameters, it is sufficient to look at the frequencies at Γ point of nanolayer [25]. For example, the frequencies of modes that correspond to the acoustic branches of nanolayer converge accordingly to zero for large NT diameters. Not all of the *A*, E_1 and E_2 modes can be Raman active, e.g., the TO mode of a BN nanolayer at Γ point (Fig. 6.9b) folds into a nanotube mode of A_1 symmetry (Fig. 6.10b) and, thus, is Raman active, whereas the LO mode of the nanolayer at Γ point (Fig. 6.9c) folds into a mode of A_2 symmetry (Fig. 6.10c), which changes a sign under reflection at a plane that contains the nanotube symmetry axis.

Figure 6.11 displays the frequencies of the Raman and IR-active modes of *zz*-BN NT (Fig. 6.5b, d) as a function of nanotube diameter where ab initio values are plotted as figured labels (which filling corresponds to active and inactive modes) while the zone-folding values are connected by lines, to guide the eye and extrapolate to larger NT diameters. The three frequency regimes can be easily distinguishable in Fig. 6.11 [25]:

(1) The low-frequency modes whose frequencies approach zero (for $D_{\mathrm{NT}} \to \infty$) are the modes derived from the acoustic branches of BN nanolayer (ZA, TA and LA, according to the classification given in Fig. 6.9).
(2) The three modes that approach $\omega \approx 818\,\mathrm{cm}^{-1}$ (for $D_{\mathrm{NT}} \to \infty$) are radial (R) modes (Fig. 6.10a) related to the optical out-of-plane (ZO) modes (Fig. 6.9a).
(3) The high-frequency regime above $1200\,\mathrm{cm}^{-1}$ consists of longitudinal (L) and transverse (T) modes (Fig. 6.10b, c respectively) which are zone-folded TO and LO modes of BN nanolayer (Fig. 6.9b, c respectively).

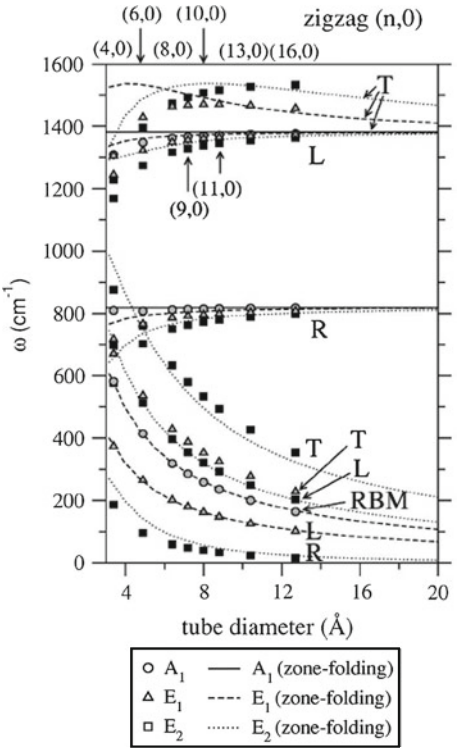

Fig. 6.11 Raman- and IR-active modes in *zz*-BN nanotubes as functions of NT diameter: comparison of ab initio and zone-folding values (marked as figured labels and lines, respectively). The shape of labels denotes the symmetry of the modes as shown in the legend positioned below. *Black filling* marks modes active in Raman spectra only, *while gray filling* stands for modes which are both Raman and IR active. R, L, and T mark the radial, longitudinal, and tangential high-frequency nanotube modes (Fig. 6.10) while RBM is a radial breathing mode [25]

Although the three different frequency regimes were discussed separately only for the case of *zz*-BN NTs (Fig. 6.11), they were also considered for the chiral and armchair nanotubes [25]. Analogically to CNTs, the inverse proportionality of RBM to the NT diameter ($\omega_{\mathrm{RBM}} \propto 1/D$) was found to be true also for BN NTs. In fact, not only the radial breathing mode, but most of the low-frequency modes display the same $1/D$ scaling. Only the frequency of the lowest E_2 mode displays $1/D^2$ proportionality [47]. For small BN NT diameters, the phonon modes deviate from the functional form A/D or A/D^2, because the linear quadratic behavior in the acoustic branches of BN nanolayer ceases to be valid further away from Γ point. Only the RBM follows the functional behavior A/D down to very low diameters [25].

A combined study of BN nanotubes by Raman and IR spectroscopy can serve to distinguish armchair nanotubes (where IR- and Raman-active modes are disjoint) from chiral and zigzag NTs, where the IR-active modes are a subset of the Raman-active modes. In particular, the radial breathing mode is both Raman and IR active for chiral and zigzag NTs, but only Raman spectra are active for armchair nanotubes, which make them a universal tool for experimental studies on single-walled nanotubes with a hexagonal morphology.

The further progress of theoretical simulations on the Raman spectra was the expansion of the bond polarization model, which was developed earlier for a descrip-

tion of the non-resonant Raman intensities of metallic CNTs [46], for the case of semiconducting BN NTs [29].

The basic assumption of the bond-polarization model [50] was that the total polarizability can be modeled in terms of the single bond contributions. Each bond was assigned a longitudinal polarizability, α_l, and a polarization perpendicular to the bond, α_p. Thus, the polarizability contribution of a particular bond d was defined as [29]:

$$\alpha_{ij}^{d} = \frac{1}{3}(2\alpha_p + \alpha_l)\delta_{ij} + (\alpha_l - \alpha_p)(\boldsymbol{R}_i\boldsymbol{R}_j - \frac{1}{3}\delta_{ij}) \tag{6.2}$$

where $\boldsymbol{R}$ is a unit vector along the bond. The second assumption was that the bond polarizabilities depend only on the bond length $|\boldsymbol{R}|$. Comparison of the non-resonant Raman spectra, calculated for *ac*- and *zz*-BN nanotubes of different diameters using both the ab initio method (as described above [25]) and the bond-polarization model [50], is given in Fig. 6.12. The Raman spectra were averaged over the polarization of the incoming and scattered light.

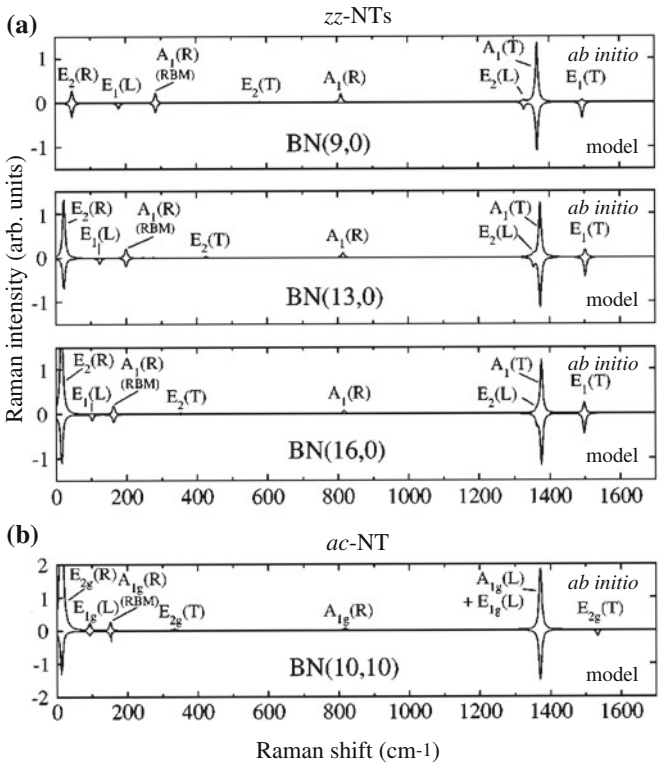

Fig. 6.12 Raman spectra for different BN NTs (**a** and **b**): comparison of ab initio calculations (*positive axis*) with the bond-polarization model (*inverted axis*) [29]. The symmetry assignment was described elsewhere [51]. The R, T and L modes are defined in Fig. 6.10 [25]

The peaks of *zz*-BN NTs below 700 cm^{-1} arise due to low-frequency phonon modes derived from the acoustic modes of BN nanolayer whose frequency scale is inversely proportional to the NT diameter (except for the E_2(R) mode, which scales with the inverse square of the diameter) [29]. The E_2(R) mode gets quite intense with the increasing D_{NT}, but its frequency is so low that it is hard to distinguish it from the strong Raleigh-scattering peak in experiments. The E_1(L) peak possesses practically vanishing intensity in the ab initio spectrum and is overestimated in the bond-polarization model. The radial breathing mode yields a clear peak that should be easily detectable in Raman measurements of BN NTs, just as in the case of CNTs. Both ab initio and bond-polarization model calculations yield a similar intensity for this peak. The high-frequency modes above 700 cm^{-1} are derived from the optical modes of BN nanolayer and change weakly with the diameter. The A_1(R) mode at 810 cm^{-1} gives a small contribution that might be detectable. The intensity decreases, however, with the increasing diameter. The bond-polarization model only yields a vanishingly small intensity for this peak. At 1370 cm^{-1} a clear signal is given by the A_1(T) mode, which has a very similar intensity both in ab initio and model calculations. The small side peak at a slightly lower frequency is due to the E_2(L) mode. The E_1(T) peak at 1480 cm^{-1} is gaining intensity with the increasing nanotube radius. The overall Raman spectrum for *ac*-BN (10,10) nanotube exhibits trends similar to those of *zz*-BN NTs [29].

6.2.3 A Growth Mechanism of Rolled-Up Single-Wall Nanotubes

While theoretical studies of CNT growth mechanisms based on different approaches are quite widespread during the last ten years [52–63], only a limited number of analogous studies on growth of BN NTs have been performed so far [15, 38, 43] although morphologically both types of hexagonal nanotubes are similar. One of the key reasons for this difference is the composition of BN NTs from the two different atomic species unlike monatomic CNTs, which makes the synthesis of the former more complicated [38]. CNTs are typically synthesized from hydrocarbon precursors when using the CVD (Chemical Vapor Deposition) method [64] and, according to the current theoretical understanding of the CNT formation process, individual carbon atoms diffuse in or on a catalytic metal nanoparticle, forming graphene-like flakes $(C_n)_{ads}$ that eventually give rise to their swelling after the appearance of pentagonal defects within a honeycomb structure [63]. A metallic substrate can assist in saturating the dangling bonds of flakes at their borders in favor of the formation of semi-fullerene-like embryos with the energy cost due to the curvature induced by the presence of periodically distributed pentagons, the appearance of which can be accelerated by a defective structure of the catalytic particle. A further step includes a gradual growth of this nucleus to a capped CNT under the influence of a permanent flux of the hydrocarbon molecules towards the interface between the metallic substrate and the graphitic adsorbate [55].

Assuming that the aforementioned ideas are relevant also to the growth of BN NTs, it is important to understand the factors that determine whether individual nitrogen and boron atoms diffusing on a catalytic surface result in the formation of capped BN embryos. The first principles calculations were performed [38] in order to confirm this prediction and to study the behavior of N_2, B_2, and BN molecules on an iron catalyst where the precursors used for producing BN NTs were already decomposed into individual B and N atoms and adsorbed upon the catalyst. The stepped *bcc*-Fe(110) surface was chosen as a typical catalytic substrate used for CVD growth. It was shown that B_2 formation dominates on flat terraces of the iron substrate, while at step edge regions BN formation is the most favorable reaction (Fig. 6.13).

The thermodynamic analysis of BN NT nucleation upon a catalytic surface was performed [15] to obtain a functional dependence of embryo's structure on the reaction parameters. At the beginning of nucleation, a few B and N atoms precipitate on the surface of a metal particle already saturated with them previously being combined into nanostructures with B and N atoms arranged in hexagons, which transform to a flat graphene-like nanolayer bonded with its edges to the metal surface (Fig. 6.14). This form of the nucleus is the most favorable because of the elimination of dangling bonds in the BN cluster as considered above. BN NT nucleus significantly differs from that of CNT, the closure of which requires the insertion of six pentagon C rings into the hexagonal network. Indeed, the insertion of pentagon (or any other odd-member rings) in BN NT nucleus results in the formation of weak B-B and N-N bonds and, therefore, is energetically unfavorable [15]. Since the closure of BN NT requires the insertion of three or four four-membered (tetragonal) rings and one octagonal ring, primary nuclei can be structurally different. Figure 6.14 shows the mapping diagram

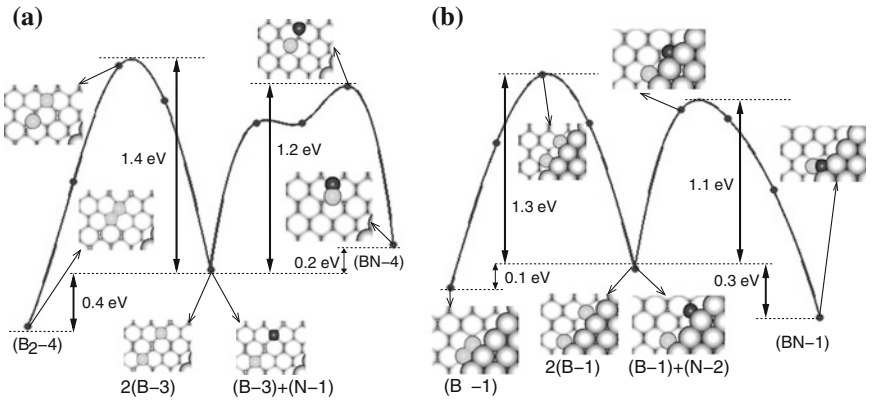

Fig. 6.13 Reaction barriers along a few reaction paths upon the stepped *bcc*-Fe(110) surface (where the external terrace is shown brighter than the internal one) for **a** reactions at the terrace $[2(B-3)] \rightarrow (B_2-4)$ and $[(B-3)+(N-1)] \rightarrow (BN-4)$ as well as for **b** reactions at the step edge $[2(B-1)] \rightarrow (B_2-1)$ and $[(B-1)+(N-2)] \rightarrow (BN-1)$. *Middle gray* and *small black* balls correspond to boron and nitrogen atom, respectively. The zero of energy for reactions $X^* + Y^* \rightarrow XY^*$ is fixed at the energy $E(X^* + Y^*)$, where both X and Y are at the same unit cell. The zero of energy for competing reactions forming B_2 and BN are set at the same value, in order to make the comparison of energy barriers easier [38]

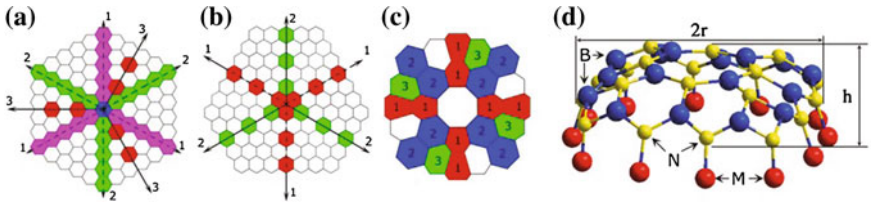

Fig. 6.14 Three principal types of BN NT nucleus: **a** with a BN hexagon at the *top* of the end cap (placement of tetragons in "1" or "2" locations results in the formation of *ac*-NTs, while placement in "3" locations results in the formation of *zz*-NTs, while arbitrary combination of "1", "2" or white results in the formation of chiral nanotubes); **b** with "star structure" (single atom of B (or N) at the *top* of the end cap (placement of tetragons only in "1" or "2" locations results in the formation of *zz*-NTs, any other combinations of locations result in the formation of chiral nanotubes); **c** octagonal ring at the top of the end cap (placement of tetragons only in "1" or "2" locations results in formation of *ac*-NTs armchair tubes, their placement in "3" locations results in the formation of *zz*-NTs, while any other combinations of locations results in the formation of chiral tubes). **d** Optimized structure of one of possible BN nuclei used for both semi-empirical calculations and thermodynamic modeling (Reprinted figure with permission from Kuznetsov et al. [15], Copyright (2007) by the WILEY-VCH Verlag GmbH & Co. KGaA, Weinheim)

used to generate armchair, zigzag and chiral caps where a combination of the mentioned rings constitutes the morphology of each nucleus. Structures of all types of end caps presented in Fig. 6.14 were optimized using semi-empirical MNDO, etc. methods, in order to analyze trends in the calculated heats of formation for each model [15].

6.2.4 Bundles of Rolled-Up Single-Wall Nanotubes

According to the experimental data, e.g., scanning electron microscopy (SEM), the ensemble of BN NTs grown from the adjacent Fe catalyst particles, using the method of laser ablation, tends to form vertical bundles [43]. The growth of these BN NTs is obtained through the optimum combination of Fe nanoparticles thickness, the laser energy density (deposition rate), and the substrate bias. For example, for the substrate with 12.5 nm thick Fe film at a substrate bias of −300 V [65], the resultant excessive deposition rate generates a coating of BN films on the Fe nanoparticles (Fig. 6.15a). Under these conditions, the deposition rate of BN films is faster than the diffusion rate of grown BN species into the Fe catalyst particles. Thus, BN films coated on the catalyst terminate the contact between Fe and the reactive growth species; this phenomenon is termed the poisoning effect. The thickness of BN films gradually decreases as the substrate bias increases (Fig. 6.15b). BN NTs start to grow at a higher substrate bias as a balance is reached between the rate of film deposition and the re-sputtering rate (Fig. 6.15c). At this total re-sputtering region, there is a suppression of the deposition of BN thin films. BN NTs grow on Fe nanoparticles according to the VLS (Vapor–Liquid–Solid) mechanism. Plasma creates a directional flux of the grown BN species with sufficient kinetic energies, to diffuse into Fe

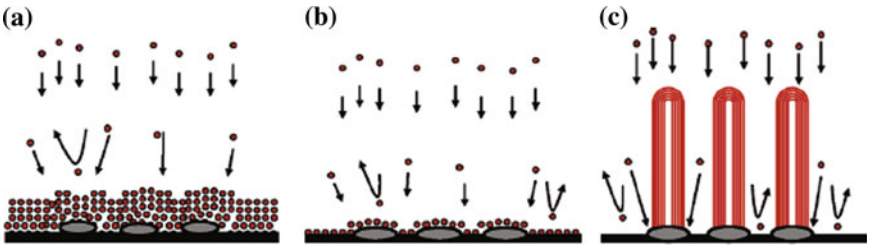

Fig. 6.15 Schematic drawing representing the growth region of BN NT bundles. **a** Deposition of BN nanoflakes on Fe nanoparticles due to low re-sputtering rate of the growth species. **b** Reduced growth rate of BN films with an energetic growth species. **c** Total re-sputtering region wherein BN NTs grow and BN films are suppressed (Reprinted figure with permission from Wang et al. [65], Copyright (2005) by the American Chemical Society)

nanoparticles, which capture and confine them in a nanoscopic space; otherwise, they are re-sputtered off. Super-saturation of Fe nanoparticles with BN vapor causes BN species to condense into the ordered nanotubular structures [65].

Although BN SW NTs can be synthesized as separated nanostructures, they were found to be more stable in bundle forms, due to a considerable inter-tube attraction caused by the polarity of B-N bonds [32]. It plays an essentially more important role than in the case of SiC NT bundle formation as considered in Sect. 5.5.2 not speaking about CNT bundles [66, 67]. Moreover, specific inter-tube interaction in BN SW NT bundles suggests the possibility of more diverse phase transitions in them under the external pressure, which could lead to new crystalline phases with unique structures, novel properties, and potential applications [33]. Nowadays, ensembles of BN NT bundles are not only the basis of many fundamental and significant designs in electronic devices and functional materials (such as super tough fibers, field effect transistors, field emission displays, etc.) but are also ideal media for atomic (e.g., Li, H, and inert gases) or molecular (e.g., H_2) storage [68].

The influence of transverse pressure on the phase transition processes of the aligned crystalline bundles of BN NTs was studied using the first principles calculations on periodic ensembles of the identical nanotubes with *ac* [30, 33] and *zz* [32] chiralities, respectively. The cohesive energy versus *ac*-bundle 2D-lattice constant dependencies shown in Fig. 6.16a illustrate that isolated SW BN NTs would be bundled together spontaneously until $a = 11.5$ Å (a total energy minimum), which corresponds to the inter-tube separation of ~3.36 Å, consistent with the experimental fact that BN NTs are usually produced in the bundle forms [69]. When a is decreased from 11.5 Å under the conditions of the transverse pressure, the total energy of a bundle increases, thus, smooth nanotube walls begin to buckle, which is accompanied by the formation of inter-tube bonds (Fig. 6.16b). At $a = 8.5$ Å, the coordination number of each atom clearly changes from 3 to 4, showing that the energy-consuming $sp^2 \rightarrow sp^3$ transition is achieved (fragment of bundle at the middle of Fig. 6.16b). With the continuously decreasing a, each NT is elongated more and more greatly along the nanotube axis until those intra-tube B-N bonds, which are not perpendicular to the NT axis (NPBs), get broken, resulting in the formation of a new layered

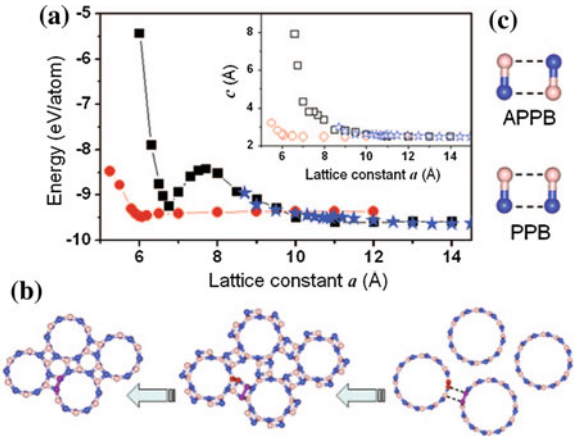

Fig. 6.16 **a** Variations of cohesive energy and lattice constant c (*inset*) versus in-plane lattice constant a for bundles of (3,3) (*circles*), (6,6) (*squares*), and (8,8) (*stars*) BN NTs. **b** Top view of atomic structures of (6,6) BN NT bundles at $a = 11.0$ (*right*), 8.5 (*middle*), and 6.75 Å (*left*). The bonds with circular and squared labels on the energy curves correspond to intra-tube B-N bonds which are not perpendicular and perpendicular to the NT axis, respectively. *Dashed lines* illustrate a pair of APPBs (*anti-parallel polar bonds*). **c** Patterns of two B-N bond arrangements, APPBs and PPBs (*parallel polar bonds*) between the adjacent nanotubes. *Light* and *dark balls* represent B and N atoms, respectively (Reprinted figure with permission from Hao et al. [33], Copyright (2008) by the American Chemical Society)

porous phase of BN at $a = 6.75$ Å [33]. This step of $sp^2 \rightarrow sp^3$ transition has an exothermic process from $a = 7.7$ down to 6.75 Å. The relative spatial orientations of polar B-N bonds of the adjacent NTs characterize the corresponding inter-tube interaction for the understanding of the bonding character in bundles under the transverse pressure: (i) in the case of the antiparallel polar bonds (APPBs) arranged between the adjacent NTs (Fig. 6.16c), the external pressure can help the neighboring nanotubes to overcome the deformation energy, to form the inter-tube bonds in the first step of phase transition crucial for the subsequent new phase formation; (ii) the parallel polar bonds (PPBs) arrangement leads to the "frustrated" B-B and N-N bonds, rather than the inter-tube hetero-nuclear B-N bonds. Thus, the results of the calculations [33] show that the BN NT bundles can undergo unique phase transitions under transverse pressure. The influence of this pressure on the band structure of *zz*-SW BN (16,0) NT bundles (with initial diameter 1.26 nm of individual shells) was analyzed via the results obtained using DFT-LCAO calculations [32]. The rate of the gradually increasing pressure was chosen to be lower for lower pressures, in order to define the structural behavior prior to a transition taking place (Fig. 6.17). After each pressure increment, the bundle was let to attain equilibrium, and then the change in cell volume was measured. No apparent systematic deviation from the circular cross section was observed below 1 GPa. Beyond this pressure, the BN NT cross section deform to an elliptic forms. Figure 6.17 clearly shows structural arrangements in nanotube bundle when pressure range is either low ($p < 1$ GPa) or high ($p > 1.0$ GPa).

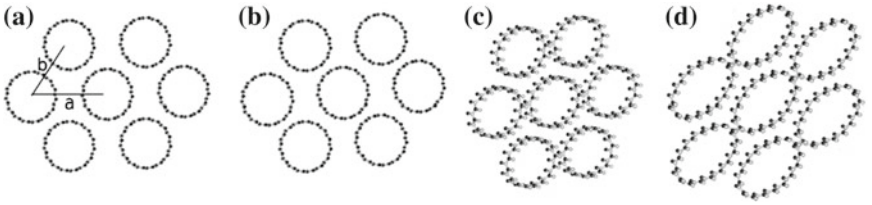

Fig. 6.17 Structure of a (16,0) SW BN NT bundle under the pressure of **a** 0 GPa, **b** 0.9 GPa, **c** 1.2 GPa, and **d** 3.5 GPa (Reprinted figure with permission from Guerini et al. [32], Copyright (2007) by the WILEY-VCH Verlag GmbH %26 Co. KGaA, Weinheim)

To quantify the volume changes occurring at the structural transition in BN NT bundles under the growth of pressure, the variations of magnitudes of UC vectors $\boldsymbol{a}$ and $\boldsymbol{b}$, defining the hexagonal basal planes (the distances between the NT centers in the adjacent cells), were considered [32]. It was observed that by increasing the pressure, both vector magnitudes diminished and their decrease was not monotonous. The first vector magnitude is discontinuous and the second one changes the slope in its dependence on pressure, both occurring at $p = 1$ GPa.

The electronic band structure was observed to change rather little with the pressure (Fig. 6.18a–d). One significant change observed at higher pressures was the splitting of the degenerated states in the conduction band bottom. The energy gap at the Γ

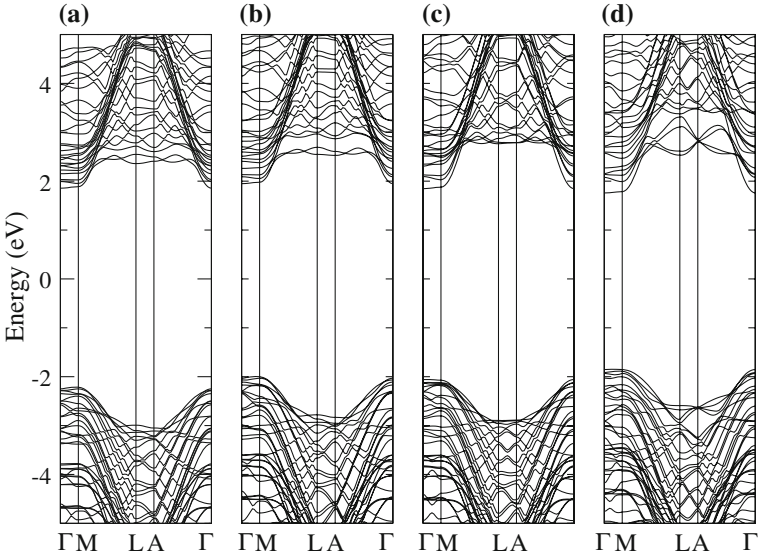

Fig. 6.18 Band structure of a (16,0) zigzag BNNTs bundle under pressure of **a** 0 GPa, **b** 0.9 GPa, **c** 1.2 GPa and **d** 3.5 GPa. The Fermi level localized in zero. The irreducible part of the hexagonal BZ for BN NT bundle is the same as for SiC NT bundle (Sect. 5.5.2) (Reprinted figure with permission from Guerini et al. [32], Copyright (2007) by the WILEY-VCH Verlag GmbH %26 Co. KGaA, Weinheim)

point was observed to diminish considerably with pressure. The value 4.10 eV at $p = 0$ decreased down to 3.61 eV at $p = 3.5$ GPa, although the system remaining a semiconductor at all the pressures considered.

A possible explanation for the different band gap dependence on the pressure in BN NT bundles (as compared to a bulk crystal) was provided as following [32]: (i) by applying the pressure to crystal, the elastic deformation is minute in most cases, due to its rigidity, whereas influence of pressure on bundles of single-wall NTs is rather different, due to their tubular geometry; (ii) although a nanotube is extremely rigid to distortions along the NT axis, it is very flexible to those, perpendicular to the axis, thus, the NT circular cross section may be deformed to an elliptical form; (iii) the instability of the NT cross section under pressure leads to deformations that cause the band gap to diminish in general. According to this idea, a transverse electric field was observed to severely reduce the band gap of a BN NT bundle [70].

6.2.5 Rolled-Up Double-Wall Nanotubes

Alternative ensembles constructed from SW BN NTs of different diameters, reproducibly synthesized and visualized, were found to be multi-wall boron nitride nanotubes with the inter-shell distance of 0.33–0.34 nm [69, 71]. Unlike CNTs, which exhibit rather random chiralities in MW NTs or bundles of SW nanotubes, a strong chirality selection (mainly *zz*-type) is observed in MW BN NTs [44]. The efficient plasma-arc method of BN NT synthesis was elaborated, which provided the production of almost exclusively double-wall nanotubes in high yield [72]. Moreover, while SW BN NTs of different chiralities with small and middle diameters should naturally undergo out-of-plane buckling, producing a dipolar shell as mentioned above (Fig. 6.6), the DW NTs may help to stabilize the growth of smooth nanotubes (containing mainly the even number of shells) [8]. Large-scale first-principles simulations on DW boron nitride nanotubes were performed earlier either for only $(n_1,0)@(n_2,0)$ chirality [22, 31] or for both $(n_1,0)@(n_2,0)$ and $(n_1,n_1)@(n_2,n_2)$ chiralities [28, 42].

The two mutual orientations of chiral and translational vectors of the constituent BN shells (Fig. 6.19) were considered for simulations of DW BN NTs [42]: coinciding and opposite (i.e., straight and inversed NT structures, respectively, corresponding to both PPB and APPB combinations of B-N bonds considered for SW BN NT bundles, Fig. 6.16). For *ac*-chirality of DW NTs, the cross-sections of inner and outer shells contain pairs of B and N atoms (B-N bonds) in the corresponding rings with both straight and inversed orientations of the chiral vector (Fig. 6.19a, b respectively), which make each of those electrostatically neutral. The difference of energies for equilibrium configurations of *ac*-DW BN NTs with the same chirality indices and straight versus inversed orientations of chiral vectors were found negligible, thus, only *a*-configurations were calculated. For *zz*-chirality, both straightly-stacked configuration, i.e., the outer B(N) ring across the inner B(N) ring (Fig. 6.19c), and the inversely-stacked configuration, i.e., N(B) across B(N) (Fig. 6.19d) were calculated because the corresponding energy difference between them is noticeable [42]. From

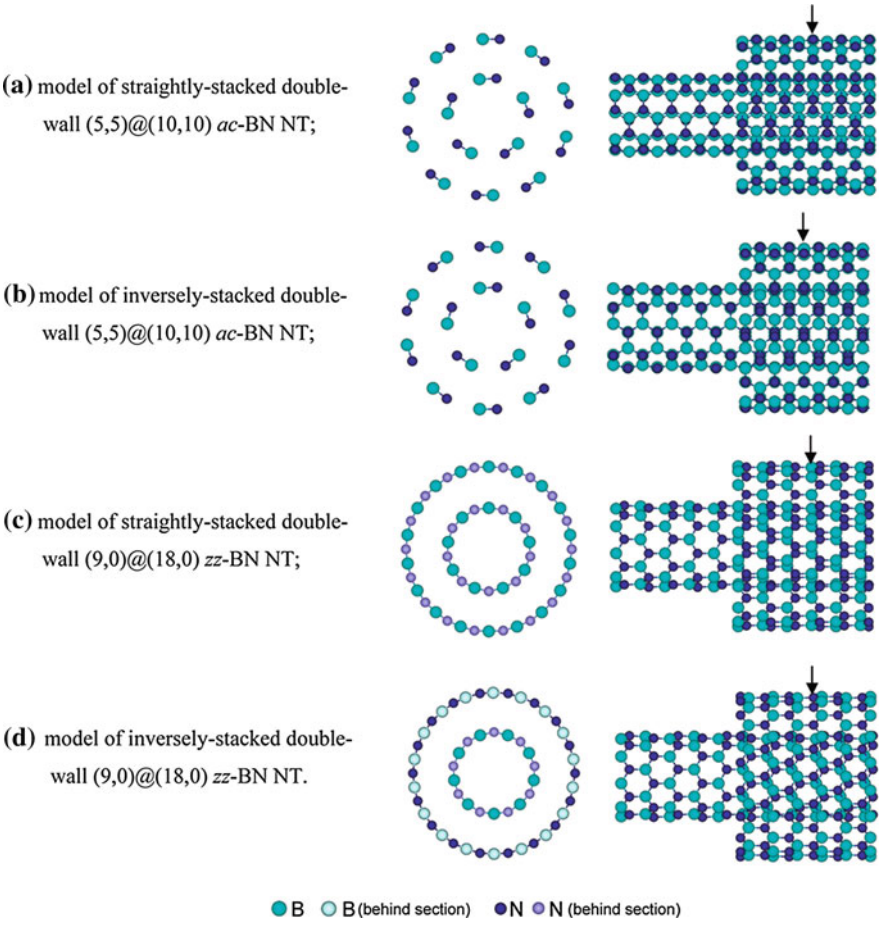

Fig. 6.19 Cross sections and lateral images for *ac*- and *zz*-chiralities of DW BN NTs corresponding to their optimized configurations. For *zz*-DW BN NTs (**c** and **d**), the atoms of the nearest ring behind the cross section are shown as *half-shaded balls*. Arrows above each lateral image of nanotube show directions of the cross sections. For convenience of visualization, lateral images of the inner shells of nanotubes have been chosen as twice as long as those of the outer shells [42]

the electrostatic point of view, the inversely-stacked configuration of *zz*-DW NTs should be energetically more favorable (i.e., positively-charged B ring of one shell is the nearest neighbor to the negatively charged N ring of the other shell, although in-wall B-N interactions are certainly more strong than those between the walls). A similar conclusion was earlier drawn elsewhere [28].

The stability of the DW NTs depends mainly on the inter-wall distance, i.e., a difference between the radii of constituent shells (ΔR_{NT}), and the diameter of the inner shell (D^{in}_{NT}). The binding energy E_{bind} between the constituent shells of a double-wall nanotube was chosen as a criterion of nanotube stability [42]:

$$-E_{bind}(D^{in}_{\rm NT}@D^{out}_{\rm NT}) = E_{tot}(D^{in}_{\rm NT}@D^{out}_{\rm NT}) - E_{tot}(D^{in}_{\rm NT}) - E_{tot}(D^{out}_{\rm NT}), \quad (6.3)$$

where E_{tot} are the calculated total energies of DW NTs and their constituent SW shells (both inner and outer) with the optimized structure. The energy curves $-E_{bind}(\Delta R_{\rm NT})$ for DW BN nanotubes of both *ac*- and *zz*-chiralities are shown in Fig. 6.20 [42]. The maxima of binding energies for these double-wall nanotubes correspond to both optimal (5,5)@(10,10) and (9,0)@(18,0) configurations as well as inter-shell distance 3.5–3.6 Å (*cf.* (5,5)@(10,10), (8,0)@(16,0) and 3.2 Å as described elsewhere [28]). The inversed B-N configuration of *zz*-DW NTs is slightly more energetically favorable than that of the straight B-B one, which confirms the presence of polarization effects in boron nitride MW NTs. Reliefs of the binding energy curves (Fig. 6.20) also give a small preference to the inversed double-wall *zz*-NTs versus *ac*-NTs. These results also favor to the experimentally observed dipolar-shell structured morphology of the MW BN NTs [8]. Obviously, the small values of $\Delta R_{\rm NT}$ and $D^{in}_{\rm NT}$ accompanied by the large values of relaxation energy result in instability of DW NTs (Fig. 6.20) while the large values of $\Delta R_{\rm NT}$ and $D^{in}_{\rm NT}$ (as well as neglecting relaxation energies) correspond to the quasi-independent non-interacting pairs of SW NTs. On the other hand, E_{bind} is sensitive to $\Delta R_{\rm NT}$ while the influence of $D^{in}_{\rm NT}$ on E_{bind} is rather negligible [42]. Fig. 6.21 shows the difference of the electronic charge re-distributions drawn for both optimal and increased values of $\Delta R_{\rm NT}$ and $D^{in}_{\rm NT}$ for double-wall *ac*- and *zz*-BW NTs (Fig. 6.19). For the optimal structures of DW NTs, considerable re-distributions of the electronic density can be observed with clearly visible polarization effects, especially around the inner shells. The latter are the largest for the inversely-stacked configuration of *zz*-BN nanotubes, while $\Delta\rho(\boldsymbol{r})$ function for *ac*-BN NTs is characterized by a more pronounced localization effects [42]. For double-wall nanotubes with large inter-wall distances (Fig. 6.21b, d and f),

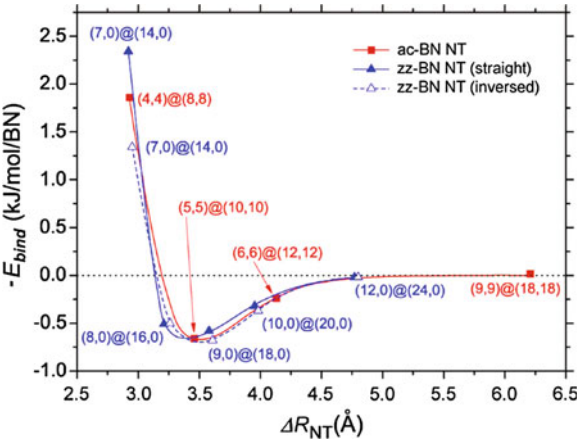

Fig. 6.20 Binding energies E_{bind} versus $\Delta R_{\rm NT}$ for the three sets of DW BN NTs with *ac*- and *zz*-chiralities (Fig. 6.19). Spline treatment of *curves* has been performed to make them smooth [42]

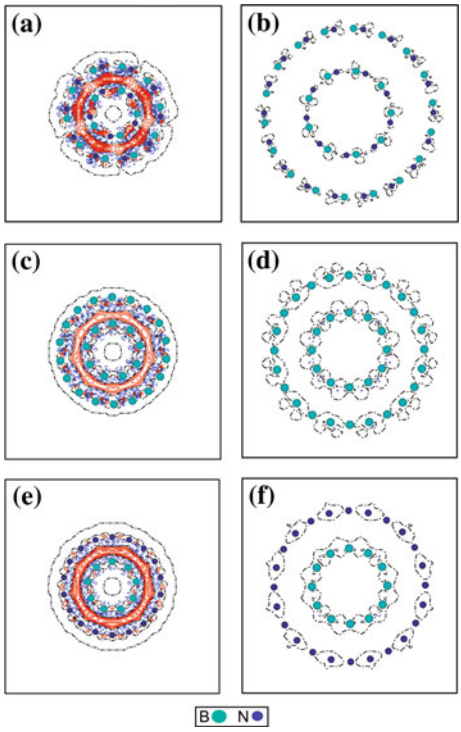

Fig. 6.21 Difference electron density plots $\Delta\rho(\boldsymbol{r})$ (the total electron densities in the perfect DW BN nanotube minus the sum of these densities in the two constituent SW BN NTs) calculated for the cross-sections of nanotubes depicted in Fig. 6.19: **a** (5,5)@(10,10), **b** (9,9)@(18,18), **c** straight (9,0)@(18,0), **d** straight (12,0)@(24,0), **e** inversed (9,0)@(18,0), **f** inversed (12,0)@(24,0). *Solid* (*red*), *dashed* (*blue*) and *dot-dashed* (*black*) isolines describe positive, negative and zero values of the difference density, respectively [42]

the interaction between the outer and inner shells is very weak, which reduces the stability of DW BN NTs, according to the reliefs of the potential curves (Fig. 6.20). The Mulliken charge population parameters calculated for both chiralities of the optimal and quasi-independent DW BN nanotube structures qualitatively confirm the results extracted from the drawn electron density re-distributions (Fig. 6.21).

For DW BN NTs, the band gap is the most dependent on the diameter of the inner shell being almost insensitive on the inter-shell distance. When comparing the calculated values of $\Delta\epsilon_{gap}$ for DW NTs with those for SW NTs, one can conclude that $\Delta\epsilon_{gap} < 6\,\text{eV}$ for chiralities (4,4), (6,0)–(10,0) of the inner shells, which correspond to $D^{in}_{\text{NT}} < 7.5\,\text{Å}$. With the further increase of D^{in}_{NT} and ΔR_{NT} the value of the band gap gradually approaches to the limit of a BN(0001) monolayer (7.09 eV) On the other hand, the comparison of gap for SW and DW BN NTs with the same outer diameter D^{out}_{NT} shows that the band gaps of the latter are noticeably smaller, by 0.5–1.5 eV (depending on a diameter of the inner shell) [42]. Thus, the band gaps for multi-wall BN NTs can be easier adjusted by the morphology composition of inner walls. For both BN(0001) nanolayer and BN NT morphologies, one-electron N($2p$) states prevail near the top of the valence band while the B($2p$) states are mainly distributed near the bottom of the conduction band [42]. Owing to a large curvature of the BN NTs of small and middle diameters which induces the hybridization between σ and π states

of both shells, the top of the valence and the bottom of the conduction bands were found to be localized on the outer and inner nanotubes, respectively [22]. Simulations of triple-wall (TW) (5,0)@(13,0)@(21,0) BN NTs [37] mainly confirmed the main conclusions drawn for DW BN NTs. An additional interest attracted theoretical study of structurally compatible DW hetero-nanotubes (CNT@BNNT and BNNT@CNT) with different sizes and combinations of chiralities which possess a number of technological applications [34]. It was found that the features of the highest occupied energy levels and the low-lying conduction bands are mainly determined by CNTs. But when the inter-tube spacing was small, these bands could be modified significantly due to an increased inter-tube interaction. In general, the valence band top and the conduction band bottom consist of mainly C(2*p*) atomic orbital, regardless of whether the CNT is the outer or the inner tube of a DW NT hetero-structure. When the inter-tube spacing was small, N(2*p*) electrons also contributed to the bands near the Fermi level because of the coupling between both shells in the double-wall hetero-structure.

6.3 Boron Nitride Nanoscrolls and Nanowires

6.3.1 Nanoscrolls

Although 1D carbon nanoscroll structures (CNScs) were known for more than half a century [73], their systematic experimental studies were begun after the reproducible synthesis of graphene [74, 75]. While CNTs could be imaged as graphene monolayers rolled-up in a way that their ends meet forming a cylinder, the rolled-up graphene monolayers in CNScs form papyrus-like nanoscroll structures (Fig. 6.22). In contrast

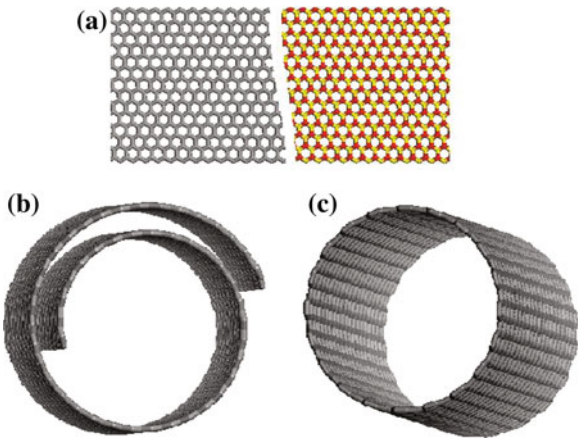

Fig. 6.22 Images of graphene/boronitrene monolayers (**a**), nanoscrolls (**b**) and nanotubes (**c**) (Reprinted figure with permission from Perim and Galvão [16], Copyright (2009) by the IOP Publishing)

to CNTs, nanoscroll diameter could be easily varied (contraction or expansion), making them extremely radially flexible. The self-scrolled tubules possess similar and even more remarkable properties than the planar graphene monolayers [76] and cylindrical CNTs [77] with potential applications in chemical doping, hydrogen storage, Li-battery technology and nano-mechanical devices [75].

Due to the similarity of honeycomb structures of both graphene and boronitrene (0001) monolayers, the morphologies of CNScs and BN NScs could be analogical (Fig. 6.22). However, in spite of a substantial number of theoretical and experimental works reported on BN NTs, as mentioned above, the reference data on BN NScs explored so far is rather scarce [16, 77]. The formation and existence of 1D nanoscrolls was also predicted for other inorganic materials, e.g., GeSi (Sect. 5.5.5). BN nanoscroll structures, simulated using the MD method, were generated by rolling a boronitrene monolayer into a truncated Archimedean-type spiral via rotation around the y' axis defined by the angle θ shown in Fig. 6.23a. This spiral is defined using the parametric equation [16]:

$$r = a\varphi + a_o, \tag{6.4}$$

where r and φ are standard cylindrical coordinates connected by non-zero constants a and a_o. The parameter a is related to the initial interlayer spacing d, i.e., $a = d/2\pi$.

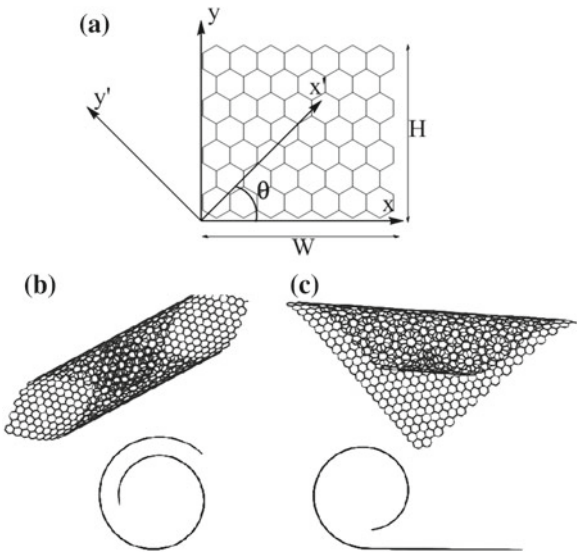

Fig. 6.23 The unwrapped honeycomb monolayer described by width W and height H where x' and y' are the scroll axes rotated by the angle θ relatively to the reference coordinate xy system (**a**). The scroll is generated by wrapping the monolayer around the y' axis. Examples of α- and β-type nanoscrolls with $\theta = 45°$ as well as their cross-sections are shown (**b** and **c**, respectively) (Reprinted figure with permission from Perim and Galvão [16], Copyright (2009) by the IOP Publishing)

Archimedean-type spirals describe well the scroll structures since they have a constant separation distance for successive turns of the spirals. While multilayer BN NScs are likely to exist, only monolayer scrolls have been considered so far [16]. The angle θ defines the scroll configuration: zigzag for $\theta = 0$, armchair for $\theta = 90°$ and chiral for $0 < \theta < 90°$. The analysis of the structural evolution during the scroll formation was restricted by two types: α (Fig. 6.23b), with no uncurled regions of the layer, and β (Fig. 6.23c), where flat and uncurled regions co-exist simultaneously. Although there are numerous other possible initial nanoscroll structures, the basic structural features can be addressed using these two structural types only as demonstrated for the CNSc case [78]. Both α- and β-BN nanoscrolls of different sizes were obtained by varying H and W values (Fig. 6.23a).

The formation of BN nanoscrolls is dominated by two major energy contributions (Fig. 6.24): an elastic energy increase caused by bending the BN layer (decreasing stability) and a free energy decrease generated by the van der Waals interaction energy of overlapping regions of the layer (increasing stability) [16]. As the structure is rolled up, the layer curvature increases before the layer overlap and so does the torsion and inversion contributions to the strain energy. Thus, the rolled nanostructure becomes less stable in relation to the undistorted (planar) configuration, which makes energy-assisted the transition from planar to rolled structures. If no external energy is provided, the curved structures will return to the more stable planar configurations. When the surfaces are overlapping, the van der Waals contributions increase the structural stability. This process can be better visualized by analyzing the van der Waals and bending energy contributions separately (Fig. 6.24b). For small nanoscroll diameters, the bending contributions outweigh the van der Waals energetic gains, thus, the structure becomes unstable and tends to evolve into planar structures [16]. There is a critical minimum of the inner diameter necessary to attain the structural stability of a nanoscroll. Beyond this limit, the rolling process would evolve spontaneously and the final structure can be even more stable than its parent planar

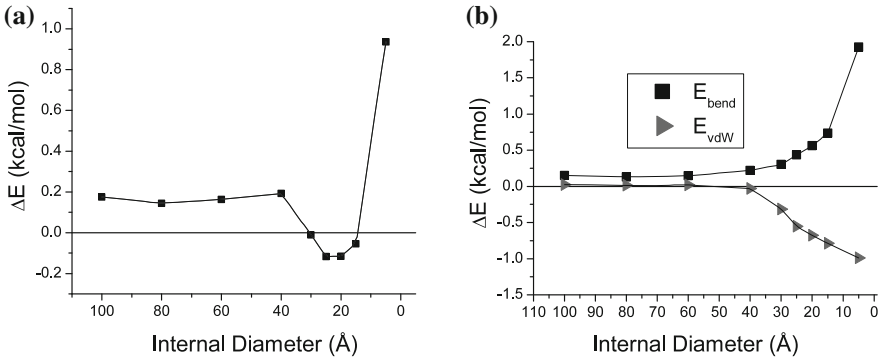

Fig. 6.24 Change in relative total energy (ΔE) during the wrapping of the plane BN monolayer into BN NSc (**a**). Contributions of bending and van der Waals terms to the total ΔE (**b**) (Reprinted figure with permission from Perim and Galvão [16], Copyright (2009) by the IOP Publishing)

configuration. For the case displayed in Fig. 6.24a, this occurs for diameters between 13 and 30 Å. Although these critical values are size- and chirality-dependent, the general behavior displayed in Fig. 6.24 is valid for all types of BN NSc structures. The armchair-type BN nanoscrolls were found to be the most stable configuration, while *zz*-NScs belong to metastable structures that can be thermally converted into armchair scrolls [16]. Chiral nanoscrolls are usually unstable and tend to evolve into *ac*- or *zz*-NScs depending on their initial geometries. Similar to the experimentally observed conically-shaped CNScs [79], BN NScs are also likely to be found in these configurations, according to performed MD simulations. The first successful synthesis route to boron nitride nanoscrolls has been reported quite recently [75].

6.3.2 Prismatic Nanowires

A number of solid substances that possess both anisotropic (e.g., layered) and isotropic crystalline modifications determine their potential capacity to form both NT and NW types of 1D structures [80, 81], as well as the possibility of phase transitions in nanosized forms of these substances. For example, 1D carbon nano-allotropes comprising graphite-like sp^2-bonded nanotubes and diamond-like sp^3-bonded nanowires, can mutually transform to each other ($sp^2 \leftrightarrow sp^3$) under certain conditions. In particular, the experimental method was elaborated for obtaining sp^3 hybridized diamond NWs from multi-wall sp^2 CNTs [82]. On the other hand, since the surface of diamond-like nanowire (characterized by d_{NW} diameter) is partially graphitized, it can be described as mixed $(sp^2)_x + (sp^3)_{1-x}$ 1D carbon nano-allotrope where x is proportional to $(1/d_{\mathrm{NW}})^2$ [83]. Similar to carbon, crystalline boron nitride, as described above, can exist in two main modifications: graphitic sp^2-hexagonal (Fig. 6.1a) and diamond-like sp^3-cubic (zinc-blende) (Fig. 6.2). The phase transition $h-\mathrm{BN} \rightarrow c-\mathrm{BN}$ occurs at $\mathrm{T} \sim 3{,}000\,\mathrm{K}$ and $p \geq 8\,\mathrm{GPa}$ [84]. Comprehensively studied BN NTs were considered in detail in Sect. 6.2. They weakly depend on the atomic structure of the walls (chirality) and the size of the nanotubes, which is an attractive factor for their use in numerous technological applications. However, experimental data on the alternative group of 1D nanostructures, i.e., monolithic BN NWs, were found to be rather scarce. These nanowires consisted of different phases: (i) a hexagonal structure in the form of a rope of vertically oriented cones rolled of boronitrene nets and embedded in one another [85], (ii) a mixed hexagonal and zinc-blende structure of nanofibres obtained from B-N-O precursor and graphite powder [86], (iii) a turbostratic structure produced from BI_3 [87], (iv) an orthorhombic structure synthesized in a hydrothermal route from the solution of H_3BO_3 in the presence of N_2H_4 H_2O and C_3H_9N microdoses incorporated inside a stainless steel autoclave [88]. Moreover, the isolation of BN nanowires in a "pure form" for the subsequent investigations was found to be a complicated problem since they were obtained, as a rule, in a mixture with other BN nanostructures (nanotubes, nanoplates, nanocrystallites, fullerenes, etc.) [89].

Similar to diamond nanowires, theoretical studies on BN NWs were performed based mainly on their densely-packed *c*-BN structure [83]. The structural, electronic

and thermal properties of BN nanowires with optimized zinc-blende morphology were carefully simulated using the DFTB and MD methods [81]. The homogeneous BN NWs represented infinitely extended 1D prismatic crystallites cut from *c*-BN crystal perpendicular to the (001), (111), and (110) section planes, called as NW types I, II, and III, respectively (Fig. 6.25). It was necessary to analyze the dependence of nanowires' stability and properties on their morphology [81]. For example, the properties of nanowires depend on the polarity of their side facets: nonpolar (equal numbers of B and N atoms per surface unit) and polar (either boron or nitrogen atoms form the external surface layers). As to the analysis of dependence of NWs properties on their size, the areas of the cross sections S_{NW} used as the dimensional NW parameter were varied in the range of 20–500 $Å^2$.

Being dependent on the NW thickness (S_{NW}) and morphology, nanowires of I-III types were found to be different from the point of view of their structural stability and phase transformation [81]. For small nanowires ($S_{NW} < 100\,Å^2$) of types I and II, the cubic structure was observed to be unstable, with a partial NW transition

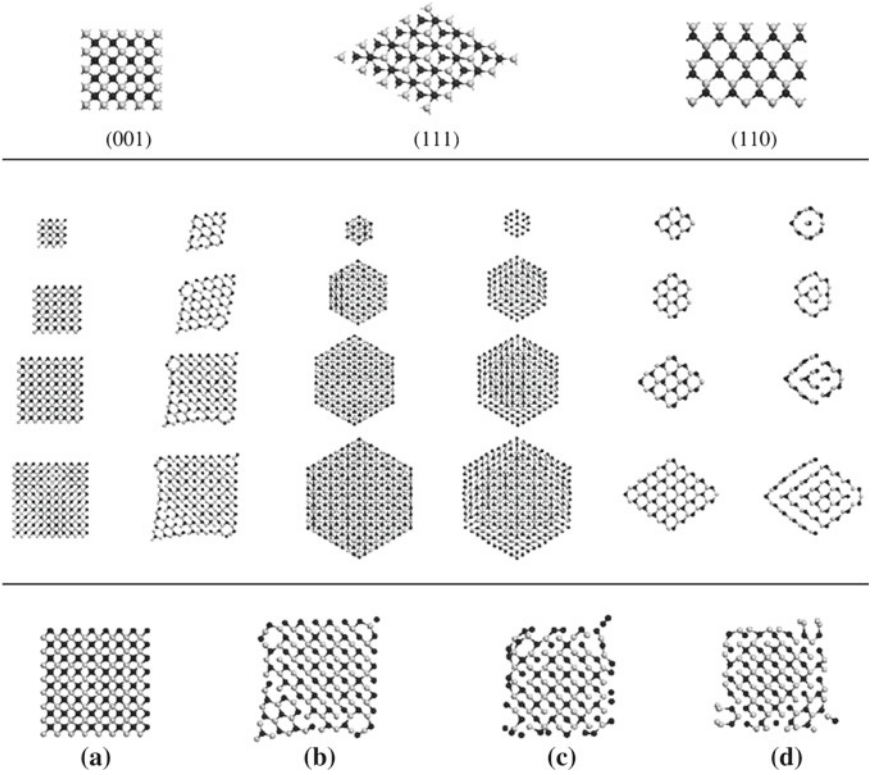

Fig. 6.25 *Top* panel: initial atomic structures of *c*-BN crystal in the directions of which nanowires of different diameters were cut: [001], type I; [111], type II; and [110], type III. *Bottom* panel: atomic structures of initial (*on the left*) and optimized (*on the right*) BN NW cross-sections [81]

to h-BN structure. Atomic rearrangements in relaxed c-BN NWs of type II (with $S_{NW} > 100\,\text{Å}^2$) resulted in the appearance of two-phase structures, with the outer layers transformed to a hexagonal structure, while the core of c-BN NW remained unchanged. Hence, one could speak about the formation of "hybrid" ($sp^2 + sp^3$) BN nanowires combining hexagonal and zinc-blende structural types. The formation of two-phase systems was also observed in the case of type I nanowires: they partially segregated with the retention of the cubic structure inside the NW core. Similar graphitization effects were also observed in the cases of reconstruction in both c-BN surface layers [90] and thin c-BN films [91]. For type III BN NWs, the cubic structure proved to be unstable during the optimization procedure in the entire range of their sizes and transformed to the hexagonal one with the foliation of the monolithic nanowire into h-BN fragments (Fig. 6.25). For the thinnest nanowires of this type ($S_{NW} < 10$–$15\,\text{Å}^2$), the energy stabilization occurred due to their transformations to hollow nanotubes with a hexagonal structure [81].

In general, the effect of the atomic rearrangement in the outer layers of BN NWs can be correlated with the lower energy stability of c-BN phase as compared with h-BN: the cohesion energy for h-BN was estimated to be 0.06 eV/atom higher than for c-BN [91]. According to the experimental observation, BN NWs were characterized by the simultaneous presence of sp^2 and sp^3 states [86]. The above described structural rearrangements in BN nanowires were also depended on (i) the type of NW facets (nonpolar or polar) and (ii) the number of dangling bonds per atom upon NW facets [81]. As a result of $sp^2 \rightarrow sp^3$ structural transformations in BN NWs, the interatomic bond lengths l_{B-N} changed noticeably, qualitatively correlating with the change in the coordination numbers of atoms, which equal 3 for the sp^2-bonded hexagonal structure and 4 for the sp^3-bonded cubic structure. Thus, for the thinnest nanowires, their average coordination numbers are noticeably less than three due to the presence of a significant number of surface atoms with dangling bonds. For the bulkiest nanowires, on the contrary, the average coordination numbers (CNs) exceed three, reflecting the presence of sp^3 atoms with $CN = 4$ inside the NW core. With the increasing size and CNs of nanowires the bond lengths l_{B-N} also increased, from 1.43 to 1.55 Å in accordance with the well-known tendency of l_{B-N} growth in boron-nitrogen systems with different atomic coordination in the following sequence: the BN molecule ($CN = 1, l_{B-N} = 1.28\,\text{Å}$) $\rightarrow$ the linear chain -B-N-B-N- ($CN = 2, l_{B-N} = 1.30\,\text{Å}$) $\rightarrow$ h-BN crystal ($CN = 3, l_{B-N} = 1.45\,\text{Å}$) $\rightarrow$ c-BN crystal ($CN = 4, l_{B-N} = 1.57\,\text{Å}$) [92]. Figure 6.26 presents the dependence of the calculated total energies for the optimized structures of BN NWs on the areas of their cross-sections [81]. It reveals that the stability of nanowires markedly increased with the growth of their diameters when the energy of the corresponding NWs approached the value of E_{tot} for the crystalline c-BN phase. At comparable values of S_{NW}, the BN nanowires of type III were found to be the most stable in the total energy (although structurally they were rather unstable, as discussed above), while NWs of type I showed the smallest stability. Obviously, the most stable BN NW configuration is type II.

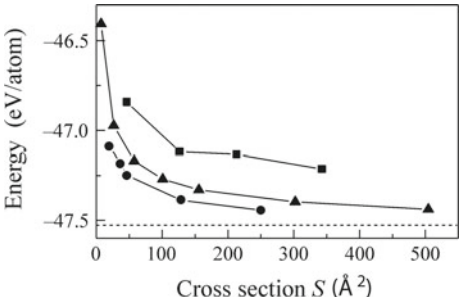

Fig. 6.26 Total energy E_{tot}, eV/atom of BN NWs versus their cross-section area S_{NW}. Nanowire types are described by the labels: square [001] (type I), triangle [111] (type II) and circle [110] (type III). The *dashed line* corresponds to the total energy of *c*-BN bulk [81]

This assumption was confirmed after performing MD simulations of all three BN NW types (Fig. 6.27) [81]. Losing their monolithic nature at already $T = 0$ K (bottom of the right panel in Fig. 6.25), the nanowires of type III became so distorted with the increasing temperature that they transformed to quasi-tubular structures (right panel of Fig. 6.27c, d). As the temperature increased, beginning with $T = 300$ K, all the type I nanowires underwent progressing thermal deformations associated, first, with the transition of the cubic structure of the "core" to the hexagonal structure; next, with their "transversal" foliation; and, starting with T ~1,000 K, the thermal decomposition of nanowires occur with the formation of *h*-BN layers and separate BN groups (as T increased up to 1,500 K). Meanwhile, BN NWs of type II proved to

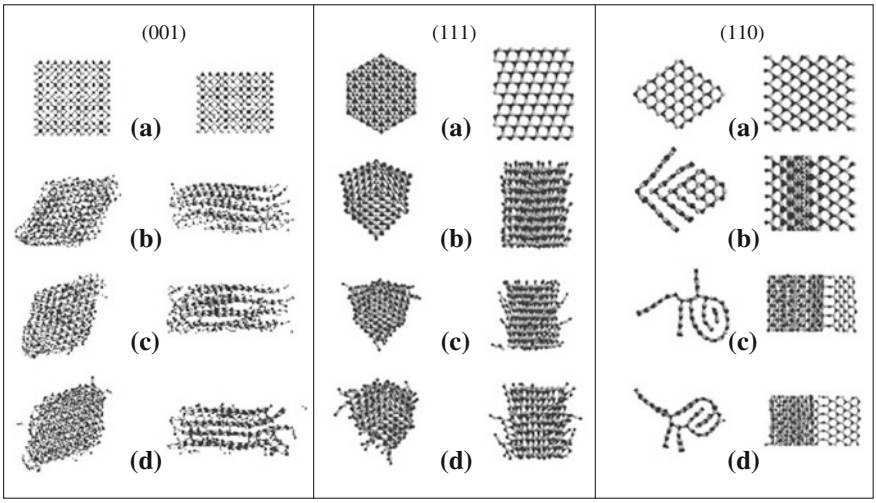

Fig. 6.27 Thermal distortions of BN NWs (types I, II, and III, as presented in Fig. 6.25) at various temperatures. Atomic structures of NW cross and longitudinal sections were shown (*left* and *right* panels in each column, respectively) are shown: (**a**) initial (*non-optimized*) atomic models and those after MD simulations at $T = 300$, 1,000, and 1,500 K (**b**, **c**, and **d**, respectively) [81]

be the most thermodynamically stable under the thermal exposure, retaining the cubic structure of the "core" up to T ~1,000 K [81]. The occurrence of B and N atoms of different coordination in the composition of each nanowire resulted in the fact that their electronic spectra (DOSs) represented a complex superposition of states corresponding to contributions of particular non-equivalent groups of atoms [81]. The width of the NW valence band (~9.0 eV) estimated using the DFTB method (Fig. 6.28) proved to be somewhat narrower than that for *h*-BN (10.4 eV) or *c*-BN (11.8 eV) crystals found earlier [93]. The band gap $\Delta\epsilon_{gap}$ also decreased, down to ~3.0–3.4 eV (approximately, by half, as compared to bulk). According to Fig. 6.28, the highest occupied and the lowest unoccupied bands were formed by the states of atoms of the outer NW layer. For less stable BN nanowires, undergoing significant structural rearrangements and having a large number of atoms with dangling bonds, both a semiconducting type (where $\Delta\epsilon_{gap}$ decreased down to 1.8–0.9 eV), and even a metallic type (that is, with a non-zero density of states at the Fermi level), of DOS spectra were obtained (right and left panels of Fig. 6.28, respectively).

DFTB simulations performed [81] well demonstrated that BN nanowires represent unique hetero-phase 1D materials in which, depending on their size and morphology, various phase transformations can occur. Some "critical" size for each NW type exists, below which *c*-NWs cannot be formed at all. Unlike homogeneous diamond-like carbon nanowires, stable BN nanowires are always two-phase systems whose "shells" have hexagonal structures and the "core" has a cubic structure. They can exhibit both semiconducting and metallic properties, which attracts enhanced technological interest. Depending on the initial structure (e.g., direction of NW axis), BN nanowires, according to MD simulations, can undergo various types of thermal deformations [81]: from the rearrangement of *c*-BN structure of their "core" into *h*-BN one, up to the formation of pseudo-tubular or layered structures from hexagonal layers.

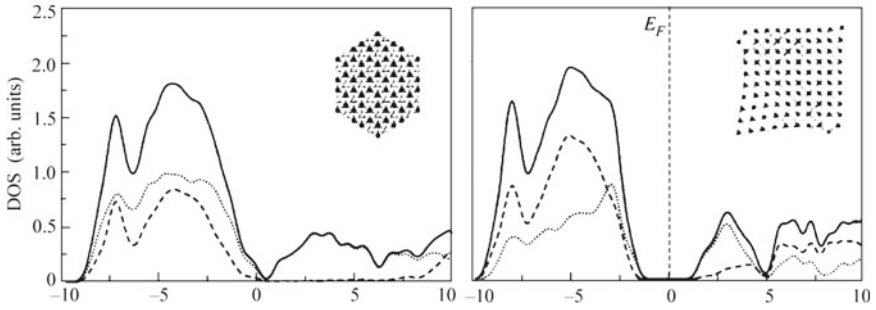

Fig. 6.28 Total densities of states (*solid lines*) of BN NWs of types I and II (at *right* and *left* panels, respectively); partial contributions of the surface (*dotted lines*) and inner (*dashed lines*) B and N atoms are given separately. The vertical line is the Fermi level ($\epsilon_F = 0$ eV) [81]

6.3.3 Monoatomic BN Linear Nanochains

Apart from prismatic-type BN nanowires with diameters varying in the range of 0.7–3.0 nm, as described above, theoretical simulations were performed also on BN nanofilaments of atomic diameters with the structure of linear chain -B-N-B-N-, which can be doped by different atoms (e.g., C and S) and functionalized [94–98]. Fragments of monoatomic BN filaments (they were called "nanowires" in aforementioned papers), which were found to be semiconducting (when using the first principles calculations), being joined to metallic electrodes (e.g., Al and Au) resulted in the appearance of the conductance along linear $(BN)_m$ chains [97, 98]. The electron transport properties of these junctions have potential applications in several components of the novel molecular electronic devices [98]. For simulations of pure BN nanochains (both terminated and infinite) and their finite fragments incorporated between electrodes, various ab initio methods were applied: (i) the standard HF-LCAO method and that combined with the Wannier-function-based formalism [95, 96], (ii) both DFT-LCAO and DFT-PW methods combined with formalism of non-equilibrium Green's function [94, 97, 98], and (iii) MD method provided for a large number of femtosecond time steps [94].

An isolated infinite monoatomic BN nanochain was found to possess a linear geometry exhibiting *sp*-type hybridization with 180° B-N-B (N-B-N) inter-bond angles since its different possible *zz*-structures led to higher total energies as compared to the linear chain (LC) [96]. It means that if the isolated BN chains could exist, they would have mainly a linear structure. A direct band gap $\Delta\epsilon_{gap}$ of monoatomic infinite BN LC (Fig. 6.29) was estimated to be 4.0 eV when using GGA-PW method with Green's function correction [94]. The other remarkable aspect of infinite BN LCs, as compared to C or Si nanochains (Sect. 5.3), is that it does not exhibit any alteration in bond populations and all the nearest boron and nitrogen atoms are equidistant. Any periodic BN structures, being hetero-nuclear in nature, have significant ionic contributions to the bonding as opposed to the purely covalent materials.

On the other hand, the charge distribution in a finite linear $(BN)_m$ nanochain terminated at the borders by B and N atoms cannot be periodically distributed along its axis. A sequence of one-electronic states is formed in this case around the energy gap corresponding to HOMOs (highest occupied molecular orbitals) and LUMOs (lowest unoccupied molecular orbitals) as shown in Fig. 6.30. These orbitals are

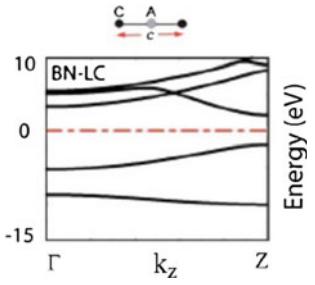

Fig. 6.29 Calculated energy band structure of infinite BN linear chain (LC) which bands are drawn for two-atom UC centered on B atom. Fermi level is shown by dot-dashed line [94]

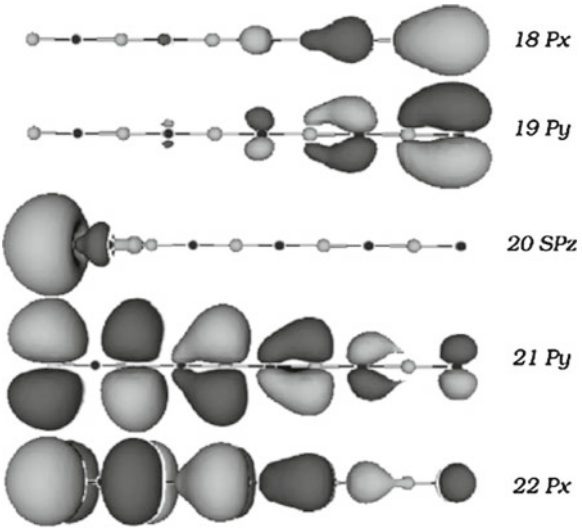

Fig. 6.30 HOMOs ($18p_x$, $19p_y$, and $20sp_z$) and LUMOs ($21p_y$ and $22p_x$) of linear $(BN)_5$ molecule oriented along z axis (Fig. 6.31) (Reprinted figure with permission from Shi et al. [97], Copyright (2006) by the American Chemical Society)

localized on either boron or nitrogen atoms, due to the difference of B and N ionicity [97]. The HOMOs are composed of degenerate (sp_z) and σ (p_x and p_y) orbitals, which are spatially localized to the left and to the right sides of a $(BN)_5$ molecule. The LUMOs are composed of two degenerate π (p_y and p_x) orbitals which are spatially delocalized in the proximity of the right side of molecule. The characteristics of molecular orbitals localized on both B and N atoms are important for understanding of conductivity in a finite linear BN chain sandwiched between two semi-infinite [001]-oriented Al nanowire electrodes (Fig. 6.31).

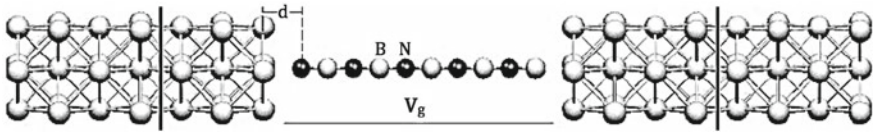

Fig. 6.31 1D model of BN LC coupled to [001]-oriented Al semi-nanowires (x and y directions were oriented perpendicular to the monoatomic BN chain fixed along z direction). 3D supercell with large vacuum gaps between nanowires in the x and y directions was chosen, which practically excluded the direct interaction of the original 1D system described as Al NW(l)-$(BN)_5$-Al NW(r) (as shown in the Figure) with its mirror images. The terminated B and N atoms were positioned symmetrically above the hollow sites of aside Al{001} facets (separated from them by distance d). The region within two black lines is the scattering region and the remaining parts are the *left* and *right* electrodes. Both NW-type Al electrodes extend to the half-infinity (in negative and positive directions). V_g determines the gate voltage [97]

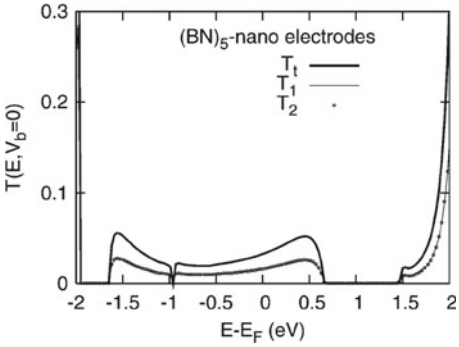

Fig. 6.32 The total transmission spectrum (T_t) and its eigen-channel decompositions (T_1 and T_2) of $(BN)_5$ LC sandwiched between two Al(100) nanoscale electrodes (Fig. 6.31). Note that only two channels contribute to the total transmission and they are equal [97]

The transport properties of BN linear chain sandwiched between two Al(001) semi-nanowires are determined by the molecular orbitals of the former and the band structures of the latter as well as by their coupling, which can explain those, e.g., the so-called eigen-channels [99]. Figure 6.32 shows the total transmission spectrum (T_t) with its eigen-channel decompositions (T_1 and T_2) of the sandwiched nanostructure. The energy E is relative to the average Fermi level of the two-probe system, i.e., $(\mu_l+\mu_r)/2$, where μ_l and μ_r are electrochemical potentials for both the left and right semi-nanowires, respectively, while V_b is the external bias voltage. The maximum value of the total transmission of BN linear chain is 0.3, which is much smaller than that (2.0) of analogous 10-atom carbon linear chain [97]. The transmission energy regions (where $T(E) > 0$) and transmission energy intervals, i.e., $T(E) = 0$, are mainly determined by Al nanoscale electrodes.

It was suggested that the value of T energy is determined by the band structure of semi-nanowires and the momentum filtering effect of finite $(BN)_5$ chain which means that only those Bloch bands of the electrodes having the same orbital character as the molecular states (Fig. 6.30) near the Fermi level (π-orbitals) conduct well [99]. On the other hand, the transmission energy intervals seem to be insensitive to BN linear chains and are determined by the band gaps of the electrodes. However, when a molecule with mainly σ orbitals is placed near the Fermi energy of the electrodes, the energy intervals are sensitive to $(BN)_5$.

Figure 6.33 shows the current-voltage (I-V) curves of BN LC coupled to Al(100) NW electrodes. The current I was estimated within the Landauer-Büttiker formalism [97]:

$$I(V_b) = \frac{2e}{h}\int_{-\infty}^{\infty}[f_l(E-\mu_l) - f_r(E-\mu_r)]T(E, V_b)dE, \tag{6.5}$$

where E, V_b, $T(E,V_b)$, μ_l and μ_r are described above, while f_l and f_r are the electron distribution functions of the left and right Al electrodes, respectively. It can be seen that the I-V curve is determined by both BN LC and Al(001) semi-nanowires (Fig. 6.31), while the NDR (negative differential resistance, which is characterized by

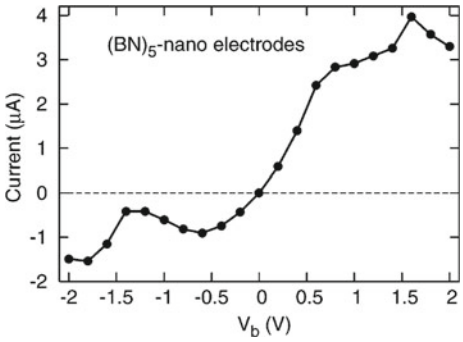

Fig. 6.33 The *I-V* curves of BN LC sandwiched between two Al(001) semi-nanowires [97]

the decrease of the current with the increase of the external bias) is the phenomenon more apparent at V_b voltage intervals –(1.4–0.6) V and 1.6–2.0 V. The origin of NDR can be understood from the changes of coupling between linear $(BN)_5$ molecule and nanoscale Al electrodes at various external biases [97]. The *I-V* curves for BN LC were found to be asymmetric as a result of its asymmetric coupling with both Al(001) semi-nanowires (according to Fig. 6.31, on the left side, nitrogen atom is bound with the left nanoscale Al electrode, while the right electrode is bound with a boron atom).

Mechanical adjustment of the spacing between nanoscale electrodes (Fig. 6.31) resulted in the ability to shift the spacing between the energy levels in a $(BN)_5$ molecule using a gate electrode [100]. The transport properties of the 1D Al NW(l)-$(BN)_5$-Al NW(r) system can be tuned using (i) variation of a distance d between BN LC and arbitrary Al electrode as well as (ii) inclusion of a gate voltage (Fig. 6.31). As shown in Fig. 6.34a, the equilibrium conductance G (determined within the Landauer-Büttiker formalism in the framework of ballistic conduction mechanism as $G = \frac{2e^2}{h} \sum_n T_n$, where T_n is the transmission probability of the mode n [101]) decreases monotonically with the growth of separation d between BN LC and each of two Al electrodes.

Figure 6.34b shows the tuning of the transport behavior of BN LC through the inclusion of the gate voltage V_g. The gate voltage drastically increases the equilibrium conductance of $(BN)_5$, which can be understood from the shift and alignment of the molecular orbitals relative to the Fermi level of the electrodes. Here, the positive gate voltage means the downshift of the energy levels in BN LC [102]. With the increase of V_g, this LC continuously switches from a weakly to a highly conducting state, which indicates that it might be a good candidate for molecular switch [97].

Figure 6.34c shows both the charge transfer from the Al electrodes to BN LC with the increase of d, which decreases monotonically, and the projection of the density of states (PDOS) of the two-probe system onto all the basis orbitals of $(BN)_5$ molecule. These plots show that the equilibrium conductance G has a different variation behavior as that of PDOS since orbitals of BN LC are well localized (in contrast, for a linear C_{10} molecule, G has the same variation behavior as that of PDOS [97]).

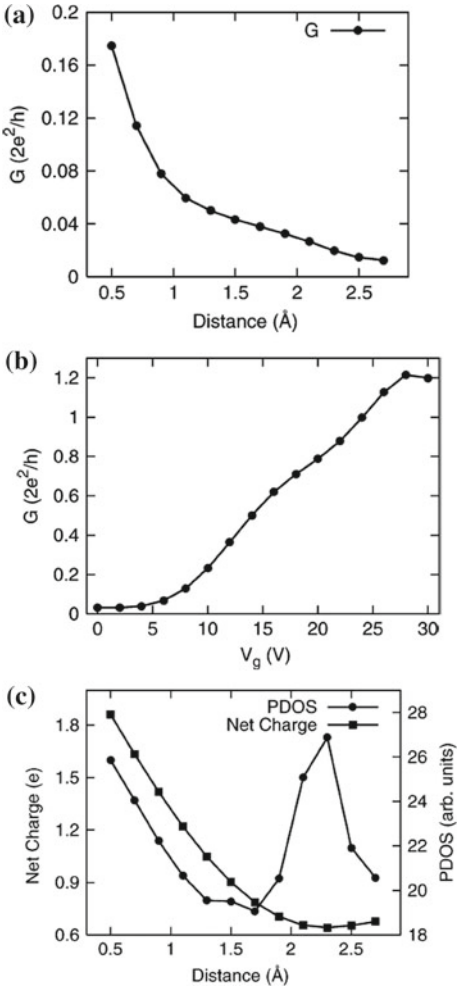

Fig. 6.34 The equilibrium conductance G of $(BN)_5$ molecule as a function of d (**a**) and V_g (**b**) as well as the corresponding PDOS at the Fermi level and charge transfer from the electrode to BN LC (**c**) [97]

6.4 Group III Metal Nitride Bulk and Nanolayers

Among the sp^3-bonded group-III metal nitrides, AlN is the largest band gap semiconductor, which $\Delta\epsilon_g$ achieves 6.2 eV, characterized by a high temperature stability, considerable thermal conductivity, low thermal expansion, resistance to chemicals used in semiconductor processing, and reliable dielectric properties [103, 104]. Moreover, small lattice mismatch between AlN and GaN lattices makes possible a synthesis of hetero-structural $Al_xGa_{1-x}N$ alloys [105], which can be used in a number of technological applications, mainly in micro- and optoelectronics, e.g., laser diodes and "solar-blind" ultraviolet photodetectors [104]. Their performance can be noticeably improved by the regulation of extrinsic impurities and intrinsic point defects

inside the crystalline samples [106–108]. There are three possible 3D crystal morphologies shared by the group-III metal nitrides: wurtzite (*w*), zinc-blende, or sphalerite (*c*), and rock salt (*rs*) [109]. As to hexagonal graphitic-type *h*-BN morphology, it cannot be realized in the group-III metal nitrides since the appearance of in-plane sp^2 Al-N (Ga-N) bond hybridization is hardly possible, which can be illustrated by a substantially higher ionicity of the latter, where the transfer of charge towards N is 2.56 *e* (2.65 *e*) [105], whereas in sp^2-bonded *h*-BN, the analogical effective charge is only 1.01 *e* accompanied by substantial covalency [3]. This difference can be a reason for essentially larger bond lengths in the group-III metal nitrides as compared to BN: 1.86 Å (1.87 Å) versus 1.46 Å respectively [110]. AlN and GaN (similarly to SiC and GeSi as considered in Sect. 5.4) crystallize in a wurtzite-type structure (Fig. 6.35b) described by $P6_3mc$ space symmetry group. As to a zinc-blende structure ($F\bar{4}3m$ group) shown in Fig. 6.35a, it was found to be metastable for AlN, although *c*-GaN phase can be stabilized using an epitaxial growth of its thin films on the (001) planes of *fcc* structures like MgO [112]. The *rs*-structure ($Fm\bar{3}m$ group) can be achieved only at very high pressures in the group-III metal nitrides, thus, it was not usually considered at all. Numerous theoretical studies of *w*- and *c*-phases of the group-III metal nitrides [104, 109] clearly show that the latter are characterized by a noticeably smaller band gap (achieving several eV decimals). Moreover, both phases differ from each other in the stacking sequence along the [0001] direction in the wurtzite structure and [111] direction in the zinc-blende one (Fig. 6.35), which cross the most

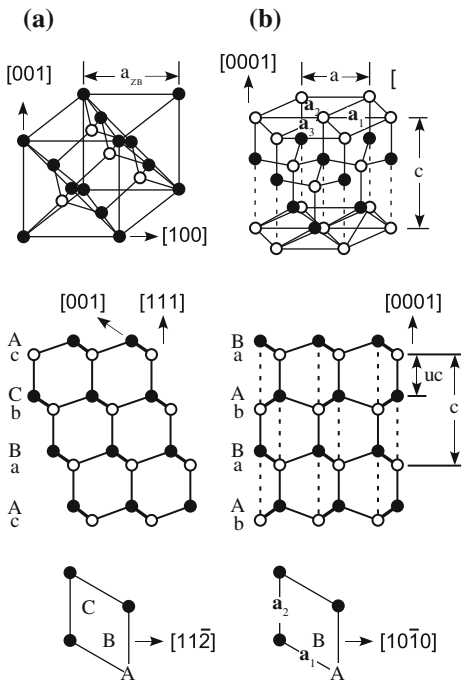

Fig. 6.35 Zinc-blende (**a**) and wurtzite (**b**) structures of the III group metal nitrides (bulk UCs in the *top* panel as well as across images of (111) and (0001) slabs, respectively, in the *middle* panel versus atop images of slab UCs in the *bottom* panel). The *open* and *closed circles* represent metal and nitrogen atoms, respectively [111]

densely packed crystallographic faces of the group-III metal nitrides. The lattice constants a_{zb} (Fig. 6.35a) for *c*-AlN and *c*-GaN were found to be 4.38 and 4.50 Å, respectively [113]. The wurtzite lattice constants *a* and *c* (Fig. 6.35b) are connected via ratio $c/a = \sqrt{8/3} \approx 1.6333$ and supplemented by the dimensionless internal parameter $u = 3/8 = 0.375$, where *uc* corresponds to the length of the bonds parallel to the [0001] axis [111]. Additionally, the wurtzite lattice contains pairs of metal and nitrogen atoms, connected by dashed lines along the [0001] direction (Fig. 6.35b) and attracted to each other by the electrostatic forces, which reduce their lengths as compared to bulk crystal. The lattice constants of wurtzite-type AlN and GaN crystals were found to be 3.31 Å (a_{AlN}), 3.19 Å (a_{GaN}), 4.98 Å (c_{AlN}) and 5.19 Å (c_{GaN}) [113], thus confirming a small lattice mismatch between both crystalline materials.

2D plane structures of the group-III metal nitrides were studied mainly for the densely-packed polar surfaces of zinc-blende (111) (Fig. 6.35a) and wurtzite (0001) (Fig. 6.35b). The corresponding ultrathin slabs can be directly compared since the [111]-ordered zinc-blende and [0001]-ordered wurtzite structures have the same coordination up to the third nearest-neighbor shell and the interface geometry (in terms of the number and direction of bonds) is the same (*cf.* Fig. 6.35a, b) [114]. A common feature found for all polar surfaces is a strong tendency towards a metal-rich surface stoichiometry (Fig. 6.36) whereas N atoms are rather thermodynamically unstable on almost all equilibrium surfaces [115, 116]. Recent studies have demonstrated that in *w*-structures, the two kinds of surfaces are the most stable: (i) the so-called *n*-type (B), where the first interlayer is shown in the lower part of Fig. 6.36, (ii) the *p*-type (A), where the outer metal atoms are positioned directly above the sub-

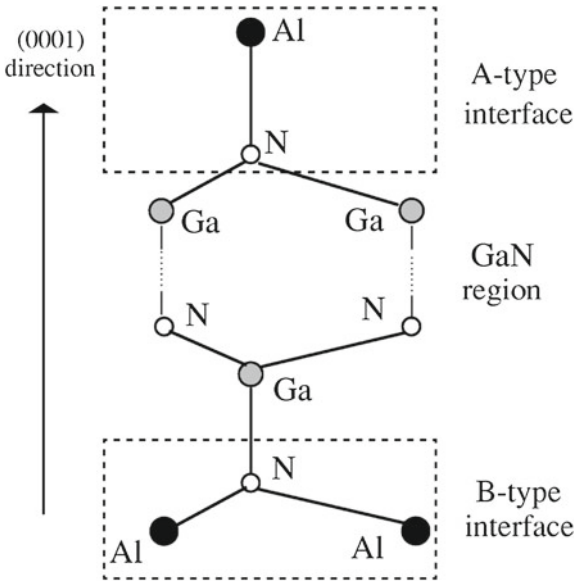

Fig. 6.36 Two types of *w*-Al/GaN(0001) interface (see explanation in the text) [114]

surface N atoms as shown in the upper part of Fig. 6.36. The *n*-type surfaces usually exhibit a smoother surface morphology leading to a higher material quality [115]. Moreover, if the *n*-type surface of group-III metal nitrides is characterized by a band gap, the width of which is 2–2.5 times smaller than that in bulk, the *p*-type surface possesses practically no noticeable gap between the conduction and valence bands since it is overlaps by the energy states of outer metal layer which is bound with subsurface layers weaker than in the case of *n*-type substrate. Similarly, the *n*-type (111) surface (the middle panel of Fig. 6.35a) is a more favorable for the zinc-blende polar substrate as compared to the *p*-type.

First principles full-potential linearized augmented plane wave (FLAPW) calculations were performed, in order to clarify the role of the interface geometry on piezoelectric fields and potential lineups in [0001] wurtzite and [111] zinc-blende Al/GaN junctions, which are structurally compatible [114], due to proximity of the corresponding lattice parameters of AlN and GaN surfaces. The electric field (its polarity and magnitude) was found to be strongly affected by atomic relaxations in the interface region. On the other hand the Schottky-barrier height (SBH) evaluated in the presence of electric fields [114] showed that their effect is relatively small (a few tenths of an eV). These calculations assess the rectifying behavior of the Al/GaN/Al contacts (Fig. 6.36), in agreement with the experimental values obtained for the SBH barrier [117]. Obviously, non-relaxed AlN (or GaN) bilayer cut from the densely-packed *n*-type slabs with either *c*-(111) or *w*-(0001) terminations (the middle panel of Fig. 6.35) practically coincide and form the buckled sp^3-bonded honeycomb nanolayers (Fig. 6.37), which atop images are the same hexagonal as a flat *h*-BN sp^2-bonded honeycomb nanolayer (Fig. 6.3). Moreover, their geometry optimization carried out using various first principles computational schemes resulted in either substantial decrease of buckling [108] or appearance of flat graphene-like nanolayers [119, 120], unlike buckled SiC and GeSi nanolayers considered in Sect. 5.4. However, unlike sp^2-bonded graphene-like AlN single-layer nanoribbons, a flat honeycomb AlN monolayer, which could be technologically important in optoelectronics and energy engineering, has not been fabricated so far, moreover, its mechanical stability is still unknown [120].

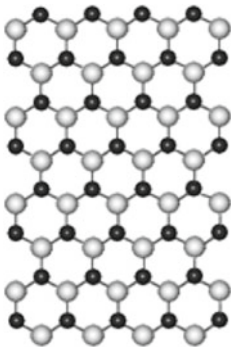

Fig. 6.37 Atop view of *n*-type densely-packed surfaces of the group-III metal nitride. N atoms are shown as *small black balls* [118]

6.5 Group III Metal Nitride Nanotubes

6.5.1 Rolled-Up Single-Wall AlN Nanotubes

1D tubular nanostructures of the group-III metal nitrides attract enhanced attention in both experiments [121–124] and theoretical simulations [108, 110, 125–140], due to numerous technological applications, for instance, in optoelectronic devices working within both ultraviolet and visible light diapasons [135] as well as in alloy-type $Al_xGa_{1-x}N$ and hetero-structural AlN/GaN-based nanoelectronics [138, 140]. AlN NTs were synthesized experimentally using either direct current (DC) arc-plasma-induced melting of aluminum in N-Ar ambient [123, 124] or treating the aluminum powder, impregnated with cobalt sulfate in advance, with NH_3/N_2 ambient in a special tubular furnace [122]. Both types of NT samples, identified using the high-resolution transmission electron microscopy (HRTEM), were accompanied by nanoparticles and nanowires. The diameters of those nanotubes were found to be either small, 2–4 nm, or large, 20–80 nm, whereas the thickness of their walls was estimated to be from 1 up to 20 nm. For synthesis of GaN NTs, *w*-ZnO NWs were used as templates [121]. Unlike earlier synthesized SW BN NTs, well visualized with graphene-like network on the nanotube wall [10], no observations of analogous SW structures in AlN and GaN NTs have been reported so far.

Nevertheless, in majority of theoretical simulations on the group-III metal nitrides NTs just smooth or slightly buckled single-walled models have been used as the simplest presentation. They were mainly characterized by two equilibrium structures possessing either *ac*- or *zz*-type chiralities (Fig. 6.38), although chiral NTs were considered as well [139] alongside with a wide range of uniform diameters (0.5–6 nm). On the other hand, theoretical models of the crystalline-type sp^3-bonded AlN NTs observed experimentally (similar to those for SiC NT as considered in Sect. 5.4.4),

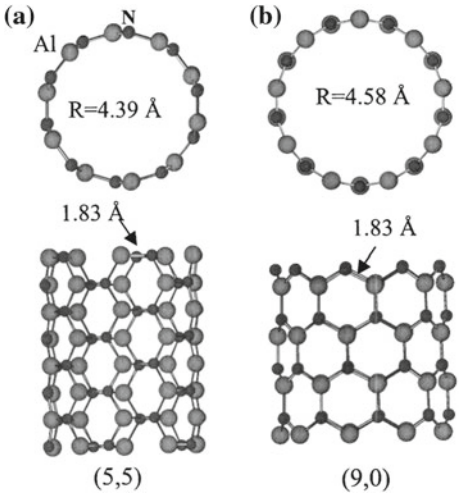

Fig. 6.38 Views of AlN SW NTs across their axes and along them for **a** armchair-type (5,5) and **b** zigzag-type (9,0) chiralities. N atoms are shown as *small black balls*. Cross-sections of both nanotubes contain values of their optimized radii (*R*) [127]

rather than cylindrical layered nanotubes, are needed [135]. For theoretical simulations on all these NT models, both finite cage-like tubules [126, 128, 129, 134] and infinite nanotubes [108, 110, 125, 127, 130–133, 135–140] were used. A wide spectrum of methods was applied in these calculations: atomistic formalism of many-body empirical potentials [110], methods of molecular dynamics [127, 129–131, 135], DFTB [125, 131], DFT-PW [125, 132, 133, 136, 138, 139], DFT-LCAO [108, 127, 130, 134, 135, 137, 140], as well as HF [126, 128]. Analogically to BN SW NTs (Fig. 6.6), a slight distortion was observed after DFT calculations in initially cylindrical honeycomb walls of AlN SW NTs, where Al atoms moved toward the axis of nanotube while N atoms were shifted in the opposite direction after relaxation, which resulted in nanotube buckling [127]. The radial buckling was found to be 0.037 and 0.035 Å for (5, 5) and (9, 0) nanotubes, respectively (Fig. 6.38). The buckling in AlN SW NTs was found to be the smallest as compared to those in BN [25] and GaN [125] SW nanotubes with similar diameters. The larger is R, the smaller will be the buckling, as shown in Fig. 6.6. For (10,10) AlN NT, the buckling was found to be only 0.018 Å. These results are correlated with a difference in hybridizations of Al and N on the curved hexagonal layer. All AlN NTs are semiconductors with band gaps ranging from 2.84 to 3.95 eV [127].

Models of *ac*- and *zz*-type AlN SW NTs with substantially larger diameter (∼6 nm) and, correspondingly, smaller structural stability were considered as (36, 36) nanotubes described by rod symmetry group $P6/m$ (Fig. 6.39a) and (64,0) NTs attributed to symmetry $P4mm$ (Fig. 6.39b), respectively [137]. It was shown that their

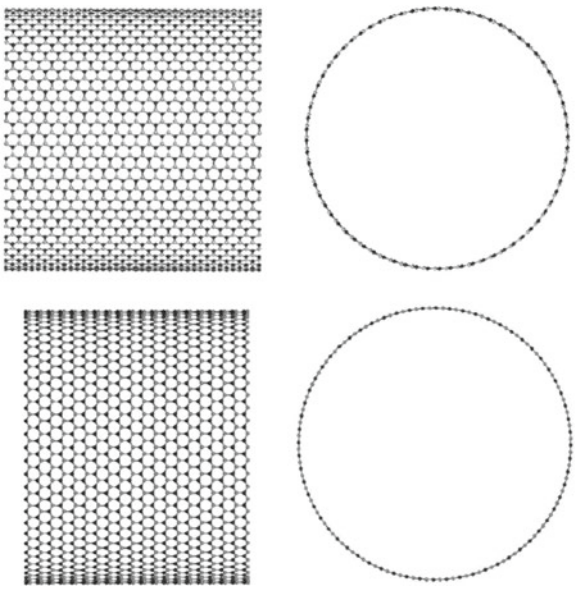

Fig. 6.39 Images of 6 nm thick AlN SW NTs along the axes of nanotubes and across them for **a** *ac*-type (36,36) and **b** *zz*-type (64,0) chiralities [137]

equilibrium bond lengths $d_{\mathrm{Al-N}}$, binding energies *per* bond E_{bind}(Al-N) and effective charges $q_{\mathrm{Al}}(q_{\mathrm{N}})$ are noticeably closer to the corresponding values of AlN bilayer (Fig. 6.37) than those for AlN SW NTs of smaller diameter (∼1 nm), by about 0.8, 0.6 and 1.3 %, respectively (which are qualitatively close for both *ac*- and *zz*-nanotubes).

To evaluate the strain energy, first of all, the optimized configuration of honeycomb AlN bilayer (Fig. 6.37) was estimated. The calculated binding energy of the AlN graphitic nanolayer was found to be 7.32 eV *per* atom, which corresponds to the nearest-neighbor Al-N distance of 1.83 Å [130]. Therefore, the energy cost *per* atom required to wrap up an AlN graphitic nanolayer into a SW NT of a given diameter and chirality (i.e., the strain energy) can be obtained from the difference between the corresponding binding energies. Figure 6.40 presents a variation of the strain energy as a function of SW NT diameters, where analogous dependencies are presented also for BN, C and GaN nanotubes [130]. The strain energies for considered nanotubes were found to be decreasing with the increasing diameters. It was also revealed that the corresponding strain energies were approximately proportional to the inverse square of the NT diameters, i.e., these nanotubes follow the classical elasticity theory. Similar to the results obtained for BN NTs [3] and GaN NTs [125], the strain energies in AlN NTs are relatively insensitive to their chirality. The energy costs to form AlN SW NTs from a graphitic nanolayer structure were found to be the lowest as compared to those necessary to form BN, GaN, and carbon nanotubes with similar diameters [130]. These are about 0.02–0.04 eV *per* atom lower than those of BN nanotubes and 0.025–0.075 eV *per* atom lower than those of GaN nanotubes (Fig. 6.40). It seems to be an advantage for the formation of AlN SW NTs, in contrast to graphene and boronitrene honeycomb monolayers. However, 2D AlN materials with a graphitic nanolayer configuration, as mentioned above, have not been synthesized experimentally so far. Obviously, the strain energy in an AlN graphitic nanolayer relative to sp^3-bonded AlN bulk structure should also be taken into account when analyzing the probability of AlN SW NTs synthesis. Such an energy was found to be 0.68 eV/atom, which is much higher than that for GaN graphitic sheet (0.36 eV/atom [125]), thus

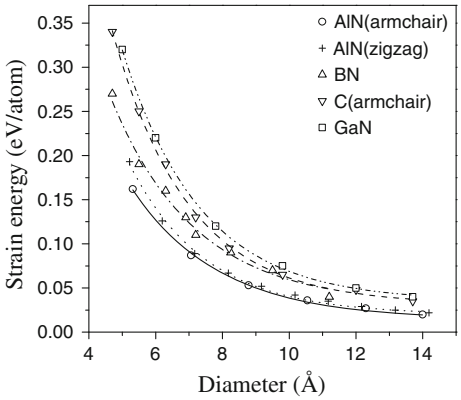

Fig. 6.40 Strain energy in *ac*- and *zz*-AlN SW NTs relative to their graphitic-like sheet structure versus diameter of these nanotubes, according to (6.1). For comparison, the strain energies in BN, GaN and carbon nanotubes are presented. The *curves* are fitted by the least-square method (Reprinted figure with permission from Zhao et al. [130], Copyright (2004) by the Elsevier B.V. All rights reserved)

indicating that AlN graphitic nanolayer is rather unstable. Indeed, its growth unlikely starts from a highly metastable phase in experiment [130], which creates a disadvantage to the formation of AlN SW NTs, because such a high strain is difficult to alleviate by growing nanotube.

Thermal stability of AlN *ac*- and *zz*-SW NTs of different diameters was studied using MD simulations based on DFT-LCAO calculations [130]. Structural transformations of AlN nanotubes with (3,3), (6,0), (9,0) and (8,8) chiralities were simulated at several temperatures up to 1,000 K (Fig. 6.41). At 300 K, no essential changes in nanotube structures were observed as compared to optimized NT configurations, since the disorder caused by atomic thermal motions was not significant at this temperature. The cross-sections of nanotubes at 600 K became more elliptic, which was explained by the softness of AlN SW NTs that could be easily deformed in a radial direction [130]. At that temperature, the structural disorder of nanotubes caused by atomic thermal motions became significant. The analysis of the pair distribution functions displayed a feature of solid-liquid coexistence, suggesting that AlN SW NTs start melting. The lattice character of nanotubes in the axial direction disappeared after relaxing these tubes at 1,000 K. The pair distribution functions at that temperature demonstrated liquid features. It allowed the authors to deduce that the highest temperature *T*, when the rolled-up AlN NTs still can stably exist, is rather low, 600 K [130], due to the high strain energy relative to cubic-type materials involved in the formation of Al SW NTs. Obviously, the structural stability of nanotubes at different temperatures depends also on the NT diameter decreasing with the growth of the latter. For example, a visible deformation of the cross-section of *ac*-nanotube with (8,8) chirality was already observed at 300 K (Fig. 6.41d).

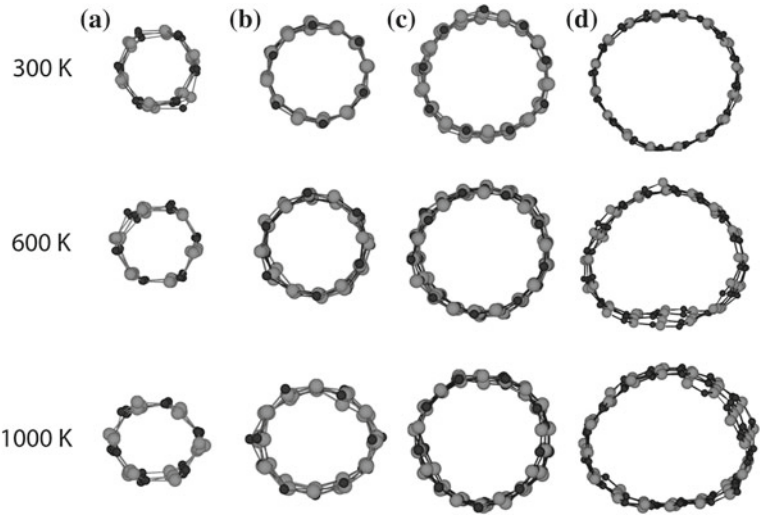

Fig. 6.41 Cross-sections of: **a** (3,3), **b** (6,0), **c** (9,0) and **d** (8,8) AlN SW NTs at the temperatures of 300, 600 and 1,000 K (Reprinted figure with permission from Zhao et al. [130], Copyright (2004) by the Elsevier B.V. All rights reserved)

6.5.2 Rolled-Up Single-Wall GaN Nanotubes

As a typical kind of a wide band-gap semiconductor with a wurtzite structure, GaN nanotubes are gaining enhanced attention due to the high efficient blue-light-emitting diodes produced from GaN materials [141] making their application quite promising for full color displays [128, 142]. Single-crystal GaN NTs with the inner diameters of 30–200 nm and wall thicknesses of 5–50 nm were successfully synthesized earlier using the epitaxial casting techniques [121]. The stability of single-wall GaN NTs was firstly studied using the first-principle DFT-LDA PW calculations on the electronic and structural properties of different GaN SW NTs [125], e.g., possessing the same (5,5) and (9,0) chiralities as shown for AlN SW NTs (Fig. 6.38). The optimized diameters of these nanotubes (D_{NT}), accompanied by buckling, were found to be 8.47 and 8.81 Å, respectively, i.e., by 4 % smaller than for AlN NTs mentioned above [127], although $d_{Al-N} < d_{Ga-N}$ [138]).

Fig. 6.42 shows the band structures and density of states calculated for the corresponding *ac*-(5,5) and *zz*-(9,0) GaN SW NTs [125]. Analogically to SiC SW NTs (Sect. 5.5.1), zigzag nanotubes possess a direct band gap, whereas armchair nanotubes have an indirect gap. The maximum of the valence-band for an *ac*-GaN NT is just near the middle of the Brillouin zone. The electronic DOSs of *ac*- and *zz*-nanotubes were found to be qualitatively similar to each other (Fig. 6.42a, b). A larger number of Ga(4*p*) and N(2*p*) states are developed by NT bond re-hybridization upon wrapping as compared with the corresponding graphitic sheet.

To study the electronic structure of ultrathin GaN SW nanotubes, both achiral, i.e., (2,2), (3,3), (3,0), (4,0) and (5.0), as well as chiral, i.e., (2,1), (3,1), (3.2), (4,1) and

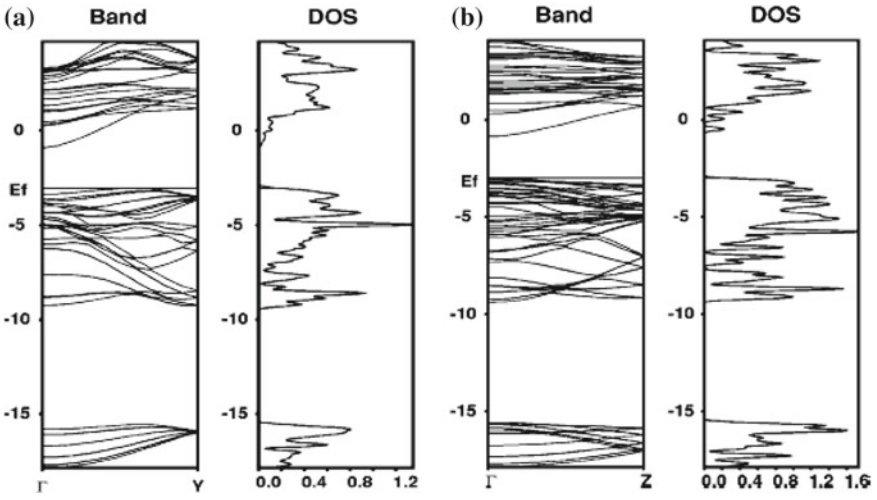

Fig. 6.42 Band structures along the nanotube axis and the corresponding density of states of (5,5) and (9,0) GaN single-wall nanotubes. *Y*(*Z*) band edges correspond to the symmetric points in the armchair (*zigzag*) nanotube [125]. **a** armchair. **b** zigzag

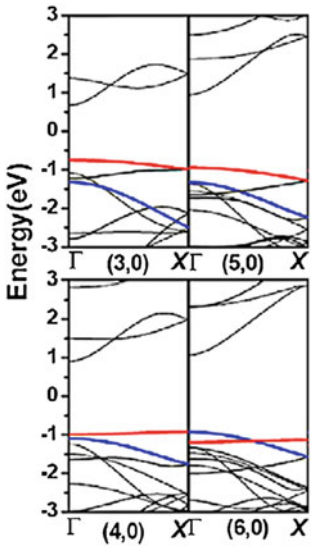

Fig. 6.43 The band structures of $(n,0)$ GaN NTs with $n = 3 - 6$. The description of details is given in the text [139]

(4,2), with NT diameters changing from 3.0 to 5.5 Å, the DFT-GGA PW calculations were performed [139]. Similar to GaN NTs of larger diameters (Fig. 6.42), both *ac*- and chiral ultrathin nanotubes were found to be the indirect-band-gap semiconductors. However, not all *zz*-NTs possessed the direct gaps, e.g., (4,0) nanotube (Fig. 6.43), i.e., the gap transition from direct- to indirect-band-gap is not merely relative to the decrease of NT diameter. Apparently, the band structures of *zz*-NTs show two different behaviors due to the different symmetry for $(2n, 0)$ and $(2n - 1,0)$ NTs. Four surface states were found near the Fermi level, which would influence the band gap (Fig. 6.43): the double degenerated localized *L*-states characterized by a narrow dispersion (red lines) and the double degenerated extended *E*-states possessing a wide dispersion (blue lines). The *L*-states are pinned at about 1.0 eV below the Fermi level for all *zz*-GaN NTs. However, the *E*-states would move downwards with decreasing diameter, switching their position with the *L*-states around Γ points for just (4,0) GaN NT. The movement of the extended *E*-states leads to the band sequence change, which results in the appearance of indirect-band-gap for (4,0) GaN NTs while other zigzag nanotubes are direct-band-gap semiconductors [139]. The movement of the extended *E*-states can be attributed to the following two factors: the π–π bond re-hybridization, due to the curvature effect of the small-diameter NTs, and the formation of soft buckling separations.

Figure 6.44 shows the dependence of the band gaps for modest-size *ac*- and *zz*-type GaN SW nanotubes on their diameters [125]. Unlike the alternating band gap of carbon zigzag nanotubes with a diamond shape, the band gaps of GaN nanotubes decrease smoothly with the decreasing diameter (Fig. 6.44). The band gap of GaN SW (n,n) NTs decreases slightly with decreasing diameter, whereas that of GaN SW $(n,0)$ NTs reduces significantly. This factor reflects the ionic character of bonding, i.e., *s* and *p* bands localized on Ga and N atoms are well separated [143]. With the

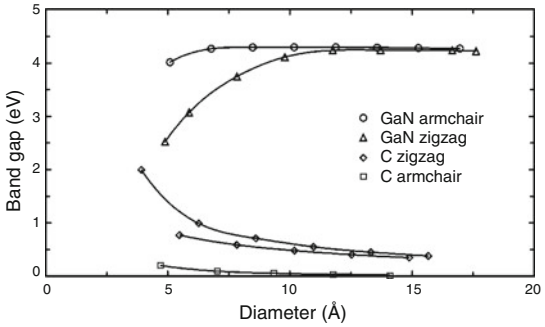

Fig. 6.44 Band gaps of *ac*- and *zz*-GaN SW NTs as a function of the diameter. For comparison, the changes of band gaps in *zz*-CNTs are shown below. (The *bottom curves* describe changes of band gap in *ac*-CNTs.) [125]

increasing nanotube diameter the band gap converges to the value of the graphitic GaN sheet. Similar dependencies of Al SW NT band gaps on nanotube diameters were obtained later [127].

An original idea for the formation of GaN SW nanotubes was suggested to use carbon nanotubes as a template [125]. GaN NTs can be synthesized at the open edges of CNTs since vertically aligned carbon nanotubes were successfully grown on glass [144]. This aligned carbon nanotube can be a suitable template for GaN NT growth. The extra energy costs necessary for the formation of GaN graphitic nanolayers can be overcome by GaN adsorption on the existing tubular form of substrates. The precise structures appearing during the GaN nucleation on carbon nanotubes is still under investigation [125]. The strain caused by the lattice mismatch between graphitic GaN (Fig. 6.37) and graphene (achieving ∼25 %), as well as the relative energetics of *ac*- and *zz*-GaN NTs can play an important role in the synthesis of GaN nanotubes on CNTs. It was found that *zz*-GaN NTs are more favorable than armchair nanotubes where the strain is relaxed within a few GaN layers. Thus, interfaces between metallic *ac*-CNTs and semiconducting *zz*-GaN NTs can be fabricated, which opens the possibility to apply this heterostructure for ultimate nanoscale photodetectors or electroluminescent devices [125].

6.5.3 Rolled-Up Single-Wall (Al,Ga)N Nanotubes

As mentioned in Sect. 6.4, GaN/AlN hetero-structures and $Al_xGa_{1-x}N$ alloys have a strong technological appeal, due to the possibility of varying their direct band gaps in a wide interval, and to their high thermal and mechanical stability [140]. The following important applications of these structures may be mentioned: LEDs (light-emitting diodes) for low-energy consumption light emission [145], blue lasers for multimedia disks [146], field effect transistors (FET) [147], and high electron mobility transistors

(HEMT) [148]. Although the reproducible synthesis of AlN and GaN single-wall nanotubes is still problematic, the results of theoretical simulations on (Al, Ga)N SW NTs would be very promising in nanoelectronics. Three types of (Al, Ga)N nanotubes have been simulated so far: alloy-type $AlGaN_2$ [138] and $Al_xGa_{1-x}N$ SW NTs [138, 140], as well as $GaN/Al_xGa_{1-x}N$ SW NT hetero-junctions [140].

The total energies of a few possible structures for a honeycomb-type $AlGaN_2$ nanosheet were estimated using the DFT-GGA PW calculations [138]. The configuration shown in Fig. 6.45a, where Ga and Al atoms were separated by N atoms, was found to be most stable. Other structures, e.g., those where Ga atoms were directly bonded to Al atoms, were found to be evidently less stable. More than one type of *zz*- and *ac*-$AlGaN_2$ NTs can exist (analogous situation was considered in Sect. 5.5.5), depending on how an $AlGaN_2$ sheet is rolled up (Fig. 6.45a), e.g., two types of zigzag nanotubes: *ZZ*1 (*n*,0) with $n = 5$–16 (Fig. 6.45b) and *ZZ*2 (0,*n*) with $n = 3$–8 (Fig. 6.45c), as well as two types of armchair nanotubes: *AC*1 (*n*,*n*) with $n = 3$–11 (Fig. 6.45d) and *AC*2 (*m*,*m*) with $m = 2$–5 (Fig. 6.45e).

Figure 6.46 shows the variation of the calculated GGA band gaps of various $AlGaN_2$ nanotubes imaged in Fig. 6.45 with the NT diameter. Those band gaps depend on both the diameter and chirality being converged to that of the honeycomb $AlGaN_2$ sheet when the diameter of the tube becomes very large [138]. The relatively smaller band gaps for the $AlGaN_2$ nanotubes with smaller diameters can be attributed to the curvature-induced strong hybridization effect. For nanotubes with the same diameter, the *AC*1 NTs have a slightly larger band gap, moreover, the band gaps of the $AlGaN_2$ NTs and a honeycomb sheet are smaller than those of bulk wurtzite $Al_xGa_{1-x}N$ alloys ($0 < x < 1$), which have tunable direct band gaps between 3.4 and 6.1 eV, depending on Al concentration. Thus, $AlGaN_2$ SW NTs can be recognized as important semiconductors for optoelectronic device applications over the visible spectral range [138].

A more generalized case of the alloy-type single-wall nanotubes, $Al_xGa_{1-x}N$ (10,0) NTs, characterized by the variable x describing Al concentration (with fixed magnitudes of 0.1, 0.3, 0.5, 0.7, 0.9), was simulated using the DFT-LCAO LDA

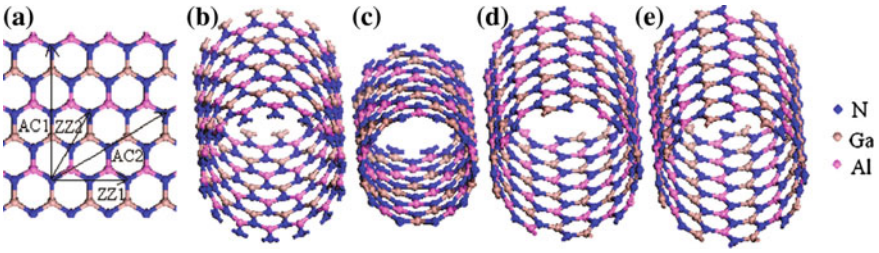

Fig. 6.45 Atomic configurations of the most stable $AlGaN_2$ sheet (**a**), containing wrapping vectors of the four types of NTs: *ZZ*1 (14,0) (**b**), *ZZ*2 (0,5) (**c**), *AC*1 (8,8) (**d**), and *AC*2 (4,4) (**e**)—the explanations are given in the text. Ga, Al, and N atoms are indicated by *light-brown*, *pink*, and *blue* spheres (Reprinted figure with permission from Pan et al. [138], Copyright (2008) by the American Chemical Society)

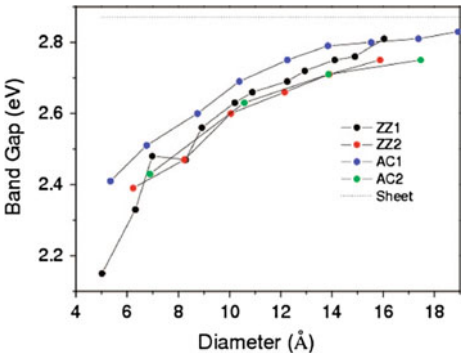

Fig. 6.46 Widths of band gaps for $AlGaN_2$ NTs (Fig. 6.45), as functions of their diameters, and optimized honeycomb sheet (Reprinted figure with permission from Pan et al. [138], Copyright (2008) by the American Chemical Society)

calculations [140]. For each concentration, five independent nanotube configurations were generated by randomly distributing Ga and Al atoms on the cation sites. The number of five was chosen because a comparison of various properties calculated for the case of $x = 0.5$ using the two sets with five and ten independent random configurations clearly demonstrated qualitatively negligible difference between the average values obtained from both sets (for each Al concentration, the standard deviations from the average values were found to be lower than 10^{-2} eV). Figure 6.47 shows alloy-type nanotubes with two particular *zz*-NT structures of $Al_{0.3}Ga_{0.7}N$ and $Al_{0.5}Ga_{0.5}N$ (the disordered analog of $AlGaN_2$ nanotube configurations which are present in Fig. 6.45b, c).

The calculated average band gap for each Al concentration can deviate from the simple linear interpolation between the extreme values from the perfect GaN and AlN nanotubes. The average band gap variation depending on the Al concentration in the alloy nanotubes was described by a non-linear equation which included the so-called bowing coefficient *b*, according to the following equation [140]:

$$E_{gap}^{Al_xGa_{1-x}N}(x) = (1-x)E_{gap}^{GaN} + xE_{gap}^{AlN} - bx(1-x), \tag{6.6}$$

where $E_{gap}^{Al_xGa_{1-x}N}(x)$ is the average band gap for arbitrary Al concentration *x*, while E_{gap}^{GaN} and E_{gap}^{AlN} are the band gaps for perfect GaN sand AlN nanotubes, respectively.

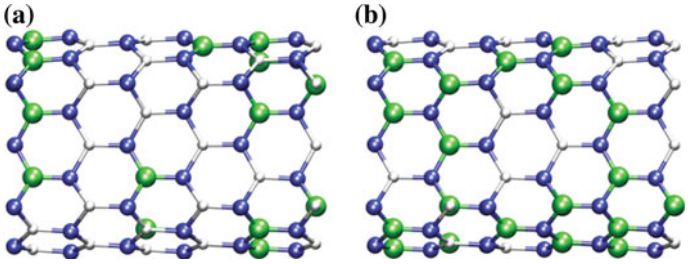

Fig. 6.47 Models of disordered $Al_xGa_{1-x}N$ (10,0) NTs with **a** $x = 0.3$ and **b** $x = 0.5$. The small, medium and large spheres represent Ga, N and Al atoms, respectively [140]

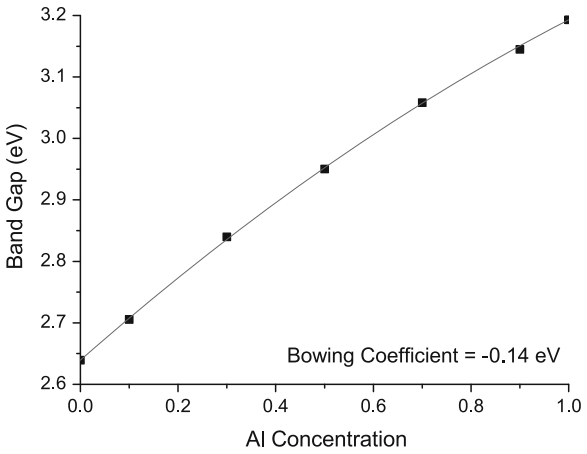

Fig. 6.48 LDA band gap variation of $Al_xGa_{1-x}N$ nanotubes as a function of Al concentration x (Reprinted figure with permission from de Almeida et al. [140], Copyright (2009) by the Elsevier B.V. All rights reserved)

Figure 6.48 shows the results for the average band gap variation with x. The total negative bowing coefficient was estimated from this plot to be ~0.14 eV [140]. Although the band gap bowing coefficient for wurtzite $Al_xGa_{1-x}N$ bulk random alloys can have a large dispersion from positive to negative values (due to the existence of different random configurations with different band gaps, as was concluded elsewhere [149]). This is not the case for $Al_xGa_{1-x}N$ alloy nanotubes, where the standard deviation in the band gap values and the total energies for different configurations of each NT with different Al concentrations is lower than 10^{-2} eV. No evidence was found on the dependence of the average distance between Al atoms in each NT and their total energies (and, consequently, the formation energies) on arbitrary Al concentration. After the corrections of LDA results based on the comparison between the experimental and theoretical data obtained for wurtzite AlN and GaN bulk, the range of allowed band gaps obtained by varying the value of x in the $Al_xGa_{1-x}N$ NTs, was changed from 3.45 to 4.85 eV (λ = 359 to 256 nm in the ultraviolet region) with a band gap variation of 1.4 eV, almost the double of that for bulk alloys [140].

The (10,0) GaN/$Al_xGa_{1-x}N$ nanotube hetero-junctions were studied for x = 0.1, 0.3, 0.5, 0.7, 0.9 and 1.0 (the limit case of GaN/AlN junction as shown in Fig. 6.49) [140]. The atomic positions and the supercell size have been fully relaxed. At the final configurations both GaN and AlN nanotubes were stressed, due to the difference between the diameters of isolated nanotubes. The maximum difference between the diameters of the nanotubes in the hetero-junction occurs for the limit case x = 1.0. The properties of the GaN/$Al_xGa_{1-x}N$ NT hetero-junctions for each Al concentration were averaged using three independent $Al_xGa_{1-x}N$ random configurations.

Figure 6.50 shows the band structure alignment profile for the GaN/AlN (10,0) NT hetero-junction. The results reveal type-I band alignment with electrons and

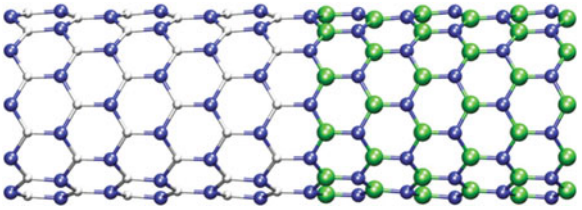

Fig. 6.49 Model of the GaN/AlN (10,0) NT hetero-junction. The *small*, *medium* and *large spheres* represent Ga, N and Al atoms, respectively [140]

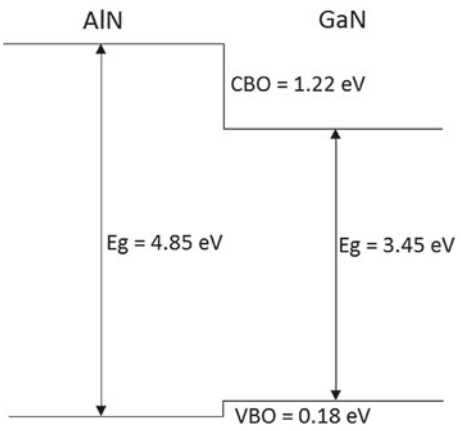

Fig. 6.50 Profile of the band structure for the GaN/AlN (10,0) NT hetero-junction. E_{gap}^{GaN} and E_{gap}^{AlN} represent the band gaps of (10,0) AlN and GaN NTs while the meanings of VBO and CBO are described in the text (Reprinted figure with permission from de Almeida et al. [140], Copyright (2009) by the Elsevier B.V. All rights reserved)

holes, both localized at the GaN side of the interface. The calculated valence and conduction band offsets (VBO and CBO, respectively) for the GaN/AlN nanotube hetero-junction were found to be 0.18 and 0.34 eV, respectively. The VBO value was obtained definitely lower than that found for *c*- and *w*-GaN/AlN bulk hetero-junctions (0.82 and 0.84 eV, respectively [150]). After the correction of band gap parameters according to the scheme based on the comparison of the experimental and theoretical data, as described above, the CB offset for the GaN/AlN NT hetero-junction increased up to 1.22 eV [140].

In spite of the promising prospects for technological applications described above, the synthesis of the stable AlN, GaN and (Al,Ga)N SW nanotubes remains a great experimental challenge because of their high strain energy as compared to the bulk materials [135].

6.5.4 Faceted AlN Nanotubes

Even if single-wall nanotubes of the group-III metal nitrides were synthesized, the further growth of the NT wall along the radial direction would not stop immediately [121, 135]. It would adsorb the incoming nitride species in the environment and form

thick-walled sp^3-bonded single-crystalline nanotubes with faceted hexagonal cross sections (similar to those of SiC NT considered Sect. 5.5.4) in order to release the strain energy. Moreover, the cylindrical multi-wall shape of GaN NT was found to be unstable and broken even at 300 K as followed from the MD simulation [131]. The surface dipoles on the lateral facets of AlN and GaN NTs facilitate the adsorption of polar group-III metal nitride species and keep the growth of hexagonal-shaped nanotube wall continuing along the radial direction [135]. The most effective way for the simulation of the sp^3-bonded faceted AlN and GaN nanotubes possessing the point symmetry D_{3h} was found to be a removal of the core nanowire symmetrically arranged around its axis from the larger NW of the same faceting (Fig. 6.51). The axial orientation of the as-synthesized hexagonal-shaped AlN (GaN) NWs and faceted AlN (GaN) NTs is always in the [0001] direction whereas the experimental data for determining their lateral facet orientations have not been available so far [135]. In analogy with single-crystalline SiC nanotubes, the corresponding six lateral facets can be chosen as attributed to the $\{10\bar{1}0\}$ family (Sect. 5.5.4), since its surface energy is smaller than that of $\{11\bar{2}0\}$ (136 vs. 143 meV/Å^2, respectively), due to a lower density of the dangling bonds on the former (0.12 vs. 0.14/Å^2). A similar result was also reported for GaN NWs, which gave 118 and 123 meV/Å^2 for $(10\bar{1}0)$ and $(11\bar{2}0)$ surfaces, respectively [151].

Figure 6.51 presents dependencies of the strain energies for AlN NWs, faceted AlN NTs of different wall thicknesses and rolled-up AlN SW NTs on their diameters, i.e., $E_{strain}(D)$ [135].

For the first two types of nanostructures, the strained energy was determined as the difference between their total energy *per* atom and that for AlN wurtzite bulk, while the diameter was evaluated by the average of the radial distance between the central axis and the outermost atoms. As defined above, E_{strain} for the rolled-up

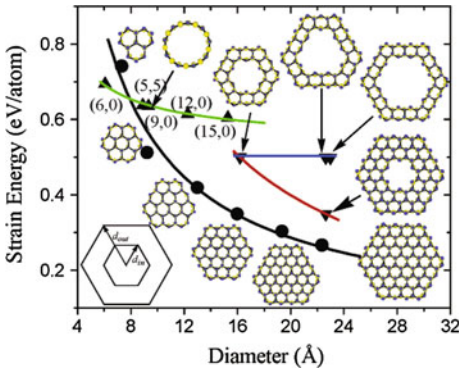

Fig. 6.51 The strain energies of AlN NWs, faceted AlN NTs and rolled-up AlN SW NT as functions of diameter. E_{strain} for different configurations of AlN NWs are represented by the *solid circles*, while the *black line* is the fitting *curve* by using the expression $E_{strain} = C/D$. The strain energies of faceted AlN NTs and single-wall AlN NTs are denoted by the *down* and *up triangles*, respectively (Reprinted figure with permission from Zhao et al. [135], Copyright (2006) by the American Chemical Society)

SW NT was estimated as the difference between the total energy of nanotube *per* atom and that for the corresponding honeycomb AlN(0001) sheet. Obviously, the strain energy of a nanowire consequently reduces with the growth of its diameter, following its inverse proportionality, i.e., $E_{strain} \sim 1/D$ [135]. The strain energy of AlN SW NT decreases monotonically with the increasing nanotube diameter and saturates at the value corresponding to the AlN graphitic-like sheet (Fig. 6.51).

However, for faceted AlN NTs, the corresponding $E_{strain}(D)$ dependencies were found quite different. The strain energies of double-wall single-crystal AlN NTs with three different diameters, but equal thickness, keep constant, ~0.50 eV/atom. The strain energy of a triple-wall faceted AlN NT is greatly reduced, to ~0.35 eV/atom, which is comparable to that of ~0.27 eV/atom for AlN NW with the same diameter.

The variation of strain energy for thick-walled faceted AlN NTs can be understood since E_{strain} in this case mainly arises from the curvature of the external and internal surfaces and the local structural distortion of the surface atoms. The main distortion occurs mainly near the surfaces, whereas the deviation of the bond lengths and bond angles in the core region from those of the perfect wurtzite AlN crystal is quite small. The strain energy of the faceted AlN NTs can be approximately evaluated by the expression [135]:

$$E_{strain}^{\mathrm{AlNNT}} = \frac{8E_{surf}}{\sqrt{3}n(d_{out} - d_{in})}, \tag{6.7}$$

where E_{surf} is the surface energy of all six $\{10\bar{1}0\}$ facets, n is the atomic density, while d_{out} and d_{in} are the outer and inner diameters of the faceted AlN NTs (shown in the inset of Fig. 6.51). The strain energy of the faceted AlN NTs is proportional to the inverse of the wall thickness and independent of the nanotube diameter. The E_{strain} of the double- and triple-wall AlN nanotubes were found to be 0.53 and 0.35 eV/atom, respectively. By using this expression, $E_{surf} \approx 136$ meV/Å^2, while $n \approx 0.14$/Å^3 for the double-wall AlN NT and 0.12/Å^3 for the triple-wall AlN NT. They are in good agreement with 0.50 and 0.35 eV/atom for faceted DW and TW AlN NTs, respectively, obtained by direct first-principles calculations. This expression is also valid for describing AlN NTs with $d_{in} = 0$, (i.e., AlN NW) and well reproduces their strain energies [135].

The band structures of *w*-AlN bulk (Fig. 6.35b), nanowire, rolled-up and faceted AlN nanotubes (Fig. 6.51), as well as H-doped AlN NW and faceted NT were evaluated using the DFT-LCAO method [135]. Wurtzite-type AlN bulk possesses a direct band gap at Γ point of the Brillouin zone (Fig. 6.52a), analogically to other group-III metal nitrides [104]. Despite underestimate of the band gap width, typical for traditional DFT methods, they are known to reproduce well both the occupied states and the dispersion of the bands [152]. The band structures of both AlN NW (Fig. 6.52b) and faceted AlN NT (Fig. 6.52c) clearly indicated that some bands appeared in the band gap of *w*-AlN, which were found to be very smooth and, thus, highly localized in a real space. An analysis of the corresponding PDOSs showed that they mainly arose from the states of atoms located on the hexagonal facets (Fig. 6.51), which are the surface states [135]. The occupied surface bands consisted of mainly the atomic

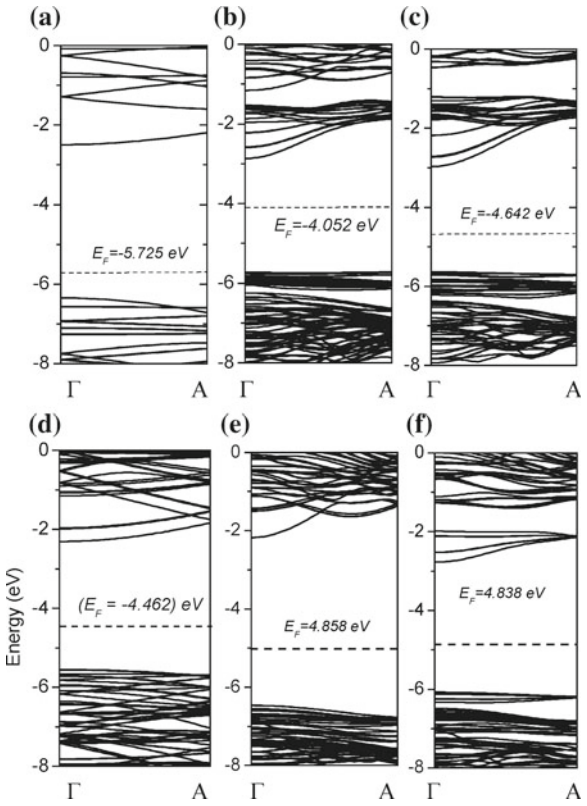

Fig. 6.52 Band structures along the direction $\Gamma(0, 0, 0)2\pi/a \rightarrow A(0, 0, 0.5)2\pi/a$ in the reciprocal space of the Brillouin zone drawn for: **a** bulk AlN (wurtzite); **b** AlN NW; **c** faceted AlN NT, **d** rolled-up (9,0) AlN SW NT, **e** H-doped AlN NW, and **f** H-doped faceted AlN NT. The dashed lines represent the Fermi levels which were directly obtained from Fermi-Dirac distribution at room temperature (Reprinted figure with permission from Zhao et al. [135], Copyright (2006) by the American Chemical Society)

N(2*p*) states, while the unoccupied surface bands arose from the Al(3*p*) states. This was found to be consistent with asymmetry of the charge distribution on the surfaces where the valence electron density is strongly accumulated around N atoms because of their strong 2*p* potentials [135]. On the other hand, the band structure of rolled-up *zz*-AlN NT bears no resemblance to that of *w*-AlN bulk, due to their structural difference (Fig. 6.52d). The width of the occupied surface bands of the AlN NW was found to be about 0.45 eV with its frontier state 0.52 eV above the top of the valence band of *w*-AlN (Fig. 6.52b). For the faceted AlN NT, the width of occupied surface bands is extended to 0.66 eV and the frontier surface state is 0.74 eV above the top of the valence band of *w*-AlN, due to the contribution from the atoms on the inner nanotube facets (Fig. 6.52c). These surface states narrow the band gap and, thus, should definitely be responsible for changes in the electronic properties of AlN NWs

and faceted NTs [135]. The surface bands located inside the band gap of the clean AlN NW disappear in the corresponding hydrogen-passivated nanowire (Fig. 6.52e). However, the surface bands remain in the band gap of H-doped faceted AlN NT, as shown in Fig. 6.52f, which is related to the unsaturated bonds at the interior facets. This also confirms that the flat bands located in band gaps of pure AlN NW and faceted NT are indeed the surface bands.

It has also been found that when the wall width of the faceted AlN NT is reduced to a single atomic layer, the hexagonal cross-section becomes unstable and transforms to a round cross-section after relaxation, forming a rolled-up *zz*-AlN SW NT [135]. On the other hand, the faceted AlN DW NT imaged in Fig. 6.51 (in the middle of the upper part) can be disintegrated into the two individual (9,0) and (15,0) rolled-up AlN SW NTs, respectively, with the corresponding strain energies 0.64 and 0.61 eV/atom (*cf.* with 0.50 eV/atom for faceted AlN DW NTs), which can form rolled-up *zz*-AlN DW NTs. When the latter coaxial nanotube was heated at 1000 K (in the framework of MD simulation), a distorted hexagonally faceted nanotube was obtained again by the formation of ionic Al-N bonds between the inner and outer round nanotube shells. Hence, the tendency of transition from faceted to rolled-up AlN NT configuration and back is quite obvious. This energy balance clearly demonstrates the difficulties in fabricating both single- and multi-wall rolled-up AlN NTs, In any case, it is a great challenge to realize the synthesis of the reproducible rolled-up AlN SW NTs [135].

6.6 Group III Metal Nitride Nanowires

6.6.1 Prismatic AlN Nanowires

Randomly oriented as well as aligned AlN NWs were fabricated using a number of alternative methods: the Al powder reaction in the NH_3/N_2 atmosphere [153], the catalytic metal-organic chemical vapor deposition [154], the radio frequency magnetron discharge sputtering of the Al-containing target in the Ar/N_2 gas mixture [86], the direct arc discharge [155], and self-patterning [156]. Group-III metal nitride nanowires provide essential number of applications, ranging from chemical and temperature sensors [157] to nanomechanical resonators [158] and field emitters [159]. The diameters of AlN NWs (d_{NW}) synthesized using different methods were estimated to be in the range of 5–100 nm. The adsorption edge of AlN NWs was found to be blue-shifted by 0.27 eV from the bulk edge as revealed by transmission spectra [160], which was attributed to the quantum size effect in the radial direction [161]. This effect makes AlN as well as other homogeneous and heterogeneous group-III metal nitride nanowires an attractive material for high performance light emitting diodes covering the spectral regime of approximately 370–480 nm [162]. Although the number of aluminium and other group-III metal nitride NWs fabricated using different techniques substantially increases, a deeper analysis of the basic process of nanowires formation is still lacking, therefore, controlling the

growth of the nanowires is still a challenging issue [163]. A number of theoretical simulations on AlN NWs have been performed so far [135, 157, 158, 163–168]. The corresponding 1D NW models were exclusively chosen as those possessing a single-crystalline *w*-AlN NW morphology (WZ, space group $P6_3mc$ as shown in Fig. 6.35) with the growth direction along the [0001] axis, although the structure of their lateral facets could not be directly identified in the experiments [135]. However, recent theoretical simulations have showed that with the decrease of nanowire diameter to the sizes of ultrathin NW a structural transformation of *w*-AlN NWs to graphite-like *h*-AlN NWs can occur (GL, which morphology is typical for BN described by $P6_3/mmc$ group as imaged in Fig. 6.1a) [158, 163, 167] although such a transformation is rather not possible in the case of AlN bulk and its various surfaces with prevailing sp^3 bonding between Al and N atoms as considered in Sect. 6.4. For simulations of 1D AlN nanowires, various ab initio methods were applied: (i) the DFT-LCAO methods as implemented in either CRYSTAL [165, 166, 168] or SIESTA [135, 158, 167] packages as well as (ii) DFT-PW methods [157, 163, 164] applied for nanowires incorporated in repeating tetragonal supercells with such a dimension that the interaction between NWs and their nearest images was negligible. Besides, periodic atomistic models applied in all theoretical studies of nanowires mentioned above, both continuous and finite element models, were used for detailed description of mechanical (e.g., elastic) NW properties and comparison with atomistic models [166, 168].

The axial orientation of arbitrary *w*-AlN nanowire coincides with the [0001] direction accompanied with hexagonal cross sections (Fig. 6.53), whereas the orientations of six NW lateral facets (faceting) can be determined via the minimum of their total surface energy $E_{surf}(d_{\mathrm{NW}})$ or strain energy $E_{strain}(d_{\mathrm{NW}})$ defined from (6.7) for the case of $d_{in} = 0$ (the profile of which is shown in Fig. 6.51). For [0001]-oriented wurtzite-type nanowires, the energetically more preferable lateral facets of AlN NWs can be considered, as shown in either Fig. 6.53b or Fig. 6.53c, densely-packed facets with different angular orientations. According to the results of ab initio

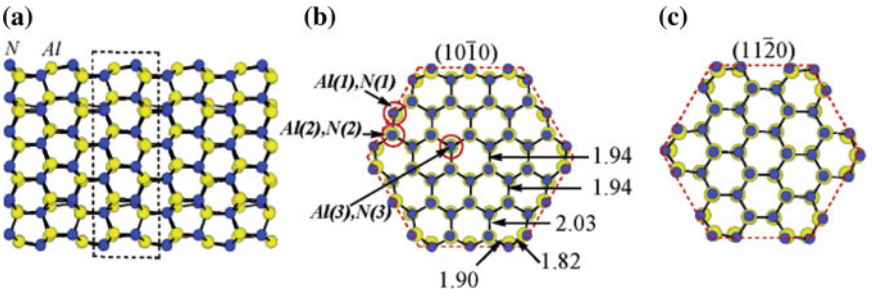

Fig. 6.53 Equilibrium configurations of [0001]-oriented AlN NWs with a different faceting: **a** aside view and **b** across view of an AlN NW with six {10$\bar{1}$0} lateral facets; **c** across view of an AlN NW with six {11$\bar{2}$0} facets. *Dash-limited rectangle* (**a**) determines the period of nanowire while *dash-limited hexagons* (**b**, **c**) determine profiles of nanowire cross-sections. The labeled atoms in central panel **b** were used for construction of the corresponding DOSs imaged in Fig. 6.54 [135]

slab calculations [135], the corresponding values of $E_{surf}(d_{NW})$ were found to be 136 and 143 meV/Å^2, respectively. Figure 6.53b, c give the equilibrium configurations of two AlN NWs with similar diameters, 16.0 and 15.6 Å, but different lateral facets, $\{10\bar{1}0\}$ and $\{11\bar{2}0\}$, respectively. $E_{strain}(d_{NW})$ of the former was calculated to be ~94 meV/atom smaller than that of the latter, while the corresponding total surface energies of these nanowires were found to be 153 and 156 meV/Å^2, respectively [135], slightly higher than those obtained for infinite two-dimensional slabs as mentioned above. These differences can be well attributed to the corner atoms of the hexagonal NW cross-section whose coordinate environment is quite different from that of the atoms on infinite two-dimensional slabs, and, thus, the Al-N bonds associated with these atoms were shortened to ~1.82 Å as compared to those of other surface and internal atoms (Fig. 6.53b). Thus, AlN NWs with $\{10\bar{1}0\}$ faceting can be considered as the energetically most preferable.

The analysis of the projected density of states (PDOS) shows that they mainly arise from the states of the atoms positioned on the facets (Fig. 6.54), clearly indicating a presence of predominantly surface states (*cf.* with Fig. 6.52b which shows the band structure of *w*-AlN nanowire terminated by six facets). Occupied surface bands mainly arise from the states of N atoms, while unoccupied surface bands mainly arise from the states of Al atoms, respectively. This is consistent with the asymmetry of charge distribution on the surfaces where the valence electron density is strongly accumulated around the N atoms because of their strong 2*p* potentials.

When the diameter of AlN NW decreased to the ultrathin size (as was mentioned above), a phase transformation WZ → GL was repeatedly observed [158, 163, 167]. As a result, the length of *w*-AlN lattice parameter *c* (Fig. 6.55), the direction of

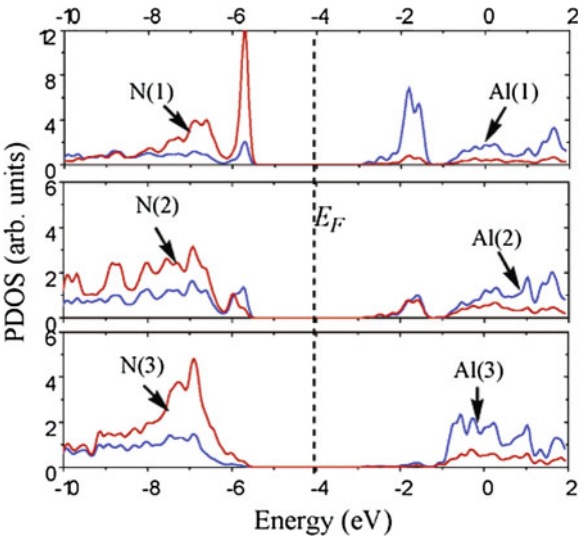

Fig. 6.54 Electron density of states projected onto different atoms labeled in Fig. 6.53b. The *dashed line* designates the Fermi level (Reprinted figure with permission from Zhao et al. [135], Copyright (2006) by the American Chemical Society)

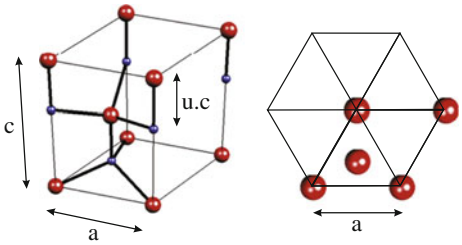

Fig. 6.55 Unit cell for wurtzite lattice structure of arbitrary binary compound (detailed description is given in Fig. 6.35b) (Reprinted figure with permission from Yvonnet et al. [168], Copyright (2010) by the Elsevier B.V. All rights reserved)

which coincides with the direction of NW axis, was found to be reduced, while cross-sections of newly-formed *h*-AlN NWs included Al and N atoms in equidistantly separated planes unlike those in *w*-AlN NWs (Fig. 6.56).

An initial atomic configuration for the construction of *h*-Al NW (GL phase), which possesses the diameter of ultrathin size (e.g., that imaged in the left panel of Fig. 6.56, which can be rather considered as ultrathin nanotubes), was chosen the pristine AlN nanowire of WZ phase corresponding to the native morphology of bulk material [158]. The initial 1D lattice parameters were chosen to be those of AlN bulk (Fig. 6.55): $a_{WZ} = 3.11$ Å and $c_{WZ} = 4.98$ Å. Then the system was consequently compressed along the nanowire axis using the maximum displacement of 0.1 Å (with total geometry optimization) while the interatomic forces were stabilized being less than 0.04 eV/Å. The final configuration obtained for the free-standing AlN NW attributed to the hexagonal GL phase where Al and N atoms were placed in alternating positions in honeycomb cross-sections, with the lattice constant $a_{GL} = 1.97$ Å, that is, the in-plane distance between two successive Al and N atoms. The distance between the nearest equidistantly separated hexagonal sections is $0.5c_{\mathrm{GL}} = 1.87$ Å, i.e., length of GL NW unit cell is $l_{\mathrm{NW}} = c_{\mathrm{GL}} = 3.74$ Å being reduced from 4.98 Å for WZ NW [158]. However, by applying a pulling force of 0.40 nN, AlN NW retains the original WZ configuration with slightly reduced lattice parameters $a_{\mathrm{WZ}} = 2.79$ and $c_{\mathrm{WZ}} = 4.86$ Å.

To understand the origin of WZ $\leftrightarrow$ GL NW phase transformation, their properties were analyzed [163]. For example, a noticeable difference between GL and WZ nanowire phases is their volume difference, which is proportional to $l_{\mathrm{NW}} \cdot (d_{\mathrm{NW}})^2$. Despite the resemblance in the atomic structure, the bulk WZ structure has a lower coordination number (4) as compared to that of GL (5). Therefore, the GL structure possesses a more negative Coulomb binding energy as compared to the WZ phase. On the other hand, the WZ structure has a stronger bond energy than the GL phase. The formation of the nanowire lost the bond energy at the surface. It means that for ultrathin nanowires with high surface-to-volume ratio, the GL structure becomes more stable due to its large Coulomb interaction energy, whereas for thicker nanowires, the WZ structure regains its stability due to a larger contribution from the bond energy [163].

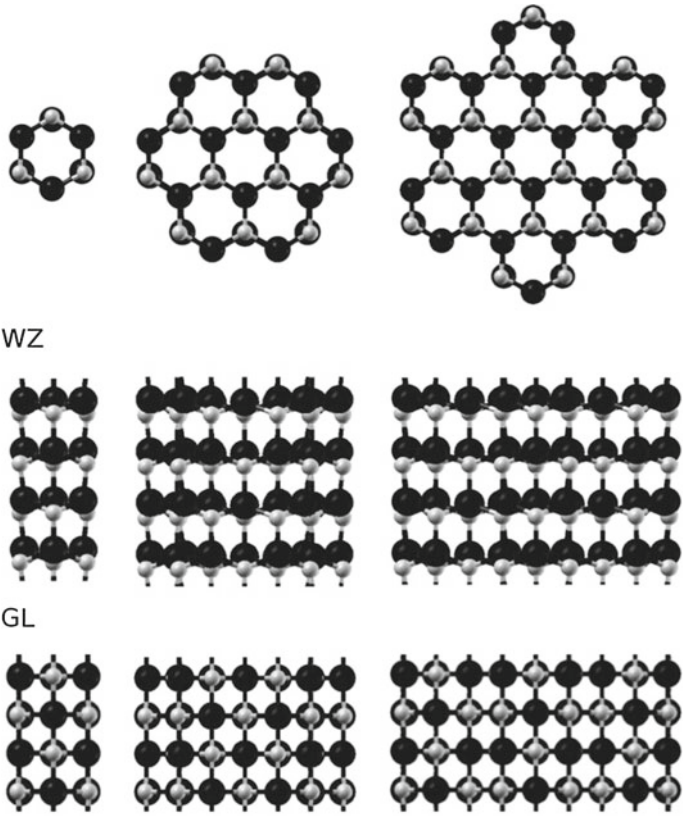

Fig. 6.56 Cross-sections (*top panel*) and lateral images (*middle and bottom panels*) of [0001]-oriented AlN NWs labeled as $R1$, $R2$ and $R3$ (possessing three different diameters) for the two structural phases, WZ and GL. The Al and N atoms are represented by *dark* and *light gray balls* respectively (Reprinted figure with permission from Mitran et al. [167], Copyright (2011) by the Elsevier B.V. All rights reserved)

The quantitative parameter, which can help for the better understanding of differences between the structures of AlN nanowires of GL and WZ phases (depending on both d_{NW} and l_{NW} parameters), is formation energy *per* Al-N pair [164]:

$$E_{form}(d_{\mathrm{NW}}, l_{\mathrm{NW}}) = [E_{tot}(n_{\mathrm{Al-N}}) - n_{\mathrm{Al-N}}\mu_{\mathrm{Al}} - 0.5n_{\mathrm{Al-N}}\mu_{\mathrm{N}}]/n_{\mathrm{Al-N}}, \quad (6.8)$$

where $n_{\mathrm{Al-N}}$ is the number of Al-N pairs *per* NW unit cell, E_{tot} the calculated total energy of AlN nanowire, μ_{Al} and μ_{N} the chemical potentials of Al and N obtained from the energies of Al atom in the face-centered cubic metal and isolated N_2 molecule, respectively. For both GL and WZ Al NWs of different diameters and UC lengths, the equilibrium periodicity of the nanowire ($l_{\mathrm{NW}} = c_{eq}$) is obtained by minimizing the total energy E_{tot}. The main goal of this comparative analysis

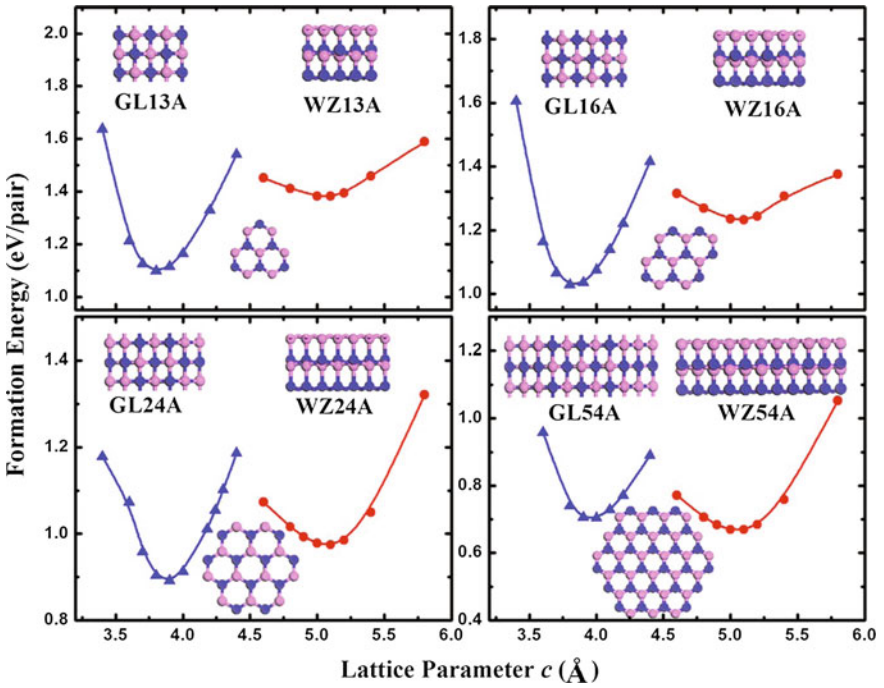

Fig. 6.57 Formation energies of GL and WZ phases of [0001]-oriented AlN nanowires as a function of NW UC length *c*. Two digits after phase labels correspond to the number of atoms in mono- (GL) or bi- (WZ) layered cross-sections. The insets are the lateral and across views of the nanowires (Reprinted figure with permission from Wu et al. [163], Copyright (2009) by the AIP Publishing LLC)

is the study of the energetic stability of different AlN nanowire phases including its dependence on the NW diameter. Figure 6.57 presents plots of energy curves $E_{form}(l_{\mathrm{NW}})$ for different values of d_{NW} for both GL and WZ phases of nanowires accompanied by their corresponding lateral and across images. The minima of energy curves shown in Fig. 6.57 directly correlate with the optimized structures of AlN NWs. Obviously, the nanowires of GL phase are energetically more stable than WZ phase NWs for ultrathin nanowire diameters only, while for thicker NWs, the GL becomes more unstable. When the diameter increases up to 54 atoms *per* Al-N layer, the NW WZ phase is more favored as the formation energy for GL54A is higher by 0.034 eV *per* Al-N pair than that for WZ54A. On the other hand, E_{form} for GL13A NW is lower by 0.285 eV/pair *per* Al-N pair than that for WZ13A, i.e., the former is substantially more stable [163].

Phase transformation WZ ↔ GL can be considered not only for morphology of nanowires possessing infinite length, but also for finite size nanorods, the length of which can be consequently increased up to infinity (NW) [163]. Figure 6.58 presents a schematic phase diagram of AlN nanorod, which suggests a possible growth route

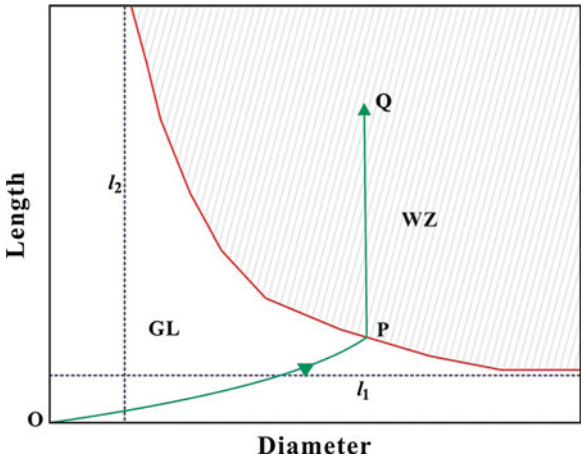

Fig. 6.58 Qualitative diagram showing areas for GL and WZ phases of [0001]-oriented AlN nanorod depending on its diameter and length. *Straight lines* l_1 and l_2 show two asymptotes of the coexistence border between both phases, where line l_1 corresponds to the transformation length for the infinite large diameter of nanorod (thickness of 2D film) while l_2 corresponds to the smallest possible diameter for AlN nanowire of the infinite length. A possible trajectory of nanorod growth $O \rightarrow P \rightarrow Q$ is described in the text (Reprinted figure with permission from Wu et al. [163], Copyright (2009) by the AIP Publishing LLC)

$O \rightarrow P \rightarrow Q$, which describes the appearance of WZ morphology. The process $O \rightarrow P$ occurs in the GL structure region, reflecting the fact that in the early stage of nanorod growth, the graphite-like structure is more favored. As the growth process continues, both the diameter of nanorod and its length grow reaching P point, where both GL and WZ phases can coexist. Further structure transformation foresees higher stability of nanorod in the WZ phase. Alongside with the structure transformation, an electric dipole moment appears associated with the WZ structure (it is zero for GL morphology). This dipole generates an electric field around the nanorod and the radicals, which are used during the synthesis procedure for the growth of AlN nanowires. Due to much larger electrostatic attractive forces, the incoming radicals are positioned on the top facets of nanorod and are barely able to have a chance to hit the sidewall [169]. In this way, the nanowire can grow along the [0001] direction with the unchanged diameter. This is described as the path $P \rightarrow Q$, which is perpendicular to the horizontal diameter axis (Fig. 6.58). Such understanding of the NW growth process suggests that in order to control the value of NW diameter, one must focus on the initial precursor, i.e., the GL nanorod structure [163]. To control effectively the first stage of growth, the WZ phase always must grow at the point P of the phase diagram, then uniform nanowires with the fixed diameter could be synthesized. Analogous mechanism was also suggested for the growth of GaN and ZnO nanowires [163, 170].

6.6.2 Thermal and Vibrational Properties of AlN Nanowires

Besides ab initio simulations on the structural and electronic properties of h- and w-AlN NW studied recently, as considered in previous Subsection [135, 157, 163–166], the attention was also directed towards their thermal, mechanical and vibrational properties [167]. The difference in nanostructure properties from those in bulk is caused by ultrathin nanowire diameters, which results in the physical reorganization of the atoms at lateral NW surface. For a high surface-to-volume ratio, the effects of the surface states are significant [164], effectively reducing the band gap, which has consequences in the optical absorption and electronic transport. Moreover, the AlN NWs experience a size-dependent phase transition WZ $\leftrightarrow$ GL as described above [163].

It is expected that thermal properties of nanowires are dramatically influenced whenever they are switched between different structural (phase) configurations [167]. Such transitions may occur due to the tensional or compressional stress caused by either thermal or mechanical perturbations, leading to the overall alteration of the whole system functionality. Therefore, further understanding in predicting the stress-induced phase transitions and revealing the consequences in thermal transport is needed. Such a characterization demands the analysis of the phonon spectrum $\hbar\omega(\mathbf{k})$. The corresponding ab initio approaches were firstly focused on Si nanowires (Sect. 5.3) concerning an atomistic approximation to thermoelectric properties [171] or a characterization of the Raman-active radial breathing mode [172]. The vibrational properties of CdSe nanowires were simulated when considering the WZ phase [173]. Experimental studies of local structural transitions and the phonon dynamics are generally pursued by means of Raman spectroscopy. The obtained results confirmed a size-dependent behavior of the phonon frequencies observed for GaAs NWs, especially for those associated with the surface modes [174]. Moreover, under the hydrostatic pressure, a transition from wurtzite to rock-salt phase was established for AlN nanowires [175].

After geometry optimization of AlN NW, the corresponding force constant matrix can be determined. To achieve the accurate results beyond Γ point phonons described by energy $\hbar\omega(k_z)$, a new supercell was assembled by joining three unit cells along the nanowire axis and further determination of the forces acting on each atom [167]. By displacing the atoms in the middle unit cell, the variations of forces (i.e., elements of the force constant matrix) around the equilibrium point were computed using the SIESTA package [176], which allows one to estimate the thermal conductance and specific heat. In the limit of low temperatures, assuming the nanowire length to be smaller than the phonon mean free path, one can neglect the mechanism of phonon scattering and employ Landauer's formalism adapted to thermal conduction in order to obtain the thermal conductance [177, 178]:

$$\kappa = \frac{\hbar}{2\pi k_B \mathrm{T}} \int_0^\infty \frac{e^{\hbar\omega/k_B\mathrm{T}}}{(e^{\hbar\omega/k_B\mathrm{T}} - 1)^2} \omega^2 \Theta(\omega) d\omega, \tag{6.9}$$

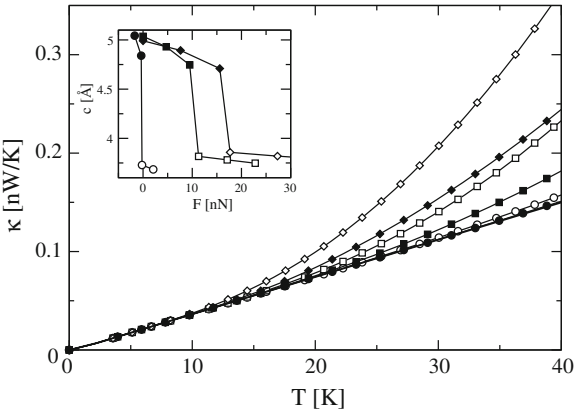

Fig. 6.59 Thermal conductance for AlN NWs under axial stress, for both WZ (*filled symbols*) and GL (*empty symbols*) phases and for different radii: $R1$ (*circles*), $R2$ (*squares*) and $R3$ (*diamonds*) as shown in Fig. 6.56. The *thick solid line* represents an ideal four-mode thermal conductance. The inset contains the variation of the lattice constant c with applied stress, indicating the transition points (Reprinted figure with permission from Mitran et al. [167], Copyright (2011) by the Elsevier B.V. All rights reserved)

where T is the temperature of the nanowire, k_B Boltzmann constant and ω phonon frequency, while $\Theta(\omega)$ represents the ballistic transmission function, which equals to the number of phonon modes at a given energy, in the case of the perfect NW structure, analogously to (5.5).

Figure 6.59 shows the thermal conductance of AlN NW at a low temperature. These data correspond to the applied pressures closest to the transition points (as shown in inset). For temperatures below $T_{ac} = 9\,K$ (when only the four acoustic modes have the major contribution to the thermal conductance), all the nanosystems converge towards the unique, almost linear dependence. Therefore, thermal conductance can be practically the same for both phases only below T_{ac}, a fact that may receive consideration in the design of the future electronic devices [167]. A value of T_{ac} is consistent with the frequency $\omega_{ac} \approx 200\,cm^{-1}$, for which the four acoustic modes are primarily occupied for both WZ and GL phases. With the temperature growth, the optical modes contribute to a thermal conductance and the behavior becomes differentiated: (i) the nanowires in the GL phase, which correspond to a higher applied pressure, have systematically higher conductance than their WZ counterparts, since the density of phonon modes is higher for the GL phase of the [0001]-oriented AlN NW (Fig. 6.60); (ii) the deviations from the declined straight line become larger with the NW size increase. Moreover, as the pressure is further enhanced beyond the transition point, the thermal conductance increases at a slower rate. Taking the $R2$ and $R3$ structures (Fig. 6.56) and applying 22.6 nN, the force necessary for reaching the GL phase is doubled, while the thermal conductance at 40 K increases to less than 3 %. Obviously, at higher temperatures, the scattering mechanism plays a more important role, as the phonon mean free path decreases

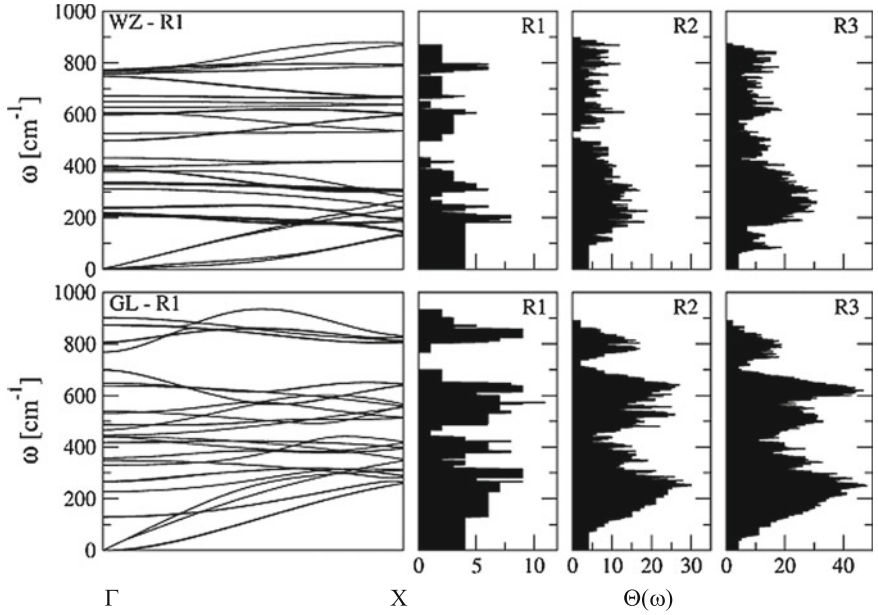

Fig. 6.60 The phonon band structure for $R1$-type AlN NW (Fig. 6.56) under stress applied for its WZ and GL phases. The phonon distributions of transmission function $\Theta(\omega)$, as defined in (6.9), are indicated for each nanowire structure [167]

[179], and the calculated curves overestimate the thermal conductance. The inset in Fig. 6.59 indicates the abrupt change in the lattice constant along the nanowire as pressure is applied, showing that the critical forces increase with the NW diameter. The quantifying behavior of the thermal conductance and heat capacity depending on NW sizes may be of crucial importance for the development of nanoscale low-temperature sensors [167]. Moreover, thermodynamical quantities that can be further derived may serve for modeling the synthesis process. In order to obtain the equilibrium configurations of AlN NWs considered in Fig. 6.56, their structures were completely relaxed [167]. This simulation step was crucial for obtaining reliable phonon dispersion curves (Fig. 6.60). The starting NW configurations were prepared in the WZ phase using bulk lattice parameters. Under no applied pressure, amongst the considered systems only the $R1$ type of nanowire changed its structure to the GL phase, which is consistent with the results obtained earlier [163], where it was argued that the GL formation energy at zero pressure is smaller. If a large enough pulling stress is applied ($\sim$0.37 nN) the $R1$ type nanowire retains the WZ structure. The NWs of larger diameter favor the morphology of WZ phase in their native, free-standing configurations. As a large enough compressive stress is applied to all nanowires, their configuration is switched to the unbuckled GL phase and the transition points are sensitive to the NW diameter. The calculated phonon spectrum of AlN NW in the direction X is presented in Fig. 6.60 for the $R1$ structure [167]. The two applied pressures ($F_{\mathrm{WZ}} = 0.37$ nN and $F_{\mathrm{GL}} = 0.21$ nN) correspond to the two phases with

different lattice constants of AlN NWs, namely, c_{GL} (3.72 Å) is considerably shorter than c_{WZ} (4.83 Å). The phonon spectrum of the aluminum nitride nanowire in the GL phase is shifted towards higher frequencies, which is the consequence of the packing, as compared to that of WZ phase. The acoustic modes were found to be essential in the description of the low temperature conductance. Altogether, there are four acoustic modes in phonon spectra of wurtzite-type nanowires: a dilatational mode, a torsional mode and two flexural modes [180]. The first two modes present a linear dispersion around the Γ point of the irreducible Brillouin zone, while the other two indicate a quadratic behavior. The maximum frequencies of the flexural modes were found to be $\omega_{WZ} = 142\,\mathrm{cm}^{-1}$ and $\omega_{GL} = 264\,\mathrm{cm}^{-1}$, which correspond to the X point in the IBZ, and are noticeably higher in the GL phase. Due to the different sizes of the IBZ in the $\Gamma \rightarrow X$ direction, resulting from the different lattice constants c_{WZ} and c_{GL}, one may conclude that there are larger average phonon group velocities of the flexural modes in the GL phase. A similar situation was observed for dilatational and rotational modes in the vicinity of the Γ point [167].

The transmission functions $\Theta(\omega)$ are also presented in Fig. 6.60 for all the considered nanowires. The GL phase introduces an overall larger phonon mode density. In particular, in the GL phase of the nanowire, there are optical modes with a lower energy as compared to the WZ case that enhance the transmission. For the $R1$ NW type, the minimum frequencies lie at $130\,\mathrm{cm}^{-1}$ and $180\,\mathrm{cm}^{-1}$ for the GL and WZ NWs, respectively, corresponding to the maximum frequencies for which $\Theta = 4$. The minimum frequency of the lowest optical modes decreases with the increasing AlN NW diameter of both structural configurations [167].

6.6.3 Elastic Properties of AlN Nanowires

Both types of hexagonal AlN NWs can be classified according to the number of circular layers in the nanowire consisting of both Al and N atoms (n_l) separated by the shortest distance d_{Al-N} (Fig. 6.61). Obviously, hexagonal nanowire consisting of n_l layers contains $N_n = 12n_l^2$ atoms *per* NW unit cell, while the number of atoms in the surface layer $N_{sn} = 12(2n_l - 1)$. Thus, the NW surface weight (in terms of the number of atoms) can be expressed as:

$$w_{sn} = \frac{2n_l - 1}{n_l^2}. \tag{6.10}$$

To simulate the elastic properties of AlN NWs, the elastic distortion of the nanowire was applied only along the NW axis, which was chosen to be the $z(3)$ axis [166]. To describe the energy of nanowire *per* atom, the simple additive model was developed:

$$e^{(NW)} = (1 - w_{sn})e^{(b)} + w_{sn}e^{(s)}, \tag{6.11}$$

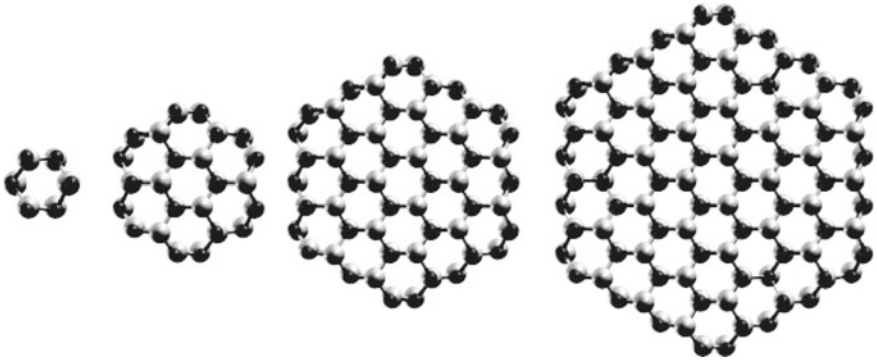

Fig. 6.61 Cross-sections of relaxed AlN nanowires with $n_l = 1, 2, 3$ and 4 (from *left* to *right*). Al and N atoms are shown as *gray* and *black*, respectively (Reprinted figure with permission from Mitrushchenkov et al. [166], Copyright (2010) by the IOP Publishing)

where w_{sn} is defined by (6.10), while $e^{(b)}$ and $e^{(s)}$ are the bulk and surface energies *per* atom of the same AlN phase as considered in the nanowire (as to the choice of the surfaces, it was determined by the facets terminating the nanowire) [166]. The energy contribution of bulk ($e^{(b)}$) was assumed to possess a uniform deformation in the xy plane ($\varepsilon_1 = \varepsilon_2$), while along the axis of periodicity (z), the elastic deformation of the nanowire was determined as ε_3. All shear deformations were set to zero. As the deformations were counted with respect to ideal bulk structure, there were no linear terms in bulk energy $e^{(b)}$ and only quadratic terms were present:

$$e^{(b)} = \frac{1}{2}\widetilde{C}_{11}^{(b)}\varepsilon_1^2 + \widetilde{C}_{13}^{(b)}\varepsilon_1\varepsilon_3 + \frac{1}{2}\widetilde{C}_{33}^{(b)}\varepsilon_3^2. \tag{6.12}$$

This expression was obtained from a classical definition of the elastic constants for ideal crystal with hexagonal structure ($C_{ij} = \frac{1}{V}\frac{\partial^2 E}{\partial\varepsilon_i \partial\varepsilon_j}$, where E is the calculated total energy *per* bulk unit cell, V its volume, which equals to $(a^2 c\sqrt{3})/2$, Fig. 6.55, while $i, j = 1, 2, \ldots, 6$), assuming that $\varepsilon_1 = \varepsilon_2$, which results in a certain transformation of the elastic constants: $\widetilde{C}_{11}^{(b)} = 2(C_{11}^{(b)} + C_{12}^{(b)})$, $\widetilde{C}_{13}^{(b)} = 2C_{13}^{(b)}$ and $\widetilde{C}_{33}^{(b)} = C_{33}^{(b)}$. With bulk cell parameters, the surface is not present in its relaxed state, therefore, the tension terms ($\tau_{ij} = \frac{1}{V}\frac{\partial E}{\partial\varepsilon_i}|_{\epsilon=0}$) should be also included in the expression of the surface energy, assuming that the surface is deformed when being relaxed [166]:

$$e^{(s)} = \frac{1}{2}\widetilde{C}_{11}^{(s)}\varepsilon_1^2 + \widetilde{C}_{13}^{(s)}\varepsilon_1\varepsilon_3 + \frac{1}{2}\widetilde{C}_{33}^{(s)}\varepsilon_3^2 + \tau_1^{(s)}\varepsilon_1 + \tau_3^{(s)}\varepsilon_3. \tag{6.13}$$

Within this simplified model, $x(1)$ deformations of volume and surface are the same. This is a quite natural assumption, especially for thick nanowires [166], as the surface must follow the deformation of the internal NW area. When applying the atomistic nanowire approximation, the surface can deform non-uniformly, especially close to the nanowire edges. Using the aforementioned additive model based

on (6.11–6.13), with bulk and surface parameters (deduced from the fitting of the slab calculations) and minimizing the energy e^{NW}, the nanowire elastic behavior and deformation were calculated as a function of the nanowire diameter [166]. The thickest nanowire calculated using the DFT-LCAO method corresponded to $n_l = 7$ and $d_{\mathrm{NW}} = 3.74\,\mathrm{nm}$. The cross section of such nanowire contains 588 Al and N atoms *per* unit cell. To simulate elastic properties for AlN NWs possessing larger diameters ($\geq$10 nm), which were experimentally synthesized earlier [86, 153–156], both continuum and finite-element models were developed [168]. The latter (FEM), characterized by discretization of the nanowire lateral surface, well reproduces the non-uniformity in distribution of deformations in the vicinity of the surface, which was obtained using the first principles calculations.

For atomistic nanowire models described above, which can be treated using first principles methods, the two significant parameters to be determined are the elastic constants and the change of the relaxed NW UC length (l_{NW}) as compared to the bulk value, although these two quantities do not describe the internal relaxation in the nanowire. To look at this more deeply, the internal structure of fully relaxed nanowires was investigated [166]. The angular relaxation was found practically negligible, as well as the along-the-wire relative relaxation. The main effect was observed for the radial relaxation, which seemed to be practically unchanged in the internal part of AlN nanowire, while the surface effects were present in the surface and subsurface layers. Figure 6.62 presents the relative radial relaxation in AlN NW for both Al and N atoms. The relaxation of the surface NW layer was found to be ~10 times larger than that in the internal NW area, thus, the surface atoms were forcedly omitted within the format of both plots, i.e., the surface effects presented in Fig. 6.62, actually correspond to the subsurface layer. According to Fig. 6.62, the internal area of AlN NW is homogeneously expanded in the same way for both types of atoms, so that it does behave

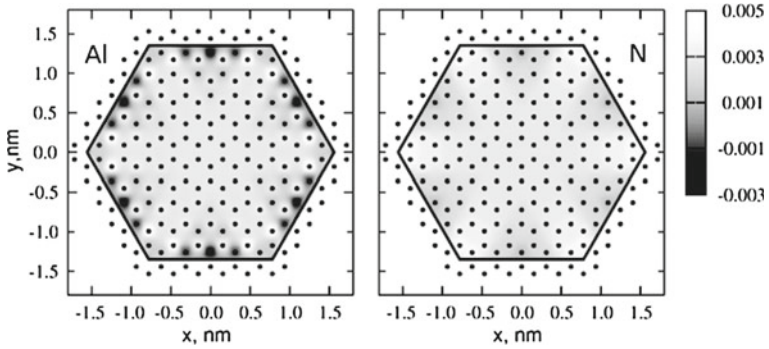

Fig. 6.62 Radial deformations in AlN NWs with the $n_l = 6$ using bulk value of c parameter (Fig. 6.55) for atoms of Al (*left panel*) and N (*right panel*). Coordinates are given in nanometers (for the center of NW, $x = y = 0$). *Thick lines* represent the ideal NW diameter $d(n_l) = 2(n_l - 1)a$ (which is expressed via a parameter of bulk) corresponding to the volume of the internal (excluding the surface) area of the nanowire. The ideal (*bulk*) positions of atoms are shown by *small filled circles* (Reprinted figure with permission from Mitrushchenkov et al. [166], Copyright (2010) by the IOP Publishing)

as an isotropic bulk crystal. The relaxation around the NW center can be taken as the macroscopic parameter which should be reproduced by the NW elastic model. Cross-sectional elastic deformations were defined as $\varepsilon_{rel}^{\mathrm{NW}} = \frac{r-r_0}{r_0}$, where r is the relaxed radial distance of a given atom from the NW axis, and r_0 the unrelaxed (bulk) value.

Similar simulations were performed also for AlN(0001) slab system containing the same number of layers between the two external surfaces as in the case of AlN nanowire (Fig. 6.62). Figure 6.63 presents the comparison of the internal relaxation parameters of the NW described by $n_l = 6$ and the corresponding slab ($n_l = 12$). For a correct comparison between these parameters, the along-the-nanowire cell parameter c was fixed to its bulk value, and all other parameters were fully relaxed. For the plotted slab data, the values of relative deformations along the in-plane $y(2)$ axis were chosen: $\varepsilon_{rel}^{slab} = \frac{y-y_0}{y_0}$. The same parameter was plotted for NW: in this case, y axis corresponds to the vertical direction in Fig. 6.62. As a result, the following conclusions were drawn [166]:

(i) while the nanowire is uniformly expanded under the free relaxation, the slab system is mostly compressed by the similar amount;
(ii) surface effects are negligible for nanowires below two external layers, while for slab systems, long-range anisotropic effects exist far away from the surface, thus, the internal area of the slab does not behave like homogeneous isotropic media, but rather has deformations alternating between the adjacent atomic layers;
(iii) the surface is slightly less flat in nanowires as compared to a slab system of the same width.

On the whole, the anisotropy of slab elasticity could be easily understood as a consequence of the surface anisotropy. However, six differently oriented facets of

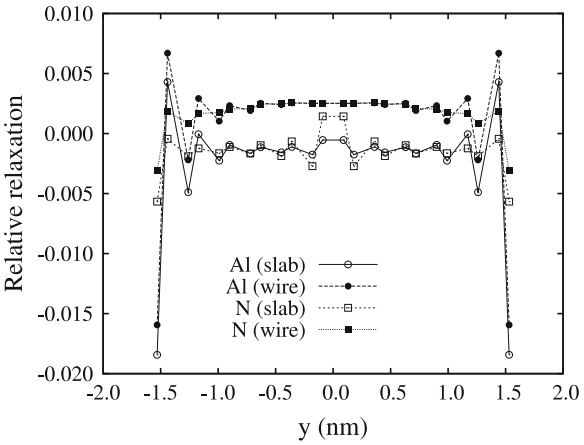

Fig. 6.63 Plots of functions $\varepsilon_{rel}(y)$ for AlN NW ($n_l = 6$) and the corresponding AlN(0001) slab ($n_l = 12$). Inset presents the labels of *elastic curves* for Al and N atoms forming nanowire and slab (Reprinted figure with permission from Mitrushchenkov et al. [166], Copyright (2010) by the IOP Publishing)

AlN NW substantially reduce their anisotropy, especially in the internal NW area leading to its isotropic behavior. Thus, one could expect that the surface parameters obtained from the slab calculations need to be somehow adjusted to the properly described nanowires [166]. This was a possible way to avoid difficulties with the definition of the nanowire diameter and UC volume when performing first principles calculations: to slightly adjust the surface parameters obtained from the slab calculations, in order to accurately reproduce elastic behavior of the calculated nanowires. For example, using bulk parameters and adjusted surface parameters of AlN, one could minimize the energies $e^{(\mathrm{NW})}$, $e^{(b)}$ and $e^{(s)}$ relatively to elastic deformations ε_1 and ε_3, as defined by (6.11)–(6.13). (In practice, the C_{33} and τ_3 constants are quite different for the bulk and surface, therefore they need adjustment, the same as τ_1, which is quite sensitive to the surface structure; however, C_{11} could be fixed as for bulk). Dependence on the NW surface weight w_{sn} defined by (6.10) could provide simple analytic expressions for $\varepsilon_r^{rel}(w)$, $\varepsilon_3^{rel}(w)$, and $C_{33}^{rel}(w)$ based on the results of ab initio calculations [166] as shown in Fig. 6.64.

Obviously, the approaches with initial slab parameters could reproduce the Young's modulus (correlated with C_{33}^{rel} value since for neglecting the along-wire strain, $C_{33}^{rel} = C_{33}^{(b)}|_{\epsilon_3=0}$ [166]) and the radial xy deformation (ε_r^{rel}), but this is not true for the along-wire z relaxation (ε_3^{rel}), which is indeed a sensible parameter. However, the adjusted surface parameters corresponding to the model can well reproduce the calculated ab initio values. The largest deviations from the simple approach correspond to the point $n_l = 3$, because the nanowire in that case is, certainly, too thin, and equals $n_l = 7$, most likely because of the lower accuracy of ab initio calculations on polyatomic systems of larger sizes [166]. The coefficients adjusted within the atomistic model can be transformed into standard *per*-volume (in GPa) and *per*-surface (in Nm^{-1}) parameters which are used in the FEM model mentioned above [168]. Obviously, this approach can be applied to nanowires of a larger diameter where ab initio calculations are no longer possible. Also, it opens up prospects for future simulations, e.g., application of this approach to a variety of other NW types, including non-hexagonal ones.

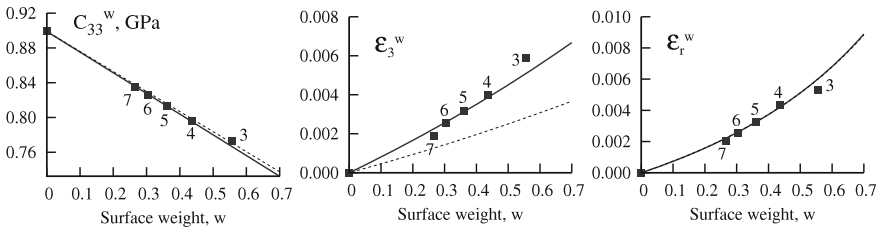

Fig. 6.64 The results obtained for atomistic first principles simulations on elastic parameters plotted as functions of surface weight. Ab initio results for nanowires are marked with square dots and numbers corresponding to the value of n_l. The bulk system corresponds to $w_{sn} = 0$. *Dashed* and *solid lines* correspond to the initial and adjusted surface parameters, respectively (Reprinted figure with permission from Mitrushchenkov et al. [166], Copyright (2010) by the IOP Publishing)

6.6.4 Prismatic GaN Nanowires and Their Elasticity

Due to the proximity among a considerable number of properties for AlN and GaN bulk, low-index densely-packed surfaces and buckled honeycomb-type nanotubes (except for a large difference between their band gaps: 6.2 vs. 3.5 eV in bulk, respectively [104]), most nanowire properties for both nitride compounds have to be qualitatively similar. This is why the current Subsection is devoted to the discussion of mainly those results that were not presented in the previous Subsections, e.g., atom-centered GaN NWs possessing triangular-type shaped cross-sections [181, 182] (for AlN, mainly hollow-centered hexagonal shaped NW models have been considered so far); (ii) H-terminated GaN nanowires and the comparison of their properties with those of clean GaN NWs (hydrogenation of their lateral facets was found to be energetically advantageous, due to a higher reactivity of dangling bonds [182, 183]); (iii) a simplified approach to estimate the NW elasticity [181]. Routine description of the calculated geometry and electronic structure, analogous to that reported for AlN NWs [135, 157, 164], was given for GaN NWs as well [169, 182, 184]. Moreover, ab initio simulations were performed for several types of defective GaN NWs containing either point vacancies [185, 186] or dopants substituted native atoms [187, 188], the electronic and magnetic properties of which could be regulated when changing the point defect concentration. For simulations of GaN nanowires, infinite (1D) models were mainly applied (e.g., periodic nanorod [169]), and for their calculations, the following methods were used: DFT-LCAO [181–184, 186], DFT-PW [169, 185, 187, 188] and MD [169]. In the experimental studies of GaN NW synthesis, mainly wurtzite morphology of nanowires was observed [189–191], although they were also reported in the zinc blende structure as obtained in conditions of synthesis at elevated temperatures in the presence of free Ga^+ ions [192]. The diameters of synthesized nanowires typically ranged from 5 to 100 nm [193, 194]. A few different GaN NW growth directions were also reported, e.g., [0001] [189, 191], $\{10\bar{1}0\}$ [195, 196] and $\{11\bar{2}0\}$ [191, 196]. The majority of synthesized GaN nanowires, especially [0001]-oriented, typically formed hexagonal shapes of cross-sections [197], although in nanowires with $\{11\bar{2}0\}$ direction of the NW axis, triangularly shaped forms were observed as well [198]. In some experiments, the growth of GaN NWs was accompanied by the presence of hydrogen species, which saturated their lateral facets, thus, making nanowires energetically more stable [183, 199]. GaN NWs with internal *p–n* junctions were fabricated through incorporation of Mg dopants [200], while Mn-doped GaN NWs displayed a ferromagnetic behavior already at room temperature [201].

In a comprehensive first-principles study of the atomic and electronic structures of various gallium nitride nanowires (Fig. 6.65), their dependence on the NW shape and diameter as well as the influence of facet hydrogenation were examined [182]. All nanowires imaged in Fig. 6.65 possess a family of lateral $\{10\bar{1}0\}$ facets, the surface energy of which is lower as compared to the $\{11\bar{2}0\}$ surface (118 vs. 123 meV/Å^2, respectively) [151], i.e., $\{10\bar{1}0\}$ NW faceting is energetically more preferable, similar to the same hierarchy observed for AlN NW facets as considered in Sect. 6.5.1 (Fig. 6.53). Triangular- and hexagonal-shaped GaN NWs imaged in Fig. 6.65 can be

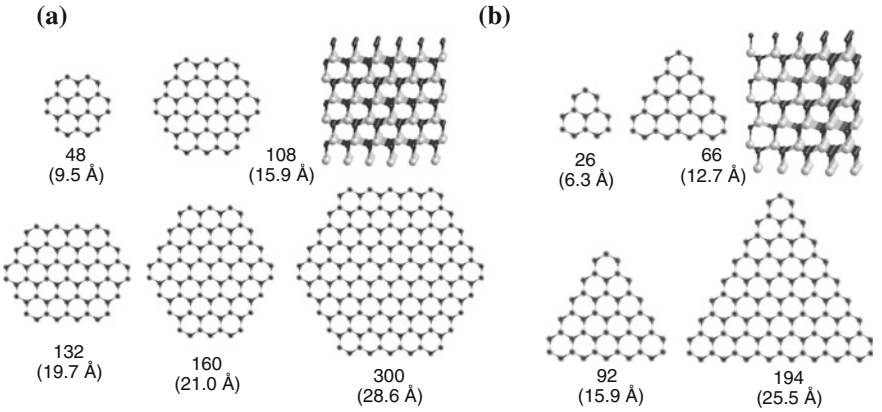

Fig. 6.65 Cross-sections and aside views of [0001]-oriented GaN NWs of different sizes and shapes (A is hexagonal and B triangular ones). The number of atoms per UC and diameters (in parentheses) are labeled for each model. N and Ga atoms are indicated as *dark* and *light balls*, respectively [182]

described by different rod groups: $P3m1$ and $P6_3mc$, respectively (except the two nanowires containing 132 and 160 atoms per UC, the cross-sections of which form distorted hexagons with either elongated or shrank contours regarding the x axis directed across NW).

Analogically to AlN NWs, Ga-N bonds were found essentially compressed at unsaturated aside nanowire facets (6.0–7.0 %) as compared to those in GaN bulk (2.01 Å) [169, 182, 183, 187] and at the center of GaN nanowires (which were contracted only by ~0.6 %). The GaN $\{10\bar{1}0\}$ slab was also reported to possess values of $d_{\mathrm{Ga-N}}$ decreased by ~6 % as compared to bulk [151]. With the increasing d_{NW}, the averaged value of $d_{\mathrm{Ga-N}}$ also increased (as can be expected) slowly approaching the bond length in bulk [182].

The saturation of dangling bonds of GaN nanowires with hydrogen resulted in the appearance of Ga-H and N-H quasi-bonds upon the NW facets [183]. (Sect. 5.2.2 contains, for comparison, across and aside images showing the hydrogen atom distribution upon faceted Si NTs.) For a single H atom, the calculated energies of bonding with nanowires were found to be 2.99 eV for the N-H bond ($d_{\mathrm{N-H}} \approx 1.04$ Å) and 1.63 eV for the Ga-H bond ($d_{\mathrm{Ga-H}} \approx 1.04$ Å). This was in a good agreement with the corresponding values obtained earlier for a hydrogenated GaN surface [202]. When comparing $d_{\mathrm{Ga-H}}$ calculated for both H-saturated and unsaturated nanowires, these bond lengths changed qualitatively in a similar way, although $d_{\mathrm{Ga-H}}$ values of the former were found to be substantially smaller [182]. For example, in a H-passivated GaN nanowire, the contraction of Ga-N bonds parallel to its [0001] axis achieved 1.0–1.7 % at the NW edge and less than 0.2 % at the NW center. Figure 6.66 presents the band structures for unsaturated GaN nanowires of diameters selected as either "small" or "large" and possessing either hexagonal or triangular shapes (although qualitatively similar results were obtained for all the other NW models shown in Fig. 6.65), which were calculated using the DFT-LCAO method [182]. It is evident

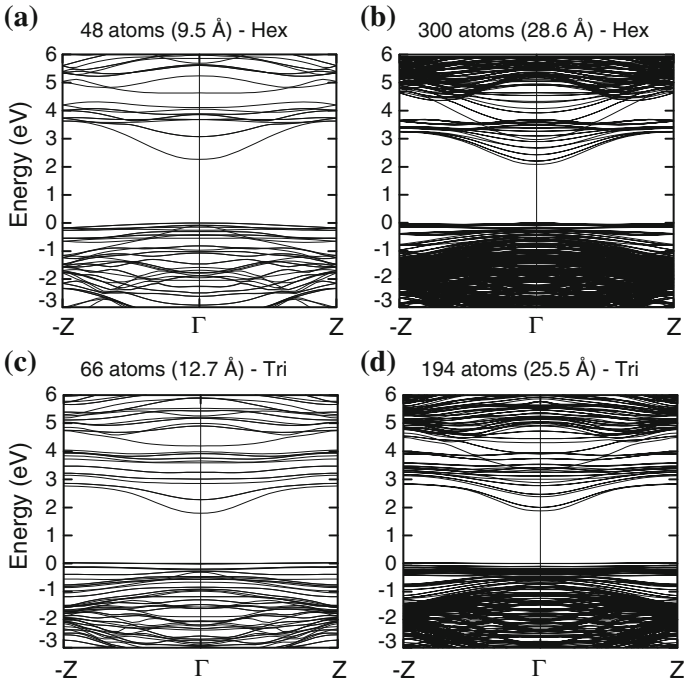

Fig. 6.66 The band structures for unsaturated GaN NWs of different diameters and shapes. The energy zero is set at the highest occupied level (VBM). "Hex" and "Tri" represent *hexagonal* and *triangular* shapes of nanowires, respectively [182]

that the corresponding NW dangling bonds produce the edge-induced states (bands) in the band gaps located above the valence band maximum (VBM) and below the conduction band minimum (CBM). The band gap of unsaturated GaN nanowires, i.e., the gap between both edge-induced states, is not changed significantly with the growth of the nanowire diameter since they are quite well localized. The analysis of the calculated total and projected DOSs for GaN nanowires of different diameters and shapes [182] clearly showed that Ga($3p$) orbitals predominantly contribute to the edge states that appear near and below the CBM while N($2p$) orbitals contribute to the edge states appearing at and above the VBM in the band structure plots as shown in Fig. 6.66.

Figure 6.67 presents the band structures for H-saturated GaN nanowires possessing the same diameters and shapes as considered in Fig. 6.66. When NWs were saturated with hydrogen atoms, the dangling bonds disappeared, i.e., the bands attributed to them were found to be from the nanowire band gap, thus, $\Delta\epsilon_{gap}^{satur} > \Delta\epsilon_{gap}^{unsatur}$. It means that the hydrogen atoms have a stabilizing effect on the bonding molecular orbitals pushing the anti-bonding molecular orbitals up. Such a behavior is typical for both the small and large nanowires of both hexagonal and triangular shapes [182].

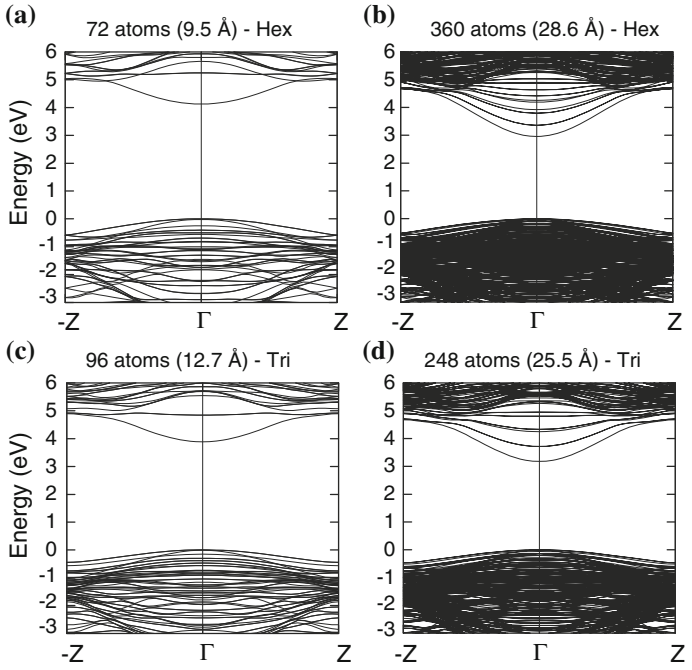

Fig. 6.67 The band structures for H-saturated GaN NWs of different diameters and shapes. Other details of presented plots are described in caption of Fig. 6.66 [182]

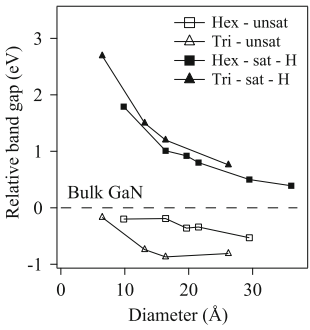

Fig. 6.68 Relative band gap as a function of nanowire diameter as calculated using the DFT-LCAO method. Values of $\Delta\epsilon_{gap}$ are relative to the calculated bulk GaN band gap [182]

Moreover, the band gap of H-saturated GaN nanowires noticeably decreased with the increasing d_{NW}, unlike unsaturated NWs (Fig. 6.66).

The calculated band gaps as a function of the NW diameter, i.e., $\Delta\epsilon_{gap}(d_{\mathrm{NW}})$, for hexagonal and triangular nanowires are shown in Fig. 6.68 [182]. For H-saturated nanowires, the essential decrease of $\Delta\epsilon_{gap}$ with the growing diameter eventually approaches the bulk band gap values. For unsaturated nanowires, a little change in the band gaps with the increasing diameter was found, illustrating the influence of the

localized edge-like dangling bond states in the band gap, as mentioned previously. For the unsaturated NWs, the band gaps of triangular nanowires were noticeably smaller than of hexagonal nanowires; however, for H-saturated NWs, this trend was reversed, although the difference was found to be much smaller [182]. For the given effective value of d_{NW}, the triangular and hexagonal nanowire calculations contained slightly different numbers of GaN units, so when examining the band gap as a function of the number of atoms, the band gaps of H-saturated hexagonal- and triangular-shaped NWs look similar (Fig. 6.68). However, for the unsaturated nanowires the trend remains, with the band gap being consistently smaller for the triangular NWs, which could be explained by both a smaller stability of triangular NWs and a higher energy of the occupied edge-induced states, as compared to the hexagonal nanowires [182]. The energetic stability of nanowires possessing different diameters and shapes is directly correlated with their formation energy E_{form}: the smaller is d_{NW}, the higher the energy. To estimate E_{form} *per* atom for unsaturated GaN NWs, (6.8) could be slightly modified since that energy for AlN NW was defined *per* Al-N bond [164], while for a H-saturated nanowire, the definition of the formation energy should contain the member describing the hydrogen atom [182]:

$$E_{form}(d_{\mathrm{NW}}) = [E_{tot}(n_{\mathrm{GaN}}) - n_{\mathrm{GaN}}\mu_{\mathrm{Ga}} - 0.5n_{\mathrm{GaN}}\mu_{\mathrm{N}}]/2n_{\mathrm{GaN}}, \tag{6.14}$$

$$E_{form}(d_{\mathrm{NW}}) = [E_{tot}(n_{\mathrm{GaN}}, n_{\mathrm{H}}) - n_{\mathrm{GaN}}\mu_{\mathrm{Ga}} - 0.5n_{\mathrm{GaN}}\mu_{\mathrm{N}} - n_{\mathrm{H}}\mu_{\mathrm{H}}]/(n_{\mathrm{GaN}} + n_{\mathrm{H}}), \tag{6.15}$$

where n_{GaN} and n_{H} are the numbers of GaN pairs and H atoms *per* NW unit cell, E_{tot} the calculated total energy of the saturated GaN nanowire, μ_{Ga}, μ_{N} and μ_{H} the chemical potentials of Ga, N and H obtained from energies of the Ga atom in the face-centered cubic metal and isolated N_2 and H_2 molecules, respectively.

The formation energies per atom for unsaturated and saturated nanowires as functions of the nanowire diameter, according to definitions given in (6.14) and (6.15), are presented in Fig. 6.69. The corresponding energy curves show the increasing NW stability with the growth of d_{NW} approaching the stability found in bulk GaN [182]. Obviously, the hexagonal nanowires are slightly more stable than triangular nanowires of the same size, although when all dangling bonds were saturated, the

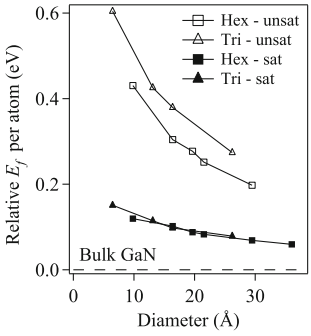

Fig. 6.69 Relative formation energy *per* atom as a function of d_{NW} for [0001]-oriented unsaturated and H-saturated GaN NWs. Energies are relative to the heat of formation *per* atom of GaN bulk. Other details of the presented plots are described in the caption of Fig. 6.66 [182]

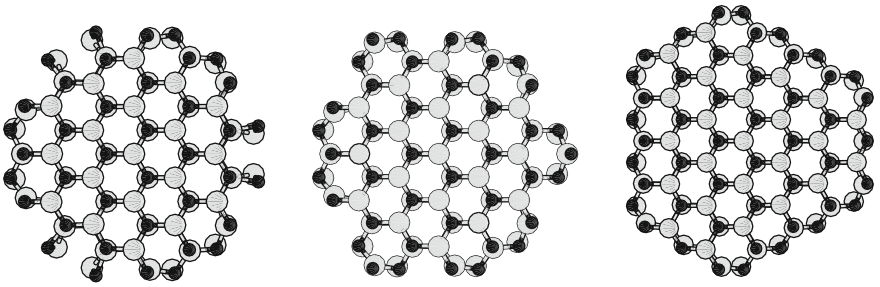

Fig. 6.70 Cross-sections of GaN nanowires considered for study of their elastic properties. The growth direction is normal to the plane of NW images. A number behind the W gives the number of atoms in NW unit cell (Reprinted figure with permission from Gulans and Tale [181], Copyright (2007) by the WILEY-VCH Verlag GmbH & Co. KGaA, Weinheim)

local bonding environment appears to be very similar to both the hexagonal- and triangular-shaped NWs with a slight priority for the former. This could be explained by the fact that for the same number of atoms, the triangular nanowires have a slightly greater circumference number of dangling bonds compared to the corresponding hexagonal nanowires. Thus, the former always experience a slightly smaller degree of "real" GaN environment as compared to the latter.

Three alternative models of atom-centered [0001]-oriented GaN nanowires with quasi-hexagonal shapes were considered (Fig. 6.70), all described by $P3m1$ rod group and containing different number of atoms per NW unit cells [181]. The first two models were terminated by alternating $\{10\bar{1}0\}$ and $\{11\bar{2}0\}$ lateral facets, while W146 NW contained only non-polar facets. W116 NW corresponds to the roundest shape amongst all three models.

The surface energies of these nanowires per formula unit were calculated using the DFT-LCAO method [181]. The high value of surface energy for W116 (0.91 eV) is not surprising due to the presence of the external atoms with two dangling bonds so that the overall number of dangling bonds is very high. In contrast, W146 had the smallest energy (0.58 eV) being energetically most preferable. The average surface energy *per* dangling bond turned out to be similar in all cases. The differences could be explained by the peculiarities of the environments for surface atoms. Since most of the surface atoms in these nanowires possess similar neighborhoods as compared to $\{10\bar{1}0\}$ and $\{11\bar{2}0\}$ slabs, some qualitative similarities were observed also between the calculated properties and electronic structures of the faceted NWs and slabs [181]. Therefore, slabs of 10 atomic layers were constructed, which was found to be enough to ensure the convergence of the surface energy and atomic relaxations with the corresponding nanowires, in order to perform slab studies instead of time- and space-consuming NW calculations that decrease computational expenses significantly. Taking into account the difference between elastic properties of the surface and core round atomic layers in nanowires, as considered in previous Subsection, a simple model for nanowire elasticity was proposed [181]. For this aim, the total energy of a nanowire per unit

cell was expressed as the sum of bulk and surface contributions:

$$E_{tot} = E_{bulk} + E_{surf} = n_b E_b + \sum_i n_{si} E_{si}, \tag{6.16}$$

where E_{bulk} is expressed using the total energy E_b of bulk crystal *per* formula unit and the number n_b of formula units in the considered unit cell. The remaining part of the total energy is the surface energy E_{surf} expressed as the sum of E_{si} contributions from n_{si} atoms belonging to different surface types (i), for example, $\{10\bar{1}0\}$ and $\{11\bar{2}0\}$. For the quantitative estimate of w-GaN elastic parameters, the energies E_b and E_{si}, were approximated by the second order polynomial expression [181]:

$$E_k(a, c) = \alpha_k(a - a_{0k})^2 + \beta_k(c - c_{0k})^2 + \gamma_k(a - a_{0k})(c - c_{0k}), \tag{6.17}$$

where k is either b or si, α_k, β_k, γ_k are elastic tensor elements, while a_{0k} and c_{0k} equilibrium lattice constants in bulk, which were determined either from bulk or surface calculations. Knowing the explicit expression for the terms in (6.16), Young's modulus for a nanowire could be estimated by a double differentiation of the total energy E_{tot} [181]:

$$E_Y = \frac{c_0}{S_0} \frac{d^2 E_{tot}}{dc^2}, \tag{6.18}$$

where S_0 is the cross section area and c_0 is the equilibrium value of NW unit cell length.

The dependence of Young's modulus versus d_{NW} calculated for hollow-centered hexagonal shaped nanowires with facets of equal sizes (Fig. 6.61) is shown in Fig. 6.71. To determine the second derivative of the total energy and to obtain

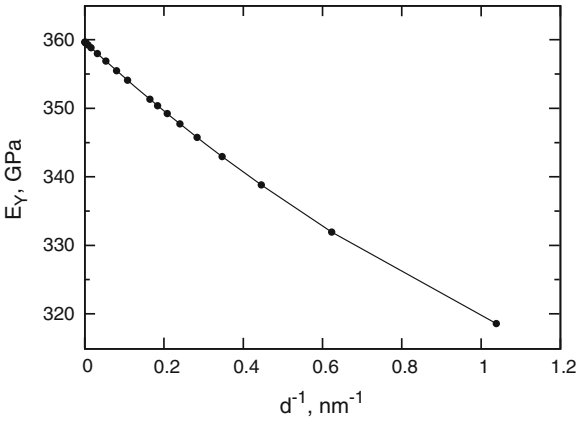

Fig. 6.71 Size dependence of the Young's modulus E_Y in *hexagonally-shaped* GaN nanowires (Reprinted figure with permission from Gulans and Tale [181], Copyright (2007) by the WILEY-VCH Verlag GmbH & Co. KGaA, Weinheim)

the Young's modulus according to (6.18), a set of constants obtained for each surface and bulk were calculated by varying GaN lattice constants and performing quadratic fit [181]. The constants obtained for bulk corresponded to the elastic moduli $C_{11} + C_{12} = 492$, $C_{33} = 403$, and $C_{13} = 103$ GPa, which were in a reasonable agreement with the experimental values based on the averages of consistent measurements ($C_{11} + C_{12} = 516$, $C_{33} = 389$, and $C_{13} = 98$ GPa [203]). The results of the performed calculations on elastic properties of GaN nanowires qualitatively reproduced bulk limit of the Young's modulus and confirmed the NW softening with the decrease of d_{NW} observed elsewhere [204]. So far, gallium nitride nanowires have covered a wider spectrum of technological applications as compared to AlN NWs, being one of the most promising building blocks in nanotechnologies related to UV-blue LEDs, detectors, lasers, high temperature and/or high power devices, as well as to potential spintronic devices [190, 205].

References

1. R. Haubner, M. Wilhelm, R. Weissenbacher, B. Lux, *High Performance Non-oxide Ceramics II, Series, Structure and Bonding*, vol. 102 (Springer, Berlin, Heidelberg, New York, 2002), pp. 1–45
2. P.B. Mirkarimi, K.F. McCarty, D.L. Medlin, Mater. Sci. Eng. R **21**, 47 (1997)
3. R.A. Evarestov, Yu.F. Zhukovskii, A.V. Bandura, S. Piskunov, J. Phys. Chem. C **114**, 21061 (2010)
4. T.E. Mosuang, J.E. Lowther, J. Phys. Chem. Solids **63**, 363 (2002)
5. K. Watanabe, T. Taniguchi, H. Kanda, Nat. Mater. **3**, 404 (2004)
6. J. Furthmüller, J. Hafner, G. Kresse, Phys. Rev. B **50**, 15606 (1994)
7. A. Lichanot, P. Azavant, U. Pietsch, Acta Crystallogr. B **52**, 586 (1996)
8. X. Blasé, A. Rubio, S.G. Louie, M.L. Cohen, Europhys. Lett. **28**, 335 (1994)
9. N.G. Chopra, R.J. Luyken, K. Cherrey, V.H. Crespi, M.L. Cohen, S.G. Louie, A. Zettl, Science **269**, 966 (1995)
10. D. Golberg, Y. Bando, M. Eremets, K. Takemura, K. Kurashima, H. Yusa, Appl. Phys. Lett. **69**, 2045 (1996)
11. A. Loiseau, F. Willaime, N. Demoncy, G. Hug, H. Pascard, Phys. Rev. Lett. **76**, 4737 (1996)
12. E. Bengu, L.D. Marks, Phys. Rev. Lett. **86**, 2385 (2001)
13. R. Czerw, S. Webster, D.L. Carroll, S.M.C. Vieira, P.R. Birkett, C.A. Rego, S. Roth, Appl. Phys. Lett. **83**, 1617 (2003)
14. D. Golberg, M. Mitome, Y. Bando, C.C. Tang, C.Y. Zhi, Appl. Phys. A **88**, 347 (2007)
15. V.L. Kuznetsov, I.N. Mazov, A.I. Delidovich, E.D. Obraztsova, A. Loiseau, Phys. Status Solidi (B) **244**, 4165 (2007)
16. E. Perim, D.S. Galvão, Nanotechnology **20**, 335702 (2009)
17. S. Guerini, V. Lemos, P. Piquini, Nanotechnology **17**, 556 (2006)
18. X. Blasé, A. De Vita, J.C. Charlier, R. Car, Phys. Rev. Lett. **80**, 1666 (1998)
19. P.W. Fowler, K.M. Rogers, G. Seifert, M. Terrones, H. Terrones, Chem. Phys. Lett. **299**, 359 (1999)
20. T. Dumitrică, H.F. Bettinger, G.E. Scuseria, B.I. Yakobson, Phys. Rev. B **68**, 085412 (2003)
21. Y.H. Kim, K.J. Chang, S.G. Louie, Phys. Rev. B **63**, 205408 (2001)
22. S. Okada, S. Saito, A. Oshiyama, Phys. Rev. B **65**, 165410 (2002)
23. D. Sánchez-Portal, E. Hernández, Phys. Rev. B **66**, 235415 (2002)
24. V.N. Popov, Phys. Rev. B **67**, 085408 (2003)

25. L. Wirtz, A. Rubio, R. Arenal, A. Loiseau, Phys. Rev. B **68**, 045425 (2003)
26. H.J. Xiang, J. Yang, J.G. Hou, Q. Zhu, Phys. Rev. B **68**, 035427 (2003)
27. W.H. Moon, H. Hwang, Physica E **23**, 26 (2004)
28. S.H. Jhi, D.J. Roundy, S.G. Louie, M.L. Cohen, Solid State Commun. **134**, 397 (2005)
29. L. Wirtz, M. Lazzeri, F. Mauri, A. Rubio, Phys. Rev. B **71**, 241402 (2005)
30. F. Zheng, G. Zhou, S. Hao, W. Duan, J. Chem. Phys. **123**, 124716 (2005)
31. H. Liu, G. Zhou, Q. Yan, J. Wu, B.L. Gu, W. Duan, D.L. Zhao, Phys. Rev. B **75**, 125410 (2007)
32. S. Guerini, V. Lemos, P. Piquini, S.S. Coutinho, Phys. Status Solidi (B) **244**, 110 (2007)
33. S. Hao, G. Zhou, W. Duan, J. Wu, B.-L. Gu, J. Am. Chem. Soc. **130**, 5257 (2008)
34. H. Pan, Y.P. Feng, J. Lin, Nanotechnology **19**, 095707 (2008)
35. Y.M. Chou, H.W. Wang, Y.J. Lin, W.H. Chen, B.C. Wang, Diam. Relat. Mater. **18**, 351 (2009)
36. P.N. Dyachkov, D.V. Makaev, J. Phys. Chem. Solids **70**, 180 (2009)
37. Y. Kinoshita, S. Hase, N. Ohno, Phys. Rev. B **80**, 125114 (2009)
38. S. Riikonen, A.S. Foster, A.V. Krasheninnikov, R.M. Nieminen, Phys. Rev. B **80**, 155429 (2009)
39. Yu.F. Zhukovskii, S. Piskunov, N. Pugno, B. Berzina, L. Trinkler, S. Bellucci, J. Phys. Chem. Solids **70**, 796 (2009)
40. Yu.F. Zhukovskii, S. Bellucci, S. Piskunov, L. Trinkler, B. Berzina, Eur. J. Phys. B **67**, 519 (2009)
41. R.K.F. Lee, B.J. Cox, J.M. Hill, Nanoscale **2**, 859 (2010)
42. R.A. Evarestov, Yu.F. Zhukovskii, A.V. Bandura, S. Piskunov, M.V. Losev, J. Phys. Chem. C **115**, 14067 (2011)
43. W.Q. Han, in *Mixed Metal Nanomaterals*, ed. by Ch. Kumar (Wiley-VCH, Weinheim, 2009), pp. 411–462
44. R. Arenal, X. Blasé, A. Loiseau, Adv. Phys. **59**, 101 (2010)
45. R.A. Jishi, M.S. Dresselhaus, G. Dresselhaus, Phys. Rev. B **47**, 16671 (1993)
46. R. Saito, G. Dresselhaus, M.S. Dresselhaus, *Phyical Properties of Carbon Nanotubes* (Imperial College Press, London, 1998)
47. O. Dubay, G. Kresse, Phys. Rev. B **67**, 035401 (2003)
48. D. Bogdan, R. Isai, A. Calborean, C. Morari, Physica E **44**, 1441 (2012)
49. J. von Neumann, E. Wigner, Physica Z **30**, 67 (1929)
50. P. Umari, A. Pasquarello, A. Dal Corso, Phys. Rev. B **63**, 094305 (2001)
51. O.E. Alon, Phys. Rev. B **64**, 153408 (2001)
52. F. Ding, K. Bolton, A. Rosén, J. Phys. Chem. B **108**, 17369 (2004)
53. Q.M. Zhang, J.C. Wells, X.G. Gong, Z. Zhang, Phys. Rev. B **69**, 205413 (2004)
54. J. Zhao, A. Martinez-Limia, P.B. Balbuena, Nanotechnology **16**, S575 (2005)
55. S. Reich, L. Li, J. Robertson, Phys. Rev. B **72**, 165423 (2005)
56. M. Cantoro, S. Hofmann, V. Scardaci, A. Parvez, S. Pisana, C. Ducati, A. Blackburn, A.C. Ferrari, J. Robertson, Nano Lett. **6**, 1107 (2006)
57. Y.A. Zhu, Y.C. Dai, D. Chen, W.K. Yuan, Surf. Sci. **601**, 1319 (2007)
58. N.I. Alekseev, N.A. Charykov, Russ. J. Phys. Chem. A **82**, 2191 (2008)
59. F. Ding, P. Larsson, J.A. Larsson, R. Ahuja, H. Duan, A. Rosén, K. Bolton, Nano Lett. **8**, 463 (2008)
60. O.V. Yazyev, A. Pasquarello, Phys. Rev. Lett. **100**, 156102 (2008)
61. H. Amara, J.M. Roussel, C. Bichara, J.P. Gaspard, F. Ducastelle, Phys. Rev. B **79**, 014109 (2009)
62. A. Börjesson, W. Zhu, H. Amara, C. Bichara, K. Bolton, Nano Lett. **9**, 1117 (2009)
63. Yu.F. Zhukovskii, S. Piskunov, E.A. Kotomin, S. Bellucci, Cent. Eur. J. Phys. **9**, 539 (2011)
64. N. Grobert, Mater. Today **10**, 28 (2007)
65. B.J. Wang, V.K. Kayastha, Y.K. Yap, Z. Fan, J.G. Lu, Z. Pan, I.N. Ivanov, A.A. Puretzky, D. Geohegan, Nano Lett. **5**, 2528 (2005)
66. M.J. López, A. Rubio, J.A. Alonso, L.C. Qin, S. Iijima, Phys. Rev. Lett. **86**, 3056 (2001)
67. M.H.F. Sluiter, Y. Kawazoe, Phys. Rev. B **69**, 224111 (2004)

68. A.B. Dalton, S. Collins, E. Muoz, J.M. Razal, V.H. Ebron, J.P. Ferraris, J.N. Coleman, B.G. Kim, R.H. Baughman, Nature **423**, 703 (2003)
69. D. Golberg, Y. Bando, Appl. Phys. Lett. **79**, 415 (2001)
70. C.W. Chen, M.H. Lee, S.J. Clark, Nanotechnology **15**, 1837 (2004)
71. A. Celik-Aktas, J.M. Zuo, J.F. Stubbins, C. Tang, Y. Bando, Acta Cryst. A **61**, 533 (2005)
72. J. Cumings, A. Zettl, Chem. Phys. Lett. **316**, 211 (2000)
73. R. Bacon, J. Appl. Phys. **31**, 283 (1960)
74. K.S. Novoselov, A.K. Geim, S.V. Morozov, D. Jiang, S.V. Dubonos, I.V. Grigorieva, A.A. Firsov, Science **306**, 666 (2004)
75. X. Chen, R.A. Boulos, J.F. Dobson, C.L. Raston, Nanoscale **5**, 498 (2013)
76. D.A. Dikin, S. Stankovich, E.J. Zimney, R.D. Piner, G.H.B. Dommett, G. Evmenenko, S.T. Nguyen, R.S. Ruoff, Nature **448**, 457 (2007)
77. E. Perim, R. Paupitz, D.S. Galvão, J. Appl. Phys. **113**, 054306 (2013)
78. S.F. Braga, V.R. Coluci, S.B. Legoas, R. Giro, D.S. Galvão, R.H. Baughman, Nano Lett. **4**, 881 (2004)
79. H. Shioyama, T. Akita, Carbon **41**, 179 (2003)
80. P.J.F. Harris, Crit. Rev. Solid State Mater. Sci. **30**, 235 (2005)
81. V.V. Ivanovskaya, A. Zobelli, G. Seifert, A.L. Ivanovskii, JETP Lett. **85**, 626 (2007)
82. L.T. Sun, J.L. Gong, Z.Y. Zhu, D.Z. Zhu, Z.X. Wang, W. Zhang, J.G. Hu, Q.T. Li, Diam. Relat. Mater. **14**, 749 (2005)
83. V.V. Pokropivny, A.L. Ivanovskii, Russ. Chem. Rev. **77**, 837 (2008)
84. S.L. Rumyantsev, M.E. Levinshtein, A.D. Jackson, S.N. Mohammmad, G.L. Harris, M.G. Spencer, M.S. Shur, in *Properties of Advanced Semiconductor Materials GaN, AlN, InN, BN, SiC, SiGe*, ed by M.E. Levinshtein, S.L. Rumyantsev, M.S. Shur (Wiley, New York, 2001), p. 6792
85. H. Zhang, J.D. Fitzgerald, L.T. Chadderton, J. Yu, Y. Chen, Phys. Rev. B **74**, 045407 (2006)
86. T. Sekiguchi, Q. Liu, T. Tanaka, J. Hu, Y. Zhu, Y. Bando, Eur. Phys. J. Appl. Phys. **27**, 107 (2004)
87. Y.J. Chen, H.Z. Zhang, Y. Chen, Nanotechnology **17**, 786 (2006)
88. J. Zhan, X. Haoa, S. Wen, M. Jiang, Physica E **25**, 409 (2005)
89. C.N.R. Rao, F.L. Deepak, G. Gundiah, A. Govindaraj, Progr. Solid State Chem. **31**, 5 (2003)
90. P. Widmayer, H.G. Boyen, P. Ziemann et al., Phys. Rev. B **59**, 5233 (1999)
91. R.M. Wentzcovitch, S. Fahy, M.L. Cohen, S.G. Louis, Phys. Rev. B **38**, 6191 (1988)
92. K. Albe, Phys. Rev. B **55**, 6203 (1997)
93. Y.N. Xu, W.Y. Ching, Phys. Rev. B **44**, 7787 (1991)
94. R.T. Senger, S. Tongay, E. Durgun, S. Ciraci, Phys. Rev. B **72**, 075419 (2005)
95. D. Jacquemin, E.A. Perpete, B. Champagne, Phys. Chem. Chem. Phys. **4**, 432 (2002)
96. A. Abdurahman, A. Shukla, M. Dolg, Phys. Rev. B **65**, 115106 (2002)
97. X.Q. Shi, Z.X. Dai, X.H. Zheng, Z. Zeng, J. Phys. Chem. B **110**, 16902 (2006)
98. M. Qiu, K.M. Liew, J. Appl. Phys. **113**, 054305 (2013)
99. C.C. Kaun, H. Guo, P. Grütter, R.B. Lennox, Phys. Rev. B **70**, 195309 (2004)
100. A.R. Champagne, A.N. Pasupathy, D.C. Ralph, Nano Lett. **5**, 305 (2005)
101. Yu.M. Galperin, *Quantum Transport*. Lecture Notes (Lund University Press, 1998)
102. S. Datta, Nanotechnology **15**, S433 (2004)
103. C. Jain, M. Willander, J. Narayan, R. van Overstraeten, J. Appl. Phys. **87**, 965 (2000)
104. P. Ruterana, M. Albrecht, J. Neugebauer, *Nitride Semiconductors: Handbook on Materials and Devices* (Wiley, New York, 2003)
105. J.M. Wagner, *Structure and Lattice Dynamics of GaN and AlN: Ab Initio Investigations of Strained Polytypes and Superlattices* (PhD Thesis, Friedrich-Schiller-Universität, Jena, 2004)
106. F. Mireles, S.E. Ulloa, Phys. Rev. B **58**, 3879 (1998)
107. J.M. Vail, D. Schindel, A. Yang, O. Penner, R. Pandey, H. Jiang, M.A. Blanco, A. Costales, Q.C. Qiu, Y. Xu, J. Phys.: Condens. Matter **16**, 3371 (2004)
108. Yu.F. Zhukovskii, N. Pugno, A.I. Popov, C. Balasubramanian, S. Bellucci, J. Phys.: Condens. Matter **19**, 395021 (2007)

109. H. Morkoç, *Nitride Semiconductors and Devices*. Springer Series in Material Science (Springer, Berlin, 1999)
110. J.W. Kang, H.J. Hwang, Comput. Mater. Sci. **31**, 237 (2004)
111. T. Hanada, in *Oxide and Nitride Semiconductors*, ed by T. Yao, S.K. Hong, Processing, Properties, and Applications. Series Advances in Materials Research, vol. 12 (Springer, Berlin, Heidelberg, 2009), pp. 1–19
112. B.K. Meyer, *III-V Nitrides Semiconductors and Ceramics: From Material Growth to Device Applications* (Elsevier Health Sciences, Amsterdam, 1998)
113. I. Vurgaftman, J.R. Meyer, J. Appl. Phys. **94**, 3675 (2003)
114. S. Picozzi, G. Profeta, A. Continenza, S. Massidda, A.J. Freeman, Phys. Rev. B **65**, 165316 (2002)
115. T.K. Zywietz, J. Neugebauer, M. Scheffler, Appl. Phys. Lett. **74**, 1695 (1999)
116. C.I. Wu, A. Kahn, Appl. Phys. Lett. **74**, 546 (1999)
117. P. Kung, M. Razeghi, Opto-Electron. Rev. **8**, 201 (2000)
118. A.N. Enyashin, S. Gemming, G. Seifert, in *Materials for Tomorrow. Theory, Experiments and Modelling*, ed. by S. Gemming, M. Schreiber, J-B. Suck. Springer Series in Materials Science, vol. 93 (Springer, Berlin, Heidelberg, New York, 2006), pp. 33–57
119. C. Zhang, J. Appl. Phys. **111**, 043702 (2012)
120. Q. Peng, X.J. Chen, S. Liu, S. De, RSC Adv. **3**, 7083 (2013)
121. J. Goldberger, R. He, Y. Zhang, S. Lee, H. Yan, H.J. Choi, P. Yang, Nature **422**, 599 (2003)
122. Q. Wu, Z. Hu, X. Wang, Y. Lu, X. Chen, H. Xu, Y. Chen, J. Am. Chem. Soc. **125**, 10176 (2003)
123. C. Balasubramanian, V.P. Godbole, V.K. Rohatgi, A.K. Das, S.V. Bhoraskar, Nanotechnology **15**, 370 (2004)
124. C. Balasubramanian, S. Bellucci, P. Castrucci, M. De Crescenzi, S.V. Bhoraskar, Chem. Phys. Lett. **383**, 188 (2004)
125. S.M. Lee, Y.H. Lee, Y.G. Hwang, J. Elsner, D. Porezag, T. Frauenheim, Phys. Rev. B **60**, 7788 (1999)
126. D. Zhang, R.Q. Zhang, Chem. Phys. Lett. **371**, 426 (2003)
127. M. Zhao, Y. Xia, D. Zhang, L. Mei, Phys. Rev. B **68**, 235415 (2003)
128. Ş. Erkoç, O.B. Malcioglu, E. Taşci, J. Mol. Struct. (Theochem) **674**, 1 (2004)
129. Y.R. Jeng, P.C. Tsai, T.H. Fang, Nanotechnology **15**, 1737 (2004)
130. M. Zhao, Y. Xia, Z. Tan, X. Liu, F. Li, B. Huang, Y. Ji, L. Mei, Chem. Phys. Lett. **389**, 160 (2004)
131. B. Xu, A.J. Lu, B.C. Pan, Q.X. Yu, Phys. Rev. B **71**, 125434 (2005)
132. E. Durgun, S. Tongay, S. Çiraci, Phys. Rev. B **72**, 075420 (2005)
133. Z. Qian, S. Hou, J. Zhang, R. Li, Z. Shen, X. Zhao, Z. Xue, Physica E **27**, 81 (2005)
134. R.R. Zope, B.I. Dunlap, Phys. Rev. B **72**, 045439 (2005)
135. M. Zhao, Y. Xia, X. Liu, Z. Tan, B. Huang, C. Song, L. Mei, J. Phys. Chem. B **110**, 8764 (2006)
136. M. Simeoni, S. Santucci, S. Picozzi, B. Delley, Nanotechnology **17**, 3166 (2006)
137. Yu.F. Zhukovskii, A.I. Popov, C. Balasubramanian, S. Bellucci, J. Phys.: Condens. Matter **18**, S2045 (2006)
138. H. Pan, Y.P. Feng, J. Lin, J. Chem. Theory. Comput. **4**, 703 (2008)
139. Y. Guo, X. Yan, Y. Yang, Phys. Lett. A **373**, 367 (2009)
140. J.M. de Almeida, T. Kar, P. Piquini, Phys. Lett. A **374**, 877 (2010)
141. S. Nakamura, T. Mukai, M. Senoh, Appl. Phys. Lett. **64**, 1687 (1994)
142. H.M. Kim, T.W. Kang, K.S. Chung, J.P. Hong, W.B. Choi, Chem. Phys. Lett. **377**, 491 (2003)
143. T. Yamamoto, H.K. Yoshida, Jpn. J. Appl. Phys. **36**, Part 2, L180 (1997)
144. W. Han, Y. Bando, K. Kurashima, T. Sato, Appl. Phys. Lett. **73**, 3085 (1998)
145. D.A. Steigerwald, J.C. Bhat, D. Collins, R.M. Fletcher, M.O. Holcomb, M.J. Ludowise, P.S. Martin, S.L. Rudaz, IEEE J. Sel. Top. Quant. Electron. **8**, 310 (2002)
146. I. Ichimura, F. Maeda, K. Osato, K. Yamamoto, Y. Kasami, Jpn. J. Appl. Phys. **39**, 937 (2000)
147. M.A. Khan, X. Hu, G. Simin, J. Yang, R. Gaska, M.S. Shur, Appl. Phys. Lett. **77**, 1339 (2000)

148. S. Rajan, A. Chini, M.H. Wong, J. Appl. Phys. **102**, 044501 (2007)
149. M. Marques, L.K. Teles, L.G. Ferreira, Phys. Rev. B **75**, 033201 (2007)
150. S.H. Wei, A. Zunger, Appl. Phys. Lett. **69**, 2719 (1996)
151. J.E. Northrup, J. Neugebauer, J. Phys. Rev. B **53**, R10477 (1996)
152. R.A. Evarestov, *Quantum Chemistry of Solids*. *The LCAO First Principles Treatment of Crystals*. Springer Series in Solid State Sciences, vol. 153 (Springer, Berlin, 2007)
153. R.K. Paul, K.H. Lee, B.T. Lee, H.Y. Song, Mater. Chem. Phys. **112**, 562 (2008)
154. J. Su, G. Cui, M. Gherasimova, H. Tsukumato, J. Han, D. Ciubaru, H. Lim, L. Pfefferle, Y. He, A.V. Nurmikko, C. Broadbridge, A. Lehman. Appl. Phys. Lett. **86**, 013105 (2005)
155. L.H. Shen, X.F. Li, J. Zhang, Y.M. Ma, F. Wang, G. Peng, Q.L. Cui, G.T. Zou, Appl. Phys. A **84**, 73 (2006)
156. G.R. Yazdi, M. Syvajarvi, R. Yakimova, Appl. Phys. Lett. **90**, 123103 (2007)
157. Z. Zhou, J. Zhao, Y. Chen, P. von Ragué Schleyer, Z. Chen, Nanotechnology **18**, 424023 (2007)
158. G.A. Nemnes, J. Nanomater. **2013**, 408475 (2013)
159. C. Xu, L. Xue, C. Yin, G. Wang, Phys. Status Solidi (A) **198**, 329 (2003)
160. Q. Zhao, H. Zhang, X. Xu, Z. Wang, J. Xu, D. Yu, G. Li, F. Su, Appl. Phys. Lett. **86**, 193101 (2005)
161. L.E. Brus, J. Chem. Phys. **80**, 4403 (1984)
162. Y.K. Song, A.V. Nurmikko, M. Gherasimova, S.R. Jeon, J. Han, Phys. Status Solidi (A) **201**, 2721 (2004)
163. Y. Wu, G. Chen, H. Ye, Y. Zhu, S.H. Wei, Appl. Phys. Lett. **94**, 253101 (2009)
164. Y. Wu, G. Chen, H. Ye, Y. Zhu, S.H. Wei, J. Appl. Phys. **104**, 084313 (2008)
165. A. Mitrushchenkov, R. Linguerri, G. Chambaud, J. Phys. Chem. C **113**, 6883 (2009)
166. A. Mitrushchenkov, G. Chambaud, J. Yvonnet, Q.C. He, Nanotechnology **21**, 255702 (2010)
167. T.L. Mitran, A. Nicolaev, G.A. Nemnes, L. Ion, S. Antohe, Comput. Mater. Sci. **50**, 2955 (2011)
168. J. Yvonnet, A. Mitrushchenkov, G. Chambaud, Q.C. He, Comput. Methods Appl. Mech. Eng. **200**, 614 (2011)
169. M.H. Tsai, Z.F. Jhang, J.Y. Jiang, Y.H. Tang, L.W. Tu, Appl. Phys. Lett. **89**, 203101 (2006)
170. Z. Gao, Y. Gu, Y. Zhang, J. Nanomater. **2010**, 462032 (2010)
171. T. Markussen, A.P. Jauho, M. Brandbyge, Phys. Rev. B **79**, 035415 (2009)
172. E. Bourgeois, M.V. Fernandez-Serra, X. Blase, Phys. Rev. B **81**, 193410 (2010)
173. M. Mohr, C. Thomsen, Nanotechnology **20**, 115707 (2009)
174. D. Spirkoska, G. Abstreiter, A. Fontcuberta i Morral, Nanotechnology **19**, 435704 (2008)
175. L. Shen, Q. Cui, Y. Ma, Q. Li, Y. Ma, B. Liu, T. Cui, J. Phys. Chem. C **114**, 8241 (2010)
176. J.M. Soler, E. Artacho, J.D. Gale, A. Garcia, J. Junquera, P. Ordejón, D. Sánchez-Portal, J. Phys.: Condens. Matter **14**, 2745 (2002)
177. D.E. Angelescu, M.C. Cross, M.L. Roukes, Superlatt. Microsctruct. **23**, 673 (1998)
178. L.G.C. Rego, G. Kirczenow, Phys. Rev. Lett. **81**, 232 (1998)
179. A. Al Shaikhi, G.P. Srivastava, Phys. Rev. B **76**, 195205 (2007)
180. J.C. Li, C.L. Wang, H. Peng, M.X. Wang, R.Z. Zhang, H.C. Wang, J. Liu, M.L. Zhao, L.M. Mei, J. Appl. Phys. **108**, 063702 (2010)
181. A. Gulans, I. Tale, Phys. Status Solidi (C) **4**, 1197 (2007)
182. D.J. Carter, J.D. Gale, B. Delley, C. Stampfl, Phys. Rev. B **77**, 115349 (2008)
183. D.Q. Fang, A.L. Rosa, Th. Frauenheim, R.Q. Zhang, Appl. Phys. Lett. **94**, 073116 (2009)
184. R. Agrawal, H.D. Espinosa, Nano Lett. **11**, 786 (2011)
185. P. Dev, H. Zeng, P. Zhang, Phys. Rev. B **82**, 165319 (2010)
186. D.J. Carter, M. Fuchs, C. Stampfl, J. Phys.: Condens. Matter **24**, 255801 (2012)
187. Q. Wang, Q. Sun, P. Jena, Nano Lett. **5**, 1587 (2005)
188. Z. Wang, J. Li, F. Gao, W.J. Weber, J. Appl. Phys. **108**, 044305 (2010)
189. C.C. Chen, C.C. Yeh, C.H. Chen, M.Y. Yu, H.L. Liu, J.J. Wu, K.H. Chen, L.C. Chen, J.Y. Peng, Y.F. Chen, J. Am. Chem. Soc. **123**, 2791 (2001)
190. J.R. Kim, H.M. So, J.W. Park, J.J. Kim, Appl. Phys. Lett. **80**, 3548 (2002)

191. Y.K. Byeun, K.S. Han, S.C. Choi, J. Electroceram. **17**, 903 (2006)
192. S. Dhara, A. Datta, C.T. Wu, Z.H. Lan, K.H. Chen, Y.L. Wang, C.W. Hsu, C.H. Shen, L.C. Chen, C.C. Chen, Appl. Phys. Lett. **84**, 5473 (2004)
193. B.S. Simpkins, L.M. Ericson, R.M. Stroud, K.A. Pettigrew, P.E. Pehrsson, J. Cryst. Growth **290**, 115 (2006)
194. B.S. Xu, L.Y. Zhai, J. Liang, S.F. Ma, H.S. Jia, X.G. Liu, J. Cryst. Growth **291**, 34 (2006)
195. H.Y. Peng, N. Wang, X.T. Zhou, Y.F. Zheng, C.S. Lee, S.T. Lee, Chem. Phys. Lett. **359**, 241 (2002)
196. T. Kuykendall, P.J. Pauzauskie, Y. Zhang, J. Goldberger, D. Sirbuly, J. Denlinger, P. Yang, Nat. Mater. **3**, 524 (2004)
197. S.D. Hersee, X. Sun, X. Wang, Nano Lett. **6**, 1808 (2006)
198. S. Gradecak, F. Qian, Y. Li, H.G. Park, C.M. Lieber, Appl. Phys. Lett. **87**, 173111 (2005)
199. M. He, P. Zhou, S. Mohammad, G. Harris, J. Halpern, R. Jacobs, W. Sarney, L. Salamanca-Riba, J. Cryst. Growth **231**, 357 (2001)
200. G. Cheng, A. Kolmakov, Y. Zhang, M. Moskovits, R. Munden, M.A. Reed, G. Wang, D. Moses, J. Zhang, Appl. Phys. Lett. **83**, 1578 (2003)
201. H.J. Choi, H.K. Seong, J. Chang, K.I. Lee, Y.J. Park, J.J. Kim, S.K. Lee, R. He, T. Kuykendall, P. Yang, Adv. Mater. **17**, 1351 (2005)
202. J.E. Northrup, R.D. Felice, Phys. Rev. B **56**, R4325 (1997)
203. R.R. Reeber, K. Wang, MRS Internet J. Nitride Semicond. Res. **6**, 3 (2001)
204. C.Y. Nam, P. Jaroenapibal, D. Tham, D.E. Luzzi, S. Evoy, J.E. Fischer, Nano Lett. **6**, 153 (2006)
205. J.C. Johnson, H.J. Choi, K.P. Knutsen, R.D. Schaller, P. Yang, R.J. Saykally, Nat. Mater. **1**, 106 (2002)

Chapter 7
Binary Oxides of Transition Metals

First-principles DFT methods complement the experimental study of the binary oxides (ZnO, TiO_2 and ZrO_2)-based nanostructures. We begin each section of this chapter with a short discussion of the results of the corresponding bulk crystal and nanosheet properties calculations. This information is important for understanding the structure and properties of binary oxide-based nanotubes and nanowires.

ZnO-layered crystals have a wurtzite structure, in which the interlayer Van der Waals interaction is weak. Therefore the conventional single-walled ZnO nanotubes are generated by rolling up one-layer slab with a hexagonal 2D lattice. The DFT(PBE) calculations of zigzag (n,0), armchair (n,n) and chiral (n_1, n_2) rolled up nanotubes show that for all types of ZnO nanotubes, the strain energies are much smaller than for BN nanotubes with the same diameters, but are somewhat sensitive to the chirality of the nanotube. The majority of the computationally studied ZnO nanowires are [0001]-oriented. These include hexagonal and triangular shaped nanowires, having six or three low energy surface facets, respectively, with the c-axis of the wire oriented along the [0001] direction.

In most theoretical simulations on TiO_2 nanotubes, the model $3D \longrightarrow 2D \longrightarrow 1D$ of structural transformations was applied, i.e., the bulk ($3D$) phase first formed a lamellar product ($3D \longrightarrow 2D$) and then was bent and rolled to a nanotubular form ($2D \longrightarrow 1D$). The lamellar product was mainly formed by the anatase (101) surface, identified as prevailing in TiO_2 NTs. A further geometry optimization of the 3-layer O-Ti-O sheet for the $2D \longrightarrow 1D$ transition results in the formation of titania nanotubes, possessing hexagonal fluorite-like (111) morphology with (n,n) and (n,0) chiralities. The results of the first-principles calculations of anatase-based six-layer nanotubes with a rectangular morphology show that rolled up (−n,n) nanotubes are energetically preferable to (n,n) nanotubes.

Two types of rutile-based [001]—and [110]—oriented nanowires are considered: Ti-atom-centered and hollow-site centered. It was found that the hollow-site centered NTs have smaller strain energy than the Ti-atom centered ones. Both LCAO and PW calculations clearly demonstrate that the more energetically preferable titania nanowires in the rutile phase display (110) facets when they are [001]-oriented and (110) and (001) facets when they are [110]-oriented. The orientation effects in the

© Springer-Verlag Berlin Heidelberg 2015

R.A. Evarestov, *Theoretical Modeling of Inorganic Nanostructures*,
NanoScience and Technology, DOI 10.1007/978-3-662-44581-5_7

morphology and electronic properties of rutile nanowires, anatase nanowires and facetted nanotubes are discussed using the results of PW DFT calculations.

In consideration of the rolled up ZrO_2 nanotubes it was taken into account that thin sheets of zirconia exhibit a variety of structures because of the existence of several crystalline bulk polymorphs. We consider cubic, tetragonal, and monoclinic faces with different (low) crystallographic indices one after another. It is found that the formation energy of ZrO_2 nanotubes with a sufficiently large diameter is mainly determined by the formation energy of the corresponding nanosheet. The analysis of nanotube formation and strain energies has determined that the most stable tubes with thin (one ZrO_2 layer) walls should have hexagonal morphology corresponding to the rolling of (111) sheets from the cubic fluorite phase. The tubes with walls composed of two ZrO_2 layers presumably have lepidocrocite morphology. The tubes with thicker walls can possess a different structure originating from the cubic, tetragonal or orthorhombic phases. The lowest strain energy was found for a nanotube with rutile morphology exhibiting zigzag ZrO bond arrangement.

The comparison of zirconia-based and titania-based nanotubes shows that the former may have smaller strain energies, while the latter may have smaller formation energies relative to the stable bulk phases.

7.1 Zinc Oxide

Zinc oxide materials are now widely applied to electronic and optoelectronic devices [1] and nano-engineering [2]. An overview of the bulk ZnO fundamental properties (electronic, phononic, magnetic and optical) is given in [3, 4].

Using different growth techniques, researchers have shown that ZnO can be grown in a wide variety of shapes and structures, possibly larger in number than any other material [5–7]. Most ZnO nanostructures are grown by three main methods: vaporliquidsolid (VLS) process, solution-based chemical synthesis, and chemical vapor deposition (CVD) [8]. Depending on the specific growth conditions, the nanostructures can be obtained with a wide range of geometric features. In particular, new nanostructured 2D- and 1D-morphologies (nanosheets, nanoribbons, nanotubes and nanowires) have been discovered and applied to gas sensing. A common feature of these nanostructures is the very high aspect ratio, which is due to the lowest surface energy of a certain crystalline facet.

Over the last decade the progress in ZnO-based nanostructures research has been very fast [9, 10]. The results of the experimental studies of ZnO-based nanostructure synthesis and growth mechanism can be found in books [2, 9, 10] and original papers [11–18].

The theoretical modeling of bulk ZnO and the ZnO-based nanostructures has become an important field in ZnO-based nanostructure research. Review [7] focuses on studies that employ DFT electronic structure calculations, useful for understanding the reaction mechanism, binding strength, charge transfer as well as other electronic and structural properties of ZnO-based nanomaterials and gas-sensor interaction. A summary and outlook for future directions of this exciting area of research is also provided.

7.1.1 Bulk Zinc Oxide and Nanolayers

At ambient conditions ZnO crystallizes in a layered wurtzite structure in which each oxygen atom is tetrahedrally coordinated with four zinc atoms along the crystallographic c-axis, and vice versa (see Fig. 7.1). The primitive unit cell consists of two formula units. The wurtzite structure of bulk ZnO with the symmetry of the nonsymmorphic space group C_{6v}^4 has a threefold rotation axis and a 6_3 improper rotation axis. Both axes are parallel to the c-direction but do not coincide with each other. Whereas the atoms of the lattice lie on the threefold axis, the 6_3 axis does not bear any atom, [19] (Fig. 7.2).

Fundamentals of the zinc oxide as a semiconductor are discussed in review article [20]. The results of the bulk ZnO DFT calculations are also reviewed in [20]. However, a common problem of most of these calculations is the use of the standard DFT exchange-correlation functionals (LDA/GGA) or parameter-dependent functionals like hybrid Heyd-Scuseria-Ernzerhof (HSE) or DFT+U. The LDA/GGA approach significantly underestimates the band gap in ZnO. On the other hand, different fractions of the HartreeFock (HF) exact exchange were used for ZnO within the HSE functional (see below).

In recent bulk zinc oxide calculations [22], the LCAO basis set (BS) and Perdew-Burke Ernzerhof (PBE0) hybrid exchange-correlation functional (implemented in the CRYSTAL09 computer code [23]) were used. The used in ZnO Hartree Fock calculations all electron BS by Jaffe et al. [24] has been chosen for Zn and O atoms; the exponents of Gaussian type orbitals smaller than 0.7 Bohr^{-2} were reoptimized for the PBE0 functional. The BS optimization in ZnO led to a considerable energy gain of 0.29 eV per primitive unit cell. The MonkhorstPack scheme [25] 6 6 4 **k**-point mesh in the Brillouin zone (BZ) was applied, the tolerances 8 8 8 8 and 16 for the Coulomb and exchange integral calculations were taken. Furthermore, the SCF convergence threshold on the total electronic energy is 10^{-7} was used for the ZnO

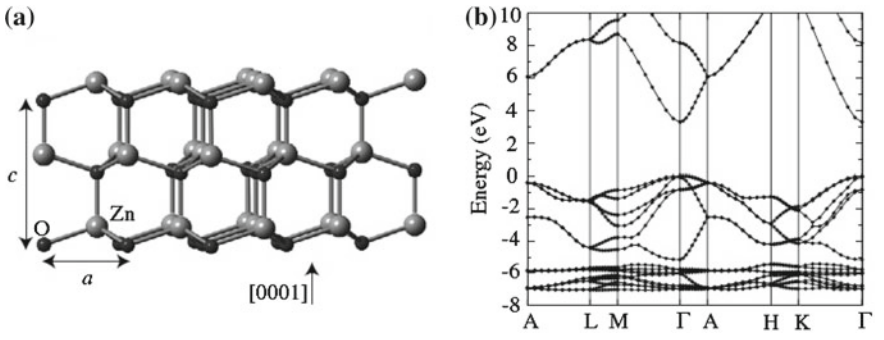

Fig. 7.1 The wurtzite crystal structure of ZnO with the lattice parameters a and c indicated in (**a**), and the band structure of ZnO calculated using the HSE hybrid functional in (**b**) [20]. The energy of the valence-band maximum was set to zero (Reprinted figure with permission from Janotti and Van de Walle [20], Copyright (2009) by the IOP Publishing)

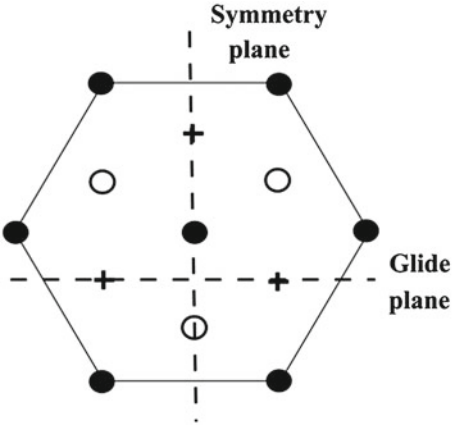

Fig. 7.2 Location of threefold rotation and 6_3 improper rotation axes and of symmetry and glide planes in the wurtzite lattice. *Filled circles* Zn (O) site within the $z = 0$ plane. *Open circles* site with an atom of the same species as within the $z = 0$ plane but located within the first *upper layer*. Each atomic site is located on a threefold rotation axis perpendicular to the $z = 0$ plane. *Crosses* location of an improper rotation axis perpendicular to the $z = 0$ plane (Reprinted figure with permission from Tronc et al. [19], Copyright (2006) by the WILEY-VCH Verlag GmbH & Co. KGaA, Weinheim)

structure optimization. High-frequency dielectric constants were estimated using the coupled perturbed HF (Kohn-Sham) method [26].

The comparison of PBE0 and HSE results made in [22] is given in Table 7.1. The calculated lattice parameters and bulk moduli agree very well with the experimental data and previous hybrid functional calculations. The Mulliken atomic charges evidence a considerable covalency of ZnO bonding (± 0.95 e for Zn and O, respectively). The underestimated band gaps in ZnO within the standard LDA, GGA-type functionals were a subject of many discussions in the literature. The band gap ΔE_g is significantly underestimated in both plane wave and LCAO calculations (0.73 eV) [27]. In order to solve this problem, one should go beyond the standard DFT functionals, e.g. by using the hybrid functional, the DFT+U approach [20] or self-interaction correction (SIC)-LDA technique [28]. It is also well established for ZnO that the DFT+U approach is unable to reproduce correctly ΔE_g by a simple variation of the U-parameter for the d electrons of the transition metal, i.e. the value of ΔE_g remains underestimated by almost 1.5 eV in comparison with the experimental value for ZnO. A very sophisticated DFT+U study on ZnO was recently performed by Boonchun and Lambrecht [29], where they separately adjusted the U parameters for the s, p, d electrons of Zn and s, p electrons of O, in order to obtain the correct ΔE_g from their accurate GW calculation. On the other hand, Oba et al. [27] have shown that the fraction of HF exact exchange must be increased to 0.375 for the HSE functional, in order to reproduce ΔE_g (3.42 eV in Table 7.1) in ZnO, if the screening parameter is set to 0.2. In calculations [22] with PBE0 $\Delta E_g = 3.56$ eV, see Table 7.1. The calculated value ΔE_g for ZnO is only by 0.12 eV larger than the experimental one.

Table 7.1 Bulk properties of Zinc Oxide [22]: a,c,u—lattice parameters; z_{Mull}—Mulliken atomic charge; z_{Born}—Born effective atomic charge (two components are separated by /); ϵ^0 and ϵ^∞ are static and high frequency dielectric constants, respectively; ΔE_g—band gap; B—bulk modulus

	PBE0 LCAO	HSE PW	Exper.
a, Å	3.26	3.25	3.25[a,b]
c, Å	5.22	5.25	5.21[a,b]
u_{frac}	0.38		0.38[a,b]
z_{Mull}(Zn), e	0.95		
z_{Mull}(O), e	−0.95		
z_{Born}(Zn), e	2.00/2.04	2.06/2.11	2.16/2.22[c]
z_{Born}(O), e	−2.00/−2.04	−2.06/−2.11	−2.16/−2.22[c]
ϵ^0_{xx}	6.67	7.72	7.80[d]
ϵ^0_{zz}	7.31	8.37	8.75[d]
ϵ^∞_{xx}	3.25	3.66	3.70[d]
ϵ^∞_{zz}	3.28	3.73	3.75[d]
ΔE_g, eV	3.56	2.5(3.42[e])	3.44[d]
B, GPa	153	144	143[a],183[b]

[a] [30]
[b] [31]
[c] [32]
[d] [33]
[e] Hartree Fock exchange 0.375 and screening parameter 0.2 from [27]

In the work of Diebold et al. [34] it was revealed using highresolution scanning tunneling microscopy (STM), that the surface morphology of wurtzite ZnO is strongly dominated by five low Miller index planes: the nonpolar prism $(10\bar{1}0)$ and $(11\bar{2}0)$ faces as well as the polar $(000\bar{1})$, (0001) and $(11\bar{2}1)$ faces, see Fig. 7.3 and [35].

The mixed-terminated $(10\bar{1}0)$ and $(11\bar{2}0)$ facets can be seen as containing exclusively neutral Zn-O ion pairs, thus leading to the nonpolarity of the two flat surfaces. The two basal planes -O-terminated $(000\bar{1})$ and Zn-terminated (0001)-are always created together by cutting the hexagonal crystal perpendicular to the c-axis, wherein the first surface is located on one side of the as-cleaved stoichiometric sheet and, concurrently, the second surface is located on the other, opposite side. The stepped surface $(11\bar{2}1)$ is constituted by terraces of four atomic rows and monatomic steps, which are $[11\bar{2}0]$ and [0001] orientations, respectively. All step edges are terminated by 2-fold coordinated oxygen sites.

The PW DFT (LDA and PBE) calculations of both the nonpolar ZnO $(10\bar{1}0)$ and $(11\bar{2}0)$ as well as the polar $(000\bar{1})$ and (0001) surfaces were performed in [36]. All the surfaces were represented by periodically repeated slabs consisting of several atomic layers and separated by a vacuum region of 9.4–12.4 Å. For the polar surfaces a dipole correction was used to prevent artificial electrostatic interactions between the repeated units. To simulate the underlying bulk structure, the slab lattice constant in the direction parallel to the surface was always set equal to the theoretical equilibrium bulk value.

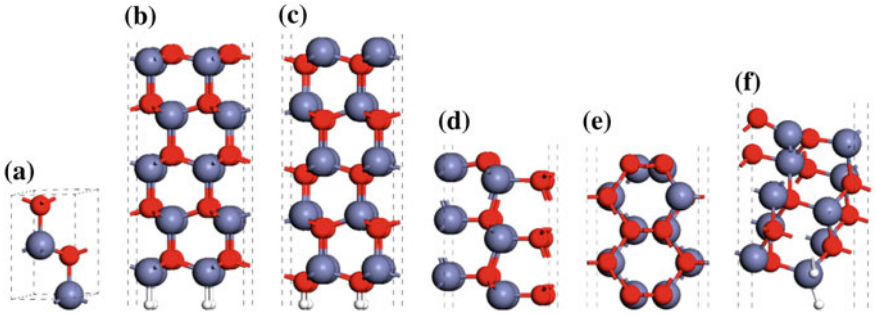

Fig. 7.3 Side views of the optimized bulk and surface structures of wurtzite ZnO: **a** bulk ZnO crystal, **b** O-terminated $(000\bar{1})$ with pseudohydrogen atoms of nuclear charge $Z = 1/2$, **c** Zn-terminated (0001) with pseudohydrogen atoms of $Z = 3/2$, **d** $(10\bar{1}0)$, **e** $(11\bar{2}0)$ and **f** $(11\bar{2}1)$ with pseudohydrogen atoms of Z = 1/2. All artificial atoms (small *white balls*) were attached to the *bottom* of the slab for each polar surface. The medium *red spheres* stand for O atoms and the large *blue spheres* for Zn atoms (Reprinted figure with permission from Tang and Luo [35], Copyright (2013) by the American Chemical Society)

The nonpolar surfaces are obtained by cutting the crystal perpendicular to the hexagonal Zn and O layers. In both cases, equivalent surfaces are created for the $(10\bar{1}0)$ and $(11\bar{2}0)$ planes so that stoichiometric slabs with the same surface termination on top and at the bottom can always be formed.

The polar surfaces were modelled by slabs consisting of Zn–O double layers, exhibiting a dipole moment perpendicular to the surface. The polar surfaces can only be stable if a rearrangement of charges between the Zn- and the O-terminated surfaces takes place. In calculations [36] the polar surfaces were stabilized by allowing the electrons to move from the $(000\bar{1})$-O surface to the (0001)-Zn surface. The charge in the top and bottom layer of the slab was modified in such a way that the dipole moment of the slab became independent of the slab thickness and the internal electric field vanishes. This charge transfer is equivalent to applying an external dipole, which compensates for the internal electric field.

The cleavage energies calculated in [36] for the two nonpolar surfaces are close -2.3 (1.6) J/m^2 in the LDA (PBE) calculations. For the two polar surfaces these energies are also close but are higher than those for the nonpolar surfaces: 4.3 (3.4) J/m^2 in LDA (PBE) calculations. These reasults were confirmed in the LDA+U calculations [37].

A precondition of the forming single-walled ZnO nanotubes is the stability of the graphene phase of the corresponding material. The component atoms in the graphitic structure adopt planar sp^2 hybridization, while those in the wurtzite structure undergo tetrahedral sp^3 hybridization. The stability of the graphitic structure of ZnO relative to Zn- and O-terminated films was discussed in [38, 39]. The experimental evidence related to the morphology of Zn-terminated polar (0001) thin films was presented in [39]. From first principles PW DFT calculations with the Perdew-Wang exchange-correlation functional and the ultra-soft Vanderbilt psedopotentials, it was also found

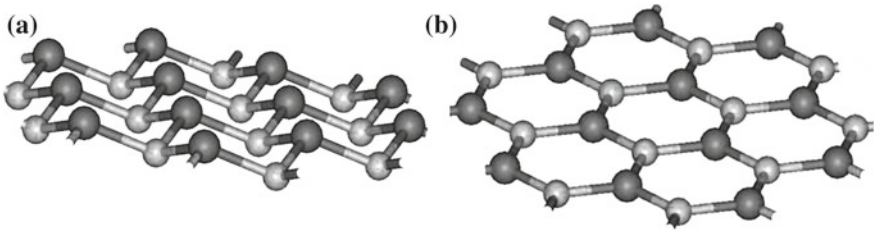

Fig. 7.4 ZnO single layers. The *left* part is a single layer taken from the wurtzite ZnO crystal while the *right* one is the optimized structure which is a planar hexagonal lattice. The *small* and *large balls* represent zinc and oxygen atoms, respectively [40]

in [39] that the graphitic structure persists up to 16 layers in the Zn-terminated film and the surface atoms exhibit trigonal sp^2 hybridization. This implies that the ultra-thin ZnO film might have a tendency to form ZnO graphitic sheets. The same conclusion was made in [40]: after the structure optimization of the single Zn–O layer in the DFT calculations a planar graphite-like structure was obtained, see Fig. 7.4.

Under appropriate conditions, single-layered ZnO graphene may coalesce in a tubular form. Moreover, the electronegative difference of 1.8 between Zn and O is comparable to the difference of 1.0 between B and N. Thus, the similarity in the bonding character of BN and ZnO may lead to an analogous growth sequence of the one-dimensional nanostructures [41], in particular single-walled nanotubes, as do C and BN. These results were confirmed in [36], where surface x-ray diffraction and scanning tunneling microscopy was made for the 2 monolayer thick ZnO(001) films grown on Ag(111). The conclusion was made that Zn and O atoms are arranged in planar sheets as in the hexagonal boron-nitride prototype structure. The observed depolarization is accompanied by a significant lateral 1.6 % expansion of the lattice parameter and a 3 % reduced Zn–O bond length within the sheets. The nonpolar structure stabilizes the atomically flat surface morphology. The transition to the bulk wurtzite structure occurs in the 34 monolayer coverage.

An alternative stabilization mechanism for the polar ZnO(0001)-Zn surface is discussed in [42]. Basing on the results of PW DFT (PAW) calculations the authors discuss various stabilization mechanisms, such as metallization of the surface layer, adsorption of OH groups or O adatoms, the formation of Zn vacancies, and large scale triangular reconstructions. The calculations indicate that isolated Zn vacancies or O adatoms are unfavorable compared to triangular reconstructions. In the absence of hydrogen, these triangular features are stable under any realistic temperature and pressure. When hydrogen is present, the reconstruction is lifted, and hydroxyl groups stabilize the ideal otherwise unreconstructed surface. The transition between the unreconstructed hydroxyl-covered surface and the triangular shaped features occurs abruptly; OH groups lift the reconstruction, but their adsorption is energetically unfavorable on the triangularly reconstructed surface.

The PW DFT (PBE) calculations [43] were performed for six bilayers of Zn- and O-terminated surfaces, in which the lower four bilayers are fixed as the bulk

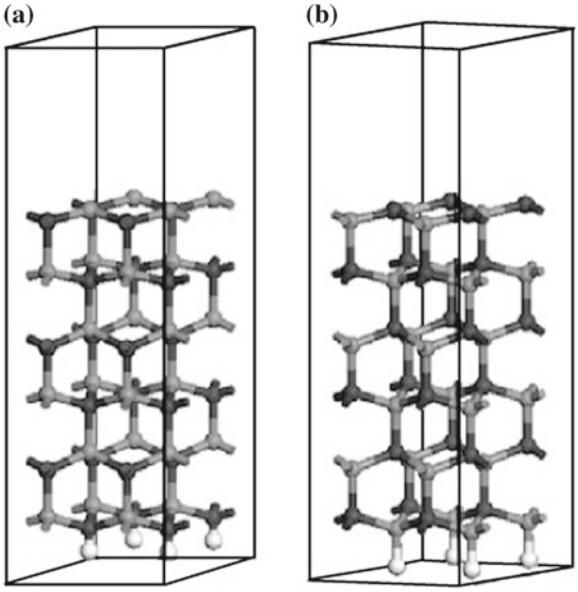

Fig. 7.5 Three-dimensional views of the *upper* part of **a** the perfect (0001) surface, and **b** the $(000\bar{1})$ surface. The *black* and the *gray* are O and Zn atoms, respectively. Four pseudohydrogen atoms (shown as *white balls*) are placed at the *bottom* of the cell (Reprinted figure with permission from Yufei et al. [43], Copyright (2010) by the IOP Publishing)

configuration while the upper two bilayers and adatoms (or adlayers) are allowed to relax. Figure 7.5 shows the schematic structures of c-axis ZnO polar surfaces, where each anion is surrounded by four cations at the corners of a tetrahedron, and vice versa.

The tetrahedral coordination is typically of sp^3 covalent bonding, but ZnO has a substantial ionic characteristic. To prevent unphysical charge transfer between the top and bottom slab surfaces, pseudohydrogens with fractional charges were used. The surface energies calculated for the 8-layer and 12-layer slab models show that the relative error is very small. By comparison, it was found that the surface energy of the Zn-terminated polar (0001) surface is bigger than that of the O-terminated polar $(000\bar{1})$ surface, which shows that the ZnO–Zn surface is more active than the ZnO–O surface. This is in good agreement with the experimental data [44].

7.1.2 Symmetry of Zinc Oxide Nanostructures

ZnO nanowires usually grow along the (0001) direction and have a hexagonal or triangular cross section, see [45, 46] and Fig. 7.6a, b. The faceted ZnO nanotubes can be regarded as nanowires with hollow interior centers that preserve their bulk-like configuration, Fig. 7.6c. The conventional single-walled and thicker ZnO nanotubes

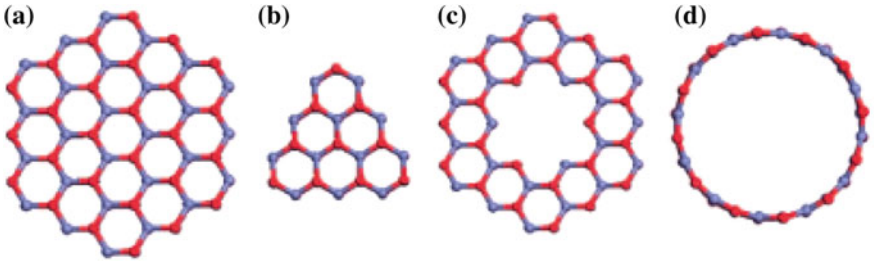

Fig. 7.6 Models of ZnO 1D nanostructures: **a** nanowires with *hexagonal cross* sections, **b** nanowires with *triangular cross* sections, **c** faceted nanotubes, and **d** conventional *single-walled* nanotubess. *Red* and *gray balls* denote O and Zn atoms, respectively (Reprinted figure with permission from Zhou et al. [46], Copyright (2008) by the American Chemical Society)

are generated by rolling up one- or multi-layer slabs with a hexagonal 2D lattice, see Fig. 7.6d.

The symmetry of wurtzite-based quantum wells and superlattices was studied in [47] which allowed the determination of the electron states symmetry and optical selection rules in these nanostructures.

The analysis of ZnO nanorods (nanowires) and faceted nanotubes symmetry was performed in [19, 48]. The hexagonal rods and tubes considered are built from the wurtzite structure of bulk ZnO, their axis being parallel to the c-axis of the wurtzite lattice. The lateral faces are assumed to be parallel to the sides of the hexagons within the (x, y) plane.

It has been shown that the symmetry of ZnO hexagonal nanorods and nanotubes depends on the location of their axes with respect to the ZnO wurtzite lattice. When the axis coincides with the threefold rotation axis of the lattice (type I structure), the point and space symmetries are described by the C_{3v} point group and the family 6 rod group RG49 (p3m1), respectively. When the axis coincides with the 6_3 improper rotation axis (type II structure), the symmetries are described by the C_{6v} point group and the family 8 rod group R70 ($p6_3mc$), respectively, see Table D.3. The site symmetry of an atom in the structure is C_{3v}, C_s, or C_1, depending on its location.

Figures 7.7 and 7.8 show type I and the type II ZnO nanotubes.

At any point of the one-dimensional Brillouin zone the direct optical transitions in the nanostructures obey the selection rules governed by the C_{3v} group (type I) or C_{6v} one (type II). The latter group is that of the Γ point of the bulk ZnO. The rules for transitions involving bound states differ from those in the bulk since they are generally governed by smaller groups. The effect of a magnetic or/and an electric field on the symmetry properties of the nanostructures was established in [19].

The conventional ZnO nanotubes are modelled by the rolling up procedure (see Chap. 2): the hexagonal lattice with the symmetry of layer group 69 (P3m1) is used to generate the chiral (n_1,n_2) and the achiral (n,n), (n,0) nanotubes.

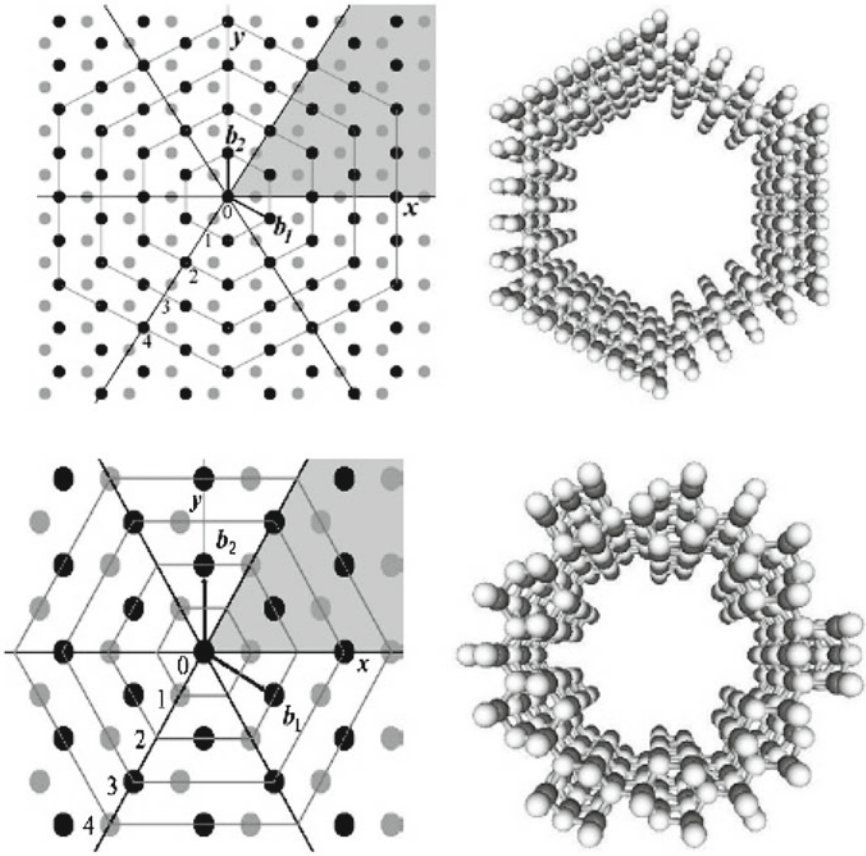

Fig. 7.7 Nanotubes of type I. *Left panels* top view of the bulk. *Points* denote zinc atoms at z = 0 (the *black* ones) and at z = c/2 (the *grey* ones). *Lines* depict positions of the vertical mirror planes. The third-order rotational axis is at their intersection. The symmetry cell is *shaded*. *Right panels* type I (*3*, *5*) and (*3*, *6*) nanotubes (Reprinted figure with permission from Milošević et al. [48], Copyright (2006) by the IOP Publishing)

The symmetry groups of the chiral NTs belong to Family 1, the symmetry groups of the achiral (n,n) and (n,0) NTs belong to families four and eight, respectfully, see C.1. The number of the atoms in the one-periodic unit cell is equal to 4n for the achiral nanotubes, the screw axis order is 2n.

At any point of the one-dimensional Brillouin zone the direct optical transitions in the achiral ZnO nanotubes obey the selection rules governed by the C_{2nv} group.

The high symmetry restrictions, introduced for the rolled up ZnO nanotubes, can increase the calculated formation energy.

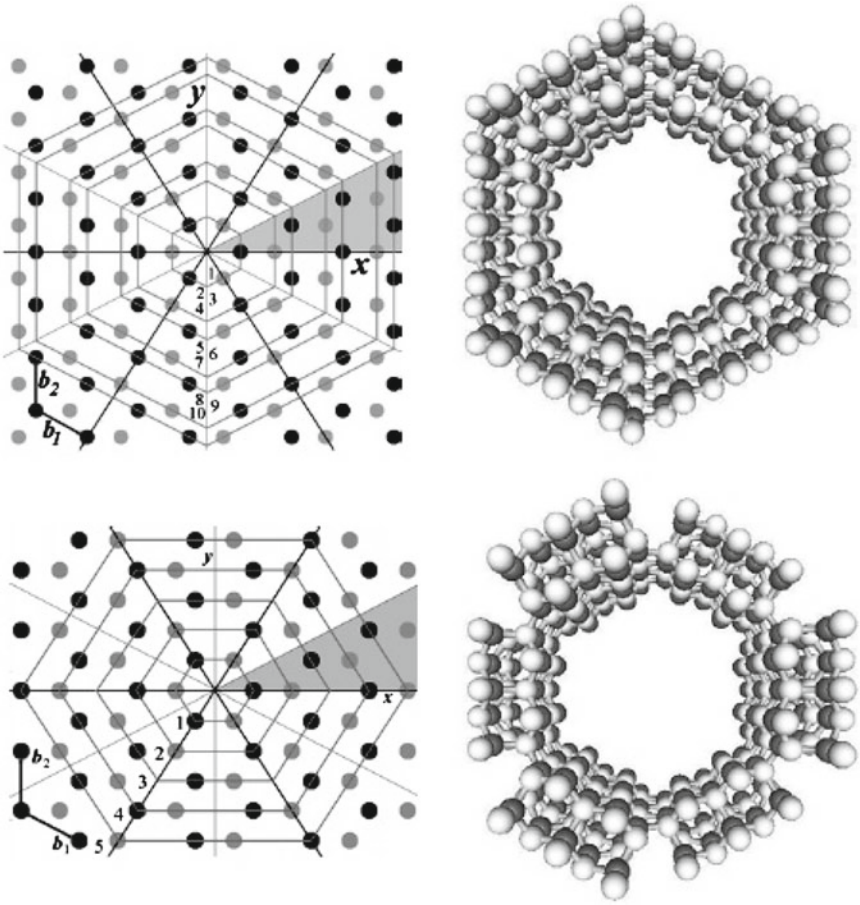

Fig. 7.8 Nanotubes of type II. *Left panels top view* of the bulk. The walls are enumerated. *Points* denote zinc atoms at z = 0 (the *black* ones) and at z = c/2 (the *grey* ones). Mirror and glide planes are indicated by *thick* and *thin* lines, respectively. The sixth-order screw axis is at their intersection. The symmetry cell is *shaded*. *Right panels* (*6*,*12*) and (*3*,*6*) nanotubes (Reprinted figure with permission from Milošević et al. [48], Copyright (2006) by the IOP Publishing)

7.1.3 ZnO Nanotubes

Different techniques have been used to grow ZnO nanotubes and study their properties [49–53].

ZnO nanotubes with a regular polyhedral shape, hollow core, and a wall thickness as small as 4 nm, were prepared in a large-area substrate by vapor phase growth [52]. The formation of the ZnO nanotubes was found to be closely related to the hexagonal structure of the ZnO crystal and the peculiar growth conditions used. In particular, high aspect ratio nanotubes are obtained by a three-step low temperature process involving ionic layer absorption, deposition of the ZnO seed layer

followed by hydrothermal annealing of the seed layer and deposition of the 1D ZnO nanostructures [49]. These ZnO nanotubes have a single-crystalline wurtzite structure with lengths exceeding 10 μ m and diameters of around 27 nm. By hydrothermal annealing, ZnO nanotubes grown along the ⟨001⟩ direction have been obtained [49].

The reaction of $Zn(NO_3)_2$ with methenamine in aqueous medium under hydrothermal conditions also gives rise to ZnO nanotubes. These nanotubes are hollow with rough surfaces, indicating a layer-stack structure. The ZnO nanotubes have a hexagonal wurtzite structure with lengths in the range of 13 μm and a wall thickness in the 50–100 nm range. The cross section is hexagonally faceted, providing strong evidence that the single nanotube grows along the c-axis direction [49], see Fig. 7.9d.

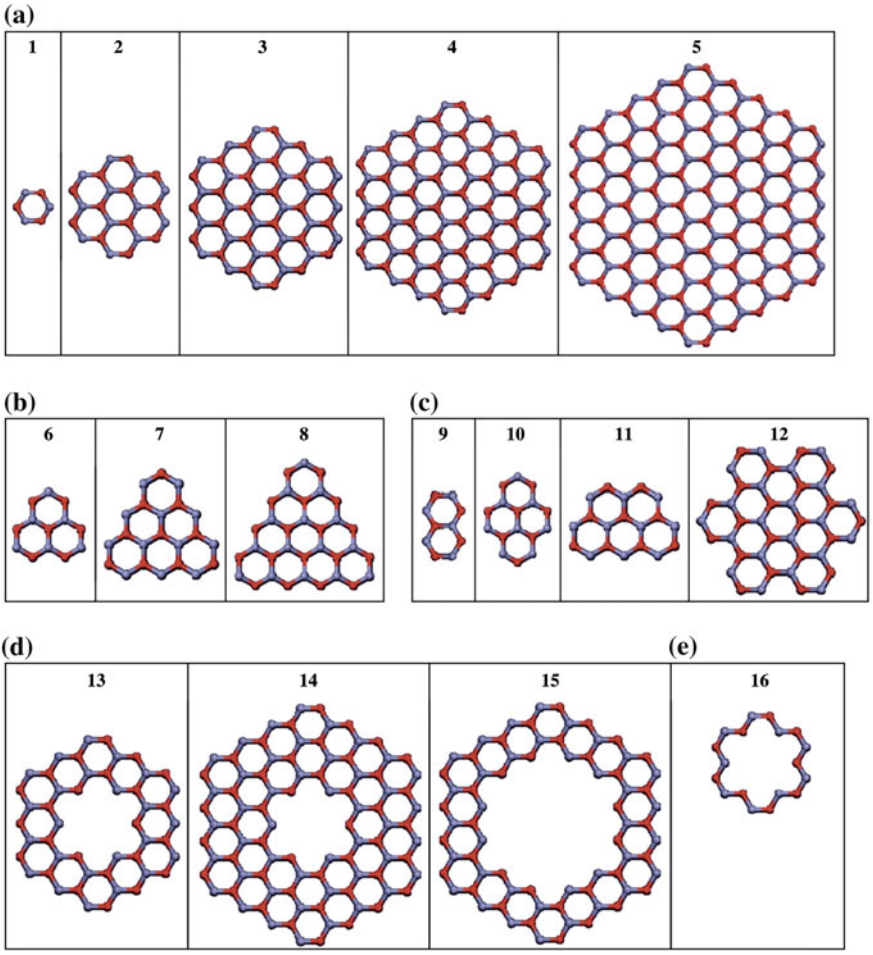

Fig. 7.9 Different nanostructures of ZnO that have been modelled using DFT: **a** hexagonal, **b** triangular, **c** other nanowires, **d** facetted (polyhedral) nanotubes, **e** facetted nanotubes (Zn atoms shown in *blue* and O atoms in *red*) (Reprinted figure with permission from Spencer [7], Copyright (2011) by the Elsevier Ltd. All rights reserved)

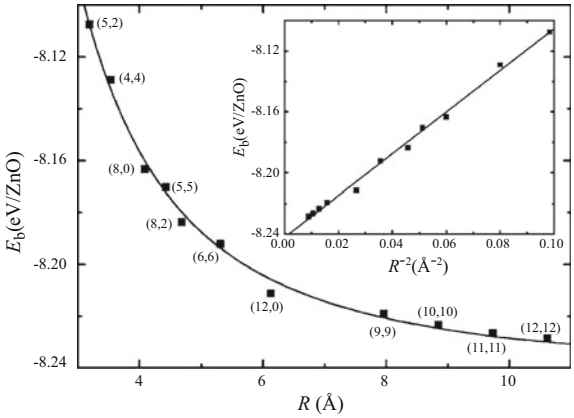

Fig. 7.10 Binding energy E_b and radius R of different SWZONTs [40]

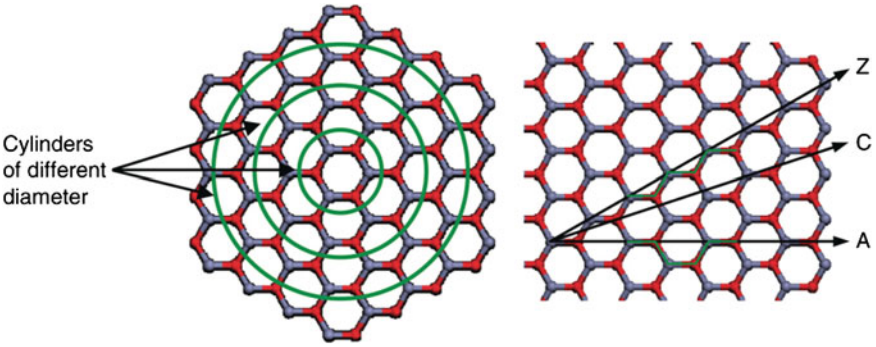

Fig. 7.11 Cleaving atoms on the ZnO surface via cylinders of different sizes (indicated in *green*) yields nanowires and nanotubes (*left*). ZnO planar sheet showing rolling directions to yield armchair (*A*), zigzag (*Z*) and chiral (*C*) nanotubes (*right*) (Reprinted figure with permission from Spencer [7], Copyright (2011) by the Elsevier Ltd. All rights reserved)

The optical properties of ZnO nanotubes were studied at room temperature in [53]. Raman peaks arising from the ZnO nanotubes were analyzed, which correspond well to those of the bulk ZnO sample.

One of the first PW DFT (LDA) calculations of the rolled up (see Fig. 7.11) single-walled ZnO nanotubes (SWZONTs) was performed in [40]. Without regard for the two ends, an SWZONT was treated as a cylinder rolled up from a single sheet of ZnO layer such that two equivalent sites of the hexagonal lattice coincide. Figure 7.10 shows the binding energy of SWZONTs with different chirality indices (n,m). From this figure one can find that (i) the binding energy for different SWZONTs is negative, which suggests that these SWZONTs can exist in principle; (ii) the binding energy E_b decreases with the increase of the radius R of SWZONTs and can be well described by (7.1). Obviously, $E_b \rightarrow -8.242$ eV/ZnO for R$\rightarrow \infty$. This value is quite close to

the binding energy −8.246 eV/ZnO of a ZnO single planar layer. The term $1.371/R^2$ reflects the curvature effect of the nanotubes.

$$E_b = -8.242 + 1.371/R^2 (\text{eV/ZnO}) \tag{7.1}$$

The classic shell theory also gives the same form, $D\Omega/R^2$, for the curvature effect, where D is the rigidity of the ZnO single layer and $\Omega = 8.91\text{Å}^2$ is the area of the parallelogram generated by the hexagonal lattice primitive translation vectors. Thus we obtain $D = 0.15$ eV, which is a lot smaller than the rigidity (1.17) eV [54] of a single graphite layer. The ZnO single layer is much softer than the graphite layer so that it is more easily wrapped up into a nanotube [40].

Table 7.2 is taken from [7] and gives references to the DFT calculations of both facetted and cylindrical shape single-walled chiral (n,m), zigzag (n,0) and armchair (n,n) ZnO-nanotubes, rolled up from the graphitic (001) ZnO plane.

To form the nanotube shape, a large supercell of bulk wurtzite ZnO is created, with one repeat unit kept in the z-direction. The supercell is then cut into cylinders of different diameters, removing the atoms outside and inside the cylinder and relaxing the structure to form a cylindrical shape. Facetted nanotubes are created the same way as the nanotubes but two cylinders of different diameters are used, with both the atoms outside the larger cylinder and those within the second smaller cylinder being removed. Both the facetted and rolled up nanotubes are infinite in the (0001) direction.

Table 7.3 shows results obtained in DFT (PBE) calculations (with the numerical atomic orbital basis set) on chiral, armchair and zigzag ZnO- nanotubes [41]. Density functional semi-core pseudopotentials (DSPP) fitted to all-electron relativistic DFT results, and a double numerical basis set including dpolarization functions (DND) were employed. The accuracy of the PBE and DND/DSPP combination was tested for the ZnO molecule and wurtzite bulk. It is seen that the zigzag nanotubes are more stable than the armchair ones, in contrast to the trend for carbon NTs. For all types of ZnO nanotubes, the strain energies are much smaller than for BN nanotubes with the same diameters [86], but are somewhat sensitive to the chirality of the nanotube. For the NTs studied in [41], the strain energies were approximately proportional to the inverse square of the tube diameter.

It is well known that DFT calculations underestimate the band gap of the bulk crystals. In particular, the DFT (PBE) calculation [41] gives for the bulk ZnO bandgap a value 0.895 eV (the experimental value is 3.25 eV, see Table 7.1). All the published DFT calculations of ZnO nanotubes (both facetted and rooled up ones) give NT band gaps that are larger than the gap of the bulk ZnO [7]. It is especially obvious from Table 7.3 showing the results of DFT(PBE) calculations [41] of single-walled ZnO nanotubes.

Previous studies have shown that DFT with hybrid functionals can give a quantitatively more accurate band gap of the bulk ZnO, see Table 7.1. The DFT(B3LYP) method, implemented in the CRYSTAL package [23], was used in [41] to calculate the band structures of bulk ZnO and ZnO (6,0) SWNT. It was found in [41] that the overall features of the ZnO (6,0) band structure are nearly the same as those based on the DFT(PBE) method, except for enlarged band gap, that is, 3.29 and 4.35 eV

Table 7.2 ZnO nanostructures modelled with wurtzite structure; including nanowires and nanotubes [7]

References	Method	Nanostructure				
		Nanowire			Nanotube	
		Hexagonal	Triangilar	Other	Facetted	SWNT
[55]	DFT: GGA(PW91) US PP	2, 3, 4			13, 14, 15	Zigzag (12, 0)
[56]	DFT: GGA(PW91) US PP	2				Zigzag (9, 0)
[57]	DFT: GGA(PW91) DNP	2				
[58]	DFT: GGA PAW		6, 7			
[59]	DFT: PW91 US PP	1, 2, 3	6	9, 10, 11		
[60]	DFT: GGA(PW91) DNP	2	7			Zigzag (12,0)
[61]	DFT: GGA DPN	1, 2, 4, 5				
[62]	DFT: LDA DPN	1, 2, 3, 4, 5				
[63]	DFT: GGA DPN	1, 2, 3, 4, 5				
[64]	DFT: GGA(PW91) PAW					Zigzag (n,o), n = 3, 5, 6, 9, 12, 15
						Armchair (n,n), n = 3, 5, 6, 9, 12, 15
[65]	DFT: GGA(PW91) PAW	2				
[66]	DFT: GGA(PW91) PAW					Zigzag (10,0) with V_O, V_{Zn}, O_{Zn}, Zn_O
						Armchair (6, 6) with V_O, V_{Zn}, O_{Zn}, Zn_O
[67]	DFT: GGA(PW91) PAW	2, 3	6			
[68]	DFT: LDA PAW				12	
[69]	DFT: GGA(PBE) DNP					Zigzag (6,0) with $1V_O$, $2V_O$, $3V_O$

(continued)

Table 7.2 (continued)

References	Method	Nanostructure				
		Nanowire			Nanotube	
		Hexagonal	Triangilar	Other	Facetted	SWNT
[70]	DFT: GGA(PBE) DND					Armchair (5,5)
[46]	DFT: GGA(PW91) PAW	3	7		13	Zigzag (8,0)
[71]	DFT: GGA(PW91) PAW	2	6	10		
[72]	DFT: GGA(PW91) PAW					Zigzag (n,0) n = 30 Armchair (n,n) n = 30
[73]	DFT: GGA(PBE) DND	2		10		
[74]	DFT: GGA(PBE) US PP	1, 2	6	9, 10		Zigzag (n,0) n = 3, 5, 6, 7, 8, 12
[41]	DFT: GGA(PBE) DND/DSPP					Zigzag (n,0) n = 3, 4, 5, 6, 9, 12, 15, 18 Armchair (n,n) n = 3, 4, 5, 6, 7, 9, 12, 15 Chiral (n,m) n = 3, 4, 5, 6, 8, m = 1, 2, 3, 4 Zigzag ((n, 0) n = 8, 12
[40]	DFT: LDA(CA/PW) TM PP					
[75]	DFT: GGA(PW91)	1, 2	6			Armchair (n,n) n = 4, 5, 6, 9, 10, 11, 12 Chiral (n,m) n = 5, 8 m = 2
[76]	DFT: GGA(PW91) PAW	1, 2, 3				
[77]	DFT: GGA PAW	1, 2, 3				
[78]	DFT: GGA					Zigzag (n,0)

(continued)

Table 7.2 (countinued)

References	Method	Nanostructure				
		Nanowire			Nanotube	
		Hexagonal	Triangilar	Other	Facetted	SWNT
[79]	DFT: GGA(RPBE) USPP					Armchair (6, 6)
[80]	DFT: GGA USPP	1, 2, 3			13	
[81]	DFT: GGA USPP	2, 3			12	
[82]	DFT: GGA USPP					Armchair (*n,n*) $n = 4, 5, 6, 7, 9, 11$
						Zigzag (*n*,0) $n = 5, 6, 9, 10, 12, 14$
						Chiral (2, 8)
[83]	DFT: LDA CA/PZ USPP					Armchair (10,10)
						Zigzag (10, 0)
[84]	DFT: LDA LCAO (6-31G)					Armchair (4,4), (5,5)
						Zigzag (*n*,0) $n = 4, 5, 6, 7, 8$
						Chiral (*n,m*) $n = 4, 5, 6, 7, 8$; m = 1, 2
						Chiral (*n*,3) $n = 4, 5, 6, 7$
						Chiral (*n*,4) $n = 5, 6, 7$
[85]	DFT: LDA NC PP	1 with V_O, V_{Zn}				

Double-ζ polarised numerical atomic orbital basis set (DPN); double numerical plus *d*-functions (DND) Troullierartins (TM); Ceperley Alder (CA); Perdewunger (PZ); Revised-Perdewurkeruzerhof (RPBE) linear combination of atomic orbitals (LCAO); ultrasoft pesudopotentails (US PP); norm-conserving pesudopotentials (NC PP)

[a] Refer to Fig. 7.9

for bulk ZnO and ZnO (6,0) SWNT, respectively which matches the experimental band gap of bulk ZnO (3.4 eV) quite well. Because both DFT-B3LYP and DFT-PBE calculations indicate that the band gap of ZnO (6,0) SWNT is larger than that of bulk ZnO, it is expected that DFT(PBE) calculations can, after all, give a qualitatively correct trend in the band structure, see Table 7.3.

ZnO rolled up nanotubes with and without defects (including vacancies and antisites) were examined in [66, 69, 83]. It was found that the presence of oxygen vacancies yields the lowest formation energies. Furthermore, antisites, that have

high formation energies in the bulk, could have relatively low formation energies in nanotubes.

Facetted ZnO NTs (structures 13, 14 and 15, Fig. 7.9) were examined in [55]. The calculated binding energy (BE) values (per atom) increased in magnitude as the size of the facetted NTs increased, showing that the larger structures are more stable. To represent the BE of infinitely large NTs the BE of a single sheet of ZnO was calculated in [55]. It was found that the smallest facetted NTs were more stable than infinitely large NTs. As it was indicated in [55] the facetted ZnO NTs unlike facetted boron nitride and carbon NTs, can only be hypothetical, due to the significant differences in the atomic radius and electronegativity of Zn and O atoms. Due to the large difference in the atomic radii, the orbital overlap is quite small resulting in weaker p bonding and hence lower stability. Furthermore, the large difference in

Table 7.3 The optimised supercell length L(Å), the average Zn-O bond length R(Å), the diameter D(Å), the number of atoms per unit cell N, the strain energy SE (eV/atom), the binding energy BE (eV/atom), bandgap Δ (eV) and net Milliken charge Q (e) of the ZnO nanotubes, the calculated band gap for the bulk ZnO is 0.895 eV [41]

Tubes	L	R	D	N	SE	BE	Δ	Q
(3,0)	16.20	1.957	3.237	36	0.196	3.215	2.265	0.718
(4,0)	16.50	1.937	4.272	48	0.094	3.317	2.013	0.729
(5,0)	16.70	1.927	5.312	60	0.053	3.358	1.937	0.738
(6,0)	16.60	1.919	6.348	72	0.035	3.376	1.917	0.744
(9,0)	16.60	1.911	8.823	108	0.013	3.398	1.921	0.754
(12,0)	16.70	1.907	12.616	144	0.004	3.407	1.915	0.757
(15,0)	16.70	1.905	15.753	180	0.002	3.409	1.907	0.76
(18,0)	16.70	1.901	18.864	216	0.002	3.409	1.879	0.761
(3,3)	9.70	1.919	5.497	36	0.064	3.347	1.852	0.741
(4,4)	9.80	1.914	7.31	48	0.036	3.375	1.977	0.752
(5,5)	9.72	1.909	9.114	60	0.028	3.383	1.909	0.752
(6,6)	9.70	1.907	10.926	72	0.022	3.389	1.912	0.761
(7,7)	9.72	1.906	12.74	84	0.019	3.392	1.909	0.763
(9,9)	9.74	1.905	16.371	108	0.016	3.395	1.905	0.766
(12,12)	9.70	1.904	21.817	144	0.013	3.398	1.905	0.767
(15,15)	9.70	1.903	27.257	180	0.011	3.4	1.906	0.768
(3,1)	20.01	1.938	3.852	52	0.124	3.287	2.02	0.72
(4,1)	8.50	1.928	4.871	28	0.067	3.344	2.12	0.732
(4,2)	15.20	1.927	5.621	56	0.045	3.366	2.021	0.741
(5,2)	12.40	1.936	6.665	52	0.045	3.366	1.915	0.745
(6,3)	14.62	1.908	8.349	84	0.024	3.387	1.858	0.749
(8,2)	8.80	1.919	9.696	56	0.016	3.395	2.042	0.759
(8,4)	15.30	1.918	11.19	112	0.005	3.405	2.021	0.758

electronegativity enhances the ionic component of the Zn-O bonds, diminishing the conjugated effect of p bonding. For boron nitride NTs, however, the atomic radii of B and N are similar and hence the overlapping of p_z orbitals between B and N results in a strong delocalised π–system and a more stable structure. Zhou et al. [46] showed that the binding energies of various facetted NTs were linearly related to the ratio of the surface atoms (number of unsaturated Zn and O atoms in the surface divided by the total number of Zn and O atoms in the system) and not to the tube size.

A more detailed discussion of the results of the ZnO nanotubes DFT calculations can be found in [7].

7.1.4 ZnO Nanowires

Several methods have been employed to synthesize ZnO nanowires [49]. In particular, they were grown by a vapour-phase transport process using a gold catalyst. Zn vapour is generated by carbo-thermal or hydrogen reduction of ZnO and the size of the nanowires is controlled by the thickness of the Au film. ZnO nanowires are single-crystalline with a wurtzite structure and grow along the c-axis. ZnO NWs were also obtained by a carbo-thermal route involving the reaction of Zn oxalate or ZnO powders mixed with activated carbon or MWNTs. The nanowires obtained are single-crystalline with a wurtzite structure and have diameters of 300–400 nm, with lengths extending to tens of microns.

The majority of 1D ZnO nanowires that have been studied computationally are [0001] oriented nanowires [7]. These include hexagonal and triangular shaped nanowires, having six or three low energy $(10\bar{1}0)$ surface facets, respectively, with the c-axis of the wire oriented along the [0001] direction, see Fig. 7.9a, b.

The hexagonal nanowire structures that have been investigated include structures 1–5 as presented in Fig. 7.9a. The nanostructures are created by building a bulk ZnO structure and cleaving atoms around a virtual ring of a specific diameter (see Fig. 7.11). Structure 1 results from cleaving the atoms around the central ZnO hexagon, indicated by the smallest ring in Fig. 7.11, while structures 2–5 are created by cleaving atoms around the larger rings indicated in Fig. 7.11. The nanowire with structure 2 features is the most commonly investigated hexagonal nanowire in the DFT studies of ZnO 1D nanostructures.

The triangular nanowires that have been investigated theoretically are shown in Fig. 7.9 (structures 6, 7 and 8). Instead of cleaving atoms around a ring, the nanowire is created by cleaving along three planes aligned at 60° to each other, producing a triangular cross section. ZnO nanowires that do not have a hexagonal or triangular cross section have also been investigated and include structures 9–12 (Fig. 7.9).

The results of the DFT calculations of ZnO nanowire stability, structure and electronic properties are discussed in [7].

A number of studies have examined the relative stability of wurtzite and hexagonal nanowires. Hexagonal (wurtzite and graphitic) and zinc blende ZnO hexagonal NWs with structure 2 and 3 were investigated in [81]. All the phases are energetically less

stable than the bulk phase, with the wurtzite phase calculated to be most energetically favourable, followed by the hexagonal and then zinc blende phases. The latter two phases change order for NWs with diameters $\geq$ 1.6 nm. A comparison of the binding energies of hexagonal and triangular nanowires (structures 1, 2 and 6 in Fig. 7.9) with wurtzite or hexagonal structures, as a function of supercell length, was made in [75]. The results obtained show that both the wurtzite and hexagonal phases correspond to distinct energy minima, indicating that the phase transition from wurtzite to hexagonal phases occurs under compression. For supercell length $\geq$ 0.44 nm the NWs exist in the wurtzite phase, while for lengths $\leq$ 0.44 nm, they exist in the hexagonal phase. The hexagonal NW with structure 1 was more stable in the hexagonal phase than the wurtzite phase, while structures 2 and 6 were more stable in the wurtzite phase. An earlier study [76] of ZnO nanowires with structures 1, 2 and 3 showed a similar trend where the wurtzite phase was more stable. In particular, their results indicated that the graphitic/hexagonal phase was more stable for the smaller NWs (structures 1 and 2) while the larger NW (structure 3) was more stable in the wurtzite phase.

Table 7.4 shows the results obtained in [73] and gives a comparison of the wurtzite and hexagonal phase NWs (structures 2, 3, 6, 10) with two bi-layers along the z-direction of the supercell, showing that both phases are distinct minima, with the binding energies becoming stronger with increasing diameter. This table gives the calculated properties of NWs with the facets $(00\bar{1}0)$ forming trigonal (W1), quadrangular (W2) and two hexagonal (W3 and W4) cross sections with a diameter of 1.5–2.0 nm, which is one of the most typical growth morphologies for ZnO nanowires found in experiments. Binding energies of ZnO nanowires increase with increasing diameters from 6.752 eV per ZnO for (W1) to 6.974 eV/ZnO for (W4), and from 6.734 eV/ZnO for (W1) to 7.072 eV/ZnO for (W4).

Compared to the bulk ZnO wurtzite solid, for ZnO nanowires with the B structure, Zn(O) atoms in the side surfaces exhibit small inward (outward) relaxation and each

Table 7.4 Theoretical structural parameters and electronic and mechanical properties of the single crystal ZnO wurtzite (B) and hexagonal (H) nanowire structures studied

Wires	N	L	R	D	E_b	□	Y	Q
W1(H)	52	8.20	2.068	7.454	6.752	1.337	537.6	0.731×763
W1(B)	52	10.80	1.978	6.617	6.734	1.888	349.1	0.716×754
W2(H)	64	8.20	2.071	8.759	6.792	1.348	532.6	0.732×765
W2(B)	64	10.80	1.986	7.657	6.806	1.780	332.9	0.717×756
W3(H)	96	8.20	2.079	10.934	6.868	1.268	303.5	0.743×762
W3(B)	96	10.80	1.989	9.934	6.913	1.681	164.1	0.723×760
W4(H)	216	8.40	2.083	18.079	9.974	1.077	182.6	0.739×764
W4(B)	216	10.60	1.999	16.458	7.072	1.346	159.5	0.723×762

The number of atoms per unit cell N, optimised supercell length L(Å), the average Zn bond length R(Å), diameter D(Å), binding energy E_b (eV/ZnO), band gap □ (eV), Young modulus Y (GPa), Millicen charges Q (e) of the single-crystal ZnO nanowires, [73]. Wires 1, 2, 3 and 4 are structures 6, 10, 2 and 3, respectively, in Fig. 7.9

polar bilayer slightly expands in the direction of the wire axis. This effect results in decreases in the average bond lengths of Zn-O (1.978, 1.986, 1.989, and 1.999 Å for W1, W2, W3, and W4, respectively), which are smaller than the theoretical Zn-O bond length 2.005 Å for the bulk phase. Both the surface oxygen and zinc atoms on the first layer relax toward the bulk region with different amplitudes, forming a buckled Zn-O dimer. For H-type ZnO nanowires, Zn(O) atoms on the side surfaces exhibit inward (outward) expansion and each polar bilayer contracts in the direction of the nanowire axis, implying the flattening of the buckled wurtzite basal plane (Zn and O atoms become coplanar). This increases the average bond lengths of ZnO (2.068, 2.071, 2.079, and 2.083 Å for W1, W2, W3, and W4, respectively), which are larger than the bulk bond length of 2.005 from calculations [73]. As a result, Zn atoms sit at equal distances from O atoms along the [0001] axis and the structure acquires an additional symmetry of a mirror plane perpendicular to the [0001] axis. This process goes on while the orientation of the basal plane remains invariant.

The coordination in the H-type nanowire is fivefold, compared to the fourfold coordination in the B structure. The formation of additional bonds along the [0001] axis implies a change in the chemical bond and charge density distributions, which differ from the graphitic structure with in-plane threefold coordination. The unusual fivefold coordination in H-type nanowires that is crystallographically similar to the rock-salt structure suggests that the observed BH transformation corresponds to enhanced ionic bonding with a higher coordination. Along the [0001] axis, the H structure has the same hexagonal symmetry as the B structure. During BH transformation with contracting supercell length, the graphitic structure is an unstable transition state.

According to calculations [73], the average binding energy of the H-type ZnO wire, W1 (H), is 0.018 eV/ZnO larger than that of the B-type W1(B), i.e. the H structure of W1 is more stable than the B structure. For the W2 wire, the binding energy difference between the H and B phase structures is only 0.014 eV per ZnO, whereas the B phase becomes energetically is preferred. The difference of binding energy between the H and B phase structures is 0.045 and 0.098 eV/ZnO for W3 and W4 wires, respectively. For ZnO nanowires of larger diameters, the H-type structure would become increasingly more and more unstable. Therefore such H phase structure can be experimentally detected since the diameter of the H wire is as small as ≈2.0 nm. This may explain why so far experiments have only observed wurtzite structures in the ZnO nanowires.

The dependence of band gaps on the structure and thickness the ZnO nanowires is also presented in Table 7.4. A well-known deficiency of the standard DFT technique, is that DFT calculations significantly underestimate the band gap of ZnO systems (in calculations [73] the Γ–point band gap for the bulk ZnO wurtzite is only 0.895 eV, much smaller than the experimental band gap 3.37 eV). As the nanowire diameter increases, the band gap decreases monotonously and approaches the bulk value. This behavior is quite different from that of single-walled ZnO nanotubes that the band gap is nearly independent of tubular structures and diameters. With the same wire diameter, the band gaps of the B phase wire are larger than that of the H phase.

Mulliken population analysis shows that the charge transfer from zinc to oxygen in the B phase wires is about 0.72–0.76 e, comparable to that in the bulk ZnO wurtzite

solid. The amount of charge transfer only slightly varies with nanowire diameter. As shown in Table 7.4, the Zn-to-O charge transfer in H phase nanowires is more pronounced than that in B phase structures, suggesting that H phase nanowires are more ionic. All the ZnO nanowires studied exhibit semiconducting behavior with direct band gap.

Table 7.4 demonstrates that the computed Youngs moduli (Y) for ZnO nanowires are significantly higher than those of bulk solid (140 GPa). Although the modulus oscillates with the wire radius, it generally decreases with increasing size. The results of the Youngs moduli calculation are in accordance with the atomic force microscopy measurements of Youngs modulus for ZnO nanowires, in which the increase in the elastic modulus for the thinner wires is attributed to the surface effect. Most importantly, the calculations [73] show strong structure dependence of Y. With the same size, the H-type wires usually have higher values of Y than those of the B phases. This indicates that the H-type wires possessing a more ionic character are mechanically stronger under external tensions.

A more detailed discussion of the results obtained in numerous DFT calculations of ZnO-based nanowires stability, structure, band gaps and density is given in [7].

We conclude this section by a short description of ZnO nanotubes and nanowires relative stability, see [56, 74, 87].

The cohesive energy values for zigzag NTs $(n,0)$ with $n = 8, 10, 12, 15, 20$, as well as a ZnO graphitic layer (representing a NT with the largest diameter) were in the range from -7.10 to -7.17 eV, which was slightly larger in magnitude than their values for the ultrathin NWs with structures 1 or 6, see Fig. 7.9, but much lower in magnitude than the NWs or facetted NTs with lower surface atom ratios [7]. For NWs with high surface-atom to bulkatom ratios, NTs are energetically preferable.

The size-dependent cohesive energy $E_c(n)$ of nanowires and single-walled nanotubes of ZnO was calculated in [74, 87] where n denotes atom number per periodic unit consisting of two ZnO layers. The calculations show that, for small n, a single-walled nanotube has a lower energy than a nanowire. A crossover point near $n \approx 38$ is predicted in [74], while the crossover point at $n \approx 48$ was found in [87].

7.2 Titanium Oxide

7.2.1 Bulk and Nanolayers

Titania (TiO_2) is a well-known semiconductor with a number of promising properties and numerous technological applications comprehensively studied in materials science [88]. The number of discovered TiO_2 polymorphs is seven [89], with rutile and anatase undoubtedly prevailing in practical applications because of their higher energetic stability as compared to other titania phases [90]. These polymorphs exhibit different properties. Anatase is the most common product of low-temperature synthesis pathways, and is an important component of materials, e.g. those developed for gasphase separation and catalysis [91]. At the same time, in order to synthesize

selected samples of rutile, which is a reliable material for both the ultrathin gate oxide in field-effect transistors and the dielectric layer in capacitors for dynamic random access memory [92], a number of experimental treatment have been performed in conditions of ultra-high vacuum (UHV) with preliminary treatments (Ar^+ ion bombardment, irradiation, high temperature) [93]. Anatase transforms irreversibly to rutile at elevated temperatures. The temperature of this transformation is not unique and the processes involved in the transformation were comprehensively reviewed in [90].

The symmetry of the TiO_2 rutile structure is described by a 3D tetragonal lattice and the space group $P4_2/mnm$ with two titania formula units per primitive cell (the upper bulk models in Fig. 2.19a–d). Table 7.5 presents the results of calculations [94] compared to those obtained from both theoretical simulations and experimental neutron scattering measurements at 15 K. The first principles calculations [94] were made by the DFT-LCAO method, as implemented in the CRYSTAL09 code [23], which describes 2D slabs and 1D nanotubes in their original space form, without spurious 3D periodicity used in the alternative planewave DFT-PW method, for example, in the VASP code [95]. A new version of the crystal code CRYSTAL14 [96] also includes the NANOROD option and extends the possibilities of nanostructure calculations.

The small-core pseudopotential [98] of the Ti atom was used in titania nanotube calculations (3*s*, 3*p*, 3*d* and 4*s*-electrons were taken as valence electrons), while the all-electron BS for the O-atom was taken from [99]. It is well known that in the LCAO calculations of crystals the BS of a free atom has to be modified as the diffuse functions cause numerical problems because of the large overlap with the core functions of the neighboring atoms in a densely packed crystal [100]. To optimize the BS, the minimization method without calculations of the total energy derivatives (the method of conjugate directions, developed by Powell [101]) was used in [102]. The diffuse exponents of valence s, p and d-orbitals have been optimized for the stable anatase phase of bulk titania. Its atomic and electronic properties have been reproduced in the good agreement with the experiment (the experimental values are given in brackets): the lattice parameters a = 3.784 Å (3.782 Å) and c = 9.508 Å (9.502 Å), the dimensionless parameter for the relative position of the oxygen atom u = 0.2074 (0.2080), although the values of the gap are still less accurate, again because of being overstimated: 4.1 eV versus 3.2 eV. Any way, these results

Table 7.5 The structure and electronic properties of optimized TiO_2 bulk (rutile phase), calculated in [94]

Calculation method	Lattice parameters			Parameters of bonds and atoms				Band gap
and reference source	a,Å	c,Å	u	$r_{Ti-O(I)}$,Å	$r_{Ti-O(II)}$,Å	q_O,e	q_{Ti},e	$\Delta\varepsilon_g$,eV
PBE	4.65	2.98	0.306	1.96	2.01	−1.095	+2.19	1.74
PBE0	4.59	2.96	0.306	1.95	1.98	−1.17	+2.34	3.83
Results of other calculations	4.54–4.65	2.93–3.00	0.303–0.307	1.91–1.95	1.97–2.04	−1.00–−1.36	+2.00–+2.72	1.8–2.1
Experimental data (15 K)	4.59	2.95	0.305	1.95	1.98	–	–	3.03

The results of other calculations and experimental data are taken from [97]

for the bulk titania (anatase) agree with the experimental data better than those given in [97] for both the plane wave (PW) and LCAO calculations when one uses different exchange-correlation potentials. A certain improvement over the substantially underestimated values of the gap for the bulk anatase in the DFT PW calculations has been achieved recently [103] using the LDA+U method (2.7 eV).

Monoperiodic translation symmetry has been adopted for nanotube calculations as it was implemented in CRYSTAL09 code [23], containing also a special input option which allows the generation of 1D nanotubes from 2D slabs.

The symmetry of the TiO_2 anatase structure is described by a 3D tetragonal lattice and the space group $I4_1/amd$ with four titania formula units per tetragonal (crystallographic) cell (the upper bulk models in Fig. 2.20a–d). Table 7.6 presents the results of our calculations [102] compared to those obtained from both theoretical simulations and experimental neutron scattering measurements at 15 K. In the anatase DFT LCAO calculations the same atomic basis set and computational parameters were used as were applied in rutile calculations. Total geometry optimization was performed both in the rutile and anatase calculations.

Tables 7.5 and 7.6 demonstrate that the parameters of the rutile and anatase bulk TiO_2 structure (a, c and u) calculated using different methods show both qualitative correlation and correspondence to the experimental values, although a certain dispersion is observed of the results obtained. The same is also true for Ti–O bond lengths inside the first (I) and second (II) coordination shells.

The calculated values of the effective charges q_O and q_{Ti} as they are found to be look quite reasonable and qualitatively comparable with the corresponding data obtained earlier [97]. As to the large difference between the experimental and calculated values of band gaps $\Delta\varepsilon_g$ between the top valence band composed mainly of O(2p) states and the bottom of the conduction band with prevailing contribution from Ti(3d) states, the standard DFT calculations essentially underestimate $\Delta\varepsilon_g$ for semiconductors and insulators. It is only when the hybrid exchange-correlation functionals, like PBE0 are applied that the band gaps can be reproduced with a relatively high accuracy. To estimate the effective atomic charges on O and Ti atoms, the Mulliken population analysis was adopted.

Table 7.6 The structure and electronic properties of optimized TiO_2 bulk (anatase phase) [102]

Calculation method	Lattice parameters			Parameters of bonds and atoms				Band gap
and reference source	a,Å	c,Å	u	$r_{Ti-O(I)}$,Å	$r_{Ti-O(II)}$,Å	q_O,e	q_{Ti},e	$\Delta\varepsilon_g$,eV
PBE	3.82	9.59	0.208	1.95	2.00	−1.10	+2.20	1.98
PBE0	3.78	9.51	0.207	1.93	1.97	−1.18	+2.36	4.09
Results of other calculations	3.70–3.80	9.50–10.01	0.202–0.208	1.90–1.95	1.96–2.04	−1.00 to −1.35	+2.08–+2.69	2.1–4.5
Experimental data (15 K)	3.79	9.52	0.208	1.94	1.98	–	–	3.18

The results of other calculations and experimental data are taken from [97]

Table 7.7 Diperiodic symmetry groups and key structural parameters of four relaxed densely packed TiO_2 rutile slabs (Fig. 2.19)

Slab models (Fig. 7.1)	Method	a,Å	c,Å	Surface area, S_{slab_UC}	S_{slab_UC}, Å^2	Minimal interlayer spacing, $h_{layer}^{(min)}$	Number of atomic planes per thinnest slab layer, $n_{layer}^{(min)}$
(110), *Pmmm*	PBE	4.63	2.98	c × a $\sqrt{2}$	19.51	a/$\sqrt{2}$	3
	PBE0	4.58	2.96		19.17		
(100), $Pm2_1n$	PBE	4.67	2.97	a × c	13.86	a	6
	PBE0	4.60	2.96		13.62		
(101), $P2_1/b11$	PBE	4.64	2.98	a × $\sqrt{a^2+c^2}$	25.59	a × c/ $\sqrt{a^2+c^2}$	3
	PBE0	4.58	2.97		25.00		
(001), $P\bar{4}2_1m$	PBE	4.64	2.98	a × a	21.53	c	2
	PBE0	4.58	2.96		20.98		

The knowledge of the relative stability of densely-packed rutile and anatase slabs is important for the study of titania nanostructures. The slab models of rutile and anatase were dealt with in Chap. 2.

The following densely-packed stoichiometric titania rutile surfaces have been previously described and systematized as stable, according to the results of DFT calculations on the corresponding slab models (their hierarchy corresponds to the growth of surface energy), see Fig. 2.19: (110), (100), (101) and (001) [88, 104–107], in accordance with the Tasker's analysis applied to predicting energetic stability for the surfaces of ionic and partly ionic metal oxides [108]. To display the relative energetics of those rutile surfaces, a Wulff construction formalism [109] can be applied when constructing a possible macroscopic TiO_2 crystal terminated by the corresponding four types of facets. The relaxation of the outermost atoms on these surfaces was found to be substantial and responsible for a large reduction of the calculated surface energies as compared to the non-optimized slabs cut from a single-crystal [104].

The following densely-packed stoichiometric titania anatase surfaces have been previously described and systematized as stable, according to the results of DFT calculations on the corresponding slab models (their hierarchy corresponds to the growth of surface energy), see Fig. 2.20: (101), (100), (110) and (001). The surface energies of the two last anatase faces are very close to each other [88, 110, 111].

The layer group symmetry of the thinnest slab layers and geometry parameters of relaxed densely-packed rutile and anatase slabs are systematized in Tables 7.7 and 7.8. Here the thinnest slab layer means a $(TiO_2)_2$ layer (the bulk rutile or anatase primitive cell contains two TiO_2 formula units). The number of atomic planes in the thinnest layer depends both on the bulk titania phase (rutile or anatase) and the surface chosen. These structural data correlate well with with the model images of all

Table 7.8 Diperiodic symmetry groups and key structural parameters of four relaxed densely packed TiO_2 anatase slabs (Fig. 2.20)

Slab models (Fig. 2.20)	Method	*a*,Å	*c*,Å	Surface area, S_{slab_UC}	S_{slab_UC}, Å^2	α, degrees	Number of atomic planes per thinnest slab layer, $n_{layer}^{(min)}$
(101), *C2/m11*	PBE	3.81	5.50	c × a sinα	19.65	110.3	6
	PBE0	3.77	5.47		19.34	110.2	
(100), *Pman*	PBE	3.78	9.54	a × c	36.06	90	1
	PBE0	3.76	9.51		35.76	90	
(110), *P112/b*	PBE	5.45	5.49	c × a sinα	25.84	120.1	2
	PBE0	5.38	5.46		25.49	119.9	
(001), *Pmmb*	PBE	3.77	3.84	a × c	14.48	90	6
	PBE0	3.71	3.80		14.10	90	

the slabs (see Figs. 2.19 and 2.20) and give detailed information on the morphology of all the surfaces.

We define the surface areas of slab unit cells S_{slab_UC} depending on the lattice parameters a and c. The numbers of atomic planes in minimal repeating layer units $n_{layer}^{(min)}$ are also given in Tables 7.7 and 7.8. These parameters describe the morphological peculiarities of four types of densely-packed rutile and anatase surfaces.

The convergence of the surface energies for all types of densely–packed slabs is demonstrated in Tables 7.9 and 7.10 using the slabs with 12, 20 and 32 formula units per surface unit cell. These slabs consist of 6, 10 and 16 thinnest slab layers, respectively.

The converged results of PBE and PBE0 calculations [94] performed on (110), (100), (101) and (001) rutile slabs of large thickness (corresponding to $N_{FU} = 32$) are systematized in Table 7.11, where they are compared between themselves and with the results of other ab initio calculations performed using different DFTmethods, see [104–107]. The relaxation of all the slab models is estimated when comparing the minimal inter-layer spacings near either the surface $h_{layer}^{(s)}$ or the mirror plane $h_{layer}^{(m)}$ in slabs with optimized geometry (Table 7.11). It has been found that $h_{layer}^{(s)}$ (s) is larger than $h_{layer}^{(m)}$ in (110) and (100) slabs, while in the other two slab types the surface layer is compressed, in accordance with the results of recent simulations [107]. The growth of slab thickness leads to the averaged optimized thickness approaching that in non-relaxed slab cut from bulk, i.e., $h_{layer}^{(m)} \rightarrow h_{layer}^{(o)}$. The effective charges on both O and Ti atoms positioned on either surface ($q_O^{(s)}$ vs. q_{Ti}^{s}) or mirror plane ($q_O^{(m)}$ vs. q_{Ti}^{m}) of 96-atom unit cells UCs per slab have been also compared (Table 7.11), the latter practically coincide with those in the rutile bulk. However, the effective charges of surface O and Ti atoms are certainly smaller than those in bulk, due to a smaller coordination number with the adjacent atoms, depending on the slab morphology, which

Table 7.9 Results of our PBE and PBE0 calculations on surface energies (E_{surf}) for four densely-packed types of relaxed TiO_2 **rutile** slabs (Fig. 2.19) containing 12, 20 and 32 formula units per surface unit cell (UC) and their comparison with the corresponding data obtained in previous DFT calculations

Slabs, computational method and verification			N_{FU} per UC	Atomic planes per slab	E_{surf}, J/m^2	N_{FU} per UC	Atomic planes per slab	E_{surf}, J/m^2	N_{FU} per UC	Atomic planes per slab	E_{surf}, J/m^2
(110), *Pmmb*	[94]	PBE	12	18	0.66	20	30	0.69	32	48	0.70
		PBE0			0.68			0.73			0.74
	literature*	LDA or GGA			0.42[c]			0.60[b]			0.89[a]
		DFT+HF			0.48[d]			0.55[c]	–		
(100), $Pm2_1n$	[94]	PBE		36	0.98	60		1.00		96	1.01
		PBE0			1.05			1.04			1.04
	literature*	LDA or GGA			0.69[c]			0.71[b]			1.12[a]
		DFT+HF			0.83[c]			–			–
(101), $P2_1/b11$	[94]	PBE		18	1.34		30	1.35		48	1.35
		PBE0			1.45			1.46			1.46
	literature*	LDA or GGA			1.05[b]			1.39[a]			
(001), $P\bar{4}2_1m$	[94]	PBE		12	1.59		20	1.60		32	1.60
		PBE0			1.65			1.70			1.70
	literature*	GGA			1.38[b]			1.36[c]			1.65[a]
		DFT+HF			–			1.59[c]			–

All the slabs considered consist of even number of atomic planes
*References [a, b, c] and [d] correspond to [104], [105], [106], [107], respectively

Table 7.10 Results of our PBE and PBE0 calculations on surface energies (E_{surf}) for four densely-packed types of relaxed TiO_2 anatase slabs (Fig. 2.20) containing 12, 20 and 32 formula units per surface unit cell (UC) and their comparison with the corresponding data obtained in previous DFT calculations

Slabs, computational method and verification			N_{FU} per UC	Atomic planes per slab	E_{surf}, J/m^2	N_{FU} per UC	Atomic planes per slab	E_{surf}, J/m^2	N_{FU} per UC	Atomic planes per slab	E_{surf}, J/m^2
(101), *C2/m11*	[94]	PBE	12	36	0.73	20	60	0.74	32	96	0.74
		PBE0			0.77			0.78			0.78
	literature*	LDA or GGA			0.49[b]						
		DFT+HF			0.61[a]				–		
(100), *Pman*	[94]	PBE		12	0.84		20	0.86		32	0.87
		PBE0			0.89			0.92			0.93
	literature*	LDA or GGA			0.58[b]						
		DFT+HF			0.82[a]			–			–
(110), *P112/b*	[94]	PBE		12	1.35		20	1.37		32	1.38
		PBE0			1.46			1.49			1.49
	literature*	LDA or GGA			1.15[b]						
		DFT+HF			1.25[a]			–			–
(001), *Pmmb*	[94]	PBE		36	1.31		60	1.37		96	1.38
		PBE0			1.48			1.54			1.57
	literature*	LDA or GGA			0.98[b]						
		DFT+HF			1.25[a]			–			–

All the slabs considered consist of an even number of atomic planes

*References [a, b] correspond to [111] and [110], respectively

Table 7.11 Results of PBE and PBE0 calculations on geometry and electronic properties for four densely-packed types of relaxed TiO_2 rutile slabs (Fig. 2.19) containing 32 formula units per surface unit cell and their comparison with the corresponding data obtained in previous DFT calculations

Slabs, number of the atomic planes in them, computational				Thicknesses of slab layers, Å		Charges on surface and mirror plane atoms, e				Band gaps
				$h_{layer}^{(s)}$	$h_{layer}^{(m)}$	$q_O^{(s)}$	$q_{Ti}^{(s)}$	$q_O^{(m)}$	$q_{TI}^{(m)}$	$\Delta\varepsilon_g$, eV
(110)	[94]	48	PBE	3.35	3.29	−0.95	+2.17	−1.10	+2.19	1.75
			PBE0	3.30	3.23	−1.02	+2.31	−1.17	+2.33	3.83
	literature*	LDA or		$\Delta h^{(s-m)}$		−0.93[d]	+2.18[d]	−1.11[d]	+2.22[d]	2.1[d]
		GGA		≈0.08[d,**]						
		DFT+HF		$\Delta h^{(s-m)}$		−1.00[c]	+2.31[c]	−1.20[c]	+2.32[c]	3.96[c]
				≈0.07[c,**]						3.60[d]
(100)	[94]	96	PBE	4.68	4.64	−1.00	+2.14	−1.10	+2.19	1.77
			PBE0	4.61	4.58	−1.07	+2.29	−1.17	+2.34	3.85
	literature*	LDA or GGA				−0.97[d]	+2.13[d]	−1.11[d]	+2.22[d]	2.0[d]
		DFT+HF		$\Delta h^{(s-m)}$ ≈0.03[c,**]		–	–	–	–	3.60[d]
(101)	[94]	48	PBE	2.49	2.51	−1.00	+2.13	−1.10	+2.19	1.79
			PBE0	2.45	2.48	−1.07	+2.27	−1.17	+2.34	3.86
	literature*	LDA or GGA		–		–	–	–	–	–
(001)	[94]	32	PBE	2.90	2.99	−1.05	+2.06	−1.10	+2.19	1.78
			PBE0	2.86	2.97	−1.13	+2.20	−1.17	+2.34	3.85
	literature*	GGA		$\Delta h^{(s-m)}$ ≈0.08[d,**]		−1.06[c]	+2.07[c]	−1.11[c]	+2.22[c]	2.0[d]
		DFT+HF		$\Delta h^{(s-m)}$ ≈0.13[c,**]		–	–	–	–	2.9[d]

* [a] correspond to [104]
[b] correspond to [105]
[c] correspond to [106]
[d] correspond to [107], respectively
** $\Delta h^{(s-m)} = h_{layer}^{(s)} - h_{layer}^{(m)}$

also confirm published results [107]. Hierarchy of surface energies calculated for all the four slabs of different thickness (Table 7.9) completely confirms the conclusions drawn earlier [104–107], whereas the growth of slab thickness results in the corresponding surface energies approaching certain limits. Thus, (110) is the energetically most stable surface while (001) is only marginally stable [104]. The calculations [94] also yield the estimate of band gap depending on the slab morphology and thickness. The thinner are the slabs, the larger are the values of $\Delta\varepsilon_g$, calculated using both PBE and PBE0 methods, which approach those for the rutile bulk with increasing slab thickness. Band gaps are qualitatively similar for slabs containing the same number of formula units per surface unit cells (N_{FU}), irrespective of slab morphology.

Obviously, the results discussed in this section are important not only in terms of verification, confirming as they do the validity of models and computational procedure used, and mainly in terms of further understanding of both the construction of four-facetted TiO_2 nanowires and, even, the possible mechanism of their growth upon the substrate.

7.2.2 Rolled-Up Single- and Double-Wall TiO_2 Nanotubes with Hexagonal Morphology

TiO_2-based nanotubes (NTs) of different morphology have been systematically synthesized and carefully studied as promising technological materials [112, 113]. One of the recently discovered nanotube applications was the doping of TiO_2 NTs by boron and nitrogen atoms [114] gradually varying their band gaps.

In most theoretical simulations on titania nanotubes, the model $3D \longrightarrow 2D \longrightarrow 1D$ of structural transformations described in [115] was applied, i.e., the bulk ($3D$) phase first formed a lamellar product ($3D \longrightarrow 2D$) and then was bent and rolled to a nanotubular form ($2D \longrightarrow 1D$). The lamellar product was mainly formed by anatase (101) surface, identified as prevailing in TiO_2 NTs [103, 116–119]. A further geometry optimization of the 3-layer O-Ti-O sheet for the $2D \longrightarrow 1D$ transition results in the formation of titania nanotubes possessing hexagonal fluorite-like (111) morphology with (n,n) and (n,0) chiralities [120]. In reality this hexagonal structure can only exist in the metastable phase of bulk titania under extremely high pressure [89].

Theoretical simulations on TiO_2 nanosheets originating from the three-layer O–Ti–O model were widespread as simpler systems for simulations [118]. When the structures of a 3-layer (101) slab cut from anatase bulk were being optimized only the structure of the (111) fluorite-type slab was recently obtained [120], which exhibits six-fold coordinated titanium atoms, and two-fold coordinated oxygens. The three-layer nanosheets cut from the fluorite phase of the bulk TiO_2 (the space group 225 $Fm\bar{3}m$) have the symmetry of the layer group 72 $P\bar{3}m1$, see Table 7.12.

Using the rolling up correspondence of the line and layer groups (see Table 2.10) one obtains line groups for special chiralities of graphene, BN and TiO_2 nanotubes (see Table 7.12). The corresponding isogonal point groups $\mathbf{P}_I$ and line groups for general chiralities (n_1, n_2) are also given in Table 7.12.

The first principles LCAO calculations on hexagonal titania nanosheets and nanotubes were performed in [102] using the hybrid Hartree-Fock/Kohn-Sham exchange-correlation functional (PBE0). TiO_2 sheets with a thickness of a few atomic layers were found to be remarkably stable [121].

The main results obtained by means of the LCAO PBE0 calculations [102] for this slab are compared with the corresponding bulk properties of the titania anatase phase in Table 7.13. The relaxation energy for the 3-layer TiO_2 slab cut from the anatase bulk and transformed into (111) fluorite-type morphology is really large, while its surface and formation energies are qualitatively similar to those calculated earlier [103, 121]. Since the optimized 3-layer slab has a hexagonal structure, its parameters cannot be compared directly with those for the titania anatase bulk.

Table 7.12 Line symmetry groups of SW BN and TiO_2 nanotubes rolled up from hexagonal nanosheets

Object	Space group for C, BN and TiO_2 bulk	Layer	Layer group	Line groups for special chiralities[a]	$\mathbf{P}_l$	Line groups for general chiralities (n_1, n_2)
Graphene, monolayer	194 $P6_3/mmc$	(0001)	80($P6/mmm$)	13i $(2n)_n/mcm$	$\mathbf{D}_{2nh}$	5 n_q22($\mathbf{D}_q$)
BN, monolayer	194 $P6_3/mmc$	(0001)	78($P\bar{6}m2$)	$4h(2n)_n/m$ $8g(2n)_nmc$	$\mathbf{C}_{2nh}$ $\mathbf{C}_{2nv}$	1 n_q($\mathbf{C}_q$)
3-layer TiO_2 slab (fluorite)	225 $Fm\bar{3}m$	(111)	72($P\bar{3}m1$)	$4h(2n)_n/m$ $8g(2n)_nmc$	$\mathbf{C}_{2nh}$ $\mathbf{C}_{2nv}$	1 n_q($\mathbf{C}_q$)

For comparison, the layer group of graphene is added
[a]Special chiralities: $g(n,0)$, $(0,n)$, $(-n,n)$; $h(n,n)$, $(-n,2n)$, $(-2n,n)$
$i(n,0)$, $(0,n)$, $(-n,n)$, (n,n), $(-n,2n)$, $(-2n,n)$

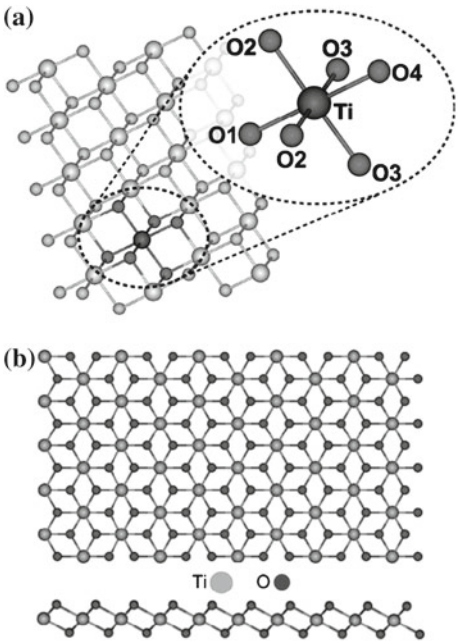

Fig. 7.12 6-fold coordination of Ti atoms in a stoichiometric three-layer *hexagonal* titania nanosheet (**a**) and its *top* and *cross-sectional* images (**b**)

Three-layer titania nanosheets with a hexagonal fluorite-like (111) structure can be rolled up to 3-layer titania SW NTs with (i) armchair-type (n,n) chirality and (ii) zigzag-type (n,0) chirality. The structural and electronic properties of several hexagonal three-layer titania nanotubes are given in Table 7.14. The optimized structures of four selected nanotubes of both chiralities (two nanotube models per each chirality) are shown in Fig. 7.13.

Table 7.13 The atomic and electronic structure of the optimized TiO_2 anatase bulk versus the fluorite-like (111) titania slab [102]

Models of TiO_2 bulk and sheets	Lattice parameters Å		Thickness h_{NT} (Å)	Bond length d_{Ti-O}[a]				Effective charge q_{Ti}[b](e)	E_{relax} per TiO_2 unit, eV	E_{surf} J/m^2	$\Delta\varepsilon_{gap}$ eV
	a	c		Ti − O1	Ti − O2	Ti − O3	Ti − O4				
Bulk	3.78	9.51	–	1.935	1.935	1.973	1.973	2.35	–	–	4.09
3-layer (fluorite-like)	2.96	–	1.92	1.95	1.96	1.97	1.98	2.45	–6.05	0.44	4.89

[a] The corresponding bonds are shown in Fig. 7.12

[b] Averaged effective charges q_O are twice smaller than q_{Ti}, with the opposite sign

As to the Ti-O bond lengths, their deformation is more noticeable for smaller values of d_{Ti-O}, gradually approaching those in a three-plane nanosheet, see Table 7.13. Obviously, this is also true for the convergence of E_{relax} with D_{NT} increasing (Table 7.14). The strain energies and band gap dependence on D_{NT} for all the four sets of three-layer TiO_2 NTs is shown in Figs. 7.14 and 7.15, respectively.

The range of nanotube diameters considered is sufficiently large, from 0.5 to 4.0 nm, with the number of atoms per NT unit cell increased from 30 to 288. The calculations with the total geometry optimization for a total of 20 one-periodic models of TiO_2 NTs of different morphologies were performed in [102].

The two curves $E_{strain}(D_{NT})$ shown in Fig. 7.14 for two chiralities of titania nanotubes confirm the conclusions drawn above from Table 7.14. When the diameters of nanotubes increase up to 40 Å all the strain energies substantially decrease and approach each other. One expects that a further increase of D_{NT} can result in slightly smaller values of E_{strain} for 3-layer nanotubes. In three-layer nanotubes of similar diameters, the difference of the strain energies for fluorite-type (n,n) and (n,0) chiralities is fairly negligible, which supports qualitatively similar results obtained earlier for these types of nanotubes [103, 116, 118]. Figure 7.15 presents $\Delta\varepsilon_{gap}$ dependence on D_{NT}. When nanotube diameters markedly increase, their band gaps $\Delta\varepsilon_{gap}$ asymptotically approach those for the corresponding 2D slabs (Table 7.13), in a similar way to hexagonal. However, the nanotube diameters considered are too small for a direct comparison with the slabs.

The line symmetry group $L_2 = Z_2P_2$ of a double-wall (DW) nanotube can be treated as an intersection of the symmetry groups L_0 and L_1 of its single-wall constituents, see Sect. 2.5 and [122, 123]. The coaxial hexagonal DW NTs $(n_1, n_1)@(n_2, n_2)$ and $(n_1, 0)@(n_2, 0)$ are commensurate; the translation period of such DW NTs is the same as for their constituents.

Table 7.15 gives the symmetry of commensurate DW TiO_2 NTs with hexagonal morphology, including both multiple DW nanotubes (armchair (n,n)@M(n,n) and zigzag (n,0)@M(n,0), part a), and nonmultiple DW nanotubes containing arbitrary SW constituents (armchair $(n_1, n_1)@(n_2, n_2)$ and zigzag $(n_1 0)@N(n_2, 0)$, part b).

LCAO PBE0 calculations of DW TiO_2 nanotubes with hexagonal morphology are made in [124] and allow one to compare their properties with those of the corresponding single-wall nanotubes. The calculations were performed using the CRYSTAL-09 computer code [23] and the HELIX option, which takes into account only rototranslational symmetry. As seen from Table 7.15, the DW NTs under consideration have twice more symmetry operations than the order of the rotohelical axis (reflections in vertical or horizontal planes are added to the rotohelical rotations). Using the TESTGEOM-NANOTUBE option as foreseen in the CRYSTAL-09 code, all the atomic coordinates in the monoperiodic unit cell were generated from 2D slabs for both constituent SW NTs separately. Added to the input, they describe the initial DW NT atomic coordinates.

The calculations of double-wall nanotubes that have large unit cells (containing up to 288 atoms in the case of (12,0) @ (36,0) and TiO_2 NTs) were performed using the full exploitation of the helical rototranslational symmetry. The coordinates of all the atoms in the nanotube unit cells were allowed to relax when the optimization procedure was performed.

Table 7.14 The structural and electronic properties of hexagonal 3-layer TiO_2 NTs (definitions of values are the same as in Tables 7.2–7.4)

Chirality of nanotube	N_A	l_{NT}, Å	D_{NT}, Å	h_{NT}, Å	d_{Ti-O}, Å				q_{Ti}, e	E_{relax}, per TiO_2, eV	E_{strain}, per TiO_2 kJ/mol	$\Delta\varepsilon_{gap}$, eV
					Ti − O1	Ti − O2	Ti − O3	Ti − O4				
$(2n)_n/m$ *group*-$\mathbf{C}_{2n,h}$ (*family* 4)												
(6,6)	36	2.991	10.06	1.86	1.89	1.94	2.00	2.05	2.42	−0.09	46.18	4.66
(9,9)	54	2.98	14.88	1.89	1.91	1.94	1.99	2.02	2.43	−0.05	20.11	4.74
(12,12)	72	2.97	19.73	1.91	1.935	1.95	1.98	1.995	2.44	−0.04	11.26	4.77
(15,15)	90	2.97	24.61	1.91	1.94	1.95	1.98	1.99	2.45	−0.04	7.20	4.79
(18,18)	108	2.97	29.51	1.91	1.945	1.955	1.97	1.98	2.45	−0.03	5.04	4.80
$(2n)_nmc$ *group*-$\mathbf{C}_{2n,v}$ (*family* 8)												
(8,0)	48	5.065	8.17	1.83	1.89	1.94	1.955	2.135	2.40	−0.33	76.43	4.65
(12,0)	72	5.10	11.70	1.88	1.915	1.945	1.96	2.03	2.43	−0.09	33.71	4.70
(18,0)	108	5.12	17.23	1.90	1.935	1.95	1.965	1.965	2.44	−0.05	14.93	4.75
(24,0)	144	5.12	22.88	1.91	1.94	1.95	1.97	1.985	2.45	−0.04	8.55	4.79
(30,0)	180	5.125	28.55	1.92	1.945	1.955	1.975	1.98	2.45	−0.04	5.52	4.82

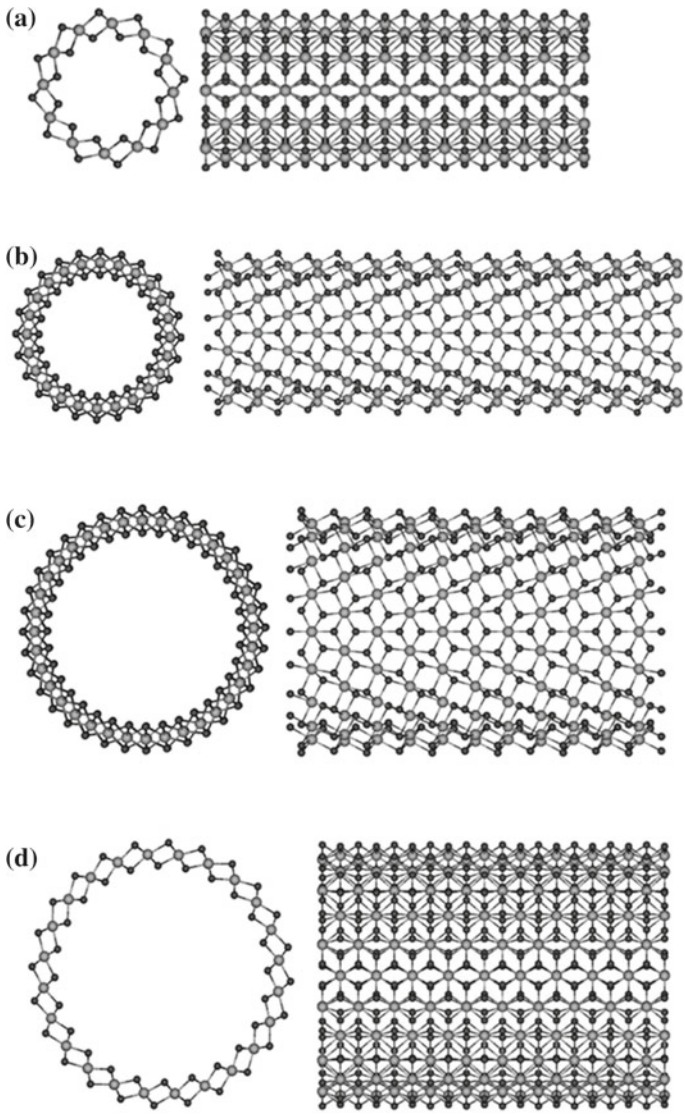

Fig. 7.13 Cross-sectional (*across*) and lateral (*aside*) images of hexagonal single-wall TiO_2 nanotubes with different chiralities and diameters. **a** Across and aside images of optimized 3-layer (6,6) TiO_2 NT with $D_{NT} = 1.01$ nm. **b** Across and aside images of optimized 3-layer (12,0) TiO_2 NT with $D_{NT} = 1.17$ nm. **c** Across and aside images of optimized 3-layer (18,0) TiO_2 NT with $D_{NT} = 1.72$ nm. **d** Across and aside images of optimized 3-layer (12,12) TiO_2 NT with $D_{NT} = 1.97$ nm

Two different commensurate DWNTs can be constructed from a given pair of SW NTs rolled up from the hexagonal sheets of TiO_2. There is no second-order symmetry axis perpendicular to the TiO_2 layers under consideration. This means that the rotation through 180° around the U axis, normal to the nanotube translation

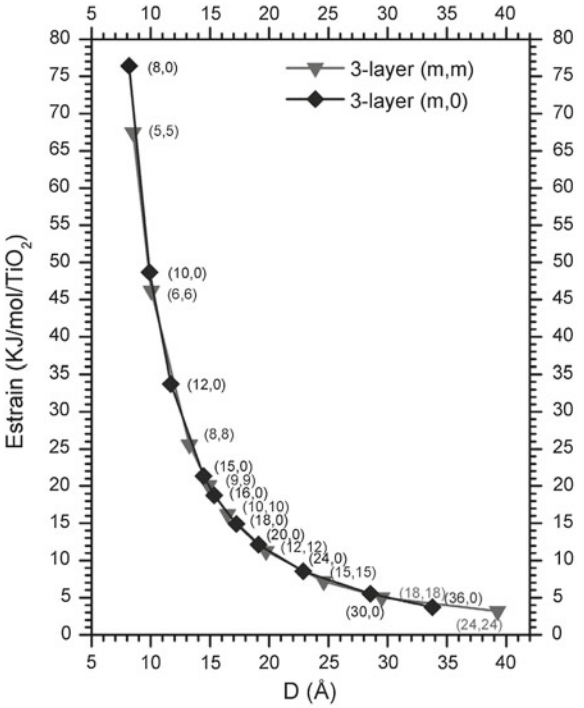

Fig. 7.14 Strain energies E_{strain} versus D_{NT} for the two sets of single-wall TiO_2 nanotubes with various chiralities

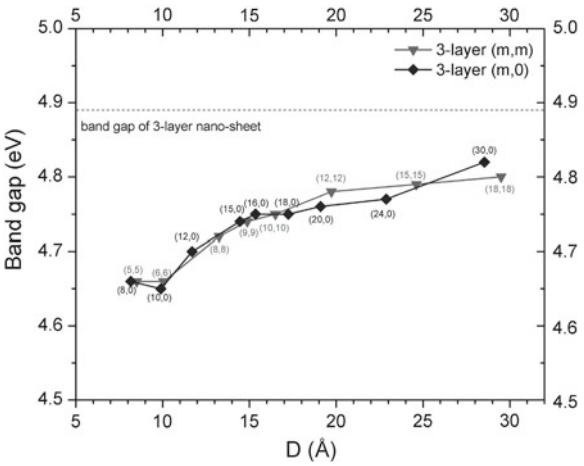

Fig. 7.15 Band gaps $\Delta\epsilon_{gap}$ versus D_{NT} for the two sets of single-wall TiO_2 nanotubes with various chiralities

Table 7.15 Symmetry of DW TiO_2 NTs with hexagonal morphology

(a) Multiple double—wall nanotubes $(n_1, n_1)@M(n_1, n_1)$ and $(n_1, 0)@M(n_1, 0)$				
DW NT chiralities	Multiple divisor M	Line group	Point group	Substance
(4,4)@(8,8)	2	$4/m$	$\mathbf{C}_{4h}$	BN
(4,4)@(12,12)	3	$8_4/m$	$\mathbf{C}_{8h}$	TiO_2
(5,5)@(10,10)	2	$\overline{10}$	$\mathbf{C}_{5h}$	BN
(6,6)@(12,12)	2	$6/m$	$\mathbf{C}_{6h}$	BN, TiO_2
(6,6)@(18,18)	3	$12_6/m$	$\mathbf{C}_{12h}$	TiO_2
(7,7)@(14,14)	2	$\overline{14}$	$\mathbf{C}_{7h}$	TiO_2
(8,8)@(16,16)	2	$8/m$	$\mathbf{C}_{8h}$	TiO_2
(8,8)@(24,24)	3	$16_8/m$	$\mathbf{C}_{16h}$	TiO_2
(9,9)@(18,18)	2	$\overline{18}$	$\mathbf{C}_{9h}$	BN
(6,0)@(12,0)	2	$6\,mm$	$\mathbf{C}_{6v}$	BN
(7,0)@(14,0)	2	$7\,m$	$\mathbf{C}_{7v}$	BN
(8,0)@(16,0)	2	$8\,mm$	$\mathbf{C}_{8v}$	BN, TiO_2
(8,0)@(24,0)	3	$16_8\,mc$	$\mathbf{C}_{16v}$	TiO_2
(9,0)@(18,0)	2	$9\,m$	$\mathbf{C}_{9v}$	BN, TiO_2
(10,0)@(20,0)	2	$10\,mm$	$\mathbf{C}_{10v}$	BN, TiO_2
(12,0)@(24,0)	2	$12\,mm$	$\mathbf{C}_{12v}$	BN, TiO_2
(12,0)@(36,0)	3	$24_{12}\,mc$	$\mathbf{C}_{24v}$	TiO_2
(b) Multiple double—wall nanotubes $(n_1, n_1)@M(n_2, n_2)$ and $(n_1, 0)@M(n_2, 0)$				
DW NT chiralities	Common divisor N	Line group	Point group	Substance
(4,4)@(9,9)	1	m	$\mathbf{C}_s$	BN
(6,6)@(10,10)	2	$4_2/m$	$\mathbf{C}_{4h}$	BN
(12,0)@(28,0)	4	$8_4\,mc$	$\mathbf{C}_{8v}$	TiO_2

vector, is not a symmetry operation and the SW rotated NT cannot be superimposed onto the original one by any rototranslational operation. When rotating one of the constituents (for example the outer shell) around the U axis, one obtains an inversed DW NT structure, which is different from the straight structure initially constructed by the folding procedure. If the U axis belongs to the one of the existing (common) mirror planes σ_h or σ_v, the total symmetry of DW NT is unaffected. For TiO_2 DW NT, the U axis should pass through the Ti atom and can coincide with the x-axis.

The binding energy E_{bind} between the constituent shells of a double-wall nanotube was chosen as a criterion for nanotube stability, see 7.2.

$$-E_{bind}\left(D_{NT}^{in}@D_{NT}^{out}\right) = E_{tot}\left(D_{NT}^{in}@D_{NT}^{out}\right) - E_{tot}\left(D_{NT}^{in}\right) - E_{tot}\left(D_{NT}^{out}\right) \quad (7.2)$$

where E_{tot} is the calculated total energy of the DW NT and its constituent SW NTs with optimized structure. Also estimated were the relaxation energies E_{relax}

(the difference between the total energies of the DW NT before and after geometry optimization) which are usually large for the small values of ΔR_{NT} and D_{NT}^{in}.

Unlike DW BN NTs, *ab initio* simulations on double-wall titania nanotubes are few.

Tables 7.16 and 7.17 present the results of the first ab initio LCAO calculations [124] on titania DW nanotubes (see also Figs. 7.17 and 7.18). Owing to the electroneutrality of each O-Ti-O shell of DW TiO_2 NTs, the inter-wall polarization effects in DW TiO_2 NTs are much less noticeable than in zz-DW BN NTs. This is why only straight configurations for both ac- and zz-chiralities of double-wall titania nanotubes with hexagonal morhphology were considered in [124].

Tables 7.16 and 7.17 contain data obtained in the calculations of DW TiO_2 NTs. Combining the latter with the binding energy curves $-E_{bind}(\Delta R_{NT})$ for titania nanotubes of both chiralities one can localize the minima of $-E_{bind}(D_{NT})$ functions which correspond to (6,6)@(12,12) and (10,0)@(20,0) configurations with inter-wall ΔR_{NT} distances 4.6–4.8 Å (ΔR_{NT} is defined as a difference between the radii of middle Ti subshells). Meanwhile, when ΔR_{NT} in DW TiO_2 NTs was reduced below the optimal values ($\leq 4.1 - 4.3$) Å structural overstrains were observed, much larger than in DW BN NTs. This is especially true for ac-nanotubes of titania (4,4)@(8,8), (6,6)@(10,10), (5,5)@(10,10), and (6,6)@(11,11), where geometry optimization resulted in the destruction of double-wall morphology and the formation of complicated nonhexagonal quasi-single-wall morphology. The binding energies estimated per formula unit for the optimal configurations of hexagonal DW NTs are considerably larger for titania as compared to boron nitrides, while the reliefs of min-

Table 7.16 The structural and electronic properties of optimized DW TiO_2 NTs

DW NT chirality indices	Initial ΔR_{NT} Å	Optimized ΔR_{NT} Å	Initial D_{NT}^{in} Å	Optinized D_{NT}^{in} Å	$E_{relaxed}$ (eV) per TiO_2 formula unit	E_{bind} (kJ/mol) per TiO_2 formula unit	Band gap $\Delta\varepsilon_{gap}$ [a] (eV)
$(n1, n1)$@$(n2, n2)$nanotubes							
(6,6)@(12,12)	4.84	4.76	10.06	10.13	−0.07	1.71	3.00[i]
(7,7)@(14,14)	5.66	5.62	11.66	11.69	−0.05	1.08	3.19[i]
(4,4)@(12,12)	6.31	6.30	7.12	7.12	−0.23	0.09	3.90[i]
(8,8)@(16,16)	6.48	6.48	13.26	13.27	−0.02	0.07	3.40[i]
(6,6)@(18,18)	9.73	9.70	10.06	10.09	−0.05	0.001	3.04[i]
(8,8)@(24,24)	13.00	12.99	13.26	13.27	−0.02	0.0001	3.49[i]
$(n1, 0)$@$(n2, 0)$nanotubes							
(8,0)@(16,0)	3.61	3.81	8.16	8.25	−0.81	−1.02	2.94[i]
(9,0)@(18,0)	4.10	4.33	9.02	8.94	−0.32	1.59	3.08[i]
(10,0)@(20,0)	4.59	4.62	9.90	9.92	−0.07	2.17	3.21[d]
(12,0)@(24,0)	5.59	5.48	11.41	11.73	−0.04	0.45	3.31[d]
(12,0)@(28,0)	7.36	7.10	11.41	11.69	−0.04	0.04	3.35[d]
(12,0)@(36,0)	9.33	9.34	11.41	11.69	−0.03	0.001	3.38[d]

[a] Indirect and direct gaps are superscripted as [i] and [d], respectively

Table 7.17 Ionic charges (q) and bond populations (p) for DW TiO_2 NTs

Nanotube configuration versus charge plot in Fig. 7.6	Outer shell				Inner shell			
	q_{O-out}[a] (e)	q_{Ti} (e)	q_{O-in}[b] (e)	p_{Ti-O}[c] (e)	q_{O-out}[a] (e)	q_{Ti} (e)	q_{O-in}[b] (e)	p_{Ti-O}[c] (e)
ac-(6,6)@(12,12)—(a)	−1.250	2.445	−1.200	0.051	−1.162	2.426	−1.257	0.056
ac-(8,8)@(24,24)—(b)	−1.241	2.457	−1.216	0.054	−1.178	2.434	−1.256	0.060
zz-(10,0)@(20,0)—(c)	−1.250	2.445	−1.198	0.048	−1.160	2.425	−1.258	0.047
zz-(12,0)@(36,0)—(d)	−1.236	2.444	−1.205	0.062	−1.173	2.431	−1.258	0.052

[a] Effective charge q_{O-out} of external shell layer (Fig. 13.6)
[b] Effective charge q_{O-in} of internal shell layer (Fig. 13.6)
[c] Averaged in-wall Ti–O bond population

ima on $-E_{bind}(\Delta R_{NT})$ curves are sharper for titania. Obviously, this is caused by a substantially larger ionic contribution to interwall interaction between the titania SW constituents (Table 7.17). In both cases, the double-wall nanotube configurations with zz-chirality are energetically more favorable compared to those with ac-chirality. As with DW BN NTs, the small values of ΔR_{NT} and D_{NT} in Table 7.16 accompanied by the large values of E_{relax} result in the instability of DW TiO_2 NTs, while the large values of ΔR_{NT} correspond to cases when the interaction within the pairs of the constituent SW NTs is almost negligible. As with to DW BN NTs, E_{bind} is rather negligible (Table 7.16).

The straightly stacked configurations for both ac- and zz chiralities of DW TiO_2 NTs with hexagonal morhphology (panels a and b of Fig. 7.16, respectively) were calculated in [124]. Unlike DW BN NTs, no permutation of Ti and O atoms occurs in the case of inverted configurations. In ac-DW TiO_2 NTs, such an inversion means the angular reorientation of O-Ti-O shells (Fig. 7.16a), which does not cause any noticeable rearrangement of the intershell bonding. A similar conclusion can also be drawn for the zz-DW TiO_2 NT, although the interwall polarization causes the Δz shift when the cross section of the nanotube contains Ti and O atoms belonging to different shells (Fig. 7.16b).

It was found in [124] that the binding energies estimated per formula unit for the optimal configurations of hexagonal DW NTs are considerably larger for titania as compared to boron nitrides. Obviously, this is caused by a substantially larger ionic contribution to the interwall interaction between the titania SW constituents. In both cases, the double-wall nanotube configurations with zz-chirality are energetically more favorable than those with ac-chirality. As with DW BN NTs, the small values of ΔR_{NT} and $D_{NT}{}^{in}$ (Table 7.16) accompanied by the large values of E_{relax} result in the instability of DW TiO_2 NTs, while the large values of ΔR_{NT} correspond to an almost negligible interaction within the pairs of constituent SW NTs. As with DW BN NTs, E_{bind} for titania nanotubes is sensitive to ΔR_{NT}, while the influence of $D_{NT}{}^{in}$ on E_{bind} is rather negligible (Table 7.16).

The comparison of the difference electronic charge redistributions drawn for both optimal and increased values of ΔR_{NT} within ac- and zz-DW NTs (both BN and TiO_2) [124] demonstrates higher electron density localization within the latter

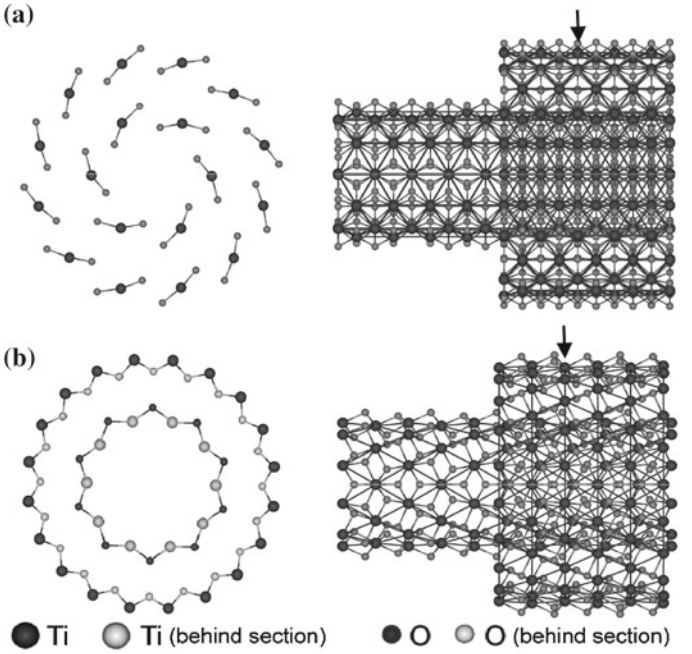

Fig. 7.16 Cross sections and lateral images of hexagonal DW TiO_2 NTs (i.e., *left* and *right* parts of models **a** and **b**, respectively) corresponding to optimized diameters for armchair and zigzag chiralities. For zz-DW TiO_2 NTs (model b), the atoms of the nearest ring behind the cross section are shown as *half-shaded balls*. The *arrows* above each lateral image are shown twice as long as the directions of the *cross sections*. For convenience, the lateral images of the *inner shells* of the nanotubes are shown as twice as long as those of the *outer shells*. **a** optimized model of double-wall (6,6)@(12,12) *ac*-TiO_2 NT. **b** optimized model of double-wall (10,0)@(20,0) *zz*-TiO_2 NT

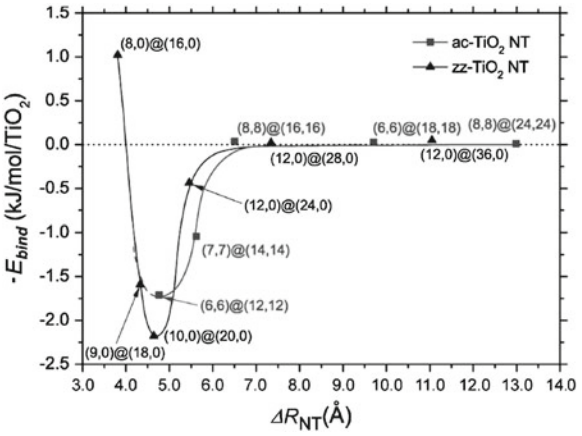

Fig. 7.17 Binding energies E_{bind} versus ΔR_{NT} for the two sets of DW TiO_2 NTs with ac- and zz-chiralities. Spline treatment of the curves was performed to make them smooth

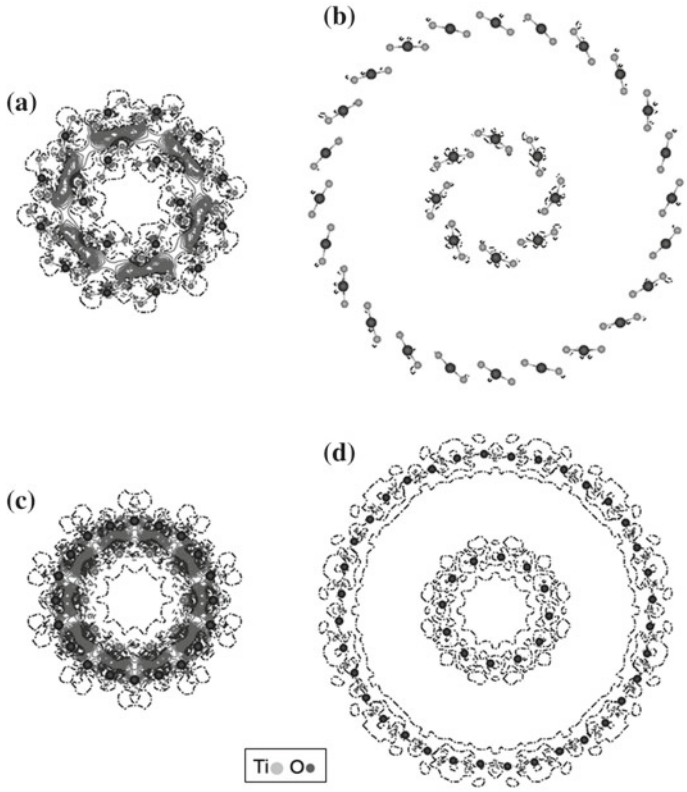

Fig. 7.18 Difference electron density plots $\Delta\rho(r)$ of DW TiO_2 NTs calculated for the cross sections of nanotubes depicted in Fig. 7.16: **a** (6,6)@(12,12), **b** (8,8)@(24,24), **c** (10,0)@(20,0), **d** (12,0)@(36,0). The *solid*, *dashed* and *dot-dashed* isolines describe positive, negative and zero values of the difference density, respectively. Isodensity curves are drawn from −0.001 to + 0.001 e $Å^{-3}$ with increments of 0.00004 e $Å^{-3}$

(especially for armchair-type nanotubes),while the comparison of the results presented in Table 7.17 show a noticeably higher bond ionicity in DW TiO_2 NTs. The bond populations between the shells in DW TiO_2 NTs were found to be close to zero. For large ΔR_{NT} in double-wall titania nanotubes (Fig. 7.13) the intershell interaction becomes weak again, i.e. the stability of these DW TiO_2 NTs is quite low, as with DW BN NTs (Figs. 7.17 and 7.18).

Unlike BN nanotubes, the difference between the values of the band gap for double-wall and single-wall TiO_2 NTs is considerably larger. An additional difference occurs for the small values of ΔR_{NT}. The band gaps of zz-DW TiO_2 NTs are indirect, while for zz-DW BN NTs, these band gaps are direct for all configurations. This can be explained by a substantially smaller stability of DW TiO_2 NTs with reduced values of ΔR_{NT}. Moreover, when both the inner D_{NT} and ΔR_{NT} increase, the band gaps of double-wall titania nanotubes are still too far from the band gap

limit of the TiO_2(111) three layer slab (4.89 eV), [102]. However, the dependence of band gaps on both ΔR_{NT} and inner D_{NT} is similar for both DW BN and TiO_2 NTs, i.e. the band gap depends the most on the diameter of the inner shell. The Mulliken population analysis shows that O(2p) states prevail near the top of the valence band, while Ti(3d) states are mainly distributed near the bottom of the conduction band.

The comparison of the total energies between optimal DW TiO_2 NTs with hexagonal fluorite-type morphology and SW TiO_2 NTs with anatase-type centered rectangular morphology [120] containing the same number of atoms per nanotube unit cell allows one to make the following conclusions. For similar chiralities, one observes that the latter are energetically preferable: (i) the energy gain for (−9,9) SW NT vs (6,6)@(12,12) DW NT with the number of atoms equal to 108 has been found to be 0.09 eV per TiO_2 formula unit; (ii) an analogous energy gain for 180-atomic unit cells of SW and DW nanotubes with chiralities (15,15) and (10,0)@(20,0) achieves 0.17 eV per TiO_2 formula unit. Therefore, the growth of anatase-type NTs is preferable.

7.2.3 *Rolled up Singlewall* TiO_2 *Nanotubes with Rectangular Morphology*

The morphology of titania nanotubes is governed by the structure of atomic layers in the bulk phases and it is much more complicated than that of carbon and BN nanotubes. The distance between two six layer slabs (1.2 Å) is two times larger than that between the neighbouring three layer slabs (0.6 Å) used in the calculations of the simplified hexagonal three layer model of TiO_2 nanotubes considered above. A more realistic six layer titania nanotube model was used in [117, 119, 125]. The model uses six atomic planes of the (101) anatase slab (three Ti- and three O- planes), and the slab obtained belongs to the rectangular lattice, see Fig. 7.19. As follows from (2.39), there are restrictions on the NT chiralities compatible with the translational symmetry.

The bulk anatase structure is described by the space group $I4_1/amd$ with four TiO_2 formula units in the tetragonal (conventional) unit cell with the edges a and c. Figure 2.20b shows a (1 0 1) slab consisting of 6 atomic planes (four oxygen and two titanium planes). The 2D translation symmetry of the slab corresponds to the centered rectangular lattice with 12 atoms in the conventional unit cell with the edges a and $\sqrt{a^2 + c^2}$. The nanotubes (−n,n) and (n,n) are constructed by rolling an anatase (1 0 1) sheet along the $(\bar{1}01)$ and (010) directions, respectively. The 1D line symmetry groups of the (−n,n) and (n,n) titania nanotubes contain $(2n)_n$ screw axis. This axis is oriented along the tube one-dimensional translation vector **a**. Just after the rolling up the reflection planes contain **a** for the (−n,n) nanotubes and are perpendicular to **a** for the (n,n) ones. During nanotube structure relaxation new symmetry elements (reflection planes and twofold axes) can appear.

Table 7.18 gives the line symmetry groups of SW TiO_2 NTs, rolled from two-periodic titania layers. Figure 7.16 shows the ways of constructing SW nanotubes for three types of titania sheets: one 3-layered with hexagonal morphology and

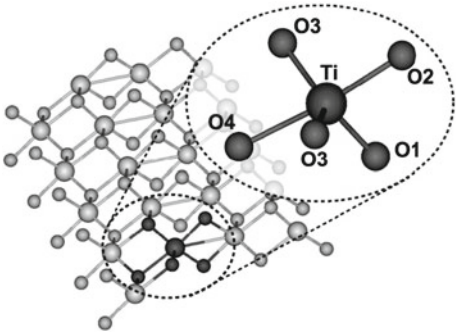

Fig. 7.19 Five-fold coordination for Ti atoms in six-layer centered rectangular titania sheets

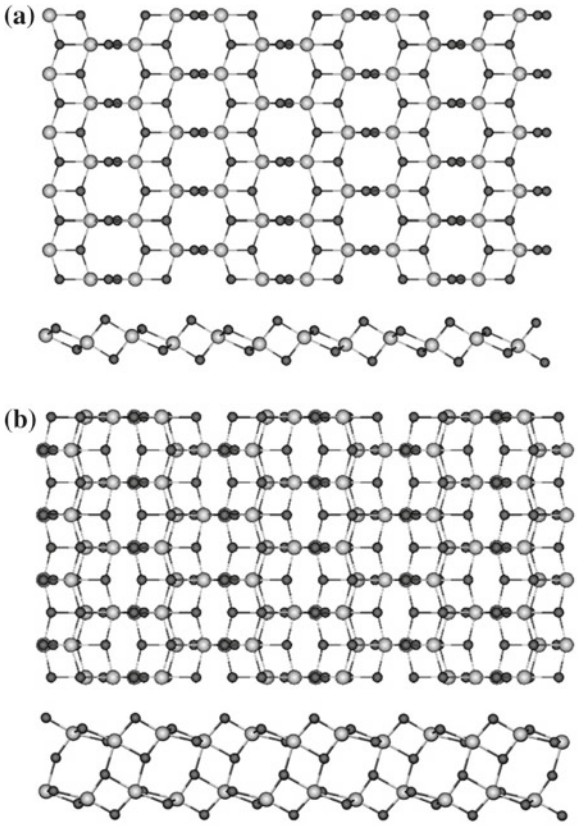

Fig. 7.20 Models of stoichiometric (101) titania sheets of different thickness optimized from the corresponding slabs with initial geometry of bulk anatase (lateral and cross sections images): **a** 6-layer slab (thickness 0.24 nm); **b** 12-layer slab (thickness 0.58 nm)

Table 7.18 Line symmetry groups of SW TiO_2 NTs, rolled from two periodic titania layers

Object	Space group for C, BN and TiO_2 bulk	Layer	Layer group	Line groups for special chiralities[a]	$\mathbf{P}_l$	Line groups for general chiralities (n_1, n_2)
3-layer hexagonal	225 $Fm\bar{3}m$	(111)	72($P\bar{3}m1$)	$4h(2n)_n/m$ $8g(2n)_nmc$	$\mathbf{C}_{2nh}$ $\mathbf{C}_{2nv}$	$1\ n_q(\mathbf{C}_q)$
6-layer centered rectangular	141 $I4_1/amd$	(101)	18($C2/m11$)	$4e(2n)_n/m$ $8d(2n)_nmc$	$\mathbf{C}_{2nh}$ $\mathbf{C}_{2nv}$	$1\ n_q(\mathbf{C}_q)$
12-layer centered rectangular	141 $I4_1/amd$	(101)	18($C2/m11$)	$4e(2n)_n/m$ $8d(2n)_nmc$	$\mathbf{C}_{2nh}$ $\mathbf{C}_{2nv}$	$1\ n_q(\mathbf{C}_q)$
6-layer primitive rectangular	63 $Cmcm$	(010)	46($Pmmn$)	$11c$ n/mmm[b] $\bar{(}2n)2m$[c]	$\mathbf{D}_{nh}$	$5\ n_q22(\mathbf{D}_q)$

[a] special chiralities: c—$(n,0)$, $(0,n)$; d—(n,n); e—$(-n,n)$
g—$(n,0)$, $(0,n)$, $(-n,n)$; $h-(n,n)$, $(-n,2n)$, $(-2n,n)$
i—$(n,0)$, $(0,n)$, $(-n,n)$, (n,n), $(-n,2n)$, $(-2n,n)$
[b] for even n
[c] for odd n

two 6-layered ones with rectangular morphology. The 3-layer model of the anatase (101) slab considered in the preceding section consists of three atomic layers (O-Ti-O), its structural optimization results in the formation of a fluorite-type (111) slab [118, 126], whose symmetry can be attributed to the layer 2D group 72($P\bar{3}m1$). It is the same for the 3-layer slab with both anatase and fluorite structures, although the space symmetry of the fluorite TiO_2 bulk crystal is described by cubic space group 225($Fm\bar{3}m$). In the case of the 6-layer model (O–O–Ti–Ti–O–O), all the six atoms of the bulk primitive unit cell are included and both centered and primitive rectangular lattices have to be considered. The 12-layer (O–O–Ti–Ti–O–O–O–O–Ti–Ti–O–O) model contains two quasi-separated 6-layer slabs. The layer group 18($C2/m11$) with a centered rectangular lattice describes the symmetry of both 6- and 12-layer slabs. The bulk titania with lepidocrocite structure can be attributed to orthorhombic space group 63 (Cmcm). The 6-layer model of the lepidocrocite (010) slab consists of six atomic layers (O–Ti–O–O–Ti–O) [127]. Layer group 46($Pmmn$) with a primitive rectangular lattice describes its symmetry. Table 7.18 gives the line symmetry groups of SW TiO_2 NTs, rolled from two periodic titania slabs.

The first-principle calculations of six layer TiO_2 NTs were made in [117, 119, 125, 127]. As the number of atoms in the six layer model of the TiO_2 nanotube quickly increases with increasing diameter the ab initio calculations are very time consuming for the structural optimization. Therefore in [117] molecular mechanics-based calculations were performed to obtain the optimized nanotube structure, while electronic band structures were obtained by performing DFT (LDA) calculations.

As in all the plane wave calculations, the three-periodic nanotube model was used in [117]: a tetragonal supercell with the lattice parameter a much larger than the nanotube translation periodicity was adopted, but the result dependence on the parameter a was not investigated. The two types (-n,n) and (n,n) of titania nanotubes (called A- and B-types,respectively [117]) were studied. It was found that A-nanotubes are energetically preferable to B-nanotubes. According to [117], the band gap of the A-nanotube was reduced by 0.60 eV as the tube diameter decreases from 12 to 5 Å. The first hybrid HF/DFT LCAO calculations of both the structure and electronic properties of the TiO_2 nanotube obtained by rolling a six-layer (1 0 1) anatase slab were made in [119, 125]. In the LCAO calculations of TiO_2 NTs no artificial 3D periodicity is necessary.

We now proceed to discuss the results of the first principles hybrid HF-DFT LCAO calculations [120, 125] on the 6- and -12 layer models of TiO_2 NTs with rectangular morphology. The CRYSTAL09 computer code [23] was used. As in the three-layer model calculations [102, 124] of TiO_2 NTs with hexagonal morphology the small-core pseudopotential [98] of the Ti atom was used (3s, 3p, 3d and 4s-electrons were taken as valence electrons), while the all-electron basis set for the O-atom was taken from [99].

The diffuse exponents of valence s, p and d-orbitals were optimized for the stable anatase phase of the bulk titania. Its atomic and electronic properties were reproduced in the good agreement with the experiment (the experimental values are given in brackets): the lattice parameters a = 3.784 Å (3.782 Å) and c = 9.508 Å (9.502 Å), the dimensionless parameter for the relative position of the oxygen atom $u = 0.2074(0.2080)$, the values of the energy gap are reproduced worse, because of being overstimated: 4.0 eV versus 3.2 eV. In any case, these results for the bulk titania (anatase) agree with the experimental data better than those given in [97] for both the plane wave (PW) and LCAO calculations when the different exchange-correlation potentials were used. A certain improvement of the substantially underestimated values of the energy gap for the bulk anatase in the DFT PW calculations has been achieved recently [103] using the LDA+U method (2.7 eV).

The structures of 6- and 12-layer anatase (101) slabs (see Fig. 7.19) were optimized in [120, 125] and their properties were calculated. Both 6- and 12-layer anatase (101) slabs keep their initial symmetry after structural optimization, although their lattice parameters differ from those in the bulk, see Table 7.20.

Six-layer titania slabs with anatase-type (101) structure can be rolled up to 6-layer titania SW NTs with (i) $(-n,n)$ chirality and (ii) (n,n) chirality. Figure 7.21a shows the optimized structures of the selected 6-layer nanotubes of both chiralities. A specific feature of these six-layer titania sheets and nanotubes is that both Ti sublayers are rearranged in the middle between the surfaces of both the sheets and nanotubes, see Figs. 7.20a and 7.21a, i.e., their optimized structure is O–O–Ti–Ti–O–O, which is different from O–Ti–O–O–Ti–O owing to the sequence of TiO_2 formula units in the bulk anatase structure.

Table 7.21 presents the results obtained after the structural optimization of 6-layer TiO_2 NTs with (i) (−n,n) chirality (for n = 3, 4, 6, 9, 12) and (ii) (n,n) chirality (for n = 6, 10, 15, 20, 24). One of the main parameters of the nanotube stability, i.e., the strain

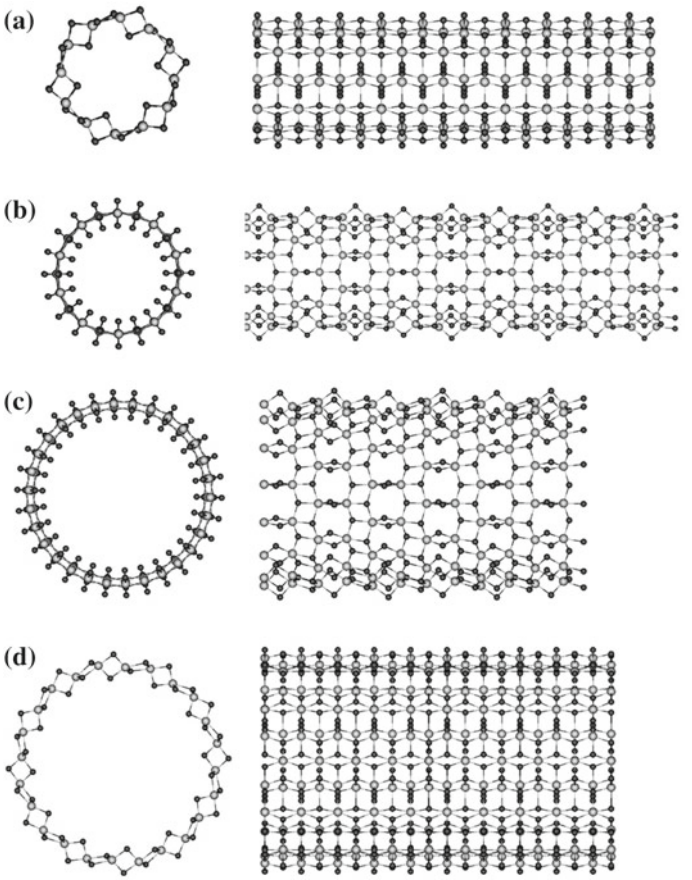

Fig. 7.21 A top (Lateral) and across (cross sections) views of 6-layered anatase-like SW TiO_2 nanotubes for different chiralities: **a** (−3,3), **b** (10,10), **c** (15,15), **d** (−6,6)

energy E_{strain}, is defined as a difference between the total energies of the optimized nanotube E_{NT} and the corresponding slab before rolling up E_{slab}, with regard to the number k of slab unit cells in the nanotube unit cell containing m formula units TiO_2 (measured in kJ/mol per TiO_2 formula unit): $E_{strain} = (E_{NT} - kE_{slab}/m)$. Obviously, the number of atoms per surface unit in (−n,n) nanotubes is markedly smaller than that in (n,n) NTs of the same diameter. Therefore the former can be calculated faster. For the small diameter D_{NT} (low chirality indices), the absolute values of both E_{relax} and E_{strain} are quite large, and trying to reduce these diameters further, one faces an enhanced instability of NTs. For example, the convergence of calculations on (4,4) nanotubes has been found to be rather poor. Since hypothetical nanotubes with an infinite diameter should coincide with sheets of the same thickness, a consequent growth of the NT diameters leads to a substantial decrease in both relaxation and strain

energies (down to zero at infinity), whereas the values of other properies (Table 7.21) approach those for the 6-layer titania slab with hexagonal structure (Table 7.20).

To analyze the dependence of E_{strain} and the energy gap on the diameter of six-layer TiO_2 NTs a sufficiently large range of nanotube diameters, from 0.5 to 4.0 nm, with the number of atoms per NT unit cell increased from 36 up to 288, was considered in [125]. Two curves $E_{strain}(D_{NT})$ shown in Fig. 7.22 demonstrate that the strain energy of six-layer NTs with (−n,n) chirality is smaller than that of (n,n) NTs of a similar diameter, i.e., the former are more stable energetically. This difference remains noticeable for nanotubes with diameters $\leq$30 Å. When the diameters of nanotubes increase to 40 Å the strain energies decrease and approach one another.

For six-layer titania nanotubes of both chiralities, $\Delta E_{gap}(D_{NT})$ curves possess maxima at the diameter range 13–17 Å (Fig. 7.23). For larger values of DNT, both the relaxation and strain energies of TiO_2 nanotubes substantially decrease, while their band gaps asymptotically approach the band gaps of the corresponding 2D slab (Table 7.20).

Table 7.19 presents the comparison of the results of calculations on four pairs of structurally similar TiO_2 nanotubes. The optimized values of D_{NT} in each pair of

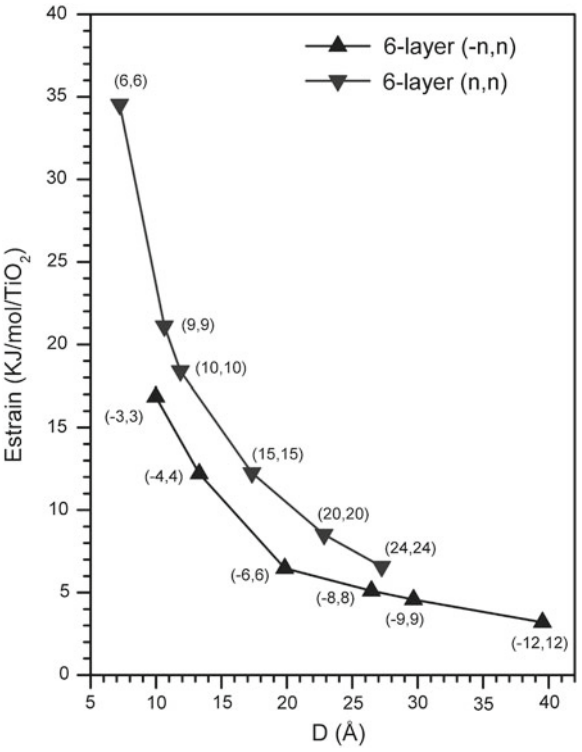

Fig. 7.22 Strain energies E_{strain} versus D_{NT} for the two sets of six-layer SW TiO_2 NTs with various chiralities

Table 7.19 The structural and electronic properties of four pairs of symmetry-compatible TiO_2 NTs ((*i*), (*d*) means indirect and direct gap, respectively)

Pairs of NTs with equal diameters	N_a	D_{NT},Å	l_{NT}, Å	h_{NT}, Å	d_{TiO}, Å				q_{Ti}, e	E_{relax}, eV/TiO_2	E_{strain}, kJ/mol *per* TiO_2	ΔE_{gap} eV
					Ti-O1	Ti-O2	Ti-O3	Ti-O4				
$(2n)n/m$ *group*												
3-layer (6,6)	36	10.06	2.99	1.86	1.89	1.94	2.00	2.05	2.42	−0.09	46.18	$4.66^{(i)}$
6-layer (-3,3)	36	9.98	3.66	2.45	1.795	1.86	1.925	2.025	2.28	−0.82	16.86	$4.92^{(i)}$
$(2n)nmc$ *group*												
3-layer (12,0)	72	11.70	5.10	1.88	1.915	1.945	1.96	2.03	2.43	−0.09	33.71	$4.70^{(i)}$
6-layer (10,10)	120	11.85	10.39	2.46	1.80	1.835	1.945	2.02	2.27	−0.45	18.39	$5.05^{(d)}$
$(2n)nmc$ *group*												
3-layer (18,0)	108	17.23	5.12	1.90	1.935	1.95	1.965	1.965	2.44	−0.05	14.93	$4.75^{(i)}$
6-layer (15,15)	180	17.33	10.33	2.43	1.785	1.87	1.92	2.01	2.27	−0.14	12.25	$5.36^{(i)}$
$(2n)n/m$ *group*												
3-layer (12,12)	72	19.73	2.97	1.91	1.935	1.95	1.98	1.995	2.44	−0.04	11.26	$4.77^{(i)}$
6-layer (-6,6)	72	19.84	3.54	2.39	1.765	1.87	1.92	2.11	2.19	−0.14	6.47	$5.26^{(i)}$

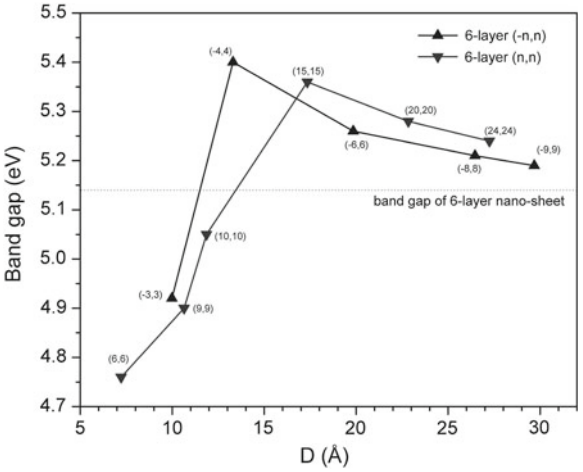

Fig. 7.23 Band gaps versus D_{NT} for the two sets of six-layer SW TiO_2 NTs with various chiralities

these NTs were selected (the relative difference of the diameters in different pairs varied from 0.57 to 1.34 %). The structural compatibility of all the four pairs can be explained by their belonging to the same line groups (Table 7.18), i.e. the chiralities of 3-layer (n,n) and 6-layer (−n,n) nanotubes can be described by the same line group $(2n)_n/m$, whereas the line group $(2n)_n mc$ corresponds to both 3-layer (n,0) and 6-layer (n,n) NTs. Alongside the proximity of diameters, this symmetry factor makes reasonable a direct comparison of the structural and electronic properties in each pair of these nanotubes. One can conclude from the data presented in Table 7.19 that in 3- and 6-layer nanotubes with close diameters described by the $(2n)_n/m$ symmetry group the number of atoms per unit cell is the same, whereas the length of the unit cell of the 6-layer nanotube is about 20 % larger. In analogous NT pairs described by the $(2n)_n mc$ symmetry group the number of atoms per unit cell is larger by about 70 % for 6-layer nanotubes, while their lengths are more than twice larger compared to 3-layer NTs. Thus, if one estimates the density of atoms per NT length, it will be larger for 3-layer nanotubes. The 6-layer NT thickness is about 30 % larger than that of 3-layer nanotubes for all chiralities. As to Ti-O bond lengths, their deformation is noticeably larger in 6-layer nanotubes, and it is not decreased for D_{NT} up to 30 Å, whereas in the 3-layer NTs, the values of $d_{\mathrm{Ti-O}}$ approach those in the three-layer slab (Table 7.2) much faster. Obviously, this is also true for the convergence of E_{relax} with DNT increasing (Table 7.20).

The chemical nature of the Ti-O bonds in both three- and six-layer titania nanotubes is slightly different. The values of effective charges q_{Ti} on titanium atoms presented in Table 7.20 clearly show that the chemical bonding in hexagonal nanotubes is more ionic. On the other hand, the calculated Ti-O bond populations in 6-layer NTs were found to be 2–3 times larger than those in 3-layer slabs achieving 0.16–0.18 e per internal wall bonds, i.e., the bonding in the former is more covalent. A series of calculations for the total and projected densities of states (DOS and

PDOS) for the TiO_2 anatase bulk, 3, 6 and 12-layer titania sheets were also made in [120]. It was found that the DoSs of the 6- and 12-layer sheets and the 6-layer nanotube are qualitatively similar to the DOSs of the bulk anatase. When both D_{NT} and the number of atoms are increased, the profiles of DOSs and PDOSs become more complicated, since the number of one-electronic states increases. The total density of states projected on different atomic states implies that the states of the highest valence band (VB) mainly arise from the 2p states of oxygen atoms, while those of the lowest conduction band (CB) come from the 3d states of Ti atoms. In 6-layer nanotubes, the contributions of O and Ti states in CB and VB states are found to be larger than in 3-layer nanotubes. It means that the $O(2p) - Ti(3d)$ bond hybridization is more pronounced at PDOSs calculated for the equilibrium six-layer TiO_2 nanotube structures, i.e., their covalent bonding is stronger.

Twelve-layer single-walled TiO_2 nanotubes with rectangular morphology were also simulated in [125]. The middle of the 12-layer TiO_2 slab consists of two sublayers containing oxygen atoms (Fig. 7.20a), and when a single-walled titania nanotube is obtained by rolling up this twelve-layer sheet its thickness is about 2.5 times larger than that of a six-layer TiO_2 nanotube. As a result, the atomic structure of the internal wall surface of this 12-layer NT is overstrained even for the moderate values of D_{NT}. A comparison of images for both six- and twelve-layer NTs with the same (−6,6) and (12,12) chiralities (Fig. 7.24) clearly shows quite small geometry relaxation of the former and a drastic change of morphology of the latter, which cannot be optimized at all, due to a divergence of the SCF calculations after several steps of geometry optimization.

This effect can be also illustrated by a drastic difference between the calculated strain energies E_{strain} for six- and twelve-layer SW TiO_2 NTs (with the initial geometry after rolling up the corresponding slabs), for (−6,6) and (12,12) chiralities: 23.76 and 41.78 versus 224.04 and 498.62 kJ/mol per TiO_2 formula unit, respectively. Thus, one can predict that for 12-layer titania nanotubes, the more preferable morphology has to be not SW but the double-walled (DW) NT consisting of a pair of six-layer nanotubes of different diameters and chirality indices.

It is seen that ab initio LCAO calculations using the hybrid PBE0 Hamiltonian allow one to perform the analysis of the atomic and electronic structure of TiO_2 sheets, as well as nanotubes simulated using different models. It was found in [120] that the structural optimization of the 3-layer slab results in a spontaneous (barrier-less) reconstruction into the hexagonal (111) fluorite structure. The structural optimization of three- and six-layer single-walled titania nanotubes leads to a growth of the NT diameter for all the morphologies considered. Noticeable differences between the calculated properties of 3- and 6-layer TiO_2 sheets and nanotubes were found. First of all, the strain energies of the six-layer nanotubes are smaller than those of the 3-layer NTs of close diameters (for $D_{NT} \leq$ 20–25 Å). The most probable reason for this 6-layer NT energetical stability is that in six-layer titania sheets and nanotubes with anatase structure both Ti sublayers are positioned in the middle between the surfaces of both the sheets and the nanotubes, i.e., their formal bulk structure is O–O–Ti–Ti–O–O. On the other hand, the relaxation energies of 6-layer NTs are larger than those of 3-layer nanotubes (especially for small NT diameters), due to a more

Table 7.20 The atomic and electronic structure of TiO_2 bulk versus various slabs

Models of TiO_2 bulk and sheets	Lattice parameters (Å)		Thickness h_{NT} (Å)	Bond length d_{Ti-O}[a] (Å)				Effective charge q_{Ti},[b] e	E_{relax} per TiO_2 unit,[c] eV	*Surface* energy E_{surf},[d] J/m^2	$\Delta\varepsilon^e_{gap}$ eV
	a	c		Ti − O1	Ti − O2	Ti − O3	Ti − O4				
bulk	3.78	9.51	–	1.935	1.935	1.973	1.973	2.35	–	–	4.09
6-layer	3.51	5.45	2.39	1.75	1.89	1.91	2.05	2.28	−1.09	0.64	5.14
12-layer	3.71	5.46	5.83	1.77	1.83	1.95	2.01	2.30	−0.55	0.67	4.92

[a] the corresponding bonds are shown in Fig. 7.19

[b] averaged effective charges q_O are twice smaller than q_{Ti}, with the opposite sign

[c] E_{relax} is a difference of energies between a slab with "bulk" geometry and that with an optimized structure

[d] $E_{surf}(n) = \frac{1}{2S}(E_n - nE_b)$, where E_n is the total energy of the n-layer slab *per* primitive surface unit cell, S its area, while E_b is the total energy per primitive bulk unit cell

[e] all band gaps considered in this table are indirect

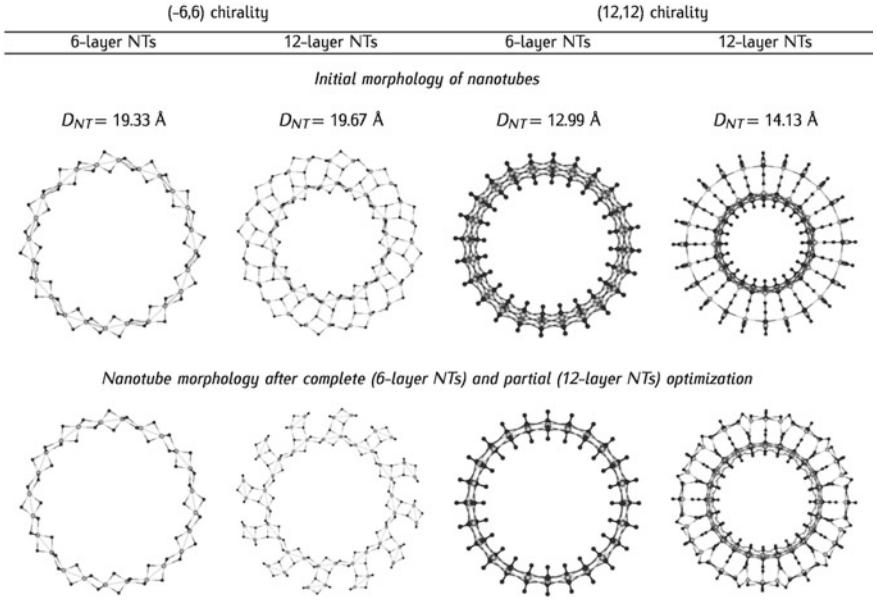

Fig. 7.24 Cross-sections of 6- and 12-layer SW TiO_2 NTs with (−6; 6) and (12; 12) chiralities, respectively (D_NT for nanotubes with initial geometry are defined as described in Table 7.21)

complicated structure of the former. The band gaps of six-layer titania nanotubes (typical semiconductor with $\Delta E_{gap} \leq 5$ eV) are found to be noticeably larger (up to 0.5 eV) compared to three-layer NTs of the same diameter. When these diameters markedly increase, the nanotube band gaps asymptotically approach those for 2D slabs of the corresponding thickness.

The strain energies of 6-layer SW TiO_2 NTs decrease with the growth of the nanotube diameter, approaching a minimum for the infinite D_{NT}. ΔE_{gap} curves for both nanotube chiralities achieve maxima at the diameter range 13–17 Å and after its further growth both gaps asymptotically approach that for the corresponding 2D slab. Twelve-layer SW TiO_2 NTs were found in [125] to be as energetically unstable as single-walled nanotubes. One can predict that for these nanotubes the most preferable morphology has to be double-walled (DW) NTs of the same chirality consisting of a pair of six-layer nanotubes of different diameters and chirality indices.

7.2.4 TiO_2 Nanowires

Titania nanowires (TiO_2 NWs) attract enhanced attention in modern nanotechnology due to a variety of promising applications such as humidity sensors, photovoltaic and photocatalytic cells, optical devices, field-effect transistors, etc. [128]. TiO_2 NWs based on the rutile phase were mainly synthesized using thermal evapora-

Table 7.21 The structural and electronic properties of six-layer SW TiO_2 NTs (Fig. 7.21)[a]

NT chirality indices	N_A	l_{NT},[b] Å	D_{NT},[c] Å	h_{NT}, Å	d_{Ti-O}, Å				q_{Ti}, e	E_{relax} eV/TiO_2,	E_{strain}, kJ/mol per TiO_2	$\Delta\varepsilon_{gap}$,[d] eV
					Ti − O1	Ti − O2	Ti − O3	Ti − O4				
(−n,n)nanotubes - $(2n)_n/m$ group												
(−3,3)	36	3.66	9.98	2.45	1.795	1.86	1.925	2.025	2.28	−0.82	16.86	4.92 $^{(i)}$
(−4,4)	48	3.60	13.30	2.41	1.775	1.89	1.94	2.01	2.21	−0.35	12.20	5.40 $^{(i)}$
(−6,6)	72	3.54	19.84	2.39	1.765	1.87	1.92	2.11	2.19	−0.14	6.47	5.26 $^{(i)}$
(−9,9)	108	3.52	29.68	2.39	1.77	1.875	1.91	2.09	2.27	−0.05	4.57	5.19 $^{(i)}$
(−12,12)	144	3.52	39.55	2.39	1.77	1.88	1.90	2.085	2.27	−0.03	3.20	5.17 $^{(i)}$
(n,n)nanotubes - $(2n)_nmc$ group												
(6,6)	72	10.32	7.22	2.44	1.79	1.835	1.96	2.01	2.27	−1.68	34.54	4.76 $^{(d)}$
(10,10)	120	10.39	11.85	2.46	1.80	1.835	1.945	2.02	2.27	−0.45	18.39	5.05 $^{(d)}$
(15,15)	180	10.33	17.33	2.43	1.785	1.87	1.92	2.01	2.27	−0.14	12.25	5.36 $^{(i)}$
(20,20)	240	10.33	22.84	2.41	1.78	1.875	1.91	2.01	2.28	−0.07	8.51	5.28 $^{(d)}$
(24,24)	288	10.33	27.24	2.41	1.78	1.875	1.895	2.01	2.28	−0.03	6.57	5.24 $^{(d)}$

[a] Definitions of values are the same as in Table 7.20
[b] Length of nanotube unit cell
[c] Diameters are given for the middle cylinders between the external and internal walls of NTs
[d] Direct and indirect band gaps are marked by superscript indices $^{(d)}$ and $^{(i)}$, respectively

tion [129, 130] via vaporliquidsolid and vaporsolid growth mechanisms, applying Ni or Au as a catalyst, and by chemical vapor deposition [131]. Such titania nanowires were found to be single crystalline with diameters of 10–100 nm possessing the [110], [132] and [001], [133] orientations of growth. On the other hand, TiO_2 NWs were recently synthesized with diameters on the Angstrem scale [134]. In this case, nanowires show effects not present in the bulk, thus opening up new applications.

A number of theoretical studies on atomic-scale TiO_2 nanowires have already been published. Simulations on the formation energy for titania nanowires showed the stability of structures assembled from Ti_2O4 building blocks (with a tetrahedral coordination of the Ti atoms instead of the usual octahedral one) [135]. Large-scale calculations on the thinnest filaments consisting of periodically repeated TiO and TiO_2 molecules along chosen 1D axes as well as on bulk-like TiO_2 [110]-oriented NWs were performed, too [136]. First-principles simulations indicated an increase in band gap values due to the quantum confinement effects of hydrogenated rutile-based TiO_2 NWs with the [001] orientation [137]. In particular, [001]—oriented nanowires were cut along the central axis passing through the Ti atoms (resulting in mirror plane symmetry but without a screw axis in nanowires).

Large-scale ab initio calculations on thermodynamically preferable TiO_2 NWs in the rutile phase [128] clearly display only the energetically preferable {110} facets in the case of their [001] orientation, as well as the alternating {110} and {001} facets in the case of the [110] NW orientation, in accordance with the Wulff construction formalism [109]. The influence of O and Ti vacancies on the energetic, structural, and electronic properties of rutile-based titania [110] nanowires and their reactivity toward water molecules were evaluated as well [138].

Two main reasons cause the simulation of both [001] and [110] orientations of rutile-based TiO_2 NWs to be a necessity, [128]: (i) the thermodynamic contribution to nanowire stability is independent of NW morphology for diameters greater than 10 nm synthesized experimentally (while ab initio calculations can be performed only for nanowires with diameters $\leq$5 nm) and (ii) the interface between a catalytic substrate and the nucleation titania seed should display a sufficiently low energy to surpass the nucleation barrier. This is why [110]- oriented rutile-based TiO_2 NWs have been synthesized more frequently so far [129–132].

The structure and electronic properties of TiO_2 anatase–based nanowires were calculated as well, with different orientations and surface terminations varied as a function of diameter [139, 140]. In particular, the stability and electronic structure of both anatase-based and rutile-based [001] nanowires were compared for a series of first-principles calculations [141]. With diameters of up to 2.1 nm in anatase-based and 3.7 nm in rutile-based nanowires, those 100-walled anatase and 110-walled rutile NWs were found to be the most stable, which retains the nonsymmorphic character of the bulk space group. As for the construction of 1D atomistic models for titania nanowires, both the Ti atom- and hollow-centered symmetry axes (i.e., translation 2-fold rotation axis and 4-fold screw axis, respectively) were considered in studies [137, 141].

According to Wulff's formalism [109], the quasi-square cross-sections of titania nanowires correspond to a minimum of dangling bonds per titania formula units [128].

From numerous possible shapes of symmetric prism models used for the simulation of rutile-based titania nanowires, [128, 136–138, 141] the two energetically most favorable configurations have been chosen in rutile-based TiO_2 nanowires calculations [94, 142]: square the rhomb-type (Figs. 7.25 and 7.26) and quasi-square rectangle-type (Figs. 7.28 and 7.29) possessing Ti atom-centered symmetry axes. As found recently [128], it is only for these shapes of TiO_2 NWs, that the total nanowire energy per formula unit achieves minimum values. The hollow site-centered TiO_2 [001] nanowire, see Fig. 7.27, has also been used in calculations [94, 141].

The construction of rutile-based nanowires for the calculations [94, 142] was made from the supercells of rutile slabs in such a way that the 2D slab surface was normal to the chosen NW periodicity direction with the subsequent removal of both slab translations and restoring the translation for the NW. The translational period of the nanowire is defined by the minimal slab unit cell along the direction normal to the slab surface. This period consists of two and four titania formula units for the orthogonal [001] and [110] nanowires, respectively. The length unit $l_{NW_{UC}}$ of the nanowires generated corresponds the minimal slab periodicity along the normal axis h^{min}_{layer} in the case of the (001) cross-sections, Fig. 2.19 d while for the (110) cross-section, NW orthogonality is provided for the double thickness $2h^{min}_{layer}$, Fig. 2.19a. Non-orthogonal [110] NWs with axes inclined from the normal by $\pi/4$ can be simulated too (as they were really observed in experiment [132]) if $l_{NW_{UC}} = h^{min}_{layer}$. On the other hand, the periodic cross-section of the 1D nanowire can be transformed from the supercell of the 2D slab possessing periodic boundary conditions (PBC). At first we consider an [001]-oriented rutile nanowire. The surface unit cell of the (001) slab with an arbitrary thickness consists of an even number of TiO_2 formula units since the two formula units of the titania bulk primitive cell are projected on the two neighbor slab planes forming periodically repeating 2D layers along the z-axis (see Fig. 2.19d and Table 7.7). There are two possibilities for the choice of four-faceted NWs since the primitive cell of the square plane lattice can be transformed into supercells with $\begin{pmatrix} n & 0 \\ 0 & n \end{pmatrix}$ or $\begin{pmatrix} n & n \\ -n & n \end{pmatrix}$ matrices which correspond to either (100), $(\bar{1}00)$, (010) and $(0\bar{1}0)$ lateral NW facets (according to Fig. 2.19d) or (110), $(\bar{1}10)$, $(1\bar{1}0)$ and $(\bar{1}\bar{1}0)$ ones (Fig. 7.25), respectively.

Table 7.9 shows that the surface energy of the (110) and related slabs is substantially smaller than that of the (001)-type of slabs. Therefore, we have to generate [001]-oriented NWs using $\begin{pmatrix} n & n \\ -n & n \end{pmatrix}$ slab supercells. Any such supercell consists of $2n^2$ minimal slab unit cells along the z-axis, i.e., $4n^2$ TiO_2 formula units (n = 1, 2, 3). To generate the nanowire, one removes the 2D periodicity of the slab, i.e., the cyclic boundary conditions for the facets and introduces periodicity along the z-axis (two TiO_2 formula units in the 1D unit cell).

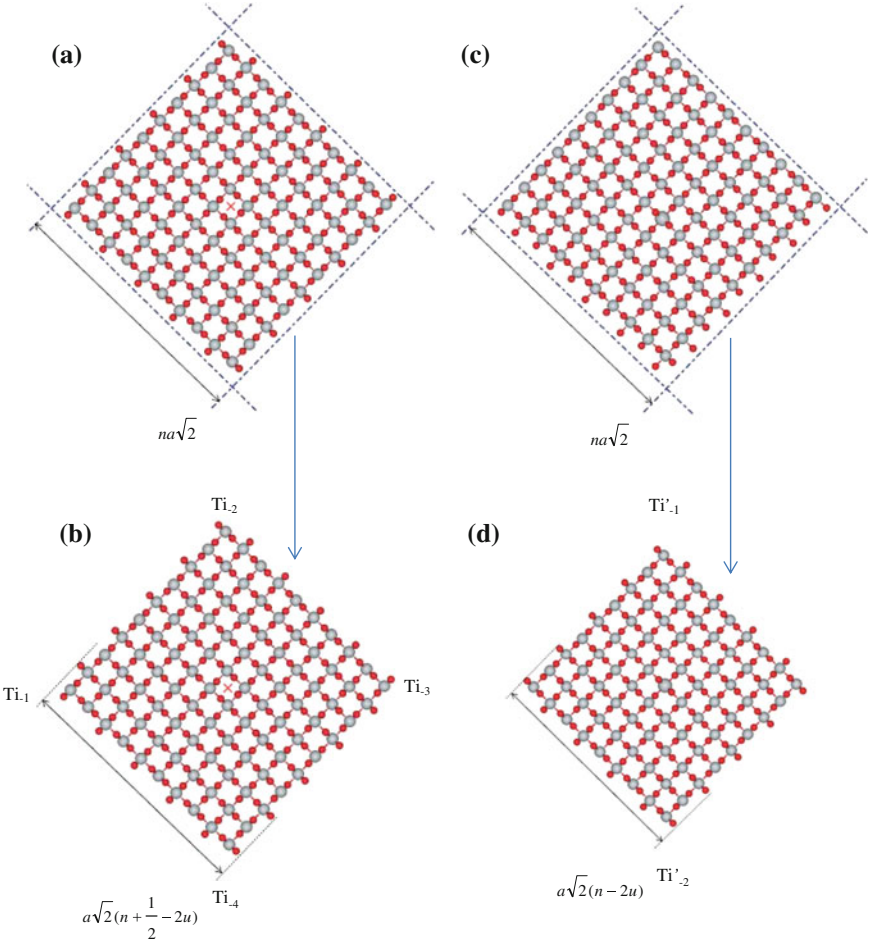

Fig. 7.25 Transformation of 5 × 5 supercells of two-plane rutile (001) slabs to cross-sections of either *hollow site*-centered (**a** → **b**) or Ti atom-centered (**c**→**d**) [001] NWs. *Dot-dashed blue lines* (**a**, **c**) show the borders of adjacent slab supercells. The centers of *hollow site*- and Ti atom-centered nanowires are shown by *crosses* and *balls*of a larger diameter, respectively. The consequent transformation of Ti_{-1}, Ti_{-2}, Ti_{-3} and Ti_{-4} (**b**), as well as Ti_{-1} and Ti_{-2} (**d**) atoms can be described by C_{4h} and D_{2h} point groups, respectively (see explanation in the text). The lengths of rhombic *square sides* in the slab supercells and NW cross-sections are defined for arbitrary extensions

Upper part of Fig. 7.25 shows the two possible types of slab supercells which differ by origins of coordinate systems centered at either the hollow site (Fig. 7.25a) or the Ti atom (Fig. 7.25c). Both rhombic-type supercells with periodic boundary conditions shown in the aforementioned models by dot-dashed lines contain the same number of formula units $4n^2$ and have the same surface area, while their size can be described by the length of square side: $na\sqrt{2}$. When removing PBC one obtains a nanowire with the translation vector perpendicular to the titania (001) rutile slab,

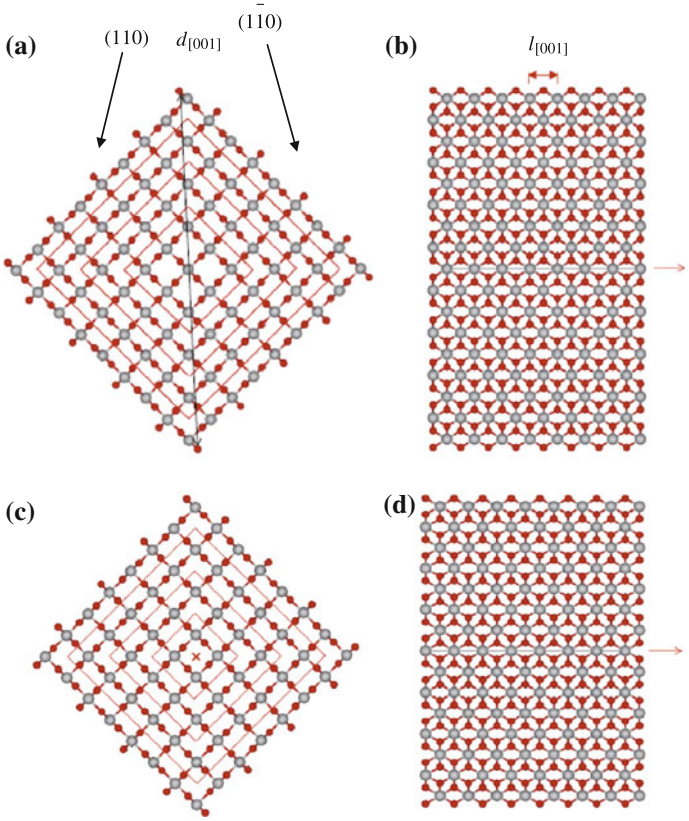

Fig. 7.26 Cross-sectional **a** and lateral **b** images of the non-optimized [001]-oriented Ti atom-centered nanowire possessing the D_{2h} symmetry and containing 81 formula units per NW unit cell with aside (110) and $(1\bar{1}0)$ facets shown in **b**. The *red* rhombs in **a** show the borders for prism models of middle, small and smallest TiO_2 NWs (49, 25 and 9 formula units per UC, respectively). The images of the [001]-oriented *hollow site*-centered titania nanowire (**c**, **d**) possessing the C_{4h} point symmetry and containing 64 formula units per unit cell are shown in a manner similar to **a** and **b**, respectively, including the prism models of middle, small and smallest TiO_2 NWs containing 36, 16 and 4 formula units per unit cell. The diameter of the nanowire is shown in **a** by a twice-terminated *arrow* ($d_{[001]}$), while its period (length of UC) is shown in **b** as ($l_{[001]}$)

whose unit length equals to thickness of slab layer unit: $l_{NW001} = h_{001}^{min}$. In the case of the hollow-centered [001] nanowire, both the NW shape and the composition of O and Ti atoms in its cross-section are the same as those in hollow-centered (001) slab supercell (cf. Fig. 7.25a, b), however, a length of its square side decreases from $na\sqrt{2}$ to $a\sqrt{2}(n + 1/2 - 2u)$ due to an absence of 2D supercell periodicity (u is the rutile structure parameter defining the positions of oxygen atoms). Symmetry of such a nanowire is described by rod group $P4_2/m$ with a screw axis. The rotations around this axis transform corner Ti_1, Ti_2, Ti_3 and Ti_4 atoms (consistently located in adjacent atomic planes) to each other. Thus, when the origin of coordinate system is centered

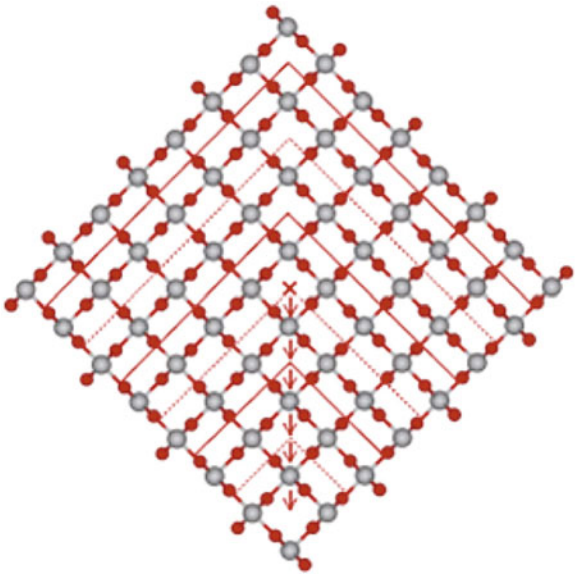

Fig. 7.27 Cross-sectional image of a non-optimized hollow site-centered TiO_2 [001] NW possessing a four-fold screw axis (its track is shown by a cross) and containing 64 formula units per NW UC. Small *arrows* show the shifts of the nanowire axis during alternating transformations from hollow site- to Ti atom-centered structures and vice versa. Two adjacent rhombohedral sides imaged by *solid lines* show the facet borders of Ti atom-centered titania nanowires, while those limited by *dashed lines* correspond to hollow site-centered TiO_2 NWs. Two other lateral facets described here fixed remain, coinciding with the lower sides of the cross-sectional image

at hollow site, one does not needs any structural transformation for transition 2D slab1D NW.

However, when removing the PBC from the supercell centered at the Ti atom one receives the cross-section of the NW requiring an additional transformation and generates a nanowire with symmetric composition of the edge O and Ti atoms similar to the composition obtained in the hollow site-centered [001]-oriented NW. To achieve this aim, the two upper rows of the edge O and Ti atoms, as well as the lowest row of the edge O atoms (Fig. 7.25c) must be removed, giving altogether $(4n1)$ formula units. The symmorphic Pmmm rod group describes the symmetry of the newly-formed Ti atom-centered nanowire (Fig. 7.25d) transforming corner Ti_1 and Ti_2 atoms (located in the same atomic plane) to each other. The length of the NW square cross section is found to be $a\sqrt{2}(n - 2u)$, while number of formula units per unit cell of this transformed nanowire is $(2n1)^2$. Obviously, the square cross-sections of Ti atom-centered nanowires (Fig. 7.25d) cannot form a 2D slab since they contain the odd number of Ti atoms in each equivalent side and cannot be translated along the side directions, resulting in the appearance of adjacent supercells which are complementary to the slab prototype. On the contrary, the cross-sections of hollow site-centered NWs containing an even number of Ti atoms (Fig. 7.25b) allow the introduction of periodic boundary conditions.

Thus, in rutile-based [001] titania nanowires (Fig. 7.26) the direction of the translation axis is orthogonal to the pair (110) and $(1\bar{1}0)$ vectors of the cross-sectional rhombic square. If the translational two-fold rotation axis goes through a Ti atom (Fig. 7.26a, b), one can see that the reflection in the horizontal plane and the rotations around the two second order axes in this plane are the symmetry operations for [001]-oriented nanowires described by the point symmetry group D_{2h} [142]. Both the cross-sectional and lateral views of this type of nanowire define its diameter, d_{NW} and length unit, l_{NW}. As to the translation axis for a [001] rutile—based nanowire with a 4-fold screw axis going through the interstitials in the middle of the squares formed by Ti atoms (Fig. 7.26c, d), its point symmetry group is C_{4h} and the corresponding rod group $P4_2/m$ is non-symmorphic, [141]. It means that the number of point symmetry operations used for the description of the [001]–oriented hollow site-centered nanowire (eight) equals that of the Ti atom-centered nanowire. Figure 7.27 clearly shows how nanowires with hollow site-centered symmetry axes can be transformed to NWs with Ti atom-centered axes and vice versa by the removal of external stoichiometric shells from the two adjacent facets.

For [110] oriented nanowires the structural generation is more complex than in the case of [001]-oriented NWs. In the former case the lateral facets are (001), $(00\bar{1})$, $(1\bar{1}0)$ and $(\bar{1}10)$. Analyzing the values of surface energies given in Table 7.9 one can suppose that the nanowires generated from (110) slab supercells have noticeably larger surface energies than [001] nanowires. The 2D lattice for a (110) slab is rectangular with the lengths of translation vectors proportional to c and $a\sqrt{2}$ (Fig. 2.19a). According to Table 7.7, the surface area of a (110) slab unit cell is a stretched rectangle, i.e., $cxa\sqrt{2}$. Moreover, unlike the (001) slab, the ratio of unit lengths in the (110) surface area is transcendental. To provide a generation of a quasi-square supercell for the (110) slab with close lengths of sides, the transformation matrix $\begin{pmatrix} 2n & 0 \\ 0 & n \end{pmatrix}$ can be used. Both choices of the coordinate system origin giving Ti atom- and hollow site-centered supercells (cf. Fig. 7.28a, c) are equivalent when periodic boundary conditions are introduced. However, after the removal of PBC one needs to make additional transformations in order to obtain stoichiometric nanowires. Rectangular quasi-square supercells with PBC shown in Fig. 7.28 by dot-dashed lines contain the same number of formula units $8n_2$ and have the same surface area, while their sizes can be described by a pair of lengths: $2nc$ and $na\sqrt{2}$ (Fig. 7.28a, c). After the removal of PBC the shapes of cross-sections in [110]-oriented NWs are the same as those in (110) slab supercells, however, the lengths of rectangle sides decrease: $c(2n1/2)$ and $a\sqrt{2}(n + 1/2 - 2u)$. For both Ti atom- and hollow site-centered [110] nanowires, additional transformations are necessary, to generate a nanowire with a symmetric composition of edge O and Ti atoms. In the first case, $(6n1)$ excessive formula units must be removed from the corresponding supercell of the (110) rutile slab (Fig. 7.28a), in order to obtain a Ti atom-centered titania nanowire, while in order to obtain a hollow site-centered [110]-oriented nanowire (Fig. 7.28c) $2n$ missing formula units must be added. These transformations generate NWs consisting of $(2n1)(4n1)$ and $2n(4n + 1)$ formula units whose symmetry is determined by the rod groups Pmmm and Pm2m for Ti atom- and hollow site-centered cases, respectively (Fig. 7.28b, d). In the former case, the symmetry group transforms Ti_1 and

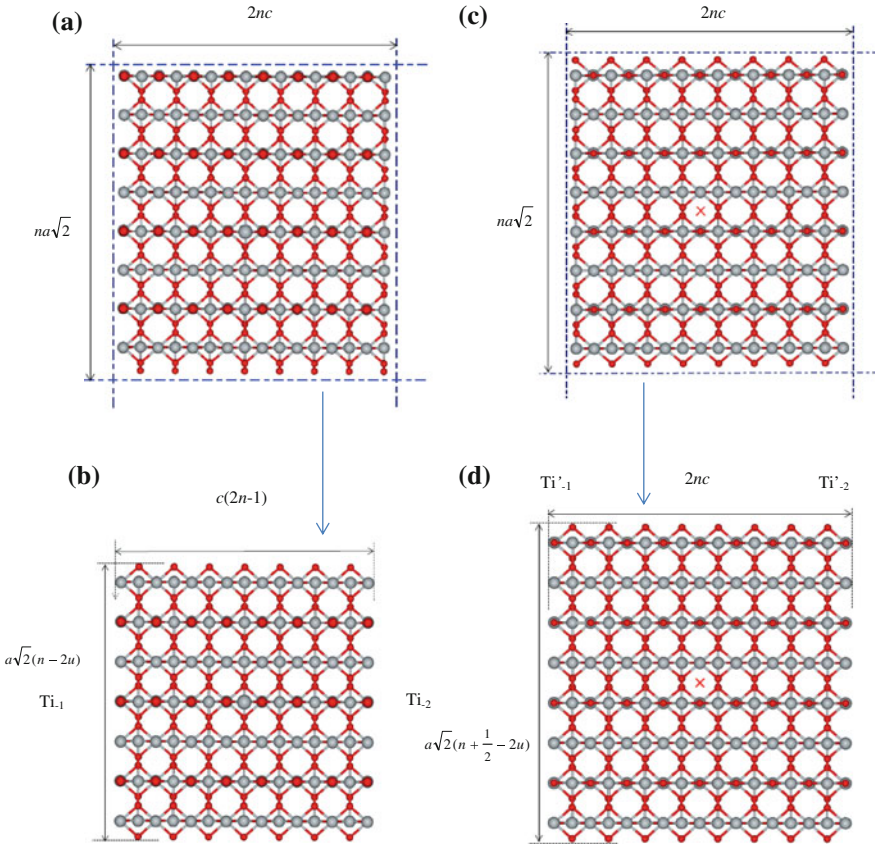

Fig. 7.28 Transformation of 84 supercells of six-plane rutile (110) slabs to cross-sections of either Ti atom-centered (**a** → **b**) or *hollow site*-centered [110] nanowires (**c**→**d**). The dot-dashed lines in Fig. 7.28a, c show the borders of adjacent slab supercells. The centers of *hollow site*- and Ti atom-centered nanowires are shown by *crosses* and *balls* of a larger diameter, respectively. The consequent transformation of Ti_{-1} and Ti_{-2} (**b**) as well as Ti_{-1} and Ti_{-2} (**d**) atoms can be described by D_{2h} and C_s point groups, respectively (see explanation in the text). The lengths of *rectangular* sides in the slab supercells and NW cross-sections are defined analytically for arbitrary extensions

Ti_2 atoms in the middle of opposite sides to each other (Fig. 7.28b), while the latter analogously transforms the titanium atoms located at the upper corners of the same side (Fig. 7.28d). Both pairs of Ti atoms are positioned in the same atomic plane. The lengths of corresponding pairs of rectangular sides are $c(2n1)$ and $a\sqrt{2}(n-2u)$ versus $2nc$ and $a\sqrt{2}(n+1/2-2u)$, respectively. Obviously, the cross-sections of [110]-oriented nanowires cannot be translated along the side directions, to provide the formation of adjacent supercells which are complementary to the prototype for the $2D \rightarrow 1D$ structural transition (Fig. 7.28).

For the orthogonal [110] TiO_2 NWs, the four formula units of the primitive cell lie in the six cross-sectional atomic planes (Fig. 7.29b). The symmetry of a [110] nanowire coincides with the symmetry of the analogous type of [001] NW if the

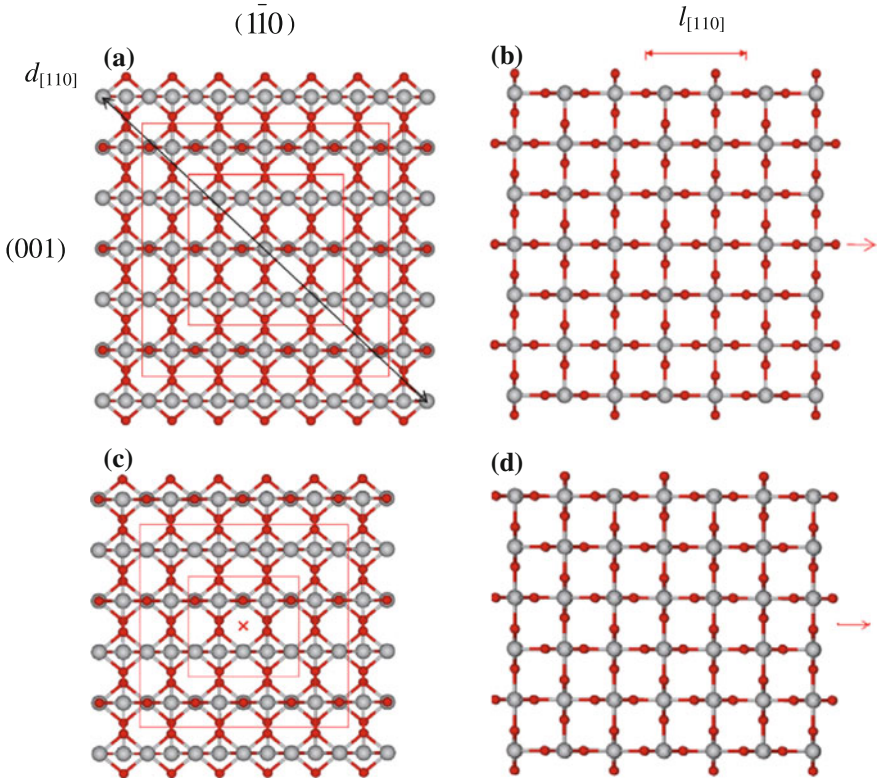

Fig. 7.29 The cross sectional **a** and lateral **b** images of a non-optimized [110]-oriented Ti atom-centered NW possessing the D_{2h} symmetry and containing 105 formula units per NW UC, with aside (001) and (110) facets (the former is shown as **b** image). The *red rectangles* in the cross-section **a** show the borders of prism models for middle and small titania nanowires containing 55 and 21 formula units per UC, respectively. The images of the [110]-oriented hollow site-centered titania nanowire (**c**, **d**) possessing the C_{2v} point symmetry and containing 78 formula units per unit cell are shown in a manner similar to **a** and **b**, respectively, including prism models of middle and small TiO_2 NWs containing 36 and 10 formula units per unit cell. The diameter of a nanowire is shown in **a** by a twice-terminated arrow ($d_{[001]}$) while its period (length of UC) is shown in **b** as ($l_{[001]}$)

translation axis with rotation by π goes through the Ti atom (the rod group Pmmm). Indeed, Fig. 7.29a, b shows that the symmetry operations for [110] NWs are reflection in the vertical (v) plane (containing the translation axis) and rotation around the two-fold translation axis in this plane. The symmetry operations also include rotations around the two-fold axis in the horizontal plane (orthogonal to the translation axis). Thus, the point group of this nanowire type is again D_{2h}, analogous to the Ti atom-centered [001] nanowire. As to the symmetry of [110] NWs with hollow site-centered symmetry axes (Fig. 7.29c, d) it can be described by a rather poor C_s point group characterized by the presence of the mirror plane across the nanowire cross-section only. However, since the lateral {110} facets of this NW configuration are described by the C_{2v} point group, the latter can be used to characterize the whole nanowire.

Let us discuss the properties of rutile-based [001] and [110] nanowires calculated in [94].

The main results of large-scale PBE and PBE0 calculations with total energy optimization on both Ti atom- and hollow site-centered titania [001] nanowires with four diameters for PBE and PBE0 exchange-correlation functionals are presented in Tables 7.22 and 7.23.

Figures 7.30 and 7.31 demonstrate the distorted structure of [001]-oriented NWs with the initial morphology discussed above. In both figures, the distorted geometry of the [001]-oriented NWs calculated using the PBE0 method is shown since PBE calculations give qualitatively similar images. Structural relaxation leads to an increase in the optimized d_{NW} and a decrease in l_{NW}. The larger the d_{NW}, the closer its equilibrium value to the initial non-optimized d_{NW} (Fig. 7.26), whereas l_{NW} also approaches the initial value of the NW unit cell length. Figures 7.30 and 7.31 demonstrate a decrease in the NW distortion with increasing d_{NW}, this distortion is more noticeable in the case of hollow site-centered nanowires. At the edges and corners of [001]-oriented NWs the Ti–O bonds have been found to be more covalent than those in the proximity of nanowire axis or in the bulk, thus explaining the appearance of structural distortion after geometry relaxation, e.g., shortening of the corner and edge Ti–O bonds. These conclusions are confirmed by the consequent decrease of the surface energy in both types of TiO_2 nanowires approaching that for the lateral {110} and $\{1\bar{1}0\}$facets, which are energetically the most favorable (Table 7.9). Comparative analysis of surface energies for the [001] and [110]-oriented nanowires is illustrated by Fig. 7.32, clearly showing energetic preference for the former, which correlates well with the recently published results of simulations on rutile-based TiO_2 NWs with varying diameters [143]. Moreover, the rutile-based NWs with hollow–centered symmetry axes have been found to be energetically slightly more stable than Ti atom-centered ones, especially when nanowire diameter increases. As the change of band gaps with increasing d_{NW}, these values approach those for the bulk beginning with the smaller gaps for ultrathin Ti atom-centered NWs. Conversely, the decrease in the calculated band gap with increasing d_{NW} has been observed for hollow site-centered nanowires beginning with large gaps in the case of small diameters, this peculiarity was confirmed in other theoretical simulations [137, 141, 143]. Analogous changes of band gap occur for slabs with increasing thickness. Irrespective of the NW type, the convergence to the value of band gap for the titania rutile bulk has been observed for both models. In [94], the results obtained for a Ti atom-centered nanofilament containing only one formula unit per NW unit cell were not analyzed since the properties of this nanostructure drastically differed from those for more thick nanowires [128]. The corresponding oscillations of surface energy and band gap for nanowires of small diameters were observed in study [143].

Figure 7.33 presents the total densities of states for rutile-based TiO_2 nanowires and those projected on the surface and internal atoms calculated using the PBE0 method for Ti atom- and hollow site-centered [001]-oriented NWs of largest diameters (Fig. 7.26 as well as Tables 7.22 and 7.23). By comparison, gray–filled areas on both plots show the total DOS for the titania rutile bulk. One can observe a slight

Table 7.22 The structural and electronic properties of optimized Ti atom-centered [001]-oriented NWs (Fig. 7.26a, b)

Nanowire size (number N_{UC} of TiO_2 formula units per UC)	Initial diameter of NW d_{NW}, Å	Optimized NW (its change) d_{NW}, Å l_{NW_UC}, (δd_{NT}, %)	Initial length of NW UC Å	Optimized NW period (its change) l_{NW_UC}, Å (δ l_{NT}, %)	Surface energy of nanowire E_{surf}, J/m^2	Band gap (its change from that of bulk) $\Delta\varepsilon_g$, eV ($\delta\varepsilon_g$, %)
PBE						
9 (*smallest*)	11.12	11.49 (+3.33)	2.98	2.91 (–2.37)	1.02	1.04 (–40.38)
25 (small)	20.24	20.71 (+2.32)		2.94 (–1.22)	0.91	1.51 (–13.25)
49 (middle)	29.40	29.94 (+1.84)		2.96 (–0.78)	0.84	1.57 (–9.67)
81 (large)	38.67	39.27 (+1.55)		2.96 (–0.57)	0.79	1.60 (–8.18)
PBE0						
9 (*smallest*)	10.98	11.27 (+2.63)	2.96	2.88 (–2.88)	1.07	3.15 (–21.59)
25 (small)	19.98	20.48 (+2.48)		2.93 (–1.26)	0.97	3.61 (–6.09)
49 (middle)	29.02	29.59 (+1.97)		2.94 (–0.82)	0.91	3.70 (–3.51)
81 (large)	38.17	38.71 (+1.41)		2.95 (–0.61)	0.86	3.74 (–2.41)

Table 7.23 The structural and electronic properties of optimized hollow site-centered [001]-oriented NWs (Fig. 7.26c, d)

Nanowire size (number N_{UC} of TiO_2 formula units per UC)	Initial diameter of NW d_{NW}, Å	Optimized NW (its change) d_{NW}, Å l_{NW_UC}, (δd_{NT}, %)	Initial length of NW UC Å	Optimized NW period (its change) l_{NW_UC}, Å ($\delta\, l_{NT}$, %)	Surface energy of nanowire E_{surf}, J/m^2	Band gap (its change from that of bulk) $\Delta\varepsilon_g$, eV ($\delta\varepsilon_g$, %)
PBE						
4 (*smallest*)	6.63	6.87 (+3.61)	2.98	2.89 (−3.01)	1.06	3.40 (95.40)
16 (small)	15.67	16.09 (+2.69)		2.94 (−1.46)	0.85	2.34 (34.48)
36 (middle)	24.82	25.33 (+2.05)		2.95 (−0.88)	0.77	2.24 (28.74)
64 (large)	33.98	34.57 (+1.72)		2.96 (−0.61)	0.75	2.03 (16.67)
PBE0						
4 (*smallest*)	6.55	6.79 (+3.73)	2.96	2.88 (−3.06)	1.11	4.53 (18.28)
16 (small)	15.47	15.89 (+2.75)		2.92 (−1.54)	0.87	4.09 (6.79)
36 (middle)	24.49	25.01 (+2.10)		2.93 (−1.02)	0.84	3.98 (3.92)
64 (large)	33.54	34.14 (+1.80)		2.95 (−0.65)	0.83	3.93 (2.61)

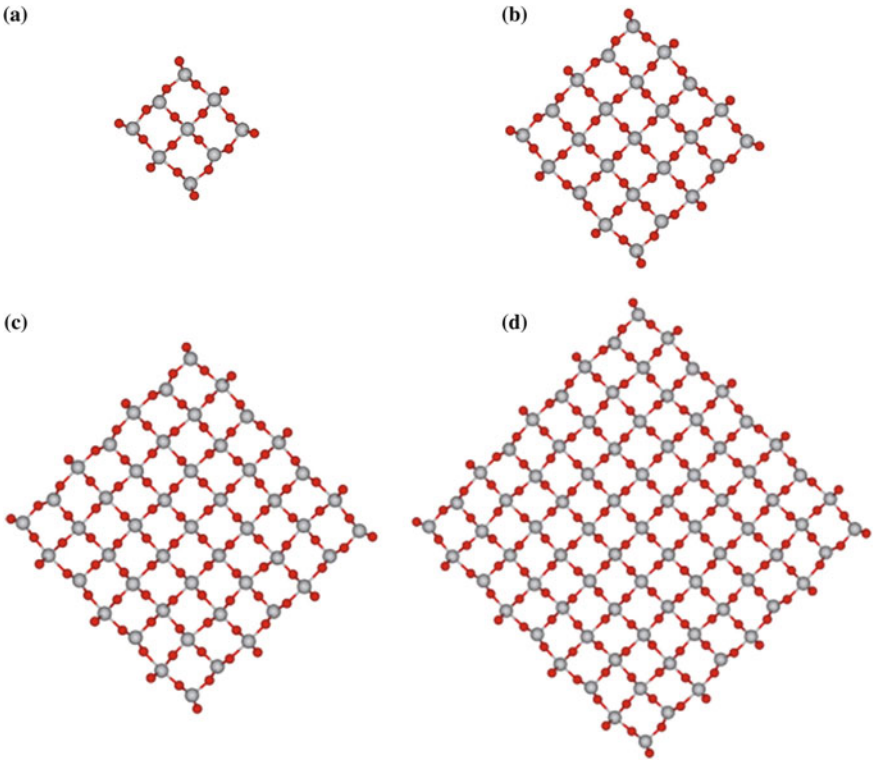

Fig. 7.30 Cross-sectional views of optimized Ti atom-centered titania [001] NWs of smallest (**a**), small (**b**), middle (**c**) and large (**d**) diameters calculated using the LCAO-PBEmethod (parameters of relaxation are present in Table 7.22). Section planes for present images are chosen to be the same as in Fig. 7.13

shift of the DOS projected on the surface (outer) or internal NW atoms towards the larger versus the lower energies, respectively, compared to the total DOS. The latter is qualitatively similar to the total DOS of the titania bulk. On the other hand, no essential qualitative difference between the DOSs for Ti atom- and hollow site-centered NWs exists. This can be explained by different coordination of surface and internal atoms. Obviously, the PDOSs of Ti and O one-electronic states imply that the states of the highest valence band (VB) zones mainly arise from the 2p states of oxygen atoms, while those of the lowest conduction band (CB) zones come from the 3d states of Ti atoms. The analysis of parameters for both 3d(Ti)–3d(Ti) and 3d(Ti)–2p(O) bonding states was performed elsewhere [143].

The results obtained in [94] for TiO_2 [110]-oriented NWs are presented in Tables 7.24 and 7.25 and Figs. 7.32, 7.34 and 7.35.

It is important to find similarities and differences between the properties of [001] and [110] types of structurally different TiO_2 NWs. The main qualitative conclusions for NW properties depending on d_{NW} are found to be close to being similar to those

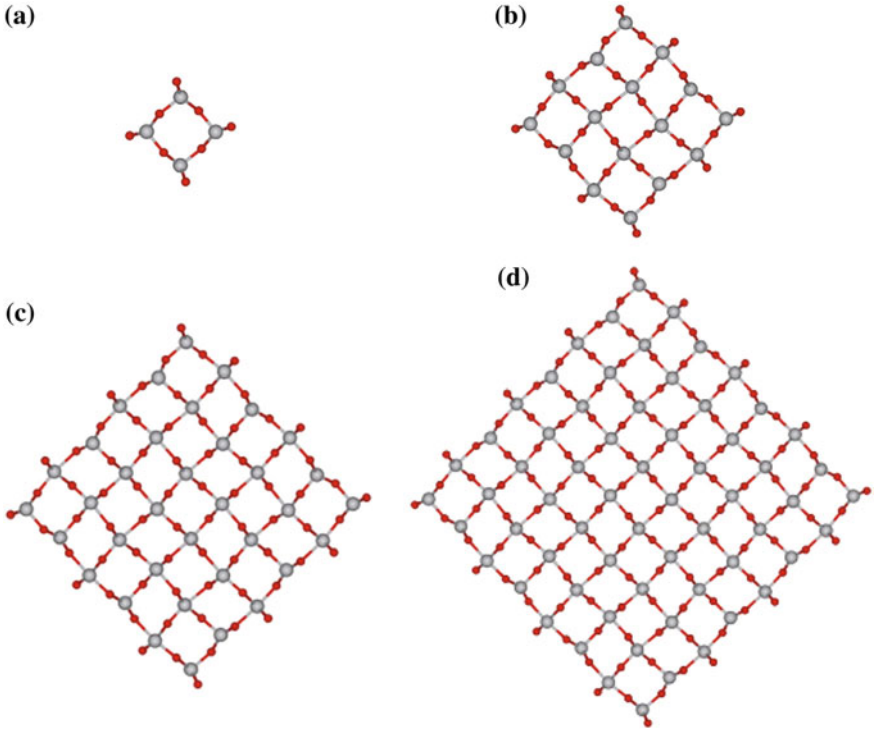

Fig. 7.31 Cross-sectional views of optimized hollow site-centered titania [001] NWs of smallest (**a**), small (**b**), middle (**c**) and large (**d**) diameters calculated using the LCAO-PBE method (parameters of relaxation are present in Table 7.23). Section planes for present images are chosen to be the same as in Fig. 7.13

drawn in [143]. However, the comparison of surface energies gives substantial energetic preference for [001]-oriented NWs over [110]-oriented nanowires, which are terminated by the alternating {001} and $\{1\bar{1}0\}$ facets (Table 7.9 clearly demonstrates that (001) rutile surfaces are less-stable).

A distorted structure of Ti atom-centered [110]-oriented NWs has been obtained using the rod group symmetry Pmmm, while relaxed hollow site-centered nanowires are described by the Pm2m rod group. As in the case of [001] nanowires, [110]-oriented NWs with hollow–centered symmetry axes have been found to be energetically slightly more stable than Ti atom-centered ones (Fig. 7.32, as well as Tables 7.24 and 7.25). Figures 7.34 and 7.35 illustrate a decrease in the [110] NW distortion with increasing d_{NW}, that is analogous to [001] NW. Again, such a distortion is more noticeable in the case of hollow site-centered nanowires.

The results for the Ti atom-centered [110]-oriented nanofilament containing only 3 formula units per NW UC, presented in [142] clearly showed that this nanofilament noticeably differs from bulk-like nanowires, which are simulated in [94].

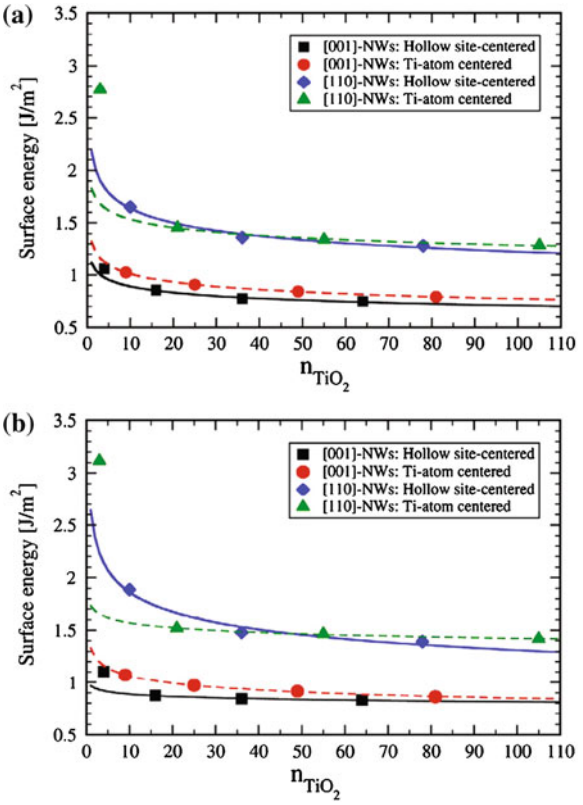

Fig. 7.32 Dependences of surface energies for Ti atom- and hollow site-centered titania nanowires of [001] and [110] orientations on the number of formula units per NW unit cells (Tables 7.11 and 7.22 and 7.23 and 7.24) calculated using the LCAO PBE (**a**) and PBE0 (**b**) methods. The labels of different shapes correspond to the calculated values of the surface energy for different NW configurations. Spline treatment of lines initially joined the nearest labels of the same shapes has been performed to obtain the smooth *curves*

The corner and edge Ti–O bonds are again more covalent and slightly shorter than those in the proximity of the symmetry axes of [110]-oriented NWs. The same is true for the change of band gaps with increasing d_{NW} since these values approach the band gap for the bulk beginning with the nanowire containing 21 formula units per unit cell. Again, in the case of Ti atom-centered TiO_2 NWs the values of the band gap increase with a growth of d_{NW}, while in the case of hollow site-centered NWs they decrease, analogously to the (110) slab with increasing thickness (cf. Tables 7.9, 7.24 and 7.25).

The conclusions, which can be drawn when analyzing the total and projected densities of states imaged in Fig. 7.36 and calculated using the PBE0 method for Ti atom–and hollow site-centered [110]-oriented titania NWs of largest diameters

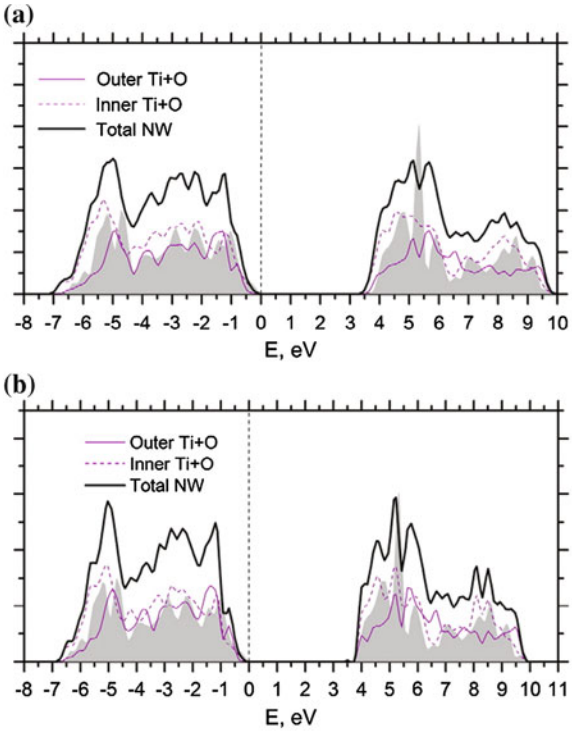

Fig. 7.33 The total densities of states (shown by *bold lines*) as well as the densities projected on either surface or internal atoms (*solid* or *dashed lines*, respectively) for [001]-oriented NWs of largest diameters (Fig. 7.26) centered on the Ti atom (**a**) and hollow site (**b**) containing 81 and 64 formula units per nanowire's UC, respectively. The *filled gray areas* correspond to the total DOS of the titania rutile bulk

(Fig. 7.29, as well as Tables 7.24 and 7.25), are qualitatively similar to those for [001]-oriented NWs.

Let us summarize the results obtained in [94] for rutile-based nanowires. 1. The procedure of the structural generation of rutile-based [001]– and [110]–oriented four-facetted TiO_2 nanowires with symmetric prism-type shapes from titania (001) and (110) slabs, respectively, was suggested in [94]. In the case of rhombic–like square hollow site-centered [001] NWs, the nanowire cross-section is structurally compatible with the corresponding supercell of the (001) rutile slab. Thus, no additional geometry transformation is required to generate this NW configuration. For the generation of other configurations of rutile-based nanowires, either addition or removal of certain number of formula units is necessary from the corresponding slab supercells after a release of the periodic 2D boundary conditions. Moreover, rutile-based NWs with hollow–centered symmetry axes have been found to be slightly more stable than the Ti atom-centered ones, especially when the nanowire diameter increases. 2. The properties of rutile-based nanowires are both size and shape depen-

Table 7.24 The structural and electronic properties of optimized Ti atom-centered [110]-oriented NWs (Fig. 7.29a, b)

Nanowire size (number N_{UC} of TiO_2 formula units per UC)	Initial diameter of NW d_{NW}, Å	Optimized NW (its change) d_{NW}, Å l_{NW_UC}, (δd_{NT}, %)	Initial length of NW UC Å	Optimized NW period (its change) l_{NW_UC}, Å (δ l_{NT}, %)	Surface energy of nanowire E_{surf}, J/m^2	Band gap (its change from that of bulk) $\Delta\varepsilon_g$, eV ($\delta\varepsilon_g$, %)
PBE						
21 (small)	11.00	11.24 (+2.19)	6.57	6.38 (−3.06)	1.45	1.46 (−16.47)
55 (middle)	19.68	20.09 (+2.09)		6.42 (−2.30)	1.34	1.61 (−7.52)
105 (large)	28.43	28.97 (+1.88)		6.45 (−1.86)	1.29	1.64 (−5.88)
PBE0						
21 (small)	10.85	11.13 (+2.52)	6.49	6.32 (−2.72)	1.52	3.65 (−4.93)
55 (middle)	19.43	19.91 (+2.45)		6.36 (−2.06)	1.46	3.76 (−1.86)
105 (large)	28.07	28.69 (+2.22)		6.38 (−1.65)	1.42	3.79 (−1.06)

Table 7.25 The structural and electronic properties of optimized Ti atom-centered [110]-oriented NWs (Fig. 7.29 c,d)

Nanowire size (number N_{UC} of TiO_2 formula units per UC)	Initial diameter of NW d_{NW}, Å	Optimized NW (its change) d_{NW}, Å l_{NW_UC}, (δd_{NT}, %)	Initial length of NW UC Å	Optimized NW period (its change) l_{NW_UC}, Å (δ l_{NT}, %)	Surface energy of nanowire E_{surf}, J/m^2	Band gap (its change from that of bulk) $\Delta\varepsilon_g$, eV ($\delta\varepsilon_g$, %)
PBE						
10 (small)	6.75	6.95 (+3.06)	6.57	6.26 (−4.92)	1.65	3.40 (95.40)
36 (middle)	15.32	15.48 (+1.02)		6.37 (−3.15)	1.36	2.34 (34.48)
78 (large)	24.05	24.26 (+0.86)		6.42 (−2.30)	1.28	2.24 (28.74)
PBE0						
10 (small)	6.66	6.86 (+3.03)	6.49	6.21 (−4.49)	1.89	4.53 (18.28)
36 (middle)	15.13	15.47 (+2.30)		6.31 (−2.79)	1.48	4.09 (6.79)
78 (large)	23.74	24.22 (+2.05)		6.36 (−2.03)	1.39	3.98 (3.92)

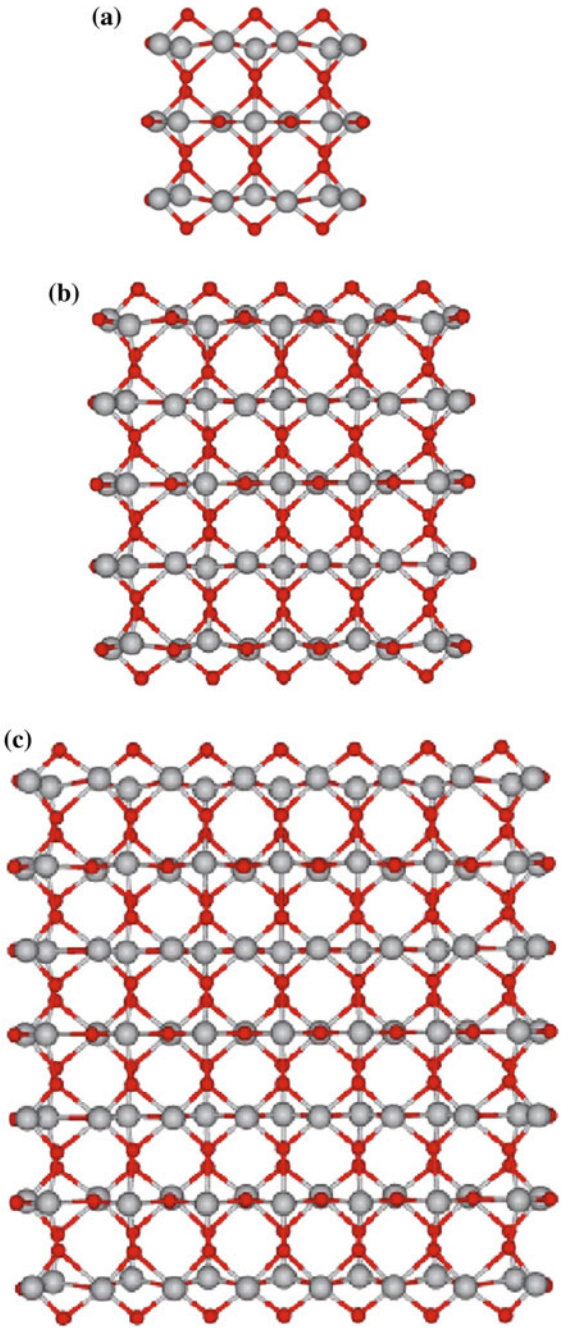

Fig. 7.34 Cross-sectional views of optimized Ti atom-centered titania [110] NWs of small (**a**), middle (**b**) and large (**c**) diameters calculated using the LCAO-PBE method (parameters of relaxation are present in Table 7.22). The section planes for the present images are chosen the same as in Fig. 7.29

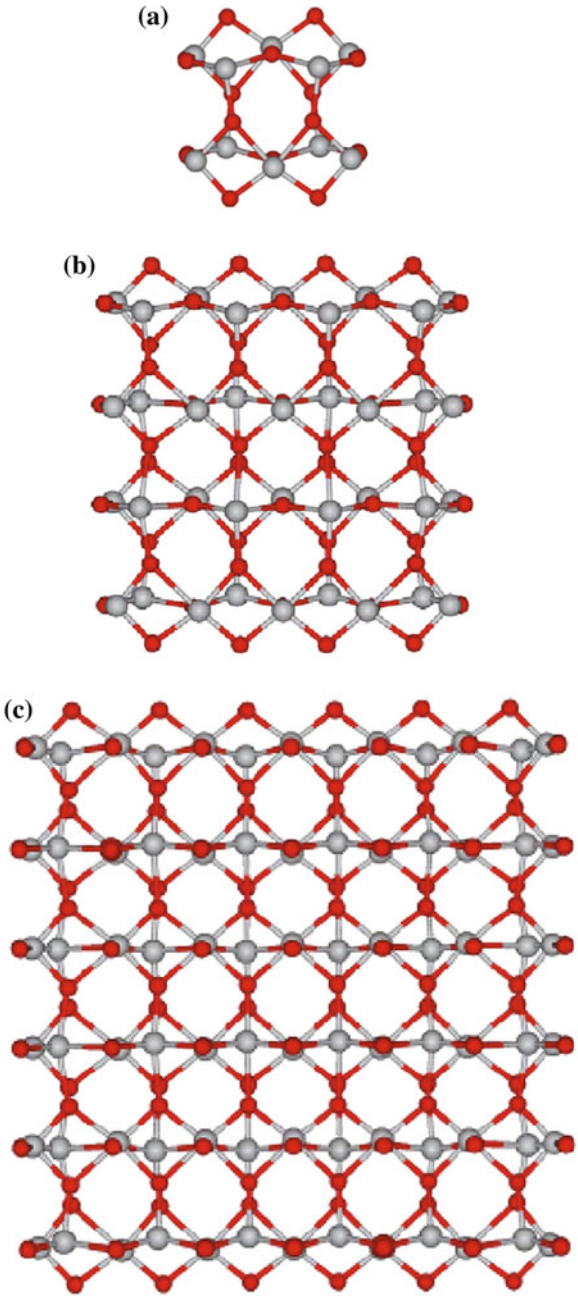

Fig. 7.35 Cross-sectional views of optimized hollow site-centered titania [110] NWs of small (**a**), middle (**b**) and large (**c**) diameters calculated using the DFT-PBE method (parameters of relaxation are present in Table 7.24). The section planes for the present images are chosen the same as in Fig. 7.29

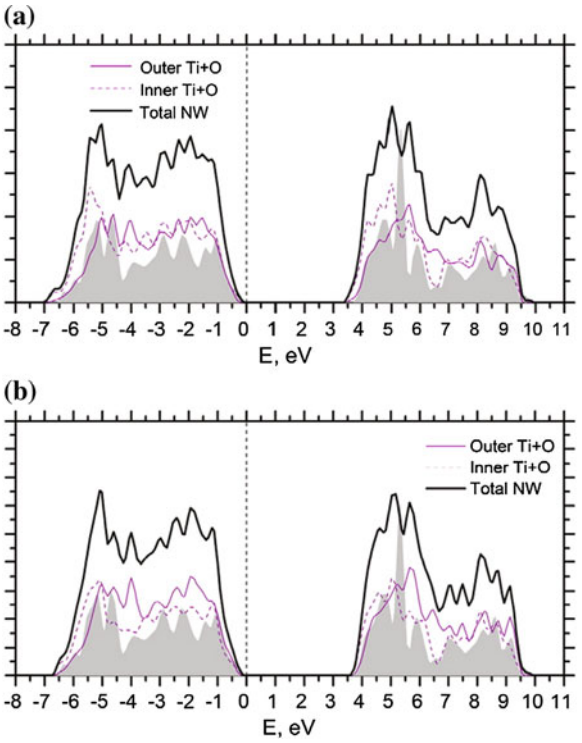

Fig. 7.36 The total densities of states (shown by *bold lines*) as well as the densities projected on either surface or internal atoms (*solid* or *dashed lines*, respectively) for [110]-oriented NWs of largest diameters (Fig. 7.29) centered on the Ti atom (**a**) and hollow site (**b**) containing 105 and 78 formula units per nanowire's UC, respectively. The *filled gray areas* correspond to the total DOS of the titania rutile bulk

dent. The large-scale calculations of the bulk crystal surface energy per formula unit allow a direct comparison of the relative stability of both 2D slabs and 1D nanowires and gives the main criterion of their stability. The values of d_{NW} slightly increase, whereas the periodicity length l_{NW} has been found to be reduced after NW geometry optimization. The larger NW diameter, the closer are its geometry parameters as well as the band gap to those of rutile-based TiO_2 bulk and non-optimized (001) and (110) slabs, whereas the NW surface energy approaches that of the facets terminating the nanowire. In the case of Ti atom-centered NWs, the values of the band gap grow with increasing d_{NW}, while in hollow site-centered NWs, these values decrease in analogous conditions, analogously to the band gaps of slabs with increasing thickness. 3. The comparative ab initio calculations using the DFT PBE and hybrid DFT HF PBE0 methods confirm that the stability of nanowires is determined mainly by the stability of their lateral facets, that is why [001]-oriented NWs terminated by {110} facets are energetically more preferable than [110] NWs terminated by alternating {110} and {001} facets. The surface energy calculation for (110) and (001) slabs allows

one to estimate the NW surface energy. Indeed, for hollow site-centered [001] and [110] nanowires the converged PBE0 surface energies are 0.83 and 1.39 J/m^2. The use of the slab averaged energies for all the facets gives 0.74 and 1.22 J/m^2. 4. Due to a structural compatibility between the TiO_2 slab supercells and the cross-sections of growing NWs, the results obtained in [94] can be used for further simulation of TiO_2 nanowire growth upon titania–containing substrate. On the other hand, some balance between the stability of supercell slabs with a large surface area and thick nanowires can exist. That is why the results of calculations [94] do not contradict experimental observations that the growth of thick TiO_2 NWs with [110] orientation (whose diameters are larger than 10 nm) can be more preferable than the stable (110) facets of the polycrystalline TiO_2/sapphire substrate [132].

Only a limited number of studies performed so far considered not just bare titania nanowires but NWs with vacancies, their chemical reactivity [144] and hydrogen-passivated NWs [137]. Such a limitation can be explained by the reduced symmetry of defective NWs, down to the P1 rod group (C_1 point group), and thus by a substantial increase of computational time. The substantial increase in the CPU time necessary for the calculations on titania nanowires described by the point group C_1 is accompanied by a noticeable limitation of NW size considered.

The LCAO calculations discussed above for bare titania nanowires use the full RG symmetry of rutile-based NWs. However the total energy per 1D unit cell and NW translation period can change if the initial structure RG symmetry is lowered. Table 7.26, see [142], clearly demonstrates that these changes are small both for [001] and [110] oriented nanowires. Therefore the calculations on titania nanowires possessing middle and large diameters $\leq$ 2 nm (which are considered to be more realistic for a comparison with the experiment [128]) become possible.

When comparing the parameters calculated for titania slabs and both NW orientations using DFT PBE and hybrid the DFTHF PBE0 methods we can observe their qualitative proximity, except for the densities of one-electron energy states including band gaps [94]. Since calculations using the hybrid method are considerably more time-consuming, especially when using plane wave codes, the parameters of

Table 7.26 Dependence of the Total Energy per TiO_2 NW Unit Cell, E_{tot_NW}, and Its Period, l, Calculated Using CRYSTAL Code[15], on Point Groups Set in Inputs for [001]- and [110]-Oriented Nanowires

Properties	Point symmetry groups			
[001]-*oriented titania nanowires containing nine formula units (Fig. 7.26)*				
	C_1	C_2	C_{2h}	D_{2h}
E_{tot_NW}, Hartree	−1877.879367	−1877.879373	−1877.879132	−1877.879132
$l_{[001]}$, Å	2.9114	2.9115	2.9108	2.9100
[110]-*oriented titania nanowires containing three formula units (Fig. 7.29)*				
	C_1	C_2	C_{2h}	D_{2h}
E_{tot_NW}, Hartree	−625.710150	−625.710162	−625.710156	−625.710151
$l_{[110]}$, Å	6.2522	6.2511	6.2511	6.2513

structure and total energy for both slabs and nanowires can be calculated using the standard GGA DFT methods. This conclusion is important as PW calculations are made mainly using the GGA methods.

The localized atomic function (LCAO) method allows one to describe single 1D nanowires, whereas the plane wave (PW) method is more widespread for large-scale calculations on low dimensional periodic systems. However, to restore the 3D periodicity in the PW nanowire calculations, the 1D nanostructure supercell is artificially introduced; i.e., the NWs are placed into a square array with sufficiently large intertube distances. At such separations, the NW-NW interaction is usually found to be rather small. However, the convergence of results obtained using DFT-PW calculations depends on the artificial interwire interactions, thus additional computational efforts should be provided to ensure their negligibility. Such an artifact is certainly absent in the LCAO nanowire calculations. From this point of view, a comparison of results obtained in DFT-LCAO and DFT-PW calculations can be very important for their verification. Such a comparison was made in [142] in the calculations of rutile-based [001] and [110]-oriented TiO_2 nanowires with Ti atom-centered symmetry axes. The details of the DFT LCAO and DFT PW computational schemes are the same as those used in the bulk rutile comparative LCAO and PW calculations (see Sect. 3.8).

Tables 7.27 and 7.28 present the results of comparative DFT– LCAO and DFT–PW calculations of rutile TiO_2 [001] and [110] Ti–atom centered NWs [142]. Both methods have been used for calculations of the key NWs structural and electronic properties depending on the orientation, shape and diameter of TiO_2 [001] and [110] NWs (i.e., the changes of the diameters d_{NW} and unit cell lengths l_{NW} of nanowires during geometry optimization, as well as effective atomic charges correlated with the formation energies per formula unit E_{rel} and band gaps). A good quantitative correlation is observed between the results of the DFT-LCAO and DFT-PW calculations. In particular, the values of d_{NW} slightly increase, whereas l_{NW} are found to be reduced after NW geometry optimization, except for the thinnest [110] NW ($d_{NW} \approx 3$ Å), whose 1D unit cell contains three formula units making this nanostructure more like a nanofilament. The larger the NW diameter is, the closer its geometry parameters as well as the band gap to those of the rutile-based TiO_2 bulk. The NW morphology affects the stability of TiO_2 NWs at very small diameters (≤ 3 Å), while at larger diameters its role is attenuated.

Both LCAO and PW calculations clearly demonstrate that the more energetically preferable titania nanowires in the rutile phase (without hydrogen passivation and the presence of vacancies) display (110) facets when they are [001]-oriented and {110} and {001} facets when they are [110]-oriented. Thus a good quantitative correlation between the results of the DFT-LCAO and DFT-PW calculations on nanowires was established in [142].

Table 7.27 Structural and Electronic Properties of Optimized Rutile-Based TiO_2 [001]-Oriented Nanowires

	Initial diameter of NW	Optimized NW diameter (its change)	Initial length of NW UC	Optimized NW period (its change)	Effective atomic charges				Total energy difference per formula unit	Band gap (its deviation from that of bulk, Table 3.3)
					Central atoms		Corner atoms			
nanowire size (number N_{UC} of TiO_2 formula units per UC)	d_{NW}, Å	d_{NT}, Å (δd_{NT}, %)	l_{NW} Å	l_{NW} Å (δl_{NT}, %)	q_O, e	q_{Ti}, e	q_O, e	q_{Ti}, e	E_{tot}/N_{UC}[a], eV	$\Delta\varepsilon_g$, eV ($\delta\varepsilon_g$, %)
DFT-LCAO-PBE calculations										
9 (smallest)	11.122	11.493 (+3.33)	2.980	2.911 (−2.37)	−1.05	+2.11	−1.16	+2.17	0.73	1.04 (−40.38)
25 (small)	20.240	20.711 (+2.32)		2.944 (−1.22)	−1.11	+2.19	−0.99	+2.16	0.39	1.51 (−13.25)
49 (middle)	29.400	29.941 (+1.84)		2.956 (−0.81)	−1.08	+2.18	−0.99	+2.16	0.26	1.57 (−9.67)
81 (large)	38.670	39.270 (+1.55)		2.963 (−0.57)	−1.10	+2.19	−0.99	+2.16	0.20	1.60 (−8.18)
DFT-PAW-PBE calculations										
9 (smallest)	11.191	11.474 (+2.53)	2.964	2.926 (−1.28)	−1.04	+2.13	−1.02	+2.18	0.51	1.14 (−36.31)
25 (small)	20.363	20.720 (+1.75)		2.960 (−0.13)	−1.11	+2.18	−1.02	+2.21	0.25	1.58 (−11.73)

(continued)

Table 7.27 (continued)

	Initial diameter of NW	Optimized NW diameter (its change)	Initial length of NW UC	Optimized NW period (its change)	Effective atomic charges				Total energy difference per formula unit	Band gap (its deviation from that of bulk, Table 3.3)
					Central atoms		Corner atoms			
nanowire size (number N_{UC} of TiO_2 formula units per UC)	d_{NW}, Å	d_{NT}, Å (δd_{NT}, %)	l_{NW} Å	l_{NW} Å (δl_{NT}, %)	q_O, e	q_{Ti}, e	q_O, e	q_{Ti}, e	E_{tot}/N_{UC}[a], eV	$\Delta\varepsilon_g$, eV ($\delta\varepsilon_g$, %)
49 (middle)	29.570	30.003 (+1.46)		2.967 (+0.10)	−1.08	+2.17	−1.03	+2.22	0.16	1.63 (−8.94)
81 (large)	38.803	39.270 (+1.21)		2.972 (+0.27)	−1.08	+2.21	−1.02	+2.21	0.12	1.65 (−7.82)
DFT-USPP-PW91 calculations										
9 (smallest)	11.218	11.484 (+2.37)	2.981	2.931 (−1.68)	−1.06	+2.17	−1.03	+2.18	0.606	1.12 (−40.74)
25 (small)	20.413	20.725 (+1.53)		2.963 (−0.60)	−1.10	+2.28	−1.03	+2.23	0.319	1.65 (−12.70)
49 (middle)	29.650	30.019 (+1.24)		2.969 (−0.40)	−1.09	+2.25	−1.03	+2.22	0.216	1.73 (−8.47)
81 (large)	38.898	39.295 (+1.02)		2.973 (−0.27)	−1.16	+2.34	−1.03	+2.13	0.165	1.76 (−6.88)

[a]Difference of E_{tot}/N_{UC} for the nanowire and bulk; i.e., zero at the energy scale corresponds to the total energy of the rutile bulk, which is also defined as a relative formation energy [141]

Table 7.28 Structural and Electronic Properties of Optimized Rutile-Based TiO_2 [110]-Oriented Nanowires

	Initial diameter of NW	Optimized NW diameter (its change)	Initial length of NW UC	Optimized NW period (its change)	Effective atomic charges				Total energy difference per formula unit	Band gap (its deviation from that of bulk, Table 3.3)
					Central atoms		Corner atoms			
nanowire size (number N_{UC} of TiO_2 formula units per UC)	d_{NW}, Å	d_{NT}, Å (δd_{NT}, %)	l_{NW} Å	l_{NW} Å (δl_{NT}, %)	q_O, e	q_{Ti}, e	q_O, e	q_{Ti}, e	E_{tot}/N_{UC}[a], eV	$\Delta\varepsilon_g$, eV ($\delta\varepsilon_g$, %)
DFT-LCAO-PBE calculations										
9 (smallest)	2.958	2.882 (−2.64)	6.572	6.251 (−5.14)	−1.05	+2.11	−1.16	+2.17	4.55	1.60 (−8.12)
25 (small)	10.996	11.237 (+2.19)		6.377 (−3.06)	−1.05	+2.19	−1.05	+2.05	0.96	1.46 (−16.47)
49 (middle)	19.683	20.094 (+2.09)		6.424 (−2.30)	−1.11	+2.19	−1.05	+2.04	0.57	1.61 (−7.52)
81 (large)	28.431	28.966 (+1.88)		6.452 (−1.86)	−1.09	+2.19	−1.05	+2.04	0.41	1.64 (−5.88)
DFT-PAW-PBE calculations										
9 (smallest)	2.964	2.827 (−4.62)	6.532	6.333 (−3.14)	−1.10	+2.20	−0.96	+2.06	2.26	1.53 (−16.99)
25 (small)	11.033	11.225 (+1.74)		6.418 (−1.78)	−1.10	+2.27	−1.01	+2.10	0.69	1.49 (−20.13)

(continued)

Table 7.28 (continued)

	Initial diameter of NW	Optimized NW diameter (its change)	Initial length of NW UC	Optimized NW period (its change)	Effective atomic charges				Total energy difference per formula unit	Band gap (its deviation from that of bulk, Table 3.3)
					Central atoms		Corner atoms			
nanowire size (number N_{UC} of TiO_2 formula units per UC)	d_{NW}, Å	d_{NT}, Å (δd_{NT}, %)	l_{NW} Å	l_{NW} Å (δl_{NT}, %)	q_O, e	q_{Ti}, e	q_O, e	q_{Ti}, e	E_{tot}/N_{UC}[a], eV	$\Delta\varepsilon_g$, eV ($\delta\varepsilon_g$, %)
49 (middle)	19.756	20.075 (+1.61)		6.457 (−1.16)	−1.10	+2.17	−1.08	+2.10	0.39	1.63 (−9.82)
81 (large)	28.539	28.943 (+1.42)		6.480 (−0.80)	−1.10	+2.16	−1.09	+2.19	0.28	1.68 (−6.55)
DFT-PAW-PBE calculations										
9 (smallest)	2.982	2.827 (−5.20)	6.548	6.333 (−3.39)	−1.06	+2.11	−0.95	+2.01	2.48	1.30 (−45.38)
25 (small)	11.087	11.198 (+1.00)		6.437 (−1.72)	−1.14	+2.27	−1.10	+2.11	0.79	1.47 (−28.57)
49 (middle)	19.845	20.055 (+1.06)		6.457 (−1.41)	−1.16	+2.25	−1.10	+2.10	0.47	1.67 (−13.17)
81 (large)	28.665	28.917 (+0.88)		6.480 (−1.05)	−1.13	+2.32	−1.19	+2.19	0.34	1.73 (−9.25)

[a]Difference of E_{tot}/N_{UC} for the nanowire and bulk; i.e., zero at the energy scale corresponds to the total energy of the rutile bulk, which is also defined as a relative formation energy [141]

7.2.5 *Orientation Effects in the Morphology and Electronic Properties of Rutile Nanowires, Anatase Nanowires and Facetted Nanotubes*

Nanostructure orientation is important in the calculation of the properties of nanostructures. The orientation effects in the morphology and electronic properties of TiO_2 nanostructures have been studied for rutile nanowires [128] and anatase nanowires [145] and nanotubes [146] by means of ab initio DFT PW calculations with structural optimization.

[001] and [110] oriented rutile NWs display the three possible morphology (the rhomb, the polyhedron, and the square), see Fig. 2.26. The knowledge of the relative surface energies is useful in predicting the shape of a nanostructure whose facets display low surface energies [128]. As we have seen above in the case of TiO_2 in the rutile phase, the (110) surface has been shown to possess the lowest surface energy, followed by the (100), (011), and (001) surfaces, respectively. Therefore [001]-oriented rutile NWs with rhomb topology (four {110} facets) are expected to have the lowest surface energy. This conclusion is confirmed both by the results of calculations [94, 128] and experimental study [133].

A short summary of the results obtained in [128] is as follows. The most thermodynamically preferable TiO_2 NWs in the rutile phase without hydrogen passivation or O vacancies display {110} facets when they are [001]-oriented and the {110} and {001} facets when they are [110]-oriented. The morphology affects the stability of the rutile TiO_2 NWs at small diameters, while at larger diameters its role is attenuated. The most stable [001]-oriented NWs are characterized by band gap values that are invariable with respect to the diameter of the nanostructures and close to that of the bulk. Such band gap behavior is anomalous with respect to the expected changes in the gap values due to quantum confinement effects. This happens because of the stabilization role of the states in the top valence bands and in the bottom conduction bands that come from atoms located close to and at the surface of these nanostructures. One can suggest that the interaction between the edges of adjacent {110} and {100} facets in NWs with the [001] axis leads to a sizable band gap reduction. In the case of [110]-oriented NWs, the presence of the flat bands, similar the localized levels in the gap region, is found to be an intrinsic feature of such nanostructures, which is not connected with the O vacancies or surface states. These flat bands composed of Ti–d states also provide a decrease in the band gaps. The calculated band structures of different NWs do not show any sign of surface dangling bonds in the gap region, indicating that the hydrogen passivation is not appropriate for these nanostructures. The absorption coefficients for rutile NWs with different morphology and orientations do not follow the changes in the gaps and do not display any shift of the absorption edge to the lower energy range. [001]-oriented NWs with a rhomb morphology can be considered as a suitable material for photovoltaic and photocatalytic cells, however an efficient way to shift the absorption edge to the lower energy range and to improve the transport properties of these NWs should be found.

According to experimental observations, there are three different growth orientations of TiO_2 NWs in the anatase phase: [001], [100] and [110], see references in [145]. The smallest experimentally observed diameter of anatase TiO_2 NWs has been detected to be 4–5 Å, [134].

Theoretical investigations of anatase NWs [139–141] mainly focus on the band gap variation with diameter and the data obtained are different and contradictory to the experimental data. The study of the orientation effects on the electronic structure of anatase-based NWs allows one to understand the situation: ab initio calculations [145] revealed a sizable anisotropy in the electronic properties of anatase TiO_2 nanowires to exist with respect to the orientation: nanowires with [001], [100] and [110] axes are found to be direct band gap, indirect band gap and degenerate semiconductor materials, respectively.

Structural optimization and band structure calculations of TiO_2 NWs were performed in [145] by utilizing the first principles total energy PAW method (see Chap. 3) and the PW basis (an energy cutoff was introduced at 420 eV). PBE exchange and correlation potentials were included, and periodic boundary conditions were applied along the nanowire axis with the unit cell parameter $a_{||}$. In order to ensure a negligible interaction between the neighboring NWs, at least 7 Å of vacuum were introduced (a further increase in the vacuum thickness did not noticeably affect the total energy). All the atoms in TiO_2 NWs were allowed to relax. The grid of $1 \times 1 \times 6$ Monkhorst-Park points was used in the calculations and the atomic relaxation was made. To ensure convergence, the final iterations were performed on the 1x1x10 grid. The optimization of $a_{||}$ was done by gradually increasing/decreasing its value along with a relaxation of the atomic positions till an equilibrium was reached. Calculations of the band structures were performed using the self-consistent charge densities. The charge distributions and transfers were analyzed by the Bader method. After the optimization the bulk lattice parameters of TiO_2 in the anatase phase were found to be $a = 3.80(3.79)$ Å and $c = 9.57(9.52)$ Å. The experimental values of these parameters are given in brackets, the LCAO PBE0 calculations give $a = 3.78$ Å and $c = 9.51$ Å, see Table 7.6.

The initial structures of TiO_2 NWs were generated in [145] on the basis of the bulk, which was specifically oriented, by cutting it along different atomic planes in order to form facets parallel to the NW axis. According to the selected orientation of NWs, $a_{||}$ was set at c, a and 2a for such nanostructures with the [001], [100] and [110] axes, respectively. The TiO_2 stoichiometry of NWs was kept invariable. As in the case of NWs, the same energy cutoff, vacuum thickness as well as the procedure of structural optimization and band structure calculation were applied for (001), (100) and (110) TiO_2 slabs which have two equal surfaces and different thickness.

The morphology of TiO_2 NWs with [001] axes can be characterized by {100} and {110} facets. The cross sections of such NWs are shown in Fig. 7.37, where cases conventionally called the square, the polyhedron and the rhomb are considered. In the square NWs only {100} facets are present, while in the rhomb NWs one can notice {110} facets. In the case of the polyhedron NWs both {100} and {110} facets, which are almost equal in size, define their shape. The diameters of these NWs are 2.6, 2.5 and 2.5 nm for the square, the polyhedron and the rhomb morphology, respectively.

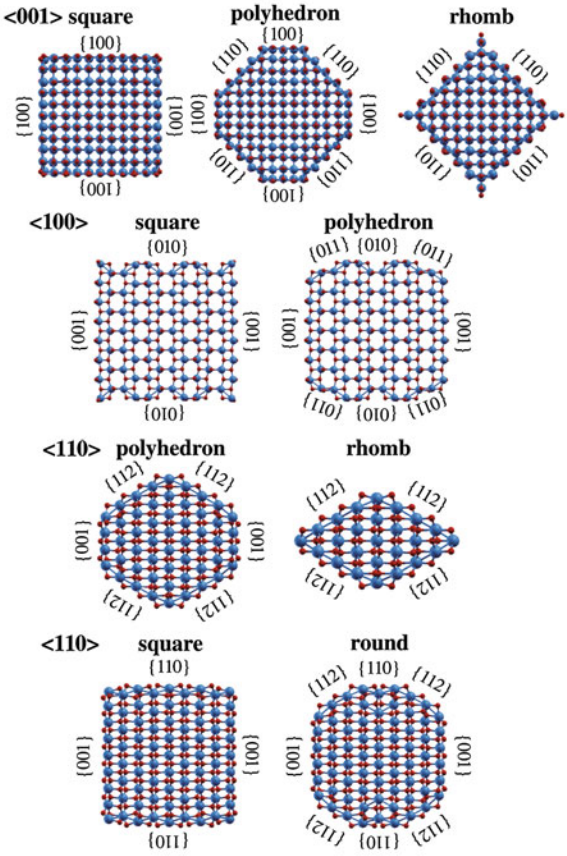

Fig. 7.37 Cross sections of TiO_2 NWs after full structural optimization. The large, *blue balls* stand for Ti atoms, the small, *red balls* represent O atoms. NW orientations, morphology and facets are indicated (Reprinted figure with permission from Migas et al. [145], Copyright (2014) by the Royal Society of Chemistry)

After the structural optimization of TiO_2 NWs only slight changes can be spotted in their shape, that are mostly caused by the O atoms. In fact, TiO interatomic distances are found to be in the range of 1.80–2.28 Å. However, in the case of the rhomb morphology there are four undercoordinated Ti atoms in the unit cell which are located at edges between adjacent{110} facets because they have only one O atom from the first coordination shell and two O atoms from the second coordination shell. Moreover, some O atoms at edges display outward relaxation, possess the largest distance from the center of the NW among the other atoms and have only one Ti atom at each edge as their neighbor with the TiO interatomic distance equal to 1.65 Å. The unit cell parameter $a_{||}$ is decreased after the optimization for all the NWs irrespective of their morphology. The largest changes in $a_{||}$ are found for the

square (2.6 %) and the rhomb (3.6 %) NWs with the smallest diameters of 1.0 and 1.4 nm, respectively.

The morphology of [100]–oriented rutile NWs can be characterized by {001}, {010} and {011} facets. In study [145] two possible cross sections were chosen : a square one with {001} and {010} facets and a polyhedron one with {001}, {010} and {011} facets, as presented in Fig. 7.37. The corresponding diameters of NWs are 3.8 and 3.4 nm for the square and the polyhedron morphology, respectively. The polyhedron morphology can be easily obtained from the square morphology by introducing {011} facets at edges between adjacent {001} and {010} facets. Structural optimization does not sizably affect the shape of the NWs with respect to the initial configurations cut from the bulk. Moreover, after relaxation the TiO interatomic distances have turned out to be in the range of 1.79–2.16 Å, which is very close to the case of [001]-oriented anatase NWs. In addition, $a_{||}$ is found to be decreased for both the square and the polyhedron NWs displaying, a 5 and 3 % reduction for a diameter of about 2.0 and 3.8 nm, respectively.

For [110]-oriented TiO_2 NWs, {001} and {112} facets were observed during the growth [147], leading to the polyhedron morphology as illustrated in Fig. 7.37. In addition to {001} and {112} facets, the appearance of {110} facets in the morphology of anatase NWs is also possible. Thus, morphology with polyhedron, rhomb, square and round cross sections was considered in [145]. Square morphology involves {110} and {001} facets orthogonal to each other in the plane of the cross section. Round morphology possesses {112} facets in between {110} and {001} facets, while rhomb morphology displays only {112} facets. For the latter case the larger rhomb diagonal (1.8 nm), which defines the diameter of the NW, is almost twice as large as the smaller diagonal (1.2 nm). The diameters of the square, the round and the polyhedron TiO_2 NWs are 2.7, 2.2 and 2.1 nm, respectively. After structural optimization the Ti-O interatomic distances are found to be in the range of 1.77–2.27 Å, which is in agreement with the data for [001]- and [100]-oriented anatase NWs. The authors of [145] also revealed that the Ti-Ti interatomic distances of Ti atoms, which are in the plane of the cross section and located on the surface of {112} and {110} facets, get shorter (2.80–2.94 Å) with respect to the bulk values. This effect is probably responsible for the expansion in $a_{||}$ since the latter one is larger than the unoptimized value by 0.8, 1.0, 2.5 and 3.5 % for the square, the round, the polyhedron and the rhomb NWs, respectively.

These results demonstrate the presence of structure anisotropy in anatase NWs with respect to their growth orientation. Such an anisotropy was also found in anatase NWs electronic properties [145]. Indeed, [001]-oriented NWs, regardless of their morphology and diameter, display a direct band gap and an almost identical dispersion of the bands close to the gap region. Similar features are typical of [100]-oriented NWs except for the indirect band-gap nature. On the contrary, anatase NWs with [110] axes and different morphology can be treated as degenerate semiconductors because the Fermi level crosses some bands at the bottom of the conduction band. This issue is attributed to a slight deviation from TiO_2 stoichiometry since two O atoms are always lacking in [110]-oriented NWs. Even though there are at least four possible places to add two O atoms and restore TiO_2 stoichiometry, these two additional O

atoms cause a significant distortion in the NW structure along with the appearance of several flat bands in the gap region. Thus, the degenerate semiconducting properties of [110]-oriented anatase NWs can be viewed as their intrinsic feature.

The calculated band-gap dependence on the diameter of anatase NWs does not follow the common $\approx 1/d^2$ law due to the quantum confinement effects and displays instead the mainly the linear dependence or even invariable values of the gap. Partly this issue can be explained by a variation in $a_{||}$ (the unit cell parameter along the NW axis) during full structural optimization, which affects the band-gap values of anatase NWs, and partly by the influence of the surface state effects. The latter should be always taken into account because surface states do not shift in energy due to quantum confinement effects and, at the same time, they characterize the top valence band and the bottom conduction band in anatase NWs. In fact, pure surface hole states usually appear at the top of the valence band in NWs with different orientations, while an admixture of surface states and bulk-like states is present in the bottom conduction band. Moreover, a similar behavior was observed for TiO_2 thin films (slabs) and the same features can be expected to occur for TiO_2 nanocrystals because their shape is characterized by facets. In addition to that, the appearance of {001} facets (or (001) surface) can lead to band-gap values in TiO_2 nanostructures being smaller than in the bulk. The prevalence of {110} facets (or (110) surface) stabilizes the band gaps at values slightly higher than the one in the bulk, whereas presence of {100} and {110} facets can result in complex band-gap behavior with the diameter in TiO_2 nanostructures similar to that of the [001]-oriented polyhedron TiO_2 NWs.

The orientation effects in the morphology and electronic properties of anatase facetted nanotubes are considered in [146]. The same computational PW DFT (PBE) method was used as was applied to study the orientatation effects in anatase TiO_2 nanowires [145]. [001]-, [100]- and [110]-oriented anatase facetted NTs with different cross sections and diameters were considered, while periodic boundary conditions were applied along the NT axis with the unit cell parameter ($a_{||}$). In order to provide a negligible interaction between the neighboring NTs at least 7 Å of vacuum were introduced because a further increase of the vacuum thickness did not noticeably affect the total energy. All the atoms in TiO_2 NTs were allowed to relax.

The initial structures of TiO_2 NTs were generated on the basis of the anatase NWs by forming a hole along the NW axis. The corresponding anatase NWs are described above. By making a hole along the NW axis centered at its middle one can easily obtain an NT, whose inner surface also possesses facets. Thus, in the case of anatase facetted NTs one can expect the same set of facets to be taken into account for both the inner and the outer surfaces. In order to describe the morphology of facetted NTs, it is convenient to use the same notations as for anatase NWs (for example: the square, the polyhedron, the rhomb) and also indicate in a similar way the shape of the hole (for example: a polyhedron NT with a square hole). According to the selected orientation of the NTs, ($a_{||}$) was set at c, a and $a\sqrt{2}$ for NTs with the [001], [100] and [110] axes, respectively.

Figure 7.38 shows the cross sections of the square anatase facetted NTs with different shapes of the hole. The #1 case is characterized by a square hole involving {100} facets, while for the #2 case a polyhedron hole is chosen along with {100} and

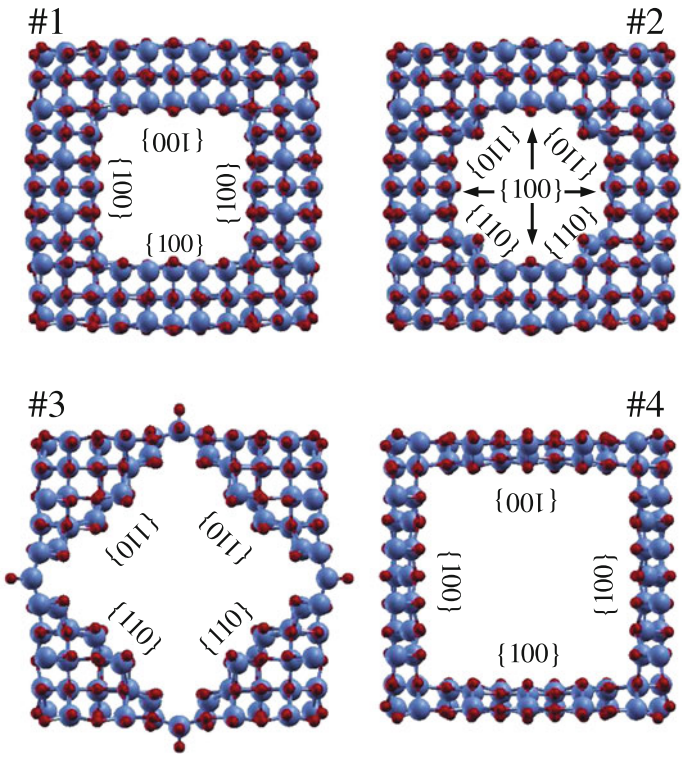

Fig. 7.38 Cross sections of [001]-oriented square anatase TiO_2 facetted NTs with different shape of the hole and diameters of 2.6 nm after full structural optimization. The corresponding square anatase NW is shown in Fig. 7.37. The large, *blue balls* stand for Ti atoms. The small, *red balls* represent O atoms. The facets of the inner surface the case numbers are indicated. For the #2 case the {100} facets are shown pointed out by *arrows* (Reprinted figure with permission from Migas et al. [146], Copyright (2014) by the Royal Society of Chemistry)

{110} facets to form the inner surface. After relaxation the thickness of NT walls consisting of three TiO_2 layers is about 0.39 nm which is comparable with the size of the bulk unit cell a. The hole size varies within 1.0–1.5 nm. The #3 case possesses a rhomb hole with {110} facets. After structural optimization the wall thickness is equal to the Ti-O interatomic distance of 1.63 Å because of the outward relaxation of the O atoms in the middle of {100} facets of the outer surface, while initially the wall in this place is only represented by one TiO_2 layer. Such a short Ti-O interatomic distance is due to the under coordinated Ti atoms, as in the case of the rhomb TiO_2 NWs. The #3 case can also be considered as a conglomerate of four touching nanocrystals which form the NT. The #4 case is similar to the #1 case except for the NT walls which have only two TiO_2 layers, however the wall thickness is enlarged to 0.30 nm with respect to 0.19 nm of the initial structure due to the outward relaxation of the surface O atoms. Structural optimization does not sizably affect the shape of the square TiO_2 NTs (the cases #1–#4) as compared with the initial structures, leading

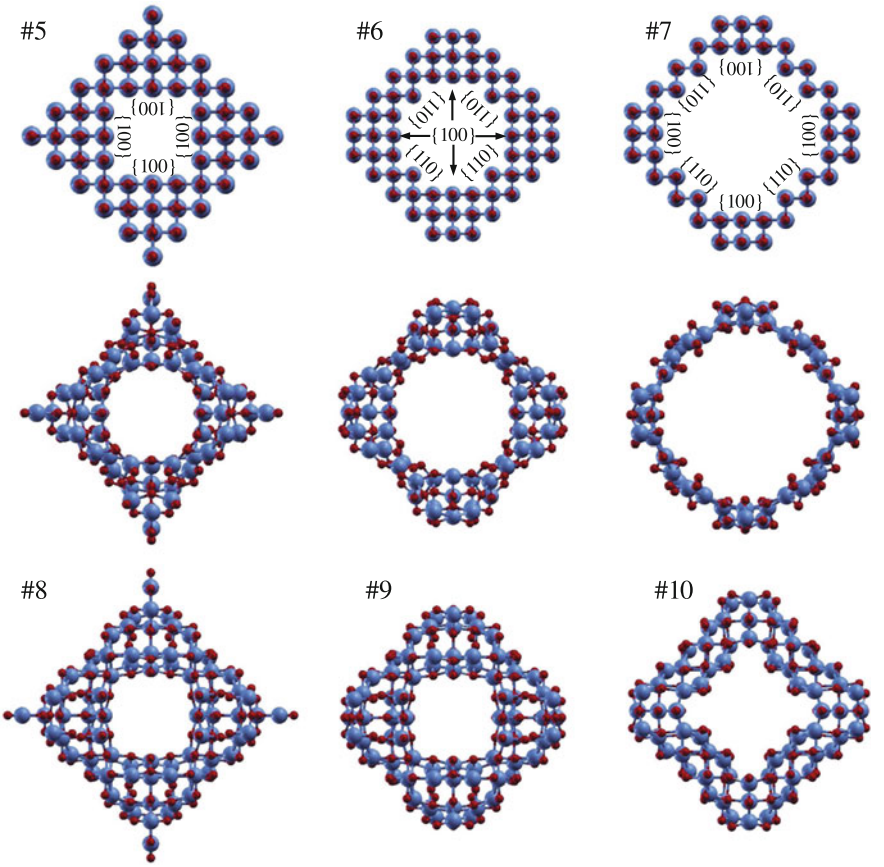

Fig. 7.39 Cross sections of [001]-oriented anatase facetted NTs with different shapes of the hole. The diameters of NTs are about 1.9–2.2 nm. The *top* and *middle panels* the #5–#7 cases as cut from the bulk and after structural optimization, respectively. The *bottom panel* the #8–#10 cases with thicker walls after structural optimization. The large, *blue balls* stand for Ti atoms. The small, *red balls* represent O atoms. The facets of the inner surface (the top panel) and the case numbers are indicated. For the #6 case the {100} facets as shown by *arrows* (Reprinted figure with permission from Migas et al. [146], Copyright (2014) by the Royal Society of Chemistry)

to the interatomic distances being close to those of TiO_2 NWs. Contrary to the TiO_2 NWs, a increases for the square TiO_2 NTs by 3.4–3.7 % and 5.1 % for the #1, #2 and #4 cases, respectively. This effect is probably due to interatomic interactions at the edges between the adjacent facets of the inner surface. However, a reduction in $a_{||}$is detected for the #3 case (1.7 %), which is most likely caused by the presence of under coordinated Ti atoms, as for the rhomb TiO_2 NWs.

The top panel of Fig. 7.39 represents the cross sections of the rhomb and polyhedron TiO_2 NTs cut from the bulk with different shapes of the hole. The #5 case shows the rhomb anatase facetted NT with a square hole characterized by the {100} facets

of the inner surface and the wall thickness in the thinnest place of about 0.27 nm (three TiO_2 layers). The polyhedron TiO_2 NT (the #6 case) possesses a polyhedron hole with {100} and {110} facets. The wall thickness is also about 0.27 nm (three TiO_2 layers). The #7 case is essentially the same as the #6 case except for the wall thickness which is reduced by half down to 0.13 nm (two TiO_2 layers). Conversely, square TiO_2 NTs (Fig. 7.38), structural optimization crucially modifies the shape of the rhomb and polyhedron TiO_2 NTs, as can be seen in the middle panel of Fig. 7.39. In fact, the hole is rounded for the #5 and #6 cases and their cross section can be also viewed as a conglomerate of nanoclusters because some the Ti and O atoms in the thinest part of the NT walls (the middle of the {110} facets of the outer surface) shift towards each other from different sides of the wall, leading to the formation of four nanocluster–like structures connected to each other by a thin isthmus. Amazingly, the #7 case, which is initially a polyhedron NT with a wall thickness of two TiO_2 layers and a polyhedron hole, has transformed into a cylindrical and single-walled-like structure. It is clearly seen that most of the O atoms on the inner and outer surfaces display outward relaxation, and the wall thickness varies in the plane of the cross section of the NT. Significant changes have been spotted for $a_{||}$, indicating its expansion of 9.5, 6.3 and 8.7 % for the #5, #6 and #7 cases, respectively. It is interesting to trace how an increase in the wall thickness of the rhomb and polyhedron NTs affects their shape. The #8 case with a square hole (Fig. 7.39, bottom panel) differs from the #5 case in the wall thickness, which is 0.40 nm (four TiO_2 layers), compared to 0.27 nm (three TiO_2 layers) of the #5 case. It is also evident that structural optimization does not modify the shape of the square hole and or the whole NT for the #8 case. Moreover, the conglomeration effect is attenuated, indicating that the wall thickness of 0.40 nm (four TiO_2 layers) for rhomb NTs turns out to be a critical one. Thus, for thicknesses smaller than 0.4 nm crucial changes in the NT shape are expected. The same conclusions can be drawn for polyhedron TiO_2 NTs. In fact, the #9 and #10 cases, which are characterized by a wall thickness of 0.40 nm (four TiO_2 layers), have square and rhomb holes, respectively. The square hole (the #9 case) has deliberately been selected with the hope to enhance the conglomeration effect observed in the #6 case; however, neither the square hole (the #9 case), nor the rhomb hole (the #10 case) causes any significant change in the NT shape. Moreover, #8 case possesses the under coordinated Ti atoms at the edges between the adjacent {110} facets. These atoms have sizable outward relaxation displaying the Ti-Ti (2.88 Å) and Ti-O (1.66 Å) distances. It is found that $a_{||}$ substantionally increases for the #8 (10.6 %) and #9 (10.4 %) cases, while a marginal reduction (0.02 %) is revealed for the #10 case.

Two types of [100]-oriented TiO_2 polyhedron NTs are shown in Fig. 7.40. The first type (the #11 case) has a square hole with a diameter of about 1.2 nm and a wall thickness close to 0.84 nm (four TiO_2 layers). The second type (the #12 case) is characterized by a polyhedron hole of 1.5–2.2 nm and it displays significantly thinner walls. In fact, 0.38 nm (two TiO_2 layers) and 0.63 nm have been determined for the walls with {001} and {011} facets, respectively. In addition, the thickness of the walls with {010} facets varies from 0.63 nm to almost zero because of a thin isthmus of TiOTi bands in the middle of these facets. However, structural optimization does not

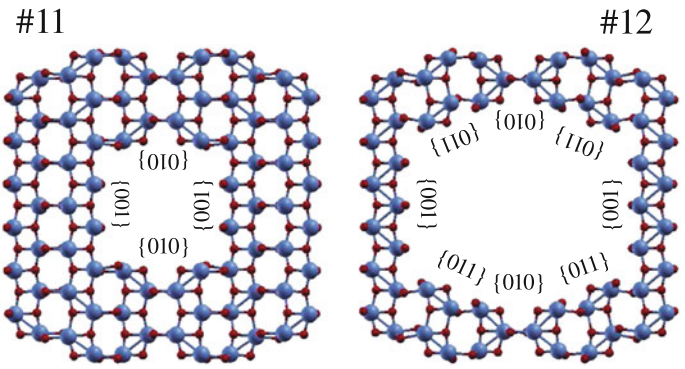

Fig. 7.40 Cross sections of [100]-oriented polyhedron anatase facetted NTs with a diameter of 3.4 nm (the corresponding NW cross sections are shown in Fig. 7.37) and different holes after full structural optimization. The large, *blue balls* stand for Ti atoms, the small, *red balls* represent O atoms. The facets of the inner surface and the case numbers are indicated (Reprinted figure with permission from Migas et al. [146], Copyright (2014) by the Royal Society of Chemistry)

affect the shape of such NTs with respect to the initial structures. Moreover, the Ti-O distances for the #11 case are similar to those of the parent NW (1.79, 2.19 Å), while for the #12 case they are 1.75, 2.28 Å. $a_{||}$ has been found to drop by 4 and 9 % for NTs with thicker (the #12 case) and thinner (the #11 case) walls, respectively. The square TiO_2 NTs are shown to display similar structural features as the polyhedron NTs. For this reason, these NTs are not predicted to have a critical wall thickness, as in the case with polyhedron and rhomb TiO_2 NTs with [001] axes because walls as thin as two TiO_2 layers preserve the shape of [100]-oriented TiO_2 NTs regardless of their morphology.

For [110]-oriented TiO_2 NTs round and polyhedron TiO_2 NTs with a polyhedron hole involving 001 and 112 facets for the inner surface were selected, whose cross sections are shown Fig. 7.41, as representatives of TiO_2 NTs with [110] axes. Thus, the round TiO_2 NTs are chosen to have two different wall thicknesses: three TiO_2 layers of about 0.60–0.62 nm (the #13 case) and two TiO_2 layers (the #14 case). After relaxation the latter case possessed a wall thickness of 0.39 nm for the walls with {001} facets, 0.26 nm for the walls with {110} facets and 0.50 nm for the walls with {112} facets. A significant increase in the wall thickness with {112} facets is attributed to an outward relaxation of the surface O atoms along with a sizable extension of the Ti-Ti interatomic distances (3.42 Å). Different from the #13 case, where no crucial change in shape can be spotted, the #14 case displays a slight inward relaxation of the walls with {112} and {110} facets, as if the NT were squeezed. This effect is more pronounced for the polyhedron TiO_2 NT with a smaller diameter and two TiO_2 layers to form walls (the #15 case), where the shape of the NT transformed into a rectangular one as if {001} and {110} facets characterized its initial morphology. It is evident that the critical wall thickness is three TiO_2 layers. The hole sizes are 1.6–1.9, 2.1–2.3 and 1.0–1.4 nm for the #13, #14 and #15 cases, respectively. Typical Ti-O

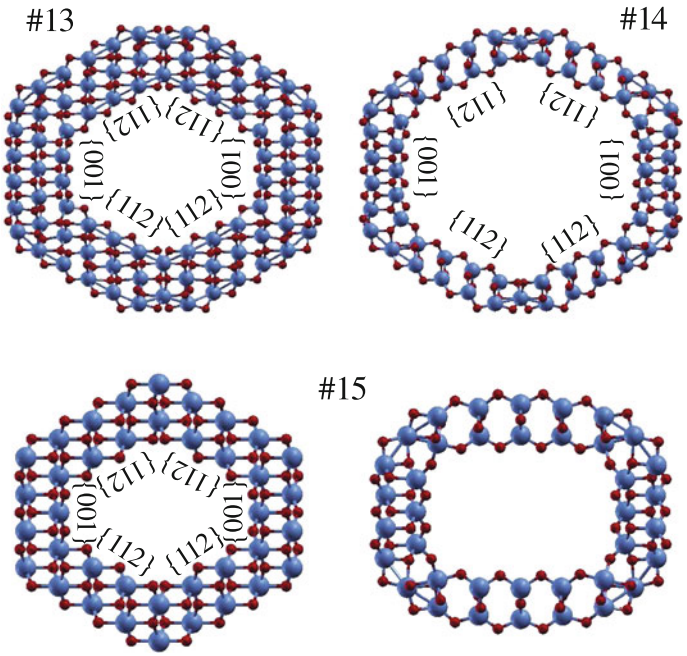

Fig. 7.41 The *top panel* cross sections of the [110]-oriented round anatase facetted NTs with a polyhedron hole and different wall thickness after full structural optimization. The diameter of the NTs is 3.1 nm. The *bottom panel* cross section of the [110]-oriented polyhedron anatase facetted NTs with a polyhedron hole before (from the *left*) and after (from the *right*) full structural optimization. The diameter of the NT is 2.1 nm. The corresponding round and polyhedron NW cross sections are shown in Fig. 7.37. The large, *blue balls* stand for Ti atoms, the small, *red balls* represent O atoms. The facets of the inner surface and case numbers are indicated (Reprinted figure with permission from Migas et al. [146], Copyright (2014) by the Royal Society of Chemistry)

interatomic distances are in the range of 1.75–2.21 A. $a_{||}$ increases by 1.7 % for the #13 case and by 3.0 % for the #15 case, while it decreases by 0.4 % for the #14 case.

Only the [001]-oriented polyhedron NT with a polyhedron hole (the #7 case, Fig. 7.39) displays a prefect cylindrical shape and a single-walled-like structure. The lateral view of an NT is presented in the top panel of Fig. 7.42 indicating the facelike structure of the NT wall. In fact, four rows of isosceles triangles in addition to chains form the wall. Moreover, each vertex of the triangle is connected to the middle of the base of a neighbor triangle. Two equal sides of the triangles have a length of 10.2 Å, whereas the base side is about 7.1 Å (Fig. 7.42, the middle panel). Since the orientation of the triangles (vertex upwards or downwards) alternates along the NT perimeter, chains as long as 10.7 Å (Fig. 7.42, middle panel) always link the vertexes of neighbor triangle bases. These chains closely resemble the thinnest anatase (101) slab of one monolayer [148]. However, some empty space or elongated holes as long as 22 Å are also clearly seen in the NT wall. The lateral views of the polyhedron

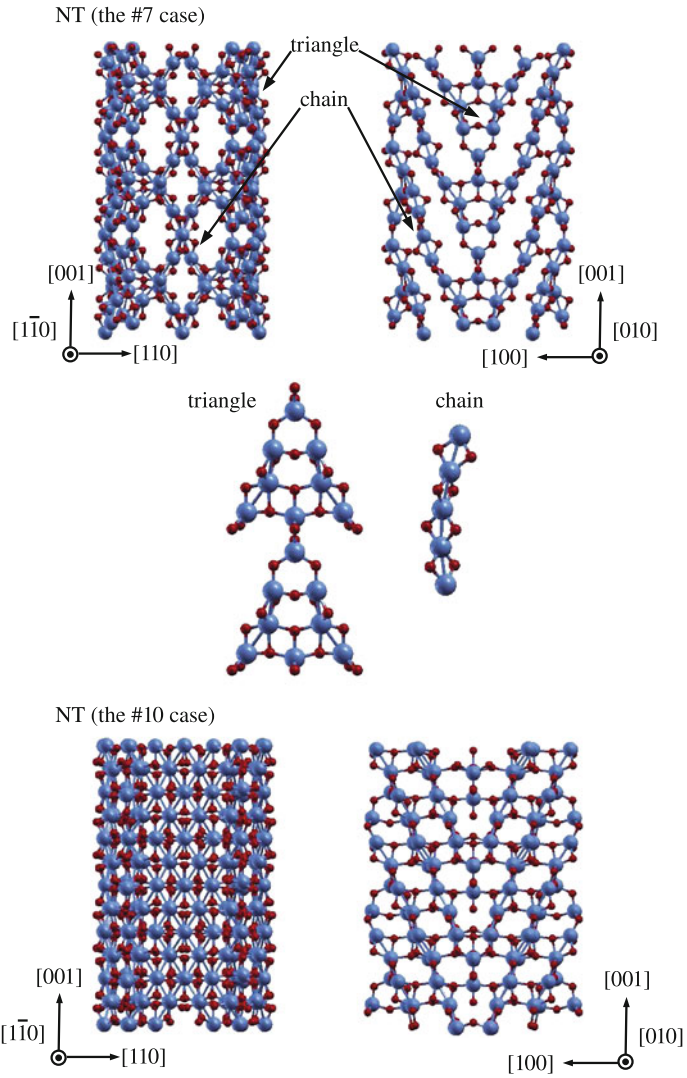

Fig. 7.42 The *top panel* different lateral views of the anatase facetted NT with a polyhedron hole (the #7 case). Three unit cells along the NT axis are presented. Crystallogrphic directions are shown. Elements of NT walls (*triangles*, which are vertex downwards oriented, and chains) are indicated by *arrows*. The *middle panel* individual elements of NT walls including *triangles*, which are vertex upwards oriented, and chains. The *bottom panel* different lateral views of the anatase facetted NT with a rhomb hole (#10 case). Three unit cells along the NT axis are presented. Crystallogrphic directions are shown (Reprinted figure with permission from Migas et al. [146], Copyright (2014) by the Royal Society of Chemistry)

TiO_2 NT with a rhomb hole (the #10 case) are also presented in Fig. 7.42 indicating that the {100} facets have a wedge structure, while the rows of chains diagonal to the NT axis are clearly seen for the {110} facets. The former ones are similar to the triangle structure observed for the #7 case, whereas the latter ones resemble the chains of the #7 case. The same can be seen from the lateral views of polyhedron TiO_2 NWs. Moreover, the #7 case (cut from the bulk initial structure) displays a lace-like structure. Thus, if the wall thickness of the polyhedron TiO_2 NT is smaller than the critical wall thickness, structural optimization rounds the NT cross section without a sizable reshuffle of atoms in the walls.

The morphology of walls of the facetted (polyhedron) TiO_2 NTs and TiO_2 NTs described and formed by rolling up a thin TiO_2 layer is different because in the latter case it is uniform while in the former case it inherits a structure which depends on the alternation of different facets. It is likely expected that in the cylindrical and single-walled- like structure (the #7 case) the interatomic distances are affected by relaxation. In fact, the Ti-O distances in the triangles and chains are in the range of 1.80–2.18 Å and 1.84–1.87 Å, respectively. Whereas the Ti–Ti distances get shorter with respect to the bulk value, shrinking down to 2.72–2.90 Å for the triangles and to 2.72 Å for the chains.

It has been revealed that the #7 case is not unique and similar cylindrical and single-walled-like structures can be formed in TiO_2 NTs with smaller and larger diameters. Figure 7.43 presents polyhedron TiO_2 NTs with polyhedron holes and diameters of 1.6 (the #16 case) and 2.7 nm (the #18 case). The lace-like structure of their walls is essentially the same as for the #7 case, while sizes of triangles get larger (the #18 case) or smaller (the #16 case) along with the length of chains. However, the polyhedron morphology of the initial NW along with a polyhedron hole is not sufficient to guarantee the cylindrical and single-walled-like structure of TiO_2 NTs. In fact, the #17 and #19 cases do not display the cylindrical shape, probably because the {100} and {110} facets are not close in size, while they can only be viewed as a single-walled-like structure with a polyhedron cross section, which is, nevertheless, visually rounded. After optimization $a_{||}$ is found to be increased by 9.7 % (the #16 case), 6.9 % (the #17 case), 8.6 % (the #18 case) and 7.9 % (the #19 case).

Experimental observations indicate that the [100] orientation occurs in cylindrical and multi-walled TiO_2 NTs [115, 149, 150]. The results discussed above suggest that the appearance of cylindrical and singlewalled- like TiO_2 NTs with [001] axes is not excluded. Moreover, one can assume that a multi-walled-like structure can easily be obtained by combining single-walled-like TiO_2 NTs with smaller and larger diameters.

Band gap variation with diameter in anatase facetted TiO_2 is affected by at least two issues. First of all, it is the value of $a_{||}$ because full structural optimization changes this lattice parameter in TiO_2 NTs by several percent with respect to the initial value corresponding to the one in the bulk. TiO_2 NTs and NWs display a similar variation in band gaps with uniaxial strain. Secondly, it is the surface states effects, which can attenuate or even block the influence of the quantum confinement effects, that can decrease the shift in the energy of band edges or lead to invariable band-gap values, which may be smaller than the one in the bulk. In the case of TiO_2

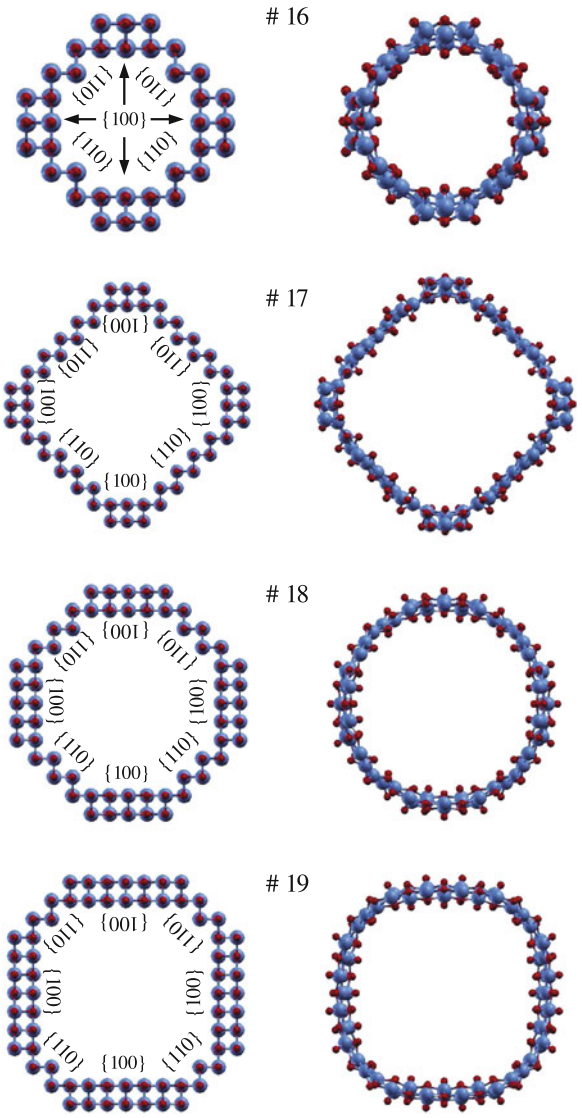

Fig. 7.43 Cross sections of [001]-oriented polyhedron anatase facetted NTs with a polyhedron hole and diameters of 1.6 nm (the #16 case) and of about 2.7 nm (the #17–#19 cases) for initial (as cut from the bulk)-*left panel*) and after full structural optimization (*right panel*). The large, *blue balls* stand for Ti atoms. The small, *red balls* represent O atoms. The facets of the inner surface and the case numbers are indicated. For the #16 case the {100} facets are shown by *arrows* (Reprinted figure with permission from Migas et al. [146], Copyright (2014) by the Royal Society of Chemistry)

NTs, where one has both outer and inner surfaces, the band-gap dependence on the wall thickness can be more complicated than in NWs. Such a dependence is shown in Fig. 7.44, where TiO_2 NTs with the same orientation have equal diameters and

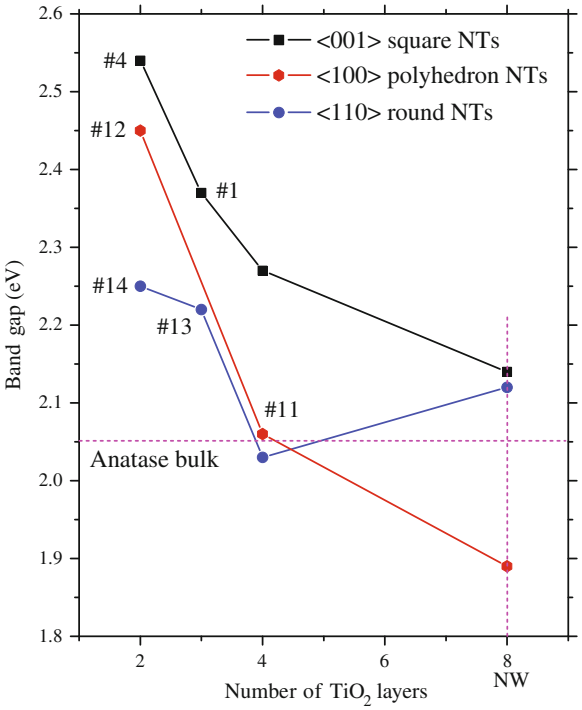

Fig. 7.44 The band gaps in [001]-, [100]- and [110]-oriented anatase facetted NTs as a function of the number of TiO_2 layers in walls. Case numbers are indicated for some of the NTs. The *horizontal dotted line* indicates the band-gap value in the anatase TiO_2 bulk, while the *vertical dotted line* corresponds to the upper limit of the wall thickness (Reprinted figure with permission from Migas et al. [146], Copyright (2014) by the Royal Society of Chemistry)

morphology. The number of TiO_2 layers forming the NT walls are used instead of thickness expressed in Å because the surface O atoms often display a sizable outward relaxation artificially increasing the wall thickness. The data for TiO_2 NWs are used as an upper limit of the NT wall thickness. It is evident that only [001]-oriented square TiO_2 NTs follow the common law of a band-gap decrease with increasing wall thickness, while a possible limiting gap value corresponds to the one in the bulk (Fig. 7.44). Conversely, [100]-oriented polyhedron TiO_2 NTs and [110]-oriented round TiO_2 NTs are predicted to have band-gap values smaller than that in the bulk (Fig. 7.44) most probably because of the presence of {001} facets. In addition, for the round TiO_2 NT with the [110] axis and a wall thickness of four TiO_2 layers the maximum of the valence band is characterized by p-states of O atoms located on the inner surfaces of the adjacent {112} facets, while the {001} facets almost disappear, leading to the band-gap value being smaller than the bulk value. Cylindrical and single-walled-like TiO_2 NTs (the #16, #7 and #18 cases) with the same wall thickness and different diameters display almost invariable band-gap values. In fact, band gaps of 3.12, 3.11 and 3.09 eV were detected for the #16, #7 and #18 cases, respectively,

indicating that changes in band-gap values of TiO_2 NTs are expected with changes in the wall thickness. Figure 7.44 shows the band-gap dependence on the effective hole size for NTs with different orientations and a fixed outer diameter, i.e. the figure represents the band gap dependence when the NTs transform into NWs.

The results of ab initio calculations [146] clearly demonstrate crucial changes in the morphology of facetted TiO_2 NTs, as obtained from TiO_2 NWs by making a hole along their axes, and these changes are closely connected with the critical wall thickness and orientation. A critical wall thickness of four and three TiO_2 layers was predicted for TiO_2 NTs with [001] and [110] axes, respectively, while [100]-oriented TiO_2 NTs do not display any variation in shape with respect to the wall thickness.

Anisotropy effects in the band dispersion of the TiO_2 NTs are very close to those of the parent TiO_2 NWs. Thus, the competitive direct/indirect character of the gap is found to be typical of [001]-oriented TiO_2 NTs because of the small dispersion of the bottom conduction bands and the top valence bands, whereas [100]-oriented TiO_2 NTs are characterized by indirect transition. The facetted TiO_2 NTs with [110] axes possess a direct band gap. Unlike the [110]-oriented TiO_2 NWs, the corresponding TiO_2 NTs have TiO_2 stoichiometry due to specific atomic arrangements on the inner and outer surfaces at the edges and such NTs do not display degenerate properties. Moreover, band-gap values smaller than that in the bulk can occur for the TiO_2 NTs due to the influence of the surface states effects. Calculations [146] have also shown an alternative way to form cylindrical and single-walled-like structures for the [001]-oriented TiO_2 NTs—without rolling up a thin titania layer into a NT.

7.3 ZrO_2

7.3.1 Bulk Zirconia

We saw above that TiO_2-based nanostructure calculations have been made by different authors who employmed different theoretical models.

As for first-principles calculations of ZrO_2-based nanostructures, however, it is only recently that they have been performed for the first time [151]. A large array of zirconia nanotubes was constructed in [151] from the nanosheets derived. In each case the positions of all the atoms were optimized to obtain the most stable nanotube structure while preserving the rototranslational symmetry. Formation and strain energies were calculated to provide nanotube stability analysis. It was found that the formation energy of ZrO_2 nanotubes with a sufficiently large diameter is mainly determined by the formation energy of the corresponding nanosheet. The closeness of the nanotube surface energy to the surface energy of the corresponding thin films confirms the principal role of the parent nanolayer structure.

Zirconia is an oxide which exhibits a large variety of polymorphs. The properties of the bulk ZrO_2 are well studied experimentally [152] and theoretically [153–160]. It has been established that ZrO_2 has three zero-pressure modifications. At high tem-

peratures (higher than 2350 °C), zirconia adopts a cubic fluorite structure ($Fm\bar{3}m$), while at low temperatures (lower than 1150 °C), a monoclinic baddeleyite ($P2_1/c$) structure is more likely preferred [161] and represents a ground state of zirconia. A tetragonal phase exists at intermediate temperatures; it can be viewed as a simple perturbation of the cubic phase in which the oxygen atoms are displaced alternately along the 4_2 axis by ±0.2 Å, resulting in a $P4_2/nmc$ symmetry.

Besides the well-known monoclinic, tetragonal, and cubic phases, two orthorhombic high pressure phases with space group symmetry Pbca (orthorhombic-I) and Pnma (orthorhombic-II) are stable above 3 and 20 GPa, respectively [162, 163]. The dense orthorhombic-II phase (isostructural with cotunnite) is of particular interest because it can be quenched to ambient conditions [163].

The relative stability of ZrO_2 phases can be influenced by the crystallite size. It is well known that small zirconia particles suspended in a host matrix do not transform from tetragonal to monoclinic, even well below the bulk transition temperature unless subjected to an external stress field or heating above 700 °K [164, 165]. Moreover, Wang et al. [112] have found that tetragonal zirconia can be obtained in particles with sizes below 40 nm at room temperature. Structure studies [166] of ZrO_2 deposition on amorphous silica have shown that thin ZrO_2 film growth starting from the formation of an amorphous phase proceeds with the preferential growth of crystallites of tetragonal and cubic structures in the direction [001]. Structure analysis of the fabricated: ZrO_2-based NT-ZNT also gives evidence that the small particle size may stabilize the virtually unstable phases. This means that ZNT can possess cubic, tetragonal or orthorhombic morphology. It should also be noted that the additional tetragonal, orthorhombic, and hexagonal phases of ZrO_2 have also been reported at high pressures and/or high temperatures [162, 167, 168].

We now proceed to consider in more detail the first-principles calculations [151] of bulk zirconia, ZrO_2 sheets and nanotubes. The hybrid exchange-correlation functional PBE0 within LCAO approximation has been employed to investigate the properties of ZrO_2 nanotubes constructed from different zirconia polymorphs, in an attempt to understand the relation between bulk zirconia atomic structure and the stability of zirconia nanotubes. Thin sheets generated from cubic, tetragonal and monoclinic phases as the precursors to nanotubes have been considered.

As the first step, the study was started with calculations of the structure and properties of the corresponding bulk crystals. At the same time, these crystals play a role of benchmark systems for testing the applicability of the computation method selected. Further, the calculations [151] demonstrated that one of the sheets considered was reconstructed to a cotunnite-type layer. Because of this, the high-pressure orthorhombic-II phase was appended to the set of three low-pressure phases. For similar reasons, the rutile-like hypothetical phase of ZrO_2 was calculated in [169]. The hypothetical anatase-like phase of ZrO_2 was studied in [169] primarily because of the prospective comparison with TiO_2 nanotubes.

The CRENBL effective small-core pseudopotential was adopted in [151] for the Zr atom [170]. This pseudopotential replaces only inner core electrons, whereas subvalence electrons (4s and 4p in Zr case), as well as valence electrons, are calculated

self-consistently. To prevent quasi-linear dependences, diffuse exponents less than 0.1 a.u. were removed from the original [170] basis and the exponents of other polarization functions were re-optimized for the periodic calculations. Oxygen atoms were treated with an all-electron basis [171]. Reciprocal space integration was performed by sampling the Brillouin zone of the cubic crystal with the $12 \times 12 \times 12$ Monkhorst Pack mesh [25], which was reduced inversely to the cell constants in other periodical systems to provide approximately uniform k-point spacing. The lattice parameters and fractional positions of all the atoms in the systems considered were fully optimized. Ionic and cell relaxations were performed until the rootmean- square forces on the atoms were less than 0.003 eV/Å in the bulk and slab systems, and less than 0.03 eV/Å in the nanotubes.

In Table 7.29 we compare the calculated properties of four ZrO_2 phases with the experimental data. As follows from this table, the theoretical structure parameters differ from the experimental estimations by (1 %) or less. The values reported are of a better quality than those obtained in other works [155, 159] using the DFT(GGA) exchange-correlation functional. Calculations [151] also reproduce the cohesion and relative energies of the different phases. The bulk moduli values were obtained via the Birch Murnaghan third-order equation of state, and they are in agreement with both the experimental and theoretical results. Table 7.29 also reports the values of the band gap, which, as expected, are much better reproduced using the hybrid exchange—correlation functional compared the plain GGA.

7.3.2 Structure and Stability of ZrO_2 Sheets

Thin sheets of zirconia exhibit a variety of structures because of the existence of several crystalline bulk polymorphs. We consistently consider cubic, tetragonal, and monoclinic faces with different (low) crystallographic indexes. A hypothetical zirconia tetragonal phase with anatase structure was also included in our consideration just for the purpose of comparison of ZrO_2 and TiO_2 nanotubes with anatase morphology. In each case the stoichiometric slabs consisting of 212 atomic planes with a thickness of 26 Å were constructed by cleaving the bulk crystals. Oxygen-terminated slabs were chosen whenever it was possible. It is known [164] that metallic terminations, as a rule, make the surface unstable to oxidation or to strong reconstruction. We do not consider non-stoichiometric slabs, so our 2D unit cells consist of an integer number of ZrO_2 formula units, as well as 1D cells of the subsequent NTs. All the surface layers were allowed to relax. There were several cases where the reconstructed structures of nanolayers generated from different phases or with different indices became identical. Consequently, the final number of unique 2D structures proved to be less than the total number of the surfaces considered.

The calculated surface energies and formation energies of the relaxed slabs are given in Table 7.30 together with the corresponding structural information. When calculating the formation energy, the values of E_{bulk}, n_{bulk} for the low-temperature

Table 7.29 Calculated and experimental[a] properties of monoclinic, tetragonal, cubic, and orthorhombic ZrO_2 phases [151]

Phase	a (Å)	b (Å)	c (Å)	Bulk modulus (GPa)	E_{form} (meV)[b]	E_g (eV)
Monoclinic[c], $P2_1/c$	5.156(5.149))	5.252(5.202)	5.290(5.320)	170(187 [172])	0; 21.8[d](22.9) [173]	5.7(5.7) [174]
Tetragonal, $P4_2/nmc$	3.598(3.598)	3.598	5.139(5.152)	208(205) [175]	52(63) [176]	6.0(5.0) [177]
Cubic(fluorite), Fm-3m	5.082(5.09)	5.082	5.082	272(194)[e]	89(120 [176])	5.5
Orthorhombic, Pnma	5.559(5.587)	3.351(3.330)	6.516(6.485)	135	230	5.1
Hypothetical tetragonal phases						
Rutile, $P4_2/mnm$	4.874	4.874	3.268		235	5.8
Anatase, $I4_1/amd$	4.032	4.032	10.650		215	6.0

[a] Experimental values are given in parenthesis. Lattice parameters are taken from [163, 178–180]
[b] Formation energy relative to the monoclinic phase
[c] $\beta = 99.244°(99.2°)$
[d] Cohesive (atomization) energy
[e] Experimental data [181] extrapolated to zero yttria content

Table 7.30 Relaxed strucure and stability[a] of ZrO_2 thin sheets generated from different bulk phases [151]

Label[b]	Final layer symmetry group	Final Number of planes	Lattice const. a(Å)	Lattice const. b(Å)	Thickness w (Å)	E_{form} (kJ/mol)	E_{surf} (J/m^2)	E_g (eV)
Cubic(fluorite) phase								
c110r2	Pmmn	4	3.26	5.41	2.03	104	0.89	6.0
c110r3*	P2/m11	9	3.19	5.03	6.82	120	1.73[c]	5.6
c110r4	$P2_1m11$	8	3.34	5.42	5.87	61	0.96	6.1
c111rh1	$P\bar{3}m1$	3	3.26	3.26	1.94	93	0.76	6.7
c111h2	$P\bar{3}m1$	6	3.41	3.41	4.85	67	0.97	6.2
Tetragonal(distorted fluorite) phase								
t001s1	$P\bar{4}m2$	3	3.46	3.46	1.93	211	1.43	6.6
t001r2	Pmmn	6	3.97	3.29	4.58	79	0.94	6.9
t110r2*	Pbaa	4	5.49	5.60	2.16	206	2.17	3.8
t110r3*	$P2_1am$	7	5.61	6.54	4.96	115	1.49[d]	6.3
Monoclinic(baddeleyite) phase								
m100r2	$P2_1/b11$	6	5.22	5.36	4.23	149	1.77	5.5
m-101r2	$P2_1$	12	5.55	6.29	3.99	141	1.34	6.4
Tetragonal (anatase) phase								
a101c2[e]	C2/m11	6	5.98	5.98	2.53	147	0.97	6.6

[a] Formation energies are relative to the monoclinic phase, and surface energies are relative to the parent phase
[b] See text for label explanation. The slabs with considerable reconstruction are marked with an asterisk
[c] Surface energy is 1.52 J/m^2 using ZrO_2 (rutile) bulk energy
[d] Surface energy is 1.25 J/m^2 using ZrO_2 (cotunnite) bulk energy
[e] The angle between the lattice vectors in the centered rectangular cell is 143.0°

monoclinic phase were used in most cases. When calculating the formation energy the following notations were used: p. xxx l n, where p is the first letter of the parent phase, xxx is the Miller index, l is the type of 2D lattice (r rectangular, c centered rectangular, s square, h hexagonal), and n is the number of ZrO_2 layers after slab relaxation or reconstruction.

The **cubic** crystal has three types of nonequivalent low index surfaces: (001), (110), and (111). However, it is clear that the first one is just a special case of the (001) surface for the less symmetric tetragonal phase. So, the last two faces were only considered in [151]. Each atomic (110) plane includes two O atoms per one Zr atom per 2D unit cell, so any number of (110) planes provides the correct stoichiometry. The single-plane sheet was excluded from the consideration because its formation energy was too high. The final relaxed or reconstructed structures of slabs consisted of 2, 3, and 4 atomic planes, as shown in Fig. 7.45. During the optimization of the (110) slab the top oxygen atoms move outward, the top zirconium atoms move inward, and the number of atomic planes is thus redoubled. The relaxation of the two-plane slab is limited to the displacements mentioned (Fig. 7.45a). However, after the initial D_{2h} (Pmmm) symmetry was removed, a deeper relaxation of the three-plane slab was found. The final structure of a 3-layer slab (Fig. 7.45b) includes nine atomic planes and it resembles the relaxed (100) rutile surface slab with the top bridging oxygens [105]. The 4-plane slab also obeys a considerable reconstruction. If the initial Pmmn symmetry is preserved, it spontaneously splits into two separated 2-layer slabs. However, after the initial symmetry is removed, the two upper layers shift along the [001] direction by approximately one fourth of the period, thus facilitating the restoration of ZrO bonds between the two middle ZrO_2 layers (Fig. 7.45c). The resulting 8-plane slab has low surface and formation energies (see Table 7.30). The 2D lattice of the (111) slabs (Fig. 7.46) has a well-known hexagonal symmetry ($P\bar{3}m1$). The zirconium atom is 6-fold coordinated in a 3-plane slab (c111h1), while in a 6-plane slab (c111h2) it is bonded to an additional O atom in the next layer. According to the data in Table 7.30, the hexagonal layers have low formation and surface energies. They are compact, very stable, and not reconstructed even if

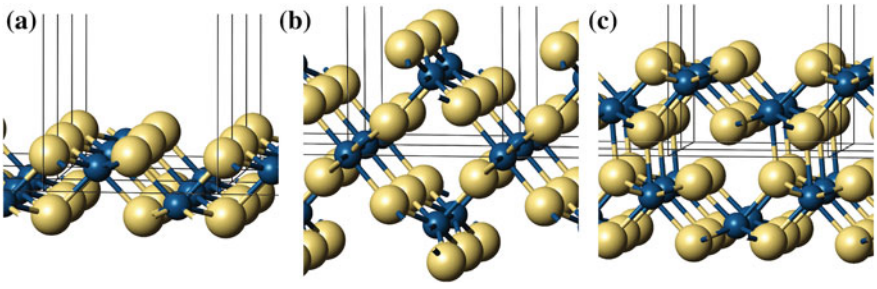

Fig. 7.45 Relaxed or reconstructed structure of nanosheets cut from the cubic ZrO_2 crystal parallel to the (110) face viewed along the [$\bar{1}$10] direction. **a** c110r2—relaxed bilayer; **b** c110r3—1×1 reconstructed trilayer with rutile morphology; and **c** c110r4—1×1 reconstructed tetralayer. *Large light balls*, O atoms; *small dark balls*, Zr atoms; *black lines*, 2D unit cell boundaries

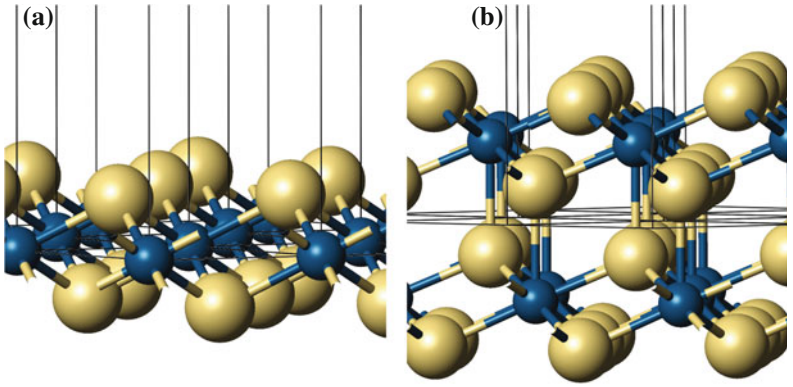

Fig. 7.46 Relaxed structure of nanosheets cut from the cubic ZrO_2 crystal parallel to the (111) face viewed along the [$\bar{1}$10] direction. **a** c111h1—relaxed monolayer and **b** c111h2—relaxed bilayer. See Fig. 7.45 for labeling

the symmetry constrains are totally removed. The ionic relaxations are small and confined to the outmost O planes.

Among the five low-index **tetragonal-phase** surfaces, (100), (001), (110), (101), and (111), the second and third ones can only be used for generating the proper thin sheets which have not been coincided previously. The last low-symmetry surface (111) has an oblique 2D lattice, so it is not suitable for NT rolling [119, 182]. It has been found that the thin slabs created from (100) and (101) t-ZrO_2 faces relax to the slabs generated from (110) and (111) cubic ZrO_2 faces, correspondingly. The relaxation of a (001) 3-plane sheet resulted in a simple structure with a square 2D lattice belonging to the P $\bar{4}$m2 layer group (Fig. 7.47a). The undercoordination of

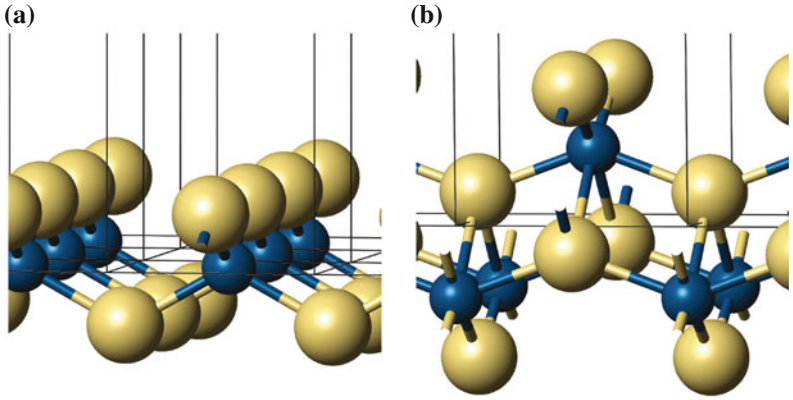

Fig. 7.47 Relaxed structure of nanosheets cut from the tetragonal ZrO_2 crystal parallel to the (001) face viewed along the [100] direction. **a** t001s1—relaxed monolayer and **b** t001r2—relaxed bilayer with lepidocrocite morphology. See Fig. 7.45 for labeling

the Zr atom in this monolayer structure (its coordination number is 4) provides large formation and surface energies, making this structure unfavorable (see Table 7.2). The adjoining of two layers together into a 6-plane slab improves the structure considerably because of the increase of the Zr coordination number up to 6 (Fig. 7.47b). Moreover, the initially equal lattice constants become different upon the optimization. The final slab structure (Fig. 7.47b) has a rectangular 2D lattice, and it is identical to that of the layer in lepidocrocite-type laminated crystals, having low formation and surface energies (Table 7.30). The (110) slabs of the tetragonal zirconia consist of alternated Zr and O planes, so that the stoichiometric sheets must include an even number of atomic planes and their initial (bulk) structure would be polar and, therefore, unstable. During the optimization, the 2-plane (110) slab with an imposed Pba2 (originating from the bulk) symmetry converts to a single flat layer. After the symmetry constrains are removed, this slab transforms to a 3-plane hexagonal sheet which has been already considered for the cubic phase. The strongly reconstructed structure of the 4-plane slab is shown in Fig. 7.48a. The reconstruction of the 6-layer (110) slab was more surprising, and a compact 7-plane structure was obtained, as displayed in Fig. 7.48b. After structure analysis the conclusion was made that this nanolayer can really be attributed to the orthorhombic-II ZrO_2 phase. The individual optimization of a 3-plane (010) cotunnite nanosheet confirmed our supposition.

The orthogonality condition [119] is satisfied for (100), (001), (101), and $(\bar{1}01)$ monoclinic faces. The monoclinic crystal was cleaved parallel to those faces to produce thin slabs with 6, 12, 12, and 12 atomic planes, correspondingly. These slabs provide the right connectivity and a sufficiently large Zr coordination number with having equal top and bottom O-terminated surfaces. However, only one pair, namely (100) and $(\bar{1}01)$, was selected for further consideration. The 12-plane (001) slab is reconstructed into the lepidocrocite-type sheet considered above, while the (101) slab is converted into a 4-plane sheet obtained after the relaxation of the (110) slab

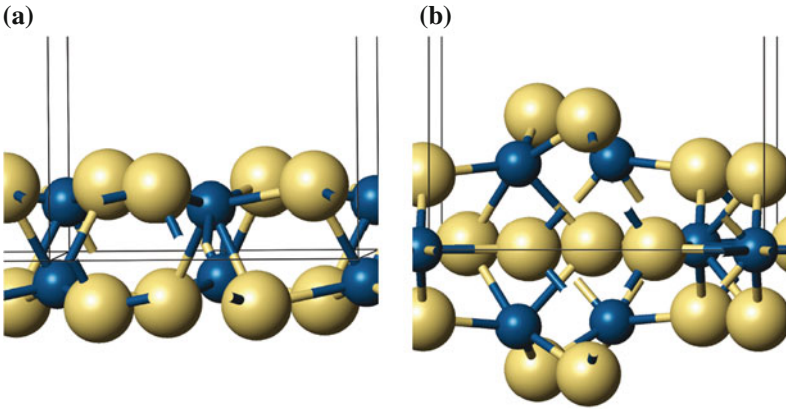

Fig. 7.48 1×1 reconstructed structure of nanosheets cut from the tetragonal ZrO_2 crystal parallel to the (110) face viewed along the [001] direction. **a** t110r2—reconstructed bilayer and **b** t110r3—reconstructed trilayer with cotunnite morphology. See Fig. 7.45 for labeling

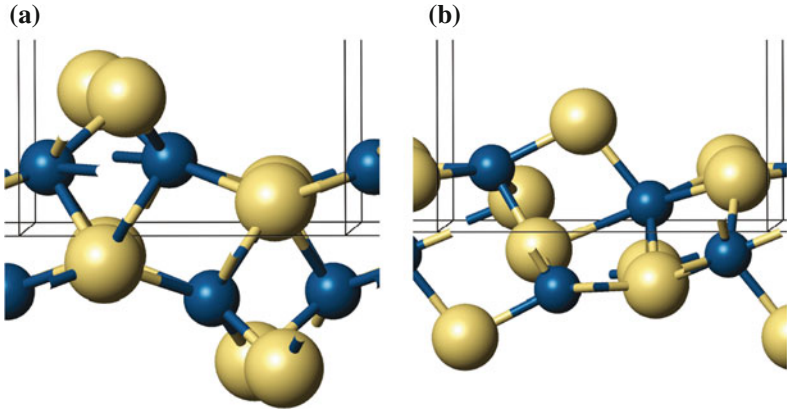

Fig. 7.49 Relaxed structure of nanosheets cut from the monoclinic ZrO_2 crystal. **a** m100r2—relaxed bilayer parallel to the (100) face viewed along the [001] direction. **b** m$\bar{1}$01r2 relaxed pseudobilayer parallel to the ($\bar{1}$01) face viewed along the [010] direction. See Fig. 7.45 for labeling

cut from the cubic phase. The final relaxed structures of (100) and ($\bar{1}$01) nanosheets are shown in Fig. 7.49. Obviously, the first possesses a 6-plane bilayer structure, while the second consists of four Zr-planes and eight O-planes. However, some of the oxygen planes almost coincide, and the actual number of the oxygen layers in the relaxed structure is 6. The final structure can be considered as a pseudobilayer because it is impossible to split the oxygen planes in between the four ZrO_2 layers.

It follows from Table 7.30 that the compact hexagonal sheet c111h1 has the smallest surface energy. Previous results [164, 183–186] for the zirconia surface energies were based on the calculation of substantially thicker slabs; nevertheless, our values are basically in accordance with the prediction that the surfaces of the cubic and/or tetragonal phases are generally more stable than the monoclinic surfaces considered here. In works [102, 119, 120, 125, 187] titania nanotubes folded from slabs of different TiO_2 bulk phases were studied. It has been found that 1- and 2-TiO_2 layer slabs cut from (101) anatase surfaces can form NT with low formation and strain energies, as discussed in the next subsection. Whereas a 3-plane layer can be reconstructed easily to a sheet with hexagonal structure, the 6-plane bilayer preserves the modified anatase structure [119]. The ab initio modeling of TiO_2 nanosheets has been performed earlier by Vittadini and coworkers [121, 188]. In particular, they have established that two TiO_2-layer (001) anatase films rearrange to very stable lepidocrocite-like nanosheets. To compare zirconia- and titania-based nanotubes, we include the zirconia 6-plane sheet with anatase structure (a101c2) in this consideration (see Table 7.30). This zirconia nanosheet possesses rather high formation energy of 147 kJ/mol in contrast to that of 71 kJ/mol for similar titania nanosheet [120]. In the last column of Table 7.30 we list the electronic band gaps, E_g, in the calculated structures. In most cases, E_g is lying in the interval from 6 to 7 eV, and it is greater than the band gap in the parent bulk phase (see Table 7.29). The only exception is the sheet

t110r2, for which $E_g = 3.8$ eV. By the way, we could not identify the parent bulk phase for this extremely reconstructed structure. We found the maximal Eg value (6.9 eV) in the lepidocrocite-like structure, t001r2, to be greater by 1 eV than that in the tetragonal ZrO_2 crystal.

7.3.3 ZrO_2 Nanotubes

The knowledge of the layer symmetry group of the precursor sheet (see Table 7.30) allows one to find the line group symmetry of nanotubes rolled up with different chiralities, see Chap. 2. The initial structures of the nanotubes considered in [151] were obtained by rolling up the relaxed or reconstructed ZrO_2 thin sheets discussed previously. The precursor sheets form 2D lattices consisting of three types: primitive rectangular (c110r2, c110r3, c110r4, t001r2, t110r3, m100r2, m$\bar{1}$01r2), centered rectangular (a101c2), and hexagonal (c111h1, c111h2). Different ZNT chiralities compatible with the 2D lattice of the listed nanosheets were considered in [151]. The nanosheets t110r2 and t001s1 were excluded from further consideration because of their large formation energy.

Two chiralities are possible for the commensurate NTs folded from simple or centered rectangular lattices: (n,0) and (0,n), or (n,n) and (−n,n), respectively [119, 120]. In the case of the hexagonal lattice, the study was restricted to the achiral NTs, (n,0) and (n,n). The line group symmetry and its family can be found for each initial NT structure using Table 2.10.

A bulk monoclinic phase has been used as the reference state for the NTs formation energy calculation just as it was done for nanolayers.

Atomic planes in slabs are transformed to atomic shells (cylinders) in tubes upon folding. The inner and outer shells undergo stress due to the stretching or shrinking of the interatomic distances in the initial relaxed slab. The smaller the tube diameter and the thicker the tube wall the larger is the strain. The most critical is the repulsion between the nearest oxygen atoms in the inner shells. Because of the shrinking, the distance between the O atoms may become less than 2.72×5 Å, thus leading to a considerable increase in repulsion. The inner and outer shells are strained in opposite directions, and reducing tension in the former may increase the tension in the latter. As a result, for any chirality and tube wall thickness w, there exists a minimum diameter d below which the NT becomes unstable and undergoes spontaneous destruction. For example, if we assume that δ is the maximal linear strain admissible for the layer, we can easily obtain the condition: $\delta \geq$ w/d. This means that the ratio w/d should have an upper limit δ for each NT type folded from a single slab. Nanotubes having w/d above this limit should possess a multi-walled structure or polygonal morphology. In this discussion we consider NTs of sufficiently large diameters (w/d ≤ 0.2) with wall thicknesses of 2–7 Å to exclude the instability mentioned. To reduce the number of calculated NT structures the stability of different NTs at a constant total number (288) of atoms was examined. In each case the positions of all the atoms were optimized to obtain the most stable ZNT structure, preserving only

the rototranslational symmetry. The resulting structural parameters, formation and strain (rolling) energies of the nanotubes are given in Table 7.31. Additionally, the selected ZNTs were recalculated at an approximately equal diameter of about 40 Å (Table 7.32). In Table 7.32, instead of the formation energies we listed the NT surface energies estimated by the equation:

$$E_{surf} = (E_{NT} - n_{NT}E_{bulk}/n_{bulk})/S_{NT};\ S_{NT} = \pi l(d_{in} + d_{out}) = 2\pi ld \qquad (7.3)$$

where l and d are the period and the average diameter of the nanotube, correspondingly. The external (d_{out}) and internal (d_{in}) diameters of the NTs were estimated as the double distance from the NT axis to the most remote or to the nearest atom (in almost all of the NTs above considered the most remote and the nearest atoms were oxygens). Therefore, the NT surface area (S_{NT}) depends on the NT average diameter and period only. Consequently, E_{surf} is insensitive to the exact definition of the radii of the NT cylindrical surfaces. The last columns of Tables 7.31 and 7.32 demonstrate the electronic band gaps in the ZNT considered. Mostly, these values are only slightly (by 0.10–0.2 eV) less than the values in the appropriate slabs because of the sufficiently large NT diameters. In the case of ZNTs based on c110r4 and t001r2 slabs, the reduction is greater: 0.4–1.1 eV. Low—energy tubes with fluorite and lepidocrocite morphology exhibit maximal E_g values. However, no overall correlation was found between the band gap and the formation energy.

To simplify the analysis of the data obtained, it is possible assume that all the ZNTs considered can be divided into three groups according to their wall thickness: (1) tubes with a wall thickness of 23 Å; (2) tubes with a wall thickness of 35 Å; and (3) tubes with a wall thickness of 57 Å. The first group includes ZNTs with thin walls consisting of 36 atomic shells (one or two compact ZrO_2 shells), while the last one includes relatively thick ZNTs with walls consisting of 79 atomic shells (three or four ZrO_2 shells). The tube walls for the middle group generally contain 6 atomic shells (two ZrO_2 shells), except for c110r3 (n,0) and m$\bar{1}$01r2, where the number of atomic shells is greater, but the intershell distance within the ZrO_2 layers is smaller.

The first group contains one type of NT folded from the rectangular 2D lattice (c110r2), one type folded from the centered rectangular 2D lattice (a101c 2), and one type folded from the hexagonal 2D lattice (c111h1). The tubes generated from the layers of cubic phase, c110r2 and c111h1, have relatively small formation and strain energies (Table 7.31). However, the data in Table 7.32 show that the tubes with hexagonal morphology (Fig. 7.50) are preferable at equal diameter. Thus, ZNTs with thin walls, if they really exist, are thought to have hexagonal morphology corresponding to the cubic zirconia phase.

The structure and energetics of nanotubes folded from TiO_2 hexagonal layers have been studied before ([102, 116, 118, 120, 187]). In particular, in previous works [102, 120, 187] the same computational approach was used. It was found that the structural optimization of the 3-plane TiO_2 slabs cut from the anatase phase resulted in a spontaneous (barrierless) reconstruction to the hexagonal (111) fluorite structure. Thus, hexagonal morphology is also preferable for NTs folded from a TiO_2 monolayer. In Table 7.33 we compare the results obtained for some tinania

Table 7.31 Relaxed structure, symmetry and stability of ZNT's consisting of 96 ZrO_2 formula units [151]

Label of initial sheet[a]	NT chirality[b]	Initial line group family[c]	Relaxed NT period l (Å)	NT wall thickness[d] w (Å)	NT average diameter[e] d (Å)	E_{form} (kJ/mol)	E_{str} (kJ/mol)	E_g (eV)
c110r2	(48,0)	11c	5.42	2.02	49.96	110	5.9	5.9
c110r2	(0,48)	11c	3.26	2.02	82.72	105	1.4	5.9
c110r3	(32,0)	6a	5.25	4.56	33.88	156	36.1	4.9
c110r3	(0,32)	3b	3.19	6.80	51.52	121	0.5	5.6
c110r4	(24,0)	6a	5.48	5.52	28.00	120	59.8	5.5
c110r4	(0,24)	3b	3.35	5.72	42.48	97	36.4	5.1
c111h1	(48,0)	8g	5.64	1.94	49.80	94	1.1	6.7
c11h1	(48,48)	4h	3.26	1.94	86.18	93	0.3	6.7
c111h2	(24,0)	8g	5.81	4.74	28.86	105	37.1	6.0
c111h2	(24,24)	4h	3.35	4.83	48.00	80.7	13.3	6.3
t001r2	(48,0)	11c	3.28	4.57	60.80	83	4.2	6.7
t001r2	(0,48)	11c	3.99	4.54	50.22	95	15.8	6.2
t110r3	(16,0)	2a	6.67	4.83	27.59	127	11.9	6.0
t110r3	(0,16)	7b	5.69	4.99	32.99	118	3.9	6.5
m100r2	(24,0)	7a	5.35	4.24	39.82	154	4.7	5.6
m100r2	(0,24)	2b	5.22	4.17	39.98	154	5.3	5.7
m-101r2	(24,0)	1	6.29	3.97	42.58	143	2.1	6.4
m-101r2	(0,24)	1	5.56	3.92	48.10	145	4.9	6.4

[a] See text for label explanation

[b] Only the chiralities (n,0), (0,n), and (n,n) were studied

[c] After rolling from the corresponding sheet and before structure optimization. Symbols a, b, c, g, h are used for chiralities (n,0); (0,n); ((n,0), (0,n)); ((n,0), (0,n), (n,n)) and ((n,n), (n,2n), (2n,n)), respectively [182]. The assignment of a, b symbols depends on crystallographic setting for rectangular groups

[d] The difference of radial distances to outmost and innermost (oxygen) atoms in relaxed structures

[e] The sum of radial distances to outmost and innermost (oxygen) atoms in relaxed structures

Table 7.32 Relaxed structure[a], stability and band gaps of selected ZNT's with an average diameter of about 40 Å [151]

Label of initial sheet	NT chirality	Number of ZrO_2 formula units	NT period l (Å)	NT wall thickness w (Å)	NT average diameter d (Å)	E_{surf} (J/m^2)	E_{str} (kJ/mol)	E_g (eV)
c110r2	(40,0)	80	5.42	2.02	41.69	0.97	8.2	5.9
c110r2	(0,24)	48	3.26	2.02	41.49	0.94	5.2	5.9
c110r3	(0,24)	72	3.19	6.79	38.69	1.74[b]	1.0	5.6
c111h1	(40,0)	80	5.64	1.94	41.51	0.77	1.6	6.7
c111h1	(24,24)	48	3.26	1.94	43.10	0.77	1.5	6.7
c111h2	(20,20)	80	3.34	4.85	40.72	1.14	14.5	6.3
t001r2	(32,0)	64	3.28	4.57	40.66	1.05	8.9	6.5
t001r2	(0,40)	80	3.99	4.52	41.86	1.23	23.2	6.1
t110r3	(0,20)	120	5.68	4.98	41.38	1.51[c]	2.7	6.5
m-101r2	(24,0)	96	6.29	3.97	42.58	1.35	2.1	6.4
a101c2	(−12,12)	48	3.80	2.53	43.35	0.98	1.1	6.6

[a] See footnotes to Table 7.31
[b] Surface energy is 1.52 J/m^2 using ZrO_2 (rutile) bulk energy
[c] Surface energy is 1.28 J/m^2 using ZrO_2 (cotunnite) bulk energy

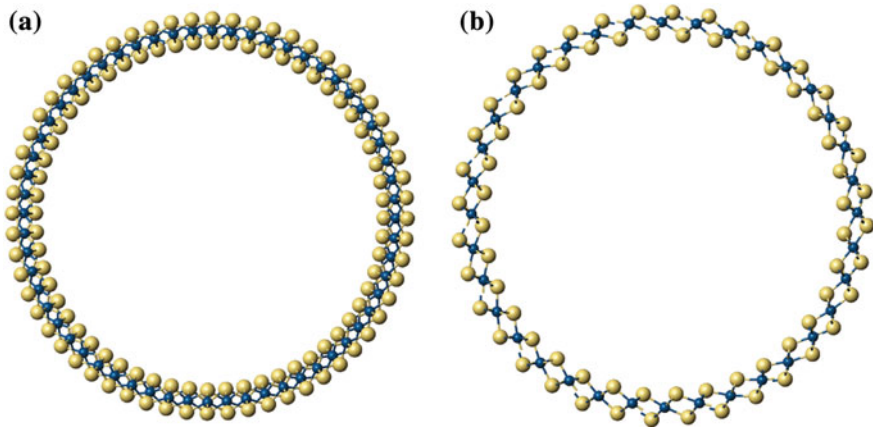

Fig. 7.50 A cross-section of the relaxed structure of zirconia nanotubes folded from the hexagonal monolayer c111h1. **a** With chirality (30,0) and **b** with chirality (18,18). See Fig. 7.45 for labeling

and zirconia nanotubes. The strain energies of TNTs reported in [102, 120, 187] are nearly two times larger than those derived here for ZNTs with an equal chirality. This means that ZNTs are more stable than TNTs relative to the precursor nanosheets.

However, the formation and surface energies of the hexagonal ZrO_2 monolayer slab (see Table 7.30) are considerably greater than the corresponding energies for the hexagonal TiO_2 monolayer slab ($E_{form} = 47$ kJ/mol, $E_{surf} = 0.44$ J/m^2). Consequently, E_{form} (ZNT) is greater than E_{form}(TNT), and ZNTs with monolayer walls should be less stable than similar TNTs relative to the parent bulk phases.

Zirconia nanotubes with anatase morphology belong to the first group possessing a wall thickness below 3 Å. Analogous titania nanotubes generated from 6-planes (101) anatase sheets were modeled in works [119, 120, 125]. Calculation results are given in Table 7.32 for ZNT a101c2 with chirality (12,12). Such chirality was found to be more favorable for TNTs [120, 125].

Comparison of similar ZNT and TNT leads to the same conclusions that were made for NTs with hexagonal morphology (see Table 7.33). Supposedly, $E_{form} \approx$ 150 kJ/mol is too high for the potential existence of anatase-type ZNTs in spite of their low strain and surface energy.

The second group includes nanotubes of different structure with a wall thickness of 45 Å. Among the ZNTs generated from the cubic phase, only the 6-shell tube of type c111h2 with hexagonal morphology and chirality (n,n) has a relatively low formation energy and the medium strain energy. During the relaxation of the NT c111h2 (20,20), the average diameter increases considerably from 38 to 41 Å. This leads to the stretching of Zr O bonds up to their break on the outward NT surface. As a result, one sees a noticeable increase in the strain energy for a 6-shell NT with hexagonal morphology compared to a similar 3-shell NT. On the other hand, nanotubes t001r2 (n,0) generated from the tetragonal phase with lepidocrocite morphology (Fig. 7.51a) have approximately the same stability, although their strain energy is

Table 7.33 Comparison of stability for selected TNTs and ZNTs with an average diameter of about 40 Å

Structure	Label of initial sheet	NT chirality	TiO_2 [102, 120, 187]			ZrO_2 [151]		
			E_{form}(kJ/mol)[a]	E_{str}(kJ/mol)	d(Å)	E_{form}(kJ/mol)[b]	E_{str}(kJ/mol)	d(Å)
Hexagonal	c111h1	(24,24)	50	3.7	39.2	89	1.5	43.1
Anatase	a101c2	(−12,12)	74	3.2	39.6	143	1.1	43.4
Lepidocrocite	t001r2	(32,0)	37	8.3	38.4	83	8.9	40.7

[a] Formation energy from the tetragonal (anatase) phase
[b] Formation energy from the tetragonal (distorted fluorite) phase

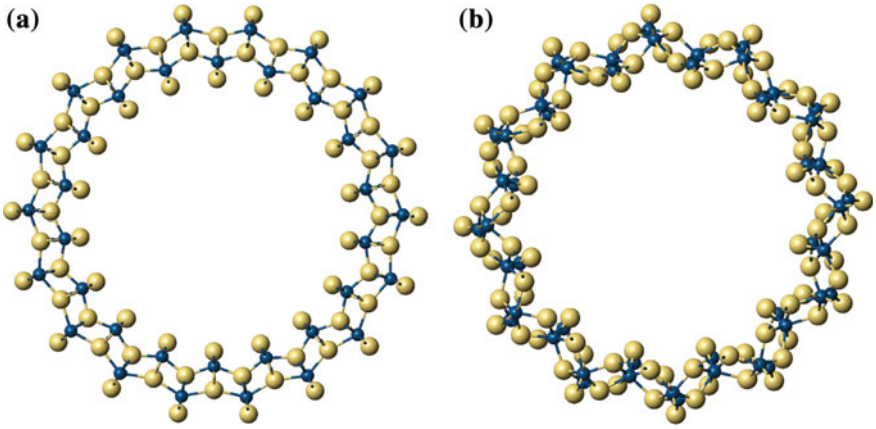

Fig. 7.51 A cross-section of the relaxed structure of zirconia nanotubes folded from the bilayers with a wall thickness of 4–5 Å. **a** Using nanosheet t001r2 with lepidocrocite morphology with chirality (18,0) and **b** using nanosheet m$\bar{1}$01r2 with baddeleyite morphology with chirality (12,0). See Fig. 7.45 for labeling

half the strain energy of c111h2 (n,n) with an equal diameter (see Table 7.32). For this reason, nanotubes with lepidocrocite structure are more preferable among other ZNTs with a wall thickness of 45 Å. As was stated above, TiO_2-layer anatase (001) films, consisting of two layers, rearrange into stable lepidocrocite-like layers [188]. Szieberth et al. [127] investigated the structure and energy of TiO_2 nanotubes with lepidocrocite morphology using a computational method which is very close to ours. Some systems were recalculated in [151] with other basis sets and gave identical results, see Table 7.33. The designated NT chirality corresponds to the choice of a and b slab vectors (see Table 7.30). The values obtained show that titania (n, 0) NTs with lepidocrocite morphology have almost the same strain energies as were found for the equivalent ZNTs. Similar to the hexagonal and anatase cases (see above), the formation energies of t001r2 (n,0) ZNTs are two times larger than the formation energies of the lepidocrocite-like TNTs.

Tubes generated from the monoclinic (baddeleyite) phase have the formation energy close to 150 kJ/mol, and consequently they are less stable than the two above-mentioned. Nevertheless, one of these ZNTs (Fig. 7.51b), namely m$\bar{1}$01r2 (n,0), may be interesting due to its flexible structure and low strain energy.

The walls with a width of 5 Å or thicker are attributed to the ZNT based on c110r4, c110r3, and t110r3 nanolayers. Presumably, the computational results for such tubes are more important. Nanotubes based on c110r4 consist of eight atomic shells and have a large strain and/or formation energy (see Table 7.31). The relatively small formation and strain energies pertain to 9-shell (with rutile morphology) and 7-shell (with cotunnite morphology) tubes with chirality (0,n). These ZNTs are depicted in Fig. 7.52a, b, respectively. The low strain energy of the first one is probably due to a spring-like ZrO bond arrangement, which provides a soft expansion and shrinking of the surface layers during the structure relaxation. The structure of the second ZNT

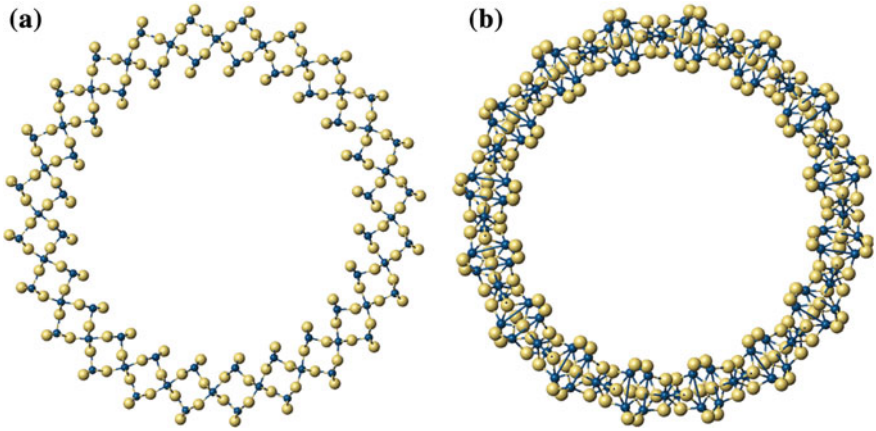

Fig. 7.52 A cross-section of relaxed structure of zirconia nanotubes folded from the trilayers with wall thickness of 5–7 Å. **a** Using nanosheet c110r3 with rutile morphology with chirality (0,24) and **b** using nanosheet t110r3 with cotunnite morphology with chirality (0,16). See Fig. 7.45 for labeling

consists of two ZrO_2 layer blocks connected with flexible one ZrO_2 layer sectors (see t110r3 slab structure in Fig. 7.48b). This explains the low strain energy of the ZNT with cotunnite morphology. Both types of tubes can be proposed as models for NT with a wall thickness greater than 5 Å, although the relatively high formation energy of those tubes (≈120 kJ/mol) should be kept in mind. Presumably, further calculations of zirconia multi-walled and/or polygonal nanotubes are needed to make more realistic the comparison between the theoretical and experimental results.

Upon relaxation, the enlargement of the initial diameter of the nanotubes considered is small, except for the above-mentioned case of ZNT c111h2, where the internal strain leads to a substantial nanotube expansion. Relaxation of the ZNT obtained from a t110r3 sheet results in a small reduction of diameter. Insignificant diameter change indicates that relaxation does not displace the atoms considerably from their positions just after folding for tube diameters of 40 Å and above, with a wall thickness less than 7 Å. This conclusion is confirmed by comparing the surface energy of the nanotubes with the surface energy of the corresponding thin films: the proximity of these values proves the principal role of the parent nanolayer structure.

The dependence of the strain energy on the tube average diameter is plotted in Fig. 7.53 for the ZNTs discussed above. It is seen that most of the selected ZNTs have low E_{str} at diameters $d > 25$. The difference in the strain energies of fluorite-type ZrO_2 monolayer tubes with chiralities (n,n) and (n,0) is quite negligible, thus supporting the similar results obtained earlier [102] for titania nanotubes folded from hexagonal layers.

Three ZrO_2-layer tubes with rutile (c110r3) morphology provide the smallest strain energy. The curves for tubes with baddeleyite (m-101r2) and cotunnite (t110r3) morphology lie slightly above. The strain energy dependence jumps down

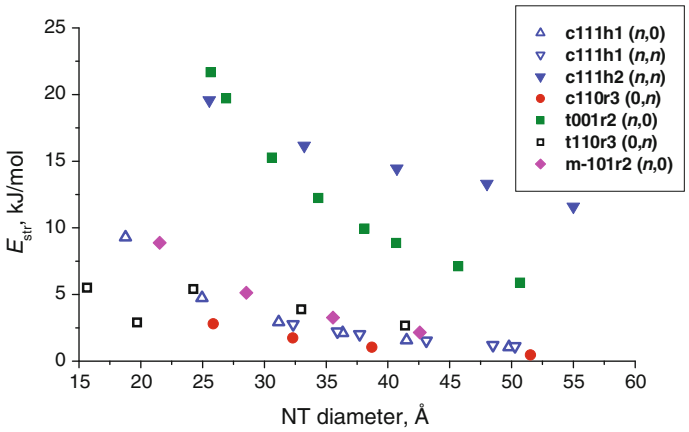

Fig. 7.53 Strain energy dependence on the average diameter for selected zirconia nanotubes (see text for nanotube labels)

for cotunnite-type tubes at d < 24 Å due to an increase of the Zr atom coordination number from 5 to 6 on the innermost tube surface. The tubes with two ZrO_2-layer walls (at lepidocrocite and hexagonal morphology) have a greater value of E_{str} than that for other cases depicted in Fig. 7.53. However, we can suppose that the importance of lepidocrocite-like structure should increase in multiwall nanotubes because of its laminate nature and low formation energy. This assumption needs examination in the subsequent calculations.

Let us summarize the most important conclusions made in [151] basing on the results of the first-principles zirconia nanotubes calculations.

It has been found that the formation energy of ZrO_2 nanotubes with a sufficiently large diameter is mainly determined by the formation energy of the corresponding nanosheet.

The proximity of the nanotube surface energy to the surface energy of the corresponding thin films confirms the principal role of the parent nanolayer structure. As a rule, the nanotube strain energy is positive and decreases with enlarging diameter. Several factors can contribute to the increase of the strain energy at relatively small nanotube diameters: (1) steric obstacles upon folding, especially those caused by repulsion between the nearby-base NT calc oxygen atoms in the inner tube shells; (2) shrinking of the chemical bonds in the inner tube shells, and (3) stretching or breaking of chemical bonds in the outer tube shells due to their expansion. The potential flexibility of the chemical bond network in the parent sheet helps to reduce the contribution of the factors listed.

The analysis of nanotube formation and strain energies has determined that the most stable tubes with thin (one ZrO_2 layer) walls should have hexagonal morphology corresponding to the rolling of (111) sheets from the cubic fluorite phase. The tubes with walls composed of two ZrO_2 layers presumably have lepidocrocite morphology. The tubes with thicker walls can possess a different structure originating from cubic,

tetragonal or orthorhombic phases. The lowest strain energy has been derived for a nanotube with rutile morphology exhibiting zigzag ZrO bond arrangement.

The comparison of zirconia-based and titania-based nanotubes shows that the former may have smaller strain energies, while the latter may have smaller formation energies relative to the stable bulk phases. One can suppose that the formation energy is a more fundamental quantity than the strain (or rolling) energy to collate the nanotubes with different chemical composition, since the former includes the latter as its part. From this point of view, titania-based single-walled nanotubes can be obtained more easily than zirconia-based single-walled nanotubes. This conclusion is in accordance with the fact that synthesized titania nanotubes may have thinner walls than those observed in the fabricated zirconia nanotubes.

References

1. C.W. Litton, D.C. Reynolds, T.C. Collins (eds.), *Zinc Oxide Materials for Electronic and Optoelectronic Device Applications* (Wiley, 2012)
2. Z.C. Feng (ed.), *Handbook of Zinc Oxide and Related Materials, Devices and Nano-Engineering*, vol. 2 (CRC Press, 2013)
3. C.F. Klingshirn, B.K. Meyer, A. Waag, A. Hoffmann, J. Jeurts, *Zinc Oxide, From Fundamental Properties Towards Novel Appliocations*. Springer Series in Materials Science, vol. 120 (Springer, Berlin, 2010)
4. Ü. Özgür, Ya.I. Alilov, C. Liu, A. Teke, M.A. Resshchikov, S. Doğan, V. Avrutin, S.J. Cho, H. Morcoc, J. Appl. Phys. **98**, 041301 (2005)
5. Z.L. Wang, J. Phys.: Condens. Matter **16**, R829 (2004)
6. Z.L. Wang, Mater. Today **7**, 26 (2004)
7. M. Spencer, Prog. Mater. Sci. **57**, 437 (2012)
8. J.R.D. Retamal, C.-Y. Chen, K.-Y. Lai, H. He Jr, *Handbook of Zinc Oxide and Related Materials, Devices and Nano-Engineering*, vol. 2 (CRC Press, 2013)
9. X.W. Sun, Y. Yang, *ZnO Nanostructures and Their Applications* (Pan Stanford Publishing, 2012)
10. M.S.R. Rao, T. Okada (eds.), *ZnO Nanocrystals and Allied Materials*. Springer Series in Materials Science, vol. 180 (Springer, Heidelberg, 2014)
11. S. Hu, Z.L. Wang, Nano Res. **4**, 1013 (2011)
12. K.W. Chae, Q. Zhang, J.S. Kim, Y.H. Jeong, G. Cao, Belstein, J. Nanotechnol. **1**, 128 (2010)
13. J. Han, F. Fan, C. Xu, S. Lin, M. Wei, X. Duan, Z. L. Wang, Nanotechnology **21**, 405203 (2010)
14. C.X. Hu, G.P. Zhu, X. Li, Y. Yang, S.T. Tan, X.W. Sun, C. Lincoln, T.A. Smith, J. Appl. Phys. **103**, 094303 (2008)
15. V.V. Pokropivny, M.M. Kasumov, Tech. Phys. Lett. **33**, 44 (2007)
16. B. Geng, X. Liu, X. Wei, S. Wang, Mater. Res. Bull. **41**, 1979 (2006)
17. A. Wei, X.W. Sun, C.X. Xu, Z.L. Dong, M.B. Yu, W. Huang, Appl. Phys. Lett. **88**, 213102 (2006)
18. W.Z. Hu, Z.Z. Ye, D.W. Ma, H.M. Lu, L.P. Zhu, B.H. Zhao, Appl. Phys. Lett. **87**, 093110 (2005)
19. P. Tronc, V. Stevanović, I. Milošević, M. Damnjanović, Phys. Status Solidi (B) **243**, 1750 (2006)
20. A. Janotti, C.G. Van de Walle, Rep. Prog. Phys. **72**, 126501 (2009)
21. J. Wróbel, J. Kurzydłowski, K. Hummer, G. Kresse, J. Piechota, Phys. Rev. B **80**, 155124 (2009)

22. D. Gryaznov, E. Blokhin, A. Sorokine, E. Kotomin, R. Evarestov, A. Bussmann-Holder, J. Maier, J. Phys. Chem. C **117**, 13776 (2013)
23. R. Dovesi, V.R. Saunders, C. Roetti, R. Orlando, C.M. Zicovich-Wilson, F. Pascale, B. Civalleri, K. Doll, N.M. Harrison, I.J. Bush, P. D'Arco, M. Llunell, *CRYSTAL09 User's Manual* (University of Torino, Torino, 2010)
24. J.E. Jaffe, A.C. Hess, Phys. Rev. B **48**, 7903 (1993)
25. H.J. Monkhorst, J.D. Pack, Phys. Rev. B **13**, 5188 (1976)
26. M. Ferrero, M. Rerat, R. Orlando, R. Dovesi, J. Comput. Chem. **29**, 1450 (2008)
27. F. Oba, M. Choi, A. Togo, A. Seko, I. Tanaka, J. Phys.: Condens. Matter **22**, 384211 (2010)
28. W. Korner, C. Elsasser, Phys. Rev. B **81**, 085324 (2010)
29. A. Boonchun, W.R.L. Lambrecht, Phys. Status Solidi (B) **248**, 1043 (2011)
30. H. Karzel, W. Potzel, M. Kofferlein, W. Schiessl, M. Steiner, U. Hiller, G.M. Kalvius, D.W. Mitchel, T.P. Das, P. Blaha, Phys. Rev. B **53**, 11425 (1996)
31. S. Desgreniers, Phys. Rev. B **58**, 14102 (1998)
32. J. Serrano, A.H. Romero, F.J. Manjon, R. Lauck, M. Cardona, A. Rubio, Phys. Rev. B **69**, 094306 (2004)
33. Springer Materials, The Landolt-Börnstein Database (2012)
34. U. Diebold, L.V. Koplitz, O. Dulub, Appl. Surf. Sci. **237**, 336 (2004)
35. Q.L. Tang, Q.H. Luo, J. Phys. Chem. C **117**, 22954 (2013)
36. C. Tusche, H.L. Meyerheim, J. Kirschner, Phys. Rev. Lett. **99**, 026102 (2007)
37. S.H. Na, C.H. Park, J. Korean Phys. Soc. **54**, 867 (2009)
38. C.L. Freeman, F. Claeyssens, N.L. Allan, J.H. Harding, Phys. Rev. Lett. **96**, 066102 (2006)
39. F. Claeyssens, C.L. Freeman, N.L. Allan, M.N. Ashfold, J.H. Harding, J. Mater. Chem. **15**, 139 (2005)
40. Z.C. Tu, X. Hu, Phys. Rev. B **74**, 035434 (2006)
41. B. Wang, Sh. Nagase, J. Zhao, G. Wang, Nanotechnology **18**, 345706 (2007)
42. G. Kresse, O. Dulub, U. Diebold, Phys. Rev. B **68**, 245409 (2003)
43. Z. Yufei, G. Zhiyou, G. Xiaoqi, C. Dongxing, D. Yunxiao, Z. Hongtao, J. Semicond. **31**, 082001 (2010)
44. F. Ostendorf, S. Torbrugge, M. Reichling, Phys. Rev. B **77**, 041405 (2008)
45. X. Wang, J. Song, Z.L. Wang, Appl. Chem. Phys. Lett. **424**, 86 (2006)
46. Z. Zhou, Y. Li, L. Liu, Y. Chen, S.B. Zhang, J. Phys. Chem. C **112**, 13926 (2008)
47. Yu.E. Kitaev, P. Tronc, Phys. Rev. B **64**, 205312 (2001)
48. I. Milošević, V. Stevanovic, P. Tronc, M. Damnjanović, J. Phys.: Condens. Matter **18**, 1939 (2006)
49. C.N.R. Rao, A. Govindaraj, *Nanotubes and Nanowires*, 2nd edn. RSC Nanoscience and Nanotechnology, vol. 18 (Royal Society of Chemistry, 2011)
50. M. Riaz, A. Fulan, G. Amin, N.H. Alvi, O. Nur, M. Willander, J. Appl. Phys. **106**, 034309 (2009)
51. Y. Xi, J. Song, R. Yang, Z. Gao, C. Hu, Z.L. Wang, J. Mater. Chem. **19**, 9260 (2009)
52. Y.J. Xing, Z.H. Hi, J.H. Song, R.M. Wang, J. Xu, Z.Q. Xue, D.P. Yu, Solid State Communs. **129**, 671 (2004)
53. Y.J. Xing, Z.H. Xi, Z.Q. Xue, X.D. Zhang, J.H. Song, R.M. Wang, J. Xu, Y. Song, S.L. Zhang, D.P. Yu, Appl. Phys. Lett. **83**, 1689 (2003)
54. O.Y. Zhong-can, Z.B. Su, C.I. Wang, Phys. Rev. Lett. **78**, 4055 (1997)
55. Y.F. Li, Z. Zhou, Y.S. Chen, Z.F. Chen, J. Chem. Phys. **130**, 204706 (2009)
56. Y. Yang, X. Yan, Y. Xiao, Z.H. Guo, Chem. Phys. Lett. **446**, 98 (2007)
57. B. Wen, R. Melnik, Chem. Phys. Lett. **466**, 84 (2008)
58. H. Xu, A.L. Rosa, T. Frauenheim, R.Q. Zhang, S.T. Lee, Appl. Phys. Lett. **91**, 031914 (2007)
59. F.C. Zhang, Z.Y. Zhang, W.H. Zhang, J.F. Yan, J.N. Yong, Chin. Phys. B **18**, 2508 (2009)
60. Z.W. Yang, B. Wen, R. Melnik, S. Yao, T.J. Li, Appl. Phys. Lett. **95**, 192101 (2009)
61. X.B. Han, L.Z. Kou, X.L. Lang, J.B. Xia, N. Wang, R. Qin, Adv. Mater. **21**, 4937 (2009)
62. H.J. Xiang, J.L. Yang, J.G. Hou, Q.S. Zhu, Appl. Phys. Lett. **89**, 223111 (2006)
63. C. Li, W.L. Guo, Y. Kong, H. Gao, Phys. Rev. B **76**, 35322 (2007)

64. H. Xu, R.Q. Zhang, X.H. Zhang, A.L. Rosa, T. Frauenheim, Nanotechnology **18**, 485713 (2007)
65. W. Fan, A.L. Rosa, T. Frauenheim, R.Q. Zhang, Solid State Commun. **148**, 101 (2008)
66. D.Q. Fang, A.L. Rosa, R.Q. Zhang, T. Frauenheim, J. Phys. Chem. C **114**, 5760 (2010)
67. J.S. Qi, D.N. Shi, B.L. Wang, Comput. Mater. Sci. **46**, 303 (2009)
68. C.C. Wang, G. Zhou, J. Li, B.H. Yan, W.H. Duan, Phys. Rev. B **77**, 245303 (2008)
69. W. An, X.J. Wu, X.C. Zeng, J. Phys. Chem. C **112**, 5747 (2008)
70. Y. Su, Q.Q. Meng, J.G. Wang, J. Phys. Chem. C **113**, 21338 (2009)
71. S-P. Huang, H. Xu, I. Bello, R.Q. Zhang, J. Phys. Chem. C **114**, 8861 (2010)
72. Y. Zhang, Y.-H. Wen, J.-C. Zheng, Z.-Z. Zhu, Phys. Lett. A **374**, 2846 (2010)
73. X. Wang, Z. Huang, T. Wang, Y.W. Tang, X.C. Zeng, Physica B **403**, 2021 (2008)
74. X. Shen, P.B. Allen, J.T. Muckerman, J.W. Davenport, J.C. Zheng, Nano Lett. **7**, 2267 (2007)
75. Y. Zhang, Y.H. Wen, J.C. Zheng, Z.Z. Zhu, Appl. Phys. Lett. **94**, 113114 (2009)
76. L.X. Zhang, H.C. Huang, Appl. Phys. Lett. **90**, 023115 (2007)
77. W. Fan, H. Xu, A.L. Rosa, T. Frauenheim, R.Q. Zhang, Phys. Rev. B **76**, 073302 (2007)
78. J.T. Dong, F.C. Zhang, W.H. Zhang, Z.Y. Zhang, Sci. China Phys. Mech. Astron. **56**, 706 (2013)
79. Y. Mao, J. Zhong, Y. Chen, Phys. E: Low-Dimen. Syst. Nanostruct. **40**, 499 (2008)
80. H. Pan, Y.P. Feng, ACS Nano **2**, 2410 (2008)
81. T.M. Schmidt, R.H. Miwa, Nanotechnology **20**, 215202 (2009)
82. Y.-R. Yang, X.-H. Yan, Z.-H. Guo, Y.-X. Deng, Chin. Phys. B **17**, 3433 (2008)
83. Z. Zhu, A. Chutia, R. Sahnoun, M. Koyama, H. Tsuboi, N. Hatakeyama, Jpn. J. Appl. Phys. **47**, 2999 (2008)
84. S.L. Elizondo, J.W. Mintmire, J. Phys. Chem. C **111**, 17821 (2007)
85. R.M. Sheetz, I. Ponomareva, E. Richter, A.N. Andriotis, M. Menon, Phys. Rev. B **80**, 195314 (2009)
86. G.Y. Guo, J.C. Lin, Phys. Rev. B **71**, 165402 (2005)
87. H. Li, Z.H. Jiang, Q. Jiang, Chem. Phys. Lett. **465**, 78 (2008)
88. U. Diebold, Surf. Sci. Rep. **48**, 53 (2003)
89. J. Muscat, V. Swamy, N.M. Harrison, Phys. Rev. B **65**, 224112 (2002)
90. D.A.H. Hanaor, C.C. Sorrell, J. Mater. Sci. **46**, 855 (2011)
91. H. Zhang, J.F. Banfield, Am. Mineral. **84**, 528 (1999)
92. U.E. Cho, S. Han, H.S. Ahn, K.R. Lee, S.K. Kim, C.S. Hwang, Phys. Rev. B **73**, 195320 (2006)
93. T.L. Thompson, J.T. Yates Jr, Chem. Rev. **106**, 4428 (2006)
94. R.A. Evarestov, Yu.F. Zhukovskii, Surf. Sci. **608**, 226 (2013)
95. G. Kresse, J. Furthmuller, *VASP the Guide* (Universität Wien, Wien, 2007)
96. R. Dovesi, V.R. Saunders, C. Roetti, R. Orlando, C.M. Zicovich-Wilson, F. Pascale, B. Civalleri, K. Doll, N.M. Harrison, I.J. Bush, P. D'Arco, M. Llunell, M. Causa, Y. Noel, *CRYSTAL14 User's Manual* (University of Torino, Torino, 2014)
97. F. Labat, P. Baranek, C. Domain, C. Minot, C. Adamo, J. Chem. Phys. **126**, 154703 (2007)
98. M.M. Hurley, L.F. Pacios, P.A. Christiansen, R.B. Ross, W.C. Ermler, J. Chem. Phys. **84**, 6840 (1986)
99. A. Schaefer, C. Huber, R. Ahlrichs, J. Chem. Phys. **100**, 5829 (1994)
100. R.A. Evarestov, *Quantum Chemistry of Solids. The LCAO First Principles Treatment of Crystals*. Springer Series in Solid State Sciences, vol. 153 (Springer, Berlin, 2007)
101. W.H. Press, S.A. Teukolski, V.T. Vetterling, B.P. Flannery, *Numerical Recipes in FORTRAN 77: The Art of Scientific Computing*, 3rd edn. (Cambridge University Press, Cambridge, 2007)
102. R.A. Evarestov, Yu.F. Zhukovskii, A.V. Bandura, S. Piskunov, J. Phys. Chem. C **114**, 21061 (2010)
103. T. He, M. Zhao, X. Zhang, H. Zhang, Z. Wang, Z. Xi, X. Liu, S. Yan, Y. Xia, L. Mei, J. Phys. Chem. C **113**, 13610 (2009)
104. M. Ramamoorthy, D. Vanderbilt, R.D. King-Smith, Phys. Rev. B **49**, 16721 (1994)

105. H. Perron, C. Domain, J. Roques, R. Drot, E. Simoni, H. Catalette, Theor. Chem. Acc. **117**, 565 (2007)
106. F. Labat, Ph Baranek, C. Adamo, J. Chem. Theor. Comput. **4**, 341 (2008)
107. A. Hallil, E. Amzallag, S. Landron, R. Tetot, Surf. Sci. **605**, 738 (2011)
108. P.W. Tasker, J. Phys. C: Solid State Phys. **12**, 4977 (1979)
109. C. Herring, Phys. Rev. **82**, 87 (1951)
110. A. Vittadini, M. Casarin, A. Selloni, Theor. Chem. Acc. **117**, 663 (2007)
111. N. Martsinovich, A. Troisi, Phys. Chem. Chem. Phys. **14**, 13392 (2012)
112. W. Wang, O.K. Varghese, M. Paulose, C.A. Grimes, J. Mater. Res. **19**, 417 (2004)
113. R. Tenne, G. Seifert, Annu. Rev. Mater. Res. **39**, 387 (2009)
114. D.J. Mowbray, J.I. Martinez, J.M. García Lastra, K.S. Thygesen, K.W. Jacobsen, J. Phys. Chem. C **113**, 12301 (2009)
115. Y.Q. Wang, C.G. Hu, X.F. Duan, H.L. Sun, Q.K. Hue, Chem. Phys. Lett. **365**, 427 (2002)
116. A.N. Enyashin, G. Seifert, Phys. Status Solidi (B) **242**, 1361 (2005)
117. Z. Liu, Q. Zhang, L.-C. Qin, Solid. State Commun. **141**, 168 (2007)
118. J. Wang, L. Wang, L. Ma, J. Zhao, B. Wang, G. Wang, Physica E **41**, 838 (2009)
119. A.V. Bandura, R.A. Evarestov, Surf. Sci. **603**, L117 (2009)
120. R.A. Evarestov, A.V. Bandura, M.V. Losev, S. Piskunov, Yu.F. Zhukovskii, Physica E **43**, 266 (2010)
121. A. Vittadini, M. Casarin, Theor. Chem. Account. **120**, 551 (2008)
122. M. Damnjanović, I. Milosević, M. Vuković, R. Sredanivić, Phys. Rev. B **60**, 2728 (1999)
123. M. Damnjanović, T.V.E. Dobradzić, I. Milosĕvić, T. Vuković, B. Nikolić, New J. Phys. **5**, 148 (2003)
124. R.A. Evarestov, Yu.F. Zhukovskii, A.V. Bandura, S. Piskunov, M.V. Losev, J. Phys. Chem. C **115**, 14067 (2011)
125. R.A. Evarestov, Yu.F. Zhukovskii, A.V. Bandura, S. Piskunov, Cent. Eur. J. Phys. **9**, 492 (2011)
126. A.N. Enyashin, S. Gemming, G. Seifert, Springer Ser. Mater. Sci. **93**, 33 (2006)
127. D. Szieberth, A.M. Ferrari, Y. Noel, M. Ferrabone, Nanoscale **2**, 81 (2010)
128. D.B. Migas, V.L. Shaposhnikov, V.E. Borisenko, F.A. d'Avitaya, J. Phys. Chem. C **114**, 21013 (2010)
129. J.M. Wu, H. Shih, Y.K. Tseng, C.L. Hsu, C.Y. Tsay, J. Electrochem. Soc. **154**, H157 (2007)
130. S.S. Amin, A. Nicholls, T.T. Xu, Nanotechnology **18**, 445609 (2007)
131. J.M. Baik, M.H. Kim, C. Larson, X. Chen, S. Guo, A.M. Wodtke, M. Moskovits, Appl. Phys. Lett. **92**, 242111 (2008)
132. J.M. Wu, H.C. Shih, W.T. Wu, Nanotechnology **17**, 105 (2006)
133. C.A. Chen, Y.M. Chen, A. Korotcov, Y.S. Huang, D.S. Tsai, K.K. Tiong, Nanotechnology **19**, 075611 (2007)
134. C. Liu, S. Yang, ACS Nano **3**, 1025 (2009)
135. D. Zhang, P. Liu, C. Liu, J. Phys. Chem. C **112**, 16729 (2008)
136. D. Cakir, O. Gulseren, Phys. Rev. B **80**, 125424 (2009)
137. H. Peng, J. Li, J. Phys. Chem. C **112**, 20241 (2008)
138. J. Nisar, A.C. Moyses, Araujo, R. Ahuja, Appl. Phys. Lett. **98**, 083115 (2011)
139. A. Iacomino, C. Giovanni, F. Train, D. Ninno, J. Phys. Chem. C **114**, 12389 (2010)
140. D.N. Tafen, J.P. Lewis, Phys. Rev. B **80**, 014104 (2009)
141. B. Aradi, P. Deak, H.A. Huy, A. Rosenauer, T. Frauenheim, J. Phys. Chem. C **115**, 18494 (2011)
142. R.A. Evarestov, D.B. Migas, Yu.F. Zhukovskii, J. Phys. Chem. C **116**, 13395 (2012)
143. T. He, Z.S. Hu, J.L. Li, G.W. Yang, J. Phys. Chem. C **115**, 13837 (2011)
144. J. Nasar, C. Moyses Araujo, R. Ahuja, Appl. Phys. Lett. **98**, 083115 (2011)
145. D.B. Migas, A.B. Filonov, V.E. Borisenko, F.A. d'Avitaya, Phys. Chem. Chem. Phys. **16**, 9479 (2014)
146. D.B. Migas, A.B. Filonov, V.E. Borisenko, N.V. Skorodumova, Phys. Chem. Chem. Phys. **16**, 9490 (2014)

147. C.A. Chen, Y.M. Chen, Y.S. Huang, D.S. Tsai, K.K. Tiongc, P.C. Liao, Cryst. Eng. Commun. **11**, 2313 (2009)
148. A.M. Ferrari, D. Sziebertha, Y. Noel, J. Mater. Chem. **21**, 4568 (2011)
149. G.H. Du, Q. Chen, R.C. Che, Z.Y. Yuan, L.-M. Peng, Appl. Phys. Lett. **79**, 3702 (2001)
150. B.D. Yao, Y.F. Chan, X.Y. Zhang, W.F. Zhang, Z.Y. Yang, N. Wang, Appl. Phys. Lett. **82**, 281 (2003)
151. A.V. Bandura, R.A. Evarestov, Comput. Mater. Sci. **65**, 395 (2012)
152. O.A. Graeve, Zirconia, in *Ceramic and Glass Materials: Structure, Properties and Processing*, ed. by J.F. Shackelford, R.H. Doremus (Springer, New York, 2008)
153. R. Orlando, C. Pisani, C. Roetti, E. Stefanovich, Phys. Rev. B **45**, 592 (1992)
154. G. Jomard, T. Petit, A. Pasturel, L. Magaud, G. Kresse, J. Hafner Phys. Rev. B **59**, 4044 (1999)
155. J.E. Jaffe, R.A. Bachorz, M. Gutowski, Phys. Rev. B **72**, 144107 (2005)
156. S. Fabris, A.T. Paxton, M.W. Finnis, Phys. Rev. B **61**, 6617 (2000)
157. X. Zhao, D. Vanderbilt, Phys. Rev. B **65**, 075105 (2002)
158. A.L. Ortiz, J. Sánchez-González, L.M. González-Méndez, F.L. Cumbrera, Ceram. Int. **33**, 705 (2007)
159. G. Fadda, L. Colombo, G. Zanzotto, Phys. Rev. B **79**, 214102 (2009)
160. Q.-J. Liu, Z.-T. Liu, L.-P. Feng, Physica B **406**, 345 (2011)
161. J.D. McCullough, K.N. Trueblood, Acta Crystallogr. **12**, 507 (1959)
162. O. Ohtaka, T. Yamanaka, T. Yagi, Phys. Rev. B **49**, 9295 (1994)
163. J.M. Haines, J.M. Leger, S. Hull, J.P. Petitet, A.S. Pereira, C.A. Perottoni, J.A.H. da Jornada, J. Am. Ceram. Soc. **80**, 1910 (1997)
164. A. Christensen, E.A. Carter, Phys. Rev. B **58**, 8050 (1998)
165. D. Vollath, F.D. Fischer, M. Hagelstein, D.V. Szab, J. Nanopart. Res. **8**, 1016 (2006)
166. A. Aarik, A. Aidla, H. Mundar, T. Uustrate, V. Sammelselg, Thin Solid Films **408**, 97 (2002)
167. H. Arashi, T. Yagi, S. Akimoto, Y. Kudoh, Phys. Rev. B **41**, 4309 (1990)
168. J.M. Leger, P.E. Tomaszewski, A. Atouf, A.S. Pereira, Phys. Rev. B **47**, 14075 (1993)
169. A.V. Bandura, R.A. Evarestov, J. Comput. Chem. **33**, 1554 (2012)
170. L.A. LaJohn, P.A. Christiansen, R.B. Ross, T. Atashroo, W.C. Ermler, J. Chem. Phys. **87**, 2812 (1987)
171. A. Schaefer, C. Huber, R. Ahlrichs, J. Chem. Phys. **100**, 5829 (1994)
172. S.-K. Chan, Y. Fang, M. Grimsditch, Z. Li, M.V. Nevitt, W.M. Robertson, E.S. Zouboulis, J. Am. Ceram. Soc. **74**, 1742 (1991)
173. C.T. Lynch (ed.), *Handbook of Materials Science*, vol. I (CRC Press, Cleveland, 1974), p. 330
174. R. Puthenkovilakam, J.P. Chang, Appl. Phys. Lett. **84**, 1353 (2004)
175. O. Ohtaka, H. Fukui, T. Kunisada, T. Fujisawa, K. Funakoshi, W. Utsumi, T. Irifune, K. Kuroda, T. Kikegawa, Phys. Rev. B **63**, 174108 (2001)
176. R. Ackermann, E.G. Rauh, C.A. Alexander, High Temp. Sci. **7**, 304 (1975)
177. L.K. Dash, N. Vast, P. Baranek, M. Cheynet, L. Reining, Phys. Rev. B **70**, 245116 (2004)
178. H. Boysen, F. Frey, T. Vogt, Acta Crystallogr. B **47**, 881 (1991)
179. J. Malek, L. Benes, T. Mitsuhashi, Powder Diffr. **12**, 96 (1997)
180. C.J. Howard, R.J. Hill, B.E. Reichert, Acta Crystallogr. B **44**, 116 (1988)
181. H.M. Kandil, J.D. Greiner, J.F. Smith, J. Am. Ceram. Soc. **67**, 341 (1984)
182. M. Damnjanović, B. Nikolić, M. Milošević, Phys. Rev. B **75**, 033403 (2007)
183. F. Haase, J. Sauer, J. Am. Chem. Soc. **120**, 13503 (1998)
184. S. Gennard, F. Corà, C.R.A. Catlow, J. Phys. Chem. B **103**, 10158 (1999)
185. A. Hofmann, S.J. Clark, M. Oppel, I. Hahndorf, Phys. Chem. Chem. Phys. **4**, 3500 (2002)
186. I.M. Iskandarova, A.A. Knizhnik, E.A. Rykova, A.A. Bagaturyants, B.V. Potapkin, A.A. Korkin, Microelectron. Eng. **69**, 587 (2003)
187. R.A. Evarestov, A.V. Bandura, M.V. Losev, Russ. J. Gen. Chem. **80**, 1152 (2010)
188. T. Orzali, M. Casarin, G. Granozzi, M. Sambi, A. Vittadini, Phys. Rev. Lett. **97**, 156101 (2006)

Chapter 8
Ternary Oxides

Owing to their novel size-dependent properties the ferroelectric nanoscale structures of the perovskites $PbTiO_3$, $BaTiO_3$, and $SrTiO_3$ (nanotubes, nanowires, nanorods) have attracted a great deal of attention [1–6]. Monoperiodic nanotube/nanowire $ATiO_3$ (A = Sr, Ba, Pb) systems offer fundamental scientific opportunities for investigating the influence of the size and dimensionality of materials with respect to their optical, magnetic and electronic properties [7–10]. Such materials have a potential application as nanosized ferroelectrics and memory elements.

The first DFT calculations for perovskite nanotubes were made in [11]. DFT studies of the ferroelectric properties of $PbTiO_3$ [10] and $BaTiO_3$ [7] nanowires allowed the finding of the critical size for ferroelectricity via polarization along the nanowire axis.

In this chapter the capacity of the DFT methods in modeling the ternary oxide-based nanostructures is illustrated with the results of $SrTi(Zr)O_3$- and $BaTiO_3$-based nanotubes and nanowires DFT calculations.

The results for $SrTiO_3$-based nanotubes with a square morphology show that the relatively stable four-layer NTs arise at greater diameters than the two-layer NTs because of a large curvature difference between the inner and the outer shells provoking a considerable stretching and shrinking of the external and internal NT surfaces. Also, the surface structure of the four-layer tubes changes considerably during atomic and cell relaxation. It was found that the nanotubes (n,0) with the TiO_2 external surface are the most stable, and their stability depends on the tube diameter only slightly. It is interesting that the broken Ti-O bonds on the tube external surface do not influence this high stability. These tubes also have a remarkably high value of the band gap, which is greater than the corresponding bulk and slab values.

Stability of the single-walled nanotubes of chiralities (n,0) and (n,n) for the cubic, and (n_1,0) and (0,n_2) for the orthorhombic $SrZrO_3$ was investigated as function of their diameter, the number of layers in the slab, and the outer surface termination (SrO or ZrO_2). The relaxed structure of ZrO_2-terminated NTs folded from the two layers of both the cubic and orthorhombic phases is very similar and corresponds to the latter phase, which is more stable.

© Springer-Verlag Berlin Heidelberg 2015

R.A. Evarestov, *Theoretical Modeling of Inorganic Nanostructures*,
NanoScience and Technology, DOI 10.1007/978-3-662-44581-5_8

The results of ab initio LCAO DFT(PBE0) calculations of stoichiometric single-walled $BaTiO_3$-based NTs of different sizes and chiralities are considered. It was found that the strain energy of the BaO-terminated 2-shell NTs is negative and exhibits a weak dependence on the tube diameter. In the case of 4-shell NTs, the TiO_2-terminated tubes are more stable than the BaO-terminated. The DFT calculations of the size dependence of the ferroelectric properties of BTO nanowires show that the ferroelectric distortion along the BTO wire axis disappears below the critical diameter of about 1.2 nm. This disappearance is related to the global contraction of the unit cell resulting from the low atomic coordinations at the wire surface.

8.1 $SrTiO_3$

8.1.1 Bulk and Nanolayers

$SrTiO_3$ (STO) is an promising ferroelectric material with an extremely high dielectric constant (the values of the order 104 were reported at low temperatures) related to the soft phonon mode behavior with temperature. At low temperatures controlled by quantum statistics the ferroelectric instability is suppressed, and the compound has been defined as a quantum paraelectric. The very high dielectric constant of the bulk STO decreases, however, significantly in thin films.

Table 8.1 shows the results of the STO bulk properties LCAO DFT(PBE0) calcualtions [12]. It is seen that the calculated lattice parameters and bulk moduli agree very well with the experimental data and previous hybrid functional calculations. The Mulliken atomic charges evidence a considerable covalency of the Ti-O chemical bonding in STO (2.32 e (Ti), −1.45 e (O), 2.03 e (Sr)).

An experimental bulk STO band structure (Fig. 8.1b) was suggested in [20] basing on an angle-resolved photoemission study of the bulk STO. Valence electron-energy loss spectroscopy (VEELS) in a dedicated scanning transmission electron microscope, vacuum ultraviolet spectroscopy and spectroscopic ellipsometry were used in [21] to determine the optical properties and the electronic structure of $SrTiO_3$. The assignments of the interband transitions in the electronic structure were determined quantitatively by comparing the VEELS spectra with vacuum ultraviolet spectra and with the calculated densities of states. The experimentally determined indirect (R–Γ) band gap energy is 3.25 eV, while the direct (R–R) band gap energy is 3.75 eV. The conduction bands in $SrTiO_3$ correspond to the bands composed mainly of Ti_{3d} t_{2g} and e_g states, followed at higher energies by the bands of Sr_{4d} t_{2g} and e_g states, and free electron like states dominating at energies above 15 eV. The upper valence band contains 18 electrons in pre-dominantly O_{2p} states, hybridized with the Ti and Sr states, and has a bandwidth of 5 eV. The interband transitions from the upper valence band to the Ti_{3d} bands and to the Sr_{4d} bands give rise to the transitions spanning from the indirect band gap energy of 3.25 eV up to 15 eV. The lower valence band contains 12 electrons in the Sr_{4p} and O_{2s} states, which are separated by 2 eV, while having a

Table 8.1 The bulk properties of $SrTiO_3$ [12]

	PBE0 LCAO	HSE[a] (LDA[b]) PW	Exper.
a, Å	3.91	3.90	3.91[c]
z_{Mull}(Sr), e	2.03		
z_{Mull}(Ti), e	2.32		
z_{Mull}(O), e	−1.45		
z_{Born}(Sr), e	2.19	(2.54)	
z_{Born}(Ti), e	7.02	(7.12)	
$z_{Born}O_1$, e	−5.60	(−5.66)	
$z_{Born}O_2$, e	−1.80	(−2.00)	
ϵ^0_{xx}	3753		3333[d] at $T = 50$ K
ϵ^{∞}_{xx}	4.64		5.82[e], 5.18[b]
ΔE_g, eV	4.17 [3.87[f]]	3.47[3.07[f]]	3.75 [3.25[f]]
B, GPa	195	192	179[g]

a-Lattice parameter; z_{Mull}-Mulliken atomic charge; z_{Born}-Born effective atomic charge; ϵ^0 and ϵ^{∞} are static and high frequency dielectric constants, respectively; ΔE_g-band gap: direct [indirect]; B-bulk modulus

[a] [13]
[b] [14]
[c] [15]
[d] [16]
[e] [17]
[f] [18]
[g] [19]

bandwidth of 5 eV. The interband transitions from the Sr_{4p} to the Ti_{3d} and Sr_{4d} bands give rise to transition energies spanning from 15 to 24 eV. Interband transitions from the O_{2s} band to the conduction bands appear at 26 eV. A very narrow band at −33 eV below the top of the valence band is composed of Sr_{4s} and Ti_{3p} states and contains eight electrons. The experimentally found valence band (ground state) properties are usually reproduced correctly in the band structure calculations.

The underestimated band gaps in STO within the standard DFT (LDA, GGA-type) functionals have been the subject of many discussions in the literature. The band gap is significantly underestimated in both plane wave ([22] and Fig. 8.1) and LCAO calculations ([23] and Fig. 8.2).

In order to solve the band gap problem, one should go beyond the standard DFT functionals, e.g. by using the hybrid functional, the DFT+U approach or GW technique. It is well known that DFT yields correct ground state properties (the lattice constant, the phonon frequency, valence bands width) of a system, while the DFT does not describe excited states correctly (the band gap, addition or removal electrons), so it is necessary to go beyond DFT to quasi-particle-like electronic structure calculations [24]. The many-body perturbation theory (MBPT) has been used to calculate the properties of excited states, and these energies can be interpreted as quasi-particle energies. Ab-initio calculations of quasi-particle energies are usually

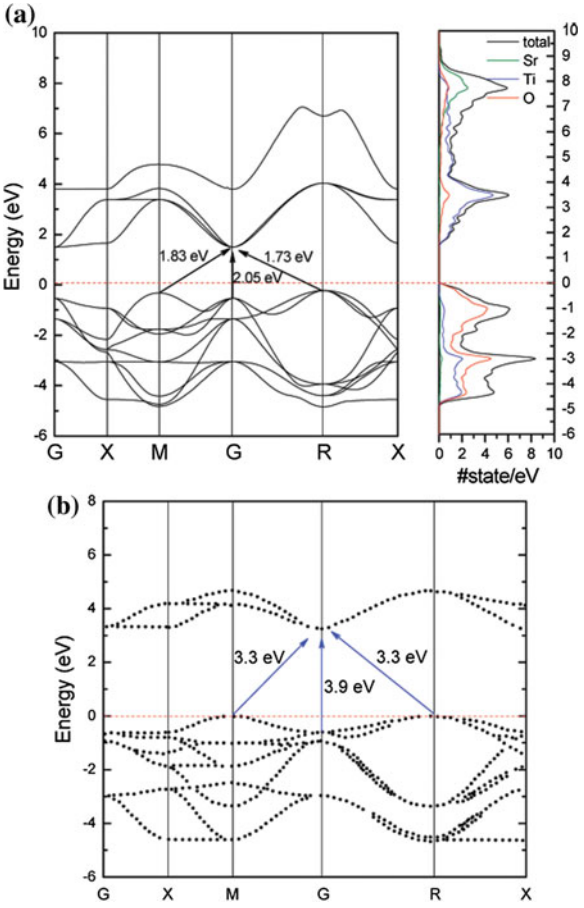

Fig. 8.1 **a** The calculated [22] and **b** the experimental [20] band structure of perovskite $SrTiO_3$. The Fermi levels are set to zero

performed within the GW approximation to the many-body perturbation theory, the self-energy is approximated as the product of the one-electron Greens function G and the dynamically screened Coulomb interaction W. The GW approximation successfully yields quasi-particle energy gaps in semiconductors (the difference with the experimental data is within 0.1 eV). In addition, it correctly predicts electron addition and removal excitations in photoemission spectroscopy. Unfortunately GW calculations require the knowledge of the inverse full dielectric matrix and for oxides these calculations are usually heavy.

The LDA+U method [25] is a simple correction method, often employed to understand the electronic structure of perovskite oxides. The drawback of the LDA+U method is that the parameter U is artificial and is not determined in a first-principles calculations also. The cubic STO electronic structure at an experimental lattice

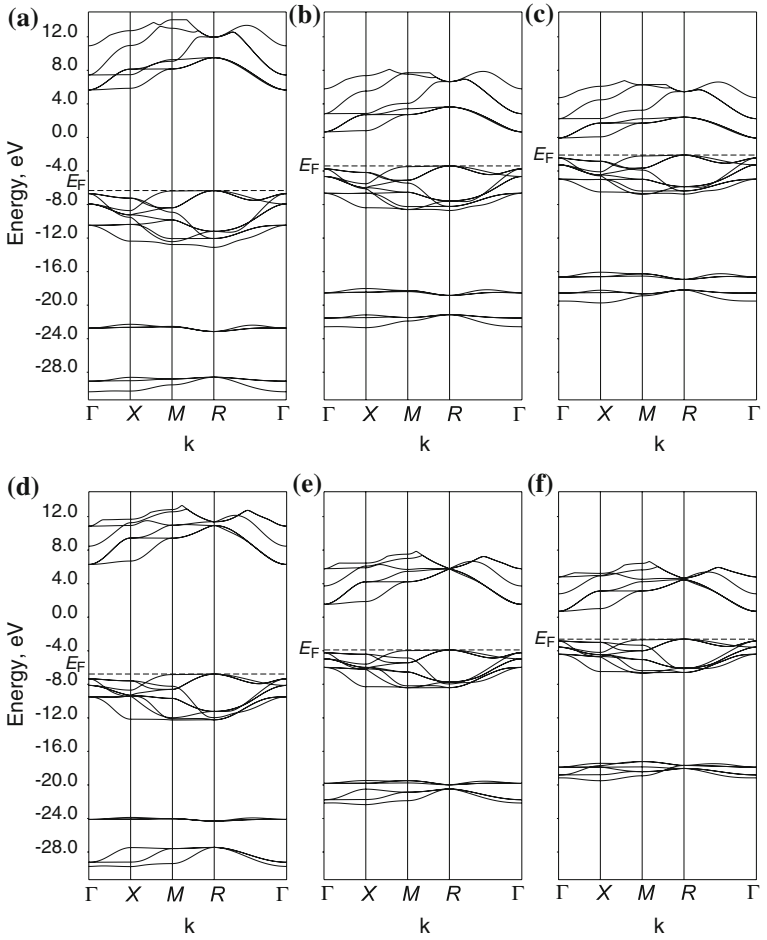

Fig. 8.2 Band structure of cubic crystals: **a–c** $SrTiO_3$, **d–f** $SrZrO_3$. HF LCAO method (**a**), (**d**); hybrid HF-DFT(PBE0) LCAO method (**b**), (**e**); DFT(PBE) LCAO method (**c**), (**f**) [23]

constant (3.905 Å) was investigated in [24] by the DFT(LDA), GW and DFT+U methods. In the latter case several U-values were examined. The valence band and the conduction band are pushed away from each other, so the band gap increases with the value of the U parameter [24]. The LDA calculation (U = 0), in agreement with the experimental data, gives that the band gap is indirect, and the band edges occur at Γ in the conduction band and at R in the valence band. In the case of U = 0 (LDA), the indirect band gap is calculated to be 1.71 eV, which is smaller than the experimentally measured band gap energy as much as 3.25 eV. The band gap increases with $U - J$ almost linearly. $U - J = 4$ eV (which is often used for the calculation of transition-metal-3d orbitals) still underestimates the experimental value. A large value of the $U - J$ parameter, 10 eV, almost gives the experimental band gap of

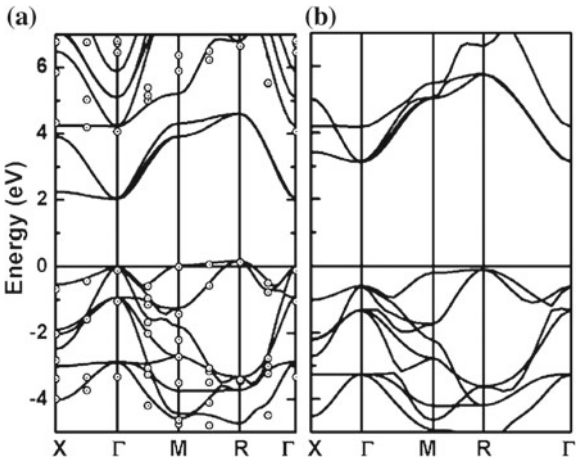

Fig. 8.3 Electronic band structure for cubic perovskite $SrTiO_3$ in the LDA and the GW methods: **a** LDA: *solid line* and GW: *open circles*; **b** $LDA + U$ method and $U - J = 10$ eV. The Fermi energy is set to zero [24]

$SrTiO_3$. A serious problem is that the electronic structures, especially around the conduction band minimum, are significantly different from the normal LDA results; therefore, the question is which one is more reliable, apart from the band gap energy.

GW calculations can be the most important guideline in understanding the electronic structure, because the measurement of the detailed electronic structure is difficult and not yet available for $SrTiO_3$. Figure 8.3a shows the calculated PW LDA band structure corrected by using the GW quasiparticle energies, which is compared to the LDA+U bands with $UJ = 10$ eV, as shown in Fig. 8.3b.

It is seen that the valence band is, by the correction of the quasi-particle energies, rigidly shifted by about 0.1 eV downwards, while the conduction bands are significantly upward shifted by about 2.0 eV, so the calculated direct band gap (at Γ) is 4.15 eV according to the GW approximation. Although these GW corrections lead to a band gap widening, the band gap calculated by using the GW calculation is found to be larger than the experimental value 3.75 eV, indicating that the plasmon-pole model should be modified if the electronic structure of a perovskite oxide is to be calculated. On the other hand, in the $LDA + U$ calculation, a large $U - J$ parameter, 10 eV, is used to get a band gap close to the experimental one. In the $LDA + U$ bands shown in Fig. 8.3b, the indirect band gap is calculated to be 3.28 eV between the Γ and the R symmery points, close to the indirect band gap measurement of 3.25 eV, and the direct band gap at Γ is found to be 3.77 eV, which is very close to direct band gap measurement of 3.75 eV. The conduction bands s of the $LDA + U$ method in Fig. 8.3b are shifted upwards by 1.22 eV compared to the LDA bands in Fig. 8.3a. However, the electronic structures detailed are very different between the $LDA + U$ and the GW calculations.

The role of relativistic effects on the $SrTiO_3$ electronic band structure was studied in [26]. The inclusion of relativistic corrections is important for the Ti_d antibonding states, which form the low-lying states of the conduction band, as well as for the Sr_p states, which are located close to the valence-band bottom, see Fig. 8.4. The top of the

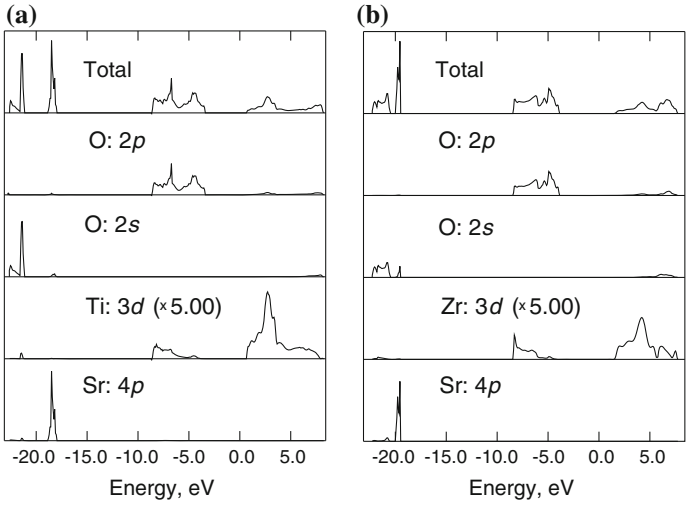

Fig. 8.4 Full and partial density of states in **a** $SrTiO_3$ and **b** $SrZrO_3$ crystals [23]

VB was found at the R point, and the minimum of the CB at the Γ point. Due to the spin-orbit interaction, a spin-orbit splitting was found to be 18.3 mev and 60.7 mev for valence states at R and Γ points, respectivly, and 28.5 mev for the conduction band Γ state. The calculated value for the indirect $R \rightarrow \Gamma$ (direct $\Gamma \rightarrow \Gamma$) band gap was 1.78 (2.14) eV, in good agreement with non-relativistic LDA calculations 1.89 (2.22) eV, [21].

It is seen from Table 8.1 that the first-principles hybrid Hartree-Fock-DFT PBE0 LCAO and HSE PW methods partly overestimate and underestimate band gaps values, respectively. However, in both cases the agreement with the experiment is better than that for the DFT calculations. The LDA, GW and $LDA + U$ STO band structure calculations use the experimental lattice constant and the fitting parameter $U - J$ i.e. they cannot be considered as the first-principles ones.

STO optical transversal (TO) and longitudinal (LO) phonon frequencies calculated in [12] at the Γ-point of the BZ (except for acoustic modes) are given in Table 8.2 and compared to the experimental and theoretical data. As is known, there are four t_{1u} modes and one t_{2u} (silent) mode in STO. According to their cubic symmetry, three t_{1u} modes are infrared active and one t_{1u} is acoustic. A peculiar feature of STO is the existence of two low frequency (soft) modes at the Γ- and R-points, which are responsible for a tendency towards ferroelectric transition (never achieved due to quantum effects) and anti-ferrodistortive phase transition observed at 105 K [27], respectively. Both modes show strong temperature dependencies, which cannot be reproduced in the harmonic approximation. Phonon frequencies calculated with PBE0 at the Γ-point are all real (see Table 8.2) and agree well with the experimental data. This is in contrast to most previous calculations, where the imaginary soft TO1 frequency was obtained employing either the standard DFT (PBE) or HSE functional.

Table 8.2 Phonon frequencies (cm^{-1}) calculated at Γ-point for $SrTiO_3$ [12]

Symmetry	PBE0 LCAO	HSE[a](LDA[b]) PW	Exper[c]
$t_{1u}(TO1)$	25	74i	15 at T=15 K
$t_{1u}(TO2)$	180	162	175,170
$t_{1u}(silent)$	268	250	265
$t_{1u}(TO3)$	547	533	545,547
$t_{1u}(LO1)$	180	(158)	171
$t_{1u}(LO2)$	480	(454)	474
$t_{1u}(LO3)$	824	(829)	795

[a] [13]

[b] [14]

[c] [28–30]

As mentioned in Chap. 2, all the surfaces in the cubic perovskite structure are type-3 surfaces that are stacks of alternately charged planes. If one relies on a formal charge values in the cubic perovskites $A^{II}B^{IV}O_3$, the (0 0 1) surface is a type-1 (non-polar) surface as the repeat unit consists of neutral SrO and TiO_2 atomic planes, see Fig. 2.21. As mentioned above, the $SrTiO_3$ bulk crystal is not fully ionic due to the covalent Ti-O bonding. This covalency is responsible for the presence of a non-vanishing dipole moment in all the repeat units parallel to the surface, which is specific to polar surfaces. The term "weak polarity" surface was suggested in [31] to characterize the electrostatic properties of such surfaces because the charge redistribution required for the cancellation of the macroscopic electrostatic field does not induce as strong a modification of the electronic structure as that predicted on truly polar surfaces (1 1 0) or (1 1 1). These polar surfaces are stacks of alternately charged planes ABO, O_2 or AO_3, B respectively, see Fig. 2.21.

The polar surfaces are generally unstable because of the large electrostatic contribution to the surface energy, [31]. Therefore most experimental and theoretical studies are made for the most stable "weak polarity" (0 0 1) $SrTiO_3$ surface, used also in the modeling of the rolled up STO nanotubes.

Recently the bonding and structure of the reconstructed (0 0 1) STO surface has been studied by the method of transmission electron microscopy [32]. The LCAO (in the single-slab model) and PW (in the repeated slab model) calculations are numerous (see, for example [33–35]. The calculations of the polar (1 1 0) and (1 1 1) STO surfaces are few, [36, 37].

We discuss here in more detail the results of a hybrid HF-DFT LCAO comparative study of the cubic $SrZrO_3$ and $SrTiO_3$ (0 0 1) surface properties in the single-slab model [34]. As known from [38], the consideration of systems with 7–8 atomic layers is sufficient to reproduce the essential surface properties of cubic perovskites. Three different slab models were used in [34]. The first (I) and the second (II) ones consist of 7 crystalline planes (either SrO- or MO_2-terminated, respectively) that are symmetrical with respect to the central mirror plane but nonstoichiometric (see Fig. 2.21). The central layer is composed of MO_2 (M = Ti, Zr) units in model I

and SrO units in model II. Both models I and II have been applied to studying the surface properties of titanates by *ab-initio* calculations [39]. Asymmetric model III is stoichiometric and includes 4SrO and $4MO_2$ atomic planes. Accordingly, it is terminated by a SrO plane on one side and by a MO_2 plane on the other side and there is no central atomic layer. Model III was included in the simulation to investigate the influence of the stoichiometry-violation in symmetrical models I and II on the calculated surface properties. For all the slabs a 1×1 surface unit cell was taken. For the 2D translations in the slabs the experimental bulk lattice constants of $SrZrO_3$ (4.154 Å) and $SrTiO_3$ (3.900 Å) were used that did not differ significantly from DFT B3PW LCAO theoretical values (4.165 and 3.910 Å, respectively).

Table 8.3 presents results obtained for charge distribution and atomic relaxations for models I and II (Mulliken atomic charges and vertical atomic displacements are given). The displacements in the normal to the surface direction are given with respect to the atomic positions in the unrelaxed bulk structure. The negative displacements correspond to the relaxation inwards, towards the bulk, while the positive ones relax outwards, i.e. to the vacuum side. It should be noted that the positions of atoms in the central plane exactly fit the corresponding bulk sites and can not relax due to the imposed mirror symmetry. There are no such restrictions for model III. However,

Table 8.3 Mulliken charges q ($|e|$) and vertical atomic displacements d (Å) for the SrO- and TiO_2-terminated slabs models (I and II, respectively)

Model[a]	Layer	$SrZrO_3$			$SrTiO_3$				
		Ion	q	d	Ion	q	d	d_{calc}[b]	d_{exper}[c]
I	1	Sr	1.86	−0.304	Sr	1.85	−0.185	−0.220	-0.25 ± 0.07
		O	−1.50	0.035	O	−1.52	0.036	0.004	-0.3 ± 0.4
	2	Zr	2.17	0.083	Ti	2.36	0.075	0.046	-0.24 ± 0.07
		O_2	−1.38	0.027	O_2	−1.45	0.040	0.000	-0.4 ± 0.7
	3	Sr	1.88	−0.058	Sr	1.87	−0.031	−0.046	0.02 ± 0.04
		O	−1.36	0.006	O	−1.43	0.009	−0.004	0.1 ± 0.2
	4	Zr	2.13	–	Ti	2.36	–	–	
		O_2	−1.35	–	O_2	−1.42	–	–	
II	1	Zr	2.16	−0.092	Ti	2.29	−0.084	−0.131	0.00 ± 0.03
		O_2	−1.26	−0.097	O_2	−1.30	−0.005	−0.062	-0.5 ± 0.3
	2	Sr	1.86	0.159	Sr	1.85	0.140	0.097	-0.01 ± 0.01
		O	−1.27	0.025	O	−1.36	0.020	−0.019	0.2 ± 0.1
	3	Zr	2.12	−0.014	Ti	2.35	−0.010	−0.027	
		O_2	−1.31	−0.008	O_2	−1.38	0.002	−0.019	
	4	Sr	1.87	–	Sr	1.87	–	–	
		O	−1.33	–	O	−1.40	–	–	

[a] Bulk charges: $SrTiO_3$: $q(Sr) = 1.88$, $q(Ti) = 2.12$, $q(O) = -1.33$; $SrZrO_3$: $q(Sr) = 1.87$, $q(Zr) = 2.53$, $q(O) = -1.47$

[b] Results of DFT PW calculations [40] using the optimized lattice constant $a = 3.86$ Å

[c] Experimental data [41] for $SrTiO_3$ at 300 K

the absolute atomic displacements cannot be calculated unambiguously in this case, due to uncertainty in the zero-level choice when the relaxed and unrelaxed structures are superimposed. This problem may be overcome by fixing the positions of the two middle layers at the bulk geometry. Model III does not satisfy this condition, so the corresponding absolute atomic displacements were not calculated in this model.

The displacement d values obtained for the $SrTiO_3$ practically coincide with the shifts from calculations [42], where almost the same LCAO procedure was used. The vertical shifts calculated for the upper Sr atoms are noticeably greater than the shifts of other atoms in both models I and II, though they are negative in the first and positive in the second case. Also, for $SrZrO_3$ they are larger than for $SrTiO_3$. The displacements of other atoms are very similar on the $SrZrO_3$ and $SrTirO_3$ surfaces, except for the inward shift of the top oxygen atom on the ZrO_2 surface which is much greater than the shift of the corresponding oxygen atom on the TiO_2 surface. The X-ray diffraction data [41] for the $SrTiO_3$ (0 0 1) surface are presented in the last column of Table 8.3. Note that the experimental values correspond to 300 K, whereas the theoretical values correspond formally to 0 K. As well as in other *ab-initio* investigations, satisfactory agreement between the theory and experiment was found only for the displacements of the top Sr atoms in model I. The comparison of the calculated and measured displacements for the deeper atoms in the $SrTiO_3$ slabs is difficult as the experimental data reveals large errors. Furthermore, in these slab simulations, as in most other studies, a cubic bulk unit cell is used to generate the surface unit cell and the corresponding symmetry (in the surface plane) is kept fixed; whereas the unit cell must be doubled and the symmetry should be lowered to tetrahedral for reproducing the ferroelectric distortions. Most certainly, surface phase transition can also take place in the case of zirconate due to the existence of lower-symmetrical orthorhombic modification at room temperature. Table 8.3 also presents the results of a previous LDA PW simulation [40] for $SrTiO_3$. The LCAO displacements satisfactory correlate with the data of PW calculations.

The Mulliken atomic charges are also given in Table 8.3. These quantities can be used for the analysis of electron redistribution in the surface layers, which may be important for the adsorption of another species on the surface. Table 8.3 clearly shows that the Sr atomic charge is close to the bulk one and exhibits insensitivity to the kind of M atom, type of termination and number of layers. Conversely, the calculated Ti and Zr charges give evidence of the considerable covalency of the M–O bonds in both crystals. It can also be seen that the deviations of the surface oxygen charges from their bulk values are relatively large and exhibit the opposite sign for the two types of surface termination. The calculated Mulliken charges are very similar to the charges obtained in [43] via the Bader density decomposition.

When models I and II are used, the surface energy E_s can be determined as sum of two parts, $E_s = E^{unrel} + E^{rel}(T)$. The first term E^{unrel} is equal to one half of the energy for the crystal cleavage into SrO- and MO_2-terminated slabs. It can be written as

$$E^{unrel} = \frac{1}{4S}\left[E^{unrel}_{slab}(\mathrm{SrO}) + E^{unrel}_{slab}(\mathrm{MO_2}) - 7E_{bulk}\right] \tag{8.1}$$

where E_{slab}^{unrel}(SrO) and $E_{slab}^{unrel}(MO_2)$ are the energies for the unrelaxed SrO- and MO_2-terminated slabs, E_{bulk} is a bulk energy per primitive cell, and S is the area of the 2D cell. The second term is the relaxation energy for the SrO- or MO_2-terminated slabs and is computed as a difference between the relaxed and unrelaxed slab energies:

$$E^{rel} = \frac{1}{2S}\left[E_{slab}^{rel}(T) - E_{slab}^{unrel}(T)\right] \tag{8.2}$$

where $T =$ SrO or MO_2.

The surface energy of model III (stoichiometric slab) equals the difference between the energy of the slab and the quadruple energy of the bulk primitive cell divided by $2S$. The results for the surface energy are summarized in Table 8.4.

For both crystals E_s for SrO termination is slightly less than that for MO_2 termination. It is important that the surface energies averaged over models I and II are very close to E_s for model III (this is valid both for the relaxed and unrelaxed systems). The values obtained show that the surface energy of $SrZrO_3$ is smaller than that of the surface energy of $SrTiO_3$ crystal. The calculated value for the surface energy of $SrTiO_3$ (1.24–1.25 J/m^2, see Table 8.4) agrees satisfactorily with the value calculated in [40] using the DFT PW framework (1.36 J/m^2).

In Table 8.4 the calculated bandgaps (BG) for slabs are compared. It is clearly seen that in all cases the BG for $SrZrO_3$ systems is wider. This agrees with the larger ionicity of $SrZrO_3$ in comparison with $SrTiO_3$. One can notice that in the case of $SrTiO_3$ the BG for model I is markedly greater than that for models II and III. The substantial reduction of BG for the TiO_2 surface relative to the bulk value is due to an extended shoulder in the valence-band electronic DOS (see below). The same reduction was found in the DFT PW calculations [40], in spite of the fact that the LDA gaps are half of the gaps calculated in GGA (see Table 8.4).

In all the figures below the zero energy is taken at the Fermi level of the bulk crystal ($SrZrO_3$ or $SrTiO_3$) and all the curves were shifted so that the centers of

Table 8.4 The calculated surface energies E_s (J/m^2) and bandgaps BG (eV)

Quantity	Relaxed				Unrelaxed		Bulk
	I	II	(I+II)/2	III	(I+II)/2	III	
$SrZrO_3$							
E_s	1.01	1.26	1.14	1.13	1.41	1.42	
BG	4.84	4.61	–	4.56	–	3.94	5.02[a]
$SrTiO_3$							
E_s	1.20	1.29	1.25	1.24	1.46	1.46	
			(1.36)[b]		(1.55)[b]		
BG	3.68	2.76	–	2.48	–	2.63	3.65[a]
	(1.86)[b]	(1.13)[b]					(1.85)[b]

[a] Experimental BG in bulk crystals: 5.9 eV for $SrZrO_3$ [44], and 3.3 eV for $SrTiO_3$ [21]
[b] The results of DFT PW calculations [40] are given for comparison in parentheses

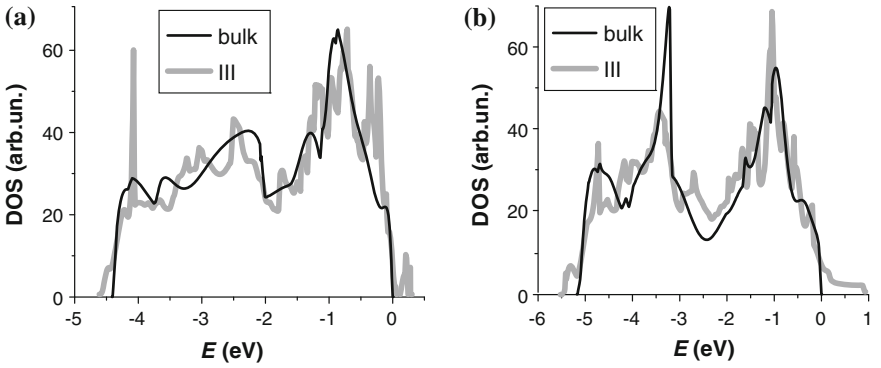

Fig. 8.5 Oxygen-projected VB DOS for bulk crystal and for surface model III **a** $SrZrO_3$; **b** $SrTiO_3$

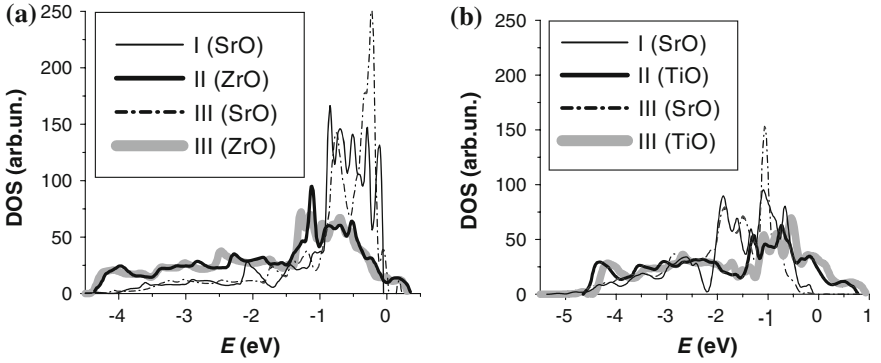

Fig. 8.6 Projected VB DOS for oxygen atom in the first surface layer for all the three models **a** $SrZrO_3$; **b** $SrTiO_3$. For model III the first oxygen projection corresponds to the SrO-side and the second to the MO_2-side

the O_{1s} bands coincide. Also, the DOS values were reduced to one oxygen atom to ensure the same scale for the bulk crystal and different slabs.

In Fig. 8.5 the total oxygen DOS for surface model III and the bulk crystal are compared. The bulk and slab VB have similar shapes and widths except for small areas at the top and bottom, that reflect the surface contributions.

These contributions are resolved in Fig. 8.6, where the DOS projected to the surface oxygens is plotted. Figure 8.6a,b demonstrate that the oxygen DOS distribution for the SrO and TiO_2 terminations are qualitatively different, whereas the distinctions between the model types (I and III or II and III) are less significant.

It is clearly seen in Fig. 8.6 that new O-subbands appear in the slabs at the top of the bulk VB. The corresponding peaks for oxygen on the SrO-terminated $SrZrO_3$ surface (in models I and III) are significantly higher than the peaks for oxygen on the ZrO_2-terminated surfaces. Also, the charge of the O atom in the first layer in the SrO-terminated slab of the $SrZrO_3$ crystal is noticeably lower than its bulk value

(1.50 vs. 1.33 in Table 8.3). This can be explained by the larger ionicity of the M–O bond in the zirconate compared with the titanate.

These features allow one to expect that a (0 0 1) SrO-terminated surface can accumulate the excess negative charge in the case of the $SrZrO_3$ crystal and it should be more basic in nature than the SrO-terminated surface of the $SrTiO_3$ crystal. In the case of $SrTiO_3$ slabs the corresponding oxygen contribution to SrO surface states is lower, whereas the new surface states originating from the TiO_2 termination form a low but extended shoulder, that is alike in models II and III. The shoulder indicated reduces the bulk BG noticeably (see Table 8.4). This means that the electronic shells on the TiO_2-terminated $SrTiO_3$ surface are more polarizable than the electronic shells on the other surface types considered. The similarities of the results obtained for the surface energy and DOS from surface models I and II on the one hand, and from model III on the other hand confirm the weak interaction between the opposite slab faces if its thickness is sufficiently large, resulting in the mutual independence of the two types of termination (SrO and MO_2) in the surface models of perovskites considered.

One can conclude that the disagreement between the theory and experiment for the vertical displacements of the $SrTiO_3$ surface atoms does not depend on the actual (LCAO hybrid HF-DFT or PW DFT) *ab-initio* method used. The dependence on the slab model and thickness may also be excluded from the possible reasons. Most probably, this discrepancy can be explained by the possible surface phase transition or surface reconstruction under the experimental conditions. *ab-initio* calculations using an extended tetragonal surface unit cell can resolve the contradiction indicated. The values obtained show that the relaxation of the top surface atoms is more prominent in the case of $SrZrO_3$ than in the case of $SrTiO_3$, and the corresponding surface energy for the zirconate is lower by about 0.1 J/m^2. This fact may be attributed to the larger ionicity of the $SrZrO_3$ bulk crystal in comparison with $SrTiO_3$ bulk crystal. The results under consideration give evidence that the SrO surface of the $SrZrO_3$ crystal is more basic than the SrO surface of the $SrTiO_3$ crystal. Based on this conclusion one can, for example, assume, that a stronger interaction of oxygen atoms on the SrO surface with the H atoms of the adsorbed water molecules (with possible water ionization) occurs in the case of zirconate than in the case of the titanate.

8.1.2 Symmetry of Rolled-Up $SrTiO_3$ *Nanotubes*

$SrTiO_3$ (STO) nanotubes were synthesized using a low-temperature hydrochemical method [8]. A titanium oxide (TiO_2) nanotube was utilized as a precursor material in order to generate the corresponding perovskite transition metal oxide nanotubes. Using the transmission electron spectroscopy (TEM) methodology, it was revealed in [8] that STO NTs have an outer diameter of 8–15 nm and an inner diameter from 4 to 7 nm. Powder X-ray diffraction patterns demonstrated the conversion of the precursor TiO_2 nanotube, composed of the crystalline phase of anatase, to crystalline STO

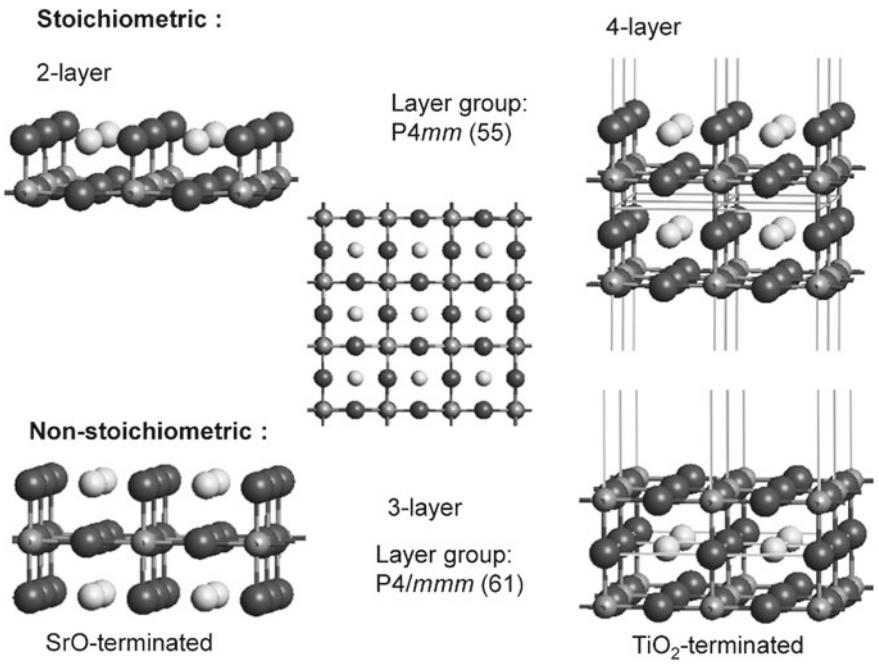

Fig. 8.7 STO slabs consisting of two or four alternating (0 0 1) SrO and TiO_2 atomic planes used for nanotubes construction (*lateral view*). The *top view* along the [0 0 1] direction is shown in the *middle*. Legend: O—*grey balls*, Ti—*small dark balls*, Sr—*light balls*

nanotubes with cubic perovskite structure. The experimental NT unit cell parameter $a = 3.89$ Å is close to $a = 3.90$ Å of the bulk cubic STO.

The full symmetry study of $SrTiO_3$ nanotubes with square morphology was given in [45] for the first time.

In the case of $SrTiO_3$, the folding procedure is applied to the most stable (0 0 1) slab cut from the bulk crystal with cubic space group $221(Pm\bar{3}m)$. The initial slab symmetry is described by the square plane lattice. The slab layer symmetry group depends on the number of layers included in the folding procedure. Figure 8.7 shows 2, 3 and 4-layer slabs cut from the bulk $SrTiO_3$ with one formula unit in the bulk unit cell.

For an even number of layers the slab layer group is $P4mm$ (55), for an odd number of layers this group becomes $P4/mmm$ (61). This follows from the scanning tables given in [46], connecting the space groups with the sectional layer groups. The latter are defined by 2D lattice Miller indices (hkl).

For the general rolling vector $\mathbf{R}(n_1, n_2)$ the symmetry of these tubes is given by the family 5 line group $\mathbf{L}^{(5)}$ (see Table C.1), which is q_p22 or q_p2 for the even and odd q, respectively. Here q is the number of square lattice cells in the supercell and defines the main rotation axis order of the nanotube. Due to the relation (2.33c)

SW nanotubes with square morphology are commensurate for any rolling vector $\mathbf{R}(n_1, n_2)$.

Let $n_1 = 5$, $n_2 = 7$. In this case $l_1/l_2 = -7/5$, $q = 74$. The greatest common divisor n_1 and n_2 is $n = 1$. The rototranslational vector $\mathbf{H}(h_1, h_2)$ is defined by $h_1 = 2$, $h_2 = 7$. As $r = h_1 l_2 - h_2 l_1 = 31$, NT $\mathbf{R}(5, 7)$ with square morphology has the rototranslational axis T_{74}^{31}.

Let now $n_1 = n$, $n_2 = 0$. In this case $q = n$, $l_1 = 0$, $l_2 = 1$, $h_1 = 0$, $h_2 = 1$, $r = 0$. Thus, for SW (n,0) STO NTs the line symmetry groups are symmorphic, belong to the family $\mathbf{L}^{(11)}$ and are n/mmm or $\bar{2n}2m$ for the even and odd n, respectively. For SW (n,n) STO NTs $q = 2n$, $l_1 = -1$, $l_2 = 1$, $h_1 = 0$, $h_2 = 1$, $r = 1$. Therefore, in this case the line symmetry groups $(2n)_n/mcm$ belong to the family $\mathbf{L}^{(13)}$. In both cases the line groups do not depend on the number of layers N in the STO slab as for layer groups 55 and 61 the folding procedure gives the line groups, that belong to the same family, see Table 2.10.

Table 8.5 presents the symmetry of SW STO nanotubes for the rolling vectors (n,0), family 11 and (n,n), family 13, respectively. This table gives also the NT diameter, defined by the length R of the rolling vector through the relation $D = R/\pi$. For STO nanotubes the square lattice parameter a=b is equal to the bulk STO cubic lattice parameter a so that $R = na$ for (n,0) and $R = na\sqrt{2}$ for (n,n). The experimental value $a = 3.905$ Å is used. The number of atoms (per monoperiodic unit cell) in two and three layer STO NTs is also given in Table 8.5. In the latter case the number of atoms is different in the tubes rolled up from SrO and TiO_2 terminated layers.

It is seen from Table 8.5 that for the tubes studied experimentally (their diameters are 4–8 nm) computer modeling is very time consuming-these tubes consist of several hundred atoms in the monoperiodic unit cell. Fortunately, the higher the NT diameter is, the larger the order of the rotohelical axis. This symmetry is fully exploited in the CRYSTAL09 and CRYSTAL14 codes for the first-principles LCAO calculations of nanotubes, see [47, 48].

The STO DW NTs $(n_1, n_1)@(n_2, n_2)$ and $(n_1, 0)@(n_2, 0)$ are commensurate; the minimal translation period of such DW NTs is the same as for the constituents.

Table 8.6 presents the symmetry of STO DW NTs. The symmetry group of DWNT (n,0)@M(n,0) belongs to the same family 11 as its SW constituents. The symmetry of DWNT (n,n)@M(n,n) depends on the parity of M. For DW NTs with an odd M, the line symmetry groups are the same as for their SW constituents and belong to family 13. For an even M, the rotations about the screw axis of the order $2n$ are changed by the rotations around the pure rotation axis of the order n so that DW NT line symmetry groups belong to family 11. As is seen from Table 8.6, the symmetry of $(n_1, n_1)@(n_2, n_2)$ and $(n_1, 0)@(n_2, 0)$ STO nanotubes depends on the parity of the numbers $n_1/GCD(n_1, n_2)$ and $n_2/GCD(n_1, n_2)$: if both of these numbers are odd, DWNT belongs to family 13; in other cases DWNT belongs to family 11.

In Table 8.6 we also present the distance d between the outer wall of the inner tube and the inner wall of the outer tube in two-layer (layer group 55) and 3-layer (layer group 61) nanotubes. This distance is calculated for $a = 3.905$ Å (translation vector for DW NTs $(n_1, 0)@(n_2, 0)$) and $a = 3.905\sqrt{2} = 5.522$ Å (translation

Table 8.5 Symmetry of $SrTiO_3$ single-wall nanotubes with square morphology

SWNT	D, Å	Line group	Point group	N_A—number of atoms in SWNT		
				Two layer, LG 55	Three layer, SrO term. LG 61	Three layer, TiO_2 term. LG 61
(a) chirality (n,0)						
(6,0)	7.46	$6/mmm$	$\mathbf{D}_{6h}$	30	42	48
(8,0)	9.94	$8mmm$	$\mathbf{D}_{8h}$	40	56	64
(12,0)	14.92	$12/mmm$	$\mathbf{D}_{12h}$	60	84	96
(16,0)	19.89	$16mmm$	$\mathbf{D}_{16h}$	80	112	128
(18,0)	22.37	$18/mmm$	$\mathbf{D}_{18h}$	90	126	144
(20,0)	24.86	$20mm$	$\mathbf{D}_{20h}$	100	140	160
(24,0)	29.83	$24/mmm$	$\mathbf{D}_{24h}$	120	168	192
(32,0)	39.78	$32/mmm$	$\mathbf{D}_{32h}$	160	224	256
(36,0)	44.75	$36/mmm$	$\mathbf{D}_{36h}$	180	252	288
(40,0)	49.72	$40/mmm$	$\mathbf{D}_{40h}$	200	280	320
(48,0)	59.66	$48/mmm$	$\mathbf{D}_{48h}$	240	336	384
(b) chirality (n,n)						
(6,6)	10.55	$12_6/mmm$	$\mathbf{D}_{12h}$	60	84	96
(8,8)	14.06	$16_8/mmm$	$\mathbf{D}_{16h}$	80	112	128
(12,12)	21.10	$24_{12}/mmm$	$\mathbf{D}_{24h}$	120	168	192
(16,16)	28.13	$32_{16}/mmm$	$\mathbf{D}_{32h}$	160	224	256
(18,18)	31.64	$36_{18}/mmm$	$\mathbf{D}_{36h}$	180	252	288
(20,20)	35.16	$40_{20}/mmm$	$\mathbf{D}_{40h}$	200	280	320
(24,24)	42.19	$48_{24}/mmm$	$\mathbf{D}_{48h}$	240	336	384
(36,36)	63.29	$72_{36}/mmm$	$\mathbf{D}_{72h}$	360	504	576

LG 55-, LG 61-layer symmetry groups of stoichiometric and non-stoichiometric slabs, respectively

vector for DW NTs $(n_1, n_1)@(n_2, n_2)$). This distance is different for 2-layer and 3-layer nanotubes with the same chiralities of both SW constituents (see Table 8.6). However, the distance d is the same for SrO and TiO_2 terminated 3-layer tubes with the same chiralities of both SW constituents. All these distances are given for the unrelaxed tubes rolled up from the 2- or 3-layer slabs. The relaxation of the tubes can change not only the intertube distances but also the symmetry of DWNTs.

8.1.3 Calculations of Rolled-Up $SrTiO_3$ Nanotubes

Let us now discuss the results of the LCAO PBE0 calculations of STO nanotubes [11]. The initial structures of the nanotubes were obtained by rolling up the stoichiometric $SrTiO_3$ slabs consisting of two or four alternating (0 0 1) SrO and TiO_2 atomic planes

Table 8.6 Symmetry of commensurate $SrTiO_3$ double wall nanotubes with square morphology; d-distance between the outer wall of the inner tube and the inner wall of the outer tube

(a) chiralities $(n,n)@M(n,n)$ and $(n,0)@M(n,0)$								
DWNT	M	Line group	Point group	d, Å		N_A—number of atoms in DWNT		
				LG 55	LG 61	LG 55	LG 61, SrO term.	LG 61, TiO_2 term.
(6,0)@(18,0)	3	$6/mmm$	$\mathbf{D}_{6h}$	5.50	3.55	120	168	192
(12,0)@(24,0)	2	$12/mmm$	$\mathbf{D}_{12h}$	5.50	3.55	180	252	288
(6,6)@(18,18)	3	$12_6/mmm$	$\mathbf{D}_{12h}$	8.59	6.64	240	336	384
(12,12)@(24,24)	2	$12/mmm$	$\mathbf{D}_{12h}$	8.59	6.64	360	504	576
(12,0)@(36,0)	3	$12/mmm$	$\mathbf{D}_{12h}$	12.96	11.01	240	336	384
(12,12)@(36,36)	3	$24_{12}/mmm$	$\mathbf{D}_{24h}$	19.14	17.19	480	672	768
(b) chiralities $(n_1,n_1)@M(n_2,n_2)$ and $(n_1,0)@M(n_2,0)$								
DWNT	GCD (n_1,n_2)	Line group	Point group	d, Å		N_A—number of atoms in DWNT		
				LG 55	LG 61	LG 55	LG 61, SrO term.	LG 61, TiO_2 term.
(12,0)@(26,0)	2	$2/mmm$	$\mathbf{D}_{2h}$	6.75	4.80	190	266	304
(12,0)@(27,0)	3	$3/mmm$	$\mathbf{D}_{3h}$	7.37	5.42	195	273	312
(12,0)@(28,0)	4	$4/mmm$	$\mathbf{D}_{4h}$	7.99	6.04	200	280	320
(12,12)@(26,26)	2	$2/mmm$	$\mathbf{D}_{2h}$	10.35	8.40	380	532	608
(12,12)@(27,27)	3	$3/mmm$	$\mathbf{D}_{3h}$	11.23	9.28	390	546	624
(12,12)@(28,28)	4	$8_4/mmm$	$\mathbf{D}_{8h}$	12.11	10.16	400	560	640

(Fig. 8.7). Two different NTs can be constructed for each chirality: (I) with a SrO outer shell (SrO terminated), and (II) with a TiO_2 outer shell (TiO_2 terminated). The inner shell has an alternate composition for the adopted even number of planes in the slab. All the calculations were made using the periodic PBE0 LCAO method via the CRYSTAL09 [47] computer code. The basis set for the Ti and O atoms was taken from [49]. Small-core pseudopotentials [50] and the corresponding basis set were used for the Sr atom. Diffuse exponents smaller than 0.1 a.u. were removed and the exponents of other polarization functions were reoptimized for the periodic calculations. The method chosen provides a good quality of the calculated STO bulk properties. Thus, the optimized lattice constant of the cubic STO (3.89 Å) is very close to the experimental value (3.90 Å).

The optimized lattice constant of the two-dimensional square lattice is slightly decreased compared to the bulk value and becomes 3.82 Å—for a two-layer slab and 3.85 Å—for a four-layer slab. The atomic positions on the boundary planes exhibit a noticeable relaxation, which in general resembles that on the surface of the thicker

STO slabs [40, 42]. The slab thickness (difference in the z-coordinate of the top and bottom oxygens) is 1.99 Å—for a two-layer (0 0 1) slab, and 5.90 Å—for a four-layer (0 0 1) slab.

After the slab-NT rolling the positions of all the atoms were optimized to obtain the most stable NT structure preserving only the rototranslational symmetry. Other symmetry constrains on NTs (second-order U axes normal to the tube axis and reflection planes) were removed during the atomic relaxation. The one-dimensional Brillouin zone was sampled with 16 (for chiralities (n,0)) or 12 (for chiralities (n,n)) **k**-points. The lattice parameters and atomic structure of the initial slabs were optimized before the folding to provide the estimation of the NT strain energy, see (3.136).

During the slab folding the inner and outer atomic shells undergo a considerable stress due to the stretching or shrinking of the interatomic distances relative to those in the initial relaxed slab. The less the tube diameter, the greater the strain. The most critical is the repulsion between the nearest oxygen atoms in the inner shells, and as a rule the distance between them cannot be less than 2.7–2.6 Å. The atomic and cell relaxation can reduce the indicated strain, but only to some extent. The inner and outer shells are strained in the opposite directions, so reducing the tension in the former can increase the tension in the latter. For example, the expansion of the NT diameter leads to a reduction of the bond shrinking in the inner tube shell, however this also leads to an increase in the bond stretching in the outer tube shell. As a result, for each NT chirality there exists a minimum diameter, below which NT is very unstable and undergoes spontaneous destruction. According to relation between the inner and outer strain and on the chemical bond pattern in the inner and outer shells, the initial diameter of the rolled NT (which is defined by the slab lattice parameters) can increase or decrease.

In Table 8.7 the calculated properties of the two-layer STO NTs are given (See Fig. 8.8).

The external diameter d of an NT is estimated as the double distance from the NT axis to the most remote atom. Almost in all the NTs considered the most remote atom is oxygen. The tube thickness w was estimated as the difference in the distances between the atoms that are the most distant from the tube axis and those that are the closest to it. During the atomic relaxation, the period L of type I NTs (SrO outer shell) is reduced, while the period of type II NTs (TiO_2 outer shell) is increased relative to the initial (slab) value. On the other hand, the thickness of the tube walls is slightly less for the former than for the latter.

As was expected, the strain energy falls down upon the increasing of the width of the NTs. Type II NTs have rather small values of the strain energy, especially for large ($\geq$30 Å) diameters. The calculated band gap is indirect for (n,0) chirality, and - direct for (n,n) chirality. The band gap of type I NTs is slightly greater than the band gap of the two-layer slab and it decreases slowly with n. The band gap for narrow NTs of type II is considerably greater than that for the slab, but it decreases fast with n increasing. The covalent component of the chemical bonds in the outer SrO shell is weak, so the expansion does not break the narrow two-layer tubes of type I. On the other hand, such an expansion can destroy the essentially covalent Ti-O bonds in the outer shell of type II NTs. This really occurs upon the optimization of type

Table 8.7 Properties of $SrTiO_3$ two-layer nanotubes

Type I (SrO outer shell)[a]						Type II (TiO_2 outer shell)					
Chirality	L(Å)	d(Å)	w(Å)	E_{str} (kJ/mol)	E_{gap} (eV)	Chirality	L(Å)	d(Å)	w(Å)	E_{str} (kJ/mol)	E_{gap} (eV)
(8 0)	3.97	13.3	1.9	80.2	4.3	(8 0)	3.49	13.7	2.2	10.4	6.4
(12 0)	3.94	18.2	1.9	54.1	4.3	(12 0)	3.57	18.4	2.2	13.1	5.9
(16 0)	3.90	23.1	1.9	37.5	4.4	(16 0)	3.65	22.7	2.1	13.2	5.4
(20 0)	3.88	27.9	1.9	28.1	4.2	(20 0)	3.73	26.7	2.1	11.3	4.9
(24 0)	3.87	32.8	1.9	21.9	4.2	(24 0)	3.76	31.0	2.1	8.1	4.5
(32 0)	3.85	42.5	2.0	14.8	4.1	(32 0)	3.79	40.3	2.0	4.4	4.1
(6 6)	5.46	14.1	1.8	25.8	4.7	(6 6)	5.61	12.6	2.0	119.0	5.8
(8 8)	5.45	17.6	1.9	25.0	4.5	(8 8)	5.47	15.7	2.0	71.3	5.1
(12 12)	5.45	24.5	1.9	19.8	4.3	(12 12)	5.40	22.1	2.0	27.3	4.3
(16 16)	5.44	31.3	1.9	15.3	4.2	(16 16)	5.37	28.7	2.0	10.2	3.6
(20 20)	5.43	38.1	1.9	12.3	4.1	(20 20)	5.38	35.4	2.0	3.9	3.7
(24 24)	5.43	45.0	1.9	10.0	4.1	(24 24)	5.38	42.2	2.0	1.0	3.7

[a] Period L, maximal diameter d, thickness w, strain energy E_{str} and band gap E_{gap} (in slab $E_{gap} = 3.9$ eV)

II tube with chirality (6,6), which is found to be totally destroyed. The nanotubes of type II with chirality (n,0), where n is less or equal to 20, also break down to weakly bonded one-dimensional chains of $SrTiO_3$ molecules. The distance between the interacting Ti and O atoms in the neighbouring chains is about 2.4–2.6 Å. In spite of the disintegration at small n, the strain energy of the two-layer tubes (n,0) with a TiO_2 outer shell is relatively low for all the n values considered (see Table 8.7).

More interesting results should be expected for four-layer NTs because they provide more realistic models of NTs observed experimentally. Computer facilities allowed the calculation of four-layer NTs with chiralities up to (48,0) and (24,24), which comprise 480 atoms. The results obtained for four-layer NTs are given in Table 8.8.

The relatively stable four-layer NTs arise at greater diameters than the two-layer NTs because of a large curvature difference between the inner and the outer shells provoking a considerable stretching and shrinking of the external and internal NT surfaces. Also, the surface structure of the four-layer tubes changes considerably during atomic and cell relaxation. However, the period of the four-layer NTs is not changed noticeably upon the relaxation because of the relatively large tube thickness, except for type II of (n,0) NTs, where it is reduced by about 0.1–0.2 A. This reduction may be connected with the surface reconstruction observed in this case (see below). The dependence of NT thickness on the chirality and surface type is rather complex and possibly additional computations are needed to analyze it in detail. During the relaxation at large n, the diameter of the type I NT (n,0) is slightly reduced and its inner surface exhibits corrugation (see Fig. 8.9a).

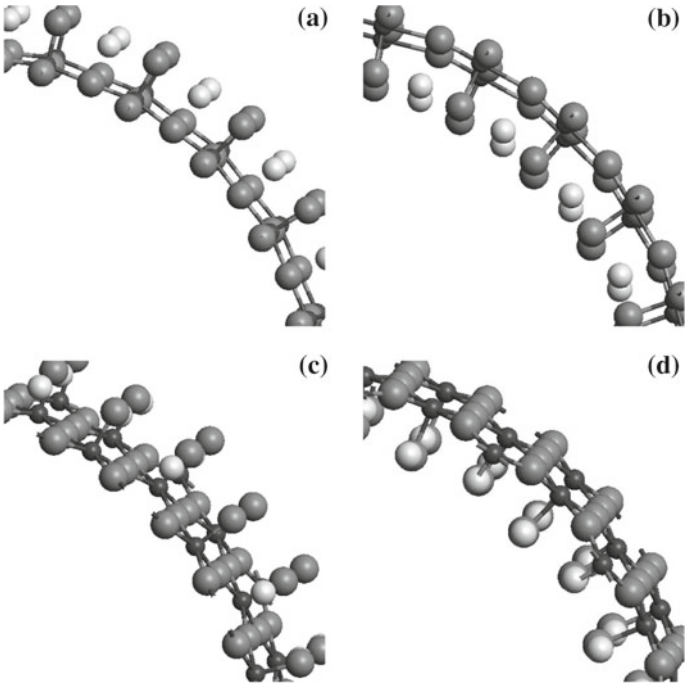

Fig. 8.8 Structure of $SrTiO_3$ NTs consisting of two atomic layers with different chirality (view along the tube axis). Chirality (20,0): **a** type I with SrO outer shell; **b** type II with TiO_2 outer shell. Chirality (16,16): **c** type I with SrO outer shell; **d** type II with TiO_2 outer shell. See Fig. 8.7 for the legend

At the same time, the diameter of the type II NT (n,0) increases and the external NT surface undergoes a very prominent reconstruction, which is accompanied by the breaking of some transverse (equatorial) Ti-O bonds and a formation of short (1.75 Å) Ti=O (titanyl) bonds. Accordingly, the reflection planes passing through the tube axis disappear and the symmetry is reduced to C_{nh}.

In the (n,n) case one observes the increasing of the NT diameter during the atomic relaxation of both surface types. For the type II NT (Fig. 8.9d) a considerable reconstruction of the external surface layer was again observed. Its optimized structure is composed of isolated TiO_2 fragments (which, however, are connected to the underneath oxygen atoms by the normal Ti-O bond with a length of 1.81 Å). The lengths of the two Ti-O bonds in a TiO_2 fragment are equal to 1.77 Å. The NT symmetry is reduced to C_{2nh}.

As can be seen from Table 8.8, the nanotubes (n,0) with the TiO_2 external surface are the most stable, and their stability only slightly depends on the tube diameter. It is interesting that the broken Ti-O bonds on the tube external surface do not influence this high stability. These tubes also have a remarkably high value of the band gap,

Table 8.8 Properties of $SrTiO_3$ four-layer nanotubes

Type I (SrO outer shell)[a]						Type II (TiO_2 outer shell)					
chirality	L(Å)	d(Å)	w(Å)	E_{str} (kJ/mol)	E_{gap} (eV)	chirality	L(Å)	d(Å)	w(Å)	E_{str} (kJ/mol)	E_{gap} (eV)
(18 0)	3.81	32.1	5.5	66.5	4.4	(18 0)	3.65	32.2	6.0	14.5	5.4
(24 0)	3.80	39.7	5.5	52.8	4.3	(24 0)	3.69	38.9	6.0	12.5	5.1
(32 0)	3.89	45.4	6.5	41.2	3.8	(32 0)	3.73	48.1	6.0	9.5	4.6
(48 0)	3.90	63.9	6.5	21.5	2.7	(48 0)	3.76	67.0	6.0	7.6	3.5
(12 12)	5.48	30.7	5.3	126.7	3.7	(12 12)	5.55	28.7	5.6	111.4	4.3
(16 16)	5.52	34.5	6.5	91.2	3.4	(16 16)	5.52	35.1	5.7	80.9	4.0
(24 24)	5.49	49.8	5.7	48.1	2.7	(24 24)	5.48	48.3	5.8	43.4	3.6

[a] Period L, maximal diameter d, thickness w, strain energy E_{str} and band gap E_{gap} (in slab $E_{gap} = 2.6$ eV)

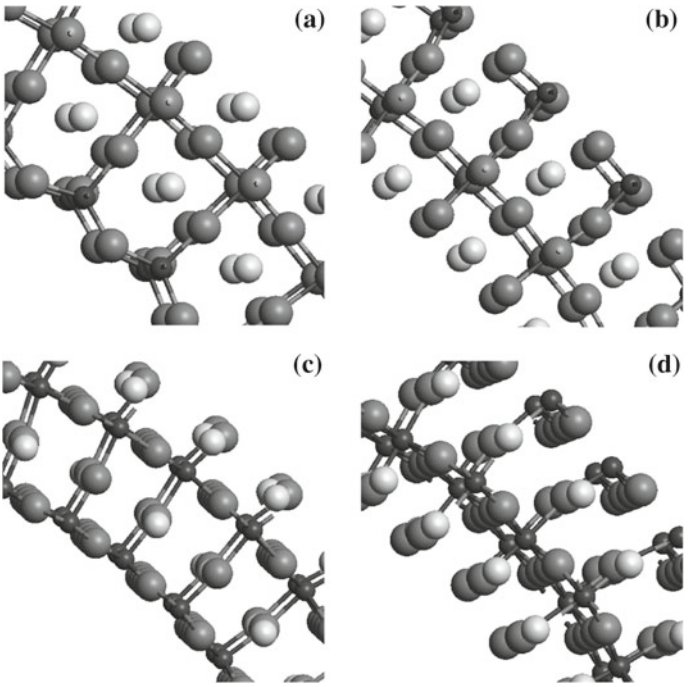

Fig. 8.9 Structure of $SrTiO_3$ NTs consisting of four atomic layers with different chirality (view along the tube axis). Chirality (48,0): **a** type I with SrO outer shell; **b** type II with TiO_2 outer shell. Chirality (24,24): **c** type I with SrO outer shell; **d** type II with TiO_2 outer shell. See Fig. 8.7 for the legend

which is greater than the corresponding bulk and slab values. As in the case of two-layer NTs, the band gap is indirect for (n,0) chirality, and direct for (n,n) chirality.

Basing on the results obtained, the following conclusions were made in [11]. In most of the cases considered the inner or outer TiO_2 shells of $SrTiO_3$ NTs undergo

a considerable reconstruction due to the shrinkage or stretching of the interatomic distances in the initial cubic perovskite structure. Two types of surface reconstruction were found: (1) the breaking of Ti-O bonds accompained by the creation of Ti=O titanyl groups in the outer surface; (2) the inner surface folding due to Ti-O-Ti bending. Based on the strain energy calculations, the largest stability was found for (n,0) NTs with a TiO_2 outer shell.

8.1.4 $SrTiO_3$ Nanowires

The increasing demand for the reduction of the size of microelectronic devices has been the motivation behind the synthesis of $SrTiO_3$ nanostructures [51]. STO nanowires have been prepared by different methods. A surface-capping soft chemical process allows the preparation of STO facetted nanowires with different diameters from a few to 200 nm [51]. A self-templated synthesis approach was used to grow ultrathin nanowires with an average diameter of 6 nm [52]. Atomic resolution scanning tunneling microscopy allowed researchers the study the structure of STO nanowires that spontaneously self-assemble on the STO (0 0 1) surface and to find the reduced STO nanowires whose widths are approximately 1 nm [53]. Also, the template-free hydrothermal process has been used to prepare mesoporous STO nanowires and the efficient photocatalytic activity of these nanowires has been demonstrated [54].

A theoretical study of the electronic and optical STO nanowire properties can provide insights into the mechanisms of photocatalytic pathways in STO nanowires and also explain the anomalious high mobility in the complicated oxide heterostructure $LaAlO_3/SrTiO_3$ nanowires [55].

To the best of our knowledge, there is only one theoretical study of STO nanowires reported so far [56]. The electronic and optical properties of the $SrTiO_3$ nanowires were examined in [56] and compared with those of the bulk material. The $SrTiO_3$ nanowires were cut along the [0 0 1] axis, in which the lateral size was equal to a period in the bulk material. The edges consisted of (1 0 0) and (0 1 0) surfaces, for the two possible terminations of the SrO and TiO_2 atomic layers, respectively.

Figure 8.10a, b show the simulation models of the SrO-terminated and TiO_2-terminated nanowires, respectively, the top views are the initial structures. Each nanowire has a cross section in which four perovskite unit cells are arranged in the x and y directions, which follows the cross section of a 4×4 unit cell. The unit cells at an edge, on a surface, and inside the nanowire are referred to as edge cell, surface cell, and inside cell, respectively, see Fig. 8.10. The terms edge bond, surface bond, and inside bond denote the chemical bonds in the corresponding cells.

The first-principles DFT(PBE) computations [56] employed a double-ζ plus polarization (DZP) atomic orbital set. Since a three-dimensional periodic boundary condition was applied in the calculations, a vacuum region (l_v) of 18 Å was introduced in both the x and y directions. This ensures that the nanowires grow along the z direction, and any undesirable interactions between the neighboring nanowires

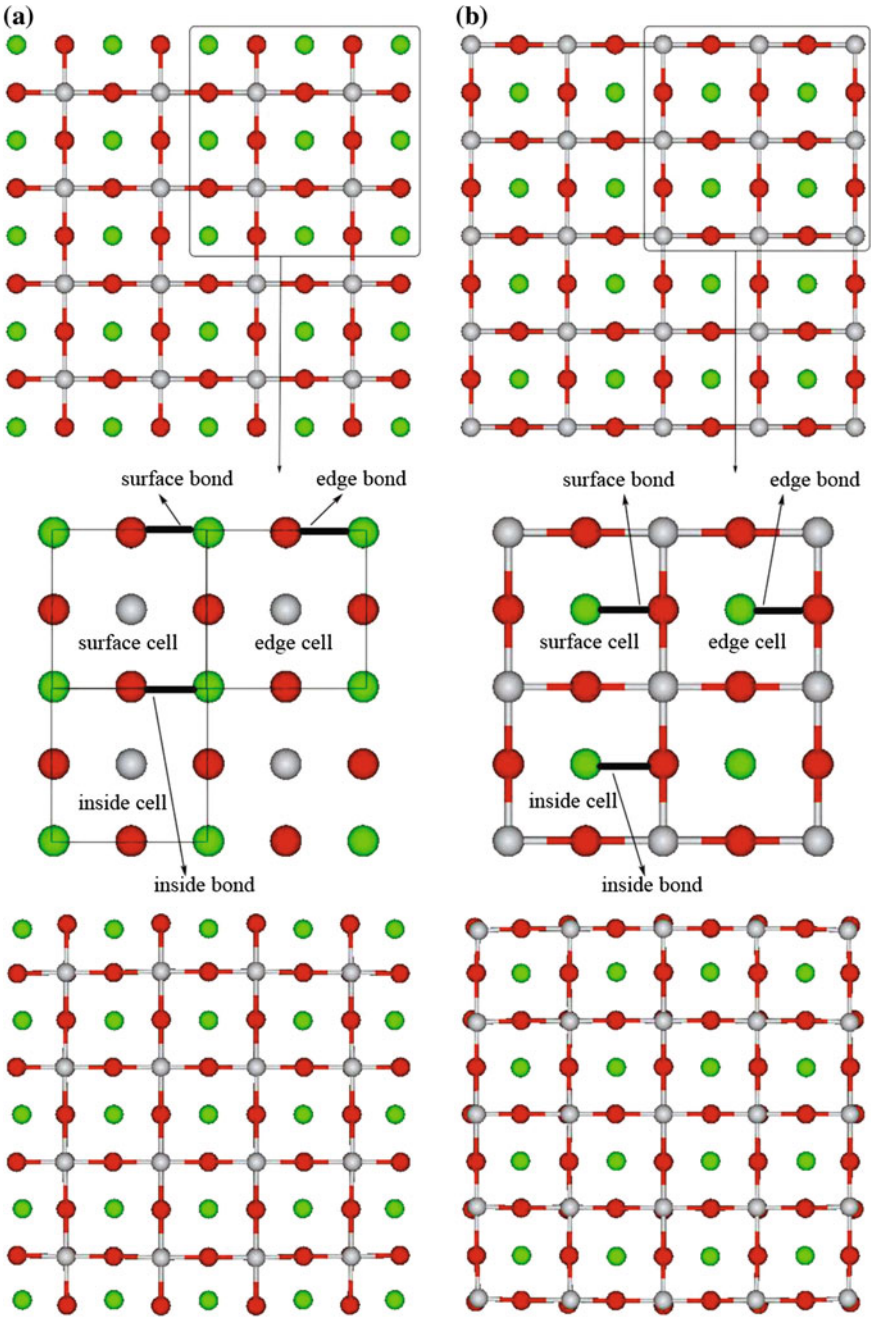

Fig. 8.10 The top view of the initial (*up*) and relaxed (*bottom*) $SrTiO_3$ **a** SrO-terminated and **b** TiO_2-terminated nanowires (In the color diagram: the *gray* indicates Ti, *red* indicates *oxygen*, and *green* indicates the Sr atom) (Reprinted figure with permission from Fu et al. [56], Copyright (2012) by the AIP Publishing LLC)

are duly avoided. The simulation cell dimensions in the x, y, and z directions are initially set to $4a + l_v$, $4a + l_v$, and a, respectively, where the theoretical lattice constant of the tetragonal bulk a is 3.905 Å. To determine the equilibrium configurations of all the nanostructures considered, all the atomic coordinates were relaxed.

The Brillouin zone integration was approximated using the **K**-points sampling scheme of the Monkhorst-Pack $5 \times 5 \times 5$ and $1 \times 1 \times 12$ **K**-point grids for bulk and nanowire calculations, respectively. The absorption spectra were obtained from the real and imaginary parts of the dielectric constant from DFT calculations. All the optimized results for $SrTiO_3$ nanowires are shown in Fig. 8.10a, b; the relaxed structures are shown in the bottom row. At the end of the optimization process, the lattice constants along the [001] axis for both nanowires decrease as compared to the bulk. The lattice constant of the SrO-terminated and TiO_2-terminated nanowires decrease from 3.905 to 3.81 and 3.85 Å, respectively. For the SrO-terminated nanowire, the strontium atoms on the surface move inwards as compared to the oxygen atoms (Fig. 8.10a).

Figure 8.11a shows the band structure of the bulk $SrTiO_3$. The **k**-vector along the symmetry lines of the first Brilliouin-zone is examined. In the band diagram, the valence and conduction band gaps are 2.37 eV along the Brillouin-zone directions G-X-M and G-R-X i.e. are underestimated compared with the experimental results (3.25 eV) because of limitations of using DFT, see the discussion above. However, the authors of [56] hope that the theoretical model used is reasonable because only the relative positions of the occupied states and empty states need to be taken into account in the comparative study of the bulk and NW band structures. The band gap modifications occurring in the nanowires are shown in Fig. 8.11b, c. The calculated band gaps of the TiO_2-terminated and SrO-terminated nanowires are 1.73 and 1.20 eV, which narrower than the band gap of the bulk perovskite $SrTiO_3$ by 0.64 and 1.17 eV, respectively. For the TiO_2-terminated nanowire, the band gap narrowing is due to the upward movement of the valence band maxima (VBM). In contrast, the band gap narrowing in the SrO-terminated nanowire is due to the downward movement of the conduction band minima (CBM).

The position of the CBM is an important parameter when one is studying the efficiency of the photocatalytic water splitting reaction. For hydrogen production, the CBM should be more negative. Compared with the bulk perovskite $SrTiO_3$, the CBM of the TiO_2-terminated nanowire do not alter. But the CBM of the SrO-terminated nanowire moves downwards by 1.2 eV, as shown in Figs. 8.11 and 8.12. According to the shift in the energy structures of the nanowires from the bulk, the band gap narrowing induces a red shift of the absorption edge. However, it seems that the overall photocatalytic water-splitting reaction efficiency of the SrO-terminated nanowire is not as high as the TiO_2-terminated nanowire because the position of the SrO-terminated nanowire CBM does not match the water splitting energy levels, given by dotted lines in Fig. 8.12.

To find the cause of the energy band shift of the nanowires partial density of states (PDOS) was analyzed in [56] for the bulk, the edge cell, surface cell, and inside cell.

Distinct peaks were observed in the PDOS for edge cell Sr atoms in the energy range from −5.5 to −4.5 eV, compared with strontium atoms in the inside cell.

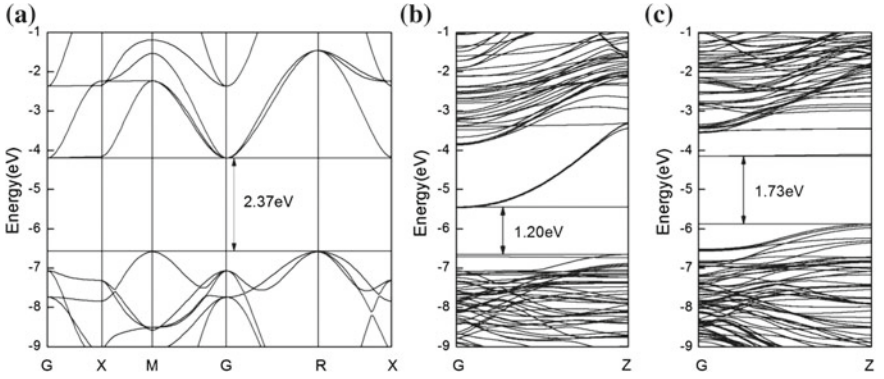

Fig. 8.11 Electronic band structure of the $SrTiO_3$ perovskite **a** bulk, **b** SrO-terminated, and **c** TiO_2-terminated nanowires along the **k**-vector [56]

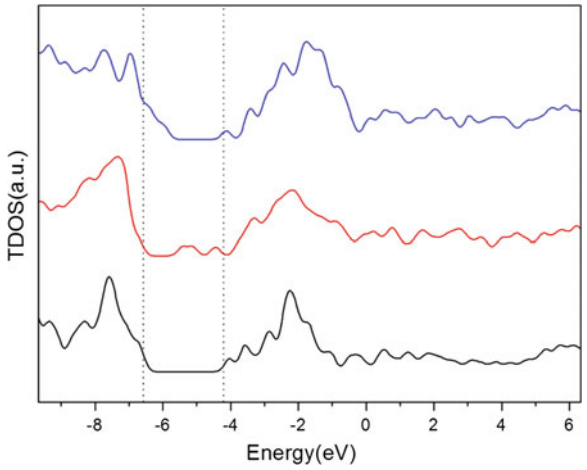

Fig. 8.12 Comparison of total density of states of $SrTiO_3$ perovskite: *black*-bulk, *red*-SrO-terminated and *blue*-TiO_2-terminated nanowires [56]

Therefore the CBM shift for the SrO-terminated nanowire is due to the Sr atoms in the edge cell. However, it is known, Sr atoms do not affect the electronic structure around the Fermi level. The peaks in the PDOS for edge and surface cell oxygen atoms in the energy range from −6.5 to −5.5 eV indicate that the VBM shift in TiO_2-terminated nanowires is due to the oxygen atoms in the edge and surface cells.

The analysis of orbital occupation, PDOS and crystal orbital overlap population (COOP) shows that a reduction of the CBM occurs through the formation of Sr-O edge bonds, because of Sr(5s) and O(2p) orbital interactions. The Sr(5s) orbital in the edge cell shows a new band of states in the CBM, which alters the bonding character of this orbital.

For TiO_2-terminated nanowires, the COOP curve for the SrO and TiO bonds in the three cells was calculated in [56]. Only the SrO bonds affect the CBM electronic structure. The peaks in the COOP for the SrO edge and surface bonds illustrate that a VBM increase occurs through Sr(5s) and O(2p) orbital interaction. The O(2p) orbital in the edge and surface cells shows a new band of states in the VBM, resulting in upward VBM movement in TiO_2-terminated nanowires compared to the perovskite $SrTiO_3$ bulk.

The SrO bonds affect the electronic structure of the two nanowires in different ways. This result may be attributed to the different positions of Sr atoms in each nanowire, as shown in Fig. 8.10. Therefore, to improve the photocatalytic activity, special attention should be paid to the orientation and surface of perovskite $SrTiO_3$ nanowires during the fabrication process.

The main conclusions made in [56] are as follows. In TiO_2-terminated nanowires, mid-band states induced by the combination of oxygen and strontium atoms on the perovskite $SrTiO_3$ nanowire surface shift the valence band toward the conduction band, which reduces the band gap. More importantly, these states do not interfere with the CBM, which plays an essential role in determining the driving force of H_2 evolution. In contrast, the electronic states induced by the combination of oxygen atoms and strontium atoms on the surface of SrO-terminated nanowires shift the conduction band toward the valence band. The optical calculated results indicate that the absorption edges shift towards the red-light region. As a result, the TiO_2-terminated nanowire proves to be a promising candidate for use in photocatalytic solar-assisted water splitting reactions, while the SrO-terminated nanowire is not suitable.

To elucidate the effects of nanowire size on photocatalysis, authors of [56] investigated the smaller nanowires with cross sections of 1×1, 2×2, and 3×3 unit cells in the same manner as they did it for the nonstoichiometric nanowires with cross section of 4×4. It was found that the unit cell dimensions have no effect on the photocatalytic characteristics. It is difficult to understand such a result, and the additional calculations, including the stoichiometric nanowires, are necessary.

8.2 $SrZrO_3$

8.2.1 Bulk and Nanolayers

Strontium zirconate $SrZrO_3$ (SZO) is of interest because of its possible high-temperature applications in fuel cells, hydrogen gas sensors and steam electrolysis [57].

Powder neutron diffraction data suggest the following sequence of phase transitions in $SrZrO_3$: from the orthorhombic Pbnm to the orthorhombic Cmcm at 970 K, the tetragonal I4/mcm at 1,100 K and lastly, to cubic $Pm\bar{3}m$ at 1,400 K [58]. The tetragonal phase has two formula units and orthorhombic phases have four formula units in the primitive cell.

The majority of SZO electronic structure calculations have been made for the cubic high-temperature phase (with one formula unit in the primitive unit cell), [59–63]. Figure 8.2d–f shows the band structure of the cubic SZO phase calculated using the LCAO basis set and the HF, DFT(PBE) and DFT(PBE0) methods. As in the case of the cubic STO phase (Fig. 8.2a–c) the band gaps are underestimated within the standard DFT functionals and overestimated in the HF method. Calculations [64] with the hybrid DFT (B3LYP) functional give the band gap 5.0 eV at the Γ point in good agreement with the experimental value 5.6 eV. Figures 8.4b and 8.13 show that: 1. the O_{2p} states form the upper valence band; 2. the Zr_d antibonding states form the low-lying states of the conduction band; 3. the Sr_p states are located close to the valence-band bottom.

As far as we know, the first ab initio DFT calculations for all the four phases of $SrZrO_3$ using both the PW and LCAO basis sets were made in [64, 65]. Later DFT PW calculations of orthorhombic [66] and six different phases [67] were performed. The results of the cubic SZO lattice dynamics calculations [63] show a soft phonon branch spreading from R to the M points of the cubic BZ. A symmetry analysis indicates that the experimentally observed low-symmetry phases of SZO can be seen as a result of the soft mode condensation at the R and M points.

The electronic structure LCAO DFT(PBE) calculations of different SZO phases were made in [64]. The DFT(PBE) band structures and densities of states for four modifications of the $SrZrO_3$ crystals are presented in Figs. 8.13a, b, 8.14a, b, 8.15a, b and 8.16a, b respectively. A comparison of the results obtained shows that, in general, the electronic structures of the cubic and tetragonal phases are similar to each other. The same is also true for two orthorhombic structures. A substantial change in the electronic structure was observed upon changing over from the tetragonal modification to the orthorhombic modification. This conclusion was also confirmed by the Mulliken atomic charges distribution, analyzed in [64]. The analysis of the total and partial densities of states for the cubic and tetragonal crystals (Figs. 8.13 and 8.14) demonstrates that the total density of states in the upper valence band is predominantly formed by the O(2p) states. It can also be seen that the Zr(4d) states make the dominant contribution to the bottom of the conduction band. Similar features of the electronic structure are observed for the orthorhombic phases.

The experimental lattice parameters of the crystallographic unit cells in the four $SrZrO_3$ phases, and those calculated in [64] are presented in Table 8.9. For the tetragonal (I4/mcm) and orthorhombic (Cmcm) modifications with the centered lattices, the crystallographic unit cell is twice as large as the primitive unit cell, and the translation vectors in all the crystals are orthogonal to each other. It can be seen from Table 8.9 that the calculated lattice constants for all the SZO modifications exceed the experimental lattice constants by 3–5 %. This overestimation is characteristic of DFT (GGA) calculations but is not very significant when different crystalline modifications are compared. A comparison of the calculated and experimental atomic coordinates given in [64] shows that the difference between the experimental and calculated values does not exceed 3–5 %.

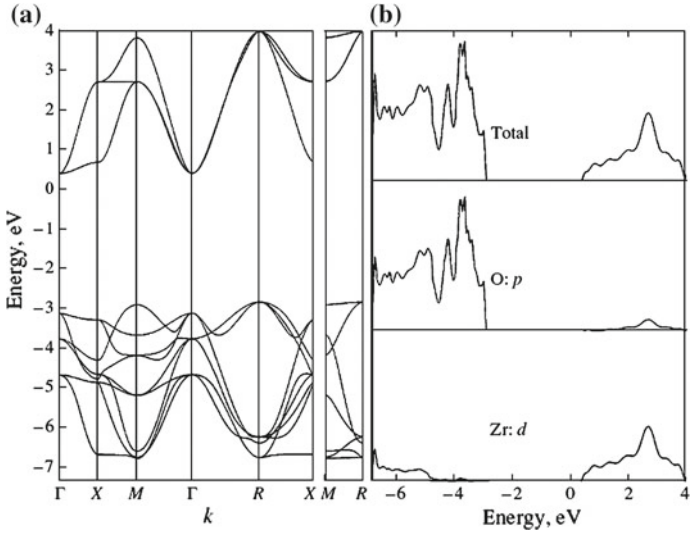

Fig. 8.13 **a** Band structure and **b** densities of states for the cubic modification (space group Pm3m) of the $SrZrO_3$ crystal [64]

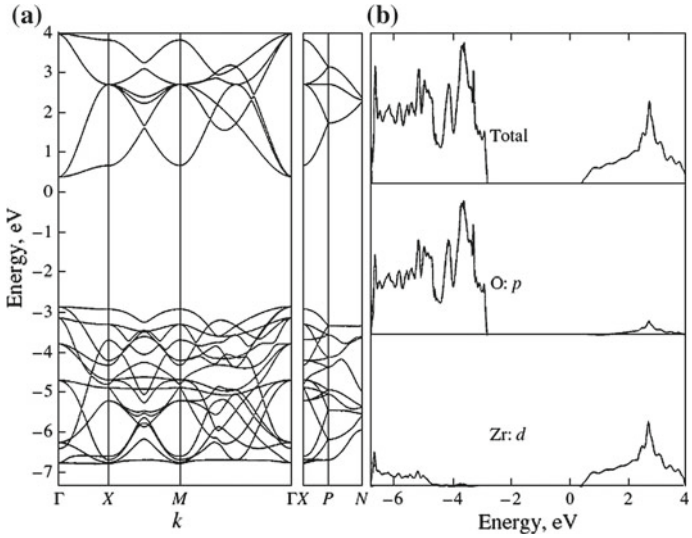

Fig. 8.14 **a** Band structure and **b** densities of states for the tetragonal modification (space group I4/mcm) of the $SrZrO_3$ crystal [64]

The first theoretical study of the cubic SZO (0 0 1) surface was made in [68] by the LCAO DFT (B3LYP) and in [69] by the FLAPW DFT(LDA) method. First-principles calculations of the electronic and structural properties of SrO and ZrO_2 terminated

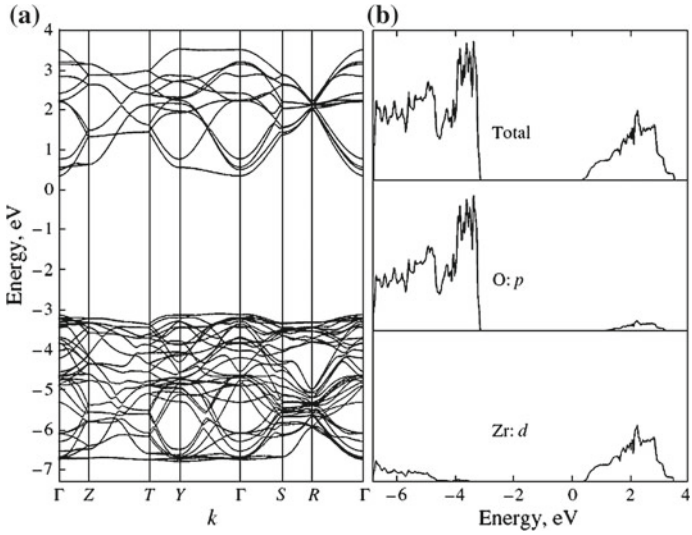

Fig. 8.15 **a** Band structure and **b** densities of states for the orthorhombic modification (space group Cmcm) of the $SrZrO_3$ crystal [64]

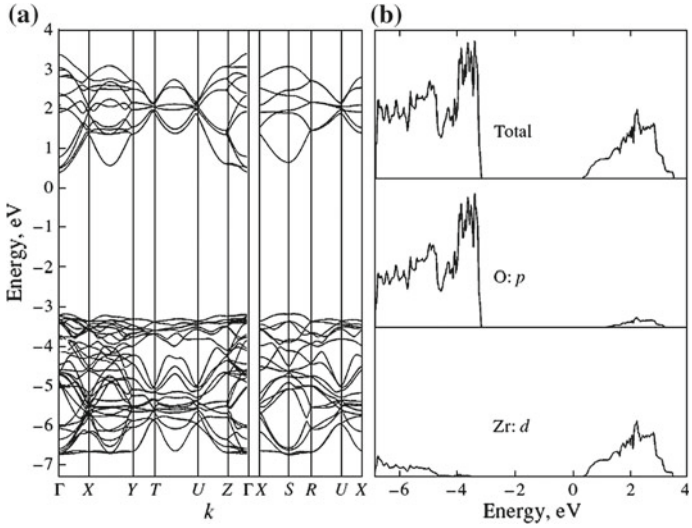

Fig. 8.16 **a** Band structure and **b** densities of states for the orthorhombic modification (space group Pbnm) of the $SrZrO_3$ crystal [64]

slabs were made in these studies. The convergence of the results with respect the slab thickness was studied in [68]. Table 8.10 shows the results for the calculations of the cleavage, relaxation and surface energies for 5, 7, 9, 11,13 and 15 planes. The results for the cleavage energy yields 1.97 eV/cell for n = 9 and 11, and 1.96 eV/cell for

Table 8.9 Optimized and experimental (in parenthesis) lattice parameters of the crystallographic unit cell in the $SrZrO_3$ crystal [64]

Phase	a (Å)	b (Å)	c (Å)
Cubic Pm3m	4.196(4.154)	4.196(4.154)	4.196(4.154)
Tetragonal, I4/mcm	5.935(5.870)	5.935(5.870)	8.393(8.309)
Orthorhombic, Cmcm	8.266(8.270)	8.368(8.273)	8.318(8.259)
Orthorhombic, Pbnm	5.847(5.786)	5.911(5.815)	8.295(8.196)

Table 8.10 Calculated cleavage E_{cl}, relaxation E_{rel}, and surface E_{surf} energies (in eV/cell) for the $SrZrO_3$ (0 0 1) surface, the bulk lattice parameter a = 4.144 Å was taken in the slab atoms relaxation [68]

	5	7	9	11	13	15
E_{cl}	1.99	1.90	1.97	1.97	1.96	1.96
$E_{rel}(ZrO_2)$	−0.19	−0.22	−0.22	−0.22	−0.22	−0.22
$E_{rel}(SrO)$	−0.75	−0.79	−0.80	−0.80	−0.79	−0.83
$E_{surf}(ZrO_2)$	1.80	1.68	1.75	1.75	1.74	1.74
$E_{surf}(SrO)$	1.24	1.11	1.17	1.17	1.17	1.17

n = 13 and 15. The values found for the surface energy, at SrO terminated surfaces, are 1.17 eV/cell for n = 9, 11, 13 and 15 planes. On the other hand, for the ZrO_2 terminated surface the calculated values are 1.75 and 1.74 eV/cell for n = 9 and 11, and 13 and 15 layers, respectively. The difference in surface energy is around 0.57 eV/cell, thus the ZrO_2 terminated is more stable than the SrO terminated surface. Consequently, 9 or 11 planes may be sufficient to describe the surface geometry and appropriate system for relaxation model studies. In order to confirm the convergence of the charge distribution with respect to the slab thickness, the Mulliken charge distribution for the ZrO_2 and SrO terminated surface models was calculated in [68]. The analysis yields convergence for n = 9–15. Therefore, an 11-plane slab model was used to describe the surface geometry and relaxation. The corresponding cleavage, relaxation and surface energies are given in Table 8.10.

Nine plane slabs were used in the FLAPW (LDA) calculations of the SZO (0 0 1) surface [69]; the results for the cleavage and relaxation energies are given in Table 8.11. The surface energy $E_{surf} = 1.22\,J/m^2$ was obtained in [69] using the equation $E_{surf} = (E_{slab}(I) + E_{slab}(II) - 9\,E_{bulk})/(4S)$, where $E_{slab}(I)$, $E_{slab}(II)$ and E_{bulk} are the total energies of the relaxed SrO-terminated slab, the relaxed ZrO_2-terminated slab, and the bulk crystal per unit cell, respectively. The factor of four comes from the fact that four surfaces are created during the cleavage procedure. Number 9 appears as the two nine plane SrO- and ZrO_2-terminated surfaces taken together represent nine bulk unit cells.

Table 8.11 shows the comparison of the results obtained for the (0 0 1) BZO surface in calculations [68–70]. The differences in the calculated cleavage and relaxation energies can be explained by the difference in 2D square lattice parameter values.

Table 8.11 Calculated cleavage, relaxation, and surface energies for $SrZrO_3$ (0 0 1), (0 1 1) and (1 1 1) [70–72]

Surface	Termination	E_{cl}	E_{rel}	E_{surf}(eV/cell)	$E_{surf}(J/m^2)$
(0 0 1)					
[70], 9planes, a = 4.195Å	ZrO_2	1.56	−0.32	1.24	1.13
	SrO	1.56	−0.43	1.13	0.91
[68],11planes, a = 4.144Å	ZrO_2	1.97	−0.22	1.75	0.82
	SrO	1.97	−0.80	1.17	0.55
[69], 9planes, a = 4.180Å	ZrO_2	1.56	−0.17	–	–
	SrO	1.56	−0.31	–	–
(0 1 1)					
	ZrO	4.94	−1.33	3.61	3.29
	Sr	4.94	−2.73	2.21	2.01
	O	3.77	−1.54	2.23	2.03
(1 1 1)					
	Zr	9.55	−1.57	7.98	7.27
	SrO_3	9.55	−0.10	9.45	8.61

In nine planes slabs three near-surface planes were relaxed; the bulk lattice parameter $a = 4.195$ Å was taken in the slab atoms relaxation

The LCAO DFT(B3LYP) studies [70, 71] demonstrate that all the calculated (0 1 1) and (1 1 1) surface energies are considerably larger than the (0 0 1) surface energies, see Table 8.11.

In the preceding section we compared the results of the $SrTiO_3$ (0 0 1) and $SrZrO_3$ (0 0 1) slab calculations. The Mulliken charges and vertical atomic displacements for both crystals (Table 8.3), the calculated surface energies and slab band gaps are given Table 8.4. It is seen that the surface energies for STO and SZO slabs of the same thickness are close. However, the band gaps both in the bulk crystal and slabs are less for STO. This is explained by a larger ionicity of the Zr-O bond compared with that of the Ti-O bond. The bulk charges are the following: $SrZrO_3$: q(Sr) = 1.88, q(Ti) = 2.12, q(O) = −1.33; $SrZrO_3$: q(Sr) = 1.87, q(Zr) = 2.53, q(O) = −1.47. The oxygen-projected valence band DOS for the bulk crystal and the stoichiometric slab model (see Fig. 8.5) are similar in both crystals. As we mentioned above, the (0 0 1) SrO-terminated surface can accumulate the excess negative charge in the case of $SrZrO_3$ crystal and it should be more basic in nature than the SrO-terminated surface of the $SrTiO_3$ crystal.

Table 8.12 lists the lattice constants a for the cubic ($Pm\bar{3}m$) and a,b,c for the orthorhombic (Pbnm) phases obtained in [73], where DFT(PBE0) calculations were made. It is seen that the use of the hybrid exchange-correlation functional decreases the difference between the experimental and calculated lattice parameters-this difference becomes less than 1 %. However, as is seen from Table 8.12, the DFT(LDA) method underestimates the lattice parameters by about 2 %.

Table 8.12 Calculated lattice parameters, formation and surface energies of nanosheets cut from $SrZrO_3$ [73]

Value	System	Parent phase and surface index		
		Cubic, $Pm\bar{3}m$	Orthorombic, $Pbnm$	
		001	001	110
	Bulk[a]	4.123	5.750, 5.819, 8.173	
	Bulk[b]	4.126	5.764, 5.810, 8.161	
Lattice	Bulk[c]	4.164	5.652, 5.664, 7.995	
constants,	Bulk[d]	4.154	5.786, 5.815, 8.196	
a, b, c, Å	2 layer slab	4.115	$a = 5.867$, $b = 5.782$ $A/\sqrt{2} = 5.802$, $B/\sqrt{2} = 5.854$	
	4 layer slab	4.104	$a = 5.766$, $b = 5.778$ $A/\sqrt{2} = 5.704$, $B/\sqrt{2} = 5.813$	
Formation	2 layer slab	282.2	276.7	275.6
energy, kJ/mol	4 layer slab	178.9	157.2	156.8
Surface energy,	2 layer slab	1.221	1.355	1.347
kJ/m^2	4 layer slab	1.437	1.568	1.571

[a] [73], LCAO DFT (PBE0)
[b] [67], PW DFT (GGA-WC [74])
[c] [63, 66], PW DFT (LDA)
[d] The experimental lattice constants [58]

A comparison of the surface energies in the cubic and orthorhombic SZO phases (with lattice parameters a and a, b, c, respectively) was made in [73]. Stoichiometric nanolayers composed of 2 and 4 alternating (0 0 1) SrO and ZrO_2 atomic planes from the cubic phase and (0 0 1) or (1 1 0) atomic layers from the orthorhombic phase were constructed. The 2D lattice of the (0 0 1) cubic SZO surface is square. The rectangular 2D lattices of the orthorhombic phase (0 0 1) and (1 1 0) surfaces have lattice constants $A = a, B = b$ and $A = c, B = \sqrt{a^2 + b^2}$, respectively. The lattice parameters and atomic structure of the initial slabs were optimized. It was proved that the obtained lattice constants of two-dimensional square or rectangular lattices are only slightly decreased compared to the bulk values (see Table 8.12). It was found that for the orthorhombic phase both the formation and surface energies are very close for the surfaces (0 0 1) and (1 1 0). We note that these energies are higher than for the cubic phase (0 0 1) surface, while the energy (for the formula unit) of the bulk orthorhombic phase is lower than that of the cubic phase.

Considered SZO nanolayers have been used in [73] as SZO nanotube precursors. Rolled up SZO nanotubes are considered in the next section.

8.2.2 Rolled-Up $SrZrO_3$ Nanotubes

To the best of our knowledge, publication [73] is the first one reporting the results of the first-principles calculations of rolled up nanotubes folded from cubic and

Table 8.13 Binding energy(ΔE) of two SWNTs in DWNT and corresponding the NTs dimensions

Chirality	ΔE, kJ/mol (per formula unit)	DWNT				After the optimization[a]	
		Before optimization		After optimization		SWNT L_1	SWNT L_2
		R_{min}, Å	R_{max}, Å	R_{min}, Å	R_{max}, Å	R_{min}, Å	R_{max}, Å
(12,12)	−58.7	8.10	14.21	5.65	13.42	5.35	13.42
(14,14)	−49.3	9.95	16.06	6.89	14.88	6.37	15.18
(16,16)	−33.2	11.80	17.90	8.20	16.33	7.39	16.96

[a] Radii R_{min} and R_{max} of NTs are estimated as the distances from the NT axis to the nearest and the most remote atom, correspondingly

orthorhombic $SrZrO_3$. The same computational parameters of the LCAO DFT(PBE0) method were used in [73] for bulk SZO, SZO nanolayers and SZO-based nanotubes calculations.

The stability of single-walled nanotubes of chiralities (n,0) and (n,n) for the cubic, and (n_1,0) and (0,n_2) for the orthorhombic SZO was investigated in relation to their diameter, the number of layers in the slab, and the outer surface termination (SrO or ZrO_2). The first (I) type of NTs was obtained by rolling up the (0 0 1) slabs of the cubic phase, the second (II) and the third (III) types were folded from the (0 0 1) and (1 1 0) slabs of the orthorhombic phase, accordingly. To estimate the NT stability the strain energy E_{str} per formula unit $E_{str}(NT) = E_l(NT) - lE_m(slab)/m$ was used, where E_l(NT)-total energy of the NT unit cell consisting of l bulk formula units, and E_m(slab)-total energy of the slab unit cell containing m bulk formula units. The atomic positions on the boundary NT surfaces exhibit a noticeable relaxation. The type I NTs folded from 2-layer slabs generally keep the initial structure while maintaining the original symmetry during the optimization procedure. However, if the symmetry decreases due to the removal of the screw rotations, the nanotube structure exhibits a considerable reconstruction, with the splitting of the ZrO_2 shells into two atomic (O and Zr) subshells, thus resembling the surface of SZO orthorhombic phases. The strain energy of those NTs is significantly less than that of the tubes with a full set of symmetry operations. The NTs generated from the layers of the cubic $SrTiO_3$ in [11] do not exhibit such behavior.

Also observed was a spontaneous splitting of the SrO-terminated (n,n) 4-layer nanotubes into two separated NTs. The resulting double-walled nanotubes are energetically more favorable than the two isolated single-walled nanotubes (see Fig. 8.17), consisting of ZrO_2 (L_1) and SrO-ZrO_2-SrO (L_2) shells, correspondingly. The atomic positions in either of these two single-walled nanotubes were optimized (see Table 8.13).

The NTs folded from the orthorhombic SZO phase (of types II and III) generally preserve the atomic distortions inherent in the orthorhombic structure. However, the concrete NT surface structure depends on the chirality, the number of layers and the termination type. The reconstruction of ZrO_2-terminated outmost surfaces due to the break of the Zr-O bonds was found in all the types of NTs simulated from 4-layer slabs.

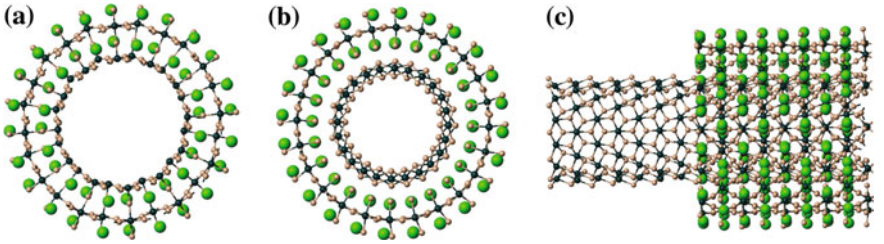

Fig. 8.17 Spontaneous splitting of type I 4-layer SrO-terminated (n,n) nanotubes into two separated NTs. Cross-section view before optimization (**a**), cross-section view after optimization (**b**), and side view after optimization (**c**). Legend: Sr-large *light balls*, Zr—small *dark balls*, O—small *light balls*, [73]

Figure 8.18 shows the dependence of the NT strain energy on its average diameter calculated as the sum of R_{min} and R_{max}. Figure 8.18 demonstrates that the strain energy of SrO-terminated NTs decreases with increasing the size of NTs, but that the strain energy of ZrO_2-terminated NTs increases. In the latter case the negative strain energy is a consequence of the large positive formation energy of the initial slabs. On the other hand, the SrO-terminated 2-layer NTs have positive or zero strain energies because of the unfavorable interaction between the O atoms in the internal ZrO_2 surface due to its shrinking. In both cases the strain energy tends to zero with increasing NT size, since the total energy of the NT converges to the total energy of the slab.

The final relaxed structure of ZrO_2-terminated NTs folded from the two layers of both the cubic and orthorhombic phases is very similar and corresponds to the latter phase, which is more stable. Raising the diameter of the (n,n) SrO-terminated SZO NTs above 50 Å promotes a transition from the cubic-like to the orthorhombic-like NT shell structure, which results a drastic fall of the strain energies (see Fig. 8.18a). Figure 8.18b effectively demonstrates that the strain energy of (n_1,0) and (0,n_2) 2-layer NTs coincides for both terminations. It means that there is no difference between the relaxed (n_1,0) and (0,n_2) type II NTs. The same can be seen in Fig. 8.18c for (n_1,0) and (0,n_2) ZrO_2-terminated 2-layer type III NTs.

In Fig. 8.18d one can see a region where the E_{str} increases with increasing the diameter of SrO-terminated type I NTs. This is just the case of spontaneous splitting of 4-layer nanotubes into two separated NTs, which was discussed above.

8.3 $BaTiO_3$

$BaTiO_3$ (BTO) has been widely investigated since the discovery of its ferroelectric properties. Because of the number of different ferroelectric phases and the ease of switching between them, BTO is also of great technological interest. Intense experimental efforts have been aimed at the synthesis of a ferroelectric based on BTO nanostructures (nanoparticles, nanowires, and nanotubes), [32, 75–86]. One

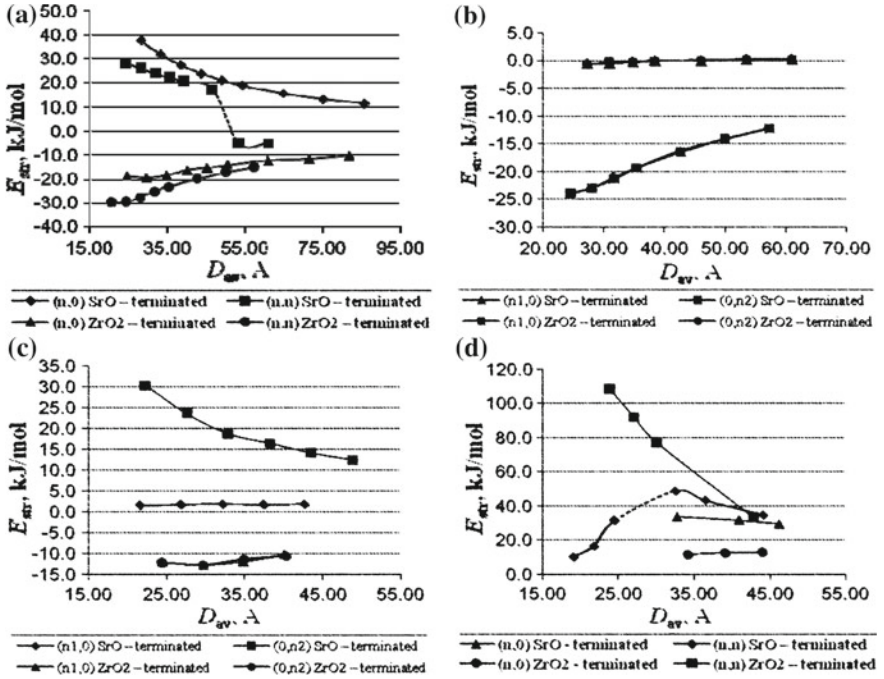

Fig. 8.18 Dependence of the strain energy E_{str} on the average tube diameter D_{av} for 2-layer type I NTs (**a**), 2-layer type II NTs (**b**), 2-layer type III NTs (**c**), and 4-layer type I (**d**) NTs

can expect the further extension of BTO nanostructures applicability (for example, as flexible and transparent nanogenerators [84]).

8.3.1 Bulk and Nanolayers

At a high temperature, BTO is stable in a paraelectric cubic structure with five atoms per unit cell (space group $Pm\bar{3}m$). At lower temperatures, BTO has three phase transitions to ferroelectric phases, see Fig. 8.19. At 393 K, BTO undergoes a structural phase transition to a tetragonal (space group P4mm) ferroelectric phase. Below 278 and 183 K, BTO has an orthorhombic (space group Amm2) and rhombohedral (space group R3m) structure, respectively [87]. All perovskite phases contain one formula unit in the primitive cell so that the phase transitions in BTO are explained by the Γ-phonon softening. We have seen above that the NT computations start with the calculations of the structure and properties of the corresponding bulk crystals as these crystals play the role of benchmark systems for checking the applicability of the accepted computation method.

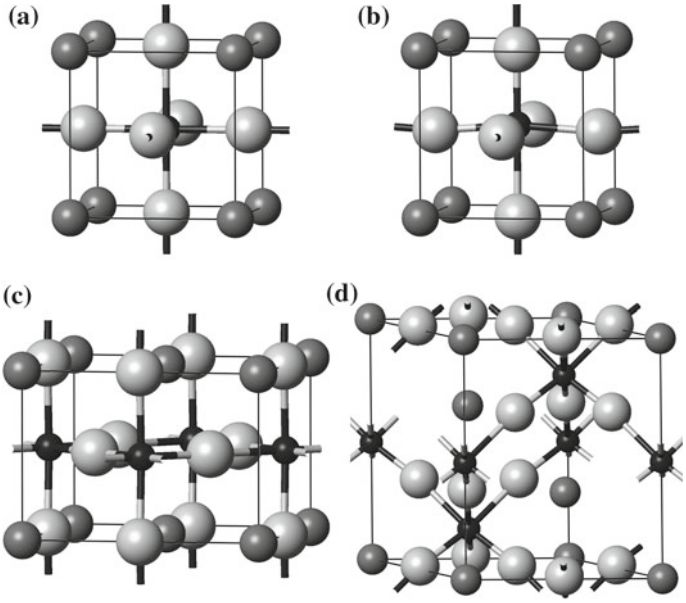

Fig. 8.19 The structure of the conventional unit cells for **a** cubic, **b** tetragonal, **c** orthorhombic, and **d** rhombohedral $BaTiO_3$. Legend: Ti—*small balls*, Ba—*middle balls*, O—*large balls*

First-principles DFT LCAO and PW calculations of the electronic, structural and vibrational properties of BTO both for cubic and noncubic (ferroelectric) phases are well-known (see [88–90] and References therein). In LCAO calculations [88, 90, 91] the ground state BTO structural and electronic properties have been studied using a number of different exchange-correlation functionals, such as the density functional theory (DFT), the Hartree-Fock (HF) approximation, and their hybrids. The results obtained for the structural and electronic properties of different phases of BTO show that apart from the band gaps (which are not ground state properties), there are a few other properties that are clearly better predicted by the hybrid PBE0 and B1WC functionals. The hybrid B1WC functional is similar to the PBE0 but mixes 16 % of the HF exchange and the Wu-Cohen-GGA [74] exchange correlation, which is tuned to remove the supertetragonality within the GGA-derived hybrid functionals. Table 8.14 shows the results obtained in LCAO calculations [88–90] using hybrid (PBE0, B1WC) exchange-correlation functionals. The agreement of the different theoretical results between themselves and with the experimental data is good: the theoretical structural parameters obtained for phases considered differ from the experimental ones by 1 % or less. The values reported in Table 8.14 are of a better quality than those obtained in other works using the local-density approximation or the generalized gradient approximation, see the referencies in [88–90]. It is important to note that both PBE0 and B1WC calculations correctly reproduce

Table 8.14 Calculated properties of BTO phases

Phase	a (Å)	b (Å)	c (Å)	Bulk modulus (GPa)[a]	E_{form}[b] (meV)	Lowest frequency at Γ (cm^{-1})	E_g (eV)
Cubic PBE0 [88]	3.986			201	0; 29.7[c]	−224i	3.7
Cubic PBE0 [89]	3.970						4.0
Cubic B1WC [90]	3.952					174i	
	(3.996)			(162)[41]	(31.6)[41]		(3.2)[42]
Tetragonal PBE0 [88]	3.971		4.073	141	−18	−137i	3.7
Tetragonal PBE0 [89]	3.965		4.131				4.0
Tetragonal B1WC [90]	3.958		4.042			125i	
	(3.997)		(4.031)	(141)[43]			(3.4)[42]
Orthorhombic PBE0 [88]	3.963	5.691	5.722	132	−24	−71i	4.2
	(3.983)	(5.674)	(5.692)				
Rhombohedral[d] PBE0 [88]	5.665	5.665	6.975	135	−30	181	4.4
Rhombohedral PBE0 [89]	5.677	5.677	6.999				4.9
Rhombohedral B1WC [90]	5.637	5.637	6.943			125	
	(5.653)		(6.959)			(173)[44]	

[a] Experimental values are given in parentheses. Lattice constants are taken from [92]; for the cubic phase-from [93]
[b] Relative to the cubic phase
[c] Cohesive (atomization) energy (eV)
[d] Hexagonal cell; in the rhombohedral cell $a = 4.013$ Å (exp. 4.004 Å); $\alpha = 89.80°$ (exp. 89.8°)

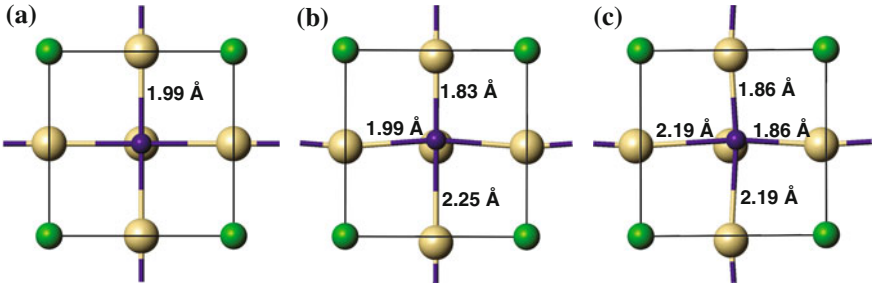

Fig. 8.20 Primitive cells of **a** cubic **b** tetragonal, and **c** orthorhombic BTO phases; top view along [1 0 0] direction. The numbers denote the calculated Ti–O bond lengths. Legend: *large light balls*—O atoms, *middle green balls*—Ba atoms, and *small dark balls*—Ti atoms [92]

the instability of the cubic and tetragonal BTO phases, giving the lowest imaginary frequencies at Γ point.

Figure 8.20 demonstrates the atomic displacements in the tetragonal and orthorhombic phases [94].

The relative stability of BTO phases can be influenced by the crystallite size. Experimental studies [32, 79–82] show that nanosized BTO systems mainly exhibit

cubic or tetragonal structure at ambient temperature. Therefore the thin nanolayers generated from the cubic, tetragonal, and orthorhombic phase were considered in [94] as the precursors to NTs.

Prior first-principles studies [37, 38, 95–102] and experiments provide evidence that the most stable BTO surfaces correspond to the (0 0 1) and (0 1 1) faces of the cubic phase. The (0 1 0) surface of the tetragonal phase was studied in [103]. It was shown that it has almost the same stability as the cubic (0 0 1) surface. To the best of our knowledge, the surfaces of the orthorhombic phase have not been studied before publication [94], where (0 0 1) and (0 1 1) nanolayers cut from the cubic phase and (0 0 1) and (0 1 0) nanolayers cut from the tetragonal phase were considered. The calculations of the (1 0 0), (0 1 0), and (0 1 $\bar{1}$) nanolayers of the orthorhombic phase were also performed for the first time in [94]. To avoid the possible mishmash, here and everywhere below, we use the Miller indices attributed to the pseudocubic (tetragonal, orthorhombic) primitive cells for the designation of crystallographic planes and directions.

An ideally cleaved cubic BTO (0 0 1) surface consists of alternating BaO and TiO_2 planes, which split into two or three close individual atomic planes upon relaxation. Any surface in ferroelectric phases with one nonzero index, (1 0 0), (0 1 0), or (0 0 1), has a similar structure composed of BaO and TiO_2 layers. Consequently, two types of terminations (BaO and TiO_2) are possible in the slab models of those surfaces. The stoichiometric slab models that have an even number of atomic planes and different terminations were considered in [94].

The symmetry operations inherited from the bulk cubic phase provide the tetragonal layer group (P4mm) of 1×1 (0 0 1) surface slabs. During the slab relaxation, O, Ba, or Ti atoms in the surface layers move with different amplitudes, which produces a surface rumpling along the [0 0 1] direction. The corresponding atomic shifts have been intensively studied in previous works, [37, 38, 95–103], where the concomitant surface energies were also calculated. However, the dependence of the calculated properties on the slab thickness was not examined properly, except in [99], where it was shown that the work function is only well converged for a slab thickness greater than 30 Å. This means that the corresponding slab model has to include 16 or more atomic planes to provide the convergence most of the physical properties. However, some of the properties may converge at a smaller thickness. To study those effects, a set of BTO slabs with a thickness up to 40 Å was calculated in [94].

Figure 8.21a presents the relaxed structure of the BTO slab including 8 BaO/TiO_2 layers, where the lengths of Ti-O bonds along the [0 0 1] direction are designated. Following [7], distortions of atomic coordinates can be quantified in terms of the differences $\Delta s(M) = |s(O) + s(O') - s(M)|$, where s = x, y, z, or the projection s^{ijk} of the atomic position on some other direction [i j k]. Oxygen atoms, O and O', are adjacent to the metal atom M (= Ti, Ba), and all the three atoms lie in one straight line in the undistorted cubic structure. Conventionally, the z axis is a normal to the surface plane, and the x and y axes lie in it. One can also distinguish the rumpling $\Delta s_\perp$ when the line O–M–O' is perpendicular to the axis s, and the bond distortion $\Delta s_{||}$ when this line is directed along the axis s. If, for example, an O–M–O' fragment is exactly linear in the noncubic structure, $\Delta s_{||}$ is equal to the difference between

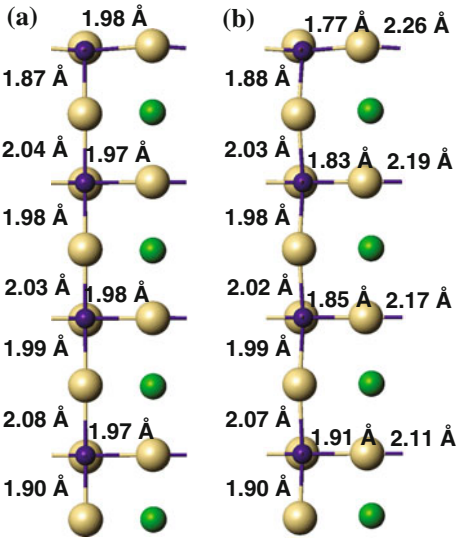

Fig. 8.21 Relaxed structure of 8-layer single-nonzero-index BTO slabs: **a** (0 0 1) nanolayer generated from the cubic phase and **b** (0 1 0) nanolayer generated from the tetragonal phase. See Fig. 8.20 for atom labeling

the lengths of two adjacent Ti–O bonds. In agreement with the previous works, a noticeable rumpling $\Delta z_{\perp}$ was found, which occurs in the outmost two layers at the TiO_2 termination and one layer at the BaO termination. However, the analysis of the thicker slabs shows that the distortion $\Delta z_{||}$ normal to the surface penetrates to the deeper layers, down to the seventh or eighth layer.

In the bulk tetragonal ferroelectric BTO phase (Fig. 8.20b), the computed value of $\Delta z_{||}$ is close to 0.42 Å, which is in good agreement with the experimental value [92] (0.37 Å). This distortion is more than two times greater than the maximal value of $\Delta z_{||} = 0.18$ Å $(= 2.08 - 1.90)$ in the outmost surface layers of the (0 0 1) slabs cleaved from the cubic phase (Fig. 8.21a). It is obvious that the tetragonal symmetry is also preserved during the cleavage parallel to the (0 0 1) plane in the tetragonal (P4mm) BTO. As pointed out in [103], the polarization normal to the surface is strongly suppressed by a depolarization field that can arise from the accumulated charge on the surfaces. This is confirmed by computations [94]: the final optimized atomic positions, the tetragonal lattice constant, and the energies of all the (0 0 1) slabs considered (including up to 20 BaO/TiO_2 layers) are the same regardless of how the initial structures were constructed. Therefore, one can conclude that the (0 0 1) thin films cut from the tetragonal phase relax to films cut from the cubic phase, and the distortions along the [0 0 1] direction are essential in the outmost surface layers only.

A different result was obtained for slabs cleaved parallel to the crystallographic plane (0 1 0) in the tetragonal phase. In this case, the former lattice vector **c** is parallel

to the surface and directed along the y axis, whereas the tetragonal symmetry is reduced to rectangular layer group 11 (Pm11). The structure of the optimized 2-layer slab is identical to that composed from the (0 0 1) planes. The deviation from the (0 0 1) relaxed films appears for slabs including four layers or more, as depicted in Fig. 8.21b. On the whole, the structure is stabilized at approximately eight layers. Two types of distortions can be defined [7] in those systems, $\Delta z_{||}$ and $\Delta y_{||}$, in the [0 1 0] and [0 0 1] pseudocubic directions, correspondingly. The first one, $\Delta z_{||}$, admits the same values, as were in the (0 0 1) slabs from the cubic phase. The second one, $\Delta y_{||}$, is noticeably greater, and it decreases only slightly from TiO_2 to BaO termination and becomes close to the bulk value (≈0.4 Å, Fig.8.21b), in the middle of the slab. The rumpling in the (0 0 1) planes, $\Delta y_{\perp}$, is about 0.15 − 0.10 Å, and does not change considerably throughout the slab.

Slabs cut parallel to the (0 1 0) surface of the orthorhombic BTO, in contrast to the (0 1 0) tetragonal surface, have ferroelectric displacements primarily along the direction perpendicular to the surface [0 1 0] direction. However, during optimization, these displacements decrease, as in the case of the (0 0 1) tetragonal surface, and the final (0 1 0) nanosheets structure (including 2D lattice parameters) is indistinguishable from that of the relaxed (0 1 0) nanosheet generated from the tetragonal phase.

The (1 0 0) surface slabs generated from the orthorhombic phase have a centered rectangular 2D lattice with angle $\gamma = 90.3°$. However, the 2-layer slab quickly relaxes to the (0 0 1) structure obtained from the cubic phase. Thicker slabs retain C1m1 symmetry, and the angle γ gradually increases with the slab thickness tending to the bulk limiting value. The atomic displacements in (1 0 0) thin films cut from the orthorhombic phase are similar to those in films cut from the tetragonal phase except for fact that the [0 1 0] and [0 0 1] directions are equivalent in the orthorhombic case.

Figure 8.22 shows the calculated dependence of the surface energy E_{surf} on the slab thickness. It is seen that the saturation of this quantity is attained at approximately at 8 BTO formula units in the 2D unit cell. In the case of single-nonzero-index surfaces, this leads to 16-layer slabs with a thickness of about 30 Å. The limiting surface energy

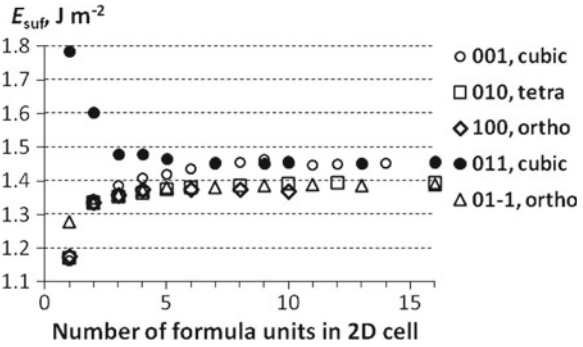

Fig. 8.22 Dependence of surface energy on thickness for BTO thin films

Table 8.15 Calculated properties of BTO thin nanosheets with a thickness of 36–38 Å

Initial phase	Pseudocubic surface index	Number of formula units in 2D cell	a (Å)	b (Å)	Thickness, w (Å)	E_{form}[a]	E_{surf} (J/m^2)	E_g (eV)
Cubic	0 0 1	10	3.97	3.97	37.95	27.7	1.46[a]	1.8
Tetragonal	0 1 0	10	3.96	4.05	37.80	25.2	1.39[b]	2.6
Orthorhombic[c]	1 0 0	10	4.01	4.01	37.78	24.3	1.37[d]	2.7
Cubic	0 1 $\bar{1}$	13	3.95	5.73	36.44	28.2	1.45[d]	3.7
Orthorhombic	0 1 $\bar{1}$	13	3.94	5.75	36.51	26.9	1.39[d]	4.1

[a] Relative to the bulk cubic phase
[b] Relative to the tetragonal phase
[c] Angle $\gamma = 90.26°$
[d] Relative to the orthorhombic phase

for the (0 1 0) surface of the tetragonal phase, however, is lower than the surface energy of the (0 0 1) surface of the cubic phase. The surface energy of (1 0 0) slabs generated from the orthorhombic phase is close to that of the (0 1 0) surface.

The stabilities and other properties of the calculated nanolayers are given in Table 8.15 for slabs with a thickness of 36–38 Å. The data presented in this table confirm that (0 0 1) nanolayers generated from the cubic phase are less stable than nanolayers cut from the tetragonal and orthorhombic phases parallel to the (0 1 0) and (1 0 0) planes, correspondingly, while the stability of the latter two is close.

While the (0 0 1) surfaces of the cubic BTO have been extensively studied [38, 95–97, 99, 103], much less is known about the (0 1 1) surfaces. The scarcity of information about these surfaces is likely to be due to the polar character of the (0 1 1) orientation. However, the (0 1 1) terminations of BTO and similar perovskites have frequently been observed, but efforts toward a precise characterization of their atomic-scale structure and corresponding electronic properties only been undertaken in a few works [98, 102]. To model this surface, stoichiometric O-terminated slabs (previously considered in [98]) were considered in [94]. It was found that this structure provides a minimum (0 1 1) surface energy relative to the cubic bulk crystal. To construct the stoichiometric (0 1 1) surface, one needs to remove extra oxygens from the outmost oxygen layers (Fig. 8.23a).

At the first stage the study of (0 1 1) nanolayers, they were cut from a cubic crystal whose inversion symmetry was kept intact (layer group P2/m11, Fig. 8.23a). This provides the equivalence of both the terminations and the zero net polarization of the slab. The slabs with a thickness of up to 40 Å were considered in [94]. Analysis of the relaxed slab structure shows that the oxygen and titanium atoms are shifted in the outmost layers along the surface, thus reproducing the atomic distortions in the (0 1 $\bar{1}$) layers of the orthorhombic Amm2 bulk phase. This is something to be expected, because the polarization along the [0 1 1] direction corresponds to the distortion in the orthorhombic ferroelectric phase [104]. That is why at the second stage, similar slabs were constructed by cleaving an orthorhombic crystal parallel

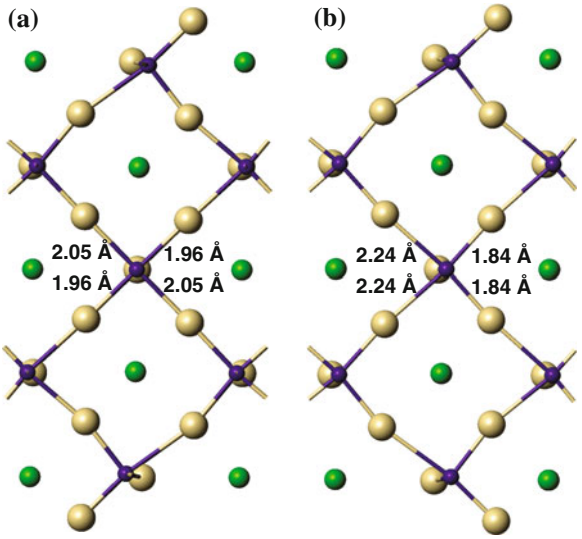

Fig. 8.23 Relaxed structure of 11-layer two-nonzero-index BTO slabs: **a** (0 1 $\bar{1}$) nanolayer generated from the cubic phase and **b** (0 1 $\bar{1}$) nanolayer generated from the orthorhombic phase. See Fig. 8.20 for atom designation

to the (0 1 $\bar{1}$) planes (Fig. 8.23b). As the [0 1 1] and [0 1 $\bar{1}$] directions in the cubic phase are equivalent, one can further refer to the (0 1 $\bar{1}$) planes in both phases. In the case of orthorhombic layers, however, the slab symmetry depends on the number l of TiOBa layers; it is $Pm2_1b$ for the even l and Pm2m for the odd l.

The results obtained are given in Table 8.15 for the thickest slabs considered, and in Fig. 8.23b for 11-layer slabs. The slabs with P2/m symmetry differ from those with Pm2m symmetry by the lateral displacements of the O atoms in the TiOBa layers. They are zero in the middle layer due to the inversion symmetry in the first case, whereas they are almost equal in all the layers except the ones next to the surface in the second case. The rumpling in the (0 1 1) planes within the orthorhombic slabs, $\Delta y_{\perp}$(Ti), is about 0.20 Å. The lateral shift of the bridging O atoms relative to the Ti atom in the subsurface layers is much greater, 0.45 Å, in both the cubic and the orthorhombic layers.

In the case of the (0 1 $\bar{1}$) orthorhombic surface, the distortions $\Delta s_{||}$ can be defined in O–Ti–O' fragments along the [0 1 0] and [0 0 1] directions. The data obtained show that the values of $\Delta s_{||}^{010}$ and $\Delta s_{||}^{001}$ in the thick nanosheets (Table 8.15) are close to those in the bulk orthorhombic phase (0.33 Å), whereas in relatively thin nanosheets (Fig. 8.23b) they are larger ($2.24 - 1.84 = 0.40$ Å).

Surface energy (relative to the orthorhombic bulk) versus slab thickness is shown in Fig. 8.22 for the (0 1 $\bar{1}$) cubic and orthorhombic cases. Figure 8.22 shows that the convergence of each curve occurs at a thickness corresponding to eight BTO formula units in a 2D cell, but the limiting surface energies of P2/m structures are noticeably

Table 8.16 Calculated properties of BTO thin nanosheets used for the preparing of NTs

Phase	Pseudo-cubic surface index	Number of formula units in 2D cell	Number of dense layers	a (Å)	b (Å)	Thickness, w (Å)	E_{form} [a]	E_{surf} (J/m^2)	E_g (eV)
Cubic	0 0 1	1	2	3.88	3.88	1.98	211	1.16[a]	3.6
Cubic	0 0 1	2	4	3.92	3.92	6.03	124	1.34[a]	2.3
Cubic	0 0 1	3	6	3.94	3.94	10.03	86	1.39[a]	2.0
Tetragonal	0 1 0	2	4	3.90	3.97	6.03	123	1.34[b]	2.6
Orthorhombic	1 0 0	2	4	3.94	3.94	6.03	123	1.34[c]	2.6
Cubic	0 1 $\bar{1}$	2	5	3.68	6.06	5.24	213	1.60[c]	4.2
Cubic	0 1 $\bar{1}$	3	7	3.88	5.80	8.01	132	1.48[c]	3.8
Orthorhombic	0 1 $\bar{1}$	2	5	3.94	5.75	5.54	176	1.33[c]	5.7
Orthorhombic	0 1 $\bar{1}$	3	7	3.82	5.91	8.11	121	1.36[c]	4.9

[a] Relative to the cubic phase
[b] Relative to the tetragonal phase
[c] Relative to the orthorhombic phase

larger. The (0 1 $\bar{1}$) and (1 0 0) thin films cut from the orthorhombic phase have a close surface energy (see Tables 8.15 and 8.16). The formation energy of systems with the same number of atoms is larger for (0 1 $\bar{1}$) layers than for single-nonzero-index layers.

Table 8.16 includes the results for extremely thin slabs used for the construction of BTO NTs (see next subsection). The data of this table demonstrate that all the slabs considered have close surface energies, except the 2-layer film, which has the lowest surface energy. However, the formation energy of this nanolayer is large ($\geq$200 kJ/mol).

Since thin BTO nanolayers are considered in [94] as precursors to NTs we summarize the main conclusions made from the results of BTO nanolayer calculations. The results obtained in [94] indicate that the thin nanolayers of different ferroelectric (tetragonal and orthorhombic) BTO phases have close surface energies and are more stable than the nanolayers of the cubic phase. The saturation of the calculated surface energy is attained on a thicknesses of about 30 Å. The formation energy of the (0 1 $\bar{1}$) nanolayers is greater than that of (0 1 0) nanolayers. It has been found that the (0 1 0) and (0 1 $\bar{1}$) faces of BTO phases can provide a basis for nanoobjects with a different structure. Because of the phase morphology of BTO, the former is more appropriate to the tetragonal structure, and the latter is more appropriate to the orthorhombic structure. The nanosheets preserved the ferroelectric displacements corresponding to the initial bulk phase, if they were composed of more than three atomic planes or dense layers. Thus, calculations [94] confirm the observation of stable ferroelectricity in thin BTO films, if they are thicker than 3–4 Å and are formed from the ferroelectric phase.

8.3.2 Rolled-Up $BaTiO_3$ Nanotubes

The major methods of $BaTiO_3$ 1D structure synthesizing can be roughly devided into two groups [78]: a hydrothermal process with or without a template, and molten-salt synthesis. $BaTiO_3$ nanotubes have been synthesized by the hydrothermal method [82, 84], via a simple wet chemical route [32]. It was found that BTO nanotubes formed a cubic phase with an average diameter of ≈10 nm and wall thickness of 3 nm at room temperature [32]. BTO arrays exhibited a distinct phase transition behavior from −190 to 300 °C [82], and the tetragonal phase was found to coexist with the cubic phase above Curie temperature. Study [78] reports a synthesis of morphology-controlled BTO nanostructures, such as spherical, cube-shaped and rod-shaped ones.

One can expect ferroelectric 1D nanostructures to provide new alternatives for developing devices not only because of the recent experiments, but also because of theoretical studies from first principles. Only two instances of BTO NTs DFT ab initio calculations have been recently reported [94, 105].

In PW DFT calculations [105] BTO nanotubes are modelled using the supercell approach. Single-layer-thick BTO films with BaO terminated (0 0 1) surfaces are rolled up about the [1 0 0] axis, as depicted in Fig. 8.24. The circumference of the nanotube is denoted by N, which is considered to be ranging from 12 to 32 in units of the BTO unit cell, and R_{in} and R_{out} denote the radii of the inner and outer surfaces. Within the supercell approach, the nearest nanotubes are separated by about 20 Å vacuum layer in both the [0 1 0] and [0 0 1] directions to avoid the neighboring interactions. The supercell lattice parameter along the [1 0 0] direction is fixed to the bulk value 3.946 Å during all calculations, while the atoms are fully relaxed.

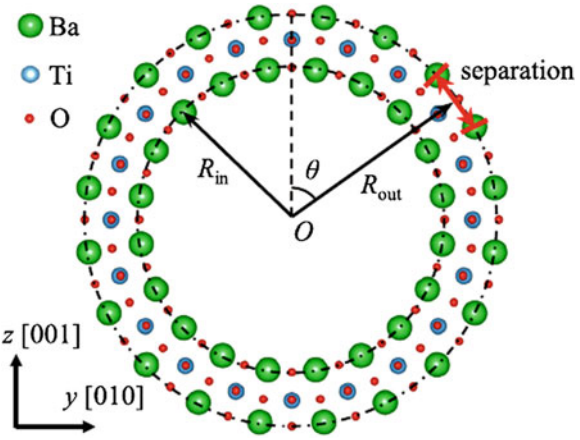

Fig. 8.24 Schematic diagram of a BTO nanotube with $N = 20$. The radii of the inner and outer surfaces are denoted by R_{in} and R_{out}, respectively. The separation refers to the distance between the nearest Ba atoms along the outer circumference of whose azimuth is denoted by θ (Reprinted figure with permission from Yin and Qu [105], Copyright (2014) by the AIP Publishing LLC)

The existence of radial polarizations in single-layer-thick BaTiO3 nanotubes was predicted in [105]. The electric polarization was confirmed and calculated by a reliable method based on electrostatic potential analysis. The polarization is found to be proportional to the strain gradient, which is induced by the bending deformation.

The results of the ab initio LCAO DFT(PBE0) calculations [94] of stoichiometric single-walled BTO NTs of different sizes are considered here in more detail. The initial structures of NTs were constructed by rolling up the relaxed BTO thin films discussed in the preceding subsection. The parent sheets have square or rectangular 2D lattices for single-nonzero-index nanolayers, respectively, and a primitive rectangular lattice for (0 1 $\bar{1}$) nanolayers.

Different BTO NT chiralities have been considered that are compatible with the 2D lattice of the selected nanosheets (see below). The majority of the calculations were made for the structures based on the cubic phase. In many cases, the results obtained for single-nonzero-index noncubic surfaces are identical to those based on the cubic (0 0 1) initial structures. This is due to the dominant role of the rotohelical symmetry that is absent in the initial slab structures. The final structure of the NTs has been obtained by the total optimization of the atomic positions with only the rototranslational symmetry preserved. Because of this, the final NT structure can belong to a line group different from the initial one. In most cases, the initial symmetry is reduced. It is essential to note that if NT optimization is performed with the total removing of the symmetry, it implicitly retains the order of the regular or screw axis assigned by the NT chirality in some test cases.

The atomic planes in slabs are transformed to atomic shells in tubes upon folding. In almost all the NTs considered, the most remote and the nearest atoms are oxygens. The inner and outer atomic shells undergo a considerable stress due to the stretching or shrinking of the interatomic distances relative to those in the initial relaxed slab. The smaller the tube diameter and the thicker the tube wall, the larger is the strain. The most critical is the repulsion between the nearest oxygen atoms in the inner shells. Because of the shrinking of the inmost layers, the distance between the O atoms can become less than 2.5–2.7 Å leading to a considerable increase in the repulsion. The inner and outer shells are strained in the opposite directions, thus reducing the tension in the former can increase the tension in the latter. As a result, for any chirality and tube wall thickness w, there exists a minimum diameter d below which the NT becomes unstable and undergoes spontaneous destruction. NTs of sufficiently large diameters were considered in [94] to prevent the instability mentioned.

The initial (0 0 1) slab symmetry is described by a square plane lattice, when the slab is cut from a bulk crystal with cubic space group 221 ($Pm\bar{3}m$). For the even number of layers, the slab layer group is 55 (P4mm). As follows from the results of [106], this layer can generate NTs with a line group belonging to family 11 (Ln/mmm, point symmetry D_{nh}) and to family 13 ($L(2n)_n$/mcm, point symmetry D_{2nh}) for the chiralities (n,0) and (n,n), respectively. The ferroelectric distortion parallel to the tube axis is only possible if the perpendicular mirror plane disappears upon NT relaxation.

To study NTs with a different wall thickness, (0 0 1) slabs consisting of 2, 4, and 6 alternating BaO and TiO_2 atomic planes, respectively, were considered. The tube thickness was estimated as half of the difference between the external and internal

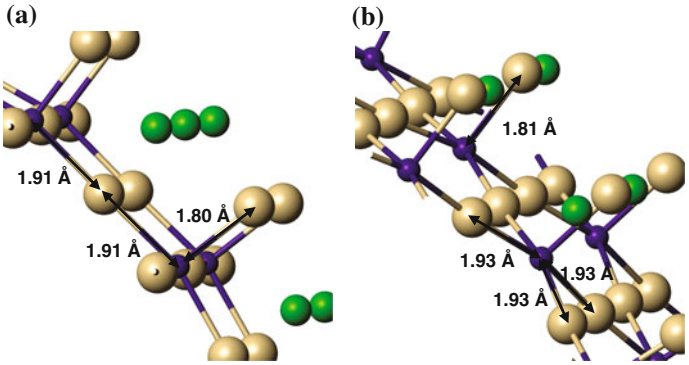

Fig. 8.25 The relaxed structure of walls for 2-shell BaO-terminated BTO NTs: **a** chirality (24,0) and **b** chirality (18,18). See Fig. 8.20 for atom labeling

diameters. The calculations were performed for achiral NTs, (n,0) and (n,n). Two different NTs can be constructed for each of the two chiralities: (i) with a BaO outer shell (TiO_2 inner shell) and (ii) with a TiO_2 outer shell (BaO inner shell). The results obtained are given in Table 8.17. It follows from this table that the properties and structure of NTs substantially depend on the wall thickness and surface composition.

During the atomic relaxation, the translation period t of the NTs (i) is almost unchanged, whereas the period of the NTs (ii) is slightly reduced relative to the initial (slab) value. The exceptions are TiO_2-terminated 4-layer NTs with chirality (n,n), where the period is slightly increased. The wall thickness w of the 2-shell NTs is approximately the same as the slab thickness (2 Å), whereas w of 4-shell NTs varies from 5.7 to 6.0 Å due to the surface reconstruction. The thickness of 6-shell NTs is noticeably less than 10 Å due to the total structure reconstruction (see later).

As discussed earlier, the structure of the 2-layer slab does not depend on the parent bulk phase: any single-nonzero-index face of the cubic, the tetragonal, or orthorhombic phases relaxed to the same 2-layer structure. Consequently, 2-shell NTs are identical for all the BTO phases. BaO-terminated NTs exhibit a noticeable relaxation without the reconstruction of TiO_2 shells and retain their initial symmetry (Fig. 8.25a, b), Ln/mmm and $L(2n)_n$/mcm for the chirality (n,0) and (n,n), respectively.

Despite the folding, the length of equatorial Ti–O bonds is adjusted by the expansion or reduction of the BaO shell, in which the covalent component of the chemical bonds is weak. Thus, Ti–O bonds keep an equal length (1.91–1.93 Å) in the TiO_2 shell, and no ferroelectric distortions can be found. According to the data in Table 8.17, BaO-terminated NTs are more favorable than the 2-layer thin films used for NT rolling.

The relaxation of 2-shell TiO_2-terminated NTs is greater than that of BaO-terminated NTs and can be regarded as a reconstruction with symmetry lowering. Thus, TiO_2-terminated NTs with the chirality (n,0) reduce their symmetry to Ln/m (C_{nh}, family 3), and NTs with the chirality (n,n) reduce their symmetry to $L(2n)_n$/m, (C_{2nh}, family 4) at $n \geq 20$, or to $L(2n)_n$mc (C_{2nv}, family 8) at $n \leq 20$. In the first two

cases, equatorial polarization (along the NT circumference) is observed. It is particularly strong in the outmost TiO_2 shell for the chirality (n,0). Moreover, for diameters less than 50 Å, a break of some transverse (equatorial) Ti–O bonds in (n,0) tubes is possible, which results in the formation of a short (1.74–1.76 Å) $Ti = O$ titanyl bonds. The overall structure of the NT with the chirality (n,0) resembles the surface of the (0 1 0) tetragonal phase nanolayers, and with the chirality (n,n) resembles the surface of (1 0 0) orthorhombic phase nanolayers (with the number of pseudoplanes greater than 2). The NTs with chirality (n,n) have a noticeable axial polarization at n $\leq$ 20; the length difference between the adjacent Ti–O bonds is close to 0.4 Å. The strain energy of TiO_2-terminated NTs is positive, but not particularly large at the chirality (n,0) (see Table 8.17).

The relatively stable 4-shell NTs arise at greater diameters than 2-shell NTs because of the large curvature difference between the inner and outer shells, which provokes considerable stretching and shrinking of the external and internal NT surfaces. As a result, a breaking of the equatorial Ti–O bonds occurs in the external shells of all the NTs considered, producing separated TiO_2 ribbons on the surface of the cylinder. The short (1.71–1.72 Å) Ti–O bonds on the external surface are separated from each other by 3 Å or even more, as illustrated in Fig. 8.26.

Nevertheless, all these NTs retain the mirror plane σ_h, so that their symmetry belongs either to family 3 (Ln/m) or to family 4 $(L(2n)_n/m)$, see Table 8.17. One exception is the BaO-terminated NT (n,0), where the mirror plane disappears because of small ($\leq$l0.1 Å) axial distortions. Consequently, the noticeable ferroelectricity is absent in the tubes under consideration. TiO_2-terminated NTs with the chirality (n,0) (Fig. 8.26a) have relatively small strain and surface energies, but they are considerably larger for NTs with the chirality (n,n), which is shown in Fig. 8.26b.

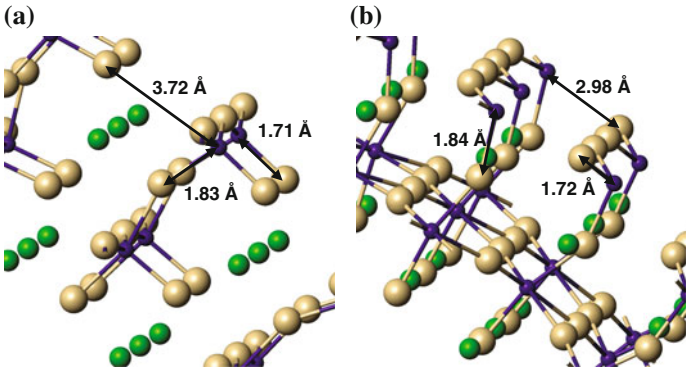

Fig. 8.26 Relaxed structure of walls for 4-shell BTO NTs folded from (0 0 1) layers of the cubic phase with TiO_2-terminated external surface: **a** chirality (24,0) and **b** chirality (16,16). See Fig. 8.20 for atom labeling

Table 8.17 Structure, stability, and band gaps of selected BTO NTs with an average diameter of about 30 Å

Number of formula units in initial 2D cell	Number of dense layers in initial cell	NT chirality[a]	Line group and family (in parentheses) of final structure	NT period t (Å)	NT wall thickness w (Å)	NT average diameter, d (Å)	E_{form}[b] (kJ/mol)	E_{str} (kJ/mol)	E_{surf}[c] (J/m^2)	E_g (eV)
(0 0 1) Cubic										
1	2	(24,0)-ba	L24/*mmm* (11)	3.89	1.95	30.95	203	−8.1	1.07	3.9
1	2	(24,0)-ti	L24/*m* (11)	3.66	2.15	33.68	232	21.0	1.20	5.6
1	2	(18,18)-ba	$L36_{18}$/*mcm* (13)	5.57	1.99	31.55	200	−11.2	1.08	3.9
1	2	(18,18)-ti	$L36_{18}$*mc* (8)	5.51	1.95	32.73	258	46.5	1.36	4.6
2	4	(24,0)-ba	L24 (1)	3.93	5.83	34.04	149	24.6	1.41	4.0
2	4	(24,0)-ti	L24/*m* (3)	3.71	6.03	36.27	136	11.8	1.28	5.0
2	4	(16,16)-ba	$L32_{16}$/*m* (4)	5.59	5.82	32.01	173	48.6	1.63	3.5
2	4	(16,16)-ti	$L32_{16}$/*m* (4)	5.76	5.73	31.24	204	79.6	1.91	4.6
3	6	(20,0)-ba	L20 (1)	3.94	9.38	31.85	144	23.6	1.82	3.9

(continued)

Table 8.17 (continued)

3	6	(20,0)-ti	L20/*m* (3)	3.67	9.76	34.06	122	1.7	1.55	4.5
(1 0 0) Orthorhombic										
2	4	(16,16)-ba	$L32_{16}mc$ (8)	5.69	5.75	31.24	186	63.6	1.79	3.3
2	4	(16,16)-ti	$L32_{16}mc$ (8)	5.96	5.64	30.96	216	93.3	1.98	4.8
(0 1 $\bar{1}$) Cubic										
3	7	(20,0)-o	L20 (1)	5.57	7.72	30.12	161	40.3	1.54	4.3
3	7	(0,20)-o	L20 (1)	4.06	8.70	31.55	122	1.5	1.54	4.9
(0 1 $\bar{1}$) Orthorhombic										
2	5	(20,0)-o	L20/*m* (3)	3.99	5.05	33.54	121	−54.8	0.97	5.5
2	5	(0,20)-o	L20 (1)	4.36	4.61	35.08	161	−15.1	1.13	5.8
3	7	(20,0)-o	L20 (1)	5.74	7.95	28.78	161	40.0	1.57	5.1
3	7	(0,20)-o	L20/*m* (3)	3.83	8.11	39.96	152	31.2	1.60	4.7

[a] The initial composition of the outside shell (termination) is designated to the right of chirality: BaO, –ba; TiO_2, –ti; O, –o

[b] Relative to the cubic phase

[c] See Table 8.16 for the reference phase

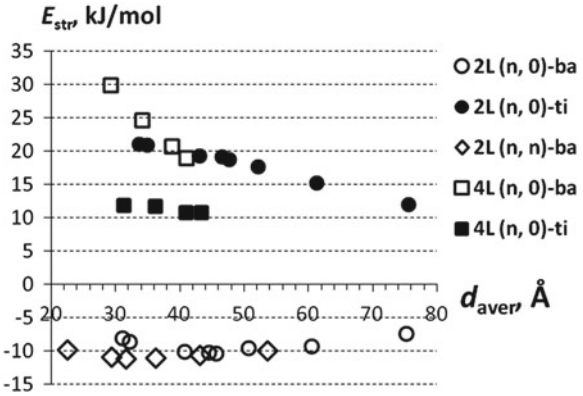

Fig. 8.27 Strain energy dependence on NT diameter for the selected tubes folded from (0 0 1) layers of the cubic phase. The number of dense layers in the initial slab: 2, 2L; 4, 4L. Terminations: BaO, –Ba; TiO_2, –Ti

Table 8.18 Stability comparison of STO [45] and BTO NTs folded from (0 0 1) layers of the cubic phases

Number of formula units in initial 2D cell	Number of dense layers in initial slab	NT chirality[a]	E_{form} (kJ/mol)		E_{str} (kJ/mol)	
			STO	BTO	STO	BTO
1	2	(32,0)-ba	256	201	14.8	−10.0
1	2	(32,0)-ti	245	231	4.4	19.3
1	2	(16,16)-ba	256	200	15.3	−10.8
1	2	(16,16)-ti	251	265	10.2	54.2
2	4	(32,0)-ba	185	142	41.2	17.4
2	4	(32,0)-ti	153	135	9.5	10.5
2	4	(16,16)-ba	235	173	91.2	48.6
2	4	(16,16)-ti	224	204	80.9	79.6

[a] The composition of the outside shell (termination) is designated to the right of chirality: BaO, –ba; TiO_2, and –ti

Figure 8.27 shows the dependence of strain energy on the NT average diameter for the selected (0 0 1) BTO NTs.

It demonstrates that the strain energy of the BaO-terminated 2-shell NTs is negative and exhibits weak dependence on the tube diameter. In the case of 4-shell NTs, the TiO_2-terminated tubes are more stable than the BaO-terminated ones. In Table 8.18, we compare the results obtained for STO [11] and BTO NTs folded from the (0 0 1) layers of the cubic phases.

The values listed in this table show that the formation energy of BTO tubes is mostly less than that of STO tubes. The calculated results indicate that the strain energy of BTO NTs with BaO-terminated external surface is noticeably less than the strain energy of STO NTs with SrO terminated external surface, whereas the opposite is right for tubes with an external TiO_2 surface. Thus, the relative stability of the BaO-terminated surface is enhanced in the case of BTO NTs. Also, it should be noted that the BaO external surface exhibits larger reconstruction than the SrO external surface in 4-shell NTs.

Relatively thick NTs have been obtained by folding the 6-layer slabs to the NTs with chirality (n,0). Such slabs cannot be folded to tubes with the chirality (n,n) at diameters that are accessible in the calculations under consideration. Because of the drastic reconstruction the final structure of 6-shell NTs is far from the initial texture of 6-layer thin films. It resembles the structure of 4-shell NTs. No noticeable axial ferroelectric distortion is found for these NTs. The strain energy of TiO_2-terminated NTs is close to zero (see Table 8.17).

The relaxed (0 1 0) slabs generated from the tetragonal phase belong to layer group 11 (Pm11). Correspondingly, such nanolayers can be rolled into NTs of family 6 (Lnmm) or family 3 (Ln/m) for the chiralities (n,0) and (0,n), respectively [106]. NTs folded from the relaxed 4-layer (0 1 0) slabs with the chiralities (24,0) and (0,24) and of two types of termination were calculated in [94]. Surprisingly, the final NT structure does not depend on the initial chirality. Moreover, the results obtained for BaO and TiO_2 terminations coincide with those obtained for the NTs with the same termination and chirality folded from the (0 0 1) cubic phase layers (see Fig. 8.26). Thus, one can conclude that the tetragonal phase does not produce new types of 4-shell NTs. On the other hand, the structure of NTs with the chiralities (n,0) or (0,n) is more likely to be attributed to the tetragonal phase.

The relaxed (1 0 0) slabs generated from the orthorhombic phase belong to layer group 13 (C1m1). NTs folded from these nanolayers correspond to family 4 ($L(2n)_n$/m) or 8 ($L(2n)_n$mc) for the chiralities (−n, n) or (n,n). Four different NTs were constructed in [94] by folding the 4-layer relaxed (1 0 0) slabs cut from the orthorhombic phase. Further optimization shows that the initial symmetry is preserved in the final structures. The structures obtained at chirality (−16,16) correspond to the line group $L32_{16}$/m and coincide with the NTs (16,16) generated from the (0 0 1) cubic phase slabs (Fig. 8.26b). The presence of the mirror plane perpendicular to the tube axis precludes axial polarization. In contrast to that, the optimization at chirality (16, 16) produced a new NT type with the symmetry $L32_{16}$ mc. The considerable axial displacements lead to the breaking of the Ti–O bonds in the outermost TiO_2 shells. The oxygen atoms in the innermost TiO_2 shell of the TiO_2-terminated NT moved in the same direction providing nonzero net polarization. The atomic displacements in the innermost TiO_2 shell of the BaO-terminated NT are considerably smaller and occur in the opposite direction. The formation energy and strain energy of the C_{2nv} structure is greater than that of the C_{2nh} structure (Table 8.17). We can also notice that both the chiralities mentioned, (−n,n) and (n,n), may be attributed to the orthorhombic phase.

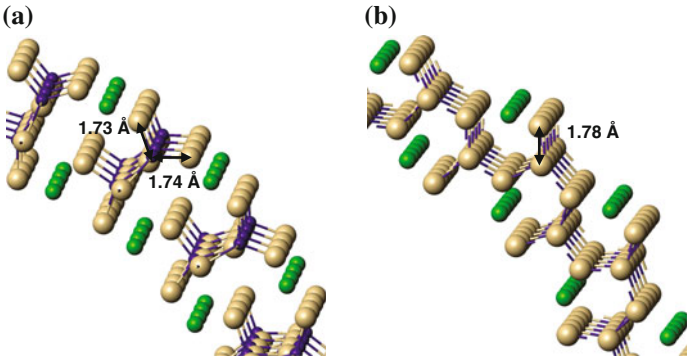

Fig. 8.28 Cross-section view on the relaxed walls of NTs folded from (0 1 $\bar{1}$) 5-layer slabs of the orthorhombic phase: **a** chirality (20,0) and **b** chirality (0,20). See Fig. 8.15 for atom labeling

Nanolayers with indices (0 1 $\bar{1}$) may belong to three different layer groups: 14 (P2/m11), 27 (Pm2m), and 28 ($Pm2_1b$). All these groups belong to families 3 (Ln/m) or 6 (Lnmm), depending on the chirality. In the case of (0 1 $\bar{1}$) BTO NTs, we study slabs of two different thicknesses (see Table 8.16). As the atomic (0 1 $\bar{1}$) planes are charged, the corresponding thin nanolayers exhibit a considerable reconstruction compared with the bulk structure. 3-layer films, in particular, consist of isolated chains of TiO_4 tetrahedra and, therefore, were not used for the tube rolling. For thicker slabs, one can also expect that the initial NTs structures will undergo considerable transformations. This really did occur during structure optimization, and the NTs generated from five (0 1 $\bar{1}$) cubic planes converted to NTs similar to those previously obtained from four (0 0 1) cubic planes. NTs with the chirality (n,0) are converted to tubes with BaO-terminated external surfaces, whereas NTs with the chirality (0,n) are converted to TiO_2-terminated 4-shell tubes. Thus, upon structure reconstruction, the shell composition changes to composition typical to single–nonzero–index perovskite layers, that is, BaO and TiO_2. A similar transformation was found for NTs generated from five (0 1 $\bar{1}$) orthorhombic layers, although they converted to structures that had not been obtained before. For the chiralities (n,0) and (0,n), the 5-layer (0 1 $\bar{1}$) films of the orthorhombic phase produce NTs with Ba^{2+} ions on the internal and external surfaces (Fig. 8.28).

It should be noted that according to some experimental evidence [2], BaO surface may really predominate in perovskite nanowires. The Ti and O atoms form an internal *skeleton* composed of TiO_4 tetrahedra with short outward Ti–O bonds (1.73–1.78 Å). TiO_4 tetrahedra join together forming weakly bonded ribbons in the NTs (n,0) (Fig. 8.28a), and weakly bonded ring disks in the NTs (0,n) (Fig. 8.28b). Both types of NTs have negative energy of rolling from the initial (0 1 $\bar{1}$) slabs and a large value of the electronic band gap, but only the NT (n,0) has low formation energy (see Table 8.17).

After optimization, 7-shell (n,0) NTs maintain the composition of shells and surfaces terminated by oxygen atoms. The final structures do not retain any symmetry

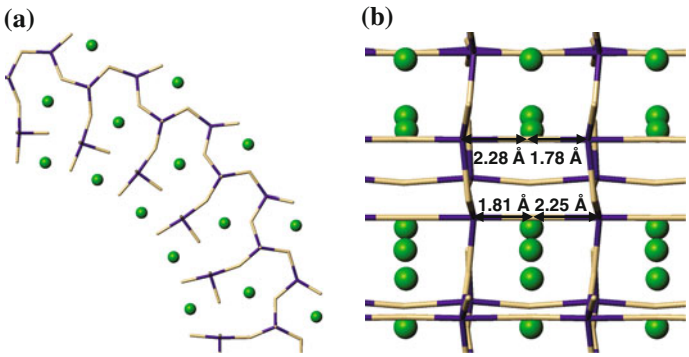

Fig. 8.29 Relaxed structure of 7-shell (0 1 $\bar{1}$) BTO NTs with the chirality (0,20) folded from layers of the cubic phase: **a** cross-sectional view and **b** side view. The Ti and O atoms are shown as sticks

elements except for rotation axis, and they belong to the first line-group family. The structures of the tubes obtained from the cubic and orthorhombic phases are remarkably similar and contain separated TiO_2 ribbons gathered together on the surface of a cylinder. This structure is similar to that for 6-shell NT obtained from (0 0 1) layers of the cubic phase, but with different positions of the Ba^{2+} ions.

The final structure of 7-shell NTs with the chirality (0,n) preserves the connectivity within and between layers but depends on the parent phase. The NT (0,20), which was rolled from the P2/m (cubic) slab, converted to the structure composed of TiO_2 and BaO shells and lost all the symmetry elements except the rotation axis (Fig. 8.29a).

The difference between the lengths of adjacent Ti–O bonds in the outmost shells along the tube axis is large ($\Delta z_{||} = 0.4$–0.5 Å). However, the displacements of the Ti atoms have opposite directions in the two external shells exhibiting antiferroelectric ordering (Fig. 8.29b). A similar NT rolled from the Pm2m slab retains shells folded from the (0 1 $\bar{1}$) layers of the orthorhombic phase as well as the mirror plane σ_h. As follows from Table 8.17, the formation energy and strain energy of this NT are remarkably larger than those for the NT folded from the (0 1 $\bar{1}$) layers of the cubic phase.

We proceed to summarize the conclusions made in [94]. It has been demonstrated that the structure and stability of BTO single-wall NTs depend on the original bulk crystal phase and the wall thickness. However, the folding of 2- and 4-layer nanosheets cleaved from different phases parallel to any single-nonzero-index plane produces the same NTs. The most stable NTs with thin 2-shell walls have a BaO external and a TiO_2 internal shell. For thicker NTs, TiO_2 composition is preferable for the outmost shells. The presence of the Ba^{2+} ions on both tube surfaces is favorable for single-wall NTs folded from (0 1 $\bar{1}$) nanosheets. In this case, a considerable structure reconstruction takes place.

The majority of relatively stable NTs have a mirror plane perpendicular to the tube axis. Some of the NTs rolled up from the orthorhombic layers show antiferroelectric arrangement of the Ti–O bonds. It means that single-walled BTO NTs can hardly

manifest ferroelectric properties. The ferroelectric properties are supposedly more probable for multiwall NTs or NTs with polygonal or polycrystalline walls.

A comparison of results obtained for BTO and STO NTs shows that the formation energy of the former is less than that of the latter in most cases. The relative stability of BaO-termination is enhanced in BTO NTs compared to STO NTs.

8.3.3 $BaTiO_3$ Nanowires

Scanned probe investigations into the ferroelectric properties of individual single-crystalline barium titanate nanowires were reported in [75]. It was shown that non-volatile electric polarization can be reproducibly induced and manipulated on these nanowires, thereby demonstrating that nanowires as small as 10 nm in diameter retain ferroelectricity. These nanowires should provide promising materials for fundamental investigations into nanoscale ferroelectricity, and they may also be useful in nanoscale nonvolatile memory applications.

A controlled measurement of voltage generation from an individual perovskite $BaTiO_3$ nanowire was successfully carried out in [77] with the development of a precision tensile mechanical testing stage integrated with high-sensitivity charge-sensing electronics. The nanowire was found to behave as a perfect nanoscale piezoelectric element showing a direct piezoelectric effect that converts mechanical energy in the form of a periodically applied mechanical load to electric energy. This study laid solid foundations for a systematic characterization of such piezoelectric nanowires and for their potential application in nanoscale energy harvesting.

X-ray diffraction study [83] shows that BTO nanowires are stabilized in the cubic form i.e. at room temperature phase of the $BaTiO_3$. A flexible nanogenerator based on a single BTO nanowire was demonstrated in [85]. The electric outputs were found to be proportional to the strain and strain rate. The growth of vertically aligned barium titanate nanowire arrays was first reported in [86], demonstrating their use as a piezoelectric NW-based sensor.

Theoretical simulation on BTO nanowires allows the study of the finite size effects influence on the structural phase transition of ferroelectric nano-sized BTO nanowires [4, 7, 107–110], the "diameter-temperature" phase diagram [111] and the strain effect on phase transitions of BTO nanowires [10, 112, 113]. The size dependence of the ferroelectric properties of BTO nanowires was first studied in [4] using DFT(LDA) calculations of model systems built from individual $BaTiO_3$ clusters that are assembled into infinite chains, themselves combined into wires of increasing diameters. These stoichiometric wires have two BaO and two TiO_2 lateral surfaces. The authors focus on the eventual disappearance of ferroelectric instability along the wire direction z. The wire diameter is specified by an integer n that corresponds to the number of TiO chains that are gathered together within the wire. The alternating TiO distances along z are called d_1 and d_2, their difference characterizes the ferroelectric distortion. Use of a numerical atomic orbital basis requred the consideration of the periodic replicas of wires separated by more than 10 Å of vacuum. The authors

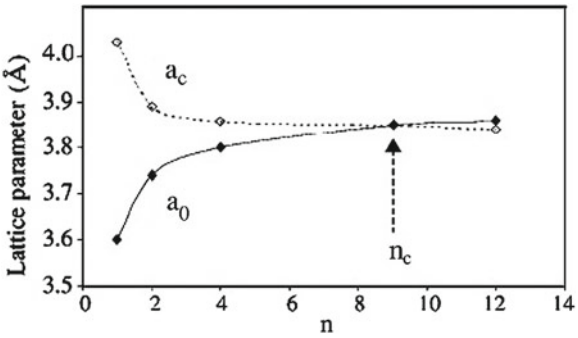

Fig. 8.30 Evolution of a_c (*white diamonds*) and a_0 (*black diamonds*) as a function of the number n of Ti-O chains in the transverse section of the wire (Reprinted figure with permission from Geneste et al. [4], Copyright (2006) by the AIP Publishing LLC)

explicitly checked that the replica of the wire generated by periodic boundary conditions did not affect the results. The n-dependence of the equilibrium 1D lattice parameter (a_0) along the NW axis was also studied.

For the thinnest wire (n = 1) the bond lengths and the equilibrium lattice constant a_0 of the relaxed structure are significantly shorter than in the bulk. This can be explained by the low coordination of the different atoms in the structure, the lack of some interactions being compensated for by the strengthening of the remaining bonds. The system remains insulating with a bandgap of 3.3 eV. The relaxed structure presents a plane of symmetry perpendicular to z ($d_1 = d_2$) and is therefore not spontaneously polarized along the wire direction, demonstrating that ferroelectricity has disappeared. However, imposing a tensile strain, one can recover the polar structural distortion along the TiO chains ($d_1 \neq d_2$) above the critical lattice constant $a_c = 4.05$ Å. This strain induced phase transition is of second order.

The fully relaxed n = 4 wire is also nonpolar along z. However, a_c has been reduced to 3.86 Å, and a_0 is now larger (3.80 Å), as expected from the increase of the mean atomic coordination numbers with respect to the n = 1 wire. Figure 8.30 shows the evolution of a_0 and a_c for wires of increasing n. It is seen that the difference a_c–a_0 progressively decreases and a crossover between both curves is observed at $n_c = 9$, which corresponds to a diameter of 1.2 nm. Above n_c, unconstrained wires are ferroelectric, whereas below this value, the spontaneous polarization only appears under tensile strain. In Fig. 8.30, a_c keeps a nearly constant value around 3.85 Å (except for n = 1), while the disappearance of the ferroelectric distortion at small sizes originates from the progressive decrease of a_0. The ferroelectric behavior of nanowires appears therefore to be monitored by the strong sensitivity of the ferroelectricity to the unit cell volume, the latter being affected by low coordination effects at free surfaces [4]. As n increases, a polar distortion recovers. However, its amplitude only progressively increases as a_0 slowly evolves to its bulk value. The main result of calculations [4] is the following: the ferroelectric distortion along the BTO wire axis disappears below a critical diameter of about 1.2 nm. This disappearance is related

to the global contraction of the unit cell resulting from the low atomic coordinations at the wire surface. Further DFT (LDA) calculations [7, 108] confirmed this result.

Both stoichiometric and nonstoichiometric BTO NWs were considered in DFT (LDA) calculations [7] using a numerical atomic orbital basis set and the supercell model with the NW axis oriented along the tetragonal c axis (taken to be along the z direction), and with the NWs separated by at least 12 Å from the neighboring images normal to the NW axis. The supercell vectors were chosen to be orthogonal, thereby allowing tetragonal ferroelectric distortions. As in calculations [4], discussed above, stoichiometric NWs contained an integral number of $BaTiO_3$ units arranged in the nxn square grid along the plane normal to the NW axis (S-n × n NWs). Infinite repetitions of the BTO units along the NW axis resulted in alternate stacking of BaO and TiO_2 planes and, consequently, in n^2 infinite –O–Ti–O– chains along the NW axis. Owing to the stoichiometry, two of the NW sidewall facets are BaO terminated and the other two are TiO_2 terminated. The inherent asymmetry of S-n × n NWs structures results in a polarization component normal to the NW axis. This asymmetry can prevent a clear understanding of the intrinsic tendency of the system to adopt certain polarization configurations. Moreover, real NWs will display facets that are either all BaO or all TiO_2-terminated, depending on which of the two surface facets is stabilized in a given chemical environment. Owing to these factors, a set of BaO– and TiO_2-terminated nonstoichiometric NWs(BaO-n × n and TiO_2-n × n) were considered in [7]. The nonstoichiometric NWs were created by adding $BaO(TiO_2)$ planes to the TiO_2(BaO) facets of S-nn × n NWs.

For each NW, two cases were considered: (1) Ti atoms constrained to be at the midpoint between the O atoms above and below (paraelectric state with net zero axial polarization, i.e., with $d_z = 0$); note, however, that these structures may have a nonzero d_x or d_y value depending on the location, stoichiometry, and surface termination; and (2) Ti atoms intentionally displaced from this central position (followed by geometry optimization) in order to determine the tendency for each system to display ferroelectric instability. For each of these two cases, the value of the c parameter (periodic distance along the NW axis) was optimized. The value of the c parameter corresponding to the most stable NW for each size and stoichiometry is displayed in Fig. 8.31 with the horizontal dashed line representing the corresponding value for the bulk BTO. Smaller c values for NWs with smaller cross sections is a consequence of the atoms (most of which are at or close to the sidewall facets) moving to increase their reduced coordination. The c value of all NWs asymptotically approaches the bulk BTO value. The BaO-n × n NWs appear to achieve this the quickest and the TiO2-n × n the slowest, with the stoichiometric variety being intermediate [7]. The $c/\overline{a}$ ratio ($\overline{a}$ is the average lateral lattice parameter) is a measure of tetragonality with larger values of this ratio correlating with an increased tendency for ferroelectric distortions. In fact, the c/a ratio is equal to 1 and 1.003, respectively, in bulk paraelectric and bulk ferroelectric BTO. For the nonstoichiometric NWs the ratio $c/\overline{a}$ increases with NW size, indicating an increased tendency for ferroelectricity with size. In BaO-n × n NWs the ratio $c/\overline{a}$ has values 0.984,1.011,1.016,1.003 (for n = 1,2,3,4, respectively); in TiO_2-n × n NWs ratio $c/\overline{a}$ has values 0.904,0.956,0.990,0.995 (for n = 1,2,3,4, respectively). The tendency for ferroelectric distortion for stoichiometric

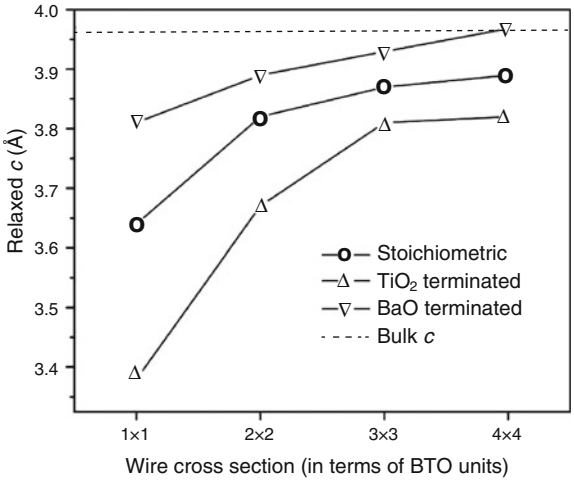

Fig. 8.31 Evolution of the equilibrium lattice constant c as a function of the wire cross section for stoichiometric and nonstoichiometric NWs (having either BaO and TiO_2 termination). The corresponding bulk tetragonal value is represented as a horizontal dashed line [7]

S-n × n NWs was quantified in terms of the ferroelectric well depth, defined as the energy difference (per BTO unit) between the reference paraelectric structure with $d_z = 0$ and the distorted ferroelectric structure (should this be stable). In the case of the S-1 × 1 and S-2 × 2 NWs, the only stable structures were the paraelectric ones. In contrast, the ferroelectric states were stable in S-3 × 3 and S-4 × 4 NWs with ferroelectric well depths of 12.8 and 13.8 meV/BTO unit, respectively, close to the corresponding value for the bulk tetragonal BTO but smaller than for the bulk rhombohedral BTO. The off-center positions along the z direction of Ti atoms were used to determine d_z for all the Ti atoms. It was found in [7] that the magnitude of the ferroelectric distortions is, in general, smaller than in the bulk BTO and that the distortions are much larger at and close to TiO_2-terminated facets than at and close to BaO-terminated facets.

In the nonstoichiometric NWs, in addition to the axial ferroelectric distortion, the transverse component of the distortion (i.e., along the plane normal to the NW axis) was considered. Among the BaO-n × n NWs, axial polarization was not stable in the BaO-1 × 1 and BaO-2 × 2 NWs, which was similar to the stoichiometric case. It is clear that axial polarization is realized only in the core of the NWs, i.e., in those BTO units that are completely surrounded by at least one BTO shell. In the outer shell region, although the d_z value is quite small, its sign is opposite to that of d_z in the core region. It can thus be concluded that BTO NWs bound by BaO facets will display core-shell polarization. In the core region, the level of the distortion, i.e., d_z value, is closer to the corresponding bulk tetragonal value than that displayed by stoichiometric NWs.

The main conclusions made in [7] are the following. The critical size for ferroelectricity in BTO NWs (with polarization along the NW axis) is about 12 Å at 0K, regardless of stoichiometry or surface terminations. The degree of polarization (quantified in terms of off-center Ti atom displacements in TiO_6 octahedra) and the energetic driving force for the ferroelectric instability (quantified in terms of the ferroelectric well depth) are comparable to those of the bulk BTO even in ultrathin nanowires. In the case of TiO_2-terminated symmetric nonstoichiometric nanowires with a size of about 16 Å, a polarization instability along the transverse direction, accompanied by a vortex polarization state, was also observed using DFT computations.

Four BTO NW models were constructed from the cubic unit cell (U) of $BaTiO_3$ and used in DFT(LDA) calculations [108]. The shape ratio of the NWs(Rods) was varied from 1:10 to 1:1 for single unit cell cross-section rods (SURs) and from 2:10 to 2:2 for double unit cell cross-section rods (DURs). Each rod ends a BaO plane or a TiO_2 plane. A1,A2 are BaO-terminated SURs and DURs,respectively; B1,B2 are TiO_2-terminated SURs and DURs, respectively. Thus the nUA1 model means nxn BaO-terminated stoichiometric nanowires for a single unit cross-section.

The authors of [108] found that a transformation of the cubic to the tetragonal phase occurs in the wire of type A. The phase transition occurs more easily in the wire of type A2. For example, A2 type wires whose length is just 4U, have a tetragonal phase, while for A1 type wires the minimum required length is 6U.

The mean values of c/a, which were averaged over unit cells of each rod showed the stability of the tetragonal phase for BaO ended SURs (type A1) with a length above 1.6 nm. For BaO ended DURs (type A2), the tetragonal phase was shown to be stable at length above 1.3 nm. These two lengths can be considered as cubic-tetragonal transition lengths. The structural-phase transition did not occur for the TiO_2 ended SURs (type B1) or DURs (type B2) at any length up to 3.2 nm. The results of DFT(LDA) computations [108] of the stoichiometric models of BTO nanowires agree with those discussed above.

An ideally cleaved cubic BTO (0 0 1) surface consists of alternating BaO and TiO_2 planes, which split into pairs of close individual atomic planes in the tetragonal cell. Any surface of the cubic or tetragonal phase with one non-zero index, (1 0 0), (0 1 0), or (0 0 1), has a similar structure composed of densely packed BaO and TiO_2 layers. According to (2.40), the [0 0 1]-directed NW 1D periodicity cell can virtually have {1 0 0} and {0 1 0}, or {1 1 0} and $\{\bar{1}\ 1\ 0\}$ low-index facets, which are orthogonal by pairs. It is well-known [40] that the {0 0 1} facets are the most common in perovskites and so they were chosen for NW calculations [107] with the tetragonal phase.

To estimate the limiting surface energy calculations were performed on (1 0 0) slabs cut from the tetragonal phase with 1–16 formula units per surface 2D unit cell [107]. As a result, the converged value of the surface energy 1.39 J/m^2 was obtained. [0 0 1]-directed NWs were constructed from the bulk 3D unit cells (see Fig. 8.32a, b), so the opposite facets have different terminations. Due to the presence of the diagonal (1 1 0) mirror plane going through the translation axis, the rod group of the [0 0 1] NW is Pm (point symmetry group C_s). NW [0 0 1] optimized structure parameters are close for the both initial cubic and tetragonal phases.

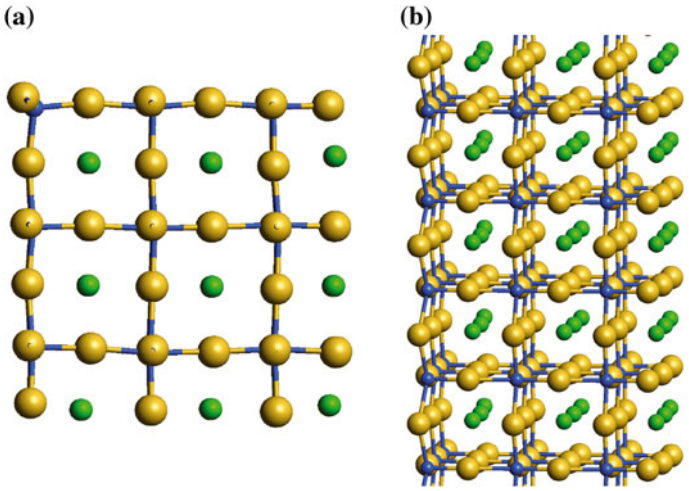

Fig. 8.32 Relaxed structure of a 3 × 3 NW cut from the tetragonal phase along the [0 0 1] direction: **a** Cross-sectional (**a**) and (1 0 0) lateral (**b**) view. Legend: *small blue balls*–Ti atoms, *small red balls*–O atoms, *large green balls*–Ba atoms, [107]

The [0 0 1] direction corresponds to the ferroelectric distortion of atoms in the both tetragonal and orthorhombic phases as compared to their positions in the cubic phase, see Fig. 8.20. The ferroelectric distortion may be important in NWs if it is parallel to the wire axis. The [0 0 1] direction in the orthorhombic base centered Amm2 phase indexed with the conventional (crystallographic) unit cell can be written as [0 1 1] using the primitive pseudocubic unit cell. [0 0 1] NWs cut from the orthorhombic phase were calculated for the first time in [107].

{0 0 1}-directed NWs based on the orthorhombic BTO phase can also have {1 0 0} and {0 1 0}, or {1 1 0} and $\{\bar{1}\ 1\ 0\}$ low-index facets satisfying (2.40). Only the first two are orthogonal to each other. They correspond to the (1 0 0) and (0 1 1) faces in the primitive pseudocubic cell, and both are known [98] to be sufficiently stable. That is why these facets were selected for the calculation of [0 0 1]-directed NWs cut from the orthorhombic BTO phase (Fig. 8.33a, b). The surface energy of the (1 0 0) and (0 1 0) faces was estimated by the calculation of the corresponding slabs of different (rising) thickness until a convergence was achieved. The resulting values of 1.37 J/m^2 and 1.39 J/m^2 for the (1 0 0) and (0 1 0) surfaces, accordingly, are very close to the surface energy of the (1 0 0) face in the tetragonal phase. [0 0 1] NWs constructed from the bulk orthorhombic BTO structure have a mirror (ordinary or glide) (0 1 0) plane going through the translational axis. The rod group of this system is Pm or Pa, depending on the parity of the number of slab periods included in a NW along the [0 1 0] direction.

The calculated properties of [0 0 1]-directed NWs based on the cubic, tetragonal and orthorhombic BTO phases are compared in Table 8.19. It can be seen that the period of all length NWs considered is close to the cubic lattice constant (3.986 Å) for NWs based on the cubic and tetragonal phases and to c-lattice constant the

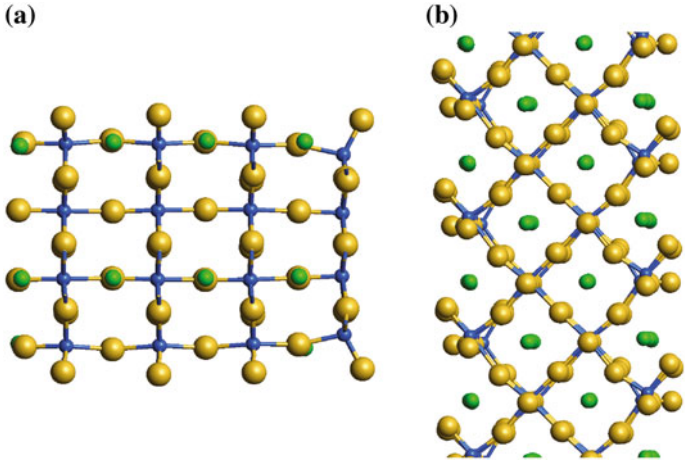

Fig. 8.33 Relaxed structure of a 4×4 NW cut from the orthorhombic phase along the [0 0 1] direction: **a** Cross-sectional (**a**) and (1 0 0) lateral (**b**) view. See Fig. 8.32 for the legend

for orthorhombic phase (5.722 Å). The surface energy of NWs obtained from the orthorhombic phase is slightly less than the surface energy of NWS obtained from the cubic and tetragonal phases. However, the formation energy (with respect to the cubic phase) exhibits a reverse trend. It should be also noted that the formation energy of perovskite-based NWs (Table 8.19) is several times greater than the formation energy of rutile-based NWs (Tables 7.22 and 7.23).

It has been found that ferroelectric displacement is absent in the center of thin (1×1, 2×2) [0 0 1] NWs, but appears in NWs thicker than 3 cubic lattice constants (about 1.2 nm). This result agrees with those found in LDA calculations [4, 7, 108] and those obtained by the application of the Landau-Ginsburg-Devonshire theory [109]. Thus, for 5×5 (tetragonal) and 5×5 (orthorhombic) NWs the displacement of the Ti atom in the center of NW is almost the same as in the bulk phase. Figure 8.34 demonstrates this for NWs cut from the tetragonal phase. Orthorhombic [0 0 1] NWs have a larger atomic relaxation at the NW edges than tetragonal NWS, and they also have nonzero shifts of O atoms along the [1 0 0] direction.

The diameter-dependent properties of ferroelectric NWs have been studied through different theoretical approaches. In [109, 111] the Landau-Ginzburg-Devonshire theory was used to investigate BTO NWs.

The size-dependent ferroelectric properties of BTO nanowires, were studied in [109], taking in account the polarization oriented along the radial direction. It was shown that the Curie temperature, mean polarization, and the area enclosed by the hysteresis loop decrease with the reducing diameter of the nanowire. However, this size effect becomes obvious only when the diameter is below 20 nm. Above this, the ferroelectric behaviors of nanowires are almost the same as those of bulk materials. Furthermore, there exists a temperature-dependent critical diameter for

Table 8.19 Calculated properties of $BaTiO_3$ nanowires

Label	Number of bulk unit cells	NW period a, Å	NW average perimeter P (maximal diameter D), Å	Average tranverse cell constant, Å	E_{form} (kJ/mol)	E_{surf} (J/m^2)	E_g (eV)
[0 0 1] Cubic (P2mm)							
1 × 1	1	3.54	–	–	446	–	5.6
2 × 2	4	3.81	23.6	3.92	246	1.82	3.6
3 × 3	9	3.87	39.4	4.00	167	1.64	2.8
4 × 4	16	3.90	55.2	3.99	127	1.57	2.4
5 × 5	25	3.92	71.0	3.99	103	1.53	2.2
[1 0 0] Tetragonal (Pm)							
1 × 1	1	3.55	–	–	446	–	5.6
2 × 2	4	3.82	23.6	3.93	246	1.83	3.6
3 × 3	9	3.90	39.4(13.9)	4.00	167	1.65	3.0
4 × 4	16	3.94	55.1(19.5)	3.98	126	1.57	2.8
5 × 5	25	3.97	70.9(25.1)	3.98	101	1.52	2.7
[0 0 1] Orthorhombic (Pa)							
1 × 1	1	6.51	–		603	–	6.6
2 × 2	4	5.48	19.4	3.88	245	1.54	5.4
3 × 3	9	5.79	34.6(12.2)	3.84	193	1.46	4.9
4 × 4	16	5.74	48.1(17.0)	3.90	147	1.44	4.1
5 × 5	25	5.73	61.8(21.9)	3.93	119	1.43	3.8

NW label is given in a^2 units for the cubic and tetragonal phases and in axb units for the orthorhombic phase. The maximal diameter $D = P/(2\sqrt{2})$

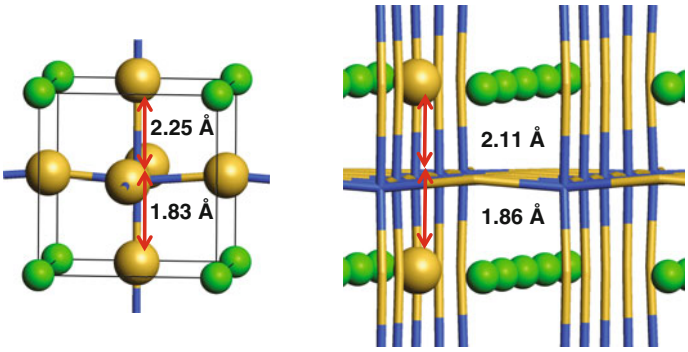

Fig. 8.34 Ferroelectric displacement of Ti atoms along the [0 0 1] direction within a 5 × 5 NW cut from the tetragonal phase

$BaTiO_3$ nanowire, below which the hysteresis loops vanish, and it is 3.6 nm at room temperature.

The diameter-temperature phase diagram and the ferroelectric behaviors of $BaTiO_3$ nanowires were studied also in [111]. Four phases- cubic, tetragonal, orthorhombic and monoclinic-have been obtained. The ferroelectric behaviors of $BaTiO_3$ NWs were studied by taking into account the effects of the gradient energy, the surface energy, the surface tension and the diameter. The ferroelectric phase transition temperatures are all depressed as the diameter decreases. The critical diameter below which the polarization disappears is 0.8 nm at 0 K. Moreover, the magnitude of the polarization and the dielectric constants largely depend on the diameter. Therefore, one can generate a specific direction of polarization by controlling the diameter of the nanowires and thus optimize the physical properties.

The shell-model-based molecular dynamics method was utilized in [113] to investigate the strain effect on the polarization distribution, piezoelectric coefficient, and hysteresis behaviors of $BaTiO_3$ nanowires. The shell model phenomenologically describes the deformation of the electronic structure of an ion due to the interactions with other atoms. In the model, two charged particles, a massive ion-core and a massless ion-shell, are used to describe each atom, enabling the capture of the dipolar moment within each unit cell. By treating the atomic interactions in the molecular dynamics framework, the shell model can save much computation cost compared to the ab initio method. However, the potential parameters in the molecular dynamics system need to be fitted by ab initio calculations, and the computational accuracy is not as high as that of the ab initio DFT methods.

In the MD simulations [113], the system temperature was kept constant at 5 K, which is near absolute zero but particles are still active and can move easily to their proper positions. First the MD simulations were performed with the aim of obtaining the spontaneous stable state, and then a gradually increasing axial strain was applied to the nanowire with sufficient relaxation time. Nanowires with diameters $d = 0.8$, 1.2, and 2.0 nm, were chosen to demonstrate the effect of the axial strain on the axial polarizations. The two critical diameters for the existence of polarization parallel and perpendicular to the axis direction are 0.8 and 1.2 nm, respectively. The nanowire with $d = 0.8$ nm has no spontaneous axial polarization at its freestanding state, but a tensile strain can recover its ferroelectricity. Similar to the definition of the critical diameter, a definition of the critical strain can also be introduced for the $BaTiO_3$ nanowire to characterize the vanishing of ferroelectricity. The critical strain increases gradually with the diameter, and asymptotically tends to a stable value. Since there is no axial spontaneous polarization in nanowires with $d \leq 1.2$ nm, the critical strain is zero in this regime.

The following conclusions were drawn in [113]. (1) A tensile strain enhances the polarization of the nanowire while a compressive strain reduces it. Ferroelectricity can be suppressed when the compressive strain increases to a critical value, i.e. the critical strain. (2) With the increase of the wire diameter, the piezoelectric coefficient increases, and finally approaches the value of the bulk material. (3) A pre-tension strain can induce the emergence of the stepwise hysteresis loop, while a pre-compression strain can lead to the disappearance of the stepwise shape.

(4) The strain effect and size effect play some equivalent roles in the ferroelectric properties of $BaTiO_3$ nanowires.

The effects of strain on the phase transitions of $BaTiO_3$ nanowires were studied in [112] by thermodynamic analysis based on the Landau theory and taking into account three components of polarization. Similar to the strain effect on phase transitions in thin films, the Curie temperature depends on mismatch strain between the nanowire and the substrate. The complete misfit strain-temperature phase diagram shows six stable ferroelectric phases for $BaTiO_3$ nanowires under different strain and temperature conditions. The calculated variation in Curie temperature vs. diameter agrees well with the existing experimental measurements. For $BaTiO_3$ nanowires with zero misfit strain the critical diameter, below which the ferroelectric phases totally disappear, is around 1.0 nm. This result agrees with that found in the ab initio DFT calculations discussed above. Concluding the discussion of BTO nanowires we note that theoretical modeling using different approaches allows one to capture the size dependence of the NW ferroelectric properties. This is important since ferroelectric nanomaterials offer a great potential for the next generation of high density storage devices [108].

References

1. S.S. Nonnemann, E.M. Galio, J.E. Spanier, Appl. Phys. Lett. **97**, 102904 (2010)
2. J.E. Spanier, A.M. Kolpak, J.J. Urban, I. Grinberg, L. Ouyang, W.S. Yun, A.M. Rappe, H. Park, Nano Lett. **6**, 735 (2006)
3. U.A. Joshi, S. Yoon, S. Baik, J.S. Lee, J. Phys. Chem. B **110**, 12249 (2006)
4. G. Geneste, E. Bousquet, J. Junquera, P. Ghosez, Appl. Phys. Lett. **88**, 112906 (2006)
5. Y. Fu, L. Bellaiche, Phys. Rev. Lett. **91**, 257601 (2003)
6. B. Hernandez, K.S. Chang, E.R. Fisher, P.K. Dorhout, Chem. Mater. **14**, 480 (2002)
7. G. Pilania, S.P. Alpay, R. Ramprasad, Phys. Rev. B **80**, 014113 (2009)
8. Y. Mao, S. Banerjee, S.S. Wong, Chem. Commun. **3**, 408 (2003)
9. Y. Mao, S. Banerjee, S.S. Wong, J. Am. Chem. Soc. **125**, 15718 (2003)
10. T. Shimada, S. Tomoda, T. Kitamura, Phys. Rev. B **79**, 024102 (2009)
11. R.A. Evarestov, A.V. Bandura, IOP Conf. Ser.: Mater. Sci. Eng. **23**, 012013 (2011)
12. D. Gryaznov, E. Blokhin, A. Sorokine, E. Kotomin, R. Evarestov, A. Bussmann-Holder, J. Maier, J. Phys. Chem. C **117**, 13776 (2013)
13. R. Wahl, D. Vogtenhuber, G. Kresse, Phys. Rev. B **78**, 104116 (2008)
14. W. Zhong, R.D. King-Smith, D. Vanderbilt, Phys. Rev. Lett. **72**, 3618 (1994)
15. L. Cao, E. Sozontov, J. Zegenhagen, Phys. Status Solidi (A) **181**, 387 (2000)
16. A.A. Sirenko, C. Bernhard, A. Golnik, A.M. Clark, J. Hao Hao, W. Si, X.X. Xi, Nature **404**, 373 (2000)
17. P. Dore, A. Paolone, R. Trippetti, J. Appl. Phys. **80**, 5270 (1996)
18. R.A. Evarestov, Yu.F. Zhukovskii, A.V. Bandura, S. Piskunov, M.V. Losev, J. Phys. Chem. C **115**, 14067 (2011)
19. K.H. Hellwege, A.M. Hellwege (eds.), *Ferroelectrics and Related Substances*, *Landolt-Boornstein*, New Series, Group III, vol. 3 (Springer, Berlin, 1969)
20. M. Takizawa, K. Maekawa, H. Wadati, T. Yoshida, A. Fujimori, H. Kumigashira, M. Oshima, Phys. Rev. B **79**, 113103 (2009)
21. K. van Benthhem, C. Elsasser, R.H. French, J. Appl. Phys. **90**, 6156 (2001)
22. H.C. Chen, C.W. Huang, J.C.S. Wu, S.T. Lin, J. Phys. Chem. C **116**, 7897 (2012)

23. R.A. Evarestov, *Quantum Chemistry of Solids. LCAO Treatment of Crystals and Nanostructures*, 2nd edn. Springer Series in Solid State Sciences, vol. 153 (Springer, Berlin, 2012)
24. M.S. Kim, C.H. Park, J. Korean Phys. Soc. **56**, 490 (2010)
25. V.I. Anisimov, J. Zaanen, O.K. Andersen, Phys. Rev. B **44**, 943 (1991)
26. M. Marques, L.K. Teles, V. Anjois, L.M.R. Scolfaro, J.R. Leite, V.N. Freire, G.A. Farias, E.F. Da Silva Jr, Appl. Phys. Lett. **82**, 3074 (2003)
27. E. Heifets, E. Kotomin, V.A. Trepakov, J. Phys.: Condens. Matter **18**, 4845 (2006)
28. J.L. Servoin, Y. Luspin, F. Gervais, Phys. Rev. B **22**, 5501 (1980)
29. J. Petzelt, T. Ostapchuk, I. Gregora, I. Rychetský, S. Hoffmann-Eifert, A.V. Pronin, Y. Yuzyuk, B.P. Gorshunov, S. Kamba, V. Bovtun et al., Phys. Rev. B **64**, 184111 (2001)
30. W.G. Stirling, J. Phys. C **5**, 2711 (1972)
31. J. Goniakowski, C. Noguera, Surf. Sci. **365**, L657 (1996)
32. G. Zhu, G. Radtke, G.A. Botton, Nature **490**, 385 (2012)
33. R.I. Eglitis, E. Heifets, E.A. Kotomin, J. Maier, G. Borstel, Mater. Sci. Semicond. Process. **5**, 129 (2003)
34. R.A. Evarestov, A.V. Bandura, V.E. Alexandrov, Phys. Status Solidi (B) **246**, 1013 (2006)
35. H.J. Zhang, G. Chen, Z.H. Li, Appl. Surf. Sci. **253**, 8345 (2007)
36. E. Heifets, W.A. Goddard III, E.A. Kotomin, R.I. Eglitis, G. Borstel, Phys. Rev. B **69**, 035408 (2004)
37. R. Eglitis, M. Rohlfing, Phys. Status Solidi (B) **250**, 1 (2013)
38. S. Piskunov, E.A. Kotomin, E. Heifets, J. Maier, R.I. Eglitis, G. Borstel, Surf. Sci. **575**, 75 (2005)
39. E. Heifets, R.I. Eglitis, E.A. Kotomin, J. Maier, G. Borstel, Surf. Sci. **513**, 211 (2002)
40. J. Padilla, D. Vanderbilt, Surf. Sci. **418**, 64 (1998)
41. G. Charlton, S. Brennan, C.A. Muryn, R. McGrath, D. Norman, T.S. Turner, G. Thornton, Surf. Sci. **457**, L376 (2000)
42. E. Heifets, R.I. Eglitis, E.A. Kotomin, J. Maier, G. Borstel, Phys. Rev. B **64**, 235417 (2001)
43. A. Asthagiri, D.S. Sholl, Phys. Rev. B **73**, 125432 (2006)
44. Y.S. Lee, J.S. Lee, T.W. Noh, D.Y. Byun, K.S. Yoo, K. Yamaura, E.T. Muromachi, Phys. Rev. B **67**, 113101 (2003)
45. R. Evarestov, IOP Conf. Ser.: Mater. Sci. Eng. **23**, 012012 (2011)
46. V. Kopsky, D.B. Litvin (eds.), *International Tables for Crystallography*. Subperiodic Groups, vol. E (Kluwer Academic, Dodrecht, 2002)
47. R. Dovesi, V.R. Saunders, C. Roetti, R. Orlando, C.M. Zicovich-Wilson, F. Pascale, B. Civalleri, K. Doll, N.M. Harrison, I.J. Bush, P. D'Arco, M.Llunell, *CRYSTAL09 User's Manual* (University of Torino, Torino, 2010)
48. I. Noel, P. D'Arco, R. Demichelis, C.M. Zicovich-Wilson, R. Dovesi, J. Comput. Chem. **32**, 855 (2010)
49. R.A. Evarestov, Yu.F. Zhukovskii, A.V. Bandura, S. Piskunov, Cent. Eur. J. Phys. **9**, 492 (2011)
50. L.A. LaJohn, P.A. Christiansen, R.B. Ross, T. Atashroo, W.C. Ermler, J. Chem. Phys. **87**, 2812 (1987)
51. S.-O. Kang, J. Choi, I. Hwang, S. Hong, B.H. Park, Y. Kim, S.J. Ahn, K.-S. Yun, J. Korean Phys. Soc. **52**, 466 (2008)
52. G.G. Yadav, G. Zhang, B. Qiu, J.A. Susoreny, X. Ruan, Y. Wu, Nanoscale **3**, 4078 (2011)
53. M.S.J. Marshall, A.B. Becerra-Toledo, L.D. Marks, M.R. Castell, Phys. Rev. Lett. **107**, 086102 (2011)
54. T-Yi Ma, H. Li, T.-Z. Ren, Z.-Y. Yuan, RSC Adv. **2**, 2790 (2012)
55. P. Irvin, J.P. Veazey, G. Cheng, S. Lu, C.-W. Bark, S. Ryu, C.-B. Eom, J. Levy Nanolett. **13**, 364 (2013)
56. Q. Fu, T. He, J.L. Li, G.W. Wang, J. Appl. Phys. **112**, 104322 (2012)
57. T. Matsuda, S. Yamanaka, K. Kurosaki, S. Kobayashi, J. Alloy. Compd. **351**, 43 (2003)
58. J. Kennedy, C.J. Howard, B.C. Chakoumakos, Phys. Rev. B **59**, 4023 (1999)
59. E. Mete, R. Shaltaf, S. Ellialtioglu, Phys. Rev. B **68**, 035119 (2003)

60. R. Terki, H. Feraoun, G. Bertrand, H. Aourag, Phys. Status Solidi (B) **242**, 1054 (2005)
61. I.R. Shein, K.I. Shein, A.L. Ivanovskii, J. Nucl. Mater. **361**, 69 (2007)
62. Z. Feng, H. Hu, S. Cui, C. Bai, Solid State Commun. **148**, 472 (2008)
63. R. Vali, J. Phys. Chem. Solids **69**, 876 (2008)
64. R.A. Evarestov, A.V. Bandura, V.E. Alexandrov, Phys. Solid State **47**, R11 (2005)
65. R.A. Evarestov, A.V. Bandura, V.E. Alexandrov, E.A. Kotomin, Phys. Status Solidi (B) **242**, R11 (2005)
66. R. Vali, Solid State Commun. **145**, 497 (2008)
67. S. Amisi, E. Bousquet, K. Katco, P. Ghosez, Phys. Rev. B **85**, 064112 (2012)
68. J.R. Sambrano, V.M. Longo, E. Longo, C.A. Taft, J. Mol. Struct. (Theochem) **813**, 49 (2007)
69. Y.X. Wang, M. Arai, Surf. Sci. **601**, 4092 (2007)
70. R.I. Eglitis, M. Rohlfing, J. Phys.: Condens. Matter **22**, 415901 (2010)
71. R.I. Eglitis, Ferroelectrics **436**, 5 (2012)
72. R.I. Eglitis, Integr. Ferroelectr. **123**, 26 (2011)
73. A.V. Bandura, R.A. Evarestov, D.D. Kuruch, IOP Conf. Ser.: Mater. Sci. Eng. **49**, 012009 (2013)
74. Z. Wu, R.E. Cohen, Phys. Rev. B **73**, 235116 (2006)
75. W.S. Yun, J.J. Urban, Q. Gu, H. Park, Nano Lett. **2**, 1 (2002)
76. R. Waser, *Nanoelectronics and Information Technology: Advanced Electronic Materials and Novel Devices* (Wiley-VCH, Weinheim, 2003)
77. Z. Wang, J. Hu, A.P. Suryavanshi, K. Yum, M.-F. Yu, Nano Lett. **7**, 2966 (2007)
78. K.-C. Huang, T.-C. Huang, W.-F. Hsieh, Inorg. Chem. **48**, 9180 (2009)
79. Y.-Y. Chen, B.-J. Yu, J.-H. Wang, R.E. Cohran, J.-J. Shyue, Inorg. Chem. **48**, 0681 (2009)
80. Y. Yang, X. Wang, C. Sun, L. Li, J. Nanotechnol. **20**, 055709 (2009)
81. B. Im, U.A. Joshi, K.H. Lee, J.S. Lee, Nanotechnology **21**, 425601 (2010)
82. Y. Yang, X. Wang, C. Sun, L. Li, J. Appl. Phys. **109**, 014109 (2011)
83. M.R.A. Bhuiyan, M.M. Alam, M.A. Momin, M.J. Uddin, M. Islam, Int. J. Mater. Mech. Eng. **1**, 21 (2012)
84. Z.-H. Lin, Y. Yang, J.M. Wu, Y. Liu, F. Zhang, Z.L. Wang, J. Phys. Chem. Lett. **3**, 3599 (2012)
85. X. Ni, F. Wang, A. Lin, Q. Xu, Z. Yang, Y. Qin, Sci. Adv. Mater. **5**, 1 (2013)
86. A. Koka, H.S. Sodano, Nat. Commun. **4**, 2682 (2013)
87. P. Goudochnikov, A.J. Bell, J. Phys.: Condens. Matter **19**, 176201 (2007)
88. R.A. Evarestov, A.V. Bandura, J. Comput. Chem. **33**, 1123 (2012)
89. Yu-S. Seo, J.S. Ahn, J. Korean Phys. Soc. **62**, 1629 (2013)
90. Yu-S. Seo, J.S. Ahn, Phys. Rev. B **88**, 014114 (2013)
91. D.I. Bilc, R. Orlando, R. Shaltar, G.M. Rignanese, J. Iniguez, Ph. Ghosez, Phys. Rev. B **77**, 165107 (2008)
92. G.H. Kwei, A.C. Lawson, S.J.L. Billinge, S.-W. Cheong, J. Phys. Chem. **97**, 2368 (1993)
93. J.W. Edwards, R. Speiser, H.L. Johnston, J. Am. Chem. Soc. **73**, 2934 (1951)
94. R.A. Evarestov, A.V. Bandura, D.D. Kuruch, J. Comput. Chem. **34**, 175 (2013)
95. X.Y. Xue, C.L. Wang, W.L. Zhong, Surf. Sci. **550**, 73 (2004)
96. Y.X. Wang, M. Arai, T. Sasaki, C.L. Wang, Appl. Phys. Lett. **88**, 091909 (2006)
97. R.I. Eglitis, G. Borstel, E. Heifets, S. Piskunov, E. Kotomin, J. Electroceram. **16**, 289 (2006)
98. R.I. Eglitis, D. Vanderbilt, Phys. Rev. B **76**, 155439 (2007)
99. M.-Q. Cai, J.-C. Liu, G.-W. Yang, X. Tan, Y.-L. Cao, W.-Y. Hu, L.-L. Wang, Y.-G. Wang, Surf. Sci. **601**, 1345 (2007)
100. J.M.P. Martirez, E.H. Morales, W.A. Saidi, D.A. Bonnell, A.M. Rappe, Phys. Rev. Lett. **109**, 256802 (2012)
101. H.L. Meyerheim, A. Ernst, K. Mohseni, I.V. Maznichenko, S. Ostanin, F. Klimenta, N. Jedrecy, W. Feng, I. Mertig, R. Felici, J. Kirschner, Phys. Rev. Lett. **108**, 215502 (2012)
102. J.L. Wang, G. Tang, X.S. Wu, Phys. Status Solidi (B) **249**, 796 (2012)
103. B. Meyer, J. Padilla, D. Vanderbilt, Faraday Discuss. **114**, 395 (1999)
104. U.V. Waghmare, J. Indian Inst. Sci. **89**, 9 (2009)
105. B. Yin, S. Qu, J. Appl. Phys. **115**, 074102 (2014)

106. M. Damnjanović, B. Nikolić, M. Milosĕvić, Phys. Rev. B **75**, 033403 (2007)
107. R.A. Evarestov, A.V. Bandura, in *Physics, Chemistry and Applications of Nanostructures*, ed. by V.E. Borisenko, S.V. Gaponenko, V.S. Gurin, C.H. Kam. Proceedings of International Conference Nanomeeting-2013 (World Scientific, 2013), p. 14
108. N.V. Chinh, N.T. Trang, B.T. Cong, P.T.H. Ngat, Proc. Natl. Conf. Theor. Phys. **36**, 131 (2011)
109. J. Hong, D. Fang, Appl. Phys. Lett. **92**, 012906 (2008)
110. A.N. Morozovska, E.A. Eliseev, M.D. Glinchuk, Phys. Rev. B **73**, 214106 (2006)
111. J.H. Qiu, J.N. Ding, N.Y. Yuan, H.X. Cao, X.Q. Wang, Y. Zhou, J. Appl. Phys. **109**, 054103 (2011)
112. J.J. Wang, E.A. Eliseev, X.Q. Ma, P.P. Wu, A.N. Morozovska, L.Q. Chen, Acta Mater. **59**, 7189 (2011)
113. Y. Zhang, J. Hong, B. Liu, D. Fang, Nanotechnology **21**, 015701 (2010)

Chapter 9
Sulfides

The layered transition metal disulfides MS_2 (M = Mo, W, Ti, Zr) have attracted a considerable attention because of their unique electronic features resulting in numerous applications in catalysis, electrochemical intercalation, and hydrogen storage technology [1, 2]. The rapidly developing nanotechnology offers great opportunities to improve the performance of MS_2-based hydrogen storage materials and rechargeable batteries.

The electronic structure comparison between the bulk, monolayered and tubular forms of $Mo(W)S_2$ disulfides is made basing on the results of LCAO DFT (PBE) first-principle calculations.

TiS_2 and ZrS_2 single- and double-wall nanotube first-principles calculations show that nanotubes obtained by rolling up the hexagonal crystalline layers with octahedral 1T morphology are the most stable.

The strain energy of TiS_2 and ZrS_2 nanotubes is greater than that of the similar TiO_2 and ZrO_2 nanotubes; however, the formation energy of the disulfide nanotubes is considerably less than that of the dioxide nanotubes.

The distance and interaction energy between the single-wall components of the double-wall nanotubes is proved to be close to those between the layers in layered crystals. The analysis of the relaxed nanotube shape using the radial coordinate of the metal atoms demonstrates a small but noticeable deviation from the completely cylindrical cross-section of the external walls in the armchair-like double-wall nanotubes.

9.1 MoS_2 and WS_2

The quasi-two-dimensional (2D) character of the transition metal disulfides stems from their arrangement in a stacking of hexagonally packed three-plane S–M–S layers, which are weakly bonded to one another by van der Waals-type forces [3]. These compounds are known to exist in two main polymorphs—with an octahedral (o) and trigonal prismatic (t) coordination of the metal atoms in the layers (see Fig. 9.1).

© Springer-Verlag Berlin Heidelberg 2015

R.A. Evarestov, *Theoretical Modeling of Inorganic Nanostructures*,
NanoScience and Technology, DOI 10.1007/978-3-662-44581-5_9

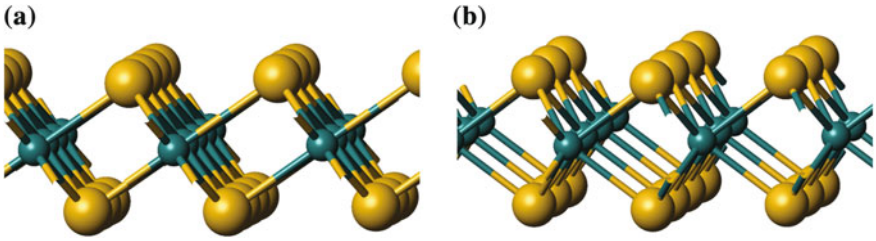

Fig. 9.1 Hexagonal layers with octahedral o (**a**) and trigonal prismatic t (**b**) coordination of the metal atoms. Legend: *small dark balls*—metal atoms, *large light balls*—sulfur atoms

Depending on the stacking sequence of the layers, a further division into several polytypes can be made. These are referred to as the 1T, 2H, 3R, 4H or 6R stacking polytypes [3]. The number in this abbreviated notation denotes the number of S-M-S layers per unit cell, and T, H and R mean trigonal, hexagonal and rhombohedral crystal systems, respectively.

9.1.1 Bulk and Nanolayers

2H–Mo(W)S_2 crystallizes in the hexagonal structure with the space group $P6_3/mmc$ (D^4_{6h}), see Chap. 2. The primitive unit cell consists of a hexagonal plane of the Mo(W) atoms sandwiched by two hexagonal planes of the S atoms. The unit cell contains two alternating layers with an ABAB stacking along the c axis, see Fig. 9.1. The structure of the bulk 2H–Mo(W)S_2 is similar to that of graphite, consisting as it does of S–Mo(W)–S layers bound by weak, van der Waals type interactions.

The electronic structure DFT calculations of 2H–Mo(W)S_2 bulk crystals have been performed for MoS_2 [4–10], WS_2 [11–13] or for both simultaneously [14, 15]. Table 9.1 shows the calculated structure parameters and band gaps in comparison with the experimental data. Table 9.1 gives the results of the DFT calculations of 2H–Mo(W)S_2 bulk crystals, using different exchange correlation functionals (local LDA, semi-local GGA(PW91, PBE), hybrid PBE0).

Figure 9.2 shows the band structure of MoS_2 and WS_2 bulk crystals calculated in [14] at the DFT (PBE, PBE0) level using LCAO basis sets. The sulfur atoms were calculated using full-electron basis sets, while for the metal elements the large-core ECP was employed, which leaves only the valence electrons to be explicitly described on the metal sites: 4d and 5sp for Mo, 5d and 6sp for W.

Figure 9.2 demonstrates that bulk MoS_2 and WS_2 are indirect-gap semiconductors. The fundamental band gap originates from the transition from the top of the valence band situated at Γ to the bottom of the conduction band halfway between the Γ and K high symmetry points. The optical direct band gap is situated at the K point. These results are similar in PBE and PBE0 computations. However, there is a significant difference in the band gap values calculated using PBE and PBE0

Table 9.1 Lattice parameters (Å), and band gaps E_g (eV) of 2H–Mo(W)S_2 bulk crystals. The experimental values of the lattice parameters a, c and the band gap E_g are taken from [16] and [17], respectively

Crystal reference	Theory			Experiment		
	a	c	E_g	a	c	E_g
MoS_2						
PBE [14]	3.173	12.696	1.2	3.160	12.595	1.23
PBE0 [14]	3.143	12.583	2.3			
LDA [4]	3.160	12.295	0.77			
LDA [5]	3.160	12.290	0.75			
PW91 [18]	3.169	12.207	0.8			
PBE [8]	3.199	12.493	0.79			
WS_2						
PBE [14]	3.164	12.473	1.3	3.154	12.362	1.35
PBE0 [14]	3.139	12.380	2.4			
LDA [12]	3.171	12.359	–			

functionals. One can see that the PBE functional performs better. The fundamental indirect band gap of bulk MoS_2 is 1.23 eV [17] and the band gap of 1.2 eV agrees perfectly at the PBE level, while it is overestimated by around 1 eV when one uses PBE0 hybrid functional. Similarly, the band gap of WS_2, with the experimental value of 1.35 eV [17] is 1.3 eV at the PBE level and 2.4 eV when PBE0 is used. The experimental direct band gaps (at the K points) of MoS_2 and WS_2 are 1.74 and 1.79 eV, respectively [17]. DFT (PBE) calculations [14] give values of 1.8 and 1.9 eV for MoS_2 and WS_2, respectively. Again, the PBE0 results are overestimated by around 1 eV. However, the PBE band gap calculation results depend on the crystal under consideration. As is seen from Tables 7.5 and 7.6, for rutile and anatase the PBE calculations underestimate the band gap by 1.3–1.2 eV giving the values of 1.74 and 1.98 eV, respectively (the experimental band gap values are 3.03 and 3.18 eV for rutile and anatase, respectively).

Figure 9.3 shows the density of states (DOS) of MoS_2, calculated in [8] at the DFT (PBE) level with the PW basis set at a pressure of 0 GPa. There are six main regions (A, B, C, D, E, F) in the DOS curve of MoS_2.

The region A in the lowest energy part of the DOS curve is derived from the Mo(4s) states, which are localized and contribute little to the bonding of Mo–S. For the region B, the DOS mainly originates from the Mo(4p) states, which are localized and also contribute little to the bonding of Mo–S. For the region C, the DOS mainly originates from the S(3s) states and Mo(4d), with small contributions from the Mo(4p) and S(3s) states. For the region D, the DOS mainly originates from the Mo(4d) states and S(3s), with small contributions from the Mo(4p) and S(3p) states. Above the Fermi level, for the region E, the DOS mainly originates from the Mo(4d) and S(3p) states, with small contributions from the Mo(5s) and S(3s) states.

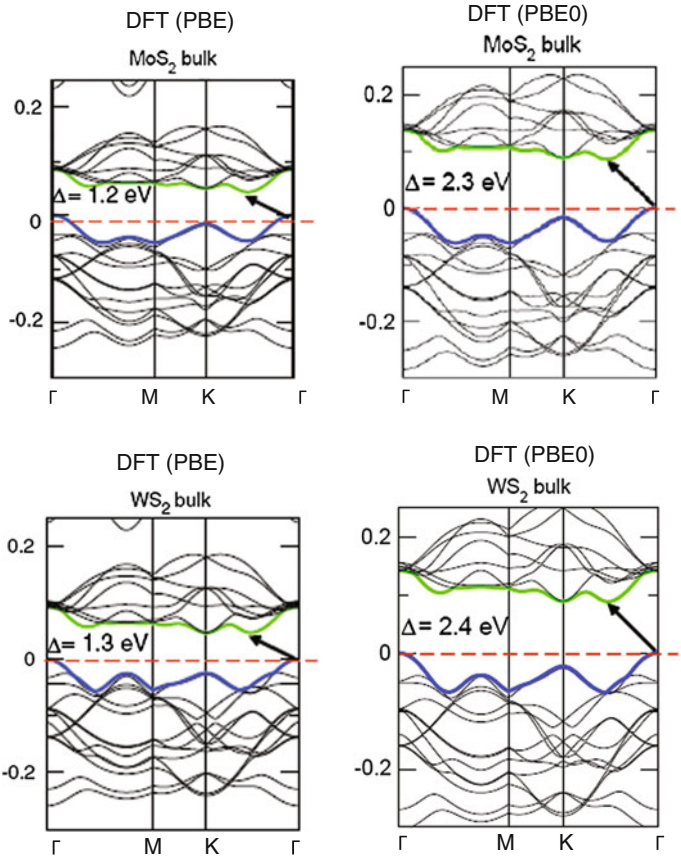

Fig. 9.2 Band structure of bulk MoS_2 and WS_2 calculated at the DFT (PBE) and DFT (PBE0) levels [14]. The *horizontal dashed lines* indicate the Fermi level E_F (Hartree). The *arrows* indicate the fundamental band gap

For the region F, the DOS mainly originates from the Mo(5s) and S(3p) states, with a small contribution from Mo(4d). The WS_2 DOS is similar to that of the MoS_2, but 5s, 5p, 4d Mo states are replaced by the 6s, 6p, 5d W states.

To investigate the influence of quantum confinement on the transition metal sulfides properties single- and few-layered MoS_2 and WS_2 were synthesized and studied experimentally by angle resolved photoelectron and optical spectroscopy [11, 19–22], by chemical methods [3, 23], by laser-thinning [24] and STM [25]. The theoretical studies of these systems were performed by DFT calculations of mono- and multi-layer models [4, 7, 10, 12, 14, 15, 26–35].

$Mo(W)S_2$ monolayers (ML) have hexagonal lattices with honeycomb structures (1H–$Mo(W)S_2$) similar to graphene and consist of two 2D parallel triangular lattices of the S atoms separated by the same lattice of the Mo(W) atoms translated by 1/3 of

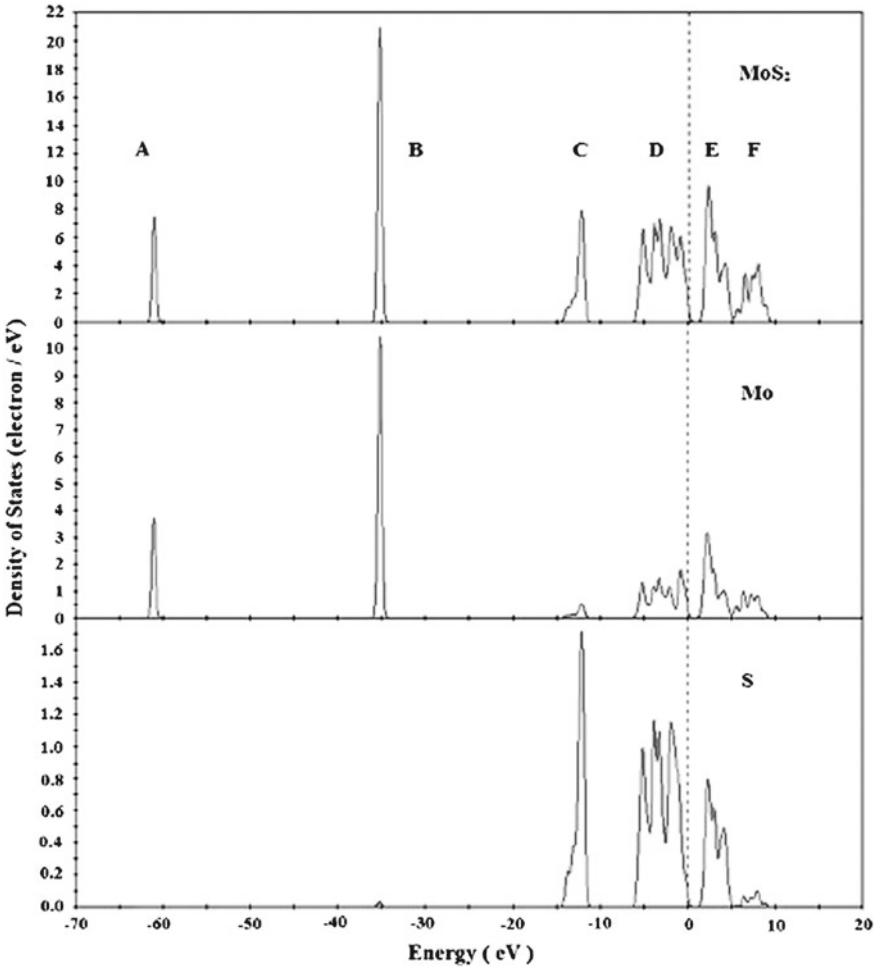

Fig. 9.3 Density of states of bulk MoS_2 (Reprinted figure with permission from Wei et al. [8], Copyright (2010) by the Elsevier B.V. All rights reserved)

the unit-cell diagonal. The S–Mo(W)–S monolayer consists of 3 atomic planes, while the graphite layer (graphene) consists of one atomic plane of carbon atoms. The layer group DG80 (p6/mmm) is the symmetry group of graphene. The layer group DG78 ($P\bar{6}m2$) is the symmetry group of the $Mo(W)S_2$ monolayer [36]. The multilayers with even numbers of S–M–S layers belong to the layer group DG72 ($P\bar{3}m1$) with inversion symmetry. The multilayers with odd numbers of S–M–S layers belong to the layer group DG78 ($P\bar{6}m2$) without inversion symmetry. The corresponding BZ is hexagonal. The bulk WS_2 valence band structure was determined experimentally by angle resolved photoelectron spectroscopy and theoretically by augmented spherical waves (ASW) [11] band structure calculations as based on the density functional

theory [11]. The experimental band structure of a single layer was determined from an electronically decoupled film prepared on a single crystalline graphite substrate by metalorganic van der Waals epitaxy. Good agreement between the experimental and calculated band structure was observed both for the bulk crystal WS_2 and the single layer. The experimental single layer band structure shows some differences compared to band structure calculations using bulk atomic positions within the layer. The authors of [11] concluded that the relaxation of the single layer occurs as a consequence of the missing interlayer interactions so that the valence band maximum for the single layer is located at the K point of the Brillouin zones and when a bulk WS_2 is thinned to a monolayer there is transition from an indirect to a direct gap semiconductor.

The same conclusion was made after Mo(W)S_2 mono- and multi-layers DFT calculations performed using different basis sets: plane waves (PW) [7, 12, 28, 29, 34, 35], augmented plane waves (APW) [31], and LCAO [4, 15, 26]. Quasiparticle self-consistent GW calculations [27, 32] give correct band gaps both for the bulk and layer structures.

DFT (LDA) PW calculations [29] of phonons in bulk, single-layer and few-layer Mo(W)S_2 confirm the stability of the single-layer structure. Indeed, it is seen from Fig. 9.4 that for both crystals the soft phonons with imaginary frequencies are absent at the single-layer phonon dispersion curves.

The electronic properties of Mo(W)S_2 layered structures with respect to the slab thickness of the systems were studied in [14]. Bulk structures as well as mono- and poly-layers were considered using LCAO DFT(PBE, PBE0) computations. Figures 9.5 and 9.6 show the band structures of MoS_2 and WS_2, respectively, calculated using the PBE0 functional and going from bulk to a monolayer. It is seen that as the number of layers decreases, the fundamental indirect band gap increases and becomes so high in the monolayer that the material changes into a 2D direct band gap semiconductor. At the same time, the optical direct gap (at the K point) stays almost unchanged (independent of the slab thickness) and close to the value of the optical direct band gap (at the K point) of a bulk system.

These results are shown in Fig. 9.7, where the band gaps of MoS_2 and WS_2 are plotted against the number of layers.

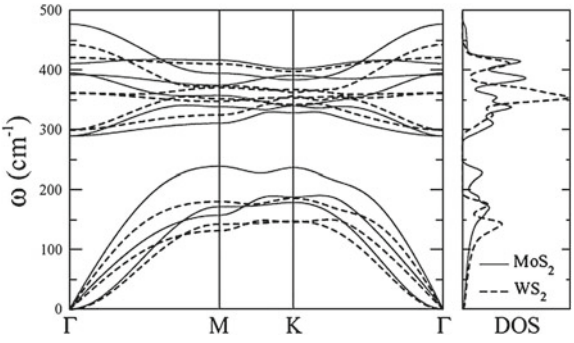

Fig. 9.4 Phonon dispersion curves for single-layer MoS_2 (*solid lines*) and WS_2 (*dashed lines*). The density of states is depicted in the *right-hand panel* [29]

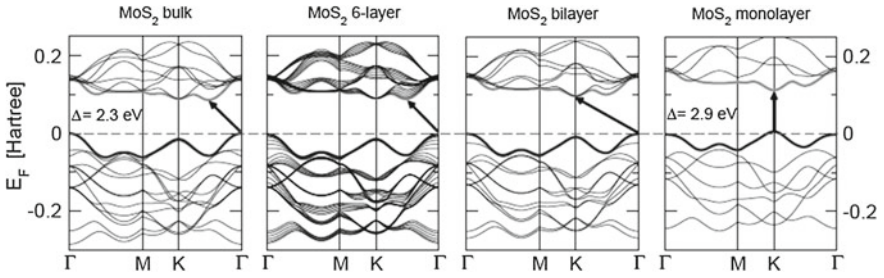

Fig. 9.5 Band structures of bulk MoS_2, its monolayer and polylayers calculated as the DFT (PBE0). The *horizontal dashed lines* indicate the Fermi level. The *arrows* indicate the fundamental band gap (direct or indirect) for a given system [14]

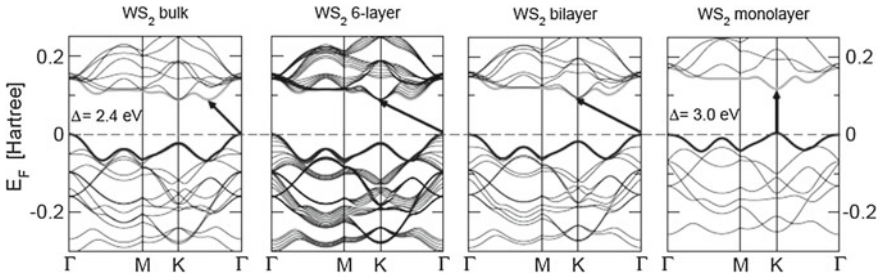

Fig. 9.6 Band structures of bulk WS_2, its monolayer and polylayers calculated as the DFT (PBE0). The *horizontal dashed lines* indicate the Fermi level. The *arrows* indicate the fundamental band gap (direct or indirect) for a given system [14]

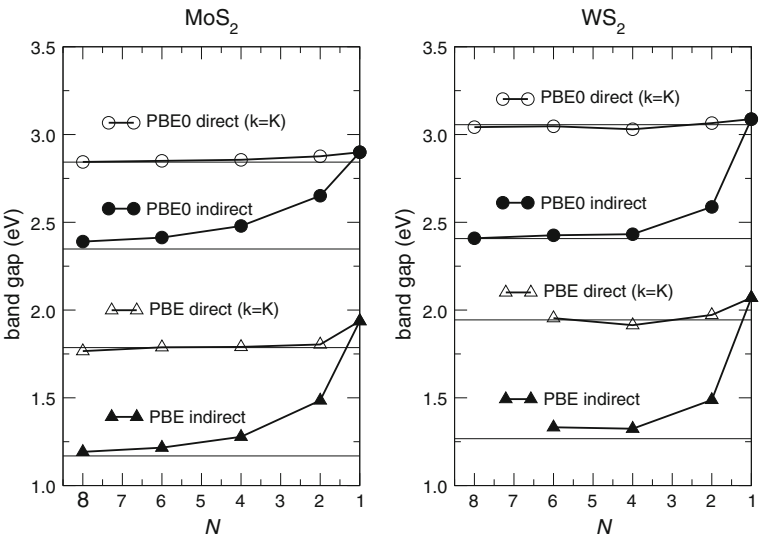

Fig. 9.7 Calculated direct and indirect band gap values of MoS_2 and WS_2 N-layer slabs. The *horizontal solid lines* indicate the band gaps of bulk structures [14]

Decreasing the number of layers causes a progressive shift in the PBE indirect gap up to 1.9 and 2.1 eV for MoS_2 and WS_2, respectively. The change in the PBE indirect gap energy is significantly larger than that of the direct gap (at the K point), which increased by around 0.1 eV. Similar results were found in [19] for MoS_2.

The band gaps of bulk structures are in the range of near infrared. Reducing the number of monolayers in the material to just a few layers causes a blue shift in the absorption features and shifts the band gap to the range of the visible light. These materials can therefore be interesting in the field of optoelectronics. These unusual electronic structures of MoS_2 and WS_2, and the resulting optical properties come from the d-electron orbitals that dominate the valence and conduction bands (see Figs. 9.8 and 9.9 for MoS_2 partial density of states, obtained in PBE and PBE0 calculations, respectively).

The projected density of states (PDOS) of MoS_2 shows that the p-states of sulfur atoms hybridize with the d-states of the transition metal atoms at the top of the valence band and the bottom of the conduction band. The core states are dominated by the s-orbitals of the chalcogenide atom (see Fig. 9.3). The results from [14] at the PBE level support the conclusion made from the photoluminescence study [23] for MoS_2: novel physical phenomena can emerge in low-dimensional nanomaterials. Bulk MoS_2, a prototypical metal dichalcogenide, is an indirect bandgap semiconductor with negligible photoluminescence. When the MoS_2 crystal is thinned

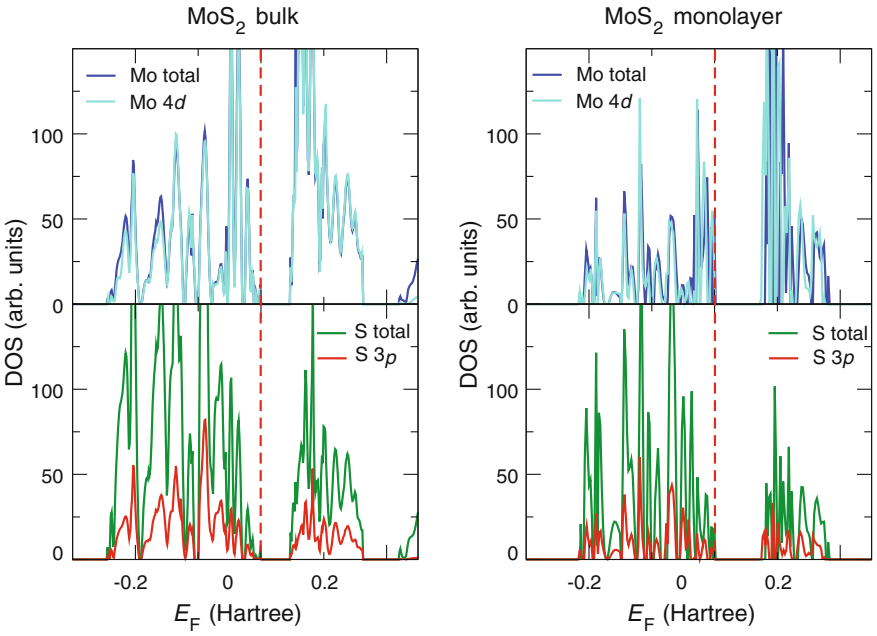

Fig. 9.8 Partial density of states of bulk MoS_2 and its monolayer calculated as the DFT (PBE). The projections of the Mo and S atoms are given together with the contributions from the 4d and 3p orbitals of Mo and S, respectively. The *vertical dashed lines* indicate the Fermi level [14]

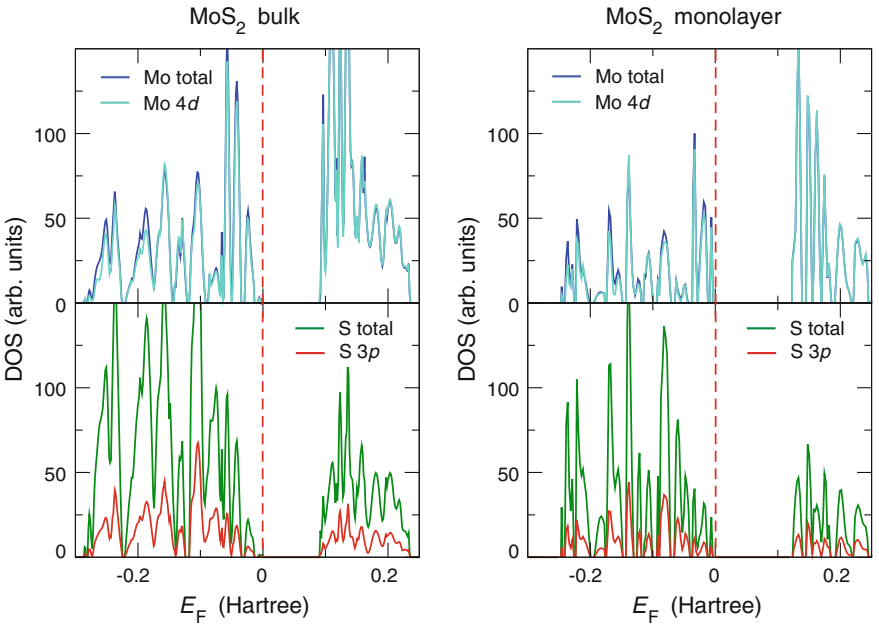

Fig. 9.9 Partial density of states of bulk MoS_2 and its monolayer calculated as the DFT (PBE0). The projections of the Mo and S atoms are given together with the contributions from the 4d and 3p orbitals of Mo and S, respectively. The *vertical dashed lines* indicate the Fermi level [14]

to a monolayer, however, a strong photoluminescence emerges, indicating an indirect to direct bandgap transition in this system. This observation shows that quantum confinement in layered d-electron materials like MoS_2 provides new opportunities for engineering the electronic structure of matter at the nanoscale with a potential application to optical devices. The results of theoretical modeling [14] show that WS_2 has very similar properties and can be considered as an alternative material.

9.1.2 Nanotubes

Taking advantage of the structural analogy between graphite and inorganic two-dimensional (2D) layered compounds (see Fig. 9.10), Tenne et al. [37] were pioneers in the preparation of concentric polyhedra and/or nanotubes of $Mo(W)S_2$ layered materials through a gas-phase reaction of H_2S with the respective metal oxides at elevated temperatures and under reducing atmosphere. The production of macroscopic quantities of WS_2 nanotubes was reported later through a modification of the gas-phase reaction, where W/WO_x was heated under a mixture of the Ar and H_2S gases. Extensive experimental studies [38–45] demonstrated that fullerene-like nanostructures and nanotubes (NTs) produced from layered materials have in common a stable, closed and hollow structure.

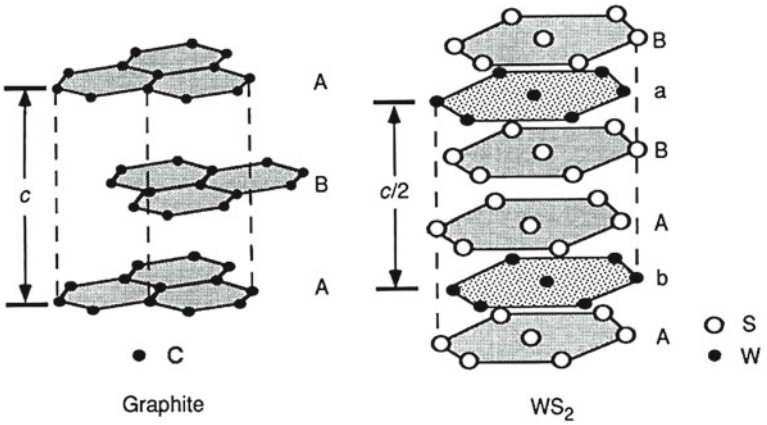

Fig. 9.10 The layered structure of graphite and WS_2. The graphite is composed of a stacking of single layers in which the bonding between the carbon atoms is sp^2. A recurrent feature motif in WS_2 is a sandwich of three sheets S–W–S with covalent tetrahedral W–S bonds and weak van der Waals bonds holding the adjacent sulphur sheets together [37]

The symmetry based properties of transition metal dichalcogenide nanotubes were studied in [36] using the line groups theory, described in Chap. 2. As we mentioned above, the multilayers with even numbers of S–M–S layers belong to the layer group DG72 ($P\bar{3}m1$); the multilayers with odd numbers of S–M–S layers belong to the layer group DG78 ($P\bar{6}m2$). In particular, the –S–M–S– monolayer symmetry layer group DG78 ($p\bar{6}m2$) is symmorphic, with the isogonal point group D_{3h} and the horizontal plane coinciding with the metal atoms plane, see Fig. 9.1.

From Table 2.10 showing the rolling up correspondence of the line and diperiodic (layer) groups one can see that the line groups of families 1, 4 and 8 correspond both to DG78 and DG72. The corresponding NT chiral vectors are (n_1,n_2)—for family 1, (n,n), (−n,2n), (−2n,n)—for family 4 and (n,0), (0,n), (n,−n)—for family 8. Figure 9.11 shows armchair (8,8) (family 4 line group) and zigzag (14,0) (family 8 line group) nanotubes rolled up from MoS_2 three-sheet single layer.

The electronic structure comparison between the bulk, monolayered and tubular forms of $Mo(W)S_2$ disulfides was presented in [15] using LCAO DFT (PBE) first-principle calculations. Figure 9.12 shows the atomic structures of the layered and tubular structures of $Mo(W)S_2$. The bulk, layers and nanotube calculations were carried out employing 3D, 2D and 1D periodic boundary conditions, respectively, as implemented in the CRYSTAL09 code [47].

Calculations [15] were performed for (n,0) zigzag and (n,n) armchair $Mo(W)S_2$ nanotubes as a function of n. The tube diameters (d) range between 12.4 and 24.9 Å for zigzag NTs, and 19.2 and 42.3 Å for armchair ones. These correspond to the index n = 11–24. The structural properties of different NTs with those of bulk/monolayered systems were compared in [15]. The lattice parameter a changes for zigzag forms and increases by around 0.14 Å when increasing d. The zigzag topologies provide longer bonds (up to 0.3 Å depending on the tube diameter) than the armchair ones.

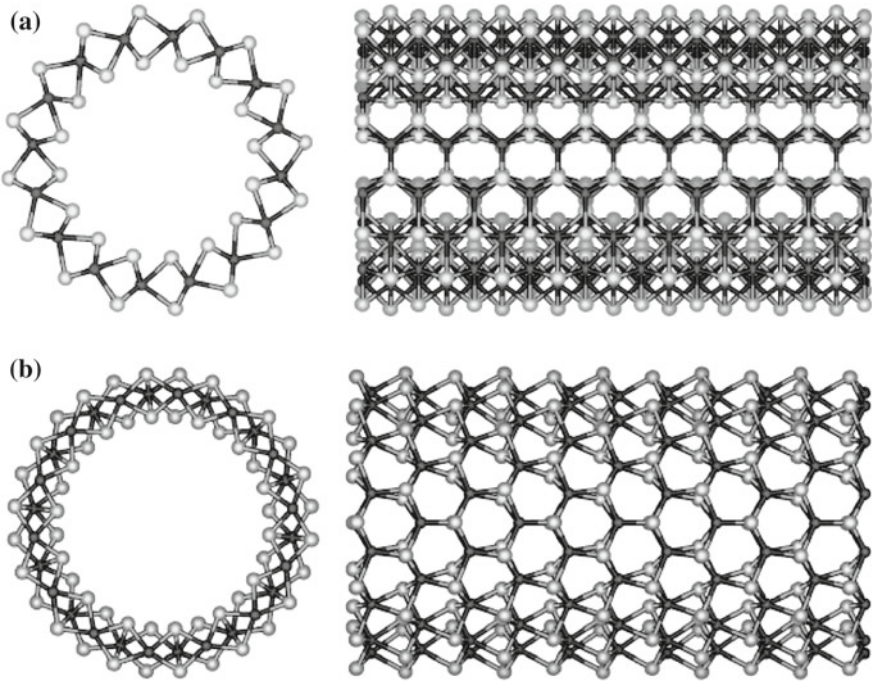

Fig. 9.11 Armchair (8,8) MoS_2 nanotube with the symmetry of the *line* group from family 4 (*top*) and zigzag (14,0) MoS_2 nanotube with the symmetry of the *line* group from family 8 (*bottom*). *Light* atoms are S; *dark* atoms are Mo [46]

The optimized bond lengths of tubes are slightly different from those of the planar sheets.

Layered structures have one type of Mo(W) S bond lengths, while in the tubular form one can distinguish the inner $Mo(W)_i$ and the outer $Mo(W)_o$. Rolling up a monolayer into a nanotube causes the elongation of the outer bond lengths by around 0.05–0.14 Å for zigzag and 0.01–0.02 Å for armchair types. On the other hand, the inner bonds shrink by 0.01 Å for both zigzag and armchair forms. The outer bonds are longer than the inner ones by 0.02–0.07 Å for armchair NTs and by 0.07–0.15 Å for zigzag tubes for both disulfides (depending on the tube diameter). These bond lengths behave differently in the tubes of the various size. With the tube diameter increasing, the inner bond lengths decrease or increase for armchair and zigzag forms, respectively. The outer bond lengths in zigzag NTs change for different chiralities, more specifically, they decrease by around 0.09 Å with the tube diameter increasing from (11,0) to (24,0) NT and stay almost unchanged in armchair structures. The metal–metal distances (within the tube circumference) are generally longer for tubular forms and decrease with increasing the diameter of the NTs. Going from (11,0) to (24,0) NT, these values decrease by around 0.06 Å in the armchair configuration and by around 0.30 Å for the zigzag. For small tube diameters, the S–S bonds are

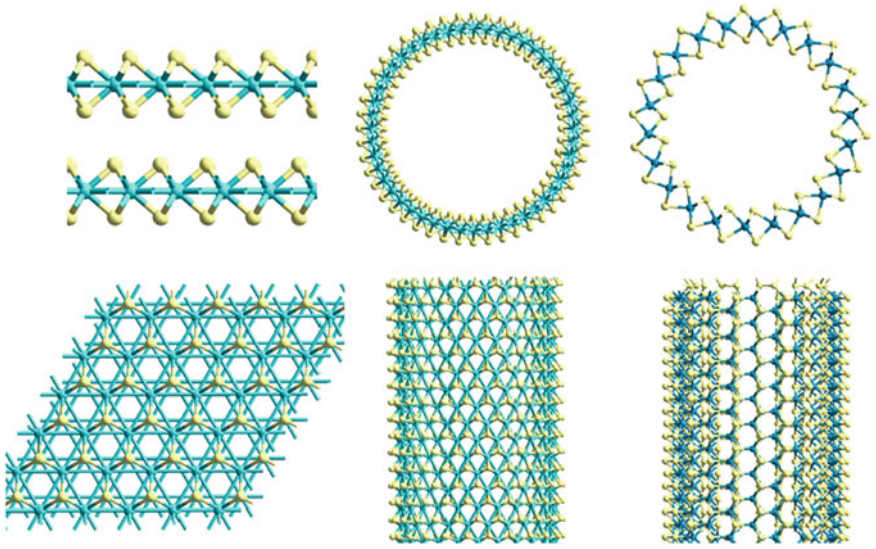

Fig. 9.12 The atomic structures of layered (*left*) and tubular (*middle* zigzag and *right* armchair) transition-metal disulfides of the Mo(W)S_2 type. The cross section (*top*) and the hexagonal sheets (*bottom*) are shown for both types of the systems [15]

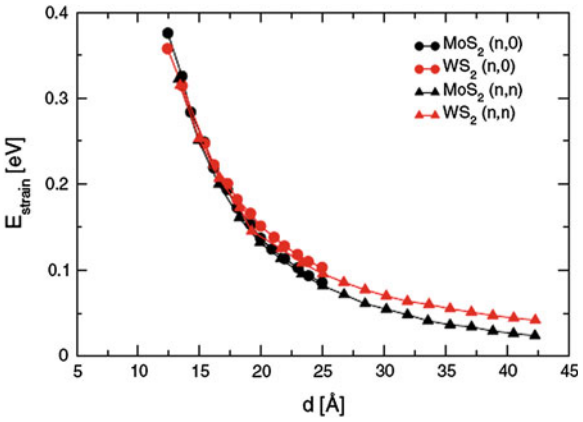

Fig. 9.13 Calculated strain energies of zigzag and armchair Mo(W)S_2-NTs as a function of the tube diameter (d). The energies are given per atom and related to the infinite monolayers of the corresponding disulfides [15]

shorter than the corresponding bonds in the layered structures, but they increase with increasing d, almost approaching the values for a bulk or a monolayer. The same results are found for both disulfides.

Figure 9.13 shows strain energies of Mo(W)S_2 NTs calculated in [15]. It is seen that the strain energies of armchair nanotubes are just slightly more favorable than

the zigzag for a given diameter for both disulfides. Also, the molybdenum forms are more stable than the tungsten ones for diameters larger than 15 Å, and this difference grows with the size of the tube. The strain energies originating from rolling up a monolayer to a tube, are one order of magnitude larger than in the case of single-walled carbon nanotubes (SWCNTs), but decrease for larger tube diameters. The result is quite understandable, as it is much easier to fold a monoatomic graphene layer than a triatomic disulfide layer.

The electronic structures of $Mo(W)S_2$ and the resulting optical properties come from the d-electron orbitals that dominate the valence and conduction bands. As we wrote in the preceding subsection, the projected DOS (PDOS) of bulk $Mo(W)S_2$ shows that the p-states of sulfur atoms hybridize with the d-states of the transition metal atoms at the top of the valence band and the bottom of the conduction band. The core states are dominated by the s-orbitals of the chalcogenide atom. The PDOS of the tubular structures do not change significantly from those of the layered forms.

Folding a monolayer of $Mo(W)S_2$ into a nanotube affects the Mulliken atomic charges mostly for small diameter sizes. Generally, the zigzag and armchair forms have the same values of q for a given tube diameter. The atomic charges approach a constant value (independent of d) for diameters larger than 25 Å. Moreover, tungsten nanotubes deviate from the layered structures much more than the molybdenum ones. The charge of metal atoms becomes less positive when the tube diameter increases. For the smallest tube sizes, these values are closer to the bulk form, and for d larger than 15 Å, they approach the charges of the monolayers.

As follows from the results of calculations [15], the band structures of zigzag NTs resemble those of the corresponding SWCNTs. However, in contrast to SWCNTs, all the $Mo(W)S_2$-NTs are semiconducting. While the band structures of (n, 0) NTs can be related to those of a monolayer, with a direct band gap, the band structures of (n, n) NTs are more related to the bulk, especially for larger tube diameters. For a given tube diameter, the band gap values of zigzag NTs are larger than those of armchair NTs. These values, in contrast to SWCNTs, increase with increasing tube diameter, going from values close to those of bulk systems (for small d) and approaching those of monolayers (for large tube sizes).

DFTB calculations of $Mo(W)S_2$ NTs were made in [46, 48]. These calculations can not be referred to as first-principles ones. In particular, the repulsive potential in the DFTB calculations [46] was obtained by fitting DFT energies for the corresponding dimers (Mo–Mo, Mo–S, S–S) as reference systems. However, this treatment gave DFTB optimized bond lengths for MoS_2 triple layers within an accuracy of 2 %, compared to the experimental data for bulk MoS_2. More, the results of the DFTB calculations for $Mo(W)S_2$ NTs are in good agreement with those obtained in the first-principles calculations [15]. Indeed, the calculated strain energies scale as $E_s = C/d^2$, where d is the tube diameter and C is a constant. In both first-principles and DFTB calculations the strain energies of armchair nanotubes are just slightly more favorable than the zigzag for a given diameter for both disulfides. The strain energy factor C (in eV/Å^2) for armchair and zigzag MoS_2 NTs on the DFTB level was 57.613 and 61.5206, in good agreement with the values 54.497 and 57.504 in the first-principles calculations [15].

The DFTB calculations [48] of the electronic properties and optical spectra of single-walled Mo(W)S_2 nanotubes used line group full symmetry, which allowed the calculation of the optical conductivity tensor and polarized optical absorption as a function of the diameter and the chiral angle of the nanotubes including large diameter tubes and highly chiral tubes. It was predicted that, due to the symmetry transformation properties of the relevant electronic states, fluorescence is not expected in the metal dichalcogenide tubes. In accordance with the measurements, the calculations show a red shift of the absorption peaks as the tube diameter increases. Also, it is found that curvature strain induces a strong chiral angle dependence of the absorption spectra.

The DFTB theoretical studies of the mechanical behavior of Mo(W)S_2 nanotubes were made in [49–51]. In [49], both tensile tests and buckling experiments of individual WS_2 nanotubes were carried out in a high-resolution scanning electron microscope. The tensile tests of MoS_2 nanotubes were also simulated by means of DFTB-based molecular dynamics. The combination of these studies provides a microscopic picture of the nature of the fracture process, giving an insight into the strength and flexibility of WS_2 nanotubes. Fracture analysis indicates that the strength of such nanotubes is governed by a small number of defects. A fraction of the nanotubes attained a theoretical strength indicating the absence of defects.

The mechanical behavior of different types of single-walled and double-walled MoS_2 nanotubes when subjected to external compressive, tensile and torsional loads was investigated in [50] using classical (force-field) molecular dynamics simulations. The forces on the atoms are determined using a reactive empirical bond-order potential parameterized for Mo–S systems. The MD simulations predict values for the Youngs modulus and torsional shear modulus of the nanotubes that are in good agreement with previous studies using different methods. Specifically, no dependence on the length and little dependence on the diameter were predicted over the range of dimensions considered in these simulations (10–30 nm lengths and 5–10 nm diameters). Simulations [50] report on the elastic properties of different MoS_2 nanotube systems as well as the interrelationships between the buckling behavior and the structural parameters of the nanotubes, such as length, diameter, chirality, and number of walls. These simulations [50] predict that the most important factor influencing the mechanical response is the number of walls present and, to a lesser extent, the diameters of the nanotubes, with the other structural parameters predicted to have little effect on the results over the range investigated. These findings are consistent with the reported density functional theory calculations and experimental data for WS_2 and MoS_2 nanotubes.

The results from systematic DFTB investigations of the structural and mechanical properties of MoS_2 and TiS_2 nanotubes in comparison to each other, to carbon nanotubes, and to the corresponding experimental results are presented in [51]. The nanotubes Youngs moduli, Poisson ratios and shear moduli as functions of diameter and chirality were obtained. It was found that the strain energy of all the systems investigated is chirality-independent. When the systems were compared, it turned out that all Mo(Ti)S_2 nanotubes have larger strain energies than carbon NTs. MoS_2 nanotubes have the largest strain energy. For small tubes ($\leq$4 nm), Youngs moduli,

Poisson ratios and shear moduli strongly depend on the tube diameter. With increasing diameter, these properties approach values corresponding to those of infinite monolayers. Additionally, the elastic constants are chirality-dependent. The elastic constants of the chiral nanotubes lie essentially in between those found for the zigzag and armchair tubes. The MD tensile tests were simulated up to the rupture of the tubes. It was found that MoS_2 nanotubes can be stretched up to 16 % and TiS_2 nanotubes up to 6–8 %, before they break. In comparison, carbon nanotubes show a larger deviation from the linear stress–strain behavior and a much higher tensile stress, while TiS_2 nanotubes can be stretched only half as much as MoS_2 nanotubes.

The influence of structural defects on the elastic constants and the stress–strain behavior of nanotubes was studied in [51]. A set of defects was chosen by removing several atoms and calculating the respective properties. The consideration of the selected defects in the nanotubes changes their Youngs moduli and Poisson ratios to different extents. For defect-free MoS_2 nanotubes, good agreement between the calculated and the experimentally determined Youngs moduli and stress–strain behavior was found. By simulating tensile tests with MoS_2 nanotubes that exhibit structural defects, larger deviations between the calculated and experimental stress–strain behavior were found. This result indicates that synthesized MoS_2 nanotubes may have a defect concentration smaller than that of CNTs.

The structure, stability and electronic properties of composite $Mo_{1-x}Nb_xS_2$ nanotubes were studied in [52] using the DFTB method. It was found that composite nanotubes (with Nb contents of 5, 10 and 25 %) are more stable than the corresponding pure tubes. This effect was even stronger for larger tube diameters. At room temperature the Nb dopant tends to arrange itself in an ordered manner along the tube axis, whereas the site entropy contribution favors a random distribution at high temperatures. All the doped nanotubes studied in [52] have metallic properties, independent of their chirality, diameters or the substitutional patterns. The density of states close to the Fermi level of Nb-substituted MoS_2 nanotubes can be varied in a wide range by the degree of doping.

The Coulomb interactions and the problem of stability of inorganic MX_2 zigzag (n,0) and armchair (n,n) nanotubes were studied in [53], where a method for calculating the Coulomb contribution to the strain energy of inorganic NTs composed of oppositely charged coaxial atomic cylinders (X–M–X), was suggested. This method makes it possible to describe the differences in the stability of inorganic NTs as a function of the ionicity of bonding and the atomic structure of the system. The numerical estimates performed in [53] show that the stability of inorganic NTs will generally decrease with an increase in the ionicity of their bonds. The method suggested can be used for calculating the Coulomb contribution to the strain energy and estimating the stability of inorganic nanostructures with a different morphology, e.g., nanorolls, fullerene-like molecules, etc. The following conclusion was made in [54]: among sulfide NTs, the most unstable are the tubes with the octahedral coordination of metal atoms (TiS_2, ZrS_2, HfS_2) and the most stable are the tubes with the trigonal-prismatic coordination of metal atoms (MoS_2, WS_2). The NTs based on ionic compounds (metal dichlorides) are less stable than the disulfide NTs.

Electron microscope images and diffraction data were interpreted in [55] to indicate bundles of sub-nanometer diameter single-wall MoS_2 nanotubes. After experimental characterization, the structure was attributed to an assembly of armchair nanotubes with interstitial iodine. Using first-principles PW DFT (PBE) total energy calculations, bundles of MoS_2 nanotubes with different topologies and stoichiometries were investigated in [56]. All of the systems are strongly metallic. Configurations with zigzag structures were found to be more stable energetically than the armchair ones, though all of the structures have similar stabilities. After relaxation, there remain several candidates which give a lattice parameter in relative agreement with the experiment. Further, spin-polarized calculations indicate that a structure with armchair tubes and iodine atoms in its center acquires a very large spontaneous magnetic moment of $12\,\mu_B$, while the other structures are nonmagnetic. Ab initio calculations [56] show that in most of the other structures, the tubes are very strongly bound together, and that the compounds should be considered as a crystal, rather than as a bundle of tubes in the habitual sense.

9.1.3 Nanowires and Nanoribbons

MoS_2 nanowires (nanorods) were synthesized by the hydrothermal method [57, 58], using MoO_3 nanorods as precursors via a sulfidation [59, 60], by redox reaction in the aqueos solution [61]. The synthesis of WS_2 nanowires (nanorods) was reported in [62] (via a solid-gas reaction with tungsten oxide nanobundles as precursors), [63] (by the hydrothermal method), [64] (the microwave-assisted method through tetrathiontungstate precursors). X-ray powder diffraction, X-ray photoelectron spectrum and field-emission scanning electron microscopy investigations of $Mo(W)S_2$ nanowire structure and properties show that these nanowires seem to be very flexible, have a tendency to form bundles, and present a stronger contrast to the regular $Mo(W)S_2$ layer.

The atomic-scale structure of Mo_6S_6 nanowires was studied in [65] using scanning tunneling microscopy and spectroscopy (STM and STS) and performing PW DFT (PBE) calculations. A novel synthesis route based on metallic Mo precursors was presented for a selected formation of elementary pure Mo_6S_6 nanowires. Mo_6S_6 nanowires selectively organize themselves as trimer bundles, and each of them consists Mo_6S_6 nanowires of an electrically conducting Mo backbone dressed with a sulfur exterior cap. Mo_6S_6 nanowires may thus be of interest as novel building blocks in nanoelectronics because they exist in a robust, singular structural conformation with uniquely defined electrical (metallic) properties. The fine structure in the experimental STS curves is well reproduced in DOS, resulting from the DFT calculations of the trimer configuration with the distance between the two outer wires fixed to the experimental value.

The structural, electronic, and transport properties of mechanically deformed Mo_6S_6 nanowires were studied in [66] using the DFTB method extended with a

Greens functions formalism. Two interesting results were presented: first, the properties of the nanowire are not affected by bending, and second, a metal-insulator transition occurs when the nanowire is twisted. This indicates that molybdenum sulfide nanowires can be used as a nanocable to flexibly transfer information between electromechanical switches, which can be also constructed from the same nanowires. Hence, these results suggest that Mo_6S_6 nanowires are unique building blocks for future nanodevices.

In order to understand the structures observed two models were built from a single MoS_2 slab and cut in such a way that it is limited by a $(10\bar{1}0)$ plane on one side and by a $(\bar{1}010)$ plane on the other [58]. The edges can be saturated with sulfur in different ways to satisfy the dangling bonds. In order to comply with the measured stoichiometry, two combinations were tested. In the first one (Fig. 9.14), the $(10\bar{1}0)$ edge was saturated with one S-atom per Mo-edge atom and the $(\bar{1}010)$ edge with two S-atoms per Mo-edge atom. For the second (Fig. 9.14), the $(10\bar{1}0)$ edge was saturated with two S per Mo atoms and the $(\bar{1}010)$ edge with one S per Mo-edge atom. Calculation [67] of the stability of these edges showed the formation of S dimers at the so-called Mo edge $(10\bar{1}0)$ when it is saturated with two S atoms. The formation of disulfide ions at MoS_2 edges to complete coordination had already been predicted and is thought to be related to the catalytic activity of this compound [58].

The structural, electronic, and magnetic properties of MoS_2 nanowires, passivated by extra sulfur, were studied in PW DFT (PBE) (with and without spin) calculations [68], using models based on experimental electron microscopy images and earlier theoretical modeling, see Figs. 9.15 and 9.16.

These models, periodic in the x direction, consist of one or two (0001) basal planes of MoS_2–2H cut in stripes limited by a $(10\bar{1}0)$ Mo edge and a $(\bar{1}010)$ S edge. The Mo edge is then saturated with sulfur. The total width of the wire is around 0.6 nm as reported in experiments, which amounts to three rows of Mo in the y direction, see Fig. 9.16. In the x direction, the periodic unit contains either three or four Mo atoms along the edges (these models are referred to as 3Mo and 4Mo). The possible distortions of the lattice that arise due to symmetric and asymmetric S edge configurations are studied. Earlier theoretical calculations showed the S monomer and S dimer edge configurations to be energetically the most favorable for the saturation

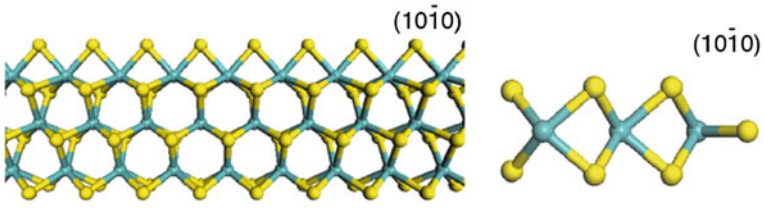

Fig. 9.14 *Side* and *top* view of the model presenting 50 % coverage on the Mo edge and 100 % on the sulphur edge (*blue spheres* represent Mo atoms and *yellow* ones represent S) (Reprinted figure with permission from Camacho-Bragado et al. [58], Copyright (2005) by the Elsevier Inc. All rights reserved)

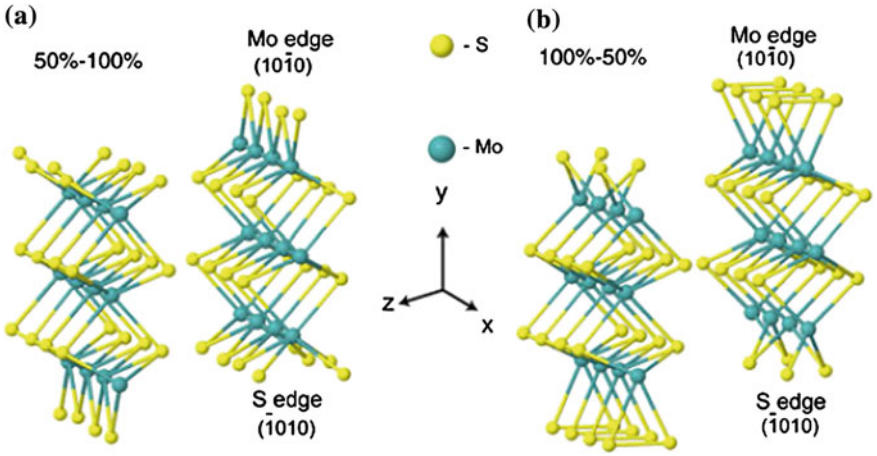

Fig. 9.15 Perspective view of the isolated double trilayer NWs (4Mo models) for two different sulfur saturations **a** 50–100 % and **b** 100–50 %. *Green* (*yellow*) *spheres*: Mo(S) atoms [68]

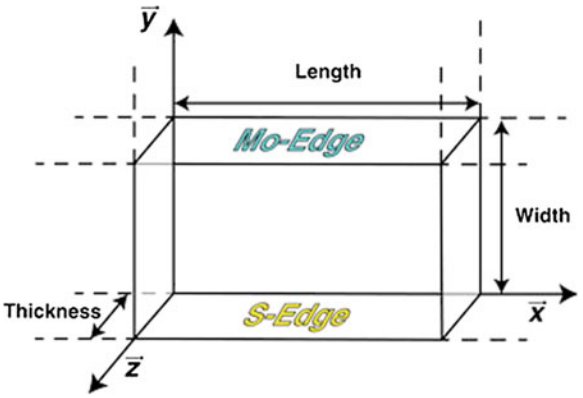

Fig. 9.16 Schematic figure of a S–Mo–S trilayer showing the M and S edge [68]

of the Mo edge. They correspond to 50 and 100 % of the sulfur coverage, respectively. Moreover, the degrees of S coverage that best match the experimental findings are 0, 50, and 100 %. Therefore, and taking also into account the measured stoichiometry, two models of sulfur saturation were tested in [68]: (i) 50 % coverage of the Mo edge (one S atom for every Mo at the edge) and no modification of the S edge (50–100 %) and (ii) 100 % coverage of the Mo edge, with two S atoms for every Mo at the edge (100–50 %). In this case, half of the S atoms are removed from the S edge to preserve stoichiometry. It was found in [68] that independently of the geometrical details and the coverage of extra sulfur at the Mo edge, quasi-one-dimensional metallic states are predominant in all the low-energy model structures despite their reduced dimensionality. These metallic states are localized mainly at the edges. In spite of the

observed pairing of the S dimers at the Mo edge, the NWs do not experience a Peierls-like metal-insulator transition. However, the electronic and magnetic character of the NWs does not depend only on the S saturation but also on the symmetry configuration of the S edge atoms. In particular, the magnetization can be enhanced through an equidistant S configuration at the Mo edge and/or the antisymmetric S configuration at the S edge. The subtle sliding of the weakly bounded planes that constitute the NWs is not as important as the saturation and configuration of the S at the edges. These results reveal a high versatility of this material due to the high stability of its metallic edge states, opening the possibility of applications not only as a nanocatalyst but also as a metallic NW.

MoS_2 **nanoribbons** (NR) may find applications in nanodevices, spintronics and photovoltaic cells through controlling the edge structure, chirality, and saturation states. However, the electronic and magnetic properties of these nanoribbons are still not fully understood, even though they are crucial for their applications in nanodevices. Theoretical modeling increases this understanding. MoS_2 nanoribbons (NRs) calculations have been performed in [69–76]. PW DFT (PW91) calculations [70] predicted the stability and magnetic and electronic properties of MoS_2 nanoribbons with either zigzag- or armchair-terminated edges. Zigzag nanoribbons exhibit ferromagnetic and metallic behavior, irrespective of the ribbon width and thickness. Armchair nanoribbons are nonmagnetic and semiconducting. These conclusions agree with those made later in DFT (LSDA) calculations [69]. The higher stability of MoS_2 nanoribbons, compared with the experimentally available triangular MoS_2 nanoclusters was discovered in [70]. The influence of the sulfur vacancy on the magnetic properties of MoS_2 NRs was studied in APW DFT (PW91) calculations [71]. This study showed that a vacancy on the S-edge with 50 % coverage intensifies the magnetization of the edge of the MoS_2 nanoribbon but such a vacancy on S-edge with 100 % coverage causes this magnetic property to disappear. It was concluded that for both coverages there are positive or negative strong gradients of the local magnetic moment near the vacancy. This may explain why lattice defects are essential for catalysis processes.

The mechanical and electronic properties of MoS_2 nanoribbons and their defects were studied in [72] using PW DFT (PW91) calculations. The phonon dispersion of the bare armchair (n,n) MoS_2 NR with $n = 12$ was calculated and the stability of the nanoribbons was ensured. Armchair nanoribbons are nonmagnetic direct band gap semiconductors; their energy band gaps vary with the width and the termination of the edge atoms with hydrogen, whereas zigzag nanoribbons are found to be ferromagnetic metals. Bare zigzag MoS_2 nanoribbons become half-metallic as a result of the (2×1) reconstruction of edge atoms and are semiconductors for minority spins, but metallic for majority spins. Their magnetic moments and spin polarizations at the Fermi level are reduced as a result of the passivation of the edge atoms by hydrogen. The functionalization of MoS_2 nanoribbons by adatom adsorption and vacancy defect creation were also studied in [72]. The nonmagnetic armchair nanoribbons attain net magnetic moment depending on where the foreign atoms are adsorbed and what kind of vacancy defect is created. The magnetization of zigzag nanoribbons

due to the edge states is suppressed in the presence of vacancy defects. The functionalization of MoS_2 nanoribbons through adatom adsorption and vacancy creation appears to be a promising way to extend the application of MoS_2.

PW DFT (PBE) calculations [74] demonstrated that the stability and electronic properties of nanoribbons strongly depend on their chirality and edge structures. The S-terminated zigzag ribbons showed the greatest edge stability, regardless of the H-saturation, because the edge atoms have fewer dangling states and should be produced in experiments. The armchair nanoribbons, with and without H-saturation, were semiconducting and non-magnetic, although the saturation of their edge states resulted in an increase in the bandgaps. The zigzag nanoribbons were ferromagnetic, and their magnetic states were enhanced by H-saturation. The metallic zigzag ribbon can be transformed into semiconductors (n- or p-type) or half-metals by controlling the dangling states with hydrogen at the edges of the structures.

The transport properties of MoS_2 (n) nanoribbons with different widths and passivation of their edges were studied in [75], using the DFTB method. The defect-free MoS_2 nanoribbons were constructed by cutting infinitely long stripes out of an ideal MoS_2 triple layer, where n denotes the number of Mo atoms across the ribbon. The armchair and zigzag MoS_2 NRs with a width up to $n = 35$ were studied. The electron transport properties are dominated for armchair as well as for zigzag MoS_2 NRs by the Mo–4d states. The edge passivation influences the electronic and transport properties of the nanoribbons. This holds especially true for nanoribbons with zigzag edges. Nearly independent of the passivation, the armchair MoS_2 nanoribbons are semiconductors and their band gaps exhibit an almost constant value. The results obtained in [75] illustrate clearly the edge priority on the electronic properties of MoS_2 nanoribbons and indicate problems for the doping of MoS_2 nanoribbons.

The bandgap tuning in armchair MoS_2 nanoribbons was studied in LCAO DFT (PBE) calculations [76] of bandgap modulation by transverse and perpendicular electric fields respectively. The field-induced bandgap modulation arises from the broken electrostatic potential symmetry in armchair MoS_2 NR owing to the application of an external field. It was shown that in the monolayer armchair MoS_2 nanoribbons the bandgap can be significantly reduced and closed by the transverse field, whereas the bandgap modulation is absent under the perpendicular field. The critical strength of the transverse field for the gap closure decreases as the ribbon width increases. In the multilayer armchair MoS_2 NR case, in contrast, it is shown that the bandgap can be effectively reduced by both transverse and perpendicular fields. Nevertheless, it seems that the two fields exhibit different modulation effects on the gap. The critical strength of the perpendicular field for the gap closure decreases with increasing number of layers, while the critical strength of the transverse field is almost independent of it. Since this gap modulation method is a viable to engineer band structure, it is to be hoped that it could be used in future nanodevices based on armchair MoS_2 NRs.

The tunable electronic and magnetic properties of WS_2 NRs were studied in [77], using the PW DFT (PBE) method. The results obtained show that the properties of WS_2 nanoribbons are greatly affected by the type of the edges: armchair nanoribbons (ANRs) remain nonmagnetic and semiconducting, just like the bulk, whereas zigzag nanoribbons (ZNRs) exhibit ferromagnetic and metallic properties. Further,

the electronic properties can be tuned by applying external strains to WS_2 nanoribbons: the band gap of ANRs experiences a direct-indirect-direct transition and the magnetic moment of ZNRs can be easily tuned by different strains. All these findings suggest that disulfide nanoribbons can exhibit extraordinary electronic and magnetic properties, and more importantly, these fascinating characteristics can be precisely modulated by controlling the edge types and applied strains.

9.2 TiS_2 and ZrS_2

9.2.1 Bulk and Nanolayers

Various morphologies of TiS_2 such as NTs, nanoclusters, fullerenes, nanodisks, whiskers, and thin films have been successfully synthesized [78–81]. The high-purity TiS_2 NTs with open-ended tips were synthesized by a chemical transport reaction [79]. A low-temperature gas reaction was used to create TiS_2 NTs with an outer diameter of ≈20 nm, an inner diameter of ≈10 nm, and an interlayer spacing of ≈0.57 nm [80]. The group 4B transition metal disulfide NTs were successfully prepared through the thermal decomposition of metal trisulfides in a hydrogen atmosphere at about 1073 K [81]. X-ray diffraction patterns indicated that all of the peaks in TiS_2 NTs could be indexed to the hexagonal phase $P\bar{3}m1$ of 1T–o-type (trigonal system with octahedral coordination of the metal atoms), see Fig. 9.17.

Among the other dichalcogenides, zirconium disulfide has also attracted attention, and corresponding nanowires, NTs, and nanobelts have been synthesized [81–83]. Thus, single ultrathin ZrS_2 discs comprising three layers of S–Zr–S repeating units were obtained [83]. The first ZrS_2 NTs were prepared by thermal decomposition of the crystalline zirconium trisulfide ZrS_3 in a stream of H_2 and Ar at 900 C [81]. Transmission electron microscopy analysis showed that the reaction product contained ZrS_2 nanorods and onions in addition to the NTs. The synthesized ZrS_2 NTs are multiwalled, and their outer and inner diameters (D_{out}, D_{in}) are relatively large: about 125 and 60 nm, respectively, which is likely to be due to specific experimental conditions. As was stated above, stable TiS_2 have smaller diameters [80].

It should be noted that only multilayered TiS_2 and ZrS_2 NTs have actually been experimentally observed [79, 80]. Evidently, there exists an additional mechanism of stabilization of multilayered NTs due to the van der Waals interaction between the neighboring walls of coaxial S–M–S cylinders similar to the interaction in the parent bulk layered crystals. The high-resolution transmission electron microscopy images demonstrate that the multilayered TiS_2 NTs predominantly have a circular shape [80]. However, among other dichalcogenides, there is evidence of the existence of the polygonal WS_2 NTs [84].

It is known [43] that some inorganic multiwall NTs can also exhibit the polygonal-cross section.

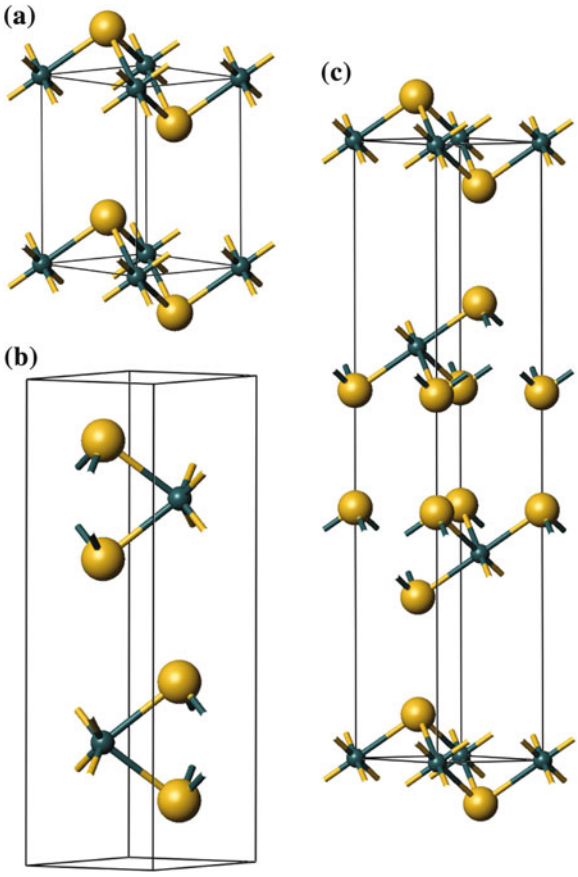

Fig. 9.17 Unit cells for TiS_2 layered polytypes: 1T–o with Pm1 symmetry (**a**), 2H–t with $P6_3/mmc$ symmetry (**b**), and 3R–o with $R\bar{3}m$ symmetry (**c**). Metal and sulfur atoms are represented by *small dark* and *large light spheres*, respectively [85]

Different layered and isotropic bulk phases TiS_2 and ZrS_2 were considered in [85, 86] as the potential precursors of NTs. The hybrid density functional theory DFT (PBE0) was applied to the investigations of the electronic and atomic structure of bulk phases, nanolayers, and nanotubes based on titanium and zirconium disulfides. The calculations were performed on the basis of the localized atomic functions (LCAO) by means of the CRYSTAL09 computer code [47]. Full optimization of all the atomic positions in the systems involved was made to study the atomic relaxation and to determine the most favorable structures.

Table 9.2 compares the calculated properties of 1T–o phase of TiS_2 and ZrS_2 with those available in literature (corresponding to zero temperature and pressure). According to the data in this table, the errors of the theoretical structure parameters do not exceed 1 %. The computational method applied—LCAO DFT (PBE0)—provides

Table 9.2 Calculated and experimental lattice parameters, atomization energy E_{at}, and band gap E_g in the 1T–o phases ($P\bar{3}m1$) of TiS_2 and ZrS_2

Reference	a (Å)	c (Å)	Fractional position of S atom, u_z	E_{at} (eV)	E_g (eV)
TiS_2					
[85]	3.411	5.656	0.244	13.9	1.4
LDA [88]	3.312	5.449	0.261		Semimetal
GGA+U[a]					1.0
Experiment[b]	3.408	5.699	0.250	14.9[c]	0.3 [97]
ZrS_2					
[85]	3.674	5.891	0.243	16.5	2.7
LDA [89]	3.598	5.660	0.257		Semimetal
PBEsol [89]	3.629	5.884	0.247		0.8
Experiment[d]	3.630	5.850	0.250	17.7[c]	1.7 [95]

[a] In [90], the relaxed cell constants have not been reported
[b] Lattice parameters from [98]
[c] Atomization energy estimated from the data in [99]
[d] Lattice parameters from [100]

good estimates of the atomization energy of TiS_2 and ZrS_2. The phonon frequencies calculated for the 1T–o phases do not have imaginary modes, thus proving the phase stability [85]. This can be regarded as a verification of the sufficient accuracy of PBE0 approximation in the special case of TiS_2 and ZrS_2 layered crystals. The success of the hybrid DFT method in reproducing the weak van der Waals-type inter-layer forces can be explained by the predominant contribution of the induced electrostatic interactions due to the big polarizability of the sulfur atom.

Table 9.3 contains the calculated properties of other phases of TiS_2 and ZrS_2. Several disulfide modifications have been mentioned in previous theoretical or experimental studies, namely the 2H and 3R modifications with both octahedral and trigonal prismatic coordination. The unit cell structure of some of them is given in Fig. 9.17. In agreement with the experimental observations, the 1T–o polymorphs (see Fig. 9.17a) were found to be the most stable among all the compounds listed in Table 9.3. The stability of other phases, as well as the stability of nanostructures can be described using the formation energy in respect to that of the 1T–o phase, $E_{form} = E/N - E_0/N_0$, where E, N and E_0, N_0 are the total energy and the number of formula units per translational unit cell in a given system and in the bulk 1T–o crystal, correspondingly. The calculated energy of the 1T–o phase is observed lower than the energy of similar polytypes, 2H–o (with $P6_3mc$ symmetry) and 3R–o (with $R\bar{3}m$ symmetry, see Fig. 9.17c), which have the same octahedral morphology but appear to be metastable. The direct optimization of the two layer (6-plane) TiS_2 slab starting from the 3R stacking sequence leads to the 1T stacking sequence [85]. This gives additional evidence that the computational method adopted can provide a sufficiently correct description of the interactions between the TiS_2 or ZrS_2 layers. Though the hexagonal (2H–t with symmetry $P6_3/mmc$, see Fig. 9.17b) and rhombohedral (3R–t

Table 9.3 Relaxed structure, stability E_{form}, and band gaps E_g of different TiS_2 and ZrS_2 phases

Polymorph	Space group	a (Å)	b (Å)	c (Å)	E_{form}[a] (meV)	E_g (eV)
TiS_2						
Hexagonal, 2H–o	186 ($P6_3mc$)	3.412	3.412	11.541	13	1.5
Cubic	227 ($Fd\bar{3}m$)	9.723	9.723	9.723 (9.739)[b]	46	0.8
Rhombohedral, 3R–o	166 ($R\bar{3}m$)	3.420	3.420	19.151	66	1.5
Rhombohedral, 3R–t	160 ($R3m$)	3.323	3.323	17.866	590	1.7
Hexagonal, 2H–t	194 ($P6_3/mmc$)	3.322	3.322	12.045	597	1.6
ZrS_2						
Hexagonal, 2H–o	186 ($P6_3mc$)	3.676	3.676	11.912	1	2.8
Cubic	227 ($Fd\bar{3}m$)	10.396	10.396	10.396	20	2.1
Rhombohedral, 3R–o	166 ($R\bar{3}m$)	3.678	3.678	19.813	31	2.9
Rhombohedral, 3R–t	160 ($R3m$)	3.562	3.562	18.389	657	1.5
Hexagonal, 2H–t	194 ($P6_3/mmc$)	3.563	3.563	12.391	664	1.4

[a] Formation energy with respect to the 1T–o phase
[b] Experimental value from [87]

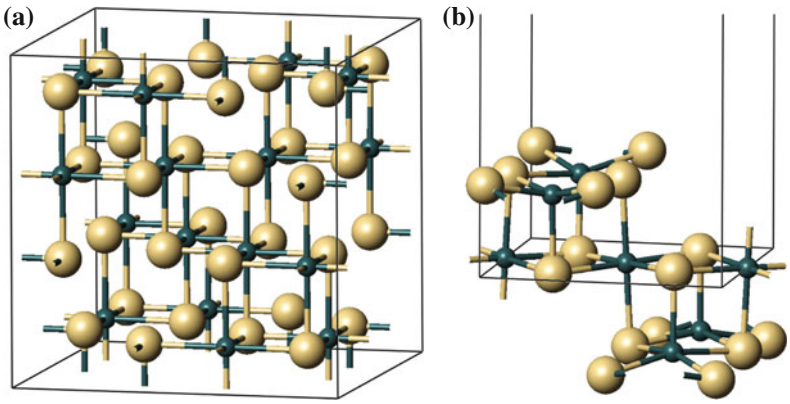

Fig. 9.18 Structure of the TiS_2 cubic polymorph. The bulk phase unit cell with $Fd\bar{3}m$ symmetry (**a**), relaxed structure of the 2D unit cell of the 9-plane 3-layer (001) slab with Pmma symmetry (**b**). Here and below, see Fig. 9.16 for the labeling of atoms [85]

with symmetry R3m) layered phases with the trigonal prismatic coordination exist for the other metal disulfides (e.g., for MoS_2, WS_2), they are noticeably less stable (by about 0.6–0.7 eV) than the polytypes 1T–o, 2H–o, and 3R–o with octahedral coordination in the case of the Ti and Zr compounds. Conversely, it was found in [85] that the cubic phase ($Fd\bar{3}m$) has a stability close to that of the 1T–o phases (see Table 9.3 and Fig. 9.18). So long as this phase had really been observed experimentally [87] for TiS_2 it was included in computations [85].

Most of the previous DFT calculations [88–91] have indicated that layered disulfides of titanium and zirconium should be semimetals. Thus, according to ab initio

band-structure calculations [91], the bulk 1T–o TiS_2 crystal is semimetallic, but its thin films are semiconductors. When the number of layers increases to 11, the TiS_2 thin film becomes semimetallic. However, at ambient conditions, the calculated electronic band structure contradicted the experiments, with both semimetal [92] and semiconductor [93, 94] states reported. There is also some evidence from an angle-resolved photoemission experiment [88] that TiS_2 is a semiconductor with a direct band gap of 0.3 ± 0.2 eV. Nevertheless, Fang et al. [91] have concluded that the photoelectron spectra are also consistent with semimetallic TiS_2 if the difference between the electronic structure of the top surface layer and the bulk is taken into account.

The band gaps calculated in [85] indicate that all the phases considered pertain to low-gap semiconductors. This disagrees with the results of previous DFT calculations [88–91] of 1T–o phases. One of the possible explanations of the appearance of a nonzero gap between the valence and conduction band states is the type of DFT Hamiltonian. As we mentioned in Chap. 3, the pure DFT (without adding the Hartree-Fock exchange in the Hamiltonian) calculations underestimate the band gap. The hybrid PBE0 functional can provide better agreement with the experimental observations, although it may slightly overestimate this property.

Zirconium sulfides were found to have an approximately 1 eV larger band gap than titanium sulfides (except for 2H–t phase, where both TiS_2 and ZrS_2 exhibit a similar value of the gap of about 1.4 eV). This seems to be reasonable because of the more ionic nature of zirconium compounds. Experimental data [95] also indicate the semiconducting properties of the 1T–o ZrS_2. It is interesting to note that the PBEsol method [96] designed specifically to improve the generalized gradient approximation (GGA) for solids, gives a nonzero band gap, while the local-density approximation (LDA) results in the semimetallic state of 1T–o ZrS_2 (see Table 9.2). The calculated band gaps of the most of the bulk crystals considered in [85] are indirect, except for cubic phases, where it is direct.

The 1T–o and 2H–t polymorphs, as well as the cubic phase of TiS_2 or ZrS_2 listed in Tables 9.2 and 9.3 were used in [85] to construct the thin slabs assumed for subsequent NT folding. Single-layer slabs parallel to the (001) crystallographic planes as depicted in Fig. 9.19 have were calculated.

As we mentioned above (see Chap. 3) the surface energy is one of the additional criteria of the sustainability of nanostructures. It can be calculated as

$$E_{surf} = (E_{slab} - E_{bulk} N_{slab}/N_{bulk})/(2S_{slab})$$

where E_{slab}, N_{slab} and E_{bulk}, N_{bulk} are the total energy and the number of formula units per translational unit cell in a nanolayer and in a bulk crystal, correspondingly. The area S_{slab} is equal to the total surface per unit cell of the nanolayer. The surface energy has a definite limit when the number of atoms is rising for a given class of nanosystems (nanolayers, NTs, nanowires) with given surface properties. In particular, one can presume that this quantity is a more appropriate measure of stability of relatively thick nanolayers due to the fast drift of the formation energy toward its bulk value with increasing number of atoms. However, for thin nanolayers and NTs, the formation

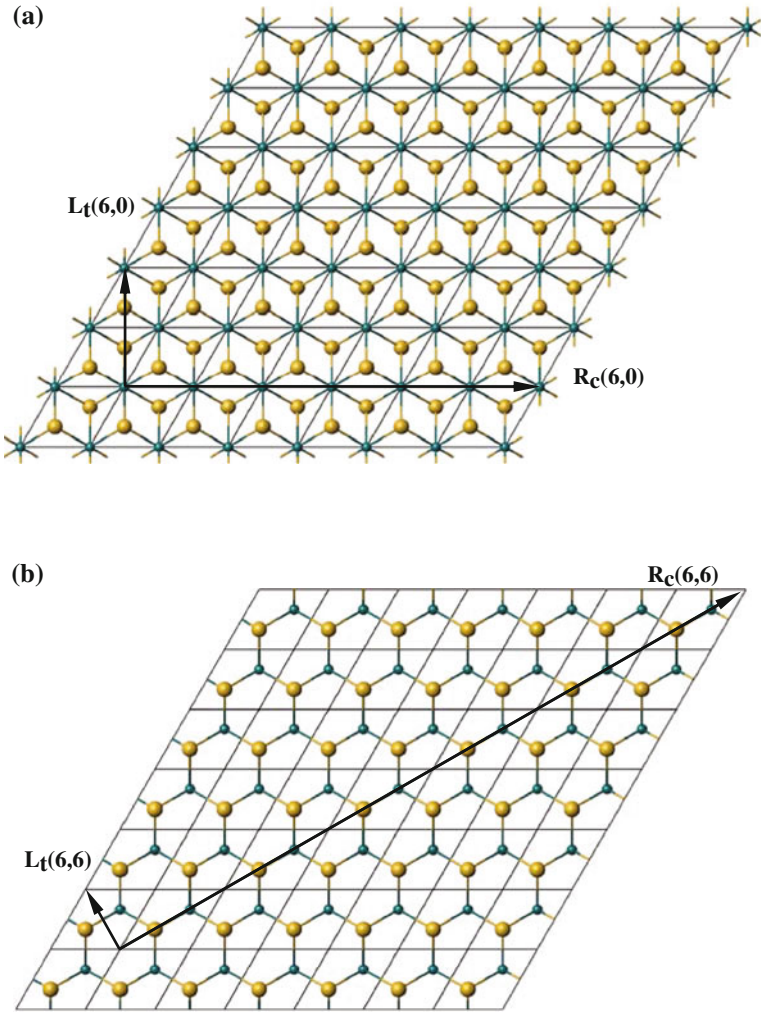

Fig. 9.19 View from above of the hexagonal layers of TiS_2 with octahedral (**a**) and trigonal prismatic (**b**) coordination of the metal atoms. The chiral vector $\mathbf{R_c}$ and the translation vector $\mathbf{L_t}$ are shown for chirality (6, 0) and (6, 6) on (**a**) and (**b**), correspondingly [85]

energy may be a more adequate characteristic of stability due to ambiguity of the surface area definition on the atomic scale. For these reasons both the formation energy of nanolayers with respect to the most stable polymorph and the surface energy of them with respect to the parent bulk phase were calculated in [85]. The slab formation and surface energies were used in [85] to select the most favorable nanolayers for the NT folding. The calculated properties of the selected slabs are given in Table 9.4.

Table 9.4 Calculated lattice parameters, formation energy E_{form}, surface energy E_{surf}, and band gap E_g of (001) nanolayers selected for disulfide nanotube folding

Crystal system and space group G of the parent bulk phase	Initial number of atomic planes	Layer group S of the relaxed structure	a (Å)	b (Å)	E_{form}[a] (kJ/mol)	E_{surf}[b] (J/m^2)	E_g (eV)
TiS_2							
1*T*–o, Hexagonal 164 ($P\bar{3}m1$)	3	72 ($P\bar{3}m1$)	3.41	3.41	7.6	0.06	1.6
Cubic 227 ($Fd\bar{3}m$)	3[c]	41 (Pmma)	7.02	6.71	53.5	0.52	1.6
2*H*–t, Hexagonal 194 ($P6_3/mmc$)	3	78 ($P\bar{6}m2$)	3.32	3.32	64.7	0.05	2.7
ZrS_2							
1*T*–o, Hexagonal 164 ($P\bar{3}m1$)	3	72 ($P\bar{3}m1$)	3.68	3.68	5.4	0.04	3.0
Cubic 227 ($Fd\bar{3}m$)	3[c]	41 (Pmma)	7.49	7.22	66.5	0.59	2.5
2*H*–t, Hexagonal 194 ($P6_3/mmc$)	3	78 ($P\bar{6}m2$)	3.56	3.56	70.8	0.03	2.5

[a] Formation energy with respect to the 1T–o phase
[b] Surface energy relative to the parent bulk phase
[c] The number of the compact layers consisting of several atomic planes

As can be expected, the formation energy, E_{form}, of the thin films obtained from the single layer of the 1T–o phase of TiS_2 or ZrS_2 (Fig. 9.19a) is close to zero. The formation energy of films generated from the 2H–t phase with trigonal prismatic coordination is close to the formation energy of the bulk phase itself, and so it is much larger than the formation energy of the isolated layer of the 1T–o phase. The surface energy is close to zero in both cases. The low value of these quantities provides the evidences that the interaction between the layers in the bulk phases mentioned is weak, and isolated single layers can be easy created.

The stability of the slabs generated from the cubic phase (Fig. 9.18a) is considerably less than that of the isolated layers of the 1T–o phase and approaches to the stability of the 2H–t phase layers.

Contrary to the conclusions made by the authors of the previous studies [101–104], the large differences between the band structure of the triple-plane layers and the bulk phases were not found in [85]. In both cases, low-gap semiconductors were found. However, the band gaps in the slabs are generally slightly larger than those of the corresponding bulk phase. A considerable increase in the gap was found for hexagonal layers with trigonal prismatic coordination and in the (001) layers of the cubic phase (see Tables 9.2, 9.3 and 9.4).

9.2.2 Rolled-Up Single-Walled Nanotubes

The atomic and electronic structure of titanium and zirconium sulfides NTs has been calculated in several theoretical works [51, 101–105].

It should be mentioned that neither the pure, nor the hybrid density functional theory (DFT) was used in those studies. An extended Hückel theory has been applied in several works [101, 102] and the DFT-based tight binding (DFTB) method has been used in others [51, 103–105]. DFTB calculations [103, 104] evidenced that the 1T–o TiS_2 triple-plane layer with octahedral coordination of the Ti atoms has a lower energy than the corresponding 2H–t hexagonal structure with trigonal prismatic coordination of the metal atoms. As a consequence of this, 1T-like tubes are also more stable compared with their 2H-analogues. The calculated [103] stability of TiS_2 tubes with 1T–o morphology was practically independent of the chirality, whereas zigzag ZrS_2 NTs were found [102] to be more stable for relatively large diameters. According to the calculations mentioned [101–104], the TiS_2 and ZrS_2 tubes are semiconductors, with a band gap of about 1.0 eV. Tibbetts et al. [106] presented a model for multiwalled NTs with a polygonal cross section and parameterized it with first-principles calculations for TiS_2. They have suggested that a tube can reduce its energy by forming a polygonal cross section. Generally, the polygonal-cross section results in a higher strain energy because the bending radius is smaller at the corners. However, the authors of [106] have claimed that this can be more than compensated for by reduced interfacial energy of the flat sectors. This energy reduction occurs because the flat sections of the NT can have a coherent interface with no tensile strain. The authors of [106] estimated this energy reduction by the parameterization of strain and interfacial energy for TiS_2 NTs via the first-principles (DFT) calculations of the flat and deformed TiS_2 sheets.

We saw in Chap. 2 that the symmetry and structure of single-walled nanotubes (SWNTs) can be simply described using the so-called layer folding, which means the construction of the cylindrical surfaces of NTs by rolling up 2D-periodic crystalline nanolayers (sheets or slabs). The knowledge of the layer symmetry group of the precursor sheet (see Table 9.4) allows one to find the symmetry line group L (presented in Table 9.5) of the NTs of any given chirality. The rolling procedure and the symmetry of NTs folded from the hexagonal layers were described in detail in Chap. 2 and monograph [107].

The SWNTs folded from the 3-plane hexagonal nanolayers of TiS_2 and ZrS_2 consist of three coaxial S–M–S (M = Ti, Zr) cylinders or atomic shells. The atomic and electronic structure of NTs of both 1T–o and 2H–t morphologies with two types of chiralities (n,0) and (n,n), known as zigzag and armchair achiral structures, was calculated in [85]. The former belongs to line group family 8 ($L(2n)_n mc$) and the latter belongs to family 4 ($L(2n)_n/m$). Simulation was performed for n in ranges from (12,0) to (40,0) and from (8,8) to (24,24), which corresponds to the NT diameters D from 15 to 50 Å. The largest diameter D value considered is comparable with the minimal inner diameters of the real TiS_2 tubes experimentally studied in [80].

Table 9.5 Relaxed structure (Translational period L, wall thickness w, and average diameter D), stability (Formation energy with respect to the most stable phase E_{form} and strain energy E_{str}), and band gaps E_g of the selected nanotubes with an average diameter of about 30 Å folded from different phases of TiS_2 and ZrS_2

Phase	Chirality	Line group family	L (Å)	w (Å)	D (Å)	E_{form} (kJ/mol)	E_{str} (kJ/mol)	E_g (eV)
TiS_2								
1T–o, Hexagonal 164 ($P\bar{3}m1$)	(28,0)	8 ($L56_{28}$mc)	5.9	2.7	30.8	13.5	5.9	1.5
	(16,16)	4 ($L32_{16}$/m)	3.4	2.7	30.4	13.7	6.1	1.6
2H–t, Hexagonal 194 ($P6_3/mmc$)	(28,0)	8 ($L56_{28}$mc)	5.7	2.9	30.0	70.1	5.4	2.7
	(16,16)	4 ($L32_{16}$/m)	3.3	2.9	29.5	70.6	5.9	2.6
Cubic ($Fd\bar{3}m$)	(12,0)	3 (L12/m)	6.7	5.8	28.6	64.6	11.1	1.4
ZrS_2								
1T–o, Hexagonal 164 ($P\bar{3}m1$)	(28,0)	8 ($L56_{28}$mc)	6.4	2.8	33.0	9.8	4.4	2.9
	(16,16)	4 ($L32_{16}$/m)	3.7	2.8	32.6	9.9	4.5	3.0
2H–t, Hexagonal 194 ($P6_3/mmc$)	(28,0)	8 ($L56_{28}$mc)	6.1	3.1	32.2	72.5	1.7	2.5
	(16,16)	4 ($L32_{16}$/m)	3.6	3.1	31.5	72.9	2.1	2.5
Cubic ($Fd\bar{3}m$)	(12,0)	3 (L12/m)	7.2	6.4	29.9	73.7	7.2	2.2

The calculated properties of NTs folded from the hexagonal nanolayers of TiS_2 and ZrS_2 are given in Table 9.5. Together with the formation energy as the measure of the NT stability it includes the strain (rolling) energy,

$$E_{str} = E_{nano}/N_{nano} - E_{slab}/N_{slab}$$

which is the NT formation energy, but with respect to the 2D-periodic precursor nanolayer (E_{slab}, N_{slab} are the total energy and the number of formula units per translational unit cell in a nanolayer with the optimized atomic structure). The data obtained show that the strain (rolling) energy E_{str} of these tubes is close to zero. Obviously, this is the consequence of the stability of isolated 3-plane layers having the hexagonal 2D lattice symmetry.

The relaxed NT structures are illustrated in Figs. 9.20 and 9.21 for both types of the chiralities. The NTs rolled up from layers with trigonal prismatic morphology exhibit a considerably larger formation energy when compared to the NTs with octahedral morphology. The same can be said about the NTs folded from the (001) slabs cut from the cubic phase of TiS_2 and ZrS_2 (see Table 9.5).

Figure 9.22 depicts the dependence of E_{str} on the average tube diameter D.

Figure 9.22a demonstrates that the strain energy of 1T–o tubes depends weakly on the tube chirality for both TiS_2 and ZrS_2. The DFTB calculations [105] gave a strain energy of approximately 7 kJ/mol for a TiS_2 NT with a diameter of 30 Å, which is in good agreement with the results presented here (6 kJ/mol). The 1T–o ZrS_2 tubes show a little bit smaller values of strain energy compared to those of TiS_2, but we do not see any preferences of the zigzag over armchair chirality revealed earlier for 1T–o ZrS_2 tubes [102] (see Fig. 9.22a). Similarly, the authors of DFTB calculations [103]

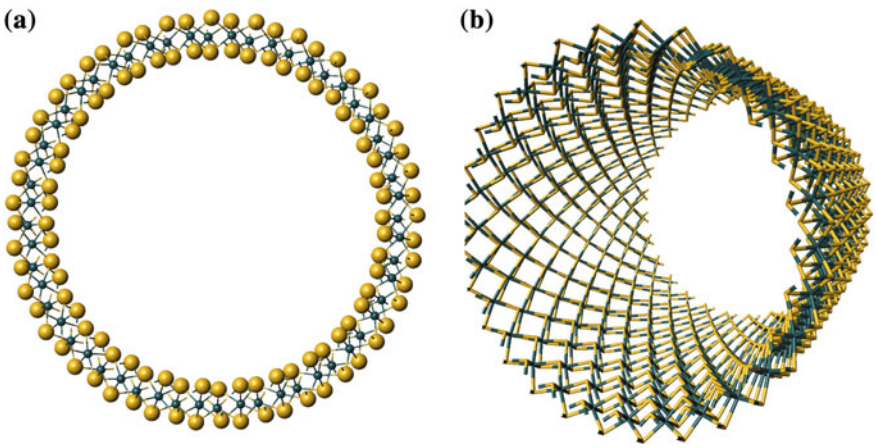

Fig. 9.20 Cross-sectional (**a**) and perspective (**b**) view of the single-wall zigzag NTs folded from hexagonal layers of the 1T–o phase of TiS_2 with chirality (28,0) [85]

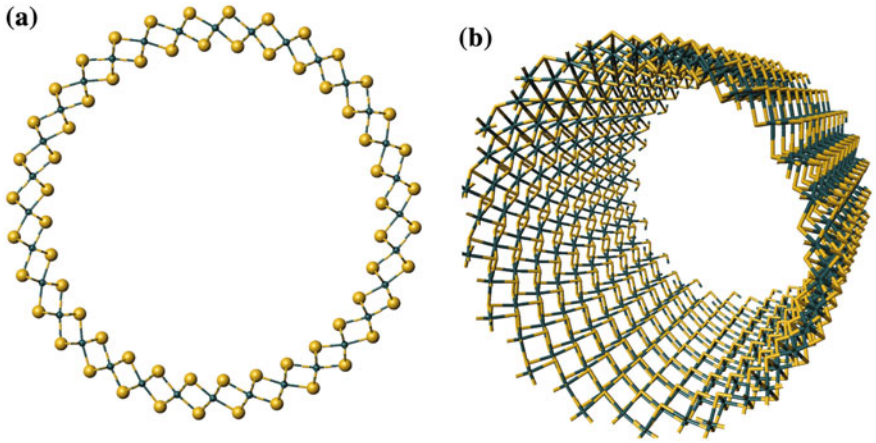

Fig. 9.21 Cross-sectional (**a**) and perspective (**b**) view of the single-wall zigzag NTs folded from hexagonal layers of the 1T–o phase of TiS_2 with chirality (16,16) [85]

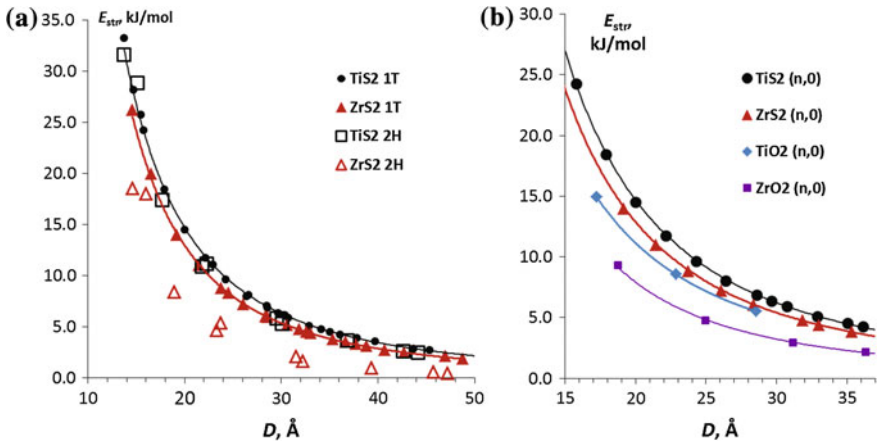

Fig. 9.22 Strain energies E_{str} versus the average diameter. **a** TiS_2 and ZrS_2 SWNT of both (n,0) and (n, n) chiralities; the *curves* are plotted for the tubes with octahedral morphology. **b** Comparison of the strain energies for sulfide and oxide [108, 109] NTs with chirality (n,0); *lines* are drawn to indicate the general dependence [85]

found that the armchair 2H–t TiS_2 tubes had slightly less strain energy than zigzag tubes of comparable diameters, whereas the DFT (PBE0) calculations [85] showed no difference. For E_{str} of 1T–o and 2H–t TiS_2 tubes, we also see a negligible difference, in contrast to the difference of about 5 kJ/mol calculated in the above-mentioned work [103]. The 2H–t ZrS_2 NTs do not fit into the general set (see Fig. 9.22a), manifesting a lower strain energy.

In all the cases depicted in Fig. 9.22a, the strain energy approximately obeys the classical D^2 law. However, the deviation from this law is significant at low NT diameters. A better approximation was obtained with a power function

$$E_{str} = \beta(D/D_0)^{-\gamma}$$

where D_0 is the units conversion factor ($D_0 = 10$ Å was assumed in [85]). The parameters β and γ were derived from the calculated data by the least-squares fitting. The values obtained are: $\beta = 62.2, 64.3, 58.0, 68.1$ kJ/mol; $\gamma = 2.08, 2.21, 2.16, 3.11$ for the TiS_2 (1T–o and 2H–t) and ZrS_2 (1T–o and 2H–t) NTs, correspondingly. It is seen that the γ value of 3.11 in the ZrS_2 2H–t NTs considerably exceeds 2, thus confirming the peculiar properties of these NTs.

In Fig. 9.22b, we compare the strain energy dependences for the oxide and sulfide zigzag NTs of the same hexagonal morphology (folded from the hexagonal $P\bar{3}m1$ layers). This figure clearly shows that the strain energy of the TiS_2 and ZrS_2 NTs is greater than the strain energy of the similar TiO_2 and ZrO_2 NTs. However, the calculated formation energy of the sulfide NTs is considerably less than the formation energy of the oxide NTs, as follows from Table 9.6, where the resulting properties are compared for the oxide- and sulfide-based NTs. The calculated band gaps of the NTs considered are given in the last columns of Tables 9.5 and 9.6. According to the data in Table 9.5, the band gaps in NTs folded from the layers of the 1T–o and 2H–t phases practically coincide with the gaps in the corresponding isolated layers (see Table 9.4) if the NT diameter is greater than or equal to 30 Å. Moreover, the NTs and single layers exhibit mostly indirect band gaps. The direct gaps were obtained in 1T–o TiS_2-based systems only.

Table 9.6 demonstrates that the band gap of the oxide-based NTs is from two to three times greater than the band gap of the sulfide-based NTs. Obviously, it is a straightforward consequence of the dielectric properties of the parent bulk crystals:

Table 9.6 Comparison of the stability of dioxide* and disulfide nanotubes with an average diameter of about 30 Å, folded from 3-plane hexagonal ($P\bar{3}m1$) layers

Composition	Chirality	E_{form}[a] (kJ/mol)	E_{str} (kJ/mol)	Band gap (eV)
TiS_2	(28,0)	13.5	5.9	1.5
	(16,16)	13.7	6.1	1.6
ZrS_2	(28,0)	9.8	4.4	2.9
	(16,16)	9.9	4.5	3.0
TiO_2	(30,0)	52.8	5.5	4.8
	(18,18)	52.3	5.0	4.8
ZrO_2	(30,0)	95.7	2.9	6.7
	(18,18)	95.5	2.8	6.7

*[111]

[a]The formation energy was calculated with respect to the most stable phases: 1*T*–o disulfide polymorphs, rutile TiO_2, and monoclinic ZrO_2

the Ti and Zr oxides are wide-gap semiconductors, whereas the corresponding sulfides are low-gap semiconductors or semimetals. The DFT (PBE0) calculations give the gap values (in eV) of 4.0 [110] or 5.5 [111] and 1.4 or 2.7 for Ti or Zr oxides and sulfides, accordingly. A possible explanation of this is the difference in the covalent contribution to the Ti-X bond, which is presumably greater in the case of X = S than in the case of X = O. As a rule, the band gap of thin layers and NTs rises with respect to the bulk value because of the quantum confinement [91] along the direction perpendicular to the layers. This increase is rather small for sulfides having a layered structure in the bulk crystals as well.

9.2.3 Rolled-Up Double-Walled Nanotubes

The line symmetry group of a double-wall nanotube (DWNT) can be found as an intersection of the symmetry groups of its single-wall constituents, see Chap. 2. The coaxial hexagonal DWNTs with $(n_1,0)@(n_2,0)$ and $(n_1,n_1)@(n_2,n_2)$ chiralities are commensurate: their translation period is the same as for the constituents. Just after rolling, the line group L of DWNT contains rotations around the screw axis, common to both SW components. Regarding the greatest common divisor N of n_1 and n_2, two possibilities for periodic DWNTs can be established [112]: (i) if both n_1/N and n_2/N are odd, L contains the screw axis $(2N)_N$ and (ii) if one or both n_1/N and n_2/N are even, L contains the rotation axis of order N. Because of the tube coaxiality, there are mainly two parameters that completely determine the relative positions of SW constituents in DWNT [113]: the angle $\Delta\phi$ and the length Δz by which the outer tube is rotated around z and translated along z, respectively, relative to the initial (just after folding from the slab) configuration characterized by $\Delta\phi = 0$ and $\Delta z = 0$. Conventionally, the maximum possible number of symmetry elements for both SWNTs coincide just after the construction. After atomic relaxation, the values of $\Delta\phi$ and Δz can differ from zero. Presumably, the rototranslational part of the DWNT symmetry group (independent of the relative SWNT positions) is not changed after relaxation. However, other common symmetry elements of SWNTs (second-order U axes normal to the translation vector, reflection and glide planes) can be lost. Thus, the total symmetry of DWNT may be reduced. Because there is no second-order rotation symmetry axis U normal to the NT axis in line group families 4 and 8, the U-rotated SWNT cannot be superimposed with the original one by any shift or rotation. As a result, two different commensurate DWNTs can be constructed [113] from a given pair of SWNTs folded from the hexagonal sheets of TiS_2 or ZrS_2. When SW constituents folded from the same slab via the same procedure are simply combined in a DWNT, one obtains a tube with a parallel stacking of the constituents. If one of the constituents is rotated around the U axis, the DWNT with an antiparallel stacking of the SW constituents will be obtained. The aspects mentioned should be taken into account during the simulation of DWNTs. The relative stability of DWNT

can be measured by the so called binding energy E_{bind} [113] that is the difference between the total energy of DWNT and the sum of the total energies of the SW components reduced to one formula unit. Obviously, the nature of the interaction between the SW components is the same as the nature of the interaction between the layers in the bulk crystals.

The TiS_2 and ZrS_2 DWNTs composed from the SWNTs of the most favorable 1T–o morphology, were studied in [85]. To investigate the dependence of the DWNT stability on the interwall distance, a set of zigzag (n,0) and armchair (n,n) DWNTs with various diameters of components was constructed. The initial difference between the average radii of the coaxial tubes was varied in the interval from 4.5 to 8.5 Å. In this study, the DWNTs with a parallel stacking of SW components was used.

Figure 9.23 shows the dependence obtained of the E_{bind} on the optimized distance between the cylinders of the Ti atoms in the inner and outer SWNT walls.

It can be seen from this figure that the most favorable distance is slightly greater (by about 0.2 Å) than the distance between the layers in the bulk crystals. The binding energy, interpolated to the most favorable distance between the SWNTs, is about of 22.5 kJ/mol for TiS_2 and 21.7 kJ/mol for ZrS_2 DWNTs. These values are smaller by 0.5–1.0 kJ/mol than the interaction energy E_{int} between the layers in the 1T–o phases estimated to be 23.6 and 22.2 kJ/mol for TiS_2 and ZrS_2, correspondingly. The binding energy of the similar TiS_2 and ZrS_2 DWNTs is slightly favorable for the former; however, the latter have smaller formation and strain energies (see Table 9.7). The average diameters and periods of the relaxed DWNTs are also included in Table 9.7. The values derived indicate that these parameters are practically unchanged compared to the values inherent in the SW components. It also follows from Table 9.5 that the energy band gaps of DWNTs are slightly reduced with respect to the SWNT band gaps, but in contrast to SWNTs, the band gaps of all DWNTs are direct.

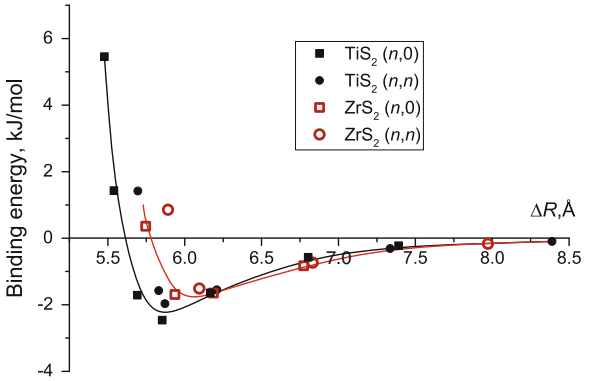

Fig. 9.23 Binding energies E_{bind} versus the distance between the walls in TiS_2 and ZrS_2 DWNT (*lines* are drawn to indicate the general dependence) [85]

Table 9.7 Relaxed structure (Translational period L, average diameter D, and interwall distance Δw), stability (Formation energy with respect to $1T$ bulk phase E_{form}, strain energy E_{str}, and binding energy E_{bind}), and band gaps of the selected TiS_2 and ZrS_2 double-wall nanotubes

DWNT	L	D	Δw (Å)	E^{a}_{form} (kJ/mol)	E_{str} (kJ/mol)	E_{bind} (kJ/mol)	Band gap (eV)
TiS_2 (n,0)							
(20,0)@(30,0)	5.9	36.1	5.69	13.63	6.03	21.71	0.9
(22,0)@(33,0)	5.9	38.8	5.85	11.53	3.93	22.46	1.1
(18,0)@(30,0)	5.9	35.3	6.17	14.58	6.98	21.64	1.1
TiS_2 (n,n)							
(12,12)@(18,18)	3.4	37.4	5.83	13.31	5.71	21.57	1.2
(18,18)@(24,24)	3.4	49.8	5.87	9.25	1.65	21.97	1.3
(14,14)@(21,21)	3.4	42.2	6.21	11.41	3.81	21.55	1.3
ZrS_2 (n,0)							
(20,0)@(30,0)	6.4	38.4	5.94	9.48	4.10	21.69	2.3
(22,0)@(33,0)	6.4	41.5	6.19	8.48	3.10	21.65	2.4
(18,0)@(30,0)	6.4	38.0	6.77	11.04	5.66	20.83	2.3
ZrS_2 (n,n)							
(12,12)@(18,18)	3.7	39.8	6.10	9.30	3.92	21.51	2.5
(18,18)@(24,24)	3.7	52.1	6.12	6.38	1.00	21.59	2.6
(14,14)@(21,21)	3.7	45.3	6.83	8.50	3.12	20.73	2.6

To investigate the influence of the stacking direction on the stability of the DWNTs, the most favorable combinations of SWNTs were used in [85]. The results of the calculations showed that the overturn of one SWNT led to a less favorable structure, although the difference in the binding energy E_{bind} is tiny (about 0.1 kJ/mol). For this reason, one can exclude the DWNTs with a reverse stacking from further consideration. Analyzing the relative shift Δz of one SW component with respect to another, it was found that Δz substantially depends on the tube chirality. The walls in the armchair DWNTs do not exhibit any valuable relative shift, thus preserving the initial C_{2nh} symmetry during the atomic relaxation. Conversely, the components of the zigzag DWNTs have a significant relative shift of about 0.4–0.5 Å for TiS_2 and ZrS_2 NTs (Fig. 9.24). Computations [85] showed that the final value of Δz does not depend on its initial value provided during the construction. The analysis of the possible relative rotation of the SW components around the common axis did not reveal a noticeable value of $\Delta\phi$. The maximum turn of one SWNT relative to another SWNT was found to be 3°.

Table 9.8 lists the data about the radial distribution of the S and Ti atoms in the DWNTs. The inner and outer radii of the DWNT are determined by the inmost and outmost S atoms, whereas the positions of the Ti atoms determine the wall average

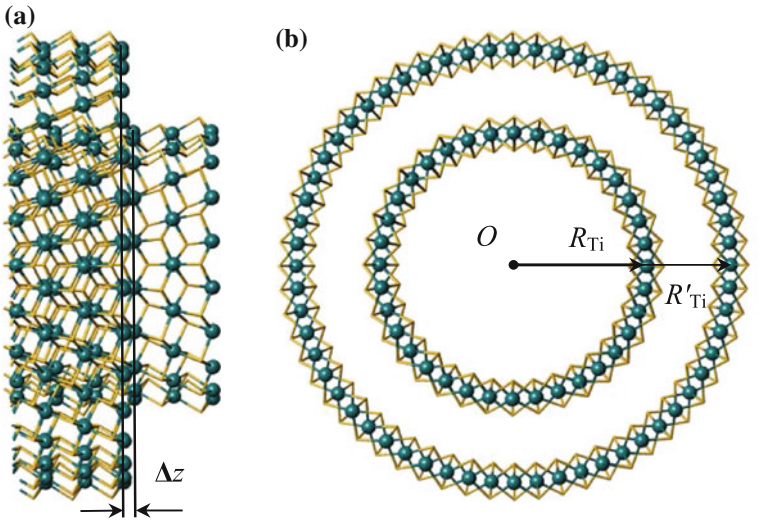

Fig. 9.24 Lateral (**a**) and cross-sectional (**b**) view of DWNT (18,0)@(30,0) folded from hexagonal layers of the 1T–o phase of ZrS_2. (The *external wall* is partially removed to show the *internal wall*.) A relative shift Δz of one SW component with respect to another is shown on (**a**). The radius vectors of Ti atoms R_{Ti} and R'_{Ti} are shown on (**b**) for *internal and external walls*, accordingly; the angle $\Delta\phi$ between R_{Ti} and R'_{Ti} describes the relative rotation of the walls about the z-axis (it is zero in the depicted case) [85]

radii. The NT thickness can be estimated as $w = R^S_{max} - R^S_{min}$. The NT thickness is slightly increased with the tube diameter; $8.4\,\text{Å} \leq w \leq 9.0\,\text{Å}$ in the case of TiS_2 tubes, and $8.8\,\text{Å} \leq w \leq 9.7\,\text{Å}$ in the case of ZrS_2 tubes.

Studying the NTs folded from the relatively thick layers of the $SrTiO_3$ crystal with perovskite structure [114], it was concluded that the polygonal shape may be favorable for perovskite NTs. The energy reduction in these systems is provided by the flat sections in the NTs that preserve the Ti–O bonding structure of the initial crystalline layers, thus reducing the bending strain. In [85], the hypothesis [106] about the polygonal shape of TiS_2 multiwall NTs was checked using the direct computations.

Several DWNT were calculated in [85] starting from both the cylindrical and polygonal shape. The initial pentagonal or decagonal structures for (20,0)@(30,0) NT, and trigonal or hexagonal (see Fig. 9.25) structures for (12,12)@(18,18) and (18,18)@(24,24) tubes were constructed. The coherence [106] of the flat segments is virtually satisfied in (20,0)@(30,0) and in (12,12)@(18,18) and (18,18)@(24,24) DWNTs at $N = 10$ and $N = 6$, respectively (see Table 9.1 in [106]). In all these cases, geometry optimization led to almost cylindrical structures which were previously obtained starting from two coaxial cylindrical SWNTs. However, a careful analysis of the relaxed DWNT shape gave evidence of a small but noticeable deviation from

Table 9.8 Relaxed wall parameters (Inner radius R^S_{min}, outer radius R^S_{max}, average radial positions of the Ti atoms in the inner and outer walls $\langle R^{Ti}_{int}\rangle$ and $\langle R^{Ti}_{out}\rangle$, and their standard deviations $\sigma(R^{Ti}_{int})$ and $\sigma(R^{Ti}_{out})$) in the selected TiS_2 and ZrS_2 doublewall nanotubes (Å)

DWNT	R^S_{min}	R^S_{max}	$\langle R^{Ti}_{int}\rangle$	$\langle R^{Ti}_{out}\rangle$	$\sigma(R^{Ti}_{int})$	$\sigma(R^{Ti}_{out})$
TiS_2 (n, 0)						
(20,0)@(30,0)	9.6	18.0	11.0	16.7	0.003	0.023
(22,0)@(33,0)	10.8	19.4	12.2	18.1	0.001	0.012
(18,0)@(30,0)	8.8	17.7	10.2	16.3	0.001	0.004
TiS_2 (n, n)						
(12,12)@(18,18)	10.0	18.7	11.4	17.3	0.007	0.103
(18,18)@(24,24)	15.5	24.4	17.0	22.9	0.018	0.161
(14,14)@(21,21)	12.1	21.1	13.5	19.7	0.009	0.046
ZrS_2 (n, 0)						
(20,0)@(30,0)	10.4	19.2	11.9	17.8	0.003	0.014
(22,0)@(33,0)	11.7	20.7	13.2	19.3	0.002	0.006
(18,0)@(30,0)	9.4	19.0	10.9	17.6	0.001	0.001
ZrS_2 (n, n)						
(12,12)@(18,18)	10.8	19.9	12.3	18.4	0.012	0.095
(18,18)@(24,24)	16.8	26.1	18.3	24.4	0.014	0.151
(14,14)@(21,21)	13.0	22.7	14.4	21.3	0.003	0.011

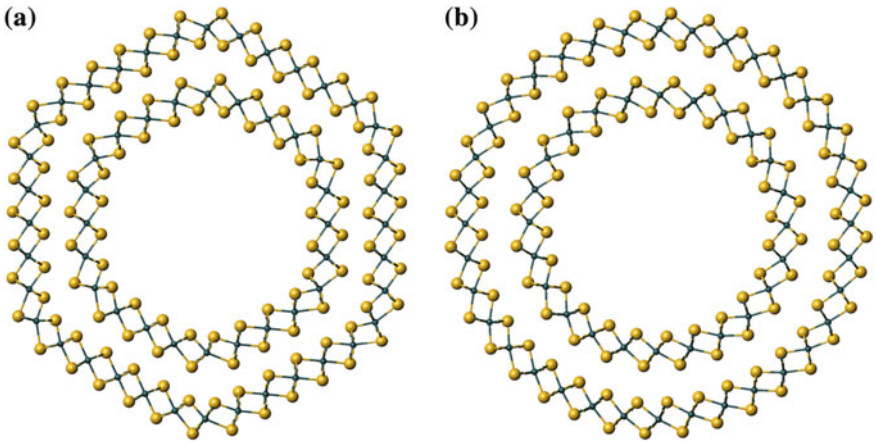

Fig. 9.25 Cross-section of DWNTs (12,12)@(18,18) folded from the hexagonal layers of the 1T–o phase of TiS_2. Prepared initial polygonal structure (**a**) and final optimized structure (**b**) [85]

the completely cylindrical shape in the relaxed NT structure regardless of initial state. These deviations were negligible in the case of zigzag DWNTs; and they were discernible in the outer component of the armchair DWNTs.

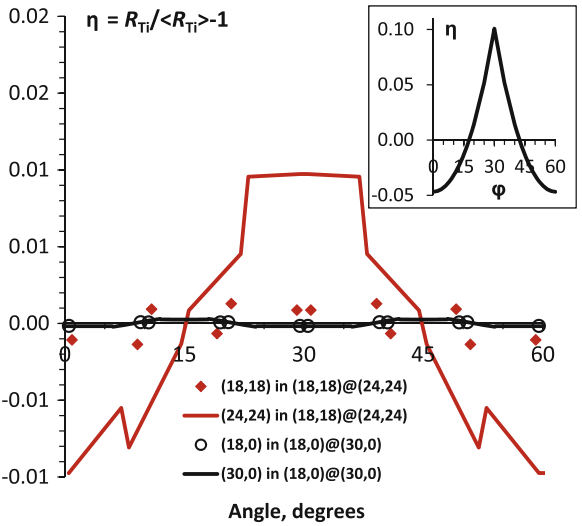

Fig. 9.26 The deviation of the Ti atom reduced radial coordinate versus its azimuth angle coordinate in the (18,0)@(30,0) and (18,18)@(24,24) TiS_2 DWNTs. (Points for (24,24) and (30,0) subtubes are connected for illustrative purpose.) The inset shows the distribution $\eta(\phi)$ for the ideal hexagon cross-section (see text for explanation) [85]

Figure 9.26 shows the relative deviation of the distance from the tube axis to the Ti atoms, $\eta = R_{Ti}/\langle R_{Ti}\rangle - 1$, versus the azimuth angle ϕ_{Ti} between the $\mathbf{R}_{Ti}$ vector and the y-axis (in our setting $\phi_{Ti} = 0$ corresponds to the position of the Ti atom on the y-axis with a minimal R_{Ti}). As is clearly seen in Fig. 9.26 only the external wall (24,24) of the (18,18)@(24,24) armchair tube has a noticeable (about 1 %) deviation from the cylindrical shape toward the flatter form, whereas the deviation of the internal wall (18,18) of the same DWNT is small. At the same time, both walls in the zigzag (18,0)@(30,0) tube have a negligible deviation from the cylindrical form. The plots depicted in Fig. 9.26 reveal a period of 60° proving that both DWNTs maintain 6-fold rotational axes. The inset in Fig. 9.26 shows the distribution $\eta(\phi)$ for the ideal hexagon cross-section. The analytical expression of such a distribution was obtained in [85] for any regular n-polygon cross-section.

The change of the NT shape is confirmed by the data of Table 9.8, where the standard deviation of the Ti remoteness from the tube axis, $\sigma(R_{Ti}) = \sqrt{\langle R_{Ti}^2\rangle - \langle R_{Ti}\rangle^2}$ is given for the selected DWNTs. The maximum standard deviation of 0.161 Å is found for the subtube (24,24) in the (18,18)@(24,24) TiS_2 NT. Although the completely polygonal tube was not obtained in [85], from the DWNTs proposed in [106] one can assume that the advantage of the multiwall NTs with a polygonal-cross section over the NTs with a circular cross-section will grow with increasing of NT diameter and it becomes more probable in the outer shells of the multiwall NTs.

References

1. F. Cheng, J. Chen, J. Mater. Res. **21**, 2744 (2006)
2. R. Tenne, in *Nanotubes and Nanofibers*, ed. by Y. Gogotsi (Taylor and Francis Group, Boca Raton, 2008), pp. 135–155
3. A.S. Golub, Ya.V. Zubavichus, Yu.L. Slovokhotov, Yu.N. Novikov, Russ. Chem. Rev. **72**, 123 (2003)
4. K. Kobayashi, J. Yamauchi, Phys. Rev. B **51**, 17085 (1995)
5. A.H. Reshak, S. Auluck, Phys. Rev. B **71**, 155114 (2005)
6. C. Li, W.L. Guo, Y. Kong, H. Gao, Phys. Rev. B **76**, 35322 (2007)
7. S. Lebegue, O. Eriksson, Phys. Rev. B **79**, 115409 (2009)
8. L. Wei, C. Jun-fang, H. Qinyu, W. Teng, Physica B **405**, 2498 (2010)
9. H. Guo, T. Yang, P. Tao, Y. Wang, Z. Zhang, J. Appl. Phys. **113**, 013709 (2013)
10. S. Zhao, J. Hue, W. Kang, Chem. Phys. Lett. **595**, 35 (2014)
11. A. Klein, S. Tiefenbacher, V. Eyert, C. Pettenkofer, W. Jaegermann, Phys. Rev. B **64**, 205416 (2001)
12. K. Albe, A. Klein, Phys. Rev. B **66**, 073413 (2002)
13. G. Arora, Y. Sharma, V. Sharma, G. Ahmed, S.K. Srivastava, B.L. Ahuja, J. Alloy. Compd. **470**, 452 (2009)
14. A. Kuc, N. Zibouche, T. Heine, Phys. Rev. B **83**, 245213 (2011)
15. N. Zibouche, A. Kuca, T. Heine, Eur. Phys. J. **B85**, 49 (2012)
16. F. Hulliger, in *Structural Chemistry of Layer Type Phases*, ed. by F. Levy (Reidel, Dordrecht, 1976)
17. K.K. Kam, B.A. Parkinson, J. Phys. Chem. **86**, 463 (1982)
18. R. Shidpour, M. Manteghian, Chem. Phys. **360**, 97 (2009)
19. K.F. Mak, C. Lee, J. Hone, J. Shan, T.F. Heinz, Phys. Rev. Lett. **105**, 136805 (2009)
20. H.R. Gutierrez, N. Perea-Lopez, A.L. Elias, A. Berkdemir, B. Wang, R. Lv, F. Lopez-Urias, V.H. Crespi, H. Terrones, M. Terrones, Nano Lett. **13**, 3447 (2013)
21. A. Berkdemir, H.R. Gutierrez, A.R. Botello-Mendez, N. Perea-Lopez, A.L. Elías, C.I. Chia, B. Wang, V.H. Crespi, F. Lopez-Urías, J-.C. Charlier, H. Terrones, M. Terrones, Sci. Rep. **3**, 1755 (2013)
22. H. Zeng, G.-B. Liu, J. Dai, Y. Yan, B. Zhu, R. He, L. Xie, S. Xu, X. Chen, W. Yao, X. Cui, Sci. Rep. **3**, 1608 (2013)
23. A. Splendiani, L. Sun, Y. Zhang, T. Li, J. Kim, C.-Y. Chim, G. Galli, F. Wang, Nano Lett. **10**, 1271 (2010)
24. A. Castellanos-Gomez, M. Barkelid, A.M. Goossens, V.E. Calado, H.S.J. van der Zant, G.A. Steele, Nano Lett. **12**, 3187 (2012)
25. H.G. Fuchtbauer, A.K. Tuxen, P.G. Moses, H. Topsoe, F. Besenbachera, J.V. Lauritsen, Phys. Chem. Chem. Phys. **15**, 15971 (2013)
26. H.S.S.R. Matte, A. Gomathi, A.K. Manna, D.J. Latte, R. Datta, S.K. Patti, C.N.R. Rao, Angew. Chem. Int. Ed. **49**, 4059 (2010)
27. C. Ataca, S. Ciraci, J. Phys. Chem. C **115**, 13303 (2011)
28. Y. Ma, Y. Dai, M. Guo, C. Niu, J. Lu, B. Huang, Phys. Chem. Chem. Phys. **13**, 15546 (2011)
29. A. Molina-Sanchez, L. Wirtz, Phys. Rev. B **84**, 155413 (2011)
30. N. Singh, G. Jabbour, U. Schwingenschlogl, Eur. Phys. J. B **85**, 392 (2012)
31. E.S. Kadantsev, P. Hawrylak, Solid State Commun. **152**, 909 (2012)
32. T. Cheiwchanchamnangij, W.R.L. Lambrecht, Phys. Rev. B **85**, 205302 (2012)
33. J. Wei, Z. Ma, H. Zeng, Z. Wang, Q. Wei, P. Peng, AIP Adv. **2**, 042141 (2012)
34. K. Kosmider, J. Fernandez-Rossier, Phys. Rev. **B 87**, 075451 (2013)
35. J. Kang, S. Tongay, J. Zhou, J. Li, J. Wu, Appl. Phys. Lett **102**, 012111 (2013)
36. I. Milošević, T. Vuković, M. Damnjanović, B. Nikolić, Eur. Phys. J. B **17**, 707 (2000)
37. R. Tenne, L. Margulis, M. Genut, G. Hodes, Nature **360**, 444 (1992)
38. R. Tenne, M. Homyonfer, Y. Feldman, Chem. Mater. **10**, 3225 (1998)

39. A. Rothschild, R. Popovitz-Biro, O. Lourie, R. Tenne, J. Phys. Chem. B **104**, 8976 (2000)
40. A. Margolin, F.L. Deepak, R. Popovitz-Biro, M. Bar-Sadan, Y. Feldman, R. Tenne, Nanotechnology **19**, 095601 (2008)
41. R. Tenne, Nat. Nanotechnol. **1**, 103 (2006)
42. R. Tenne, M. Remkar, A.N. Enyashin, G. Seifert, in *Carbon Nanotubes*, ed. by A. Jorio, G. Dresselhaus, M.S. Dresselhaus. Topics in Applied Physics, vol. 111 (Springer, Berlin, 2008), pp. 631–671
43. R. Tenne, G. Seifert, Annu. Rev. Mater. Res. **39**, 387 (2009)
44. R. Tenne, M. Redlich, Chem. Soc. Rev. **39**, 1423 (2010)
45. R. Levi, M. Bar-Sadan, R. Tenne, in *Springer Handbook for Nanomaterials*, Chapter 16, ed. by R. Vajtai (Springer, Berlin, 2013)
46. G. Seifert, H. Terrones, M. Terrones, G. Jungnickel, T. Frauenheim, Phys. Rev. Lett. **85**, 146 (2000)
47. R. Dovesi, V.R. Saunders, C. Roetti, R. Orlando, C.M. Zicovich-Wilson, F. Pascale, B. Civalleri, K. Doll, N.M. Harrison, I.J. Bush, P. D'Arco, M.Llunell, *CRYSTAL09 User's Manual*, (University of Torino, Torino, 2010)
48. I. Milošević, B. Nikolić, E. Dobardzic, M. Damnjanović, I. Popov, G. Seifert, Phys. Rev. B **76**, 233414 (2007)
49. I. Kaplan-Ashiri, S.R. Cohen, K. Gartsman, V. Ivanovskaya, T. Heine, G. Seifert, I. Wiesel, H.D. Wagner, R. Tenne, PNAS **103**, 523 (2006)
50. E.W. Bucholz, S.B. Sinnott, J. Appl. Phys. **112**, 123510 (2012)
51. T. Lorenz, D. Teich, J.-O. Joswig, G. Seifert, J. Phys. Chem. C **116**, 11714 (2012)
52. V.V. Ivanovskaya, T. Heine, S. Gemming, G. Seifert, Phys. Status Solidi (B) **243**, 1757 (2006)
53. A.N. Enyashin, Y.N. Makurin, A.L. Ivanovskii, Dokl. Phys. Chem. **399**, 293 (2004)
54. A.N. Enyashin, V.V. Ivanovskaya, A.L. Ivanovskii, Mendeleev Commun. **107**, 94 (2004)
55. M. Remskar, A. Mrzel, Z. Skraba, A. Jesih, M. Ceh, J. Demsar, P. Stadelmann, F. Levy, D. Mihailovic, Science **292**, 479 (2001)
56. M. Verstraete, J.-C. Charlier, Phys. Rev. B **68**, 045423 (2003)
57. H. Lin, X. Chen, H. Li, M. Yang, Y. Qi, Mater. Lett. **64**, 1748 (2010)
58. G.A. Camacho-Bragado, J.L. Elechiguerra, A. Olivas, S. Fuentes, D. Galvanb, M.J. Yacaman, J. Catal. **234**, 182 (2005)
59. C. Zhang, H.B. Wu, Z. Guo, X.W. (David) Lou, Electrochem. Commun. **20**, 7 (2012)
60. M. Albiter, R. Huirache-Acuna, F. Paraguay-Delgado, J.L. Rico, G. Alonso-Nunez, Nanotechnology **17**, 3473 (2006)
61. Y. Tian, J. Zhao, W. Fu, Y. Liu, Y. Zhu, Z. Wang, Mater. Lett. **59**, 3452 (2005)
62. S. Sun, Z. Li, X. Chang, Mater. Lett. **65**, 3164 (2011)
63. G. Tang, H. Tang, C. Li, W. Li, X. Ji, Mater. Lett. **65**, 3457 (2011)
64. P.K. Panigrahi, A. Pathak, Sci. Technol. Adv. Mater. **9**, 045008 (2008)
65. J. Kibsgaard, A. Tuxen, M. Levisen, E. Lagsgaard, S. Gemming, G. Seifert, J.V. Lauritsen, F. Besenbacher, Nano Lett. **8**, 3928 (2008)
66. I. Popov, S. Gemming, S. Okano, N. Ranjan, G. Seifert, Nano Lett. **8**, 4093 (2008)
67. H. Schweiger, P. Raybaud, G. Kresse, H. Toulhoat, J. Catal. **207**, 76 (2002)
68. L.F. Seivane, H. Barron, S. Botti, M.A.L. Marques, A. Rubio, X.X. Lopez-Lozano, J. Mater. Res. **28**, 240 (2013)
69. A.R. Botello-Mendez, F. Lopez-Urias, M. Terrones, H. Terrones, Nanotechnology **20**, 325703 (2009)
70. Y. Li, Z. Zhou, S. Zhang, Z. Chen, J. Am. Chem. Soc. **130**, 16739 (2008)
71. R. Shidpour, M. Manteghian, Nanoscale **2**, 1429 (2010)
72. C. Ataca, H. Sahin, E. Akturk, S. Ciraci, J. Phys. Chem. C **115**, 3934 (2011)
73. Z. Wang, K. Zhao, H. Li, Z. Liu, Z. Shi, J. Lu, K. Suenaga, S.-K. Joung, T. Okazaki, Z. Jin, Z. Gu, Z. Gao, J. Mater. Chem. **21**, 171 (2011)
74. H. Pan, Y.-W. Zhang, J. Mater. Chem. **22**, 7280 (2012)
75. E. Erdogan, I.H. Popov, A.N. Enyashin, G. Seifert, Eur. Phys. J. B **85**, 33 (2012)

76. Q. Yue, S. Chang, J. Kang, X. Zhang, Z. Shao, S. Qin, J. Li, J. Phys.: Condens. Matter **24**, 335501 (2012)
77. H. Zhang, X.-B. Li, L.-M. Liu, J. Appl. Phys. **114**, 093710 (2013)
78. S. Prabakar, C.W. Bumby, R.D. Tilley, Chem. Mater. **21**, 1725 (2009)
79. J. Chen, S.-L. Li, Z.-L. Tao, Y.-T. Shen, C.-X. Cui, J. Am. Chem. Soc. **125**, 5284 (2003)
80. J. Chen, S.-L. Li, Z.-L. Tao, F. Gao, Chem. Commun. **8**, 980 (2003)
81. M. Nath, C.N.R. Rao, Angew. Chem. Int. Ed. **41**, 3451 (2002)
82. D. Zhang, P. Liu, C. Liu, J. Phys. Chem. C **112**, 16729 (2008)
83. J. Jang, S. Jeong, J. Seo, M.-C. Kim, E. Sim, Y. Oh, S. Nam, B. Park, J. Cheon, J. Am. Chem. Soc. **133**, 7636 (2011)
84. Y.Q. Zhu, W.K. Hsu, N. Grobert, B.H. Chang, M. Terrones, H. Terrones, H.W. Kroto, D.R.M. Walton, Chem. Mater. **12**, 1190 (2000)
85. A.V. Bandura, R.A. Evarestov, J. Comput. Chem. **35**, 395 (2014)
86. R.A. Evarestov, A.V. Bandura, Phys. Scr. **89**, 044001 (2014)
87. P. Lightfoot, F. Krok, J.L. Nowinski, P.G. Bruce, J. Mater. Chem. **2**, 139 (1992)
88. Y.G. Yu, N.L. Ross, J. Phys.: Condens. Matter **23**, 055401 (2011)
89. H. Jiang, J. Chem. Phys. **134**, 204705 (2011)
90. K. Sanchez, P. Palacios, P. Wahnon, Phys. Rev. B **78**, 235121 (2008)
91. C.M. Fang, R.A. de Groot, C. Haas, Phys. Rev. B **56**, 4455 (1997)
92. C.A. Kukkonen, W.J. Kaiser, E.M. Logothetis, B.J. Blumenstock, P.A. Schroeder, S.P. Faile, R. Colella, J. Gambold, Phys. Rev. B **24**, 1691 (1981)
93. R.H. Friend, D. Jerome, W.Y. Liang, C. Mikkelsen, A.D. Yoffe, J. Phys. C: Solid State Phys. **10**, L705 (1977)
94. D.R. Allan, A.A. Kelsey, S.J. Clark, R.J. Angel, G.J. Ackland, Phys. Rev. B **57**, 5106 (1998)
95. M. Moustafa, T. Zandt, C. Janowitz, R. Manzke, Phys. Rev. B **80**, 035206 (2009)
96. J.P. Perdew, A. Ruzsinszky, G.I. Csonka, O.A. Vydrov, G.E. Scuseria, L.A. Constantin, X. Zhou, K. Burke, Phys. Rev. Lett. **100**, 136406 (2008)
97. C.Y. Chen, W. Fabian, F.C. Brown, K.C. Woo, B. Davies, B. DeLong, A.H. Thompson, Phys. Rev. B **21**, 615 (1980)
98. J.R. Dahn, W.R. McKinnon, R.R. Haering, W.J.L. Buyers, B.M. Powell, Can. J. Phys. **58**, 207 (1980)
99. V.P. Glushko, V.A. Medvedev, L.V. Gurvich (eds.), *Thermal Constants of Substances* (Wiley, New York, 1999)
100. G. Haegg, N. Schoenberg, Arkiv fur kemi **7**, 371 (1954)
101. A.N. Enyashin, A.L. Ivanovskii, Inorg. Mater. **41**, 1118 (2005)
102. V.V. Ivanovskaya, A.N. Enyashin, N.I. Medvedeva, Y.N. Makurin, A.L. Ivanovskii, Internet Electron. J. Mol. Des. **2**, 499 (2003)
103. V.V. Ivanovskaya, G. Seifert, Solid State Commun. **130**, 175 (2004)
104. V.V. Ivanovskaya, G. Seifert, A.L. Ivanovskii, Semiconductors **39**, 1058 (2005)
105. D. Teich, T. Lorenz, J.-O. Joswig, G. Seifert, D.-B. Zhang, T. Dumitrica, J. Phys. Chem. C **115**, 6392 (2011)
106. K. Tibbetts, R. Doe, G. Ceder, Phys. Rev. B **80**, 014102 (2009)
107. R.A. Evarestov, *Quantum Chemistry of Solids: LCAO Treatment of Crystals and Nanostructures*, 2nd edn. Springer Series in Solid State Sciences, vol. 153 (Springer, Berlin, 2012)
108. R.A. Evarestov, Yu.F. Zhukovskii, A.V. Bandura, S. Piskunov, J. Phys. Chem. C **114**, 21061 (2010)
109. R.A. Evarestov, A.V. Bandura, M.V. Losev, S. Piskunov, Yu.F. Zhukovskii, Physica E **43**, 266 (2010)
110. A.V. Bandura, R.A. Evarestov, Surf. Sci. **603**, L117 (2009)
111. A.V. Bandura, R.A. Evarestov, Comput. Mater. Sci. **65**, 395 (2012)
112. M. Damnjanović, T.V.E. Dobradzić, I. Milošević, T. Vuković, B. Nikolić, New J. Phys. **5**, 148 (2003)
113. R.A. Evarestov, Yu.F. Zhukovskii, A.V. Bandura, S. Piskunov, M.V. Losev, J. Phys. Chem. C **115**, 14067 (2011)
114. R.A. Evarestov, A.V. Bandura, *Nanodevices and Nanomaterials for Ecological Security*. NATO Science for Peace and Security; Series B: Physics and Biophysics (Springer, Dordrecht, 2012), pp. 75–85

Appendix A
Space Groups

Table A.1 gives the list of 230 three-periodic space groups. The point group international symbols are underlined for the space groups that appear as the first ones in the list of a given crystal class.

Table A.1 230 three-periodic space groups

N_G	G	IG	N_G	G	IG	N_G	G	IG
Triclinic								
1	C_1^1	$P\underline{1}$	2	C_i^1	$P\underline{\bar{1}}$			
Monoclinic								
3	C_2^1	$P\underline{2}$	4	C_2^2	$P2_1$	5	C_2^3	$C2$
6	C_s^1	$P\underline{m}$	7	C_s^2	Pc	8	C_s^3	Cm
9	C_s^4	Cc	10	C_{2h}^1	$P\underline{2/m}$	11	C_{2h}^2	$P2_1/m$
12	C_{2h}^3	$C2/m$	13	C_{2h}^4	$P2/c$	14	C_{2h}^5	$P2_1/c$
15	C_{2h}^6	$C2/c$						
Orthorhombic								
16	D_2^1	$P\underline{222}$	17	D_2^2	$P222_1$	18	D_2^3	$P2_12_12$
19	D_2^4	$P2_12_12_1$	20	D_2^5	$C222_1$	21	D_2^6	$C222$
22	D_2^7	$F222$	23	D_2^8	$I222$	24	D_2^9	$I2_12_12_1$
25	C_{2v}^1	$P\underline{mm}2$	26	C_{2v}^2	$Pmc2_1$	27	C_{2v}^3	$Pcc2$
28	C_{2v}^4	$Pma2$	29	C_{2v}^5	$Pca2_1$	30	C_{2v}^6	$Pnc2$
31	C_{2v}^7	$Pmn2_1$	32	C_{2v}^8	$Pba2$	33	C_{2v}^9	$Pna2_1$
34	C_{2v}^{10}	$Pnn2$	35	C_{2v}^{11}	$Cmm2$	36	C_{2v}^{12}	$Cmc2_1$
37	C_{2v}^{13}	$Ccc2$	38	C_{2v}^{14}	$Amm2$	39	C_{2v}^{15}	$Abm2$
40	C_{2v}^{16}	$Ama2$	41	C_{2v}^{17}	$Aba2$	42	C_{2v}^{18}	$Fmm2$
43	C_{2v}^{19}	$Fdd2$	44	C_{2v}^{20}	$Imm2$	45	C_{2v}^{21}	$Iba2$
46	C_{2v}^{22}	$Ima2$	47	D_{2h}^1	$P\underline{mmm}$	48	D_{2h}^2	$Pnnn$
49	D_{2h}^3	$Pccm$	50	D_{2h}^4	$Pban$	51	D_{2h}^5	$Pmma$

(continued)

© Springer-Verlag Berlin Heidelberg 2015

R.A. Evarestov, *Theoretical Modeling of Inorganic Nanostructures*,
NanoScience and Technology, DOI 10.1007/978-3-662-44581-5

Table A.1 (continued)

N_G	G	IG	N_G	G	IG	N_G	G	IG
52	D_{2h}^{6}	$Pnna$	53	D_{2h}^{7}	$Pmna$	54	D_{2h}^{8}	$Pcca$
55	D_{2h}^{9}	$Pbam$	56	D_{2h}^{10}	$Pccn$	57	D_{2h}^{11}	$Pbcm$
58	D_{2h}^{12}	$Pnnm$	59	D_{2h}^{13}	$Pmmn$	60	D_{2h}^{14}	$Pbcn$
61	D_{2h}^{15}	$Pbca$	62	D_{2h}^{16}	$Pnma$	63	D_{2h}^{17}	$Cmcm$
64	D_{2h}^{18}	$Cmca$	65	D_{2h}^{19}	$Cmmm$	66	D_{2h}^{20}	$Cccm$
67	D_{2h}^{21}	$Cmma$	68	D_{2h}^{22}	$Ccca$	69	D_{2h}^{23}	$Fmmm$
70	D_{2h}^{24}	$Fddd$	71	D_{2h}^{25}	$Immm$	72	D_{2h}^{26}	$Ibam$
73	D_{2h}^{27}	$Ibca$	74	D_{2h}^{28}	$Imma$			
Tetragonal								
75	C_4^1	$P\underline{4}$	76	C_4^2	$P4_1$	77	C_4^3	$P4_2$
78	C_4^4	$P4_3$	79	C_4^5	$I4$	80	C_4^6	$I4_1$
81	S_4^1	$P\overline{4}$	82	S_4^2	$I\overline{4}$	83	C_{4h}^1	$P\underline{4/m}$
84	C_{4h}^2	$P4_2/m$	85	C_{4h}^3	$P4/n$	86	C_{4h}^4	$P4_2/n$
87	C_{4h}^5	$I\overline{4}/m$	88	C_{4h}^6	$I4_1/a$	89	D_4^1	$P\underline{422}$
90	D_4^2	$P42_12$	91	D_4^3	$P4_122$	92	D_4^4	$P4_12_12$
93	D_4^5	$P4_222$	94	D_4^6	$P4_22_12$	95	D_4^7	$P4_322$
96	D_4^8	$P4_32_12$	97	D_4^9	$I422$	98	D_4^{10}	$I4_122$
99	C_{4v}^1	$P\underline{4mm}$	100	C_{4v}^2	$P4bm$	101	C_{4v}^3	$P4_2cm$
102	C_{4v}^4	$P4_2nm$	103	C_{4v}^5	$P4cc$	104	C_{4v}^6	$P4nc$
105	C_{4v}^7	$P4_2mc$	106	C_{4v}^8	$P4_2bc$	107	C_{4v}^9	$I4mm$
108	C_{4v}^{10}	$I4cm$	109	C_{4v}^{11}	$I4_1md$	110	C_{4v}^{12}	$I4_1cd$
111	D_{2d}^1	$P\overline{4}2\underline{m}$	112	D_{2d}^2	$P\overline{4}2c$	113	D_{2d}^3	$P\overline{4}2_1m$
114	D_{2d}^4	$P\overline{4}2_1c$	115	D_{2d}^5	$P\overline{4}m2$	116	D_{2d}^6	$P\overline{4}c2$
117	D_{2d}^7	$P\overline{4}b2$	118	D_{2d}^8	$P\overline{4}n2$	119	D_{2d}^9	$I\overline{4}m2$
120	D_{2d}^{10}	$I\overline{4}c2$	121	D_{2d}^{11}	$I\overline{4}2m$	122	D_{2d}^{12}	$I\overline{4}2d$
123	D_{4h}^1	$P4/\underline{mmm}$	124	D_{4h}^2	$P4/mcc$	125	D_{4h}^3	$P4/nbm$
126	D_{4h}^4	$P4/nnc$	127	D_{4h}^5	$P4/mbm$	128	D_{4h}^6	$P4/mnc$
129	D_{4h}^7	$P4/nmm$	130	D_{4h}^8	$P4/ncc$	131	D_{4h}^9	$P4_2/mmc$
132	D_{4h}^{10}	$P4_2/mcm$	133	D_{4h}^{11}	$P4_2/nbc$	134	D_{4h}^{12}	$P4_2/nnm$
135	D_{4h}^{13}	$P4_2/mbc$	136	D_{4h}^{14}	$P4_2/mnm$	137	D_{4h}^{15}	$P4_2/nmc$
138	D_{4h}^{16}	$P4_2/ncm$	139	D_{4h}^{17}	$I4/mmm$	140	D_{4h}^{18}	$I4/mcm$
141	D_{4h}^{19}	$I4_1/amd$	142	D_{4h}^{20}	$I4_1/acd$			
Rhombohedral								
143	C_3^1	$P\underline{3}$	144	C_3^2	$P3_1$	145	C_3^3	$P3_2$
146	C_3^4	$R3$	147	C_{3i}^1	$P\overline{3}$	148	C_{3i}^2	$R\overline{3}$
149	D_3^1	$P\underline{312}$	150	D_3^2	$P321$	151	D_3^3	$P3_112$
152	D_3^4	$P3_121$	153	D_3^5	$P3_212$	154	D_3^6	$P3_221$
155	D_3^7	$R32$	156	C_{3v}^1	$P\underline{3m1}$	157	C_{3v}^2	$P31m$

(continued)

Table A.1 (continued)

N_G	G	IG	N_G	G	IG	N_G	G	IG
158	C_{3v}^3	$P3c1$	159	C_{3v}^4	$P31c$	160	C_{3v}^5	$R3m$
161	C_{3v}^6	$R3c$	162	D_{3d}^1	$P\bar{3}1\underline{m}$	163	D_{3d}^2	$P\bar{3}1c$
164	D_{3d}^3	$P\bar{3}m1$	165	D_{3d}^4	$P\bar{3}c1$	166	D_{3d}^5	$R\bar{3}m$
167	D_{3d}^6	$R\bar{3}c$						
Hexagonal								
168	C_6^1	$P\underline{6}$	169	C_6^2	$P6_1$	170	C_6^3	$P6_5$
171	C_6^4	$P6_2$	172	C_6^5	$P6_4$	173	C_6^6	$P6_3$
174	C_{3h}^1	$P\bar{\underline{6}}$	175	C_{6h}^1	$P6/\underline{m}$	176	C_{6h}^2	$P6_3/m$
177	D_6^1	$P\underline{662}$	178	D_6^2	$P6_122$	179	D_6^3	$P6_522$
180	D_6^4	$P6_222$	181	D_6^5	$P6_422$	182	D_6^6	$P6_322$
183	C_{6v}^1	$P6\underline{mm}$	184	C_{6v}^2	$P6cc$	185	C_{6v}^3	$P6_3cm$
186	C_{6v}^4	$P6_3mc$	187	D_{3h}^1	$P\bar{6}\underline{m2}$	188	D_{3h}^2	$P\bar{6}c2$
189	D_{3h}^3	$P\bar{6}2m$	190	D_{3h}^4	$P\bar{6}2c$	191	D_{6h}^1	$P6/\underline{mmm}$
192	D_{6h}^2	$P6/mcc$	193	D_{6h}^3	$P6_3/mcm$	194	D_{6h}^4	$P6_3/mmc$
Cubic								
195	T^1	$P\underline{23}$	196	T^2	$F23$	197	T^3	$I23$
198	T^4	$P2_13$	199	T^5	$I2_13$	200	T_h^1	$P\underline{m\bar{3}}$
201	T_h^2	$Pn\bar{3}$	202	T_h^3	$Fm\bar{3}$	203	T_h^4	$Fd\bar{3}$
204	T_h^5	$Im\bar{3}$	205	T_h^6	$Pa\bar{3}$	206	T_h^7	$Ia\bar{3}$
207	O^1	$P\underline{432}$	208	O^2	$P4_232$	209	O^3	$F432$
210	O^4	$F4_132$	211	O^5	$I432$	212	O^6	$P4_332$
213	O^7	$P4_132$	214	O^8	$I4_132$	215	T_d^1	$P\bar{4}\underline{3m}$
216	T_d^2	$F\bar{4}3m$	217	T_d^3	$I\bar{4}3m$	218	T_d^4	$P\bar{4}3n$
219	T_d^5	$F\bar{4}3c$	220	T_d^6	$I\bar{4}3d$	221	O_h^1	$Pm\underline{\bar{3}m}$
222	O_h^2	$Pn\bar{3}n$	223	O_h^3	$Pm\bar{3}n$	224	O_h^4	$Pn\bar{3}m$
225	O_h^5	$Fm\bar{3}m$	226	O_h^6	$Fm\bar{3}c$	227	O_h^7	$Fd\bar{3}m$
228	O_h^8	$Fd\bar{3}c$	229	O_h^9	$Im\bar{3}m$	230	O_h^{10}	$Ia\bar{3}d$

Appendix B
Layer Groups as Subroups of Space Groups

Table B.1 shows the correspondence DG $\leftrightarrow$ G$/T_3$ between three-dimensional diperiodic (DG) and three-periodic (G) space groups. This correspondence was at first given by Wood [1] in the setting that differs for rectangular diperiodic groups from that given in Table B.1 (the setting in this Table corresponds to the standard setting of [2]).

Table B.2 presents the non-standard factorization of the diperiodic space groups. The generalized translational group, Z describes the periodical arrangement of the elementary motifs along two independent directions (these two directions are assumed to be in the xy-plane).

Table B.1 Correspondence between three-dimensional two-periodic (DG) and three-periodic (G) space groups (DG $\leftrightarrow$ G$/T_3$), [2]

DG		G		DG		G		DG		G	
1	$P1$	C_1^1	1	28	$Pm2_1b$	C_{2v}^2	26	55	$P4mm$	C_{4v}^1	99
2	$P\bar{1}$	C_i^1	2	29	$Pb2_1m$	C_{2v}^2	26	56	$P4bm$	C_{4v}^2	100
3	$P112$	C_2^1	3	30	$Pb2b$	C_{2v}^3	27	57	$P\bar{4}2m$	D_{2d}^1	111
4	$P11m$	C_s^1	6	31	$Pm2a$	C_{2v}^4	28	58	$P\bar{4}2_1m$	D_{2d}^3	113
5	$P11a$	C_s^2	7	32	$Pm2_1n$	C_{2v}^7	31	59	$P\bar{4}m2$	D_{2d}^5	115
6	$P112/m$	C_{2h}^1	10	33	$Pb2_1a$	C_{2v}^5	29	60	$P\bar{4}b2$	D_{2d}^7	117
7	$P112/a$	C_{2h}^4	13	34	$Pb2n$	C_{2v}^6	30	61	$P4/mmm$	D_{4h}^1	123
8	$P211$	C_2^1	3	35	$Cm2m$	C_{2v}^{14}	38	62	$P4/nbm$	D_{4h}^3	125
9	$P2_111$	C_2^2	4	36	$Cm2a$	$4C_{2v}^{15}$	39	63	$P4/mbm$	D_{4h}^5	127
10	$C211$	C_2^3	5	37	$Pmmm$	D_{2h}^1	47	64	$P4/nmm$	D_{4h}^7	129
11	$Pm11$	C_s^1	6	38	$Pmaa$	D_{2h}^3	49	65	$P3$	C_3^1	143
12	$Pb11$	C_s^2	7	39	$Pban$	D_{2h}^4	50	66	$P\bar{3}$	C_{3i}^1	147
13	$Cm11$	C_s^3	8	40	$Pmam$	D_{2h}^5	51	67	$P312$	D_3^1	149
14	$P2/m11$	C_{2h}^1	10	41	$Pmma$	$4D_{2h}^5$	51	68	$P321$	D_3^2	150

(continued)

© Springer-Verlag Berlin Heidelberg 2015

R.A. Evarestov, *Theoretical Modeling of Inorganic Nanostructures*,
NanoScience and Technology, DOI 10.1007/978-3-662-44581-5

Table B.1 (continued)

DG		G		DG		G		DG		G	
15	$P2_1/m11$	C_{2h}^2	11	42	$Pman$	D_{2h}^7	53	69	$P3m1$	C_{3v}^1	156
16	$P2/b11$	C_{2h}^4	13	43	$Pbaa$	D_{2h}^8	54	70	$P31m$	C_{3v}^2	157
17	$P2_1/b11$	C_{2h}^5	14	44	$Pbam$	D_{2h}^9	55	71	$P\bar{3}12/m$	D_{3d}^1	162
18	$C2/m11$	C_{2h}^3	12	45	$Pbma$	D_{2h}^{11}	57	72	$P\bar{3}2/m1$	D_{3d}^3	164
19	$P222$	D_2^1	16	46	$Pmmn$	D_{2h}^{13}	59	73	$P6$	C_6^1	168
20	$P2_122$	D_2^2	17	47	$Cmmm$	D_{2h}^{19}	65	74	$P\bar{6}$	C_{3h}^1	174
21	$P2_12_12$	D_2^3	18	48	$Cmma$	D_{2h}^{21}	67	75	$P6/m$	C_{6h}^1	175
22	$C222$	D_2^6	21	49	$P4$	C_4^1	75	76	$P622$	D_6^1	177
23	$Pmm2$	C_{2v}^1	25	50	$P\bar{4}$	S_4^1	81	77	$P6mm$	C_{6v}^1	183
24	$Pma2$	C_{2v}^4	28	51	$P4/m$	C_{4h}^1	83	78	$P\bar{6}m2$	D_{3h}^1	187
25	$Pba2$	C_{2v}^8	32	52	$P4/n$	C_{4h}^3	85	79	$P\bar{6}2m$	D_{3h}^3	189
26	$Cmm2$	C_{2v}^{11}	35	53	$P422$	D_4^1	89	80	$P6/mmm$	D_{6h}^1	191
27	$Pm2m$	C_{2v}^1	25	54	$P42_12$	D_4^2	90				

The numbers of 17 plane groups are underlined

Table B.2 The non-standard factorization of the diperiodic groups [3]

DG	H	I	PZ	Int.symb.	DG	H	I	PZ	Int.symb
1	C_{2h}	C_1	T	p1	41	D_{2h}	D_{2h}	$C_{2v}T_h$	$p\frac{2}{a}\frac{2_1}{m}\frac{2}{m}(\frac{2_1}{m}\frac{2}{m}\frac{2}{a})$
2		S_2	S_2T	$p\bar{1}$	42		D_{2h}	$D_{1d}T'_h$	$p\frac{2}{n}\frac{2}{m}\frac{2_1}{a}(\frac{2}{m}\frac{2_1}{a}\frac{2}{n})$
3		C_2	C_{2T}	p211(112)	43		D_{2h}	$D_12_1T_h$	$p\frac{2}{a}\frac{2}{b}\frac{2_1}{a}(\frac{2}{b}\frac{2_1}{a}\frac{2}{a})$
4		C_{1h}	$C_{1h}T$	pm11(11m)	44		D_{2h}	$C_{2h}T'_v$	$p\frac{2}{m}\frac{2_1}{b}\frac{2_1}{a}(\frac{2_1}{b}\frac{2_1}{a}\frac{2}{m})$
5		C_{1h}	T_h	pb11(11a)	45		D_{2h}	$C_22_1T_h$	$p\frac{2}{a}\frac{2_1}{b}\frac{2_1}{m}(\frac{2_1}{b}\frac{2_1}{m}\frac{2}{a})$
6		C_{2h}	$C_{2h}T$	$p\frac{2}{m}11(11\frac{2}{m})$	46		D_{2h}	$C_{2v}T'_h$	$p\frac{2}{n}\frac{2_1}{m}\frac{2_1}{m}(\frac{2_1}{m}\frac{2_1}{m}\frac{2}{n})$
7		C_{2h}	C_{2T_h}	$p\frac{2}{b}11(11\frac{2}{a})$	47		D_{2h}	$D_{2h}T'$	$p\frac{2}{m}\frac{2}{m}\frac{2}{m}$
8	D_{2h}	D_1	D_{1T}	p112(211)	48		D_{2h}	$C_{2v}T'_h$	$c\frac{2}{a}\frac{2}{m}\frac{2}{m}(\frac{2}{m}\frac{2}{m}\frac{2}{e})$
9		D_1	2_1	$p112_1(2_111)$	49	D_{4h}	C_4	C_{4T}	$p4$
10		D_1	$D_{1T'}$	c112(211)	50		S_4	S_4T	$p\bar{4}$
11		C_{1v}	$C_{1v}T$	$p11m(m11)$	51		C_{4h}	$C_{4h}T$	$p4/m$
12		C_{1v}	T_v	$p11a(b11)$	52		C_{4h}	$C_4T'_h$	$p4/n$
13		C_{1v}	$C_{1v}T'$	$c11m(m11)$	53		D_4	D_{4T}	$p422$
14		D_{1d}	$D_{1d}T$	$p11\frac{2}{m}(\frac{2}{m}11)$	54		D_4	$C_42'_1$	$p42_12$
15		D_{1d}	S_22_1	$p11\frac{2_1}{m}(\frac{2_1}{m}11)$	55		C_{4v}	$C_{4v}T$	$p4mm$

(continued)

Table B.2 (continued)

DG	H	I	PZ	Int.symb.	DG	H	I	PZ	Int.symb
16(18)		D_{1d}	$D_{1d}T'$	$c11\frac{2}{m}(\frac{2}{m}11)$	56		C_{4v}	$C_4T'_v$	$p4bm$
17(16)		D_{1d}	S_2T_v	$p11\frac{2}{a}(\frac{2}{b}11)$	57		D_{2d}	$D_{2d}T$	$p\bar{4}2m$
18(17)		D_{1d}	$S_2T'_v$	$p11\frac{2_1}{a}(\frac{2_1}{b}11)$	58		D_{2d}	$S_42'_1$	$p\bar{4}2_1m$
19		D_2	D_2T	$p222$	59		D_{2d}	$D_{2d}T$	$p\bar{4}m2$
20		D_2	C_22_1	$p222_1(2_122)$	60		D_{2d}	$S_4T'_v$	$p\bar{4}b2$
21		D_2	$C_22'_1$	$p22_12_1(2_12_12)$	61		D_{4h}	$D_{4h}T$	$p\frac{4}{m}\frac{2}{m}\frac{2}{m}$
22		D_2	D_2T'	$c222$	62		D_{4h}	$D_{2d}T'_h$	$p\frac{4}{n}\frac{2}{b}\frac{2}{m}$
23		C_{2v}	$C_{2v}T$	$p2mm(mm2)$	63		D_{4h}	$C_{4h}T'_v$	$p\frac{4}{m}\frac{2_1}{b}\frac{2}{m}$
24(27)		D_{1h}	$D_{1h}T$	$pmm2(m2m)$	64		D_{4h}	$D_{2d}T'_h$	$p\frac{4}{n}\frac{2_1}{m}\frac{2}{m}$
25(29)		D_{1h}	$C_{1h}2_1$	$pm2_1a(b2_1m)$	65	D_{6h}	C_3	C_3T	$p3$
26(28)		D_{1h}	$C_{1v}2_1$	$pbm2_1(m2_1b)$	66		S_6	S_6T	$p\bar{3}$
27(30)		D_{1h}	D_1T_v	$pbb2(b2b)$	67		D_3	D_3T	$p312$
28(24)		C_{2v}	C_2T_v	$p2ma(ma2)$	68		D_3	D_3T	$p321$
29(31)		D_{1h}	D_1T_h	$pam2(m2a)$	69		C_{3v}	$C_{3v}T$	$p3m1$
30(33)		D_{1h}	2_1T_h	$pab2_1(b2_1a)$	70		C_{3v}	$C_{3v}T$	$p31m$
31(34)		D_{1h}	$D_1T'_h$	$pnb2(b2n)$	71		D_{3d}	$D_{3d}T$	$p\bar{3}1\frac{2}{m}$
32		D_{1h}	$C_{1v}T'_h$	$pnm2_1(m2_1n)$	72		D_{3d}	$D_{3d}T$	$p\bar{3}\frac{2}{m}1$
33(25)		C_{2v}	$C_2T'_v$	$p2ba(ba2)$	73		C_6	C_6T	$p6$
34(26)		C_{2v}	$C_{2v}T'$	$c2mm(mm2)$	74		C_{3h}	$C_{3h}T$	$p\bar{6}$
35		D_{1h}	D_1hT'	$cmm2(m2m)$	75		C_{6h}	$C_{6h}T$	$p6/m$
36		D_{1h}	$D_1T'_h$	$cam2(m2e)$	76		D_6	D_6T	$p622$
37		D_{2h}	$D_{2h}T$	$p\frac{2}{m}\frac{2}{m}\frac{2}{m}$	77		C_{6v}	$C_{6v}T$	$p6mm$
38		D_{2h}	D_2T_h	$p\frac{2}{a}\frac{2}{m}\frac{2}{a}(\frac{2}{m}\frac{2}{a}\frac{2}{a})$	78		D_{3h}	$D_{3h}T$	$p\bar{6}m2$
39		D_{2h}	$D_2T'_h$	$p\frac{2}{n}\frac{2}{b}\frac{2}{a}(\frac{2}{b}\frac{2}{a}\frac{2}{n})$	79		D_{3h}	$D_{3h}T$	$p\bar{6}2m$
40		D_{2h}	$C_{2h}T_v$	$p\frac{2}{m}\frac{2_1}{m}\frac{2}{a}(\frac{2_1}{m}\frac{2}{a}\frac{2}{m})$	80		D_{6h}	$D_{6h}T$	$p\frac{6}{m}\frac{2}{m}\frac{2}{m}$

The sequental numbers of diperiodic groups and their International symbols are given according to [1]. The sequental numbers and the International symbols from [2] are given in brackets if they differ from those in [1]. For each diperiodic group DG, the holohedry H, the isogonal point group I, the factorization PZ and the international symbol according to [1], are given

Appendix C
Line Groups

Table C.1 is taken from [4]. All line groups are divided into 13 families, each family includes infinitely many line groups. Among these families there are 5 symmorphic (families 2, 3, 6, 9, 11) for which factorization (2.22) coincides with the standard one. The families 1 and 5 contain both incommensurate and commensurate (symmorphic and nonsymmorphic) line groups.

Table C.1 Line Groups. For each family F different factorizations, the roto-helical subgroup $L^{(1)}$, generators, and the isogonal point group P_I, are given in the first line

F N_F	q even	Factorizations International	q odd	$L^{(1)}$ F^+	Coset representatives $\ell_i^{(F)}$	P_I
1		$T_Q \times C_n$		$T_Q \times C_n$	$(C_Q\|f), C_n$	C_q
1		L_{q_p}		1		
2		$T \wedge S_{2q}$		$T \times C_q$	$(E\|a), S_{2q}$	S_{2q}
2	$L\overline{2q}$		$L\overline{q}$	1	S_{2q}	
3		$T \wedge C_{qh}$		$T \times C_q$	$(E\|a), C_q, \sigma_h$	C_{qh}
2	Lq/m		$L\overline{2q}$	1	σ_h	
4		$T^1_{2n}C_{nh} = T^1_{2n}S_{2n}$		$T^1_{2n} \times C_n$	$(C_{2n}\|a/2), C_n, \sigma_h$	C_{2nh}
2		$L(2n)_n/m$		1	σ_h	
5		$T_Q \wedge D_n$		$T_Q \times C_n$	$(C_Q\|f), C_n, U$	D_q
2	Lq_p22		Lq_p2	1	U	
6		$T \times C_{qv} = C_{qv} \wedge T'$		$T \times C_q$	$(E\|a), C_q, \sigma_v$	C_{qv}
2	Lqmm		Lqm	6	σ_v	
7		$C_q \wedge T'$		$T \times C_q$	$(\sigma_v\|a/2), C_q$	C_{qv}

(continued)

© Springer-Verlag Berlin Heidelberg 2015

R.A. Evarestov, *Theoretical Modeling of Inorganic Nanostructures*,
NanoScience and Technology, DOI 10.1007/978-3-662-44581-5

Table C.1 (continued)

F N_F	q even	Factorizations International	q odd	$L^{(1)}$ F^+	Coset representatives $\ell_i^{(F)}$	P_I
2	Lqcc		Lqc	7	$(\sigma_v\|a/2)$	
8		$C_{nv} \wedge T^1_{2n} = C_{nv} \wedge T'_d$		$T^1_{2n} \times C_n$	$(C_{2n}\|a/2), C_n, \sigma_v$	C_{2nv}
2		L$(2n)_n mc$		8	σ_v	
9		$T \wedge D_{qd} = T' \wedge D_{qd}$		$T \times C_q$	$(E\|a), C_q, U_d, \sigma_v$	D_{qd}
4	L$\overline{2q}2m$		L$\overline{q}m$	6	σ_v, U_d, S_{2q}	
10		$T'S_{2q} = T'_d D_q$		$T \times C_q$	$(\sigma_v\|a/2), S_{2q}$	D_{qd}
4	L$\overline{2q}2c$		L$\overline{q}c$	7	$(\sigma_v\|a/2), S_{2q}, (U_d\|a/2)$	
11		$T \wedge D_{qh} = T'D_{qh}$		$T \times C_q$	$(E\|a), C_q, U, \sigma_v$	D_{qh}
4	Lq/mmm		L$\overline{2q}m2$	7	σ_v, U, σ_h	
12		$T'C_{qh} = T'D_q$		$T \times C_q$	$(\sigma_v\|a/2), C_q, \sigma_h$	D_{qh}
4	Lq/mcm		L$\overline{2q}2c$	7	$(\sigma_v\|a/2), U, (S_{2q}\|a/2)$	
13		$T^1_{2n}D_{nh} = T^1_{2n}D_{nd} =$		$T^1_{2n} \times C_n$	$(C_{2n}\|a/2), C_n, U, \sigma_v$	D_{2nh}
		$T'_d D_{nh} = T'_d D_{nd}$				
4		L$(2n)_n/mcm$		8	σ_v, U, σ_h	

$N_F = |L^{(F)}|\|L^{(1)}|$, the international symbol (of commensurate groups only), family F^+ of the positive subgroup L^+ (for positive $F = F^+$), and the coset representatives $\ell_i^{(F)}$ for $i > 1$ of (2.25) (when $N_F = 4$, the first one gives L^+). T'_d and U_d are glide plane and horizontal axes bisecting vertical mirror planes, while $S_{2q} = C_q\sigma_h$. For families 1 and 5, the order q of the isogonal principle axis is given by $Q = q/r$ (for commensurate groups), otherwise q is infinite [4]. In families 4,8,13 $q = 2n$ is even

Appendix D
Rod Groups as Subgroups of Space Groups

Table D.1 gives the correspondence between rod and space groups—their international notation, the number of the corresponding SG and its Schönflis symbol.

75 rod groups can be distributed over 13 families, as is shown in Table D.2.

Table D.3 is taken from [4] and presents rod groups in the form accepted for a line group classification.

Table D.1 Rod Groups (RG) as subperiodic subgroups of Space Groups (SG)

RG		SG		RG		SG		RG		SG	
1	P1	1	C_1^1	26	$P4_3$	78	C_4^4	51	$P\bar{3}m1$	164	D_{3d}^3
2	$P\bar{1}$	2	C_i^1	27	$P\bar{4}$	81	S_4^1		$P\bar{3}1m$	162	D_{3d}^1
3	P211	(3)	C_2^1	28	P4/m	83	C_{4h}^1	52	$P\bar{3}c1$	165	D_{3d}^4
	P121	(3)	C_2^1								
4	Pm11	(6)	C_s^1	29	$P4_2/m$	84	C_{4h}^2		$P\bar{3}1c$	163	D_{3d}^2
	P1m1	(6)	C_s^1								
5	P1c1	(7)	C_s^2	30	P422	89	D_4^1	53	P6	168	C_6^1
	Pc11	(7)	C_s^2	31	$P4_122$	91	D_4^3	54	$P6_1$	169	C_6^2
6	P12/m1	(10)	C_{2h}^1	32	$P4_222$	93	D_4^5	55	$P6_2$	171	C_6^4
	P2/m11	(10)	C_{2h}^1	33	$P4_322$	95	D_4^7	56	$P6_3$	173	C_6^6
7	P12/c1	(13)	C_{2h}^4	34	P4mm	99	C_{4v}^1	57	$P6_4$	172	C_6^5
	P2/c11	(13)	C_{2h}^4	35	$P4_2cm$	101	C_{4v}^3	58	$P6_5$	170	C_6^3
8	P112	(3)	C_2^1		$P4_2mc$	105	C_{4v}^7	59	$P\bar{6}$	174	C_{3h}^1
				36	P4cc	103	C_{4v}^5	60	P6/m	175	C_{6h}^1
9	$P112_1$	4	C_2^2	37	$P\bar{4}2m$	111	D_{2d}^1	61	$P6_3/m$	176	C_{6h}^2
10	P11m	(6)	C_s^1		$P\bar{4}m2$	115	D_{2d}^5	62	P622	177	D_6^1
				38	$P\bar{4}2c$	112	D_{2d}^2	63	$P6_122$	178	D_6^2

(continued)

© Springer-Verlag Berlin Heidelberg 2015

R.A. Evarestov, *Theoretical Modeling of Inorganic Nanostructures*,
NanoScience and Technology, DOI 10.1007/978-3-662-44581-5

Table D.1 (continued)

RG		SG		RG		SG		RG		SG	
11	P112/m	(10)	C_{2h}^1		$P\bar{4}c2$	116	D_{2d}^6	64	$P6_222$	180	D_6^4
12	$P112_1/m$	11	C_{2h}^2	39	P4/mmm	123	D_{4h}^1	65	$P6_322$	182	D_6^6
13	P222	16	D_2^1	40	P4/mcc	124	D_{4h}^2	66	$P6_422$	181	D_6^5
14	$P222_1$	17	D_2^2	41	$P4_2/mmc$	131	D_{4h}^9	67	$P6_522$	179	D_6^3
15	Pmm2	(25)	C_{2v}^1		$P4_2/mcm$	132	D_{4h}^{10}	68	P6mm	183	C_{6v}^1
16	Pcc2	27	C_{2v}^3	42	P3	143	C_3^1	69	P6cc	184	C_{6v}^2
17	$Pmc2_1$	(26)	C_{2v}^2	43	$P3_1$	144	C_3^2	70	$P6_3mc$	186	C_{6v}^4
	$Pcm2_1$	(26)	C_{2v}^2	44	$P3_2$	145	C_3^3		$P6_3cm$	185	C_{6v}^3
18	Pm2m	(25)	C_{2v}^1	45	$P\bar{3}$	147	C_{3i}^1	71	$P\bar{6}m2$	187	D_{3h}^1
	P2mm	(25)	C_{2v}^1	46	P312	149	D_3^1		$P\bar{6}2m$	189	D_{3h}^3
19	P2cm	(28)	C_{2v}^4		P321	150	D_3^2	72	$P\bar{6}c2$	188	D_{3h}^2
	Pc2m	(28)	C_{2v}^4	47	$P3_112$	151	D_3^3		$P\bar{6}2c$	190	D_{3h}^4
20	Pmmm	47	D_{2h}^1		$P3_121$	152	D_3^4	73	P6/mmm	191	D_{6h}^1
21	Pccm	49	D_{2h}^3	48	$P3_212$	153	D_3^5	74	P6/mcc	192	D_{6h}^2
22	Pcmm	(51)	D_{2h}^5		$P3_221$	154	D_3^6	75	$P6_3/mmc$	194	D_{6h}^4
	Pmcm	(51)	D_{2h}^5	49	P3m1	156	C_{3v}^1		$P6_3/mcm$	193	D_{6h}^3
23	P4	75	C_4^1		P31m	157	C_{3v}^2				
24	$P4_1$	76	C_4^2	50	P3c1	158	C_{3v}^3				
25	$P4_2$	77	C_4^3		P31c	159	C_{3v}^4				

The numbers of SG generating different RG or RG with different settings are given in brackets

Table D.2 Rod Groups Distribution over Line Group Families (q—order of the rotation or screw axis), F—family number, N, N_c—number of groups and classes in family F

RGF	Class	Internat. Symbol (odd q,even q)	N, N_c	q = 1	q = 2	q = 3	q = 4	q = 6
1	C_q	q, q_p	16	1(1)	8(112), 9((112_1)	42(3) 43(3_1) 44(3_2)	23(4), 24(4_1) 25(4_2), 26(4_3)	53(6), 54(6_1) 55(6_2), 56(6_3) 57(6_4), 58(6_5)
		Classes	**5**	$\mathbf{C_1}$	$\mathbf{C_2}$	$\mathbf{C_3}$	$\mathbf{C_4}$	$\mathbf{C_6}$
5	D_q	$q2, q22$ q_q2, q_p22	16	3(211)	13(222), 14((222_1)	46(312) 47(3_112) 48(3_212)	30(422), 31(4_122) 32(4_222), 33(4_322)	62(622), 63(6_122) 64(6_222), 65(6_322) 66(6_422), 67(6_522)
		Classes	**5**	$\mathbf{D_1}$	$\mathbf{D_2}$	$\mathbf{D_3}$	$\mathbf{D_4}$	$\mathbf{D_6}$
2	S_{2q}	$\overline{q}, \overline{2q}$	3	2($\bar{1}$)	27($\bar{4}$)	45($\bar{3}$)		
		Classes	**3**	$\mathbf{S_2}(C_i)$	$\mathbf{S_4}$	$\mathbf{S_6}(\mathbf{C_{3i}})$		
3	C_{qh}	$\overline{2q}, q/m$	5	10(11m)	11($112/m$)	59($\bar{6}$)	28($4/m$)	60($6/m$)

(continued)

Table D.2 (continued)

RGF	Class	Internat. Symbol (odd q,even q)	N, N_c	q = 1	q = 2	q = 3	q = 4	q = 6
4	C_{qh}	$(2n)_n/m$	3		$12(11 2_1/m)$		$29(4_2/m)$	$61(6_3/m)$
		Classes	**5**	$\mathbf{C_{1h}}$	$\mathbf{C_{2h}}$	$\mathbf{C_{3h}}$	$\mathbf{C_{4h}}$	$\mathbf{C_{6h}}$
6	C_{qv}	qm, qmm	6	$4(m11)$	$15(mm2)$	$49(3m1)$	$34(4mm)$	$68(6mm)$
7	C_{qv}	qc, qcc	5	$5(c11)$	$16(cc2)$	$50(3c1)$	$36(4cc)$	$69(6cc)$
8	C_{qv}	$(2n)_n mc$	3		$17(mc2_1)$		$35(4_2mc)$	$70(6_3mc)$
		Classes	**5**	$\mathbf{C_{1v}}$	$\mathbf{C_{2v}}$	$\mathbf{C_{3v}}$	$\mathbf{C_{4v}}$	$\mathbf{C_{6v}}$
9	D_{qd}	$\overline{q}\ m, \overline{2q}\ 2m$	2	$6(2/m11)$	$37(\overline{4}\ 2m)$	$51(\overline{3}\ m1)$		
10	D_{qd}	$\overline{q}\ c, \overline{2q}\ 2c$	3	$7(2/c11)$	$38(\overline{4}\ 2c)$	$52(\overline{3}\ c1)$		
		Classes	**3**	$\mathbf{D_{1d}}$	$\mathbf{D_{2d}}$	$\mathbf{D_{3d}}$		
11	D_{qh}	$\overline{2q}\ m2, q/mmm$	5	$18(2mm)$	$20(mmm)$	$71(\overline{6}\ m2)$	$39(4/mmm)$	$73(6/mmm)$
12	D_{qh}	$\overline{2q}\ 2c, q/mcc$	5	$19(2cm)$	$21(ccm)$	$72(\overline{6}\ c2)$	$40(4/mcc)$	$74(6/mcc)$
13	D_{qh}	$(2n)_n/mmc$	3		$22(mcm)$		$41(4_2/mmc)$	$75(6_3/mmc)$
		Classes	**5**	$\mathbf{D_{1h}}$	$\mathbf{D_{2h}}$	$\mathbf{D_{3h}}$	$\mathbf{D_{4h}}$	$\mathbf{D_{6h}}$
	total	**75 rod groups, 31 crystal classes**						

In families 4, 8, 13 $q = 2n$ is even

Table D.3 Rod Groups (international and factorized notation) listed by families F of line groups according to the order q of the principal axis of the isogonal group, [4]

F	$q = 1$	$q = 2$	$q = 3$	$q = 4$	$q = 6$
1	1 $L1 = TC_1$	8 $L2 = TC_2$ 9 $L2_1 = T_2C_1$	42 $L3 = TC_3$ 43 $L3_1 = T_3C_1$ 44 $L3_2 = T_3^2C_1$	23 $L4 = TC_4$ 24 $L4_1 = T_4C_1$ 25 $L4_2 = T_4C_2$ 26 $L4_3 = T_4^3C_1$	53 $L6 = TC_6$ 54 $L6_1 = T_6C_1$ 55 $L6_2 = T_6C_2$ 56 $L6_3 = T_6C_3$ 57 $L6_4 = T_6^2C_2$ 58 $L6_5 = T_6^5C_1$
2	2 $L\overline{1} = \mathbf{TS_2}$	27 $L\overline{4} = \mathbf{TS_4}$	45 $L\overline{3} = \mathbf{TS_6}$		
3	10 $L\overline{2} = \mathbf{TC_{1h}}$	11 $L2/m = \mathbf{TC_{2h}}$	59 $L\overline{6} = \mathbf{TC_{3h}}$	28 $L4/m = TC_{4h}$	60 $L6/m = TC_{6h}$
4		12 $L2_1/m = \mathbf{T_2C_{1h}}$		29 $L4_2/m = T_4^1C_{2h}$	61 $L6_3/m = T_6^1C_{3h}$
5	3 $L12 = \mathbf{TD_1}$	13 $L222 = \mathbf{TD_2}$ 14 $L2_122 = T_2C_1$	46 $L32 = \mathbf{TD_3}$ 47 $L3_12 = T_3C_1$ 47 $L3_22 = T_3^2D_1$	30 $L422 = TD_4$ 31 $L4_122 = T_4D_1$ 32 $L4_222 = T_4D_2$ 33 $L4_322 = T_4^1D_2$	62 $L622 = TD_6$ 63 $L6_122 = T_6D_1$ 64 $L6_222 = T_6D_3$ 65 $L6_322 = T_6^1D_3$ 66 $L6_422 = T_6^2D_2$ 67 $L6_522 = T_6^5D_1$
6	4 $L1m = \mathbf{TC_{1v}}$	15 $L2mm = \mathbf{TC_{2v}}$	49 $L3m = \mathbf{TC_{3v}}$	34 $L4mm = TC_{4v}$	68 $L6mm = TC_{6v}$
7	5 $L1c = \mathbf{T'C_1}$	16 $L2cc = \mathbf{T'C_2}$	50 $L3c = \mathbf{T'C_3}$	36 $L4cc = T'C_4$	69 $L6cc = T'C_6$
8		17 $L2_1mc = \mathbf{T_2C_{1v}}$		35 $L4_2mc = T_4C_{2v}$	70 $L6_3mc = T_6C_{3v}$
9	6 $L\overline{1}m = \mathbf{TD_{1d}}$	37 $L\overline{4}2m = \mathbf{TD_{2d}}$	51 $L\overline{3}m = \mathbf{TD_{3d}}$		
10	7 $L\overline{1}c = \mathbf{T'S_2}$	38 $L\overline{4}2c = \mathbf{T'S_4}$	52 $L\overline{3}c = \mathbf{T'S_6}$		
11	18 $L\overline{2}2m = \mathbf{TD_{1h}}$	20 $L2/mmm = \mathbf{TD_{2h}}$	71 $L\overline{6}2m = \mathbf{TD_{3h}}$	39 $L4/mmm = TD_{4h}$	73 $L6/mmm = TD_{6h}$
12	19 $L\overline{2}2c = \mathbf{T'C_{1h}}$	21 $L2/mcc = \mathbf{T'C_{2h}}$	72 $L\overline{6}2c = \mathbf{T'C_{3h}}$	40 $L4/mcc = T'C_{4h}$	74 $L6/mcc = T'C_{6h}$
13		22 $L2_1/mcm = \mathbf{T_2D_{1d}}$		41 $L4_2/mcm = T_4D_{2d}$	75 $L6_3/mcm = T_6D_{3d}$

References

1. E.A. Wood, *80 Diperiodic Groups in Three Dimensions* (Bell System Monograph No 4680, New York, 1964)
2. V. Kopsky, D.B. Litvin (eds.), *International Tables for Crystallography*. Subperiodic Groups, vol. E (Kluwer Academic Publishers, Dodrecht/Boston/London, 2002)
3. I. Milosević, B. Nikolić, M. Damnjanović, M. Krčmar. J. Phys. A: Math. Gen. **31**, 3625 (1998)
4. M. Damnjanović, I. Milosĕvić, *Line Groups in Physics*. Lecture Notes in Physics, vol. 801 (Springer, Berlin, 2010)

Index

A
Adiabatic approximation, 188

B
Band representation, 93
  MgO and Si crystals, 95
  $SrZrO_3$ crystal, 95
Basic translation vectors, 13
Basis sets in molecular calculations
  localized atomic-like orbitals
    correlation-consistent basis, 125
    Gaussian-basis notations, 124
    Gaussian-type orbitals, 120
    polarization functions, 122
    Slater-type orbitals, 118
Basis sets in periodic calculations
  localized atomic-like orbitals, 118
    basis set superposition error, 132
    Gaussian-type basis, 128
    molecular-basis adaptation, 125
  plane waves, 115
  portable basis
    TZVP, 132
Boundless crystal, 13
Bravais lattice, 13
  2D (plane), 48
  base-centered, 15
  body-centered, 15
  cubic, 17
  face-centered, 15
  hexagonal, 17
  monoclinic, 16
  orthorhombic, 17
  parameters, 15
  point symmetry, 14
  primitive, 15
  tetragonal, 17
  triclinic, 16, 17
  type, 14
Brillouin zone
  special points
    Monkhorst–Pack, 152
  symmetry line, 89
  symmetry point, 89
Bulk crystals
  AlN, GaN
    calculations, 384
    structure, 383
  band structure
    MgO, TiO_2, 191
  $BaTiO_3$
    calculations, 580, 581
    structure, 579, 581
    symmetry, 579
  BN
    structure, 349, 350
  Boron, 218
    electronic properties, 219
    structure, 219
  density of states
    $SrTiO_3$, $SrZrO_3$, 194
    projected density of states, 194
  electron-density maps
    Cu_2O, 195
  Germanium-structure, 254
  group-III metal nitrides
    structure, 383
  MeB_2
    structure, 239, 240
  MoS_2
    density of states, 613
  MoS_2, WS_2
    band structure, 612

© Springer-Verlag Berlin Heidelberg 2015

R.A. Evarestov, *Theoretical Modeling of Inorganic Nanostructures*,
NanoScience and Technology, DOI 10.1007/978-3-662-44581-5

calculations, 612
structure, 611
phonon symmetry
TiO_2, 204
Silicon
structure, 254
$SrTiO_3$
band structure, 547, 550
calculations, 546
Density of states, 550
phonon calculations, 551
$SrZrO_3$
band structure, 547
Density of states, 550
TiS_2
structure, 631
TiS_2, ZrS_2
calculations, 635
structure, 634
vibrational frequences
TiO_2, 206
calculation, 202
Bulk properties
SiC, GeC
structure, 306

C
Conventional unit cell, 17
Crystal structure
cubic
diamond, 32
fluorite, 32
perovskite, 33
zincblende, 33
database, 30
description, 29
hexagonal
AlB_2, TiB_2, 44
BN, 43
graphite, 42
graphite, boron nitride, molybdenite, 40
MoS_2, 41
TiS_2, TiB_2, 41
wurtzite ZnS, 44
orthorhombic
$BaTiO_3$, V_2O_5, lepidocrocite, 39
tetragonal
$BaTiO_3$, $PbTiO_3$, 39
$SrTiO_3$, 37
anatase, 34
$BaTiO_3$, 39
rutile, 34
ZrO_2, 37
type, 9, 28
Crystal system
cubic, 14
hexagonal, 14
monoclinic, 14
orthorhombic, 14
rhombohedral, 14
syngony, 14, 15
tetragonal, 14
triclinic, 14
Crystallographic point groups
international notation, 17
Schönflies notation, 17

D
Density-functional theory (crystals)
LCAO approximation, 117
HSE03 hybrid functional, 176
Kohn–Sham equations, 171
linear-scaling method, 173
screened Coulomb hybrid functional, 178
Density-functional theory (molecules)
generalized-gradient approximation
GGA
exchange-correlation functionals, 164
PBE functional, 165
Hohenberg–Kohn theorems, 154
Kohn–Sham equations, 156, 158
local density approximation LDA
exchange-correlation functionals, 161
local spin density approximation LSDA, 162
orbital-dependent exchange-correlation functionals
hybrid functionals, 167, 169
Thomas-Fermi model, 153
Density Functional Tight Binding (DFTB)
bulk crystals, 114
parameters, 114

E
Effective core potentials
nonrelativistic
energy-consistent, 137
generation, 138
Hay–Wadt potentials, 140
separable embedding potentials, 141
valence basis-sets, 139

relativistic, 142
Stevens–Basch–Krauss potentials, 141
Stuttgart-Dresden potentials, 141
Electron correlation
spin correlation, 145

F
Fullerene-like
SiC
structure, 325

G
Group
plane, 48
space, 9, 11
subperiodic, 44

H
Hartree-Fock method
LCAO approximation
crystals, 150, 151
restricted for open shells ROHF, 148
restricted RHF, 147
unrestricted UHF, 148

I
Induced representations
of space group
q-basis, 92
Irreducible representations, 9, 11
of space group
full representation, 90
of translation group
k vector, 84
Bloch functions, 85
Brillouin zone, 85

L
Layer group
Brillouin zone, 97
element, 49
irreducible representations, 97
setting, 45
site-symmetry, 50
table, 657
Line groups, 63
factorization, 61, 62
families, 60
irreducible representations, 100
family 4, 100
family 8, 101
first family, 100
orbits, 66, 67
stabilizer, 67

M
Monoatomic crystal, 14

N
Nanochains
BN
calculations, 379
structure, 378, 379
Nanolayers
AlN, GaN
calculations, 385
structure, 385
$BaTiO_3$
calculations, 582–585, 587
stability, 585
structure, 582
Boron
structure, 219–221
symmetry, 222
Germanium
calculations, 260
MeB_2
structure, 241
MoS_2
density of states, 618
MoS_2, WS_2
phonon calculations, 616
structure, 615, 616
SiC
calculations, 309
structure, 256, 307
SiC, GeSi
calculations, 307
Silicon, Germanium
calculations, 256, 257
structure, 254
$SrTiO_3$, $SrZrO_3$
(0 0 1), density of states, 556
surface (0 0 1), 553
surface (0 0 1) energy, 555
TiS_2, ZrS_2
calculations, 636
structure, 635
Nanoribbons
MoS_2
band gap, 630
calculations, 629
properties, 629

- WS_2
  - calculations, 631
- Nanoscrolls
  - BN
    - structure, 371, 373
  - GeSi
    - structure, 320
- Nanotubes
  - AlB_2
    - calculations, 246, 247
  - AlN
    - band structure, 398
    - faceted structure, 397
    - stability, 389
    - strain energy, 388, 397, 398
    - structure, 386
  - AlN calculations, 387
  - AlN, GaN
    - calculations, 387
  - AlN/GaN
    - band gap, 394
    - band structure, 393
    - calculations, 395
    - structure, 393
  - $BaTiO_3$
    - calculations, 589, 596, 597
    - properties, 590
    - strain energy, 594
    - structure, 590, 591
  - BeB_2,MgB_2
    - calculations, 244
  - BeB_2,MgB_2,AlB_2
    - calculations, 242
  - BN
    - band structure, 366
    - bundle calculations, 364
    - bundle structure, 363
    - double-wall, band structure, 369
    - double-wall, binding energy, 367
    - double-wall, electronic structure, 368
    - double-wall, structure, 366
    - growth mechanism, 360, 361
    - phonon calculations, 356, 357
    - polyhedral, calculations, 352
    - pressure influence, 364
    - Raman spectra, 359
    - rolled up, calculations, 353
    - structure, 351
    - thermodynamics, 362
  - Boron
    - bundle calculations, 228, 230, 231
    - bundle structure, 228
    - calculations, 223, 225–227
    - double-wall, 232
    - double-wall, calculations, 233, 235
    - electronic structure, 232
    - structure, 224
  - double-wall
    - symmetry, 75
  - GaN
    - band gap, 391
    - band structure, 390
  - Germanium
    - calculations, 261
  - GeSi
    - binding energy, 322
    - calculations, 322
  - MeB_2
    - calculations, 241, 242, 245, 246
    - structure, 241
  - MgB_2
    - calculations, 245
  - MoS_2
    - bundles, 626
    - defective, 625
    - strain energy, 622
    - symmetry, 620
  - MoS_2, WS_2
    - calculations, 623
    - DFTB calculations, 624
    - structure, 620
  - multiwall
    - symmetry, 76
  - rolled up
    - single-wall, 68
    - symmetry, 67, 69
    - symmetry implementation, 107, 108
  - SiC
    - band structure, 311
    - bundles, density of states, 314
    - bundles, structure, 313, 314
    - calculations, 258, 313
    - density of states, 318
    - double-wall, calculations, 316
    - double-wall, structure, 315
    - faceted, structure, 317
    - properties, 319
    - stability, 259
    - structure, 307

SiC, GeC
structure, 310
structure calculations, 310
Silicon
calculations, 258, 266
double-wall, 260, 263, 264
phonon calculations, 266
stability, 259
structure, 261, 262, 265
$SrTiO_3$
calculations, 566
double wall, symmetry, 559, 560
single wall, calculations, 561–564
single wall, symmetry, 559
symmetry, 545
$SrTiO_3$,$BaTiO_3$
comparison, 594
TiB_2
calculations, 248–250
TiO_2 double wall
calculations, 466
TiO_2 single wall
calculations, 459
rectangular, 470, 473
rectangular, calculations, 473
symmetry, 458
TiS_2, ZrS_2
calculations, 640
comparison with dioxides, 642
double-wall, calculations, 645
double-wall, stability, 644
double-wall, structure, 646, 647
double-wall, symmetry, 643
strain energies, 640
structure, 638, 640
WS_2
structure, 619
ZnO-symmetry, 436
ZrO_2-calculations, 533, 538
ZrO_2-symmetry, 530
Nanowires
AlN
band structure, 398
calculations, 401
density of states, 402
elastic constants, 411, 413
elastic properties, 410, 414
formation energy, 405
phase transitions, 406
phonon calculations, 410
structure, 400, 403
thermal properties, 407, 409
$BaTiO_3$
calculations, 600–603
ferroelectricity, 604
MD simulations, 607
properties, 604
structure, 598
BN
DFTB calculations, 377
MD simulations, 377
stability calculations, 374, 375
structure, 373
structure calculations, 373
Boron
calculations, 238
calculations, electronic properties, 238
structure, 236, 237
GaN
band gap, 419
band structure, 415, 416
formation energy, 419
stability, 420
structure, 415
surface energy, 420, 421
Young's modulus, 422
Ge/Si and Si/Ge
band structure, 340
calculations, 337
Germanium
band gap calculations, 305
calculations, 298, 299, 301, 302
stability calculations, 302, 304
structure, 298
GeSi
band structure, 338
calculations, 333–335, 337
structure, 331, 333, 336
MoS_2
calculations, 628
MoS_2, WS_2
models of the structure, 627
structure, 626
SiC
band gap, 329
band structure, 329
calculations, 323, 324
electronic structure, 328, 329
structure, 323, 324
Silicon
calculations, 269, 271, 273, 275–279, 281, 282
calculations of mechanical properties, 295

elastic properties, 293
MD calculations, 285
mechanical properties calculations, 296–298
phonon calculations, 289–293
phonon properties, 283, 286, 288
structure, 269, 271, 283
thermal properties, 283, 284, 286
vibrational spectra, 292
Wulff construction, 271, 273
Young's modulus, 294
Silicon, Germanium
comparison, 301
structure, 268
$SrTiO_3$
calculations, 566, 568
ZnO
symmetry, 436

O
Orbits of points, 9, 12, 28
crystallographic, 24

P
Periodic boundary conditions, 13
Primitive unit cell, 13

R
Reference unit cell, 14
Relativistic theory
molecules, 142
Rod groups
as line groups, 64, 663
axial point groups, 63
correspondence to space groups, 63, 663
elements, 63
families, 64, 663
family 4, 64
first family, 64
realization, 65

S
Single wall nanotubes, 70
hexagonal lattice, 71
rectangular lattices, 74
square lattice, 73
Site-symmetry group, 24
oriented, 28
Space group, 20
designations, 21
elements, 20
nonsymmorphic, 21
symmorphic, 21
table, 21
Supercell
for centered lattices, 19
transformation, 18
Surfaces of crystals
models
single slab, 45
Surfaces types
type-2
TiO_2 (110), 53
Symmetry operations, 12
Symmetry properties
of crystalline orbitals, 82
of molecular orbitals, 82
time-reversal transformation, 83

T
Translation
improper or fractional, 20
proper, 20

U
U_2N_3-crystal
calculations, 144
UF_6 molecule, 143

W
Wavevector
little group, 90, 99
point-symmetry group, 88
star, 90, 99
Wyckoff positions, 9, 28
notation, 24
parameter-dependent, 24
parameter-free, 24